



# IAP-SAT Final Report (2012 - 2020)

- Part I: IAP Space Program
- Part II: Basics for Satellite Bus
- Part III: Mission Simulation (scilab)
- Part IV: Satellite Bus
  - Inertial Measurement Unit
  - Chemical Propulsion Unit
  - Electrical Propulsion Unit
  - COM Unit
  - Hardware-in-the-Loop (HIL) Testrig
- Part V: Payload
  - IAP-SWRDA (Radio Astronomy HI Line Sensor): Basics, Design, Realization
  - IAP-OSM (Optical Spectrometer): Basics, Design
  - IAP-IRS (Infrared Sensor): Basics, Design, Manufacturing Plan
  - IAP-GAMS (Gamma Astronomy Measurement System): Basics, Concept for Instrument: Scintillator



# Content

IAP-SAT FINAL REPORT .....	I
(2012 - 2020).....	I
• PART I: IAP SPACE PROGRAM .....	I
• PART II: BASICS FOR SATELLITE BUS.....	I
• PART III: MISSION SIMULATION (SCILAB).....	I
• PART IV: SATELLITE BUS.....	I
• PART V: PAYLOAD.....	I
LAST UPDATE: 23.07.2020 11:24 .....	I
<b>PART I: IAP SPACE PROGRAM.....</b>	<b>I</b>
<b>1 IAP SPACE PROGRAM 2012 - 2020 .....</b>	<b>II</b>
1.1 PROGRAM OVERVIEW .....	II
1.2 SCIENTIFIC PROGRAM.....	II
1.2.1 <i>Conception for IR Sensor and Gamma Astronomy Sensor</i> .....	<i>ii</i>
1.2.2 <i>Pulsar Radio Astronomy Sensor</i> .....	<i>ii</i>
1.2.2.1 The SRWDA Project .....	iii
1.2.2.2 Ground Station for Radio Astronomy: IAP_SRWDA.....	iii
1.3 SATELLITE DESIGN AND CONSTRUCTION .....	III
1.4 OLD PROGRAM (LAST UPDATED DEZ. 12).....	IV
1.5 AIM OF IAP_SRWDA-.SAT PROJECT .....	V
1.6 MISSION OVERVIEW FOR IAP-SAT .....	V
1.7 SATELLITE & BALLON SYSTEM FOR COMMUNICATION .....	VI
1.8 OPEN TASKS (UPDATED 2019).....	VII
<b>2 PROJECT MANAGEMENT.....</b>	<b>IX</b>
2.1 ORGANISATION .....	IX
2.2 IAP ORGANIGRAM.....	X
2.3 DOCUMENTATION .....	X
2.4 YEARLY WORKING PACKAGES, TIME PLANS, COSTS .....	X
2.4.1 <i>IAP 2012</i> .....	<i>X</i>
2.4.2 <i>IAP 2013</i> .....	<i>X</i>
2.4.2.1 Costs IAP 2013.....	<i>xi</i>
2.4.3 <i>Working packages 2014</i> .....	<i>xi</i>
2.4.3.1 Costs IAP 2014 (planned).....	<i>xii</i>
2.4.4 <i>Working Packages and Time Plan 2015</i> .....	<i>xii</i>
2.4.5 <i>IAP-SAT 2016</i> .....	<i>xiii</i>
2.4.5.1 Project Status at Beginning of actual project phase (2016).....	<i>xiii</i>
2.4.5.2 Goal of actual phase .....	<i>xiii</i>
2.4.5.3 Overview Planning & Budget IAP 2016.....	<i>xiii</i>
2.4.5.4 To do with internal ressources .....	<i>xiii</i>
2.4.5.5 Master Thesis Tasks to complete the IAP-SAT prototype.....	<i>xiv</i>
2.4.5.6 Time Plan FOG Development .....	<i>xiv</i>
2.4.6 <i>Overview Planning &amp; Budget IAP-SAT 2017</i> .....	<i>xv</i>
2.4.6.1 To do for CNCLab.....	<i>xv</i>
2.4.6.2 To do with internal ressources .....	<i>xv</i>
2.4.7 <i>IAP-SAT 2020</i> .....	<i>xvi</i>
2.4.7.1 Time Plan for COM System (Last update: 16.2.2020).....	<i>xvi</i>

2.5	ESTIMATED COSTS OF IAP-SAT (SATELLITE DEVELOPMENT AND THE LAUNCHING) .....	XVIII
2.6	MASTER THESIS CONCERNING HIL AND MISSION SIMULATION .....	XIX
2.7	MASTER AND PHD TASKS CONCERNING THE ELECTRICAL PROPULSION UNIT .....	XXII
2.8	CORRESPONDENCE WITH ISTANBUL UNIVERSITY CONCERNING TRAINEE STUDENT .....	XXIV
<b>PART IIA: BASICS FOR SATELLITE BUS .....</b>		<b>29</b>
<b>3</b>	<b>GENERAL BASICS CONCERNING SATELLITE TECHNOLOGY .....</b>	<b>30</b>
3.1	METEOROLOGY .....	30
3.2	SATELLITE.....	30
3.2.1	<i>Definition</i> .....	30
3.3	ORBIT .....	30
3.3.1	<i>Laws of motion</i> .....	30
3.3.2	<i>Laws of gravitation</i> .....	31
3.4	LOW EARTH ORBIT .....	33
3.4.1	<i>LEO basics</i> .....	34
3.5	SUN SYNCHRONOUS ORBIT .....	34
3.6	METEOROLOGICAL SATELLITE .....	36
3.6.1	<i>Components of meteorological satellite</i> .....	36
3.6.1.1	Satellite bus (platform): power source, battery, control system, communication system, thermal protection.....	37
3.6.1.2	Payload.....	40
3.7	EXAMPLE OF A METEOROLOGICAL SATELLITE.....	40
3.8	EXAMPLE: DUBAISAT-1 ORBIT SPECIFICATIONS .....	41
3.9	GROUND TRACKING .....	42
3.10	ELECTROSTATIC PLASMA THRUSTERS .....	43
3.11	ELECTROMAGNETIC PROPULSION SYSTEMS.....	43
<b>4</b>	<b>ELEMENTS SATELLITE BUS .....</b>	<b>45</b>
4.1	SATELLITE BUS DESIGN TASKS OVERVIEW.....	45
4.1.1	<i>Example: 10 ccm Student Nanosatellite OUFTI-1 of University of Liège</i> .....	45
4.2	DESIGN OF THE ENERGY SUPPLY SYSTEM .....	45
4.3	MISSION SIMULATION .....	48
4.4	PAYLOAD INTEGRATION .....	49
<b>5</b>	<b>CANDIDATE SOFTWARE TOOLS .....</b>	<b>50</b>
5.1	TOOLS .....	50
5.1.1	<i>FreeCAD</i> .....	50
5.1.2	<i>Scilab/Scicos</i> .....	50
5.1.2.1	Scicos.....	51
5.2	POSSIBLE DEVELOPMENT ENVIRONMENT FOR COMMUNICATION AND CONTROL.....	51
5.3	NEARSPACECRAFT SIMULATOR DEVELOPMENT.....	52
<b>6</b>	<b>EXAMPLE SATELLITE SYSTEMS.....</b>	<b>53</b>
6.1	FLYING LAPTOP EXAMPLE, STUTTGART UNIVERSITY, GERMANY .....	53
6.1.1	<i>Star tracker system</i> .....	54
6.2	GÖKTÜRK PROJECT.....	54
6.3	DUBAISAT-1.....	56
6.4	LOW ORBIT SATELLITES AT VERY LOW ALTITUDE .....	56
<b>PART IIB: SYSTEM CONCEPT FOR SATELLITE BUS .....</b>		<b>58</b>

---

<b>7</b>	<b>SYSTEM CONCEPT .....</b>	<b>59</b>
7.1	OVERVIEW .....	59
7.1.1	<i>Satellite Bus</i> .....	59
7.1.2	<i>Electrical Propulsion System</i> .....	59
7.1.3	<i>Power Supply System</i> .....	71
7.1.4	<i>Structures and Mechanisms</i> .....	73
7.1.5	<i>Thermal Control System</i> .....	73
7.1.6	<i>Flight Control System (FCS) on board of satellite – Attitude control system (ACS)</i> .....	75
7.1.6.1	Gear .....	76
7.1.7	<i>Command and Data Handling</i> .....	77
7.2	EDUCATION AND PUBLIC OUTREACH .....	77
7.3	FIRST MOCKUP MODEL .....	78
7.4	PROTOTYPE .....	79
<b>8</b>	<b>TELEMETRY (SATELLITE BUS COMMUNICATION) CONCEPTION .....</b>	<b>80</b>
8.1	FROM SBEP PROJECT .....	80
8.2	SATELLITE SIDE .....	81
8.2.1	<i>System Design</i> .....	81
8.2.2	<i>Working packages</i> .....	82
8.3	GROUND STATION SIDE .....	83
8.3.1	<i>GUI Alternative 1: Using the old alternative Lotte program</i> .....	83
8.3.2	<i>GUI Alternative 2: In Scilab</i> .....	84
8.4	TRANSCIEVER TECHNOLOGY.....	84
8.4.1	<i>Specification</i> .....	84
8.4.1.1	STEP 1 (until 15 June 2013) .....	85
	Development environment for STEP 1.....	86
8.4.1.2	STEP 2 (until 30 June 2013) .....	86
8.4.1.3	STEP 3: Improvements.....	87
8.4.1.4	Antenna improvement .....	88
8.4.1.5	Channel Coding.....	88
8.5	PAYLOAD COMMUNICATION: SCS-SMS INCLUDING AES .....	88
<b>9</b>	<b>TELEMETRY (SATELLITE BUS COMMUNICATION) PROTOTYPE .....</b>	<b>89</b>
9.1	OVERVIEW .....	89
9.1.1	<i>Synthesize transceiver STD-402</i> .....	89
9.2	BASE STATION SIDE .....	89
9.3	SATELLITE SIDE .....	89
9.3.1.1	Hardware part .....	90
9.3.1.2	ACU actuator .....	90
9.3.1.3	GPS sensor .....	91
9.3.1.4	PIC board .....	91
9.3.1.5	Antenna control board .....	95
9.3.2	<i>Software part</i> .....	95
9.3.2.1	Communication code .....	95
9.3.2.2	Control and stability code.....	97
9.3.2.3	Coding code.....	97
9.3.2.4	Antenna control code.....	97
9.4	SYSTEM CODING .....	97
9.4.1	<i>Introduction</i> .....	97
9.4.2	<i>Source Coding</i> .....	98

9.4.2.1	Using Huffman theory .....	99
9.4.2.2	Write the Huffman code (c programming) .....	101
9.4.3	<i>Encryption</i> .....	105
9.4.3.1	Advanced Encryption Standard (AES) .....	105
9.4.3.2	<i>AES</i> algorithm .....	105
9.4.3.3	Encryption and Decryption AES flow chart .....	109
9.4.3.4	AES program (C programming) .....	110
<b>PART III: MISSION PLANNING AND SIMULATION.....</b>		<b>111</b>
<b>10</b>	<b>MISSION PLANNING.....</b>	<b>112</b>
<b>11</b>	<b>MISSION SIMULATION WITH MAPLE.....</b>	<b>113</b>
<b>12</b>	<b>MISSION SIMULATION 2012: SHUTTLE FLIGHT SIMULATION INTO ORBIT .....</b>	<b>114</b>
<b>13</b>	<b>GROUND TRACK VISUALIZATION .....</b>	<b>118</b>
13.1.1	<i>Tools for visualization of the ground track of satellites: Gpredict and OpenSat .....</i>	<i>118</i>
<b>14</b>	<b>SIMULATION OF IAP-SAT MISSION 2015 .....</b>	<b>121</b>
14.1	SPECIFICATION OF IAP-SAT'S PARAMETERS.....	121
14.2	DESCRIPTION AND MODELING OF IAP-SAT .....	121
14.3	VISUALIZATION OF THE GROUND TRACK OF IAP-SAT .....	122
<b>15</b>	<b>PRESENTATION FILM 2015 .....</b>	<b>125</b>
15.1	PAYLOAD PROGRAM .....	125
15.2	PRESENTATION FILM OF MIS .....	125
<b>16</b>	<b>MISSION SIMULATION WITH CELESTLAB (2020).....</b>	<b>126</b>
16.1	CELESTLAB DEMO TOOL .....	126
16.1.1	<i>Visibility:</i> .....	<i>126</i>
	Ground Station Visibility: .....	126
16.2	PRINCIPLE AND TASK .....	127
16.3	TRAJECTORY SIMULATION OF OPERATIONAL FLIGHT OF IAP-SWRDA_SAT (LOW EARTH ORBIT) .....	128
16.4	TRAJECTORY SIMULATION OF TRANSPORT VEHICLE FOR IAP-SAT .....	136
<b>17</b>	<b>MISSION PLANNING.....</b>	<b>140</b>
<b>PART IV: SATELLITE BUS ELEMENTS .....</b>		<b>143</b>
<b>INERTIAL MEASUREMENT UNIT.....</b>		<b>144</b>
<b>18</b>	<b>REALIZATION OF INERTIAL MEASUREMENT UNIT (IMU).....</b>	<b>145</b>
18.1	IMU-SENSOR: LSM9DS0 .....	146
18.2	LSM9DS0 HOOKUP GUIDE .....	147
18.2.1	<i>Covered In This Tutorial</i> .....	<i>147</i>
18.2.2	<i>About the LSM9DS0</i> .....	<i>148</i>
18.2.3	<i>Choose Your Own Adventure: SPI or I<sup>2</sup>C</i> .....	<i>149</i>
18.2.4	<i>Breakout Overview</i> .....	<i>149</i>
18.2.5	<i>The Pinout</i> .....	<i>149</i>
	Power Supply .....	150
	Communication.....	151
	Interrupts .....	152
18.2.6	<i>Basic Arduino Example</i> .....	<i>152</i>

---

18.2.7	<i>Download and Install the Library</i> .....	152
18.2.7.1	Simple Hardware Hookup (I <sup>2</sup> C).....	152
18.2.7.2	Open the LSM9DS0_Simple Example .....	155
18.2.8	<i>Resources and Going Further</i> .....	164
18.3	SOFTWARE ON RASPBERRY CONCERNING IMU .....	165
<b>19</b>	<b>BASE STATION IN LABORATORY</b> .....	<b>167</b>
<b>20</b>	<b>FIBER OPTIC GYRO BASICS</b> .....	<b>168</b>
<b>21</b>	<b>FIBER OPTIC GYRO DEVELOPMENT TEST RIG AND FIBER OPTIC GYROSCOPE SENSOR</b> .....	<b>173</b>
21.1	SAGNAC EFFECT.....	173
21.1.1	<i>Definition:</i> .....	173
21.1.2	<i>Experiment:</i> .....	174
	<b>i. Schema:</b> .....	174
	<b>ii. Materials:</b> .....	174
	<b>ii.1. Fiber optic cable [TBD]</b> .....	174
	<b>ii.2. Fiber optic coupler [TBD]</b> .....	175
	<b>ii.3. Detector circuit</b> .....	175
	<b>ii.4. Laser [TBD]</b> .....	176
21.2	FOG .....	177
21.3	FREECAD FILES .....	178
21.4	REFERENCES: .....	178
21.5	ORDERED MATERIALS (OKTOBER 2016).....	178
21.5.1.1	Fiber optic cable .....	180
21.5.1.2	Fiber optic coupler.....	181
21.5.1.3	Single Fibre Collimator and FC/PC to FC/PC Adapter .....	182
21.5.1.4	Packed .....	184
<b>STAR CAMERA</b> .....		<b>186</b>
<b>22</b>	<b>CONCEPT FOR STAR CAMERA</b> .....	<b>187</b>
22.1	SPECIFICATIONS OF A STAR CAMERA FOR CUBESAT APPLICATIONS .....	187
22.2	DESIGN AND PROTOTYPE OF A STAR CAMERA (OPAL).....	188
<b>CHEMICAL PROPULSION UNIT</b> .....		<b>192</b>
<b>23</b>	<b>BASICS FOR SATELLITE CHEMICAL PROPULSION UNITS</b> .....	<b>193</b>
23.1	ELEMENTS OF CHEM. PROULSION UNITS FOR SATELLITES .....	193
23.1.1	<i>Space Propulsion Tanks</i> .....	194
23.1.2	<i>Space Propulsion Valves</i> .....	196
23.2	INSTRUMENTS FOR TEST ENVIRONMENT FOR CHEMICAL PROPULSION UNIT: .....	200
23.2.1	<i>Types of Valves</i> .....	200
23.2.1.1	Check Valve .....	200
23.2.1.2	Tank Vent Valve.....	200
23.2.1.3	High Pressure Gas Valve .....	201
23.2.1.4	Gas Bleed Valve: .....	201
23.2.1.5	Drain Valve .....	202
23.2.2	<i>Pressure Regulator</i> .....	202
23.2.3	<i>Restricting Orifice</i> .....	204
23.2.3.1	Single stage multi-hole restriction orifice. ....	206
23.2.3.2	Multi-stage restriction orifice plate assembly. ....	206

23.3	PROCESS FOR THE CONTROL OF THE MIXTURE RATIO OF FUEL AND OXIDIZER FOR A LIQUID FUEL MOTOR BY MEASURING FLOWS, AND CONTROL SYSTEMS FOR CARRYING OUT THIS PROCESS .....	207
23.3.1	<i>Classical Control for Bi-Propellant Rocket Engine</i> .....	209
23.3.2	<i>Further Literature</i> .....	209
23.4	COMBUSTION OF THE OXIDIZER/FUEL MIXTURE .....	211
<b>24</b>	<b>CONSTRUCTION OF TEST RIG FOR CHEMICAL PROPULSION UNIT .....</b>	<b>215</b>
24.1	SCHEMATIC FLOW DIAGRAM .....	215
24.2	SPECIFICATION .....	216
24.3	COST ESTIMATION .....	218
24.4	TOTAL ASSEMBLY (FREECAD).....	219
24.5	COMPONENTS:.....	220
24.5.1	<i>Oxidizer/Fuel Tank</i> .....	220
24.5.2	.....	220
24.5.3	<i>High Pressure Gas Supply Tank</i> .....	221
24.5.4	<i>Frame</i> .....	222
24.5.5	<i>Satellite Thrust Chamber</i> .....	223
24.5.6	<i>Filters</i> .....	223
24.5.7	<i>Gas fill valve</i> .....	224
24.5.8	<i>Filler Neck</i> .....	225
24.5.9	<i>Restriction Orifice (RO) – Flow Control Instrument</i> .....	226
24.5.10	<i>Pressure Regulator</i> .....	226
24.6	2D SKETCHES .....	228
24.6.1	<i>Fuel / Oxidizer Tank</i> .....	228
24.6.2	<i>High Pressure Supply Tank</i> .....	232
24.7	COSTS .....	234
24.8	PRESSURE CALCULATION .....	235
24.8.1	<i>Pressure of the Fuel/Oxidizer Tanks</i> .....	236
24.8.2	<i>Pressure of the High-Pressure Supply Tank</i> .....	236
24.9	AVAILABLE COMPONENTS FOR THE CHEMICAL PROPULSION UNIT TEST .....	237
<b>25</b>	<b>MIXTURE RATIO CONTROL AND CHAMBER PRESSURE CONTROL FOR ORBIT ATTITUDE CONTROL ENGINE TEST RIG OF IAP-SAT .....</b>	<b>239</b>
25.1	PRINCIPLE AND TASK .....	239
25.2	PROPELLANTS USED .....	240
25.3	BASIC COMPONENTS .....	242
25.3.1	<i>Flowmeter</i> .....	242
25.3.2	<i>Solenoid Valve</i> .....	243
25.4	ASSEMBLY .....	244
25.5	FUEL - OXIDIZER MIXING CONTROL.....	245
25.5.1	<i>Start learning on Raspberry</i> .....	245
25.5.1.1	Step 1 reading book.....	245
25.5.1.2	Step 2 Watch on YouTube .....	245
25.5.1.3	Step 3 Writing code on Raspberry pi.....	246
25.5.1.4	Step 4 Hardware .....	246
25.5.1.5	Step 5 Result.....	247
25.5.2	<i>Programming with Python</i> .....	247
25.5.2.1	Step 1: write code in new script to control led.....	247
25.5.2.2	Step 2: Hardware.....	248

25.5.2.3	Note: In the table below focus on gpio pins .....	249
25.5.2.4	Testing code for flow sensor .....	249
25.5.2.5	New test of flow meter sensor .....	250
25.5.3	<i>The code of flow meter sensor:</i> .....	251
25.5.4	<i>Hardware for flowmeter sensor: new RaspberryPi</i> .....	251
25.5.5	<i>Test Results</i> .....	253
25.5.6	<i>Pins of raspberry pi 3:</i> .....	254
25.5.7	<i>The code of servo motor (Servo Motor driven Automatic Valve instead of solenoid valve) .....</i>	254
25.5.8	<i>Valve</i> .....	255
25.5.9	<i>Mixing Control Testing Algorithm (Valve is moving according to flow sensor) .....</i>	257
25.5.9.1	References of control DC motor:.....	258
25.5.10	<i>Hardware of servo motor and flow sensor</i> .....	259
25.5.11	<i>Hardware of on/off relay</i> .....	262
<b>ELECTRICAL PROPULSION UNIT .....</b>		<b>265</b>
<b>26</b>	<b>CONCEPT FOR THE ELECTRICAL PROPULSION UNIT .....</b>	<b>266</b>
26.1	PRIMITIVELY MODELING THE CHOSEN PULSED PLASMA THRUSTER (PPT).....	266
26.2	MODELING OUR PPT DESIGN IN FREECAD .....	266
26.2.1	<i>Modelling “fuel continues supplying system” .....</i>	267
26.2.2	<i>2D projections of important parts of the propulsion system .....</i>	268
<b>27</b>	<b>PPT ELECTRICAL PROPULSION UNIT .....</b>	<b>269</b>
27.1	CONCEPT FOR THE ELECTRICAL PROPULSION UNIT.....	269
27.2	EIGENFELDANTRIEB (PPT) .....	269
27.3	GEPULSTES PLASMATRIEBWERK .....	269
27.3.1	<i>Prinzip:</i> .....	269
27.4	TEST ENVIRONMENT FOR ELECTRICAL PROPULSION (FROM [BÖHRK ET. AL. 2007]).....	272
27.5	REALIZATION .....	273
<b>28</b>	<b>ELECTRICAL PROPULSION TEST RIG .....</b>	<b>274</b>
<b>29</b>	<b>ELECTRIC-PROPULSION TEST STAND (CONCEPT, DESIGN, MANUFACTURING).....</b>	<b>275</b>
29.1	BASICS .....	275
29.1.1	<i>Vacuum Chamber Technology</i> .....	275
29.1.1.1	Choosing the Right Vacuum Materials.....	275
29.1.1.2	Desorbing Water in Vacuum Systems: Bakeout or UV? .....	279
29.1.1.3	Vacuum pump .....	283
	How to Convert an Air Compressor Into a Vacuum Pump.....	283
29.1.2	<i>Electrical Propulsion</i> .....	283
29.1.3	<i>Detector</i> .....	284
29.1.3.1	Langmuir Probe .....	284
29.1.3.2	Rokowski coil .....	285
29.2	GAMS UNIT DESIGN .....	287
29.2.1	<i>Concept</i> .....	287
29.3	PRINCIPLE .....	287
29.4	ROKOWSKI COIL.....	288
29.4.1	<i>Aim</i> .....	288
29.4.2	.....	288
<b>COM UNIT .....</b>		<b>289</b>

<b>30</b>	<b>TELEMETRY SYSTEM WITH HARCKRF</b>	<b>290</b>
30.1	TIME PLAN	290
30.2	INTRODUCTION	291
30.2.1	<i>Links and references:</i>	293
30.2.2	<i>SDR (Software defined radio):</i>	294
30.2.3	<i>HDSDR:</i>	294
30.2.4	<i>SDRSharp:</i>	295
30.2.5	<i>GnuRadio:</i>	297
30.2.5.1	<i>Links:</i>	298
30.3	GETTING STARTED	298
30.3.1	<i>Getting Started with HackRF and GNU Radio</i>	300
30.3.2	<i>HackRF with Raspberry PI:</i>	301
30.4	SYSTEM 1	304
30.5	SYSTEM 2	305
30.6	SYSTEM 3	305
	<b>POWER SUPPLY AND BATTERY</b>	<b>306</b>
	<b>IAP-SAT INTEGRATION</b>	<b>308</b>
<b>31</b>	<b>ATTITUDE CONTROL SYSTEM (ACS) COMPONENTS</b>	<b>309</b>
31.1	MAGNETOMETER	309
31.2	SUN SENSOR	311
31.3	GPS	311
31.4	FIBER OPTIC GYRO UNIT	311
31.5	STAR TRACKER SYSTEM	313
31.6	OTHER COMPONENTS	314
31.6.1	<i>OBC</i>	314
31.6.2	<i>PAMCAM</i>	315
31.7	CONCEPT FOR POWER SUPPLY AND BATTERY	315
31.8	CONCEPT FOR THE PROPULSION UNIT	318
31.8.1	<i>Primitively modeling the chosen Pulsed Plasma Thruster (PPT)</i>	318
31.8.2	<i>Modeling our PPT design in FreeCad</i>	318
31.8.2.1	<i>Modelling “fuel continues supplying system”</i>	319
31.8.2.2	<i>2D projections of important parts of the propulsion system</i>	320
31.9	FREECAD FILES	320
<b>32</b>	<b>INTEGRATION OF IAP-SAT</b>	<b>322</b>
32.1	INTEGRATION OF IMU AND RADIOASTRONOMY HI SENSOR (2017)	322
32.2	INTEGRATION OF CHEM. PROPULSION (2020)	323
	<b>HARDWARE-IN-THE-LOOP (HIL) TESTRIG</b>	<b>324</b>
<b>33</b>	<b>BASICS FOR EMBEDDED TEST AND SIMULATION ENVIRONMENT</b>	<b>325</b>
33.1	SATELLITE SYSTEM STRUCTURE	325
33.2	BLOCK DIAGRAMS IN SIGNAL AND CONTROL THEORY	325
33.3	AOCS SUBSYSTEM STRUCTURE	326
<b>34</b>	<b>IAP-SAT HARDWARE-IN-THE-LOOP (HIL) SYSTEM DESIGN AND REALIZATION</b>	<b>330</b>
34.1	ACS ON-BOARD ALGORITHMS ARCHITECTURE	330
34.2	CONCEPT FOR SIMULATION ENVIRONMENT	330

34.2.1	<i>Space Environment</i> .....	330
34.2.2	<i>Matlab testing interface</i> .....	332
34.3	HIL SYSTEM ARCHITECTURE .....	334
34.3.1	<i>Simulation on scilab/scicos</i> .....	335
34.3.1.1	Parameters and equations used in the simulation .....	335
34.3.1.2	Modeling of the components of IAP-SAT in Scicos .....	336
Model of gyroscope .....	337	
Model of accelerometer .....	338	
Model of actuators .....	340	
Model of space .....	341	
Integration of diagrams .....	345	
34.3.1.3	Test of simulation .....	347
34.4	C CODE OF CONTROL ALGORITHM AT THE BOARD COMPUTER .....	349
34.5	LINKING THE SOFTWARE SIMULATION ON THE SERVER WITH THE ONBOARD-COMPUTER .....	350
34.5.1	<i>Helping in building a program that simulates the satellite's movement in a space environment</i> 355	
34.5.2	<i>Working with shell programs to maintain the feedback system</i> .....	356
34.6	RECEIVING METEOROLOGICAL DATA .....	357
<b>35</b>	<b>OPERATION OF HIL TEST RIG</b> .....	<b>364</b>
35.1	RESULTS OF THE SIMULATION IN SCICOS .....	364
35.1.1	<i>Simulation of gyroscope</i> .....	364
35.1.2	<i>Simulation of accelerometer</i> .....	365
35.1.3	<i>Simulation of actuators</i> .....	366
35.1.4	<i>Results of the integration of diagrams</i> .....	368
35.1.5	<i>Test of simulation</i> .....	370
Results of case 1 .....	370	
Results of Case 2 .....	371	
Results of case 3 .....	372	
35.1.6	<i>Integration of the Hardware-in-the-Loop (HIL) test rig</i> .....	374
35.2	RECEIVING METEOROLOGICAL DATA .....	375
	<b>PART V: PAYLOAD (SCIENTIFIC PROGRAM)</b> .....	<b>380</b>
<b>36</b>	<b>CONCEPT FOR SCIENTIFIC PROGRAM</b> .....	<b>381</b>
36.1	DATA COLLECTION FROM GROUND STATION .....	381
36.1.1	<i>System Design</i> .....	381
36.2	SATELLITE BASED RADIO ASTRONOMY SENSOR .....	382
<b>37</b>	<b>IMAGE PROCESSING TECHNIQUES FOR PAYLOAD SENSORS</b> .....	<b>383</b>
37.1	EDGE DETECTION .....	383
	<b>HI LINE RADIO ASTRONOMY SENSOR</b> .....	<b>385</b>
	<b>IAP-SWRDA</b> .....	<b>386</b>
Abstract .....	387	
Master Thesis Task .....	388	
Presentation (May 2015) .....	389	
Table of contents .....	403	
List of figures .....	404	
List of Keywords .....	404	

<b>38</b>	<b>INTRODUCTION TO SWRDA .....</b>	<b>407</b>
38.1	BACKGROUND.....	407
38.2	THE SRWDA PROJECT .....	407
38.3	OBJECTIVES .....	407
38.4	OUTLINE.....	407
<b>39</b>	<b>BASICS .....</b>	<b>408</b>
39.1	21-CM RADIO ASTRONOMY BASICS .....	408
39.2	RADIO WAVE RECEIVING.....	409
39.3	SOFTWARE DESIGNED RADIO .....	409
39.4	BASIC SDR RECEIVER ARCHITECTURE .....	410
<b>40</b>	<b>SYSTEM DESIGN .....</b>	<b>412</b>
<b>41</b>	<b>HARDWARE CONCEPTION .....</b>	<b>414</b>
41.1	PLATFORM SELECTION .....	414
41.1.1	<i>Hackrf platform</i> .....	414
41.1.2	<i>BladeRF Platform</i> .....	415
41.1.3	<i>Ettus Research's USRP B100</i> .....	415
41.1.4	<i>Rtl_SDR (RTL2832+ E4000):</i> .....	416
<b>42</b>	<b>HARDWARE REALIZATION.....</b>	<b>417</b>
42.1	HARDWARE OF RTL SDR (RTL2832+E4000): .....	417
42.1.1	<i>RTL2832</i> .....	417
42.1.2	<i>Tuner E4000</i> .....	417
42.2	HARDWARE OF USRP .....	419
42.2.1	<i>USRP B100 as motherboard</i> .....	419
42.2.2	<i>WBX 50-2200 MHz Rx/Tx as daughterboard</i> .....	420
42.2.3	<i>FPGA</i> .....	421
42.2.4	<i>ADC converter</i> .....	423
42.3	LOW NOISE AMPLIFIER LNA.....	423
42.4	HYDROGEN LINE FILTER .....	424
42.5	PREAMPLIFIER:.....	426
42.6	ANTENNA AND FEED HORN.....	427
<b>43</b>	<b>SOFTWARE.....</b>	<b>429</b>
43.1	GNU RADIO .....	429
43.2	GNU RADIO ARCHITECTURE .....	430
43.3	GNU RADIO COMPANION (GRC).....	431
43.4	BASIC BLOCKS.....	433
43.4.1	<i>RTL SDR source</i> .....	433
43.4.2	<i>WX GUI blocks</i> .....	433
43.5	SOFTWARE DESIGN.....	434
43.6	SOFTWARE IMPLEMENTATION .....	434
43.6.1	<i>RTL Source</i> .....	435
43.6.2	<i>FFT filter</i> .....	436
43.7	TEST AND MEASUREMENTS .....	436
<b>44</b>	<b>FUTURE WORK.....</b>	<b>438</b>
<b>45</b>	<b>LITERATURE .....</b>	<b>439</b>

<b>46</b>	<b>APPENDIX .....</b>	<b>440</b>
A.1	SOFTWARE .....	440
	<i>Python code</i> .....	440
A.2	HARDWARE .....	449
	<i>SDR RTL 2382+4000</i> .....	449
	<i>IF Amplifier</i> .....	449
	<i>Low noise amplifier</i> .....	450
	<i>Motherboard USRP B100</i> .....	451
A.3	LIST OF OFF-THE-SHELF ELECTRONIC COMPONENTS AND ASSEMBLIES .....	454
A.4	MECHANICAL COMPONENTS .....	455
<b>IAP-OSM (OPTICAL SPECTROMETER) .....</b>		<b>457</b>
<b>47</b>	<b>1 BASICS .....</b>	<b>458</b>
47.1	SPECTROSCOPY .....	458
47.1.1	<i>Theory</i> .....	458
47.1.2	<i>Type of radiative energy</i> .....	459
47.1.3	<i>Nature of the interaction</i> .....	460
47.1.4	<i>Type of materials</i> .....	461
47.2	SPECTROMETER .....	462
47.2.1	<i>Types of spectrometer</i> .....	463
47.2.1.1	Optical spectrometer .....	463
47.2.1.2	Spectroscopes .....	464
47.2.1.3	Mass spectrometer .....	465
47.2.1.4	Time-of-flight spectrometer .....	465
47.2.1.5	Magnetic spectrometer .....	465
47.3	TYPES OF OPTICAL SPECTROMETERS .....	465
47.3.1	<i>General dispersive spectrometer design</i> .....	466
47.4	CCD DETECTOR .....	468
47.4.1	<i>Overview</i> .....	468
47.4.2	<i>Driving a linear CCD</i> .....	468
47.4.3	<i>CCD output handling</i> .....	468
47.4.4	<i>Driving the CCD with a microcontroller</i> .....	470
47.4.5	<i>Communication interfaces</i> .....	471
47.4.5.1	Comparison of different interfaces .....	471
47.4.5.2	Hardware for USB communication .....	471
47.4.6	<i>Brief description of USB protocol</i> .....	472
<b>48</b>	<b>DESIGN AND REALIZATION OF A SPECTROMETER PROTOTYPE .....</b>	<b>474</b>
48.1	OPTICAL SETUP .....	474
48.1.1	<i>Diffraction grating source</i> .....	476
48.1.1.1	Microcontroller circuit .....	476
48.1.2	<i>Supply circuit</i> .....	478
48.1.3	<i>Spectrometer casing</i> .....	478
48.2	MINIMAL CIRCUIT BETWEEN USB AND MICROCONTROLLER .....	479
48.3	MICROCONTROLLER FIRMWARE .....	480
48.4	CCD DRIVING .....	482
48.4.1	<i>USB communication</i> .....	484
48.5	THE MAIN LOOP .....	487

48.6	COMPUTER SOFTWARE .....	489
48.6.1	<i>Command line backend for USB communication</i> .....	489
48.6.2	<i>Data preprocessing according to calibration</i> .....	490
48.6.3	<i>Python module backend</i> .....	490
48.6.4	<i>Graphical user interface</i> .....	490
48.6.5	<i>Calibration</i> .....	492
48.7	RESULTS .....	493
48.8	CONCLUSION .....	494
<b>49</b>	<b>DESIGN OF IAP-OSM .....</b>	<b>496</b>
49.1	OPTICAL SETUP .....	497
49.2	MATERIALS FOR OPTICAL SETUP .....	497
49.3	SCHEMATIC OF SPARKFUN TRIAD SPECTROSCOPY SENSOR - AS7265X (QWIIC).....	498
49.4	SOFTWARE DESIGN CONSIDERATIONS AND ARDUINO .....	498
49.5	REFERENCES .....	500
<b>IAP-IRS</b>	<b>.....</b>	<b>501</b>
<b>50</b>	<b>BASICS OF INFRARED SCIENCE &amp; TECHNOLOGY .....</b>	<b>503</b>
50.1	INFRARED ASTRONOMY (NEAR INFRARED, MID INFRARED, FAR INFRARED).....	503
50.1.1	<i>NEAR INFRARED</i> .....	504
50.1.2	<i>MID INFRARED</i> .....	505
50.1.3	<i>FAR INFRARED</i> .....	506
50.2	DEFINITION OF INFRARED AND THE ORIGIN OF THE INFRARED RADIATION .....	506
50.2.1	<i>The definition of the infrared band</i> .....	507
50.3	INSTRUMENTATION / SENSORS TECHNOLOGY.....	510
50.3.1	<i>IRAS</i> .....	510
50.3.1.1	The most important results of IRAS.....	511
50.4	INFRARED SATELLITE OBSERVATORIES.....	512
50.4.1	<i>Infrared Space Observatory (ISO)</i> .....	513
50.4.1.1	Scientific instruments and observing strategy.....	514
50.4.1.2	Most important results.....	515
<b>51</b>	<b>IAP-IRS UNIT DESIGN (PBS DETECTOR) OVERVIEW (PRESENTATION) .....</b>	<b>518</b>
<b>52</b>	<b>BASICS .....</b>	<b>529</b>
52.1	INTRODUCTION TO LEAD SALT INFRARED DETECTORS (KONDAS, FEBRUARY 1993) .....	530
52.2	STRUCTURE .....	531
52.3	THEORETICAL BACKGROUND .....	533
52.3.1	<i>Basic principle</i> .....	534
52.3.2	<i>Biasing</i> .....	534
52.3.3	<i>Noise</i> .....	534
<b>53</b>	<b>OVERVIEW (WILLIAM V. CUMMINGS JR., 1951) .....</b>	<b>535</b>
<b>54</b>	<b>IR PHOTOCONDUCTIVE DETECTORS .....</b>	<b>537</b>
54.1	PHOTOCONDUCTORS VS. PHOTODIODES .....	537
54.2	USAGE NOTES.....	537
54.3	THEORY OF OPERATION .....	537
54.4	FREQUENCY RESPONSE .....	538
54.5	TEMPERATURE CONSIDERATIONS.....	539

---

54.6	TYPICAL PHOTOCONDUCTOR AMPLIFIER CIRCUIT .....	539
54.7	SIGNAL TO NOISE RATIO .....	540
54.8	NOISE EQUIVALENT POWER.....	540
54.9	DARK RESISTANCE .....	540
54.10	DETECTIVITY (D) AND SPECIFIC DETECTIVITY (D*) .....	540
<b>55</b>	<b>ROOM-TEMPERATURE, THIN-FIL, PBS PHOTOCONDUCTIVE DETECTOR HARDENED AGAINST LASER DAMAGE .....</b>	<b>542</b>
<b>56</b>	<b>PBS SYNTHESIS.....</b>	<b>549</b>
56.1	PREPARE REACTANTS .....	549
56.2	DEGAS THE MIXTURE .....	549
56.3	INJECTION .....	549
56.4	CLEANING .....	549
56.5	PbS/POLYMER NANOCOMPOSITE OPTICAL MATERIALS WITH HIGH REFRACTIVE INDEX.....	550
<b>57</b>	<b>CONCLUSION .....</b>	<b>551</b>
	Heat sink: .....	554
	Sapphire window overview:.....	554
	Substrate quartz: .....	555
	Thermoelectric cooler.....	557
<b>58</b>	<b>THERMOELECTRICALLY COOLED IR DETECTORS BEAT THE HEAT .....</b>	<b>562</b>
58.1	THERMOELECTRIC COOLERS .....	562
58.2	CHOOSING A COOLER.....	563
58.3	NEAR-INFRARED DETECTORS .....	564
58.4	PRINCIPLE OF THERMOELECTRIC COOLING .....	565
58.4.1	<i>Peltier effect</i> .....	566
<b>59</b>	<b>LEAD SULFIDE QUANTUM DOTS SYNTHESIS.....</b>	<b>567</b>
59.1	OVERVIEW .....	567
59.2	SIGNIFICANCE .....	567
59.3	PROCEDURE.....	567
59.4	PbS/POLYMER NANOCOMPOSITE OPTICAL MATERIALS WITH HIGH REFRACTIVE INDEX.....	568
<b>60</b>	<b>SYNTHESIS AND OPTICAL PROPERTIES OF THE SEMICONDUCTOR PBS NANOBELTS .....</b>	<b>570</b>
60.1	INTRODUCTION .....	570
60.2	EXPERIMENTAL SECTION .....	570
60.2.1	<i>Reagents &amp; Equipments:</i> .....	570
60.3	RESULTS AND DISCUSSIONS .....	572
60.4	CONCLUSION .....	574
<b>61</b>	<b>MATERIALS .....</b>	<b>576</b>
<b>62</b>	<b>REFERENCES TO IAP-IRS .....</b>	<b>577</b>
62.1	REFERENCES AND FURTHER READING TO THE 2.6 .....	577
62.2	FOR PBS SENSOR.....	578
<b>SUPPLIERS DATA .....</b>		<b>579</b>
	Electronics, Control .....	579
	Satellite Parts .....	579

CNC Fine Mechanics (2D) .....	579
3D Printing (Plastics) .....	580
CNC .....	580
<b>IAP-GAMS (GAMMA ASTRONOMY SENSOR) .....</b>	<b>581</b>
<b>PROJECT STATUS AT BEGINNING OF ACTUAL PROJECT PHASE.....</b>	<b>582</b>
<b>63 PROJECT MANAGEMENT.....</b>	<b>584</b>
63.1 ORGANISATION WITHIN IAP .....	584
63.2 WORKING PACKAGES AND TIME PLAN .....	584
63.2.1 <i>To do with internal resources</i> .....	584
63.2.2 <i>To do with external resources</i> .....	584
<b>64 BASICS .....</b>	<b>585</b>
64.1 GAMMA ASTRONOMY .....	585
64.1.1 <i>PAMELA Experiment</i> .....	586
64.2 NUCLEAR PROCESSES, NEUTRON AND GAMMA RAY PHYSICS .....	586
64.2.1 <i>Introduction</i> .....	586
64.2.1.1 Overview .....	587
64.2.1.2 Learning Outcomes.....	587
64.2.2 <i>Structure of the Nucleus</i> .....	588
64.2.2.1 Fundamental Interactions and Elementary Particles.....	588
64.2.2.2 Protons, Neutrons, and the Nuclear Force .....	590
64.2.2.3 Nuclear Chart.....	591
64.2.2.4 Nuclear Mass and the Liquid Drop Model .....	594
64.2.2.5 Excitation Energy and Advanced Nuclear Models .....	596
64.2.2.6 Nuclear Fission and Fusion .....	599
64.2.3 <i>Nuclear Reactions</i> .....	600
64.2.3.1 Radioactivity and Nuclear Decay .....	600
64.2.3.2 Nuclear Reactions.....	603
64.2.3.3 Interactions of Charged Particles with Matter .....	605
64.2.3.4 Interactions of Photons with Matter .....	607
Photoelectric effect.....	609
Raleigh scattering.....	610
Compton scattering .....	610
Pair production .....	611
Photonuclear reactions.....	611
64.2.3.5 Interactions of Neutrons with Matter .....	613
64.2.4 <i>Fission and Nuclear Chain Reaction</i> .....	615
64.2.4.1 Fission Cross Sections .....	616
64.2.4.2 Fission Products and the Fission Process.....	617
64.2.4.3 Nuclear Chain Reaction and Nuclear Fission Reaction cores .....	619
64.2.4.4 Reaction core Physics and the Transport Equation .....	620
64.2.5 <i>Bibliography</i> .....	621
64.3 DOSIMETRY, DOSE LIMITATIONS, AND GUIDANCE .....	623
64.3.1.1 Dose Definitions .....	624
Exposure .....	624
Absorbed, equivalent, and effective dose .....	625
Committed dose .....	628
Derived quantities.....	628
64.3.1.2 Background Radiation Exposure.....	630
64.3.1.3 International Guidance.....	632

---

UNSCLEAR.....	633
ICRP.....	634
ICRP 103.....	634
IAEA.....	635
64.3.2 Summary.....	636
64.4 RADIATION INSTRUMENTATION.....	636
64.4.1.1 Basics of Detection.....	636
Ionization.....	637
Excitation.....	637
Resolving time.....	638
Energy response and efficiency.....	640
Counting statistics and decision levels.....	643
Particle counting versus spectroscopy.....	646
64.4.1.2 Gas-Based Detectors.....	649
Proportional counters.....	650
Geiger-Müller counters.....	650
64.4.1.3 Scintillation-Based Detectors.....	652
Scintillators.....	652
Photomultiplier tubes (PMT).....	653
64.4.1.4 Semiconductor-Based Detectors.....	653
64.4.1.5 Portable Instrumentation.....	656
General-purpose survey meter.....	656
Area contamination meter.....	656
Neutron meter.....	656
Portable gamma spectrometer.....	657
64.4.1.6 Specialized Detectors.....	658
64.4.1.7 Dosimetry Techniques.....	658
Thermo-luminescent dosimetry (TLD).....	658
Electronic personal dosimeter (EPD).....	660
Liquid scintillation counting (LSC).....	661
64.4.1.8 Summary.....	663
64.5 GAMMA DECAY.....	663
64.6 GAMMA SPECTROSCOPY.....	664
64.6.1 <i>Detektor</i> .....	664
64.6.2 <i>Gamma-Gamma Coincidence Spectroscopy using Fast Scintillators</i> .....	666
64.6.3 <i>Detectors for neutron scattering</i> .....	666
64.7 SCINTILLATORS IN DEEP.....	668
64.7.1.1 Overview.....	668
64.7.2 <i>Scintillation Materials and their applications</i> .....	669
64.7.2.1 Radiation Detection with Plastic scintillators.....	672
Background.....	672
Description.....	672
Advantages.....	672
Potential Applications.....	673
64.7.2.2 Multi-anode photomultiplier tube: Phillips XP1704.....	673
64.7.2.3 Proton beam Scintillator-CCD camera system.....	673
64.7.2.4 The Mini Gamma-Ray Camera.....	674
Comparison of MGRC with Standard Gamma Camera.....	675
64.7.2.5 Q&A.....	681
64.7.2.6 Manufacturing mini gamma-ray camera.....	683
64.7.2.7 GSO scintillator.....	684
64.7.3 <i>Scintillators and Photomultipliers</i> .....	686

<b>65</b>	<b>GAMS UNIT DESIGN .....</b>	<b>687</b>
65.1	CONCEPT .....	687
<b>66</b>	<b>REALIZATION .....</b>	<b>688</b>
<b>67</b>	<b>TEST RIG.....</b>	<b>689</b>
67.1	COSTS .....	689
<b>68</b>	<b>NEXT WORKING PACKAGES .....</b>	<b>691</b>
<b>69</b>	<b>SUPPLIERS DATA .....</b>	<b>692</b>
69.1	ELECTRONICS, CONTROL .....	692
69.2	SATELLITE PARTS .....	692
69.3	CNC FINE MECHANICS (2D) .....	692
69.4	3D PRINTING (PLASTICS) .....	693
69.5	CNC .....	693
<b>REFERENCES .....</b>		<b>694</b>
69.6	FURTHER READING .....	694
69.7	REFERENCES FROM [ESSENTIAL] .....	695
<b>IR SENSOR (BASICS AND CONCEPT) .....</b>		<b>701</b>
<b>OPTICAL SPECTROSCOPY .....</b>		<b>702</b>
<b>GAMMA ASTRONOMY SENSOR (BASICS AND CONCEPT).....</b>		<b>703</b>
<b>70</b>	<b>REFERENCES.....</b>	<b>704</b>
<b>71</b>	<b>SUPPLIERS DATA .....</b>	<b>707</b>
71.1	ELECTRONICS .....	707
71.2	SATELLITE PARTS .....	707
71.3	CNC FINE MECHANICS (2D) .....	707
71.4	3D PRINTING (PLASTICS) .....	708
71.5	CNC(تصنيع قطع).....	708

## Part I: IAP Space Program

# 1 IAP Space Program 2012 - 2020

## 1.1 Program Overview

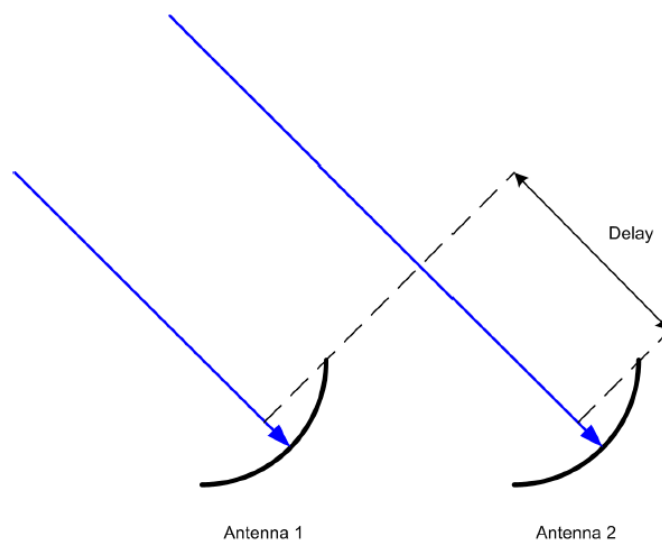
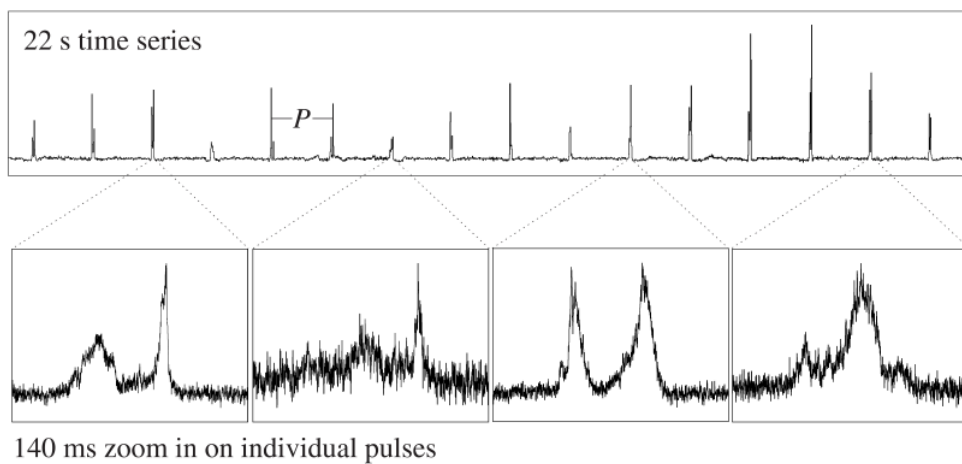
The program has three parts or aspects:

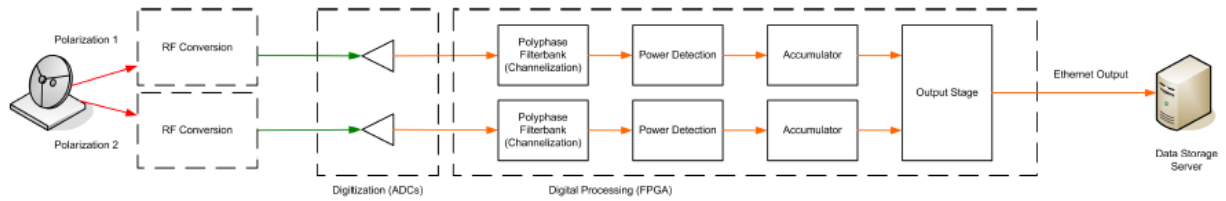
- Scientific Program
- Satellite Design and Construction
- Mission Simulation Control for a Shuttle System hired from Japan/India/China/...

## 1.2 Scientific Program

### 1.2.1 Conception for IR Sensor and Gamma Astronomy Sensor

### 1.2.2 Pulsar Radio Astronomy Sensor





**1.2.2.1 The SRWDA Project**

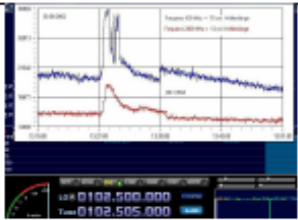
The radio astronomical IAP project supernova radio wave detector and analyzer (SRWDA) aims to detect and analyze HI radio signals from supernova remnants. At the base station a set of antennas, which gives also direction

information of the signals, is aimed to be connected to a computer which acts as Software Defined Radio (SDR). Afterwards an analyzing program is aimed to be installed.

Later the detectors are planned to be installed on satellites to improve the resolution and to suppress disturbing signals from earth stations.

**1.2.2.2 Ground Station for Radio Astronomy: IAP\_SRWDA**

Last update: 06 December 2013

	External I/O DLL		I	
	To connect the 4 antenna array correctly to the HDSDR program	The free software defined radio HDSDR	I/Q interface (normally to soundcard)	SRWDA Analyzer Analysis software package

Actual Working Packages:

- Development of Prototype with parts of IAP ECS

Financial and man power needs for 2014:

- 1 persons (e.g. as PhD thesis) with student support (e.g. as master thesis)
- 1.000 USD material

Actually a master thesis is undergone in this project [Kassar 2014].

**1.3 Satellite Design and Construction**

The architecture of a satellite mission

The draft of a satellite mission  
Design and planning of a satellite  
Design of the energy supply system  
Draft of the position control system  
Design of the drive system  
Performance Evaluation of Propulsion Systems  
Description of the Analysis Tool  
Design of the radio link  
Design of the on-board data processing system  
Design of the thermal control system  
Design of the structure and mechanisms  
Reliability and product assurance

## 1.4 Old Program (last updated Dez. 12)

Das IAP-Programm umfasst für den Zeitraum Jan 2013 – Dez 2015 folgende Einzelpakete:

- A. Programmpaket Mission (Start bis LEO – Übergang in Erdflucht – Einschwenkung in Mondorbit – Abtrennung des Landmoduls vom Mutterschiff – Landung des Landmoduls auf dem Mond – Start und Flug zum Mutterschiff im Mondorbit)
- B. Programmpaket wissenschaftliche Mission (Messen von kosmischer Strahlung, Vorauswertung, Senden zur Erde)

Programmpaket A:

- SW-Programmumgebung unter Linux
- Implementierung von PN Navigation und anderen regelungstechnischen Algorithmen (inkl. Lenkung), Benutzung von MATLAB/Simulink (Student Vers. bei Amazon 77 EUR)
- Implementierung von Image Processing (Bildsequenzen)
- Benutzung von CFD/Numerical Combustion SW
- Migrierung des alternative Lotte Systems zu einem Landemodul

Programmpaket B:

- SW-Programmumgebung unter Linux
- Wissenschaftliches teilchenphysikalisches Programmpaket
  
- MATLAB/SIMULINK Einarb. Satellitenregelung
- SIM-Programm Einarbeitung

### 1.5 Aim of IAP\_SRWDA-.SAT project

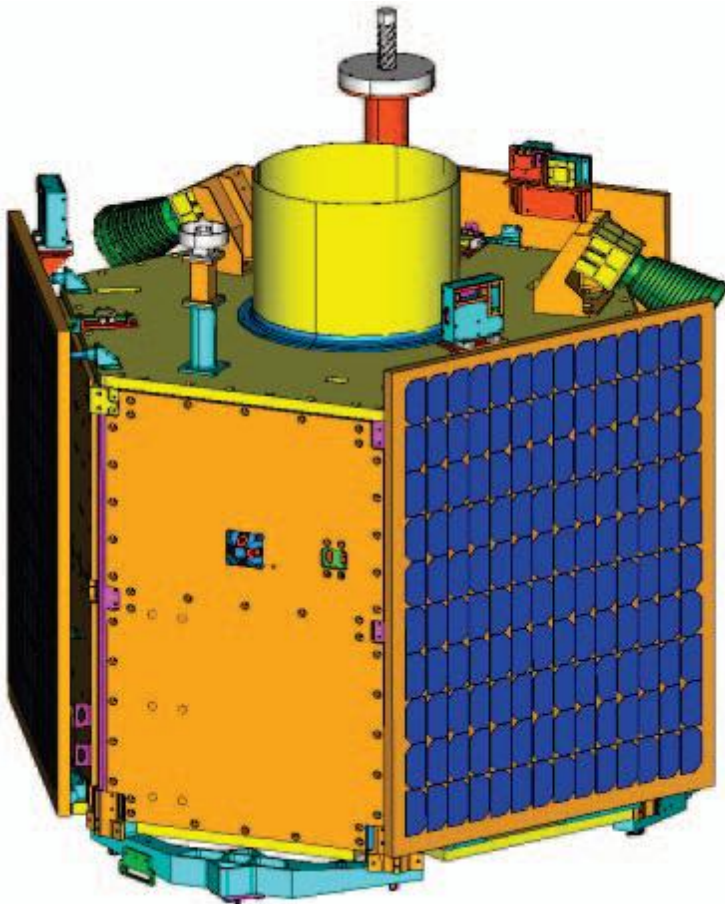
- initialization of a small private space program (mission planning, communication, telemetry (ground tracking), FCS) which is expendable to commercial usage
- initialization of astrophysics scientific program

### 1.6 Mission Overview for IAP-Sat

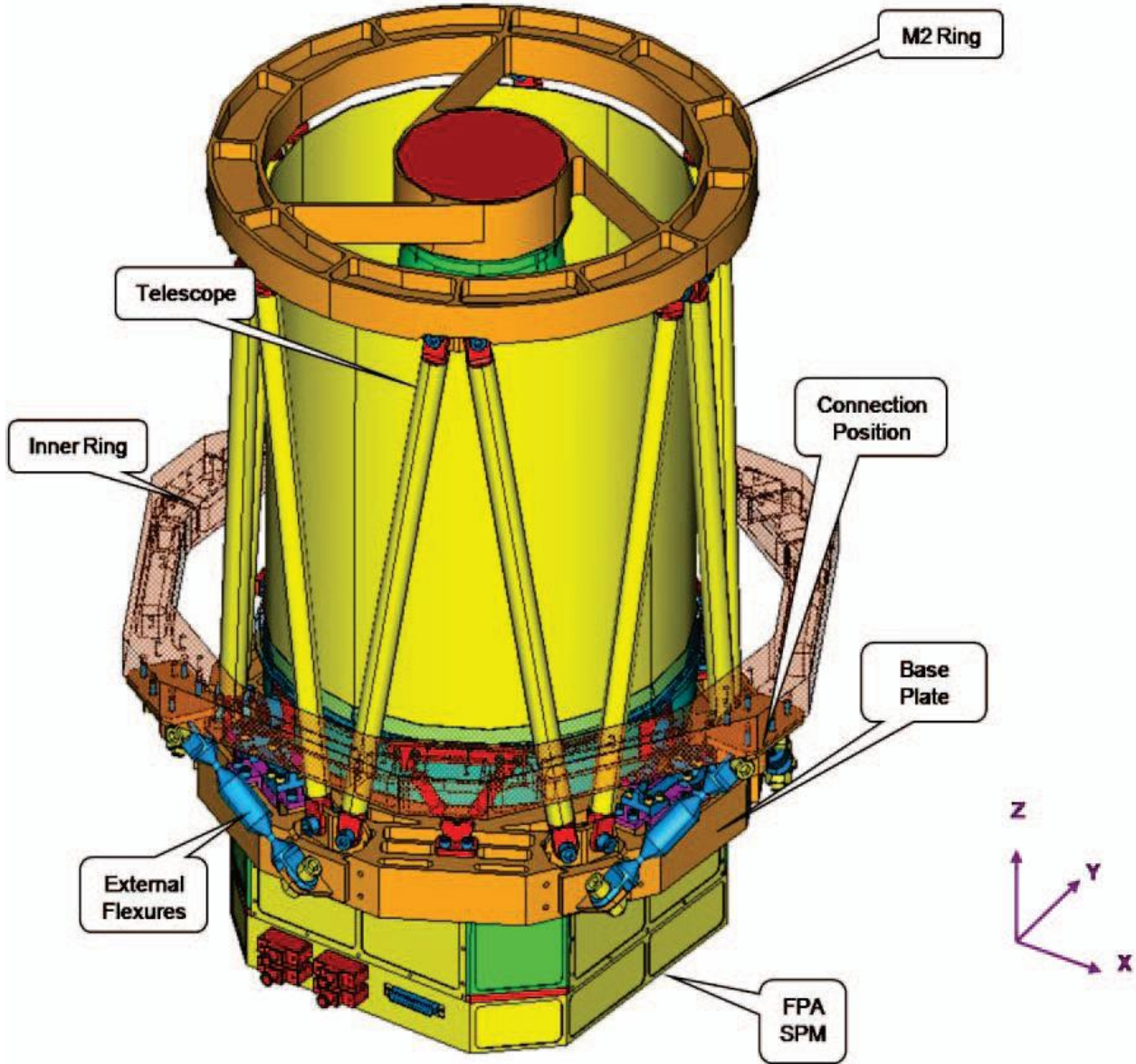
The satellite shall be based on technology of Turkish Göktürk and DubaiSat-1



Göktürk



DubaiSat-1



Dubai Medium Aperture Camera (DMAC)

### 1.7 Satellite & Ballon System for Communication

## 1.8 Open Tasks (updated 2019)

# TEMOLeb-SatellitePlatform

(Communication Satellite Platform) نظام قمر اصطناعي للإتصالات



المركز التقني للإتصالات والمعلوماتية



## 3000 Kg Payload COM Unit for GEO

**Payload** **Telecommunications**




**Transporter**  About 5000\$/kg  
For 3000 kg = 15 Mio \$

Pre-Development (2012-2019)

**Sensors IMU**

IMU or Inertial Measurement Unit

The IMU has the following parts:

- Gyro
- Accelerometer
- Magnetometer



**Communication SDR**

The radio astronomical IAP project supernova radio wave detector and analyzer SRWDA

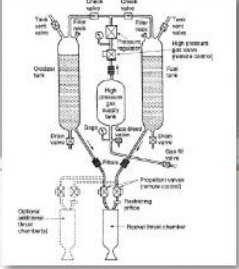


**Chemical Prop. Unit**

The satellite chemical propulsion system is based on this system

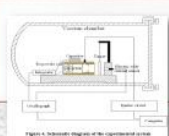
- Methane tank
- Oxygen tank
- Thrust chamber

Transporter propulsion system design

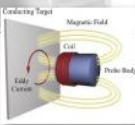


**Electrical Prop. Unit**

Pulsed Plasma Thruster



EDDY current sensor

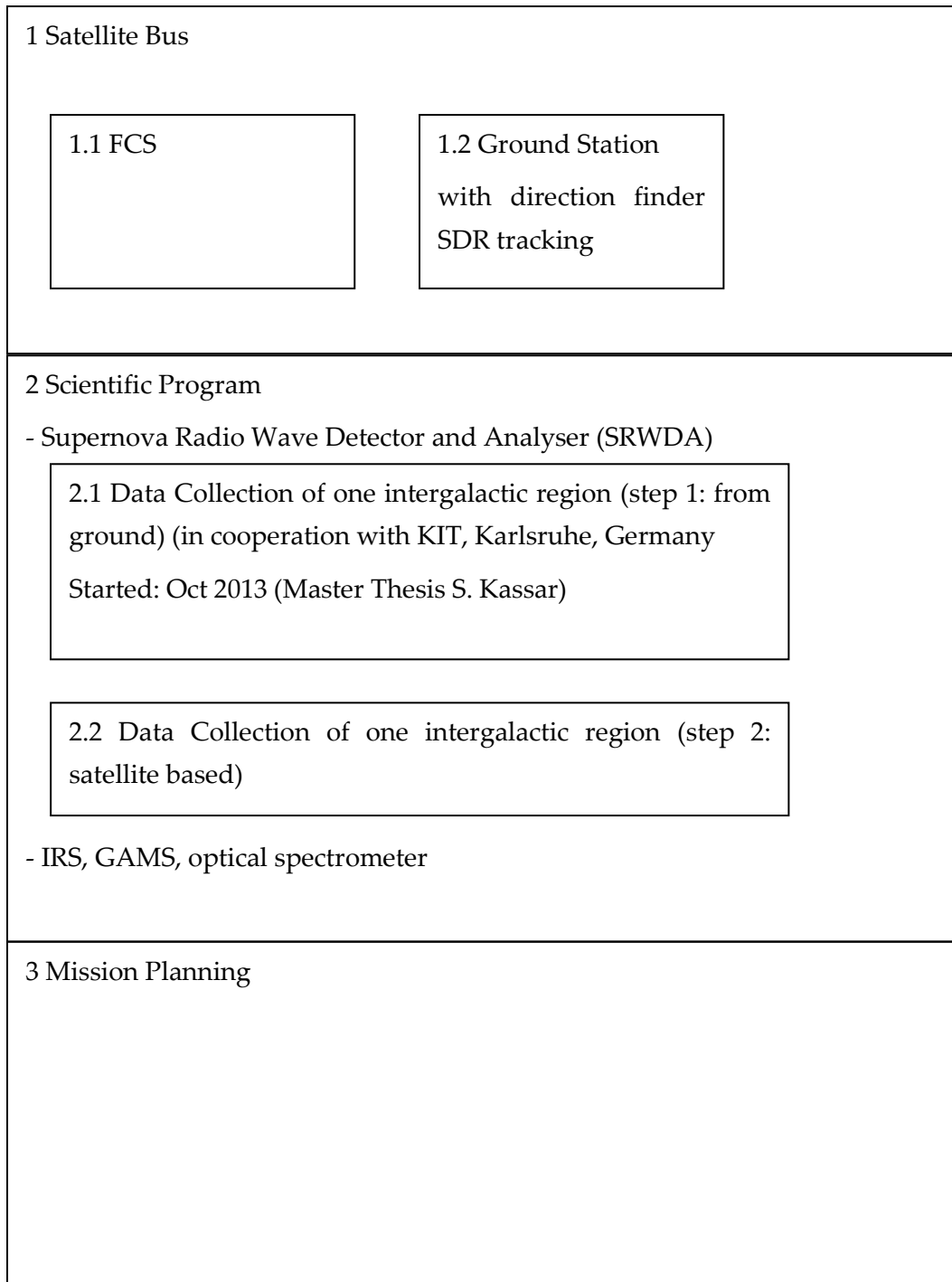



Open Tasks

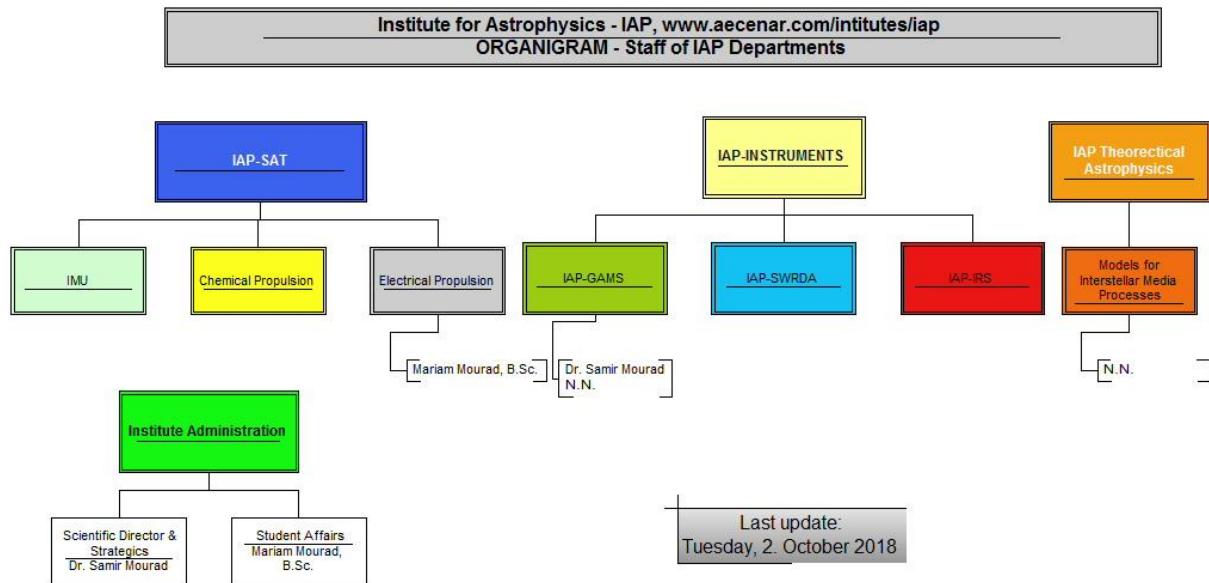
Tasks	Needed Human Resource	External Cost	Year
TEMOLeb-Mintad Gas filling	2 Technicians, 4 MM (man months)	5000\$	2019
TEMOLeb-Mintad& TEMOLeb-SAT solar panels and system	-	2000\$	2019
TEMOLeb-Mintad Control System development & Validation (simulink/scilab)	Eng., 5 MM	400\$	2019
TEMOLeb-Mintad Actuators, Wings integration	2 Technicians, 2 MM	1000\$	2019
TEMOLeb-Mintad Sensors integration	Eng., 1 MM	300\$	2019
TEMOLeb-SAT Actuator (chem.)	1 Technician, 1 MM	1500\$	2019
TEMOLeb-SAT Platform integration	1 Technician, 1/2 MM	500\$	2019
TEMOLeb-Mintad Telemetry Unit	2 Eng., 6 MM	3000\$	2020
TEMOLeb-SAT Telemetry Unit	2 Eng., 6 MM	3000\$	2020
TEMOLeb-Mintad COM Unit (Payload)			2020
TEMOLeb-SAT COM Unit (Payload)			2020

## 2 Project Management

### 2.1 Organisation



## 2.2 IAP Organigram



## 2.3 Documentation

Satellite Bus	Satellite Bus Prototype - Conception - HIL Testrig - Intergration of Prototype	IAP-SAT Reports 1-6 (2012-2020), Final Report
Payload	Radioastronomy Sensor	[Kassar 2014]
Shuttle	Modeling of shuttle (motor, body) Mission Planning	IAP-TRANSPORTER (planned 2018)
Operation of satellite	Ground Station with direction finder SDR tracking	planned 2019

## 2.4 Yearly Working Packages, Time Plans, Costs

### 2.4.1 IAP 2012

July – September 2012

Mission Simulation

Costs: 500 \$

### 2.4.2 IAP 2013

June – Dec 13 : Conception Phase

Milestone (Dec 13): First Mock-up model

## 2.4.2.1 Costs IAP 2013

2013	Materialkosten	Arbeiterlöhne	Einnahmen	Ausgaben/Mona	Bilanz/Monat	Bilanz/Jahr	
Januar				0	0		
Februar				0	\$0		
März				0	\$0		
April				0	\$0		
Mai		-\$800		-800	-\$800		
Juni	-\$300	-\$800		-\$1.100	-\$1.100		
Juli		-\$960		-\$960	-\$960		
August				\$0	\$0		
September		-\$800		-\$800	-\$800		
Oktober	-\$150	-\$760		-\$910	-\$910		
November		-\$800		-\$800	-\$800		
Dezember		-\$480		-\$480	-\$480		
	-\$450	-\$5.400					-\$5.050

## 2.4.3 Working packages 2014

WP No.	Working package content	Time span, material costs	Development environment (HW, SW)	Responsible	Status
1	Implementing Space Model, Sensor Model and Actuator Model (only Resistojet) in scicos Sources: M.Yassir Diss.	24.7.-7.8.	HP Server, scicos		
2	Star camera: Fixing on Orion -> star coordination card in memory, Vergleich mit aufgenommenem Bild	8.8.-31.8.			
3	Resistojet Thruster Prototype	24.7.-7.8.	ProE		
4	Development and Test Bench System Design	31.7.-1.8.	Word		

## 2.4.3.1 Costs IAP 2014 (planned)

		Engineer need (MM)	Specialized Worker/Facharbeiter (MM)	Student (1/2 MM)	Personnel Costs	Material Costs	Duration (months)	Needed Staff
IAP_SRWDA-SAT	mock-up model				\$1.000	\$300	1	1 Student (A1)
	specification prototype				\$1.000		1	1 Student (A1)
	prototype (COM, FCS) aus ECS u. alt. Lotte übernehmen				\$4.000	\$1.200	6	1 Master Student (electrical engineering)
	mission simulation				\$2.000		1	1 Student (A1)
	Specification MPD propulsion system				\$1.000		3	1 Student (A1)
	MPD propulsion system				\$5.000	\$2.000		
IAP_SRWDA-SAT Ground Station	Migration from IAP_SRWDA Ground Station				\$3.000	\$1.000	1	1 Student (A1)
IAP_SRWDA Ground Station	Integration Ground Station Prototype					\$1.000	3	1 Master Student (electrical engineering) Suheeb

Sum: 22.500 \$

## 2.4.4 Working Packages and Time Plan 2015

WP No.	Working package content	Time span, costs	Development environment (HW, SW)	Responsible	Status
1	Specification, Cost Analysis. Result: Presentation Film	Mar-Apr 2015 (2 man months)	FreeCAD, Gpredict, OpenSat	Master Student Fatima Al Chaar	finished
2	Hardware-in-the-Loop test rig without adaption to board computer	May-Aug 2015 (4 man months)	Scicos, ubuntu, C compiler	Master Student Fatima Al Chaar	Finished
3	Concept for Propulsion Unit	July/August 2015 (1 man month)		Practical Student Ibrahim Ghanem	finished
4	Implementation of control algorithm at On-Board-Computer and Closed-Loop-Integration of HIL				open
5	Visualization of satellite movement in orbit based on scilab simulation data				open
6	Specification of battery system			Practical Student Ibrahim Ghanem	finished
7	Specification, Design of star			Practical Student	Partly

	camera and algorithm			Houssam Barbara	finished
--	----------------------	--	--	--------------------	----------

### 2.4.5 IAP-SAT 2016

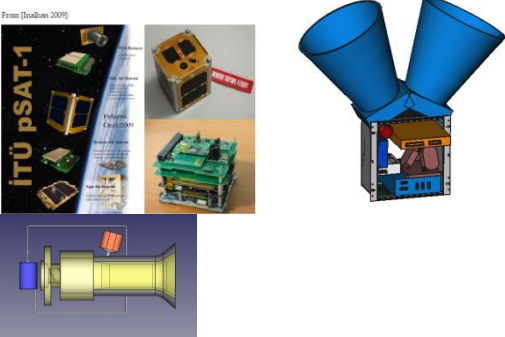
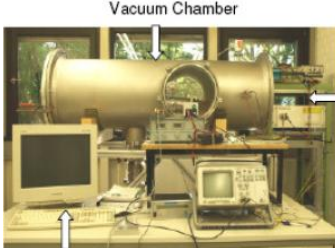
#### 2.4.5.1 Project Status at Beginning of actual project phase (2016)

- Presentation film
- HIL test rig
- Concept for propulsion unit, concept for battery

#### 2.4.5.2 Goal of actual phase

- On-Board-Computer Integration with Control Algorithm
- Visualization of satellite movement in orbit based on scilab simulation data
- Integration
- Fiber Optic Gyro development test rig
- Mission Simulation of Orbiting IAP-SAT

#### 2.4.5.3 Overview Planning & Budget IAP 2016

<p><b>IAP</b></p>	<p>Completing IAP-SAT Prototype</p>  <p>Budget: 5000\$</p>	<p>Building Experimental Rig for Electrical Satellite Propulsion Unit</p>  <p>Data Readout at 200MHz Figure 3. One of the I-MPD Test Facilities</p> <p>Budget: 1500\$</p>
-------------------	---	--

#### 2.4.5.4 To do with internal resources

WP No.	Working package content	Time span, costs	Development environment (HW, SW)	Responsible	Status
1	Implementation of control algorithm at On-Board-Computer and Closed-Loop-Integration of HIL				open
2	Visualization of satellite				open

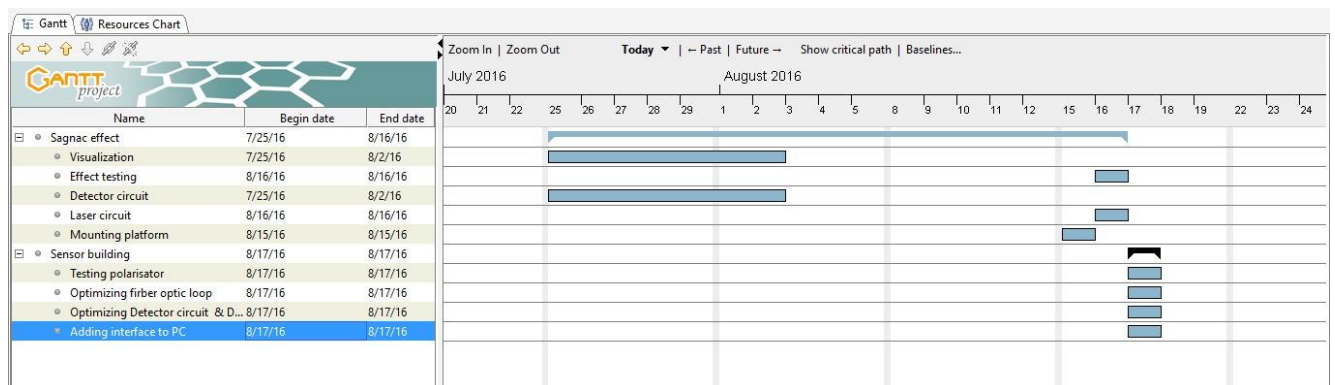
	movement in orbit based on scilab simulation data				
3	Specification, Design of star camera and algorithm			Practical Student Houssam Barbara	Partly finished

### 2.4.5.5 Master Thesis Tasks to complete the IAP-SAT prototype

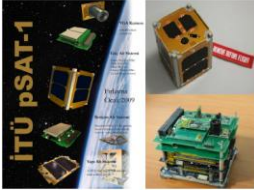
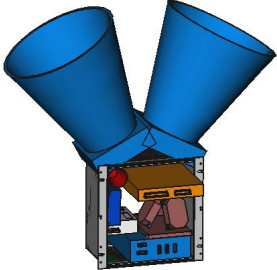
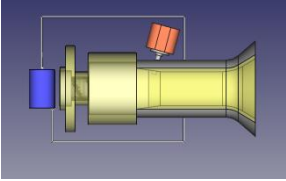
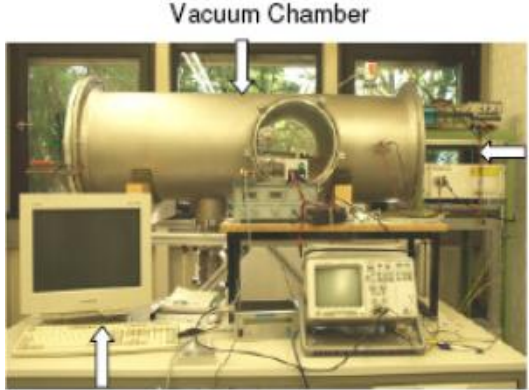
From <http://aecenar.com/job-opportunities>

Title	Keywords	Preferred Faculty/ Student Profile	AECENAR Project
Development of a star tracking camera for a meteorological satellite		Electronics	IAP-SAT
Integration of GPS and star tracking to multisensor attitude control system for a meteorological satellite		Electronics	IAP-SAT
Development of a PPT propulsion unit for attitude control for a meteorological satellite		Electronics / Mechanical Engineering	IAP-SAT
Study (including vibration) and Planning of bringing a meteorological satellite into orbit		Mechanical Engineering	IAP-SAT
Development of a electrical propulsion unit (Pulsed Plasma Thruster (PPT)) for attitude control of a small meteorological satellite		Electronics / Mechanical Engineering	IAP-SAT

### 2.4.5.6 Time Plan FOG Development



### 2.4.6 Overview Planning & Budget IAP-SAT 2017

<p>Completing IAP-SAT Prototype, Budget: <b>1500\$</b></p> <div style="display: flex; justify-content: space-around; align-items: center;">   </div> 	<p>Building Experimental Rig for Electrical Satellite Propulsion Unit, Budget: <b>500\$</b></p>  <p><b>Figure 3. One of the I-MPD Test Facilities</b></p>
--	---

#### 2.4.6.1 To do for CNCLab

10.8.17: paid 600\$

WP No.	Working package content	Time span, costs	Development environment (HW, SW)	Due Date	Status
1	IMU (Gyro+Acc.) 6DOF	1d, 50\$			
2	OnBoardComputer	1d, 100\$			
3	Star Camera	3d, 50\$			
4	Electrical Propulsion Unit	3d			
5	Telemetry	1d			
6	Integration to IAP-SAT	2d			
7	Earth Station	2d			
8	Visualization of satellite movement in orbit based on scilab simulation data				

Working start: 18.8. **Due Date for total system: 1.9.17**

#### 2.4.6.2 To do with internal resources

WP No.	Working package content	Time span, costs	Development environment (HW, SW)	Responsible	Status
3	Development of a PPT			Mariam	

	propulsion unit for attitude control of IAP-SAT			Mourad	
--	---	--	--	--------	--

## 2.4.7 IAP-SAT 2020

### 2.4.7.1 Time Plan for COM System (Last update: 16.2.2020)

Title	Description	Estimated Time	Status
Task 1: Introduction			
HackRF	Introduce HackRF and getting start with, a brochure summarize the main info should be prepared and established	5 days	Done
SDR (Software Defined Radio)	Introduce and understand SDR workflow and check for its available software	5 days	Done
Task 2: Getting Start			
Receiving signal	Use available SDR software to receiving signal using HackRF	2 days	Done
Transmitting signal	Use available SDR software to transmitting signal using HackRF	2 days	Done
Pentoo OS	Prepare Pentoo OS on a machine or USB image to be used with the HackRF	2 days	Done
GnuRadio	Getting start with GnuRadio compain and make some tutorials	3 days	Done
Raspberry&GnuRadio	Install GnuRadio on Raspberry Pi OS and make some testes	4 days	In progress
Task 3: System 1 (Send and receive system "separately")			
Make a Sender	Build a system to send a RF signal	4 days	

	using a HackRF and Raspberry Pi.		
Make a Receiver	Build a system to receive a RF signal using a HackRF and developed SDR software	7 days	
Task 4: System 2 (Send \ Receive system)			
Raspberry S\R	Update the Raspberry Pi system to make it two way communication sys (send \ receive)	3 days	
SDR software S\R	Update the developed SDR software to make it two way communication sys. (send \ Receive)	3 days	
Task 5: System 3: Lotte System			
Arduino > Raspberry	Connect Arduino to Raspberry and send and receive data from it using USB connection	5 days	
Raspberry > HackRF	Use HackRF to send Arduino data, and to receive command for it	10 days	
HackRF > Gui	Use a Windows developed software to receive sent data from the raspberry side to be access	10 days	

Total time: 65 days,

Spent time: 20 days,

Remaining time: 45 days

## 2.5 Estimated Costs of IAP-SAT (satellite development and the launching)

Satellite Development Cost and Launch Cost						
Working Package	Material Cost	Man Month	Qualification	Salary/MM	Personnel Cost per item	Total item cost
Camera	\$40,000	6	Eng	\$5,000	\$30,000	\$70,000
Chemical Propulsion System	\$50,000	10	Eng	\$5,000	\$50,000	\$100,000
Gyroscopes	\$20,000	10	Eng	\$5,000	\$50,000	\$70,000
Accelerometers	\$20,000	10	Eng	\$5,000	\$50,000	\$70,000
Tank for fuel	\$10,000	5	Eng	\$5,000	\$25,000	\$35,000
Tank for oxygen	\$10,000	5	Eng	\$5,000	\$25,000	\$35,000
Solar panels including battery system	\$15,000	10	Eng	\$5,000	\$50,000	\$65,000
Communication's board	\$5,000	10	Eng	\$5,000	\$50,000	\$55,000
Board Control Computer	\$10,000	10	Eng	\$5,000	\$50,000	\$60,000
Antenna system	\$10,000	10	Eng	\$5,000	\$50,000	\$60,000
Integration	\$10,000	5	Eng	\$5,000	\$25,000	\$35,000
Test	\$10,000	15	Eng	\$5,000	\$75,000	\$85,000
Launch	\$1,600,000			\$5,000	\$0	\$1,600,000
Ground Station	\$100,000			\$5,000	\$0	\$100,000
				Total Cost		\$2,440,000
Operational Cost per year						
Working Package	Material Cost	Man Month	Qualification	Salary/MM	Personnel Cost per item	Total item cost
Maintenance	\$40,000	12	Eng	\$5,000	\$60,000	\$100,000
Ground Station	\$20,000	36		\$3,000	\$108,000	\$128,000
				Total Cost		\$228,000

**Table1: Costs of development and launching of IAP**

With the consideration of the maintenance and operational cost, the total cost of IAP-SAT is around 2,668,000\$. The satellite's expected life time is at least 5 years.

## 2.6 Master Thesis concerning HIL and mission simulation<sup>1</sup>



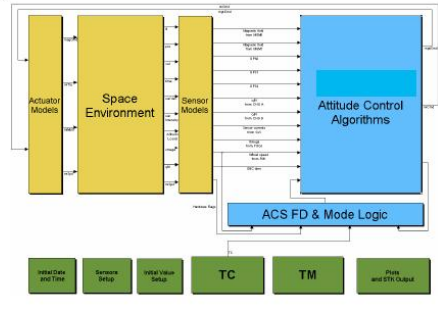


Bismillah

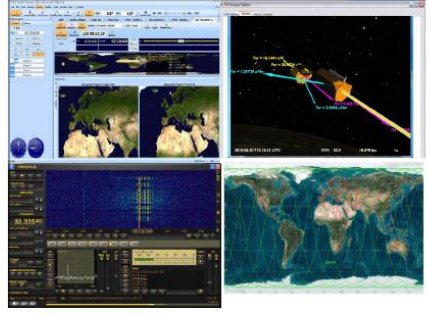
Ras Nhache/Batroun  
www.aecenar/institutes/iap  
12.2.2015




IAP Laboratory at Ras Nhache/Batroun, Lebanon



Simulation Environment



In such a way the Graphical User Interface shall be

Master Thesis

**Simulation of the system and of the operational flight of IAP-SAT to take meteorological data to monitor and estimate the energy supply potential of large scale photovoltaic energy plants to control a national alternative energy supply program**

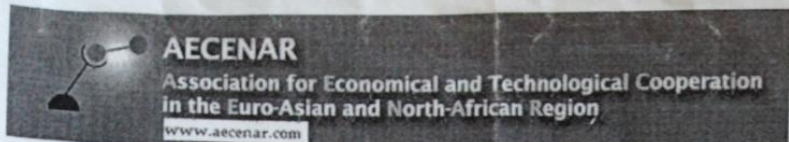
**Detailed description and working plan**

Modeling of actual IAP-SAT hardware and software components in octave	8 weeks
Modeling of IAP-SAT mechanical components with ProE	3 weeks
Integration to a operation flight model and visualization in IAP-ECS environment	3 weeks
Documentation	3 weeks

**Keywords:** Control of national energy mix programs, large scale photovoltaic plants, meteorological data, *Low Earth Orbit Satellite, Flight Mechanics&Dynamics, Matlab Simulink/Scilab*

**Contact:** Samir Mourad, Email: [samir.mourad@aecenar.com](mailto:samir.mourad@aecenar.com), Mobile +961 76341526

<sup>1</sup> The master thesis was worked out by Fatima Al Chaar, Student of Energetic Physics at Lebanese University, Tripoli

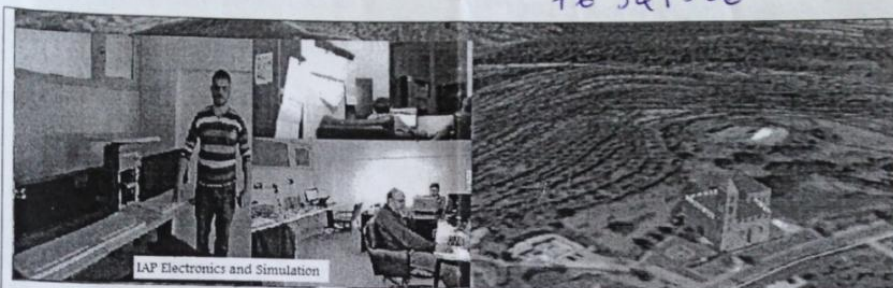


Ras Nhache/Batroun  
www.aecenar/institutes/iap  
12.2.2015

Bismillah

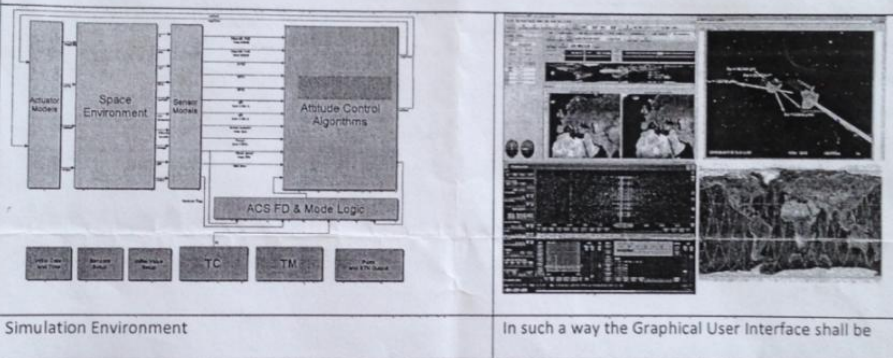
76 341526

OK



IAP Electronics and Simulation

IAP Laboratory at Ras Nhache/Batroun, Lebanon



Simulation Environment

In such a way the Graphical User Interface shall be

Master Thesis

Simulation of the system and of the operational flight of IAP-SAT to take meteorological data to monitor and estimate the energy supply potential of large scale photovoltaic energy plants to control a national alternative energy supply program

Detailed description and working plan

Modeling of actual IAP-SAT hardware and software components in octave	8 weeks
Modeling of IAP-SAT mechanical components with ProE	3 weeks
Integration to a operation flight model and visualization in IAP-ECS environment	3 weeks
Documentation	3 weeks

**Keywords:** Control of national energy mix programs, large scale photovoltaic plants, meteorological data, Low Earth Orbit Satellite, Flight Mechanics&Dynamics, Matlab Simulink/Scilab

**Contact:** Samir Mourad, Email: [samir.mourad@aecenar.com](mailto:samir.mourad@aecenar.com), Mobile +961 76341526



## 2.7 Master and PhD Tasks concerning the electrical propulsion unit



Ras Masqa/Tripoli, Lebanon 24-12-2018

### Master Thesis:

#### Eddy current sensor for the PPT test stand

IAP aims to control the position of the satellite IAP-SAT with a PPT (Pulsed Plasma Thruster). For this reason we have to test the specific Impulse of this thruster. We decided to use for the measurements an eddy current sensor.

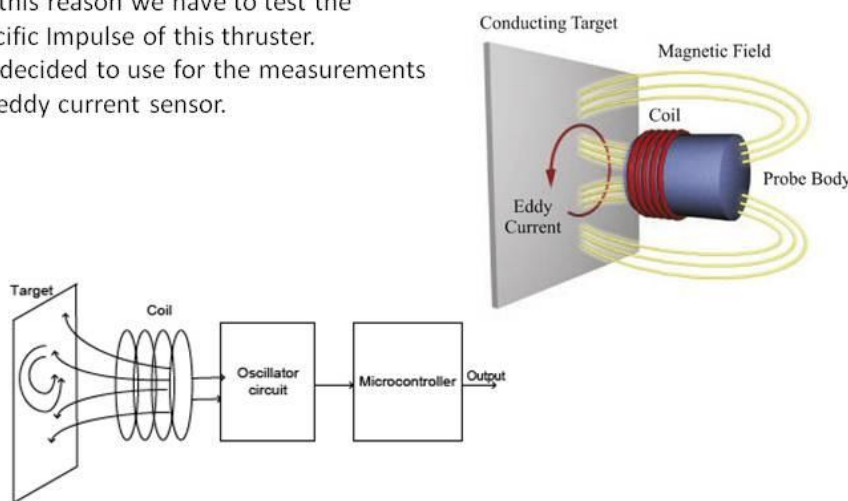


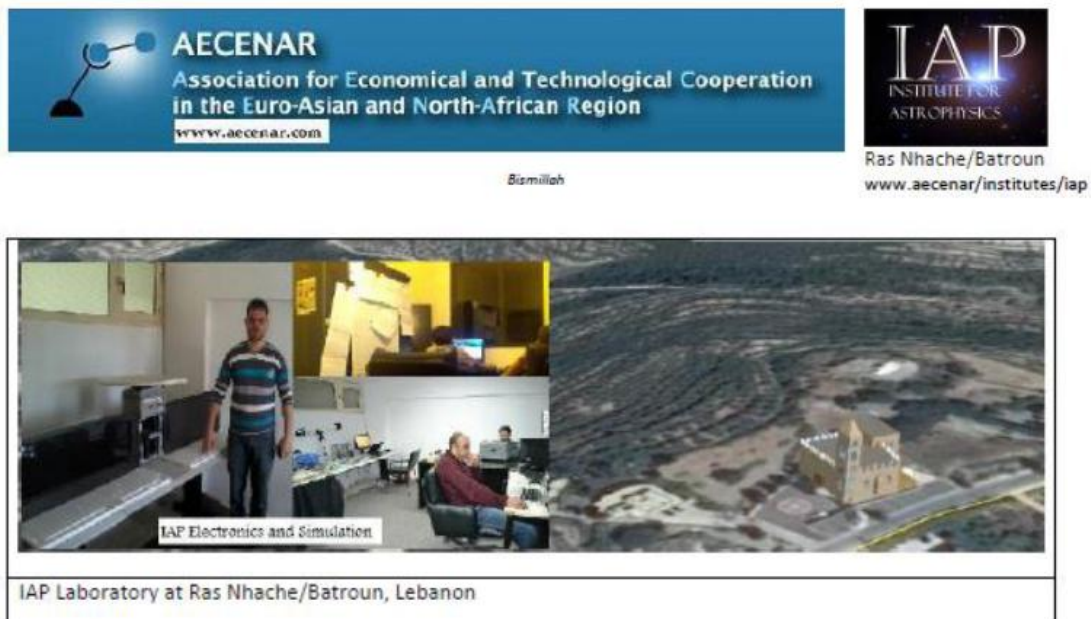
**Figure 4.** Components of eddy current displacement sensor.

#### Tasks:

- Design of the different components of the detector
- Construction
- Taking measurement data
- Analysis of results

#### Contact:

Dr. Samir Mourad,  
 Mob. +961 76 341526 (Lebanon),  
 WhatsApp +49 178 7285578 (Mob. Germany)



IAP-SAT is the first Lebanese meteorological satellite. It will be used to take meteorological data to estimate the state of weather in Lebanon.

In 2015 there was established a hardware-in-loop test rig for IAP-SAT where the space environment was simulated. One of the next steps shall be the development of an electrical propulsion unit based on pulsed plasma thruster (PPT) technology. In two PhD theses there shall be investigated the PPT thruster and its interaction with Van Allen Belt magnetic field.

#### PhD Thesis:

##### CFD Simulation of interaction of IAP-SAT PPT with Van Allen magnetic field

Detailed description an working plan:

- Development of appropriate optimized CFD algorithm package able to undergo a fast simulation of PPT similar magnetic field environments
- Taking Simulation Data for interaction of IAP-SAT PPT with Van Allen Belt magnetic field.

Keywords: Electrical Space Propulsion Units, pulsed plasma thruster (PPT) technology, computational fluid dynamics.

Contact: Samir Mourad, Email: [samir.mourad@aecenar.com](mailto:samir.mourad@aecenar.com), Mobile +961 76341526



Ras Nhache/Batroun  
www.aecenar/institutes/iap

Bismillah



IAP Laboratory at Ras Nhache/Batroun, Lebanon

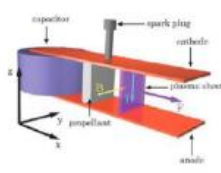


Figure 3.4: Working Principle of SIMP-LEX [60, 48]

From [Navraz et. al. 2005]:

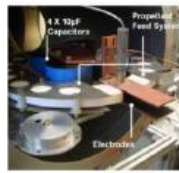
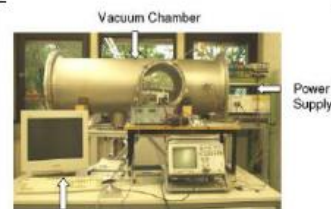


Figure 3.5: Test of SIMP-LEX propellant feed system [60, 48]



Data Readout at 200MHz  
Figure 3. One of the I-MPD Test Facilities

similar project environment at IRS, Stuttgart (

IAP-SAT is the first Lebanese meteorological satellite. It shall be used to take meteorological data to estimate the state of weather in Lebanon. In 2015 there was established a hardware-in-loop test rig for IAP-SAT where the space environment was simulated. One of the next steps shall be the development of an electrical propulsion unit based on pulsed plasma thruster (PPT) technology. In two PhD theses there shall be investigated the PPT thruster and its interaction with Van Allen Belt magnetic field.

**PhD Thesis: Measurement of interaction of IAP-SAT PPT with a laboratory Van Allen belt environment**

Detailed description an working plan:

- Development of IAP-PPT unit
- Development of measurement environment
- Taking measurement data

Keywords: Electrical Space Propulsion Units, pulsed plasma thruster (PPT) technology, Van Allen Belt magnetic field

Contact: Samir Mourad, Email: [samir.mourad@aecenar.com](mailto:samir.mourad@aecenar.com), Mobile: +961 76341526

**2.8 Correspondence with Istanbul University concerning trainee student**

Letter of practicant acceptance 30 June 2015:



**T.C**  
**İstanbul Teknik Üniversitesi**  
**Makine Fakültesi Dekanlığı**

İstanbul Teknik Üniversitesi Makine Mühendisliği Bölümü öğrencisi İbrahim Ghanem, numaralı 030120916'ın firmamızda (22.7.2015 – 22.8.2015) tarihleri arasında, haftada 5 gün, staj yapması uygun görülmüştür.

Bilgilerinize

Saygılarımızla

A handwritten signature in black ink, appearing to read 'Samir Mourad', is positioned above the printed name.

Samir Mourad, Director

**AECENAR Center Lebanon**

Ras Nhache, Qubaisi Building, Main Road, District: Batroun – North Lebanon, **Lebanon**

رأسنحاش، مركز القبيسي جانب مسجد القبيسي – قضاء البترون – لبنان الشمالي - لبنان

**Contact**

**Samir Mourad**, *Director*

Mobile Lebanon ++961 76 341 526

Mobile Germany ++49 (0)176 93516187

Email: samir.mourad@aecenar.com

**AECENAR Bureau Germany**

Hermann-Treiber-Str. 17, 69123 Heidelberg, **Germany**

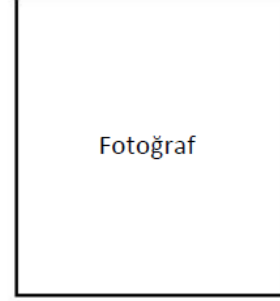
Email: info@aecenar.com

Website: www.aecenar.com

For practicants report:



İ.T.Ü.  
Makina Fakültesi



## STAJ DEFTERİ

Öğrencinin;

Adı ve Soyadı : İbrahim Ghanem

Numarası : 030120916

Program/Yarıyıl : Mechanical engineering / 5

STAJ YAPILAN

KURUMUN ADI : AECENAR

BÖLÜM	YAPILAN İŞ	TARİH		GÜN SAYISI	BÖLÜM SORUMLUSU
		Başlangıç	Bitiş		
General	Acquainting with company's projects	27/7	28/7	2	Samir Mourad
Control	Helping in feedback system	29/7	7/8	8	Samir Mourad
Design	PPT FreeCad desgin	10/8	14/8	5	Samir Mourad
Desgin	Battery SolidWorks desgin	17/8	21/8	5	Samir Mourad

(Firma Kaşesi/Mührü)

YAPILAN İŞ:

YAPILAN İŞ:	İŞ YERİ
KURUMUN ADI : AECENAR	
BÖLÜM : IAP-SAT	
<b>STAJYER ÖĞRENCİNİN DEĞERLENDİRİLMESİ (İş yeri yetkilileri tarafından doldurulacak)</b>	
1: Zayıf.....5: Mükemmel şeklinde notlandırınız.	
İŞ YERİNE UYUM	: 5
ÇALIŞKANLIK	: 5
YETERLİLİK	: 4
KARAR VERME	: 4
İŞ DİSİPLİNİ	: 4.5
TAKIM ÇALIŞMASINA YATKINLIK	: 4.5
<b>DÜŞÜNCE VE ÖNERİLER (VARSA):</b>	
ابراهيم غانم عمل جيدا ما طلبناه منه ونتمنى له كل خير وندعوا الله ان يستعمله لافادة البشرية. ونامل ان يرجع عندنا مرة اخرى	
(Firma Kaşesi/Mührü)	
	
Tarih	
.....28./..10....../..2015.....	
<b>SORUMLUNUN;</b>	
ADI ve SOYADI	: Samir Mourad
ÜNVANI	: Qubaisi Building, Main Road, Ras Nhache/Batroun, North Lebanon, Lebanon
İMZASI	: 

## YAPILAN İŞ:

YAPILAN İŞ:	İŞ YERİ
KURUMUN ADI : AECENAR	
BÖLÜM : IAP-SAT	
<b>STAJYER ÖĞRENCİNİN DEĞERLENDİRİLMESİ (İş yeri yetkilileri tarafından doldurulacak)</b>	
1: Zayıf.....5: Mükemmel şeklinde notlandırınız.	
İŞ YERİNE UYUM	: 5
ÇALIŞKANLIK	: 5
YETERLİLİK	: 4
KARAR VERME	: 4
İŞ DİSİPLİNİ	: 4.5
TAKIM ÇALIŞMASINA YATKINLIK	: 4.5
<b>DÜŞÜNCE VE ÖNERİLER (VARSA):</b>	
ابراهيم غانم عمل جيداً ما طلبناه منه ونتمنى له كل خير وندعوا الله ان يستعمله لافادة البشرية. ونامل ان يرجع عندنا مرة اخرى	
(Firma Kaşesi/Mührü)	
	
Tarih	
.....28./..10....../..2015.....	
<b>SORUMLUNUN;</b>	
ADI ve SOYADI	: Samir Mourad
ÜNVANI	: Qubaisi Building, Main Road, Ras Nhache/Batroun, North Lebanon, Lebanon
İMZASI	: 

## Part IIa: Basics for Satellite Bus

### 3 General Basics concerning satellite technology

#### 3.1 Meteorology

Meteorology is the study of weather, climate, and forces that cause changes in our environment. It uses math and physics to understand the atmosphere, which is consisted of layers of gases and moisture surrounding the earth. Most weather takes place in the lowest level of the atmosphere, known as the troposphere. Within meteorology there are a number of specialty fields which include climatology, severe storms and tornadoes, tropical cyclones, hydrology, and agriculture. [23]

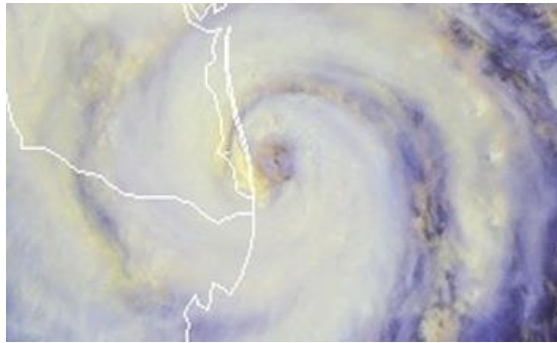


**Figure 3.1: Meteorological image**

Meteorology has application in many diverse fields such as military, transport, agriculture, construction and energy production. It offers a range of practical applications which make a major contribution to human safety and the security of air and sea transport.

#### 3.2 Satellite

##### 3.2.1 Definition

A satellite is an object that goes, or orbits, around a larger object, such as a planet. While there are natural satellites, like the moon, hundreds of man-made satellites also orbit around the earth (Fig.3.2). [24]



**Figure 3.2: Artificial satellite**

#### 3.3 Orbit

##### 3.3.1 Laws of motion

A satellite's orbit is the curved path it follows around earth (Fig.3.3).

The basis for classical mechanics Laws of motion (Newton's laws):

1. Everybody continues in its state of rest or of uniform motion in a straight line unless it is compelled to change that state by a force impressed upon it.
2. The rate of change of momentum is proportional to the impressed force and is in the same direction as that force.

*Momentum = mass × velocity, so Law (2) becomes  $F = d(mv)/dt = m dv/dt = ma$  for constant mass*

3. For every action, there is an equal and opposite reaction. [5]

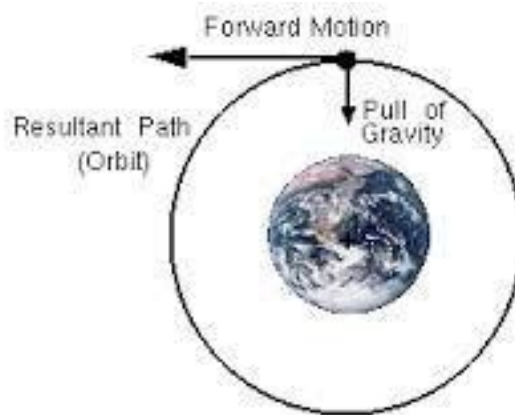


**Figure 3.3: Third law of Newton**

### 3.3.2 Laws of gravitation

The force of attraction between any two particles is

- Proportional to their masses
- Inversely proportional to the square of the distance between

them

i.e.  $F = G \cdot m_1 \cdot m_2 / r^2$  (treating the masses as points)

Where  $G$  = gravitational constant =  $6.673 \times 10^{-11} \text{ Nm}^2 / \text{kg}^2$

So, the followed laws explain how a satellite stays in orbit.

Law (1): A satellite would tend to go off in a straight line if no force were applied to it.

Law (2): An attractive force makes the satellite deviate from a straight line and orbit around earth.

The Laws of Gravitation:

This attractive force is the gravitational force between the earth and the satellite. Gravity provides the inward pull that keeps the satellite in orbit. Assuming a circular orbit, the gravitational force must equal the centripetal force.

$$m \cdot v^2/r = G \cdot m \cdot m_E/r^2$$

Where:  $v =$  tangential velocity

$r =$  orbit radius  $= R_E + h$  (i.e. not the altitude of the orbit)

$R_E =$  radius of Earth

$h =$  altitude of orbit = height above Earth's surface

$m =$  mass of satellite

$m_E =$  mass of Earth

$v = \sqrt{Gm_E/r}$ , so  $v$  depends only on the altitude of the orbit (not on the satellite's mass).

The period of the satellite's orbit is  $T = 2\pi r/v = 2\pi r/\sqrt{Gm_E/r} = 2\pi \sqrt{r^3/Gm_E}$ .

Again, this is only dependent on the altitude, increasing as the orbit's altitude increases. [24]

Form of orbit:

Kepler's Laws were based on observations of the motions of planets.

- 1) All planets travel in elliptical orbits with the Sun is at one focus (Fig. 3.4) → defines the shape of orbits.

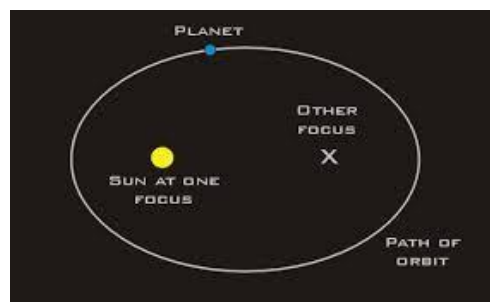


Figure 3.4: First law of Kepler (elliptical orbit)

- 2) The radius from the earth to the satellite sweeps out equal areas in equal time → determines how orbital position varies in time

- 3) The square of the period of a satellite's revolution is proportional to the cube of its semi major axis.

$$T^2 = 4\pi^2 a^3 / GM; \text{ so } (T_1/T_2)^2 = (r_1/r_2)^3$$

The pull of gravity is stronger closer to the earth, so a satellite in a low orbit must travel faster than one in a geostationary orbit (Fig. 3.5). [25]

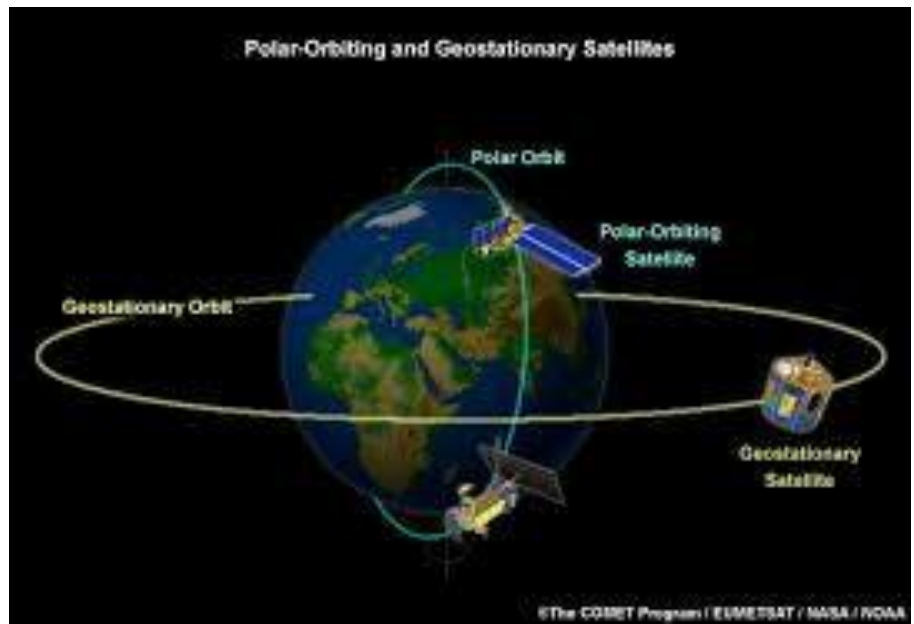


**Figure 3.5: Third law of Kepler (satellite polar orbiting is faster than geostationary orbiting because of radius)**

### 3.4 Low earth orbit

The Low Earth Orbit (LEO) is used for the vast majority of satellites. As the names imply, Low Earth Orbit is relatively low in altitude; the definition of LEO stating that the altitude range is between 200 and 1200 km above the Earth's surface (Fig. 3.6).

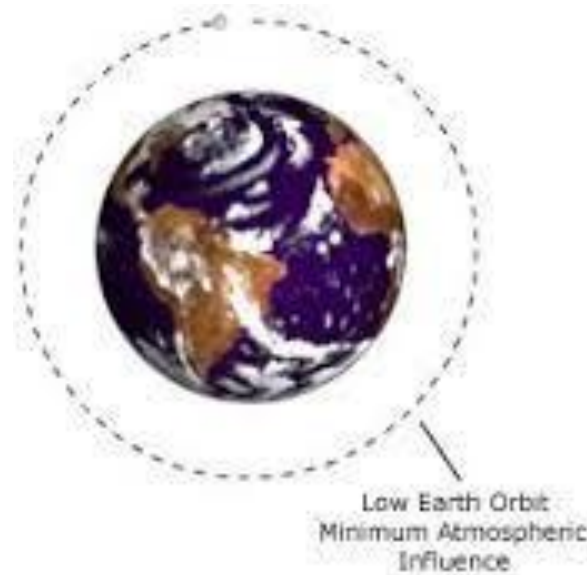


**Figure 3.6: Low earth orbit**

### 3.4.1 LEO basics

LEO is still very close to the Earth, especially when compared to other forms of satellite orbit including geostationary orbit. The low orbit altitude leads to a number of characteristics:

- Orbit times are much less than for many other forms of orbit. The lower altitude means higher velocities are required to balance the earth's gravitational field. Typical velocities are very approximately around 8 km/s, with orbit times sometimes of the order of 90 minutes.
- Radiation levels are lower than experienced at higher altitudes.
- Less energy is expended placing the satellites in LEO than higher orbits.
- Some speed reduction may be experienced as a result of friction from the low, as a result of the increasing drag from the presence of gasses at low altitudes. [2]

### 3.5 Sun synchronous orbit

Sun-synchronous orbit (SS-O) is a special case of the polar orbit. Like a polar orbit, the satellite travels from the north to the south poles as the earth turns below it (Fig. 3.7). [2]

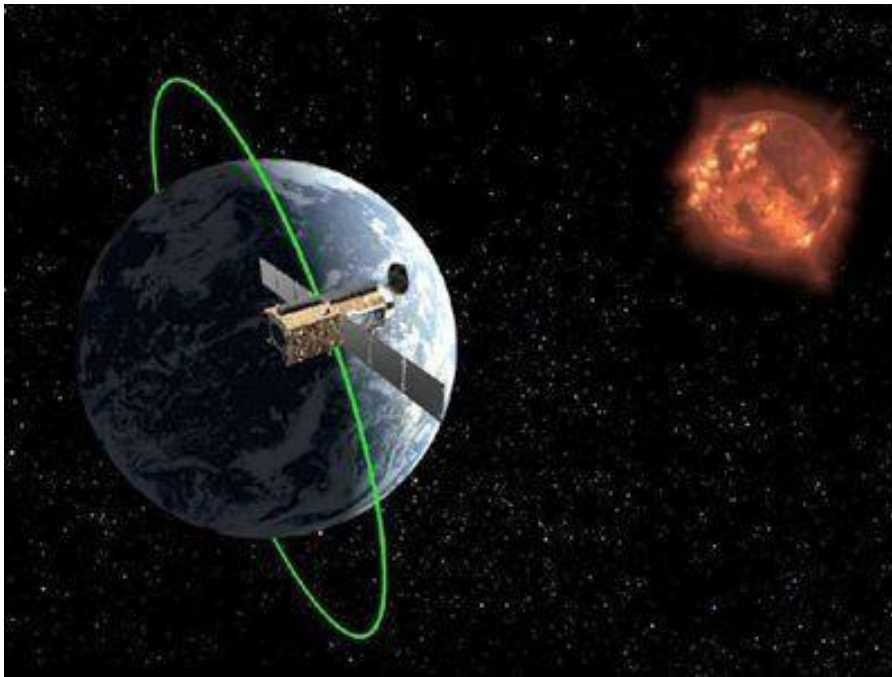


Figure 3.7: Sun synchronous orbit

A Sun-synchronous orbit is a geocentric orbit which combines altitude and inclination in such a way that an object on that orbit will appear to orbit in the same position, from the perspective of the Sun, during its orbit around the Earth (Fig. 3.8). [26]

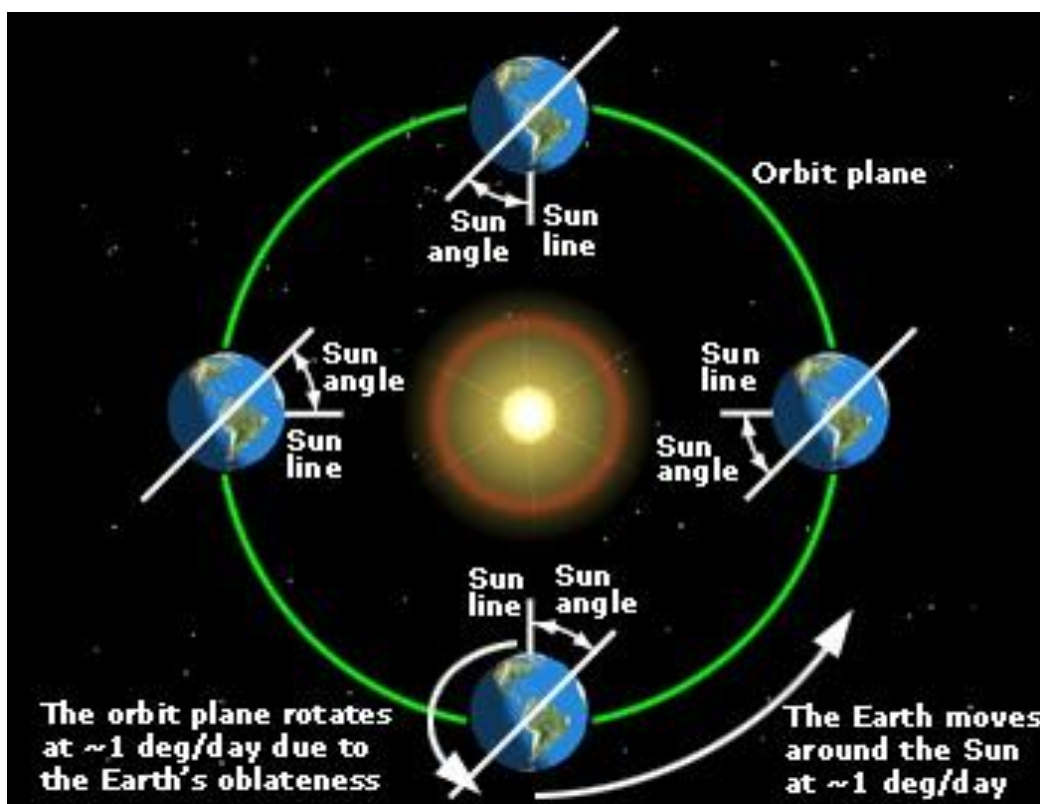
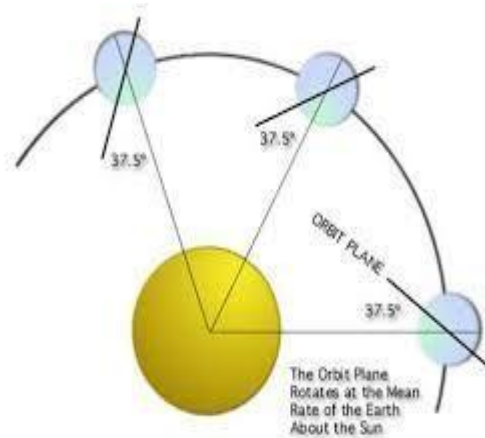


Figure 3.8: Sun synchronous orbit (conservation of the angle between the sun and the orbit plane)

The uniformity of Sun angle is achieved by tuning the inclination to the altitude of the orbit. The plane of the orbit is not fixed in space relative to the distant stars, but rotates slowly

about the earth's axis. Typical sun-synchronous orbits are about 600–800 km in altitude, with periods in the 90–100 minutes range, and inclinations of around 98. [26]



**Figure 3.9: Sun synchronous orbit**

Only the solar panels can be redirected to optimize the electric power depending on the position of the sun (Fig. 3.10).

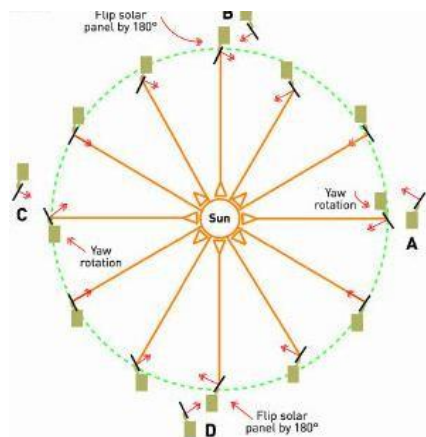


**Figure 3.10: Sun synchronous orbit (only the solar panels can rotate)**

### 3.6 Meteorological satellite

Meteorological satellite is an artificial satellite that gathers data concerning the earth's atmosphere and surface in order to aid meteorologists in understanding weather patterns and producing weather forecasts.

Satellite Meteorology refers to the study of earth's atmosphere and oceans using data obtained from remote sensing devices flown on board satellites orbiting the earth. Satellite makes measurements indirectly by sensing electromagnetic radiations coming from the surfaces below.

These weather satellites are often placed in a sun-synchronous orbit. These satellites are in polar orbits. The orbits are designed so that the satellite's orientation is fixed relative to the sun throughout the year, allowing very accurate weather predictions to be made. Most meteorological satellites orbit the earth 15 to 16 times per day. [1]

#### 3.6.1 Components of meteorological satellite

A meteorological satellite comprises two parts: satellite bus and payload.

### 3.6.1.1 Satellite bus (platform): power source, battery, control system, communication system, thermal protection...

#### i. Power source



**Figure 3.11: Solar panels of the satellite**

It is the solar panels in satellite; just like many other machines, satellites also need electrical power to function.

The sun is a very powerful, clean and convenient source of power, particularly for satellites. The only thing needed is a means to convert the energy contained in the sun's radiation – mainly light and ultraviolet rays – into electrical power. The most efficient way to achieve this today is by using panels composed of semiconductor photovoltaic cells. 'Solar panels', as they are usually called. [1]

#### ii. Battery



**Figure 3.12: Battery of the satellite**

Satellites orbiting the earth pass through a shadow region on the opposite side of the earth from the sun. Depending on the type of orbit; this can happen just a few times a year or every few hours. During these so-called 'eclipses', the solar panels cannot produce electrical energy and the satellite would not only be unable to operate, but would also freeze to incredibly low temperatures (eventually around  $-270^{\circ}\text{C}$ ) if a backup power source were not available. Electrical energy therefore has to be stored on board the spacecraft when in sunlight for consumption during these eclipses.

Batteries are used to store the energy, so that the satellite can continue to work when the Sun is eclipsed. [1]

#### iii. Control thermal system

Space is not a friendly environment either. Satellites have to survive temperature variations of more than 200°C – rather like someone standing in front of a fireplace with a blazing fire while an air conditioner pumps freezing air onto his back. [1]

Satellites orbiting the earth are subjected to similar extreme temperature variations. The delicate electronics on man-made satellites would not operate efficiently over this temperature range, so it is necessary to insulate the satellite from the space environment. Active thermal control systems such as resistive heaters, thermo-electric coolers, heat pipes... are critical tools for managing the temperature in localized areas of the satellite. Heating systems consume valuable electrical power. Cooling systems also consume power and actually only concentrate thermal energy in a small volume that must still be passively radiated into space. [21]

#### iv. **Control system (sensors, actuators)**

To position itself in space, a satellite has to maneuver using its own small propulsion (e.g. electrical or chemical propulsion). It also has to maintain its orientation, using thrusters and gyroscopes, otherwise it will tumble along its orbit and its antenna will drift out of alignment with the earth. [1]

##### a. **Sensors**

###### 1) Gyroscope

Gyro Rate Sensors determine the attitude by measuring the rate of rotation of the satellite. They are located internal to the satellite and work at all points in an orbit. Since they measure a change instead of absolute attitude, gyroscopes must be used along with other attitude hardware to obtain full measurements. At least three gyro sensors are used in a satellite. [30]

###### 2) Accelerometer

An accelerometer is a device that measures proper acceleration. The proper acceleration measured by an accelerometer is not necessarily the coordinate acceleration (rate of change of velocity). [30]

##### b. **Actuators**

Satellite propulsion is characterized in general by its complete integration within the satellite. Its function is to provide forces in the space to:

- position, adjust, and maintain orbits of satellite: used for orbit control
- orient the satellite: used for attitude control

The propulsion is a reaction Jets which produce a control force by the expenditure of mass; These systems are based on jet propulsion devices that produce thrust by ejecting stored matter, called the propellant. [28]

Satellite propulsion can be classified according to the source of energy utilized for the ejection of propellant:

- 1) Chemical propulsion (based on the principle of converting chemical energy into kinetic energy of the exhaust gases) uses heat energy produced by a chemical reaction to generate gases at high temperature and pressure in a combustion chamber. These hot gases are accelerated through a nozzle and ejected from the system at a high exit velocity to produce thrust force (Fig. 3.13).

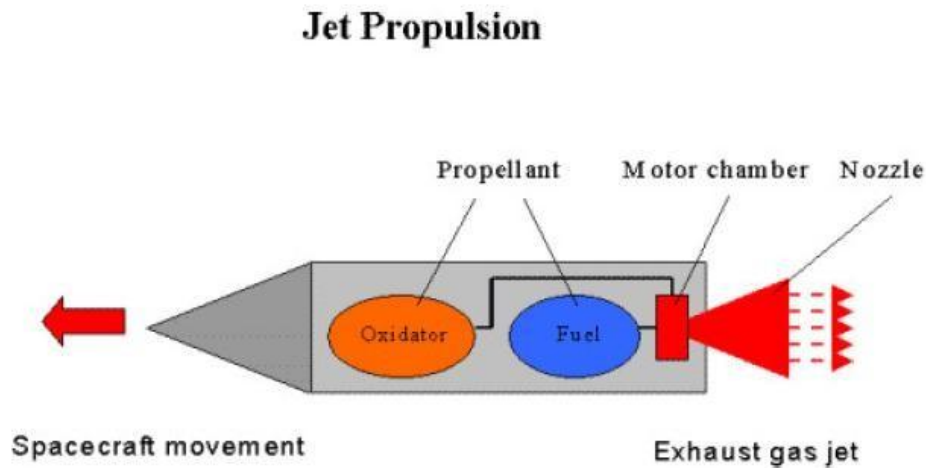


**Figure 3.13: Chemical propulsion**

It uses two separate propellants, a liquid fuel and liquid oxidizer. These are contained in separate tanks and are mixed only upon injection into the combustion chamber (Fig. 3.13). [4]

- 2) Electrical propulsion uses electric or electromagnetic energy to eject matter at high velocity to produce thrust force. [4]
- 3) Hall Effect thrusters

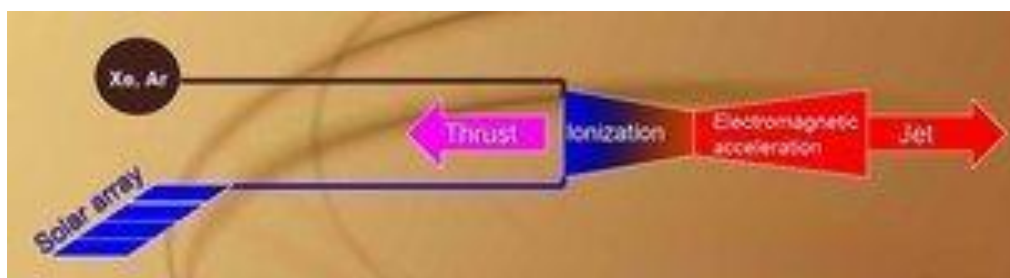


**Figure 3.14: Hall Effect propulsion**

Hall Effect thrusters have been classed as both electrostatic and electromagnetic propulsion systems. An electrostatic field accelerates the ions in the propellant stream but that field is, to a large extent, produced by the actions of plasma electrons interacting with a magnetic field, giving both classes a claim to the technique.

In Hall Effect thrusters, also referred to as closed drift thrusters, a heavy gas, xenon in most implementations to date, is ionized and accelerated by an electric field. An electron current passing through and being impeded by a magnetic field establishes the acceleration field. The processing electrons in this magnetic field follow a closed drift path, giving rise to one of the names for this technique. The flow of the drifting electrons, which is perpendicular to both the applied magnetic field and the current flow in the plasma, is due to the Hall Effect, the source of the other name for this type of thruster (Fig. 3.14). [15]

#### v. **Communication system**

Outside the protection of the Earth's atmosphere, the level of radiation (UV, X-rays, gamma-rays and all sorts of energetic particles) is much higher and more destructive than on the earth. Before they can even begin to operate in space, satellites have to survive the bone-shaking launch. Then the solar panels have to be opened and antennas, which are often stowed to take less space in the launcher, deployed before the satellite enters its operational orbit.

Once in orbit, a satellite usually carries out multiple functions, with different payloads or instruments. It then sends information to a ground station about the condition of its payload and its systems, and it receives instructions back from the ground operators. All this has to work well, with little possibility of recovery, not to mention repair. Apart from very special cases, there is no way backing. [1]

#### **3.6.1.2 Payload**

The main mission is carried out by the primary payload instruments, the imager and the sounder. The imager is a multichannel instrument that senses infrared and visible reflected solar energy from the Earth's surface and atmosphere. The sounder provides data for vertical atmospheric temperature and moisture profiles, surface and cloud top temperature, and ozone distribution. [3]

The meteorological mission needs an imager (camera) as payload.

### **3.7 Example of a meteorological satellite**

NOAA (National Oceanic and Atmospheric Administration) is a three-axis stabilized American spacecraft (Fig. 3.15). It has launched into an 870-km circular, near-polar orbit with an inclination angle of  $98.73^\circ$  to the Equator. The total orbital period will be approximately 102.14 minutes. The sunlight period will average about 72 minutes, and the Earth shadow period will average about 30 minutes. Because the Earth rotates, the satellite observes a different portion of the Earth's surface during each orbit. The nominal orbit is planned to be sun-synchronous, and rotates eastward about the Earth's polar axis  $0.986^\circ$  per day. The precession keeps the satellite in a constant position with reference to the sun for consistent illumination throughout the year. [11]



Figure 3.15: NOAA satellite

### 3.8 Example: DubaiSat-1 orbit specifications

The frame consists of spacecraft (S/C) adaptors, six longerons, rails, inner ring, inner rods and three decks. Six longerons are connected to six rails at the bottom, middle, and top deck. The inner ring provides structure stiffness and stability for DMAC payload. Three S/C adaptors are connected to the shear brackets and mechanically couple the satellite and separation adaptor of the launch vehicle (LV); Dnepr Rocket. Each one of the S/C adaptors has two S/C-based separation sensors and one LV-based separation sensor to monitor separation condition between the satellite and the launch vehicle. The umbilical connector is attached on the lower surface of the bottom deck with its mounting support bracket. The key system features of DubaiSat-1 are introduced in Table 1.

Table 1: DubaiSat-1 key system features.

Parameters	Features
Orbit	Sun-Synchronous Low Earth Orbit
Nominal Altitude	680 km
Inclination	98.13 deg
Mass	~ 200 kg (Bus: 150 kg)
Dimension	Ø 1,200 x 1,200 (mm) - Hexagonal
Attitude Accuracy	0.2° (Full 3-axis stabilized)

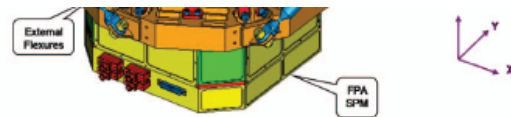


Figure 2: DMAC Mechanical Structure.

The main characteristics of the DMAC are shown in the following table (Table 2).

Table 2: DMAC main system features.

Parameters	Features
Spectral Bands	Pan: 420-720 nm (the Pan and MS data are co-registered) MS1: 420-510 nm (Blue) MS2: 510-580 nm (Green) MS3: 600-720 nm (Red) MS4: 760-890 nm (Near Infrared)
Spatial Resolution	2.5m (Pan), 5m (MS)
Swath Width	20 km
FOR (Field Of Regard)	720 km (this provides an event monitoring capability)
Detector	Charged Coupled Device (CCD)
Quantization	8-bits
Instrument mass, power, and size	32 kg, < 60 W (max), Ø 420 mm x 610 mm

### 3.9 Ground Tracking

FROM ORBIT TO EARTH: MAPPING THE GROUND TRACK

angle  $\psi$  described by the satellite's radius vector since the ascending node crossing (fig. 3.8). The angle  $\psi$  is the difference between  $\theta$ , the true anomaly of  $S_1$ , and  $\omega$ , the orbit's argument of perigee (calculation of  $\theta$  as a function of  $\Delta t$  is discussed on page 15).

Once the coordinates of  $S_1$  have been established, this point on the track can be plotted on a planisphere. The track can in this way be constituted point by point over a complete orbital revolution and then extended in like manner from the next ascending node crossing. These operations are summarised graphically in figure 3.9 for a number of satellite crossing points effected at regular time intervals.

**Impact of orbit modifications**

The ground track being determined by the five orbital elements, it is necessarily affected by changes in any of these, whether intentional or attributable to natural causes (see pages 14-16).

Modifying  $\Omega$ , the right ascension of the ascending node, which is to say nodal precession (see page 14) has the effect of adding the direct or retrograde rotation of the orbital plane

Figure 3.10. Modification of a track by nodal precession. The distance AB between two successive Equator crossings of an ascending track depends solely on the orbital period  $P$ . Nodal precession is left out of account. The latter does however modify distance AB, increasing it if the orbit is direct, decreasing it if it is retrograde. There is no precession at 90° orbital inclination.

Figure 3.9. The track is transferred to a map. The position of the ascending node, which serves as the starting point for the track, is determined by adding the value of  $\Omega$  to the position of the vernal equinox.

From orbit to Earth: mapping the ground track

Transposing the track onto a map

The process required to go from the trajectory of an orbiting satellite to the plotting on a map of the corresponding ground track can be broken down into a series of operations.

The first step is to establish the five orbital elements together with a positioning quantity for the satellite. For the latter it is convenient to take the point in time  $t$  at which the satellite crosses the ascending node  $N$ , which is taken to be the starting point for the track. The starting point is thus on the Equator, its longitude being that of the vernal equinox at  $t$  increased by angle  $\Omega$ , the right ascension of the ascending node.

After a period of time  $\Delta t$  the satellite reaches a position  $S_1$ , corresponding to track position  $s_1$ . The coordinates of this position can be derived from the orbital inclination and the

Figure 3.8. The coordinates of a point on the track. The latitude  $l$  and longitude  $l'$  of point  $P$  are calculated from inclination  $i$  and the angle  $\psi$ , described by the satellite's radius vector since the ascending node crossing  $N$ .

Assuming a fixed Earth:  
 $\sin l = \sin i \sin \psi$   
 $\sin l' = \sin i \cos i \cos \psi$

Assuming a rotating Earth, latitude is the same as for a fixed Earth, while longitude has to be adjusted by the angle through which the Earth has turned during the time,  $t$ , taken by the satellite to travel from  $N$  to  $P$ , i.e.  $360(t/P) \times 15$  (for times in minutes and angles in degrees).

1. As seen from the orbital plane: the satellite takes the same time to go from  $N$  to  $S_1$  from  $S_1$  to  $S_2$ , etc. This time is a function of the angles  $\theta$  and  $\omega$ .

2. As seen from a plane perpendicular to the orbital plane, where the latitudes of the points on the track are seen to vary.

### Ground tracks and orbital cycles

Figure 3.21. Succession of descending tracks over a Landsat-1, -2 and -3 orbital cycle. Above: descending tracks during the first day of the cycle. The distance between the track described in one revolution and the track described in the subsequent revolution is known as the tracking interval. On completion of 14 revolutions, track  $n = 14$  is located to the west of track  $n$  since the combined length of 14 tracking intervals exceeds that of the Equator. Track  $n = 14$  is executed on day two of the cycle. Below: descending tracks over the 18 day orbital cycle. On track  $n = 14$  the descending node pass occurs at a point on the Equator located at distance  $d$  to the west of track  $n$ . This is because 14 tracking intervals exceed by distance  $d$  the length of the Equator. The cumulative effect of these daily offsets over the 18-day cycle is to leave the track on day 18 again coincident with the track on the first day - since  $d$  divides exactly 18 times into tracking interval  $P$ .

40 | GROUND TRACKS

more detailed treatment, in figs. 3.19 and 3.20. The first shows the ground tracks of a satellite in a medium-inclination prograde low Earth orbit - the class of orbit occupied by most manned spacecraft and space stations. The example given here is that of Skylab.

The second represents the ground tracks described by a satellite in retrograde orbit at an altitude of 600 km to 900 km. This class of orbit is typically that of sun-synchronous remote sensing satellites whose tracks are of particular importance since it is these which determine the ground area observed.

Figure 3.19. Tracks described by International Space Station over a 24-hour period. Orbit altitude is 385 km and inclination 51.6°. The orbital period is 92.18 minutes and the distance at the Equator between two successive tracks in the same direction is 2668.4 km.

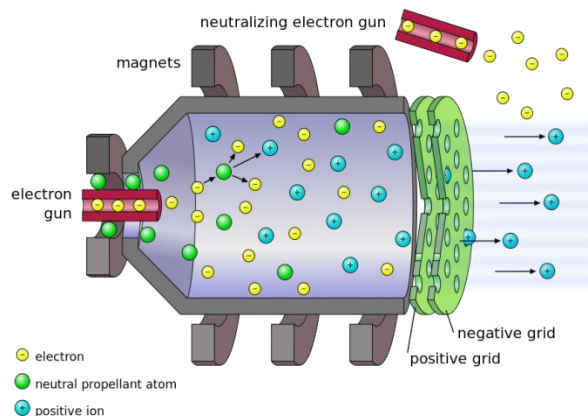
Figure 3.20. Tracks described by HCMM over a 24-hour period. Orbit altitude is 630 km and inclination 97.5°. The orbital period is 97.2 minutes and the distance at the Equator between two successive tracks in the same direction is 2712 km.

### 3.10 Electrostatic Plasma Thrusters

The purpose of this research was finding the best Plasma Thruster for the satellite project in order to mechanically model a prototype of it.

Electrostatic thrusters are a branch of Plasma Thrusters that uses high voltage electric fields to accelerate ions out of the propulsion providing thrust. The core principle of this technology lies in first ionizing the propellant then accelerating it out using an electric field. Many different propulsion systems under this domain were analyzed and each one's adequacy to our project was checked.

- Ion Bombardment



In these types of thrusters Xenon fuel is ionized in a discharge chamber by bombarding it with electrons using an electron gun. The formed plasma (positively charged gas) diffuses into a high-voltage electric field formed between 2 charged gridded plates where it is accelerated to high speeds out of the exhaust. In order to prevent the spacecraft from acquiring a negative net charge (which will block the system), electrons are injected into the exiting plasma in order to neutralize it. [1]

The following types of electrostatic thrusters were also analyzed in detail:

- Colloid ion
- Contact ion
- Field Emission (FEFP)
- Microwave or Radiofrequency ion
- Plasma separator ion
- Radioisotopic ion
- Hall Effect

[1] <http://www.daviddarling.info/encyclopedia/E/electronbomthruster.html>

### 3.11 Electromagnetic propulsion systems

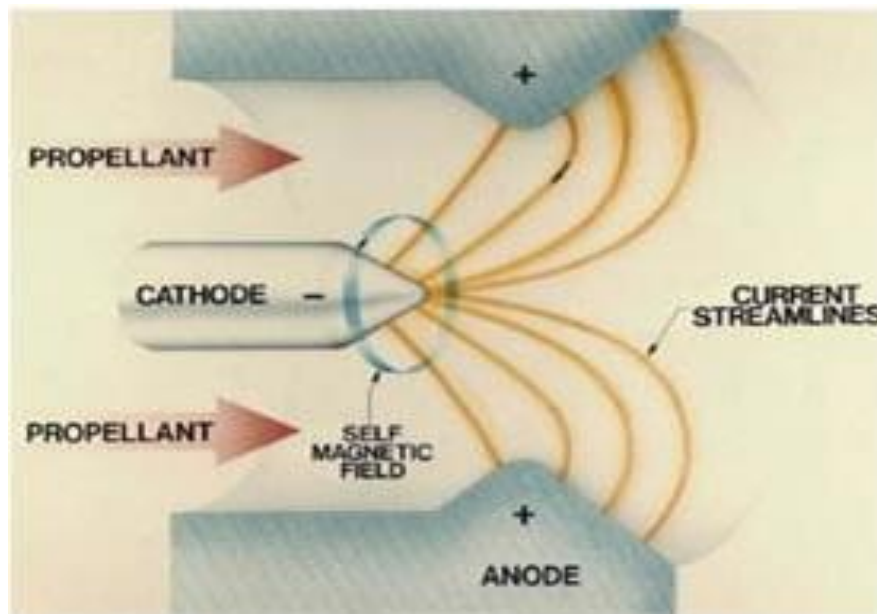
Electromagnetic propulsion technology generally consists of 2 steps:

1. Production of plasma in an ionization chamber
2. Accelerating the plasma to the exhaust velocity by electromagnetic forces

Electromagnetic thrusters have higher efficiencies over their electrostatic counterparts. This is due to the fact that plasma in these thrusters can be brought up to very high temperatures and densities resulting in the ability to confine and direct this plasma. As a result, higher exhaust velocities and more economic propellant usage are achieved.

Electromagnetic technology embodies several propulsion systems each using different techniques and processes. All of these systems were carefully studied and analyzed in order to choose the best system that mechanically fulfills the IAP-satellite project's requirements.

- Magnetoplasmadynamic



This type of thruster consists of a cathode rod centered in the middle and a cylindrical anode that surrounds the cathode. The high-voltage electric field between the anode and the cathode ionizes the fuel injected into the system. The positively charged ions complete the circuit and the resulting current flow induces a magnetic field. The interaction between both magnetic and electric fields produces a Lorentz force that acts on the plasma and accelerates it to high speeds.[1]

Other systems were also analyzed:

- Pulsed plasma
- Helicon plasma
- Inductive pulsed plasma
- Electron-cyclotron-resonance
- Variable specific-impulse plasma

[1] <http://www.daviddarling.info/encyclopedia/M/MPDthruster.html>

## 4 Elements Satellite Bus

### 4.1 Satellite Bus Design Tasks Overview

The architecture of a satellite mission

Design of a satellite mission

Design and planning of a satellite

Design of the energy supply system

Design of the attitude control system

Design of the propulsion system

Performance Evaluation of Propulsion Systems

Description of the Analysis Tool

Design of the telemetry system (radio link)

Design of the on-board data processing system

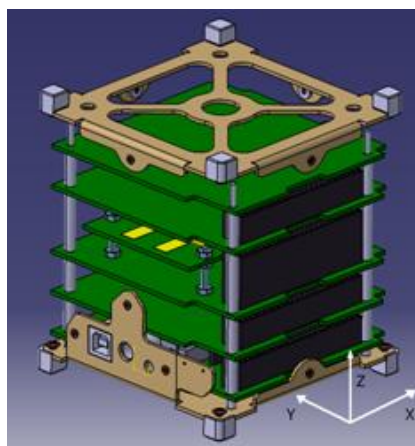
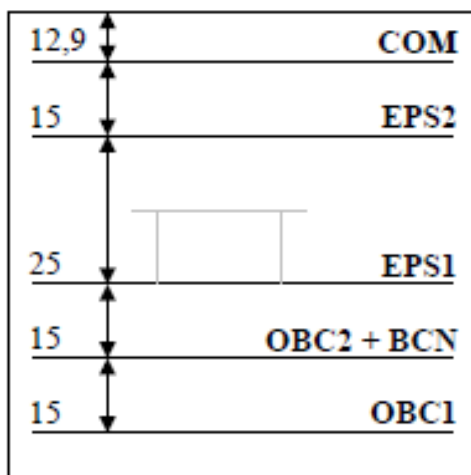
Design of the thermal control system

Design of the structure and mechanisms

Reliability and product assurance

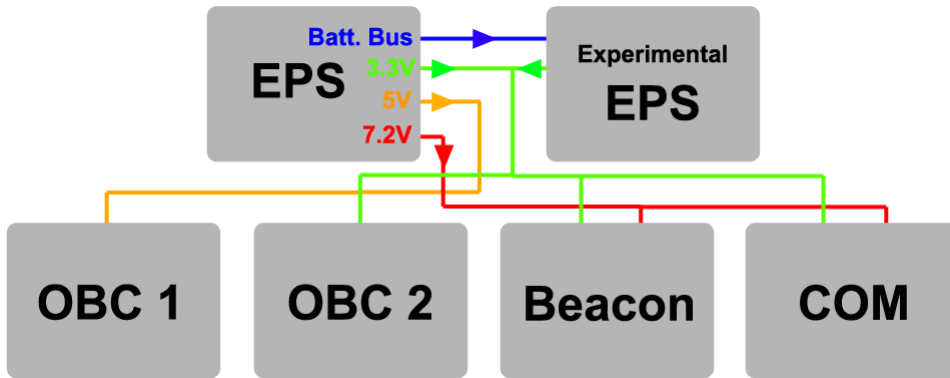
#### 4.1.1 Example: 10 ccm Student Nanosatellite OUFTI-1 of University of Liège

(OUFTI-1 is designed for communications in D-STAR, an amateur-radio communication protocol)

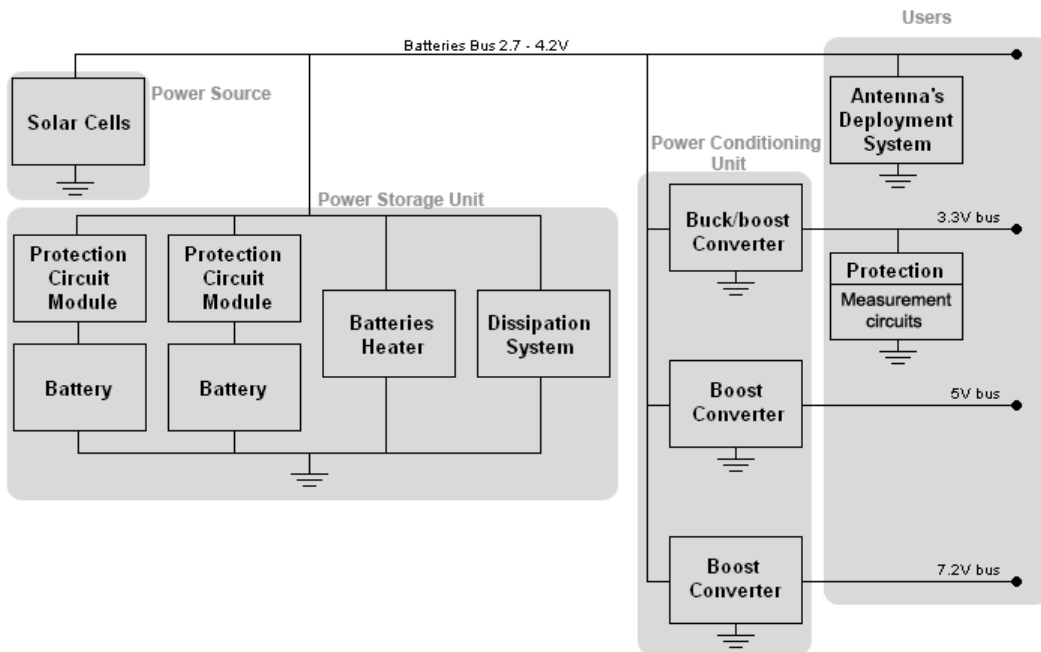


### 4.2 Design of the energy supply system

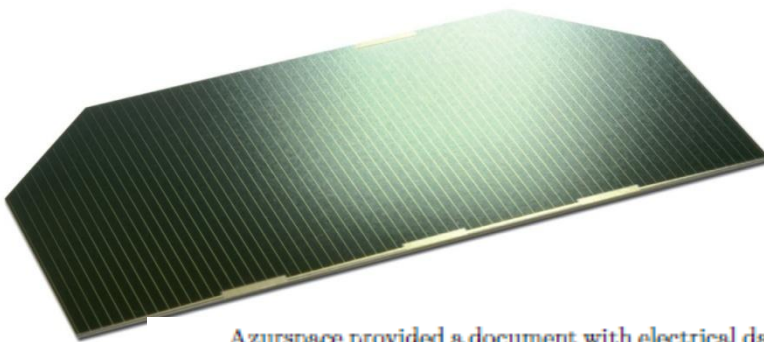
based on: Pierre THIRION, Design and Implementation of On-board Electrical Power Supply of Student Nanosatellite OUFTI-1 of University of Liège (Master Thesis)



OUFTI-1  
subsystems  
and power  
buses



Block  
diagram of  
EPS.



The commercialized model, the “3G - 28%”, has an efficiency of 28% at Begin Of Life (BOL), the dimensions of the solar cells are 80mm x 40mm with cropped corners, for a total surface of 30.18cm<sup>2</sup>.

Azurspace provided a document with electrical data for the 30% cells (table 3.1). The short circuit current is thus 528.15 mA for one cell, and the current at max. power is 513.06mA.

Open Circuit Voltage $V_{OC}[mV]$	2,716
Short Circuit Current $J_{SC}[mA/cm^2]$	17.5
Voltage at max. Power $V_{pmax}[mV]$	2,427
Current at max. Power $J_{pmax}[mA/cm^2]$	17.0
Maximum Power $P_{pmax}[mW/cm^2]$	41
Average Efficiency $\eta_{bare}[\%]$	30.1

Table 3.1: Electrical characteristics of Azurspace 3G - 30% solar cells at 28°C and for the AM0 spectrum [23].

### Electrical Design of EPS

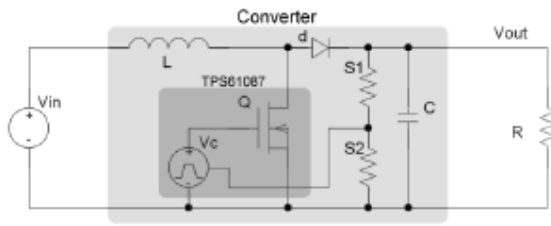


Figure 5.6: Simplified schematics of the 7.2V converter.

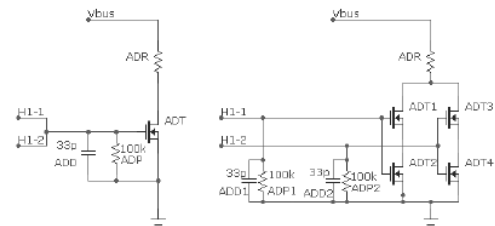


Figure 5.42: Propositions for the antennas deployment system.

## Matlab code for the I-V curves of solar panels

The first function gives the current in one solar cell as a function of the voltage (in V), the insolation G (with  $G_{nom} = 1350W/m^2$  as unity), and the temperature (in C).

function I = Cell\_GaAs(V,G,TaC)

%Code produced by the team from the CubeSat SwissCube

%and modified by Philippe Ledent (OUFTI-1) (september 2008)

% Pierre Thirion (OUFTI-1) (april 2009)

%

%Model of 30% efficiency solar cell from Azurspace : I=f(V,T)

%Use of function : I = Cell\_GaAs(V,G,TaC)

%V = Voltage on cell terminals [V]

%G = relative insolation [-] (G=1 => 1367 W/m^2)

%TaC = temperature of the cell in operation [Celsius]

%Boltzman constant

k = 1.38e-23;

%Electric charge

q = 1.60e-19;

.....

.....

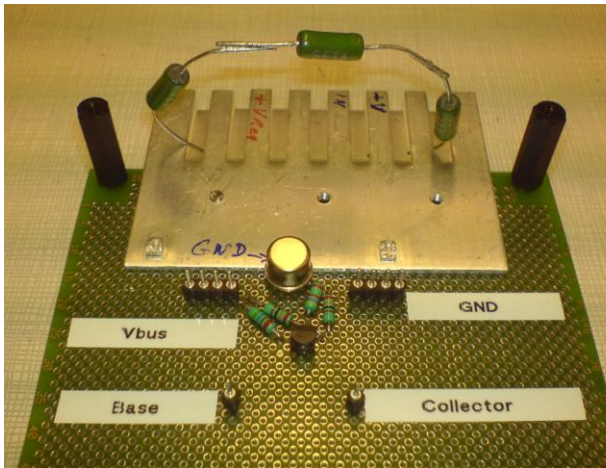


Figure C.1: Prototype of the shunt regulator.

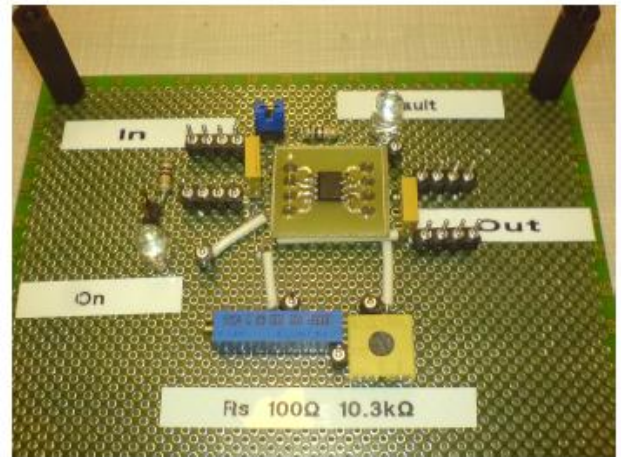
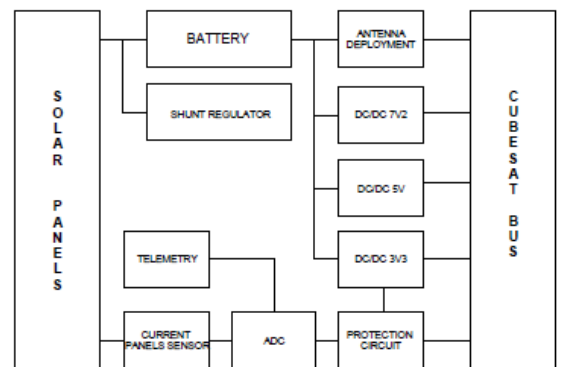


Figure C.2: Prototype of the protection circuit.



Figure C.3: Engineering model of the EPS card.

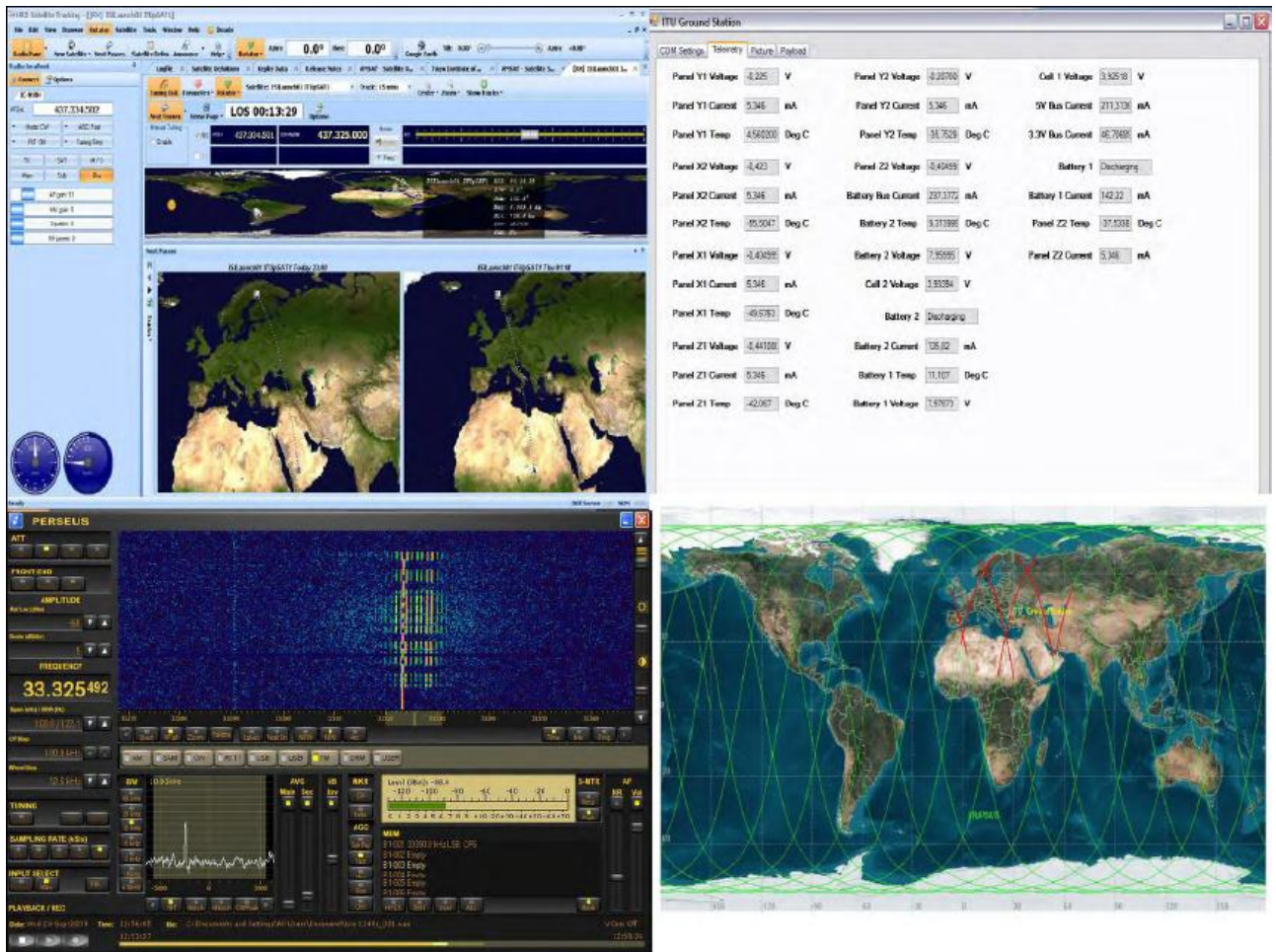
DESIGN TOP LEVEL :



### 4.3 Mission Simulation

From [Inalhan 2009]:





#### 4.4 Payload Integration



Integration des Engineering Modells der Oberstufe

## 5 Candidate Software Tools

### 5.1 Tools

#### 5.1.1 FreeCAD

Computer-aided design (CAD) (Fig. 3.16) is the use of computer systems to assist in the creation, modification, analysis, or optimization of a design. CAD software is used to increase the productivity of the designer, improve the quality of design, improve communications through documentation, and to create a database for manufacturing. CAD output is often in the form of electronic files for print, machining, or other manufacturing operations. [9]

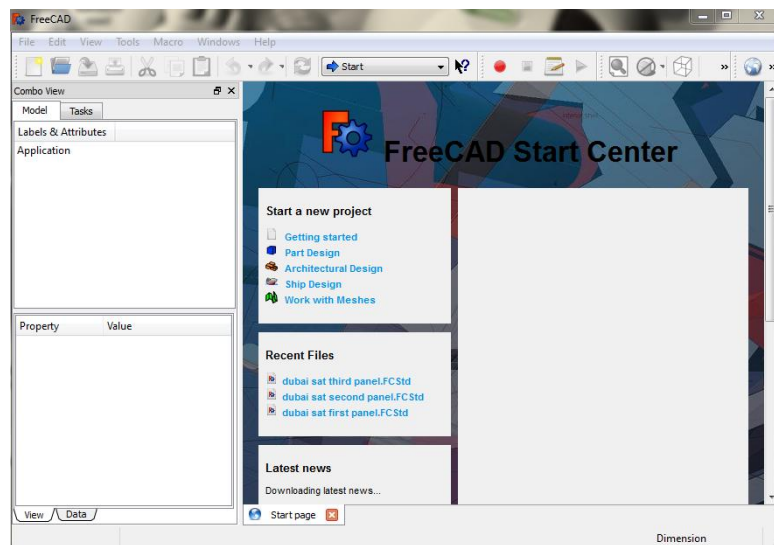


Figure 5.1: Window of FreeCAD

#### 5.1.2 Scilab/Scicos

The software used in this project is scilab/Scicos (ubuntu version).

Scilab is a free open-source software package for scientific computation. It includes hundreds of general purpose and specialized functions for numerical computation, organized in libraries called toolboxes that cover such areas as simulation, optimization, systems and control, and signal processing. One important Scilab toolbox is Scicos.

Scilab is one of the major open-source alternatives to MATLAB. It is similar enough to MATLAB, and Scicos is the open source equivalent to Simulink from the MathWorks. [16]

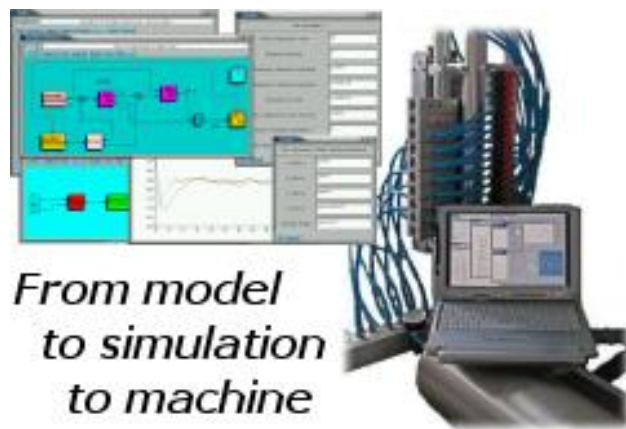
Scicos is a scilab toolbox for modeling and simulating dynamical systems. It is particularly useful for modeling systems where continuous-time and discrete time components are disconnected.

The graphic editor of the toolbox Scicos allows the user to describe his dynamic system in a completely modular way. One of the basic module from which scicos diagram is constructed is the block. A block in Scicos defines an operation that can evolve continuously or discretely in time. By interconnecting blocks with links, the user can construct his algorithm. A large number of mostly used blocks are saved in palettes, these blocks provide elementary operations needed to construct models diagram. [29]

### 5.1.2.1 Scicos

From [www.scicos.org](http://www.scicos.org) :

Scicos: Block diagram modeler/simulator



**Scicos** is a graphical dynamical system modeler and simulator developed in the Metalau project at [INRIA, Paris-Rocquencourt center](http://www.inria.fr). With **Scicos**, user can create block diagrams to model and simulate the dynamics of hybrid dynamical systems and compile models into executable code. **Scicos** is used for signal processing, systems control, queuing systems, and to study physical and biological systems. New extensions allow generation of component based modeling of electrical and hydraulic circuits using the [Modelica](http://www.modelica.org) language.

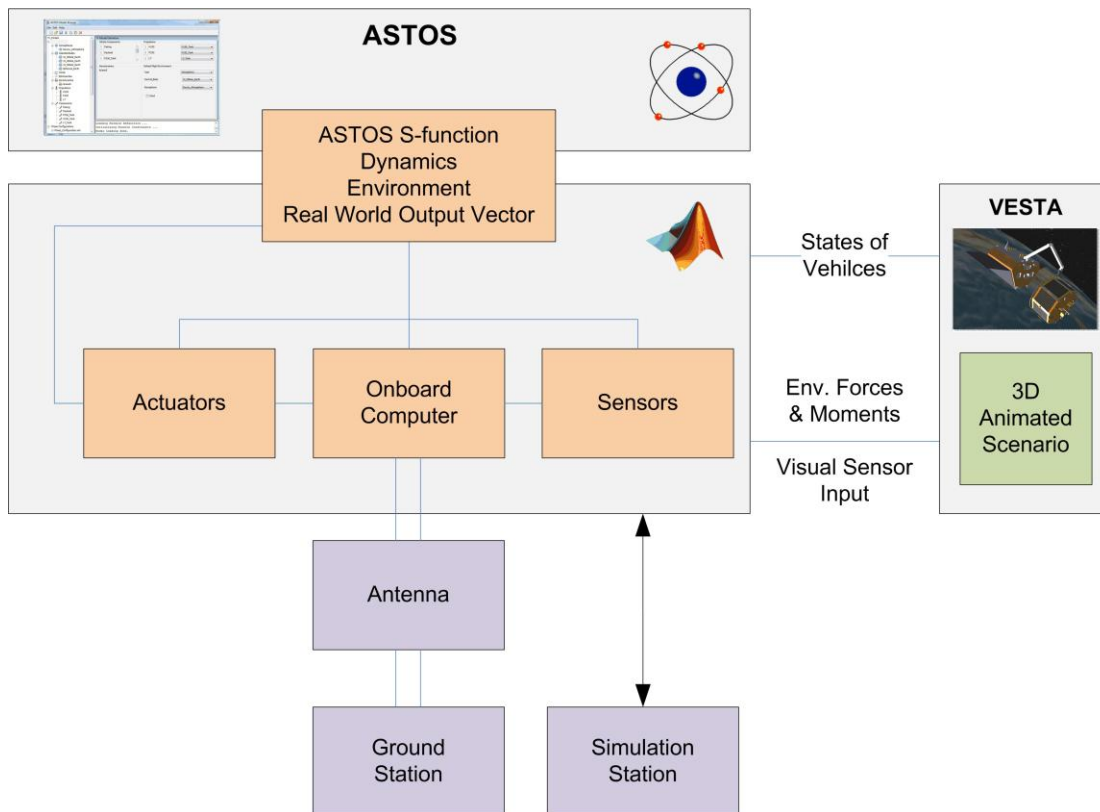
**With Scicos you can:**

- Graphically model, compile, and simulate dynamical systems
- Combine continuous and discrete-time behaviors in the same model
- Select model elements from [Palettes](#) of standard blocks
- Program new blocks in C, Fortran, or Scilab Language
- Run simulations in batch mode from Scilab environment
- Generate C code from Scicos model using a *Code Generator*
- Run simulations in real time with and real devices using [Scicos-HIL](#)
- Generate *hard real-time* control executables with [Scicos-RTAI](#) and [Scicos-FLEX](#)
- Use [implicit blocks](#) developed in the Modelica language.
- Discover new Scicos capability using additional toolboxes.

## 5.2 Possible Development Environment for Communication and Control

Communication and Control shall be developed under Matlab/Simulink or Octave or Scilab/Scicos. Then there must be generated autocode, which has to be put on a suitable HW.

### 5.3 NearSpacecraft Simulator Development



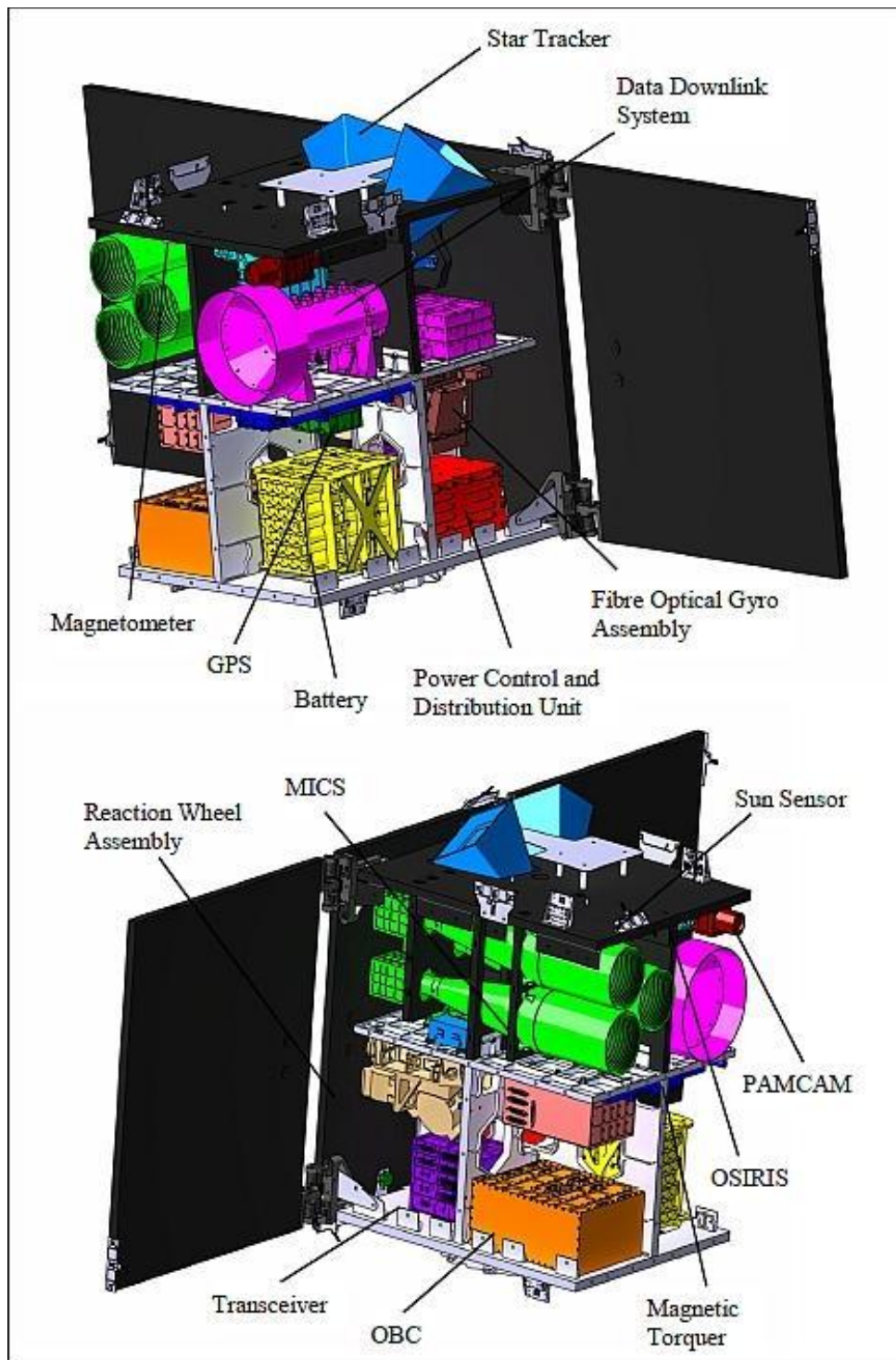
The tool SRSIM is a multi-purpose spacecraft simulation test bench, employed primarily to validate Guidance, Navigation and Control System designs for the various near space missions the IFR (University of Stuttgart) is involved in. The Matlab/Simulink based SRSIM is a six degree of freedom space dynamics simulator including advanced modeling of the space environment through the ASTOS software package. This allows to precisely include effects such as solar radiation pressure, atmospheric drag and magnetic field interactions. In addition, it includes an advance visualization environment called VESTA, that is also responsible for the calculations of any surface-related disturbances and provides input to optical sensors such as Navigation Cameras and Star Trackers.

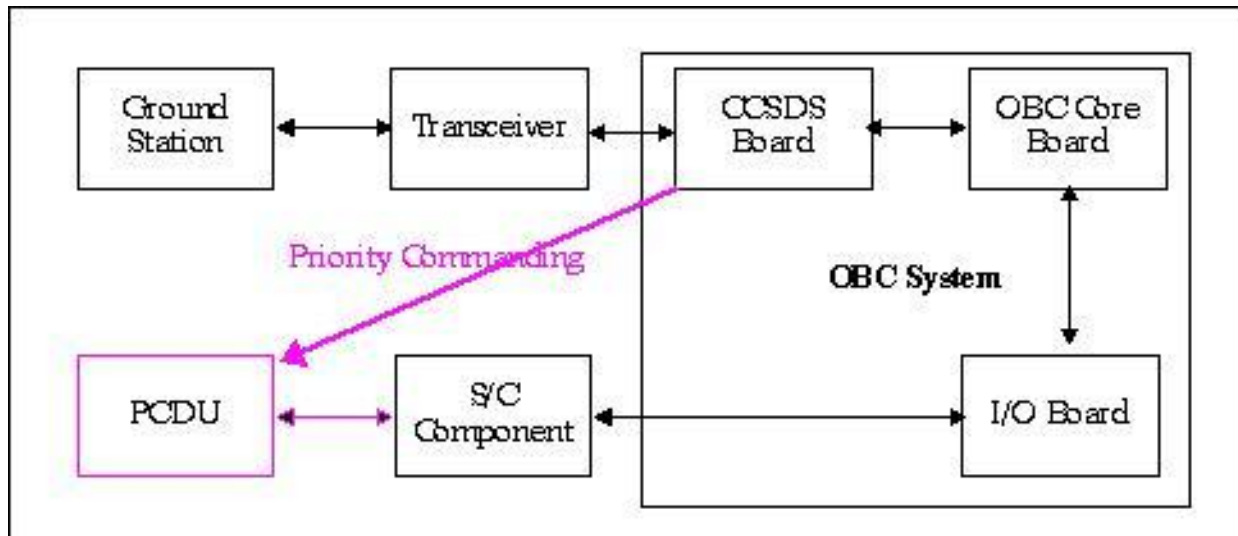
## 6 Example Satellite Systems

### 6.1 Flying Laptop Example, Stuttgart University, Germany



CAD model of satellite: Flying Laptop, Stuttgart University, Germany





### 6.1.1 Star tracker system<sup>2</sup>

The star tracker system is employed in FLP to obtain the  $\_ne$  attitude knowledge. The selected sensor is the micro-Advanced Stellar Compass ( $\_ASC$ ) developed by the Technical University of Denmark (DTU). The  $\_ASC$  is the latest generation of the Advanced Stellar Compass (ASC) which was used in not less than 15 di\_erent projects carried out by NASA, ESA, CNES, DLR and other leading space agencies. The  $\_ASC$  is light in weight is more suitable for the small and micro-satellites.

The Star Tracker System of Flying Laptop consists of two camera head units (CHU), one micro-data Processing Unit ( $\_DPU$ ), and two ba\_es as shown in the Figure 3.18. Two CHUs are included in this design to avoid the Star Tracker blinding and to allow a single failure in this system. The  $\_DPU$  could drive up to 4 CHUs and its electronics is fully redundant. The  $\_DPU$  uses 486 microprocessor to process the optical data acquired by CHU. It is equipped with 64 kB PROM, 8 MB  $\_ash$  and 8 MB RAM. During normal operation, the  $\_DPU$  creates a digital image of the acquired analogue data received from the CHUs every 0.5 s and stores it in the internal RAM. In further computing, the lens distortion is compensated and the image is adjusted for adequately bright objects. The amount of bright objects that are found in an image can be influenced by varying a software

## 6.2 Göktürk project<sup>3</sup>

Göktürk – Project of Reconnaissance and Surveillance Satellite System

Developments in Space Technologies and TAF Satellite Need, as well as the developments experienced with regard to space since 1970s grew in 1990s and led to the emergence of new trends; visual satellites, in particular, became a part of our lives. Extension of usage area of visual satellites, and rise of the benefits gained thanks to innovations in technology have

<sup>2</sup> From [Yassir 2010]

<sup>3</sup> last update: 2011, taken from homepage of Turkish Airforces

made the necessity of such systems in terms of military indisputable. Within this framework, TURAF initiated studies towards having satellite systems, so that TAF can take its part within this historical evolution process. In order to determine the technical specifications of the electro optical reconnaissance and surveillance satellite foreseen to be acquired in the first phase, satellite image requirements of TAF have been examined and the Air Force Command triggered the Project of Reconnaissance and Surveillance System, in the wake of the evaluations carried out.



### Project Description

Within the scope of the Reconnaissance and Surveillance Satellite System named as GÖKTÜRK; a satellite which will be deployed on the low earth orbit (650-700 km) and which carries a very high-resolution Electro optical (E-O) camera and a fixed and mobile satellite earth station to form the earth section of the system will be obtained, with a view to satisfy the satellite image need of TAF for target intelligence, without any territorial water and air space restrictions and in daytime and under favorable weather conditions. In addition thereto, a Satellite Assembly Integration and Test (SAIT) center will be established within the scope of the project.

### Technical specifications of Göktürk Project:

1. **Electro optical camera system** on the satellite will be able to take 4-band color and black-white images.
2. In order to make the best of sunlight, the satellite will be deployed on the **low orbit** (at 650-700 km altitude) compatible with the circular sun.
3. It will have imaging capabilities in **spot, stereo, stripe and wide-area modes**.
4. Communication can be established with the satellite, by means of the earth station based in Ankara, and the images taken by the satellite when it is out of the communication cone will be stored to be transferred to the earth station afterwards.
5. In line with the orbit properties, images will be acquired across the world via satellite. On the orbit, a cycle of the satellite is approximately 98 minutes and it will complete 14 cycles per day around the world.

### Earth Station

The following functions are intended to be created in the earth station to be built within the scope of the project;

6. Satellite command control,
7. Satellite tasking and image downloading,
8. Image processing,
9. Planning image requests, archive management and image distribution.

It is further intended that the Satellite Earth Station will have an expansion potential to support operation of the satellites that will take part in the future within the reconnaissance and surveillance satellite system architecture.

**Usage Concept**

Reconnaissance and Surveillance Satellite System will be used in line with the needs of TAF; in peace, crisis and war. In addition, meeting possible satellite image demands of Public Institutions and fulfilling possible image requests of friendly and allied countries within the scope of peacekeeping operation and/or antiterrorism are further projected.

**Activity Calendar**

The agreement concerning the project, procurement activities of which were initiated within the Undersecretariat for Defense Industries (UDI) in 2005, was executed on 16 July 2009. The satellite is envisaged to be placed into the orbit in 2013. With the reconnaissance and surveillance satellite system added in the inventory, the reconnaissance architecture will have gained substantial system ability and in the future, efficient imagery intelligence production ability will be obtained by using satellite images together with reconnaissance aircraft and unmanned aerial vehicles.

**6.3 DubaiSat-1**

The frame consists of spacecraft (S/C) adaptors, six longerons, rails, inner ring, inner rods and three decks. Six longerons are connected to six rails at the bottom, middle, and top deck. The inner ring provides structure stiffness and stability for DMAC payload. Three S/C adaptors are connected to the shear brackets and mechanically couple the satellite and separation adaptor of the launch vehicle (LV); Dnepr Rocket. Each one of the S/C adaptors has two S/C-based separation sensors and one LV-based separation sensor to monitor separation condition between the satellite and the launch vehicle. The umbilical connector is attached on the lower surface of the bottom deck with its mounting support bracket. The key system features of DubaiSat-1 are introduced in Table 1.

**Table 1: DubaiSat-1 key system features.**

Parameters	Features
Orbit	Sun-Synchronous Low Earth Orbit
Nominal Altitude	680 km
Inclination	98.13 deg
Mass	~ 200 kg (Bus: 150 kg)
Dimension	Ø 1,200 x 1,200 (mm) - Hexagonal
Attitude Accuracy	0.2° (Full 3-axis stabilized)

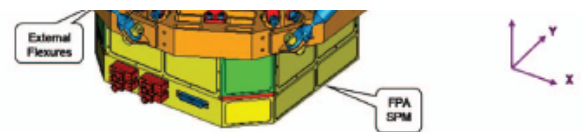


**Figure 2: DMAC Mechanical Structure.**

The main characteristics of the DMAC are shown in the following table (Table 2).

**Table 2: DMAC main system features.**

Parameters	Features
Spectral Bands	Pan: 420-720 nm (the Pan and MS data are co-registered) MS1: 420-510 nm (Blue) MS2: 510-580 nm (Green) MS3: 600-720 nm (Red) MS4: 760-890 nm (Near Infrared)
Spatial Resolution	2.5m (Pan), 5m (MS)
Swath Width	20 km
FOR (Field Of Regard)	720 km (this provides an event monitoring capability)
Detector	Charged Coupled Device (CCD)
Quantization	8-bits
Instrument mass, power, and size	32 kg, < 60 W (max), Ø 420 mm x 610 mm

**6.4 Low Orbit Satellites at very low altitude**

[https://www.quora.com/Which-satellite-occupies-the-lowest-earth-orbit-and-at-what-altitude?redirected\\_qid=1431376:](https://www.quora.com/Which-satellite-occupies-the-lowest-earth-orbit-and-at-what-altitude?redirected_qid=1431376)

The lowest that I know of was KH7-16, with a perigee of 92 km and an apogee of 155 km, for a semi-major axis of 123 km.

[https://www.n2yo.com/satellite/?s=41475:](https://www.n2yo.com/satellite/?s=41475)

**CADRE (41475U)**, CADRE is classified as [Amateur radio](#)

**NORAD ID:** 41475 ⓘ

**Int'l Code:** 1998-067HV ⓘ

**Perigee:** 270.7 km ⓘ

**Apogee:** 279.2 km ⓘ

**Inclination:** 51.6 ° ⓘ

**Period:** 89.9 minutes ⓘ

**Semi major axis:** 6645 km ⓘ

**RCS:** Unknown ⓘ

**Launch date:** [November 20, 1998](#)

**Source:** United States (US)

**Launch site:** TYURATAM MISSILE AND SPACE COMPLEX (TTMTR)

**Uplink (MHz):**

**Downlink (MHz):** 437.485/3404.000

**Beacon (MHz):**

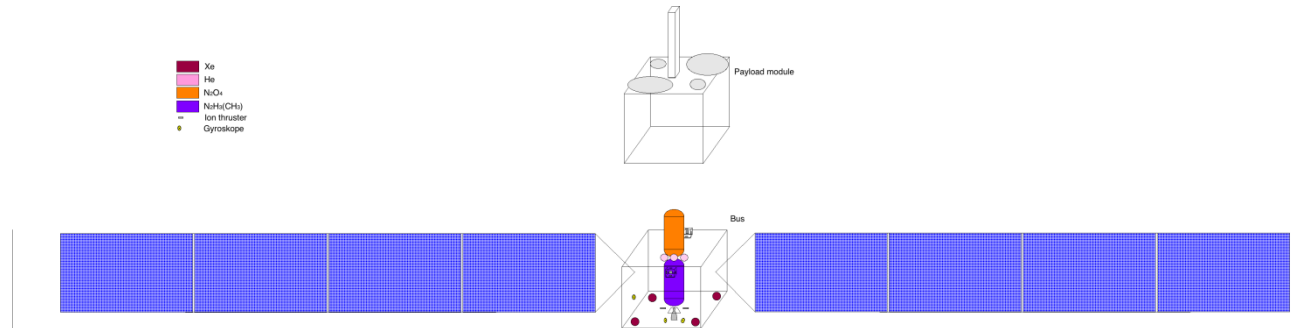
**Mode:** 9600bps GMSK 1Mbit OQPSK

## **Part IIb: System Concept for Satellite Bus**

## 7 System Concept

Many is taken from [Laufer 2009].

### 7.1 Overview



#### 7.1.1 Satellite Bus

The bus necessary for such a satellite consists of the following subsystems: propulsion system, power supply system, structures and mechanisms, thermal control, communication, command and data handling, attitude determination and control.

#### 7.1.2 Electrical Propulsion System

SIMP-LEX is a low mass, robust and easy-to-integrated system consisting of a cluster of four pulsed MPD thrusters using solid propellant (PTFE, Polytetrafluorethylene, a.k.a. Teflon). A pulsed plasma thruster consists of four main parts in general: a capacitor bank, two electrodes, the propellant and a spark plug (see figure 3.4). After the capacitors are charged, the spark plug is triggered forming a short-time arc discharge. This discharge ionizes the solid propellant along its surface closing the main circuit through a plasma sheet formed by the ablated and ionized propellant. The circuit yields a current loop resulting in an induced magnetic field. The magnetic field component perpendicular to the plasma current leads to a Lorentz force and accelerates the plasma creating an impulse. The MPD thrusters provides an average thrust of approx. 1.5 mN each with a specific impulse of 1950 s pulsed at 0.5 Hz and consuming around 120 W per engine. Using a pulsed plasma thruster system as the main engine during the cruise phase demands lifetime tests and investigations especially of the solid propellant feed system (see figure 3.5) since an expected operational lifetime of up to 20,000 hours is required. For this case, the system is designed to feed the propellant from the side using a helical shape with up to two loops on each side for the *LUNAR MISSION BW1* [60].

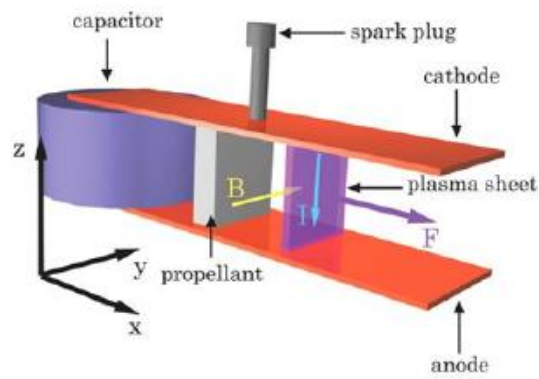


Figure 3.4: Working Principle of SIMP-LEX[60, 48]

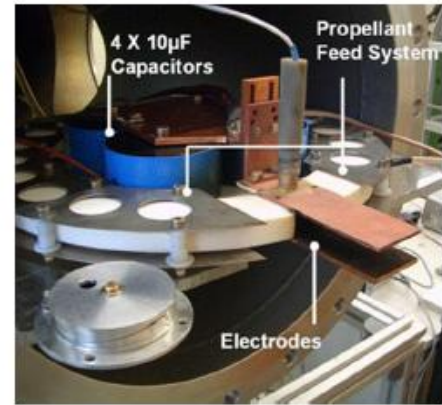


Figure 3.5: Test of SIMP-LEX propellant feed system[60, 48]

From [Nawaz et. al. 2005]:

### I. Introduction

At the *Institut für Raumfahrtssysteme* in Stuttgart, Germany, an instationary pulsed magnetoplasmadynamic thruster (I-MPD, also referred to as pulsed plasma thruster, PPT) is being built. This project was initiated when the *Small Satellite Program* was started at IRS in 2002. This program includes the launch of four satellites, developed at this institute. One of the satellites, BW1, is an all electrical satellite bound to the moon<sup>[1]</sup>. Two types of electric thrusters will provide the  $\Delta v$  necessary. One of them is a thermal arcjet with a thrust level of around 100 mN<sup>[2]</sup>; the other is the I-MPD thruster SIMP-LEX (Stuttgart Instationary Magnetoplasmadynamic Thruster for Lunar Exploration). The first will be used for phases that require higher

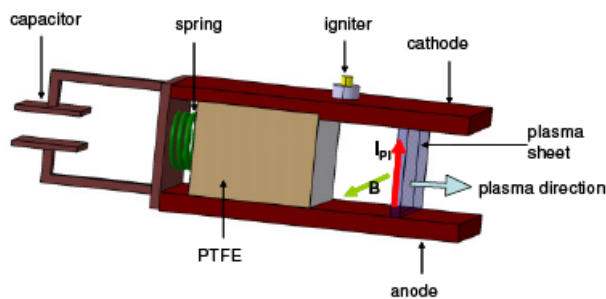


Figure 1. Working Principle of an I-MPD

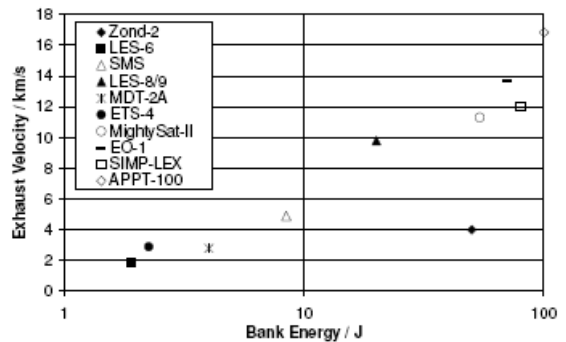


Figure 2. Overview of Exhaust Velocity over Bank Energy for Various I-MPDs<sup>[3,4,5,6]</sup>

thrust levels, such as the ascent phase immediately after separation from launcher, elevating the orbit above the Van Allen belt. A cluster of I-MPDs serve as cruise propulsion system. The I-MPD was chosen as cruise thruster because of its simple design, its reliability as well as its capability to easily adjust to different power levels due to its pulsed energy release without loss of performance. On small satellites, power is usually one of the tightest constraints. Although SIMP-LEX is the first I-MPD thruster in Stuttgart, the development of such a thruster at IRS can draw from over 30 years of expertise in the field of electric propulsion.

In principle, a parallel plate I-MPD consists of two parallel electrode plates between which a solid propellant block (Polytetrafluorethylen, PTFE) is placed, see Fig.1. The capacitor is charged externally and discharges across the surface of the PTFE, forming PTFE-plasma, once the igniter is fired. An electrical circuit with current  $I_{pl}$  and its own magnetic field  $B$  is formed. Consequently, the plasma is accelerated outwards along the electrodes according to the Lorentz law resulting in an impulse bit on the thruster in the opposite direction.

Figure 2 shows an overview of several I-MPD thrusters. Filled icons indicate the mission was already launched. SIMP-LEX will have a bank energy of around 80 J and its expected exhaust velocity is 12 000 m/s. In order to serve as a cruise propulsion system the cluster of I-MPDs will have to provide a total average thrust of 6 mN.

### A. Test Facility Setup

In its final stage, the test facility for the I-MPD will be comprised of three vacuum chambers: one in which the thrust is measured, one for conducting life expectancy tests, and one for optimizing components and geometry of the thruster. Currently, the first two have been setup, where the facility in which the thrust is measured also serves for geometry and current investigations. It is shown in Fig. 3. The pressure in the vacuum chambers reaches about  $10^{-5}$  mbar prior to firing the thruster.

The electronics providing the voltage to the capacitor as well as the voltage peak to the spark plug was developed by ASP GmbH in Friedrichshafen. Its bread board stage allows for different voltage settings for charging the capacitor as well as various pulse frequencies in the automatic firing mode.

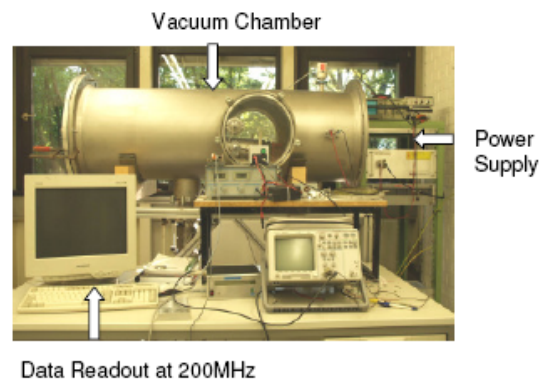


Figure 3. One of the I-MPD Test Facilities

### B. Thruster Setup

The current setup of the I-MPD thruster is shown in the pictures in Fig. 4. It shows its parallel plate geometry, as well as its highly modular setup. This setup allows for easy changes of components and geometry which are currently being optimized. Fig. 4 a) shows the configuration of the capacitor, the copper electrodes and the igniter. The distance  $h$  between the electrodes in Fig. 4 b) can be changed incrementally by using a different set of holes in the red half shell for mounting the electrode plates, as seen in the left picture. The width  $d$  of the electrodes as well as their length can be varied freely. The current values for the thruster can be seen in

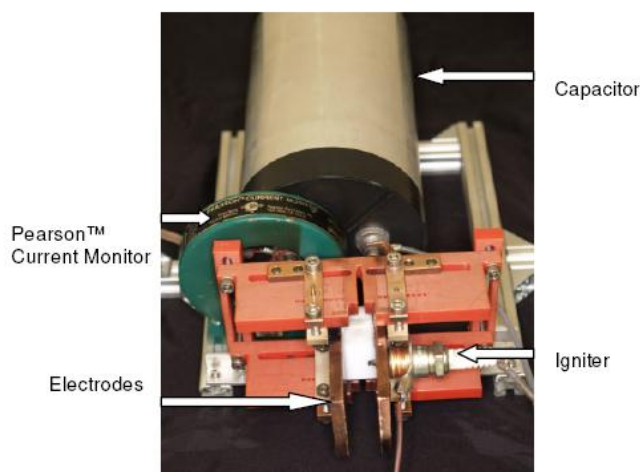


Figure 4a. Current Setup of SIMP-LEX

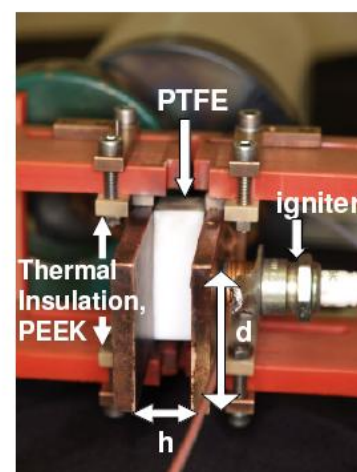


Figure 4b. Close-Up Front View of SIMP-LEX

Table 1. However, they are still subject to optimization.  $L$  is the distance the plasma covers from the propellant surface to the end of the electrodes. First tests at a pulse frequency of 1.2 Hz showed that it is necessary to insulate the PE (Polyethylen) half shells (red) thermally from the plasma and the copper electrodes. This was realized by placing PEEK spaceholders between the electrodes and the half shell and by moving the half shell backwards, away from the plasma.

Capacity	1 x 40 $\mu$ F
Maximum Voltage	2200V
h	20 mm
d	40 mm
L	47 mm

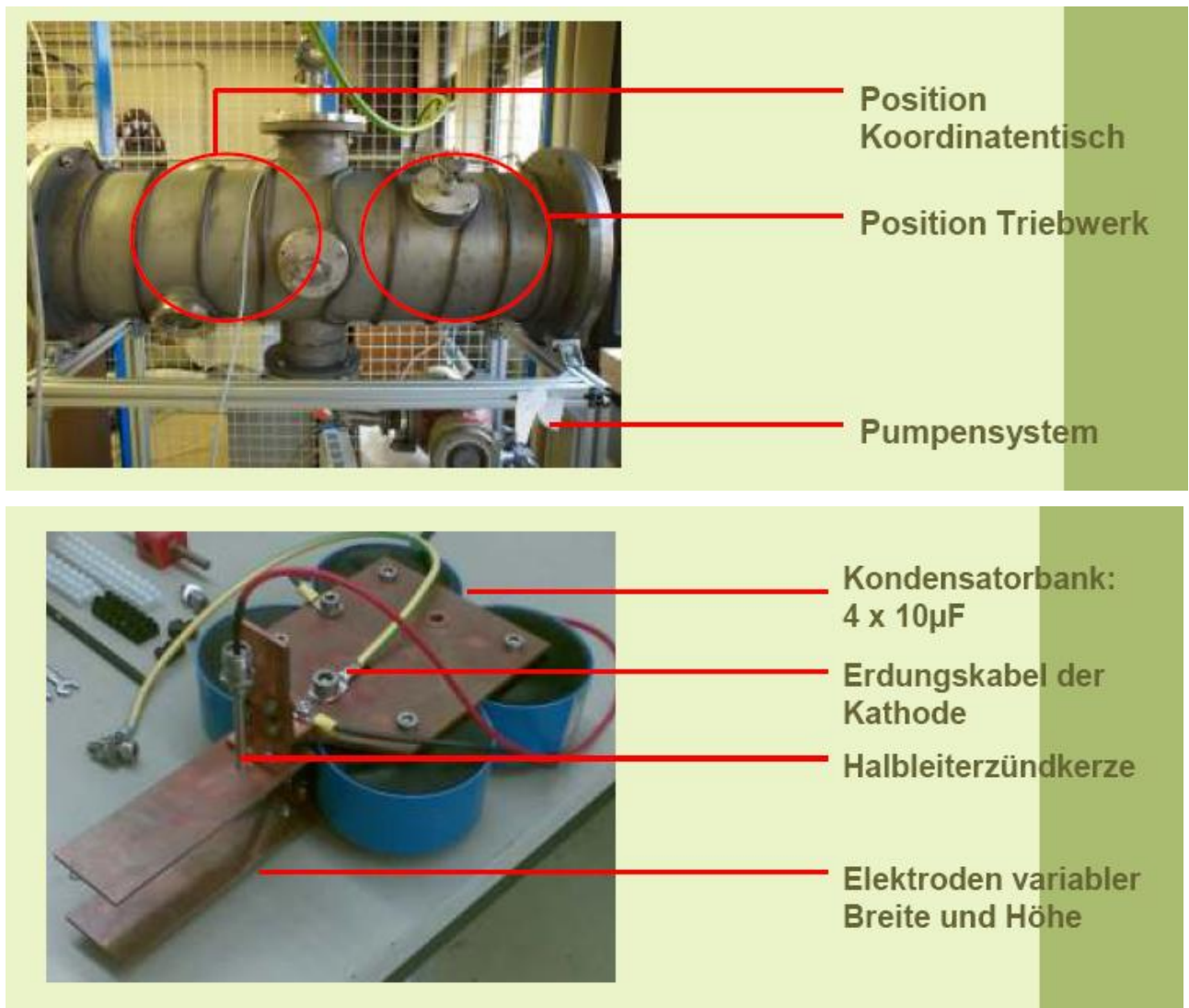
**Table 1. Current I-MPD Design Parameters**

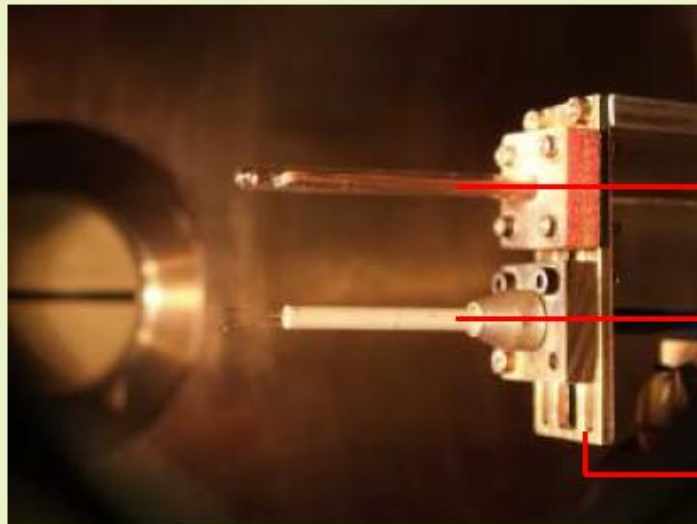
### C. Measurement of Plasma Current and Mass Bit Ablated

Figure 4 also shows the Pearson™ current monitor, placed between the electrodes and the capacitor. It serves as a Rogowski coil and outputs a voltage proportional to the current through the coil.

The mass bit is measured by comparing the weight of the propellant bar before and after at least 150 pulses. The balance used has a precision of 10  $\mu$ g.

From [Böhrk et. al. 2007]:

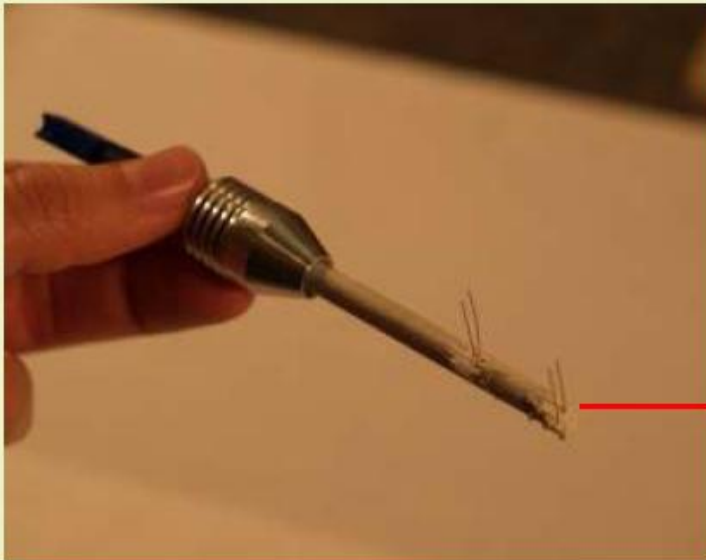




Magnetfeldsonde

Elektrostatische  
Tripelsonde

Sondenhalterung auf  
Koordinatentisch



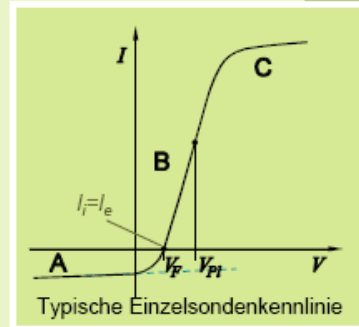
Elektrostatische  
Flugzeitsonde

$$\lambda_e \approx \lambda_i \approx \lambda_{ei} = \frac{16\pi(\epsilon_0 k T_e)^2}{e^4 n_e \ln \Lambda}$$

$$\Lambda = 12\pi \frac{(\epsilon_0 k T_e)^{3/2}}{n_e^{1/2} e^3}$$

$$\lambda_D = \sqrt{\frac{\epsilon_0 k T_e}{e^2 n_e}}$$

$$r_L = \frac{mv_{\perp}}{ZeB}$$

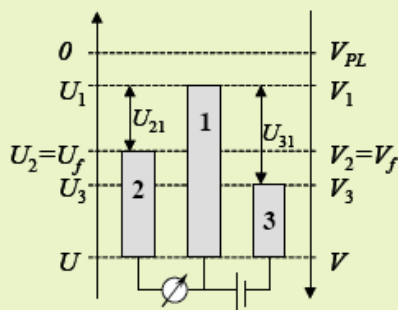


$r_p$	$0,2 \times 10^{-3} \text{m}$	$s$	$2 \times 10^{-3} \text{m}$
$\lambda_D$	$3 \times 10^{-6} \text{m}$	$\lambda_{e,i}$	$1,3 \times 10^{-2} \text{m}$
$m_i$	$5,14 \times 10^{-26} \text{kg}$ [5]	$r_{L,i}$	$3 \times 10^{-2} \text{m}$
		$r_{L,e}$	$1 \times 10^{-6} \text{m}$

- Plasma des I-MPD: dünne ( $r_p > \lambda_D$ ) stoßfreie ( $\lambda_{e,i} > r_p$ ) Raumladungsschicht
- $r_{L,e} < r_p < r_{L,i}$  moderates B-Feld
- Elektronenenergien maxwellverteilt

[5] Scharlemann, C., Investigation of Thrust Mechanisms in a Water fed Pulsed Plasma Thruster, Ph.D.-Thesis, Ohio State University, 2003

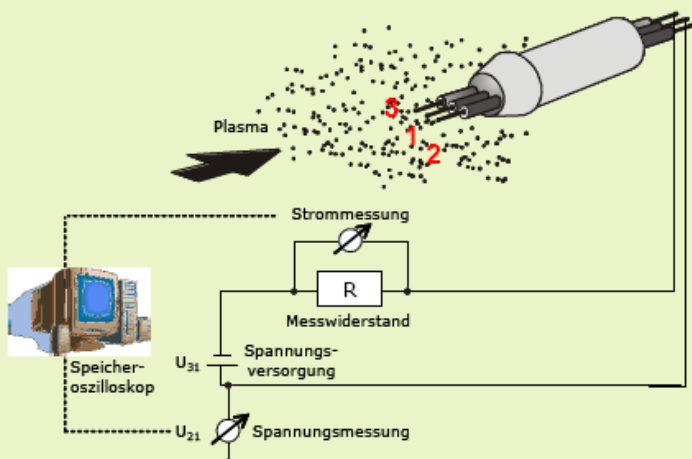
### Elektrostatische Tripelsonde



$$I_1 = A j_i(U_1) - A j_e \exp\left(-\frac{eU_1}{kT_e}\right)$$

$$I_2 = 0 = A j_i(U_2) - A j_e \exp\left(-\frac{eU_2}{kT_e}\right)$$

$$I_3 = I_1 = A j_i(U_3) - A j_e \exp\left(-\frac{eU_3}{kT_e}\right)$$



$$I_1 = A_{j_i}(U_1) - A_{j_e} \exp\left(-\frac{eU_1}{kT_e}\right)$$

$$I_2 \stackrel{0}{=} A_{j_i}(U_2) - A_{j_e} \exp\left(-\frac{eU_2}{kT_e}\right)$$

$$I_3 = I_1 = A_{j_i}(U_3) - A_{j_e} \exp\left(-\frac{eU_3}{kT_e}\right)$$

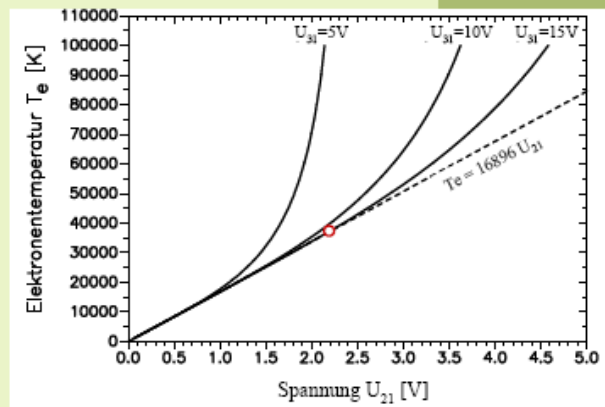
$$\frac{I_1 - I_2}{I_1 - I_3} = \frac{1}{2} = \frac{1 - \exp(-eU_{21}/kT_e)}{1 - \exp(-eU_{31}/kT_e)}$$

$$U_{21} = \frac{kT_e}{e} \left[ \ln 2 - \ln \left( 1 + \exp\left(-\frac{eU_{31}}{kT_e}\right) \right) \right]$$

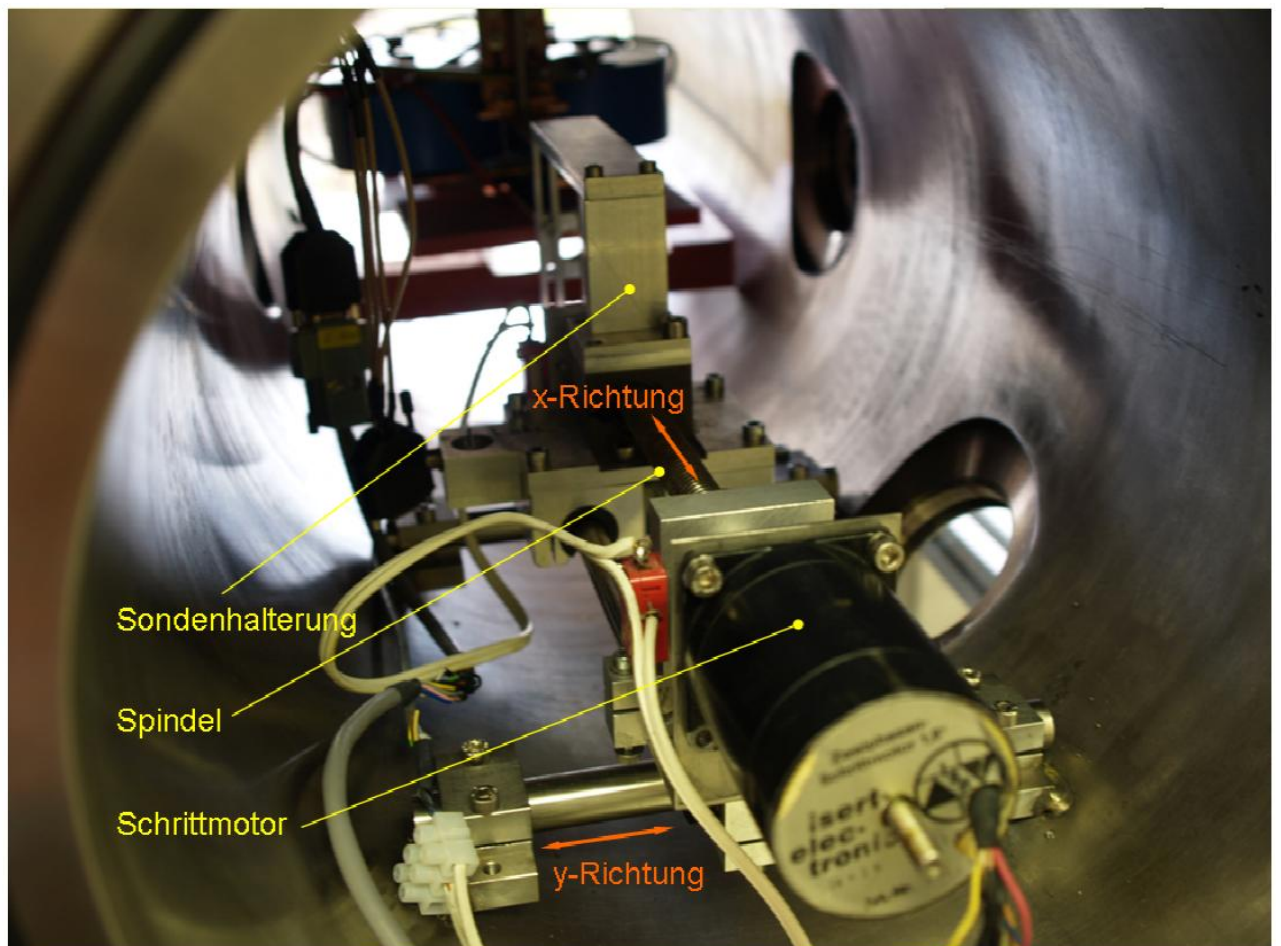
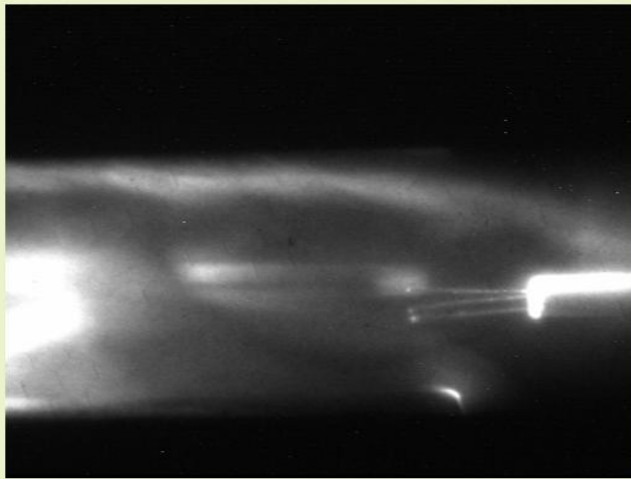
Der Wert der Exponentialfunktion wird für relativ große Doppelsondenspannungen ( $U_{31} \geq 10\text{V}$ ) vernachlässigbar klein. Somit gilt in guter Näherung :

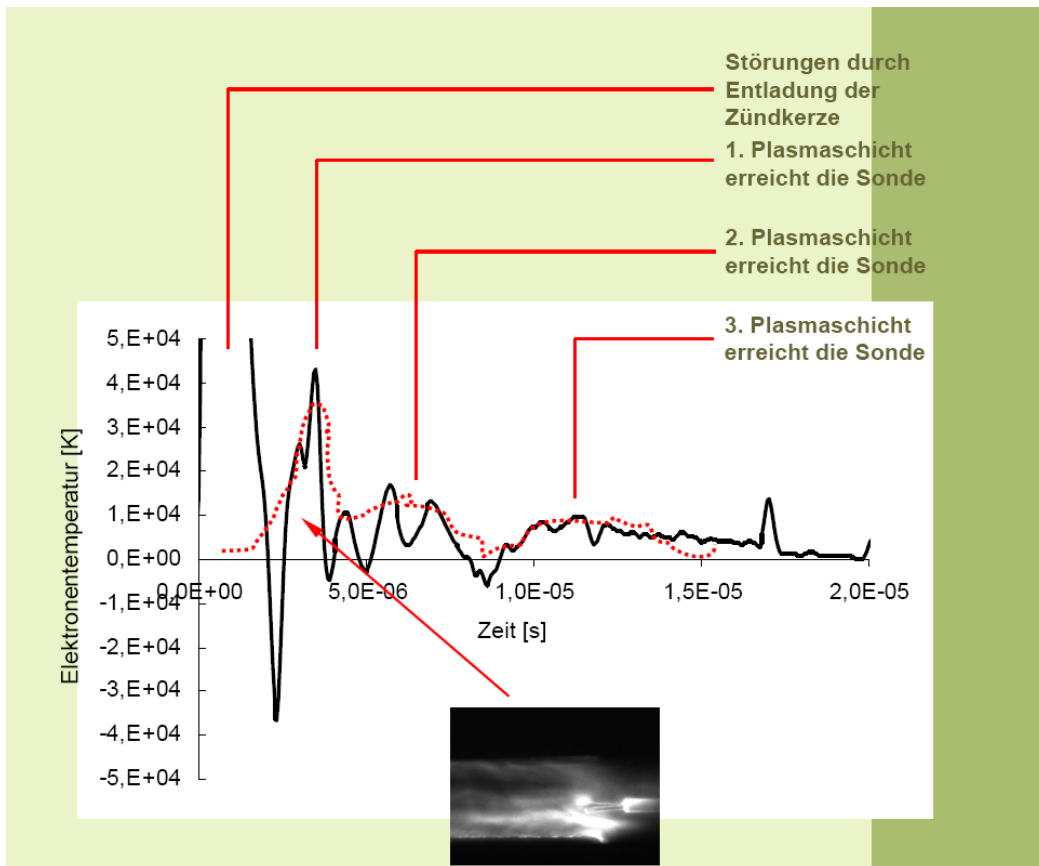
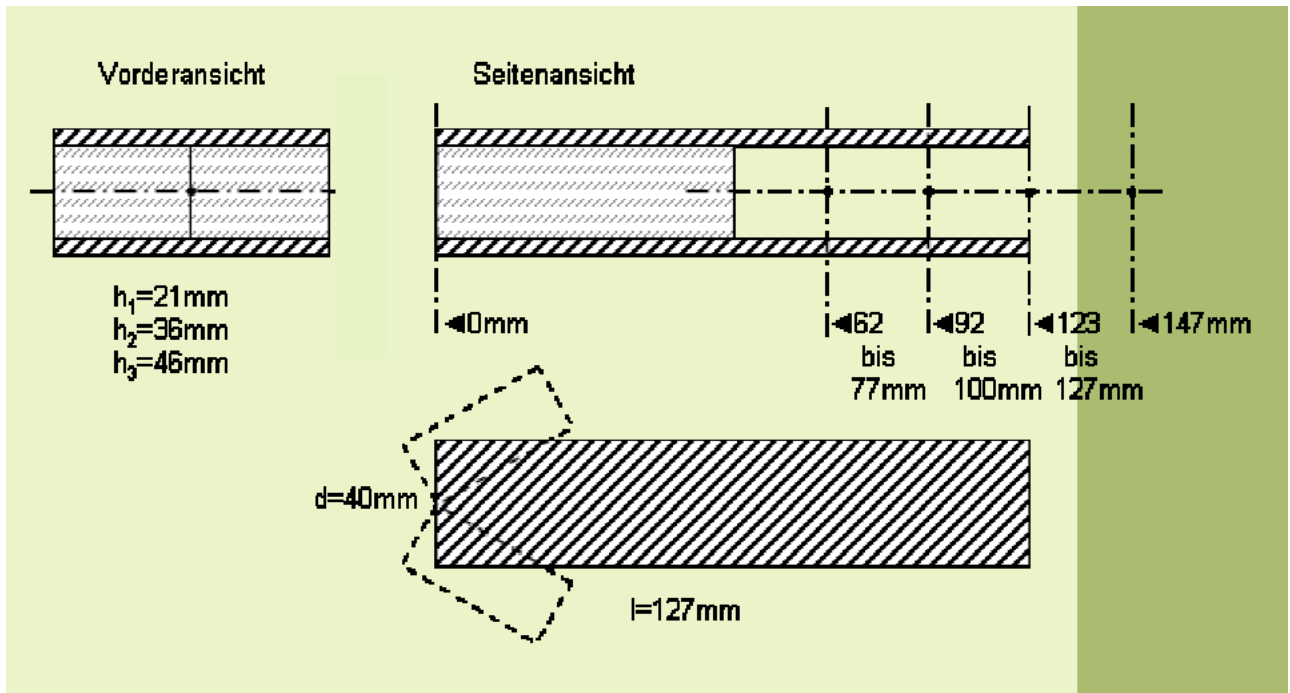
$$T_e = \frac{eU_{21}}{k \ln 2}$$

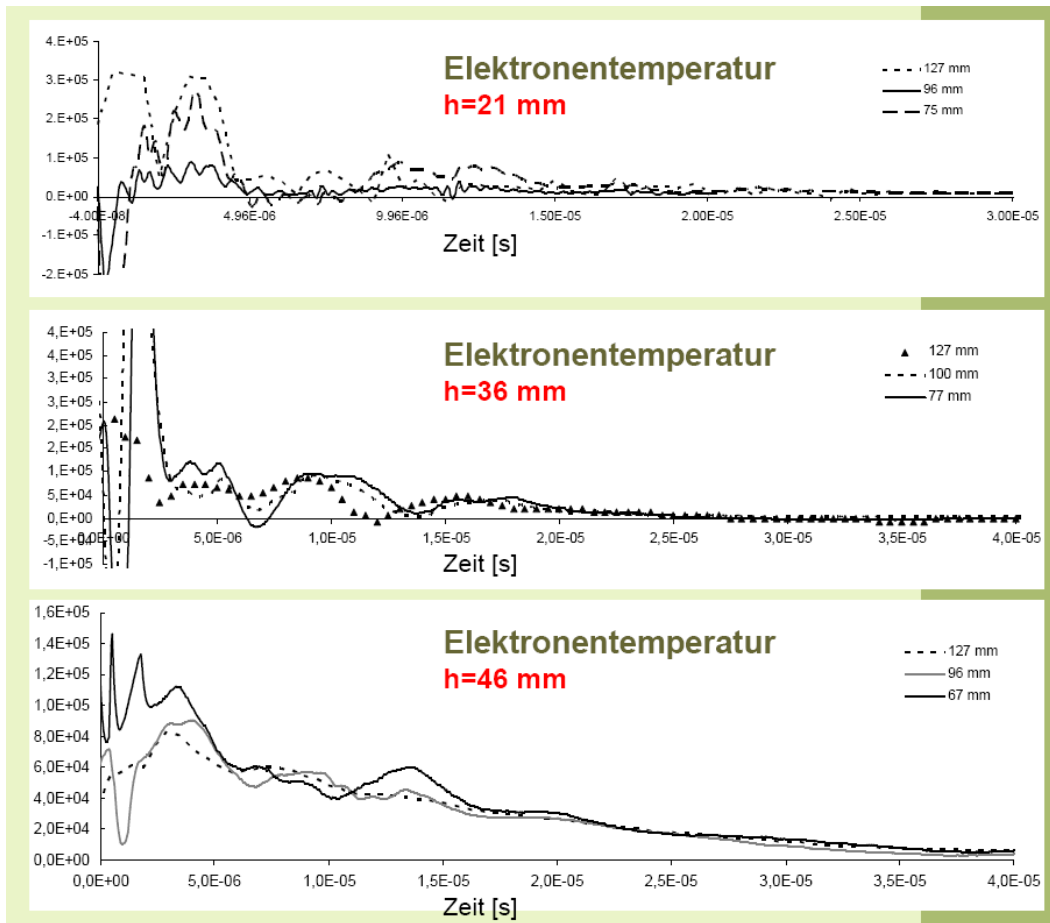
## Elektrostatistische Tripelsonde

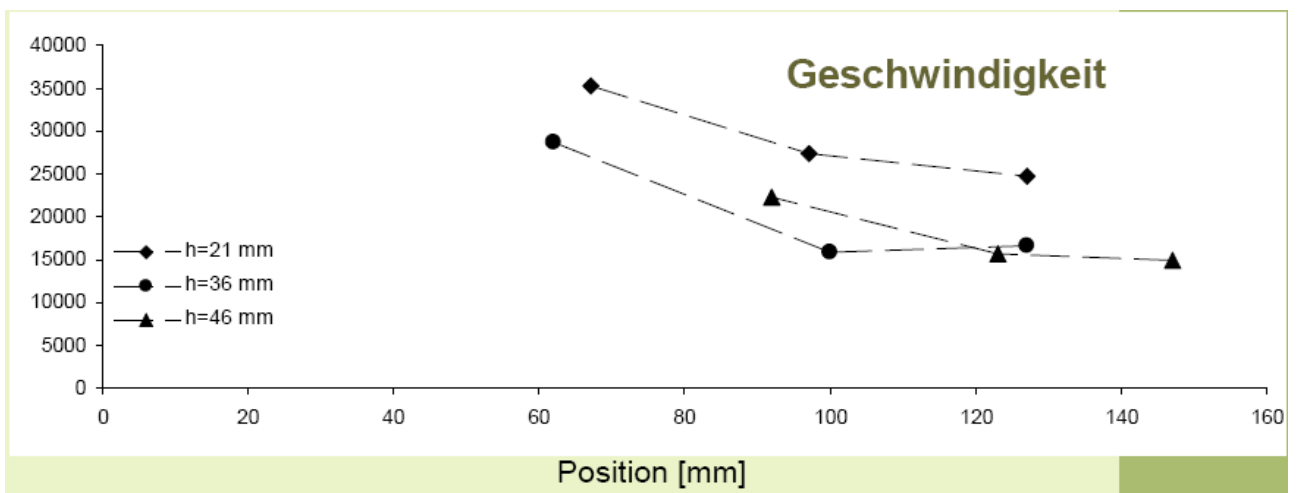
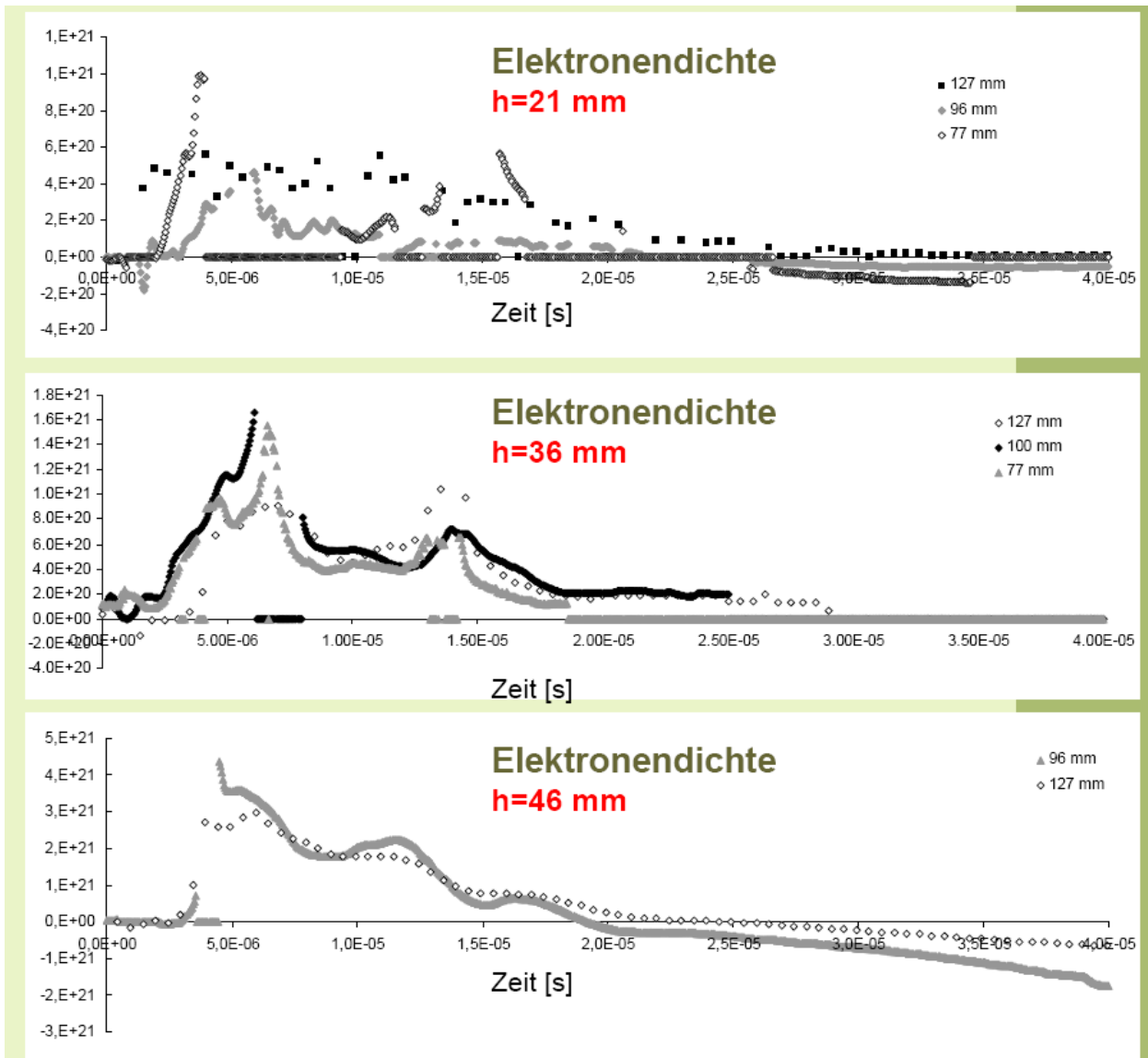


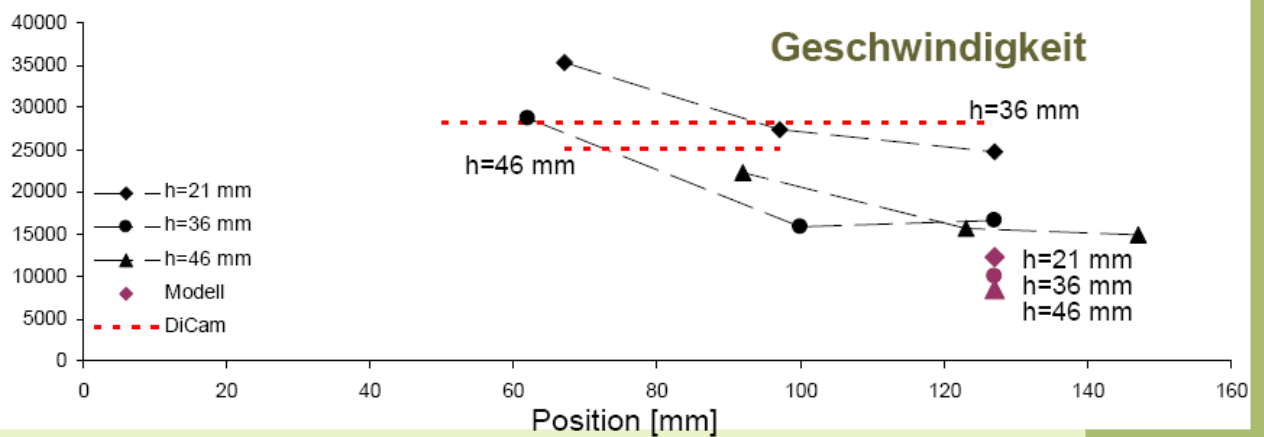
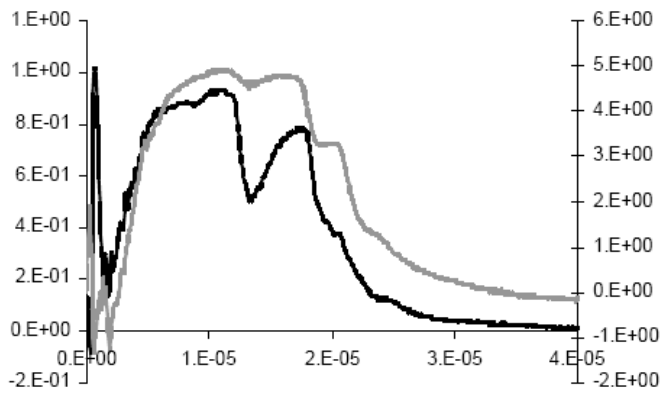
Elektronentemperatur  $T_e$  in Abhängigkeit von  $U_{21}$  und  $U_{31}$











**Elektrostatische Sondenmessungen am I-MPD Simp-LEX erfolgreich durchgeführt**

**Messungen zwischen den Elektroden**

**Vergleichbarkeit mit Ergebnissen aus „Messungen“ mit Hochgeschwindigkeitskamera**

**Höchste Elektronentemperatur bei h=21 mm:  $T_e=20-30\text{eV}$**

**Höchste Elektronendichte bei h=46 mm:  $n_e=4 \times 10^{21}\text{m}^{-3}$**

**Höchste Geschwindigkeit bei h=21 mm:  $v=25-35\text{ km/s}$**

### 7.1.3 Power Supply System

#### The Li-ion advantage

Today's satellite makers are looking for technologies that reduce the overall size of the satellite because of the costs of manufacturing and launching the satellite. A lighter, smaller battery allows more mass/volume on the satellite for more transponders (communication satellites), heavier science components (NASA missions) or lower launch costs. Although Ni-H<sub>2</sub> significantly reduces satellite weight compared to NiCd, lithium-ion (Li-ion) technology reduces weight even more due to its higher specific energy.

Lower thermal dissipation is another source of weight reduction for Li-ion. Combined with higher energy and better charge efficiency, this lets the satellite maker reduce the size of the satellites' solar panels.

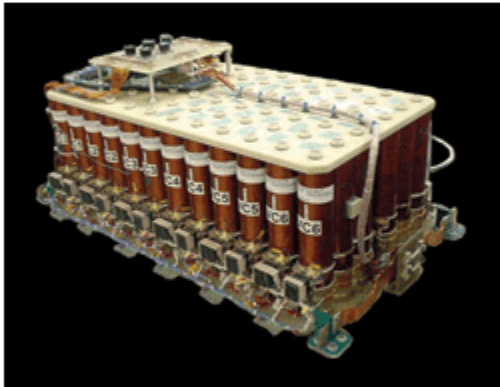


Fig. 2. Soft batteries used in satellites

Li-ion has numerous other advantages over NiCd and Ni-H<sub>2</sub>, including low self-discharge, wide operating temperature, and superior charging efficiency. Li-ion batteries retain about 96% to 98% of their charge even after a month of storage and need no recharging when they are about to be launched, as is the case with Ni-H<sub>2</sub>. Li-ion batteries can operate from 0° to 40°C, and they are easily recharged, further simplifying operation and maintenance. ■

For more on batteries, visit <http://www2.electronicproducts.com/Power.aspx>.

### Base: 10 ccm Student Nanosatellite OUFTI-1 of University of Liège (OUFTI-1 is designed for communications in D-STAR, an amateur-radio communication protocol)

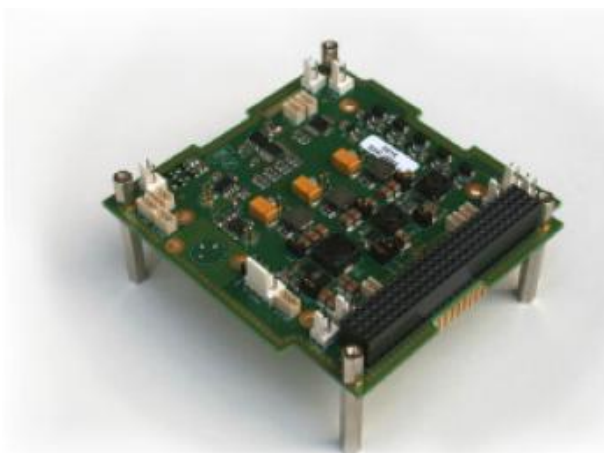
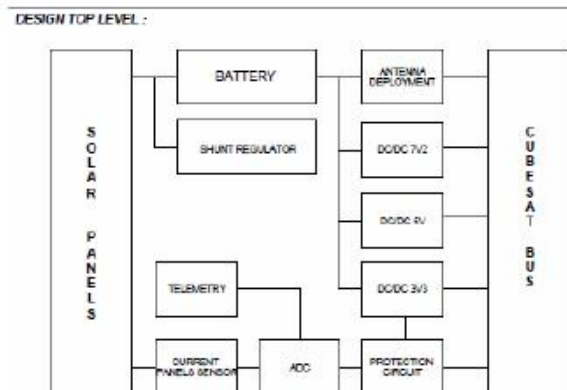


Figure C.3: Engineering model of the EPS card.



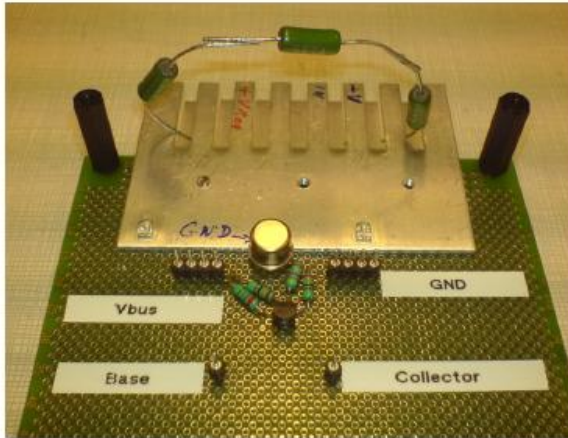


Figure C.1: Prototype of the shunt regulator.

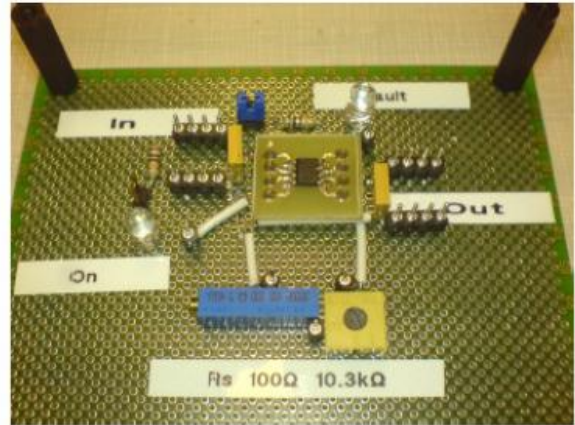


Figure C.2: Prototype of the protection circuit.

Rechargeable Lithium-ion Batteries

QL015KA



PERFORMANCE

- Lithium ion rechargeable cell
- Battery design for long cycle life (>100,000 cycles)

CHEMISTRY

- LNCAO

MAIN APPLICATIONS

- Military
- Aerospace

KEY FEATURES

- Domestic production
- Long LEO and GEO cycle life
- High reliability
- Zero-Volt™

SPECIFICATIONS

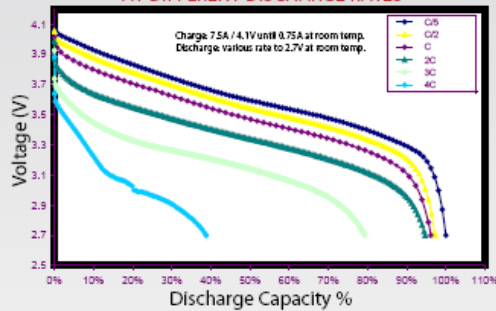
ELECTRICAL CHARACTERISTICS

Nominal Capacity	15 Ah
Nominal Voltage	3.6 V
Maximum Recommended Continuous Discharge Current	1 C
Operating Discharge Temperature	15°C to 35°C

PHYSICAL CHARACTERISTICS

Height	88.3 mm
Width	54.5 mm
Thickness	38.0 mm
Weight	380 g
Volume	182 cc
Gravimetric Energy Density	142 Wh/kg
Volumetric Energy Density	296 Wh/L

CELL LEVEL VOLTAGE CURVES AT DIFFERENT DISCHARGE RATES



QL1820



PERFORMANCE

- Lithium ion rechargeable cell
- Battery design for long cycle life (>20,000 cycles)

CHEMISTRY

- LNCAO

MAIN APPLICATIONS

- Military
- Aerospace

KEY FEATURES

- Domestic production
- Long LEO and GEO cycle life
- High reliability
- Zero-Volt™

[www.quallion.com](http://www.quallion.com)

Quallion LLC | 12744 San Fernando Road | Sylmar, CA 91342 | 818.833.2000

### 7.1.4 Structures and Mechanisms

Initial investigations were performed in preparation for a full scale mock-up and to check the feasibility of the accommodation of all subsystems[66]. Early trade-off evaluations led to structural options to accommodate and position subsystems and components[25]. Further studies refined the selected structural options in preparation for the spacecraft prototype (see figures 3.7 and 3.8)[52].

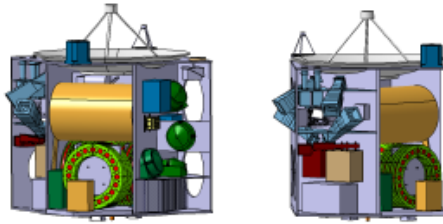


Figure 3.7: Structure option — View on propulsion module[52]      Figure 3.8: Structure option — View on star trackers and other subsystems[52]

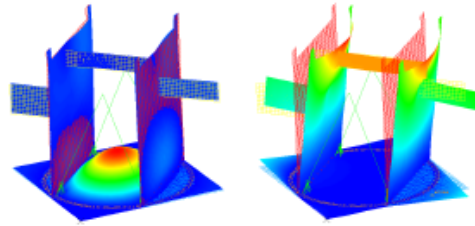
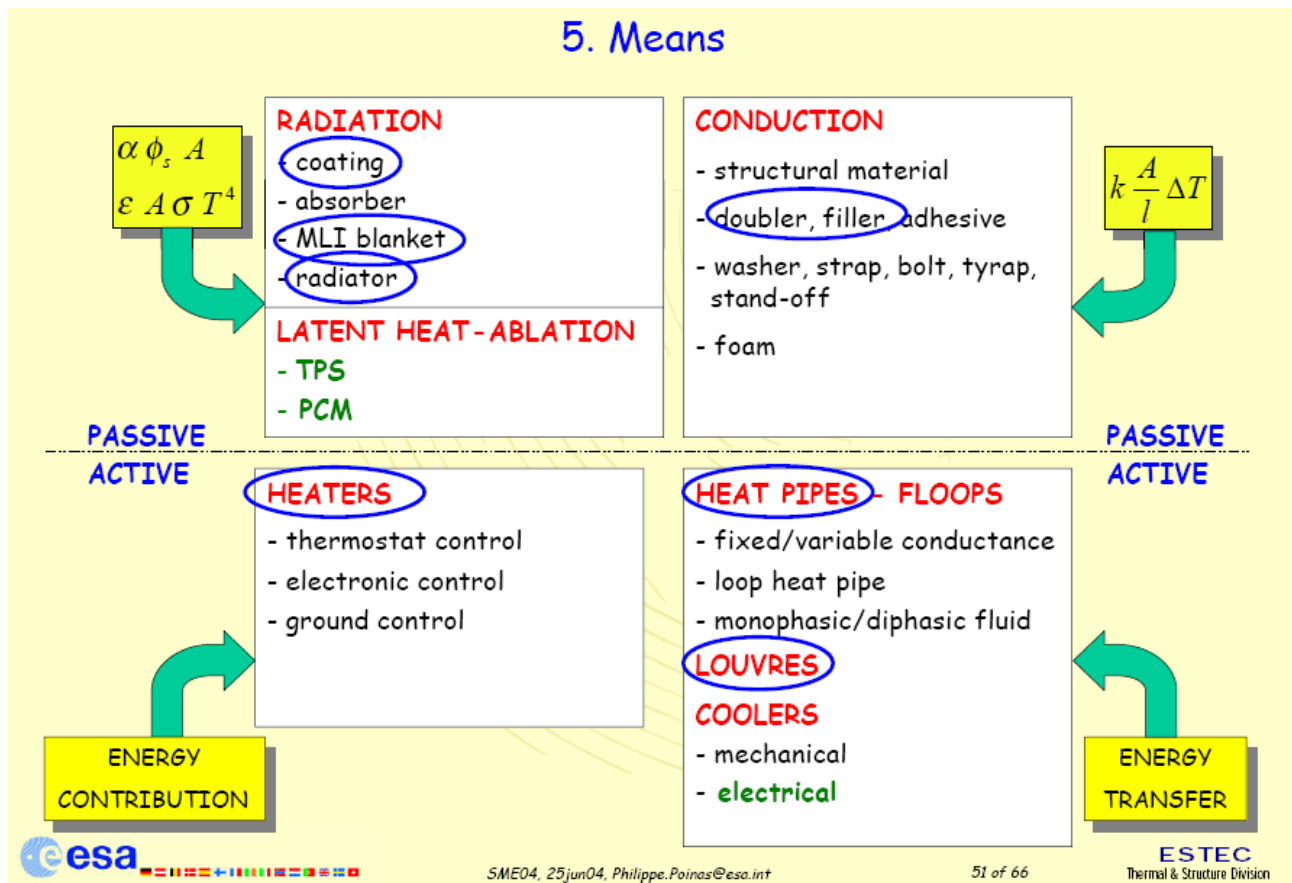


Figure 3.9: FEM analysis, longitudinal eigenfrequency[52]      Figure 3.10: FEM analysis, lateral eigenfrequency[52]

Analysis of different materials were performed to reduce the structural mass. Initial options using carbon fibre fold core sandwich material was replaced by honeycomb sandwich structures due to less complex production and usage as well as availability[26, 52]. Further studies must still be performed in order to determine the final structural design of the satellite bus incorporating all mechanisms and solar panel structure.

### 7.1.5 Thermal Control System



## 5. Means

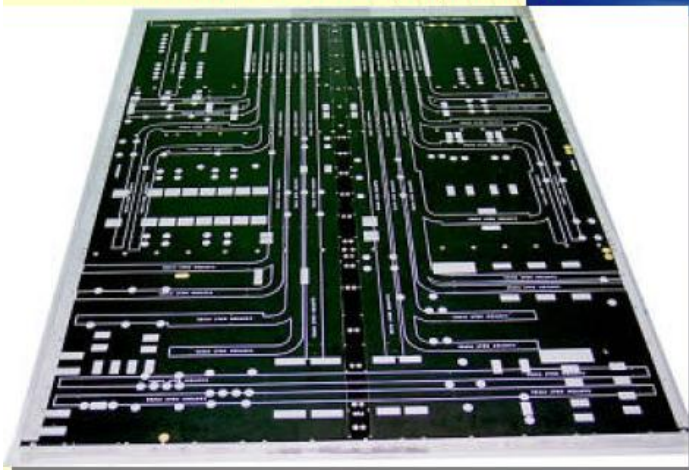
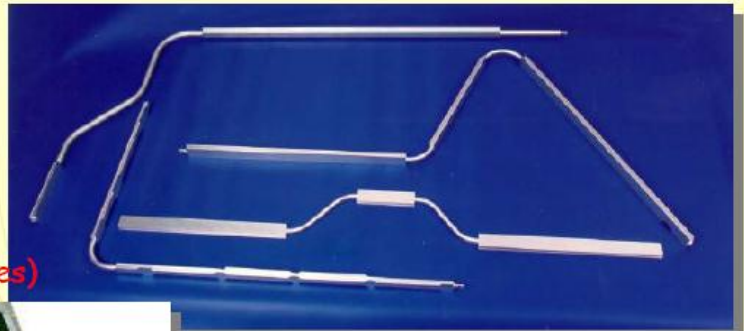
- **Passive Systems Pros/Cons**
  - no mechanical moving parts or moving fluids, no power consumption
    - simple to design/implement/test
    - low mass and cost
    - highly reliable
  - BUT low heat transport capability
    - except heat pipes
- **Active Systems Pros/Cons**
  - mechanical moving parts or moving fluids or electrical power required
    - complex design
    - generate constraints on S/C design and test configurations
    - high mass and cost
    - less reliable than PTC means

### 5. Means - ATC - Heat Pipes

Ø 12 mm



Telecom Panel Heat Pipe (Swales)

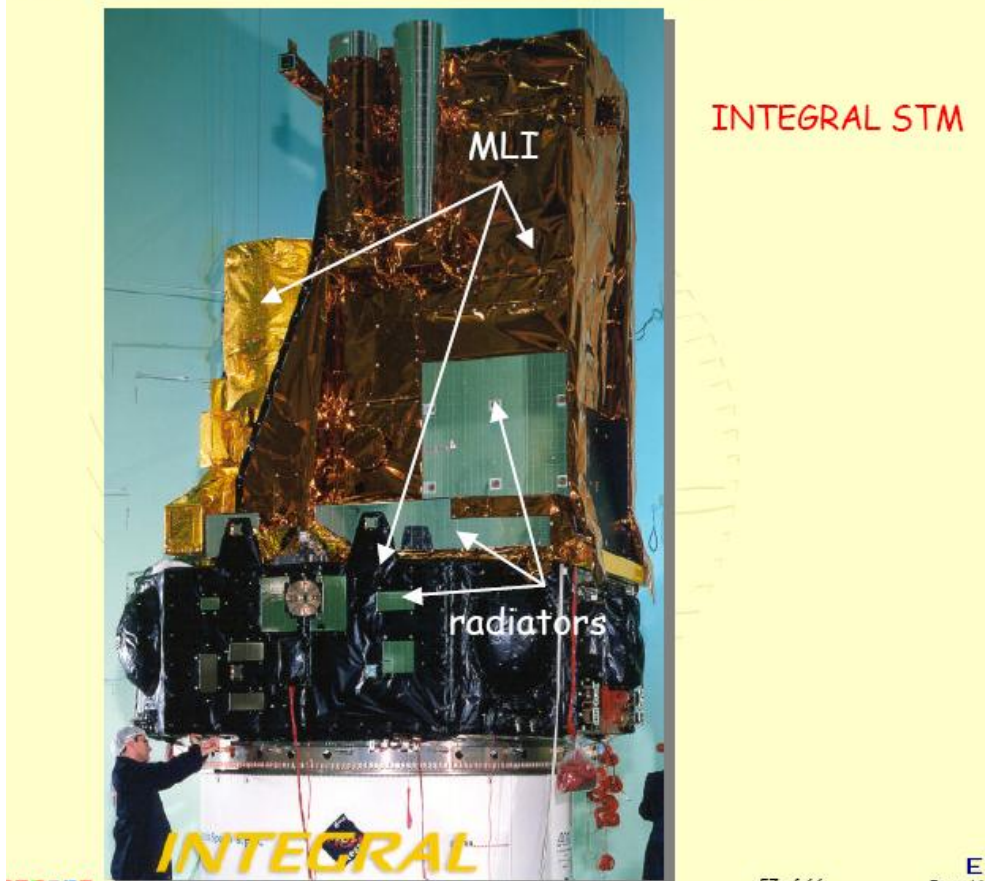


bi-tube

saddle



## 5. Means - PTC - Radiation, Radiators



### 7.1.6 Flight Control System (FCS) on board of satellite - Attitude control system (ACS)

All possible elements of [Mourad et. al. 2006] shall be used.

### 7.1.6.1 Gear

From: Robert H. Berning III and Olivier Viout, Development of the Upgraded DC Brush Gearmotor FOR SPACEBUS PLATFORMS



Figure 2—Upgraded brush gearmotor (UBGM).

the existing motor design revealed inefficient processes, high brush drag and use of discontinued brush material.

The brush assembly consists of a carbon-composite brush, shunt wire, cap and spring. Eight different brush materials were considered and four were selected for testing. All brushes were tested for motor performance, resistance, drag, spring force, brush wear, commutator wear, smearing, debris and manufacturing yield. Brush material options 2 and 3 were eliminated due to low motor torque. Brush material option 1 was selected due to poor performance of option 4 in a vacuum. Table 2 lists development brush performance. The selected brush material is softer than the existing brush material, resulting in higher motor torque, lower brush drag and less commutator wear.

The motor trade study considered all assemblies and machined parts. The producibility of the existing motor is poor, due to the need for frequent rework resulting in high production costs. Stack fabrication, coating and attachment methodology were upgraded to current Moog procedures. All uncontrollable and unnecessary processes were replaced or eliminated. For instance, existing BGM commutators are machined after final armature assembly, putting the completed armature at risk. UBGM commutator processing was moved to the piece part level to lower the risk to hardware. The soldering process was updated to the current standard. Table 3 shows increased motor torque with new brush mate-

rials, design and manufacturing changes.

The overall development of the upgraded brush gearmotor was successful. All issues discovered during the Six-Sigma process were addressed. After development was completed, a qualification unit (Fig. 2) was fabricated to specification, using production processes and tooling. The unit was subjected to qualification testing that included vibration, thermal-vacuum exposure and life tests. The qualification unit successfully passed all qualification and life tests with no findings.

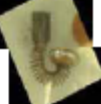
#### Lessons Learned

While the upgraded brush motor development and qualification were successful, the methodology in some areas needs improvement. The following documents the major lessons learned during development and qualification:

*Understand derived requirements.* A firm understanding of the requirements (actual and derived) is needed prior to development. At the onset of the development process, the gearhead bushings were identified as a cause of BGM performance problems. A total redesign of the gearhead was started, with heritage design practices, processes and software utilized in the new gearhead. Gear design parameters were optimized to allow for greater allowable tolerances and used compatible material combinations to reduce galling and thermal expansion issues. Optimization of the gearhead for producibility adversely affected performance, however.

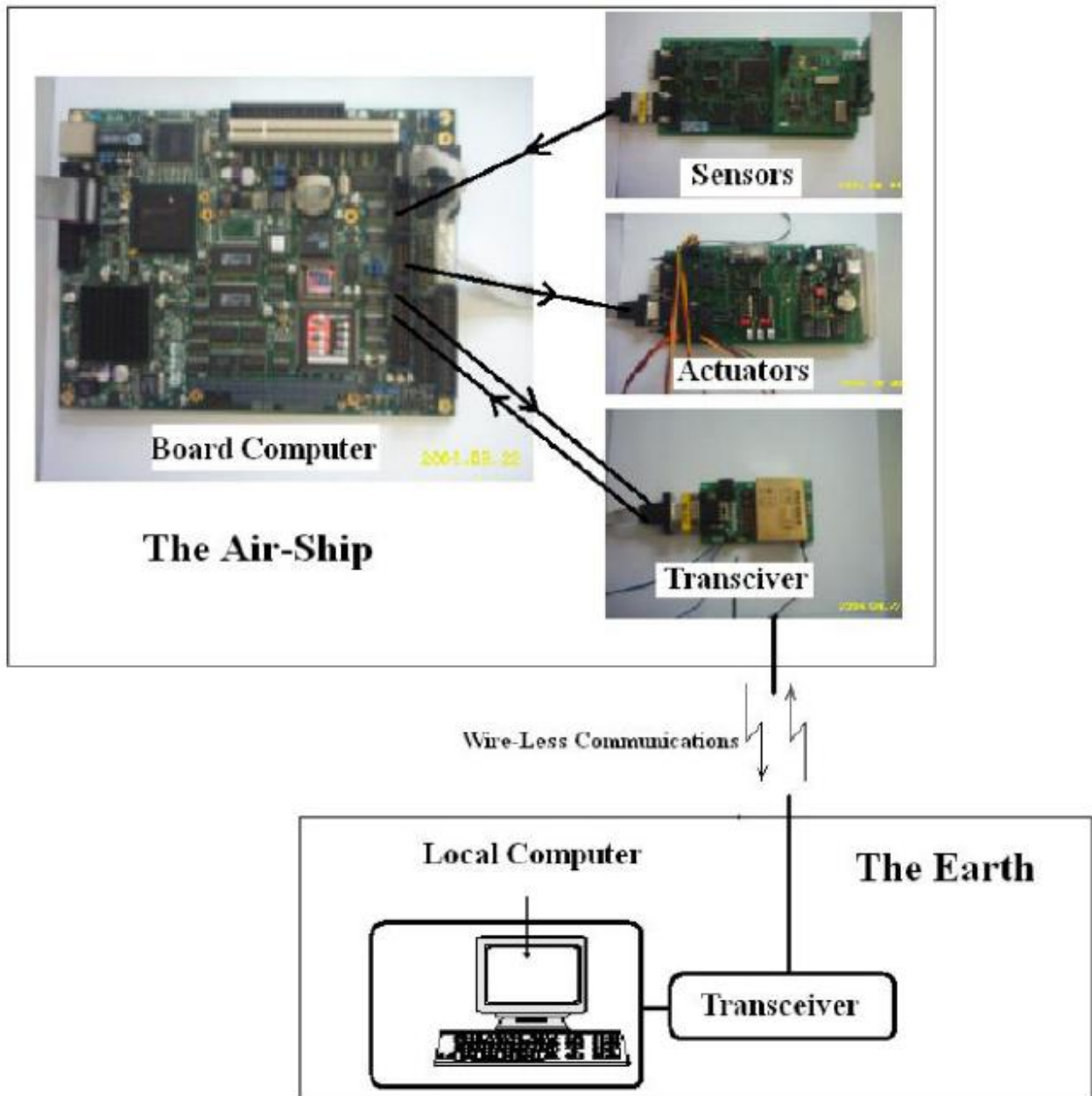
Since the BGM motor torque output is relatively low, it

continued

				
New Brush	A1	A2	B1	B2
Percent Reduction	~14%	~14%	~14%	~17%

### 7.1.7 Command and Data Handling

All possible elements of [Mourad et. al. 2006] shall be used.



Also the elements from SBEP conception (May-July 2013).

See chapter "Telemetry"

## 7.2 Education and Public Outreach

To gain visibility within the scientific and engineering community as well as in the general public an education and public outreach program will be an important element of the project. Up-to-date communications involves classical instruments like press releases for broadcasting and print media coverage but also online media like web-based home pages, blogs and wiki-based information systems. Initiating partnerships with telecommunication and web media providers should favorably

To link the scientific community and the general public amateur astronomy groups will also be involved in payload experiments and the organization and management of ground-based observations (e.g. space and ground based imaging of transient lunar phenomena). These groups will establish a network to education and public outreach institutions like public observatories, science museums, planetariums and others to support an successful outreach program.

### 7.3 First Mockup Model

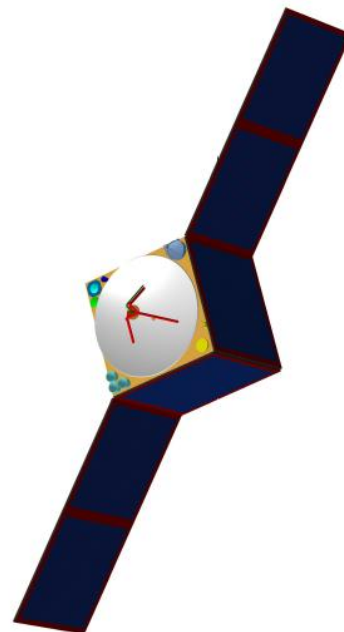
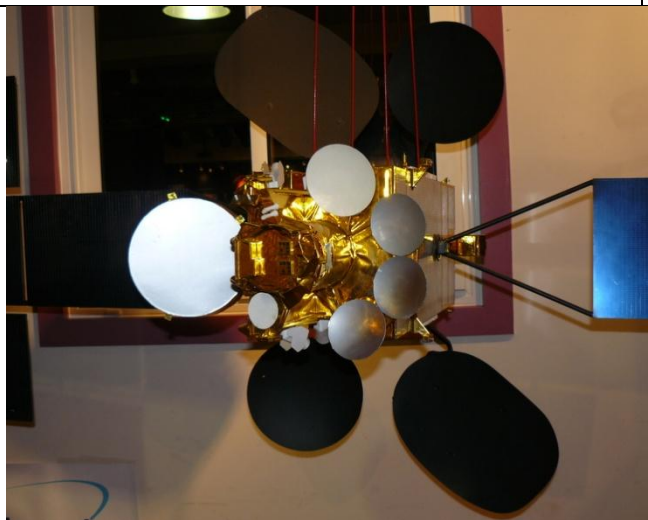


Figure 3.18: Accommodation of the strawman payload (left corner: MICS2, upper corner: SPOSH (bba), PAMCAM2 (dark blue), right corner: LUDENA, center: TICS2) [6]

## 7.4 Prototype

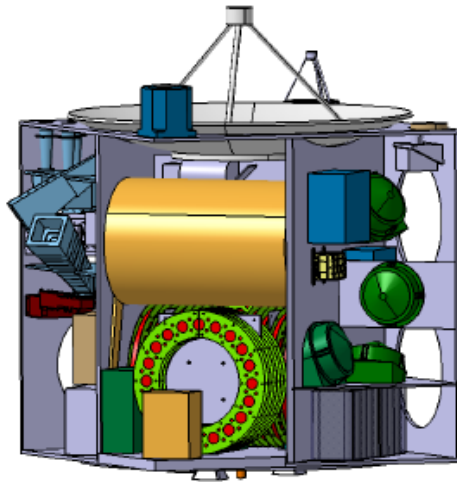


Figure 6.5: Prototype design —  
View on propulsion module[52]

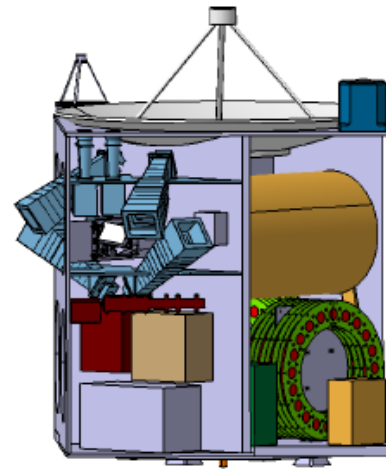
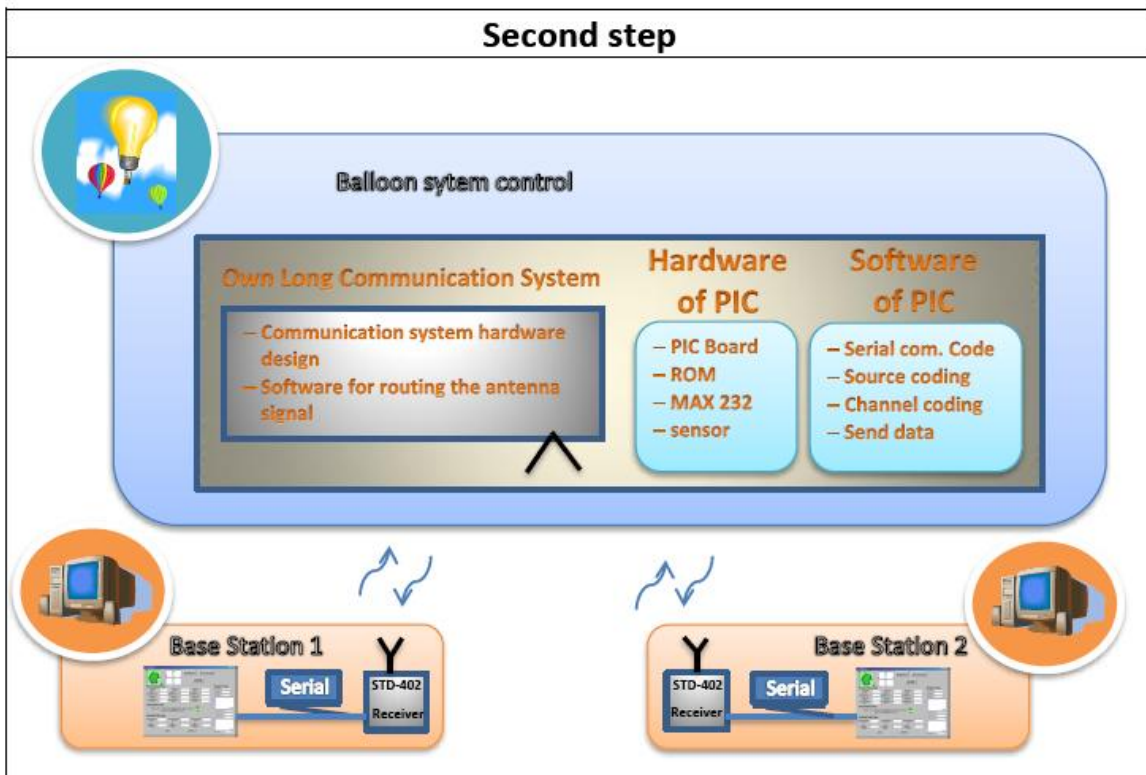
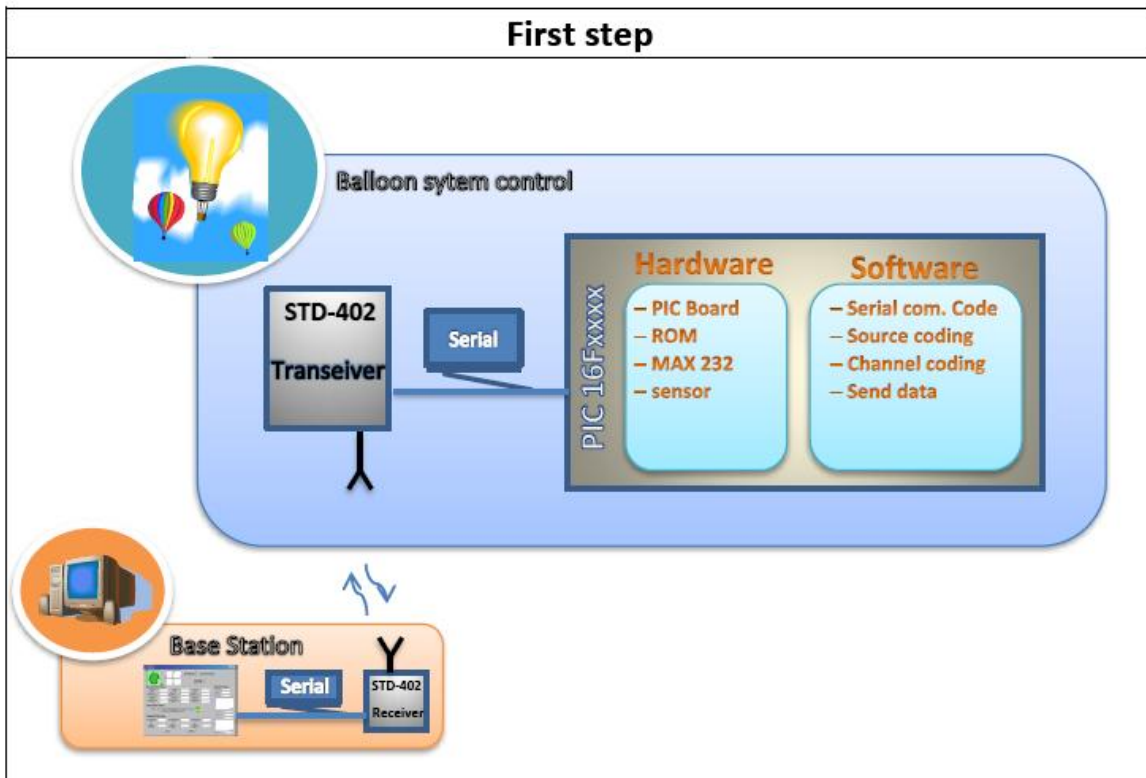


Figure 6.6: Prototype design —  
View on star trackers and other  
subsystems[52]

## 8 Telemetry (Satellite Bus Communication) Conception

### 8.1 From SBEP project<sup>4</sup>



<sup>4</sup> From [IAP\_SBEP]

## 8.2 Satellite side<sup>5</sup>

### 8.2.1 System Design

In general, the microcontrollers has to do the following (see figure 8.1):

- Establish a communication with the base station
- Control the Stratosphere balloon (stability and travel system)
- Source coding, encrypt code and channel coding
- Do a phased array

In our project we use the C programming language to program the microcontroller. A side to the software, there are some hardware should be build also will discuss it later.

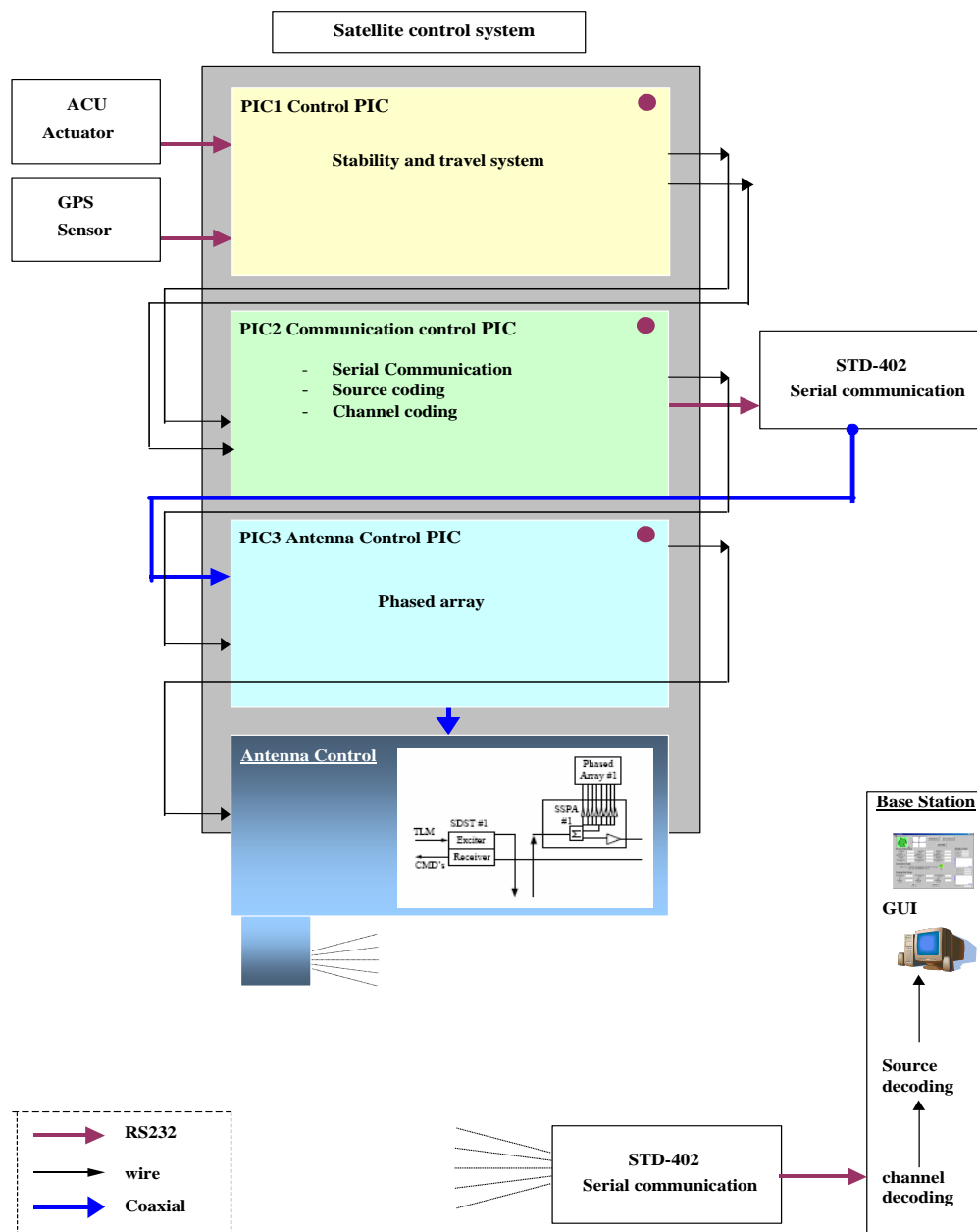


Figure 8.1: Satellite control system

<sup>5</sup> Migration from [IAP\_SBEP]

As we see in **figure1** the first PIC is connected to the ACU actuator ([Mourad et. al. 2006], Thesis of Jamal Ebeidieh) and to the GPS sensors board ([Mourad et. al. 2006], project of Mohamed Subhan) and connected to the base PIC to interact. The second PIC which is the base PIC is connected to the other PIC and to the STD-402 transceiver. The third PIC is connected to the base PIC and to the circuit of antenna control for a phased array antenna goal.

### 8.2.2 Working packages

WP No.	Working package content	Time span, material costs	Development environment (HW, SW)	Responsible	Status
1	Development of the base station GUI	0,5 MM	PC, Windows, VC++		
2	Development of Control for Stabilization of the stratoBallon (using alternativeLotte HW), scilab/xcos	2 MM			
2a	Requirements				
2b	Lotte MatrixX Code -> MATLAB				
2c	Generating Autocode, Loading on alternativeLotte Control Card				
3	Installation of a communication system for sending the data from the ballon to the base station (using a commercial radio sonde) (Payload 1)	Sep			
4		Sep			
4a	Modeling of communication path to stratosphere with octave	1 MM			
4b	Development of HW	3 MM			

### 8.3 Ground station side



#### 8.3.1 GUI Alternative 1: Using the old alternative Lotte program

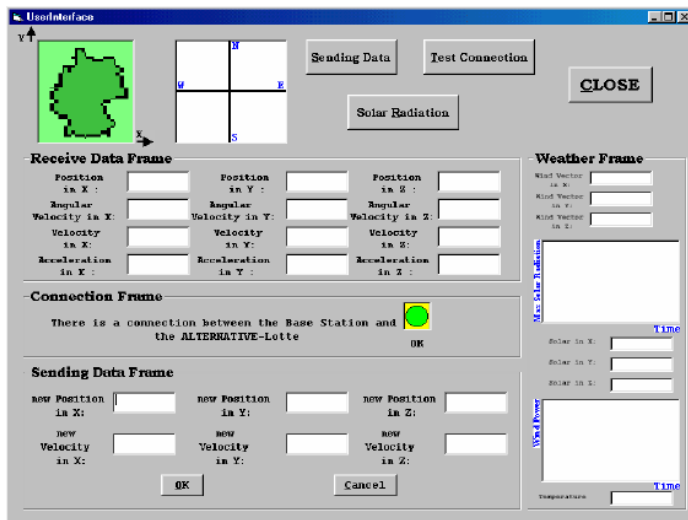
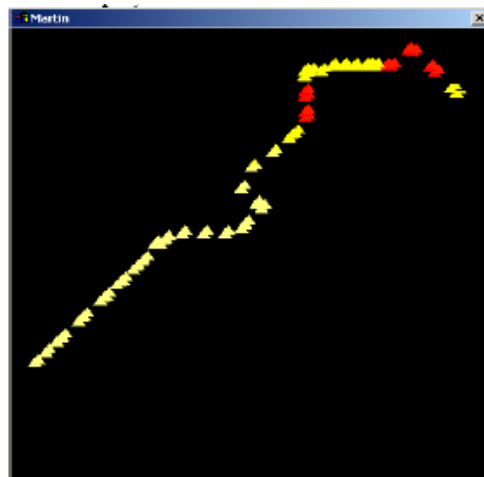
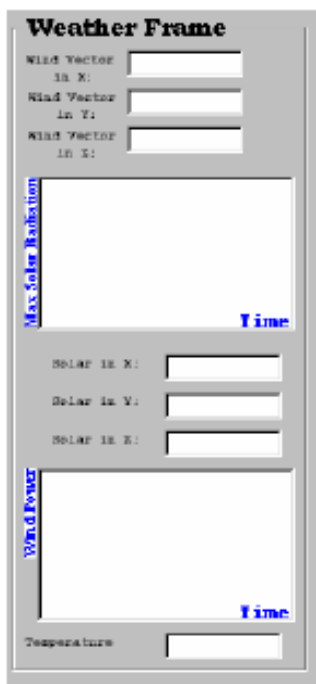
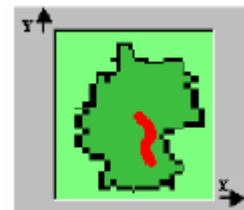
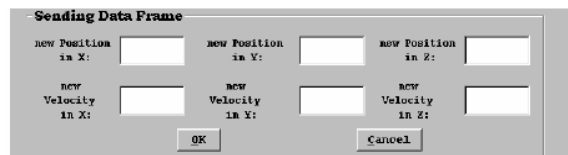
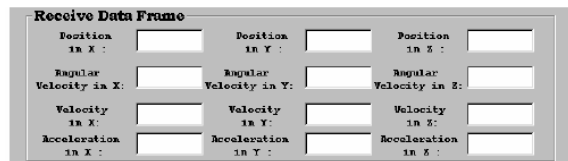
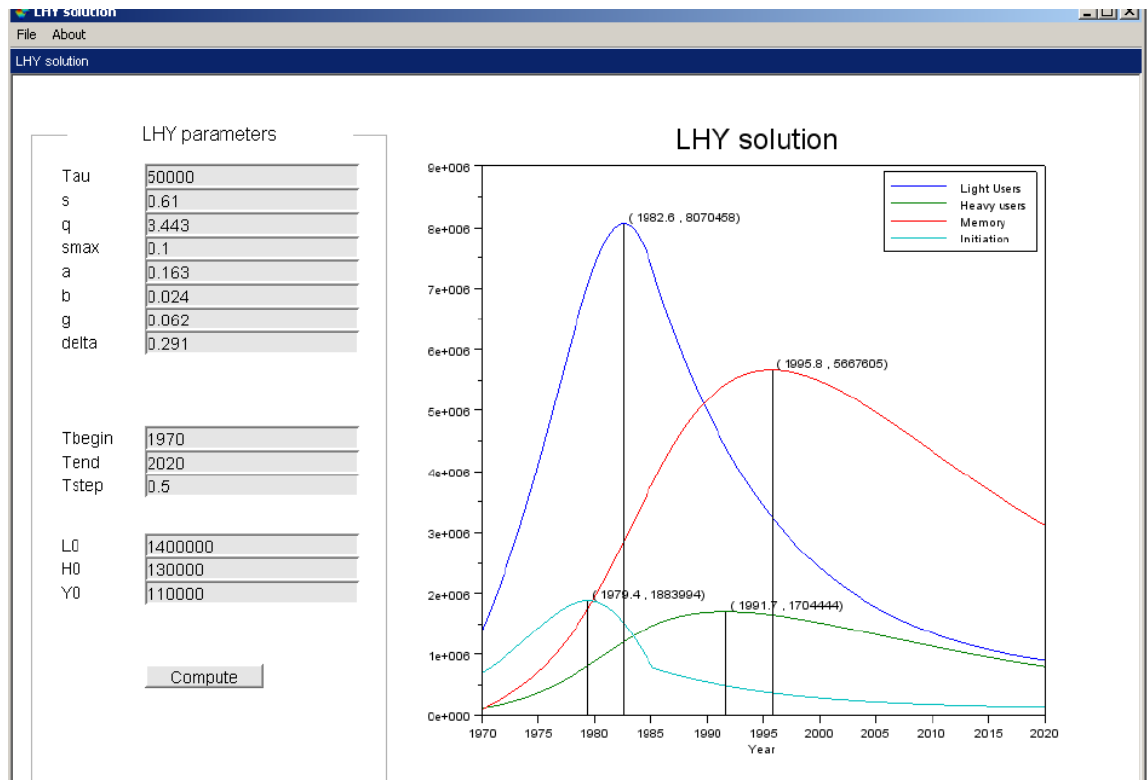


Figure 3.1: User Interface



Advantage: already programmed, only little changes necessary

### 8.3.2 GUI Alternative 2: In Scilab



See LHY\_Tutorial\_GUI.pdf

## 8.4 Transceiver Technology

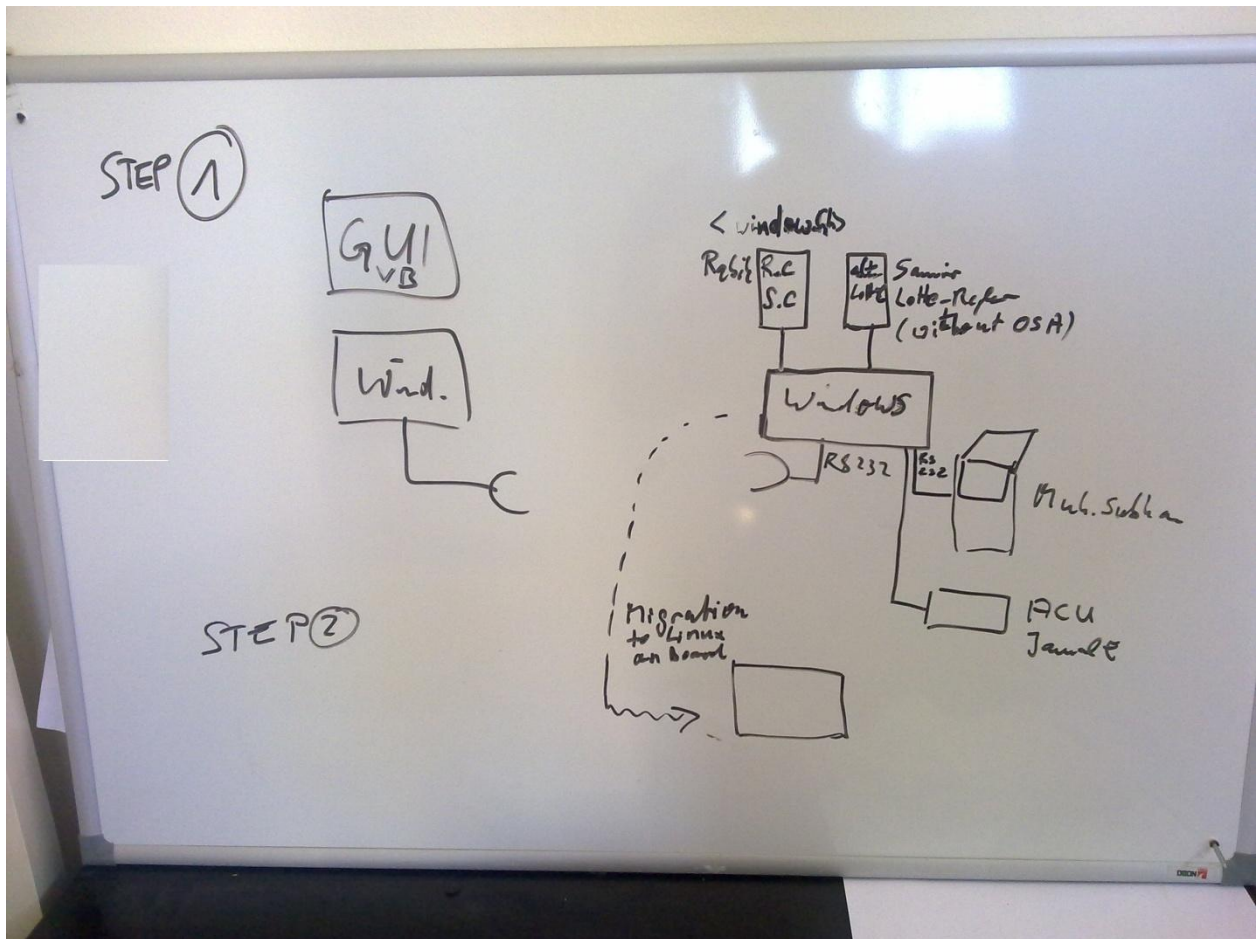
The transceiver technology shall use channel coding as on satellite communication technology (turbo codes). There exist MATLAB satellite communication simulation packages.

The design can be started based on the alternative Lotte transceiver (see Ref. [Mourad et. al. 2006], Thesis of Rabih al-Farkh). To improve the sending and receiving the antenna shall be modified.

There be used phased array technology both at sending and at receiving site.

### 8.4.1 Specification

It was decided, that the GUI and communication system of the former "alternative Lotte" project (Alternative 1) shall migrated, because this will reduce the development time insha Allah.



The ground station is a PC.

GUI:

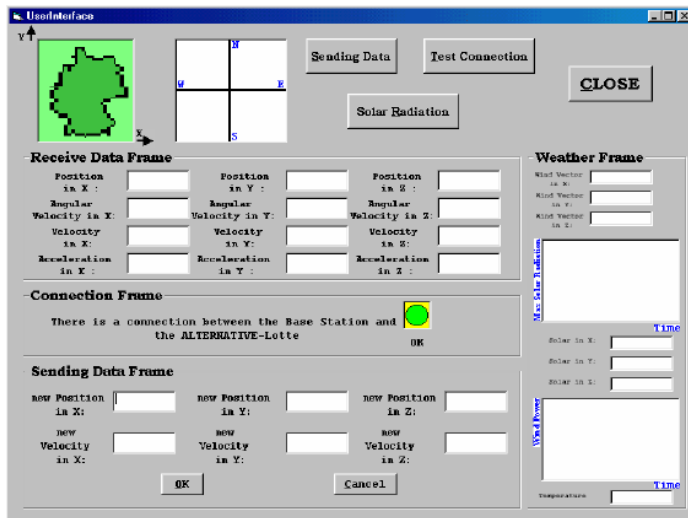


Figure 3.1: User Interface

#### 8.4.1.1 STEP 1 (until 15 June 2013)

Communication and Control modules of the board computer shall be integrated on a Windows PC, HW (Sensor card, actuator card and comm.) shall be mounted with 3 serial ports (RS 232) to the PC.

At this stage also a GUI for the board computer is implemented (migration of KAHROUB solar circuit windows program and integration of the code of Rabih (Receive.C, Send.C) into it).

FCS is from

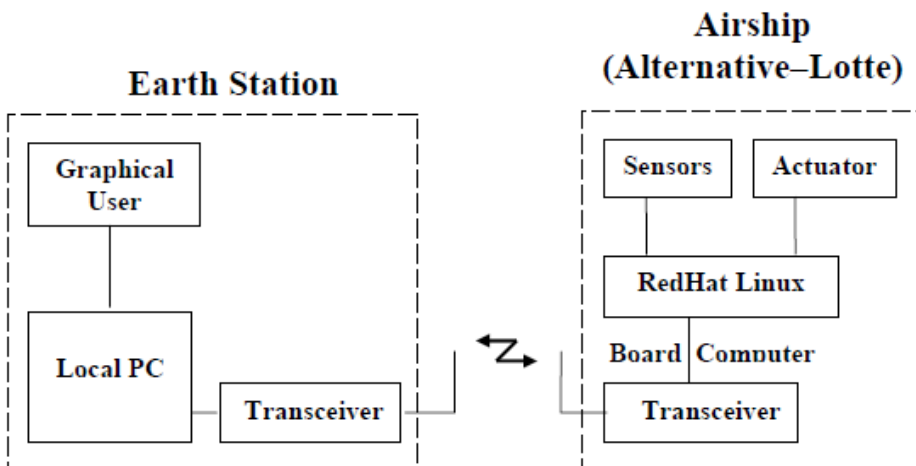
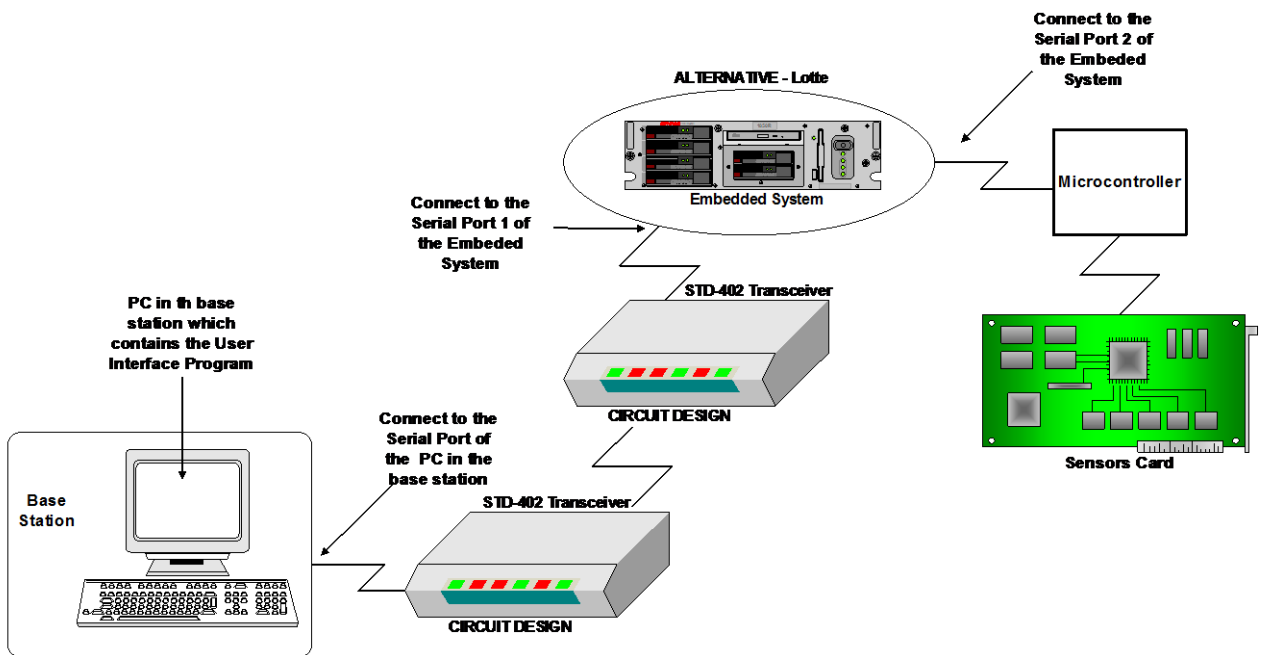
D:\AECENAR\IAP\Alternative Lotte\Regelung an Bord\osa\_lotte\lotte\_regler neufassung von Textdatei.txt

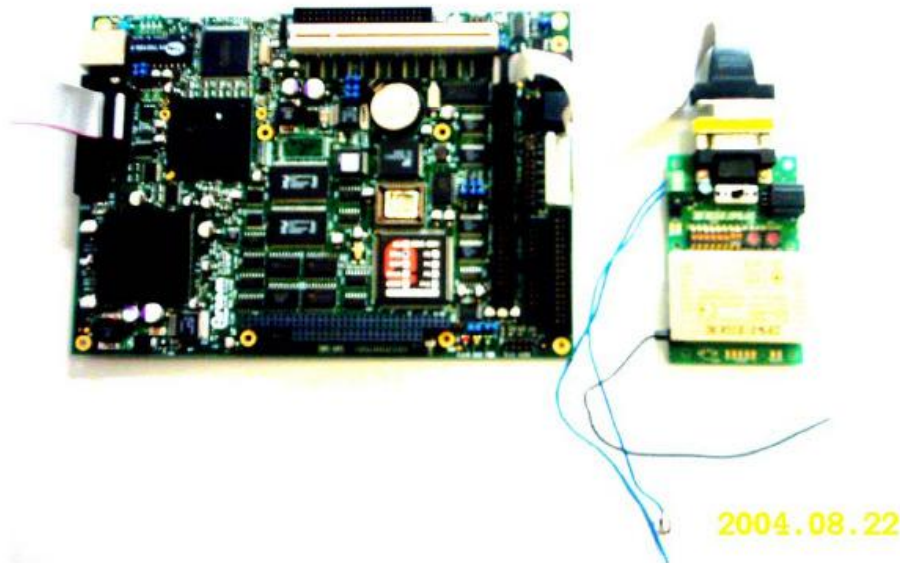
(Migration of former MATRIXX autocode file D:\AECENAR\IAP\Alternative Lotte\Regelung an Bord\osa\_lotte\Copy of Lotte\_Regler.c)

**Development environment for STEP 1**

Visual Basic 6.0 (for Ground Station PC), C Compiler: MinGW, MSYS

**8.4.1.2 STEP 2 (until 30 June 2013)**





The communication is at 433 MHz. C Compiler for the microcontroller of the board.

### 8.4.1.3 STEP 3: Improvements

The two STD-42 transceivers can only communicate at distances < 500 m.

The SBEP system must have the ability to communicate up to about 60 km, because the balloon shall go up to 40 km (stratosphere) and due to unavoidable drifts the distance between the base station and the balloon will extend 50 km.

For this reason the following improvements shall be done:

1. send and receive antenna lobes shall be directed with phased array antennas.
2. channel coding must be added before sending to the user data

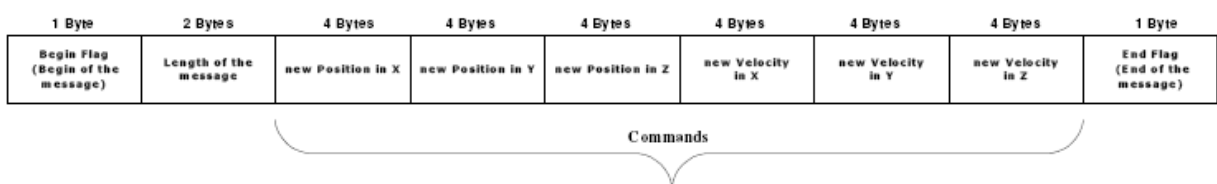


Figure 3.13: User Data Protocol \_ Send Message

and decoded after receiving the data.

### 8.4.1.4 Antenna improvement

166

Uplink, Downlink and Overall Link Performance; Intersatellite Links

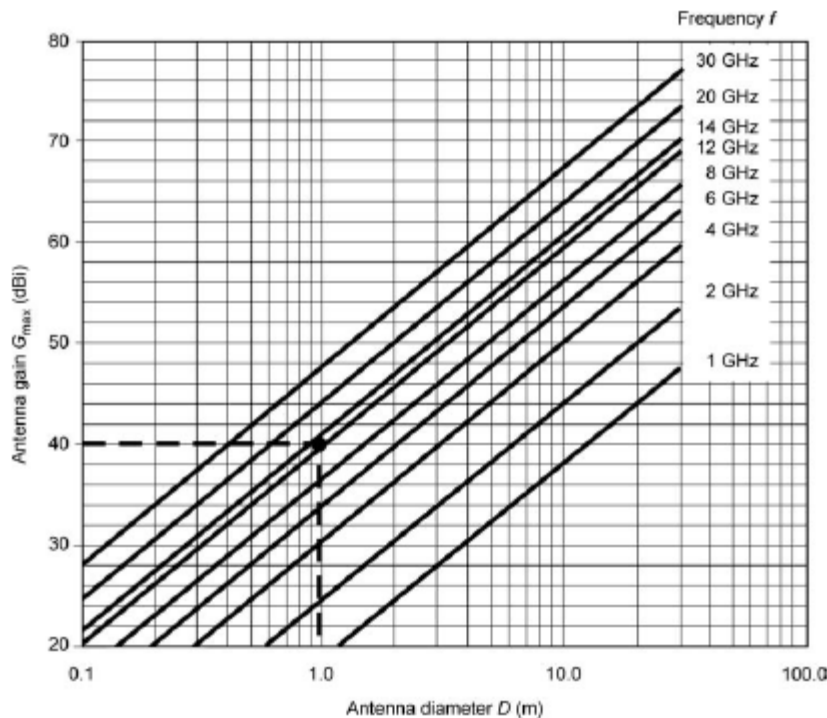


Figure 5.2 Maximum antenna gain as a function of diameter for different frequencies at  $\eta = 0.6$ . A 1 m antenna at 12 GHz has a gain of 40 dBi.

whose value depends on the chosen illumination law. For uniform illumination, the coefficient has a value of  $58.5^\circ$ . With non-uniform illumination laws, which lead to an attenuation at the reflector boundaries, the 3 dB beamwidth increases and the value of the coefficient depends on the particular characteristics of the law. The value commonly used is  $70^\circ$  which leads to the following

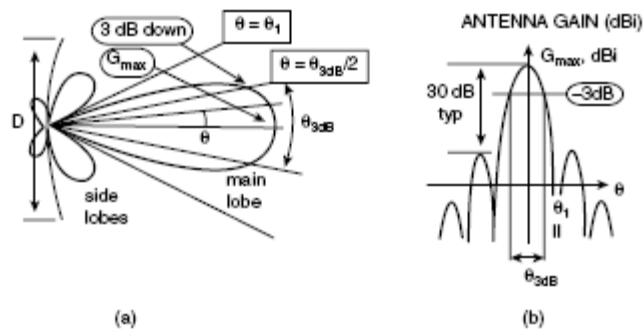


Figure 5.3 Antenna radiation pattern: (a) polar representation and (b) Cartesian representation.

From [Maral et. al. 2009].

### 8.4.1.5 Channel Coding

There shall be implemented a turbo code.

## 8.5 Payload Communication: SCS-SMS including AES

See [IAP\_ECS]

## 9 Telemetry (Satellite Bus Communication) Prototype<sup>6</sup>

### 9.1 Overview

In our project, the satellite communicates with a base station wirelessly by two Synthesize transceivers STD-402. The base station is a computer connected to a Synthesize transceiver and on the computer there is a GUI user interface, in the satellite there are microcontrollers connect together and the hall system connect to the base station by a Synthesize transceiver.

#### 9.1.1 Synthesize transceiver STD-402

The transceiver to be used is **MB-STD-RS232**. It is a bi-directional semi-duplex radio modem having RS232 serial interface. It uses CIRCUIT DESIGN's standard 434 MHz FM Narrow Band transceiver module **STD-402** transceiver for RF part. This transceiver was selected because of its frequency of 434 MHz. For this frequency there is no extra permission necessary. Another reason is that this transceiver is a cheap one.

Further details see [Mourad et. al. 2006], Thesis of Rabih al-Farkh

### 9.2 Base station side<sup>7</sup>

In the base station side, a GUI user interface should build to interact with the satellite by sending and receiving data.

See [Mourad et. al. 2006], Thesis of Rabih al-Farkh, Chapters 3-4

### 9.3 Satellite side

In the satellite side, there are some PIC microcontrollers which should be programmed to do its work. In general, the microcontrollers aim to do the follow (see figure1):

- Establish a communication with the base station
- Control the Stratosphere balloon (stability and travel system)
- Source coding, encrypt code and channel coding
- Do a phased array

In our project we use the C programming language to program the microcontroller. A side to the software, there are some hardware should be build also will discuss it later.

---

<sup>6</sup>

<sup>7</sup> most of this information is from the **Alternative-lotte** project of **Rabih al\_Farkh**

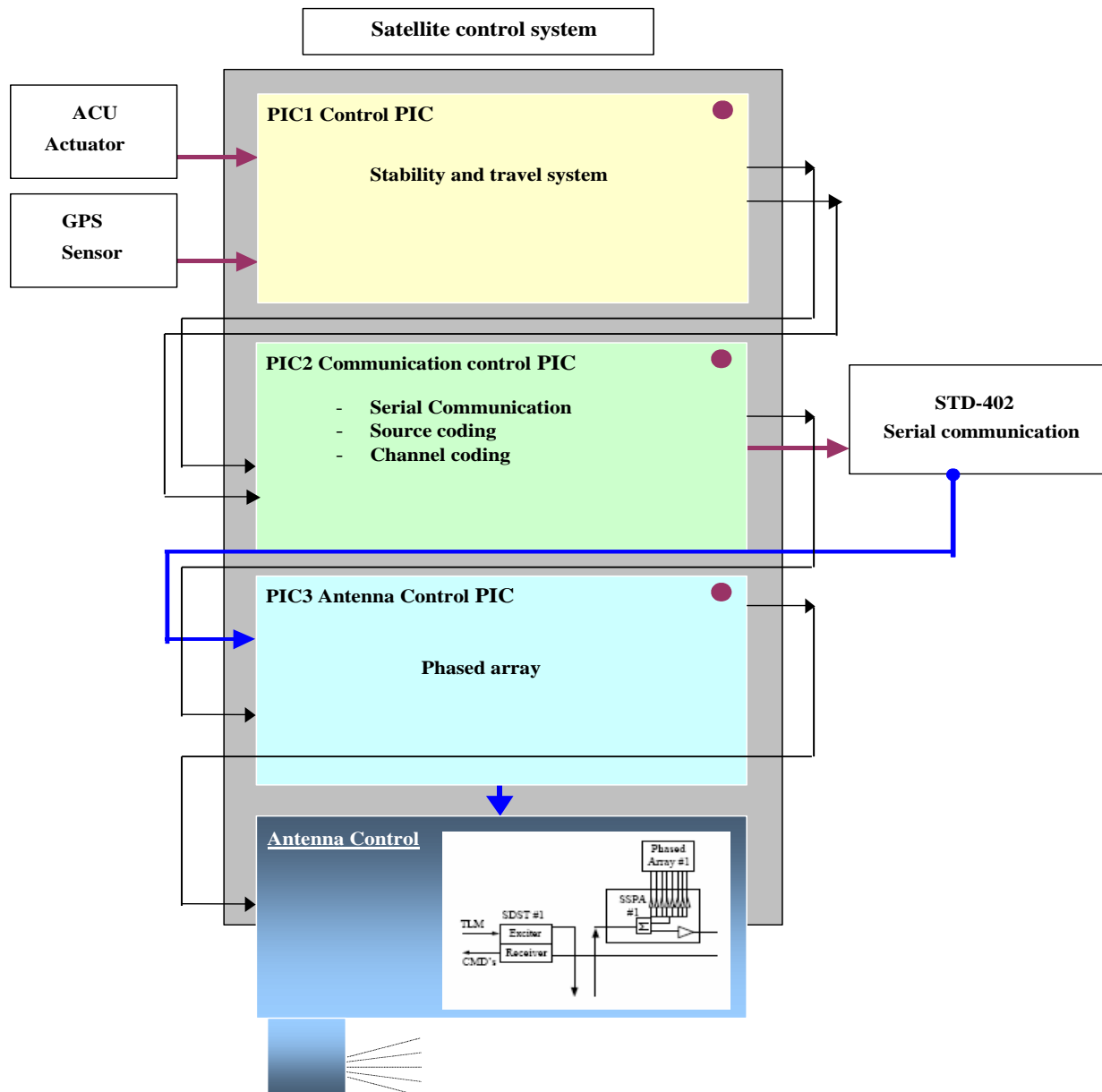


**Figure1: Satellite control system**

As we see in **figure1** the first PIC is connected to the ACU actuator (project of Jamal Ebeidieh) and to the GPS sensors board (project of Mohamed Subhan) and connected to the base PIC to interact. The second PIC which is the base PIC is connected to the other PIC and to the STD-402 transceiver. The third PIC is connected to the base PIC and to the circuit of antenna control for a phased array antenna goal.

### 9.3.1.1 Hardware part

We can divide the hardware part of our project as follow:

### 9.3.1.2 ACU actuator<sup>8</sup>

The ACU actuator is the project of Mr. Jamal Ebeideh. You can go back to his project report as a reference for this part.

<sup>8</sup> Source: <https://www.aecenar.com/download/ACUactuator>

### 9.3.1.3 GPS sensor<sup>9</sup>

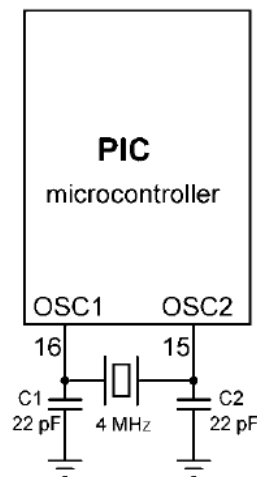
The ACU actuator is the project of Mr. Mohamed Subhan. You can go back to his project report as a reference for this part.

### 9.3.1.4 PIC board<sup>10</sup>

The PIC microcontroller needs a minimum support component to do its work. A PIC microcontroller, even though it may have been programmed, is not of much use unless it is supported by a number of components, such as the timing components and the reset circuit.

#### Timing components and design

A PIC microcontroller requires an external clock circuit (some PIC microcontrollers have built-in clock circuits) to function accurately. For accurate timing applications, the clock circuitry consists of a crystal, and two small capacitors. Figure bellow shows the circuit diagram of a PIC microcontroller with a 4-MHz crystal clock circuit. The crystal and the capacitors are connected to the OSC1 and OSC2 inputs of the microcontroller.

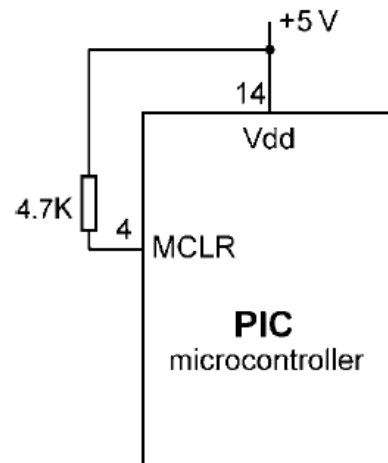


#### Power source and Reset circuit

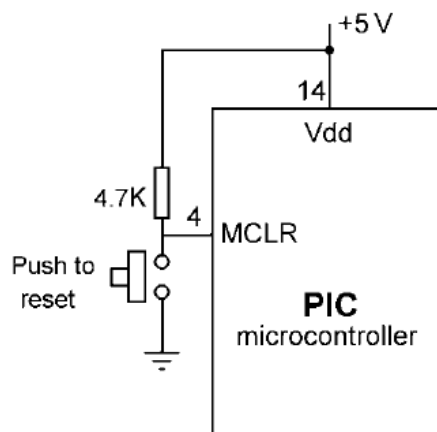
A PIC microcontroller starts executing the user program from address 0 of the program memory when power is applied to the chip. As shown in Figure bellow, the reset input (MCLR) of the microcontroller is usually connected to the 5V supply voltage through a 4.7K resistor.

<sup>9</sup> Source: <https://www.aecenar.com/download/GPSSensors>

<sup>10</sup> Some information of this part is copy with change from: PICBASIC PROJECT for Dogan Ibrahim



There are many applications where the user may want to force reset action e.g. by pressing an external button so that the program re-starts to execute from the beginning. External reset is very useful during microcontroller-based system development and testing. Figure below shows how an external reset button can be connected to a PIC microcontroller. Normally the MCLR input is at logic 1, and goes to logic 0 which resets the microcontroller when the reset button is pressed. The microcontroller goes back to the normal operating mode when the button is released.

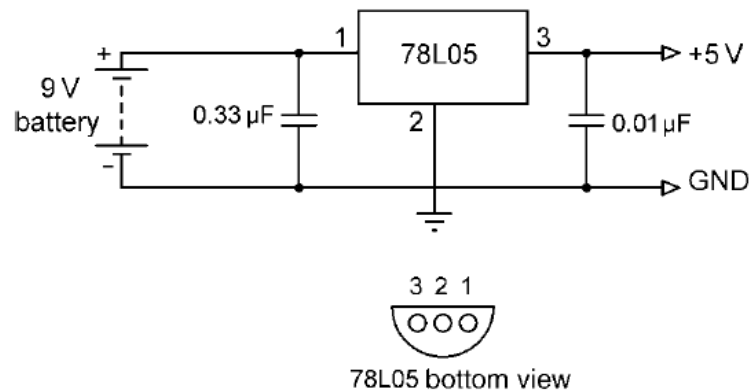


### Power supply

Every electronic circuit requires a power supply to operate. The required power can either be provided from a battery, or the mains voltage can be used and then reduced to the required level before it is used in the circuit (e.g. a mains adaptor). In this section, we shall look at the design of a power supply circuit to power our PIC microcontroller circuits.

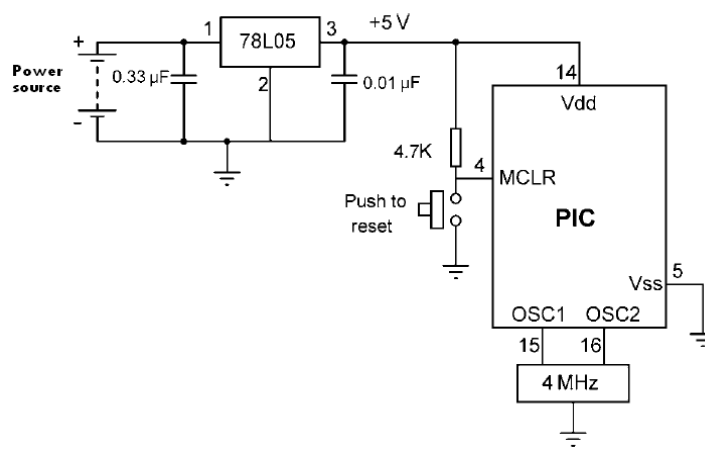
PIC microcontrollers can operate from a power supply voltage in the range 2 to 6V. The standard power supply voltage in digital electronic circuits is 5 V and this is the voltage with which the PIC microcontrollers are mostly operated. Unfortunately, it is not possible to obtain 5 V using standard alkaline batteries only. The nearest we can get is by using three batteries, which gives 4.5 V and this is not enough to power standard logic circuits. The simplest solution to drop the voltage from 9 to 5 V is by using a potential divider circuit using two resistors. Although a potential divider circuit is simple, it has the major

disadvantage that the voltage at the output depends on the current drawn from the circuit. As a result of this, the output voltage will change as we add or remove components from our circuit. Also, the output voltage falls as the battery is used. A voltage regulator circuit is needed to convert the 9 V battery voltage into 5V, independent of the current drawn from the supply. A basic voltage regulator circuit consists of a regulator integrated circuit and filter capacitors. Figure bellow shows a low-cost voltage regulator circuit using the 78L05-type voltage regulator IC, and two filter capacitors. 78L05 is a 3-pin IC with a maximum current capacity of 100 mA.

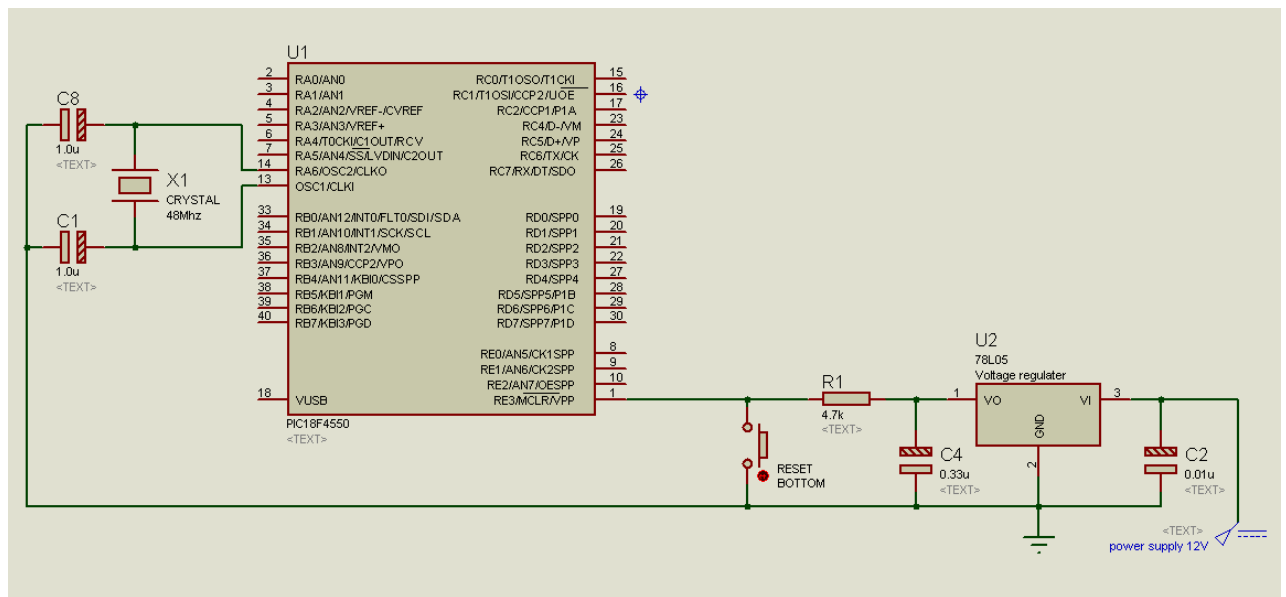


One of the pins of 78L05 is connected to the +V terminal of the battery in parallel with a 0.33- $\mu$ F capacitor. One of the pins is connected to the -V terminal of the battery. The third pin provides the +5 V output and a 0.01- $\mu$ F capacitor should be used in parallel with this pin. In applications where a larger current is required, the 7805 regulator IC can be used. This is pin compatible with the low-power 78L05 and it has a maximum current capacity of 1 A. 78L05 should be used with a suitable heat-sink in applications drawing more than a few hundreds of mill-amperes.

The complete circuit diagram of our PIC based basic system, together with the power supply, is shown in Figure bellow. The circuit is now fully functional, what is required now is to write our program and load it into the program memory of the microcontroller.



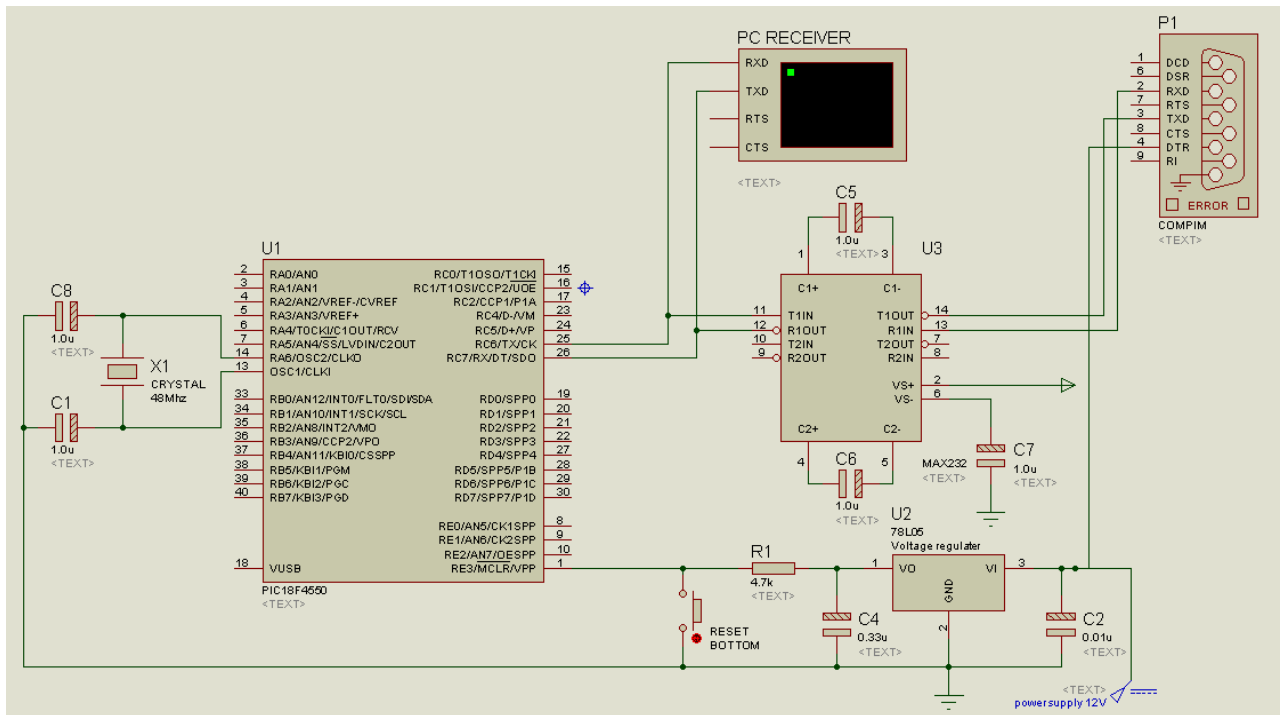
This circuit is tested on simulation software (Proteus isus7) under the design bellow:



### Serial communication component

PIC microcontroller has serial communication module (USART) which operates using CMOS logic levels which changes between +5V and 0V to represent logic 1 and 0. However computer serial port (RS232C) operates in different voltage levels. It represents logic 0 with -10V and logic 1 with +10V. So obviously we can't directly connect PIC MCUs USART pins to computer. We need to convert voltage levels. For this task there is specially designed serial level converter ICs available in most common one is MAX232 which is used here. This IC receives signals from -10 to +10V from computer side and converts them into 0 and 5V which can be used in microcontroller

When using MAX232 IC it is essential to connect C2 capacitor as close as possible to MAX232 chip. Otherwise your circuit may not work. Also it is good idea to keep serial cable from computer to MAX232 reasonably short. The new Proteus design is shown in the figure bellow:



The virtual terminal was added only for testing purpose.

### 9.3.1.5 Antenna control board

Not yet . . .

### 9.3.2 Software part

We can divide the software part of our project as follow:

#### 9.3.2.1 Communication code <sup>11</sup>

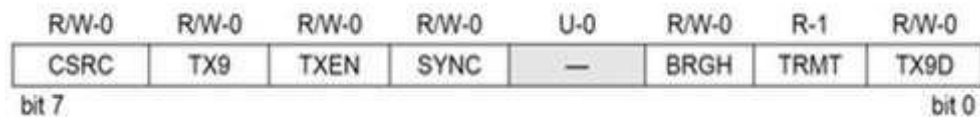
To communicate with external components such as computers or microcontrollers, the PIC micro uses a component called **USART – Universal Synchronous Asynchronous Receiver Transmitter**. This component can be configured as:

- A Full-Duplex asynchronous system that can communicate with peripheral devices, such as CRT terminals and personal computers
- A Half-Duplex synchronous system that can communicate with peripheral devices, such as A/D or D/A integrated circuits, serial EEPROMs, etc.

To enable the serial communication with PIC microcontroller we must set different parameters within two registers:

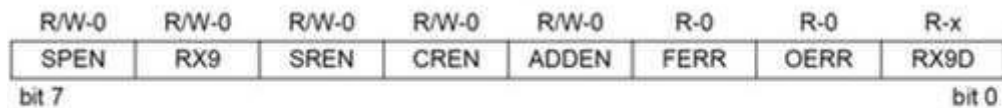
<sup>11</sup> Reference: some information in this part was copied with change from: [http://www.microcontrollerboard.com/pic\\_serial\\_communication.html](http://www.microcontrollerboard.com/pic_serial_communication.html)

## 1. TXSTA – Transmit Status and Control Register



MicrocontrollerBoard.com

## 2. RCSTA – Receive Status and Control Register



MicrocontrollerBoard.com

The send information will be stored inside **TXREG** register, which acts as a temporary buffer storage of information prior to transmission. While the receive information will be store in the **RSR** register, which acts as a temporary buffer storage.

Each transmission is transmitted in the particular rate (BAUD). The baud rate is measured in units of **bps** (bit per second). This is done by setting the system clock to the value needed. To do so, we need to “write” a hexadecimal number to the **SPBRG** register. The value written to the **SPBRG** register set the clock cycle to the value we want for the BAUD rate.

The size of **SPBRG** register is 8-bit. In asynchronous mode, the baud rate of transmission of the information can be set to high speed or to low speed. The rate selection, as already seen, is made by the BRGH bit in TXSTA register:

1 = High speed

0 = Low speed

For each baud rate we need to calculate the value being placed in the SPBRG differently:

$$\text{SPBRG} = (\text{Fosc} / (16 \times \text{Baud rate})) - 1, \quad \text{BRGH} = 1 \text{ High Speed}$$

$$\text{SPBRG} = (\text{Fosc} / (64 \times \text{Baud rate})) - 1, \quad \text{BRGH} = 0 \text{ Low Speed}$$

In our case, we have: Fosc=48Mhz, Baud rate=9600

$$\text{For High Speed} \Rightarrow \text{SPBRG} = 0x137 \quad \text{hex}$$

$$\text{For Low Speed} \Rightarrow \text{SPBRG} = 0x4D \quad \text{hex}$$

Then the code for serial sending is (C programming):

```
void SendToSerial(char m)
{
    SPBRG = 0x4D; // 4D hex or 77 decimal (baud rate=9600), Low
                 speed: SPBRG = (Fosc / (64 x Baud rate)) - 1
    TXSTA = 0x22; // determining the setting for the
```

```

transmitter
    RCSTA= 0x90; // determining the setting for the
receiver
    TXREG = m;
    while (PIR1bits.TXIF==0) {}
}

```

### 9.3.2.2 Control and stability code

Not yet ...

### 9.3.2.3 Coding code

This code part will discuss in the system coding chapter (next chapter), and includes:

- Source Coding and Decoding code
- Encryption and Decryption code
- Channel Coding and Decoding code

All of this code will discuss in C language.

### 9.3.2.4 Antenna control code

Not yet ...

## 9.4 System coding

In the engineering sense, coding can be classified into four areas:

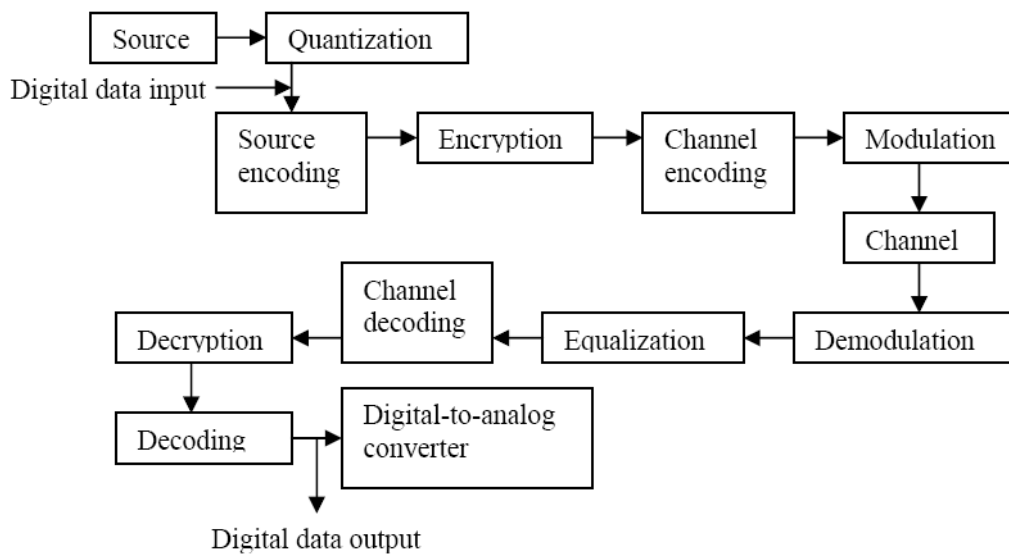
- Encryption: to encrypt information for security purpose.
- Data compression: to reduce space for the data stream.
- Data translation: to change the form of representation of the information so that it can be transmitted over a communication channel.
- Error control: to encode a signal so that error occurred can be detected and possibly corrected.

### 9.4.1 Introduction<sup>12</sup>

The main aim of any communication schemes is to provide error-free data transmission. In a communication system, information can be transmitted by analog or digital signals. For analog means, the amplitude of the signal reflects the information of the source, whereas for digital case, the information will first be translated into a stream of '0' and '1'. Then two different signals will be used to represent '0' and '1' respectively. As can be referred to the following illustration, the main advantage of using digital signal is that errors introduced by noise during the transmission can be detected and possibly corrected. For wireless communication channels, noise can be introduced in various ways.

<sup>12</sup> Reference: [http://www.mathdb.org/notes\\_download/elementary/number/ne\\_N6.pdf](http://www.mathdb.org/notes_download/elementary/number/ne_N6.pdf)

Figure 1 shows the flow of a simple digital communication system:



#### 9.4.2 Source Coding

Suppose a word 'Zebra' is going to be sent out. Before this information can be transmitted to the channel, it is first translated into a stream of bits ('0' and '1'). The process is called **source coding**. There are many commonly used ways to translate that. For example, if ASCII code is used, each alphabet will be represented by 7-bit so-called the code word. The alphabets 'Z', 'e', 'b', 'r', 'a', will be encoded as

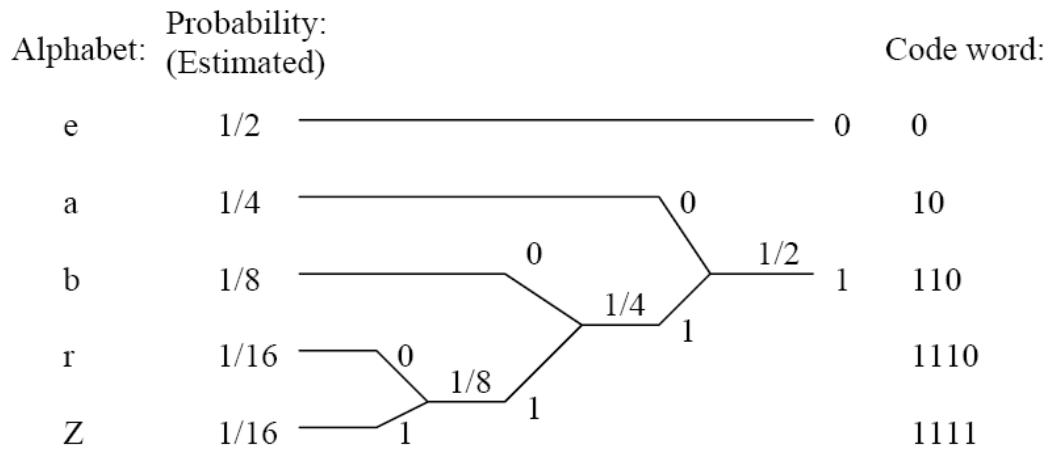
'1010101', '0110110', '0010110', '0010111', '0001110'

The **ASCII code** is an example of fixed-length code, because each of the code word is of the same length (7 bits). However, in the view of efficient communication, the occurrence of 'Z' is not as often as that of 'e' and 'a'. If there is a way of encoding information such that the alphabets with higher probability of occurrence are assigned with shorter code words, and longer for the other letters which seldom come out, then on the whole it may be able to conserve the number of bits to be sent to the channel while sending the same information. This is what the variable length code can do. The following illustrates the **Huffman Codes**, which was developed by David Huffman in 1951.

Rules:

- ✓ Order the symbols ('Z', 'e', 'b', 'r', 'a') by decreasing probability and denote them as  $S_1$ , to  $S_n$  ( $n = 5$  for this case).
- ✓ Combine the two symbols ( $S_n, S_{n-1}$ ) having the lowest probabilities. Assign '1' as the last symbol of  $S_{n-1}$  and '0' as the last symbol of  $S_n$ .
- ✓ Form a new source alphabet of ( $n-1$ ) symbols by combining  $S_{n-1}$  and  $S_n$  into a new symbol  $S'_{n-1}$  with probability  $P'_{n-1} = P_{n-1} + P_n$ .
- ✓ Repeat the above steps until the final source alphabet has only one symbol with probability equals to 1.

Figure 2: The process of coding the word 'Zebra' by Huffman Code



### 9.4.2.1 Using Huffman theory

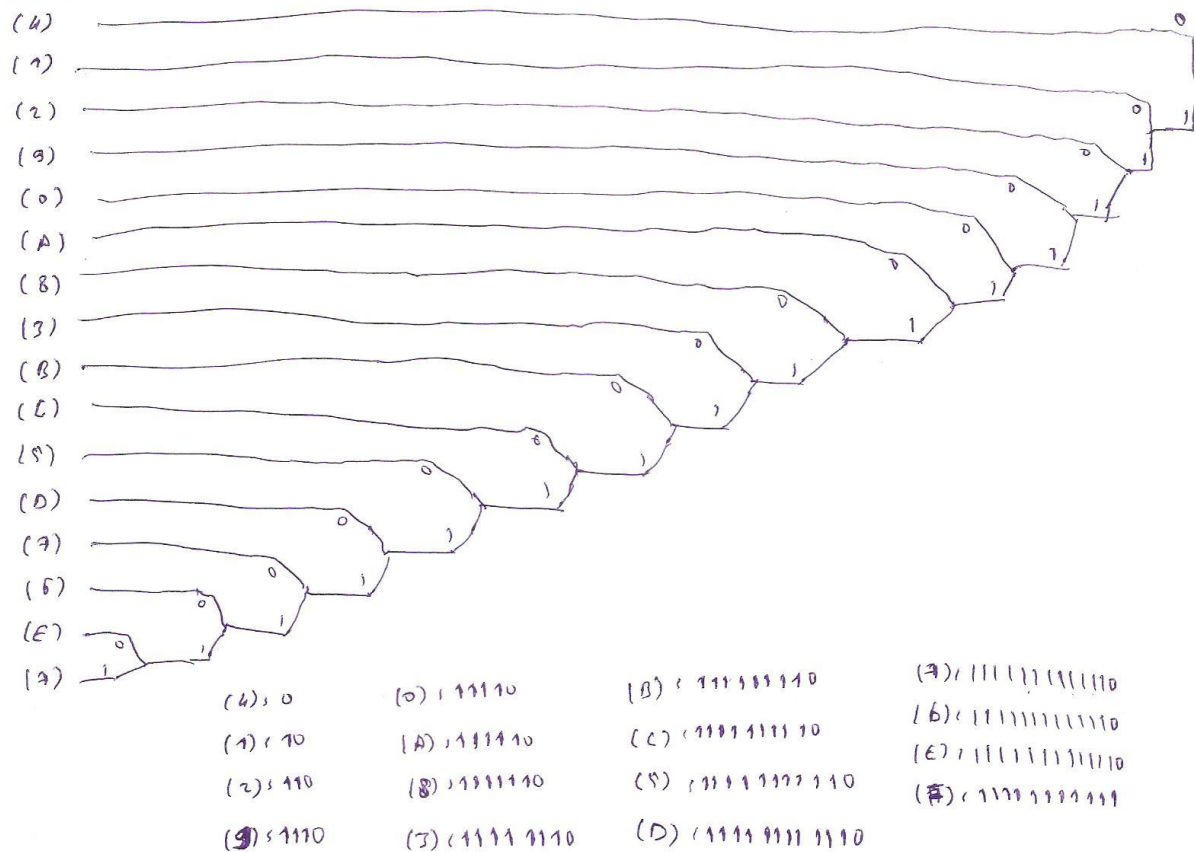
In the stratosphere balloon project, the Stratosphere balloon send to the base station a data message contain hexadecimal character with message length equal to 116. Hexadecimal data mean that we need a tree of 16 roots (0, 1, 2, 3, 4, 5, 6, 7, 8, 9, A, B, C, D, E, and F) to use it in the Huffman coding strategy.

The probability of each character can't know by us but we can use some message data and calculate the percentage in it. For this purpose, I use 10 data message and the percentages were as follow:

- |               |               |               |              |
|---------------|---------------|---------------|--------------|
| (0): 70/1160  | (1): 161/1160 | (2): 106/1160 | (3): 59/1160 |
| (4): 202/1160 | (5): 58/1160  | (6): 41/1160  | (7): 43/1160 |
| (8): 61/1160  | (9): 75/1160  | (A): 67/1160  | (B): 54/1160 |
| (C): 50/1160  | (D): 47/1160  | (E): 40/1160  | (F): 36/1160 |

Then we can sort the character as follow:

$$4 > 1 > 2 > 9 > 0 > A > 8 > 3 > B > C > 5 > D > 7 > 6 > E > F$$



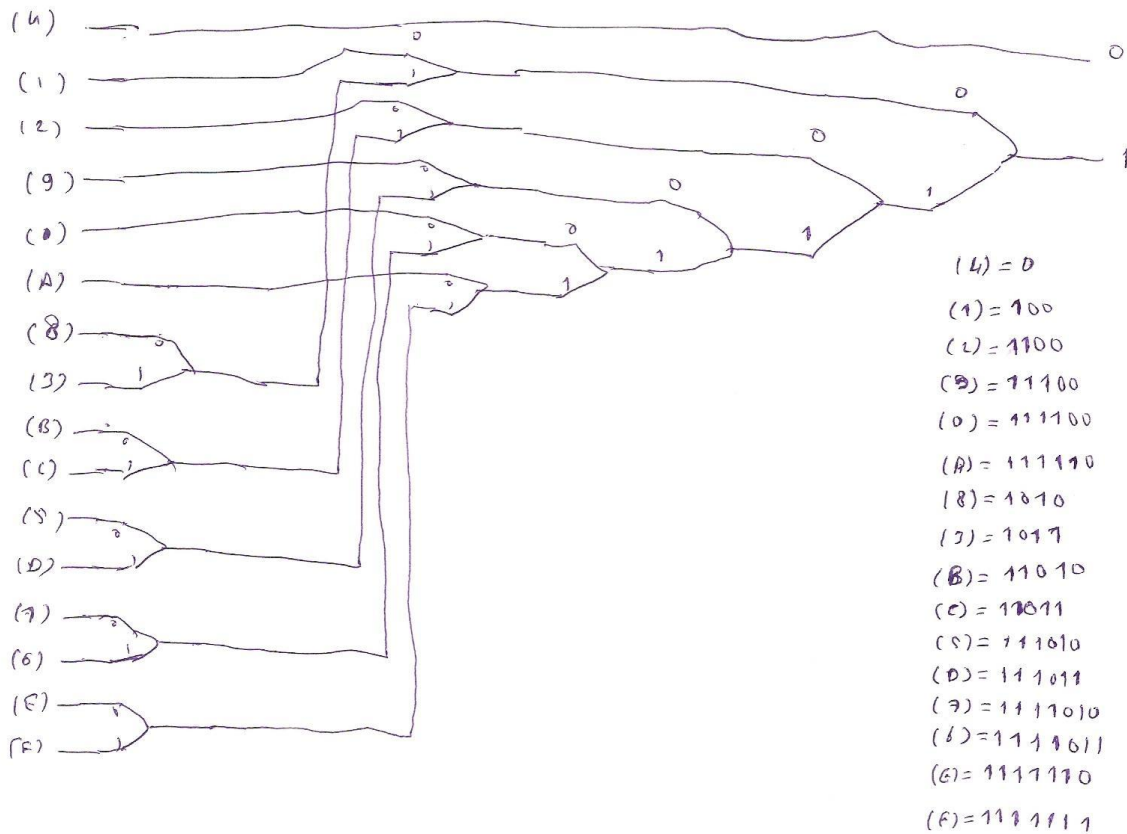
By trying to solve a Huffman code using this tree we get:

Let try with this msg: 41A73C42

The code will be:  
010111110111111111111111011111110111111111100110

We can advanced this tree to reduce the number of bits, the tree bellow reduce the number of bits for each character





By trying to solve the same Huffman code using the new tree we get:

Message : 41A73C42

The code will be: 01001111101111101010111101101100

9.4.2.2 Write the Huffman code (c programming)



As we see in the last part that each Hex characters have one binary code as the following table:

Table1: our Huffman code table

0	111100	4	0	8	1010	C	11011
1	100	5	111010	9	11100	D	111011
2	1100	6	1111011	A	111110	E	1111110
3	1011	7	1111010	B	11010	F	1111111

Now, let's start with the coding side:

The **coding** part is done by 16 (if) conditions for the 16 Hex characters we have it:

Let's start:

```
void Source_Coding(char msg[])
{
    int i, lenght;
    char c0[7] = "111100";
    char c1[7] = "100";
    char c2[7] = "1100";
    char c3[7] = "1011";
    char c4[7] = "0";
    char c5[7] = "111010";
    char c6[7] = "1111011";
    char c7[7] = "1111010";
    char c8[7] = "1010";
    char c9[7] = "11100";
    char cA[7] = "111110";
    char cB[7] = "11010";
    char cC[7] = "11011";
    char cD[7] = "111011";
    char cE[7] = "1111110";
    char cF[7] = "1111111";
    lenght = strlen(msg);
    for(i=0; i <= lenght; i++){
        if (msg[i] == '0')    Send_STRING(c0);
        else if (msg[i] == '1') Send_STRING(c1);
        else if (msg[i] == '2') Send_STRING(c2);
        else if (msg[i] == '3') Send_STRING(c3);
        else if (msg[i] == '4') Send_STRING(c4);
        else if (msg[i] == '5') Send_STRING(c5);
        else if (msg[i] == '6') Send_STRING(c6);
        else if (msg[i] == '7') Send_STRING(c7);
        else if (msg[i] == '8') Send_STRING(c8);
        else if (msg[i] == '9') Send_STRING(c9);
        else if (msg[i] == 'A') Send_STRING(cA);
```

```

else if (msg[i] == 'B') Send_STRING(cB);
else if (msg[i] == 'C') Send_STRING(cC);
else if (msg[i] == 'D') Send_STRING(cD);
else if (msg[i] == 'E') Send_STRING(cE);
else if (msg[i] == 'F') Send_STRING(cF);

//      else set the error bit in the sending message
}

//      Delay10KTCYx(1000);
}

```

In the other hand, in the **decoding** side is done also by some (if) conditions as follows:

```

For(i=0; i<= msglenght; ){
If (code[i] = 0) {i++; m = '4'; break;}
Else {      // the first 1 on the code
I++;
if (code[i] = 0){      // the code now is: 10
if (code[i] = 0) {i++; m = '1'; break;}
else {      // the code now is: 101
i++;
if(code[i] = 0) {i++; m = '8'; break;}
else {i++; m = '3'; break;}
}
Else {      // the code now is: 11
I++;
If(code[i] = 0) {      // the code now is: 110
I++;
If(code[i] = 0) {i++; m = '2'; break;}
Else {
i=i+2;
If(code[i] = 0) { m = 'B'; i++; break;}
Else { m = 'C'; i++; break;}
}
}
Else {      // the code now is: 111

```

```

        I++;
        If(code[i] = 0) {           // the code now is: 1110
            i++;
            If(code[i] = 0) {m = '9'; i++; break;}
            Else{                   // the code now is: 11101
                I++;
                If(code[i] = 0) {m = '5'; i++; break;}
                Else { m = 'D'; i++; break;}
            }
        Else{                       // the code now is: 1111
            I++;
            If(code[i] = 0){        // the code now is: 11110
                I++;
                If(code[i] = 0) { m = '0'; i++; break;}
                Else{               // the code now is: 111101
                    I++;
                    If(code[i] = 0){i++; m = '7'; break;}
                    Else {i++; m = '6'; break;}
                }
            Else{                   // the code now is: 11111
                I++;
                If(code[i] = 0){ i++; m = 'A'; break;}
                Else{               // the code now is: 111111
                    If(code[i] = 0){i++; m = 'E'; break;}
                    Else{i++; m = 'F'; break;}
                }
            }
        }
    }
} // end of the conditions of the first character
} // end of the loop

```

### 9.4.3 Encryption<sup>13</sup>

One of the most widely used block cipher algorithms is the **Data Encryption Standard (DES)**, adopted in 1977 by the American National Standards Institute (ANSI).

After more than twenty years of use with continuous aging due to advances in cryptography, the National Institute of Standards and Technology (NIST). On 2 October 2000 the NIST announced that the new encryption technique, named **Advanced Encryption Standard (AES)**, would use the Rijndael algorithm, designed by two well-known specialists, Joan Daemen and Vincent Rijmen from Belgium.

#### 9.4.3.1 Advanced Encryption Standard (AES)<sup>14</sup>

AES is based on a design principle known as a substitution-permutation network, and is fast in both software and hardware. AES is a variant of Rijndael which has a fixed block size of 128 bits, and a key size of 128, 192, or 256 bits. By contrast, the Rijndael specification *per se* is specified with block and key sizes that may be any multiple of 32 bits, both with a minimum of 128 and a maximum of 256 bits.

AES operates on a 4×4 column-major order matrix of bytes, termed the *state*, although some versions of Rijndael have a larger block size and have additional columns in the state. Most AES calculations are done in a special finite field.

The key size used for an AES cipher specifies the number of repetitions of transformation rounds that convert the input, called the plaintext, into the final output, called the cipher-text. The number of cycles of repetition is as follows:

- 10 cycles of repetition for 128-bit keys.
- 12 cycles of repetition for 192-bit keys.
- 14 cycles of repetition for 256-bit keys.

Each round consists of several processing steps, each containing five similar but different stages, including one that depends on the encryption key itself. A set of reverse rounds are applied to transform cipher-text back into the original plaintext using the same encryption key.

#### 9.4.3.2 AES algorithm

1. KeyExpansion—round keys are derived from the cipher key using Rijndael's key schedule.
2. InitialRound
  1. AddRoundKey—each byte of the state is combined with the round key using bitwise **xor**.

---

<sup>13</sup> Reference: Microchip AN821 Advanced Encryption Standard Using the PIC16XXX page:1

<sup>14</sup> Reference: [http://en.wikipedia.org/wiki/Advanced\\_Encryption\\_Standard](http://en.wikipedia.org/wiki/Advanced_Encryption_Standard)

### 3. Rounds

1. *SubBytes*—a non-linear substitution step where each byte is replaced with another according to a lookup table.
2. *ShiftRows*—a transposition step where each row of the state is shifted cyclically a certain number of steps.
3. *MixColumns*—a mixing operation which operates on the columns of the state, combining the four bytes in each column.

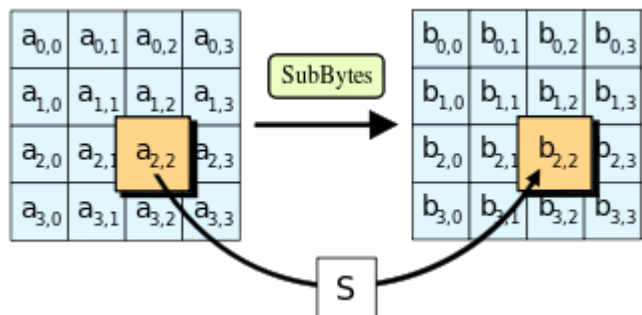
#### 4. AddRoundKey

### 4. Final Round (no *MixColumns*)

1. *SubBytes*
2. *ShiftRows*
3. AddRoundKey

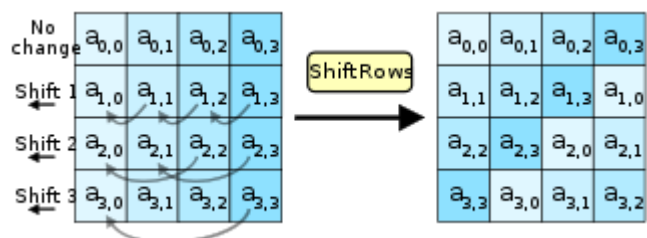
## The *SubBytes* step

In the *SubBytes* step, each byte in the state matrix is replaced with a SubByte using an 8-bit substitution box, the Rijndael S-box. This operation provides the non-linearity in the cipher. The S-box used is derived from the multiplicative inverse over  $GF(28)$ , known to have good non-linearity properties. To avoid attacks based on simple algebraic properties, the S-box is constructed by combining the inverse function with an invertible affine transformation. The S-box is also chosen to avoid any fixed points (and so is a derangement), and also any opposite fixed points.



## The *ShiftRows* step

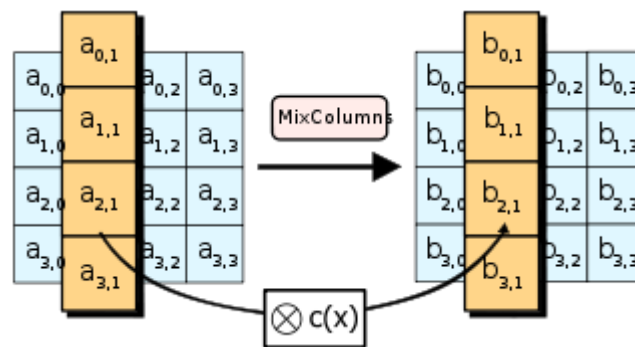
The *ShiftRows* step operates on the rows of the state; it cyclically shifts the bytes in each row by a certain offset. For AES, the first row is left unchanged. Each byte of the second row is shifted one to the left. Similarly, the third and fourth rows are shifted by offsets of two and three respectively.



For blocks of sizes 128 bits and 192 bits, the shifting pattern is the same. Row  $n$  is shifted left circular by  $n-1$  bytes. In this way, each column of the output state of the *ShiftRows* step is composed of bytes from each column of the input state. (Rijndael variants with a larger block

size have slightly different offsets). For a 256-bit block, the first row is unchanged and the shifting for the second, third and fourth row is 1 byte, 2 bytes and 3 bytes respectively — this change only applies for the Rijndael cipher when used with a 256-bit block, as AES does not use 256-bit blocks. The importance of this step is to make columns not linear independent. If so, AES becomes four independent block ciphers.

### The MixColumns step



In the MixColumns step, the four bytes of each column of the state are combined using an invertible linear transformation. The MixColumns function takes four bytes as input and outputs four bytes, where each input byte affects all four output bytes. Together with ShiftRows, MixColumns provides diffusion in the cipher.

During this operation, each column is multiplied by the known matrix that for the 128-bit key is:

$$\begin{bmatrix} 2 & 3 & 1 & 1 \\ 1 & 2 & 3 & 1 \\ 1 & 1 & 2 & 3 \\ 3 & 1 & 1 & 2 \end{bmatrix}$$

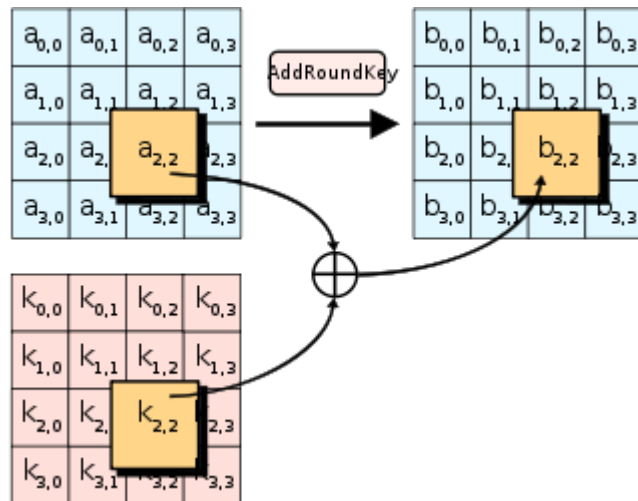
The multiplication operation is defined as: multiplication by 1 means no change, multiplication by 2 means shifting to the left, and multiplication by 3 means shifting to the left and then performing xor with the initial unshifted value. After shifting, a conditional xor with 0x1B should be performed if the shifted value is larger than 0xFF.

In more general sense, each column is treated as a polynomial over GF(28) and is then multiplied modulo  $x^4+1$  with a fixed polynomial  $c(x) = 0x03 \cdot x^3 + x^2 + x + 0x02$ . The coefficients are displayed in their hexadecimal equivalent of the binary representation of bit polynomials from GF(2)[x]. The MixColumns step can also be viewed as a multiplication by a

particular MDS matrix in a finite field. This process is described further in the article Rijndael mix columns.

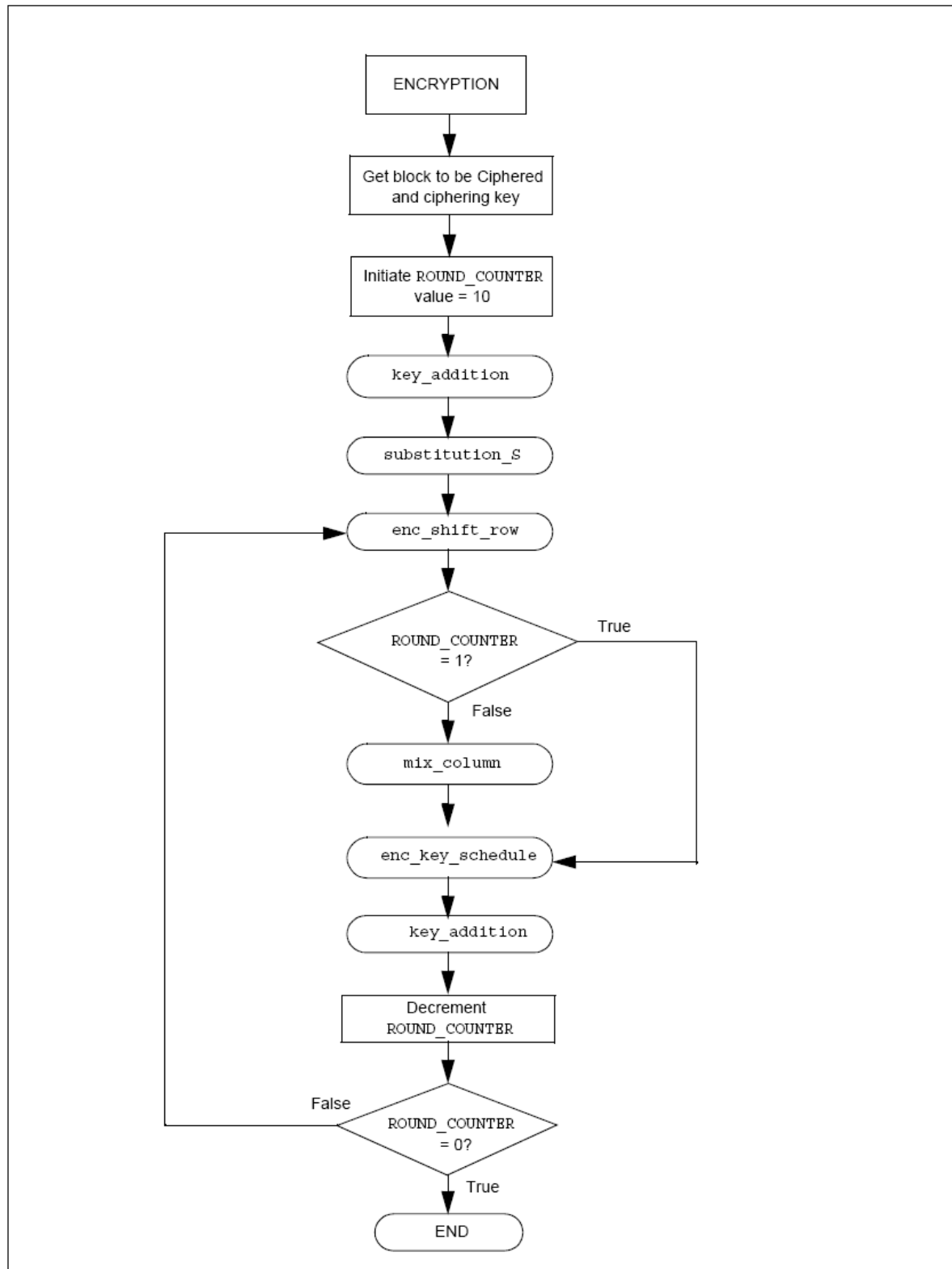
### The AddRoundKey step

In the AddRoundKey step, the subkey is combined with the state. For each round, a subkey is derived from the main key using Rijndael's key schedule; each subkey is the same size as the state. The subkey is added by combining each byte of the state with the corresponding byte of the subkey using bitwise XOR.



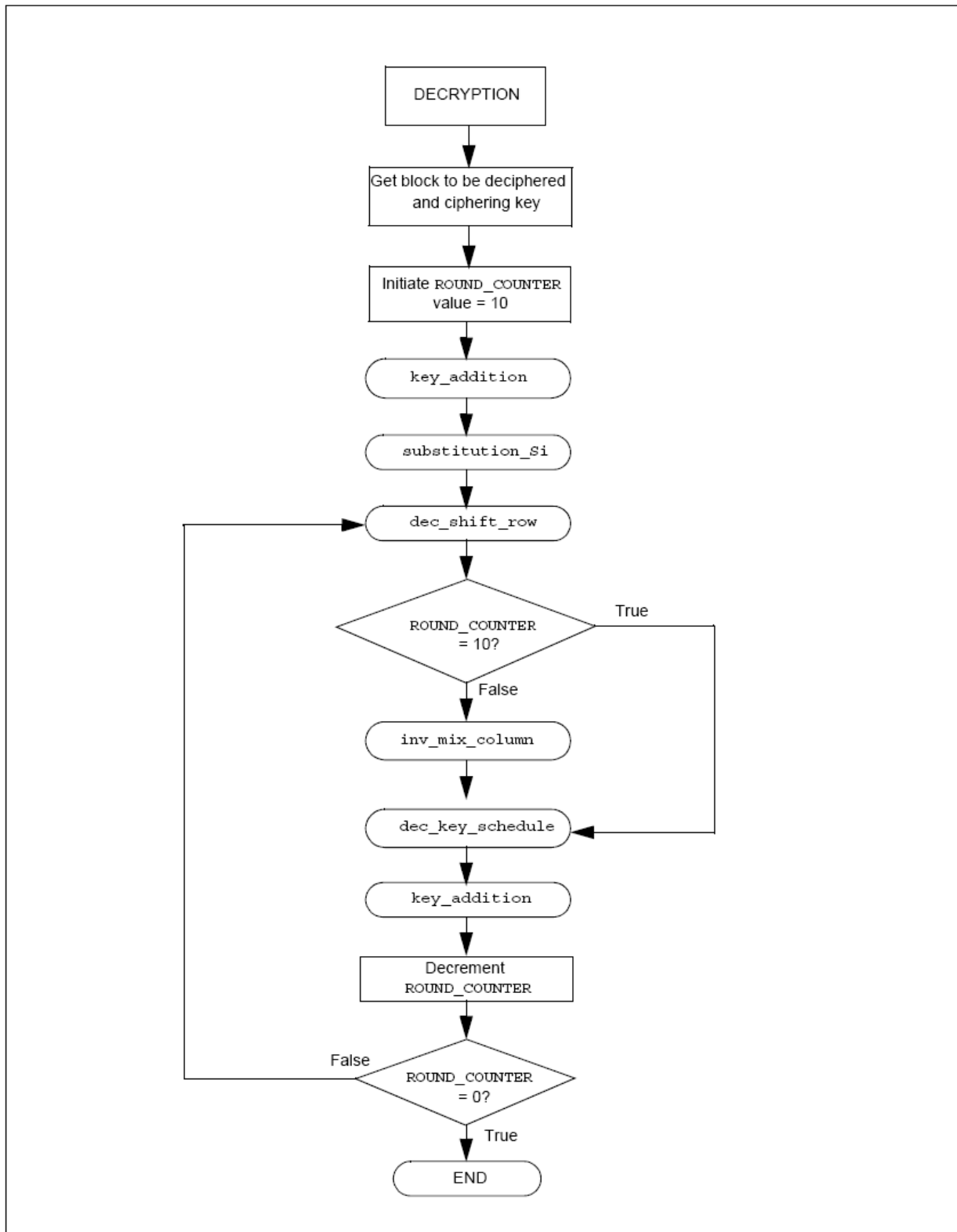
### 9.4.3.3 Encryption and Decryption AES flow chart <sup>15</sup>

#### Encryption flow chart



<sup>15</sup> Reference: Microchip AN821 Advanced Encryption Standard Using the PIC16XXX page:18, 19

## Decryption flow chart



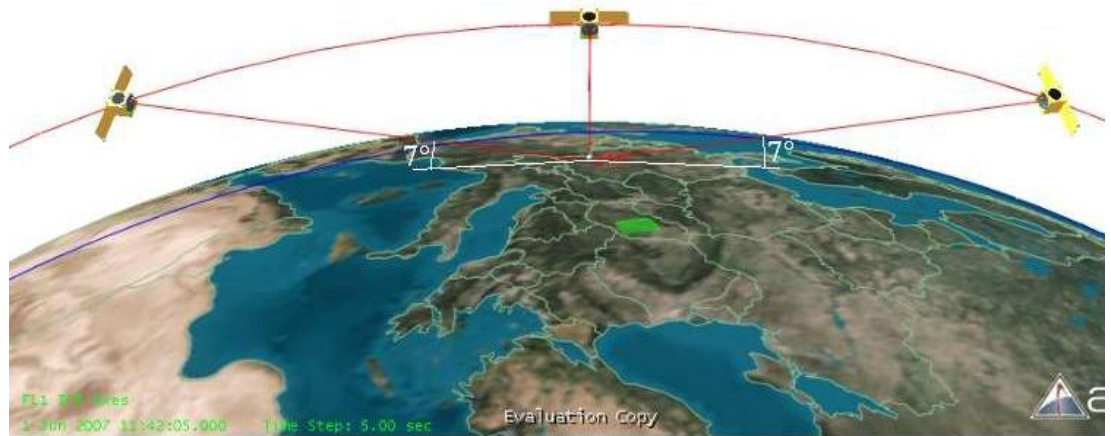
## 9.4.3.4 AES program (C programming)

See [IAP\_ECS]

## Part III: Mission Planning and Simulation

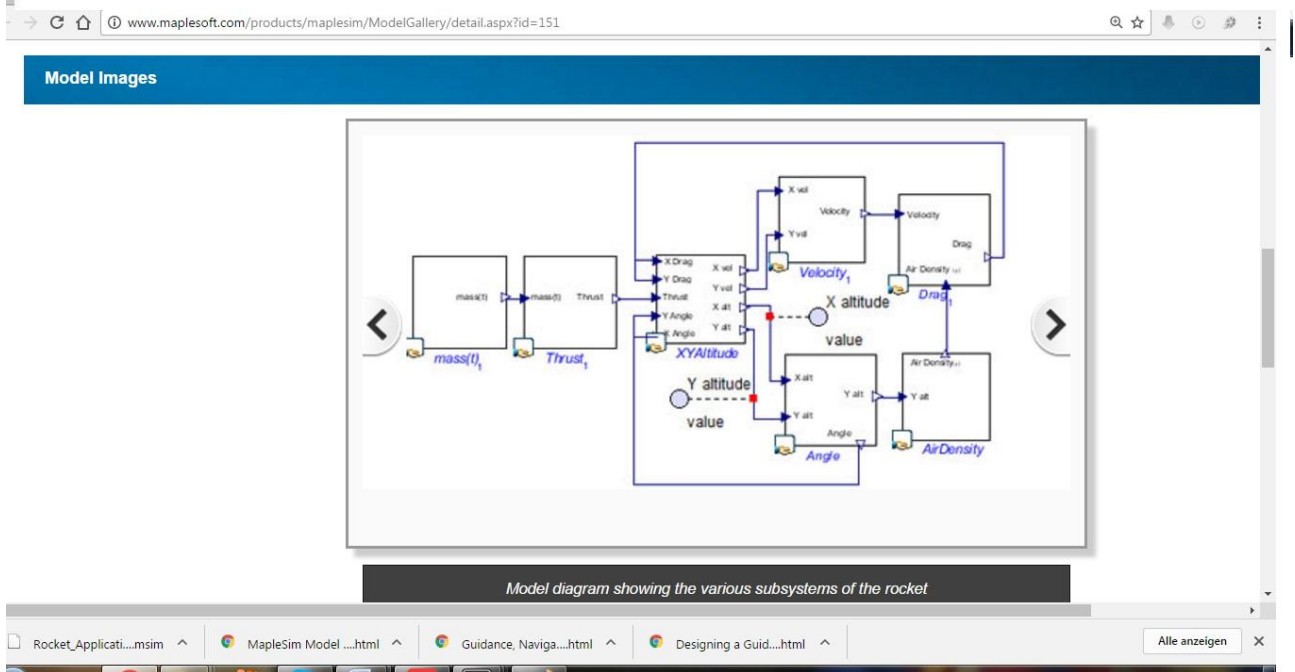
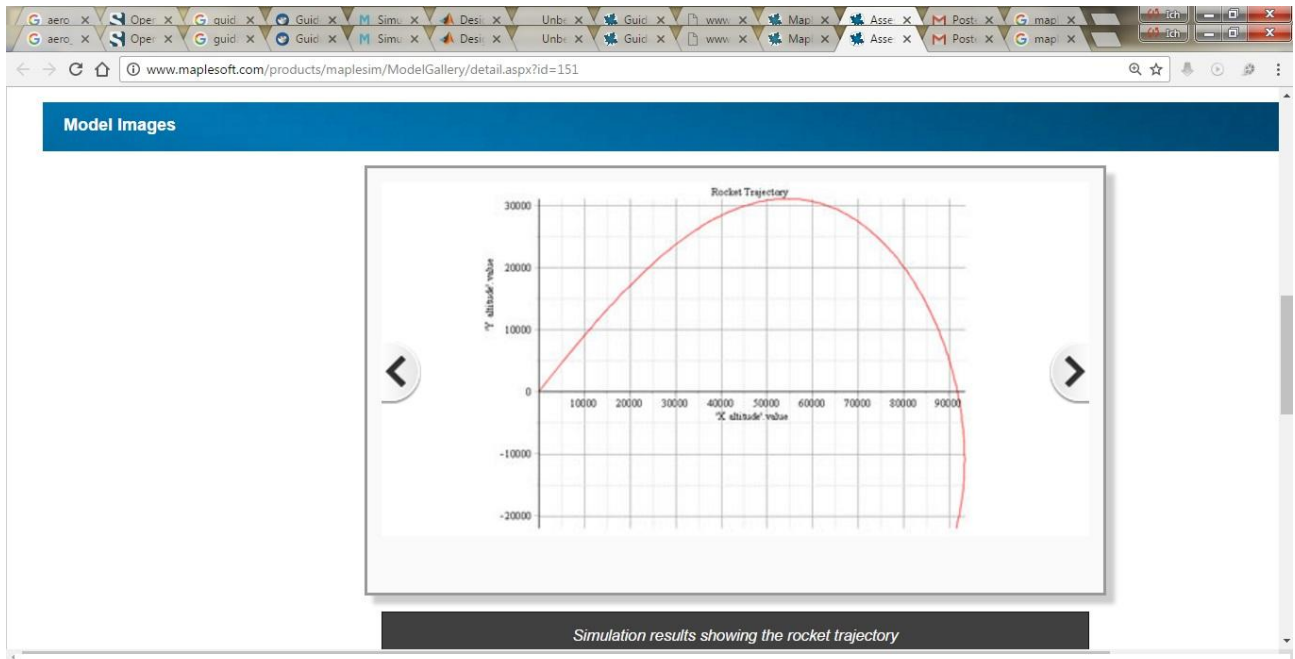
## 10 Mission Planning

- Tracked Downlink (fixed direction to receiver station)

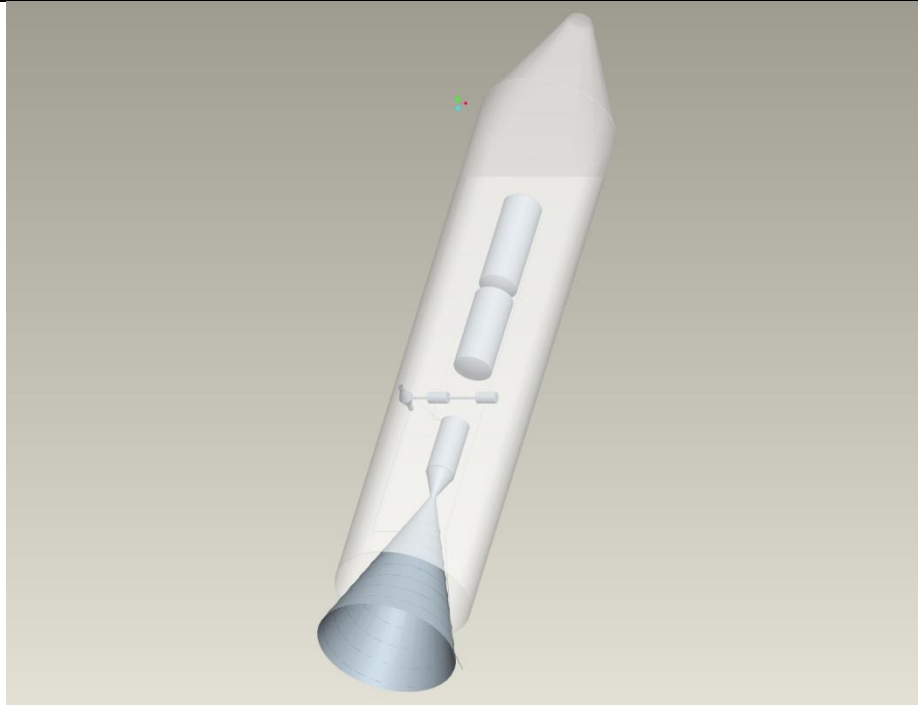


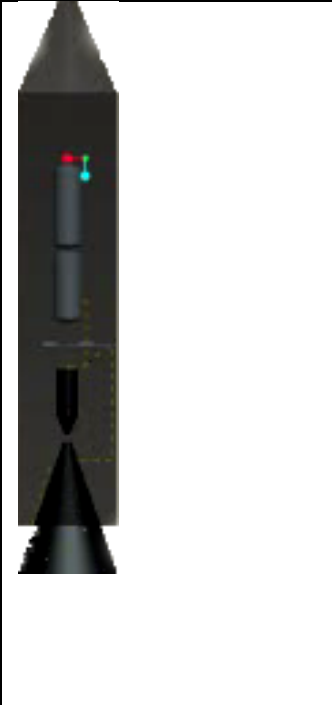
Target pointing mode (from [Yasir 2010], p.22)

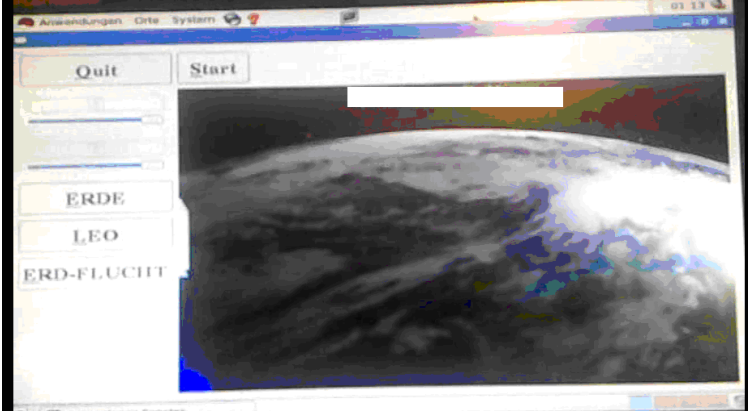
# 11 Mission simulation with Maple

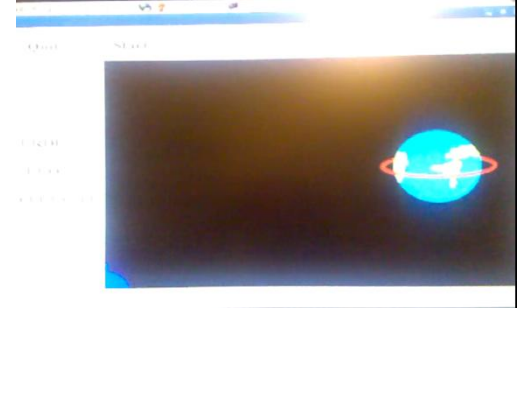


## 12 Mission Simulation 2012: Shuttle Flight simulation into orbit









```

s gamma 317 - 43.121498 h 317 - 1887127.250000 x 317 - 1990971
s gamma 318 - 43.119830 h 318 - 1895233.875000 x 318 - 1999628
s gamma 319 - 43.116578 h 319 - 1903342.000000 x 319 - 2008287
s gamma 320 - 43.114109 h 320 - 1911451.500000 x 320 - 2016948
s gamma 321 - 43.111649 h 321 - 1919562.500000 x 321 - 2025612
s gamma 322 - 43.109188 h 322 - 1927674.875000 x 322 - 2034278
s gamma 323 - 43.106728 h 323 - 1935788.500000 x 323 - 2042946
s gamma 324 - 43.104267 h 324 - 1943903.500000 x 324 - 2051616
s gamma 325 - 43.101807 h 325 - 1952019.750000 x 325 - 2060289
s gamma 326 - 43.099350 h 326 - 1960137.375000 x 326 - 2068963
s gamma 327 - 43.096893 h 327 - 1968256.250000 x 327 - 2077640
s gamma 328 - 43.094437 h 328 - 1976376.250000 x 328 - 2086318
s gamma 329 - 43.091980 h 329 - 1984497.500000 x 329 - 2094999
s gamma 330 - 43.089523 h 330 - 1992620.000000 x 330 - 2103682
s gamma 331 - 43.087067 h 331 - 2000743.625000 x 331 - 2112366
s gamma 332 - 43.084610 h 332 - 2008868.375000 x 332 - 2121053
s gamma 333 - 43.082153 h 333 - 2016994.250000 x 333 - 2129741
s gamma 334 - 43.079697 h 334 - 2025121.250000 x 334 - 2138432
s gamma 335 - 43.077240 h 335 - 2033249.250000 x 335 - 2147124
s gamma 336 - 43.074783 h 336 - 2041378.250000 x 336 - 2155818
s gamma 337 - 43.072330 h 337 - 2049508.250000 x 337 - 2164514
s gamma 338 - 43.069878 h 338 - 2057639.250000 x 338 - 2173212
s gamma 339 - 43.067425 h 339 - 2065771.250000 x 339 - 2181912
s gamma 340 - 43.064972 h 340 - 2073904.250000 x 340 - 2190613
    
```

```
#include "/home/iap/gtk+-uebungen/gtk-2.0/gtk/gtk.h"
```

```
#include <unistd.h>
```

```
void loeschen_funk(GtkWidget *widget, gpointer daten);
int raketenflugberechnung_ebeneErde();

int main(int argc, char *argv[])
{
    GtkWidget *hauptfenster;
    GtkWidget *schalter;
    GtkWidget *vbox;

    gtk_init(&argc, &argv);

    hauptfenster = gtk_window_new(GTK_WINDOW_TOPLEVEL);
    gtk_widget_set_usize(GTK_WIDGET(hauptfenster), 180,120);
    gtk_window_set_title(GTK_WINDOW(hauptfenster), "Mondprojekt");

    gtk_signal_connect(GTK_OBJECT(hauptfenster), "destroy",
        GTK_SIGNAL_FUNC(loeschen_funk), NULL);
    gtk_container_set_border_width(GTK_CONTAINER(hauptfenster), 20);

    vbox = gtk_vbox_new(TRUE, 0);
    gtk_container_add(GTK_CONTAINER(hauptfenster), vbox);

    /*Schalter einrichten*/
    schalter = gtk_button_new_with_label("Raketenflug berechnen");
    gtk_signal_connect(GTK_OBJECT(schalter), "clicked",
        GTK_SIGNAL_FUNC(raketenflugberechnung_ebeneErde), 0 );
    gtk_box_pack_start(GTK_BOX(vbox), schalter, TRUE, FALSE, 0);
    gtk_widget_show(schalter);

    /* Fenster sichtbar machen. */
    gtk_widget_show(vbox);
```

```
gtk_widget_show(hauptfenster);

gtk_main();

g_print("main() wird nun beendet.\n");
return 0;
}

void loeschen_funk(GtkWidget *Widget, gpointer zdaten)
{
    g_print("Beenden : Destroy-Signal wurde empfangen.\n");
    gtk_main_quit();
}

/*-----*/
/*      Berechnung      */
/*-----*/

/*globale Variablen und Arrays.*/

float v[500];
float F = 30000;
float F_W = 0;
float c_W = 0.8;
float A_R = 0.8;
float luft_dichte = 0.002;
float m = 1000;
int g = 10;
float gamma_grad[500];
float gamma_rad;
float sin_gamma;
float cos_gamma;
float h[500];
float x[500];
int delta_t = 2;
int i;
```

```

int raketenflugberechnung_ebeneErde()
{
v[0] = 0;
gamma_grad[0] = 90;
h[0] = 0;
x[0] = 0;

for(i = 0; i < 500; i++)
{
sleep(2);

gamma_rad = gamma_grad[i] * 3.1415/180;
sin_gamma = sin(gamma_rad);
cos_gamma = cos(gamma_rad);
v[i+1] = ( (F-F_W) / m - (g*sin_gamma) ) * delta_t + v[i];
F_W = c_W * A_R * (luft_dichte/2) * v[i] * v[i];
gamma_grad[i+1] = ((-2*g)/(v[i]+v[i+1]))*cos_gamma*delta_t+gamma_grad[i];
h[i+1] = 0.5 * (v[i] + v[i+1]) * sin_gamma * delta_t + h[i];
x[i+1] = 0.5 * (v[i] + v[i+1]) * cos_gamma * delta_t + x[i];
gamma_grad[2] = 45;

if (m < 10)
    m = m - 10;

printf("v_%d = %f m/s \t gamma_%d = %f \t h_%d = %f \t x_%d = %f \n" \
    , i, v[i], i, gamma_grad[i], i, h[i], i, x[i]);
}
return 0;
}

```

## 13 Ground Track Visualization

### 13.1.1 Tools for visualization of the ground track of satellites: Gpredict and OpenSat

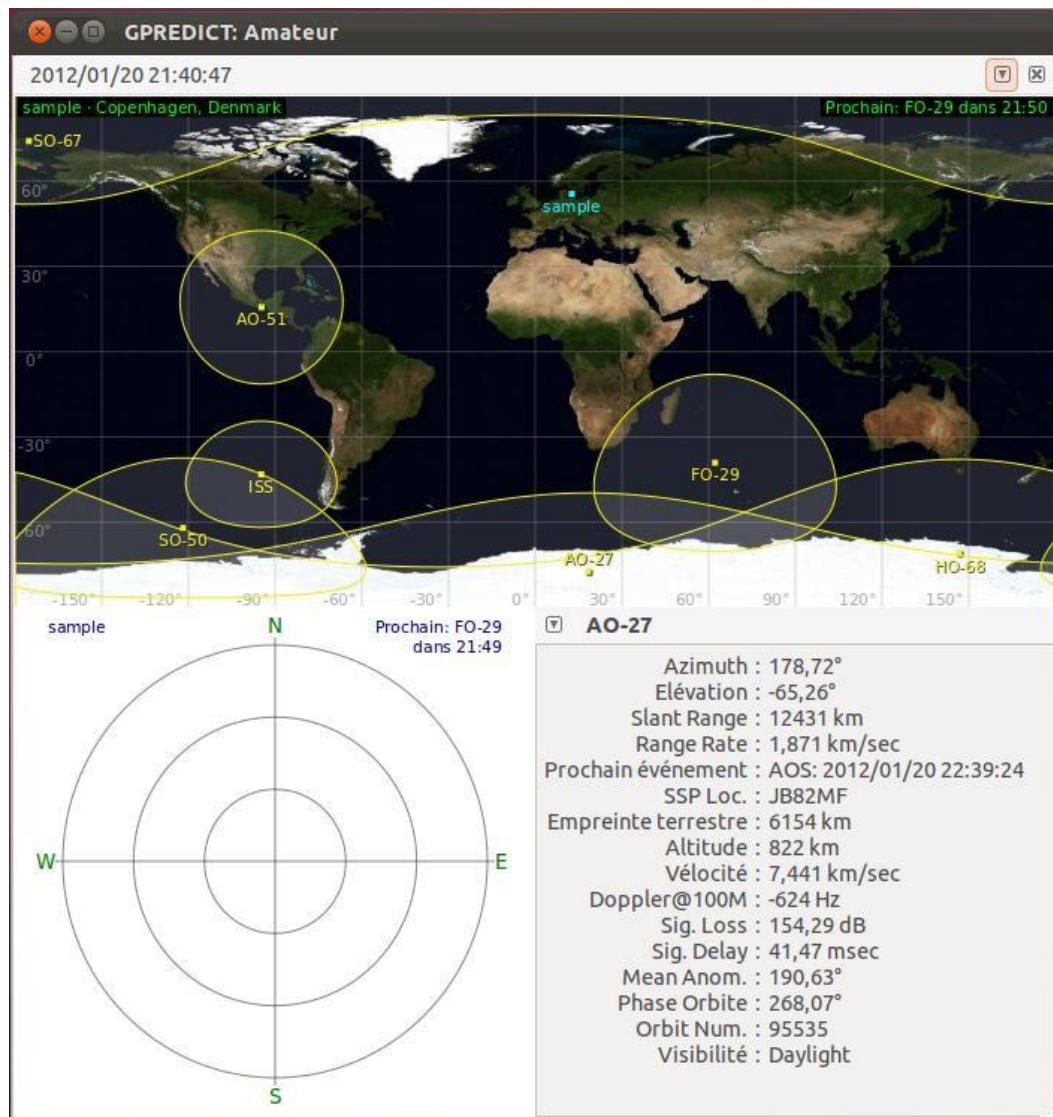


Figure 13.1: Gpredict software

To simulate the satellite around the earth, a specific program is necessary.

We want to take such open source program and adapt it to our specific requirements. We want to have a program which tracks our satellite (IAP-SAT). The source code of gpredict is used to make our program.

Gpredict is a real-time satellite tracking and orbit prediction program (Fig. 3.17). A satellite tracking program is a computer program that predicts the position and velocity of a satellite at a given time using a mathematical model of the orbit. It can also predict the time of future passes for a satellite, and provide you with detailed information about each pass. [13]

Gpredict can track an unlimited number of satellites and display their position and other data in lists, tables, maps, and polar plots (Fig. 3.18).

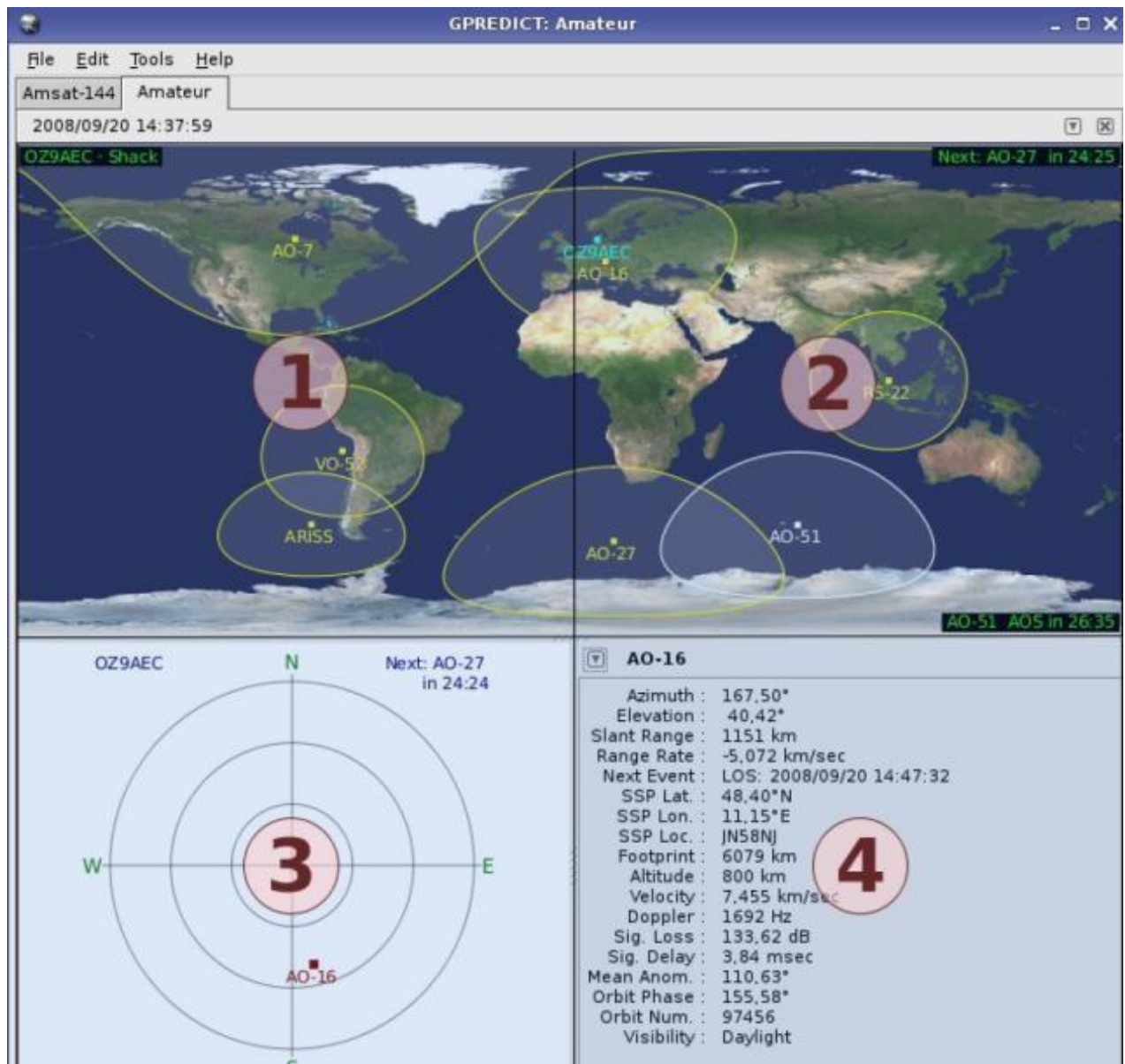


Figure 13.2: Window of Gpredict (list, map and polar plot)

### Opensat

It is open source software, which also follows all satellites in the atmosphere, and gives their ground tracking (Fig. 3.19 and Fig. 3.20), as Gpredict.



Figure 13.3: Open-Satellite software

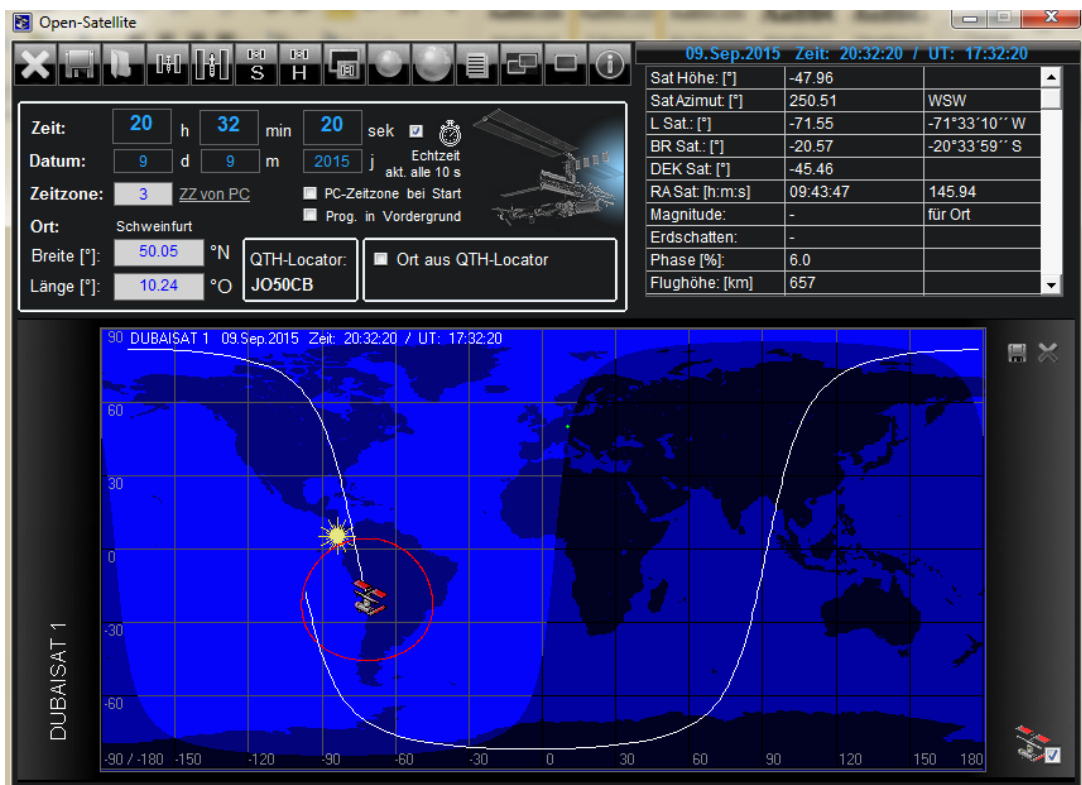


Figure 13.4: Window of OpenSatellite

## 14 Simulation of IAP-SAT mission 2015

### 14.1 Specification of IAP-SAT's parameters

IAP-SAT is the first Lebanese meteorological satellite. It will be used to take meteorological data to estimate the state of weather in Lebanon.

This satellite has the same parameters of Dubai-SAT;

It will be placed on a sun-synchronous low earth orbit, on a nominal altitude of 680 Km. [10]

The parameters of this satellite are presented in the following table (Table 2.1):

Parameters	Features
Orbits	Sun-synchronous Low Earth Orbit
Altitude	680 Km
Inclination	98.13°
Mass	200 Kg (Payload: 50Kg, Bus:150Kg)
Dimension	Hexagonal: 1.2×1.2(m)
Attitude Accuracy	0.2°

**Table 14.1: Parameters of IAP-SAT**

### 14.2 Description and Modeling of IAP-SAT

This satellite contains, according to its mission:

- A camera
- Sensors: 3 gyroscopes, 3 accelerometers
- Actuators: 4 electrical propulsions (Hall Effect thrusters)
- Board of communication
- Board computer
- Battery
- Antenna
- 3 solar panels

After the specification of IAP-SAT and fixing its parameters, this satellite will be modeled. The program CAD is used to attain this object (Fig. 2.2).

IAP-SAT has a shape close to that of DubaiSat.

We construct geometrical shapes depending on the shape of the body represented by this geometric shape, for example: a hexagonal shape represents the body of the satellite, a rectangular shape represents the computer board; a cylindrical shape represents the antenna. Then, we approach and we collect all these forms together in a specific manner to obtain the model of our satellite.

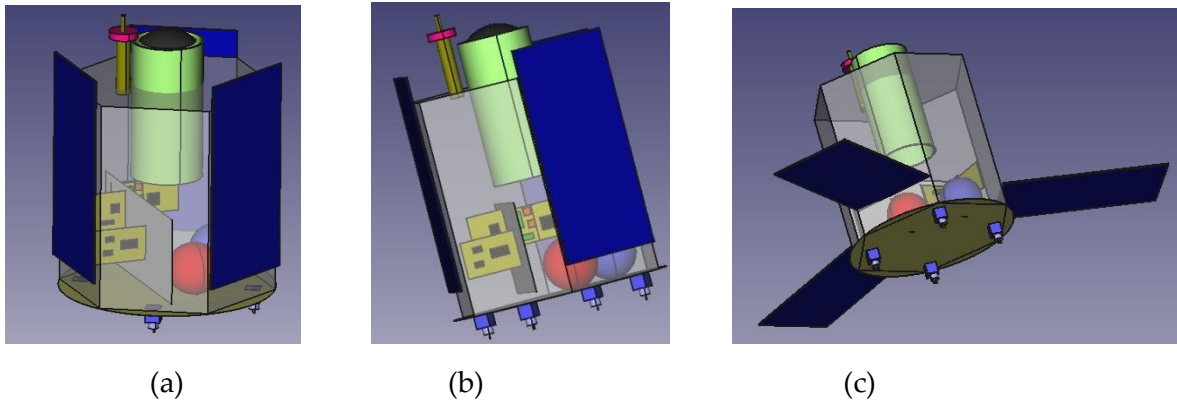


Figure 14.1 (a, b, c): Model of IAP-SAT in FreeCAD

### 14.3 Visualization of the ground track of IAP-SAT

After modeling this satellite, it will be constructed and launched to take the needed meteorological data. This satellite attains the sun-synchronous low earth orbit, and starts to turn around the earth. The ground station detects these moves by showing the ground track for this satellite when it changes its position with the time. We use the OpenSatellite software to follow the satellite and obtain its ground tracking represented in the next figures (Fig.2.3 and Fig. 2.4), and we can estimate the position of this satellite which changes with time, so we obtain the prediction of its ground tracking.

09.Sep.2015 Zeit: 20:28:00 / UT: 17:28:00		
Sat Höhe: [°]	-53.12	
Sat Azimut: [°]	237.00	WSW
L Sat: [°]	-67.53	-67°31'44" W
BR Sat: [°]	-36.34	-36°20'25" S
DEK Sat: [°]	-55.40	
RA Sat: [h:m:s]	09:32:23	143.10
Magnitude:	-	für Ort
Erdschatten:	-	
Phase [%]:	14.0	
Flughöhe: [km]	659	
Abstand SSP: [km]	12250	
Slantrange: [km]		
Velocity: [km/s]	7.53	
Umlauf: [min]	98.23	
Rev-Nr.:	32733	
Alter TLE Daten [d]:	2228.60	<a href="#">Bitte TLE updaten</a>
Achse a [km]:	7036	große Achse
Achse b [km]:	7020	kleine Achse
Höhe Mond: [°]	-13.94	
Azimut Mond: [°]	312.11	NW
L_Mond: [°]	-121.54	-121°32'17" W
BR_Mond: [°]	14.35	14°21'11" N
DEK_Mond: [°]	14.26	
RA_Mond: [h:m:s]	08:35:38	128.91 (geoz.)
Mondphase:	11.3 % ab	
Höhe Sonne: [°]	2.16	
Azimut Sonne: [°]	275.58	W
L_Sonne: [°]	-82.66	-82°39'22" W
BR_Sonne: [°]	5.27	05°16'27" N
DEK_Sonne: [°]	5.24	
RA_Sonne: [h:m:s]	11:11:09	167.79

Figure 14.2: Window of OpenSatellite when DubaiSat is selected

IAP-SAT is not in the atmosphere now, so we try to follow the ground tracking of the closest satellite; it is Dubaisat.

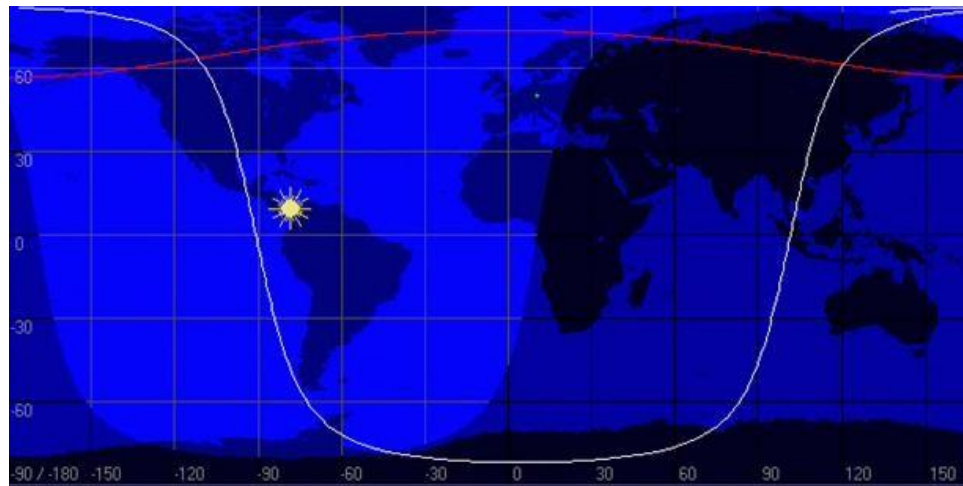


**Figure 14.3: One complete rotation around the earth**

The satellite accomplishes one rotation around the earth in 90 minutes.

After 90 minutes, it takes another position for a new rotation. The difference between the previous and the next track is shown in the figure 2.4:

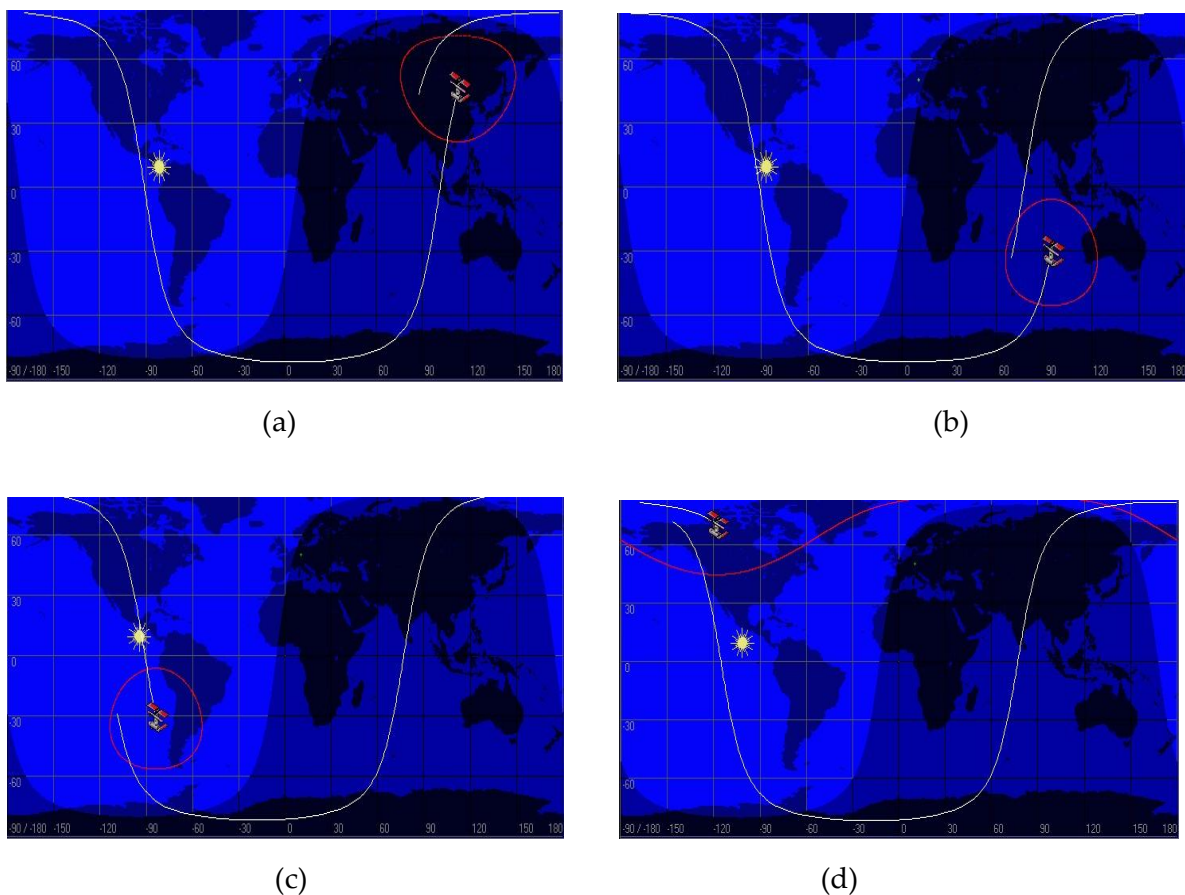


**Figure 14.4 (a, b, c, d): Ground tracking of DubaiSat**

The satellite follows the connected line, and the other line is the previous trajectory of this satellite before 90 minutes.

The satellite realizes about 16 rotations in the day. All these rotations are shown in the figure 2.5:

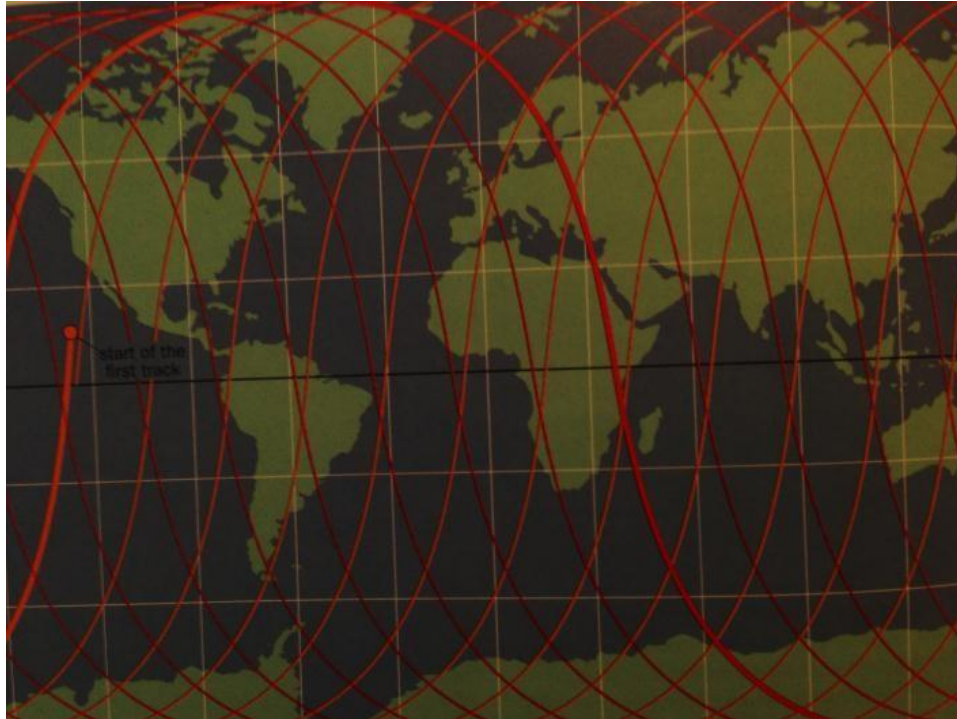


**Figure 14.5: All rotations of the satellite around the earth during the day**

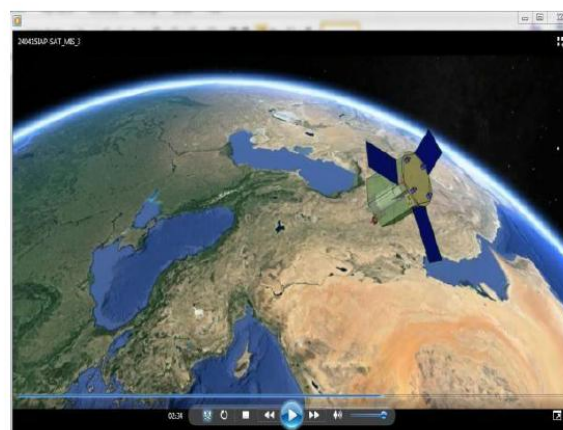
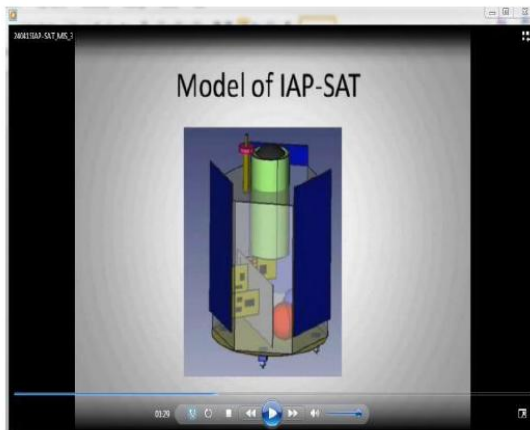
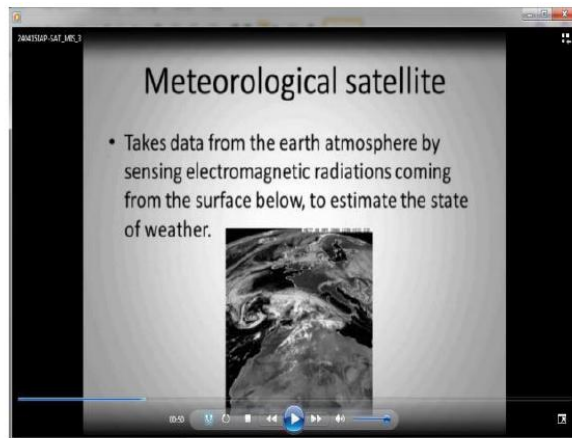
## 15 Presentation Film 2015

### 15.1 Payload Program

Earth Surveillance to take meteorological data to take meteorological data to monitor and estimate the energy supply potential of large scale photovoltaic energy plants to control a national alternative energy supply program. The satellite shall be based on technology of Turkish Göktürk and DubaiSat-1

### 15.2 Presentation Film of MIS

After modeling, specification, prediction of position and tracking the satellite, we make a film of this mission simulation. This film contains all results of the first part of the project (specification). Screenshots of this film are represented in the following figure:



## 16 Mission Simulation with CelestLab (2020)

### 16.1 CelestLab Demo Tool

CelestLab is a numerical tool which is an add-on to Scilab in which it deals with satellite and orbit simulation, tracking and behavior. The CelestLab has a large library to allow the simulation or space application. The CelestLab provide the user with some demos to create standard simulation application. The used can change the initiation parameters in order to display the needed results. Once you add the CelestLab Library you can access the Demo tools.

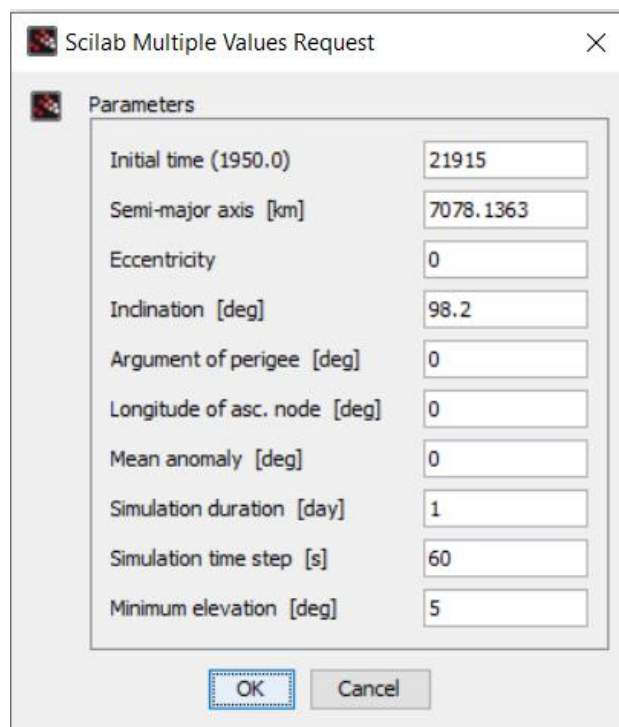
#### 16.1.1 Visibility:

This feature in the CelestLab Demo tool help the user to simulate the movement of the satellite. This tool has eight main sections:

- 1) *Accessibility at equator*
- 2) *Ground station pointing error*
- 3) *Ground station visibility space time coverage*
- 4) *Visibility duration*
- 5) *Visibility parameter*
- 6) *Visibility parameter 2*
- 7) *Visibility pass*

#### Ground Station Visibility:

As for the round Station Visibility. The user should specify the following parameter **presented in figure** . This tool will display a 2D map of the earth with the orbit pass way of the satellite. The display will all be in 2Dimension.



The image shows a dialog box titled "Scilab Multiple Values Request" with a close button (X) in the top right corner. Below the title bar is a section labeled "Parameters" containing a list of input fields with their corresponding values:

Parameter	Value
Initial time (1950.0)	21915
Semi-major axis [km]	7078.1363
Eccentricity	0
Inclination [deg]	98.2
Argument of perigee [deg]	0
Longitude of asc. node [deg]	0
Mean anomaly [deg]	0
Simulation duration [day]	1
Simulation time step [s]	60
Minimum elevation [deg]	5

At the bottom of the dialog box are two buttons: "OK" and "Cancel".

Figure 16-1: Visibility parameters panel

Once we have all the Initial data set, the tool will present the orbit pass on the earth map, **Check figure** , the figure has the degrees which specify the position of the orbit place. Once

we have the orbit we can use the right click on the map to specify the position in which we want to check the visibility time.

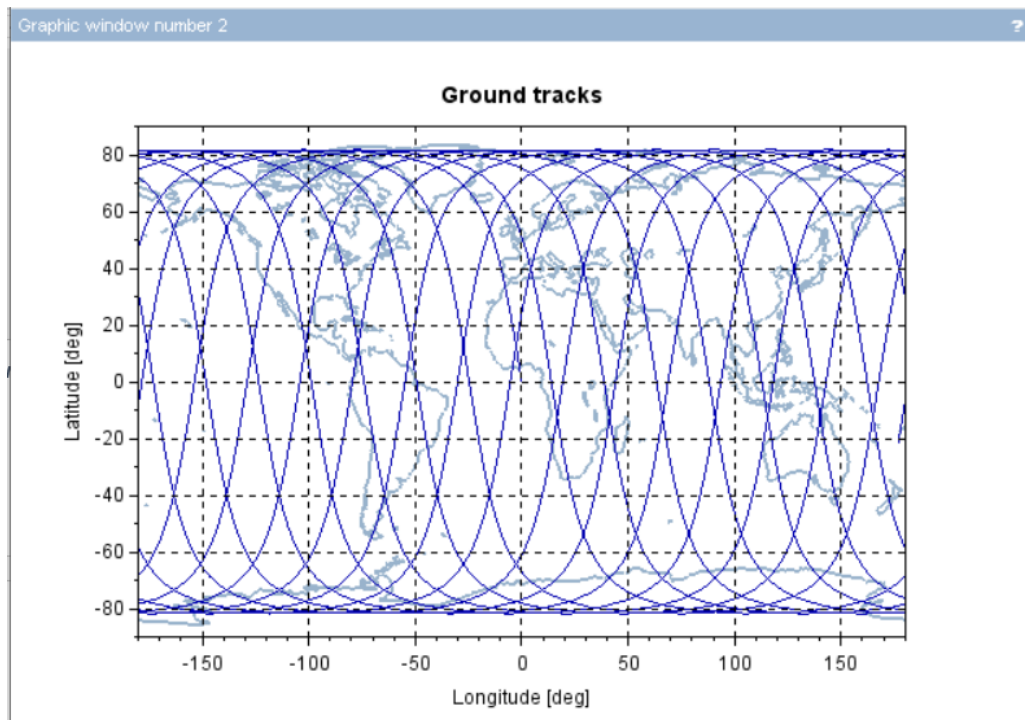


Figure 16-2: Orbit pas of the satellite on a 2D Earth Map

Once the position is specify, the visibility pass windows will present the time in which the satellite is visible from the location specified. **Check figure**

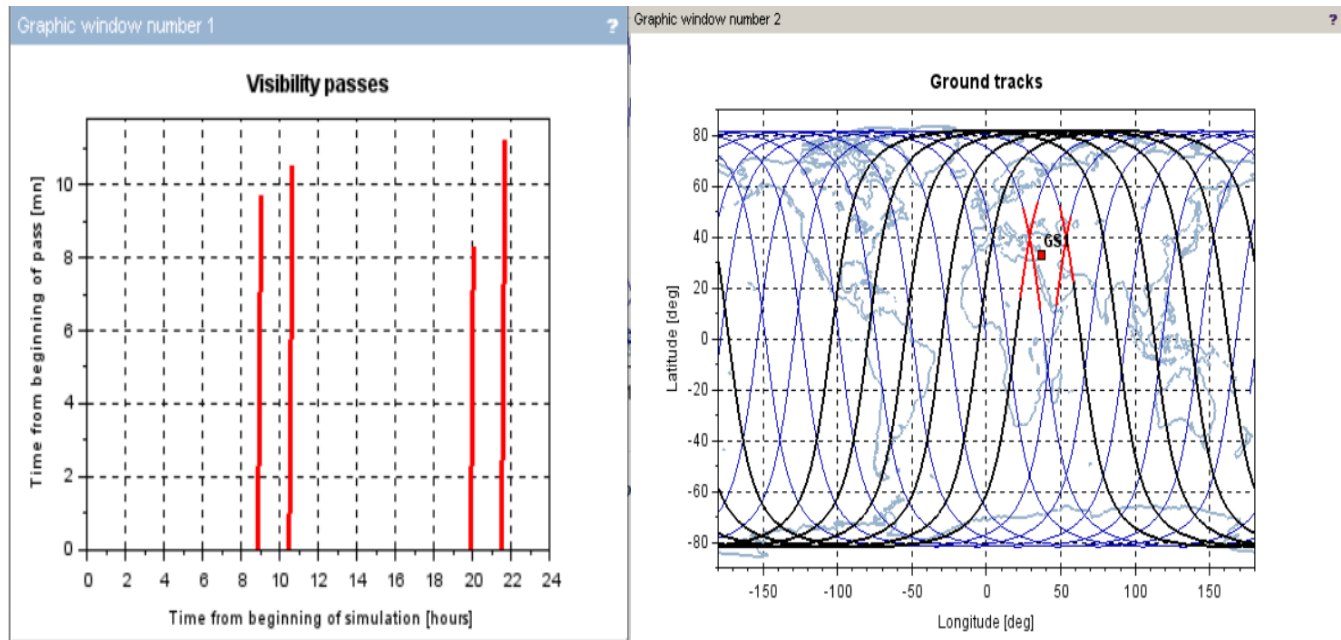


Figure 16-3: Orbit pass and satellite vision time

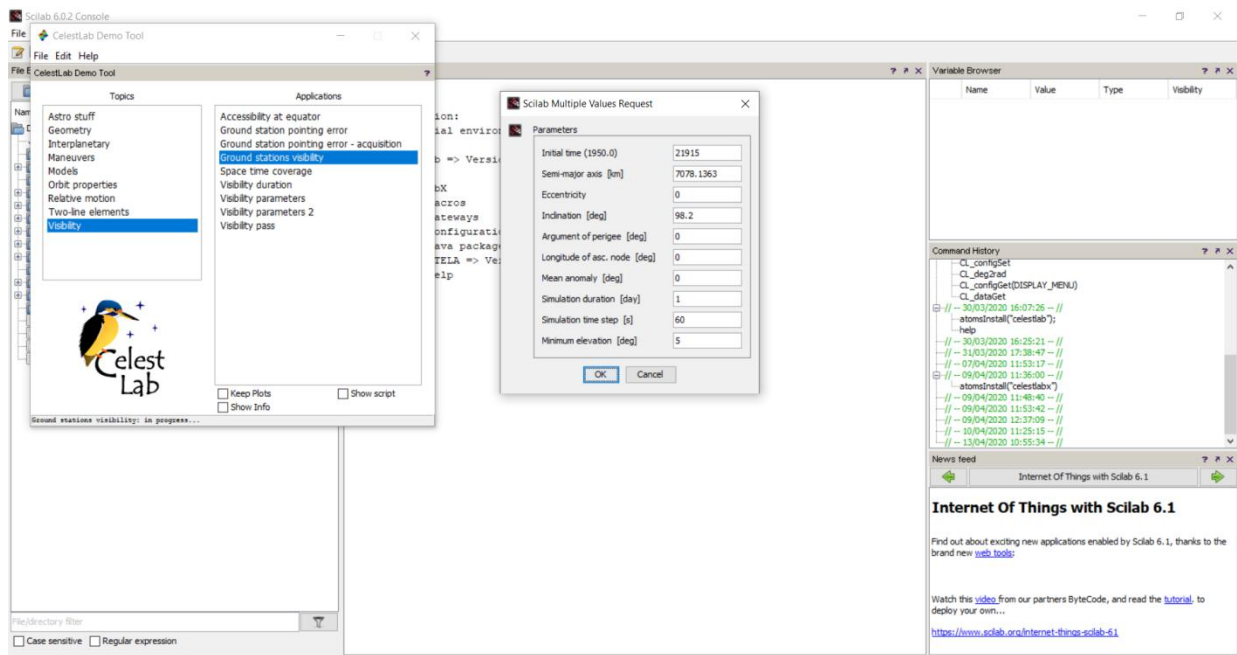
## 16.2 Principle and Task

TODO:

- Trajectory Simulation of Operational Flight of IAP-SWRDA\_SAT (Low Earth Orbit)
- Trajectory Simulation of Operational Flight of IAP-SWRDA\_SAT (Low Earth Orbit)
- Trajectory Simulation of Transport Vehicle for IAP-SWRDA\_SAT

- Trajectory Simulation of Transport Vehicle for IAP-COMSAT

## 16.3 Trajectory Simulation of Operational Flight of IAP-SWRDA\_SAT (Low Earth Orbit)<sup>16,17</sup>

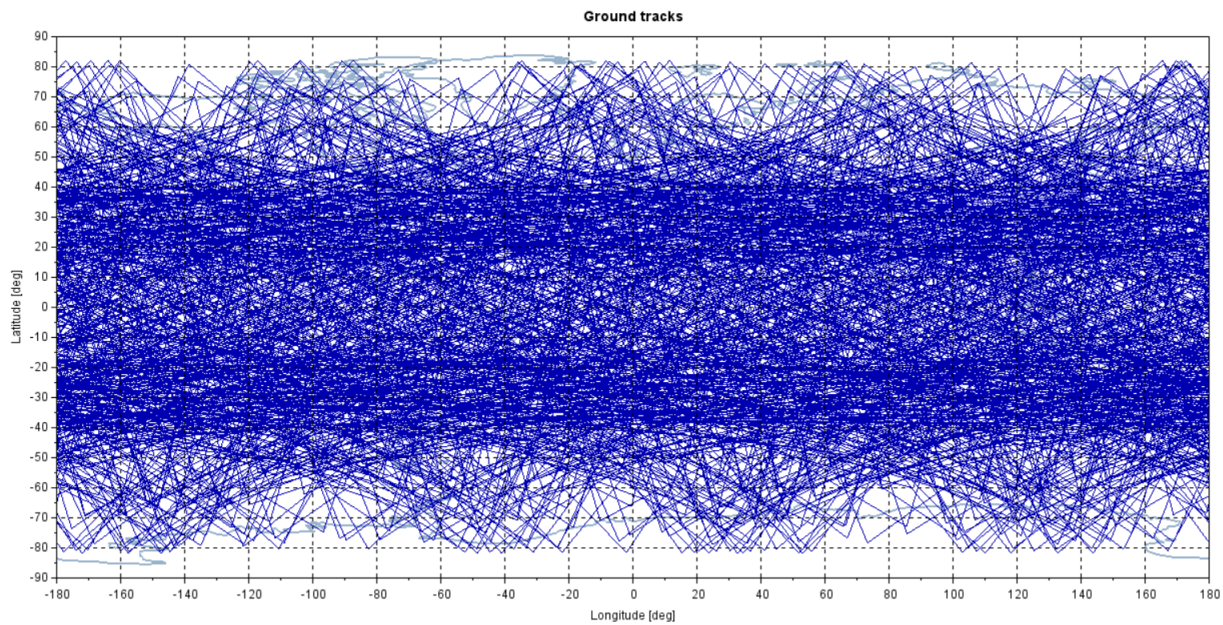


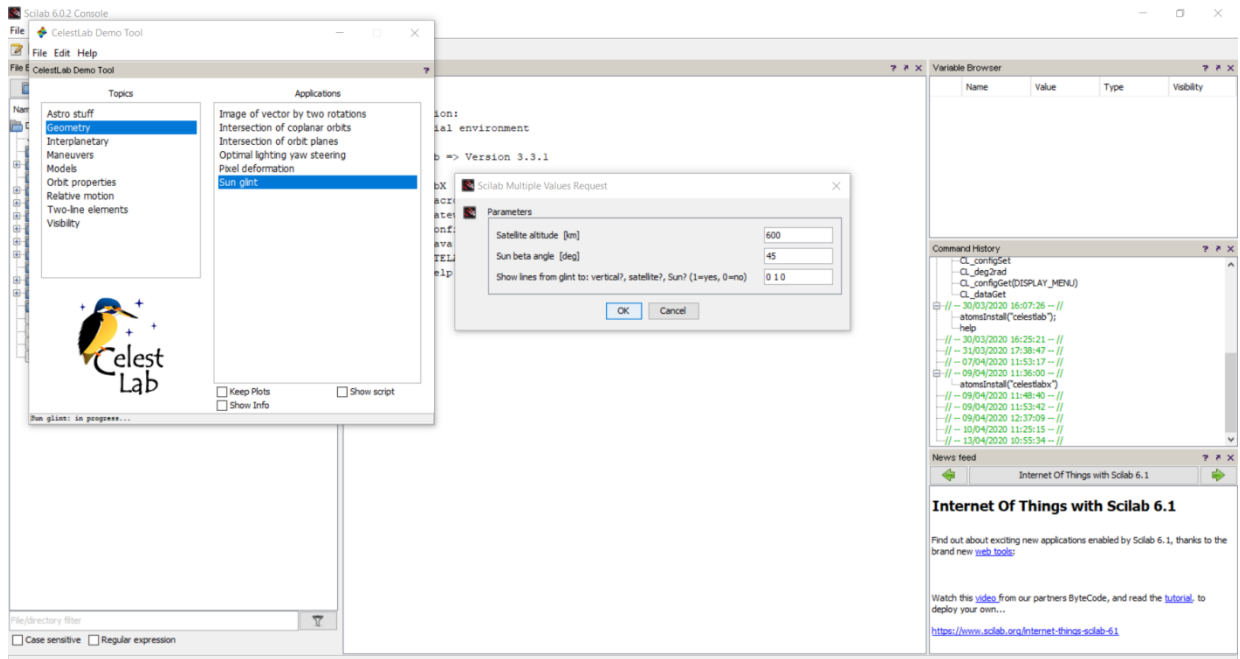
- 1) Semi major axis [Km]: in geometry, the major axis is used for ellipse which is the longest diameter axis. The semi major axis is one half the major axis
- 2) Eccentricity: a dimensionless parameter that determines the amount by which its orbit around another body deviates from a perfect circle. A value of 0 is a circular orbit, values between 0 and 1 form an elliptic orbit.
- 3) Inclination [deg]: measures the tilt of an object's orbit around a celestial body. It is expressed as the angle between a reference plane and the orbital plane or axis of direction of the orbiting object.
- 4) Argument of perigee [deg]: the angle between the perigee (maximum) and the ascending node, measured in the orbital plane.
- 5) Longitude of asc. node [deg]: the angle measured in the equatorial plane between the ascending node of the orbit and the x-axis. The ascending node is defined to be the intersection between the Earth's equatorial plane and the satellite's orbit as it goes from the southern hemisphere to the northern one.
- 6) Mean anomaly [deg]: the time that has passed since the last passage at perigee, as a function of the orbital period, and expressed as an angle.
- 7) **Simulation duration [day]**: specify the time in days which we want the simulation to be done. For one hour we need to put 0.0416 day which is equivalent to it.
- 8) **Simulation time step [sec]**: the simulation step is the interval which the simulation will be done. The smaller the value the more accurate the simulation. Still the small values requires high computation power.

<sup>16</sup> [https://en.wikipedia.org/wiki/Low\\_Earth\\_orbit](https://en.wikipedia.org/wiki/Low_Earth_orbit)

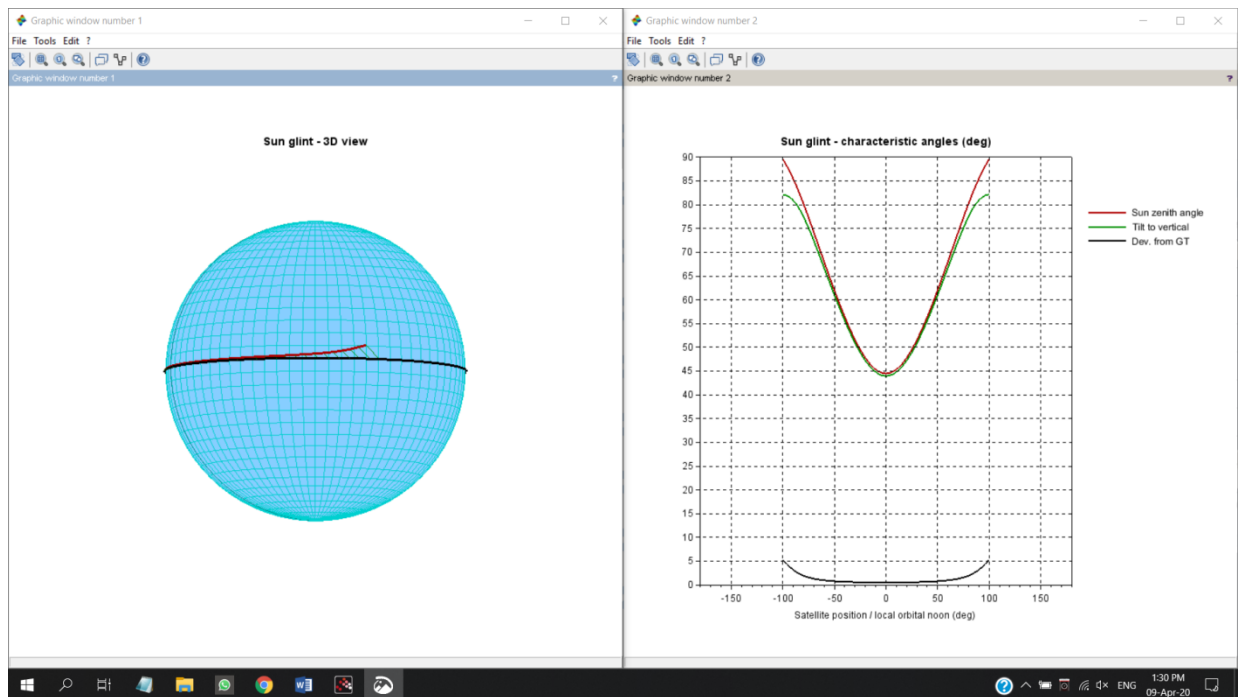
<sup>17</sup> <https://scholarworks.aub.edu.lb/bitstream/handle/10938/10252/t-6038.pdf?sequence=1&isAllowed=y>

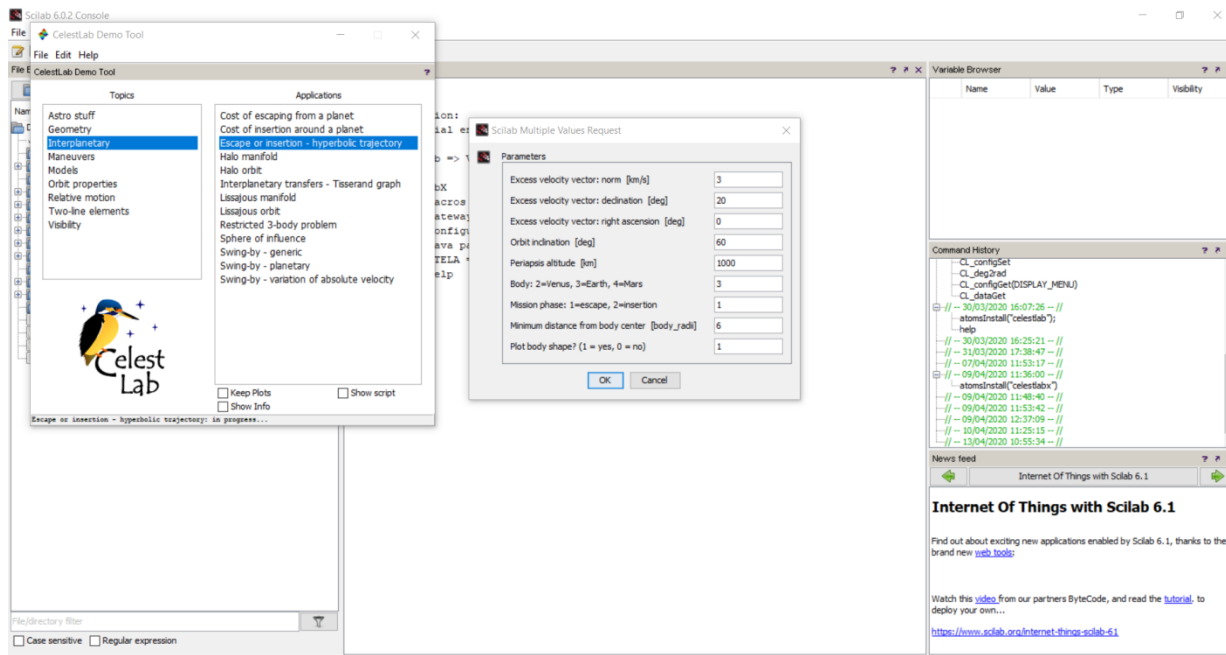
Initial Time	21915
Semi major axis [Km]	600
Eccentricity	0.1
Inclination [deg]	98
Argument of perigee [deg]	10
Longitude of asc. node [deg]	45
Mean anomaly [deg]	123
Simulation duration [day]	1
Simulation time step [sec]	60
Minimum elevation [deg]	5



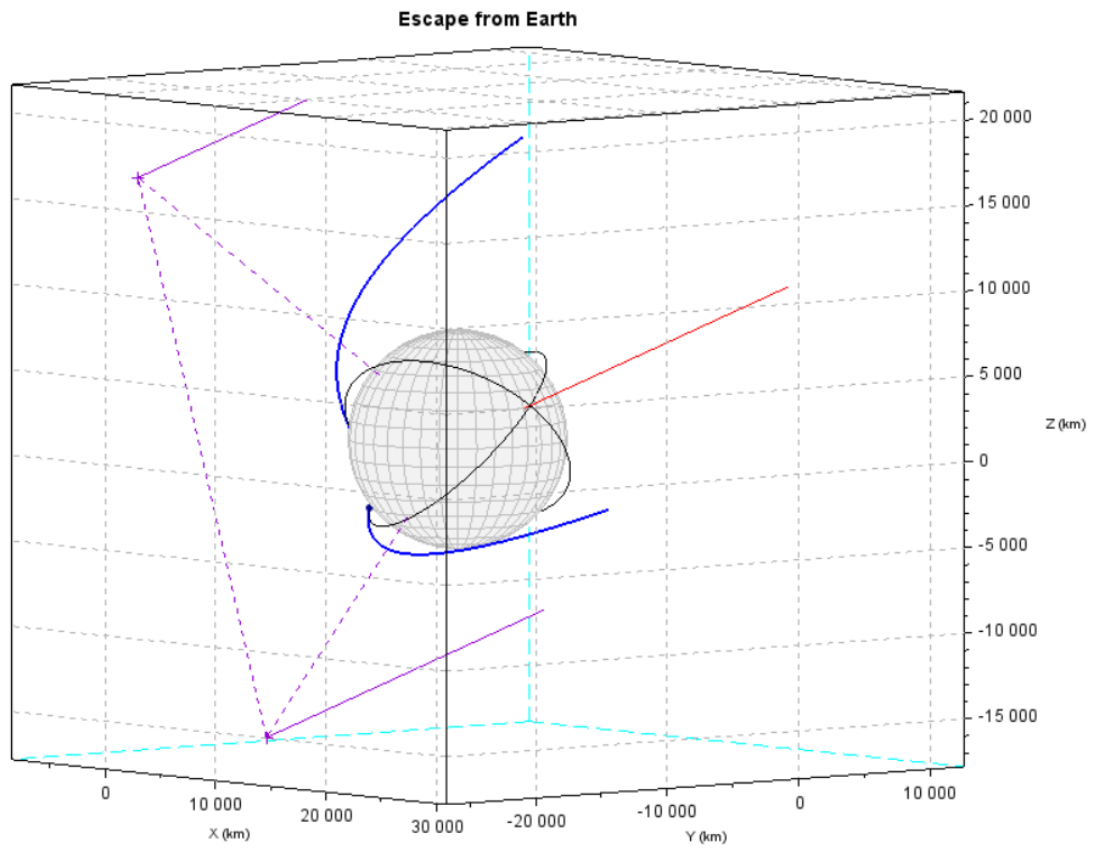


Satellite Altitude [km]	600
Sun beta angle [deg]	45
Show lines from glint to: satellite	1

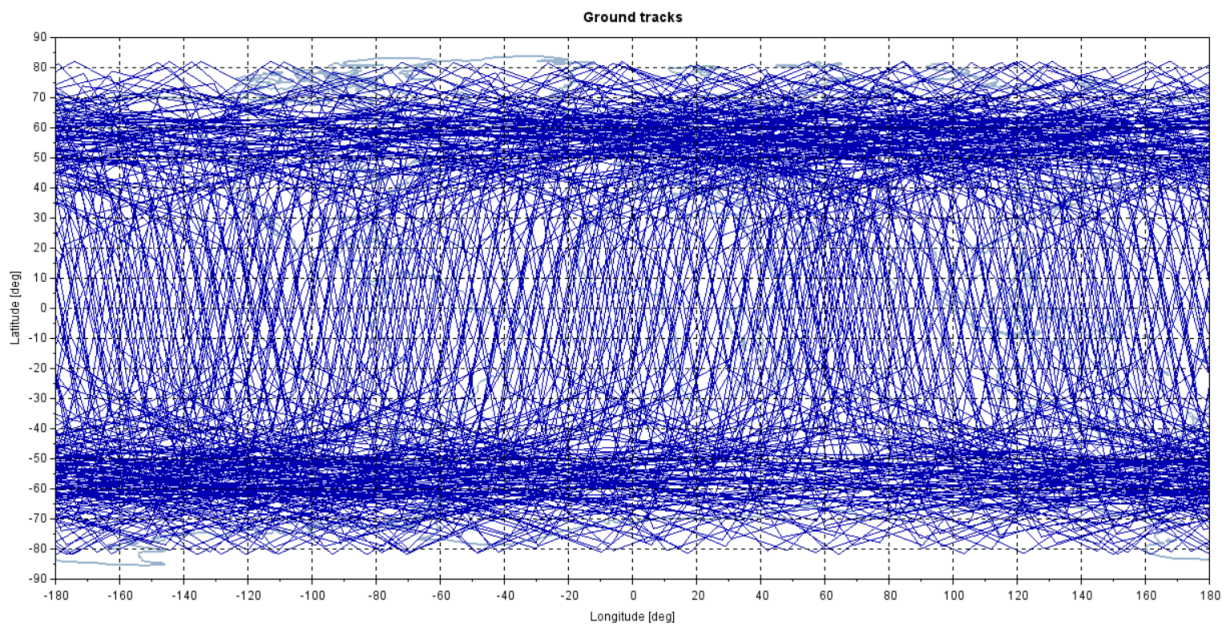




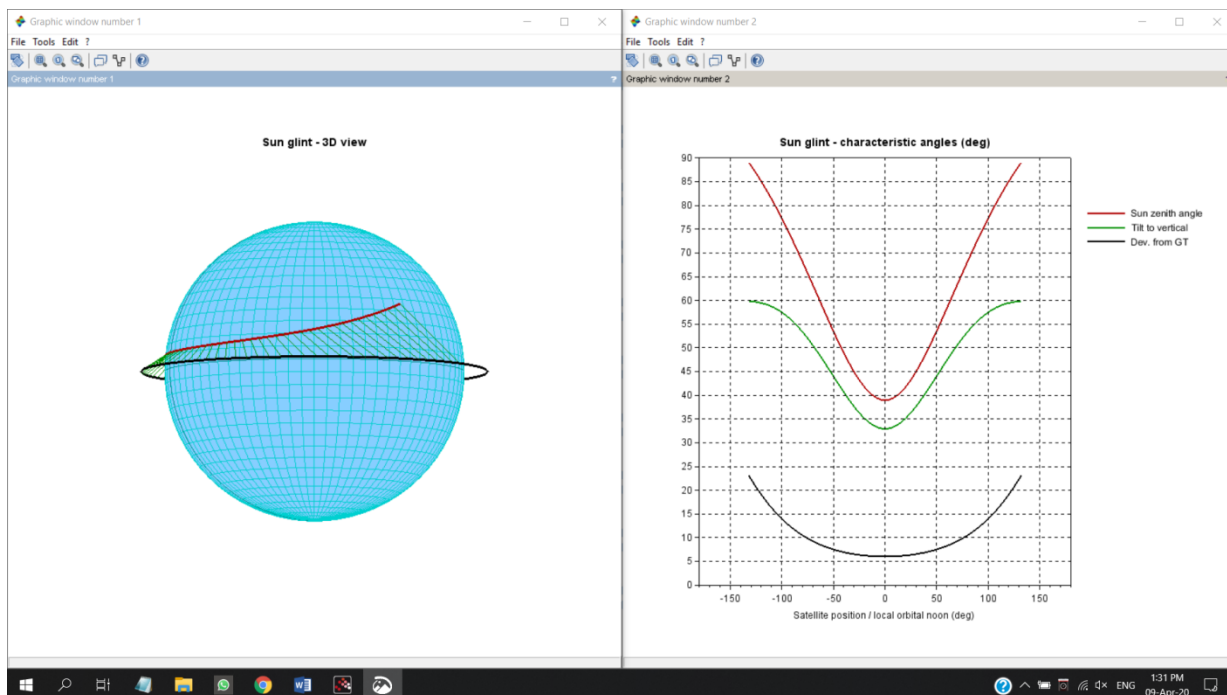
Excess velocity vector: norm [km/s]	3
Excess velocity vector: declination [deg]	20
Excess velocity vector: right ascension [deg]	0
Orbit inclination [deg]	45
Periapsis altitude [km]	600
Body: 2=Venus, 3=Earth, 4=Mars	3
Mission phase: 1=escape, 2=insertion	1
Minimum distance from body center [body_radii]	5
Plot body shape? (1=yes, 2=no)	1



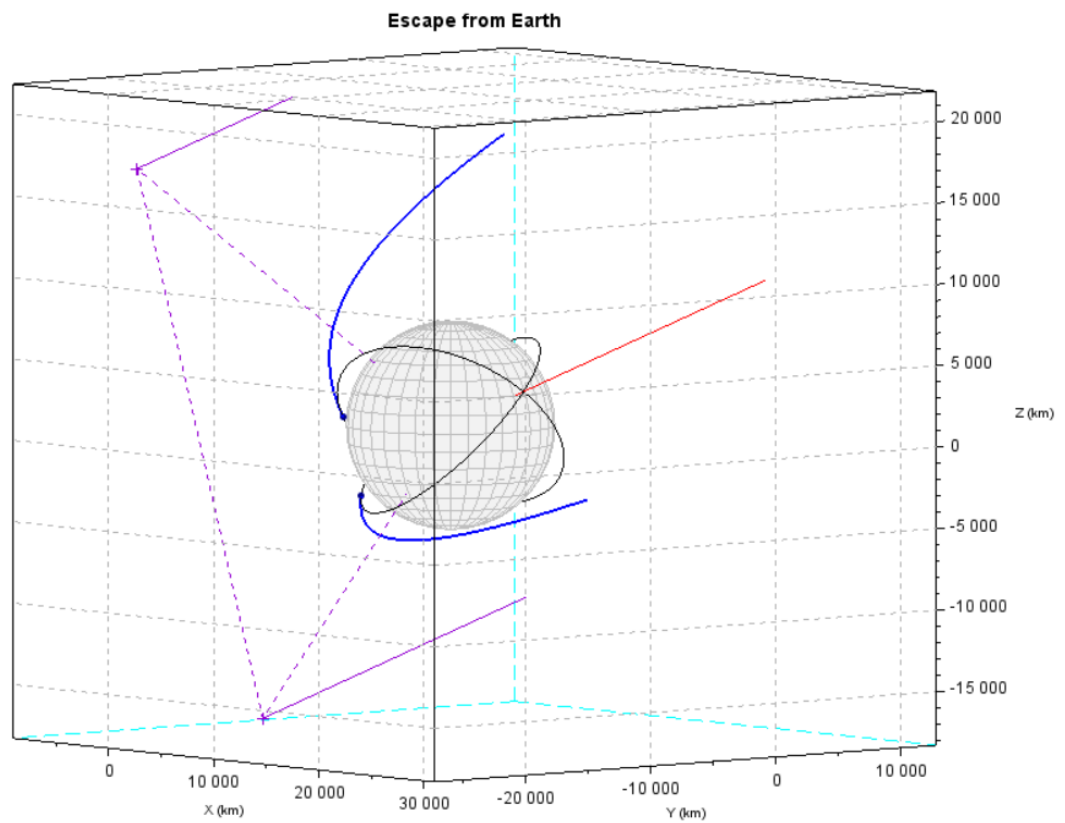
Initial Time	21915
Semi major axis [Km]	1000
Eccentricity	0.1
Inclination [deg]	98
Argument of perigee [deg]	10
Longitude of asc. node [deg]	45
Mean anomaly [deg]	123
Simulation duration [day]	1
Simulation time step [sec]	60
Minimum elevation [deg]	5



Satellite Altitude [km]	1000
Sun beta angle [deg]	45
Show lines from glint to: satellite	1

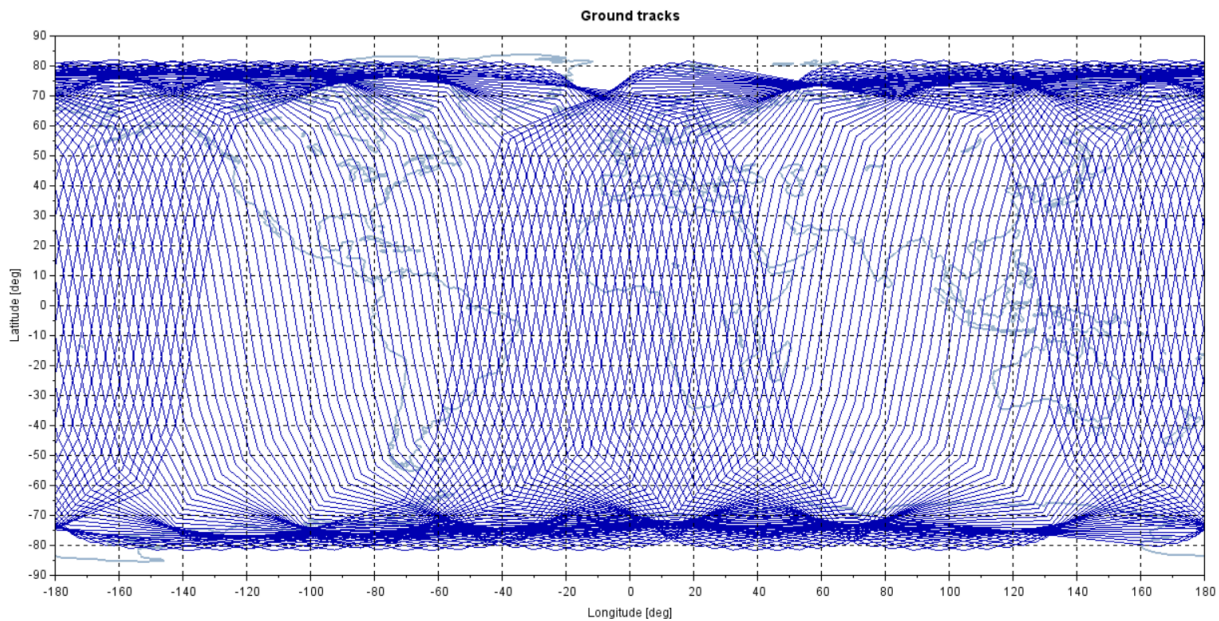


Excess velocity vector: norm [km/s]	3
Excess velocity vector: declination [deg]	20
Excess velocity vector: right ascension [deg]	0
Orbit inclination [deg]	45
Periapsis altitude [km]	1000
Body: 2=Venus, 3=Earth, 4=Mars	3
Mission phase: 1=escape, 2=insertion	1
Minimum distance from body center [body_radii]	5
Plot body shape? (1=yes, 2=no)	1

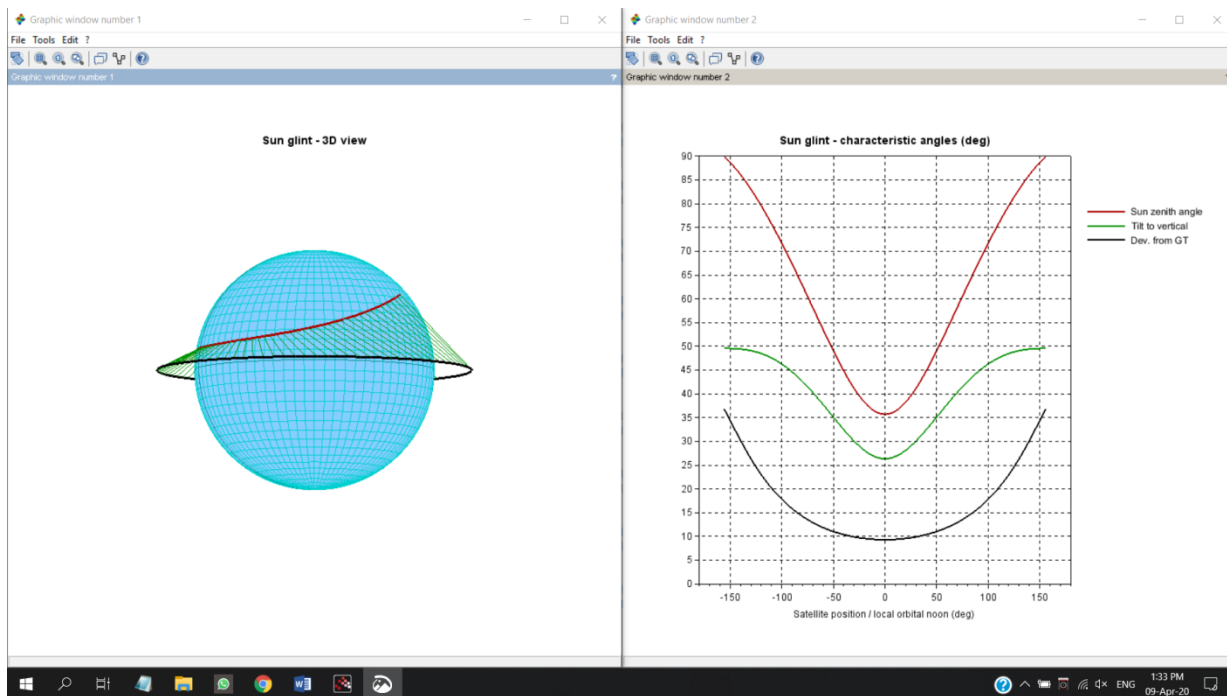


Initial Time	21915
Semi major axis [Km]	2000
Eccentricity	0.1
Inclination [deg]	98
Argument of perigee [deg]	10
Longitude of asc. node [deg]	45
Mean anomaly [deg]	123

Simulation duration [day]	1
Simulation time step [sec]	60
Minimum elevation [deg]	5

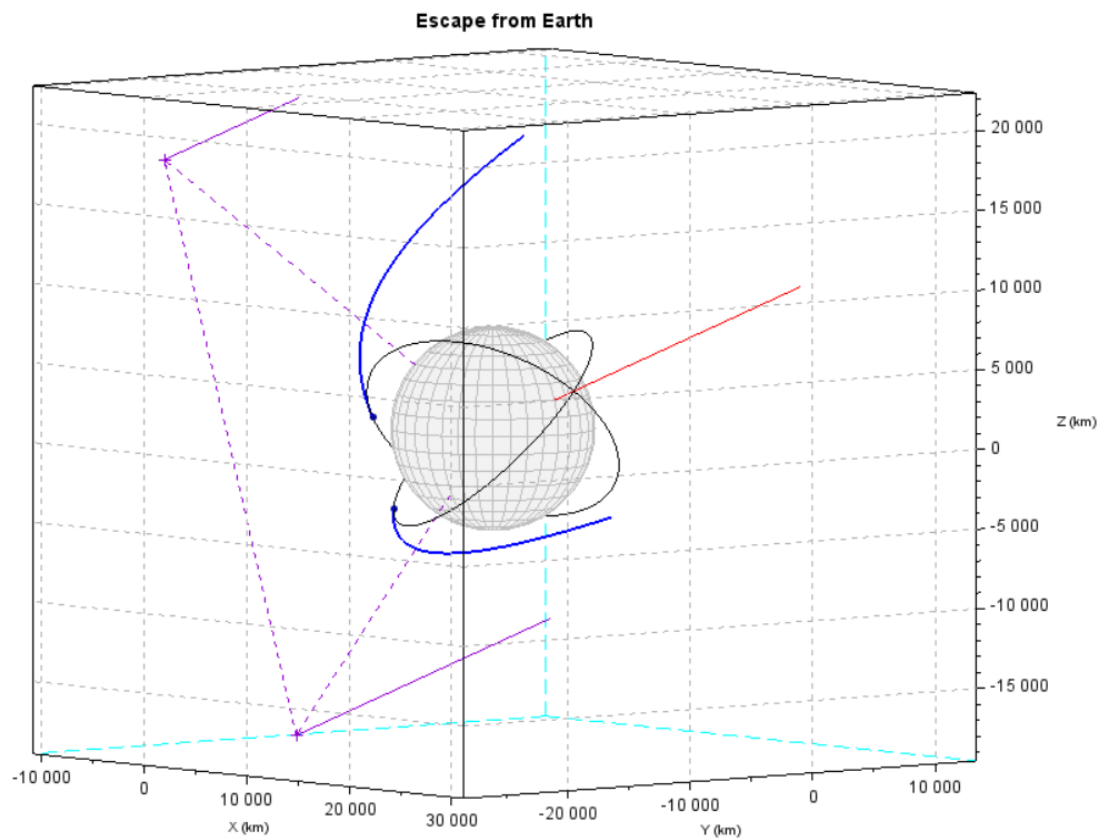


Satellite Altitude [km]	2000
Sun beta angle [deg]	45
Show lines from glint to: satellite	1



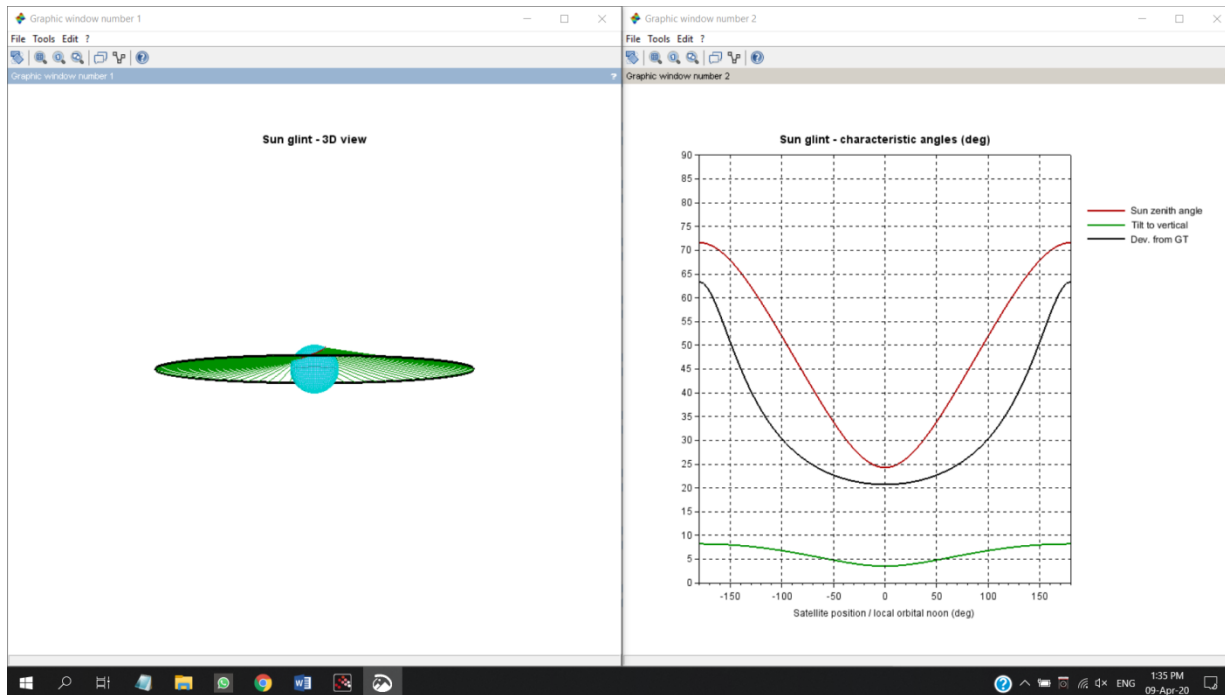
Excess velocity vector: norm [km/s]	3
-------------------------------------	---

Excess velocity vector: declination [deg]	20
Excess velocity vector: right ascension [deg]	0
Orbit inclination [deg]	45
Periapsis altitude [km]	2000
Body: 2=Venus, 3=Earth, 4=Mars	3
Mission phase: 1=escape, 2=insertion	1
Minimum distance from body center [body_radii]	5
Plot body shape? (1=yes, 2=no)	1

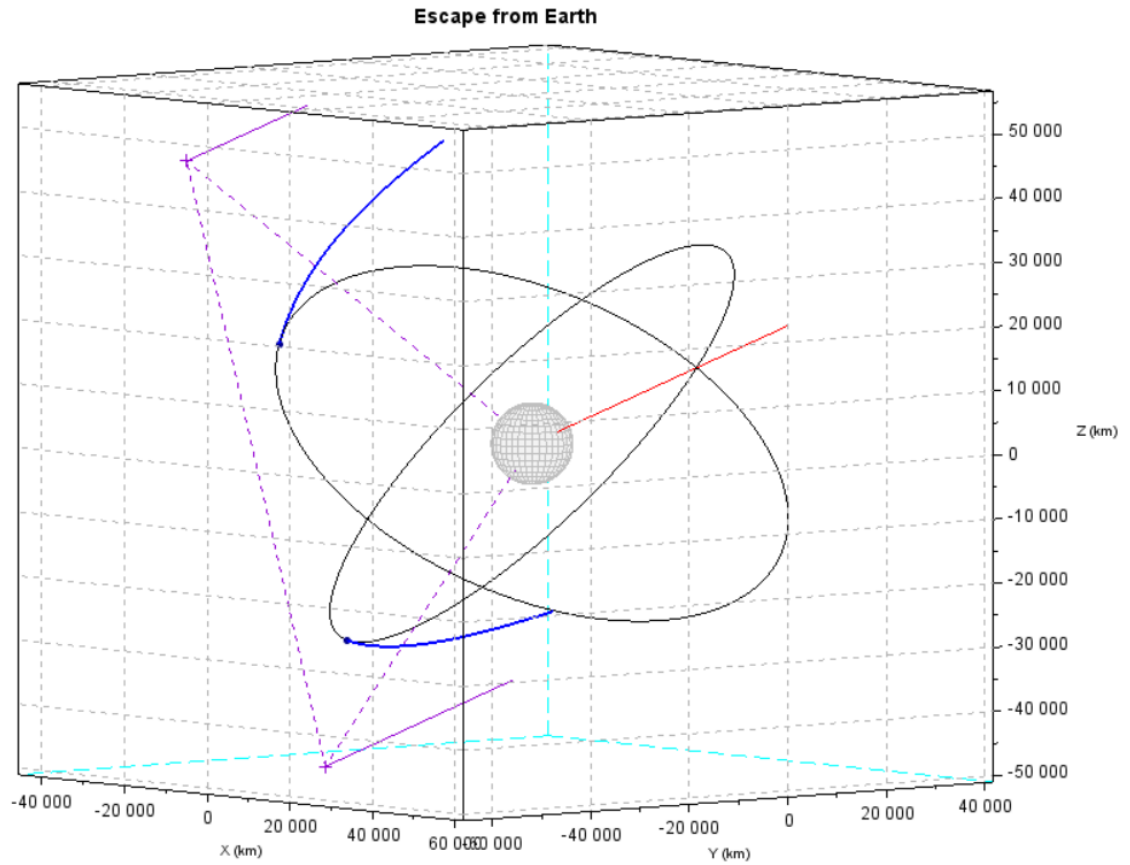


## 16.4 Trajectory Simulation of Transport Vehicle for IAP-SAT

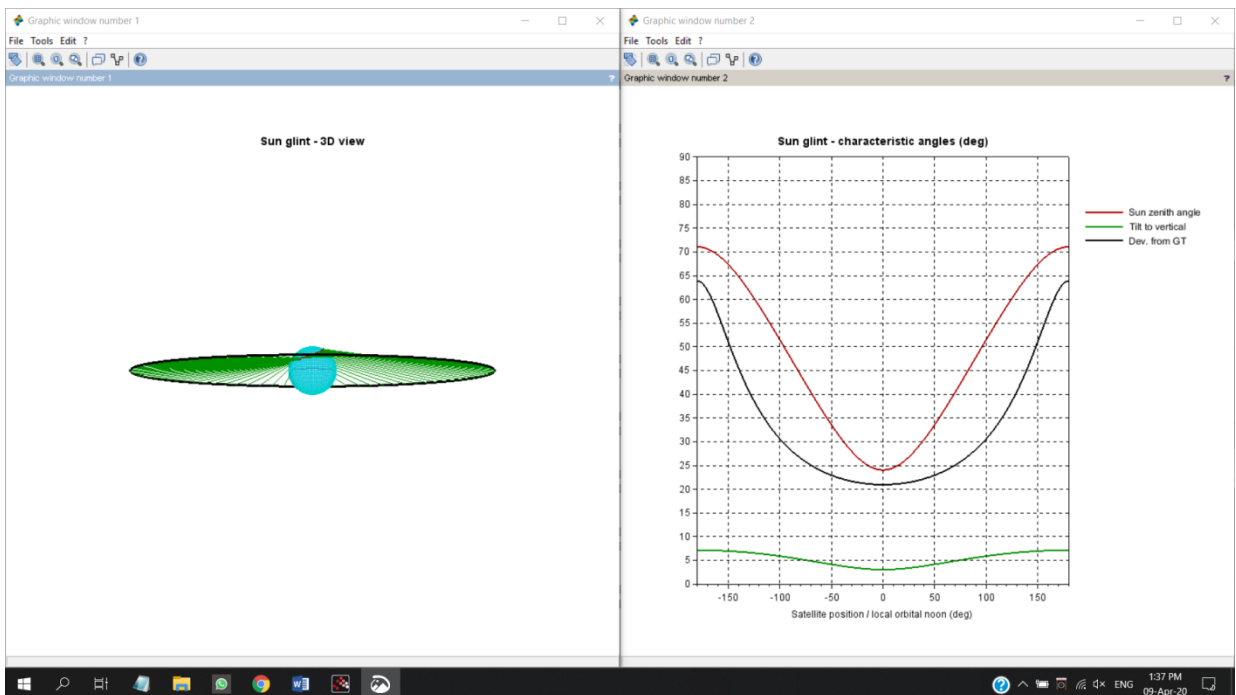
Satellite Altitude [km]	36000
Sun beta angle [deg]	45
Show lines from glint to: satellite	1



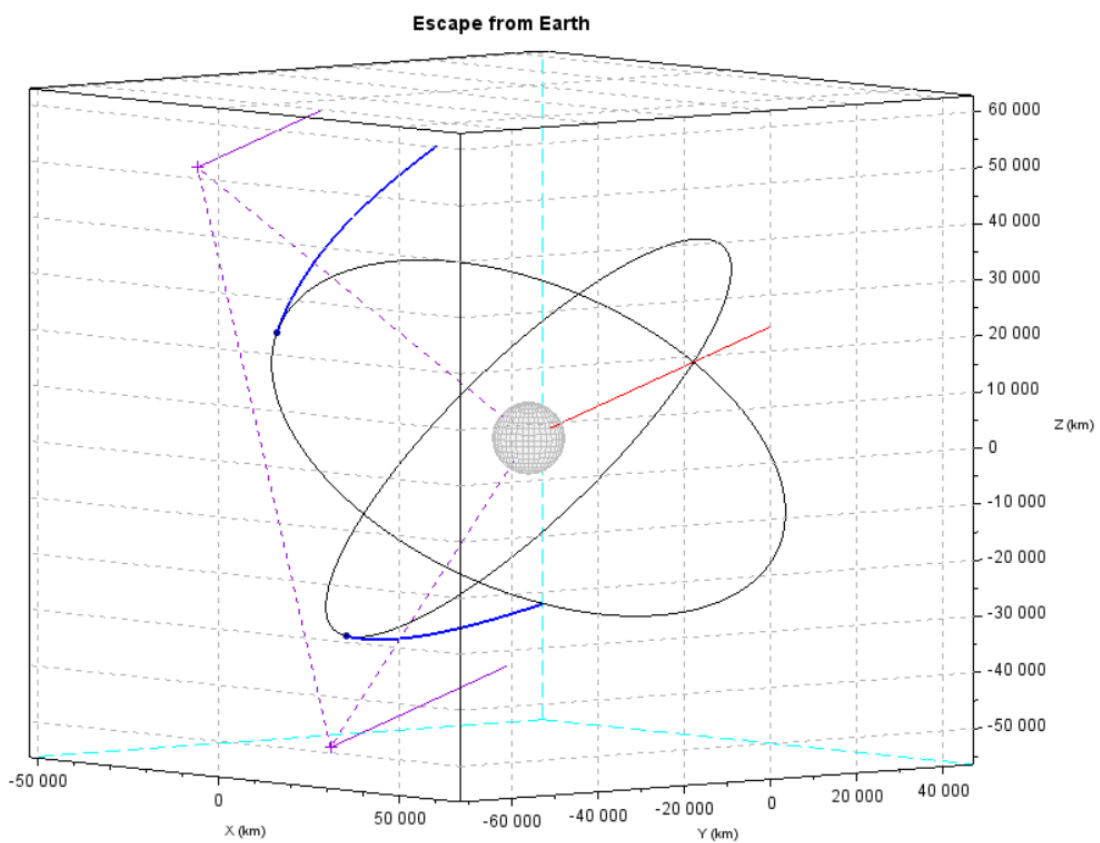
Excess velocity vector: norm [km/s]	3
Excess velocity vector: declination [deg]	20
Excess velocity vector: right ascension [deg]	0
Orbit inclination [deg]	45
Periapsis altitude [km]	36000
Body: 2=Venus, 3=Earth, 4=Mars	3
Mission phase: 1=escape, 2=insertion	1
Minimum distance from body center [body_radii]	5
Plot body shape? (1=yes, 2=no)	1



Satellite Altitude [km]	42164
Sun beta angle [deg]	45
Show lines from glint to: satellite	1



Excess velocity vector: norm [km/s]	3
Excess velocity vector: declination [deg]	20
Excess velocity vector: right ascension [deg]	0
Orbit inclination [deg]	45
Periapsis altitude [km]	42164
Body: 2=Venus, 3=Earth, 4=Mars	3
Mission phase: 1=escape, 2=insertion	1
Minimum distance from body center [body_radii]	5
Plot body shape? (1=yes, 2=no)	1



## 17 Mission Planning<sup>18</sup>

Milestone Date	Spaceflight Deliverables	Spacecraft Provider Deliverables
Contract Signing <i>Typically L-12+ months</i>	<ul style="list-style-type: none"> <li>- Procure deployment system</li> <li>- Requirements for CAD &amp; FEM, thermal models</li> <li>- ICD Template</li> <li>- Apply for export licensing (as required)</li> </ul>	<ul style="list-style-type: none"> <li>- Completed spacecraft questionnaire</li> </ul>
Kickoff <i>LSA signature+2 months</i>	<ul style="list-style-type: none"> <li>- Mission Schedule</li> <li>- Safety submission template delivery</li> </ul>	<ul style="list-style-type: none"> <li>- Spacecraft CAD model</li> <li>- Spacecraft FEM</li> <li>- Spacecraft Test Plan</li> </ul>
Mission CDR <i>Launch-9 months</i>	<ul style="list-style-type: none"> <li>- Updated mission schedule</li> <li>- Current best estimate launch campaign schedule</li> <li>- Preliminary Integration Schedule</li> <li>- Preliminary Launch Operations Plan</li> </ul>	<ul style="list-style-type: none"> <li>- Updated CAD model (if applicable)</li> <li>- Updated FEM (if applicable)</li> <li>- Thermal Model</li> <li>- Updated Spacecraft Mas</li> <li>- Completed Safety Submission</li> <li>- Spacecraft launch site operations plan</li> <li>- Spacecraft licensing information sent to appropriate agency</li> </ul>
System Readiness Review <i>Launch-3 months</i>	<ul style="list-style-type: none"> <li>- Updated mission analyses results (if applicable)</li> <li>- Final integration schedule</li> <li>- Final launch operations plan</li> <li>- A list of facilities and services available for spacecraft checkout</li> </ul>	<ul style="list-style-type: none"> <li>- Verification compliance to ICD requirements (i.e. test reports)</li> <li>- Updates to CAD, FEM, thermal model, and Safety Package (if applicable)</li> </ul>
Integration Process Start <i>Launch-60 days</i>	<ul style="list-style-type: none"> <li>- Identify last access to the spacecraft</li> <li>- Spaceflight provides the integration facility</li> </ul>	<ul style="list-style-type: none"> <li>- Final as-measured spacecraft mass and best estimated wet-mass</li> <li>- Delivery of Spacecraft and associated electrical and mechanical GSE to integration facility for system level integration</li> <li>- Delivery of spacecraft mass simulator to integration facility for system level integration</li> </ul>
Launch Readiness Review <i>Launch-1 day</i>	<ul style="list-style-type: none"> <li>- Approximate separation time</li> </ul>	<ul style="list-style-type: none"> <li>- Launch Readiness Review (LRR)</li> </ul>
Launch <i>Launch+0 hours</i>	-	-
Spacecraft Separation <i>Launch+4 hours</i>	<ul style="list-style-type: none"> <li>- Separation confirmation and state vector</li> </ul>	-
Acquisition Notification <i>Spacecraft Acquisition+12 hours</i>	-	<ul style="list-style-type: none"> <li>- Indication of spacecraft acquisition, state-of-health assessment</li> </ul>

<https://www.nasa.gov/smallsat-institute/space-mission-design-tools>

<https://public.ccsds.org/Pubs/529x0g1.pdf>

<sup>18</sup> <https://spaceflight.com/wp-content/uploads/2019/02/Spaceflight-Mission-Planning-Guide-Rev-G.pdf>

Table 3-2 Description of Deliverables

Item	Deliverables from Spacecraft Provider to Spaceflight
1	Spacecraft Questionnaire – The spacecraft questionnaire includes the orbit requirements, interface details, mass properties, preliminary drawings, and unique spacecraft requirements, etc.
2	Verification Artifacts – Provide documentation to serve as verification artifacts of all ICD requirements (includes spacecraft system design information, test plans and results, Certificates of Compliance, etc.)
3	Spacecraft CAD Model – CAD model showing the outer mold line configuration, shape, and dimensions of the satellite.
4	Mass Properties Report – Current best estimate mass properties are tracked from spacecraft questionnaire through Mission Readiness Review. The values should include the nominal values and 3 $\sigma$ uncertainties.
5	Safety Package – The Safety Package is a data package that provides detailed technical data on all hazardous items including drawings, schematics, RF Radiation, and assembly and handling procedures (format is dependent upon Launch Range).
6	Spacecraft Launch Operations Plan – Each spacecraft must specify any handling constraints, environmental constraints, personnel requirements, equipment requirements, launch site checkout procedures, integration procedures, and the duration of these tasks for their satellite.
7	Spacecraft Finite Element Model (microsats only) – A spacecraft FEM is required for inclusion in Coupled Loads Analysis.
8	Spacecraft Thermal Model (microsats only) – A spacecraft thermal model is required for inclusion in an integrated thermal analysis
9	Spacecraft licensing - Copies of all licenses, permits, clearances, authorizations, and approvals necessary for the transportation of, communication with, operation, launch and orbital deployment of the spacecraft including, but is not limited to all licenses from: the Federal Communications Commission (“FCC”) or spacecraft provider’s applicable national administration/agency; and if applicable, the National Oceanic and Atmospheric Administration (“NOAA”).

Item	Deliverables from Spaceflight to Spacecraft Provider
1	ICD – Interface Control Document defining mission, interface, and operational spacecraft requirements necessary to successfully execute the launch service, including acceptable verification methods and verification artifacts for each of the requirements.
2	Deliverable input guidance – Provide deliverable templates and feedback on draft submissions.
3	Schedule – Description of the mission planning timeline and status of readiness activities to ensure the team is on-track to meet mission milestones.
4	Mission Unique Design Analyses – Provide current best estimates through coordination with launch vehicle team for launch environments, targeted orbital parameters, and deployment timing.
5	Spacecraft and Mission Readiness Review – Provide readiness status for spacecraft, Spaceflight hardware and facilities to execute launch campaign.
6	State vector and deployment confirmation – Actual insertion parameters and separation confirmation on orbit.

		Done/Undone
1	Spacecraft Questionnaire	Undone: interface details, mass properties
2	Verification Artifacts	all undone
3	Spacecraft CAD Model	not done for the satellite
4	Mass Properties Report	all undone
5	Safety Package	all undone
6	Spacecraft Launch Operations Plan	Done: environmental constraints, equipment requirements
7	Spacecraft Finite Element Model (microsats only)	all undone
8	Spacecraft Thermal Model (microsats only)	all undone
9	Spacecraft licensing	all undone



**Part IV: Satellite Bus Elements**

## Inertial Measurement Unit

## 18 Realization of Inertial Measurement Unit (IMU)<sup>19</sup>

The IMU has the following parts:

- Gyro
- Accelerometer
- Magnetometer

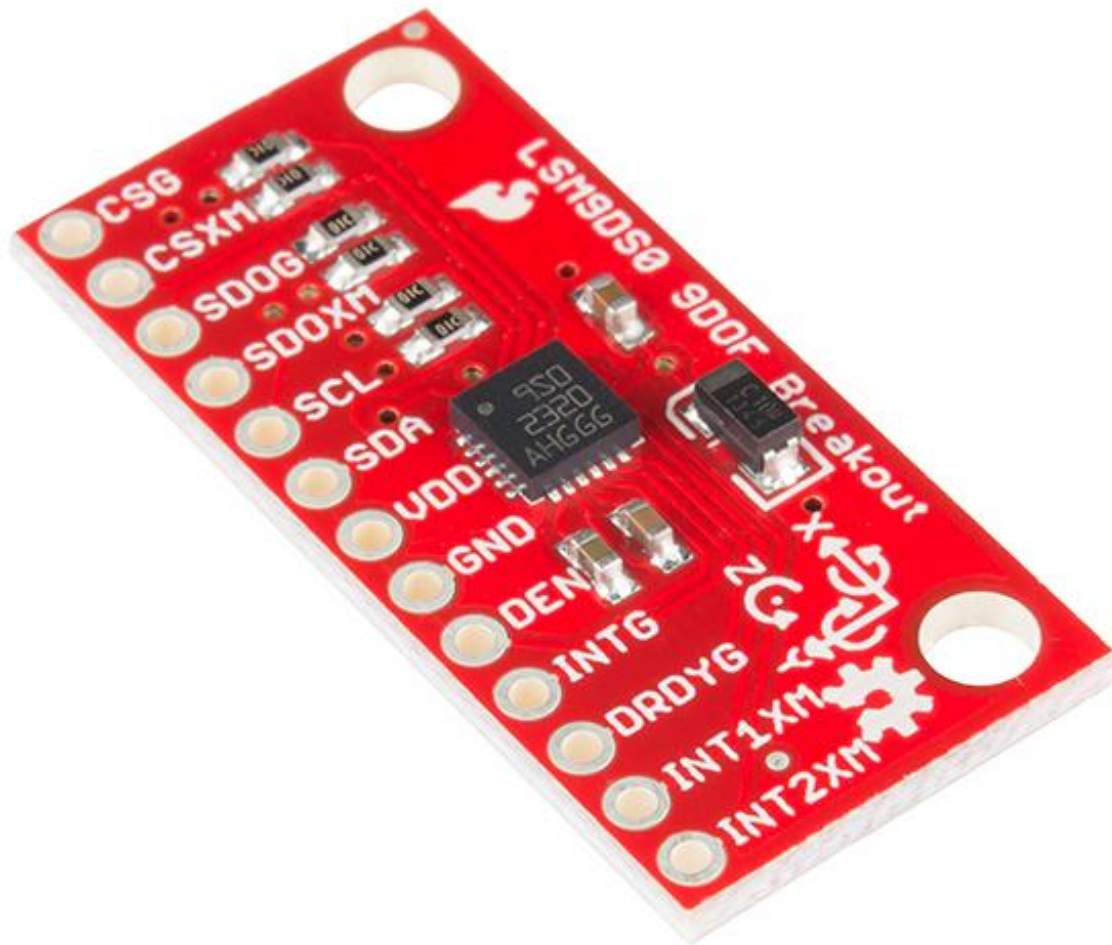


The software runs on a raspberry pi.



<sup>19</sup> done by CNCLab (Rami Nassouh)

## 18.1 IMU-Sensor: LSM9DS0



LSM9DS0 IMU Breakout - 9DoF

Price : 39.95\$

Mark : SparkFun Electronics®

Serial number : SEN0080

### Description:

This is the LSM9DS0, a versatile motion-sensing system-in-a-chip that houses a 3-axis accelerometer, 3-axis gyroscope, and 3-axis magnetometer. That's right, 9 degrees of freedom (9dof) from a single IC!

Each sensor in the LSM9DS0 supports a wide range of, well, ranges: the accelerometer's scale can be set to  $\pm 2$ , 4, 6, 8, or 16 g, the gyroscope supports  $\pm 245$ , 500, and 2000  $^{\circ}/s$ , and the magnetometer has full-scale ranges of  $\pm 2$ , 4, 8, or 12 gauss. Additionally, the LSM9DS0 includes an I2C serial bus

interface supporting standard and fast mode (100 kHz and 400 kHz) and an SPI serial standard interface.

## FEATURES

3 acceleration channels, 3 angular rate channels, 3 magnetic field channels

$\pm 2/\pm 4/\pm 6/\pm 8/\pm 16$  g linear acceleration full scale

$\pm 2/\pm 4/\pm 8/\pm 12$  gauss magnetic full scale

$\pm 245/\pm 500/\pm 2000$  dps angular rate full scale

16-bit data output

SPI / I2C serial interfaces

Analog supply voltage 2.4 V to 3.6 V

Programmable interrupt generators

Embedded self-test

Embedded temperature sensor

Embedded FIFO

## 18.2 LSM9DS0 Hookup Guide<sup>20</sup>

### 18.2.1 Covered In This Tutorial

This tutorial is devoted to all things LSM9DS0. We'll introduce you to the chip itself, then the breakout board. Then we'll switch over to example code, and show you how to interface with the board using an Arduino and our [SFE LSM9DS0 Arduino library](#).

- The tutorial is split into the following pages:
- [About the LSM9DS0](#) – An overview of the LSM9DS0, examining its features and capabilities.
- [Breakout Overview](#) – This page covers the LSM9DS0 Breakout Board – topics like the pinout, jumpers, and schematic.
- [Hardware Assembly](#) – Assembly tips and tricks, plus some information about the breakout's dimensions.
- [Basic Arduino Example](#) – How to install the **Arduino library**, and use a simple example sketch.
- [Advanced Arduino Example](#) – A more advanced Arduino sketch – using the library – showing off features like switch the sensors' scales and data rates.
- [Using the Arduino Library](#) – An overview of the SFE\_LSM9DS0 Arduino library.

---

<sup>20</sup> [https://learn.sparkfun.com/tutorials/lsm9ds0-hookup-guide?\\_ga=2.72099031.592506407.1511257598-1712679554.1505480322](https://learn.sparkfun.com/tutorials/lsm9ds0-hookup-guide?_ga=2.72099031.592506407.1511257598-1712679554.1505480322)

## 18.2.2 About the LSM9DS0

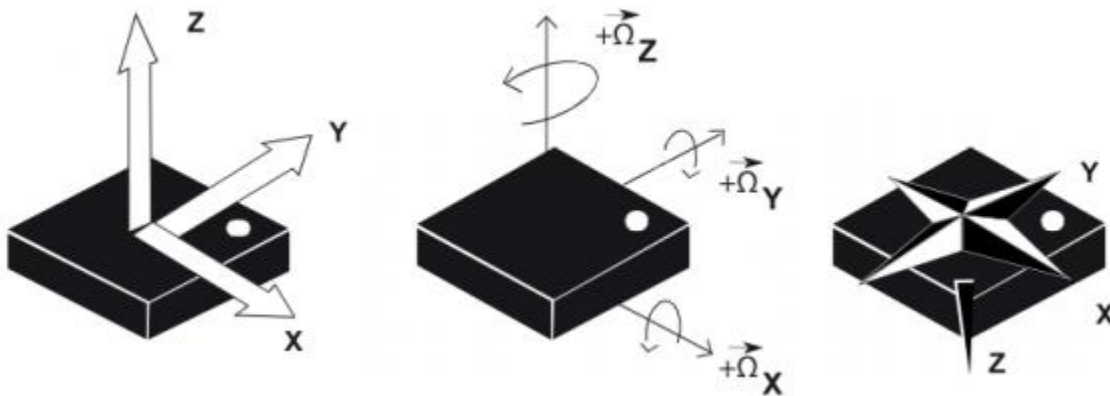
The LSM9DS0 is one of only a handful of IC's that can measure three key properties of movement – angular velocity, acceleration, and heading – in a single IC.

The [gyroscope](#) can measure **angular velocity** – that is “how fast, and along which axis, am I rotating?” Angular velocities are measured in **degrees per second** – usually abbreviated to DPS or  $^{\circ}/s$ . The LSM9DS0 can measure up to  $\pm 2000$  DPS, though that scale can also be set to either 245 or 500 DPS to get a finer resolution.

An [accelerometer](#) measures **acceleration**, which indicates how fast velocity is changing – “how fast am I speeding up or slowing down?” Acceleration is usually either measured in  $m/s^2$  (meters per second per second) or *g*'s (gravities [about  $9.8 m/s^2$ ]). If an object is sitting motionless it feels about 1 *g* of acceleration towards the ground (assuming that ground is on earth, and the object is near sea-level). The LSM9DS0 measures its acceleration in *g*'s, and its scale can be set to either  $\pm 2$ , 4, 6, 8, or 16 *g*.

Finally, there's the [magnetometer](#), which measures the power and direction of **magnetic fields**. Though they're not easily visible, magnetic fields exist all around us – whether you're holding a tiny ferromagnet or feeling an attraction to [Earth's magnetic field](#). The LSM9DS0 measures magnetic fields in units of **gauss** (Gs), and can set its measurement scale to either  $\pm 2$ , 4, 8, or 12 Gs.

By measuring these three properties, you can gain a great deal of knowledge about an object's movement. 9DOF's have tons and tons of applications. Measuring the force and direction of Earth's magnetic field with a magnetometer, you can approximate your **heading**. An accelerometer in your phone can measure the direction of the force of gravity, and estimate **orientation** (portrait, landscape, flat, etc.). Quadcopters with built-in gyroscopes can look out for sudden rolls or pitches, and correct their momentum before things get out of hand.



The LSM9DS0 measures each of these movement properties in three dimensions. That means it produces **nine pieces of data**: acceleration in x/y/z, angular rotation in x/y/z, and magnetic force in x/y/z. On the breakout board, the z-axis runs normal to the PCB, the y-axis runs parallel to the short edge, and the x-axis is parallel to the long edge. Each axis has a positive and negative direction as well, noted by the direction of the arrow on the label.

The LSM9DS0 is, in a sense, two IC's smashed into one package – like if you combined an [L3G4200D gyro](#) with an [LSM303DLMTR accel/mag](#). One half of the device takes care of all-things gyroscope,

and the other half manages both the accelerometer and magnetometer. In fact, a few of the control pins are dedicated to a single sensor – there are **two chip select pins** (CSG for the gyro and CSXM for the accel/mag) and **two serial data out pins** (SDOG and SDOXM).

### 18.2.3 Choose Your Own Adventure: SPI or I<sup>2</sup>C

In addition to being able to measure a wide variety of movement vectors, the LSM9DS0 is also multi-featured on the hardware end. It supports both **SPI** and **I<sup>2</sup>C**, so you should have no difficulty finding a microcontroller that can talk to it.

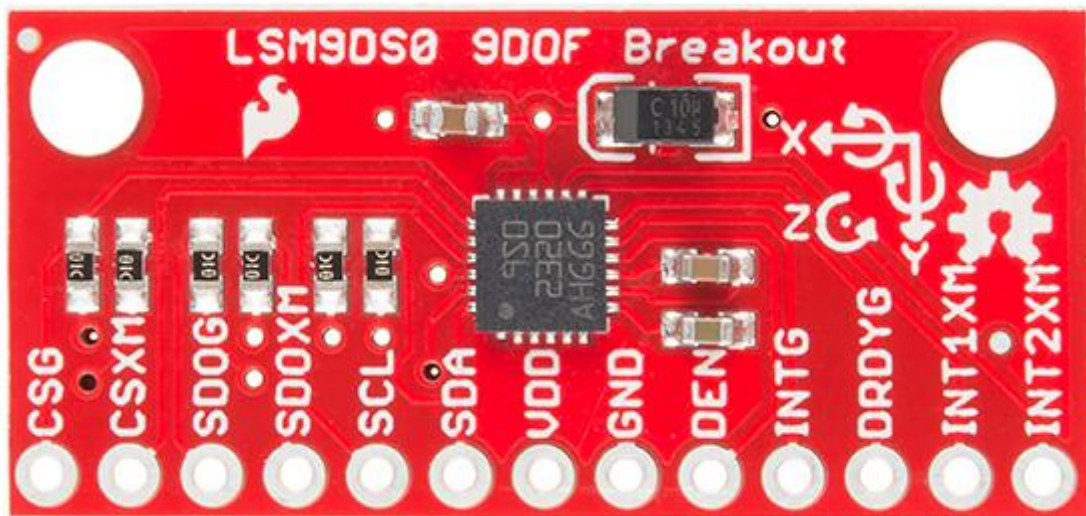
For much more detailed information about the IC, we encourage you to [check out the datasheet](#)<sup>[21]</sup>

### 18.2.4 Breakout Overview

Now that you know everything you need to about the LSM9DS0 IC, let's talk a bit about the breakout board it's resting on. On this page we'll discuss the pins that are broken out, and some of the other features on the board.

### 18.2.5 The Pinout

In total, the LSM9DS0 Breakout breaks out 13 pins.



Here's an overview of each of the pin functions:

Pin Label	Pin Function	Notes
CSG	Chip Select Gyro	This pin selects between I <sup>2</sup> C and SPI on the gyro. Keep it HIGH for I <sup>2</sup> C, or use it as an (active-low) chip select for SPI.

<sup>21</sup> <https://cdn.sparkfun.com/assets/f/6/1/f/0/LSM9DS0.pdf>

		<b>HIGH (1):</b> SPI idle mode / I <sup>2</sup> C <b>enabled</b> <b>LOW (0):</b> SPI <b>enabled</b> / I <sup>2</sup> C disabled.
<b>CSXM</b>	Chip Select Accel/Mag (XM)	This pin selects between I <sup>2</sup> C and SPI on the XM. Keep it HIGH for I <sup>2</sup> C, or use it as an (active-low) chip select for SPI. <b>HIGH (1):</b> SPI idle mode / I <sup>2</sup> C <b>enabled</b> <b>LOW (0):</b> SPI <b>enabled</b> / I <sup>2</sup> C disabled.
<b>SDOG</b>	SPI: Gyroscope MISO I <sup>2</sup> C: Gyro address select	In SPI mode, this is the gyroscope data output (SDO_G). In I <sup>2</sup> C mode, this selects the LSb of the I <sup>2</sup> C address (SA0_G)
<b>SDOXM</b>	SPI: Accel/Mag MISO I <sup>2</sup> C: XM address select	In SPI mode, this is the XM data output (SDO_XM). In I <sup>2</sup> C mode, this selects the LSb of the I <sup>2</sup> C address (SA0_XM)
<b>SCL</b>	Serial Clock	I <sup>2</sup> C and SPI serial clock.
<b>SDA</b>	SPI: MOSI I <sup>2</sup> C: Serial Data	SPI: Device data in (MOSI) I <sup>2</sup> C: Serial data (bi-directional)
<b>VDD</b>	Power Supply	Supply voltage to the chip. Should be regulated between <b>2.4V and 3.6V</b> .
<b>GND</b>	Ground	0V voltage supply
<b>DEN</b>	Gyroscope Data Enable	Mostly unknown. The LSM9DS0 datasheet doesn't have much to say about this pin.
<b>INTG</b>	Gyro Programmable Interrupt	An interrupt that can be programmed as active high/low, push-pull, or open drain. It can trigger on over/under rotation speeds.
<b>DRDYG</b>	Gyroscope data ready	An interrupt that can indicate new gyro data is ready or buffer overrun.
<b>INT1XM</b>	Accel/Mag Interrupt 1	A programmable interrupt that can trigger on data ready, over-acceleration or "taps".
<b>INT2XM</b>	Accel/Mag Interrupt 2	A programmable interrupt that can trigger on data ready, over-acceleration or "taps".

These pins can all be classified into one of three categories: communication, interrupts, or power.

### Power Supply

The VDD and GND pins are where you'll supply a voltage and 0V reference to the IC. The breakout board does not regulate this voltage, so make sure it falls within the allowed supply voltage range of the LSM9DS0: **2.4V to 3.6V**. Below is the electrical characteristics table from the datasheet.

Symbol	Parameter	Test conditions	Min.	Typ. <sup>(1)</sup>	Max.	Unit
Vdd	Supply voltage		2.4		3.6	V
Vdd_IO	Module power supply for I/O		1.71	1.8	Vdd+0.1	
Idd_XM	Current consumption of the accelerometer and magnetic sensor in normal mode <sup>(2)</sup>			350		μA
Idd_G	Gyroscope current consumption in normal mode <sup>(3)</sup>			6.1		mA
Idd_G_LP	Gyroscope supply current in sleep mode <sup>(4)</sup>			2		mA
Idd_Pdn	Current consumption in power-down mode <sup>(5)</sup>			6		μA
VIH	Digital high-level input voltage		0.8*Vdd_IO			V
VIL	Digital low-level input voltage				0.2*Vdd_IO	V
VOH	High-level output voltage		0.9*Vdd_IO			V
VOL	Low-level output voltage				0.1*Vdd_IO	V
Top	Operating temperature range		-40		+85	°C

The communication pins are not 5V tolerant, so they'll need to be regulated to within a few mV of VDD.

Another very cool thing about this sensor is how **low-power** it is. In normal operation – with every sensor turned on – it'll pull around **6.5mA**.

### Communication

CSG, CSXM, SDOG, SDOXM, SCL, and SDA are all used for the I<sup>2</sup>C and SPI interfaces. The function of these pins depends upon which of the two interfaces you're using.

If you're using using I<sup>2</sup>C here's how you might configure these pins:

- Pull CSG and CSXM HIGH. This will set both the gyro and accel/mag to I<sup>2</sup>C mode.
- Set SDOG and SDOXM either HIGH or LOW. These pins set the I<sup>2</sup>C address of the gyro and accel/mag sensors.
- Connect SCL to your microcontroller's SCL pin.
- Connect SDA to your microcontroller's SDA pin.
- The board has a built-in 10kΩ pull-up resistor on both SDA and SCL lines. If that value is too high, you can add a second 10kΩ resistor in parallel to divide the pull-up resistance to about 5kΩ.

Or, if you're using **SPI**:

- Connect CSG and CSXM to two individually controllable pins on your microcontroller. These chip-selects are active-low – when the pin goes LOW, SPI communication with either the gyro (CSG) or accel/mag (CSXM) is enabled.

- SDOG and SDOXM are the serial data out pins. In many cases you'll want to connect them together, and wire them to your microcontroller's **MISO** (master-in, slave-out) pin.
- Connect SCL to your microcontroller's SCLK (serial clock) pin.
- Connect SDA to your microcontroller's **MOSI** (master-out, slave-in) pin.

## Interrupts

There are a variety of interrupts on the LSM9DS0. While connecting up to these is not as critical as the communication or power supply pins, using them will help you get the most out of the chip.

The accelerometer- and magnetometer-specific interrupts are **INT1XM** and **INT2XM**. These can both be programmed to interrupt as either active-high or active-low, triggering on events like data ready, tap-detection, or when an acceleration or magnetic field passes a set threshold.

**DRDY** and **INTG** are devoted gyroscope interrupts. DRDY can be programmed to go high or low when new gyroscope readings are ready to read. INTG is a little more customizable, it can be used to trigger whenever angular rotation exceeds a threshold on any axis.

### 18.2.6 Basic Arduino Example

This example will show you how to download and install the `SFE_LSM9DS0` library, and use it in its most basic form. We'll use I<sup>2</sup>C and ignore the interrupts, which means we'll be using as few wires and Arduino pins as possible.

### 18.2.7 Download and Install the Library

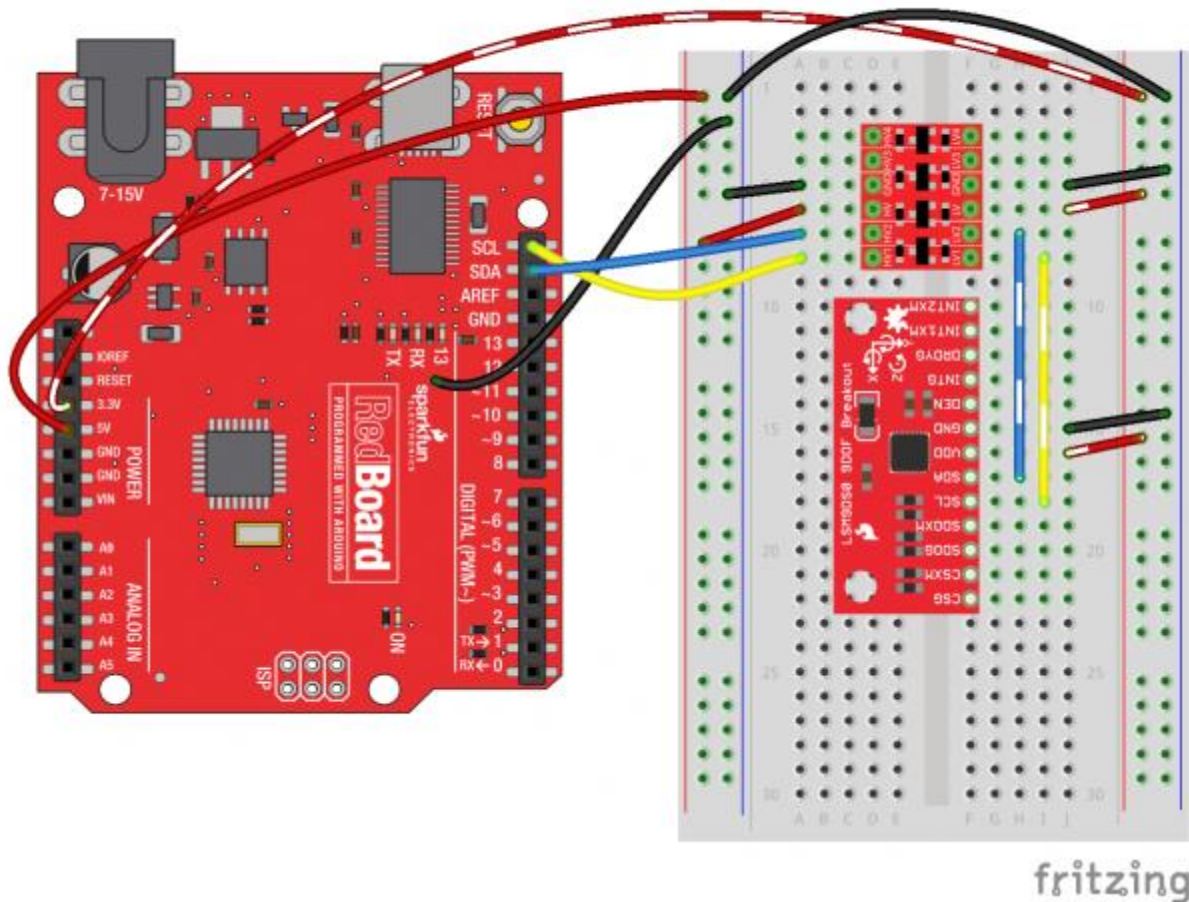
We've written a full-featured Arduino library to help make interfacing with the LSM9DS0's gyro and accelerometer/magnetometer as easy-as-possible. Visit the [GitHub repository](#) to download the most recent version of the library, or click the link below:

**[DOWNLOAD THE SFE LSM9DS0 ARDUINO LIBRARY](#)**

For help installing the library, check out our [How To Install An Arduino Library tutorial](#). You'll need to move the `SFE_LSM9DS0` folder into a *libraries* folder within your Arduino sketchbook.

#### 18.2.7.1 Simple Hardware Hookup (I<sup>2</sup>C)

The library will work with either I<sup>2</sup>C or SPI. Since we're trying to be as frugal with our Arduino pins as possible, I<sup>2</sup>C it is! Here's a fritzing diagram for this example:

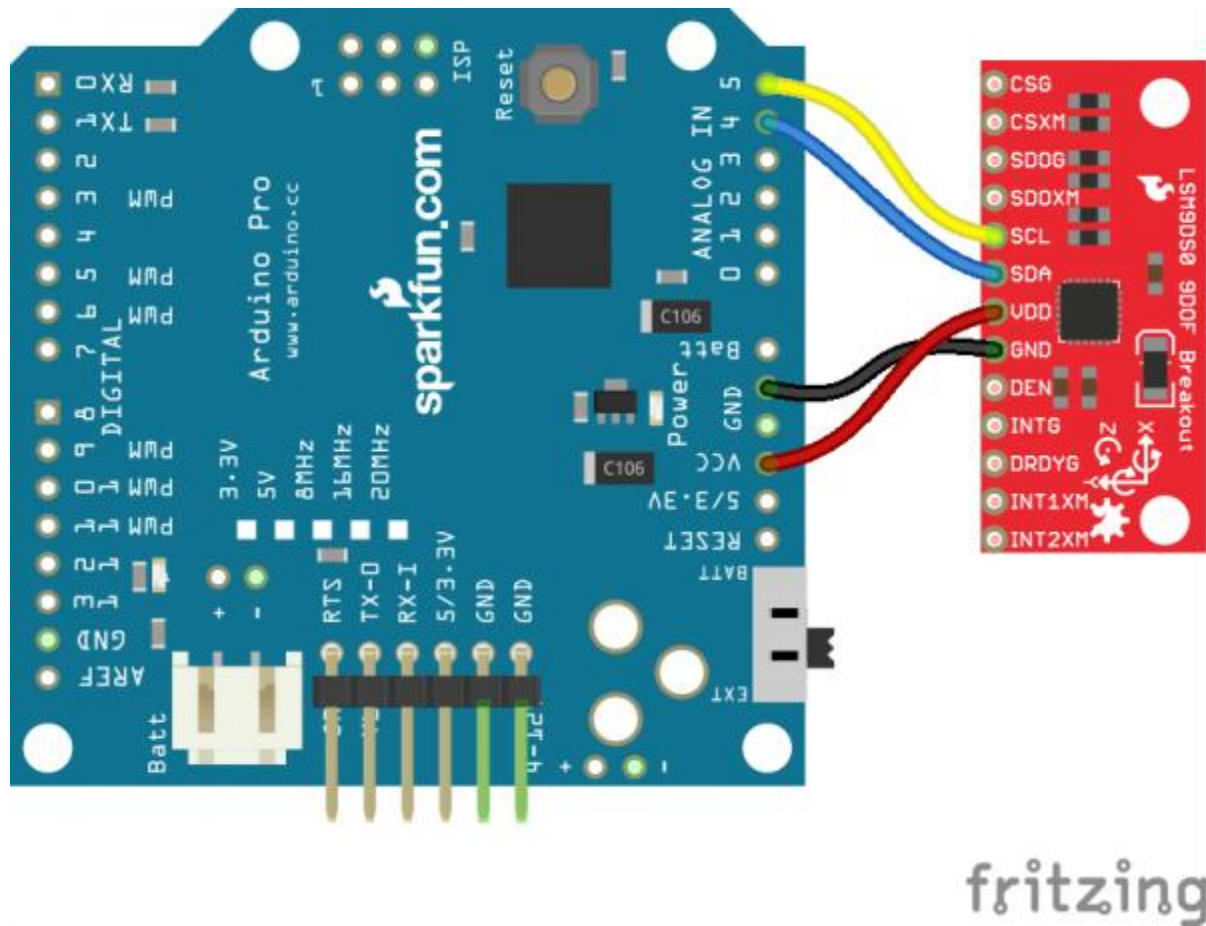


fritzing

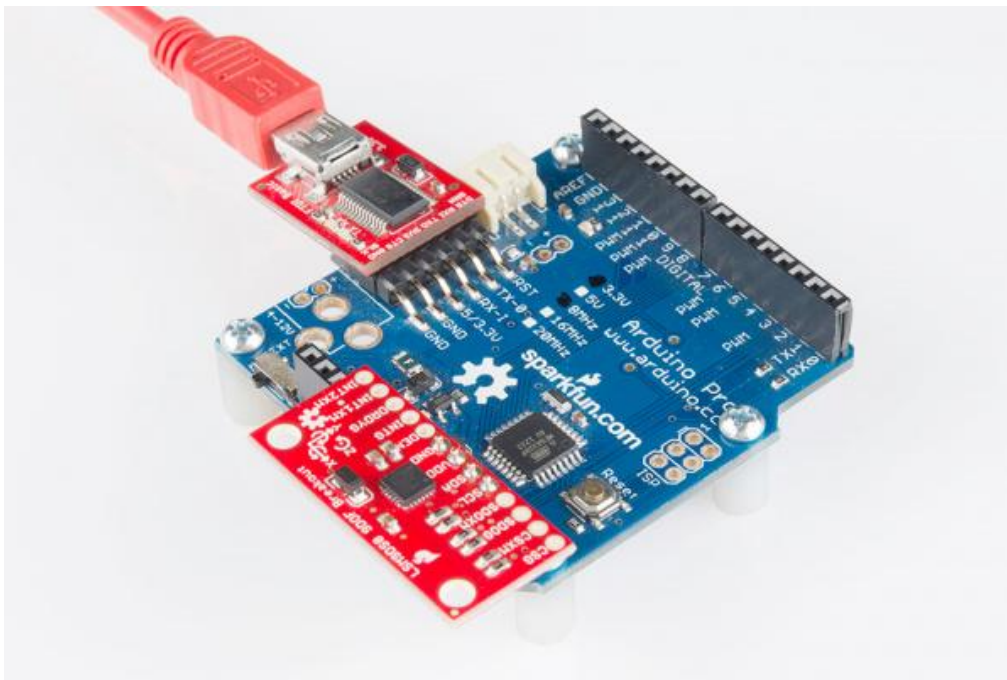
Connecting the LSM9DS0 to a RedBoard via a [Bi-Directional Logic Level Converter](#).

This hookup relies on all of the **jumpers** on the back of the board being set (as they should be, unless they've been sliced). If the jumpers have been disconnected, connect all four CS and SDO pins to 3.3V. Since we're using I<sup>2</sup>C all we have to do is connect SDA to SDA and SCL to SCL. Unfortunately, since the LSM9DS0's **maximum operating voltage is 3.6V**, we need to use a [level shifting board](#) to switch between 3.3V and 5V.

Alternatively, if you have a 3.3V-operating Arduino – like the [3.3V/8MHz Pro](#) – you can connect SDA and SCL directly from microcontroller to sensor.



Heck, you can even mount the breakout board on top of the Arduino Pro. If you do this, you'll need to set A3 HIGH and A2 LOW. The sensor pulls little enough current that the Arduino's I/O pins can power it!



*The wireless hookup: mounting an LSM9DS0 on top of an Arduino Pro. Pull A2 LOW and A3 HIGH to power the breakout.*

### 18.2.7.2 Open the LSM9DS0\_Simple Example

Once you've installed the library, open Arduino (or restart it if it was already open). You'll find this first example under the **File > Examples > SFE\_LSM9DS0 > LSM9DS0\_Simple**:

```
COPY CODE/*****
```

```
LSM9DS0_Simple.ino
```

```
SFE_LSM9DS0 Library Simple Example Code
```

```
Jim Lindblom @ SparkFun Electronics
```

```
Original Creation Date: February 18, 2014
```

```
https://github.com/sparkfun/LSM9DS0\_Breakout
```

The LSM9DS0 is a versatile 9DOF sensor. It has a built-in accelerometer, gyroscope, and magnetometer. Very cool! Plus it functions over either SPI or I2C.

This Arduino sketch is a demo of the simple side of the SFE\_LSM9DS0 library. It'll demo the following:

- \* How to create a LSM9DS0 object, using a constructor (global variables section).
- \* How to use the begin() function of the LSM9DS0 class.
- \* How to read the gyroscope, accelerometer, and magnetometer using the readGryo(), readAccel(), readMag() functions and the gx, gy, gz, ax, ay, az, mx, my, and mz variables.
- \* How to calculate actual acceleration, rotation speed, magnetic field strength using the calcAccel(), calcGyro() and calcMag() functions.
- \* How to use the data from the LSM9DS0 to calculate orientation and heading.

Hardware setup: This library supports communicating with the LSM9DS0 over either I2C or SPI. If you're using I2C, these are the only connections that need to be made:

```
LSM9DS0 ----- Arduino
```

```
SCL ----- SCL (A5 on older 'Duinos')
```

```
SDA ----- SDA (A4 on older 'Duinosaurs')
```

```
VDD ----- 3.3V
```

```
GND ----- GND
```

(CSG, CSXM, SDOG, and SDOXM should all be pulled high jumpers on the breakout board will do this for you.)

If you're using SPI, here is an example hardware setup:

```
LSM9DS0 ----- Arduino
```

```
CSG ----- 9
```

```
CSXM ----- 10
```

```
SDOG ----- 12
```

```
SDOXM ----- 12 (tied to SDOG)
```

```
SCL ----- 13
```

```
SDA ----- 11
```

```
VDD ----- 3.3V
```

```
GND ----- GND
```

The LSM9DS0 has a maximum voltage of 3.6V. Make sure you power it off the 3.3V rail! And either use level shifters between SCL and SDA or just use a 3.3V Arduino Pro.

Development environment specifics:

```
IDE: Arduino 1.0.5
```

```
Hardware Platform: Arduino Pro 3.3V/8MHz
```

```
LSM9DS0 Breakout Version: 1.0
```

This code is beerware. If you see me (or any other SparkFun employee) at the local, and you've found our code helpful, please buy us a round!

Distributed as-is; no warranty is given.

```

*****/

// The SFE_LSM9DS0 requires both the SPI and Wire libraries.
// Unfortunately, you'll need to include both in the Arduino
// sketch, before including the SFE_LSM9DS0 library.
#include <SPI.h> // Included for SFE_LSM9DS0 library
#include <Wire.h>
#include <SFE_LSM9DS0.h>

////////////////////////////////////

// Example I2C Setup //

////////////////////////////////////

// Comment out this section if you're using SPI
// SDO_XM and SDO_G are both grounded, so our addresses are:
#define LSM9DS0_XM 0x1D // Would be 0x1E if SDO_XM is LOW
#define LSM9DS0_G 0x6B // Would be 0x6A if SDO_G is LOW
// Create an instance of the LSM9DS0 library called `dof` the
// parameters for this constructor are:
// [SPI or I2C Mode declaration],[gyro I2C address],[xm I2C add.]
LSM9DS0 dof(MODE_I2C, LSM9DS0_G, LSM9DS0_XM);

////////////////////////////////////

// Example SPI Setup //

////////////////////////////////////

/* // Uncomment this section if you're using SPI
#define LSM9DS0_CSG 9 // CSG connected to Arduino pin 9
#define LSM9DS0_CSXM 10 // CSXM connected to Arduino pin 10
LSM9DS0 dof(MODE_SPI, LSM9DS0_CSG, LSM9DS0_CSXM);
*/

```

```
// Do you want to print calculated values or raw ADC ticks read
// from the sensor? Comment out ONE of the two #defines below
// to pick:

#define PRINT_CALCULATED

//#define PRINT_RAW

#define PRINT_SPEED 500 // 500 ms between prints

void setup()
{
  Serial.begin(115200); // Start serial at 115200 bps

  // Use the begin() function to initialize the LSM9DS0 library.
  // You can either call it with no parameters (the easy way):
  uint16_t status = dof.begin();

  // Or call it with declarations for sensor scales and data rates:
  //uint16_t status = dof.begin(dof.G_SCALE_2000DPS,
  //
  //                               dof.A_SCALE_6G, dof.M_SCALE_2GS);

  // begin() returns a 16-bit value which includes both the gyro
  // and accelerometers WHO_AM_I response. You can check this to
  // make sure communication was successful.

  Serial.print("LSM9DS0 WHO_AM_I's returned: 0x");
  Serial.println(status, HEX);
  Serial.println("Should be 0x49D4");
  Serial.println();
}

void loop()
{
  printGyro(); // Print "G: gx, gy, gz"
  printAccel(); // Print "A: ax, ay, az"
```

```
printMag(); // Print "M: mx, my, mz"

// Print the heading and orientation for fun!
printHeading((float) dof.mx, (float) dof.my);
printOrientation(dof.calcAccel(dof.ax), dof.calcAccel(dof.ay),
                dof.calcAccel(dof.az));

Serial.println();

delay(PRINT_SPEED);
}

void printGyro()
{
    // To read from the gyroscope, you must first call the
    // readGyro() function. When this exits, it'll update the
    // gx, gy, and gz variables with the most current data.
    dof.readGyro();

    // Now we can use the gx, gy, and gz variables as we please.
    // Either print them as raw ADC values, or calculated in DPS.
    Serial.print("G: ");

#ifdef PRINT_CALCULATED
    // If you want to print calculated values, you can use the
    // calcGyro helper function to convert a raw ADC value to
    // DPS. Give the function the value that you want to convert.
    Serial.print(dof.calcGyro(dof.gx), 2);
    Serial.print(", ");
    Serial.print(dof.calcGyro(dof.gy), 2);
    Serial.print(", ");
    Serial.println(dof.calcGyro(dof.gz), 2);
#endif
}
```

```
#elif defined PRINT_RAW

  Serial.print(dof.gx);

  Serial.print(", ");

  Serial.print(dof.gy);

  Serial.print(", ");

  Serial.println(dof.gz);

#endif

}

void printAccel()

{

  // To read from the accelerometer, you must first call the

  // readAccel() function. When this exits, it'll update the

  // ax, ay, and az variables with the most current data.

  dof.readAccel();

  // Now we can use the ax, ay, and az variables as we please.

  // Either print them as raw ADC values, or calculated in g's.

  Serial.print("A: ");

#ifdef PRINT_CALCULATED

  // If you want to print calculated values, you can use the

  // calcAccel helper function to convert a raw ADC value to

  // g's. Give the function the value that you want to convert.

  Serial.print(dof.calcAccel(dof.ax), 2);

  Serial.print(", ");

  Serial.print(dof.calcAccel(dof.ay), 2);

  Serial.print(", ");

  Serial.println(dof.calcAccel(dof.az), 2);

#else

  Serial.print(dof.ax);

  Serial.print(", ");
```

```
Serial.print(dof.ay);

Serial.print(", ");

Serial.println(dof.az);

#endif

}

void printMag()

{

    // To read from the magnetometer, you must first call the

    // readMag() function. When this exits, it'll update the

    // mx, my, and mz variables with the most current data.

    dof.readMag();

    // Now we can use the mx, my, and mz variables as we please.

    // Either print them as raw ADC values, or calculated in Gauss.

    Serial.print("M: ");

#ifdef PRINT_CALCULATED

    // If you want to print calculated values, you can use the

    // calcMag helper function to convert a raw ADC value to

    // Gauss. Give the function the value that you want to convert.

    Serial.print(dof.calcMag(dof.mx), 2);

    Serial.print(", ");

    Serial.print(dof.calcMag(dof.my), 2);

    Serial.print(", ");

    Serial.println(dof.calcMag(dof.mz), 2);

#elif defined PRINT_RAW

    Serial.print(dof.mx);

    Serial.print(", ");

    Serial.print(dof.my);
```

```
Serial.print(", ");

Serial.println(dof.mz);

#endif

}

// Here's a fun function to calculate your heading, using Earth's
// magnetic field.
// It only works if the sensor is flat (z-axis normal to Earth).
// Additionally, you may need to add or subtract a declination
// angle to get the heading normalized to your location.
// See: http://www.ngdc.noaa.gov/geomag/declination.shtml

void printHeading(float hx, float hy)
{
    float heading;

    if (hy > 0)
    {
        heading = 90 - (atan(hx / hy) * (180 / PI));
    }
    else if (hy < 0)
    {
        heading = - (atan(hx / hy) * (180 / PI));
    }
    else // hy = 0
    {
        if (hx < 0) heading = 180;
        else heading = 0;
    }

    Serial.print("Heading: ");
    Serial.println(heading, 2);
}
```

```
}

// Another fun function that does calculations based on the
// accelerometer data. This function will print your LSM9DS0's
// orientation -- it's roll and pitch angles.

void printOrientation(float x, float y, float z)
{
    float pitch, roll;

    pitch = atan2(x, sqrt(y * y) + (z * z));
    roll = atan2(y, sqrt(x * x) + (z * z));
    pitch *= 180.0 / PI;
    roll *= 180.0 / PI;

    Serial.print("Pitch, Roll: ");
    Serial.print(pitch, 2);
    Serial.print(", ");
    Serial.println(roll, 2);
}
```

After uploading the code, open up your **serial monitor** and **set the baud rate to 115200 bps**. You should see something like this begin to stream by:



## 18.3 Software on Raspberry concerning IMU



RTIMULib-master.zip

Name	Änderungsdatum	Typ	Größe
AccelCalDlg.cpp	22.06.2015 06:47	CPP-Datei	10 KB
AccelCalDlg.h	22.06.2015 06:47	H-Datei	3 KB
CMakeLists.txt	22.06.2015 06:47	Textdokument	3 KB
IMUThread.cpp	22.06.2015 06:47	CPP-Datei	5 KB
IMUThread.h	22.06.2015 06:47	H-Datei	3 KB
MagCalDlg.cpp	22.06.2015 06:47	CPP-Datei	11 KB
MagCalDlg.h	22.06.2015 06:47	H-Datei	3 KB
main.cpp	22.06.2015 06:47	CPP-Datei	2 KB
RTIMULibDemo.cpp	22.06.2015 06:47	CPP-Datei	16 KB
RTIMULibDemo.h	22.06.2015 06:47	H-Datei	4 KB
RTIMULibDemo.pri	22.06.2015 06:47	Qt Project Include...	2 KB
RTIMULibDemo.pro	22.06.2015 06:47	Qt Project file	2 KB
RTIMULibDemo.ui	22.06.2015 06:47	Qt UI file	3 KB
SelectFusionDlg.cpp	22.06.2015 06:47	CPP-Datei	3 KB
SelectFusionDlg.h	22.06.2015 06:47	H-Datei	2 KB
SelectIMUDlg.cpp	22.06.2015 06:47	CPP-Datei	9 KB
SelectIMUDlg.h	22.06.2015 06:47	H-Datei	2 KB

Name	Änderungsdatum	Typ	Größe
IMUDrivers	22.06.2015 06:47	Dateiordner	
CMakeLists.txt	22.06.2015 06:47	Textdokument	4 KB
RTFusion.cpp	22.06.2015 06:47	CPP-Datei	5 KB
RTFusion.h	22.06.2015 06:47	H-Datei	5 KB
RTFusionKalman4.cpp	22.06.2015 06:47	CPP-Datei	7 KB
RTFusionKalman4.h	22.06.2015 06:47	H-Datei	4 KB
RTFusionRTQF.cpp	22.06.2015 06:47	CPP-Datei	6 KB
RTFusionRTQF.h	22.06.2015 06:47	H-Datei	3 KB
RTIMUAccelCal.cpp	22.06.2015 06:47	CPP-Datei	4 KB
RTIMUAccelCal.h	22.06.2015 06:47	H-Datei	3 KB
RTIMUCalDefs.h	22.06.2015 06:47	H-Datei	3 KB
RTIMUHal.cpp	22.06.2015 06:47	CPP-Datei	11 KB
RTIMUHal.h	22.06.2015 06:47	H-Datei	5 KB
RTIMULIB LICENSE	22.06.2015 06:47	Datei	2 KB
RTIMULib.h	22.06.2015 06:47	H-Datei	2 KB
RTIMULib.pri	22.06.2015 06:47	Qt Project Include...	4 KB
RTIMULibDefs.h	22.06.2015 06:47	H-Datei	3 KB
RTIMUMagCal.cpp	22.06.2015 06:47	CPP-Datei	8 KB
RTIMUMagCal.h	22.06.2015 06:47	H-Datei	5 KB
RTIMUSettings.cpp	22.06.2015 06:47	CPP-Datei	64 KB
RTIMUSettings.h	22.06.2015 06:47	H-Datei	18 KB
RTMath.cpp	22.06.2015 06:47	CPP-Datei	17 KB
RTMath.h	22.06.2015 06:47	H-Datei	7 KB



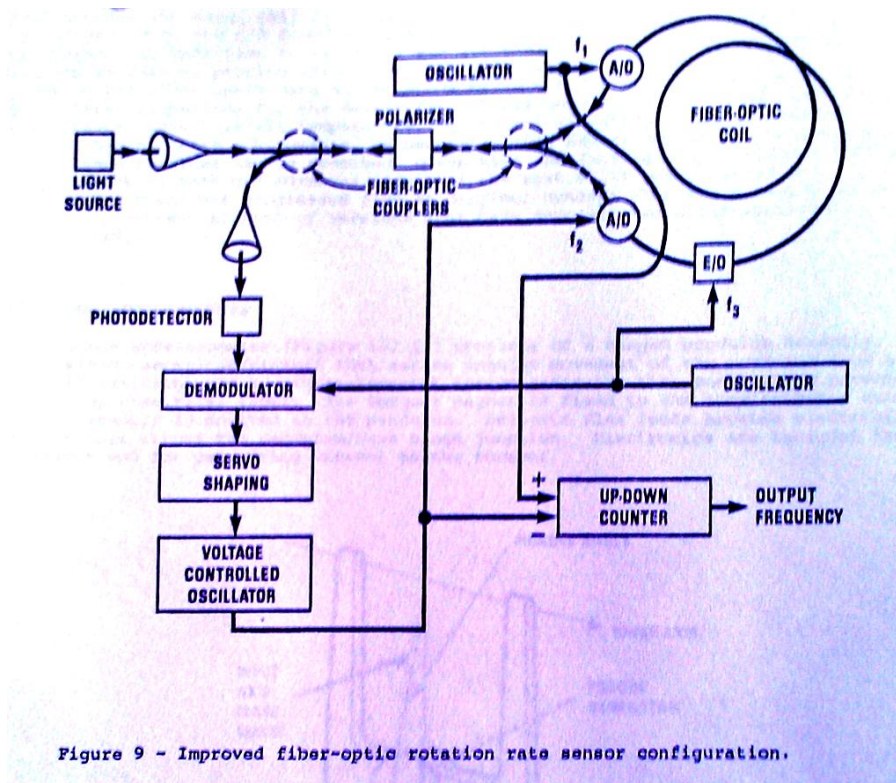
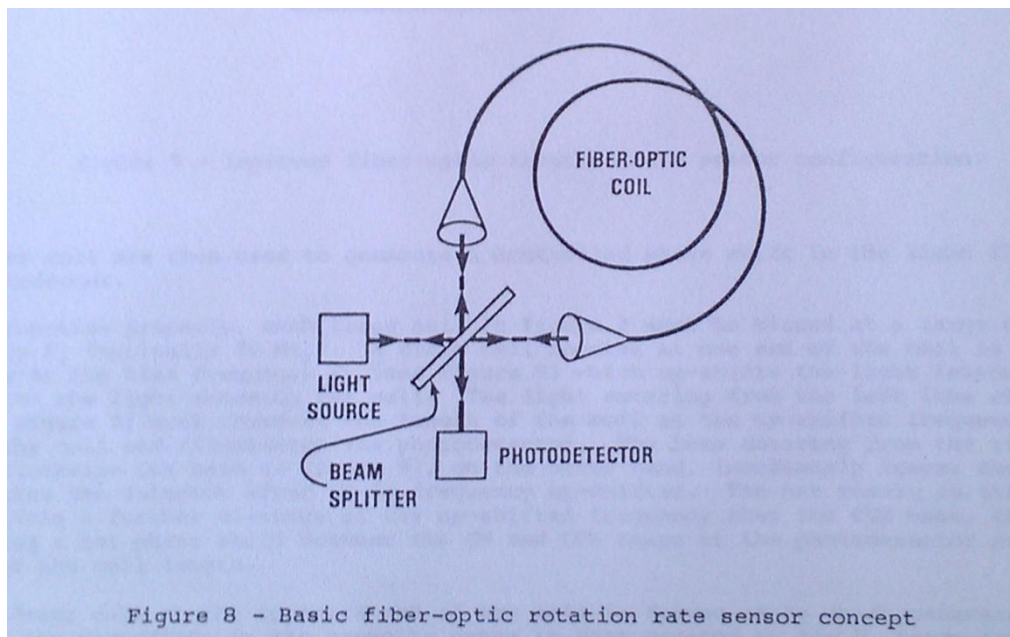
## 19 Base Station in Laboratory

On-Board-Computer: Raspberry Pi

with remote desktop via WiFi: visualization of IMU.



## 20 Fiber Optic Gyro Basics



From

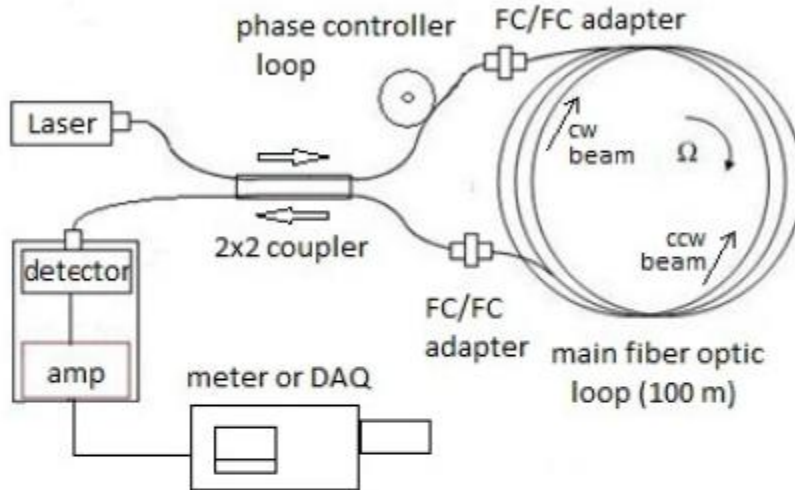
### Single Mode Fiber Optic Sagnac Interferometer with Wireless Data Collection

Doug Marett

Skyhunt, Toronto, ON Canada

*Fiber optic Gyroscope, IFOG, FOG, Sagnac Interferometer, wireless data acquisition*

**Figure 1: Fiber optic Sagnac interferometer block diagram (all components co-rotate on a platform)**



## II. MATERIALS

The essential parts for this project were as follows:

- FP-MQW 1.3  $\mu\text{m}$  laser with FC/PC connector
- 2 x 2 coupler (single mode) with FC/PC connectors
- Phase controller loop and mount
- 100 m or 1000 m single mode fiber optic loop
- PIN diode IR detector with amplifier
- Output voltmeter or wireless DAQ

**Figure 2: Parts for the Sagnac interferometer**

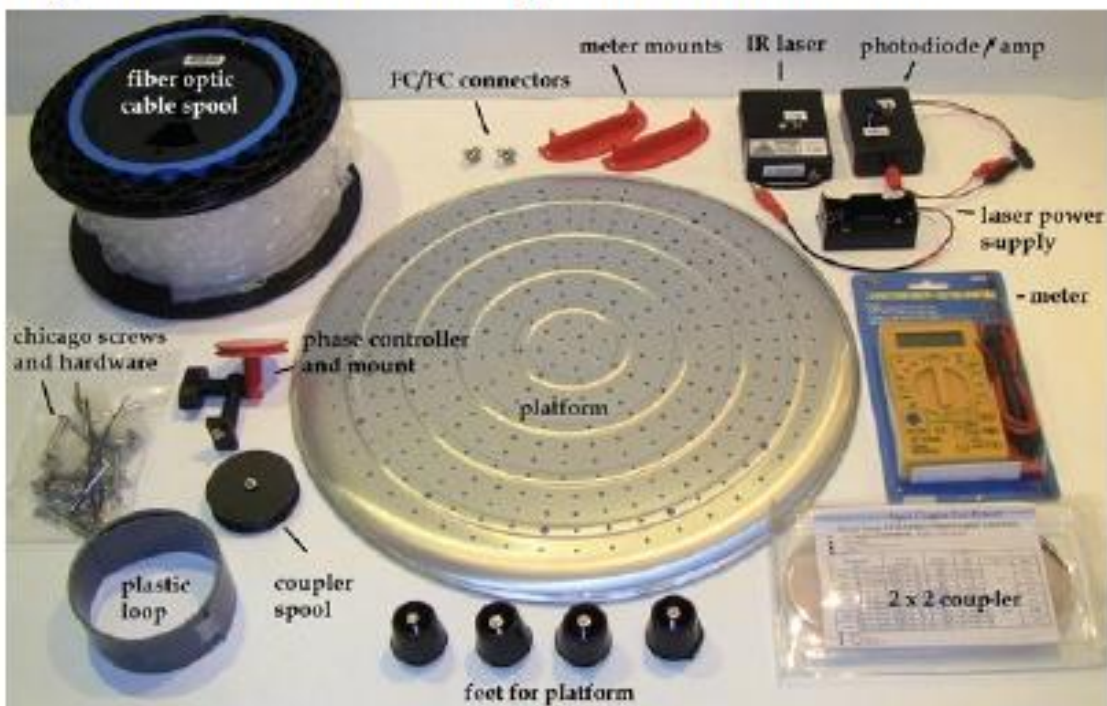


Figure 3: Phase Controller Detail

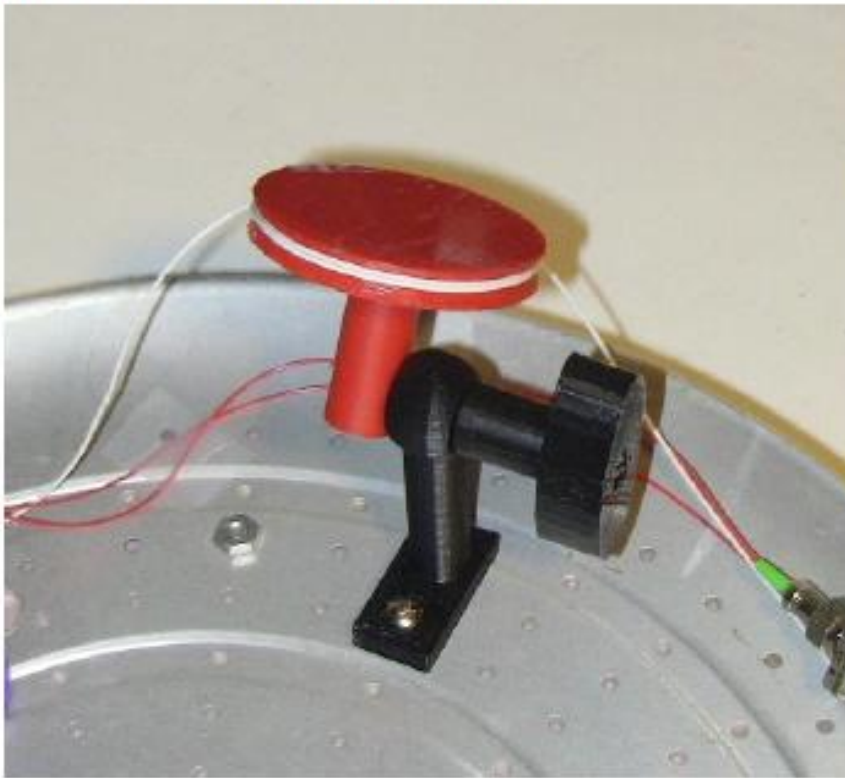


Figure 4: Assembled Sagnac interferometer

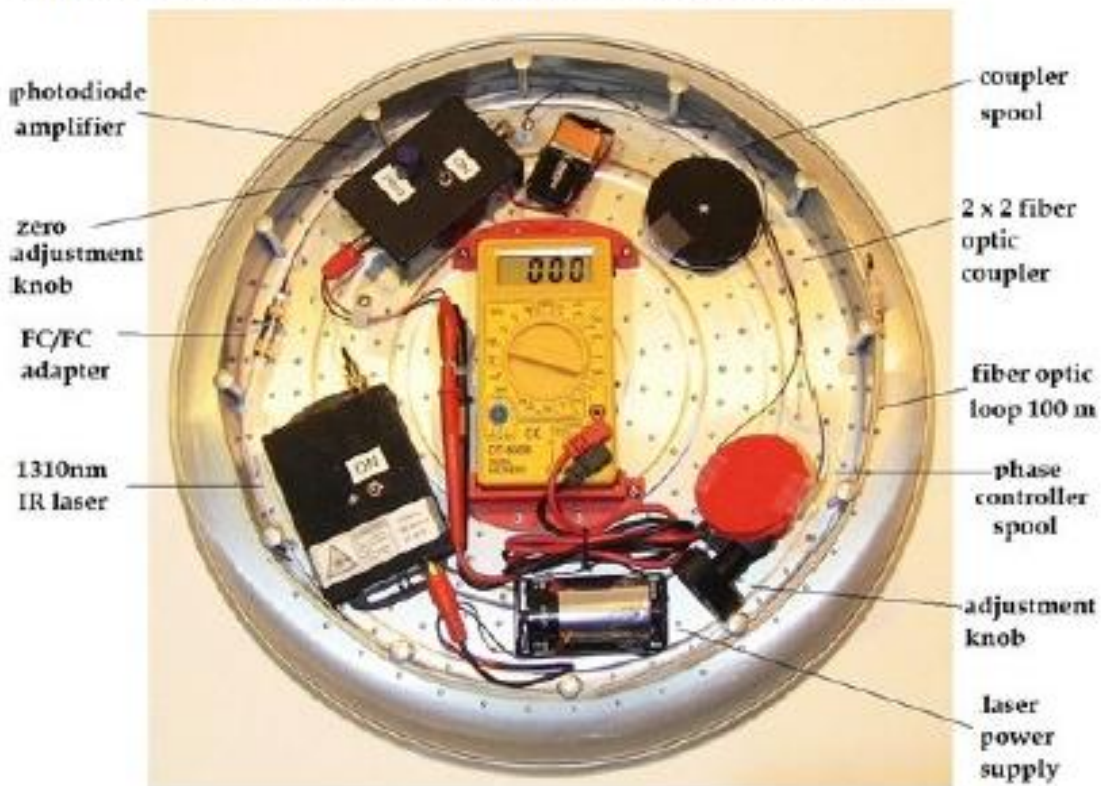
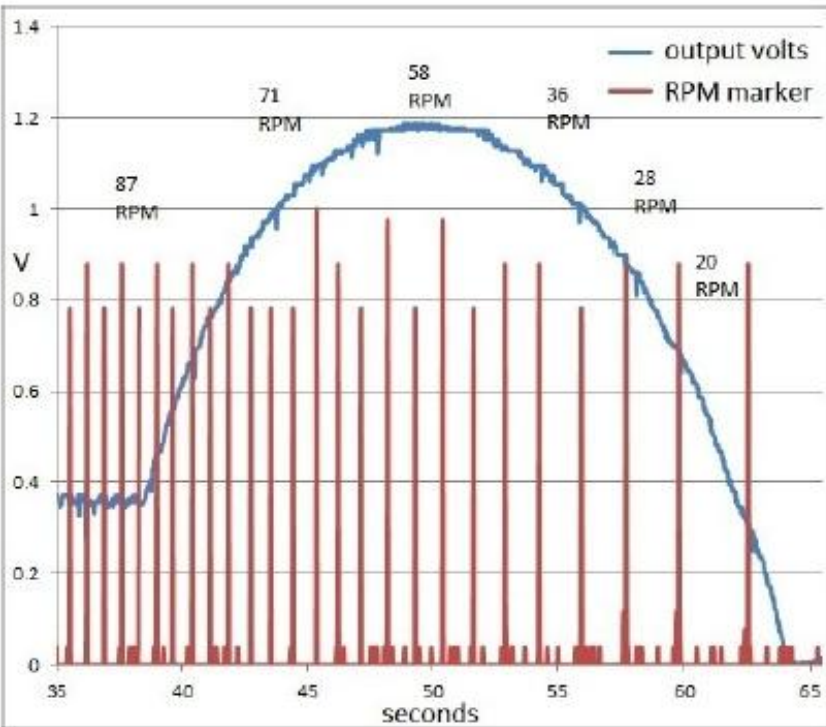
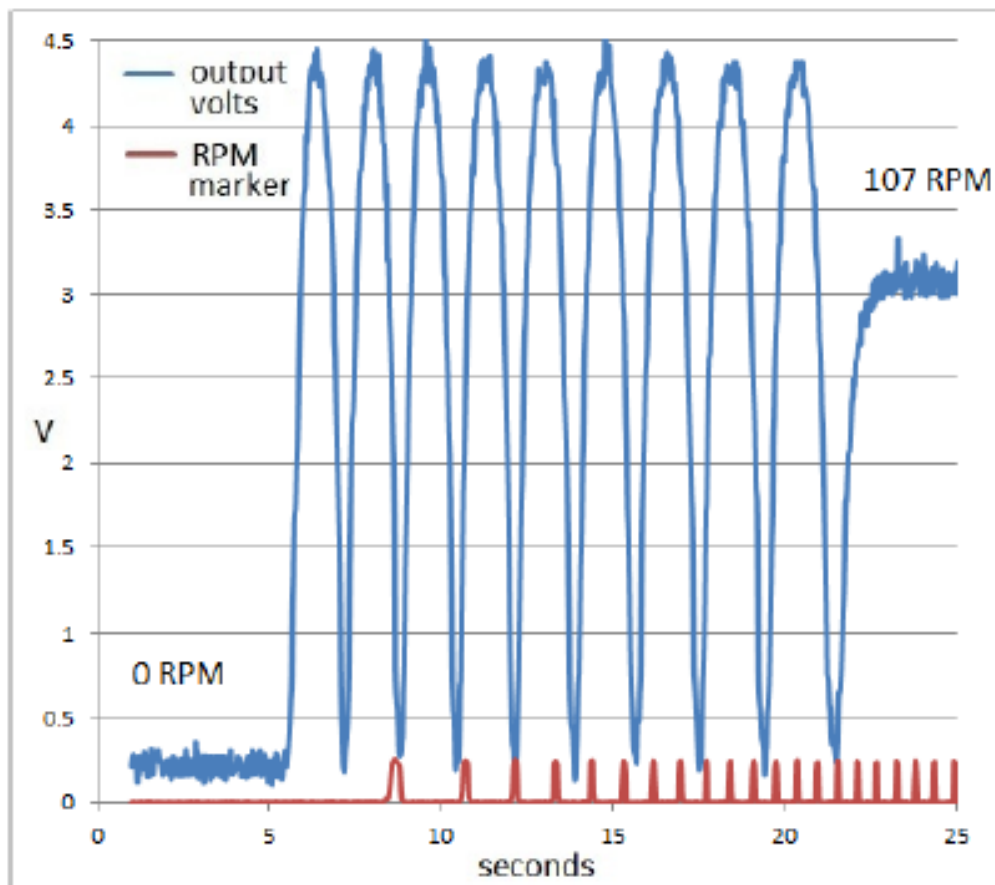


Figure 5: Interferometer output volts versus RPM collected using a wireless DAQ (100 m loop)



**Figure 6: Interferometer output volts verses RPM collected using a wireless DAQ (1000 m loop)**



---

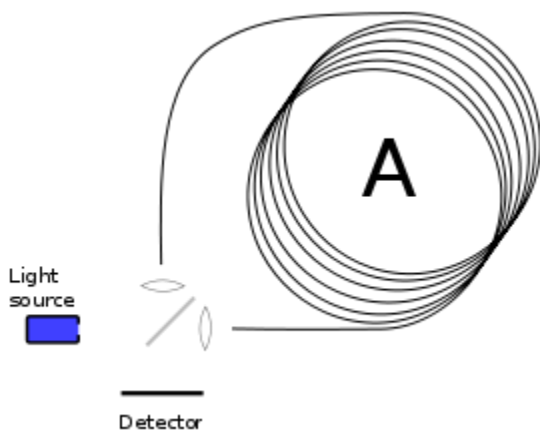
## 21 Fiber Optic Gyro development test rig and Fiber optic gyroscope sensor

### 21.1 Sagnac effect

#### 21.1.1 Definition:

The Sagnac effect (also called Sagnac interference), named after French physicist Georges Sagnac, is a phenomenon encountered in interferometry that is elicited by rotation. The Sagnac effect manifests itself in a setup called a ring interferometer. A beam of light is split and the two beams are made to follow the same path but in opposite directions. To act as a ring the trajectory must enclose an area. On return to the point of entry the two light beams are allowed to exit the ring and undergo interference. The relative phases of the two exiting beams, and thus the position of the interference fringes, are shifted according to the angular velocity of the apparatus. This arrangement is also called a Sagnac interferometer.

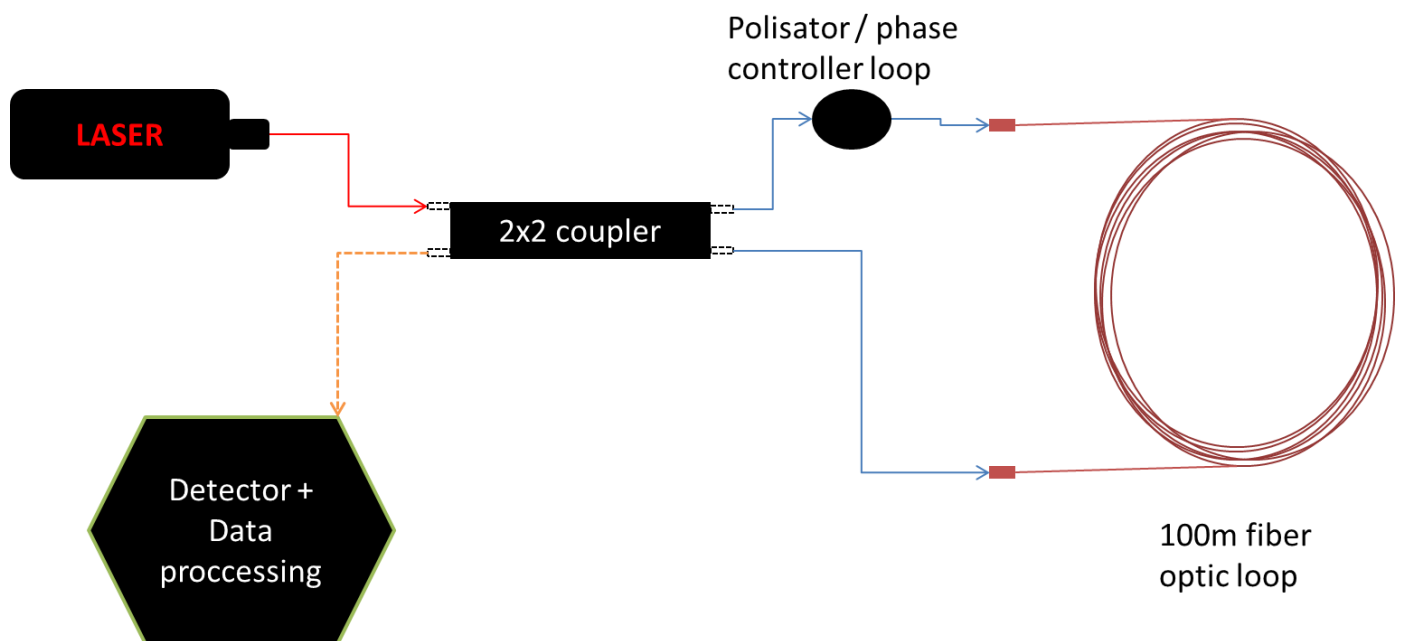
[1]



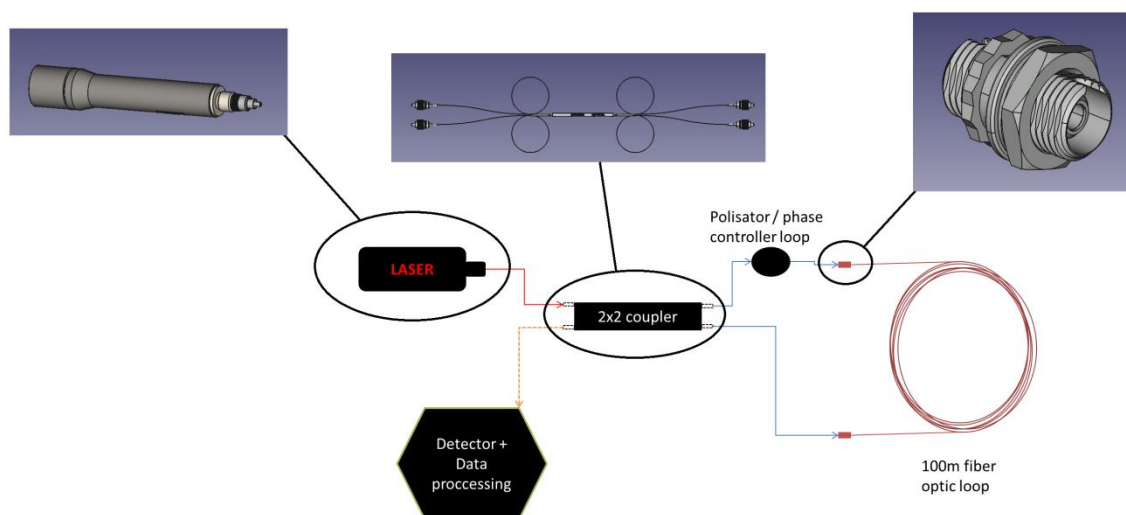
Title: *Figure 1. Schematic representation of a Sagnac interferometer.*

## 21.1.2 Experiment:

## i. Schema:



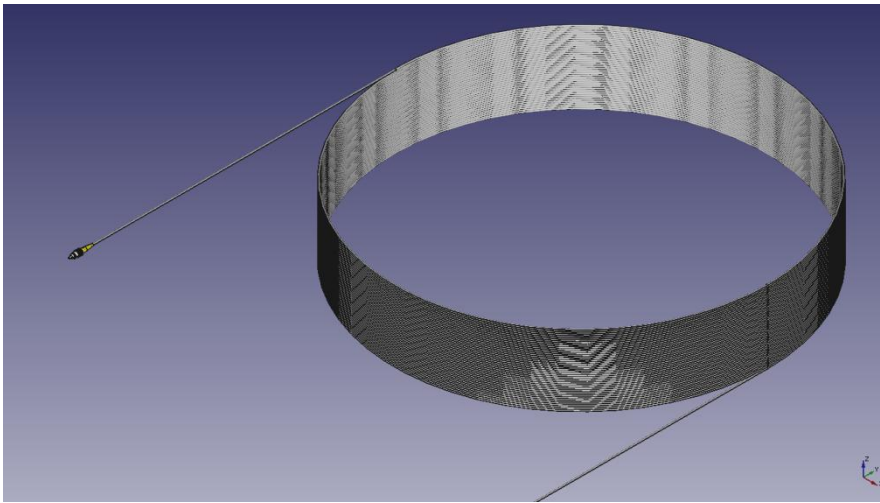
Title: *Figure 2. Sagnac effect schema.*



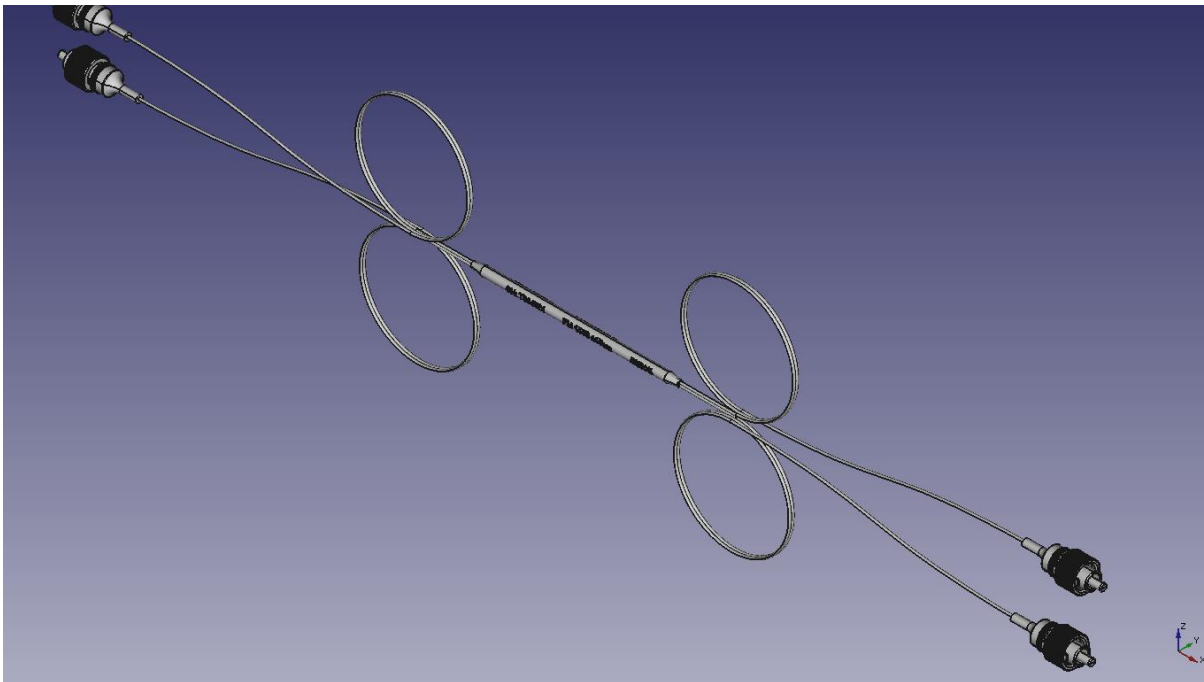
## ii. Materials:

- Single or Multi mode fiber optic cable ( 10 - 40 m ) with FC/UPC connectors.
- Fiber optic coupler 2x2 (50:50 split) with FC/UPC connectors.
- Detector circuit.
- Laser.
- (Polarisator) We won't use a polarisator in the first stage of sagnac effect experiment

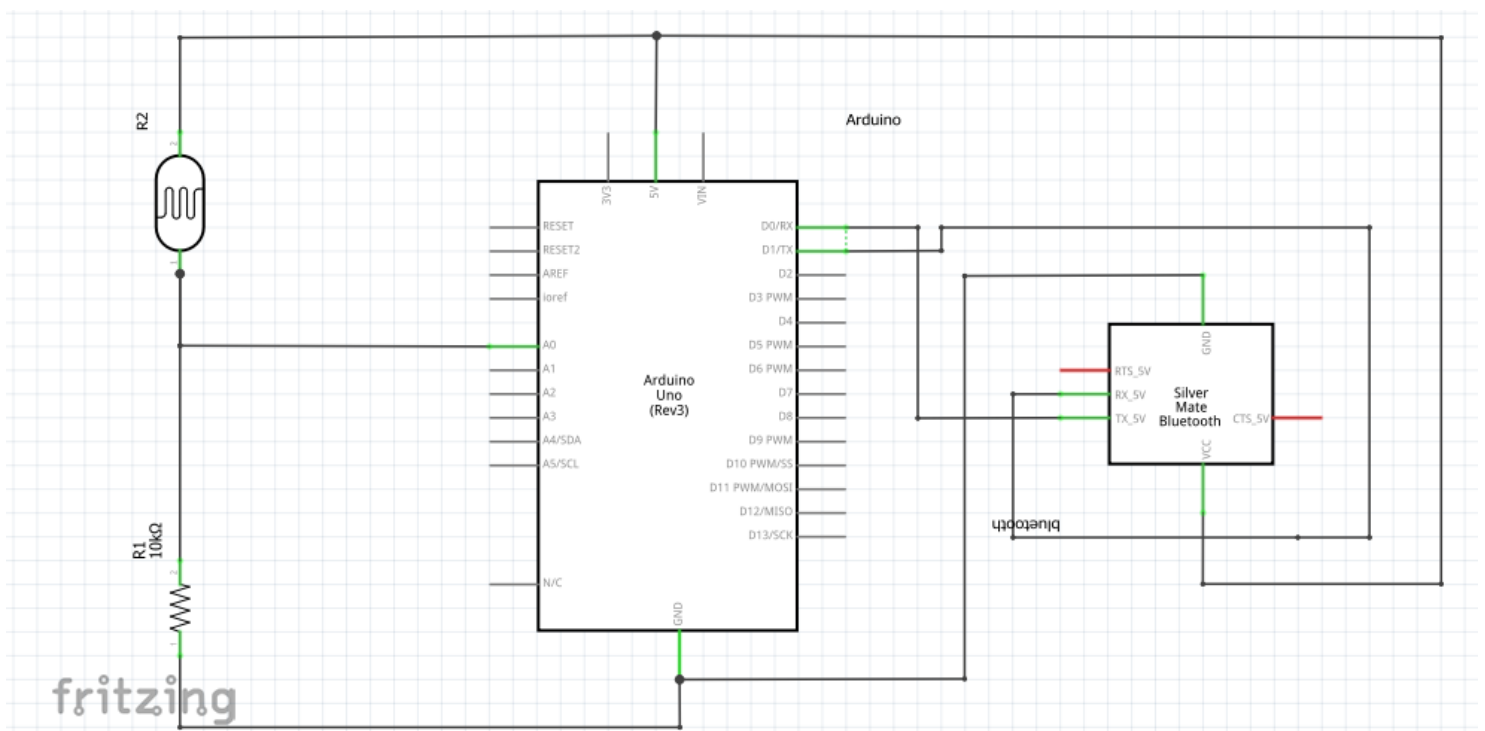
## ii.1. Fiber optic cable [TBD]



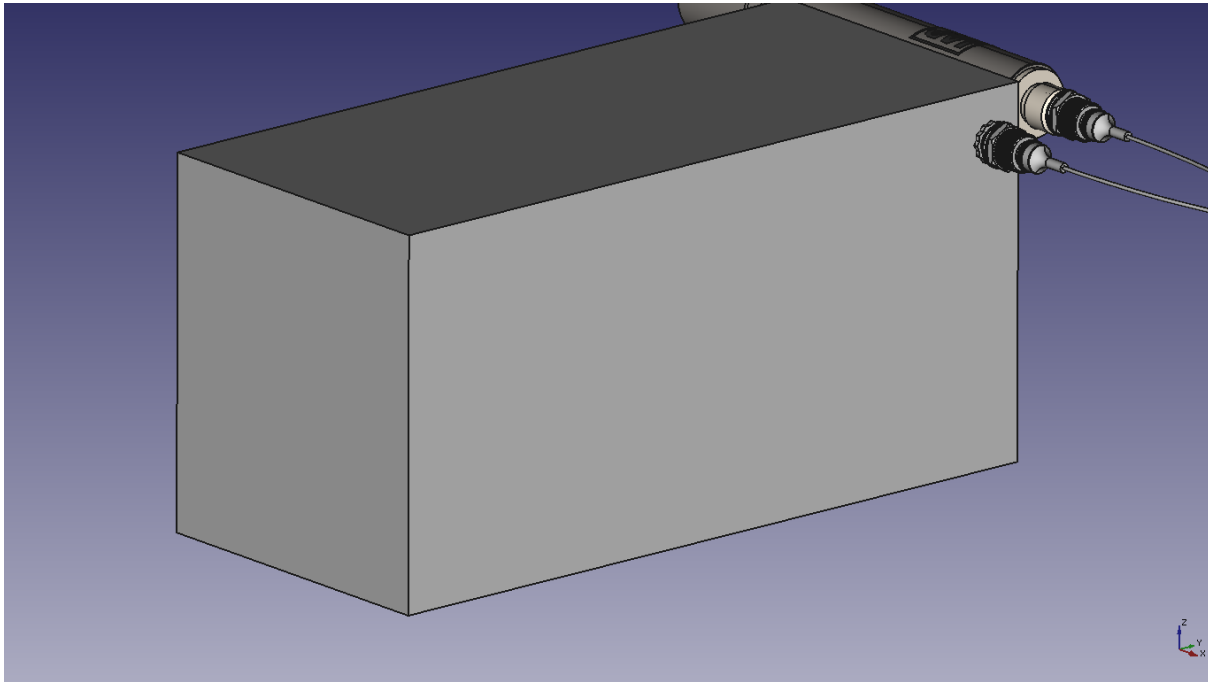
**ii.2. Fiber optic coupler [TBD]**



**ii.3. Detector circuit**



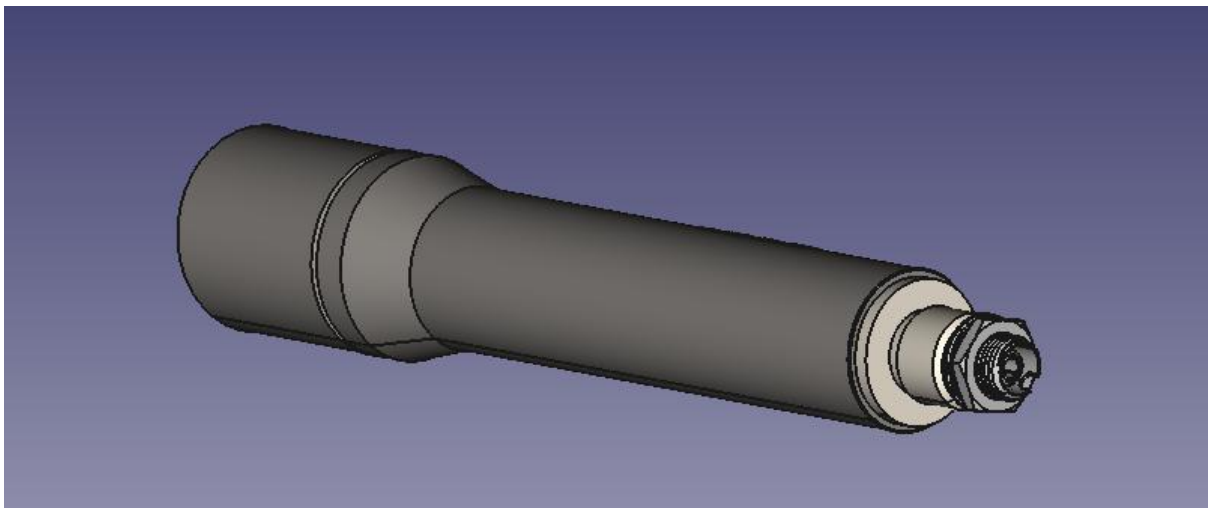
Title: *Figure 3. Detector schema.*



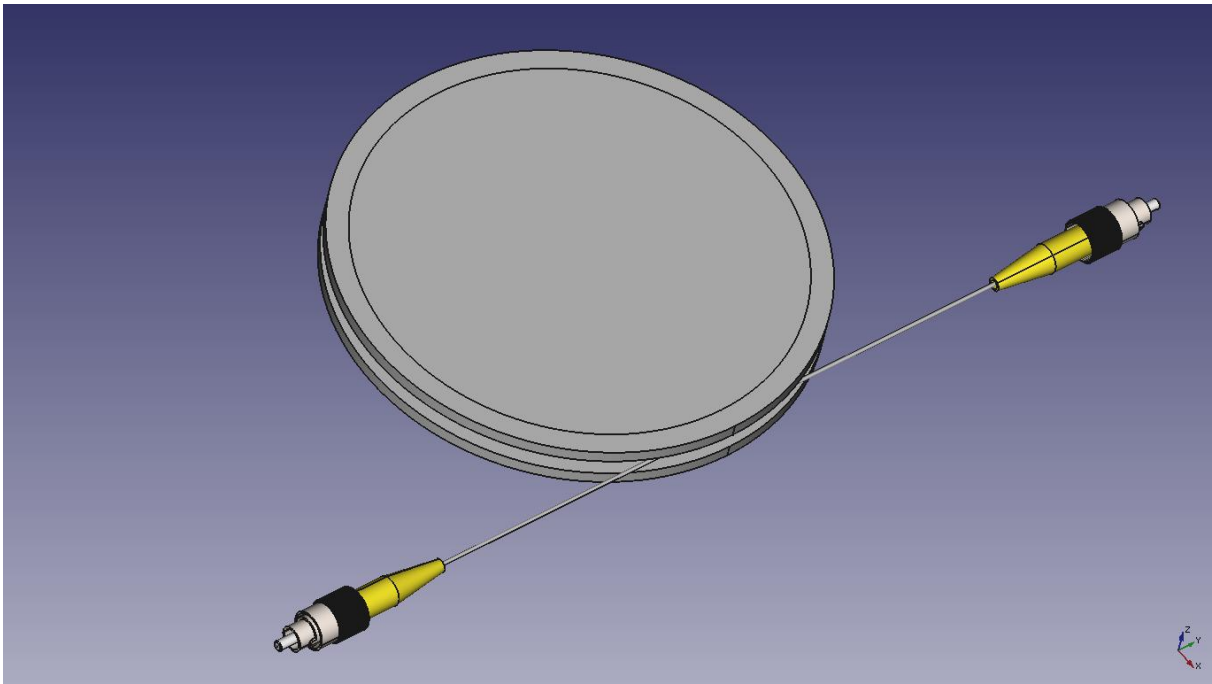
Component:

- \* Arduino UNO
- \* Bluetooth slave client
- \* Resistor 10k ohm
- \* Photodiode

**ii.4. Laser [TBD]**



**ii.5. Polarisator [TBD]**



21.2 FOG

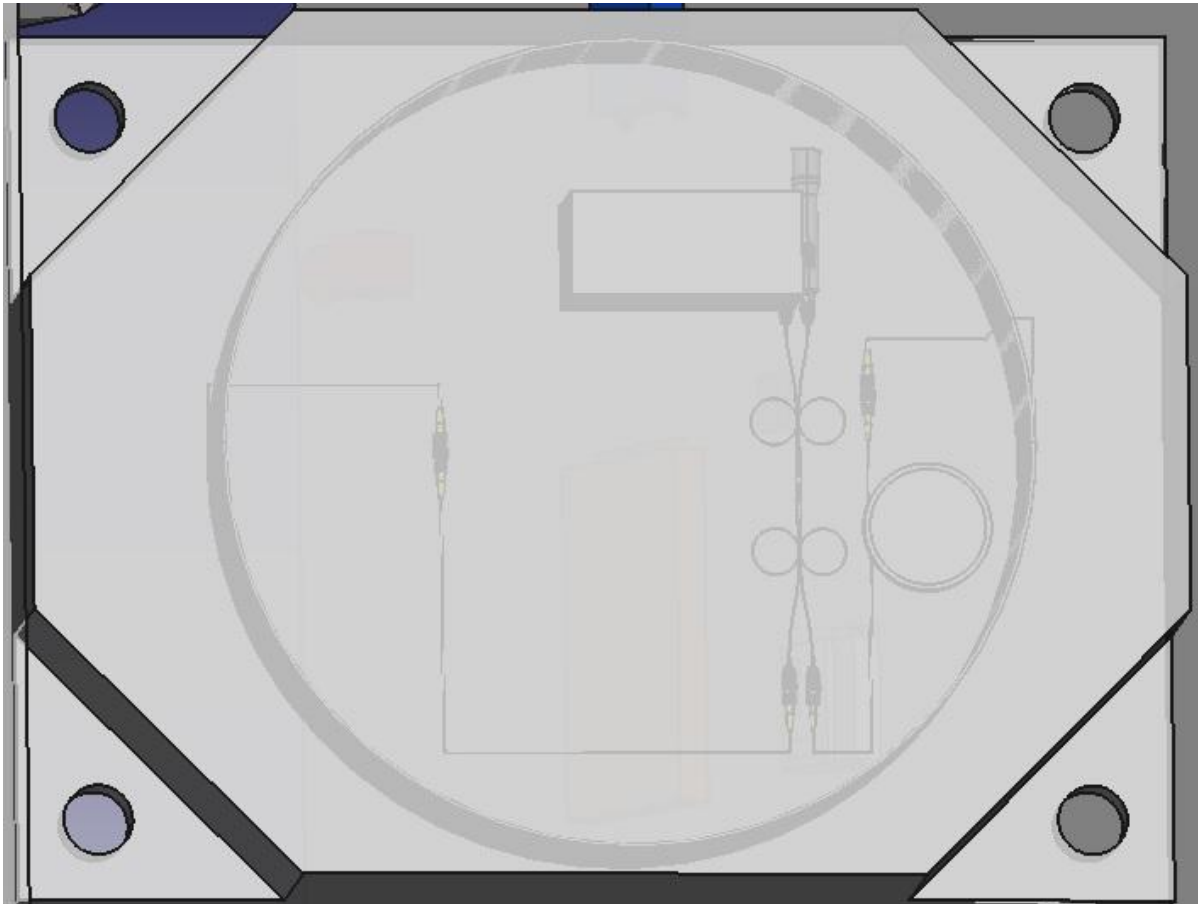


Fig.: FOG Sensor

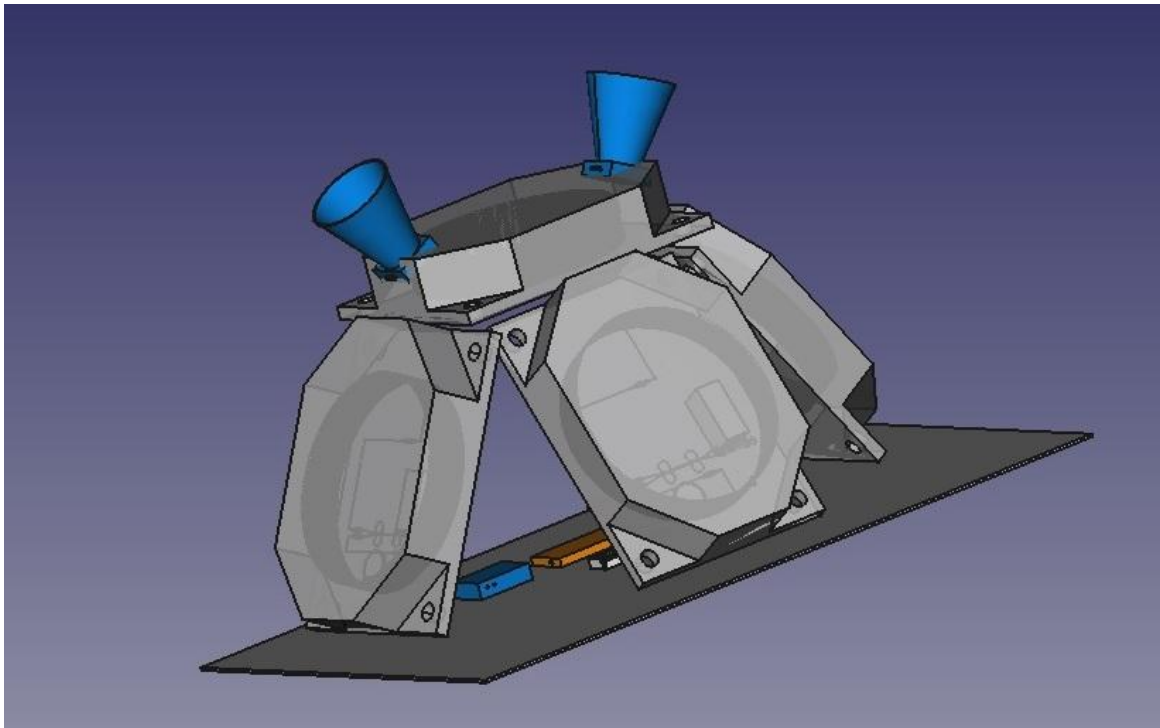


Fig: FOG integration in satellite (4 FOG sensors)

### 21.3 FreeCAD files

	 081016IAP-SAT_Integration.FCStd
--	---

### 21.4 References:

[1]: [https://en.wikipedia.org/wiki/Sagnac\\_effect](https://en.wikipedia.org/wiki/Sagnac_effect)

#### Useful links:

- <https://www.youtube.com/watch?v=AwcQsbgy7AY>
- <http://laserpointerforums.com/f42/diy-homemade-laser-diode-driver-26339.html>
- regulator: <https://www.youtube.com/watch?v=ljJWWGPjc-w>
- <http://www.instructables.com/id/How-to-Build-a-Bench-Top-Power-Supply/>
- <http://www.instructables.com/id/How-to-build-a-laser-general-guide/>

We can buy diode laser from: [http://www.ekt2.com/EKT/Educational/Led\\_AND\\_Laser/Laser/](http://www.ekt2.com/EKT/Educational/Led_AND_Laser/Laser/)

### 21.5 Ordered Materials (Oktober 2016)

- Single or Multi mode fiber optic cable ( 100 m ) with FC/PC connectors.
- Fiber optic coupler 2x2 with FC/UPC connectors.
- Single Fibre Collimator with FC/PC Connector
- FC/PC to FC/PC Adapter and FC/APC to FC/PC Adapter



# Shenzhen Bynet Communication Technology Co., Ltd

Add: 3/F, Building 7, Jiayiyuan Science and Techno. Park, Hua ning Road, Dalang, Longhua Town, Shenzhen, China, 518109  
 Tel: 86-755-33673743 Fax: 86-755-33673745  
 E-mail: sales13@szbynet.com Website: www.szbynet.com

## Proforma Invoice

Invoice No.:

Invoice Date: 14/Oct/2016

Buyer:

Shipping Date:

Add.:

Shipped by:

Attn:

Destination: Lebanon

Tel:

P/O NO.

No.	Item Number	Goods and Description	QTY (PCS)	U/PRICE (USD)	T/PRICE (USD)
<b>PRICE TERM: FOB SHENZHEN</b>					
	1	Optical Fused Coupler FBT 2x2/ mini module Fiber Optical Splitter	4	4.28	17.10
	2	Fiber optical FC/PC to FC/PC Adapter and FC/APC to FC/PC Adapter	10	0.35	3.53
	3	patch cord cable single-mode simplex 3 mm 100m with FC/PC Connectors	5	6.42	32.10
	4	Single Fiber Collimator with FC/PC connector/ferrule	4	3.20	12.80
	5	shipping fee			95.78
<b>TOTAL</b>					<b>161.31</b>

**TOTAL: SAY USD SEVENTY THREE DOLLAR AND SIXTY TWO CENT**

**Payment term: 30 days credit date of invoice**

**1. Payment to the seller's following account when order confirmation:**

BENEFICIARY: OVEROCEAN PHOTONICS TECHNOLOGY LIMITED  
 ACCOUNT NO.: 2204593108001  
 ACCOUNT BANK: Wing Hang Bank (China) Limited Shenzhen Branch  
 BANK ADDRESS: 5F, Shun Hing Square, Di Wang Commercial Centre, No. 5002, Shennan Road East, Shenzhen China  
 SWIFT CODE: WIHBCNBXSZB

**2. Bynet will only be held liable for local bank charges only.**

Buyer:

Seller: Shenzhen Bynet Communication Technology Co., Ltd

Authorized Signature

Authorized Signature



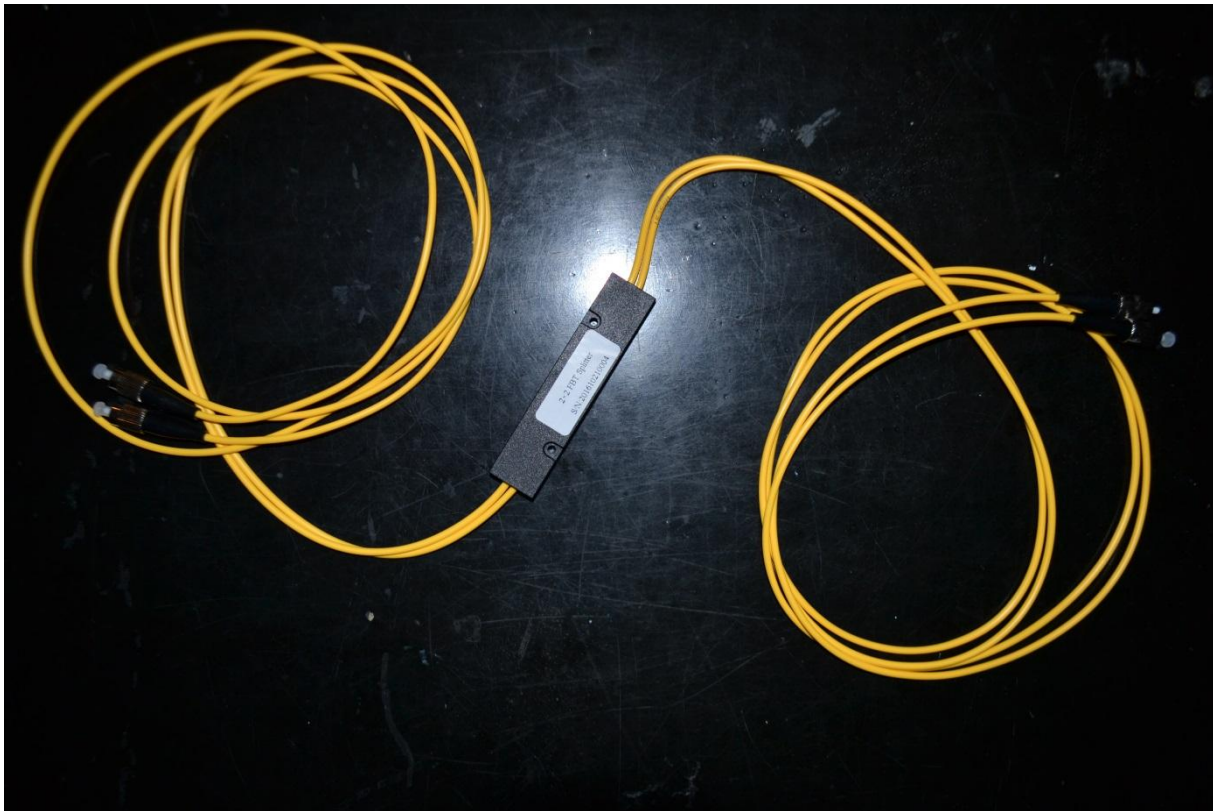
Additionally: Customs (in Lebanon: about 60\$) (about 100% of original material cost without shipping)

21.5.1.1 Fiber optic cable



### 21.5.1.2 Fiber optic coupler



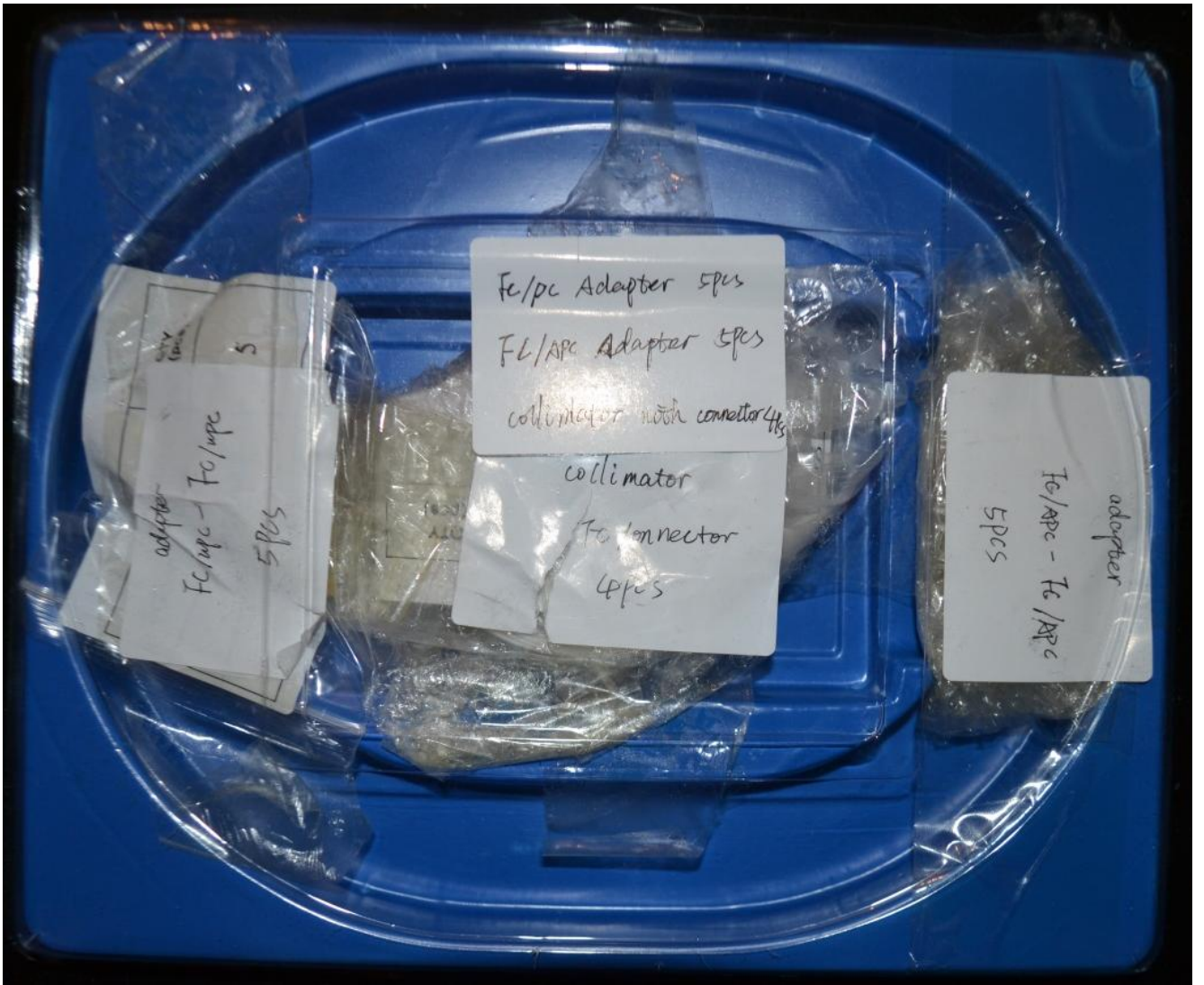


### 21.5.1.3 Single Fibre Collimator and FC/PC to FC/PC Adaptor



FC Adaptor







21.5.1.4 Packed





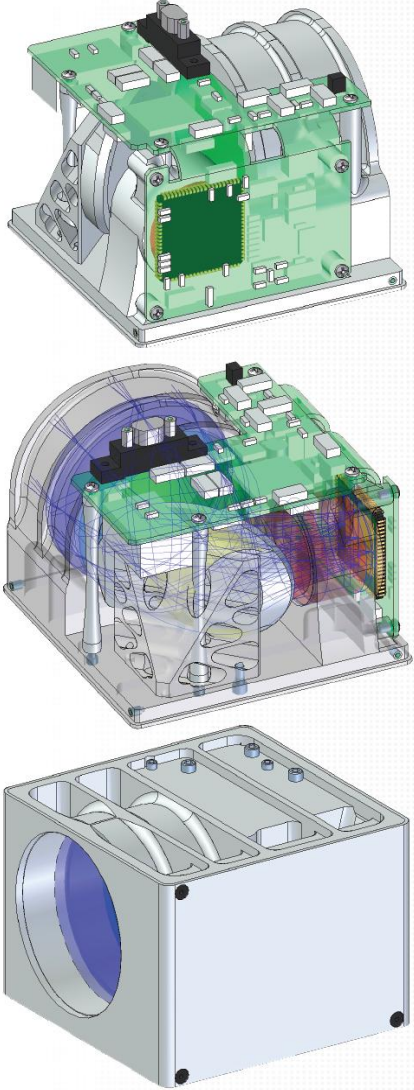
## Star Camera

## 22 Concept for star camera<sup>22</sup>

### 22.1 Specifications of a Star Camera for CubeSat Applications

# STAR CAMERA

COMPACT, LIGHT-WEIGHT, & LOW POWER STAR IMAGING FOR NANO- & PICO-SATELLITES



The Space Dynamics Laboratory (SDL) has developed a miniature Star Camera based on its Digital Imaging Space Camera (DISC) product line. The DISC Star Camera is a science-enabling technology for missions that require more stringent pointing knowledge than is currently available on extremely small satellites. Using a radiation-hardened focal plane, it is able to detect down to magnitude 6 stars.

**STAR TRACKER OPTION**

Also available is SDL's DISC Star Tracking Algorithm with a complete 'Lost in Space' solution for each image. The algorithm computes a quaternion that rotates the bore of each image to the J2000 inertial coordinate frame of the Hipparcos Star Catalog.

**SPECIFICATIONS**

**POWER** < 1 W

**MASS** 0.8 kg

**DIMENSIONS** 96 × 96 × 70 mm

**FEATURES**

- Designed specifically for star imaging
- Sized to fit in a CubeSat
- HAS2 RadHard CMOS FPA
- 60 mm aperture, 13° FOV
- SpaceWire interface
- High-quality, custom optics
- Optional radiation tolerant version

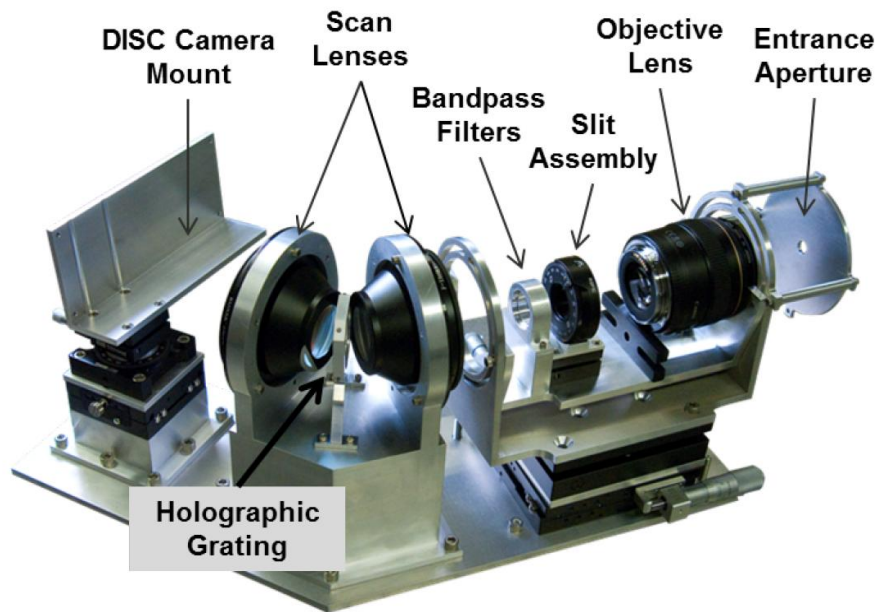


**Space Dynamics**  
LABORATORY  
Utah State University Research Foundation

1695 North Research Park Way • North Logan, Utah 84341 • Phone 435.713.3400 • [www.sdl.usu.edu](http://www.sdl.usu.edu)

<sup>22</sup> practical work of Houssam Barbara

## 22.2 Design and Prototype of a Star Camera (OPAL)



Prototype OPAL. (Image: Jacob Givens)

High spatial and temporal resolution data on temperatures and winds in the thermo-sphere are needed by both the space weather and earth climate modeling communities. To address this need, Space Dynamics Laboratory (SDL) started the Profiling Oxygen Emissions of the Thermosphere (POET) program. POET consists of a series of sensors designed to fly on sounding rockets, CubeSats, or larger platforms, such as IridiumNEXT Sensor-PODS. While each sensor design is different, they all use characteristics of oxygen optical emissions to measure space weather properties.

### Interferogram Simulation

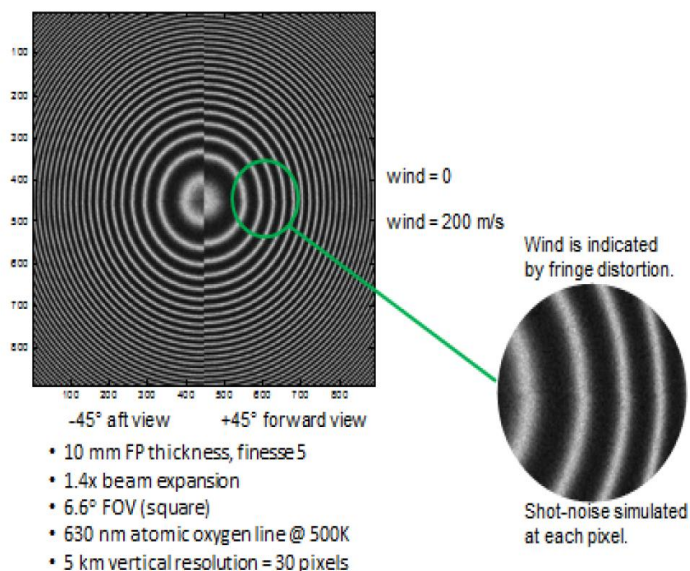


Fig. 2.8: Interferogram simulation.

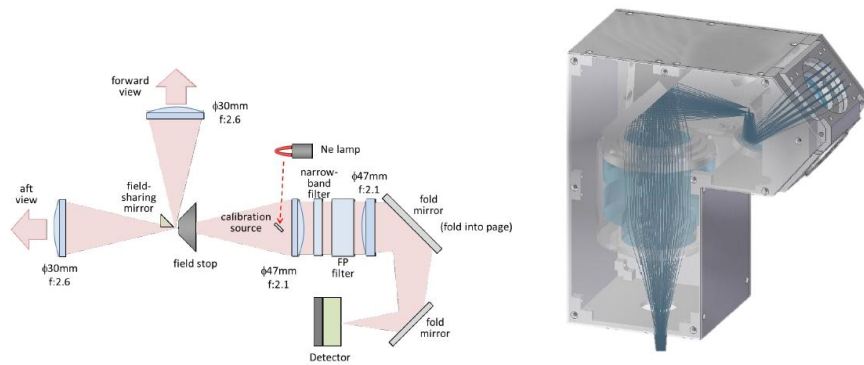


Fig. 2.9: SEDI Optics. Left image is unfolded. Right image shows optics to scale, folded into CubeSat form factor.

paired with a standard CMOS or CCD detector or an electron multiplying charge coupled device (EMCCD). The EMCCD is preferred due to greater sensitivity and reduced noise characteristics. The preferred device is CCD97-00 Back Illuminated 2-Phase Electron Multiplying CCD sensor by e2v Technologies, which is shown in Figure 2.10. A space rated electronics board for this sensor will be custom built by SDL.

### 2.3 Could SEDI Replace OPAL?

It is possible to determine temperature from Doppler broadening of known emission lines. Since SEDI has the sensitivity to measure Doppler shifts, it could also measure Doppler broadening. Unfortunately, the high spectral sensitivity of SEDI requires a large

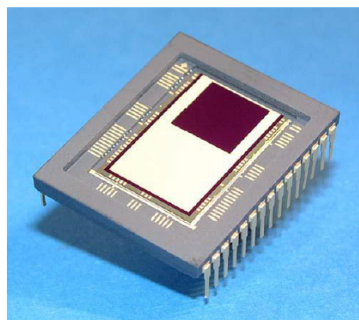


Fig. 2.10: Electron Multiplying Charge Coupled Device (EMCCD) by e2v Technologies.

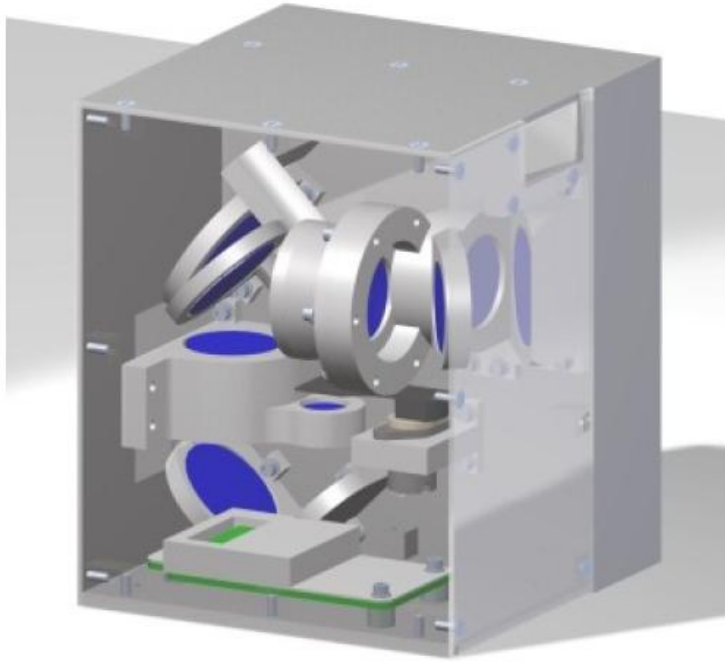


Fig. 2.11: OPAL optics and electronics in a 1-U volume.

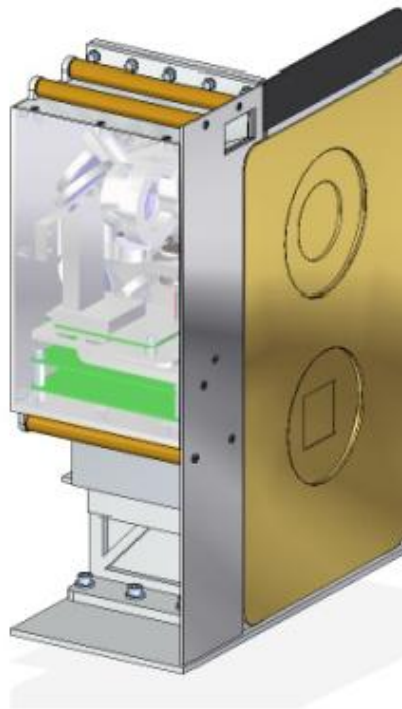


Fig. 2.12: OPAL in a SensorPODS configuration.

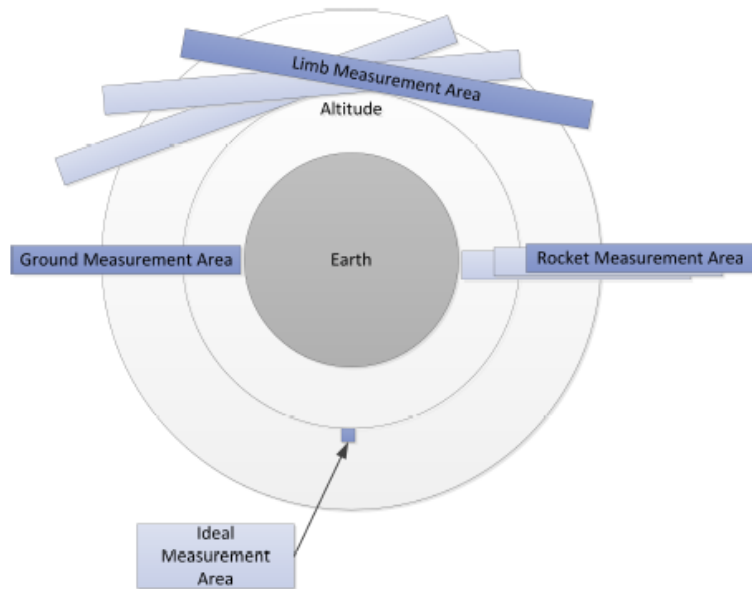


Fig. 2.13: Measurement areas from different platforms.

constellation will provide spatial and temporal resolution never before possible at a cost consistent with NASA Edison or similar programs. OPAL will operate from a 3U CubeSat platform shown in Figure 2.14.

## Chemical Propulsion Unit

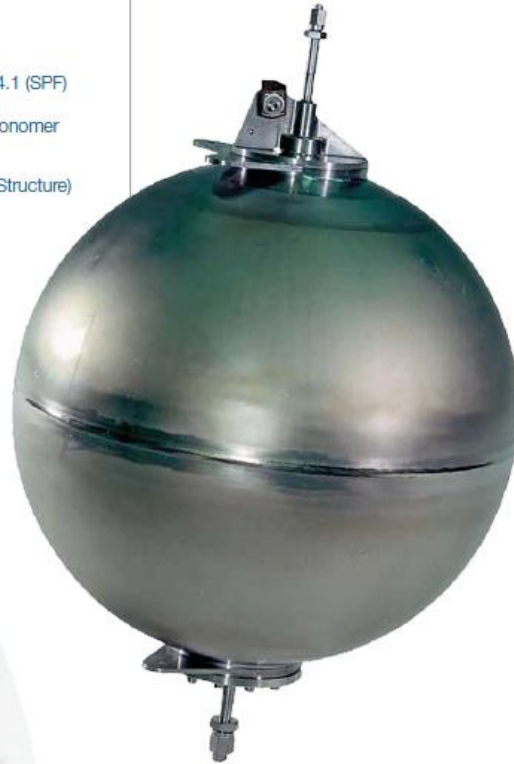


## 23.1.1 Space Propulsion Tanks

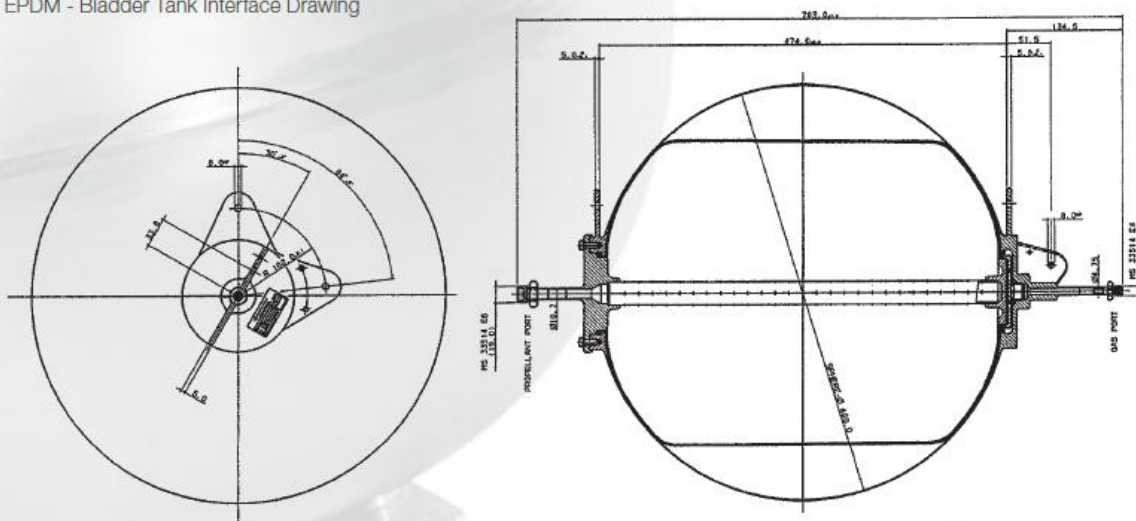
## EPDM - BLADDER TANK BT 01/0

## EPDM - Bladder Tank BT 01/0

Tank Net Volume	58 Litres
Max. Propellant Volume	39 Litres
Propellant	Hydrazine ( $N_2H_4$ )
Pressurant Gas	Helium (He) or Nitrogen ( $N_2$ )
Maximum Expected Operating Pressure (MEOP)	26 bar
Proof Pressure (1.5 x MEOP)	39 bar
Burst Pressure (2.0 x MEOP)	52 bar
Interface Fixation	5 Fixation Holes $\phi$ 8H7
Materials	
- Pressure Vessel	Ti6Al4V Hemispheres 3.7164.1 (SPF)
- Gas & Propellant Ports	Ti6Al4V (3.7164.1)
- Bladder	Ethylene-Propylene-Diene Monomer (EPDM)
Tank Mass	< 8.5 kg (exclusive Support Structure)
Project Application	Ariane 5 SCA, ARD

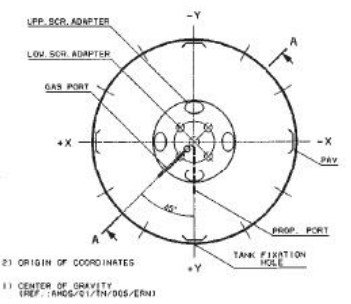
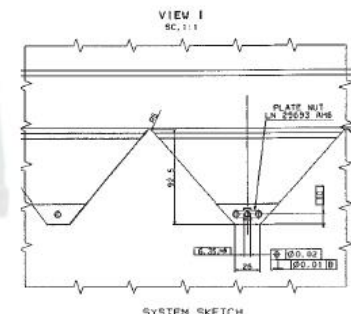
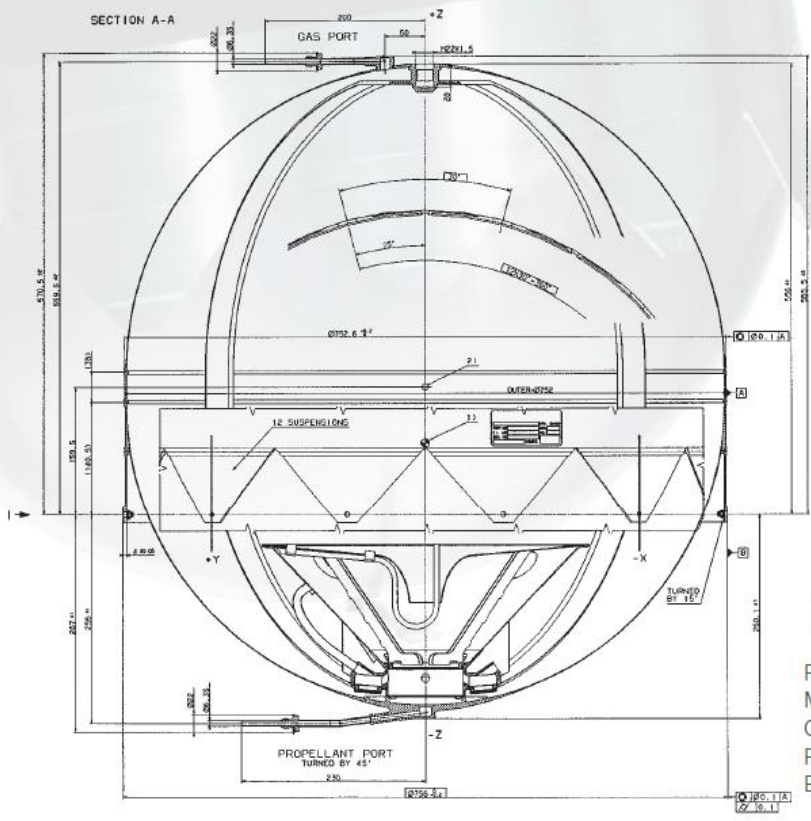


EPDM - Bladder Tank Interface Drawing



# SURFACE TENSION PROPELLANT TANK OST 21/0

Surface Tension Propellant Tank OST 21/0	
Tank Net Volume	235 Litres
Propellants	MON respectively MMH
Geometrical Shape	Spherical with a cylindrical intersection
Interface Fixation	12 Suspension Tabs with floating nuts M6 x 1 (e.g.)
<b>Materials</b>	
- Pressure Vessel	Ti6Al4V STA (3.7164.7)
- Suspension/Ports	Ti6Al4V (3.7164.1)
- PMD	Ti99.4 (3.7034.1) and Ti6Al4V (3.7164.1)
- Screens	304L (1.4306); qualified also for Ti99.4 (3.7025.1)
Tank Mass	16 kg
Project Involvement	Amos



Pressurant Gas: Helium (He) or Nitrogen (N<sub>2</sub>)  
 Maximum Expected  
 Operating Pressure (MEOP): 22.0 bar  
 Proof Pressure (1.5 x MEOP): 33.0 bar  
 Burst Pressure (2.0 x MEOP): 44.0 bar

### 23.1.2 Space Propulsion Valves

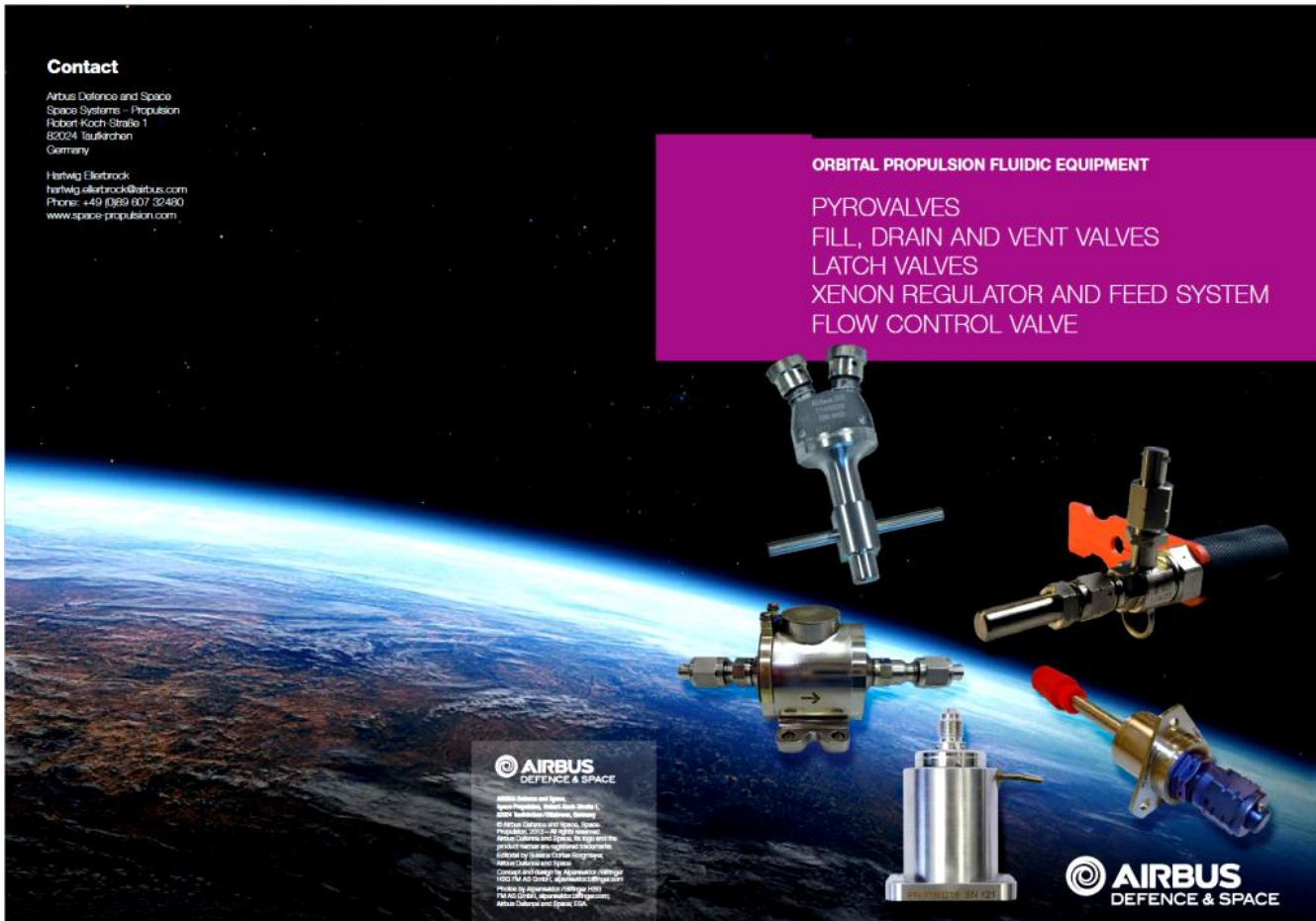
**Contact**

Airbus Defence and Space  
 Space Systems - Propulsion  
 Robert Koch Straße 1  
 82024 Taufkirchen  
 Germany

Hartwig Ellertbrock  
 hartwig.ellertbrock@airbus.com  
 Phone: +49 (0)89 807 32490  
 www.space-propulsion.com

**ORBITAL PROPULSION FLUIDIC EQUIPMENT**

PYROVALVES  
 FILL, DRAIN AND VENT VALVES  
 LATCH VALVES  
 XENON REGULATOR AND FEED SYSTEM  
 FLOW CONTROL VALVE



**AIRBUS**  
DEFENCE & SPACE

Airbus Defence and Space, Space Systems, Robert Koch Straße 1, 82024 Taufkirchen, Germany. © Airbus Defence and Space, Space Systems, 2012. All rights reserved. Airbus Defence and Space, its agents and product names are registered trademarks owned by Airbus Defence and Space. Control and design by Airbus Defence and Space. Airbus Defence and Space, USA.

**AIRBUS**  
DEFENCE & SPACE

To assure the highest possible quality, reliability and performance of our spacecraft propulsion systems and thrusters, Airbus Defence and Space designs, develops and produces its own valves for the control of propellants and pressurants. These space qualified valves, proven over again in major international programs, are available separately or as part of a complete propulsion system.

The range of valves available include:

- Pyrovalves
- Fill, Drain and Vent Valves
- Latch Valves
- Xenon Regulator Feed System
- Flow Control Valve

**ORBITAL PROPULSION FLUIDIC EQUIPMENT**



Pyrovalve



Fill and Drain Valve



Ground Halt Coupling



Latch Valve



Xenon Regulator Feed System (XRFS)



Flow Control Valve

## PYROTECHNICAL VALVES

Pyrovalves are widely used on spacecrafts and launchers where reliable one shot devices are needed for permanent opening or closing of a fluid circuit. Due to its excellent leak tightness capability prior to and after firing in combination with its low mass and low complexity, the pyrovalve presents state of the art propulsion system equipment suitable to fulfil the various mission needs.

Airbus Defence and Space offers a family of Normally Closed (NC) and Normally Open (NO) Pyrotechnical Valves with various different interlocks in order to fulfil the specific customer needs. The available product portfolio covers screwed as well as weldable interfaces (1/4" and 3/8"). All valve types are provided with redundant ESA standard initiators (square) which provides the energy needed for actuation.

The main function of the Pyrotechnical Valve is to definitively shut down or open a fluid circuit. Furthermore, as part of the propulsion subsystem they must ensure a minimal pressure drop as well as perfect external and internal leak tightness prior to and after actuation. The latter is achieved by an all welded design in combination with a flexible titanium membrane, which physically separates the combustion chamber from the hydraulic flow section. This membrane ensures a perfect pressure tightness between the pyrotechnic chambers and the fluid circuits before, during and after the actuation.

The Pyrotechnical Valve provides a highly reliable, fast acting, zero liquid leakage compact design at low equipment mass. Only a small pulse of electrical power is required for valve actuation.



Pyrovalve Key Technical Characteristics	
<b>Initiators</b>	Redundant ESA Standard Initiators
<b>Design</b>	All-welded Titanium design
<b>Fluid Compatibility</b>	Helium, Argon, Xenon, Nitrogen, MON, MMH, Hydrazine, Deionized Water, IPA
<b>Response Time (Mechanical)</b>	< 7ms
<b>Mass</b>	< 0.160 kg (depending on type)
<b>Qualified Operating Temperature</b>	-90°C < T < 100°C
<b>Qualified Operating Pressure (MEOP)</b>	310 bar
<b>Proof Pressure</b>	1.5 x MEOP (465 bar)
<b>Burst Pressure (NO and NC)</b>	
<b>Pre firing</b>	> 4x MEOP (rupture pressure: > 1240 bar)
<b>Post firing</b>	> 2.5x MEOP (rupture pressure: > 775 bar)
<b>Leakage</b>	
<b>Normally Open</b>	Internal leak after firing: < 1x10 <sup>-4</sup> scc/s (G-ke) External leak before/after firing: < 1x10 <sup>-4</sup> scc/s (G-ke)
<b>Normally Closed</b>	Internal leak before firing: < 1x10 <sup>-4</sup> scc/s (G-ke) External leak before/after firing: < 1x10 <sup>-4</sup> scc/s (G-ke)

## Pyrovalve Heritage and Future Missions

The heritage of Airbus Defence and Space regarding Pyrotechnical Valves goes back to 1984, when the 1st generation has been developed by Aerospatial Les Mureaux with support from ESA. Following successful qualification in 1987, the first generation of Pyrovalves was produced until the year 2000. In 1999 a harmonisation and improvement of the first Pyrovalve generation was introduced and successfully qualified in 2001. Following 2 years of production all Pyrovalve activities were transferred from Airbus DS Les Mureaux to Airbus DS Lampoldshausen in 2004. The transfer was finished in 2006 with a successfully performed First Article validation program.

As of today, Airbus DS has delivered more than 600 NC and more than 600 NO Pyrotechnical valves to leading satellite manufacturers. More 500 FM units were already successfully actuated on various spacecrafts without any failure. The production stability is continuously monitored and verified throughout specific Destructive Lot Acceptance Test (DLAT) campaigns. Meanwhile more than 200 units were successfully actuated during extensive DLAT testing including vibration and shock testing, low and high temperature firings as well as under- and overcharge testing. This demonstrates the excellent reliability of the Pyrotechnical Valves manufactured by Airbus DS.

Spacecraft	Launch Year	Spacecraft	Launch Year	Spacecraft	Launch Year
Ariane-5	since 1996	Arabsat 6A	2010	Eutelsat W5A	2012
Arabsat 4B	2006	Arabsat 6B	2010	Eutelsat W6A	2012
Anik F3	2007	COM-5	2010	METOP-B	2012
SkyNet 5B	2007	Aksat 2B	2010	SkyNet 5D	2012
Arabsat 4 AR	2008	Eutelsat W3B	2010	VEGA	2012
Astra 1M	2008	KA-SAT	2010	Yamal 402	2012
ATV FM1	2008	ATV FM 2	2011	ATV FM 4	2013
HotBird 9	2008	Ekspres AM4	2011	Alphasat	2013
Nimiq-4	2008	Arabsat 6C	2011	AMOS 4	2013
SkyNet 5C	2008	SSOT (Myriade)	2011	Astra 2E	2013
Amazonas-2	2009	YAHSAT 1A	2011	GAIA	2013
MILSAT W7	2009	YAHSAT 1B	2011	SES-6	2013
HotBird 10	2009	Astra 1N	2011	ARSAT 1	2014
MILSAT-A	2009	Eisa FM1	2011	Astra 2G	2014
Palapa D	2009	Eisa FM2	2011	Astra 5B	2014
Spirale 1	2009	Eisa FM3	2011	ATV FM5	2014
Sprae 2	2009	Eisa FM4	2011	Arabsat 6B	2015
Thor-6	2009	Atlantic Bird	2011	LISA-PATHfinder	2015
Aksat 2A	2010	Eutelsat W3C	2011	BepiColombo	2016
Nilesat 201	2010	Aptar 7A	2012	ExoMars	2016
RASCOM-2	2010	Astra 2F	2012	METOP-C	2017
MILSAT-B	2010	ATV FM 3	2012		



## FILL AND DRAIN VALVE

Airbus DS offers a wide range of Fill and Drain / Vent valves for spacecraft applications incorporating either two or three inlets against leakage pending on customer demand. Propellant loading / venting valves are designed to provide three independent inlets, while gas type or test port FCVs provide 2 independent ones.

With regard to the selected materials, the propellant type and test port FCVs provide an excellent compatibility with state of the art storable propellants such as MMH / Hydrazine / MON-1 as well as MON-3. Space high pressure gas type FCV are available for operation with Helium (He) and Xenon (Xe). In gases all types are compatible with standard test agents (IPA / HFE 7100 / deionized water) and gases (He, N<sub>2</sub>).

In general six different valves types are available, each providing a different interface to prevent misconnection on spacecraft level. These types differ mainly in thread size and orientation.

The following design attributes and features are common to all six FDV types:

- All piece parts of the valve are machined from titanium alloy (Ti6Al4V) leading to a light weight unit with 0.25 inch / 6.4mm outlet diameter tube stub, which forms a weldable connection to the titanium tubing of the subsystem.

- The interface to the subsystem structure is provided by a triangular flange with triple-screw attachment (thread size M5).

- An all welded housing containing a spring supported guided valve poppet equipped with the primary seal. This ensures that the valve is kept closed in non actuated conditions.

- In flight configuration the valve poppet sealing will be additionally protected and sealed by mounting a cap.

- Low pressure drop over at high mass flows ensured by design. The flow area is at least as large as the connected tubing.

For servicing a dedicated Ground Half Coupling (GHC) has to be mounted. For each FDV type there is a respective GHC permitting only mating of the correct type. By this means a safe and easy to handle, leak-tight connection between the propulsion system and the ground support equipment is guaranteed.

Each GHC provides a robust specific opening / closing mechanism to safely operate the FDV. No specific tooling is required.

## Fill and Drain Valve Heritage and Future Missions

Since their original qualification in 1983, thousands of fill, drain and vent valves have been produced and delivered for a variety of spacecraft programmes including Eutelsat W3A, Amazonas, Intarsat 4 F1, Anik F3, SkyNet 5A, SkyNet 5B, Amos 2, Astra, Star 1, Galaxy 17, Hispasat, MSG-4, Microsats, Herschel/Panck, Planck, Spacabus, Eurostar communication satellites, Mars Express, Venus Express and ESA's Automated Transfer Vehicle. The outstanding flight heritage underlines the excellent reliability of the Airbus DS Fill and Drain / Vent valves.



Ground Half Coupling



Fill and Drain Valve Propellant Loading

Fill & Drain Valves - 2 Failure Tolerant (3 inlets against external leakage)	
<b>Operating Media</b>	Various fluids (Propellants and Pressurants)
<b>Mass</b>	< 0.09 kg
<b>Total Length</b>	100 ± 1 mm
<b>Standard Tube Dimensions</b>	
- outer diameter	6.4 ± 0.02mm
- inner diameter	4.9 ± 0.01mm
- inner diameter (at weld JF)	5.58 ± 0.02mm
<b>Tube Length</b>	43 mm
<b>Adapter Thread</b>	Fuel Loading 9/16" - 18 UNLF - 3A - RH Fuel Venting 7/16" - 20 UNLF - 3A - RH Ox Loading 9/16" - 18 UNLF - 3A - LH Ox Venting 7/16" - 20 UNLF - 3A - LH  Note: All of the above threads require corresponding ground half couplings
<b>MEOP</b>	
- Fuel / Ox Loading / Venting	Up to 33 bar
<b>Burst pressure</b>	1240 bar
<b>Sinusoidal Vibration</b>	Up to 20 g
<b>Random Vibration</b>	Up to 5 g <sup>2</sup> /Hz (56.3g RMS)
<b>Pyrotechnic Shock</b>	Up to 3250 g
<b>All European</b>	Yes



FDV Fuel Venting



Low Pressure Helium Valve



	Fuel Fill Valve	Fuel Vent Valve	High Pressure Helium Valve
<b>Operating Media</b>	Monomethyl Hydrazine (MMH)	Monomethyl Hydrazine (MMH)	Helium (High Pressure)
<b>Mass</b>	< 0.09 kg	< 0.09 kg	< 0.06 kg
<b>Total Length</b>	108.8 ± 1 mm	107.2 ± 1 mm	94.5 ± 1 mm
<b>Standard Tube Dimensions</b>			
- outer diameter	6.4 ± 0.02mm	6.4 ± 0.02 mm	6.4 ± 0.02 mm
- inner diameter	5.58 ± 0.11 mm	5.58 ± 0.02 mm	4.98 ± 0.02 mm
<b>Tube Length</b>	43 mm	43 mm	43 mm
<b>Adapter Thread</b>	9/16" - 18 UNJF - 3A - RH. Requires corresponding ground half coupling	7/16" - 20 UNJF - 3A - RH. Requires corresponding ground half coupling	M 12 x 1.5 - RH. Requires corresponding ground half coupling
<b>Life</b>			
- Operational Life	About 16 years	About 16 years	About 16 years
- Storage Life	Up to 5 years in a protected environment	Up to 5 years in a protected environment	Up to 5 years in a protected environment
<b>Open/Close Cycles</b>	40 Cycles	40 Cycles	40 Cycles
<b>Standard Operating Temp.</b>	-30°C to 80°C	-30°C to 80°C	-30°C to 80°C
<b>Leakage</b>			
- external Leakage	< 1x10 <sup>-4</sup> scc/sec GHe	< 1x10 <sup>-4</sup> scc/sec GHe	< 1x10 <sup>-4</sup> scc/sec GHe
- internal Leakage	< 2.8x10 <sup>-4</sup> scc/sec GHe	< 2.8x10 <sup>-4</sup> scc/sec GHe	< 2.8x10 <sup>-4</sup> scc/sec GHe

Low Pressure Helium Valve	Oxidiser Fill Valve	Oxidiser Vent Valve	High Pressure Xenon Valve
Helium (Low Pressure)	Nitrogen Tetroxide (MON)	Nitrogen Tetroxide (MON)	Xenon (High Pressure)
< 0.06 kg	< 0.09 kg	< 0.09 kg	< 0.06 kg
94.5 ± 1 mm	108.8 ± 1 mm	107.2 ± 1 mm	115 ± 1 mm
6.4 ± 0.02 mm	6.4 ± 0.02 mm	6.4 ± 0.02 mm	6.4 ± 0.02 mm
5.58 ± 0.02 mm	5.58 ± 0.02 mm	5.58 ± 0.02 mm	4.9 ± 0.1 mm
43 mm	43 mm	43 mm	61 mm
7/16" - 20 UNJF - 3A - RH. Requires corresponding ground half coupling	9/16" - 18 UNJF - 3A - LH. Requires corresponding ground half coupling	7/16" - 20 UNJF - 3A - LH. Requires corresponding ground half coupling	M 14 x 1.5 - FH. Requires corresponding ground half coupling
About 16 years	About 16 years	About 16 years	About 16 years
Up to 5 years in a protected environment	Up to 5 years in a protected environment	Up to 5 years in a protected environment	Up to 5 years in a protected environment
40 Cycles	40 Cycles	40 Cycles	40 Cycles
-30°C to 80°C	-30°C to 80°C	-30°C to 80°C	-30°C to 80°C
< 1x10 <sup>-4</sup> scc/sec GHe	< 1x10 <sup>-4</sup> scc/sec GHe	< 1x10 <sup>-4</sup> scc/sec GHe	< 1x10 <sup>-4</sup> scc/sec GHe
< 2.8x10 <sup>-4</sup> scc/sec GHe	< 2.8x10 <sup>-4</sup> scc/sec GHe	< 2.8x10 <sup>-4</sup> scc/sec GHe	< 2.8x10 <sup>-4</sup> scc/sec GHe

## LATCH VALVES

The Airbus DS low pressure latching valve (named hereafter LPLV or LV) is a solenoid-operated, bi-stable valve constructed essentially of stainless steel and qualified to operate with a number of different working media, including hydrazine and its most common derivatives.

The LPLV provided by Airbus DS represents the switchable, fully reliable safety barrier in the propellant flow between tank and thrusters. It is equipped with a back-relief-function protecting the downstream lines and equipment against over-pressure (e.g. due to environmental effects).

For switching 2 electromagnetic coils are to be activated to change the status of the valve to open or closed. Switching can be performed by using a non-regulated supply within a range of 22VDC < 28VDC < 38 VDC. At room temperature the LPLV can be closed or opened within a switch-time of 30ms while the cycle-time is defined to 50ms.

A microswitch is installed for position indication, activated by a pin, which is directly mounted on the LPLV-anchor.

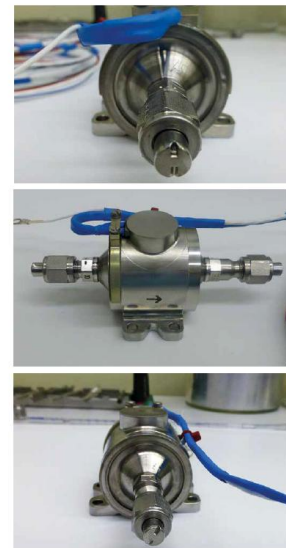
The variant with welded interface is identical to the screwed-interface one except for the tubing connection.

Latch Valve Technical Characteristics		
Characteristics	Nominal Value	Remarks
<b>Tubing Interface</b>	1/4 inch	Screwed or welded versions available
<b>Mass</b>	545 g	
<b>Operating voltage</b>	22-32 VDC	Up to 50VDC for 50ms switching pulses
<b>Response time</b>	< 30 ms	Opening and Closing;
<b>Coil resistance</b>	37,5 Ω ± 1,5 Ω	At ambient temperature
<b>Max.operating pressure</b>	24,25 bar	Specified value; higher values possible
<b>Back-Relief Pressure</b>	8 to 14 bar	
<b>Flow Rate and Pressure Drop</b>	< 0.15 bar at 4.5 g/s	Flow rates up to > 20g/s usable
<b>Fluid Compatibility</b>	Water, hydrazine, MMH, NTO, IPA, He, N <sub>2</sub> , Xe and others	
<b>Opening/Closing cycles</b>	> 500	
<b>Operating Temperature</b>	9° C to 50° C for use with hydrazine	
<b>Electrical connection</b>	Flying leads AWG26, 2m long	
<b>Leakage</b>		
- external Leakage	< 10 <sup>-4</sup> scc/s	
- internal Leakage	< 5 scc/h GHe	



## Latch Valve Heritage and Future Missions

Spacecraft	Launch Year
Glottio	1984
Hipparcos	1986
Meteosat	1986-88
DFS	1987
Eureca	1990
HAPS	1990
ISO	1992
SOHO	1995
Galileo IOC	2010-14
Pilades	2011-13
Spot 6	2012
Sentinel-1A	2014
Kazakhstan Gharysh Sapary	2014
Spot 7	2014
Sentinel-2A	2015
Saosat-ingenio	2015
CSO	2016
Sentinel-1B	2016
Sentinel-2B	2016
Sentinel-5 Precursor	2016



## XENON REGULATOR FEED SYSTEM (XRFS)

The XRFS is a bang-bang pressure regulator. It uses a system of valves, plenum volume, pressure transducers and flow restrictors to down regulate the high pressure of the xenon propellant and/or which it is stored in the Xenon Storage Tank to the supply pressure required by the Xenon Flow Controller (XFC).

The main components of the XRFS are:

- The inlet filter protects the XRFS and the thruster modules downstream from any anomalous particles contamination which could degrade the performance of the XRFS and the thruster modules
- The base plate supports all the components and the brackets
- The pipeworks feed the gas
- The valve block at the base of the plenum is equipped with normally closed solenoid valves

- The valves are arranged in 2 parallel redundant branches. Each branch a serial arrangement of 3 isolated and regulating solenoid valves is capable of fulfilling the mission requirements
- The inserted flow restrictors limit the plenum filling rate
- The plenum volume which is sized in order to ensure the beginning of life valve 'open' times limits the number of regulator valve cycles required by the system mission life
- The two high pressure and four low-pressure transducers (TAF) monitor the inlet and outlet pressure
- Thermal hardware. Electronic circuits with thermostats measure the XRFS temperature. Heaters and thermostats ensure the maintaining of a minimum hardware temperature of +27 °C

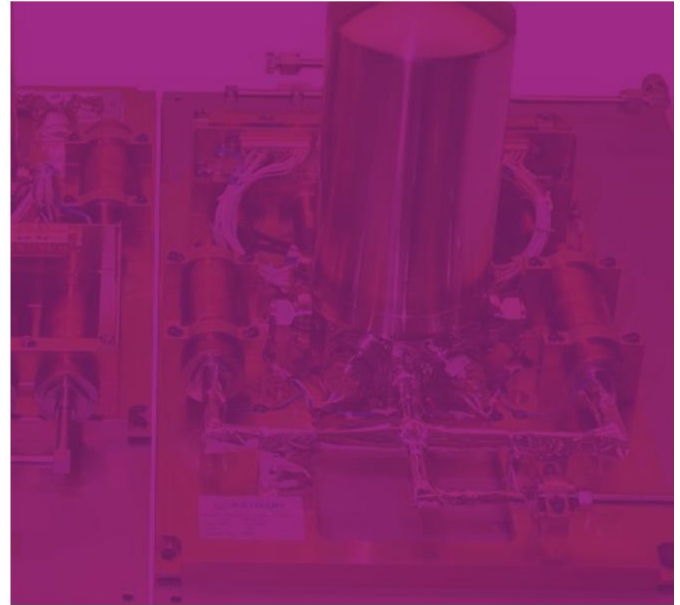
The XRFS provides a high degree of redundancy (series and parallel) and failure tolerance, to ensure the reliability and function during the whole mission.

### XRFS Heritage and Future Missions

Project	Launch Year
INMARSAT 4 FPM	2005
INMARSAT 4 FM2	2005
INMARSAT 4 FM3	2008
KASAT	2010
YASAT 1A	2011
YASAT 1B	2012
DIRECT TV 15	2015
SES 10	2016
SkyBrazil-1	2016



XRFS Key Technical Characteristics	
Regulator Type	"Bang-bang" type regulator (pulsing valves) with two parallel redundant regulation branches, each branch being twice redundant.
Flow Control	The maximum possible flow rate is limited by upstream pressure and smallest diameter in the system's flow path. The actual flow is controlled by regulation of the pressure within the plenum.
Inlet Pressure	3 to 120 bar
Outlet Pressure	2.65 bar ± 0.2 bar
Leakage	- external Leakage < 1x10 <sup>-6</sup> scc/s GHe - internal Leakage < 2x10 <sup>-6</sup> scc/s GHe
Flow Rate	> 6 mg/s gaseous xenon
Flow Restrictor	48900 Lohms
Total propellant throughput	300 kg max
Mass	< 5.9 kg
Dimensions	443.5 mm x 278 mm x 228 mm (plenum)
Temperature Range	27 °C to 45 °C (operating)
Design Life	15 years
Cycle Life	1.000.000 qualified
Reliability	> 0.998
Mechanical Interface	1/4" diameter titanium pipes (T3A2.5V)
Electrical Interface	D-Sub Connectors

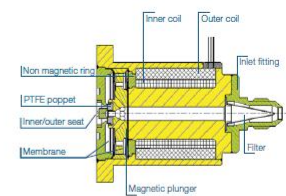
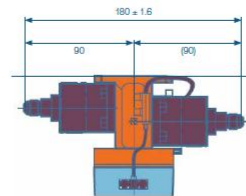


## 400N APOGEE ENGINE FLOW CONTROL VALVE

The 400N flow control valve is an electromagnetic controlled, normally closed valve with a non sliding fit suspended armature design and has redundant electric coils. The moving part, called magnetic plunger, is actuated with the magnetic force induced by the coil when supplied by direct current voltage.

With no voltage applied, the magnetic plunger returns to closed position thanks to the two preloaded membrane springs. The spring preload compresses the PTFE poppet on the metallic seats and enables to meet the required tightness level. After energizing of the coil, the valve opens and the flow passes through an annular gap. At the inlet of the valve a 40µm filter is located to protect the PTFE seat for any pollution.

More than 100 units were successfully build and more than 80 successfully used on Airbus DS 400N engine in orbit.



400N Apogee Engine Flow Control Valve (FCV) Key Technical Characteristics		
Valve type		Dual-coil-solenoid monostable bipropellant engine valve (Normally-Closed), non sliding fit
Operating Voltage per Coil	VDC	21 to 27
Coil resistance	Ohms	20 ± 1 at 21°C
Power dissipation	Watt	38.4 at 27 VDC
Response time (20°C)	ms	< 30
Pull-in	VDC	< 18,3
Drop-out	VDC	> 1.5, < 5
Holding Voltage per Coil	VDC	> 7.5
Max inlet pressure (operational domain)	bar	34
Burst pressure	bar	88
Flow Rate / Pressure Drop		max 1.1 bar at 70 g/s H2O
Compatible Media		NTO, MMH, water
Seat material		PTFE
Other materials in contact with media		AISI 430, AISI 347, Incoloy
Leakage		
- external Leakage	scc/s	< 1x10E-6
- internal Leakage	scc/s	< 5x10E-4
Electrical connection		AWG24 flying leads acc. ESA ECSS 3901.002 1.7m (4 single wires)
Media inlet connector		AN4 7/16 - 20 UNJF - 3A
Inlet filter		Mash type, stainless steel, <40µm
Temperatures		
Operating	°C	0°C to 115°C
Acceptance	°C	-5°C to 120°C
Qualification	°C	-10°C to 125°C
Number of open/close cycles		5000
Life time	years	16



## 23.2 Instruments for Test Environment for Chemical Propulsion Unit:

The main element that will be used for the propulsion unit are tanks, valves, filters and gauges. With the necessary controlling board and electric elements.

### 23.2.1 Types of Valves

The type of disk will decide the type of valve. Most common types of Check valves are

- Swing Type.
  - Top Hinged
  - Tilting disk
- Lift Type
  - Piston Type
  - Ball type
- Dual Plate Type
- Stop Check Valve

#### 23.2.1.1 Check Valve<sup>23</sup>

The valve that used to prevent backflow in a piping system is known as a check valve. It is also known as a non-return valve or NRV. The pressure of the fluid passing through a pipeline opens the valve, while any reversal of flow will close the valve. It allows full unobstructed flow and automatically shuts as pressure decreases. The exact operation will vary depending on the mechanism of the valve.

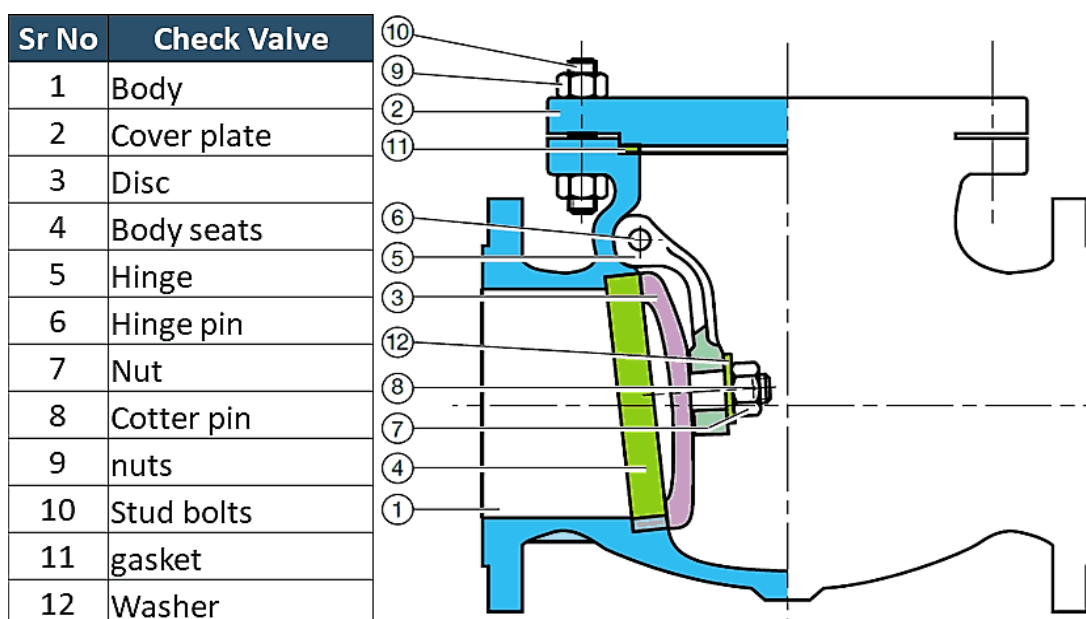


Figure 23-1: Schematic and description of Check Valve

#### 23.2.1.2 Tank Vent Valve<sup>24</sup>

Prevents vapors from the tank from escaping into the atmosphere. Once the pressure build to a certain level the vent will allow the escape of some vapor to sustain the desired pressure

<sup>23</sup> <https://hardhatengineer.com/what-is-check-valves-types-parts/>

<sup>24</sup> <https://www.samarins.com/glossary/vent-valve.html>



Figure 23-2: Tank Vent Valve

### 23.2.1.3 High Pressure Gas Valve<sup>25</sup>

There are five main types of high pressure gas valves.

- a) **Relief:** Fluid power systems operate within a preset pressure range. This range is a function of the forces the system must generate to do the required work; if these forces are not controlled or limited, they can cause damage to the (sometimes extremely) expensive equipment and fluid power components. Relief valves act as the safeguards which limit maximum pressure by diverting excess oil when the pressures get too high.
- b) **Reducing:** Reducing valves are the most practical components when it comes to maintaining secondary, lower pressure in a hydraulic system. They're the only high pressure valve on this list that remains open and close when subjected to sufficient downstream pressure. They come in two types: direct acting and pilot operated.
- c) **Sequence:** Some circuits have more than one actuator, so it's necessary to drive these actuators (such as cylinders) in a specific order or sequence. Limit switches, timers, and other electrical control devices are used for this purpose.
- d) **Counterbalance:** These high pressure valves are primarily used to set pressure in part of a circuit, usually to counterbalance a weight or external force. The valve's main port is connected to the cylinder's rod end, and the pressure setting is slightly higher than that required to keep the load from free-falling.
- e) **Unloading:** Unsurprisingly, unloading valves are used to unload pumps. They direct pump output flow (which is usually the output of one pump in a multi-pump system) directly to a reservoir at low pressure once system pressure has been reached. When an external pilot signal acting on the opposite end of the valve spool exerts a force large enough to exceed that exerted by the spring, the valve spool shifts and diverts pump outflow to the reservoir.

### 23.2.1.4 Gas Bleed Valve:

A bleed valve for bleeding air from a compressor at start-up of a gas turbine engine is self-actuated. The bleed valve moves between open and closed positions based on the pressure within a compressor. The bleed valve is driven to an open position at low pressure conditions and to a closed position once the pressure within the compressor chamber becomes higher and closer to operating pressures. So we can say its normal open valve and tend to close when turbine start up.

<sup>25</sup> <https://www.tigervalve.com/how-do-high-pressure-hydraulic-valves-work>

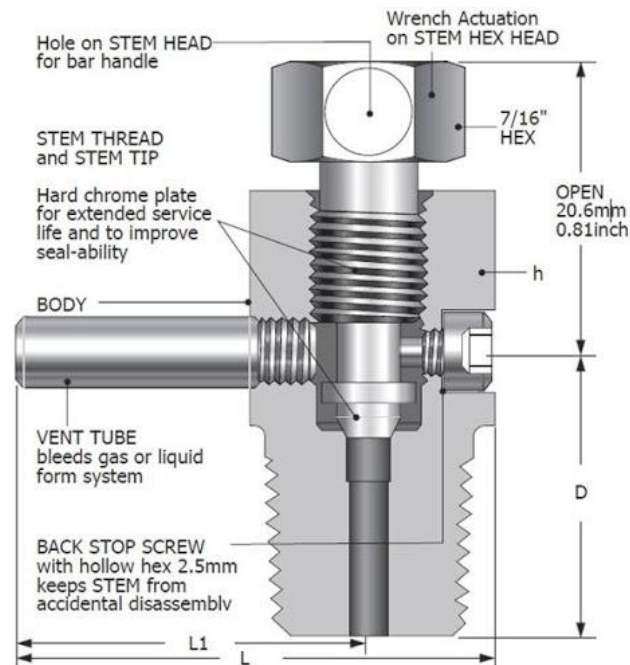


Figure 23-3: Bleed valve used to add or remove liquid from gases or vice versa

### 23.2.1.5 Drain Valve<sup>26</sup>

A drain valve is a mechanical device used to release excess or unwanted quantities of liquid or gas from a storage tank, vessel or container. The valve is usually opened by turning a screw or handle, although some drain valves are automatically opened when a set pressure or temperature is reached. When the valve is opened, liquid or air drains from the storage tank due to gravity or pressure differential.



Figure 23-4: Drain valve

### 23.2.2 Pressure Regulator

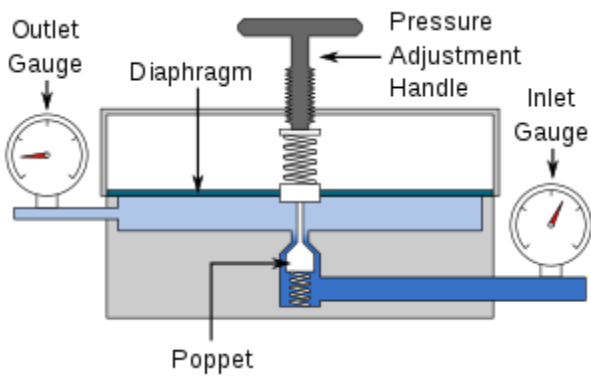
A **pressure regulator** is a control [valve](#) that reduces the input pressure of a fluid to a desired value at its output. Regulators are used for gases and liquids, and can be an integral device with an output

<sup>26</sup> <https://www.wisegeek.com/what-is-a-drain-valve.htm>

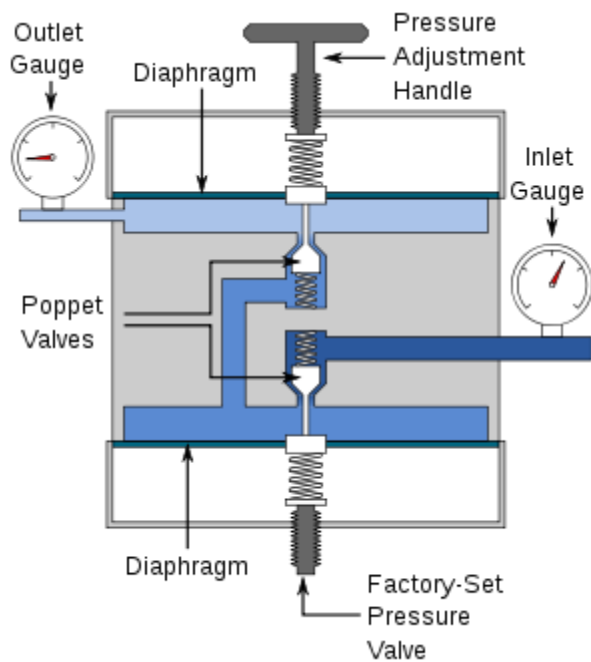
pressure setting, a restrictor and a sensor all in the one body, or consist of a separate pressure sensor, controller and flow valve.



Oxygen and MAPP gas cylinders with two-stage pressure regulators



Single-stage pressure regulator



Two-stage pressure regulator



### 23.2.3 Restricting Orifice<sup>27</sup>

A Restrictive Flow Orifice (RFO) is a type of orifice plate. They are used to limit the potential danger, damage, or wastage of an uncontrolled flow from, for example, a compressed gas cylinder. They are generally not limiting the flow during normal operation but if a fault or failure occurs causing uncontrolled flow the orifice will present a restriction, limiting the flow. The area of the orifice determines the rate of flow at the outlet of a given process fluid for the specified pressure and temperature. For safety a restriction orifices must be inserted into the pipeline when a reduction of pressure or a limitation of the flow rate is required.

---

<sup>27</sup> [https://en.wikipedia.org/wiki/Restrictive\\_flow\\_orifice](https://en.wikipedia.org/wiki/Restrictive_flow_orifice)

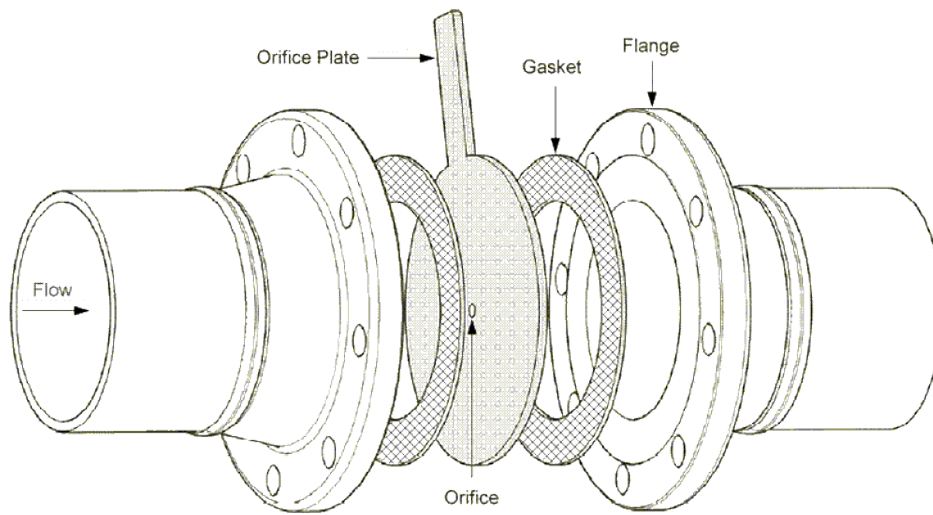


**Figure 23-5: Schematic of a single stage restriction orifice**

Orifice plate is a thin plate with an orifice in the middle. It is placed in a pipe where the volumetric flow measurement needs to be done.



**Figure 23-6: Single stage restriction Orifice Plate**

When the fluid flows through the orifice in the plate, fluid velocity changes and according to Bernoulli's equation pressure also changes. By measuring the difference between pressure values immediately before and after the orifice plate, volumetric flow calculation can be done. In case of restriction orifice, the size of the orifice is chosen in order to have desired pressure drop across the restriction orifice. This effect is known as choked flow across the orifice.

As the name suggests, function of a restriction orifice is to restrict the flow and kill pressure downstream of the orifice. The restriction orifice size for given flow and downstream pressure limit can be calculated using [EnggCyclopedia's restriction orifice sizing calculator for gases](#) and [EnggCyclopedia's restriction orifice sizing calculator for liquids](#).

### 23.2.3.1 Single stage multi-hole restriction orifice.

A single stage multi-hole restriction orifice plate is used to abate the noise generated by the device due to high velocity through the bore which offers restriction to the incoming fluid. The flow at the inlet is now channeled into several streams through the multiple holes and this reduces the noise which would be otherwise will be above the acceptable limit if a single hole device is used.



Figure 23-7: Orifice Plate with multi-holes

### 23.2.3.2 Multi-stage restriction orifice plate assembly.

These devices are used where the pressure reduction ratio is very high and cannot be achieved by a single stage orifice plate. Thus a multistage device essentially consists of a number of single stage device built in a single spool. Like a single stage device it can be of single hole multi stage design or multi-hole multi-stage design or combination of both.

The Restriction Orifices are arranged in eccentric manner, diametrically opposite each other during fabrication of MRO.

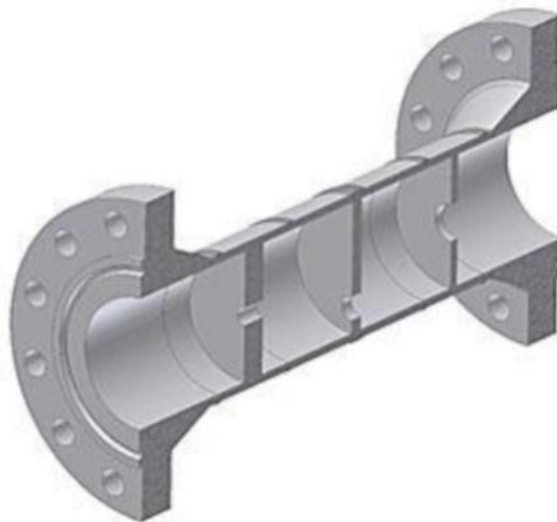
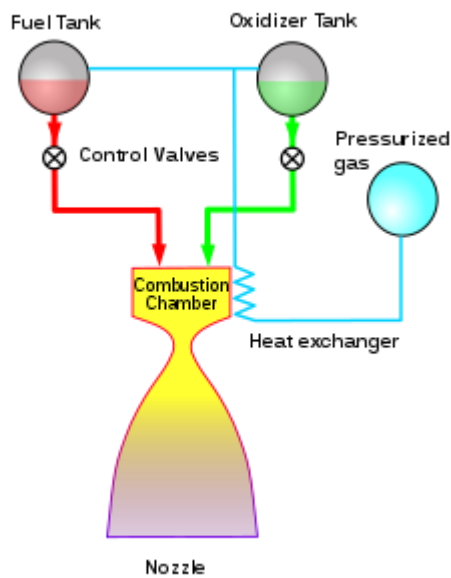


Figure 23-8: Multi-stage restriction orifice plate assembly.

### 23.3 Process for the control of the mixture ratio of fuel and oxidizer for a liquid fuel motor by measuring flows, and control systems for carrying out this process



From:

<https://ntrs.nasa.gov/archive/nasa/casi.ntrs.nasa.gov/19920004056.pdf><https://ntrs.nasa.gov/archive/nasa/casi.ntrs.nasa.gov/19920004056.pdf>

#### OVERVIEW OF ROCKET ENGINE CONTROL

Carl F. Lorenzo and Jeffrey L. Musgrave  
National Aeronautics and Space Administration  
Lewis Research Center MS 77-1  
Cleveland, OH 44135

#### Abstract

This paper broadly covers the issues of Chemical Rocket Engine Control. The basic feedback information and control variables used in expendable and reusable rocket engines, such as the Space Shuttle Main Engine are discussed. The deficiencies of current approaches are considered and a brief introduction to Intelligent Control Systems for rocket engines (and vehicles) is presented.

#### INTRODUCTION

The purpose of this paper is to give a broad overview of Chemical Rocket Engine (CRE) control as background for Nuclear Thermal Rocket Engine control. The paper will discuss the fundamental (underlying) physical issues in CRE control. A brief discussion of modern CREs and their control will follow. This will include a discussion of the Space Shuttle Main Engine (SSME). Recent advanced control approaches for the SSME will be presented along with the benefits which ensue. Current research into Intelligent Control Systems for the SSME which allows high levels of adaptability to engine degradations will be discussed. Finally the connections of current chemical rocket engine controls research to nuclear rocket controls will be explored.

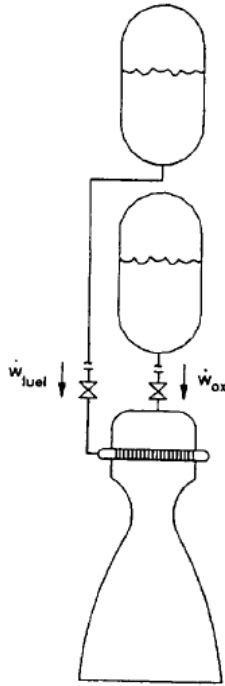
**FUNDAMENTALS OF CHEMICAL ROCKET ENGINE CONTROL**

FIGURE 1. Pressure Fed Bi-Propellant Rocket Engine Schematic.

The fundamentals of CRE control are best explained by starting with a simplified configuration (Figure 1). This pressure fed rocket engine supplies propellants through appropriate feedlines, control valves and injector elements to a main combustion chamber by pressurizing the supply tanks. The chamber requires the propellants to be delivered in a predetermined ratio (mixture ratio), defined as

$$MR = \frac{\dot{w}_{ox}}{\dot{w}_{fuel}} \quad (1)$$

and at a flow rate level related to the desired thrust. The fundamental function of a rocket engine control is to control thrust (inferred by chamber pressure) and the mixture ratio. The mixture ratio is important since for any propellant combination and pressure level, it sets the combustion temperature and hence the performance and the maximum material temperature. It is also important in terms of propellant utilization.

The basic dynamic equations are found in (Lee et al. 1953). The chamber pressure ( $P_c$ ) to total weight flow ( $\dot{w}_T$ ) transfer function is given by

where ( $c^*/A_T g$ ) is a proportionality constant,  $\sigma$  is the combustion delay and  $\tau$  is the chamber fill time ( $\tau \sim c^* A_T V_c / RT_c$ ) where  $c^*$  is the characteristic exhaust velocity,  $A_T$ ,  $T_c$ , and  $V_c$  represent the throat area, combustion temperature, and

$$\frac{P_c(s)}{\dot{w}_T(s)} = \left( \frac{c^*}{A_T g} \right) \left( \frac{e^{-\sigma s}}{\tau s + 1} \right) \quad (2)$$

main chamber volume respectively. In linear form the injectors are flow resistors so that

$$\dot{w}_T(s) = \dot{w}_{fuel}(s) + \dot{w}_{ox}(s) = k_1(P_{t_{fuel}}(s) - P_c(s)) + k_2(P_{t_{ox}}(s) - P_c(s)) \quad (3)$$

where  $P_i$  is the injector pressure. The feedline can be represented in lumped parameter form (continuity and momentum equations) or distributed hyperbolic form (wave equation). In this configuration there are two inputs, namely the valve areas (positions) which control the individual propellant flows and hence the chamber pressure and mixture ratio.

A classical control for this simplified configuration is shown in Figure 2. The following observations are made. Chamber pressure responds to total weight flow. Therefore the chamber pressure flow loop would usually (but not necessarily) go with the propellant having the higher flow rate say  $O_2$  in an  $H_2 - O_2$  engine. Also the two loops tend to be interactive and to minimize excursions of the error signals, one loop is tuned to be the "fast" loop and the other slower. Experience shows that the mixture ratio should be the fast loop. This minimizes excursions in MR away from the set point which in turn keeps the gas and metal temperatures at the design conditions. The chamber pressure is the "slower" loop and its bandwidth is set by thrust response requirements. The type of control shown here would normally require three measurements

$P_c$ ,  $\dot{w}_{fuel}$ , and  $\dot{w}_{ox}$  with two control inputs (valve areas)

$A_{fuel}$  and  $A_{ox}$ . These basic ideas dominate CRE control design for much more complex cycles.

### 23.3.1 Classical Control for Bi-Propellant Rocket Engine

From:

<https://ntrs.nasa.gov/archive/nasa/casi.ntrs.nasa.gov/19920004056.pdf><https://ntrs.nasa.gov/archive/nasa/casi.ntrs.nasa.gov/19920004056.pdf>

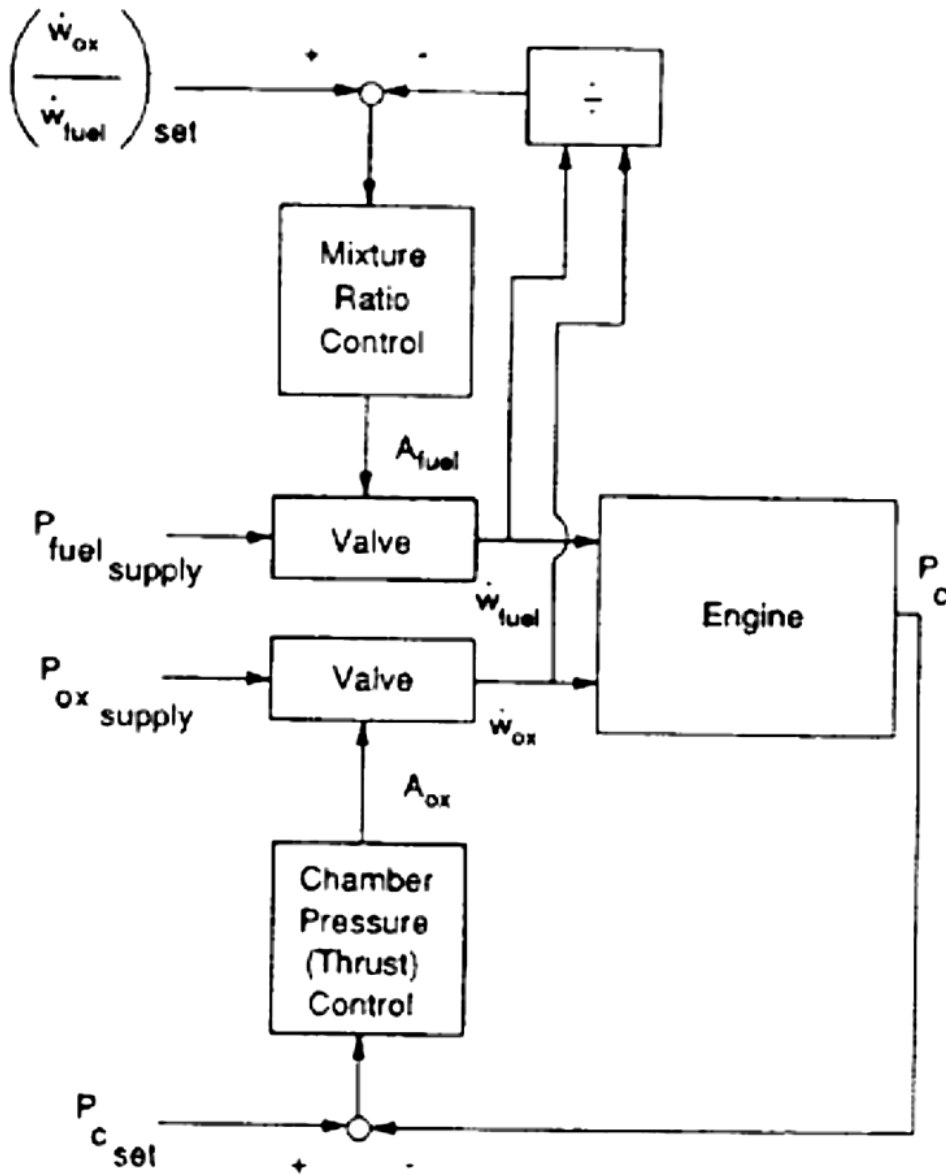


FIGURE 2. Classical Control for Bi-Propellant Rocket Engine.

### 23.3.2 Further Literature

[https://en.wikipedia.org/wiki/Pressure-fed\\_engine](https://en.wikipedia.org/wiki/Pressure-fed_engine)

<https://pdfs.semanticscholar.org/f45b/553398867943f824682ab56af28152dc90d7.pdf>

<https://patents.google.com/patent/US4541238>

[https://en.wikipedia.org/wiki/Air%E2%80%93fuel\\_ratio](https://en.wikipedia.org/wiki/Air%E2%80%93fuel_ratio)

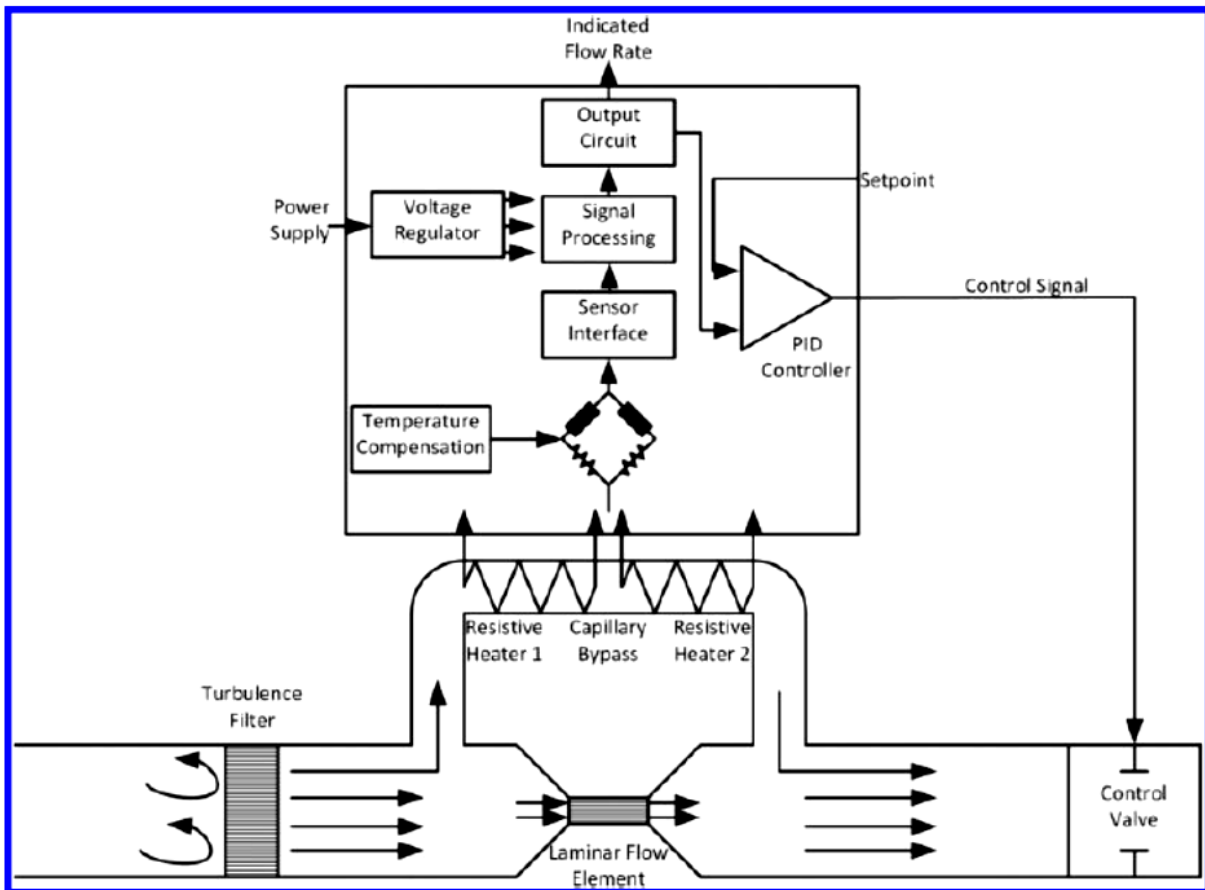


Fig. 1 Diagram of a typical thermal mass flow controller.

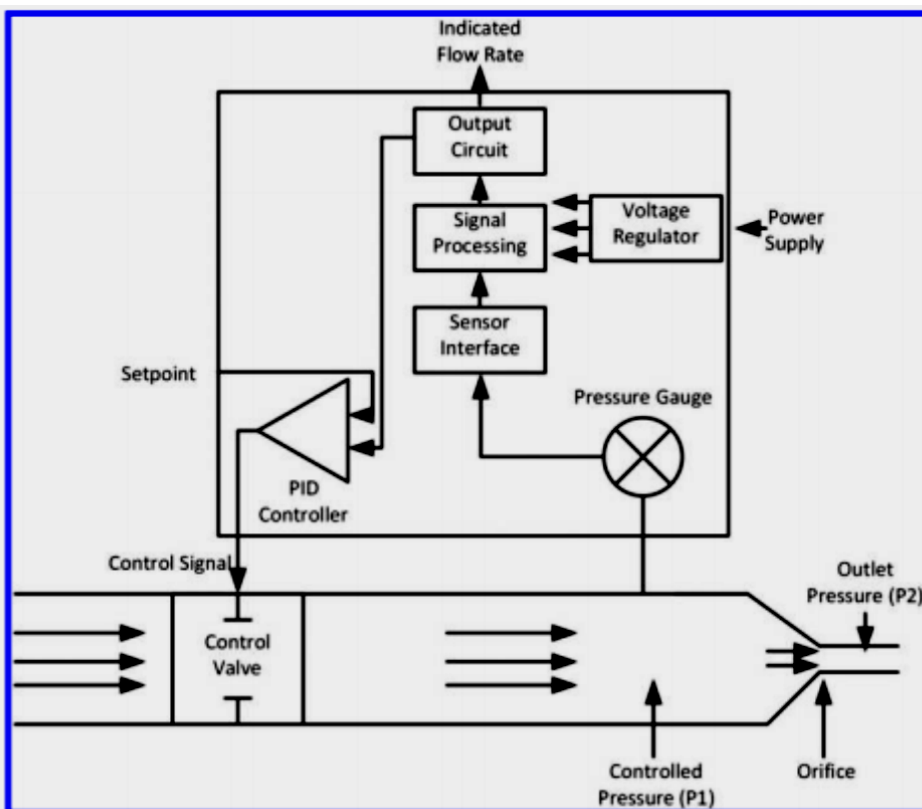


Fig. 3 Diagram of a typical pressure-based mass flow controller.

## 23.4 Combustion of the Oxidizer/Fuel Mixture<sup>2829</sup>

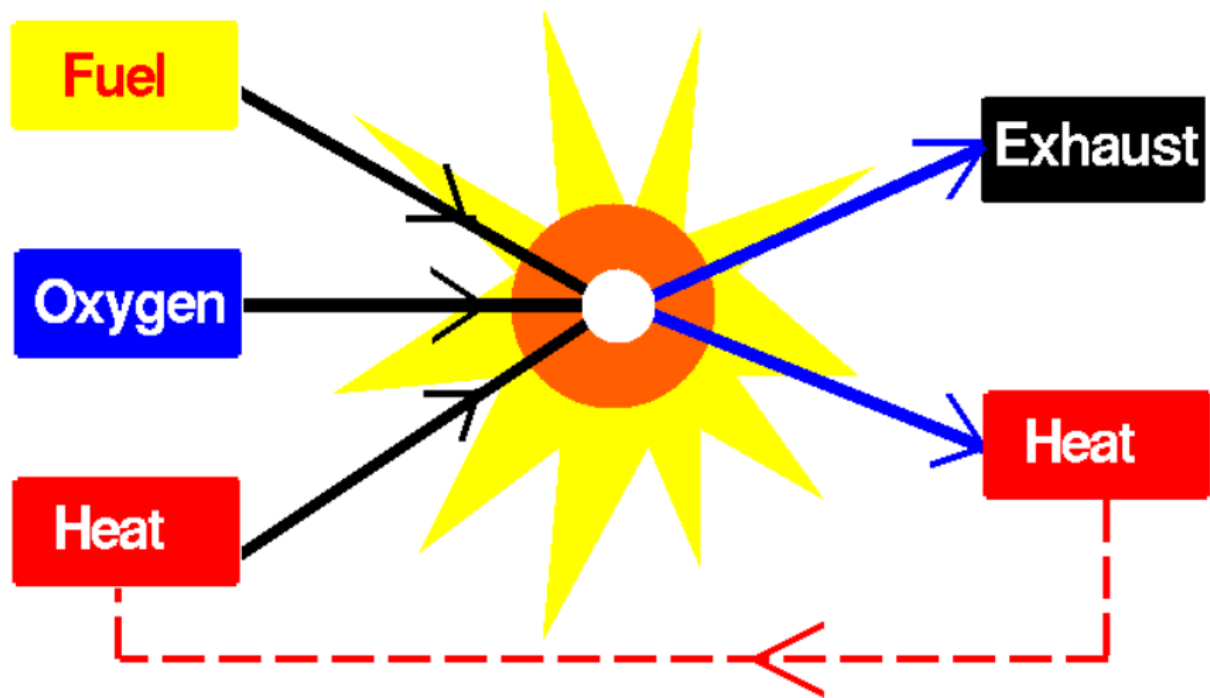
NASA NATIONAL AERONAUTICS AND SPACE ADMINISTRATION

+ Text Only Site  
+ Non-Flash Version  
+ Contact Glenn

FIND IT @ NASA :  + GO

+ ABOUT NASA + NEWS & EVENTS + MULTIMEDIA + MISSIONS + MY NASA + WORK FOR NASA

# Combustion



To launch a [rocket](#) or to move a rocket through space, we must use a [propulsion system](#) to generate [thrust](#). Thrust is generated through an application of Newton's [third law](#) of motion; a working gas is accelerated to the rear of the rocket engine, and the re-action is a thrust force applied to the engine in the forward direction. In [solid](#) and [liquid](#) fueled rocket engines, the working gas is produced through the burning of a fuel to produce power. Burning a fuel is called **combustion**, a chemical process that we study in middle or high school.

<sup>28</sup> <https://www.grc.nasa.gov/WWW/K-12/rocket/combst1.html>

<sup>29</sup> <https://www.grc.nasa.gov/WWW/K-12/rocket/>

Rocket Propulsion Analysis (Standard Edition, evaluation copy - trial version)

File View Run Help

Express Thermodynamic Analysis

Chamber pressure:  atm

System:

Mixture ratio:  O/F mixture mass ratio (oxidizer/fuel)

Oxidizer:						Fuel:									
Species	MF	T	Unit	p	Unit	Species	MF	T	Unit	p	Unit				
O2(L)	1		K		MPa	C2H5...	1		K		MPa				
Sum of all the mass fractions: 1						Sum of all the mass fractions: 1									
Add		Define new		Remove		Normalize		Add		Define new		Remove		Normalize	

Nozzle exit conditions

pressure:  atm

expansion area ratio:  (A<sub>e</sub>/A<sub>t</sub>)

expansion pressure ratio:  (p<sub>c</sub>/p<sub>e</sub>)

Sections are designated as follows: c = combustion chamber, t = nozzle throat, e = nozzle exit.

Engine performance:

Parameter	Sea level	Optimum expansion	Vacuum	Unit
Characteristic velocity		1649.78		m/s
Effective exhaust velocity	2691.08	2691.08	2926.34	m/s
Specific impulse (by mass)	2691.08	2691.08	2926.34	N·s/kg
Specific impulse (by weight)	274.41	274.41	298.40	s
Thrust coefficient	1.6312	1.6312	1.7738	

Propellant mixture ratio O/F<sup>30</sup> [N·s/kg]: 1.3

!! For Fuel: 75% Ethanol and Oxidizer: Liquid Oxygen.

(At P<sub>c</sub>=68 atm – P<sub>e</sub>=1 atm e=exit, c=combustion chamber)

Rockets burn huge amounts of fuel very quickly to reach escape velocity of at least 25,000 mph (7 miles per second or 40,000 km/h).

<sup>30</sup> <http://www.braeunig.us/space/propel.htm>

## ROCKET PROPELLANT PERFORMANCE

Combustion chamber pressure,  $P_c = 68 \text{ atm (1000 PSI)}$  ... Nozzle exit pressure,  $P_e = 1 \text{ atm}$

Oxidizer	Fuel	Hypergolic	Mixture Ratio	Specific Impulse (s, sea level)	Density Impulse (kg-s/l, S.L.)
Liquid Oxygen	Liquid Hydrogen	No	5.00	381	124
	Liquid Methane	No	2.77	299	235
	Ethanol + 25% water	No	1.29	269	264
	Kerosene	No	2.29	289	294
	Hydrazine	No	0.74	303	321
	MMH	No	1.15	300	298
	UDMH	No	1.38	297	286
Liquid Fluorine	50-50	No	1.06	300	300
	Liquid Hydrogen	Yes	6.00	400	155
FLOX-70	Hydrazine	Yes	1.82	338	432
	Kerosene	Yes	3.80	320	385
Nitrogen Tetroxide	Kerosene	No	3.53	267	330
	Hydrazine	Yes	1.08	286	342
	MMH	Yes	1.73	280	325
	UDMH	Yes	2.10	277	316
	50-50	Yes	1.59	280	326
Red-Fuming Nitric Acid (14% $N_2O_4$ )	Kerosene	No	4.42	256	335
	Hydrazine	Yes	1.28	276	341
	MMH	Yes	2.13	269	328
	UDMH	Yes	2.60	266	321
Hydrogen Peroxide (85% concentration)	50-50	Yes	1.94	270	329
	Kerosene	No	7.84	258	324
Nitrous Oxide	Hydrazine	Yes	2.15	269	328
	HTPB (solid)	No	6.48	248	290
Chlorine Pentafluoride	Hydrazine	Yes	2.12	297	439
Ammonium Perchlorate (solid)	Aluminum + HTPB (a)	No	2.12	277	474
	Aluminum + PBAN (b)	No	2.33	277	476



## 24 Construction of Test Rig for Chemical Propulsion Unit

### 24.1 Schematic Flow Diagram

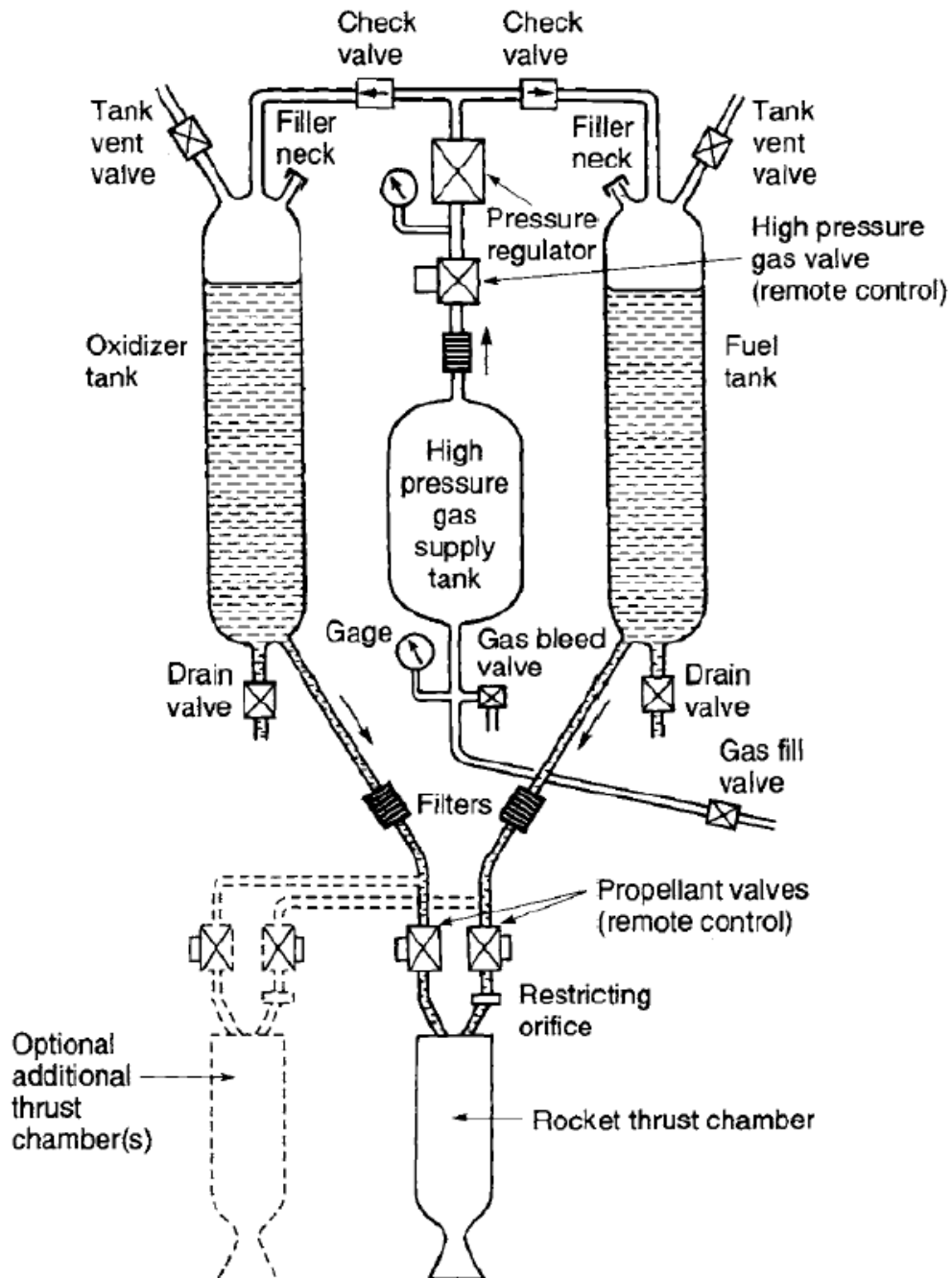


Figure 24-1: Schematic Flow Diagram of a liquid propellant rocket engine with a gas pressure feed system. The dashed lines show a second thrust chamber, but some engines have more than a dozen thrust chambers supplies by the same feed system, also shown are components needed for start and stop, controlling tank pressure, filling propellants and pressurizing gas, draining or flashing out remaining propellant, tanks pressure relief or venting, and several sensors.

## 24.2 Specification

### CHEMICAL ORBITAL PROPULSION MODULE

**Chemical Orbital Propulsion Module for transfer orbit, attitude maneuver during transfer orbit, station keeping and deorbiting.**

Commercial telecommunication satellites and institutional missions that rely on bigger platforms fly with Airbus Defence and Space b-propellant subsystems and components. Our customers worldwide rely on an impressive heritage and success rate. Airbus Defence and Space orbital propulsion modules are used for transfer orbit, attitude maneuver during transfer orbit, station keeping and deorbiting.

**Main Subsystems and Components:**

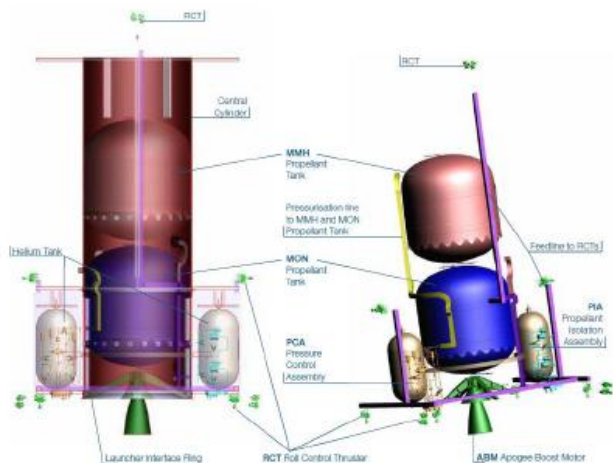
**Propulsion System**

- Fuel Tank (700L – 1450L)
- Oxidizer Tank (700L – 1450L)
- 10N Thrusters – RCT
- 400N Apogee Boost Motor
- Pressure Control Assembly – PCA
- Propellant Isolation Assembly – PIA
- Helium Tank 5L – 90L
- Pyrovalves
- Fill and Drain Valves
- Pressure Regulator
- Pressure Transducer

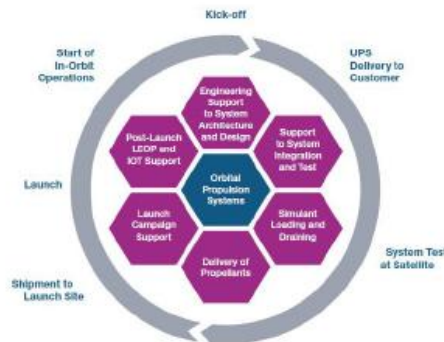
Central Cylinder with Launcher Interface Ring  
Propulsion Thermal Control

**Key Features**

- Reduced interface management
- Modular design
- Advantageous symmetry
- Fully integrated subassembly
- Multiple spare provision equipment
- Provision of complete services around propulsion

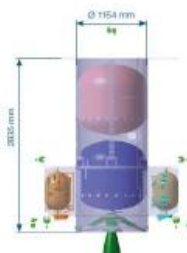


Airbus Defence and Space provides the complete range of services around the Unified Propulsion System (UPS), from engineering support for system architecture and design up to propellant loading and Launch Early Operations Phase (LEOP)



**Bi-propellant UPS B2**

Propellant Loading Mass: 1695 kg



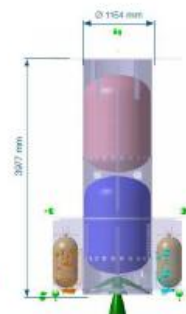
**Bi-propellant UPS B3**

Propellant Loading Mass: 2441 kg



**Bi-propellant UPS C3**

Propellant Loading Mass: 3194 kg



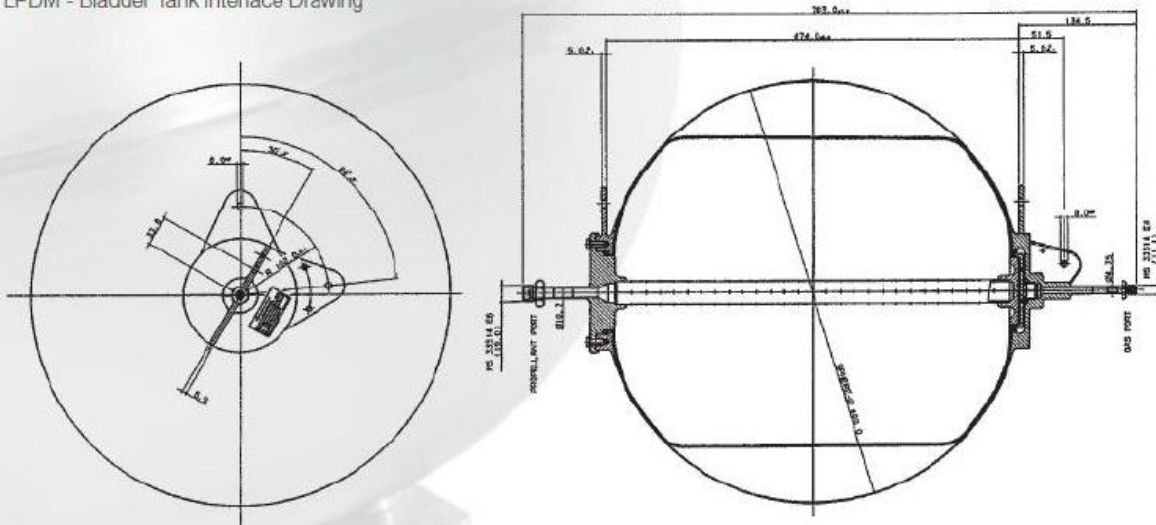
## EPDM - BLADDER TANK BT 01/0

### EPDM - Bladder Tank BT 01/0

Tank Net Volume	58 Litres
Max. Propellant Volume	39 Litres
Propellant	Hydrazine (N <sub>2</sub> H <sub>4</sub> )
Pressurant Gas	Helium (He) or Nitrogen (N <sub>2</sub> )
Maximum Expected Operating Pressure (MEOP)	26 bar
Proof Pressure (1.5 x MEOP)	39 bar
Burst Pressure (2.0 x MEOP)	52 bar
Interface Fixation	5 Fixation Holes ø 8H7
Materials	Ti6Al4V Hemispheres 3.7164.1 (SPF) Ti6Al4V (3.7164.1) Ethylene-Propylene-Diene Monomer (EPDM)
Tank Mass	< 8.5 kg (exclusive Support Structure)
Project Application	Ariane 5 SCA, ARD



EPDM - Bladder Tank Interface Drawing

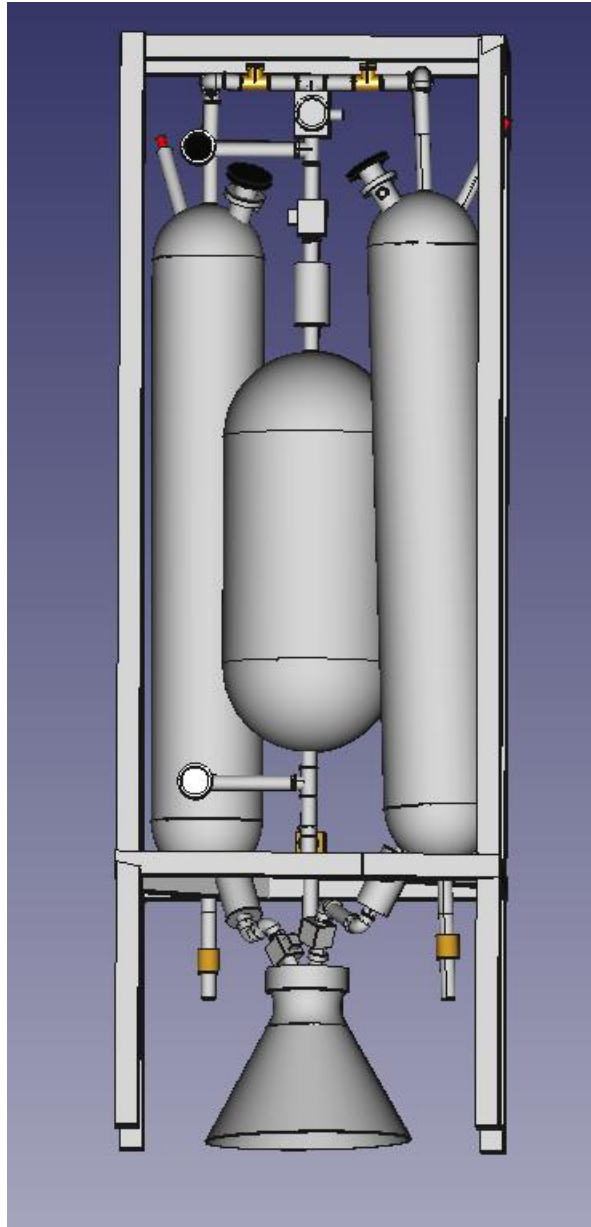


## 24.3 Cost Estimation

### IAP-SAT Testrig chem. Prop. Parts List

		Cost
1	Oxidizer Tank (LOX)	\$300
2	Fuel Tank (Bioethanol)	\$100
3	High pressure tank (He)	\$250
4	Thrust Chamber	\$80
5	High pressure gas valve (remote control)	\$200
6a	Propellant valve (remote control)	\$200
6b	Propellant valve (remote control)	\$200
7	Restricting orifice	\$50
8a	Filter	\$50
8b	Filter	\$50
9a	Drain valve (Abflussventil)	\$20
9b	Drain valve	\$20
10	Gas fill valve	\$30
11	Gas bleed valve	\$30
12	Gauge	\$50
13	Filter	\$30
14	Pressure Regulator	\$50
15	Gauge	\$20
16a	Tank vent valve	\$20
16b	Tank vent valve	\$20
17a	Check valve	\$20
17b	Check valve	\$20
	Total	\$1.810

## 24.4 Total Assembly (FreeCAD)



Assembly



Total Assembly.FCStd

## 24.5 Components:

In this section, the main element needed for building the propulsion unit will be presented. All the elements will be drawn using FreeCAD and will have a 3D shape.

### 24.5.1 Oxidizer/Fuel Tank

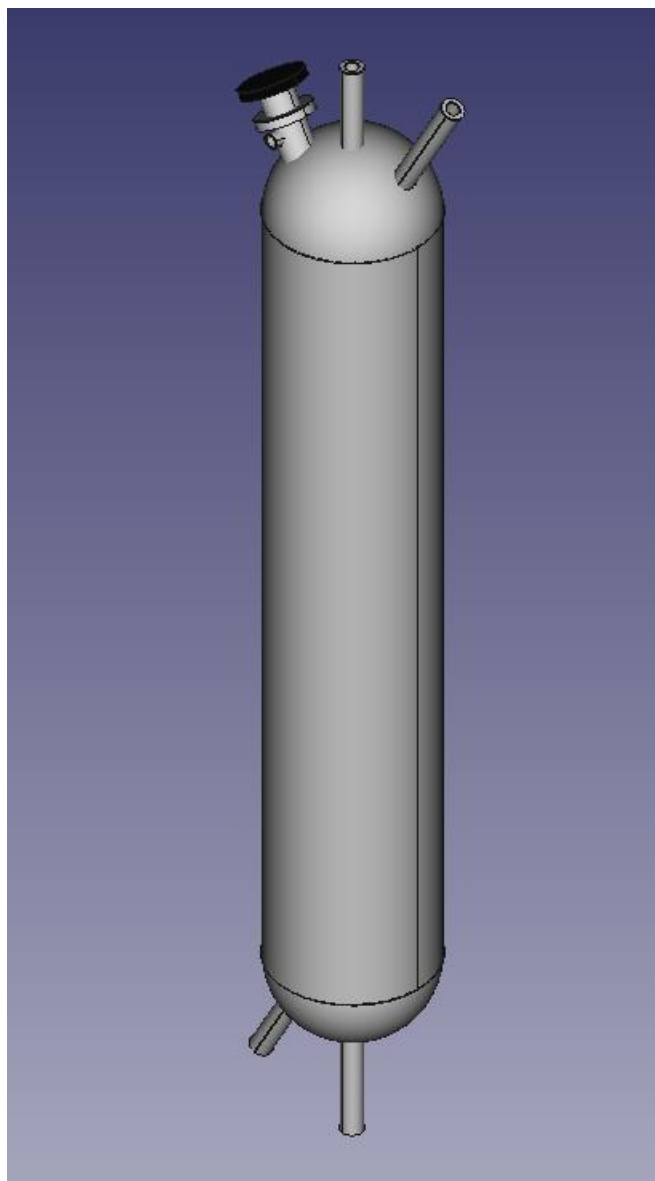


Figure 24-2: Oxidizer and fuel tank

Oxidizer and Fuel Tanks	 FUel.FCStd
-------------------------	---

### 24.5.2

Oxidizer Tank Storage Temperature: 90.17 K, -182.83 °C.

### 24.5.3 High Pressure Gas Supply Tank

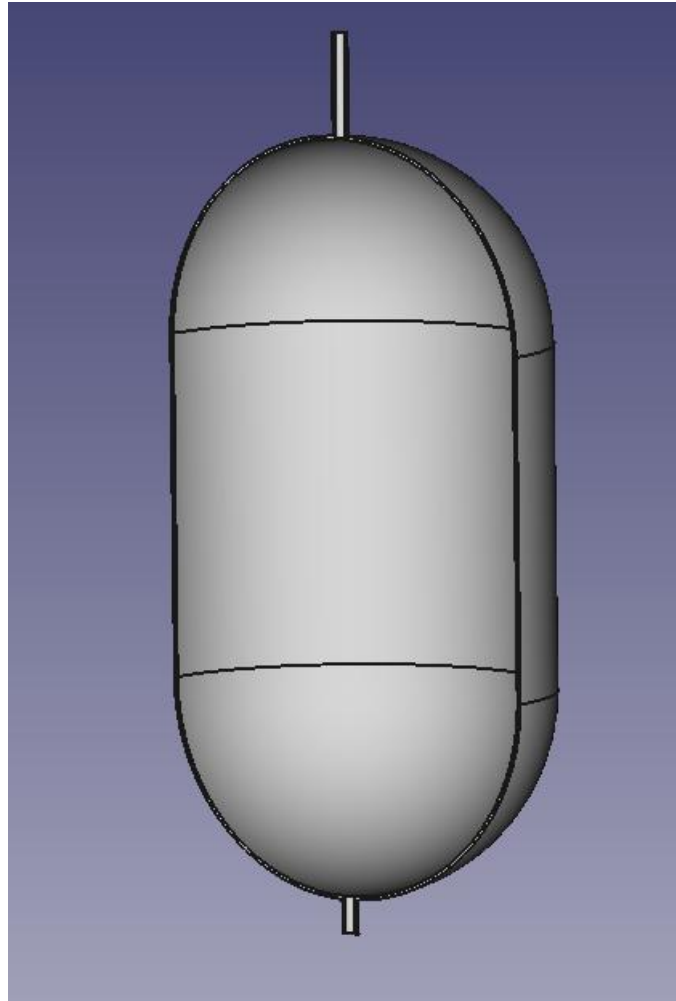


**Figure 24-3: High pressure gas tank**

High Pressure Gas Supply Tank	 HP gas supply tank.FCStd
-------------------------------	--

Pressurant Tank (Helium): Pressure 400bar, Temp 300K

24.5.4 Frame

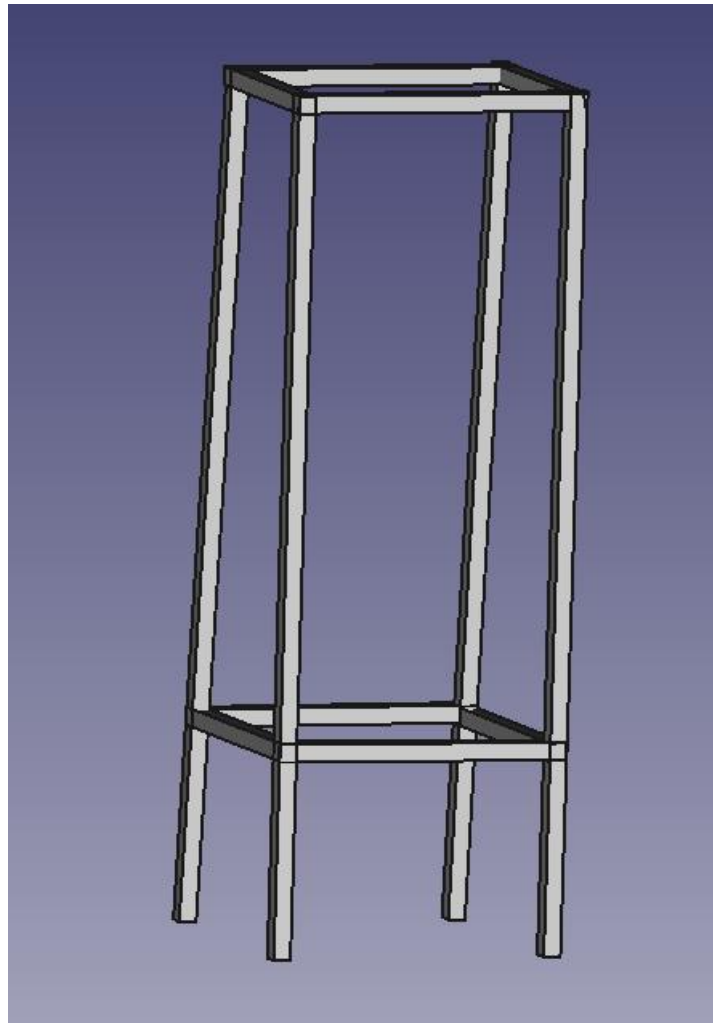


Figure 24-4: Test rig

Test Rig	 Test Rig1.FCStd
----------	--

### 24.5.5 Satellite Thrust Chamber

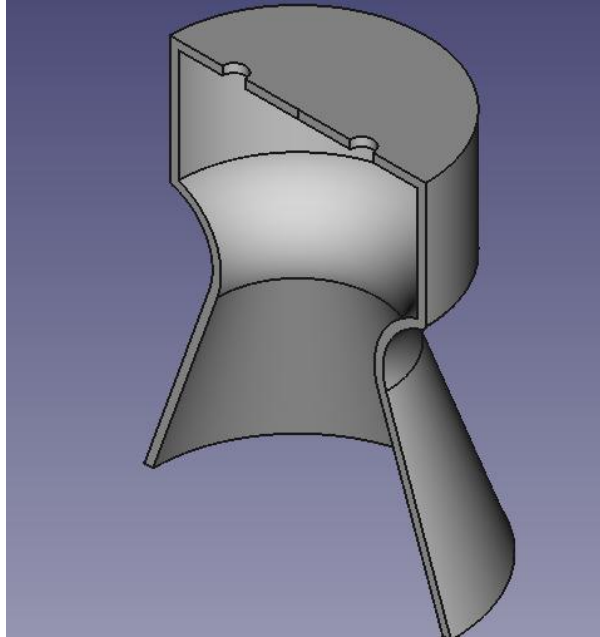


Figure 24-5: Thrust Chamber

Rocket Thrust Chamber	 thrust.FCStd
-----------------------	---

### 24.5.6 Filters

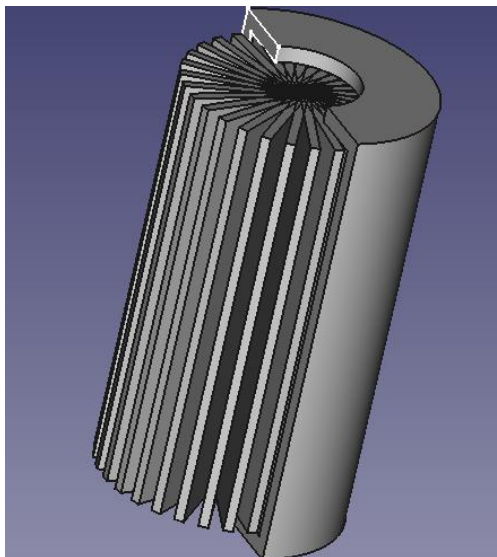
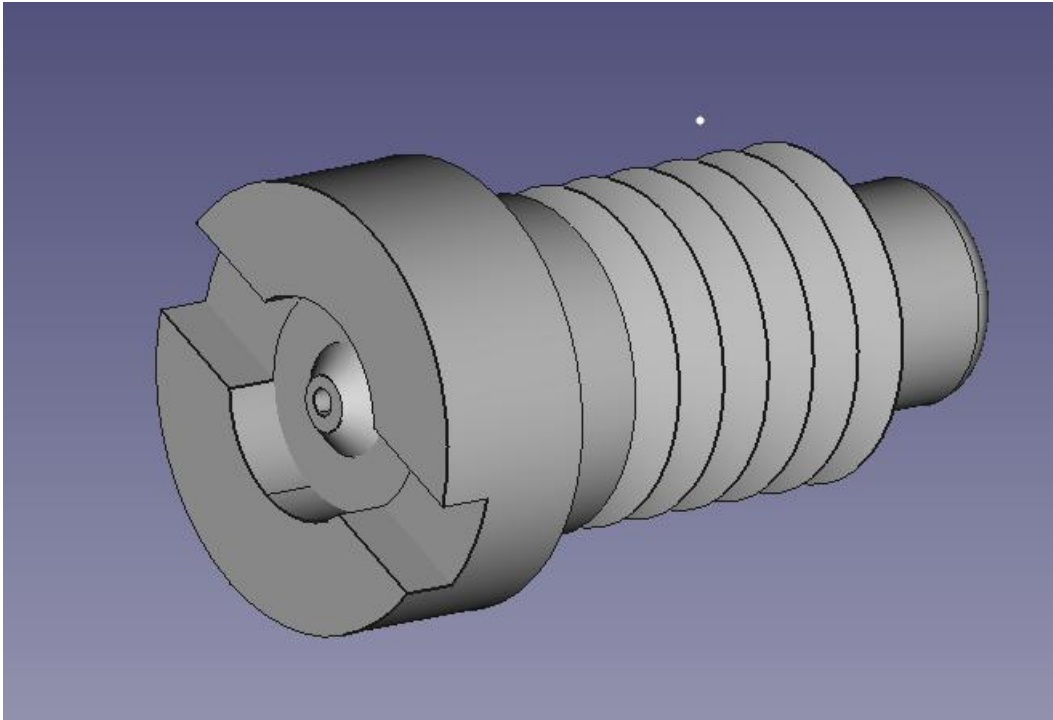


Figure 24-6: Filter used for pressured gasses

Filters	 Filter.FCStd
---------	---

**24.5.7 Gas fill valve****Figure 24-7 Gas Fill Valve**

<b>Gas Fill Valve</b>	 Gas Fill valve.FCStd
-----------------------	---

### 24.5.8 Filler Neck

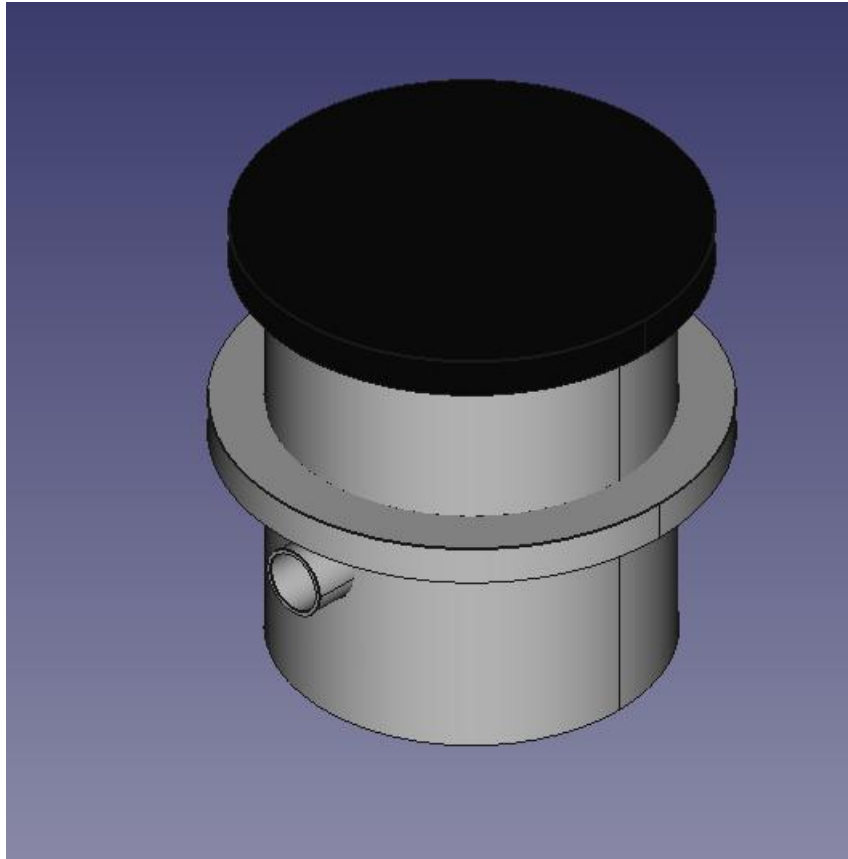
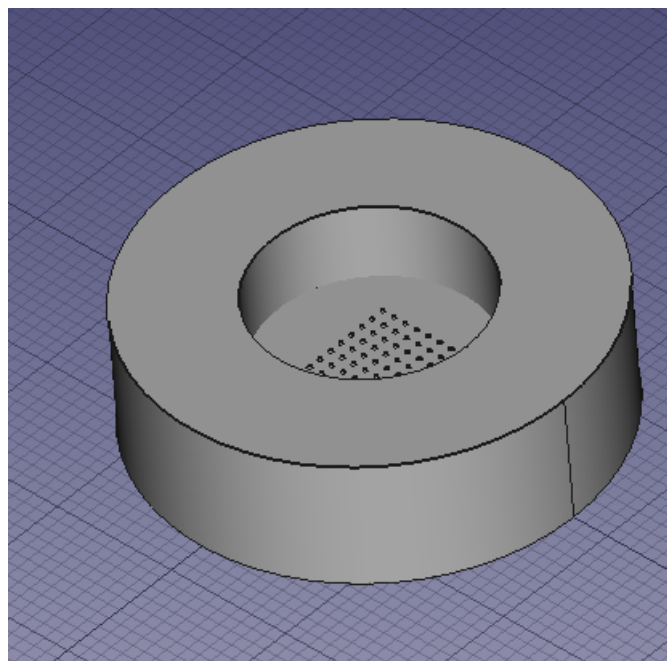


**Figure 24-8 Filler Neck**

<p><b>Filler Neck</b></p>	 <p>Filler neck.FCStd</p>
---------------------------	--

### 24.5.9 Restriction Orifice (RO) - Flow Control Instrument

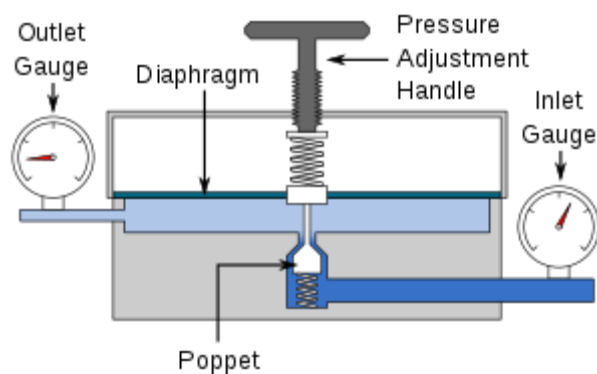


Restriction Orifice

Restricting  
Orifice.FCStd

### 24.5.10 Pressure Regulator

A **pressure regulator** is a control [valve](#) that reduces the input pressure of a fluid to a desired value at its output. Regulators are used for gases and liquids, and can be an integral device with an output pressure setting, a restrictor and a sensor all in the one body, or consist of a separate pressure sensor, controller and flow valve.

**Figure 24-9: Single-stage pressure regulator**

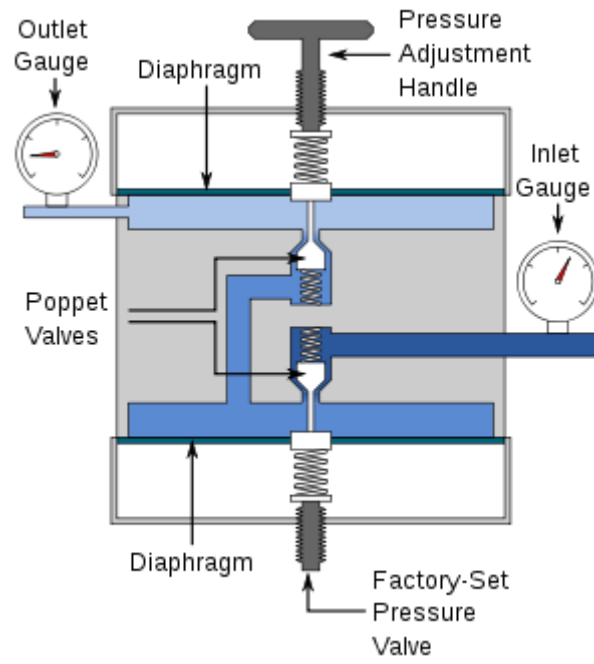


**Figure 24-10: Two-stage pressure regulator**

## 24.6 2D Sketches

### 24.6.1 Fuel / Oxidizer Tank

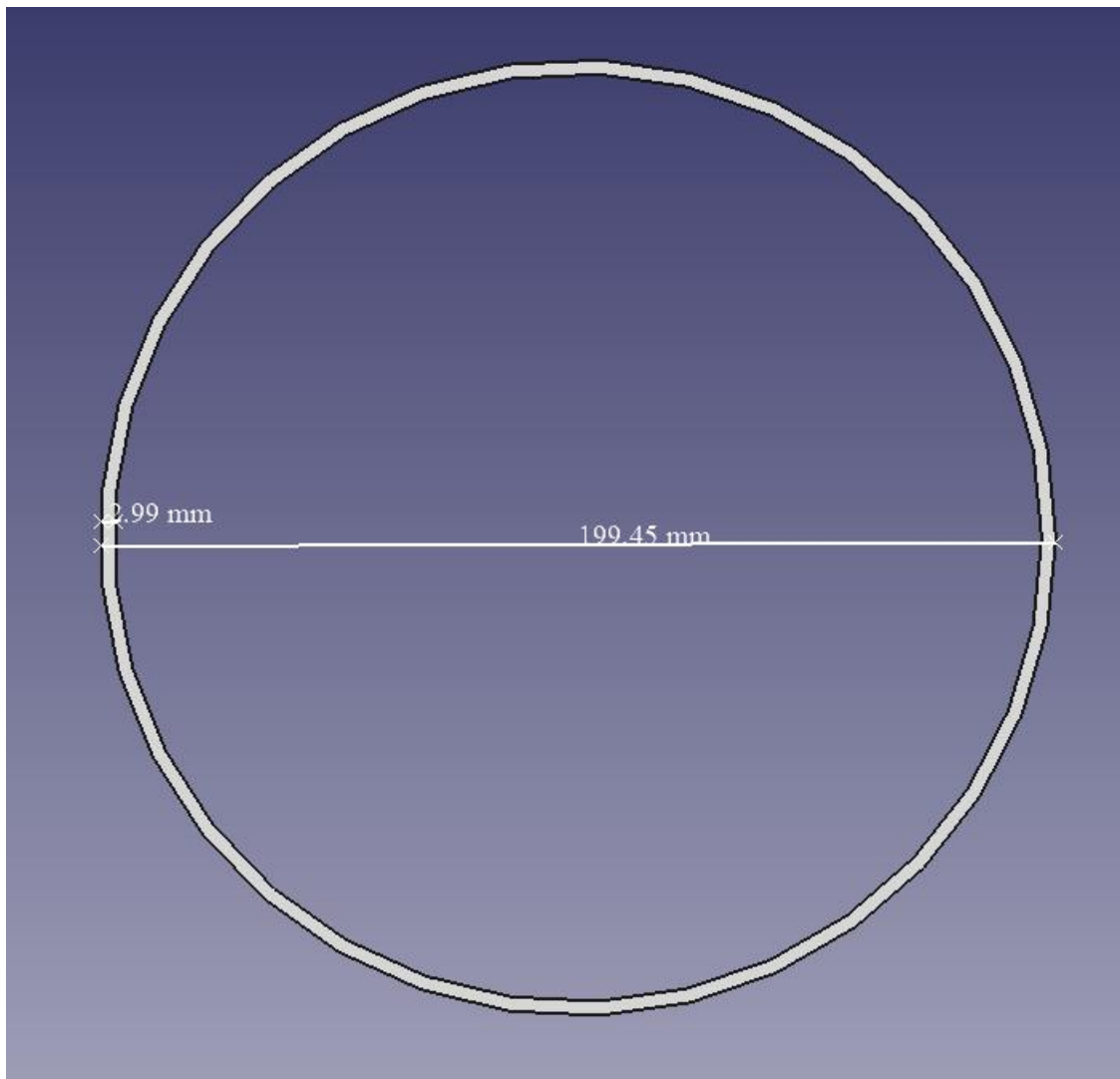
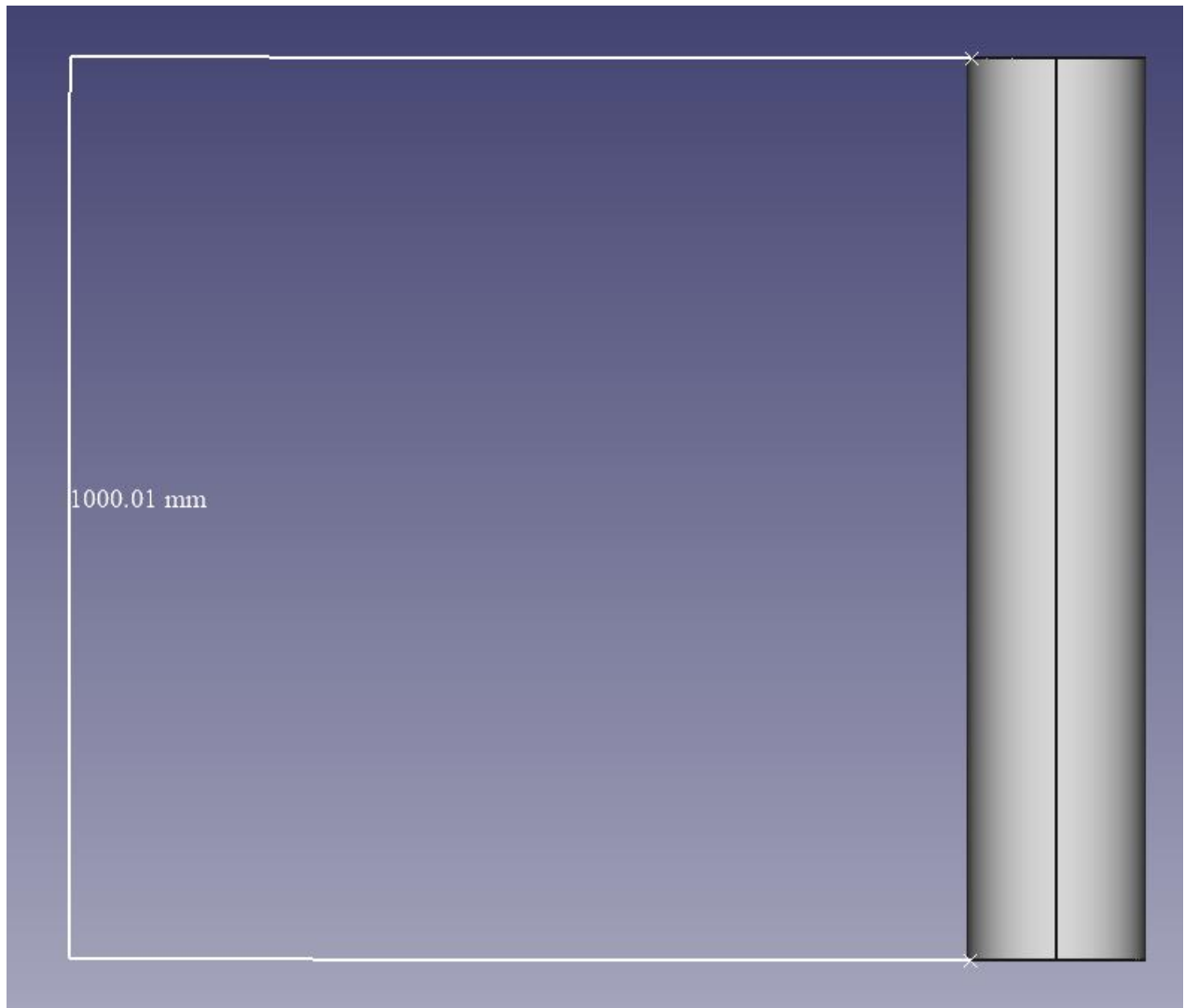
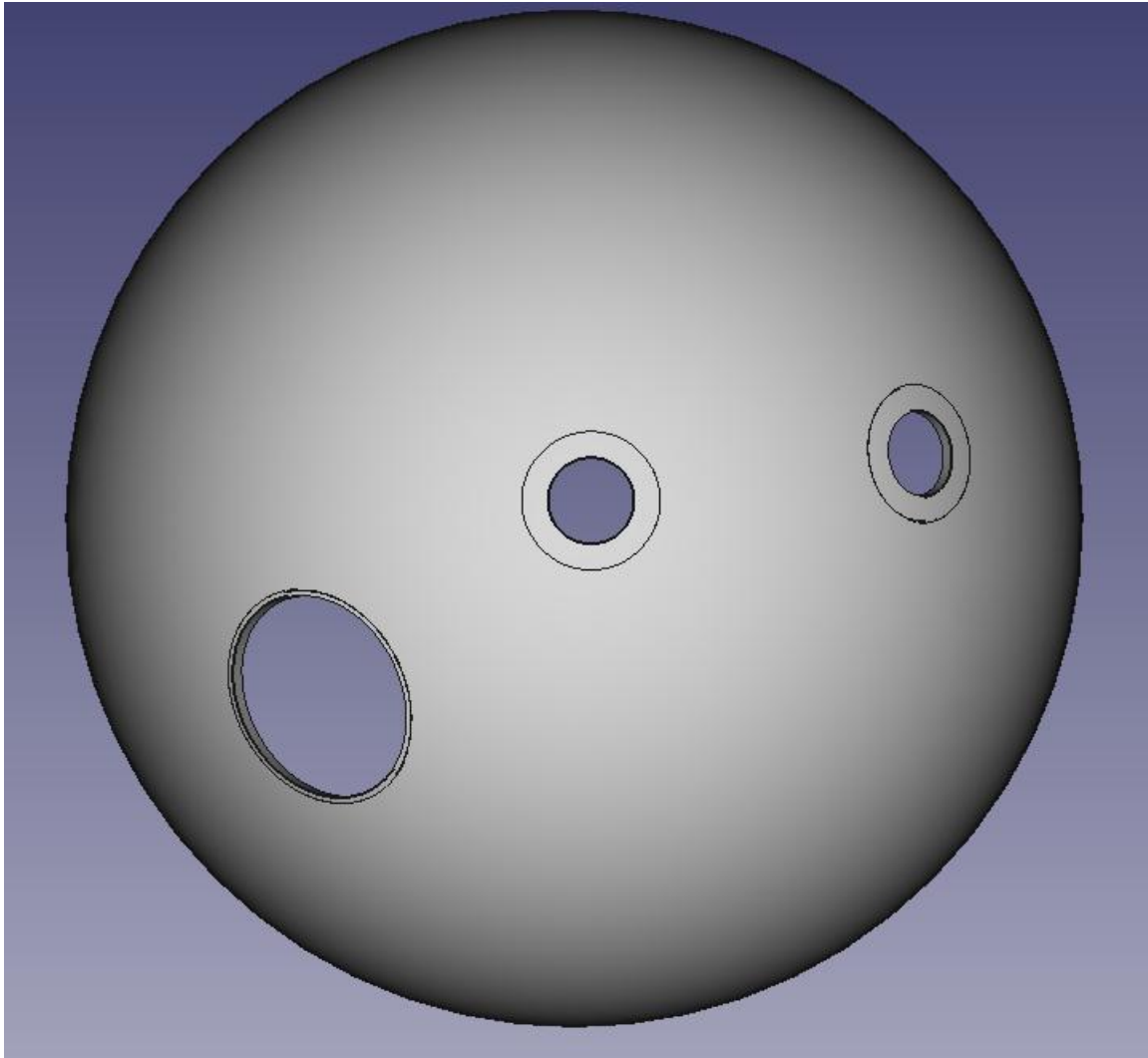


Figure 24-11. Diameter & Thickness of Tank



**Figure 24-12. Length of Tank**



**Figure 24-13.Upper Tank Cap (Radius 100mm - Thickness 3mm)**

2 x 27mm holes.

1 x 51mm hole.

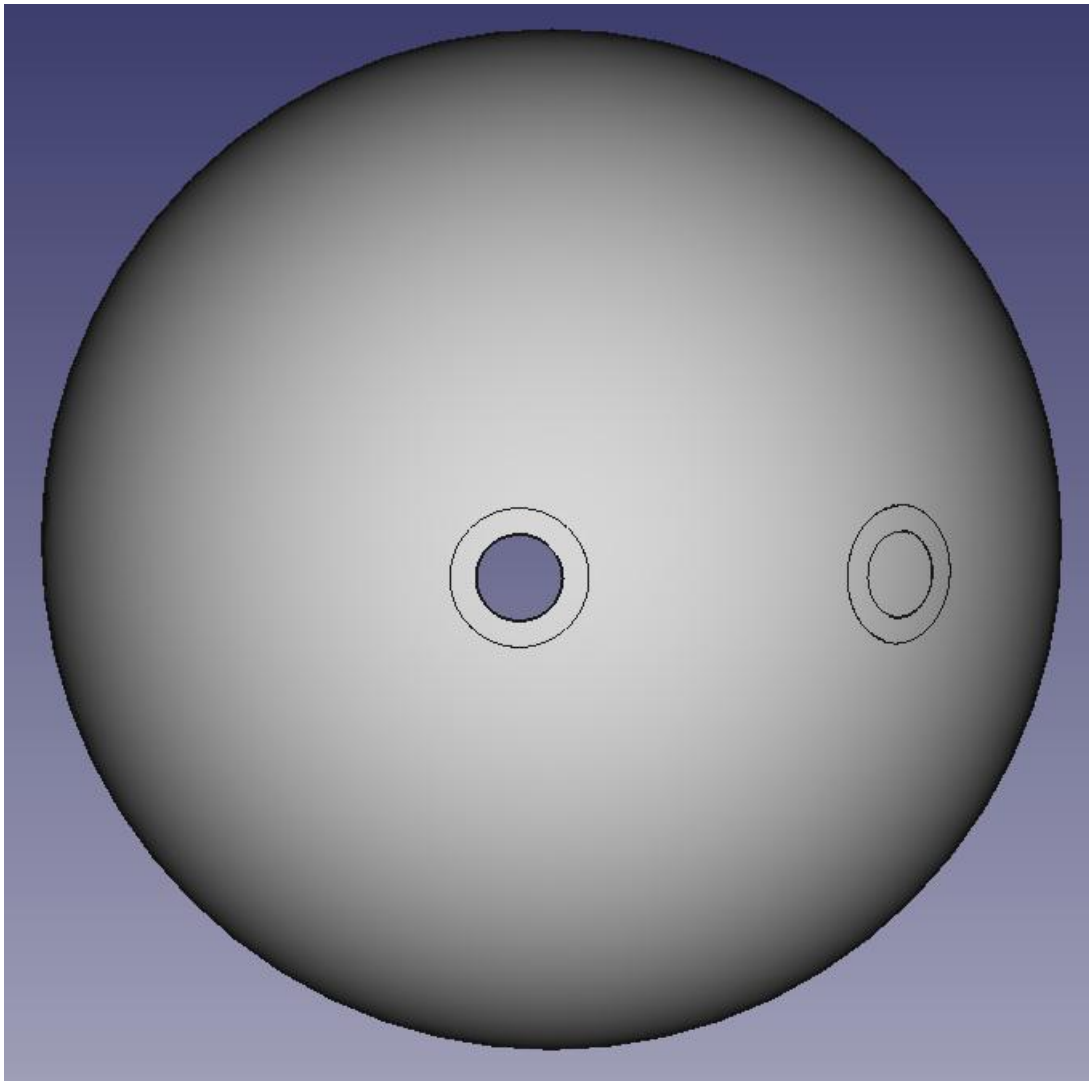


**Figure 24-14. Bottom Tank Cap**

2 x 27mm holes.

### 24.6.2 High Pressure Supply Tank

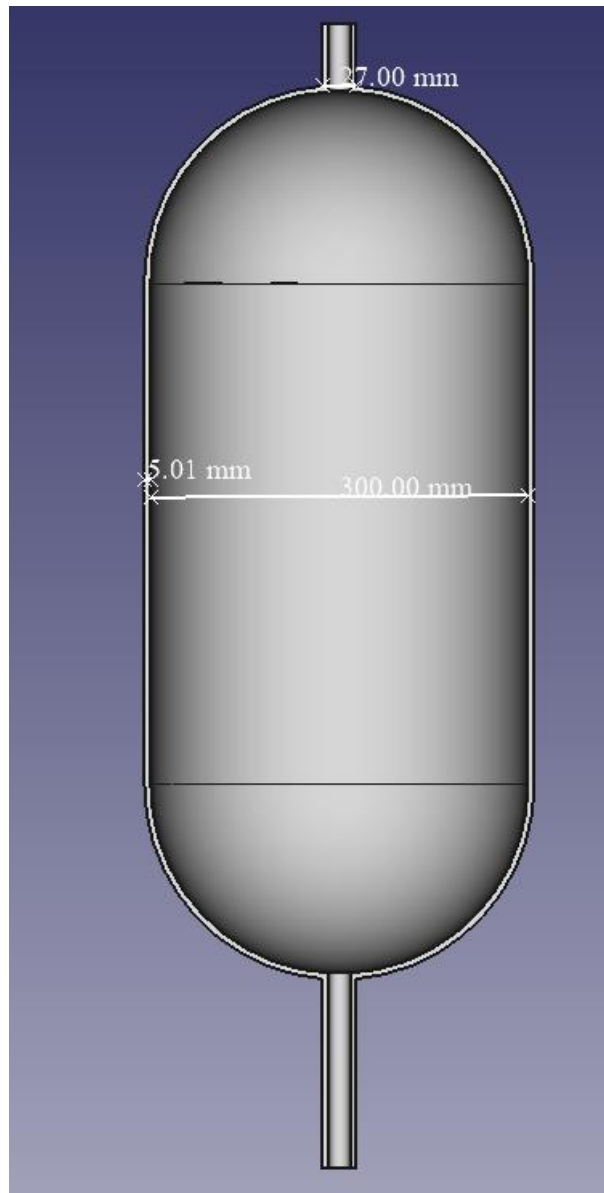


**Figure 24-15. Diameter & Thickness of HP Supply Tank**

5 mm thickness.

150 mm radius.

2 x 27 mm holes at the top and bottom of the tank.

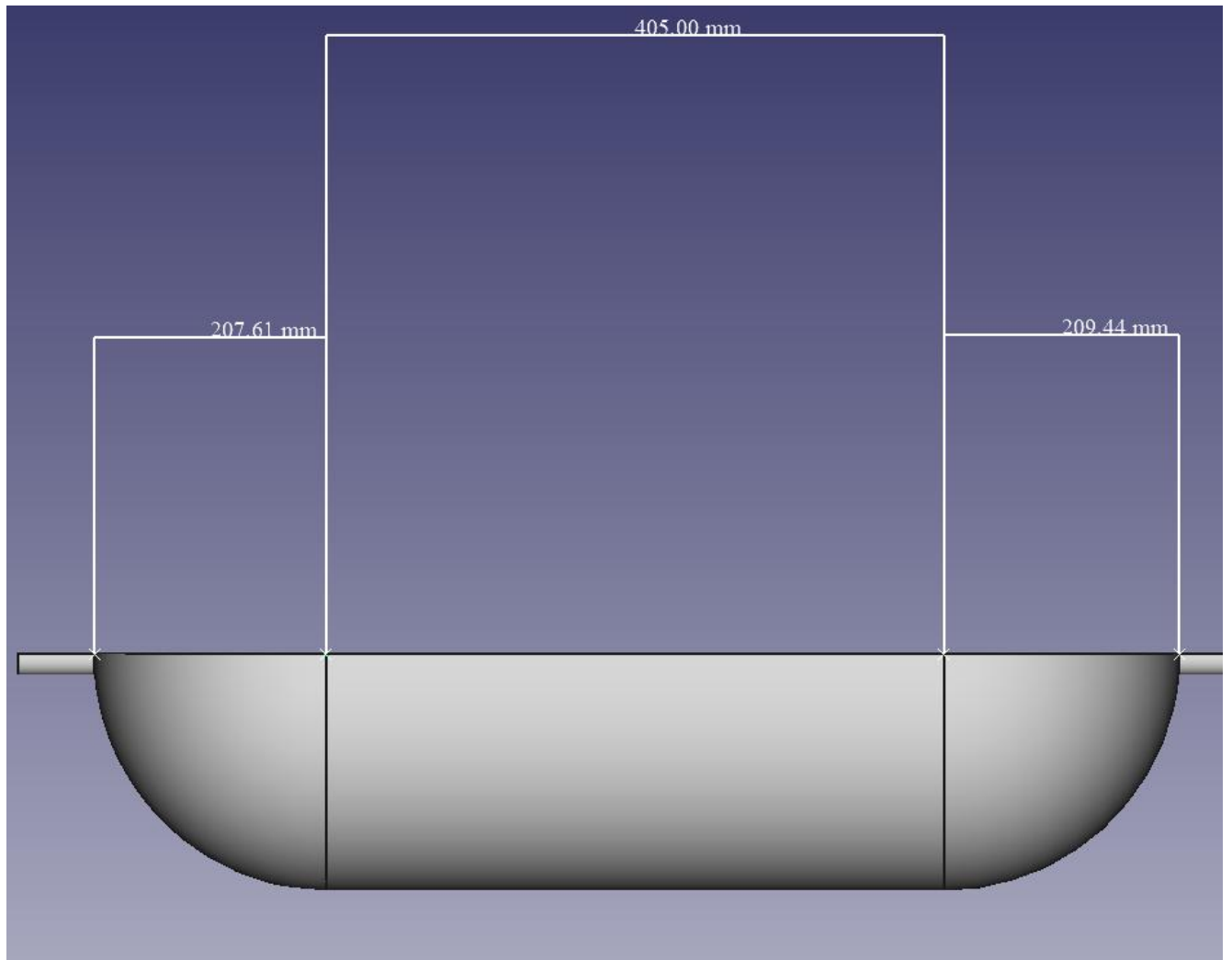


Figure 24-16. Length of HP Tank

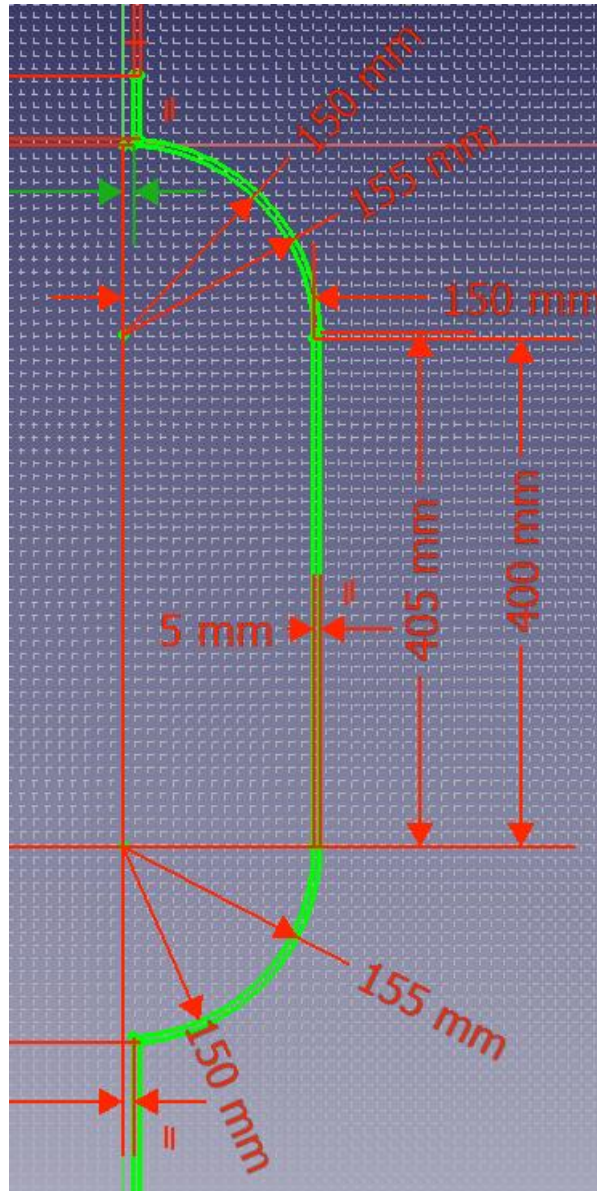


Figure 24-17. Sketch of HP Tank

## 24.7 Costs

Table 24-1: IAP-SAT Test rig chem. Prop. Parts List

		Number of Pieces	Cost	Total Cost	
1	Oxidizer Tank (LOX)	1	\$300	300\$	
	Oxidizer (H2O2)		120\$	120\$	Local
2	Fuel Tank (Bioethanol)	1	\$100	100\$	
	Fuel (Bioethanol)				
3	High pressure tank	1	\$250	250\$	

	(He)				
4	Thrust Chamber	1	\$80	80\$	
5	High pressure gas valve (remote control)	1		50\$	Alibaba <sup>31</sup>
			50\$		
6	Propellant valve (remote control)	2	\$200	400\$	
7	Restricting orifice	1	\$200	200\$	Alibaba <sup>32</sup>
8	Filter	3	\$50	150\$	
9	Drain valve	2	\$20	40\$	Alibaba <sup>33</sup>
10	Gas fill valve	1	\$16	16\$	Alibaba <sup>34</sup>
11	Gas bleed valve	1	\$10	10\$	Alibaba <sup>35</sup>
12	Gage	2	\$60	120\$	Alibaba <sup>36</sup>
13	Pressure Regulator	1	\$50	50\$	
14	Tank vent valve	2	\$20	40\$	
15	Check valve	2	\$80	160\$	Alibaba <sup>37</sup>
			Total	2086\$	

## 24.8 Pressure Calculation

Using **Barlow's formula** relates the internal pressure that a pipe can withstand to its dimensions and the strength of its material.

$$P = (2 \cdot S \cdot t) / D$$

where

$P$  = pressure,  $S$  = allowable stress,  $t$  = wall thickness,  $D$  = outside diameter.

This formula figures prominently in the design of autoclaves and other pressure vessels.

For material Stainless Steel 306, assume  $S=115$  MPa

<sup>31</sup> [https://www.alibaba.com/product-detail/anson-valves-gas-valve-type-high\\_60186147305.html?spm=a2700.7724857.discountZoneStyleB\\_top.3.452c2c75eO62gp](https://www.alibaba.com/product-detail/anson-valves-gas-valve-type-high_60186147305.html?spm=a2700.7724857.discountZoneStyleB_top.3.452c2c75eO62gp)

<sup>32</sup> [https://www.alibaba.com/product-detail/Liquid-Restriction-Orifice-Stainless-Steel-Water\\_62239053995.html?spm=a2700.7724857.normalList.10.2f157542AdaVvw&s=p&bypass=true](https://www.alibaba.com/product-detail/Liquid-Restriction-Orifice-Stainless-Steel-Water_62239053995.html?spm=a2700.7724857.normalList.10.2f157542AdaVvw&s=p&bypass=true)

<sup>33</sup> [https://www.alibaba.com/product-detail/KLPT-Two-position-AC220V-Low-Price\\_60632633020.html?spm=a2700.7724857.normalList.37.7056422aEvftw1](https://www.alibaba.com/product-detail/KLPT-Two-position-AC220V-Low-Price_60632633020.html?spm=a2700.7724857.normalList.37.7056422aEvftw1)

<sup>34</sup> [https://www.alibaba.com/product-detail/act-gnv-cng-gas-filling-valve\\_62043748852.html?spm=a2700.7724857.discountZoneStyleB\\_top.2.e5544be382dGoI](https://www.alibaba.com/product-detail/act-gnv-cng-gas-filling-valve_62043748852.html?spm=a2700.7724857.discountZoneStyleB_top.2.e5544be382dGoI)

<sup>35</sup> [https://www.alibaba.com/product-detail/Brass-copper-invar-kovar-Monel-Inconel\\_62386469364.html?spm=a2700.7724857.normalList.52.191f6546A0aVYY](https://www.alibaba.com/product-detail/Brass-copper-invar-kovar-Monel-Inconel_62386469364.html?spm=a2700.7724857.normalList.52.191f6546A0aVYY)

<sup>36</sup> [https://www.alibaba.com/product-detail/Digital-air-pressure-gauge-vacuum-pressure\\_60649448376.html?spm=a2700.7735675.normalList.249.f2bc58e5CXhqr&s=p](https://www.alibaba.com/product-detail/Digital-air-pressure-gauge-vacuum-pressure_60649448376.html?spm=a2700.7735675.normalList.249.f2bc58e5CXhqr&s=p)

<sup>37</sup> [https://www.alibaba.com/product-detail/RF-TriClamp-Weld-Thread-Sanitary-Stainless\\_62267985811.html?spm=a2700.7735675.normalList.79.1608490fwCCKSe&s=p](https://www.alibaba.com/product-detail/RF-TriClamp-Weld-Thread-Sanitary-Stainless_62267985811.html?spm=a2700.7735675.normalList.79.1608490fwCCKSe&s=p)

### **24.8.1 Pressure of the Fuel/Oxidizer Tanks**

Thickness = 3 mm

Diameter = 200 mm

Pressure = 34.5 bar

### **24.8.2 Pressure of the High-Pressure Supply Tank**

Thickness = 5 mm

Diameter= 300 mm

Pressure = 38.3 bar

## 24.9 Available Components for the Chemical Propulsion Unit Test



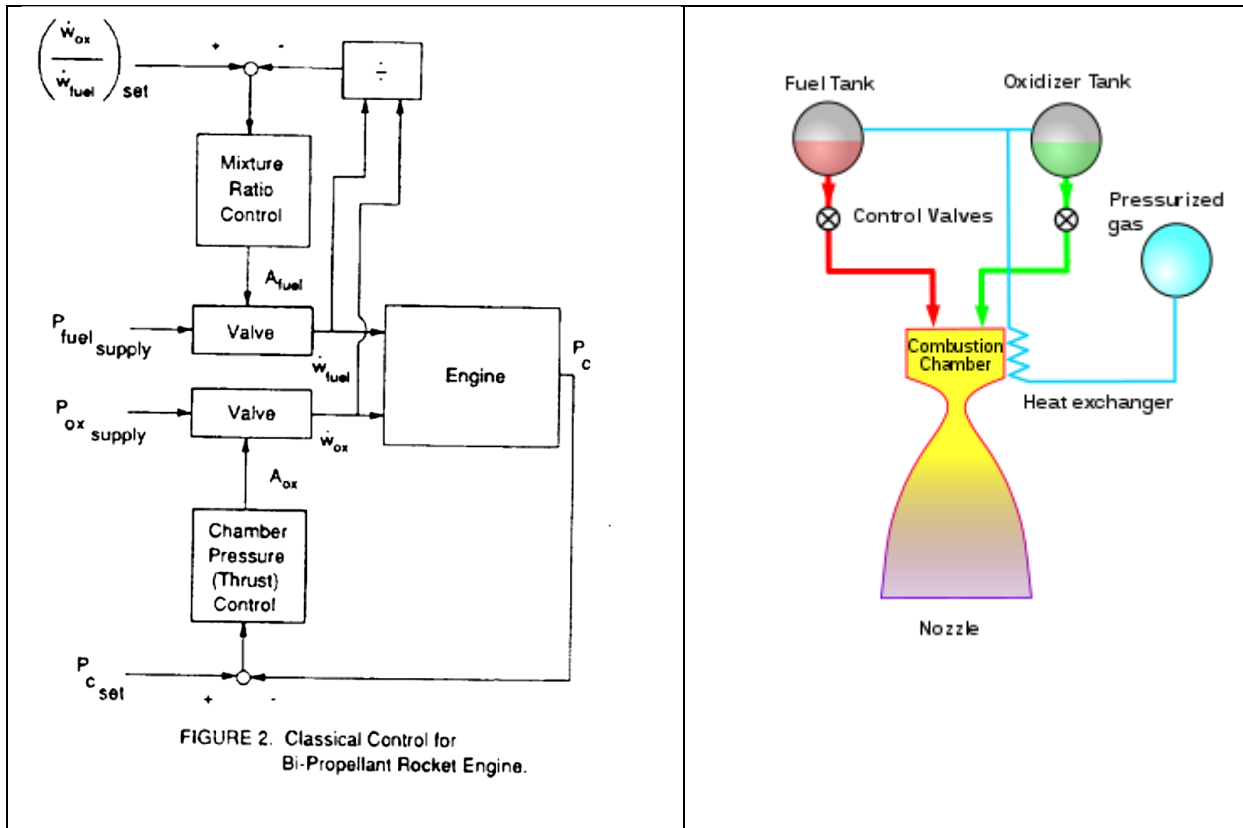
**Figure 24-18. Test Rig and Tanks**



**Figure 24-19. Burner**

## 25 Mixture Ratio Control and Chamber Pressure Control for Orbit Attitude Control Engine test rig of IAP-SAT

### 25.1 Principle and Task



Oxidizer (Hydrogen Peroxide)
Fuel (Ethanol)

Trainee Task: Control with Arduino (Control Design, Implementation and Realization with Arduino)

Keywords: Control, PID, Combustion Mixture

**Sensors:** Flowmeters, Pressure transducers.

Only two actuators (control valves upstream from pre-burners) are used to control the system in a continuous way.

Measured states can be combustion temperatures, cavity pressures, turbo-pumps speed and some mass flows.

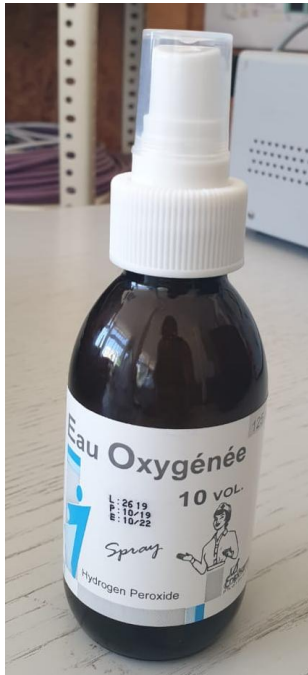
Concerning control inputs, valve positions can be measured; and sometimes there are other physical parameters or quantities relevant to determine, such as fuel and oxidizer temperatures or vibrations.

The sensors required for their control loop are mentioned: flow-rate sensors are installed prior to the chamber, apart from the typical pressure sensor inside the chamber.

In actual engines in flight, most mass flows are normally not measured. Hence, estimators have to be used.

## 25.2 Propellants Used

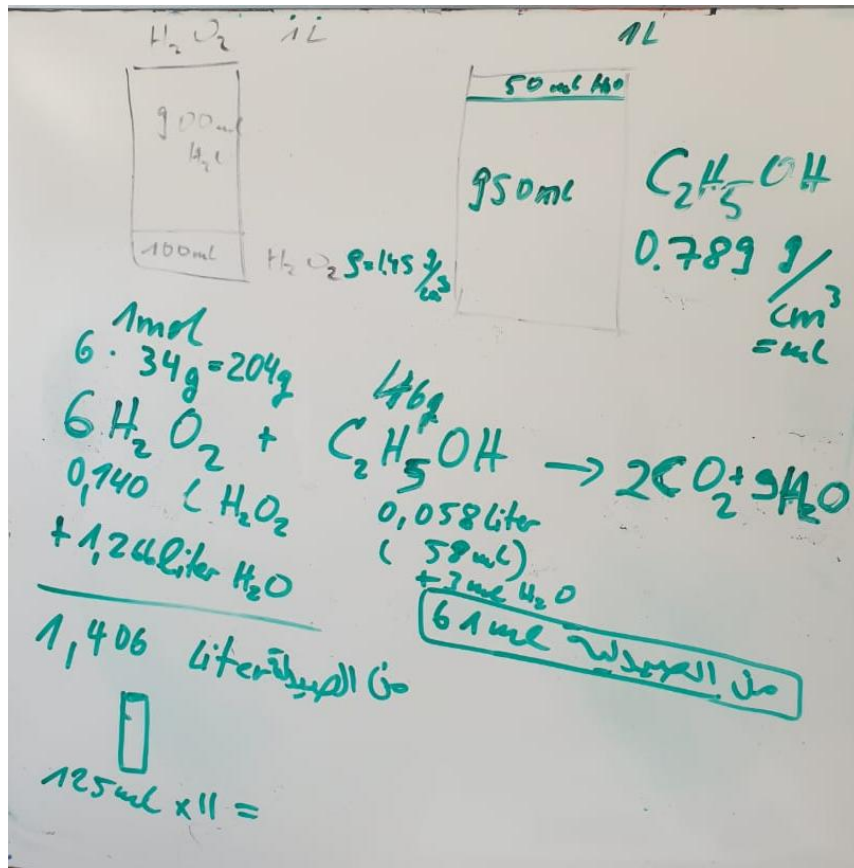
We have:



Oxidizer: Hydrogen Peroxide 10%



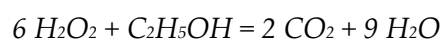
Fuel: Ethanol 95%



Oxidizer: For 1 liter of (H<sub>2</sub>O<sub>2</sub>) Hydrogen Peroxide 10%: 100ml H<sub>2</sub>O<sub>2</sub> + 900ml H<sub>2</sub>O

Fuel: For 1 Liter of (C<sub>2</sub>H<sub>5</sub>OH) Ethanol 95%: 950ml C<sub>2</sub>H<sub>5</sub>OH + 50ml H<sub>2</sub>O

When mixing:



For H<sub>2</sub>O<sub>2</sub>: (density 1.45g/ml)

1 mole = 34g

6x34g = 204g

204g / 1.45h/ml = 0.14 liter

0.14 liter H<sub>2</sub>O<sub>2</sub> + 1.26 liter H<sub>2</sub>O = 1.4 liter needed from Pharmacy (125ml x 11)

For C<sub>2</sub>H<sub>5</sub>OH: (density 0.789g/ml)

1 mole = 46g

46g / 0.789g/ml = 0.058 liter

58ml C<sub>2</sub>H<sub>5</sub>OH + 3 ml H<sub>2</sub>O = 61ml needed from Pharmacy

O/F: 1406/61= 23

 Rocket Propulsion Analysis (Standard Edition, evaluation copy - trial version)

File View Run Help

Express Thermodynamic Analysis

Chamber pressure:  bar

System:

Mixture ratio:  optimum optimize mixture ratio for max delivered  $I_s$

Oxidizer:

Species	MF	T	Unit	p	Unit
H2O2...	1		K		MPa
Sum of all the mass fractions: 1					

Fuel:

Species	MF	T	Unit	p	Unit
C2H5...	1		K		MPa
Sum of all the mass fractions: 1					

Buttons: Add Define new Remove Normalize

Nozzle exit conditions

pressure:  atm

expansion area ratio:  (Ae/At)

expansion pressure ratio:  (pc/pe)

Sections are designated as follows: c = combustion chamber, t = nozzle throat, e = nozzle exit.

Engine performance:

Parameter	Sea level	Optimum expansion	Vacuum	Unit
Characteristic velocity		1399.88		m/s
Effective exhaust velocity	1590.27	1590.27	1977.26	m/s
Specific impulse (by mass)	1590.27	1590.27	1977.26	N-s/kg
Specific impulse (by weight)	162.16	162.16	201.62	s
Thrust coefficient	1.1360	1.1360	1.4124	

## 25.3 Basic Components

### 25.3.1 Flowmeter<sup>38</sup>



Quantity: 2

<sup>38</sup> <https://cnclablb.com/water-flow-sensor.html?search=Water%20flow%20sensor>

Price per unit: 15,775 L.L (11% VAT excluded)

**Specification:**

The lowest rated working voltage: DC4.5 5V-24V

Maximum operating current: 15 mA (DC 5V)

Working voltage range: DC 5~18 v

Load capacity: = 10 mA (DC 5V)

Use temperature: = 80°C

Operating humidity range: 35%~90%RH (no frost)

Allowing pressure: pressure 2.0Mpa

Temperature: -25~+80 °C

External threads: 1/2"

Outer diameter: 20mm

Intake diameter: 9mm

Outlet diameter: 12mm

Application:

Water heaters, credit card machines, water vending machine, flow measurement device!

**25.3.2 Solenoid Valve<sup>39</sup>**



Quantity: 2

Price per unit: 28,429 L.L (11% VAT excluded)

---

<sup>39</sup> <https://cnclablb.com/g34-12v-pp-normally-closed-solenoid-valve-water-diverter-device.html?search=valve>

**Specification:**

Material: PP

Voltage: about 12V DC

Rated power: about 5W

Operation model: normally closed (N/C)

Pressure: about 0.02 - 0.8Mpa

Port size: about G3/4

Fluid temperature: about 0-100 degrees Celsius

Usage: water and low viscosity fluids

**Flow characteristics:**

about 0.02Mpa>2L/min;

about 0.10Mpa>10L/min;

about 0.30Mpa>16L/min;

about 0.80Mpa>28L/min

**25.4 Assembly**

Chemical Propulsion Unit test rig after connecting the solenoid valves and flowmeter sensors.

## 25.5 Fuel - Oxidizer Mixing Control

The control of the test rig is realized with python on a Raspberry Pi 3. In the following is described how to learn to work with this environment for whom is totally new to this.

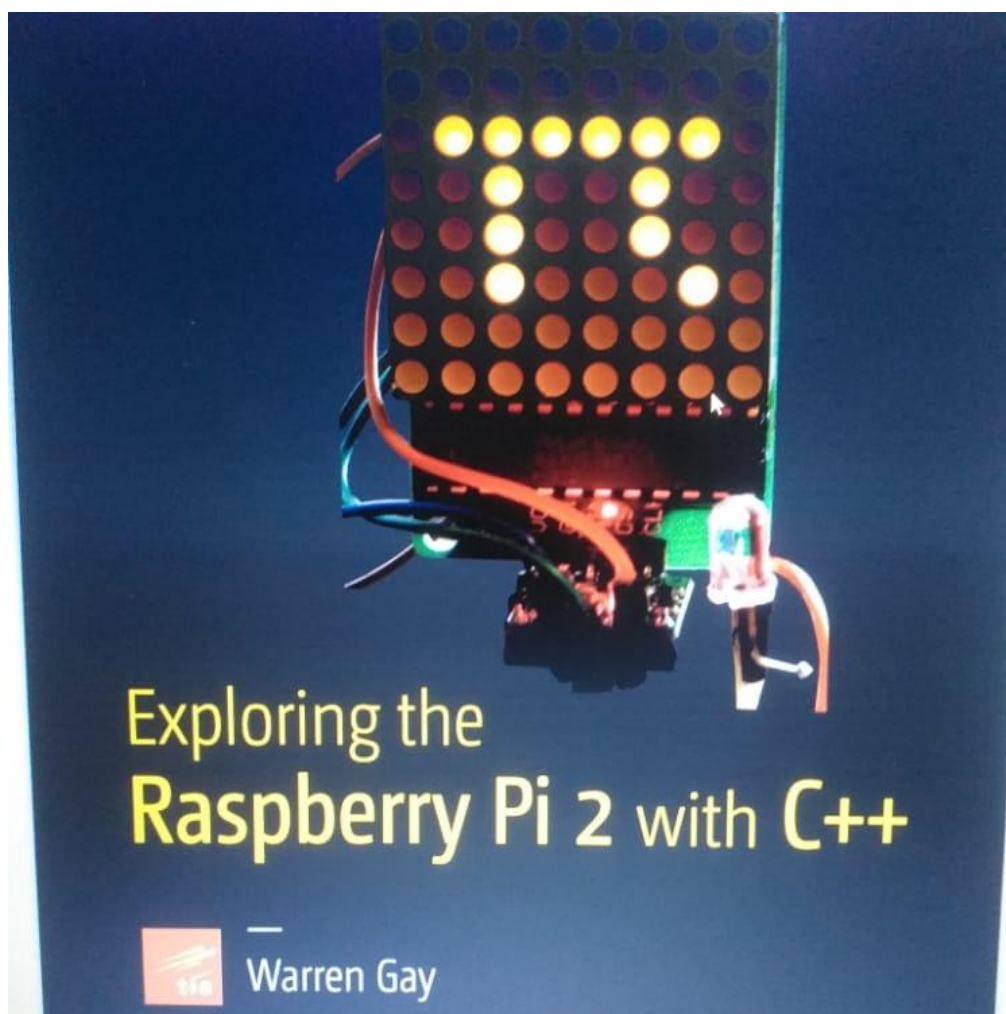
### 25.5.1 Start learning on Raspberry

#### 25.5.1.1 Step 1 reading book

Reading a book about raspberry pi and how to write code in c ++

The link of this book:

<https://bbooks.info/b/w/8873f497932991f0a46529d6b98eea3373f9ad81/exploring-the-raspberry-pi-2-with-c.pdf>



#### 25.5.1.2 Step 2 Watch on YouTube

We watched a YouTube video related to LED control

The title of this video: Writing to GPIO pins in C using wiringPi on the raspberry Pi



### 25.5.1.3 Step 3 Writing code on Raspberry pi

```

MERCHANTABILITY or FITNESS FOR A PARTICULAR PURPOSE. See the
GNU Lesser General Public License for more details.

You should have received a copy of the GNU Lesser General Public License
along with wiringPi. If not, see <http://www.gnu.org/licenses/>
.....
*/

#include <stdio.h>
#include <wiringPi.h>

// LED Pin - wiringPi pin 0 is BCM_GPIO 17.
#define LED 17

int main (void)
{
    printf ("Raspberry Pi blink\n");
    wiringPiSetup ();
    pinMode (LED, OUTPUT);

    for (;;)
    {
        digitalWrite (LED, HIGH); // On
        delay (500); // ms
        digitalWrite (LED, LOW); // Off
    }
}

int X;
for (x=0; x<5; x++)
{
    digitalWrite (LED, HIGH); // On
    delay (500); // ms
    digitalWrite (LED, LOW); // Off
    delay (500);
}
pinMode 0 ;

```

### 25.5.1.4 Step 4 Hardware

We installed a resistor with LED on breadboard and connected it on Raspberry PI



### 25.5.1.5 Step 5 Result

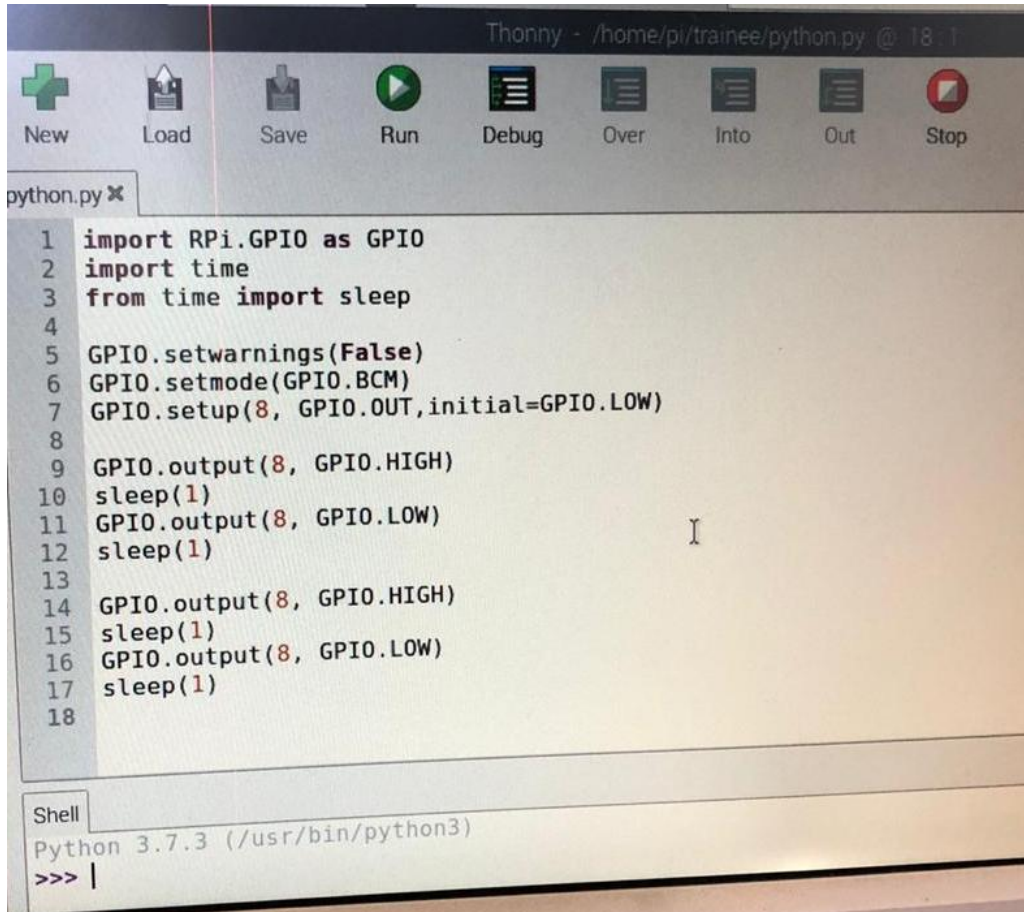
Some pictures while working and controlling the LED:



### 25.5.2 Programming with Python

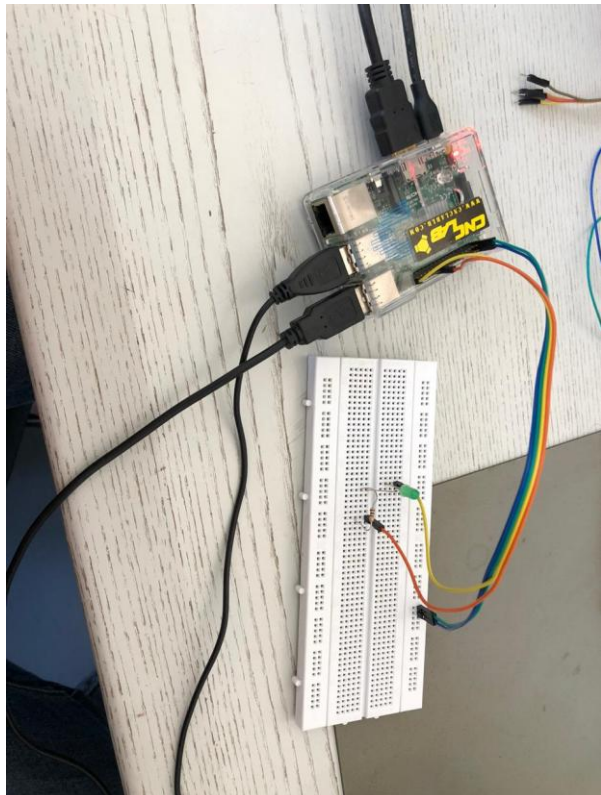
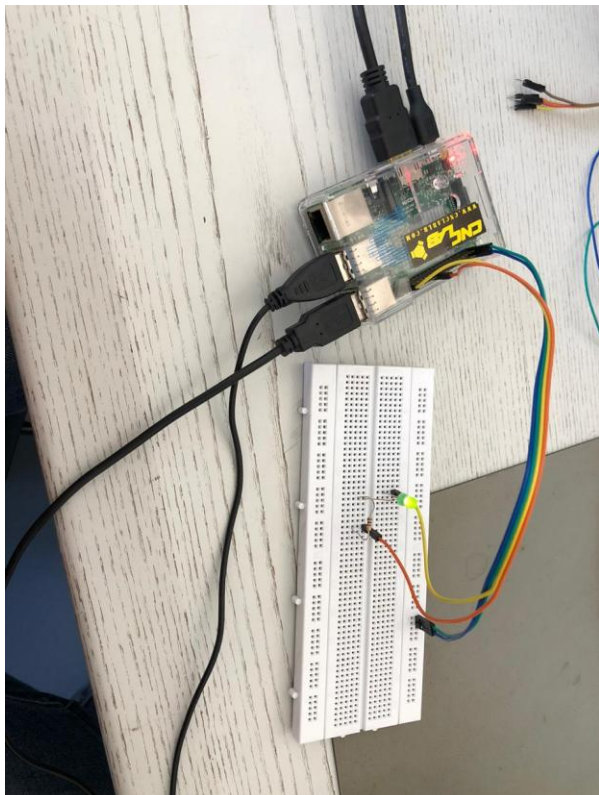
#### 25.5.2.1 Step 1: write code in new script to control led

Attention: using this raspberry pi you must focus to `GPIO.setmode(GPIO.BCM)` NOT `.BOARD`



```
Thonny - /home/pi/trainee/python.py @ 18 1
New Load Save Run Debug Over Into Out Stop Z
python.py ✕
1 import RPi.GPIO as GPIO
2 import time
3 from time import sleep
4
5 GPIO.setwarnings(False)
6 GPIO.setmode(GPIO.BCM)
7 GPIO.setup(8, GPIO.OUT, initial=GPIO.LOW)
8
9 GPIO.output(8, GPIO.HIGH)
10 sleep(1)
11 GPIO.output(8, GPIO.LOW)
12 sleep(1)
13
14 GPIO.output(8, GPIO.HIGH)
15 sleep(1)
16 GPIO.output(8, GPIO.LOW)
17 sleep(1)
18
Shell
Python 3.7.3 (/usr/bin/python3)
>>> |
```

### 25.5.2.2 Step 2: Hardware



25.5.2.3 Note: In the table below focus on gpio pins

Pin #	Name	Beschreibung
3	GPIO2	Input/Output. Oder I2C-Kabel SDA (I2C1_SDA).
5	GPIO3	Input/Output. Oder I2C-Kabel SCL (I2C1_SCL).
7	GPIO4	Input/Output. Oder liefert Ausgang für Grundtakt (GPCLK0) an externe Schaltkreise.
8	GPIO14	Input/Output. Oder UART Sendepin (UART_TXD).
10	GPIO15	Input/Output. Oder UART (UART_RXD).
11	GPIO17	Input/Output.
12	GPIO18	Input/Output.
13	GPIO27	Input/Output.
15	GPIO22	Input/Output.
16	GPIO23	Input/Output.
18	GPIO24	Input/Output.

175

19	GPIO10	Input/Output. Oder SPI Masterkabel Eingang (SPI_MOSI).
21	GPIO9	Input/Output. Oder SPI Masterkabel Ausgang (SPI_MISO).
22	GPIO25	Input/Output.
23	GPIO11	Input/Output. Oder SPI Clock Kabel (SPI_SCLK).
24	GPIO8	Input/Output. Oder SPI Device Select 0 (SPI_CE0).
26	GPIO7	Input/Output. Oder SPI Device Select 1 (SPI_CE0).
27	ID_SC	Reserviert.
28	ID_SC	Reserviert.
29	GPIO5	Input/Output.
31	GPIO6	Input/Output.
32	GPIO12	Input/Output.
33	GPIO13	Input/Output.
35	GPIO19	Input/Output.
36	GPIO16	Input/Output.
37	GPIO26	Input/Output.
38	GPIO20	Input/Output.
40	GPIO21	Input/Output.

Sie akzeptieren keine 5V und

25.5.2.4 Testing code for flow sensor

```
#!/usr/bin/env python
#flowsensor.py
import RPi.GPIO as GPIO
import time, sys

FLOW_SENSOR = 23

GPIO.setmode(GPIO.BCM)
GPIO.setup(FLOW_SENSOR, GPIO.IN, pull_up_down = GPIO.PUD_UP)

#global count

#count = 0
```

```

def countpulse(channel,start_counter):
    print ("Bismillah")
    print (channel)
#    global count
    start_counter = 1
    count = 0
    if start_counter == 1:
        count += 1
#print count
#flow = count / (60 * 7.5)
#print(flow)
    channel= GPIO.add_event_detect(FLOW_SENSOR, GPIO.FALLING,
callback=countpulse)

    while True:
        try:
            start=count - 1
            time.sleep(1)
            start=count - 1
            flow = (count * 60 * 2.25 / 1000)
            print ("The flow is:" , flow)
            '#%.3f Liter/min' % (flow)
            count = 0
            time.sleep(5)

        except KeyboardInterrupt:
            print ('\ncaught keyboard interrupt!, bye')
            print ("No flow")
            GPIO.cleanup()
            sys.exit()

countpulse (1,2)

```

### 25.5.2.5 New test of flow meter sensor

```

import RPi.GPIO as GPIO
import time, sys
pulse_pin = 25
GPIO.setmode(GPIO.BCM)
GPIO.setup(pulse_pin, GPIO.IN,pull_up_down = GPIO.PUD_UP)

def countPulse1(channell):
    count+=1
    print("Number of revolution of wheel of flow sensor:")
    print(count)

GPIO.add_event_detect(pulse_pin, GPIO.RISING, callback=countPulse1)

try:
    while True:
        print("Inside while starting")
        time.sleep(10)
        print("Inside while ending")
        time.sleep(10)
except KeyboardInterrupt:
    print ('\ncaught keyboard interrupt!, bye')
    GPIO.cleanup()
    sys.exit()

```

- Today, we're going to modify the code to suit our work with a flow meter sensor
- We will also connect the sensor to the raspberry pi and we will try to reach a result
- We'll also connect the valve to the raspberry pi and we'll control it
- We will write all the writing work on the word

### 25.5.3 The code of flow meter sensor:

```
import RPi.GPIO as GPIO
import time, sys

FLOW_SENSOR = 23

GPIO.setmode(GPIO.BCM)
GPIO.setup(FLOW_SENSOR, GPIO.IN, pull_up_down = GPIO.PUD_UP)

global count
count = 0

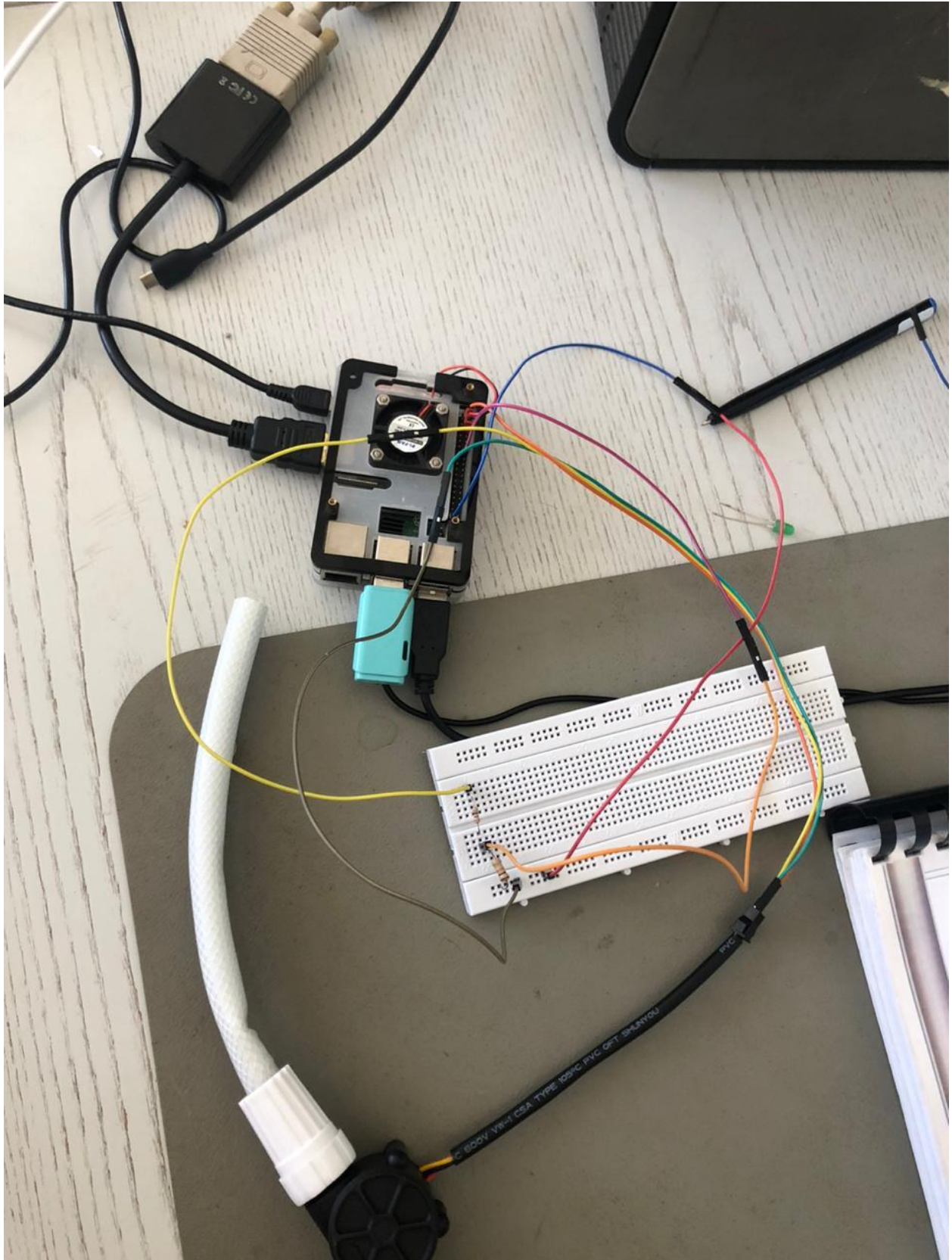
def countPulse(channel):
    global count
    if start_counter == 1:
        count = count+1
    #     print count
    #     flow = count / (60 * 7.5)
    #     print(flow)

GPIO.add_event_detect(FLOW_SENSOR, GPIO.FALLING, callback=countPulse)

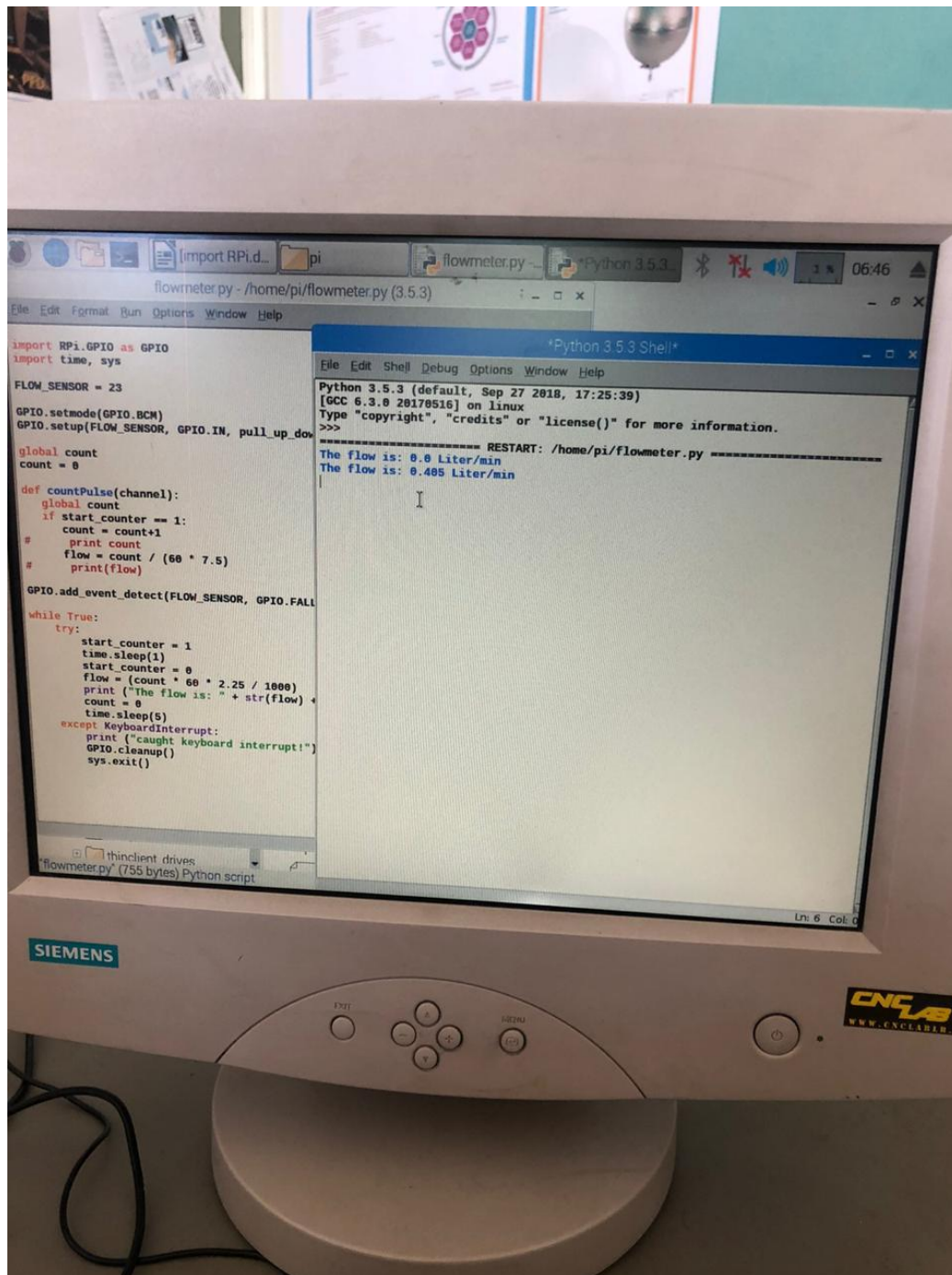
while True:
    try:
        start_counter = 1
        time.sleep(1)
        start_counter = 0
        flow = (count * 60 * 2.25 / 1000)
        print "The flow is: %.3f Liter/min" % (flow)
        count = 0
        time.sleep(5)
    except KeyboardInterrupt:
        print '\ncaught keyboard interrupt!, bye'
        GPIO.cleanup()
        sys.exit()
```

### 25.5.4 Hardware for flowmeter sensor: new RaspberryPi

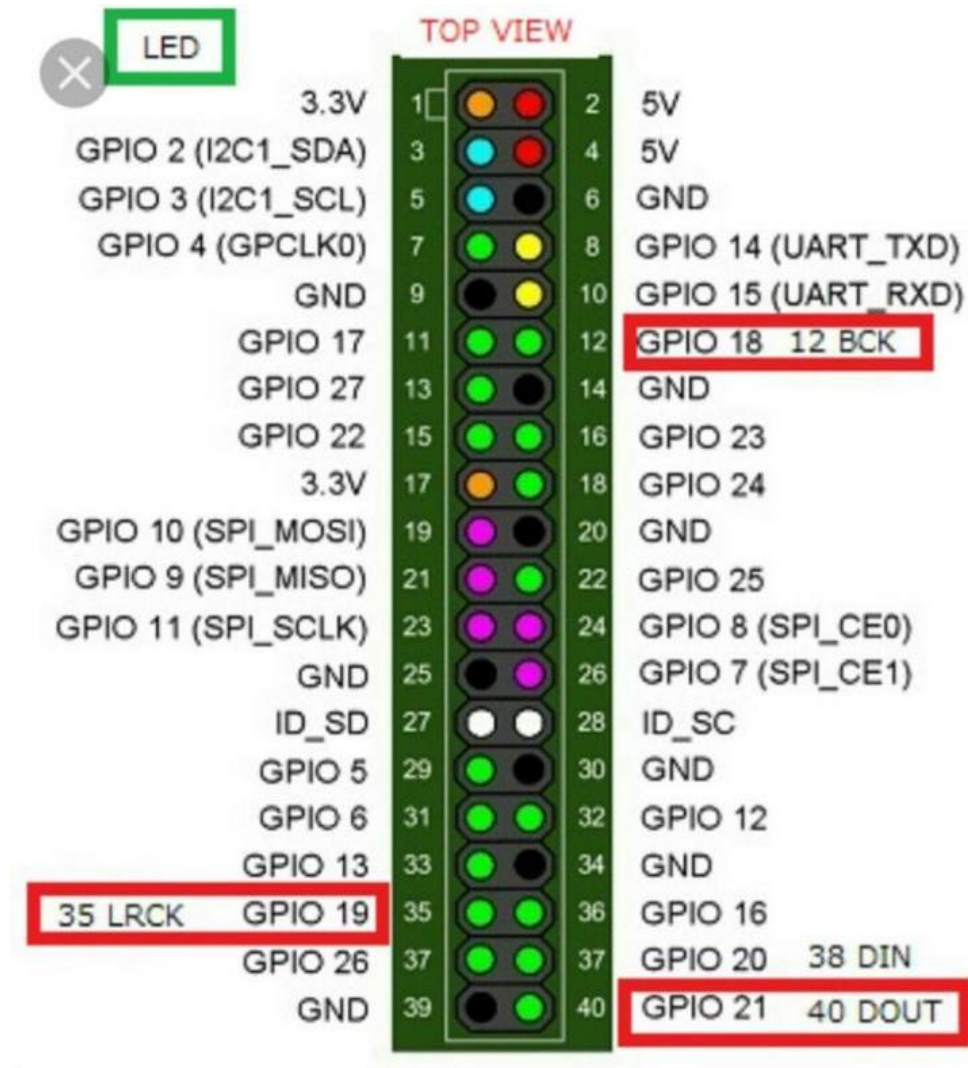




### 25.5.5 Test Results



## 25.5.6 Pins of raspberry pi 3:



## 25.5.7 The code of servo motor (Servo Motor driven Automatic Valve instead of soleonid valve)

```
# Import libraries
import RPi.GPIO as GPIO
import time

# Set GPIO numbering mode
GPIO.setmode(GPIO.BOARD)

# Set pin 11 as an output, and set servol as pin 11 as PWM
GPIO.setup(11,GPIO.OUT)
servol = GPIO.PWM(11,50) # Note 11 is pin, 50 = 50Hz pulse

#start PWM running, but with value of 0 (pulse off)
servol.start(0)
print ("Waiting for 2 seconds")
time.sleep(2)

#Let's move the servo!
print ("Rotating 180 degrees in 10 steps")

# Define variable duty
duty = 2

# Loop for duty values from 2 to 12 (0 to 180 degrees)
```

```
while duty <= 12:
    servol.ChangeDutyCycle(duty)
    time.sleep(1)
    duty = duty + 1

# Wait a couple of seconds
time.sleep(2)

# Turn back to 90 degrees
print ("Turning back to 90 degrees for 2 seconds")
servol.ChangeDutyCycle(7)
time.sleep(2)

#turn back to 0 degrees
print ("Turning back to 0 degrees")
servol.ChangeDutyCycle(2)
time.sleep(0.5)
servol.ChangeDutyCycle(0)

#Clean things up at the end
servol.stop()
GPIO.cleanup()
print ("Goodbye")
```

### 25.5.8 Valve





### 25.5.9 Mixing Control Testing Algorithm (Valve is moving according to flow sensor)

```
# Import libraries
import RPi.GPIO as GPIO
import time, sys

FLOW_SENSOR = 23
SERVO = 11

# Set GPIO numbering mode
GPIO.setmode(GPIO.BCM)

# Set pin 23 as input for the flow sensor
# Set pin 11 as an output, and set servol as pin 11 as PWM
GPIO.setup(FLOW_SENSOR, GPIO.IN, pull_up_down = GPIO.PUD_UP)
GPIO.setup(SERVO, GPIO.OUT)

global count
count = 0
start_counter = 0

def countPulse(channel):
    global count
    if start_counter == 1:
        count = count+1
    #    print count
    flow = count / (60 * 7.5)
    #    print(flow)

servol = GPIO.PWM(11,50) # Note 11 is pin, 50 = 50Hz pulse

GPIO.add_event_detect(FLOW_SENSOR, GPIO.FALLING, callback=countPulse)

#start PWM running, but with value of 0 (pulse off)
servol.start(0)
print ("Waiting for 2 seconds")
time.sleep(2)

#Let's move the servo!
print ("Rotating 180 degrees in 10 steps")

# Define variable duty
duty = 2

# Loop for duty values from 2 to 12 (0 to 180 degrees)
while duty <= 12:
    servol.ChangeDutyCycle(duty)
    time.sleep(1)
    duty = duty + 1

# Wait a couple of seconds
time.sleep(2)

# Turn back to 90 degrees
print ("Turning back to 90 degrees for 2 seconds")
servol.ChangeDutyCycle(7)
time.sleep(2)

#turn back to 0 degrees
print ("Turning back to 0 degrees")
```

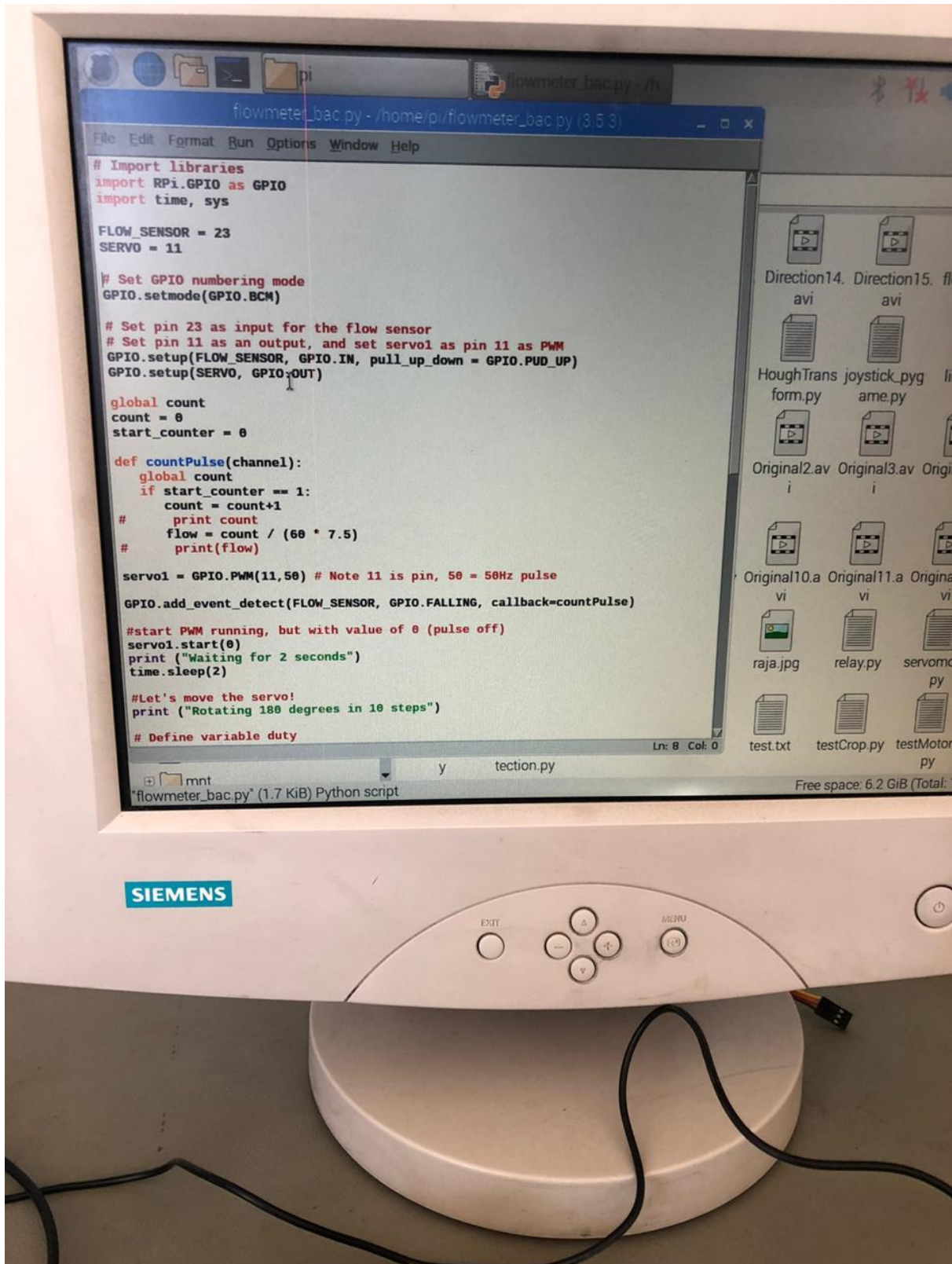
```
servo1.ChangeDutyCycle(2)
time.sleep(0.5)
servo1.ChangeDutyCycle(0)
time.sleep(2)

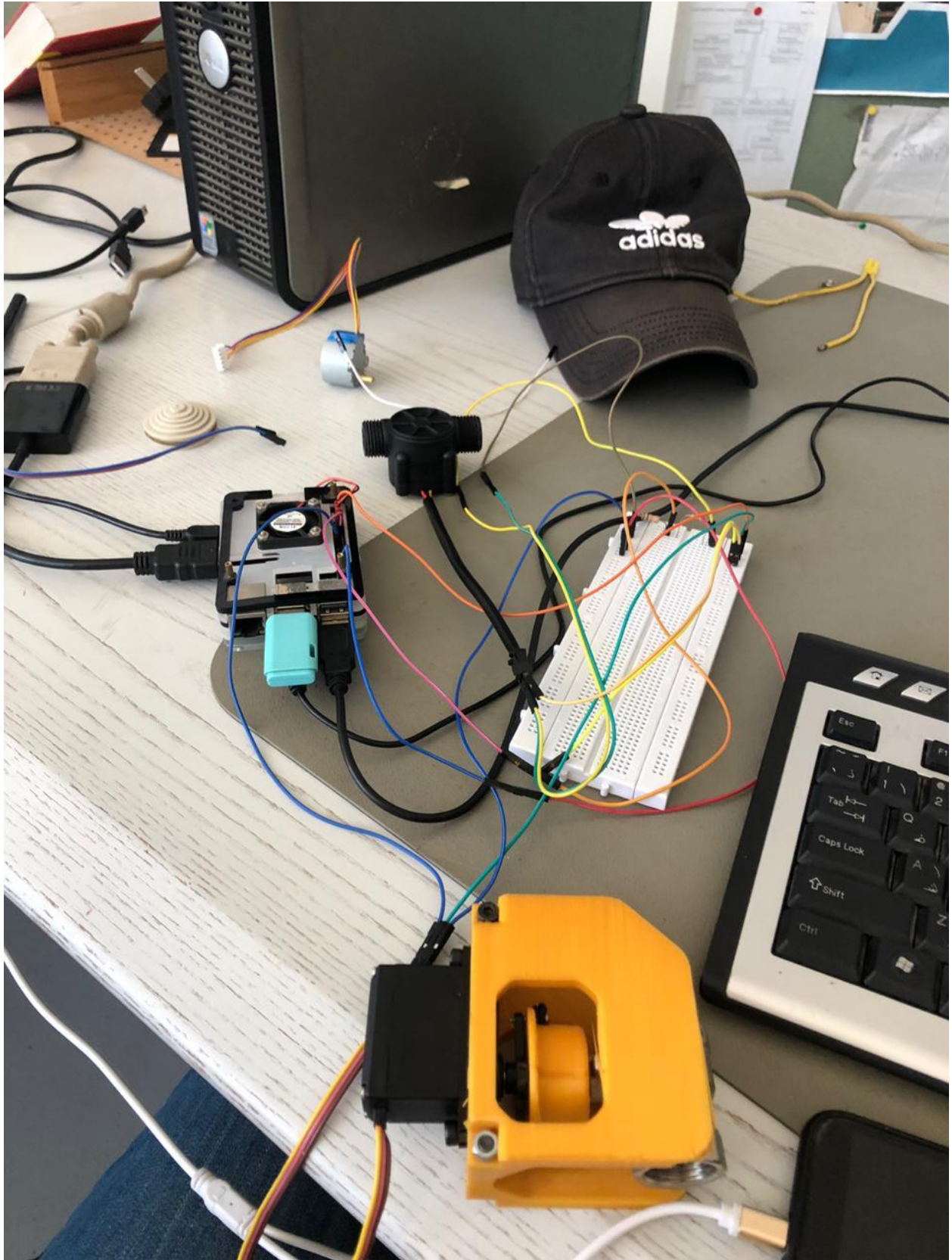
while True:
    try:
        start_counter = 1
        time.sleep(1)
        start_counter = 0
        flow = (count * 60 * 2.25 / 1000)
        print ("The flow is: " + str(flow) + " Liter/min" )
        count = 0
        time.sleep(2)
    except KeyboardInterrupt:
        servo1.stop()
        print ("caught keyboard interrupt!")
        GPIO.cleanup()
        print ("Goodbye")
        sys.exit()
```

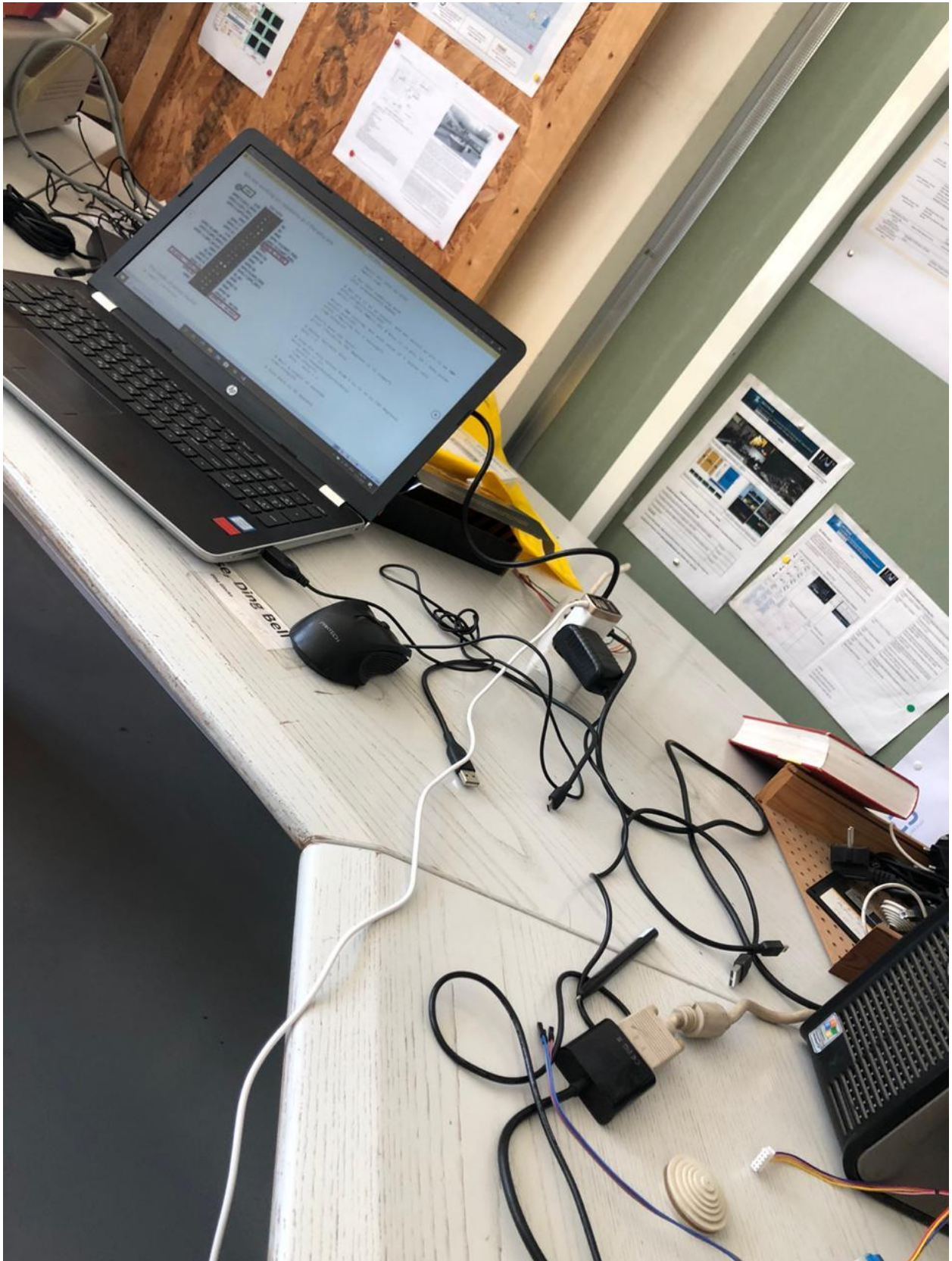
### **25.5.9.1 References of control DC motor:**

<https://www.aranacorp.com/en/control-a-dc-motor-with-raspberry-pi/>

25.5.10 Hardware of servo motor and flow sensor

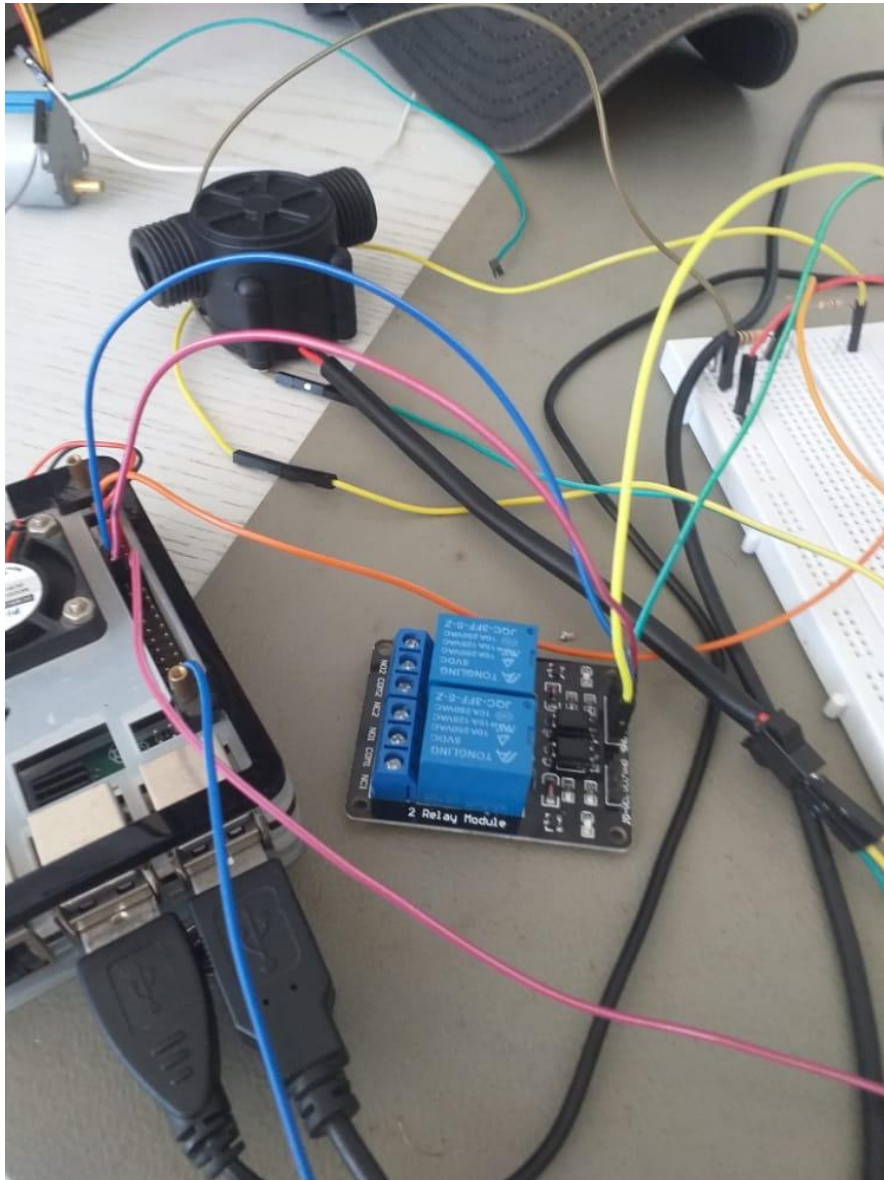


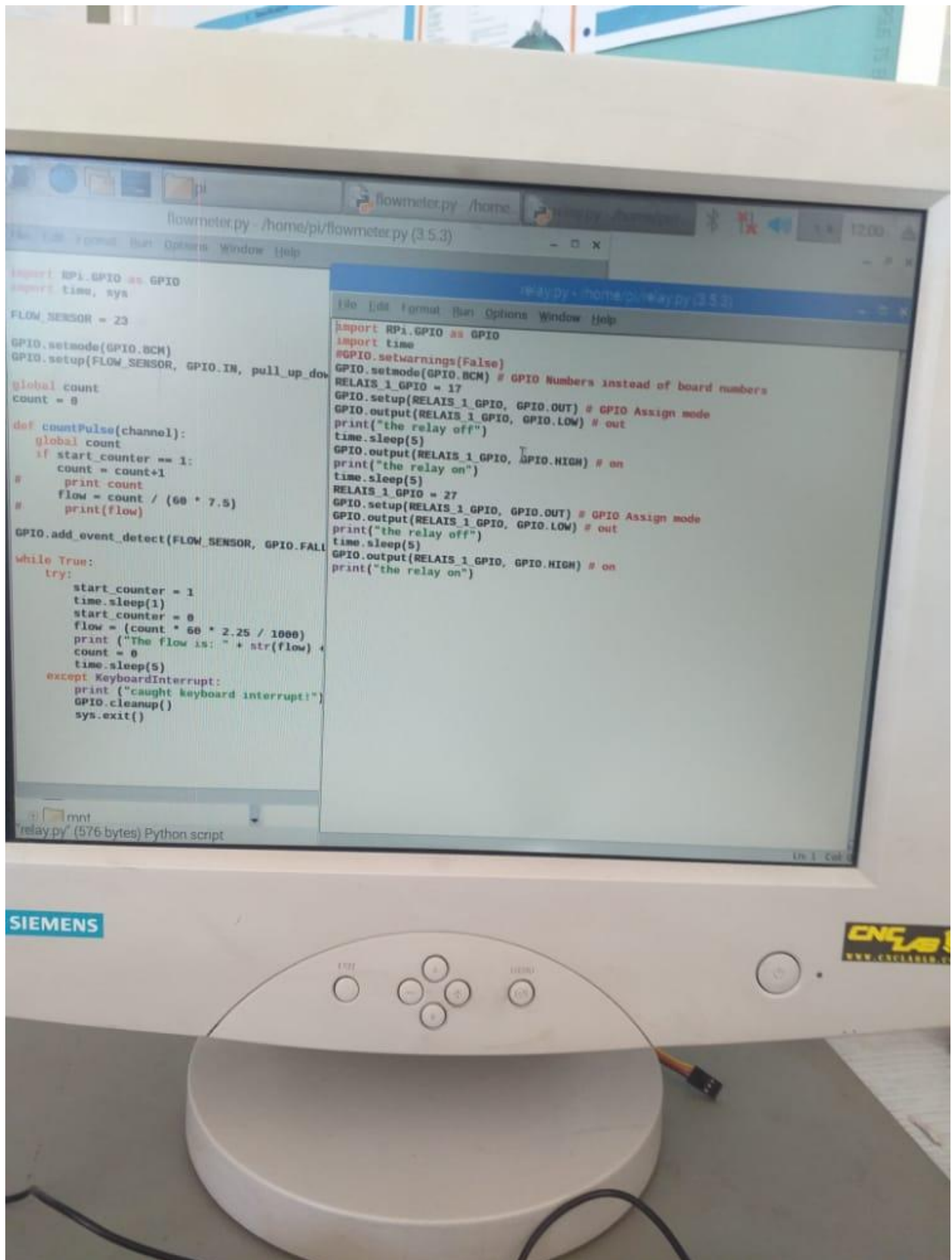




**25.5.11 Hardware of on/off relay**

Because the valve has two directions of moving (1. opening 2. closing) a H bridge is needed  
When the valve open





## Electrical Propulsion Unit

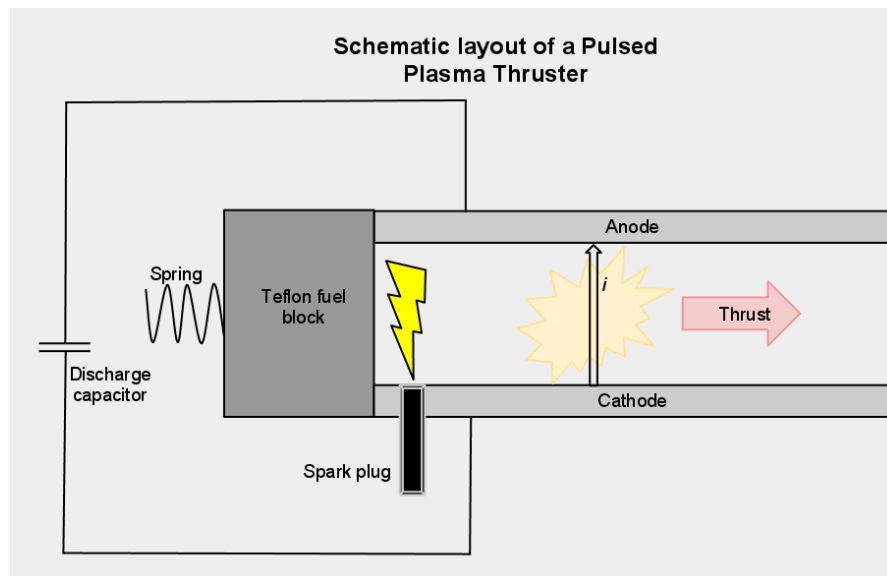
## 26 Concept for the Electrical Propulsion Unit<sup>40</sup>

### 26.1 Primitively modeling the chosen Pulsed Plasma Thruster (PPT)

Amongst all the inspected Propulsion systems, PPT was chosen and it had to be designed on FreeCad.

PPT's working mechanism was carefully studied and its different components were identified.

The primitive 2D sketch that our design depends on is below.



The components necessary for the PPT are:

- Parallel anode/cathode plates
- Spark igniter
- Teflon circular block
- Spring system
- High voltage capacitor

**Mechanism:** The first step of PPT mechanism is plasma formation. An igniter directed to the solid fuel bar produces a spark that ablates and sublimates the surface of the propellant forming plasma. Since the plasma is positively charged, it completes the circuit between the 2 plates. The interaction between the formed electric and magnetic field produces a Lorentz force that acts on the plasma and accelerates it out of the exhaust at high speeds.

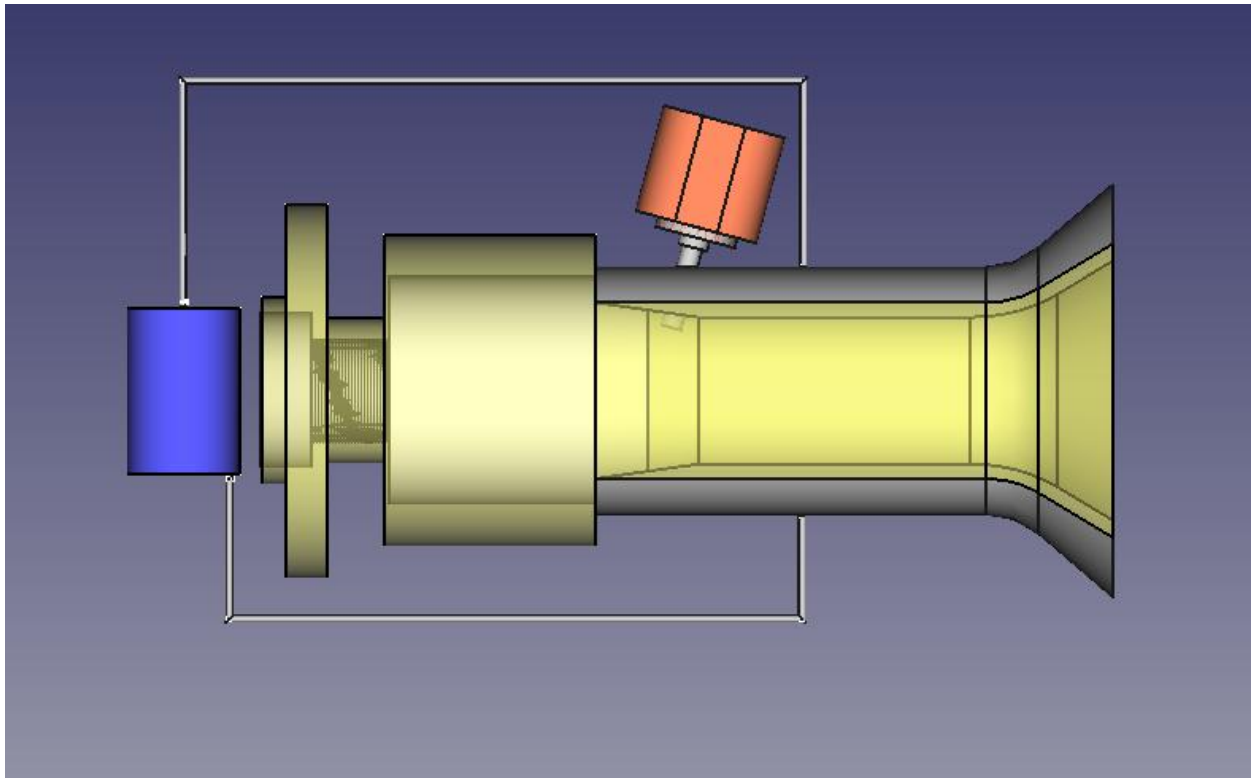
### 26.2 Modeling our PPT design in FreeCad

After identifying the different components of our PPT system and taking into consideration its working mechanism, the propulsion system was modelled on FreeCad.

The following is the FreeCad model of the PPT:

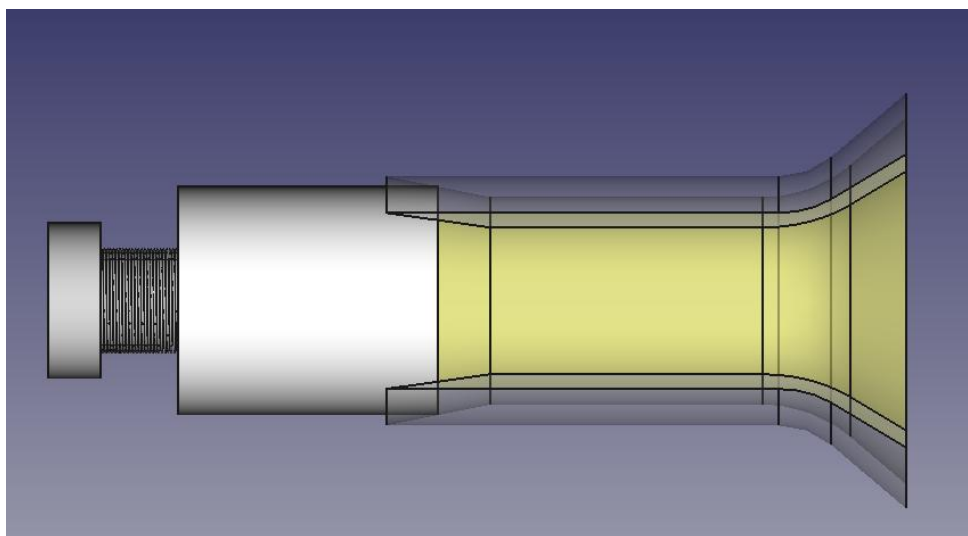
---

<sup>40</sup> From Ibrahim Ghanim, Practical Work at AECENAR Ras Nhache, July/August 2015



### 26.2.1 Modelling “fuel continues supplying system”

Most of propulsion systems use fluid fuel which its supply is easily provided by maintaining a pressure difference between the fuel reservoir and the ionization chamber. However pulsed plasma thrusters use solid fuel, that’s why its continuous fuel supply was insured by a spring system mounted on the fuel rod.

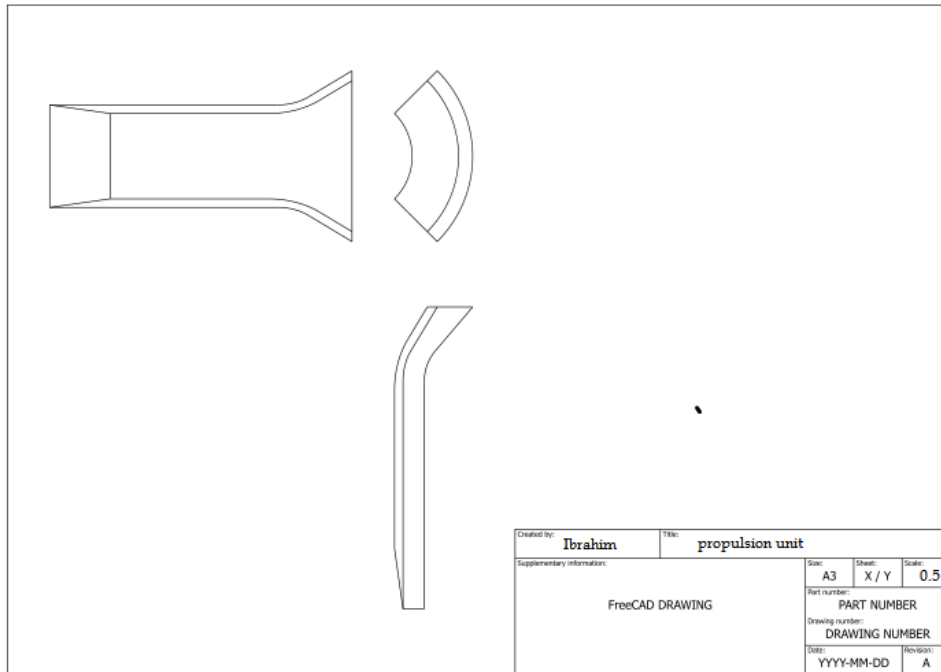


The propulsion unit is designed with a cone shaped ending such that its outer nozzle is slightly larger than the fuel rod and its inner nozzle is smaller than the fuel rod. A compressed spring is mounted to the end of the fuel rod such that the rod is always under pushing force. When the igniter produces a spark and the outer surface of the fuel rod gets

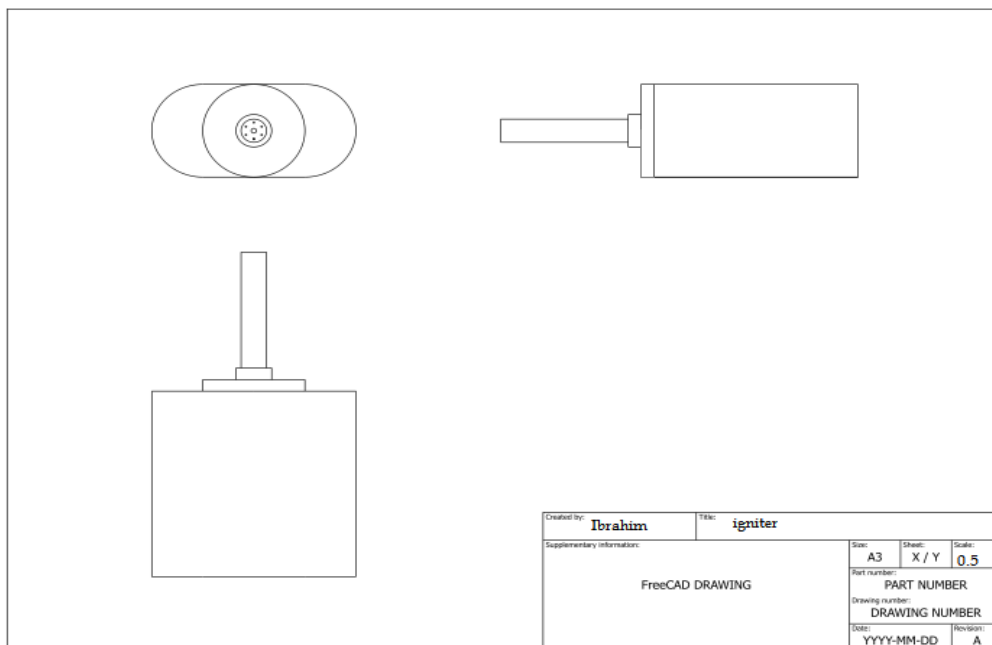
ablated and sublimated, the spring system pushes the rod inward such that it returns to its previous position in the propulsion unit.

### 26.2.2 2D projections of important parts of the propulsion system

#### 1) Propulsion unit



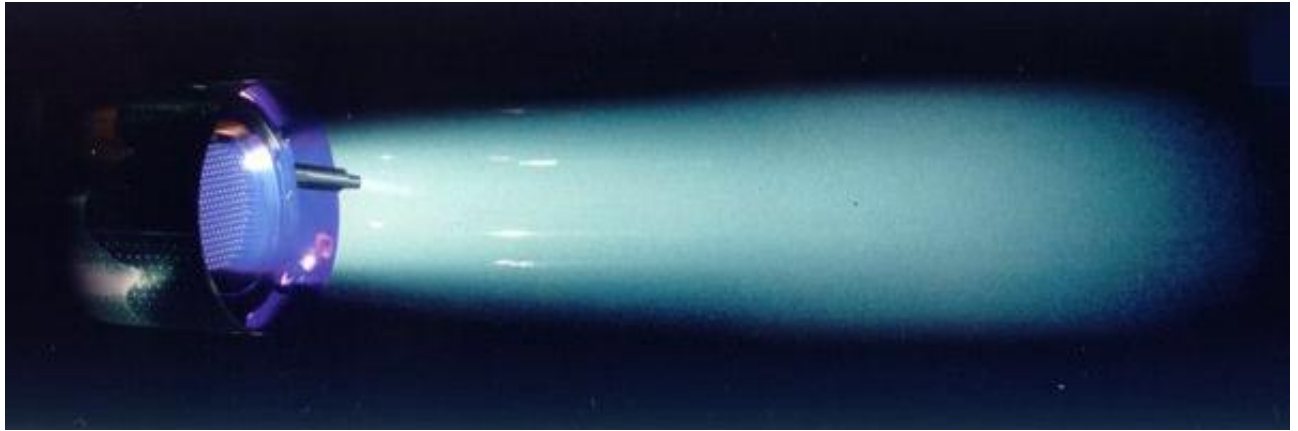
#### 2) Igniter



## 27 PPT Electrical Propulsion Unit

### 27.1 Concept for the Electrical Propulsion Unit

See IAP-SAT Report 3 (2015)



Änderung: Eigenfeldantrieb (PPT oder PTT) statt Ionenantrieb; da wir damit schon in einer früheren Studie begonnen haben.

### 27.2 Eigenfeldantrieb (PPT)

Betriebszustand: stationär gepulst

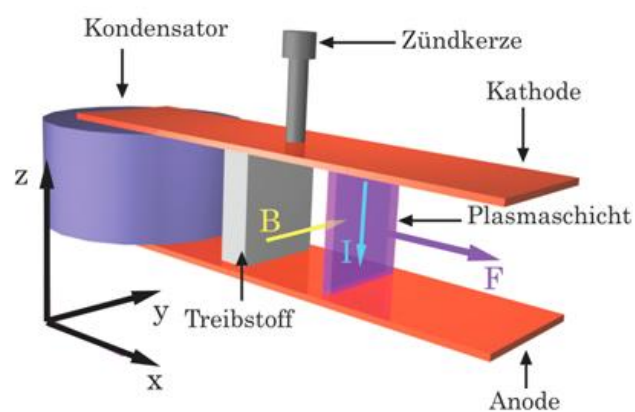
Treibstoffe: Gase, Teflon

Ionisationsgrad: 0.5-1

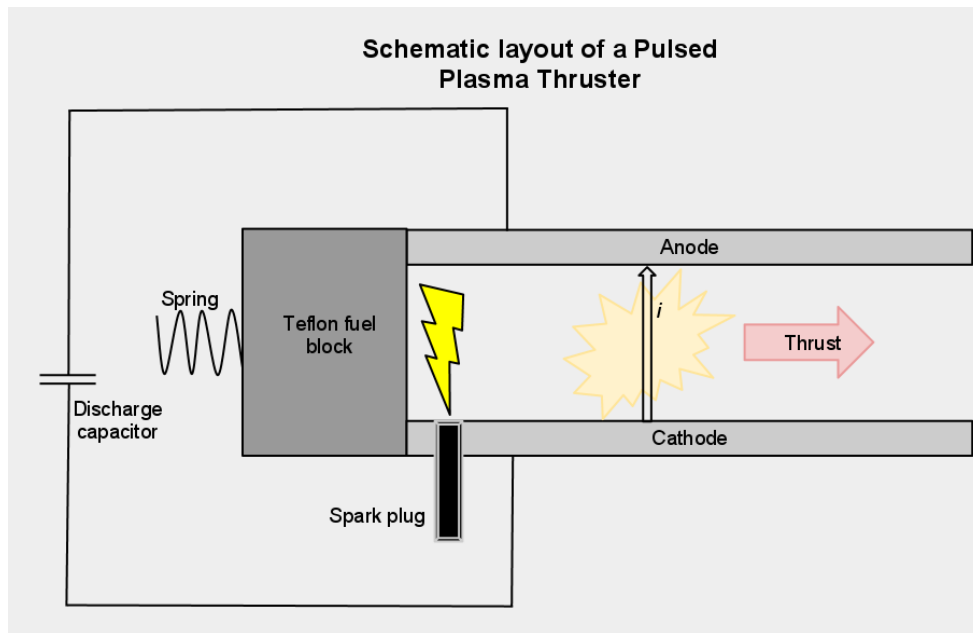
(T.6.1 aus Raumfahrtsysteme)

### 27.3 Gepulstes Plasmatriebwerk

#### 27.3.1 Prinzip:



Funktionsprinzip des gepulsten Plasmatriebwerks



$$F = - (p_0 A_t c_{FeI} + \mu_0 / (4\pi) I^2 (3/4 + \ln(r_a / r_k))) e_z$$

$$F = I \times B$$

$A_t$  : Düsenhalsquerschnitt

$\mu_0$  : magnetische Feldkonstante

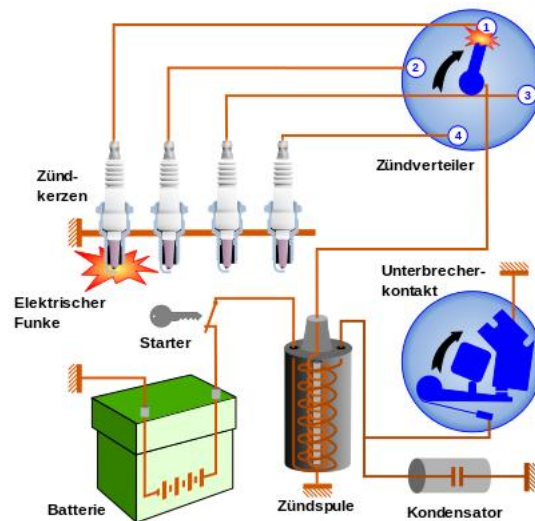
$c_{FeI}$  : Schubkoeffizient

$r_a$  : Anodenradius: groß

$r_k$  : Kathodenradius: fest

Treibstoff: Teflon: fest. Spart Behälter und weitere Komplikationen wie z.B Temperaturerhaltung.

Zünder:



Die Solarplatten versorgen den Zünder-Schaltkreis mit Gleichstrom.

Der Unterbrecherkontakt sorgt für alternativen Strom. Der ist notwendig um mit der Zündspule, die die Rolle eines Transformators spielt, die Spannung zu erhöhen.

Der Zündkondensator hat meistens  $0.22 \mu\text{F}$ .

Kondensator:

bei Zündung auf 500 V aufladen

$$V = Z_c I$$

$$Z_c = 1 / (j C \omega) \Rightarrow C = 1 / (j Z_c \omega) = 1 / (j (V/I) 2 \pi f)$$

$$\omega = 2 \pi f$$

circuit 1

4 thrusters

\*En but de chercher la valeur du condensateur, on prends par hypothèse que:

Force  $F = 860 \mu\text{N}$

Vitesse  $v = 13.7 \text{m/s}$

Puissance  $P = 70\text{W}$

On a :  $P = U \cdot I^2$  ;  $I = (P/U)^{1/2} = (70/500)^{1/2} = 0.374\text{ A}$

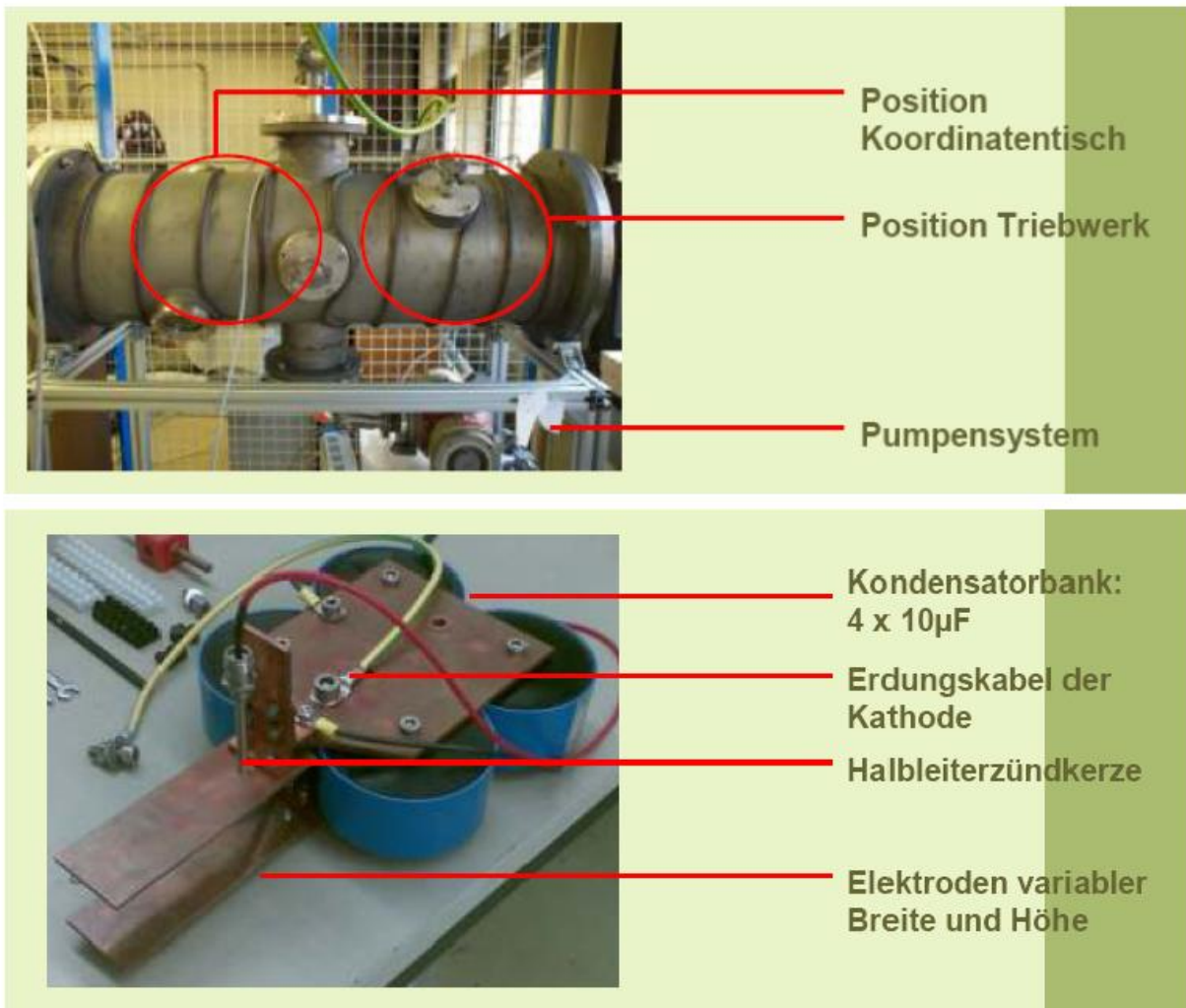
$I = q \cdot U$  ;  $q = I/U = 0.374/500 = 0.027\text{ C}$

$F = q \cdot v \wedge B = i \wedge B = i \cdot B \cdot \sin(i, B) = i \cdot B$  ;  $B = F/i = (860 \cdot 10^{-6})/0.374 = 2.299 \cdot 10^{-3}\text{ T}$

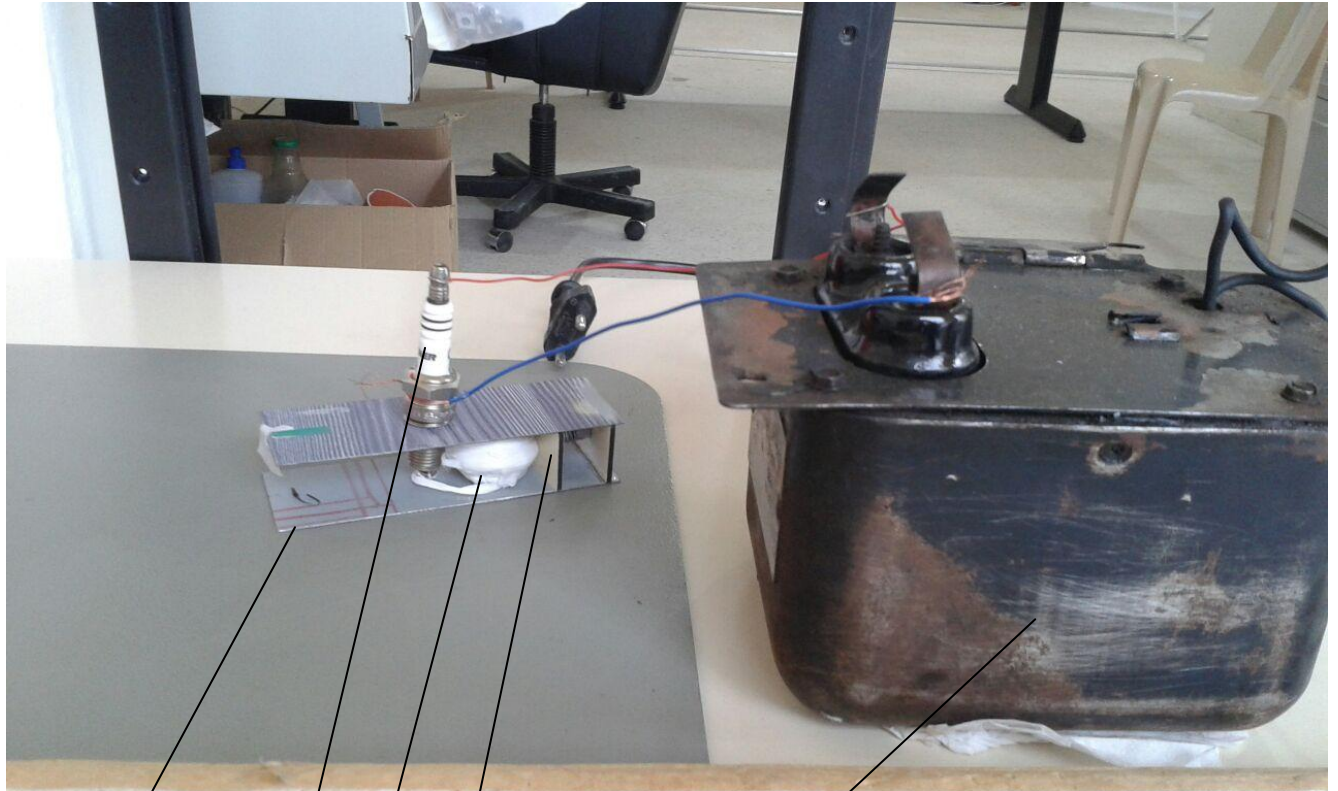
$q = C \cdot U$  ;  $C = q/U = 0.027/500 = 54\ \mu\text{F}$

## 27.4 Test Environment for Electrical Propulsion (from [Böhrk et. al. 2007])

From [Böhrk et. al. 2007]:



## 27.5 Realization



Aluminium

Teflon

Plastic (Isolator)

spark plug

Transformer

## 28 Electrical Propulsion Test Rig



AECENAR

بسم الله الرحمن الرحيم  
Association for Economical and Technological Cooperation  
in the Euro-Asian and North-African Region

IAP  
INSTITUTE FOR  
ASTROPHYSICS

## محطة تجريبية للدفع الالكتروني

Project of IAP institute by AECENAR

**الهدف:** عندما يكون القمر الاصطناعي في الفضاء، يحتاج إلى آلية تثبت و تصحح مساره. نستخدم لذلك الدفع الالكتروني، الذي لا يعمل إلا في غرفة فراغ. لدراسة فعاليته نحتاج لمنظومة من العدادات الكاشفة.

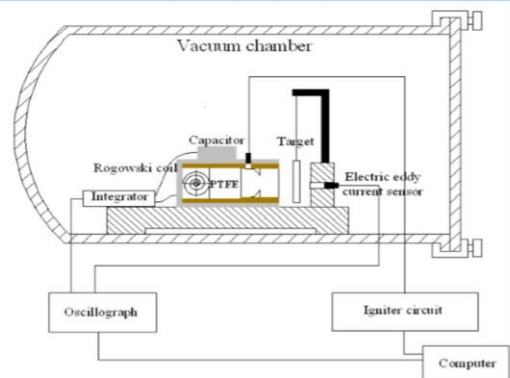
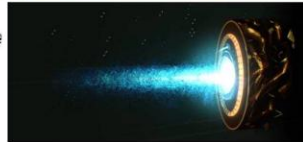


Figure 4. Schematic diagram of the experimental system

PPT

يتميز الPPT عن سائر منظومات الدفع الالكتروني بأنه سهل التصنيع ومثين فلا يتأثر كثيراً بالتصادمات الحاصلة في الفضاء.

### الدفع الالكتروني



Pulsed  
Plasma  
Thruster

يتميز الدفع الالكتروني عن الدفع الكيميائي بأنه خفيف الوزن، لا يلوث، يمكن استخدامه لمدة طويلة في الفضاء (10 سنين)

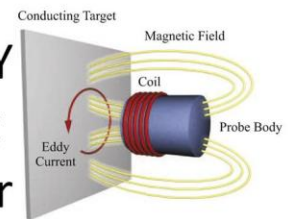
### غرفة فراغ



تضيق الجزينيات في الهواء فلا تعطي مفعولها و لا نستطيع أن نقيسها، و في حالتنا لا يتكون البلازما من الأصل إلا في غرفة فراغ شبه تام.

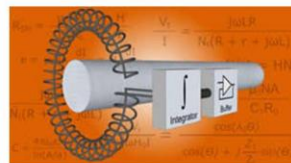
### عداد كاشف

EDDY  
current  
sensor



يقوم الECS بقياس فرق المسافة بين الtarget و الProbe الذي نشأ بتصادم البلازما بالهدف.

### ROGOWSKI coil



يقيس الRC التيار (current) العائد بعد عملية الدفع.

AECENAR - IAP

www.aecenar.com/institutes/iap

## 29 Electric-Propulsion Test stand (Concept, Design, Manufacturing)

### 29.1 Basics

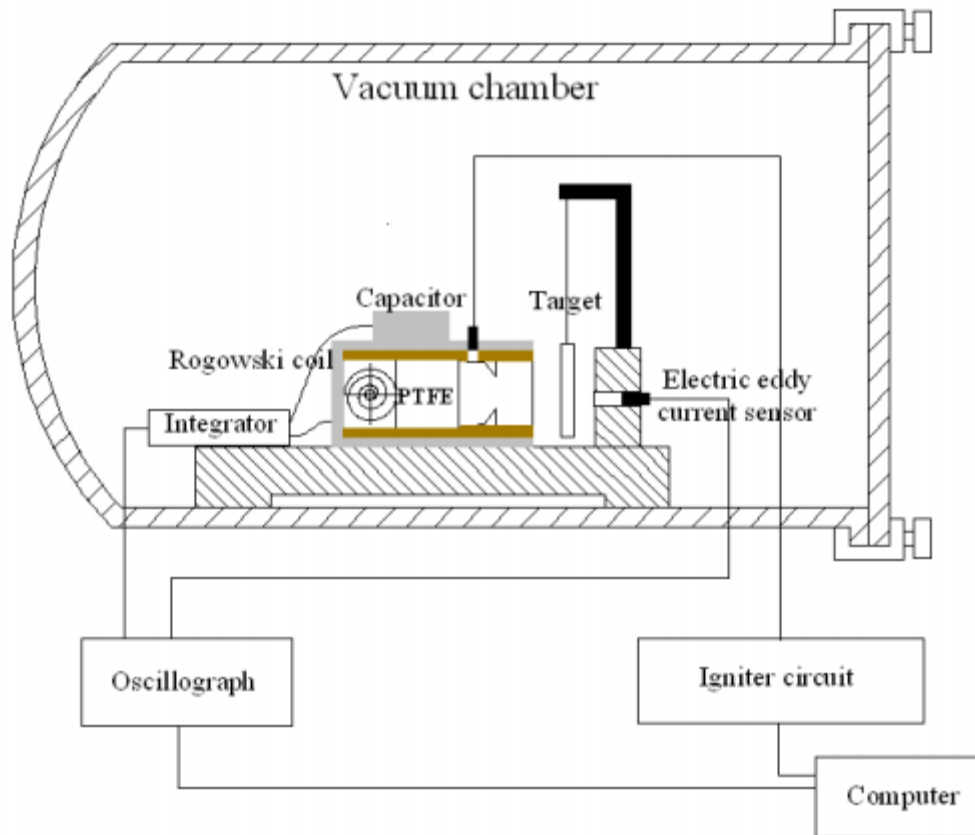


**Figure 4. Schematic diagram of the experimental system**

#### 29.1.1 Vacuum Chamber Technology

All experiments were performed in the vacuum chamber (1 m diam., 1.8 m length) with two turbomolecular pumping systems ( 2,000 L/s  $\times$  2 EA ), a mechanical booster pumping system and a rotary pumping system. Its degree of vacuum was maintained in the range of  $10^{-4}$  Pa ( $10^{-6}$ Torr) during each PPT operation.

##### 29.1.1.1 Choosing the Right Vacuum Materials

A Journal of From Practical and Useful Vacuum Technology

By Phil Danielson

An in-depth review of each and every material exposed to the vacuum system is absolutely essential to ensure a successful system design.

It's no secret to its practitioners that vacuum technology is a demanding discipline. The technology is unforgiving to the point that you can do almost everything right, but if you make one mistake, the chamber might not pump down to it's required level. This means that a lot of decisions need to be made. Crucial decisions. When you consider that the total complexity of a vacuum system is greater than the sum of the complexity of its parts, the

message comes home to you in dire clarity. Each part interacts with every other part, and that's why a mistake can kill the project. Worse yet, a few really small mistakes can be worse than one big one. Although this can be daunting, it's not really as daunting as it sounds.

A little detailed thinking within the basic vacuum relationship  $Q$  (Gas Load) =  $S$  (Pumping Speed)  $\times$   $P$  (Pressure) will provide the guidance and technique. A low value for  $Q$  will result in a lower  $P$  with any given  $S$ . If, then, we try to keep the total gas load as low as possible, we have to realize that the most important gas load(s) in most vacuum systems emanate from the materials exposed to the vacuum. The gas within the chamber prior to pumpdown has to be removed of course, but this is a much simpler process than dealing with the gas from the materials. All engineering solutions are a series of successive compromises, and the choice of vacuum materials is no exception. Choosing the materials to use in a vacuum system design is not just a case of finding the materials with the lowest gas loads, but to also consider the various physical or chemical properties that will fulfill the process's requirements.

<b>Approximate outgassing rates to use for choosing vacuum materials or calculating gas loads</b>	
<i>(All rates are for 1 hour of pumping)</i>	
<b>Vacuum Material</b>	<b>Outgassing Rate</b> <i>(torr liter/sec/cm<sup>2</sup>)</i>
Stainless Steel	$6 \times 10^{-9}$
Aluminum	$7 \times 10^{-9}$
Mild Steel	$5 \times 10^{-6}$
Brass	$4 \times 10^{-6}$
High Density Ceramic	$3 \times 10^{-9}$
Pyrex	$8 \times 10^{-9}$
<b>Vacuum Material</b>	<b>Outgassing Rate</b> <i>(torr liter/sec/linear cm)</i>
Viton (Unbaked)	$8 \times 10^{-7}$
Viton (Baked)	$4 \times 10^{-8}$

The universal materials problem that runs through any and all vacuum technology is the vacuum chamber itself. The material(s) of construction is required to provide as little gas load as possible while still being strong enough to withstand the forces exerted by the external atmospheric pressure. The strength issue is easily dealt with by making the walls thick enough or by adding additional bracing or supports either internally or externally, but the main problem is found in assessing the possible gas loads. Chambers are commonly constructed of metals, glasses, ceramics, or plastics. All of these materials have in common consideration that the internal surfaces will be covered with layers of sorbed water molecules which will have to be desorbed during the pumpdown. Since most of the water molecules are sticking to themselves in a bed, the base material doesn't matter very much

until enough water has desorbed to leave only a single monolayer on the surface. At this point, things change. You need a material that doesn't bond too strongly to the water molecules. This starts ruling out a lot of plastic materials, but more importantly, you have to start thinking about gas coming out of the material's bulk. This, along with surface desorption, is what we call outgassing. Coupled to this effect is permeation of gases from the atmosphere through the chamber's walls, and this includes sealant and/or gasket materials such as elastomer O-rings.

Other than the consideration of strength and permeation, the same criteria should be applied to any material exposed to the vacuum. Permeation occurs with most materials, but is often too small an effect to be of concern. For example, the small amount of atmospheric helium that permeates into Pyrex bell jar through the glass's tiny micropores is too small to be of concern at  $10^{-6}$  -  $10^{-7}$  torr, but might be a real problem in a Pyrex system that is expected to operate at  $10^{-11}$  torr. In general, though, we can look at materials exposed to the vacuum by mainly assessing the outgassing rate. Additionally, gas loads can arise by vaporization of the material itself or from components of the material. High vapor pressure materials are an obvious problem in terms of contamination of the vacuum space or the process.

Metals are arguably the most prevalent vacuum chamber materials, with stainless steel (SS) far ahead of other metals such as mild steel (MS) or aluminum (Al) alloys. Since MS is usually used only for systems that require moderate vacuums above 10<sup>6</sup> torr, it would seem that a choice between SS or Al would be sufficient, but this is only the beginning of the selection process. For example, deciding to use SS doesn't mean any and all SS alloys. Free-machining alloys such as 303 SS contain sulfur (S), but the vapor pressure of the S is too high for high vacuum systems. 304 SS, though, is the most common choice. This helps narrow things down, but ultrahigh vacuum (UHV) usually requires the low-carbon 304L alloy. What we're describing here is the process of picking down through the layers to merely define the overall description of the material, but we have to get deeper yet. The final choice of material will also depend upon the surface finish to minimize surface area with its resultant lowest desorption rate per unit area. Then the surface cleaning

needs to be evaluated to ensure that organic contamination is removed and that no porous welding scale remains. All of this seemingly tiresome detail work is absolutely required to assure that the minimum gas load is presented by the material. For example, if Al had been chosen, you'd have to make sure the surface hadn't been anodized since the oxide film absorbs large quantities of water vapor and then slowly desorbs them into the vacuum space.

Sealing materials and gaskets are another extremely important consideration. Total gas loads emanating from elastomer O-rings can be greater than those from the chamber's surface. So,

if you're going to use O-ring seals, you have to do everything possible to reduce the gas loads. This means using vacuum-baked Orings that have been carefully handled with lint-free gloves and haven't been solvent cleaned since the solvents are absorbed and cause swelling. Swelling increases outgassing and atmospheric permeation. When analyzing the expected gas loads, then, it might be feasible to consider using metal gaskets and avoiding the O-ring's gas loads entirely.

There are a number of other materials that will probably be used in a vacuum system for very specific applications that are process dependent. This overall category includes ceramics and glasses that might be used as thermal or electrical insulators, components of internal arrays, or even plastic substrates. In each case, the same careful assessment is required to ensure that the gas loads are as small as possible. For example, ceramics are considered to be good vacuum materials, but only if high-density sintered materials are used. This differentiates between the insulator in a UHV-rated feedthrough and a piece of firebrick. Porous materials contain massive amounts of gas. Even normally acceptable metals such as Al need to be looked at carefully. Household Al foil is often found in systems where it is used as a chamber liner. This material is coated with peanut oil used as a lubricant in its manufacture, and it is virtually impossible to remove with solvent cleaning.

In addition to gas load effects, the physical properties of materials need consideration. Internal arrays are often assembled with SS nuts and bolts that are likely to become heated by the process. This results in extreme surface galling that can make it impossible to disassemble the pair, but a thin coating of Milk of Magnesia (unflavored)

### **QUESTIONS TO ASK YOURSELF WHEN CHOOSING VACUUM MATERIALS**

1. Have I added up the total gas loads from all the materials?
2. Have I defined each material well enough?
3. What would happen to the total gas load if I substituted for any single material?
4. Does any single material's gas load dominate over the others?
5. Have I compromised too far or too many times?
6. Am I really sure that I've looked at every material?
7. Have I made any mistakes?

brushed on the threads before assembly makes disassembly easy. Sliding surfaces can also cause galling or sticking problems with pairs such as SS-to-SS, but a coating of molybdenum disulfide can act as a vacuum-compatible lubricant. These are only a few of the many

examples of the materials problems that need to be considered, and a successful system requires a full analysis.

There are a number of materials that need to be avoided whenever possible. High vapor pressure metals can be a problem, and they can sneak in easily if close attention isn't given. Zinc and cadmium-plated nuts and bolts are a prime example. If these materials become heated during the process, they can sublime within the system to cause metallic contamination. Additionally, they can form thin oxide coatings that sorb large quantities of water vapor. The zinc content of brass is often a problem in any but the most non-stringent requirements. Any material, then, that might vaporize under vacuum needs to be treated with suspicion. This includes many plastic materials.

Although vacuum technology is unforgiving of mistakes, a careful analysis, in depth, of the materials that will be exposed to the vacuum system will help avoid those dire mistakes that can kill a design. Any process will require a number of successive compromises, but adding up the many gas loads will allow a sensible series of compromises. This is one of those cases where "the devil's in the details" really makes sense.

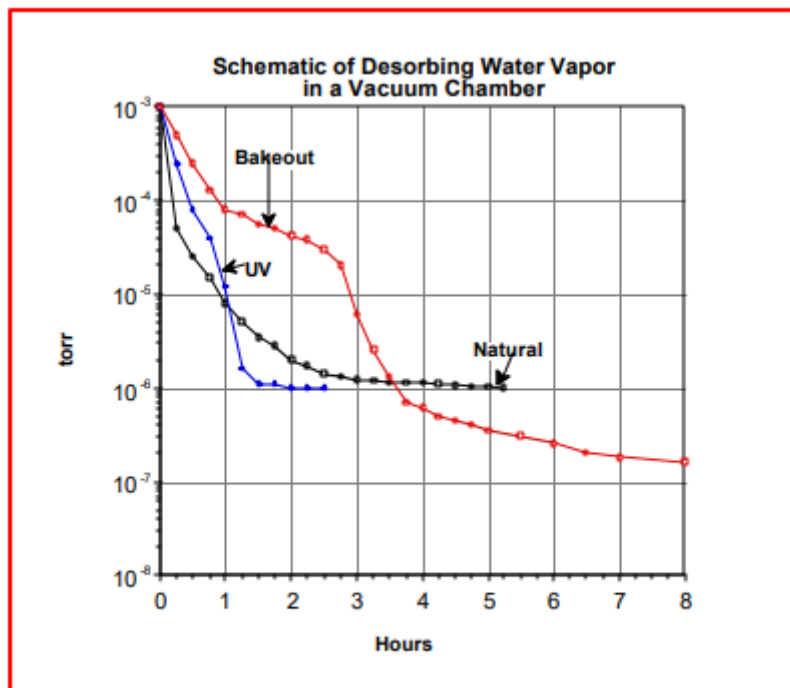
Reprinted by permission by R&D Magazine, all rights reserved. Cahners Business Information. A shorter version appeared in R&D Magazine, April 2003.

#### **29.1.1.2 Desorbing Water in Vacuum Systems: Bakeout or UV?**

Shorter pumpdown times or lower pressures can be achieved by using either bakeout or UV energy to desorb water vapor. Here's how to make the choice. Water vapor, desorbing from the internal surfaces of vacuum systems, is a problem that's common to vacuum technology as a whole. Every time a vacuum system is opened to ambient air with its attendant humidity, the internal surfaces become covered with layers upon layers of water molecules. Every item placed within a vacuum system is likewise covered with water molecules. Every pumpdown cycle from atmosphere will go through two overlapping stages. Firstly, the permanent gases making up the air mixture in the system's volume, such as nitrogen (N<sub>2</sub>) and oxygen (O<sub>2</sub>) will be pumped away. Secondly, the water molecules desorbing from the internal surfaces must be pumped away. Once the pressure is in the low millitorr range, the desorbing water makes up over 99% of the total gas load. If, for example, you turn on a residual gas analyzer (RGA) in the high 10<sup>-4</sup> torr range during a pumpdown from air, the O<sub>2</sub> and N<sub>2</sub> will drop off-scale almost immediately while the water vapor peak will seem to be fixed. Alternatively, if you pump a system down to its ultimate pressure of, say 10<sup>-6</sup> or 10<sup>-7</sup> torr, and then backfill it to atmospheric pressure with dry N<sub>2</sub>, it will pump back down to its ultimate pressure again in minutes instead of hours. This is explained by the fact that the pumpdown rate is not controlled by the amount of water vapor within the chamber but by its desorption rate from the internal surfaces. Since a certain amount of sorbed water had already been removed by the first pumpdown, the desorption rate is still at the same

lowered level it had been prior to the N<sub>2</sub> backfilling, and the low pressure equilibrium could be quickly re-established. The time vs pressure pumpdown curve, then, will be controlled by the changing desorption rate of the water molecules from the system's internal surfaces. During a pumpdown, the desorption rate will be initially high due to the fact that the last formed layers will have weaker water-to-water bonds<sup>1,2</sup> than those closer to the chamber wall. With pumping time, the desorption rate will drop lower and lower as the stronger-bonded molecules are exposed. Taking the fundamental vacuum relationship  $Q=SP$  as desorption rate = pumping speed x pressure, it is easy to see A Journal of From Practical and Useful Vacuum Technology By Phil Danielson that the desorption rate needs to fall to some given point before a given pressure can be achieved with a fixed pumping speed. The normal desorption of water vapor requires that the molecules absorb enough energy to overcome their bonds before they can desorb to be pumped away. This is usually due to thermal energy transferred from the chamber itself to the molecules. It follows, then, that if additional energy is applied to the molecules, the desorption rate can be increased while the energy is being applied. If this is done on a temporary basis during a pumpdown, a much lower final desorption rate will result when the energy source is removed, since only the more tightly bonded molecules will remain undesorbed.

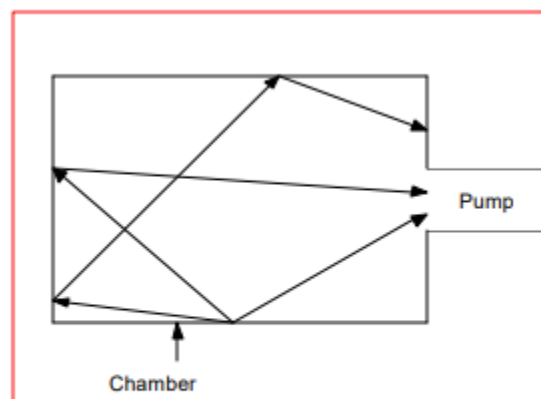
There are two efficient and effective methods of energy transfer that are commonly used: heat and ultraviolet (UV) light. Although each method has its own advantages and disadvantages, the choice of which method to use for a given application depends upon the performance goals to be achieved. In general, the goals can be simplified to two options. The goal might be to achieve a lower pressure in a given time, or it might be to achieve a given pressure in a shorter time. Both methods of energy transfer will accomplish either of these goals, but each method needs to be considered in light of the application and the system itself.



*Pumpdown performance of an O-ring sealed system showing the effects of both desorption techniques against no forced desorption.*

Bakeout is the term most commonly used to refer to the application of heat to stimulate desorption. In many minds it's associated only with ultrahigh vacuum (UHV) systems. Granted, it's pretty nigh impossible to achieve UHV without bakeout, but UHV systems have many more considerations beyond mere bakeout. The proper pumps, seals, and materials are just a few examples. Heat can be applied to almost any vacuum system to temporarily increase desorption. Heat, applied externally to the chamber, is the most common method, with heaters mechanically clamped or bolted to the outer surfaces for good thermal contact. For UHV systems, 2500 C is usually the required/recommended temperature. This temperature is high enough that Viton can't be used because it degrades rapidly at temperatures above 1800 C, and perfluoro elastomers that can withstand the temperature have too high a permeation rate<sup>3</sup>, as does Viton, to allow UHV pressures to be attained. This leaves metal gaskets as the only reasonable choice for bakeout at these temperatures. Bakeout, however, can be useful for O-ring-sealed systems that are used in the high vacuum region. The water vapor desorption rate is a function of both time and temperature. A lower temperature will just require a longer time at that temperature to provide whatever degree of diminution of the desorption rate is required by the pumpdown specifications. This means that a temperature of, say, only 1000 C will increase the desorption rate during the temperature cycle to reduce the pressure achieved in a given time than would be possible if no means of additional energy transfer were to be provided. The problem here is time. If a stainless steel chamber is heated by external heaters, the low thermal conductivity and high heat capacity of the stainless steel will greatly lengthen the

time between application of heat to the thermal energy reaching the sorbed water vapor inside the chamber. Conversely, the time to cool will be long as well. If, as in most practical vacuum systems, there are internal arrays, the heat has to be transferred through some solid connection with the heated wall. This can require very long time periods. The time lag problem disappears, in a practical sense, if aluminum chambers are used since aluminum has a very high thermal conductivity. One way around the time lag problem is to heat the inside of the chamber with infrared (IR) bulbs mounted inside the chamber. UHV compatible IR bakeout systems are commercially available. UV energy avoids some of the problems of thermal energy. A UV bulb(s), mounted within a chamber will transfer energy to the sorbed water molecules if the bulb emits the correct wavelength<sup>4</sup> of UV light. If you think of spectroscopy, the mechanism for energy transfer is fairly simple. Specific molecules will absorb specific wavelengths of light. The sorbed water molecules will absorb the UV light until they become sufficiently excited to overcome the water-to-water bonds and desorb. The UV light is reflected internally enough that line-of-sight exposure is not required. UV excitation is a very efficient method of energy transfer since the energy is absorbed directly by the water molecule and only negligible amounts of heat are radiated. A pumpdown time can usually be cut in half if only a total UV energy 2.5 mw/in.<sup>2</sup> of chamber surface area is provided while doubling the energy to 5 mw/in.<sup>2</sup> can usually cut the time to one-third.



*Behavior possibilities of a desorbing water vapor molecule showing the statistical chance of re-sorbing or entering the pump.*

Choosing the best method for a given application requires an understanding of the behavior of desorbed water molecules. A water molecule, once desorbed, will not necessarily be pumped away. Although a desorbed molecule might enter the pump, it's more likely that it will impinge upon another spot in the chamber. When it impinges, it might resorb or it might merely bounce. This results in a chaotic condition of molecules desorbing, re-sorbing, and generally moving around within the chamber until they finally wander into the pump. If thermal desorption is being used, the higher temperature of the chamber will reduce the amount of re-sorption and increase the chances of a molecule entering the pump. If, though, the chamber is not heated isothermally where the temperature is not constant throughout, the molecules will tend to selectively re-sorb on colder spots. Upon cooling the chamber, the previously colder spots will become an enhanced source of water vapor. Although this problem is avoided with UV energy which will flood the whole chamber, the UV energy will

not penetrate into the trapped volume of virtual leaks or reach the surfaces of O-rings recessed between flanges. Thermal energy, though, will tend to drive water vapor out of these sources. Another major difference to consider is the fact that UV energy is only useable on surfaces. If a "gassy" material needs to be placed within a chamber that's either hygroscopic or porous, UV energy will only desorb water from the material's surface while thermal energy will drive it out of the material's bulk. This means that UV energy will effectively desorb the water from the surface, but that water will then diffuse out of the bulk to the surface and cause continual desorption. The specific application will then help make the choice between the two methods of energy transfer. A batch system that is continually cycled from air-to-high vacuum will probably be better served by UV desorption since the pumpdown time can be shortened enough to provide many more product runs per day. A system, sealed with Viton O-rings, could have the pumpdown time reduced by 1/2 to 2/3 of the time usually required to achieve a given pressure. The same amount of UV energy could also achieve about a decade lower pressure in the same amount of time as is usually required. The resultant pressure could be even lower if vacuum pre-baked Orings were used. Systems and applications that require UHV pressures will require thermal energy at temperatures too high for O-rings so metal gaskets will be required, and the inability of UV to penetrate to the O-rings is no longer a concern. The time penalty for heat-up and cool-down cycles becomes less important when the need is to reduce the desorption rate of the water vapor to almost nothing. In many applications, a combination of both methods used together can utilize the main advantages of both to achieve UHV or even just lower high vacuum pressures in a shorter time.

#### References

- 1 See #15, "Sources of Water Vapor in Vacuum Systems"
- 2 See #16, "How To Assess Gas Loads in Vacuum System Design"
- 3 See #14, "Gas Loads and O-Rings"
- 4 US Patent Number 4660297

Reprinted with permission by R&D Magazine, all rights reserved. Copyright 2001. Cahners Business Information. A shorter version appeared in R&D Magazine, January 2001.

### **29.1.1.3 Vacuum pump**

#### **How to Convert an Air Compressor Into a Vacuum Pump**



### **29.1.2 Electrical Propulsion**

Because the tendency of satellite design to be towards small and low cost, the need for miniaturizing the propulsion systems have become apparent. Pulsed Plasma Thruster (PPT) is one of the promising propulsion system for attitude control, station keeping, de-orbit, formation flying, and drag compensation of the small, micro- and nano-satellite because of

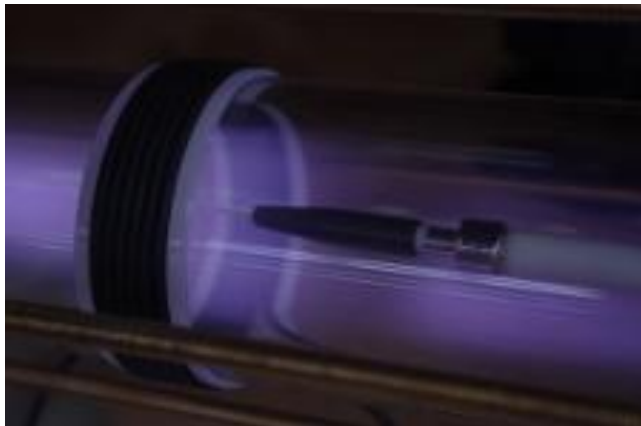
the following reasons. 1) Simplicity. No tankage, seals nor mechanical valves. 2) Light weight and high reliability. Only two power supplies. : Capacitor charge power supply and ignition power supply. Only one moving device. : Solid propellant feed mechanism to discharge chamber. 3) Small impulse bit (impulse per shot) level. Precise total impulse control.

### 29.1.3 Detector

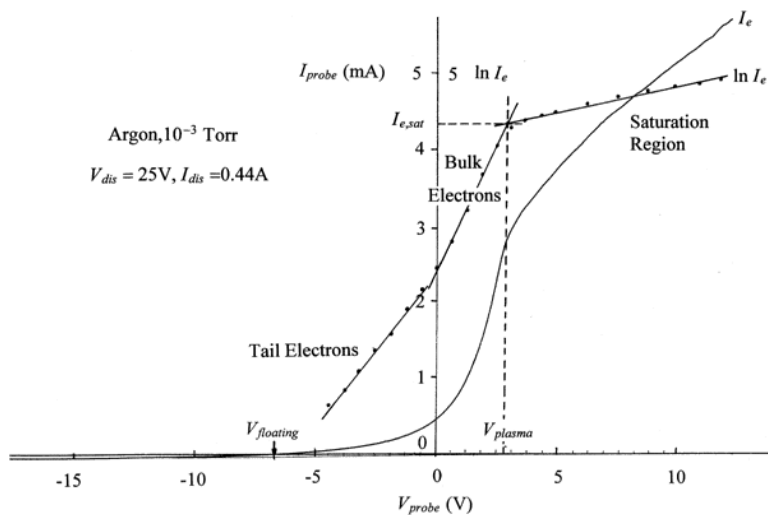
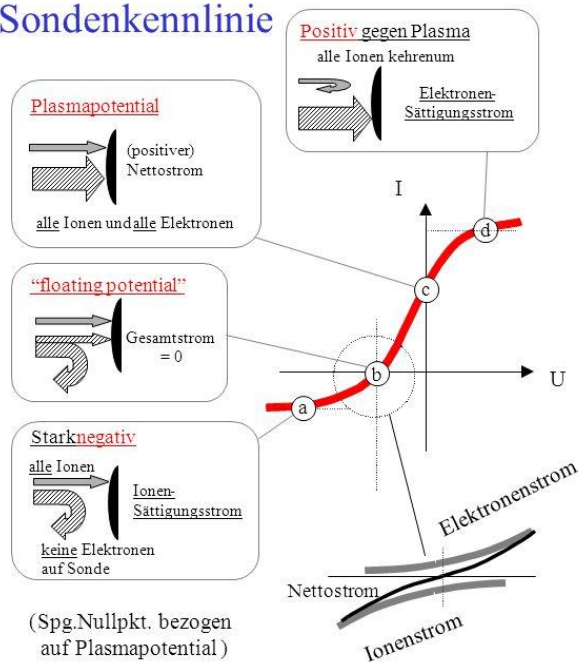
Since the electric Propulsion is a pulsed plasma thruster, we have to detect plasma.

One of the most frequently employed methods for plasma diagnostics is the Langmuir probe.

#### 29.1.3.1 Langmuir Prope



## U/I- Sondenkennlinie



But this sonde have a disadvantages

which makes the application of probe method more difficult or impossible in plasma containing fluctuations, oscillations and waves.

### 29.1.3.2 Rokowski coil

A Rogowski coil is an electrical transducer used for measuring AC currents such as high speed transients, pulsed currents of a power device, or power line sinusoidal currents at 50 or 60 Hz. The Rogowski coil has a flexible clip-around sensor coil that can easily be wrapped around the current-carrying conductor for measurement and can measure up to a couple thousand amperes of very large currents without an increase in transducer size.

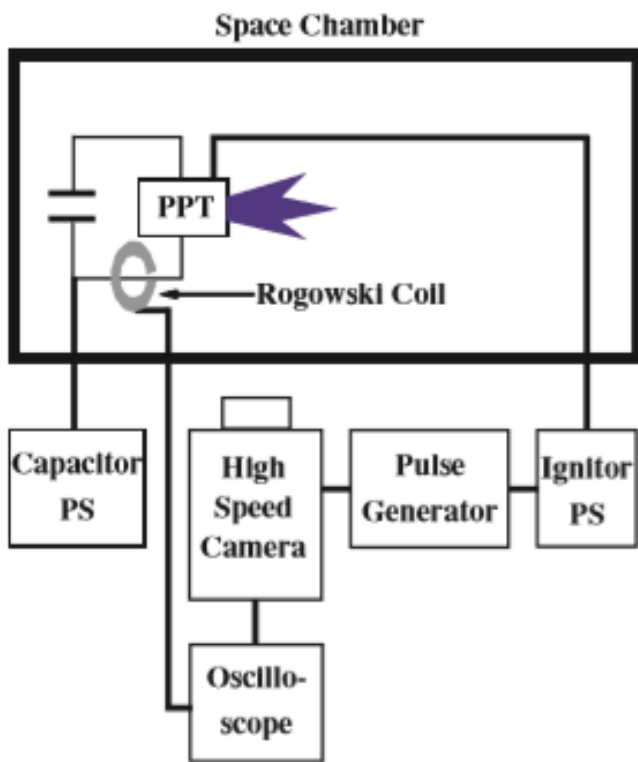
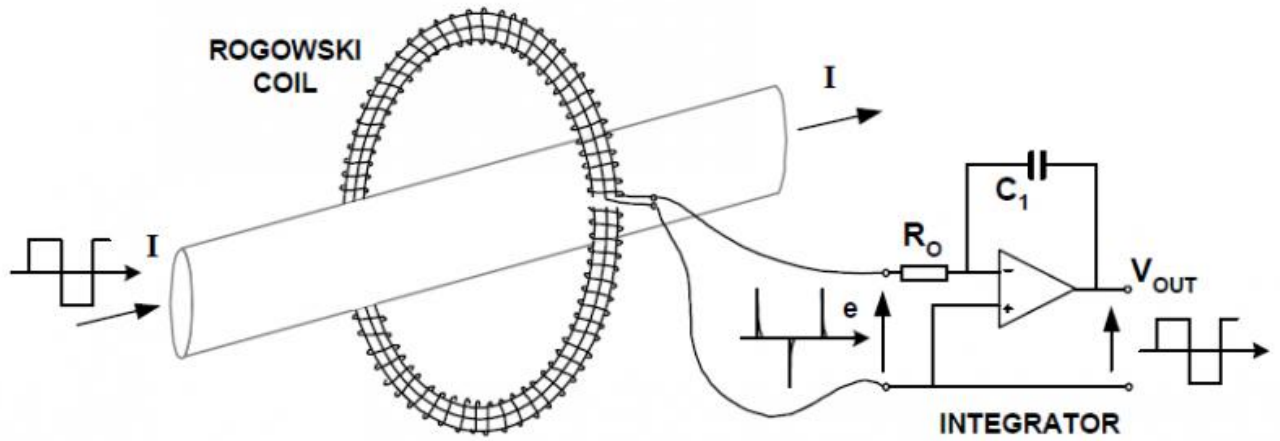


Fig. 3 Experimental Apparatus of High Speed Camera Experiment.

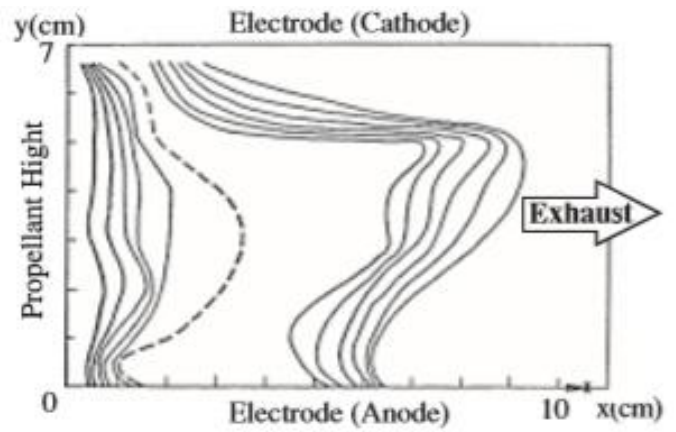
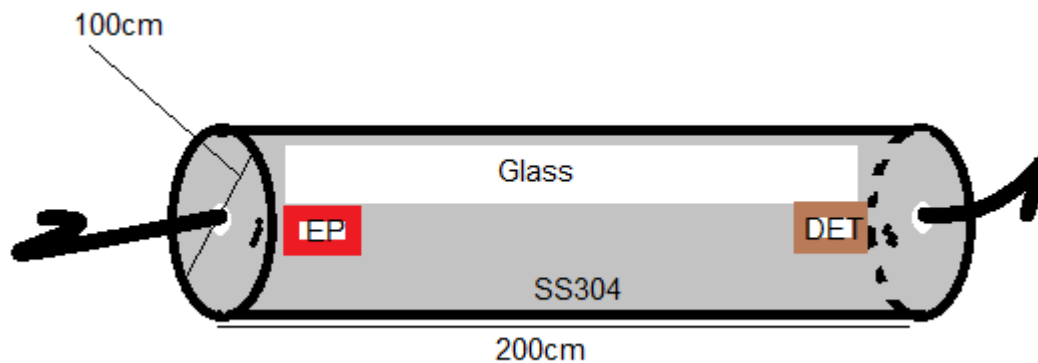


Fig. 5 Current Distribution Measured with a Small Rogowski Coil at the Current Reversal. (AFOSR-TR-77-0623 by Palumbo and Begun<sup>9</sup>)

## 29.2 GAMS Unit Design

### 29.2.1 Concept

Conclusion:



We will back out the desorbed water in a homogeneous way.

My Idea is to heat a metal coat in fire until it will be heated homogeneous to more than 250°. Then we overcoat the vacuum chamber. In this way the VC will be heated with contact (faster) and homogeneous. Therefore, the desorbed water is backed out without resorption on a colder wall of the VC. In addition, the complex structures of the EP and the DET will be backed out.

We shall use metal gaskets instead of o-rings,

Thin coating of Milk of Magnesia (unflavored) for nuts and bolts,

And Molybdenum Disulfide Coatings (MoS<sub>2</sub> Coatings) as a vacuum-compatible lubricant for SS-to-SS pairs.

Acetone followed by isopropyl alcohol 70% to clean the VC

(<https://www.youtube.com/watch?v=iZ9ieSHOZsg>)

inschaAllah. Eddy current and Rogowski coil Detector system (Concept)

## 29.3 Principle

The eddy current position sensor is similar to the inductive position sensor. A coil of wire is used as the probe as shown in Figure 3. This coil may have a ferromagnetic core or an air core as the inductive sensor. The operating frequencies of eddy current sensor are much higher than for the inductive sensors and operate in the region of 150 kHz to a few MHz. At these frequencies the eddy current losses are large and proportional to the coil's position relative to the target. Targets used with inductive and eddy current sensor must be a conductive material. The resolution of the eddy current sensor depends on the conductivity of the target material. The higher the conductivity of the target material the better is its displacement resolution. The higher excitation frequency means eddy current sensors are less susceptible to noise caused by power amplifier switching<sup>5-7</sup>.

An eddy current displacement sensor consists of two components as shown in Figure 4. The sensor coil and sensor drive electronics with signal processing block which can be a circuit or a microprocessor algorithm. An AC current in the sensor coil generates an oscillating magnetic field, which induces eddy currents in the surface of the target<sup>8,9</sup>. The coil impedance changes with

distance from target and this variation is converted to a line output by the sensor's signal processing electronics.

When the sensor coil is driven by an AC current, it generates an oscillating magnetic field that induces eddy currents in any nearby metallic target. The eddy currents flows in a direction opposite to that of the coil, reducing the magnetic fluxes in the coil and so its inductance. The eddy currents also dissipate energy, increasing the coil's resistance. As shown in Figure 3, the coil and the target constitute the primary and (shorted) secondary of a weakly coupled air-core transformer. Movement of the target changes the coupling, and this movement is reflected as an impedance change at the terminals of the coil<sup>10-12</sup>.

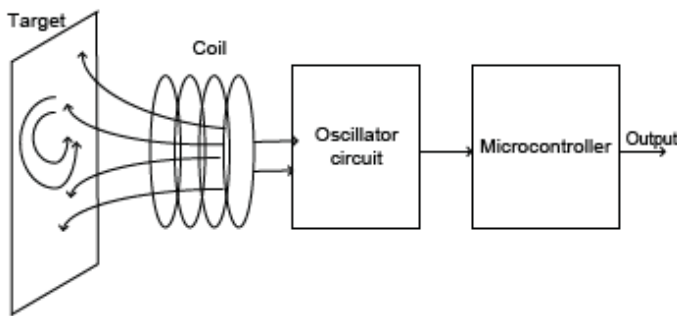


**Figure 4.** Components of eddy current displacement sensor.

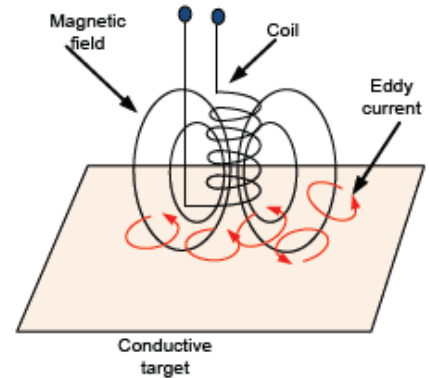
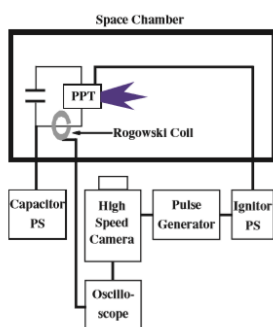


**Figure 3.** Eddy current displacement sensor working principle.

## 29.4 Rokowski coil

### 29.4.1 Aim



**29.4.2** Fig. 3 Experimental Apparatus of High Speed Camera Experiment.

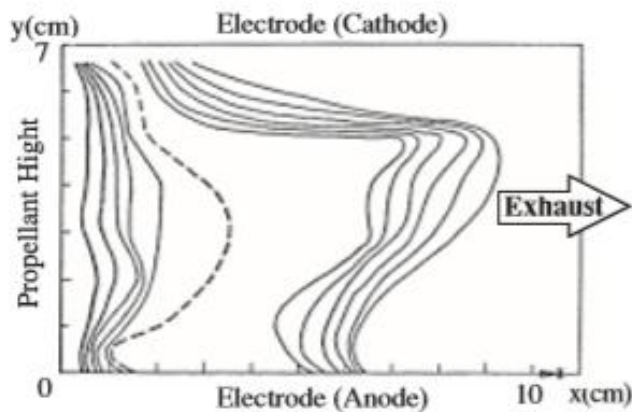


**Fig. 5** Current Distribution Measured with a Small Rogowski Coil at the Current Reversal. (AFOSR-TR-77-0623 by Palumbo and Begun<sup>®</sup>)

## COM Unit

## 30 Telemetry System with HarckRF

By MMJZ



### 30.1 Time Plan

Title	Description	Estimated Time	Status
Task 1: Introduction			
HackRF	Introduce HackRF and getting start with, a brochure summarize the main info should be prepared and established	5 days	Done
SDR (Software Defined Radio)	Introduce and understand SDR workflow and check for its available software	5 days	Done
Task 2: Getting Start			
Receiving signal	Use available SDR software to receiving signal using HackRF	2 days	Done
Transmitting signal	Use available SDR software to transmitting signal using HackRF	2 days	Done
Pentoo OS	Prepare Pentoo OS on a machine or USB image to be used with the HackRF	2 days	Done

GnuRadio	Getting start with GnuRadio compain and make some tutorials	3 days	Done
Raspberry&GnuRadio	Install GnuRadio on Raspberry Pi OS and make some tests	4 days	Done
Task 3: System 1 (Send and receive system “separately”)			
Make a Sender	Build a system to send a RF signal using a HackRF and Raspberry Pi.	4 days	In Progress
Make a Receiver	Build a system to receive a RF signal using a HackRF and developed SDR software	7 days	In Progress
Task 4: System 2 (Send \ Receive system)			
Raspberry S\R	Update the Raspberry Pi system to make it two way communication sys (send \ receive)	3 days	
SDR software S\R	Update the developed SDR software to make it two way communication sys. (send \ Receive)	3 days	
Task 5: System 3: Lotte System			
Arduino > Raspberry	Connect Arduino to Raspberry and send and receive data from it using USB connection	5 days	
Raspberry > HackRF	Use HackRF to send Arduino data, and to receive command for it	10 days	
HackRF > Gui	Use a Windows developed software to receive sent data from the raspberry side to be access	10 days	

Total time: 65 days,

Spent time: 25 days,

Remaining time: 40 days

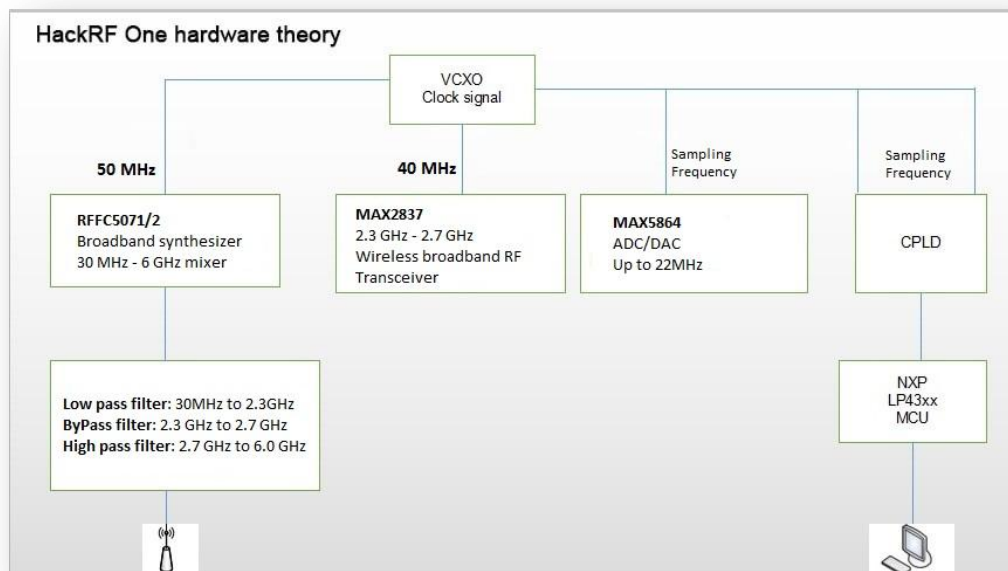
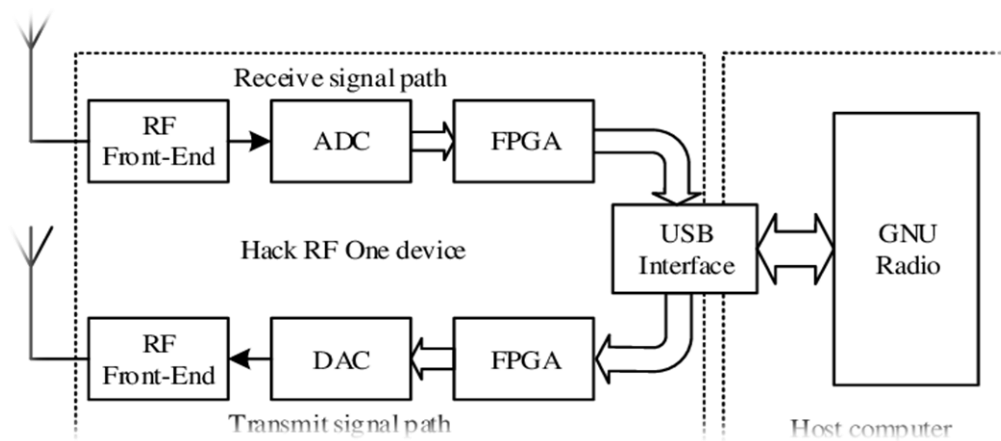
### 30.2 Introduction

**HackRF One** from **Great Scott Gadgets** is a Software Defined Radio peripheral capable of transmission or reception of radio signals from 1 MHz to 6 GHz. Designed to enable test and development of modern and next generation radio technologies, **HackRF One** is an open source hardware platform that can be used as a USB peripheral or programmed for stand-alone operation.

#### Specifications:

- 1 MHz to 6 GHz operating frequency

- Half-duplex transceiver
- Up to 20 million samples per second
- 8-bit quadrature samples (8-bit I and 8-bit Q)
- Compatible with GNU Radio, SDR#, and more
- Software-configurable RX and TX gain and baseband filter
- Software-controlled antenna port power (50 mA at 3.3 V)
- SMA female antenna connector
- SMA female clock input and output for synchronization
- Convenient buttons for programming
- Internal pin headers for expansion
- Hi-Speed USB 2.0
- USB-powered
- Open source hardware



### Parameters:

- Frequency band: 1MHz-6Ghz
- Data bandwidth: 20MHz

- Sampling accuracy ( ADC/DAC) : 8BIT
- Sampling speed ( ADC/DAC): 20Mbps
- Maximum transmitting power: 10dbm
- 64QAM transmitting EVM: 1.5%
- Complex sampling bandwidth: 20Mhz

To invoke DFU mode: Press and hold the DFU button. While holding the DFU button, reset the HackRF One either by pressing and releasing the RESET button or by powering on the HackRF One. Release the DFU button.

The DFU button only invokes the bootloader during reset. This means that it can be used for other functions by custom firmware.

#### **Hardware:**

- Mixer RFFC5072: 80MHz-4200MHz
- Wireless bandwidth RF transceiver MAX2837: 2.3Ghz-2.7Ghz
- Processor LPC4330: Main frequency 204MHz
- Amplifier MGA-81563: 0.1-6Ghz, 3V, 14dbm
  - The RF switch determines whether to amplify via a 14db amplifier
  - The signal is filtered by high pass or loss pass filter
  - Signal RFFC5072 chip mixing to 2.6GHz fixed medium frequency
  - The firmware supports variable intermediate frequency options: range 2.15 GHz to 2.75 GHz
  - Signal into the MAX2837 chip mixing to the baseband, output differential IQ signal (MAX2837 chip can limit the bandwidth of the signal)
  - The MAX5864 chip digitizes the baseband signal and sends it to CPLD
  - The LPC4320/4330 processor sends the sampled data to computer via USB
  - RFFC5072 and MAX2837 are protected in a shield to prevent interference from the outside world or other chips on the board, and to prevent static electricity from penetrating some chips

#### **30.2.1 Links and references:**

Official site: <https://greatscottgadgets.com/hackrf/one/>

HackRF Lessons of Michael Ossmann: <https://greatscottgadgets.com/sdr/>

Source files on github: <https://github.com/mossmann/hackrf>

Portapack source files on github: <https://github.com/sharebrained/portapack-hackrf>

#### **Files:**



HackRF\_Poster.pdf

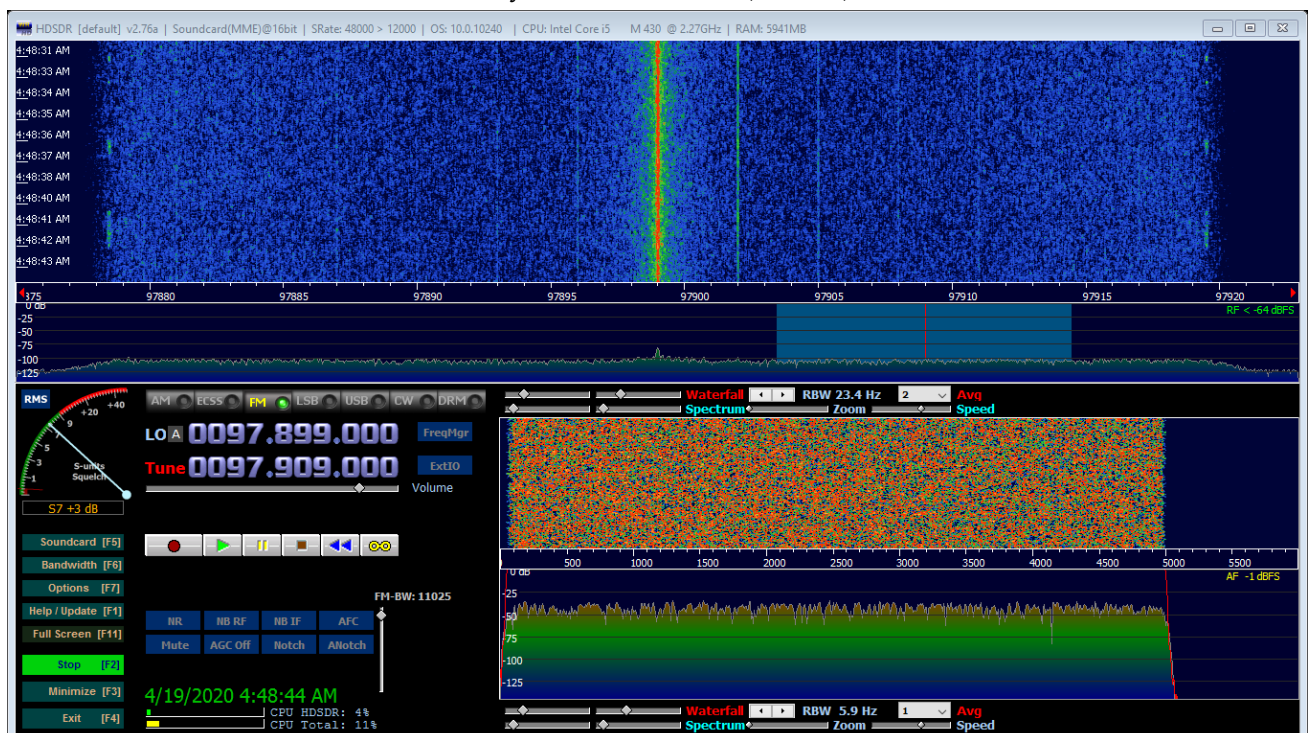
### 30.2.2 SDR (Software defined radio):

Software-defined radio (SDR) is a radio communication system where components that have been traditionally implemented in hardware (e.g. mixers, filters, amplifiers, modulators/demodulators, detectors, etc.) are instead implemented by means of software on a personal computer or embedded system.

There are a lot of SDR software globally like: HDSDR, SDRSharp...

### 30.2.3 HDSDR:

HDSDR is a freeware Software Defined Radio (SDR) program for Microsoft Windows 2000/XP/Vista/7/8/8.1/10. Typical applications are Radio listening, Ham Radio, SWL, Radio Astronomy, NDB-hunting and Spectrum analysis. HDSDR (former WinradHD) is an advanced version of Winrad, written by Alberto di Bene (I2PHD).



Main features:

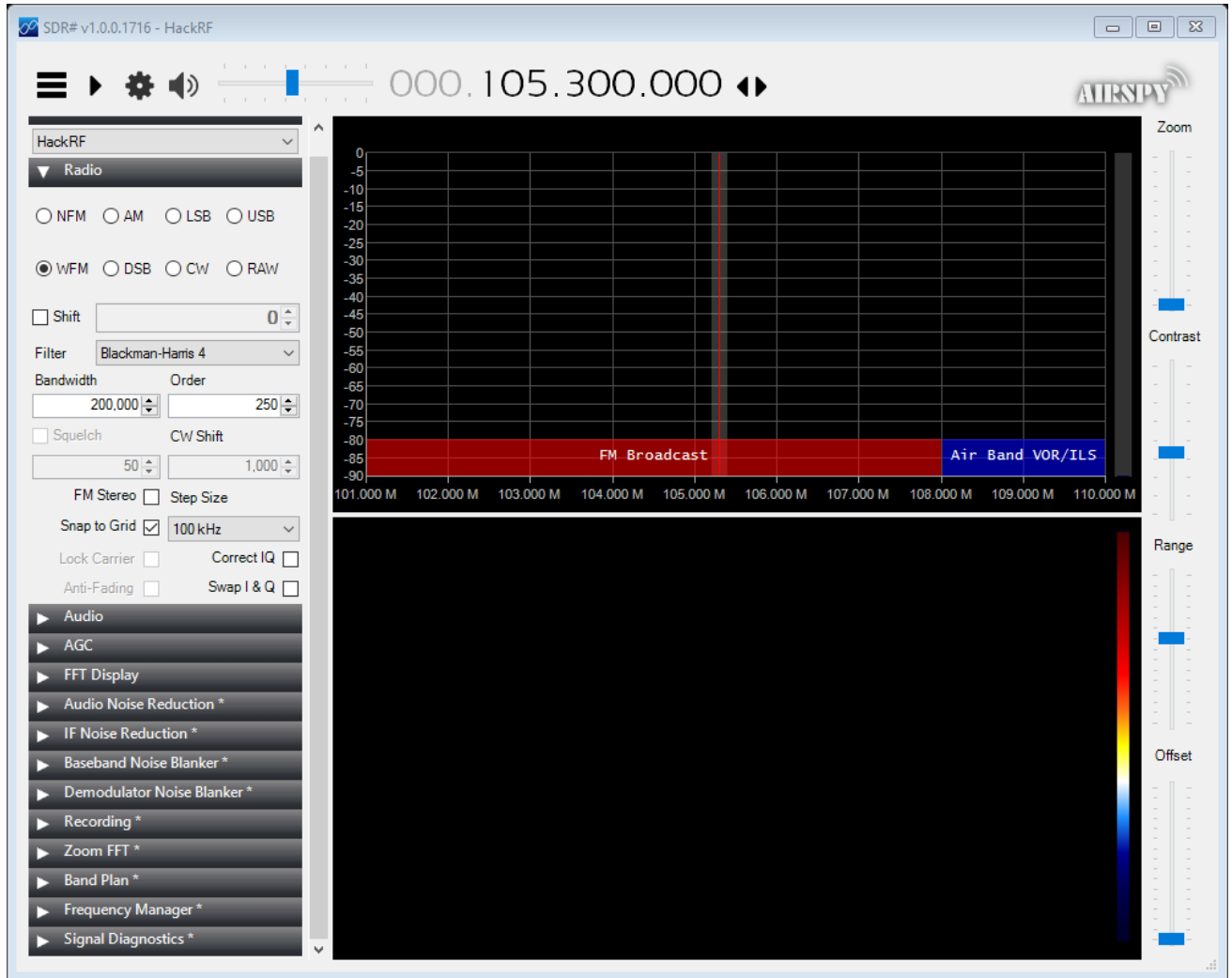
- separate large spectrum and waterfall display for input and output signals
- RF & AF spectrum and waterfall is optically zoomed to fit window width independently of FFT resolution bandwidth (RBW)
- flexible and efficient usage of the screen area from 640x480 (Netbooks) up to 8k
- extreme low-speed waterfall - helpful for pattern noise detection or short wave condition monitoring
- AM, ECSS, FM, SSB and CW demodulation
- basic transmit (TX) functionality in modes SSB, AM, FM & CW
- I/Q modulated signal pair for the TX input signal (Microphone) is produced on the TX output
- squelch, noise reduction, noise blanker, adjustable band pass filter, anti-alias filter
- automatic notch filter and up to 10 manual adjustable notch filters
- record and playback RF, IF and AF WAV files with recording scheduler

- Frequency Manager for Eibi, Ham Bands, Radio Bands, User frequency lists
- DDE client for Ham Radio Deluxe, Orbitron, WXtrack, SatPC32, Wisp and PstRotator (Howto)
- Omni-Rig support (CAT) to control additional hardware
- support for various hardware through Alberto's (I2PHD) ExtIO DLL interface
- ExtIO frequency options for IF-Adapter, Upconverter, Downconverter, Undersampling and calibration
- All HDSDR program options can be stored and loaded per "profile", to ease use of different receivers
- autocorrelation and cepstrum display for demodulated audio
- some command line options with profile management

Link: <http://www.hdsdr.de/>

#### **30.2.4 SDRSharp:**

Airspy is a line of Popular Software-Defined Radio (SDR) receivers developed to achieve High Performance and Affordable Price using innovative combinations of DSP and RF techniques. The goal is to satisfy the most demanding telecommunications professionals and radio enthusiasts while being a serious alternative to both cost sensitive and higher end receivers. Airspy Radios feature world class reception quality and ease of use thanks to the tight integration with the de facto standard free SDR# software for signal acquisition, analysis and demodulation.



Link: <https://airspy.com/download/>

### 30.2.5 GnuRadio:

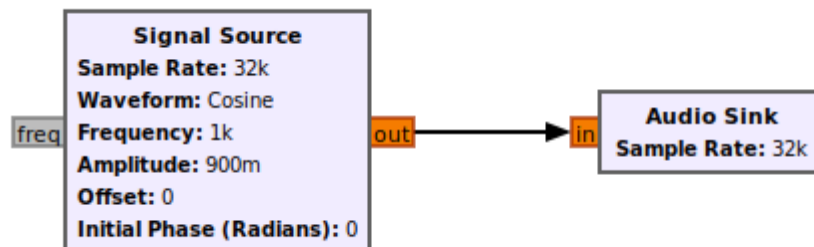
GNU Radio is a free & open-source software development toolkit that provides signal processing blocks to implement software radios. It can be used with readily-available low-cost external RF hardware to create software-defined radios, or without hardware in a simulation-like environment. It is widely used in research, industry, academia, government, and hobbyist environments to support both wireless communications research and real-world radio systems.

#### What is GNU Radio?

GNU Radio is a framework that enables users to design, simulate, and deploy highly capable real-world radio systems. It is a highly modular, "flowgraph"-oriented framework that comes with a comprehensive library of processing blocks that can be readily combined to make complex signal processing applications.

GNU Radio has been used for a huge array of real-world radio applications, including audio processing, mobile communications, tracking satellites, radar systems, GSM networks, Digital Radio Mondiale, and much more - all in computer software.

It is, by itself, not a solution to talk to any specific hardware. Nor does it provide out-of-the-box applications for specific radio communications standards (e.g., 802.11, ZigBee, LTE, etc.), but it can be (and has been) used to develop implementations of basically any band-limited communication standard.



#### Why would I want GNU Radio?

Formerly, when developing radio communication devices, the engineer had to develop a specific circuit for detection of a specific signal class, design a specific integrated circuit that would be able to decode or encode that particular transmission and debug these using costly equipment.

Software-Defined Radio (SDR) takes the analog signal processing and moves it, as far as physically and economically feasible, to processing the radio signal on a computer using algorithms in software.

You can, of course, use your computer-connected radio device in a program you write from scratch, concatenating algorithms as you need them and moving data in and out yourself. But this quickly becomes cumbersome: Why are you re-implementing a standard filter? Why do you have to care how data moves between different processing blocks? Wouldn't it be better to use highly optimized and peer-reviewed implementations rather

than writing things yourself? And how do you get your program to scale well on a multi-core architectures but also run well on an embedded device consuming but a few watts of power? Do you really want to write all the GUIs yourself?

Enter GNU Radio: A framework dedicated to writing signal processing applications for commodity computers. GNU Radio wraps functionality in easy-to-use reusable blocks, offers excellent scalability, provides an extensive library of standard algorithms, and is heavily optimized for a large variety of common platforms. It also comes with a large set of examples to get you started.

### 30.2.5.1 Links:

Official site: <https://www.gnuradio.org/>

GNU Radio wiki tutorials: <https://wiki.gnuradio.org/index.php/Tutorials>

GNU Radio API manual: <https://www.gnuradio.org/doc/doxygen/>

## 30.3 Getting started

### HSDR:

Download HSDR from here <http://www.hdsdr.de/index.html>

While you are there read the other pages, note the link to Alberto's original help and YouTube.

Execute the installation.

Later versions of Windows have security features that make altering the contents of "Program Files" difficult. A way round this might be to change the default and install HSDR somewhere different "C:\HSDR" perhaps.

Note the folder where it installs, you will usually need to find it in order to place a DLL file in there.

Look here <http://hdsdr.de/hardware.html> for DLLs and instructions for use with many radios, SDR and conventional .

Used ExtIO dll:



ExtIO\_HackRF.dll



ExtIO\_RTL2832.dll

Open HSDR and try to receive any local radio signal

<Add screenshot here>

### SDRSharp:

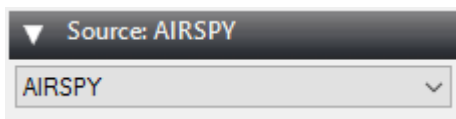
Airspy is a plug-and-play device and does not require any particular driver installation on Windows Vista, 7, 8, 8.1 and 10. You just plug Airspy and Windows will download and install the right driver for you.

There are exceptions where the original configuration of the PC does not allow the automatic installation of this class of devices. In such case, a driver should be installed manually with the following procedure:

- Download and unzip the WinUSB Compatibility Driver
- Open the device manager and select Airspy
- Select “Update Driver” then “Browse My Computer” to the inf file

### Using SDR#

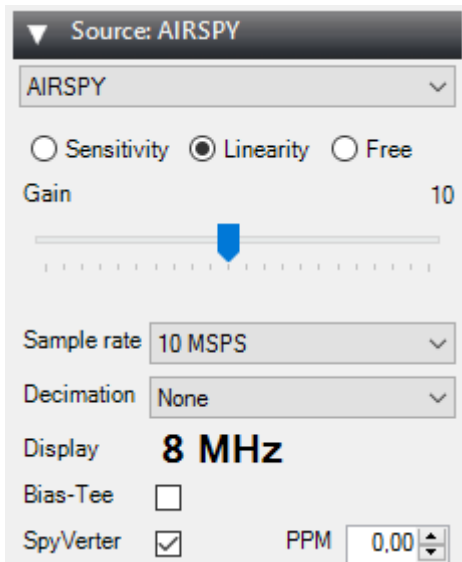
Airspy was designed by the same people who developed the SDR# software so it’s the obvious choice for running Airspy and leverage all its powerful features. First, go to the download page and get a copy. Then run SDRSharp.exe and select the “AIRSPY” front-end:



Then next step is the gain configuration. As depicted in this screen shot, there are many gain modes:

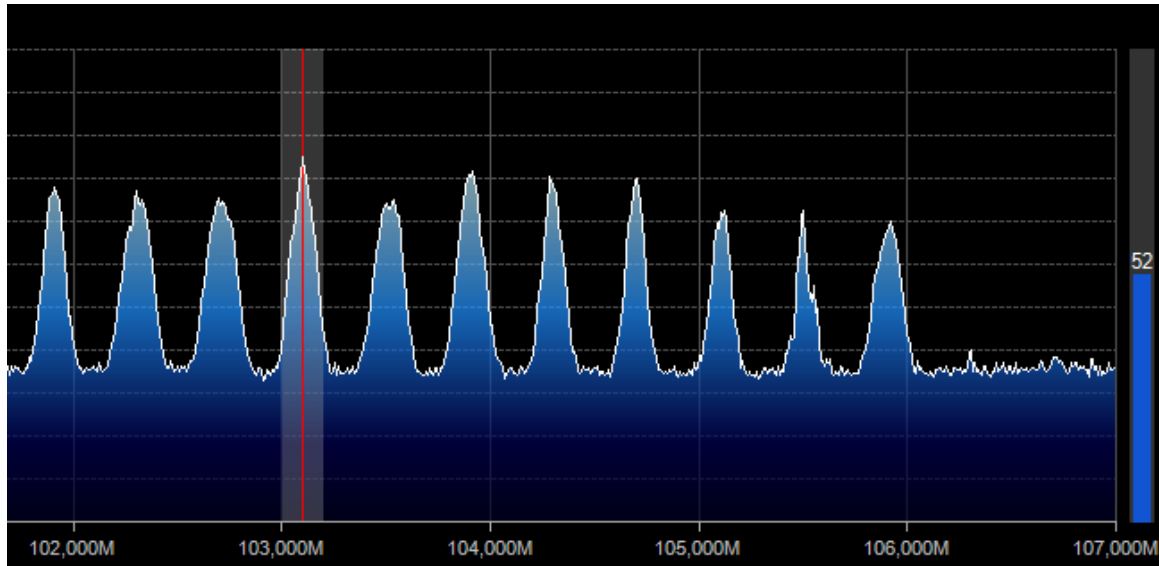
- Sensitivity
- Linearity
- Free (Custom)

The “Linearity” mode is the one you want to start with:



The following fine tuning procedure ensures you have the maximum SNR on the signal of interest while preserving the dynamic range:

- Start with the minimum gain
- Increase the gain until the noise floor rises by about 5dB
- Fine tune to maximize the SNR (the blue bar graph on the right)



In any case, you should make sure the RF noise floor just overrides the quantization noise floor of the ADC, but no more.

### 30.3.1 Getting Started with HackRF and GNU Radio<sup>41</sup>

The easiest way to get started with your HackRF and ensure that it works is to use Pentoo, a Linux distribution with full support for HackRF and GNU Radio. Download the latest Pentoo .iso image from one of the mirrors listed at <http://pentoo.ch/download/>. Then burn the .iso to a DVD or use [UNetbootin](#) to install the .iso on a USB flash drive. Boot your computer using the DVD or USB flash drive to run Pentoo. Do this natively, not in a virtual machine. (Unfortunately high speed USB operation invariably fails when people try to run HackRF from a virtual machine.)

Once Pentoo is running, you can immediately use it to [update firmware](#) on your HackRF or use other HackRF command line tools. For a walkthrough, watch [SDR with HackRF, Lesson 5: HackRF One](#).

To verify that your HackRF is detected, type `hackrf_info` at the command line. It should produce a few lines of output including "Found HackRF board." The 3V3, 1V8, RF, and USB LEDs should all be illuminated and are various colors.

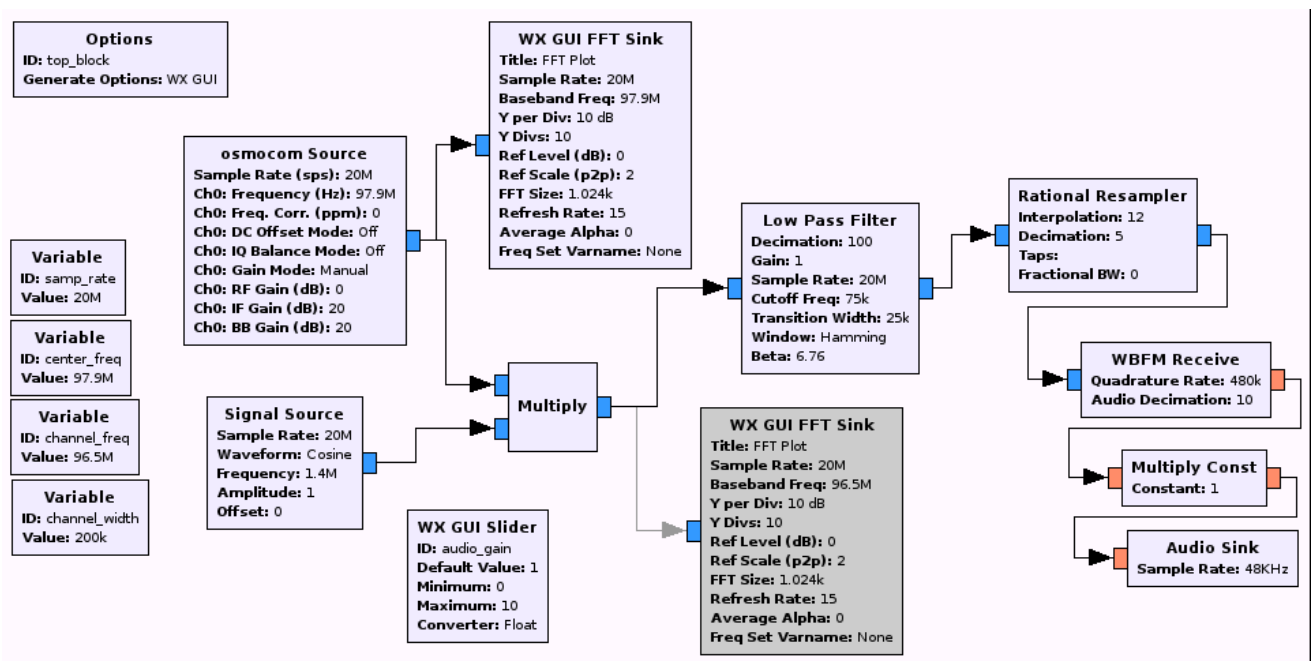
You can type `startx` at the command line to launch a desktop environment. Accept the "default config" in the first dialog box. The desktop environment is useful for GNU Radio Companion and other graphical applications but is not required for basic operations such as firmware updates.

Now you can use programs such as `gnuradio-companion` or `gqrx` to start experimenting with your HackRF. Try the Examples below. If you are new to GNU Radio, an excellent place to start is with the [SDR with HackRF](#) video series or with the [GNU Radio guided tutorials](#).

---

<sup>41</sup> <https://github.com/mossmann/hackrf/wiki/Getting-Started-with-HackRF-and-GNU-Radio>

Try FM radio flow graph: Create a flow graph in GNU Radio Companion like the one in the video or the screenshot below. Test the flow graph by listening to a strong FM radio signal.



This flow graph is the done on the first lesson of Michael Ossmann tutorials, complete the list to be more familiar with the HackRF and gnuRadio.

<Add screenshot here for output>

### 30.3.2 HackRF with Raspberry Pi:

There is some files and tools should be installed on the Raspbian system of the raspberry Pi to make the ability to use HackRF. As the Raspbian is not a high performance OS, the installation will be a little bit complex.

#### PiSDR:

You can find on the cloud some raspbian image updated with these tools and SDR software pre-installed and ready to go such PiSDR

The PiSDR is a Raspbian based operating system for the Raspberry Pi pre-loaded with multiple Software Defined Radio software. It was created to serve as a fast and reliable bootstrap for SDR projects.

Link: <https://pisdr.luigifreitas.me/#getting-started>

#### Installation on RaspberryPi 3<sup>42</sup>

##### What will we need

We would need Raspberry Pi 3 or Raspberry Pi Zero W 1.1, which has 64-bit ARMv7 processor. Please note that gr-gsm cannot be installed on Raspberry Pi 1 (we tested Model B),

<sup>42</sup> <https://github.com/ptrkrysik/gr-gsm/wiki/Installation-on-RaspberryPi-3>

since it has ARMv6 processor. Some GNU Radio components are not supported on ARMv6 architecture.

On RPi we will install Debian based Linux operating system Raspbian Jessie (we used version from 2016-03-18).

### **Update software on Raspberry Pi**

First we need to change default password with the command `passwd`. After that we need to install new updates:

```
sudo apt-get update
```

```
sudo apt-get upgrade
```

### **Expand space on a SD card and set-up the device**

Next step is to expand space on a SD card. We invoke the tool to do that with `sudo raspi-config`. In menu we select *Expand space*. We also need to set timezone, in which country we will use Wi-fi, keyboard settings (under *Internationalisation Options*). **Do not change language settings!** If system language is not English, some strange errors in Python start to appear.

Now we need to reboot the machine with `sudo reboot`.

### **Update firmware on Raspberry Pi**

Right after that we need to update Raspberry firmware with command `sudo rpi-update`. When this is finished, we need to stop the machine with `sudo shutdown -h now` and physically plug off the power. After some seconds we power it up again.

### **Secure the device**

Now it is good time to setup firewall, enable NTP client, change hostname... maybe we also want to set up VNC console. We assume you are able to secure the device, for some quick steps.

**Do not skip this step, security is important.**

### **Increase swap space**

Sometimes you will need more memory for compiling. You can "add" new memory with increasing swap space. Open the configuration file:

```
sudo nano /etc/dphys-swapfile
```

... and look for default value in Raspbian, which is: `CONF_SWAPSIZE=100`

Change it to: `CONF_SWAPSIZE=1024` After that you need to stop and start the service that manages the swapfile on Raspbian:

```
sudo /etc/init.d/dphys-swapfile stop
```

```
sudo /etc/init.d/dphys-swapfile start
```

Now can then verify the amount of memory and swap space by issuing the following command: `free -m`

**Install screen**

Since compiling can take a long time, it may also be a good idea to install screen: `sudo apt-get install screen`.

**Installation of software needed for gr-gsm****Install Kalibrate**

First, we will install Kalibrate:

```
sudo apt-get install libtool autoconf automake libfftw3-dev librtlsdr0 librtlsdr-dev libusb-1.0-0 libusb-1.0-0-dev
```

```
git clone https://github.com/asdil12/kalibrate-rtl.git
```

```
cd kalibrate-rtl
```

```
git checkout arm_memory
```

```
./bootstrap
```

```
./configure
```

```
make
```

```
sudo make install
```

**Install GNU Radio**

Now we need to install GNU Radio, which is quite simple:

```
sudo apt-get install gnuradio gnuradio-dev gnu // In fact, there's no such package named "gnu", so just install gnuradio gnuradio-dev
```

**Install libosmocore**

We need to compile libosmocore...

```
sudo apt-get install cmake
```

```
sudo apt-get install build-essential libtool shtool autoconf automake git-core pkg-config  
make gcc
```

```
sudo apt-get install libpcsclite-dev libtalloc-dev gnutls-dev libsctp-dev
```

```
git clone git://git.osmocom.org/libosmocore.git
```

```
cd libosmocore/
```

```
autoreconf -i
```

```
./configure
```

```
make
```

```
sudo make install
```

```
sudo ldconfig -i
```

```
cd
```

**...and install some other things**

```
sudo apt-get install swig python-docutils
```

```
sudo apt-get install gr-osmosdr rtl-sdr
```

```
sudo apt-get install libboost-dev
```

```
sudo apt-get install osmo-sdr libosmosdr-dev
```

```
sudo apt-get install libusb-1.0.0 libusb-dev
```

```
sudo apt-get install libboost-all-dev libcxxunit-dev swig doxygen liblog4cpp5-dev python-scipy
```

### Install gr-gsm

Now we are ready for the final step:

```
git clone https://github.com/ptrkrysik/gr-gsm.git
```

```
cd gr-gsm
```

```
mkdir build
```

```
cd build
```

```
cmake ..
```

```
make
```

```
sudo make install
```

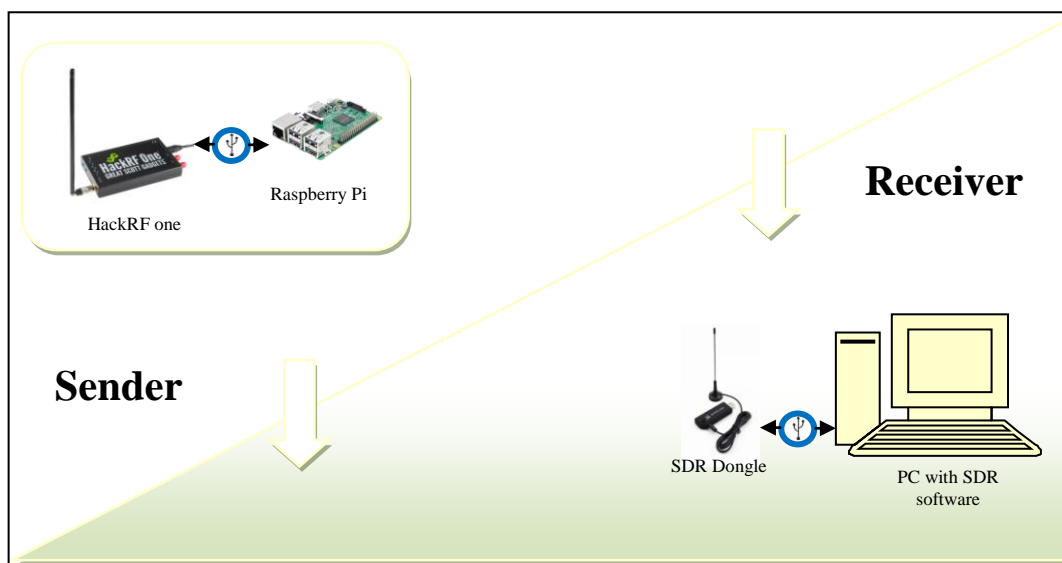
```
sudo ldconfig
```

### install HackRf lib:

Step 1: sudo apt-get update -y

Step 2: sudo apt-get install -y hackrf

## 30.4 System 1



System 1: Send and receive system (separately)

<https://zr6aic.blogspot.com/2018/04/setting-up-my-raspberry-pi-as-bacar.html>

<https://github.com/F5OEO/rpitiX>

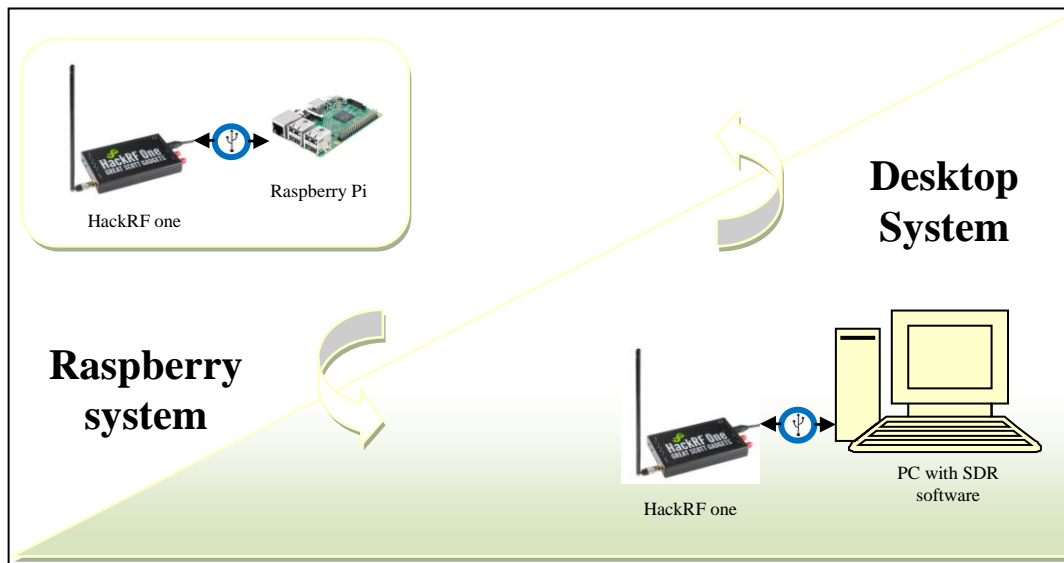
<https://www.rtl-sdr.com/transmitting-fm-am-ssb-sstv-and-fsq-with-just-a-raspberry-pi/>

<https://medium.com/@rxseger/sdr-first-project-initial-setup-node-hackrf-gnu-radio-on-linux-os-x-rpi-3-w-fm-tuner-ee16cdc8fd82>

[https://www.reddit.com/r/RTLSDR/comments/dy29a3/hackrf\\_on\\_windows/](https://www.reddit.com/r/RTLSDR/comments/dy29a3/hackrf_on_windows/)

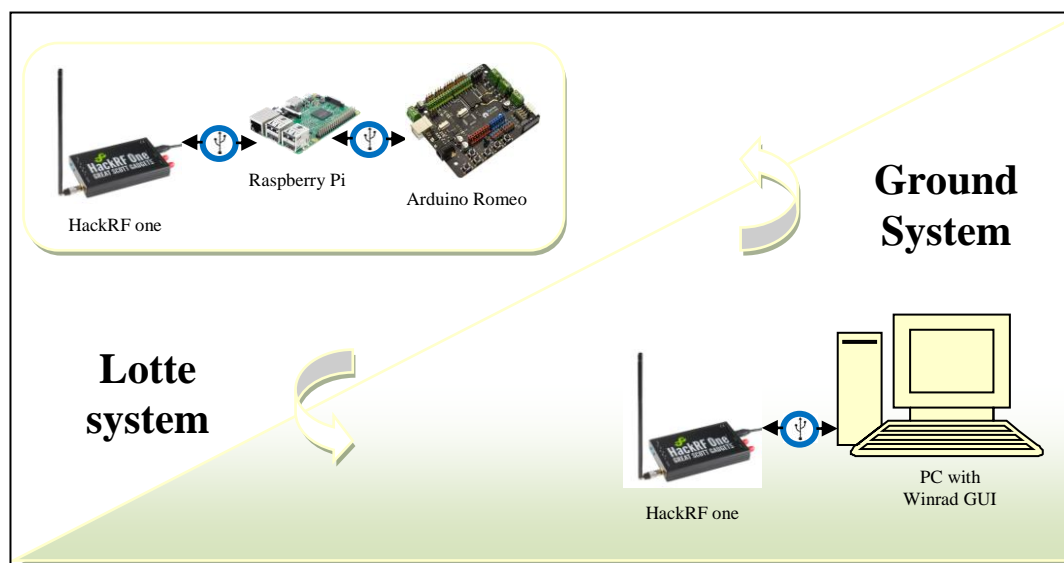
<https://github.com/mossmann/hackrf/issues/457>

### 30.5 System 2



System 2: Send \ Receive system

### 30.6 System 3



System 3: Lotte System

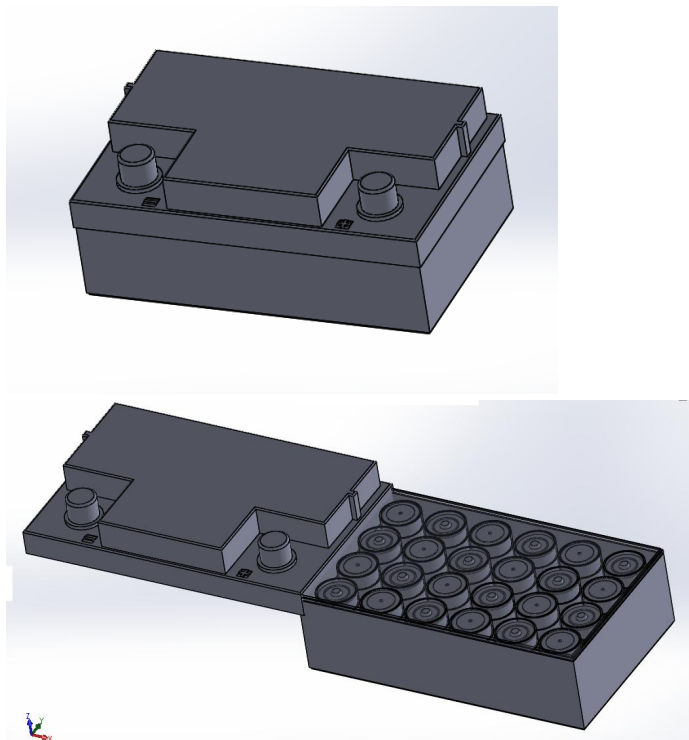
## Power Supply and Battery

Satellites need electric energy to pursue operation. This energy is acquired from solar power using solar cells which transform radiation energy into electricity. New developments in solar panel's technology have increased the efficiency of such systems to 30%. However the satellite will be deprived of such source of energy during eclipses, that is when the satellite is passing through the shadow of the earth. This phenomenon becomes more profound for LEO satellites which pass through an eclipse every 100 minutes and which the eclipse represents up to 40% of the total cycle time. In order to provide the continuity of electric energy supply, satellites are equipped with rechargeable batteries. These batteries simply charge during times when solar energy is available and discharge during shadow periods.

The first utilized battery in a spacecraft was the silver-zinc battery which provided high energy density. However because Ag-Zn batteries have low cycle life, they were replaced by Ni-Cd batteries that dominated the space industry for 20 years. After that, various batteries were used however restrictions and robust standards imposed on batteries used in space industry rendered many of them obsolete.

Aerospace industry now adopted the lithium-ion-based batteries in its satellite projects since lithium has:

- High energy density
- High specific energy
- Long cycle life
- Ability to be charged and discharged fast
- Compact shape



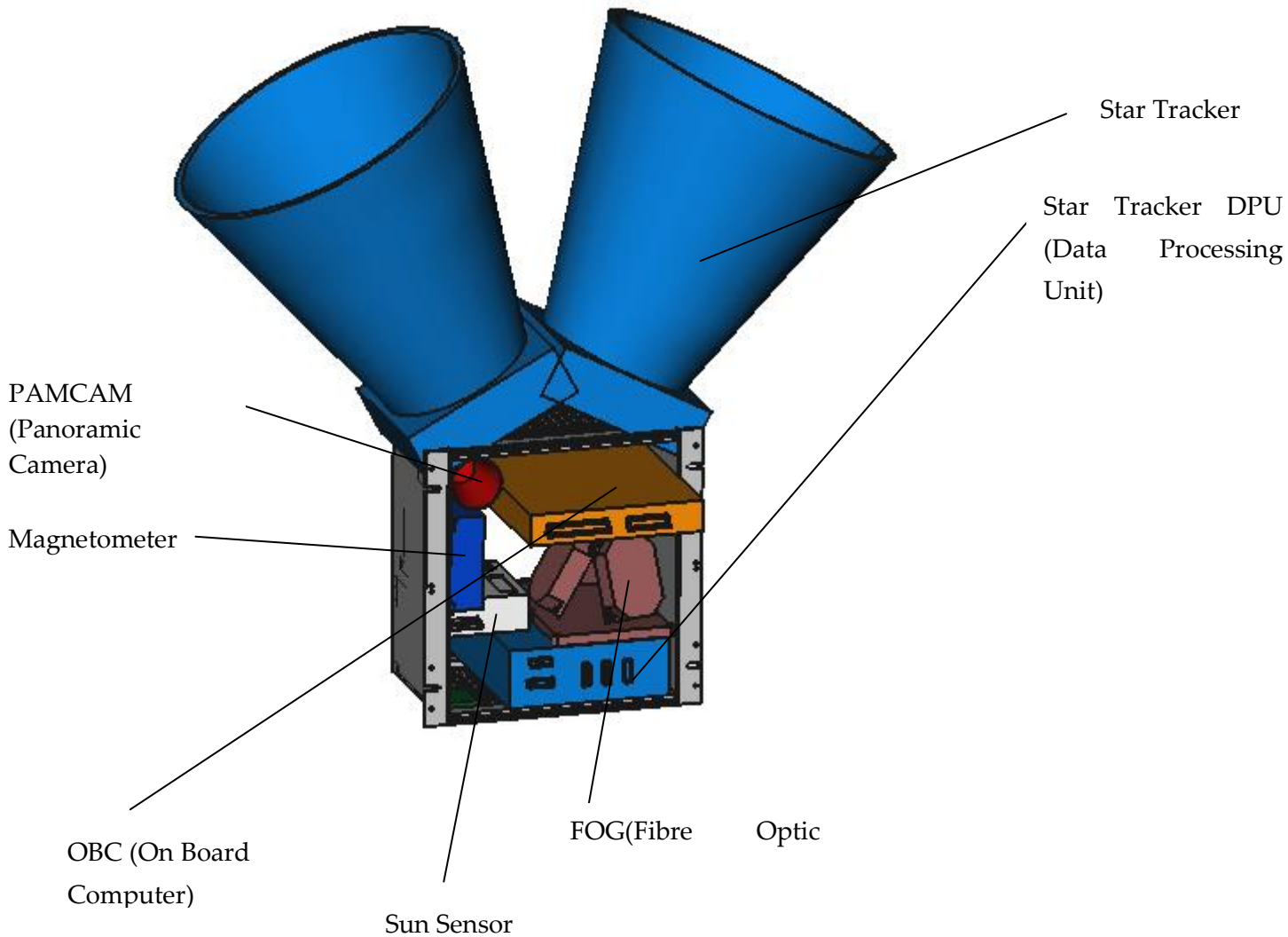


## IAP-SAT Integration



### 31 Attitude Control System (ACS) Components

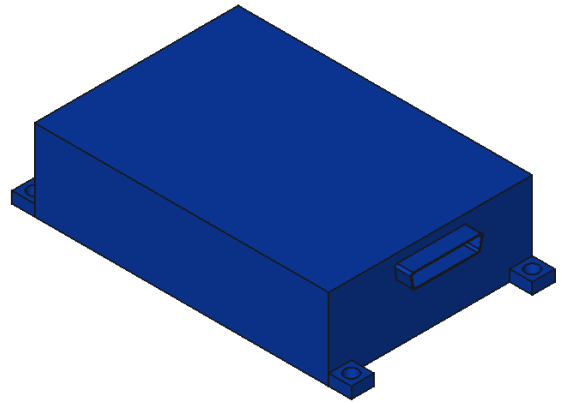
Type	ACS Components
Sensors	3-axis Magnetometers
	sun sensors
	GPS Receiver
	Star Tracker camera head units
	Rate Gyros
Actuators	



#### 31.1 Magnetometer

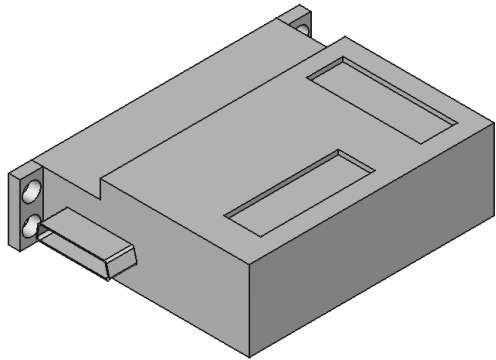
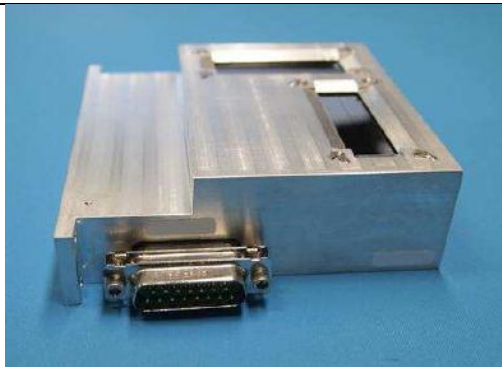
Specification form © Surrey Satellite Technology Ltd., Tycho House, 20 Stephenson Road, Surrey Research Park, Guildford, Surrey, GU27YE, United Kingdom, Tel: +44(0)1483803803 | Fax: +44(0)1483803804 | Email: info@sstl.co.uk | Web: www.sstl.co.uk

Sensitivity	$\pm 10$ nT
Range	$\pm 60$ $\mu$ T
Bandwidth	10 Hz
Temperature Channel	1x 0 - 5V Analogue
Field Measurement	3x 0 - 5V Analogue
Mass	190 g
Dimensions (H x W x L)	36 x 90 x 130 mm
Power Supply	Supply $\pm 12$ V Consumption <300mW
Temperature	-20 to +50°C operating -40 to +80°C non-operating
Random Vibration	15Grms in all axis
Radiation Tolerance	5kRad (Si)

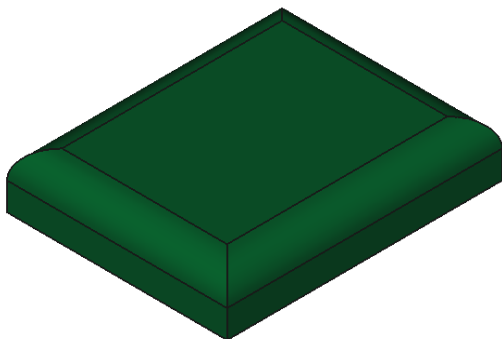


### 31.2 Sun sensor

Specification form © Surrey Satellite Technology Ltd., Tycho House, 20 Stephenson Road, Surrey Research Park, Guildford, Surrey, GU27YE, United Kingdom, Tel: +44(0)1483803803 | Fax: +44(0)1483803804 | Email: info@sstl.co.uk |

Sensors	2 orthogonal axes	 
Sensor field of view	± 50°	
Accuracy	1.0° (95%)	
Analogue output	4x 0 - 5V per channel	
Mass	~210g	
Dimensions (H x W x L)	95x 107 x 35 mm	
Power consumption	Sunlit: <100 mW; Dark: <10 mW	
Power Supply	± 12V	
Temperature	-30 to +60° C operating -40 to +80° C non-operating	
Random Vibration	15Grms in all axis	
Radiation Tolerance	5kRad (Si)	

### 31.3 GPS



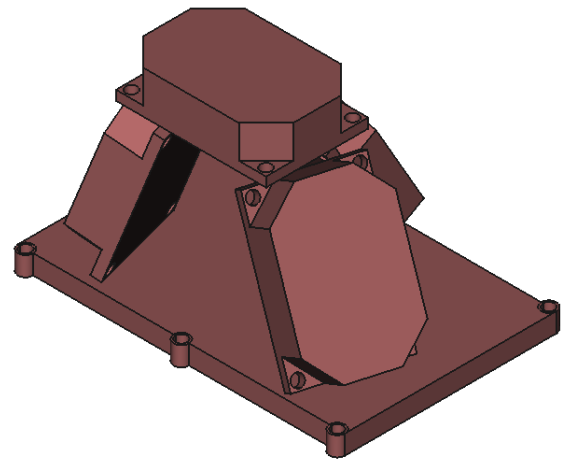
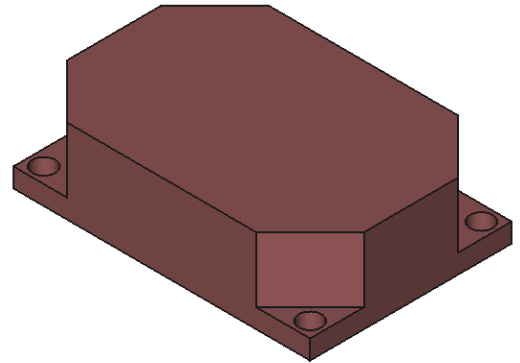
### 31.4 Fiber optic gyro unit

Specification form © Surrey Satellite Technology Ltd., Tycho House, 20 Stephenson Road, Surrey Research Park, Guildford, Surrey, GU27YE, United Kingdom, Tel: +44(0)1483803803 | Fax: +44(0)1483803804 | Email: info@sstl.co.uk |

Fiber Optic Gyro unit is composed of four fiber optic gyros (FOG) used in a tetrahedron like configuration for the measurement of the body angular rates. The tetrahedron like configuration allows autonomous detection of a single failure.

The type of the sensor is C-FORS

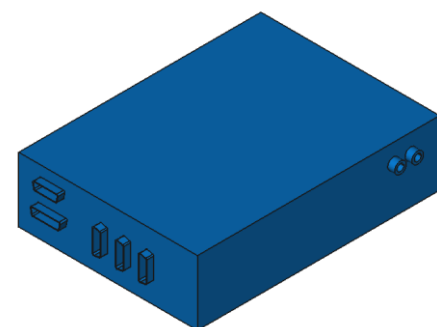
Parameters	FOG C-FORS Sensor
Sensor Performance	
Rate bias	$\leq 2^\circ/\text{h}$ ( $1 \sigma$ )
Random walk	$\leq 0.15^\circ/\sqrt{h}$
Scale Factor	$\leq 1000$ ppm ( $1 \sigma$ )
Axis misalignment	$\leq 10$ mrad (Absolute) $\leq 1$ mrad (Stability)
Maximum measurement range	$\pm 1000^\circ/\text{s}$
Initialization time	$\leq 120$ ms
Mechanical Properties	
weight	$\leq 130$ g
Dimensions	78 mm x 53 mm x 22 mm
Case	Hermetically sealed
Electrical Properties	
Power Consumption	2.8 W
Communication Interface	IBIS
Supply voltage	+5.0 V -5.0 V +3.3 V



### 31.5 Star tracker system

Specification form © Surrey Satellite Technology Ltd., Tycho House, 20 Stephenson Road, Surrey Research Park, Guildford, Surrey, GU27YE, United Kingdom, Tel: +44(0)1483803803 | Fax: +44(0)1483803804 | Email: info@sstl.co.uk |

Physical Characteristics	
Dimensions (mm)	DPU: 155 x 210 x 56 30° baffle CHU: Ø147 x 283 (H)
Power	16 – 50 V unregulated DPU: 6.5W, CHU: 0.5W
Mass (kg)	DPU: <1.2 , 30° baffle CHU: 1.4
Radiation	5 kRad (Si)
Random vibration	15 G <sub>rms</sub> in all axis
Lifetime	7.5 years LEO Orbit (< 800Km)
Temperature	-30° C to +15° C performance -20° C to +50° C operating -30° C to +60° C non-operating
Performance Properties	
Relative Accuracy	X/Y < 3 arcsec (1σ) Z < 25 arcsec (1σ)
Bias	X/Y < 5 arcsec (1σ) Z < 3.5 arcsec (1σ)
Maximum rate/acceleration	6 deg/sec / 2.5 deg/s <sup>2</sup>
Attitude Acquisition Time	8 s from power ON
Update Rate	1 Hz to 16 Hz
Sun/Earth Exclusion Angle	30 Degrees
Moon Exclusion Angle	Robust to Moon in field of view (22.6 x 22.6 deg)
Time synchronisation	PPS input via LVDS. RS485 or optional RS422
TM/TC interface	CAN-SU or Optional (RS422 & SpaceWire)

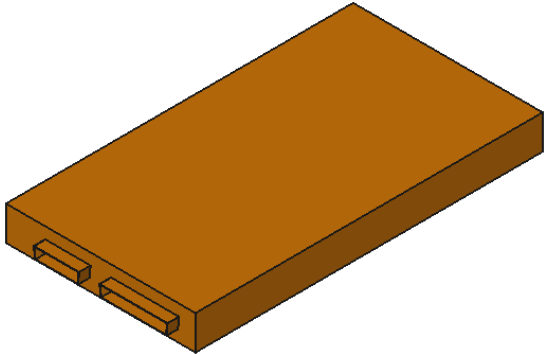


## 31.6 Other Components

### 31.6.1 OBC

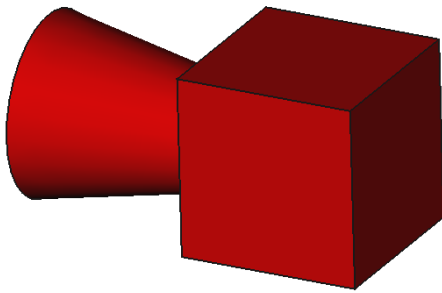
Specification form © Surrey Satellite Technology Ltd., Tycho House, 20 Stephenson Road, Surrey Research Park, Guildford, Surrey, GU27YE, United Kingdom, Tel: +44(0)1483803803 | Fax: +44(0)1483803804 | Email: info@sstl.co.uk |

Performance Properties	
Processor	IBM PPC750FL 500 Dhrystone 2 MIPS 296 Whetstone MWIPS
Operating System	VxWorks, Others may be available on request
Memory	512MiBytes (EDAC 16,8) 24MiBytes MRAM 4MiBytes Flash (EDAC 16,8)
Interfaces	MIL-STD-1553B 2 x Dual CAN bus 8x LVDS Inputs/ 8x LVDS Outputs 4x Opto Isolated Inputs 4x Opto Driver Outputs 12x RS485/ MLVDS Transceiver RS422 receiver/transmitter links
Protocols	MIL-STD-1553 (optional), Spacewire (optional), CAN-SU, UART (optional RS422/RS485), HDLC, Pulse-Per-Second Synchronisation Others available on request




Physical Characteristics	
Dimensions	306x167x 30mm (single board)
Power at 28V	<10W
Mass	1.5kg
Radiation	5kRad (Si)
Random Vibration	10 G <sub>rms</sub> in all axis
Lifetime	up to 7.5years
Temperature	-20° C to +50 ° C operating -30° C to +60 ° C non-operating

### 31.6.2 PAMCAM



This so called Panoramic Camera (PAMCAM) should be able to take color images in order to increase the public outreach of the Small Satellite Program.

### 31.7 Concept for Power Supply and Battery<sup>43</sup>

Satellites need electric energy to pursue operation. This energy is acquired from solar power using solar cells which transform radiation energy into electricity. New developments in solar panel's technology have increased the efficiency of such systems to 30%. However the satellite will be deprived of such source of energy during eclipses, that is when the satellite is passing through the shadow of the earth. This phenomenon becomes more profound for LEO satellites which pass through an eclipse every 100 minutes and which the eclipse represents up to 40% of the total cycle time. In order to provide the continuity of electric energy supply, satellites are equipped with rechargeable batteries. These batteries simply charge during times when solar energy is available and discharge during shadow periods.

The first utilized battery in a spacecraft was the silver-zinc battery which provided high energy density. However because Ag-Zn batteries have low cycle life, they were replaced by Ni-Cd batteries that dominated the space industry for 20 years. After that, various batteries were used however restrictions and robust standards imposed on batteries used in space industry rendered many of them obsolete.

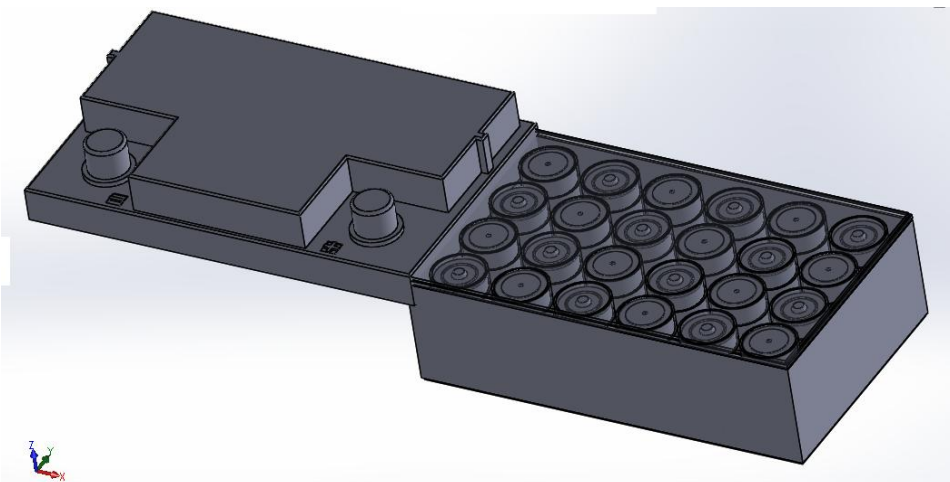
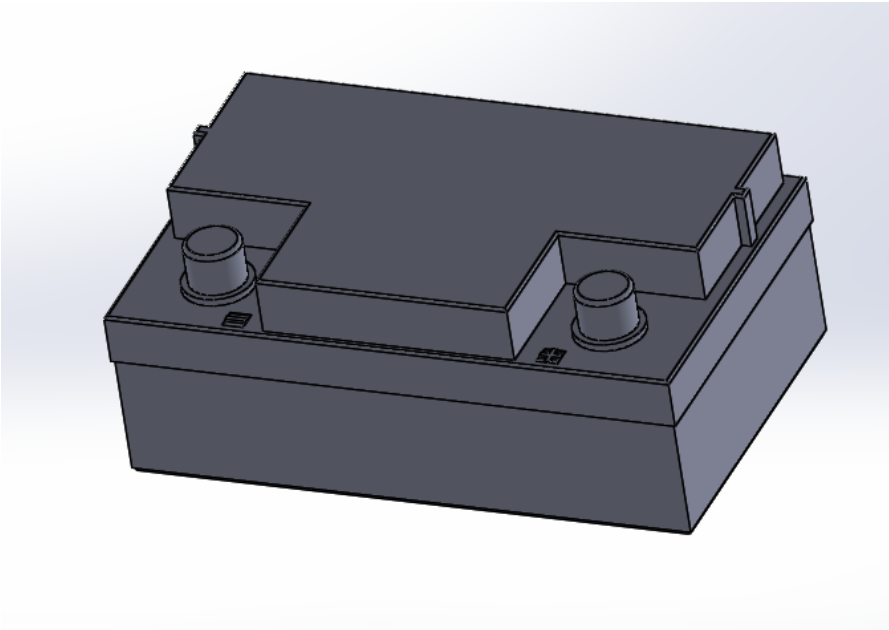
Aerospace industry now adopted the lithium-ion-based batteries in its satellite projects since lithium has:

- High energy density
- High specific energy
- Long cycle life

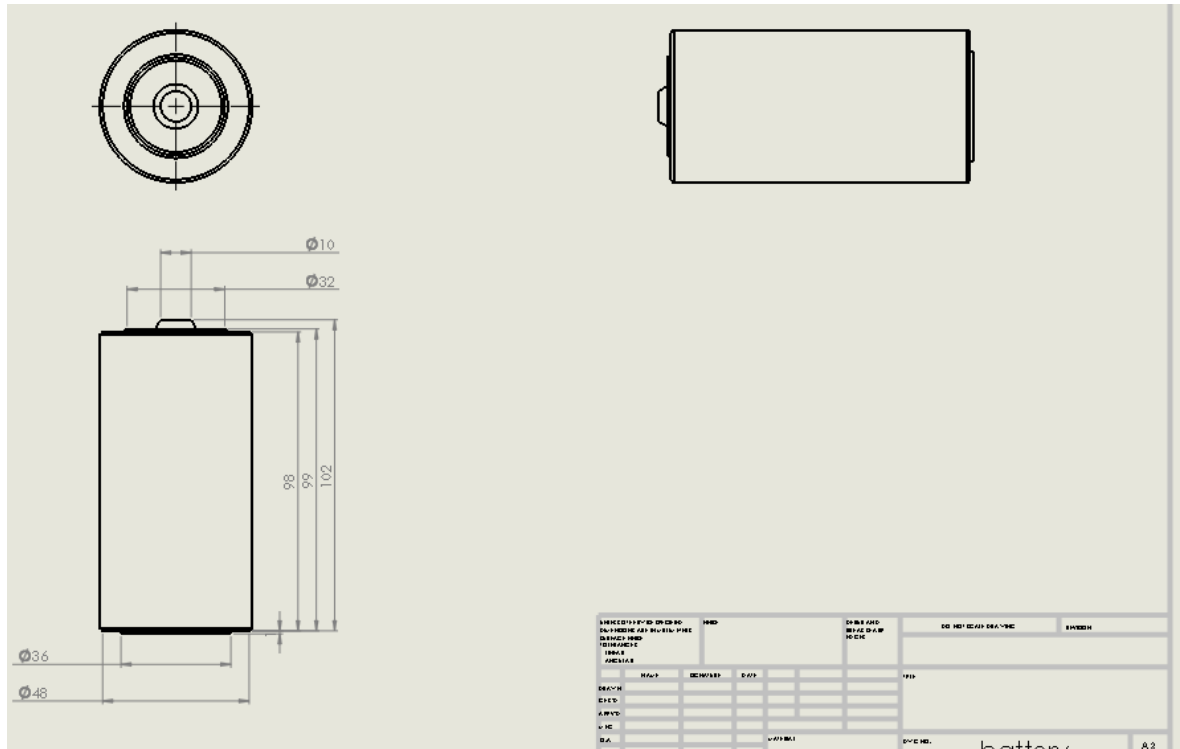
---

<sup>43</sup> From Ibrahim Ghanim, Practical Work at AECENAR Ras Nhache, July/August 2015

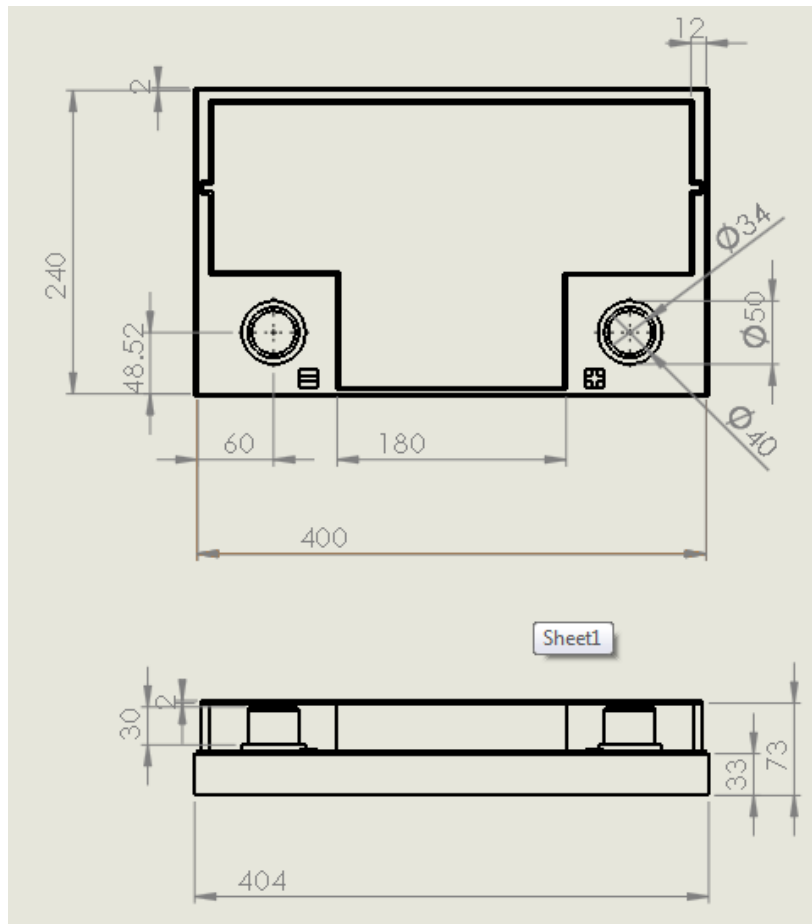
- Ability to be charged and discharged fast
- Compact shape



**Battery:**



**Body:**



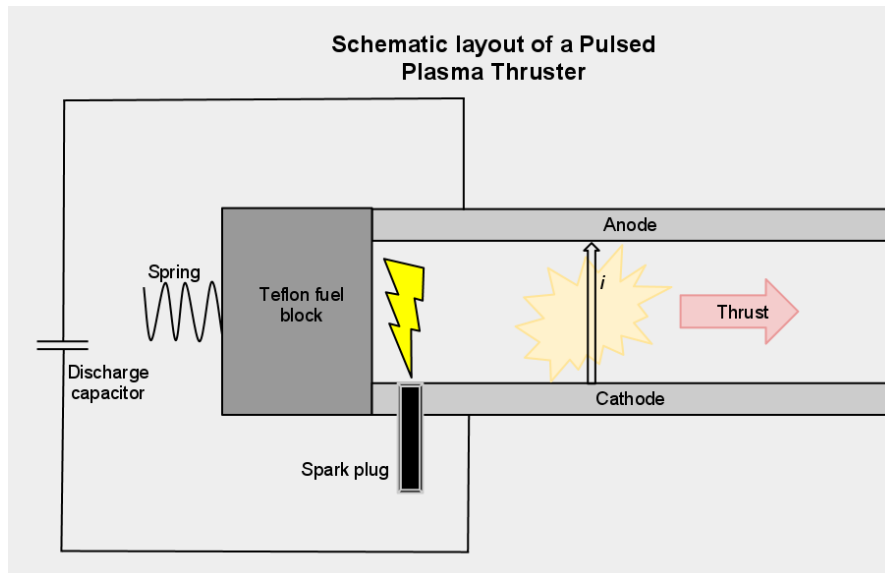
## 31.8 Concept for the Propulsion Unit<sup>44</sup>

### 31.8.1 Primitively modeling the chosen Pulsed Plasma Thruster (PPT)

Amongst all the inspected Propulsion systems, PPT was chosen and it had to be designed on FreeCad.

PPT's working mechanism was carefully studied and its different components were identified.

The primitive 2D sketch that our design depends on is below.



The components necessary for the PPT are:

- Parallel anode/cathode plates
- Spark igniter
- Teflon circular block
- Spring system
- High voltage capacitor

**Mechanism:** The first step of PPT mechanism is plasma formation. An igniter directed to the solid fuel bar produces a spark that ablates and sublimates the surface of the propellant forming plasma. Since the plasma is positively charged, it completes the circuit between the 2 plates. The interaction between the formed electric and magnetic field produces a Lorentz force that acts on the plasma and accelerates it out of the exhaust at high speeds.

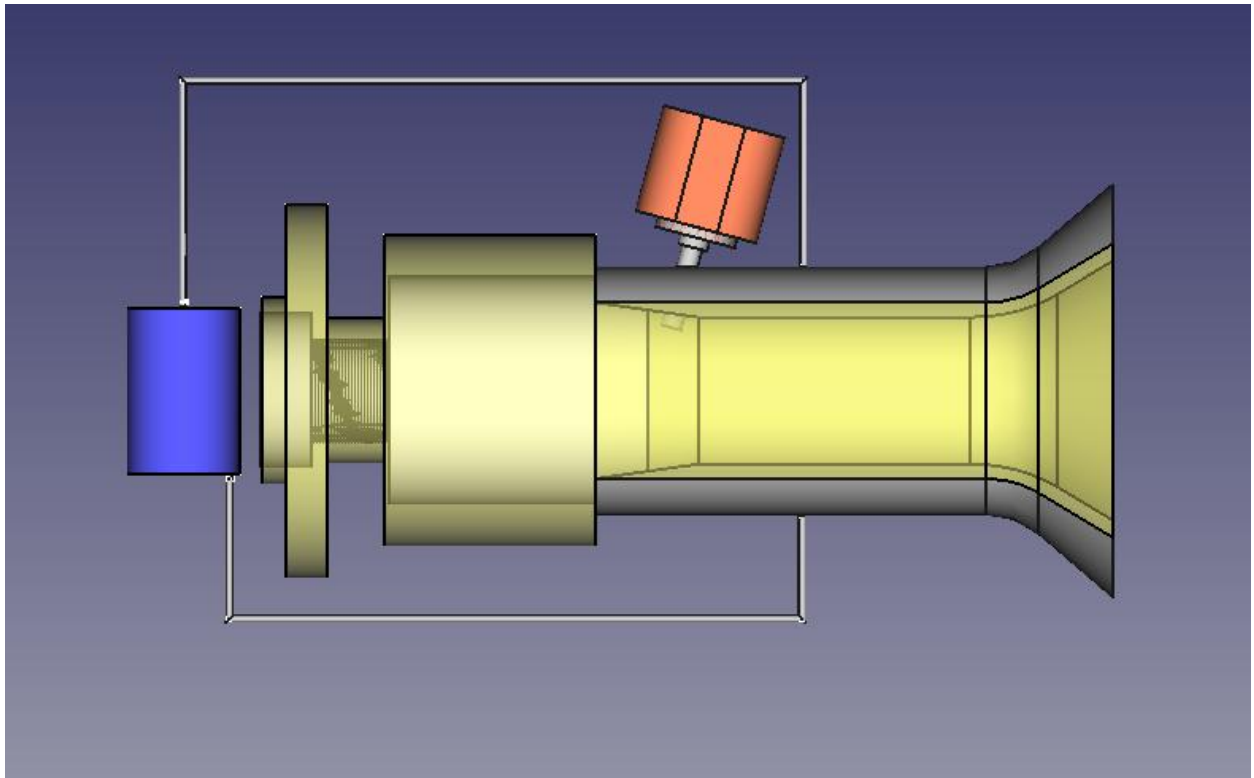
### 31.8.2 Modeling our PPT design in FreeCad

After identifying the different components of our PPT system and taking into consideration its working mechanism, the propulsion system was modelled on FreeCad.

The following is the FreeCad model of the PPT:

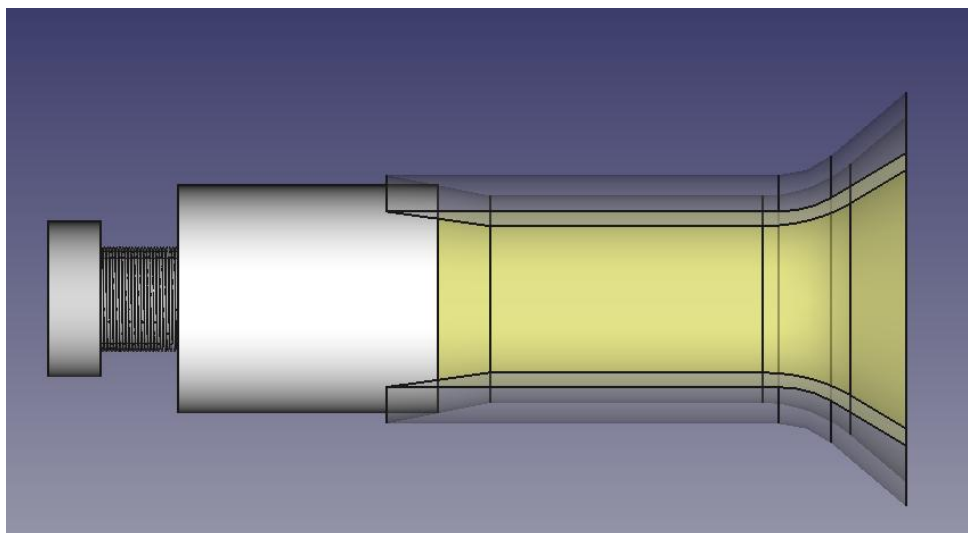
---

<sup>44</sup> From Ibrahim Ghanim, Practical Work at AECENAR Ras Nhache, July/August 2015



### 31.8.2.1 Modelling “fuel continues supplying system”

Most of propulsion systems use fluid fuel which its supply is easily provided by maintaining a pressure difference between the fuel reservoir and the ionization chamber. However pulsed plasma thrusters use solid fuel, that’s why its continuous fuel supply was insured by a spring system mounted on the fuel rod.

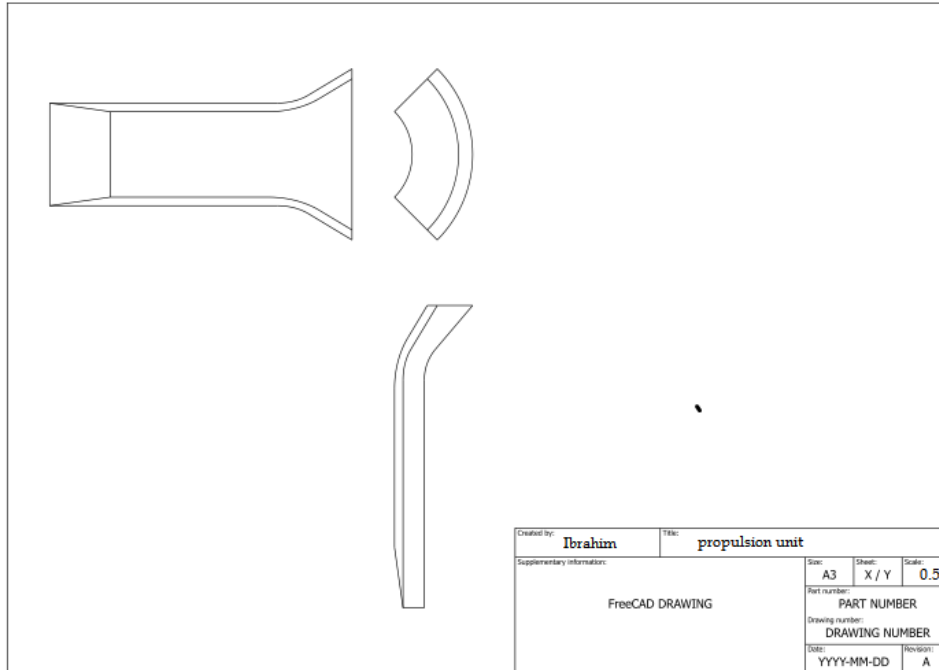


The propulsion unit is designed with a cone shaped ending such that its outer nozzle is slightly larger than the fuel rod and its inner nozzle is smaller than the fuel rod. A compressed spring is mounted to the end of the fuel rod such that the rod is always under pushing force. When the igniter produces a spark and the outer surface of the fuel rod gets

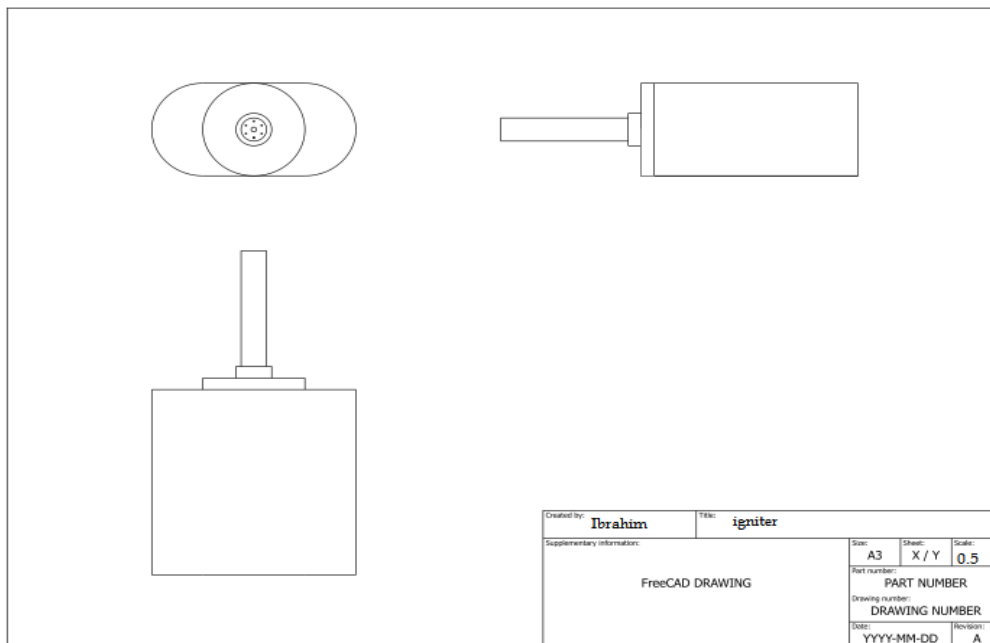
ablated and sublimated, the spring system pushes the rod inward such that it returns to its previous position in the propulsion unit.

### 31.8.2.2 2D projections of important parts of the propulsion system

#### 3) Propulsion unit

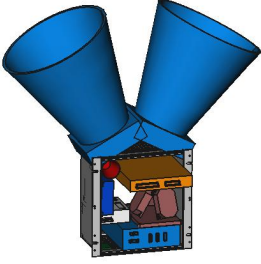
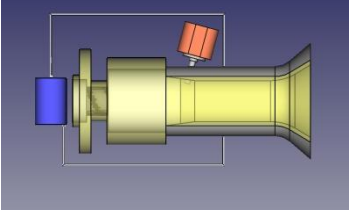


#### 4) Igniter



## 31.9 FreeCAD files

--	--

	 <p>170116IAP-SAT_Integration.FCStd</p>
	 <p>propulsion chamber.FCStd</p>

## 32 Integration of IAP-SAT

### 32.1 Integration of IMU and radioastronomy HI sensor (2017)



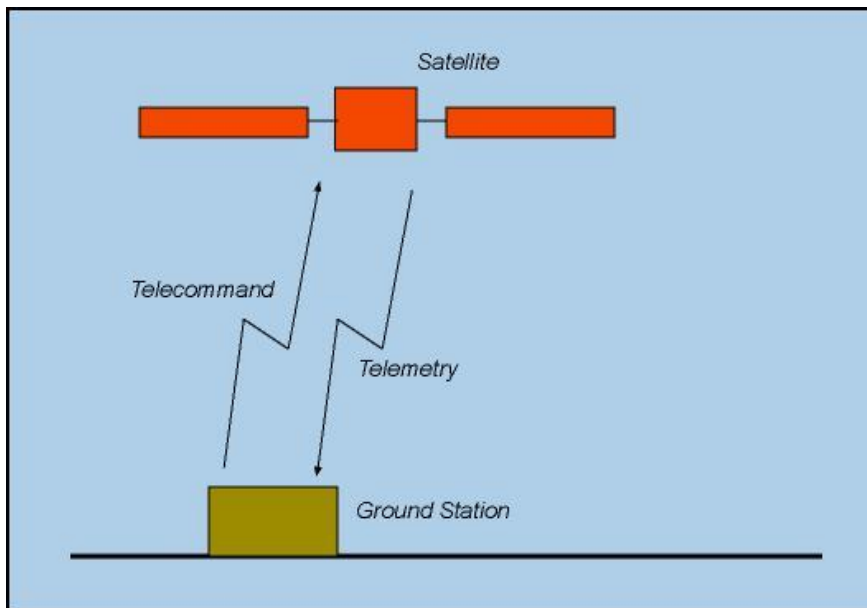
### 32.2 Integration of chem. propulsion (2020)



## Hardware-in-the-Loop (HIL) Testrig

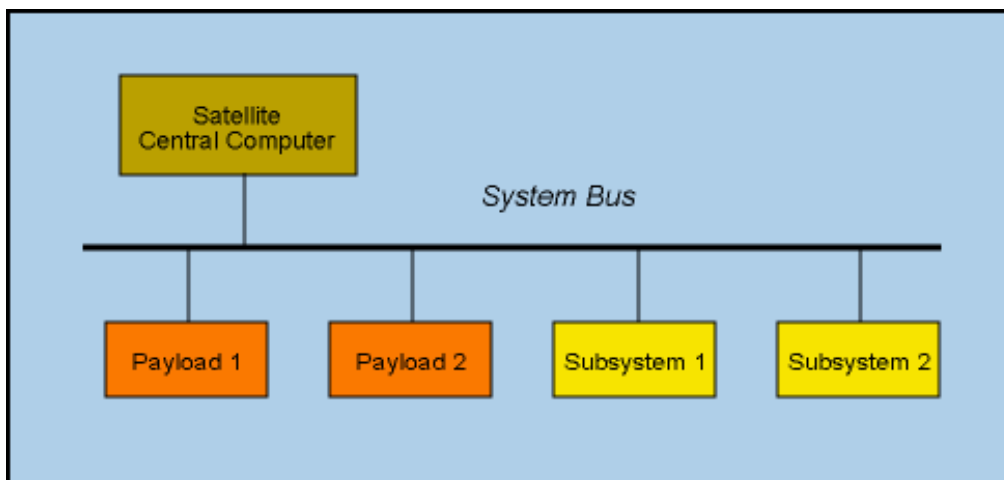
### 33 Basics for Embedded Test and Simulation Environment

#### 33.1 Satellite System Structure



The figure at the side shows a "black box" view of a satellite system. The satellite is controlled from a *ground station* through a radiofrequency link. Depending on the mission, the link with the ground station

may be continuous or extend only over a section of the orbit.



The figure at the side shows a typical internal architecture of a satellite system.

#### 33.2 Block Diagrams in Signal and Control Theory

The block diagram modeling may provide control engineers with a better understanding of the composition and interconnection of the components of a system.

It can be used, together with transfer functions, to describe the cause-effect relationships throughout the system.

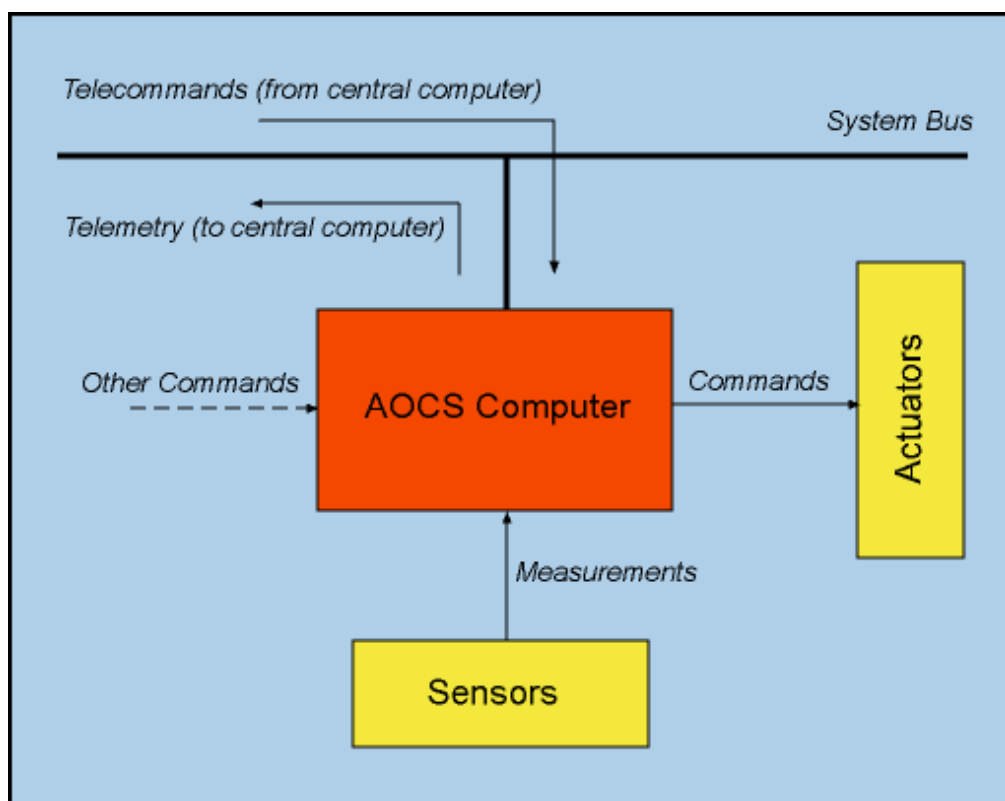
The common elements in block diagrams of most control systems include:

- Comparators
- Blocks representing individual component transfer functions, including:

- Input sensor
- Output sensor
- Actuator
- Controller
- Plant (the component whose variables are to be controlled)
  - Input or reference signals
  - Output signals
  - Disturbance signal
  - Feedback loops [17]

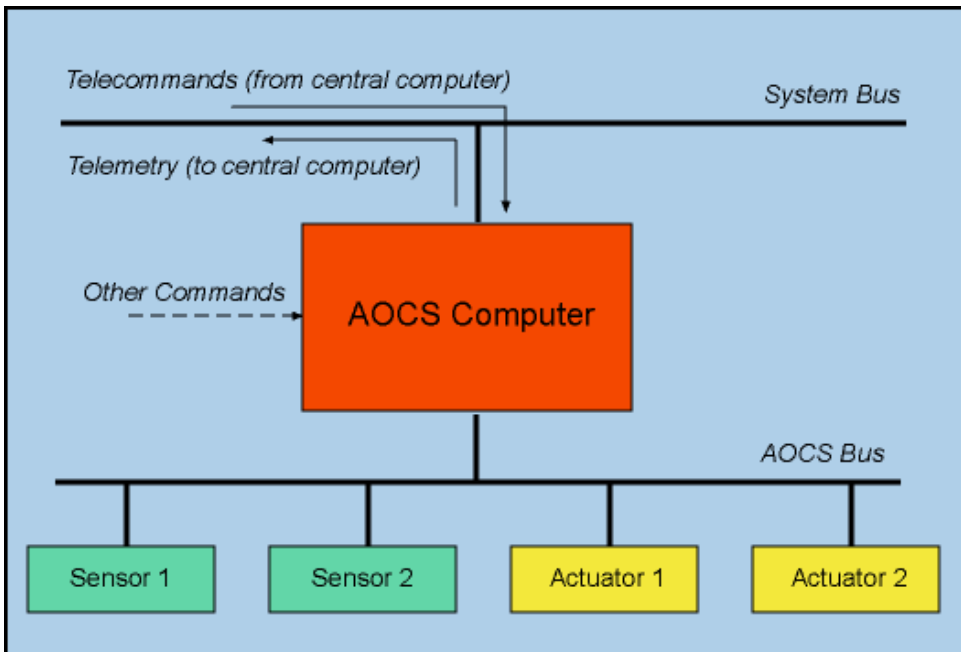
### 33.3 AOCS Subsystem Structure

The AOCS subsystem is one of the subsystems of a satellite. Its main function is to control the attitude and the orbit of the satellite.



The figure at the side shows an AOCS subsystem with its external interfaces. The figure assumes an AOCS with a dedicated computer separate from the central satellite computer. In an alternative configuration, the AOCS is hosted on the central computer.

The AOCS receives [telecommands](#) from the central computer and it forwards [telemetry data](#) to it over the [system bus](#). It periodically acquires measurements (on the satellite attitude and orbital position) from a set of [sensors](#) and uses them to compute control signals that are sent to a set of [actuators](#). Other commands, for special contingencies (such as for instance forcing the AOCS into safe mode), may be routed over dedicated command lines.



Because of its complexity, the AOCS is often organized around a dedicated AOCS bus over which communications between the AOCS computer and the AOCS sensors and actuators take place. The resulting structure is shown in the figure at the side.

## SIMULATION ENVIRONMENT

An essential requirement in order to develop and verify various attitude control algorithms is the availability of space environment model. Such a tool provides necessary infrastructure at the preliminary stage to examine and validate the algorithms prior to hardware implementation.

A simulator was set up to develop and verify attitude control algorithms for the FLP.

The simulator was developed in Matlab/Simulink environment. The top level diagram of the simulator is shown in the Figure 7.1. The structure of the simulator is kept close to the overall structure of ACS algorithms. The yellow blocks in the top level diagram represents the space environment along with the ACS hardware. The blocks in the blue color contain all the functions that have to be implemented on the FPGA-based OBC and the blocks in the green color show the user interface which is required to initialize the inputs and monitor the output of the simulator.

A fabulous support provided by EADS Astrium in a form of Astrium STARS library tool box must be acknowledged here. This tool box contains several key functions which not only helped but also accelerated the development of the space environment.

Each block shown in the top level diagram is discussed briefly in this chapter to provide an overview of the simulator. The blocks and sub-blocks of this simulator are well documented in [44] and [45]. The main blocks of the simulator are

- Space environment

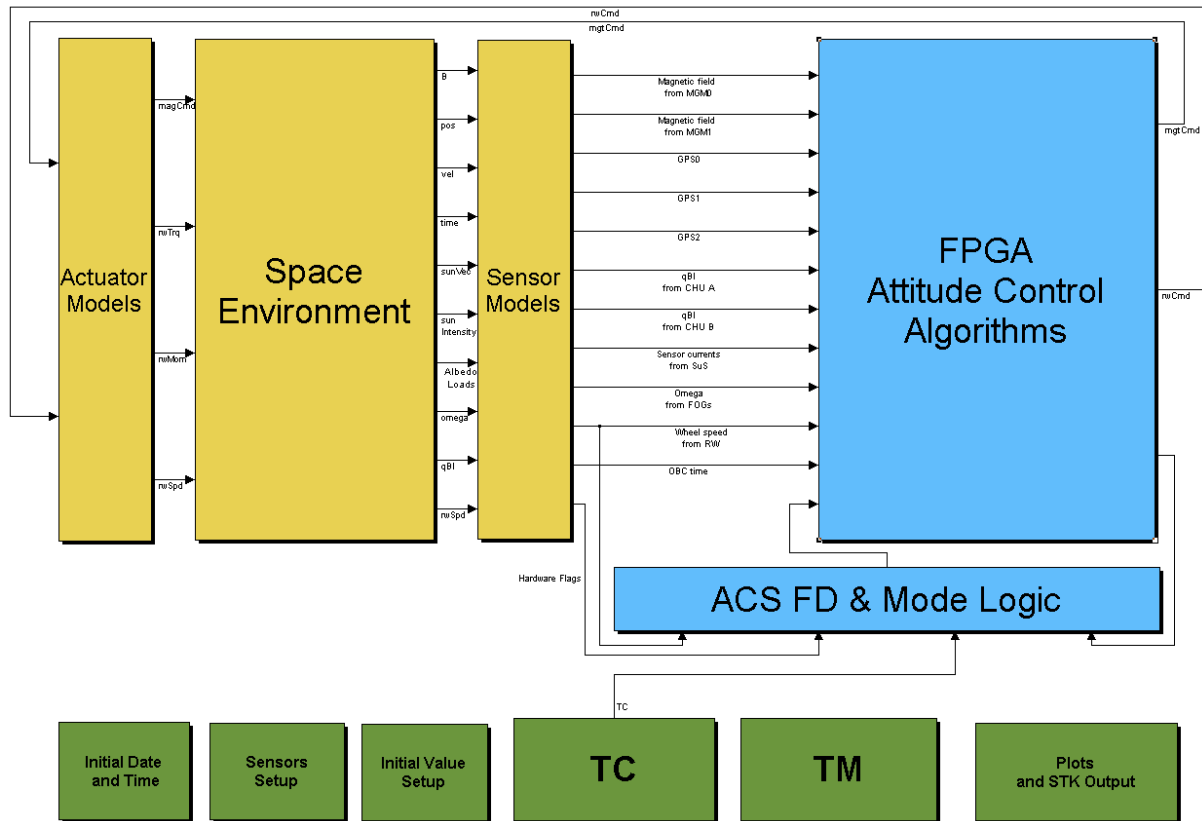


Figure 7.1: Top level diagram of the simulator

- Sensor models
- Actuator models
- User interface
- ACS algorithms
- ACS FD and mode logic

## Space environment

This block emulates the space environment for the simulation. The core of this block is the orbit generator which connects all the other blocks. The main blocks in space environment are shown in the Figure 7.2 and are listed below.

1. Epoch clock
2. Orbit propagator
3. Spacecraft dynamics and attitude block
4. Earth's magnetic field model

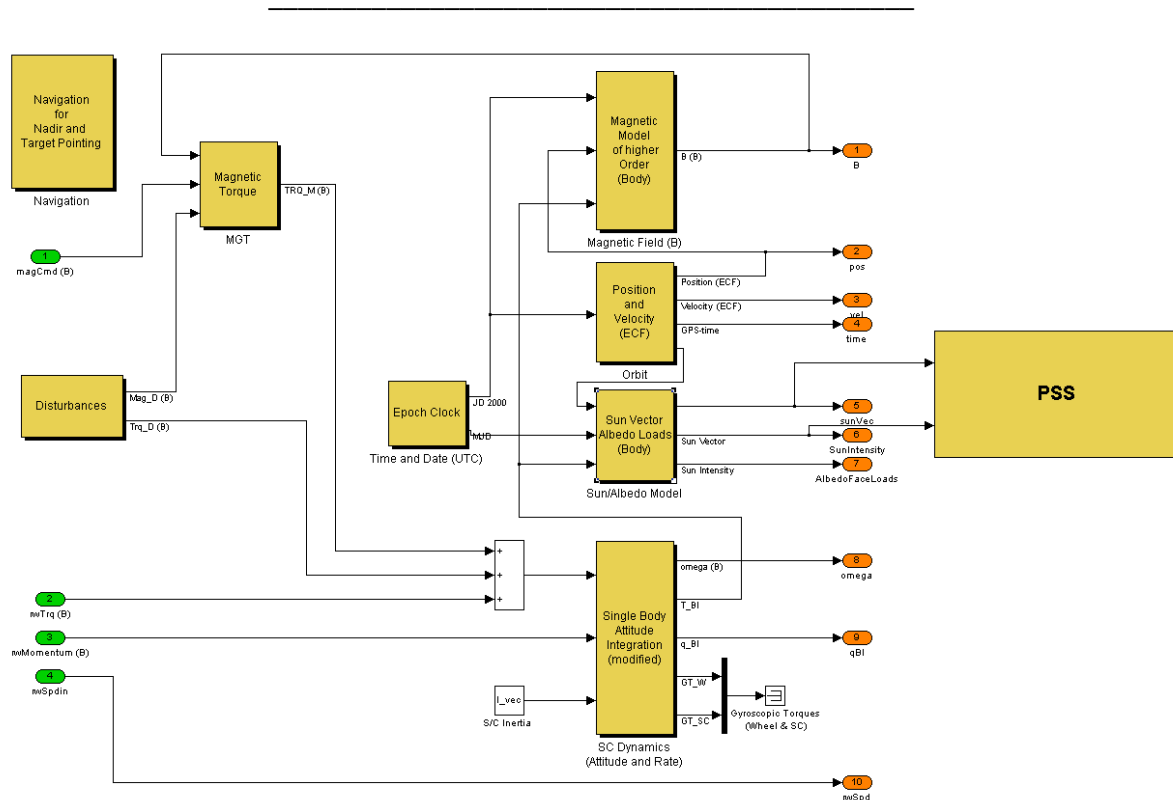


Figure 7.2: Space environment

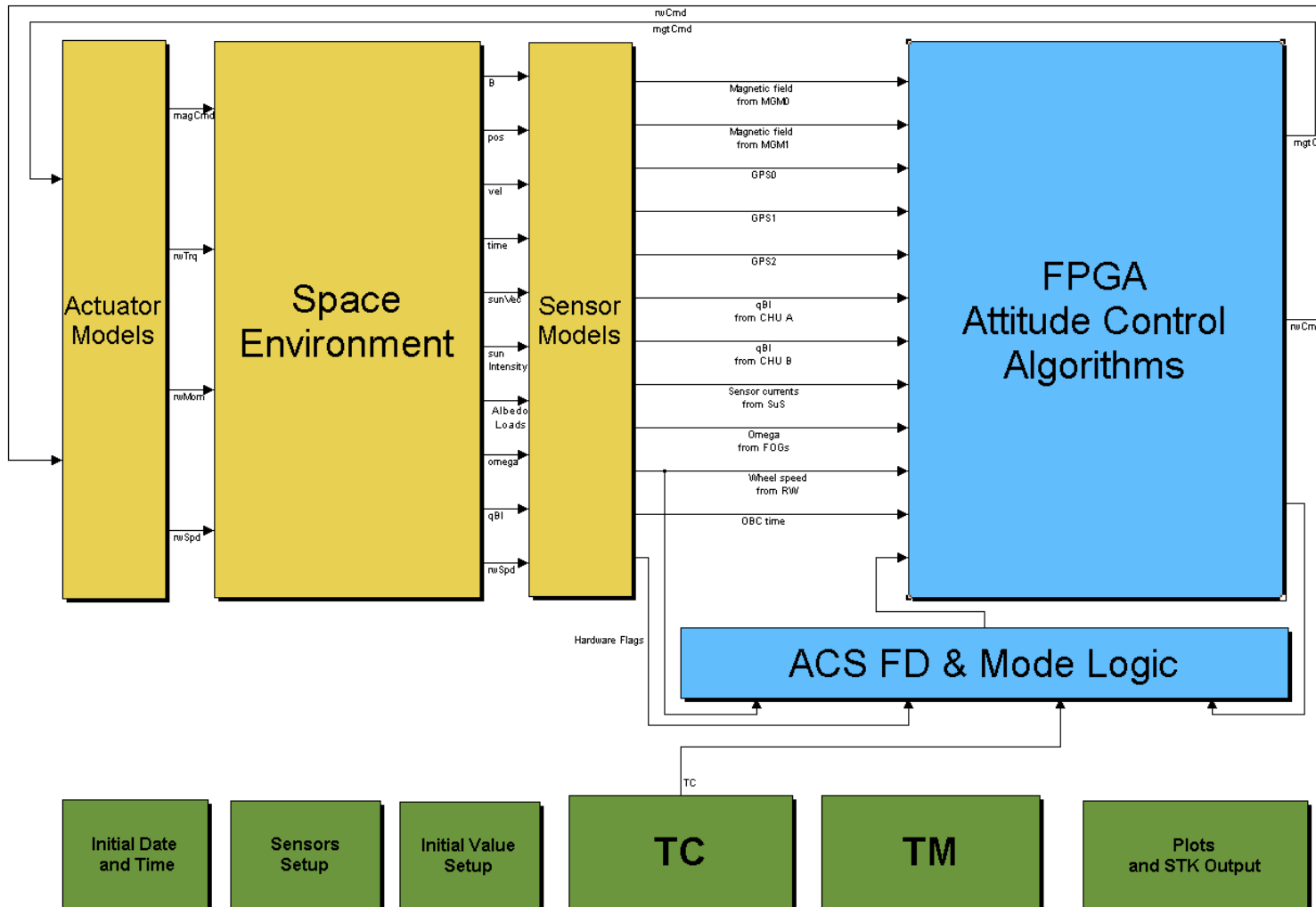
- 5. Sun vector and eclipse flag generator
- 6. Modeling albedo effect
- 7. Power subsystem (battery) model

## 34 IAP-SAT Hardware-in-the-Loop (HIL) System Design and Realization

### 34.1 ACS On-Board Algorithms Architecture

tbd ([Yassir 2010])

### 34.2 Concept for Simulation Environment<sup>45</sup>



#### 34.2.1 Space Environment

This block emulates the space environment for the simulation. The core of this block is the orbit generator which connects all the other blocks. The main blocks in space environment are shown in the Figure 7.2 and are listed below.

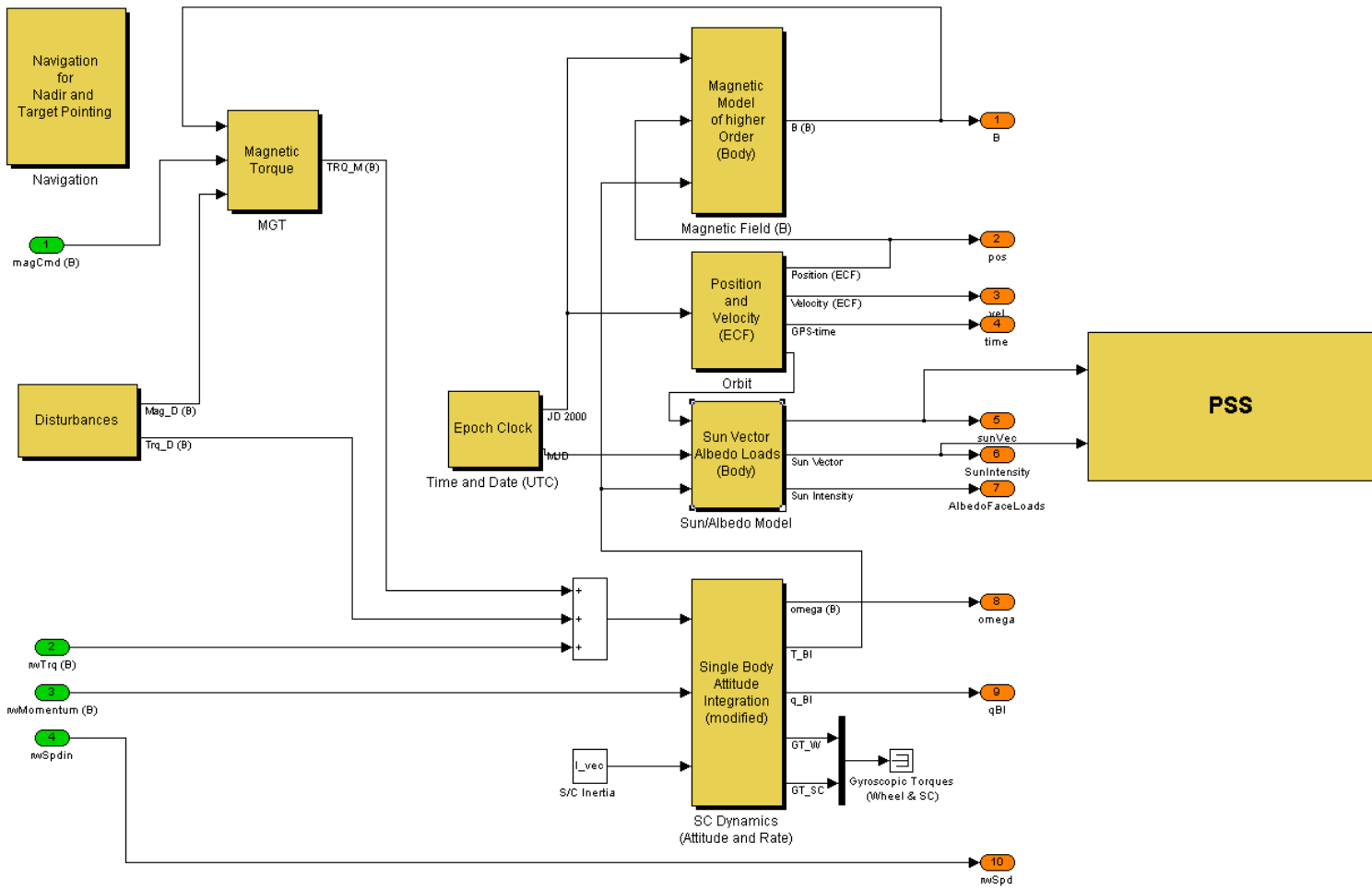
1. Epoch clock
2. Orbit propagator
3. Spacecraft dynamics and attitude block
4. Earth's magnetic field model

<sup>45</sup> Mostly based on [Yassir 2010]

5. Sun vector and eclipse flag generator

6. Modeling albedo effect

7. Power subsystem (battery) model



34.2.2 Matlab testing interface

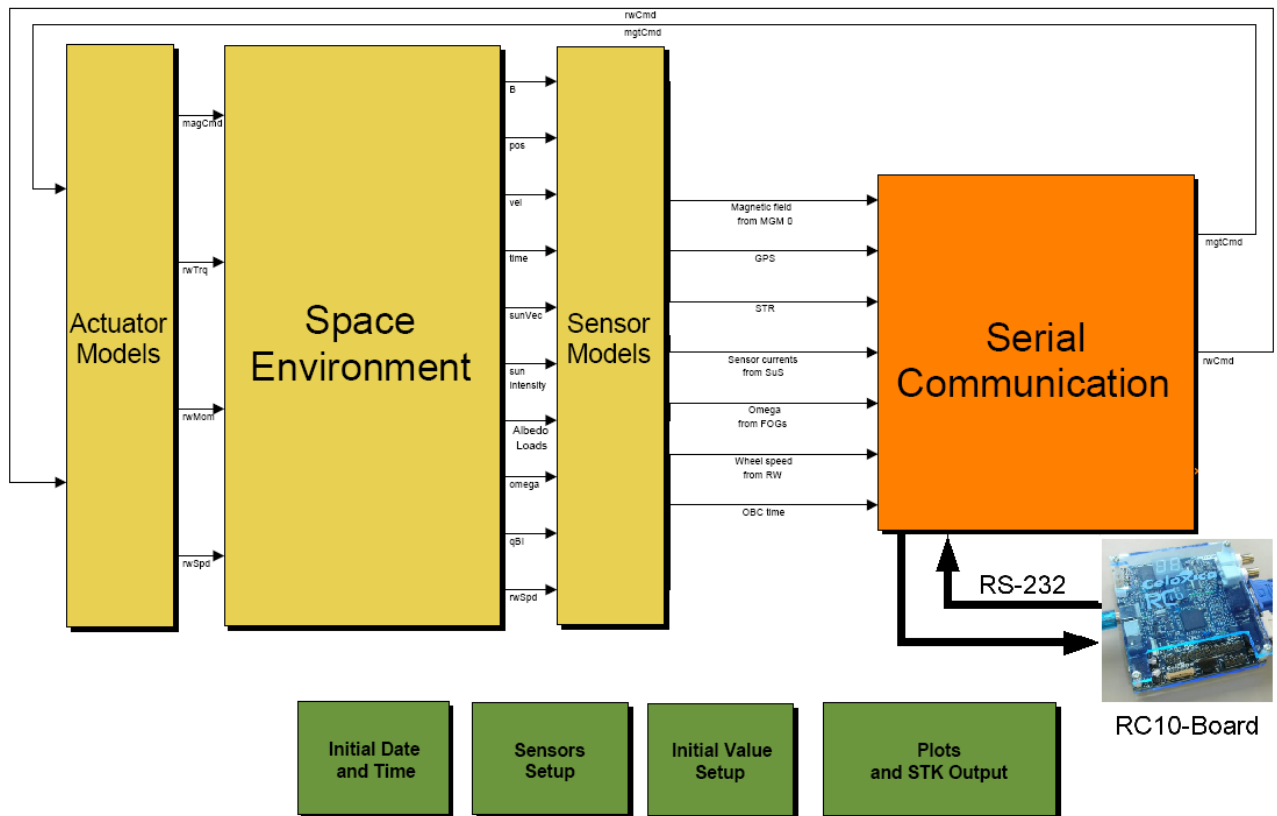
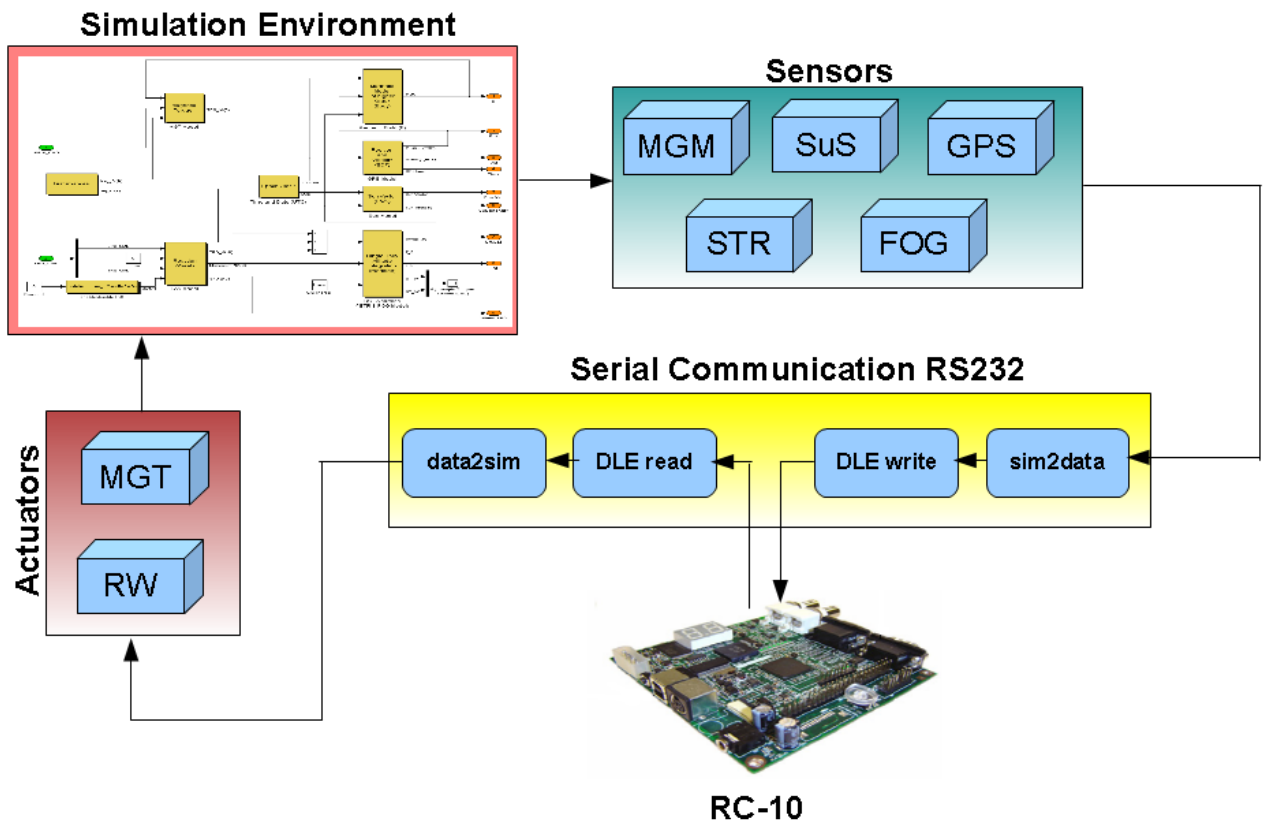


Figure 8.3: Top level diagram of testing algorithms with scicos



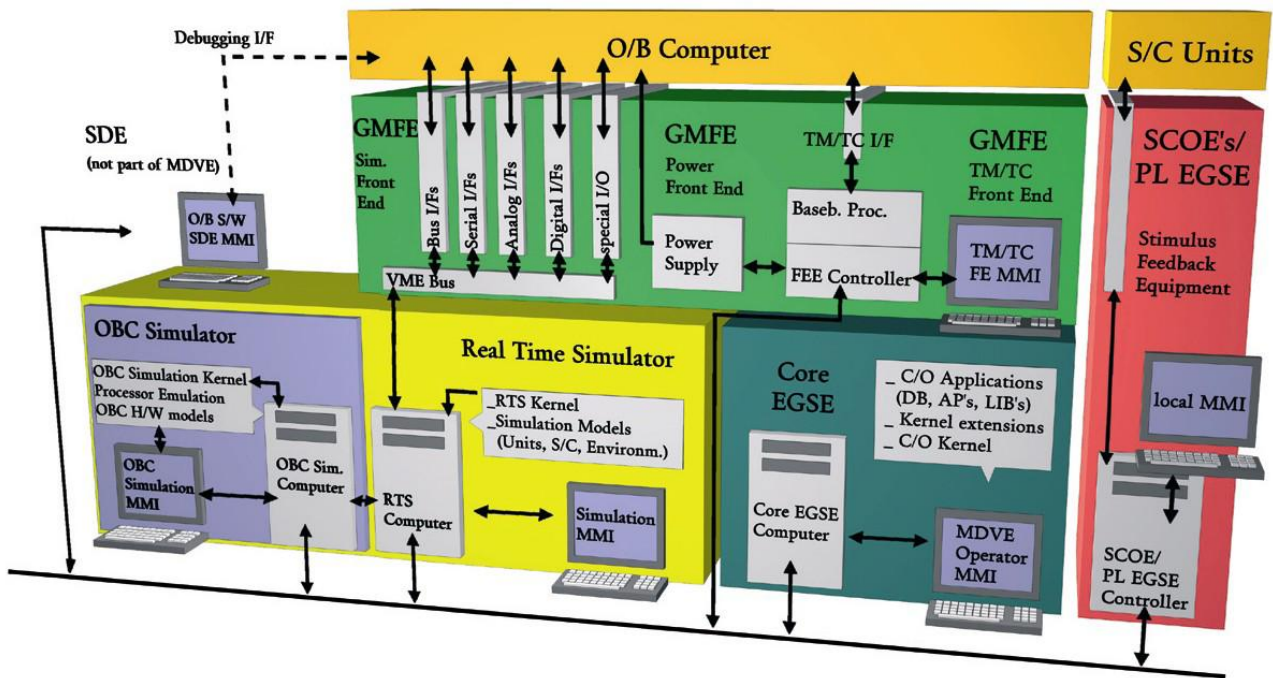


Figure 8.6: Model based development and verification environment

MDVE will be used in various project phases for a number of design, development and verification tasks in different working environments. The most important MDVE standard configurations are:

1. Development SVF (DEV-SVF)
2. Software Verification Facility (SVF)
3. System Testbed (STB)
4. Extended Real-Time Testbed (FlatSat)
5. Spacecraft simulator for the mission control center.

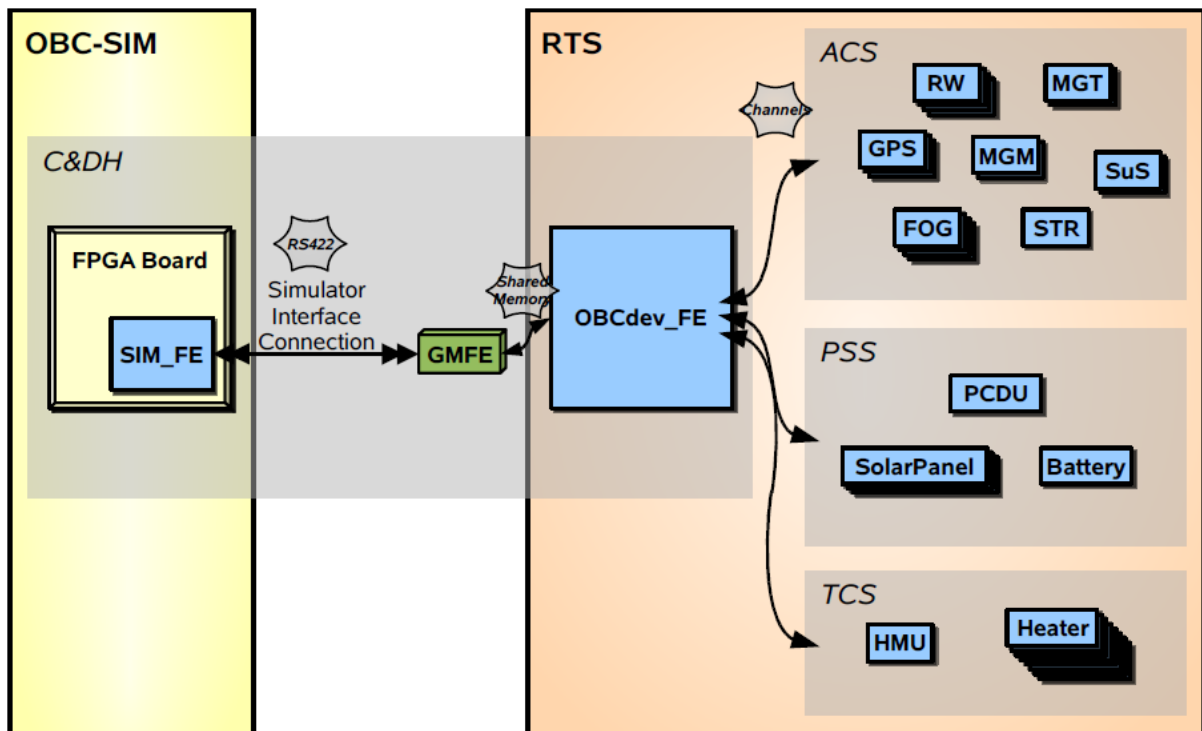


Figure 8.7: Simulator Interface with OBC

### 34.3 HIL System architecture

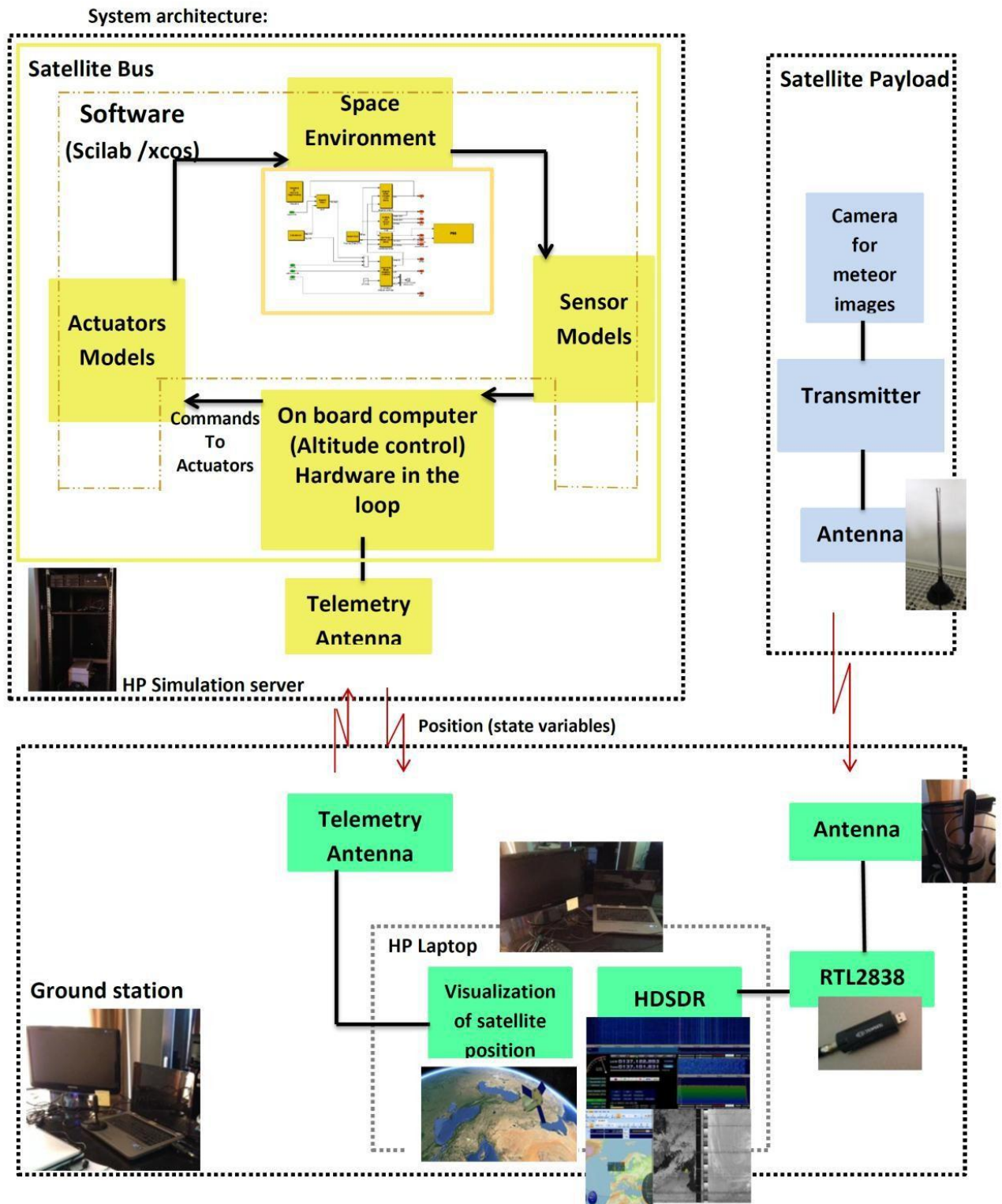


Figure 34.1: System architecture of the satellite's function

IAP-SAT is launched; it attains the sun synchronous low earth orbit with a fixed orientation and starts to turn around the earth.

This satellite changes its orientation and its inclination due to disturbance and perturbation in the atmosphere. The electronic systems on board a satellite include attitude determination and control, communications, command and telemetry, and computer systems. Sensors also refer to the electronic components on board a satellite.

The most important consideration that must be made in the design process is the environment in which the satellite systems and components must operate and endure.

One of the most vital roles that electronics and sensors play in the mission and performance of a satellite is to determine and control its attitude, or how it is orientated in space.

The orientation of a satellite varies depending on the mission. The satellite may need to be stationary and always pointed at earth, which is the case for a weather satellite. However, it may also be needed to fix the satellite on a given axis. The attitude determination and control system ensures the right and correct behavior of the satellite.

Another system which is vital to a satellite is the command and telemetry system, so much in fact, that it is the first system to be redundant. The communication from the ground to the satellite is the responsibility of the command system. The telemetry system handles communications from the satellite to the ground. Signals from ground stations are sent to command the satellite and precise the task that should be accomplished by the satellite, while telemetry reports back on the status of those commands including satellite vitals and mission specific data. [27]

### 34.3.1 Simulation on scilab/scicos

#### 34.3.1.1 Parameters and equations used in the simulation

##### Equations of motion:

The only force applied on the satellite is the gravitation force:  $F_{grav} = (G * M_{sat} * M_{Central}) / R^2$

Orbital Speed Equation: 
$$v = \sqrt{\frac{G * M_{central}}{R}}$$

The Acceleration Equation: 
$$a = \frac{G * M_{central}}{R^2}$$

Orbital Period Equation: 
$$\frac{T^2}{R^3} = \frac{4 * \pi^2}{G * M_{central}}$$

With R= 6378.14 Km

$$h = 680 \text{ Km}$$

$$G = 6.67 * 10^{-11} \text{ N} * \text{m}^2 * \text{kg}^{-2}$$



### Model of gyroscope

Gyroscopes are devices that sense rotation in three-dimensional space without reliance on the observation of external objects. [12]

Rate gyroscopes, also referred to simply as gyros, do not provide a measure of attitude, but are commonly used in satellite as they provide a measurement of angular velocity. Fusing the gyro with attitude measurements provides more accurate attitude estimates than the attitude measurements alone, with the degree of improvement dependent on a number of factors such as the sensor sampling frequency, satellite dynamics, and gyro noise characteristics. [14]

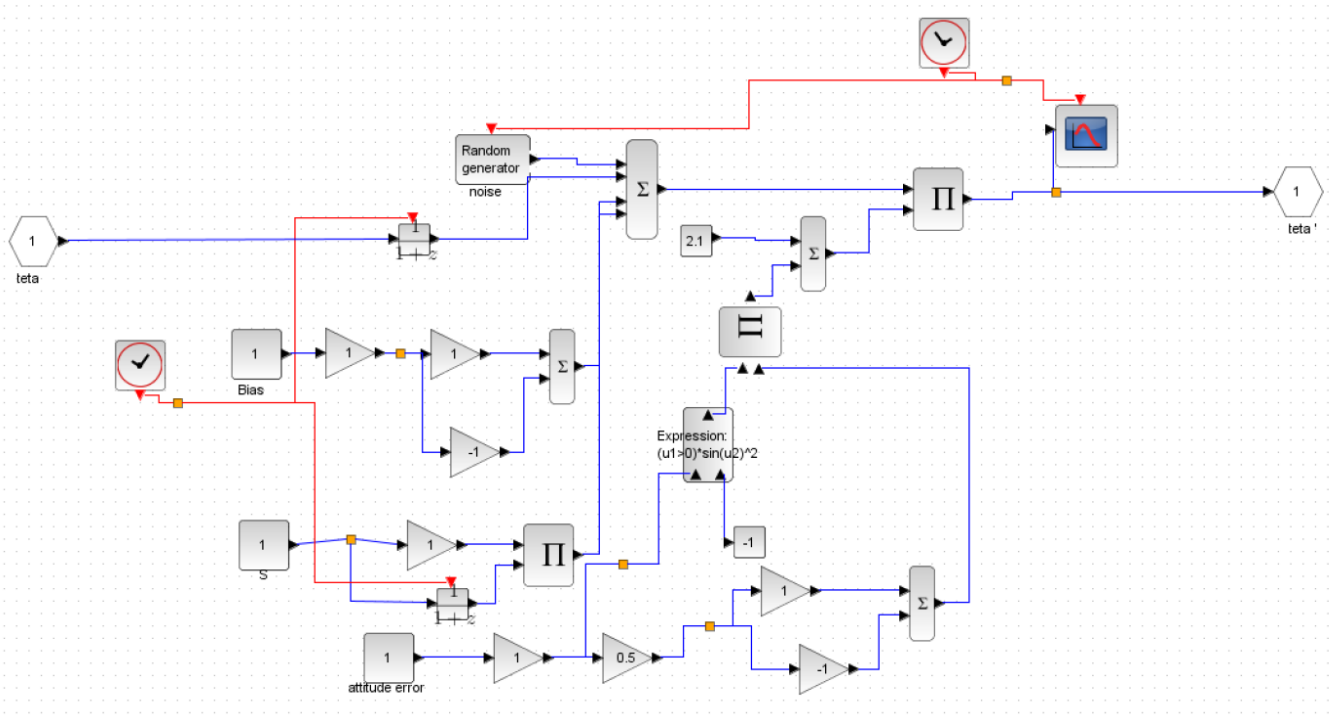
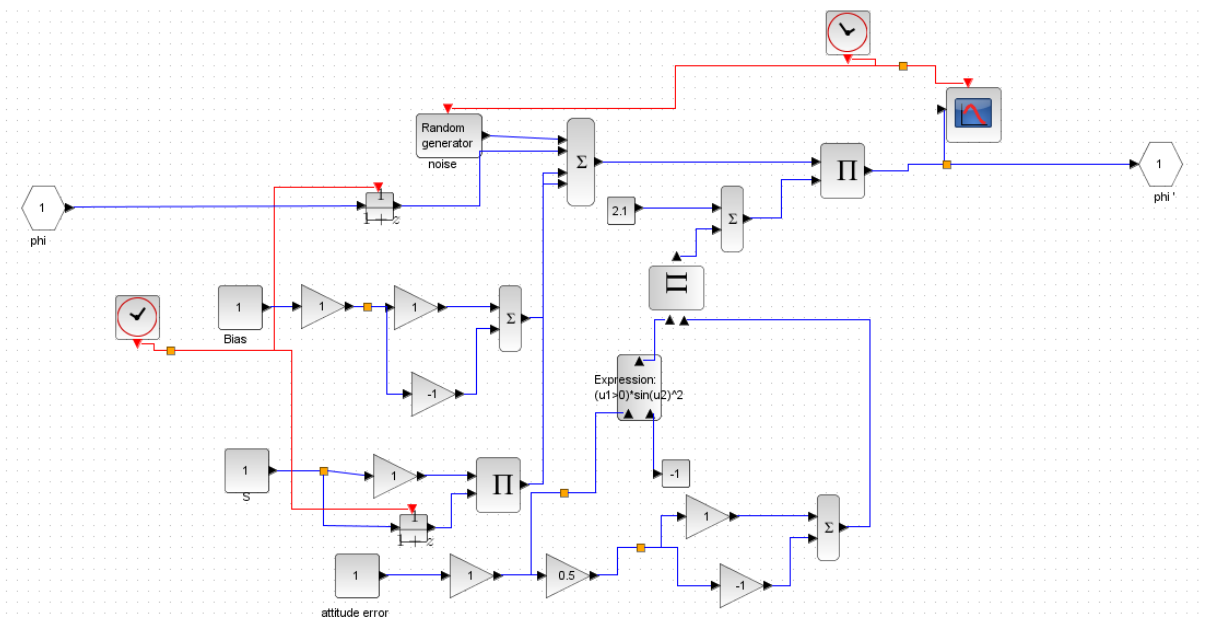


Figure 34.3: Diagram of gyroscope (representative of theta angle)





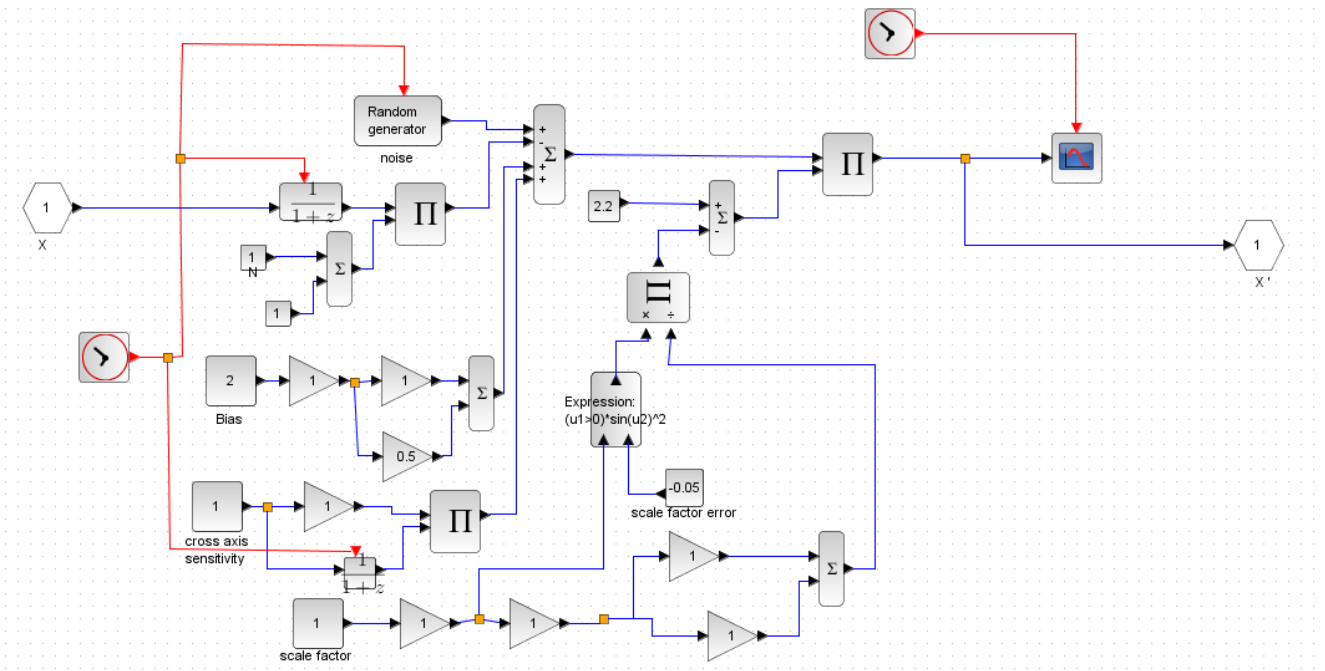


Figure 34.6: Diagram of accelerometer (representative of X position)

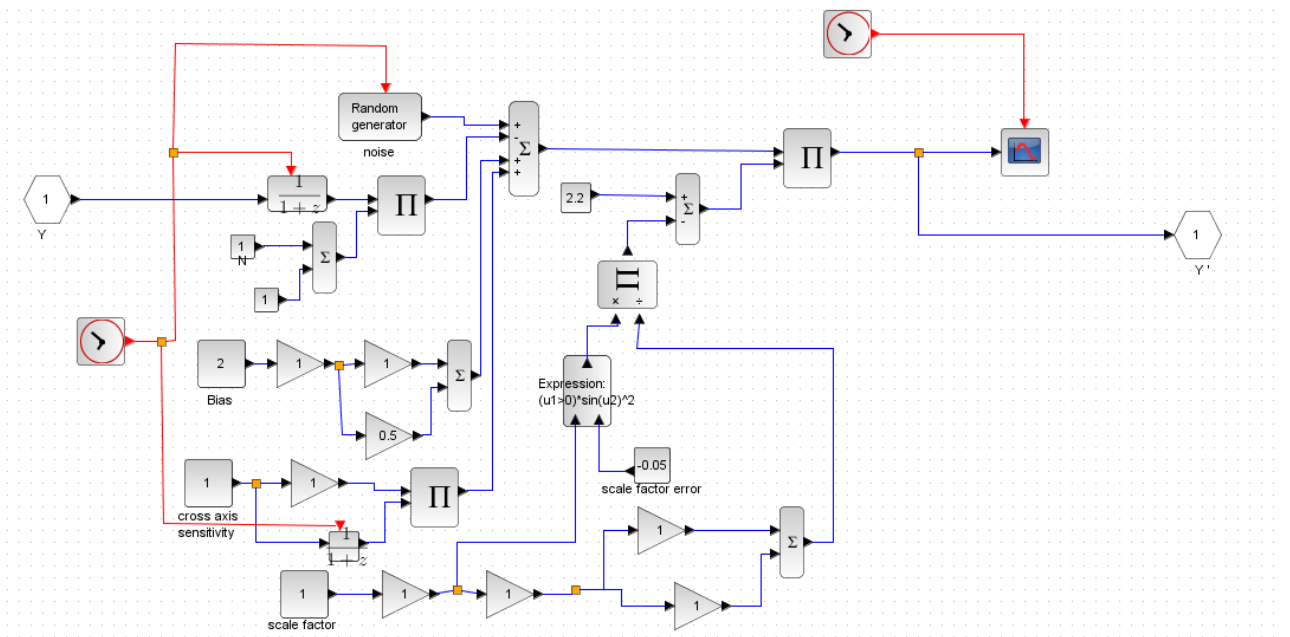
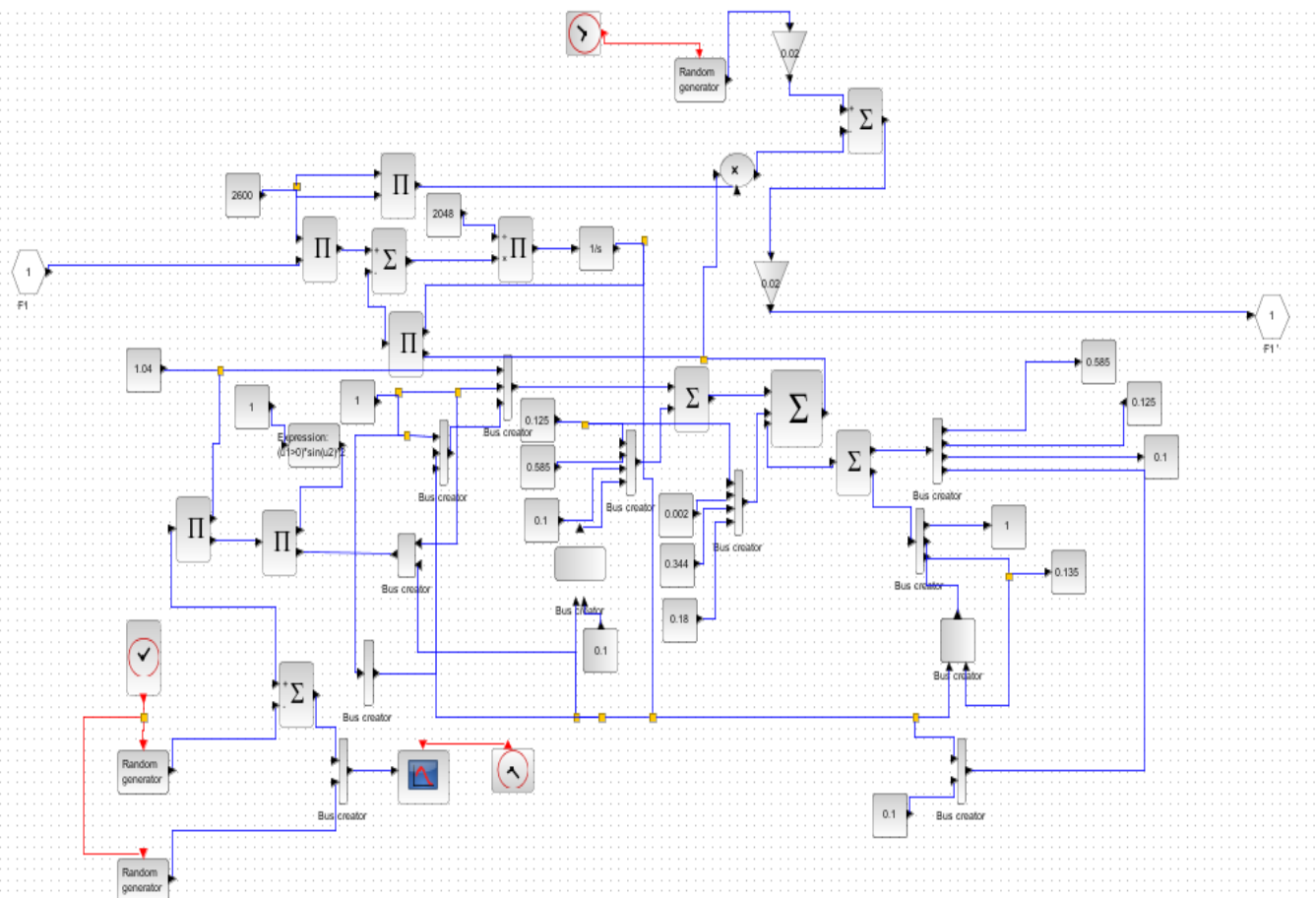


Figure 34.7: Diagram of accelerometer (representative of Y position)





**Figure 34.9: Diagram of Hall Effect propulsion (first propulsion F1)**

As input of the Hall Effect thrusters (Fig.6.9), we have the force (rate of momentum); this input creates an impulse to reset the satellite in its correct position and the right orientation. The output of the actuators is the real values of this force after passing by the random generator, noise...

There are 4 actuators, each one has the same diagram, but with F1, F2, F3 and F4 as inputs.

### Model of space

As we mentioned above, the most important consideration that must be made in the design process is the environment in which the satellite systems and components must operate and endure.

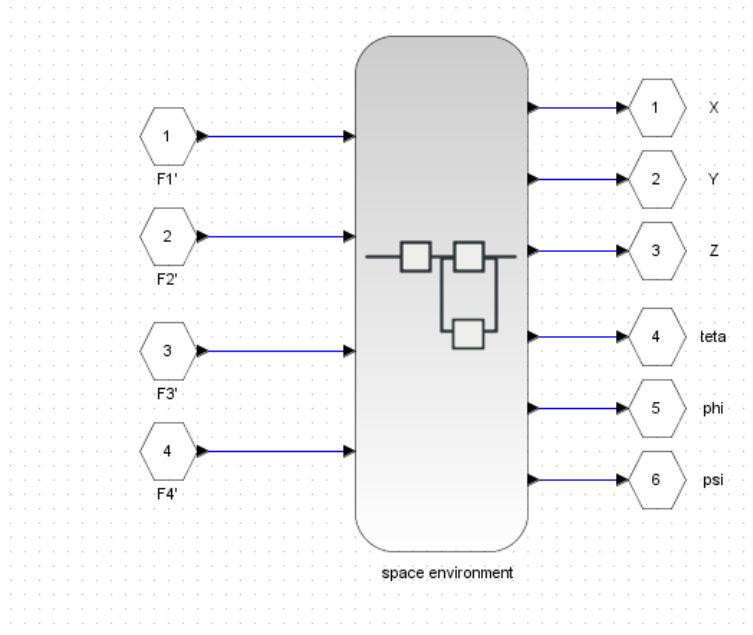


**Figure 34.10: Diagram of the space environment**

The diagram of the space environment is formed by four diagrams (Fig.6.10):

Diagram representing the positions and angles, another representing system dynamics (attitude and rate) , one represents the magnetic field and the last represents the sun vector.

[6]

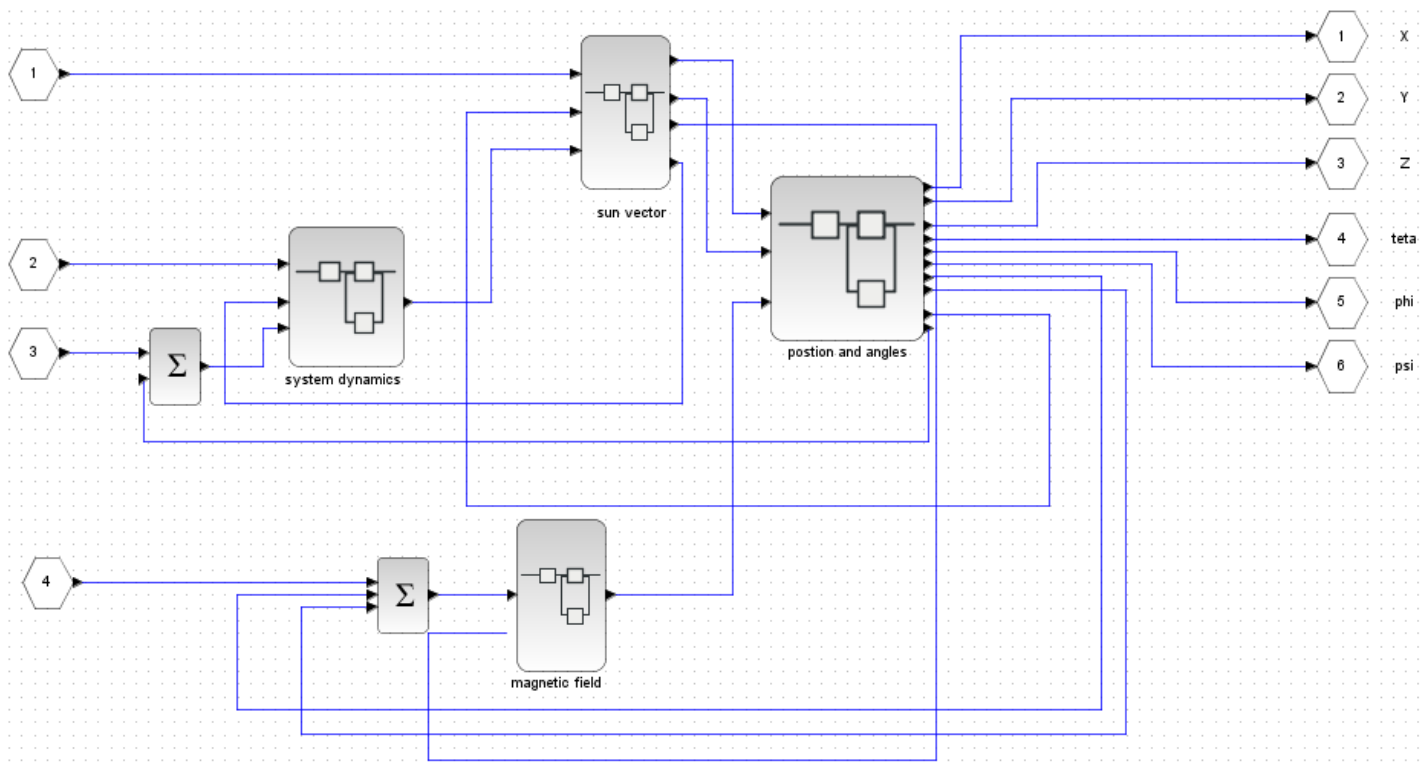


**Figure 34.11: Diagram of the space environment with details of its components**

The details of each related blocks in Fig.6.11, are shown in the next figures:

a- System dynamics

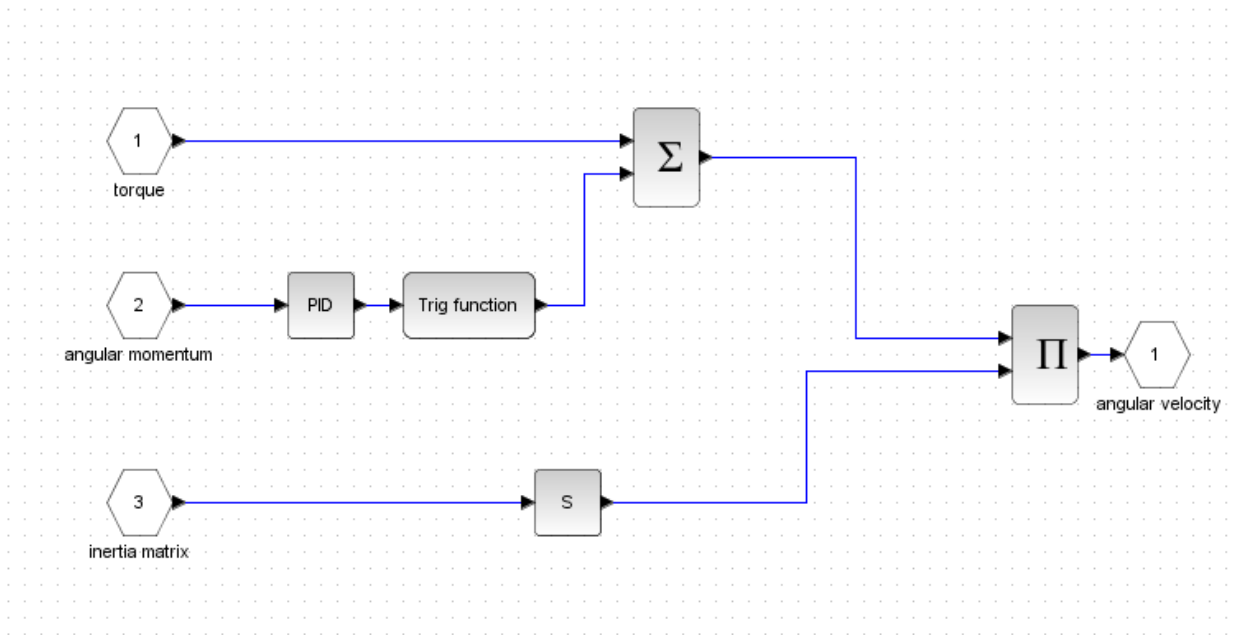


Figure 34.12: Diagram of the system dynamics

In the simulation of the system dynamic (Fig.6.12), the inputs are: the torque, the angular momentum and the inertia matrix.

This diagram gives as output the vector of the angular velocity.

b- Sun vector

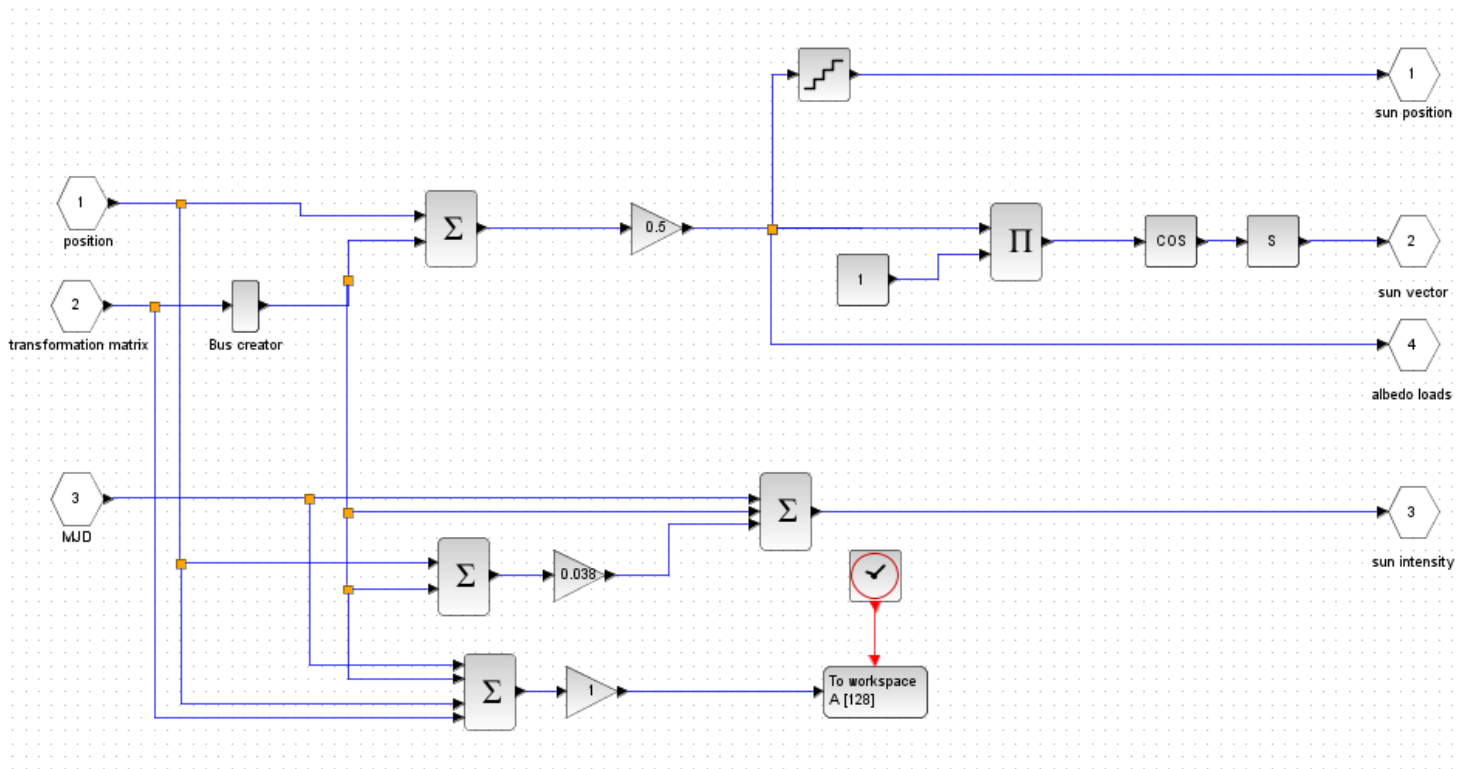


Figure 34.13: Diagram of the sun vector

In this diagram (Fig. 6.13), we have simulated the sun vector by entering as inputs the position, the transformation matrix and the MJD (Modified Julian Date). The outputs of this diagram are the sun position, the sun vector, the albedo loads and the sun intensity.

c- Positions and angles

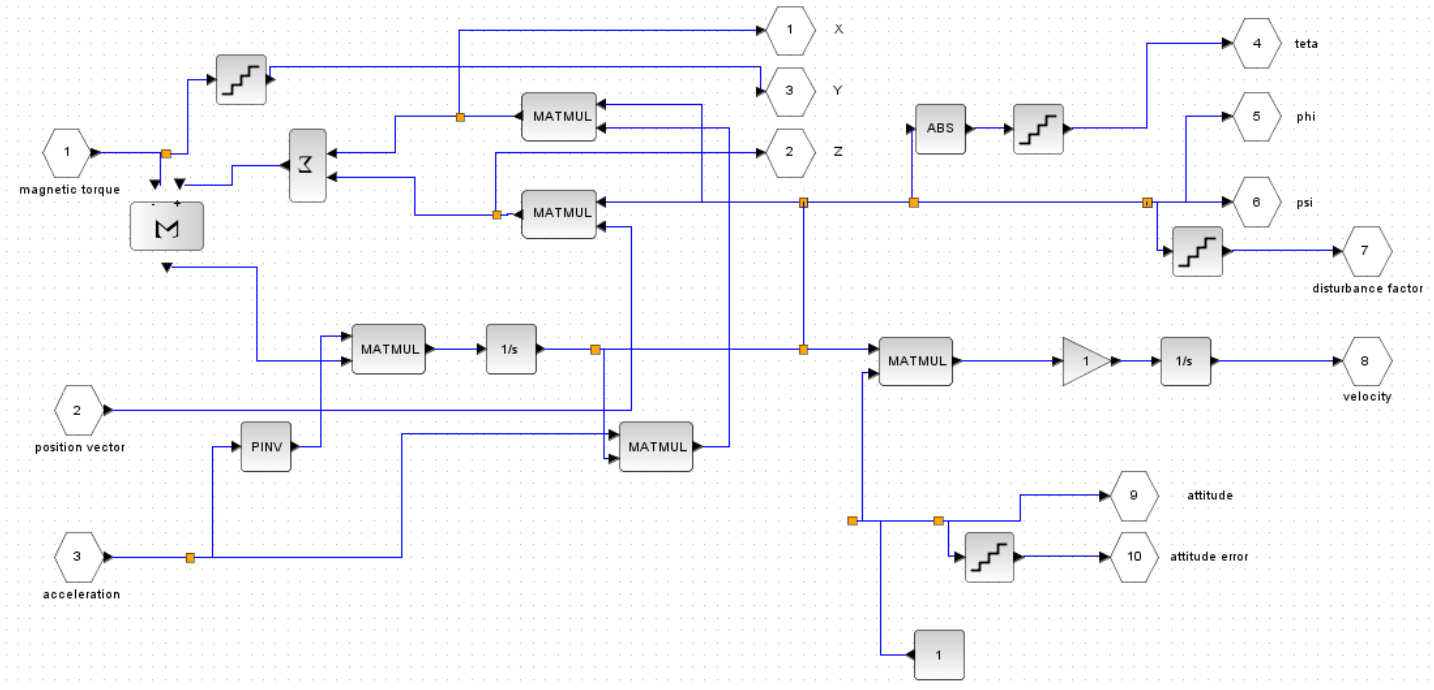
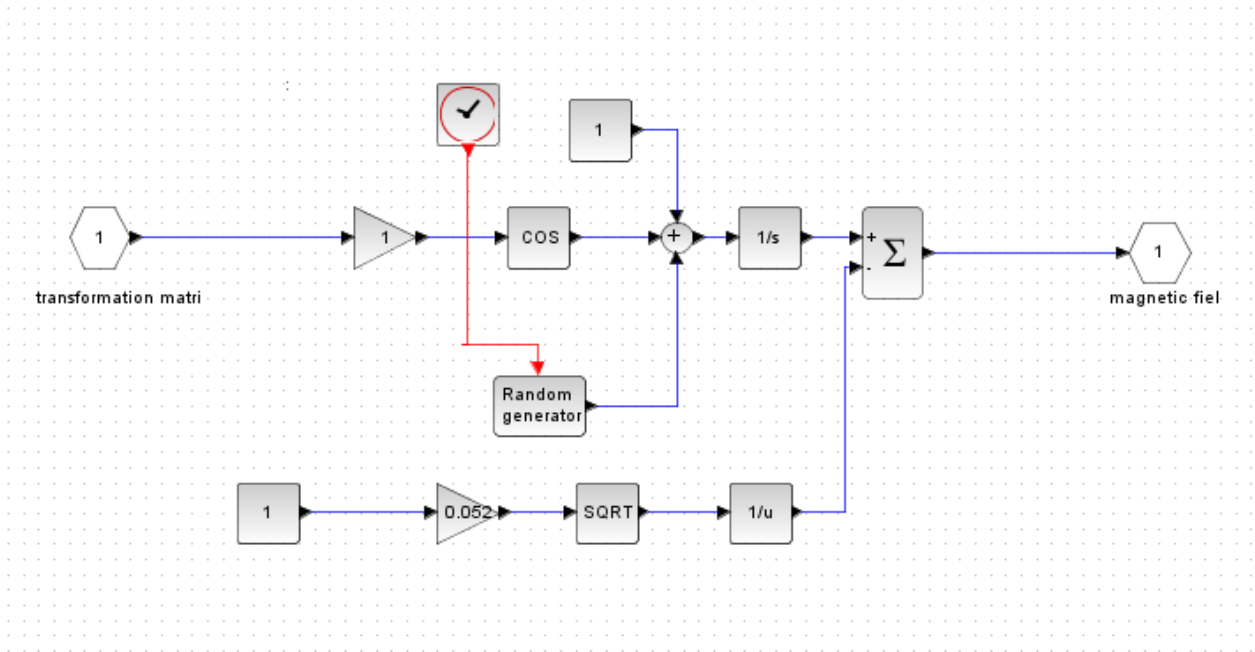


Figure 34.14: Diagram of the positions and angles

The diagram of positions and angles (Fig.6.14) has as inputs the magnetic torque, the position vector and the acceleration.

The outputs of this diagram are the position (X, Y and Z), the angles (teta, phi and psi), the velocity, the attitude, the attitude error and the disturbance factor.

## d- Magnetic field



**Figure 34.15: Diagram of the magnetic field**

The magnetic field is simulated by using the transformation matrix as input, and we obtain as output the magnetic field (Fig.6..15).

### Integration of diagrams

To simulate our satellite, all this models (model of space, actuators and sensors) will be integrated to obtain one diagram (Fig. 6.16).

In this diagram, we have integrated the four diagrams of actuators, the diagram of the space environment and the diagrams of sensors (three diagrams for the gyroscope and three for the accelerometer).

The sensors measure the values of position and orientation of the satellite from space, and give them real values.

By passing to the board computer, these values are checked and compared to the correspondent values.

If these values are not the fixed values to our mission, the corresponding actuators are activated to reset the satellite in the best situation.

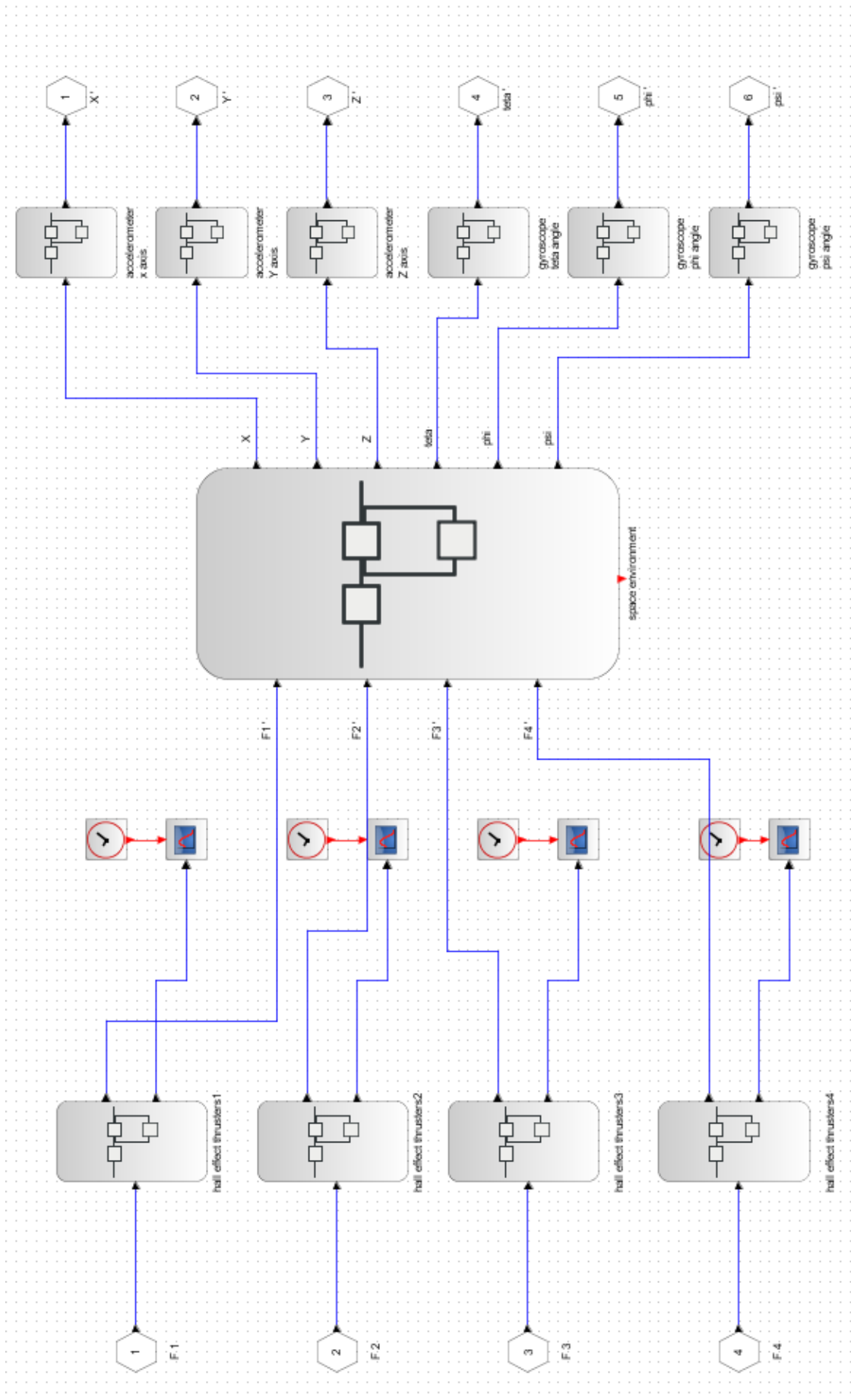


Figure 34.16: Integration of all diagrams (final model of simulation)

### 34.3.1.3 Test of simulation

Now we try to test our simulation, by giving different inputs (forces) to the actuators and see the difference in the result.

Many cases are experimented.

Case 1:

The first case is to consider that the last propulsion will not function, so the value of  $F_4$  will be zero, and the other forces will take each one the correspondent value to put the satellite on the requested orientation.

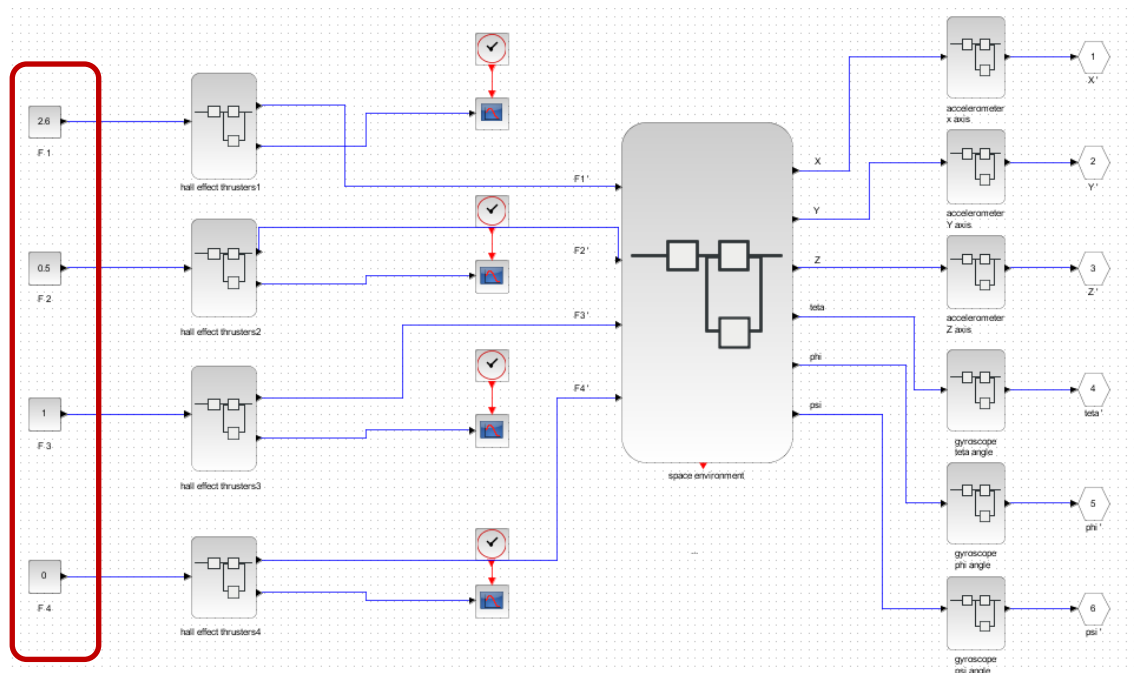


**Figure 34.17: First case of the simulation's test**

Case 2:

The second case is to consider that the input of the second propulsion will be a variable force (a step function), and the fourth force will also be zero.

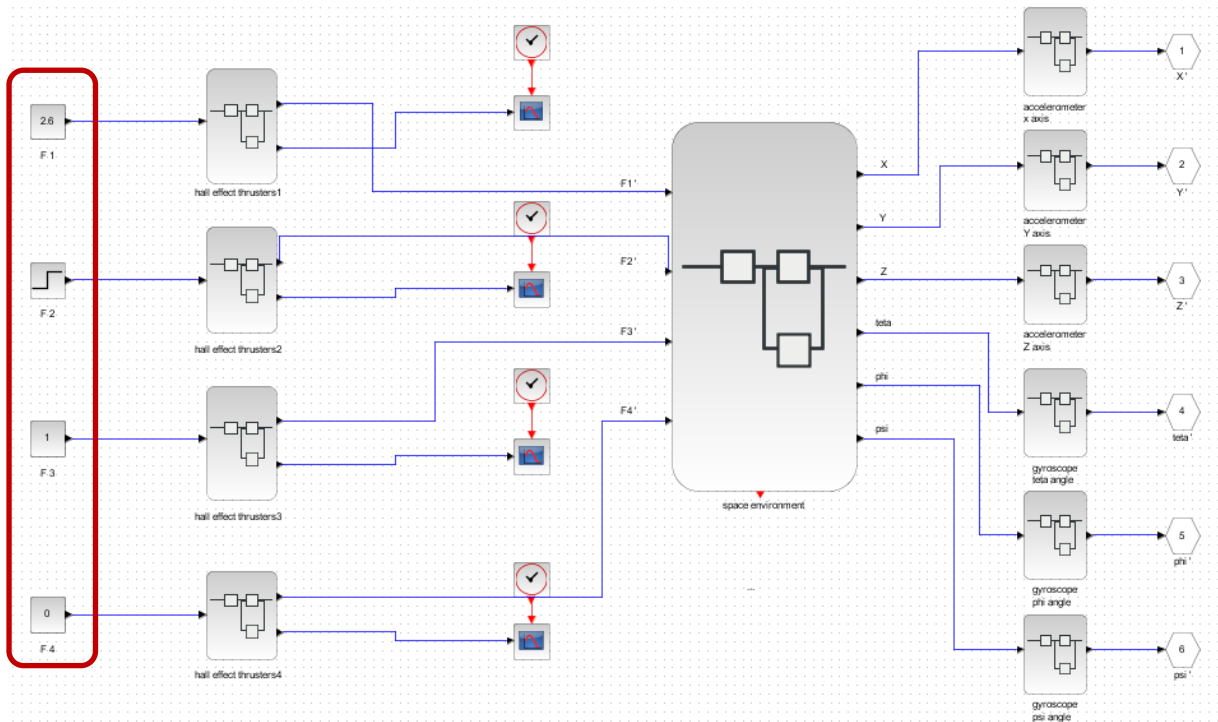


Figure 34.18: Second case of the simulation's test

Case 3:

This last case is to consider that it is necessary to activate the first propulsion (value of F1 different to zero), and the others have all the value zero for the force.

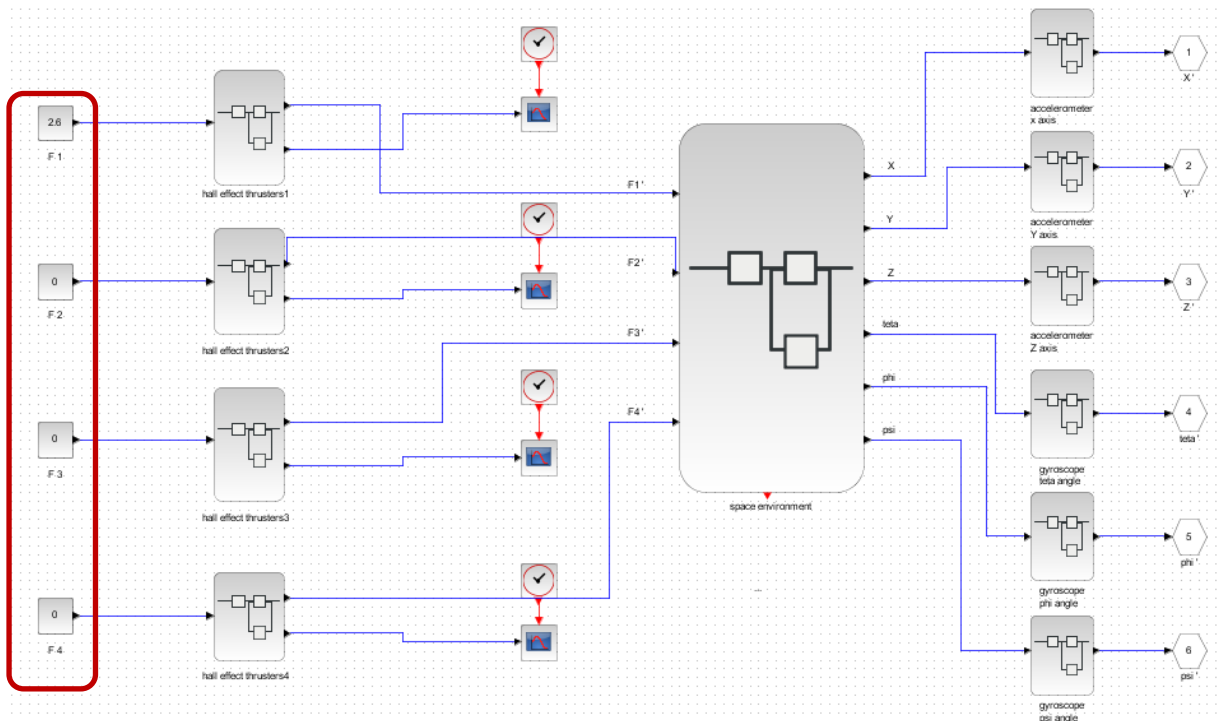


Figure 34.19: Third case of the simulation's test

### 34.4 C code of Control Algorithm at the Board Computer

The next figure represents the first attempt of writing the C-code, which will examine the outputs of the sensors on the board computer.

Fatima Char: This code is written by my colleague, during his master training; however, I have finished my project before that he accomplished his project.



```

3.sce x read.c x
#include <stdio.h>
#include <stdlib.h>

int main()
{
    float num;
    FILE *cfptr;
    FILE *fptr;

    if ( ( cfptr = fopen( "/home/arcom/JAYCE.txt", "r" ) ) == NULL ) {
        printf("file could not be opened. \n");
    }

    else {
        fseek ( cfptr, 10 * sizeof(float), SEEK_SET);
        fscanf( cfptr, "%f", &num) ;
        fclose (cfptr);
    }

    if ( ( fptr = fopen( "/home/arcom/ibra.txt", "w" ) ) == NULL ) {
        printf("file could not be opened. \n");
    }

    else {
        fprintf(fp, "%f\n", num);
        fclose (fp);
    }

    system("PAUSE");
    return 0;
}

```

Figure3: The C-code first trial

A similar code, but more detailed and delicate, will close our loop, and complete this task.

from "Result of Master Thesis in Short":

Next step in our project was the hardware in the loop.

We have simulated all the non-present components of the satellite (sensors, actuators and space environment) as block diagrams in Scilab/Scicos. We have integrated all these diagrams to obtain one diagram representative of the real state and function of the satellite.

Then, a closed loop was simulated between the sensors that provide the actuators positions and angles, and the actuators that generate forces to change the attitude and put the satellite on the orbit again after a possible disturbance based on the data of the sensors.

As perspectives, we got success in writing a C-code which reads the outputs of the simulation from a C-binary file and transforms them to a txt file. This txt file is sent and read on the computer board; however, this task remains incomplete and need more investigation.

Therefore, the next task consists of writing a new C-code with the duty of examining these outputs and sending the request inputs to the diagram of simulation. These inputs are sending as txt file and should be again transformed to a C-binary file to be read by the simulation. This task must be more examined and investigated.

### 34.5 Linking the software simulation on the server with the OnBoard-Computer

The sensors (gyroscope and accelerometer) take information about position, inclination and orientation of the satellite from the space environment and send this information to the computer board.

In the test of simulation (paragraph 6.1.1.3), we have manually changed the inputs of actuators to assay how the outputs of sensors change with the forces given by the propulsion. But in our system, this test will be realized automatically, by using the board computer.

This computer board is connected to the actuators. If the needed position and the orientation are not reached, the actuators are automatically activated to control these parameters.

By the action of the actuators, the space environment has a new position and orientation which are detected again by the sensors.

With this method, we arrive to control the attitude of the satellite on its orbit.

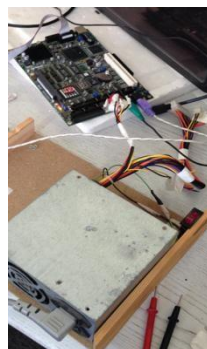
The modeling of the space environment, the sensors and the actuators is a software simulation realized with the scilab/scicos software on the HP server (paragraph 2.2.2). But the board computer is hardware, and it will be connected to this software simulation.

To join this software with the board computer and to attain the real control of the satellite, the board computer will read the outputs of sensors, to give the inputs for the actuators.

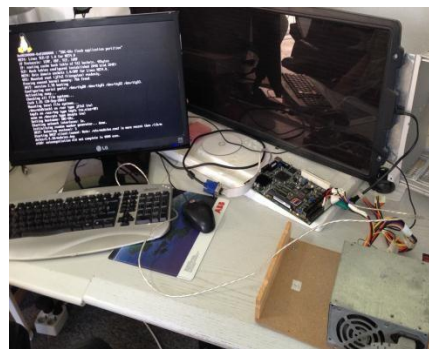
The computer board is activated, and we have connected this board with a screen, as shown in the figures 34.20, and the board should be connected to the internet.



(a)



(b)



(c)

**Figure 34.20 (a, b, c): Activation of the board computer**

The simulation of the sensors, actuators and space environment is done on the HP server. This HP server will be connected to the same network.

```
SBC-GX login: arcom
Password:
arcom@SBC-GX arcom$ ssh meae@192.168.1.1
meae@192.168.1.1's password:
Last login: Wed May 13 13:28:11 2015 from 192.168.1.103
[meae@server ~]$
```

**Figure 34.21: Screen appeared after the login to the server**

We have to login firstly to the board computer in order to enter to the HP server.

Now all files on the server can be shown on the screen of board computer (Fig.6.22).

```
nss-mdns-0.10.tar
nss-passwords_0.1.1-1_kfreebsd-1386.deb
old
OpenFOAM
OpenI95.exe
opencad-2015.03-1
opencad-2015.03-1.src.tar
OpenSCAD-2015.03-x86-64.zip
pluto
promotion1_fzk
rpm-4.11.0.1
rpa-4.11.0.1.tar.bz2
scicos_block_editing1.png
scicos_block_editing2.png
Scicos_block_Guyro.png
scicoslab-x11-4.3-1.e15.1386.rpm
scicoslab-x11-4.3-1.e15.1386.rpm_FILES
spa_environ
tools
uebung
usr
xenacs-21.4.20.tar.tar
xenacs-21.4.20.tar
[meae@server ~]$
```

**Figure 34.22: Appearance of all files present on the server on the screen of board computer**

After this connection, we have to transfer the simulation in scilab/scicos to the board computer of the satellite by writing a C-code, because the board can't read the scicos file extension (.zcos).

The C-file will recognize the data in scicos file, and transform it to a format that can be read by the computer board.

Firstly, we arrive to read the inputs and the outputs of the scicos diagram from a C-binary file, by using the blocks in the palette of scicos.

Then, a method is necessary method to read this binary file as a txt file to link this software with the hardware.

Let's try to apply our method on a simple model simulated using Scicos (Fig.6.23).

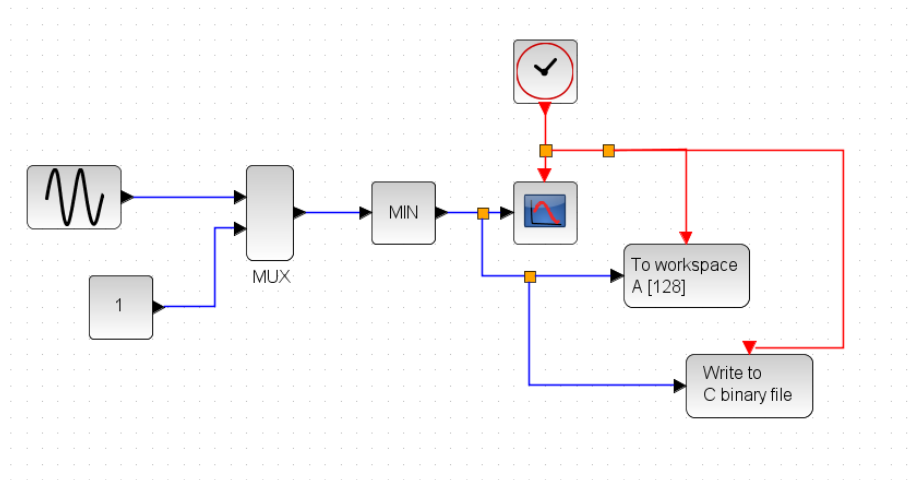


**Figure 34.23: Example of a randomly simulation**

The first step is to write the output of the file Scicos in a C binary file then to save this output in the workspace.

In the SciNotes, we write a code to run the simulation automatically (Fig.6.24).

```

3.sce (/home/jisa/Desktop/new/3.sce) - SciNotes
3.sce x
1 cd /home/jisa/Desktop/new/
2 importXcosDiagram("/home/jisa/Desktop/new/1.zcos")
3
4 typeof(scs_m)//The diagram data structure
5
6 //This diagram uses 3 context variables.:
7 //-.Amplitude.: the sin function amplitude
8 //-.Pulsation.: the sin function pulsation
9 //-.Tf.....: the final simulation time
10 scs_m.props.context//the embedded definition
11
12 //first batch simulation with the parameters embedded in the diagram
13 xcos_simulate(scs_m, .4);
14 quit;
15

```

**Figure 34.24: code written in SciNotes**

A binary file is created after the simulation, see fig.6.25.

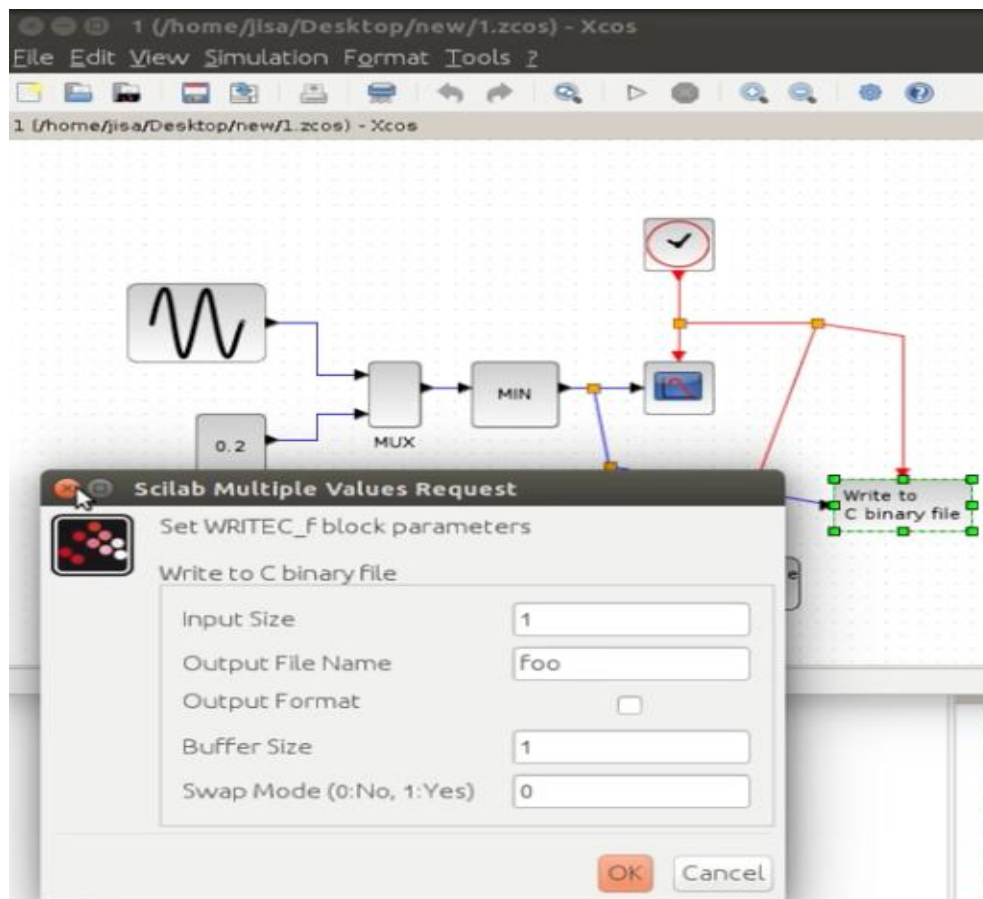


Figure 34.25: Output saved in the C-binary file (foo)

This file is named foo. Second step is to write the C-code (Fig.6.26).

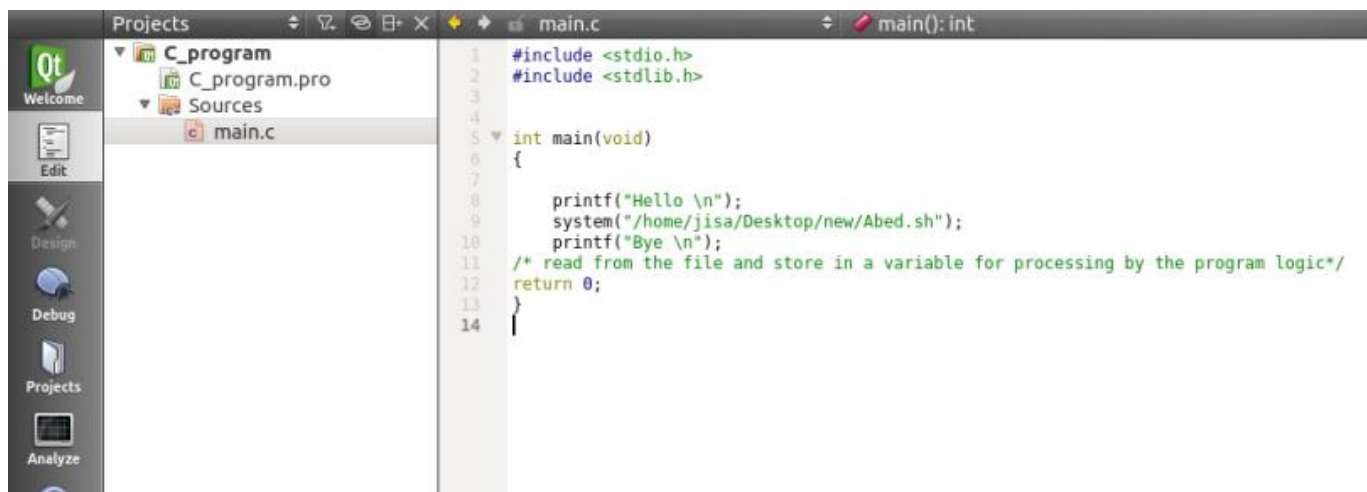


Figure 34.26: C-code written to integrate the hardware in the loop

In this code, we have a command line which let the program follows the commands written in a shell file: (*System ("/home/jisa/Desktop/new/Abed.sh")*). This shell file is shown in the figure 6.27:

```

Abed.sh x
scilab -f /home/jisa/Desktop/new/3.sce
echo Opening Scilab Simulation...
sleep 0.25
echo Simulation is Done...
sleep 0.25
echo foo \file is created...
sleep 0.25
cd /home/jisa/Desktop/new
sleep 0.25
echo Directory is Changed to Desktop\new...
sleep 0.25
echo Converting foo from binary to text...
sleep 0.25
hexdump -v -e '1/4 "%f "' -e '\n' <foo> JAYCE
sleep 0.25
echo Converting is completed...
sleep 0.25
echo JAYCE.txt is created...
sleep 0.25
echo Sending File JAYCE.txt to arcom...
\\ you need to install sshpass
sleep 0.25
sshpass -p "arcom" scp -o StrictHostKeyChecking=no /home/jisa/Desktop/new/JAYCE arcom@192.168.1.100:/home/arcom
sleep 0.25
echo JAYCE.txt is sent...

```

**Figure 34.27: Shell file containing all the steps to integrate the hardware**

In this script, we have written all commands which conduct our program:

First command is to run the program scilab. Then, we write the directory of the file .zcoss of simulation (the example file that i will transfer to the board computer) to open it.

The delay between two commands is 0.25s.

When the simulation of the file is done, a binary file foo (Fig.6.28) is created.

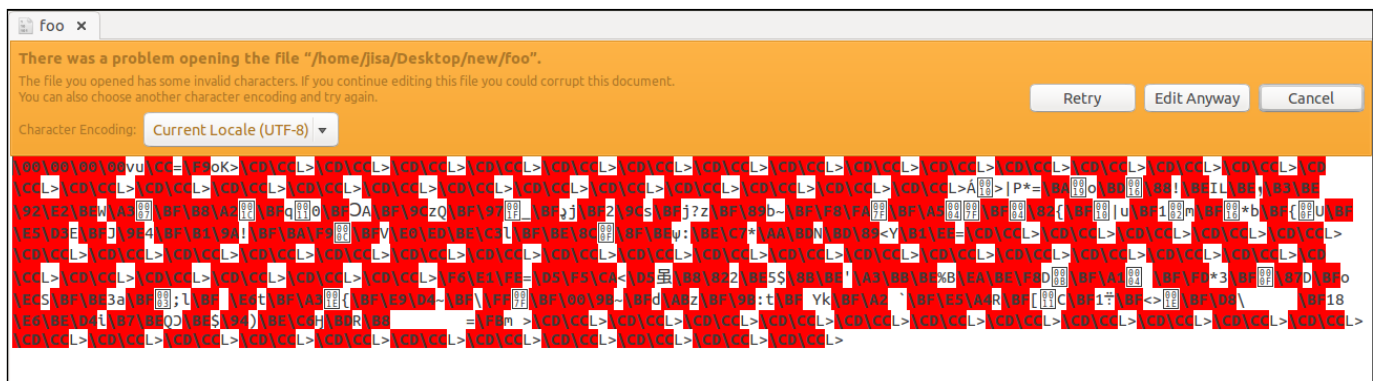


**Figure 34.28: The binary file foo**

So we write now in the shell file a command line to transfer this binary file to a txt file. This txt file is named Jayce (Fig.6.29).



Please note that the recommended version of Scilab is 5.5.2. This page might be outdated.  
See the recommended documentation of this function

Scilab manual >> xcoss > palettes > Sinks palette > WFILE\_f

## WFILE\_f

Write to file

### Block Screenshot



Then we tried the "Code generation" feature of Xcos in order to transform our control block diagrams into C code then implement the "C File Processing Functions" to write inputs/outputs to a text file.

However we failed to compile the generated standalone code due to linker errors. Even after intensive research in programming forums and adding linkers for the designated libraries to the compiler... all the attempts to debug the errors were in vain.

Line	File	Message
		[Linker error] undefined reference to `cstblk_'
		[Linker error] undefined reference to `cstblk_'
		[Linker error] undefined reference to `summation'
		[Linker error] undefined reference to `cscope'
		[Linker error] undefined reference to `cstblk_'
		[Linker error] undefined reference to `cstblk_'
		[Linker error] undefined reference to `summation'
		[Linker error] undefined reference to `cscope'
		[Linker error] undefined reference to `cscope'
		[Linker error] undefined reference to `cstblk_'
		[Linker error] undefined reference to `cstblk_'
		[Linker error] undefined reference to `summation'
		[Linker error] undefined reference to `cscope'
		ld returned 1 exit status

### 34.5.2 Working with shell programs to maintain the feedback system

The work was conducted with the help of a Linux specialist.

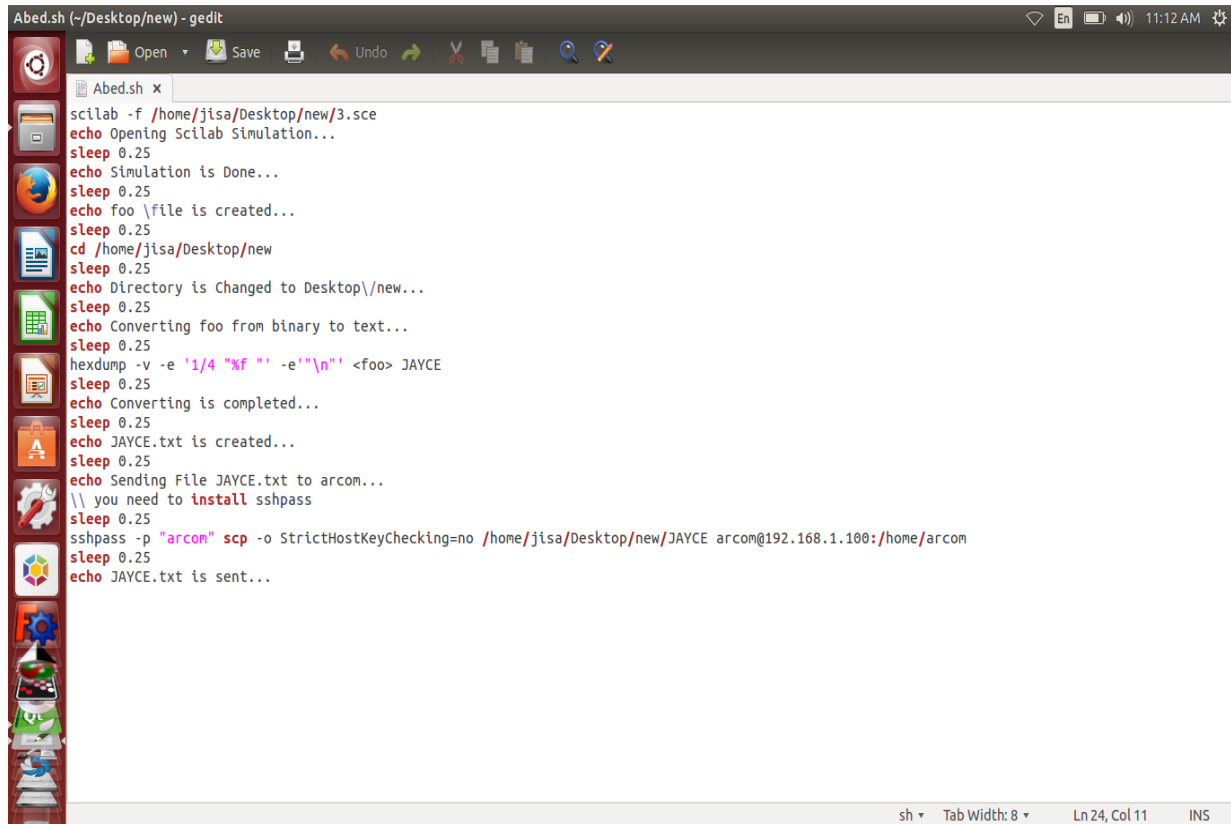
A shell script is a computer program designed to be run by the UNIX shell in order to execute designated commands.

The solution which is manifested in the shell script for the feedback system was as follows:

- 1) write the output of the sensor program in a text file but in binary form (writing the output of the simulation in binary format is provided by WRITEC\_f block in XCos)
- 2) convert the binary file into float format using the shell command hexdump
- 3) send this file to the Arcom board which has an embedded linux operating system and which is mounted on the satellite

4) execute the C program on the arcom board which processes the sensor data then sends commands to the actuators.

The first successful prototype for the shell program was the following:



```

Abed.sh x
scilab -f /home/jisa/Desktop/new/3.sce
echo Opening Scilab Simulation...
sleep 0.25
echo Simulation is Done...
sleep 0.25
echo foo \file is created...
sleep 0.25
cd /home/jisa/Desktop/new
sleep 0.25
echo Directory is Changed to Desktop\new...
sleep 0.25
echo Converting foo from binary to text...
sleep 0.25
hexdump -v -e '1/4 "%f "' -e "\n" <foo> JAYCE
sleep 0.25
echo Converting is completed...
sleep 0.25
echo JAYCE.txt is created...
sleep 0.25
echo Sending File JAYCE.txt to arcom...
\\ you need to install sshpass
sleep 0.25
sshpass -p "arcom" scp -o StrictHostKeyChecking=no /home/jisa/Desktop/new/JAYCE arcom@192.168.1.100:/home/arcom
sleep 0.25
echo JAYCE.txt is sent...

```

where 3.sce scilab program opens the Xcos simulation and saves the result in binary format to foo.txt file.

### 34.6 Receiving meteorological data

This satellite bus is connected to the ground station by the communication system and telemetry, and the ground station is also connected to the payload of satellite by telemetry.

From the payload system, we obtain image of the meteorological data.

The camera takes photo for the earth's surface, and sends this data to the ground station as signals. The ground station receives these signals and decodes it to obtain the represented image of weather.

For example, let's see the meteorological satellite NOAA followed by the ground station (Fig. 6.30).

NOAA turns around the earth on a low earth orbit. The prediction of its position in function of time is shown by the program Gpredict, and it turns under the frequency 137.915.5 MHz:

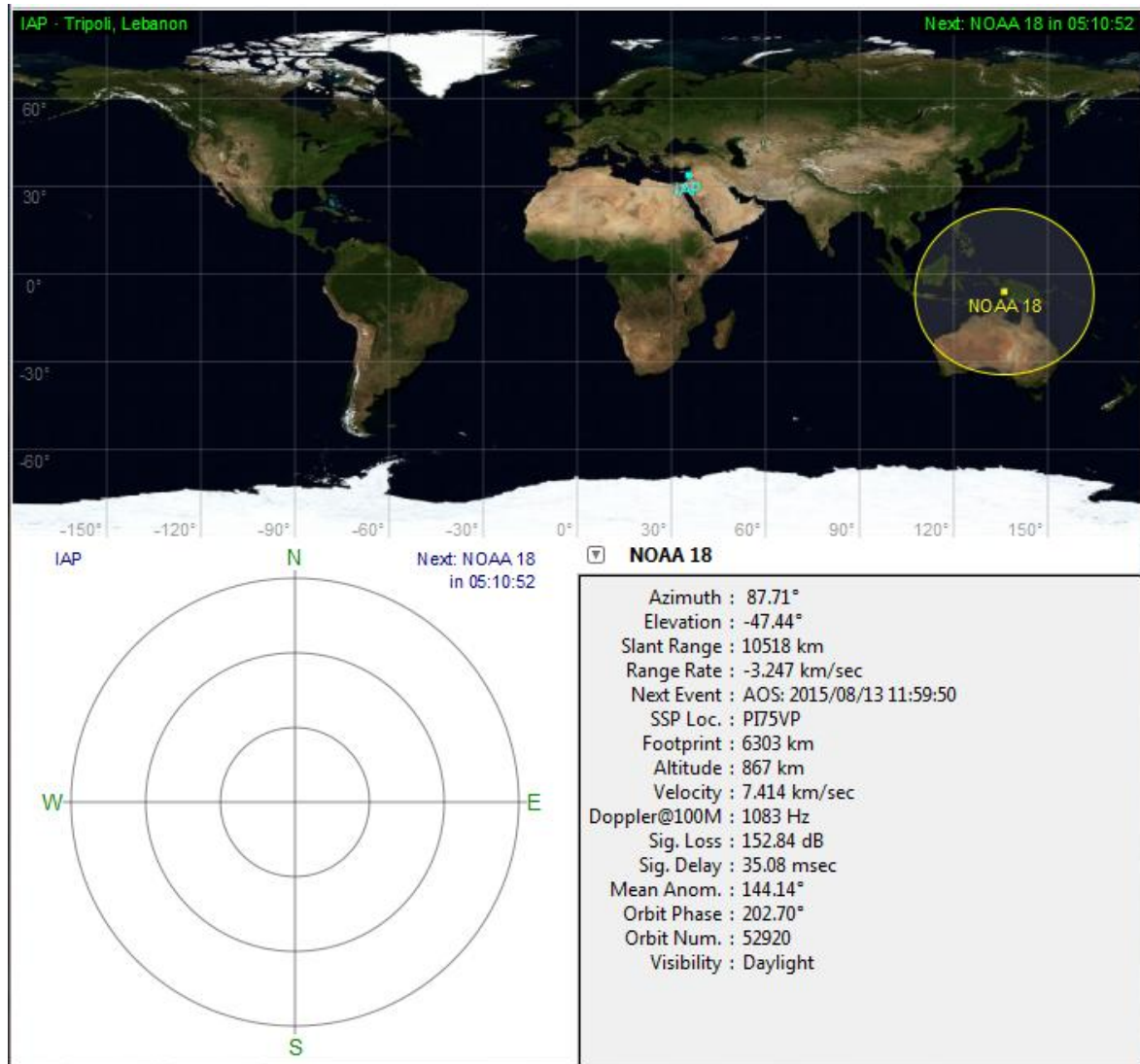


Figure 34.30: Gpredict following NOAA-SAT

How to receive and read this signal?

We need as hardware:

- An antenna to detect the frequency of satellite
- A RTL
- Our computer

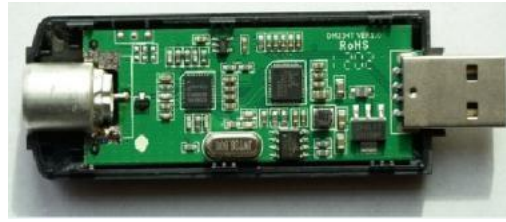
As software:

- Zadig
- ExtIO\_RTL2832
- HDSDR program
- WXtoImg program

First, we have to plug the USB dongle receiver RTL2832 (Fig.6.31), and to install the driver.

**RTL:**

(a)



(b)

**Figure 34.31 (a, b): The RTL**

RTL-SDR is the cheapest method to get into the world of SDR (Software Defined Radio) - method of receiving (RTL-SDR has no capability to transmit) and processing radio transmission using your PC. Using it you can receive everything that is transmitted between about 20~2000 MHz depending on second chip on the device.

In brief it can hear i.e.:

- Ordinary FM radio stations
- Police radio transmissions
- Plane and ship tracking information
- GPS and meteorological satellites
- International Space Station and other space equipment that transmits below 2 GHz
- every other device that you know transmits on these frequencies. [7]

Next we have to download Zadig.

Zadig is a Window application that installs generic USB drivers, such as WinUSB, to help you access USB devices (Fig. 34.32).

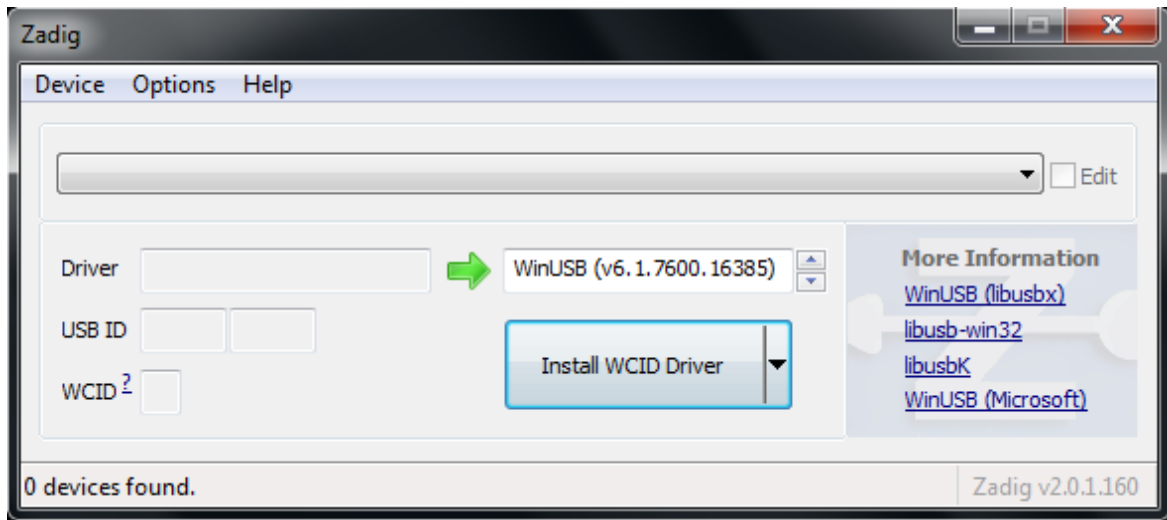


Figure 34.32: Installation of Zadig

We searched for devices, to install the driver RTL.

After finding devices, we choose the name of this device, Bulk-In, interface (Interface 0), then we click reinstall device.

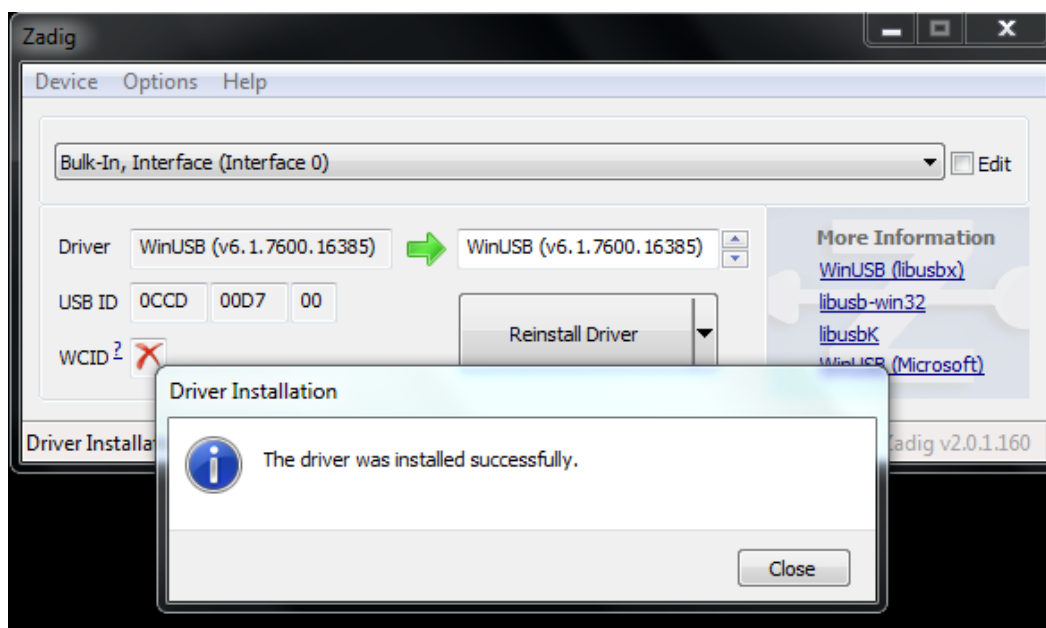


Figure 34.33: Installation for the driver RTL in Zadig

The next step is to download ExtIO\_RTL2832. It is a software defined radio program that supports the ultra-cheap RTL-SDR.

The HDSDR software (Fig.6.34) doesn't communicate with the SDR hardware directly. It communicates with the SDR radio hardware through an External Input Output Dynamic Link Library (ExtIO-DLL) file, which is a type of plug-in.

Then, we download the software HDSDR (High Definition Software Defined Radio).



Figure 34.34: HSDR

Before starting this program, we have to copy ExtIO\_RTL2832.DLL into our HSDR installation directory (default=C:\Program Files (x86)\HSDR).

Now, we open HSDR and select ExtIO\_RTL2832.DLL:

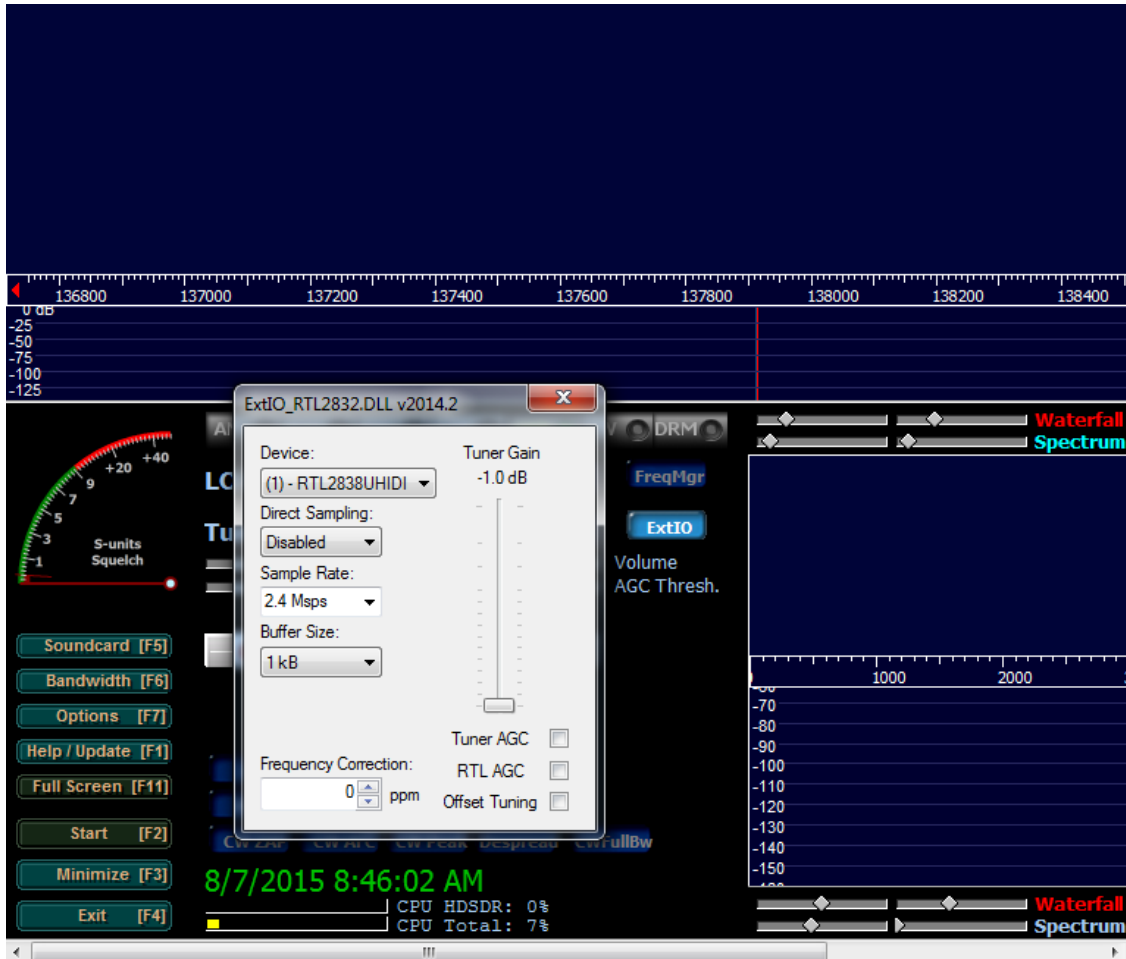


Figure 34.35: Choosing the driver RTL in HSDR

We verify our driver RTL2832, and we fix in HSDR the request frequency (to receive meteorological data from NOAA satellite, the request frequency is 137.915.5 MHz).

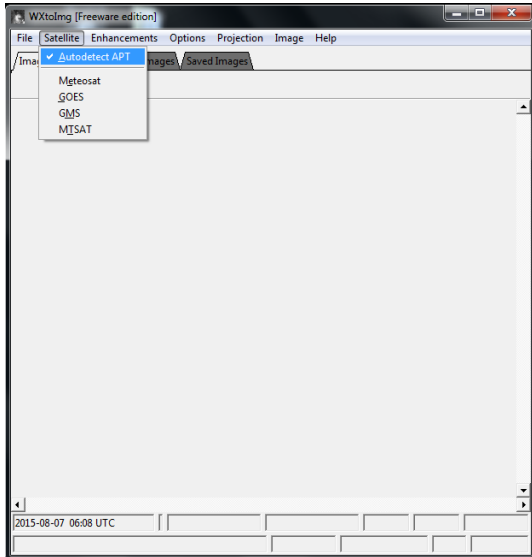
By using an antenna (Fig. 6.36), we can receive a real signal from the NOAA satellite, and visualize this signal in HSDR.



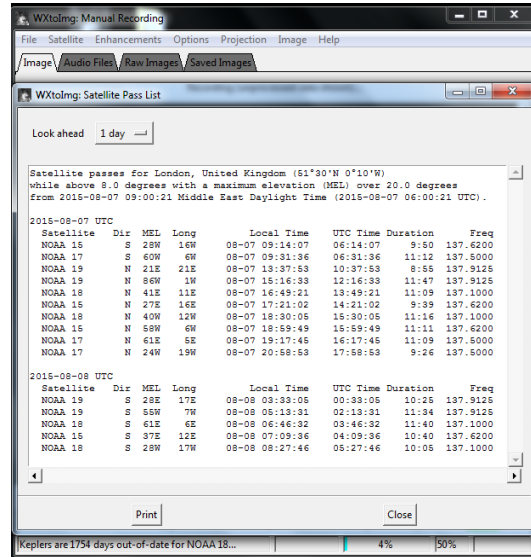
Figure 34.36: Antenna multidirectional used in our experience

We also install the program WXtoImg (program which transferred the signal to a meteorological image). WXtoImg (Fig. 6.37) is a fully automated APT (automatic picture transmission) and WEFAX (weather fax) weather satellite decoder. The software supports recording, decoding, editing, and viewing. It supports real-time decoding, map overlays, advanced color enhancements, 3-D image [31]

When we start WXtoImg, it will detect the satellite NOAA, because of fixing its frequency in HDSDR.



(a)



(b)

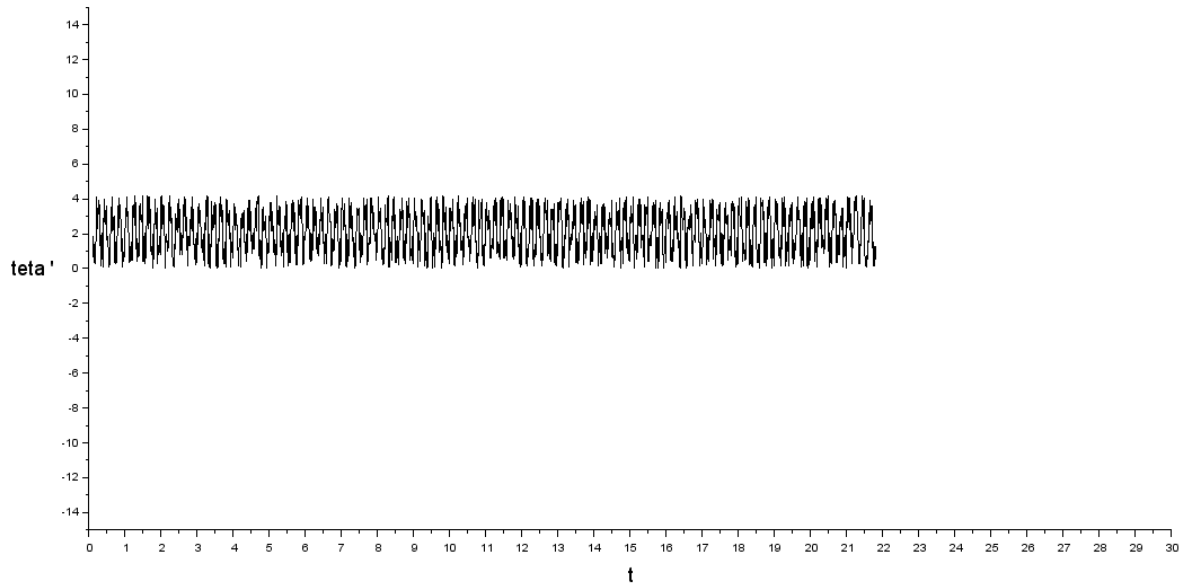
Figure 34.37 (a, b): WXtoImg program

## 35 Operation of HIL test rig

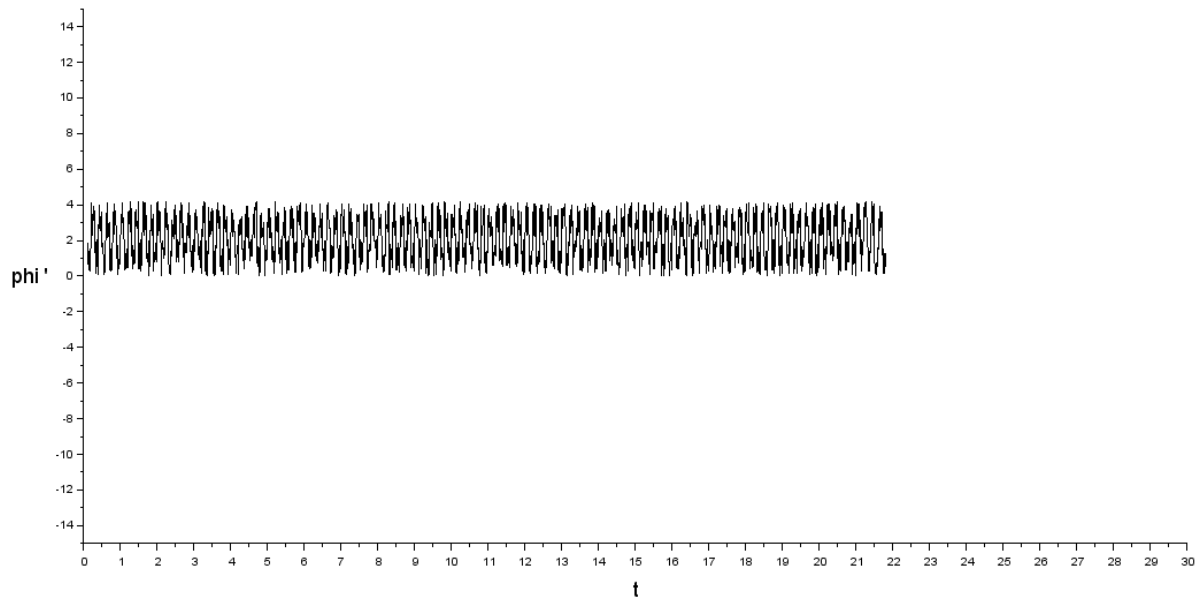
### 35.1 Results of the Simulation in Scicos

#### 35.1.1 Simulation of gyroscope

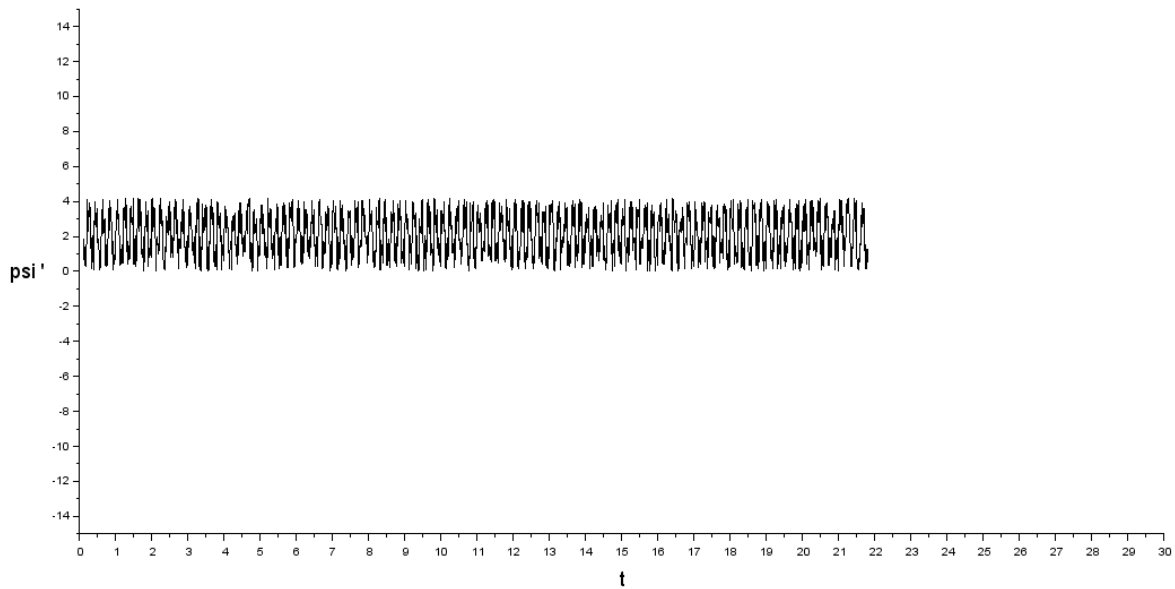
When we execute the diagrams which represent the simulation of gyroscope, the results are shown in the next figures (Graph 7.1, 7.2 and 7.3):



**Graph 35.1: Variation of  $\theta'$  (angle with x-axis) function of time**



**Graph 35.2: Variation of  $\phi'$  (angle with Y-axis) function of time**



**Graph 35.3: Variation of  $\psi'$  (angle with Z-axis) function of time**

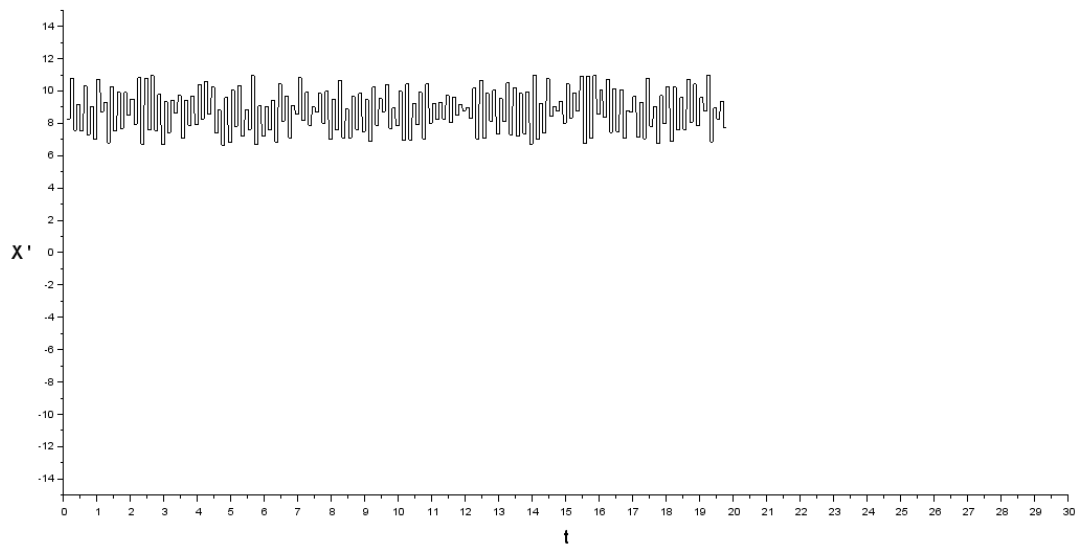
These graphs represent the simulation of the diagrams represented in the figures (2.8, 2.9, 2.10).

It is obvious that the values of the angles with the X-axis (Y-axis and Z-axis) change, they are not the same values entered as inputs to these diagrams.

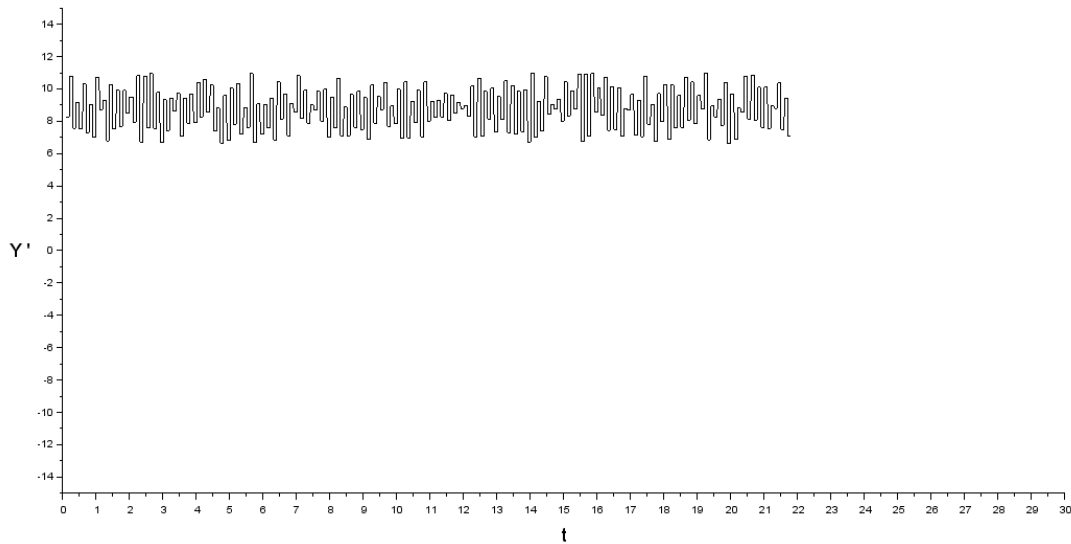
As we see in those graphs, the angle teta ( $\phi$ ,  $\psi$ ) changes to be teta' ( $\phi'$ ,  $\psi'$ ), after passing by the bias, the attitude error, the random generator...

### 35.1.2 Simulation of accelerometer

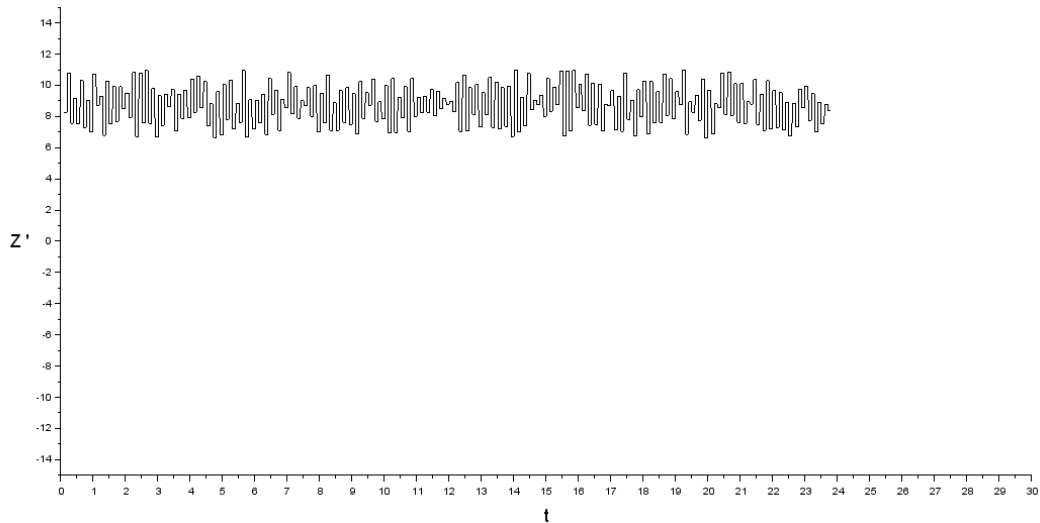
In this section, we will see the results obtained after executing the diagrams representative of the accelerometers simulation.



**Graph 35.4: Variation of the position  $X'$  with time**



**Graph 35.5: Variation of the position  $Y'$  with time**

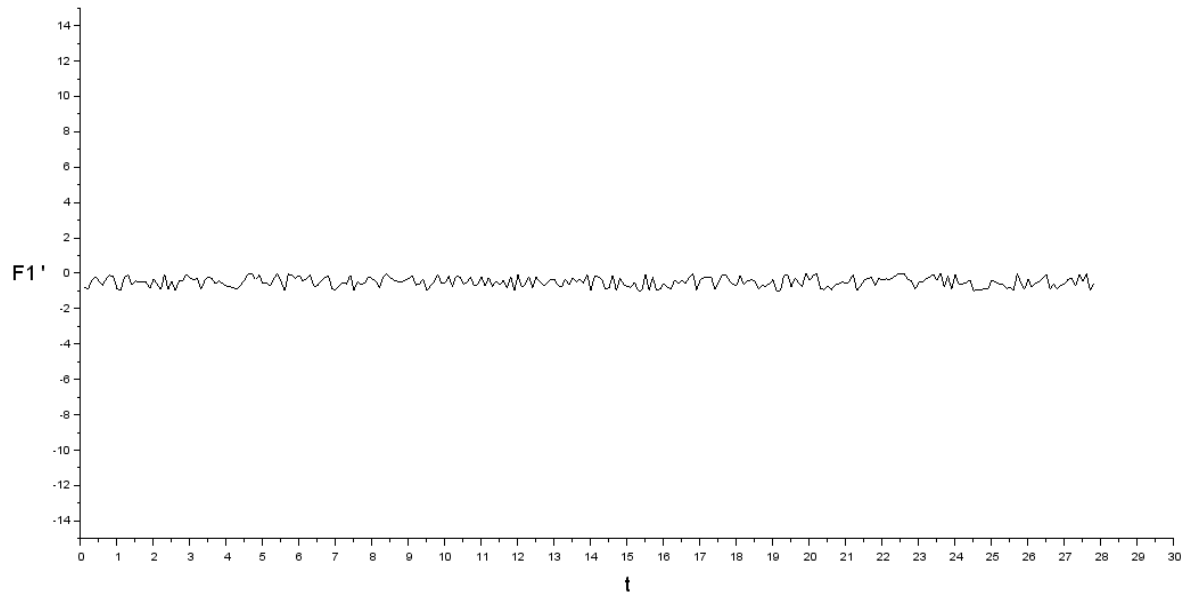


**Graph 35.6: Variation of the position  $Z'$  with time**

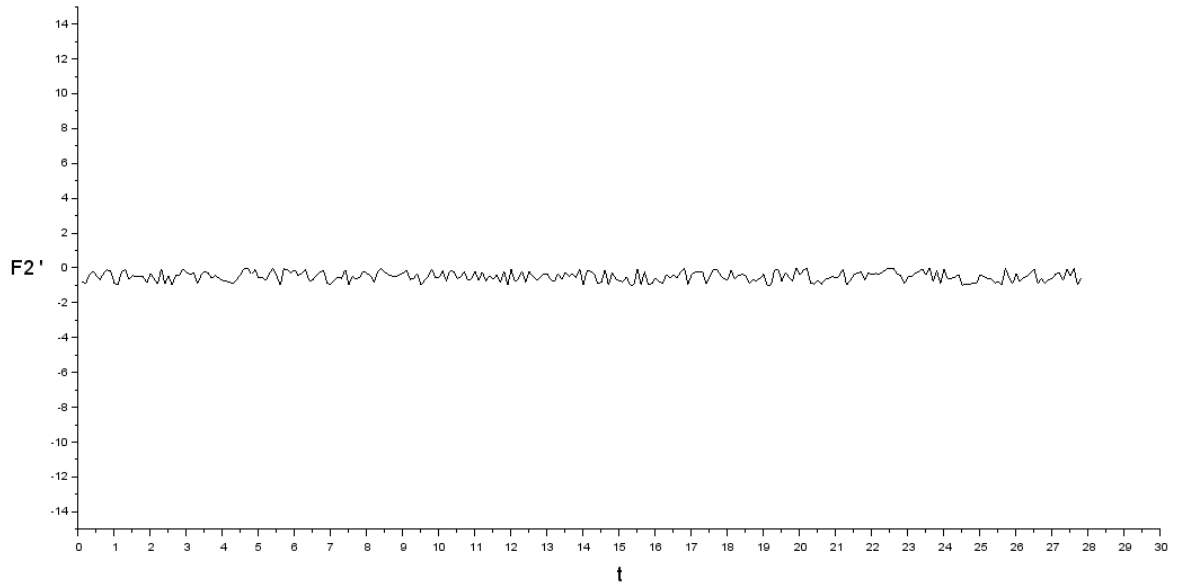
In these graphs (Graph 7.4, 7.5 and 7.6), we see the variation of the position  $X'$ ,  $Y'$ ,  $Z'$  with the time ( $X'$ ,  $Y'$  and  $Z'$  are the real values of  $X$ ,  $Y$  and  $Z$  positions after passing by the diagram of the accelerometer simulation that we have already seen them in figures (2.11, 2.12 and 2.13).

### 35.1.3 Simulation of actuators

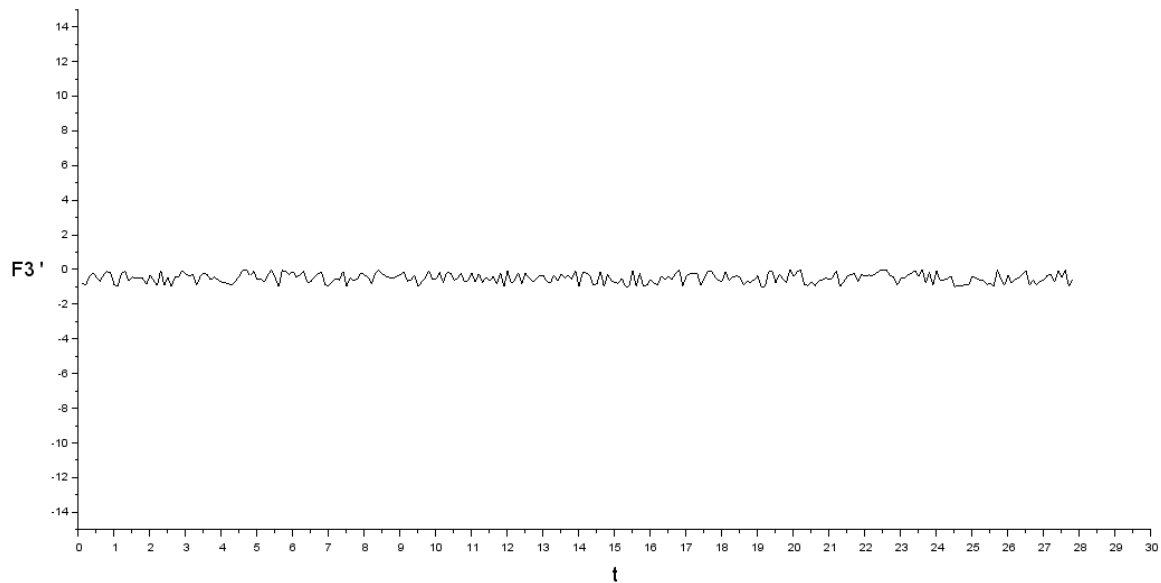
The results of the actuators simulation are represented in the next figures.



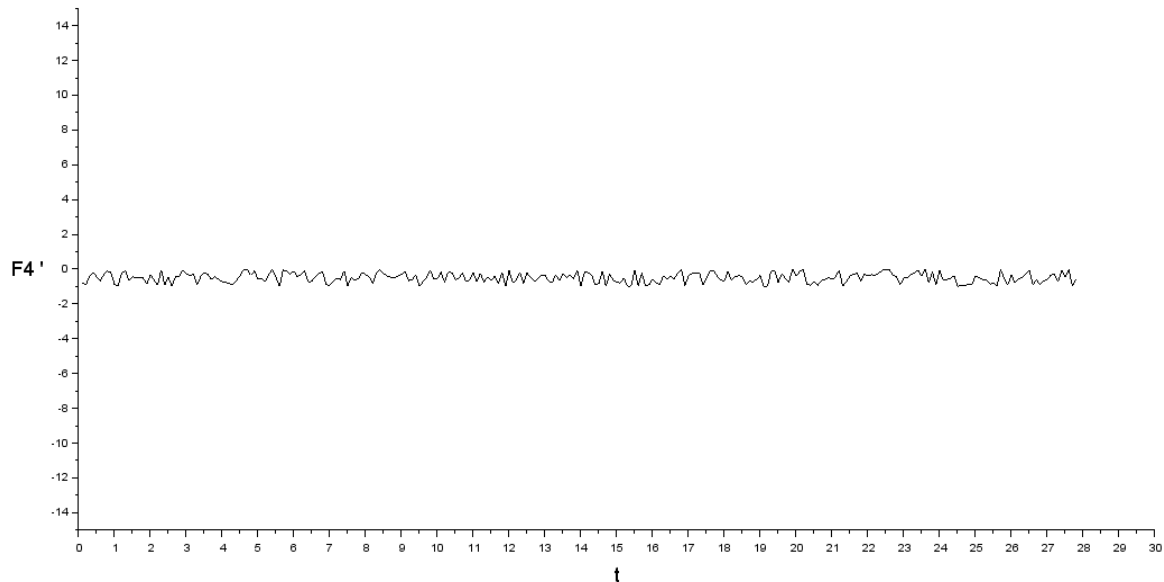
**Graph 35.7: Variation of F1' with time**



**Graph 35.8: Variation of F2' with time**



**Graph 35.9: Variation of F3' with time**



**Graph 35.10: Variation of F4' with time**

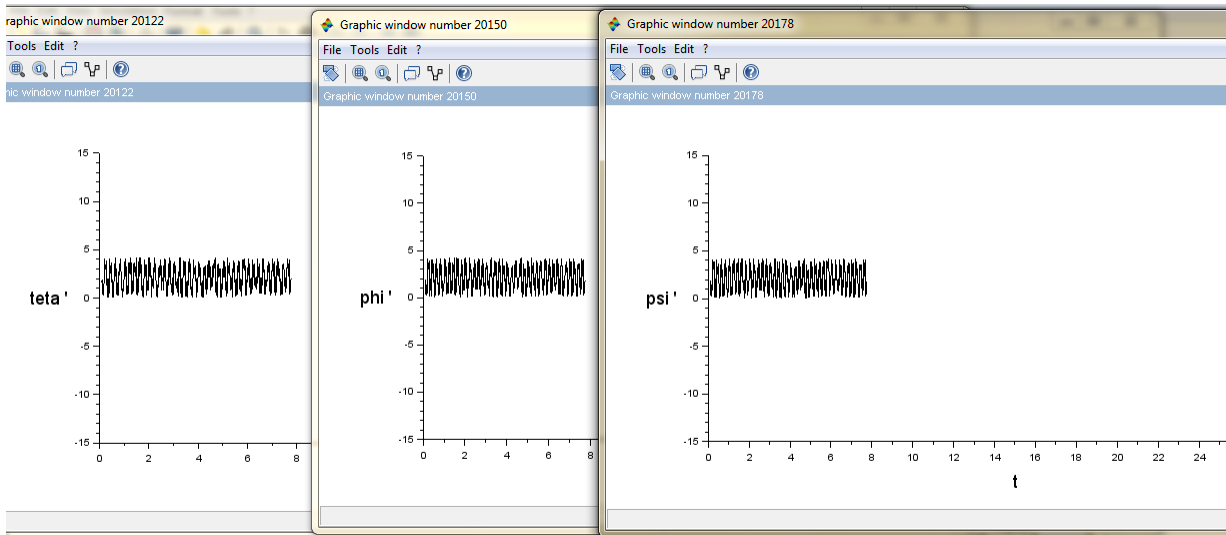
It is clear in the previous graphs (Graph 7.7, 7.8, 7.9 and 7.10), that the values of the forces given to the propulsion to control the attitude of the satellite; these forces ( $F'$ ) are also different than the real values given as inputs because of random generator and others blocks (represented in the figure 2.14). In the four previous graphs, we see the variation of  $F'$  ( $F1'$ ,  $F2'$ ,  $F3'$ ,  $F4'$ ) with time.

#### 35.1.4 Results of the integration of diagrams

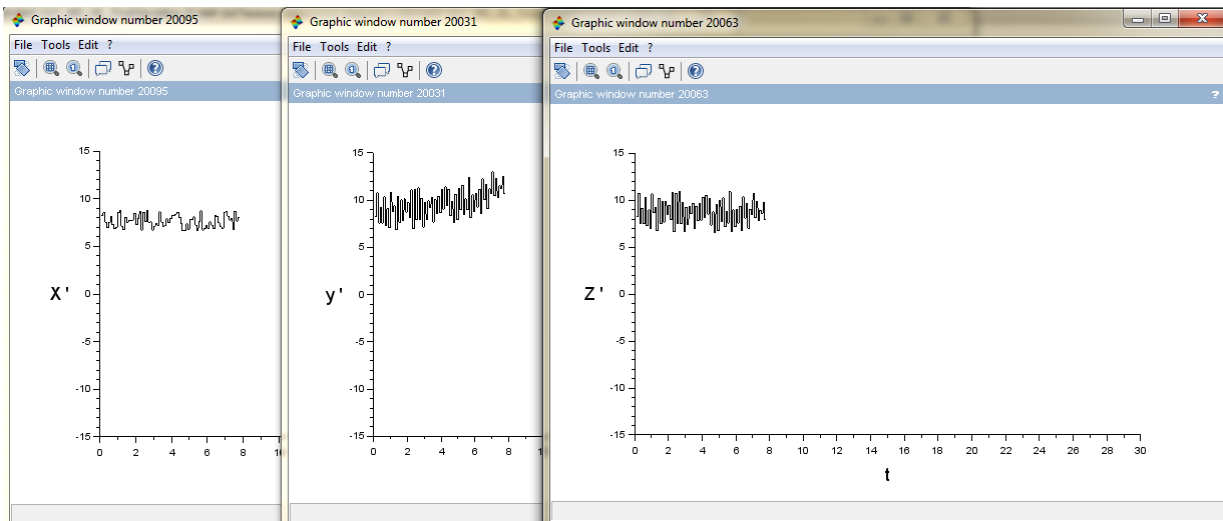
To represent our system, it is necessary to integrate all the previous diagrams to simulate the state when the satellite is really in the atmosphere.

The results of this simulation (represented in figure 6.16) are the next (graph 7.11, 7.12 and 7.13):

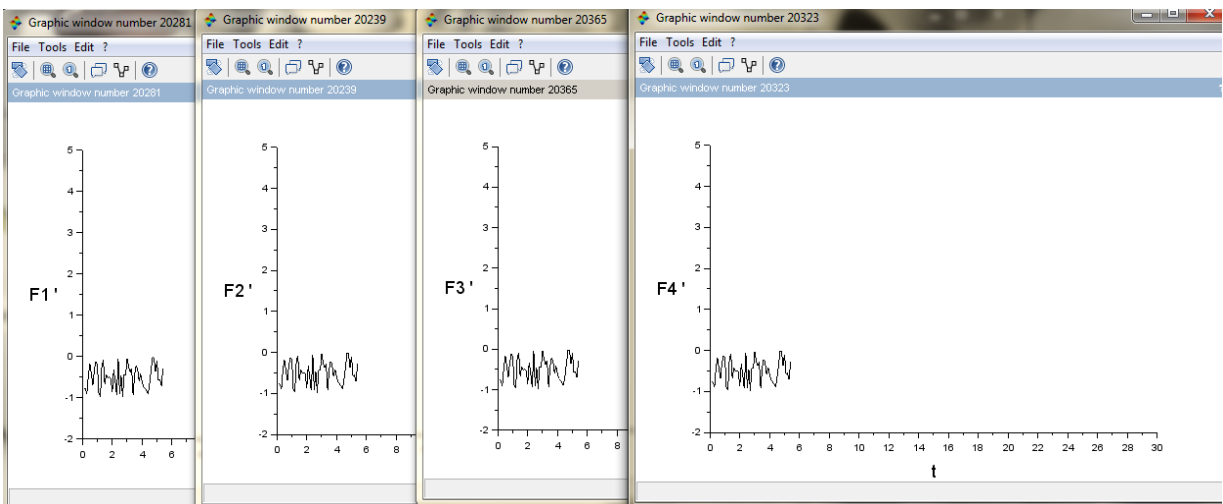
# Operation of HIL test rig



**Graph 35.11: Variation of the angles with time**



**Graph 35.12: Variation of the position with time**



**Graph 35.13: Variation of forces with time**

When the model is executed, all these graphs appear in the same time to represent how the orientation and the position change with the forces during the time of the simulation.

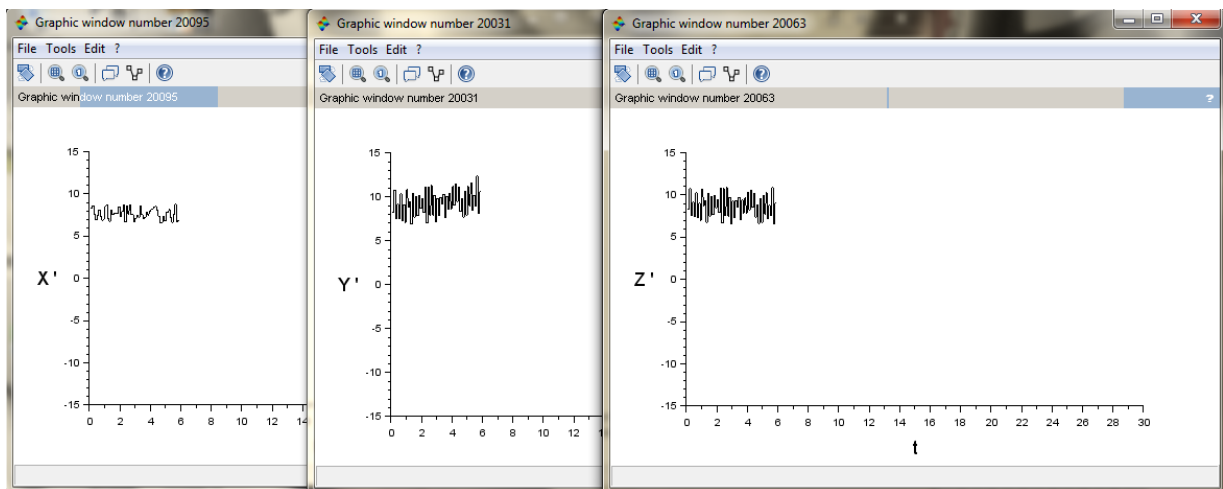
So we arrive to simulate our satellite by representing all the components of the satellite in scicos, and by integrating all these models to obtain the representative diagram.

### 35.1.5 Test of simulation

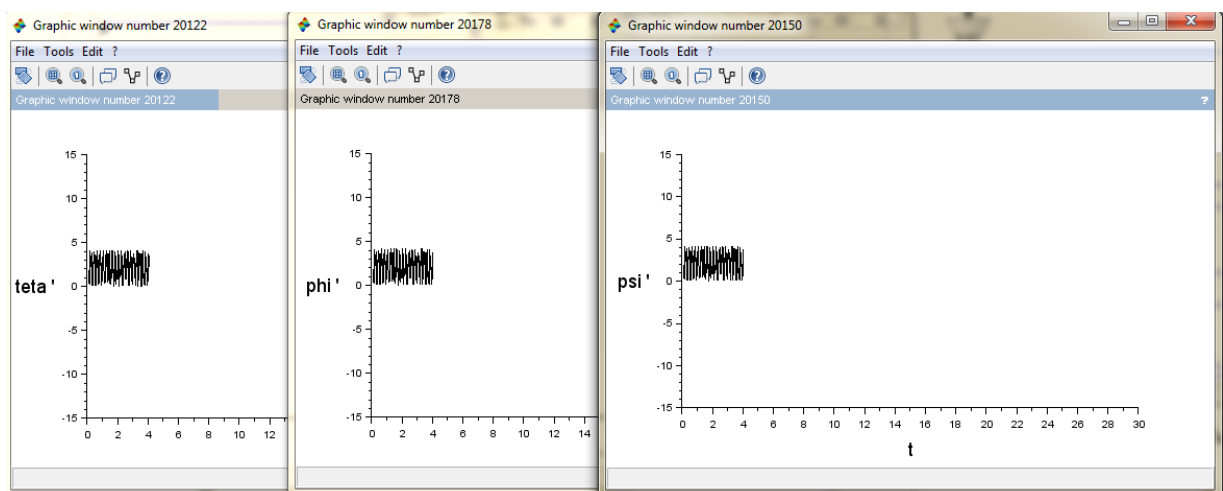
In this section, we will see the result of the simulation when we change the values of forces.

#### Results of case 1

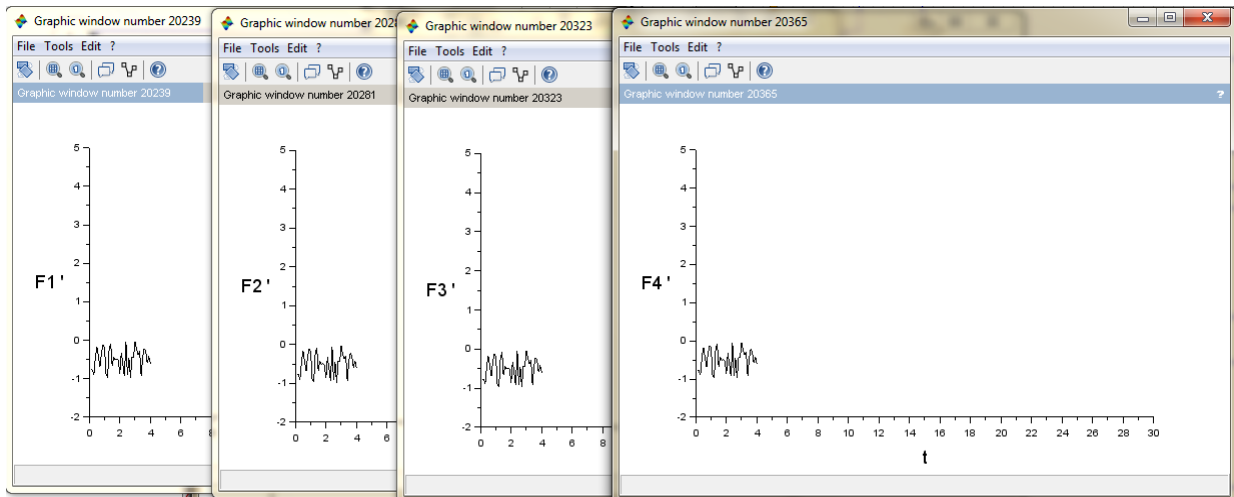
The first case is the case with the value zero of  $F_4$  (figure 6.17).



**Graph 35.14: Variation of position with time**



**Graph 35.15: Variation of position with time**

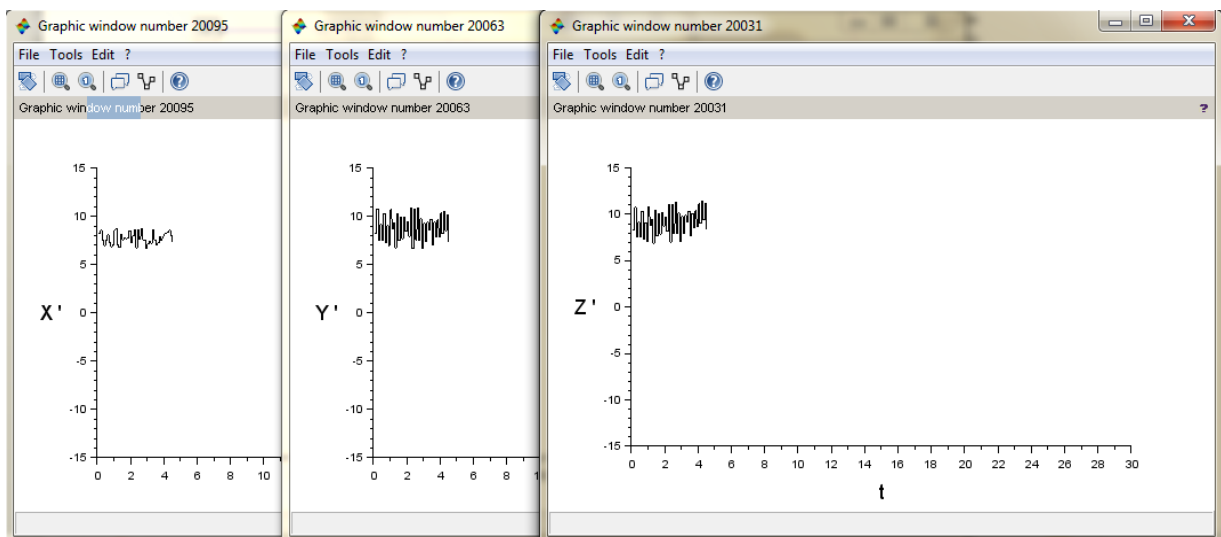


**Graph 35.16: Variation of forces with time**

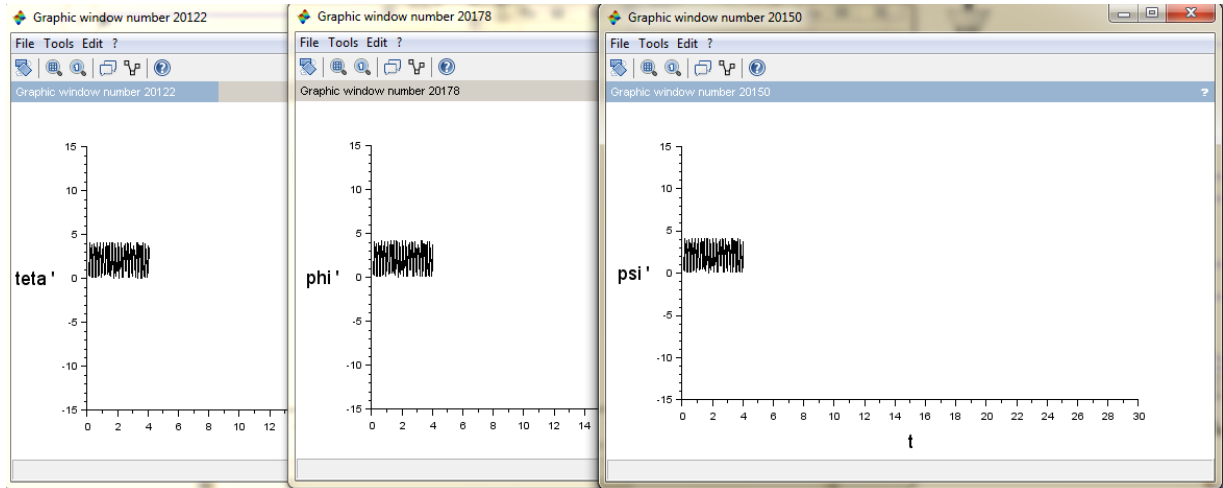
We see a small difference in the graphs of position. We can detect that the variation of  $Y'$  and  $Z'$  with time is different when all the forces have a nonzero value.

**Results of Case 2**

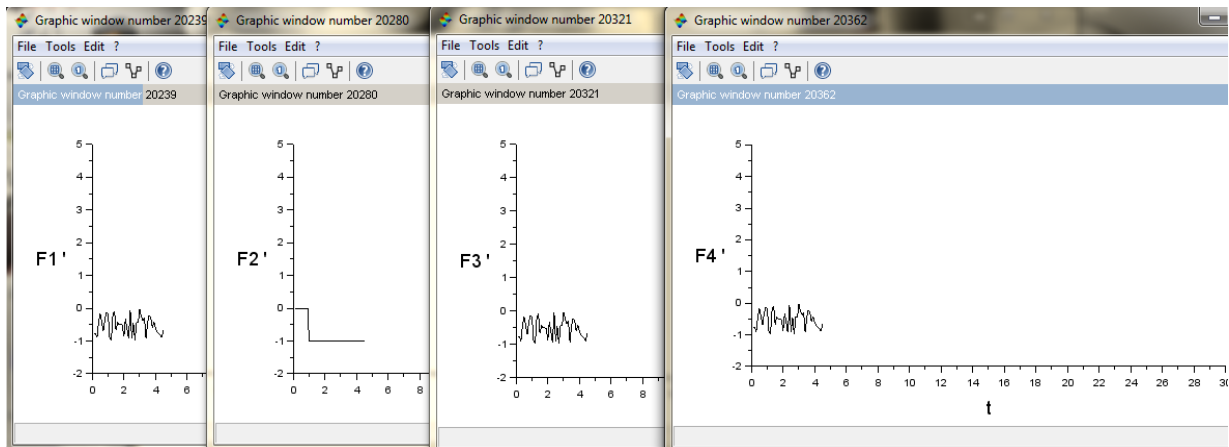
This case represents the test when  $F4$  is zero, and  $F2$  is a step function (figure 6.18).



**Graph 35.17: Variation of position with time**



**Graph 35.18: Variation of angles with time**



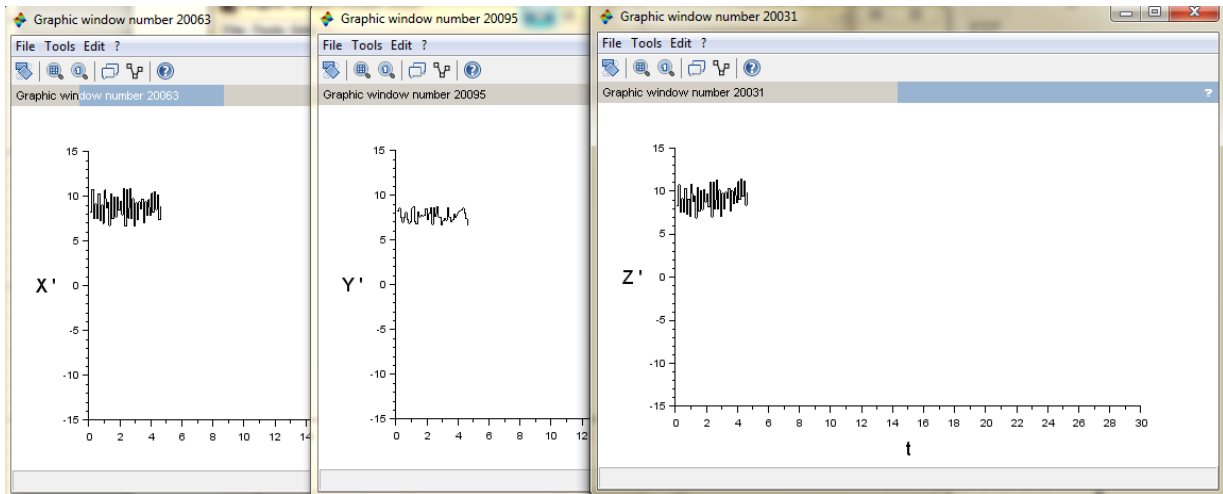
**Graph 35.19: Variation of forces with time**

We can see clearly the change of the graph of position ( $Z'$  only), and the change in the graphs of actuators. The graph of the second propulsion is different; it is as a step function with a little change due to noise and other blocks.

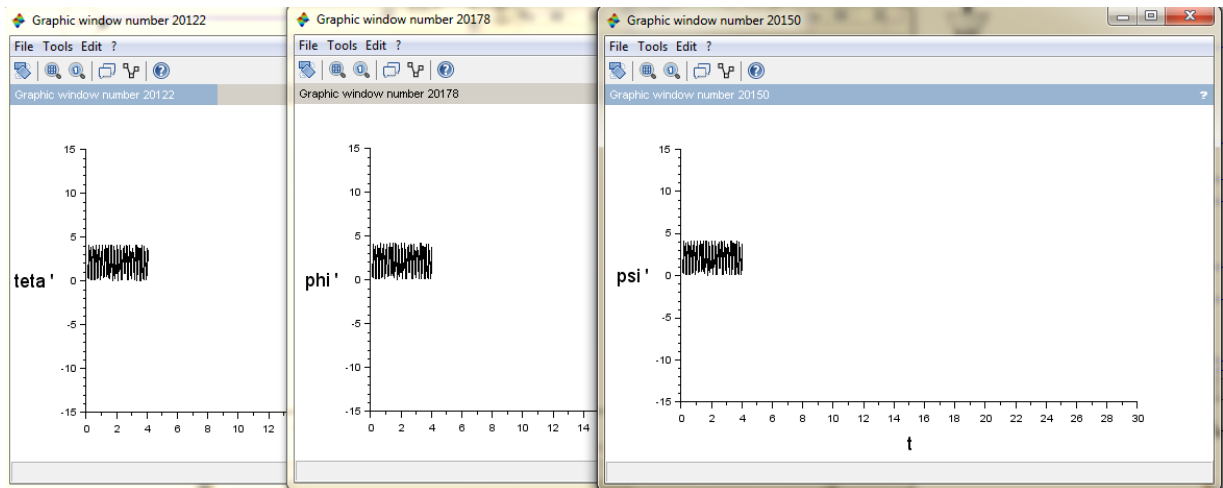
### Results of case 3

In this case, all the forces have zero as value, exception  $F1$  (Figure 6.19).

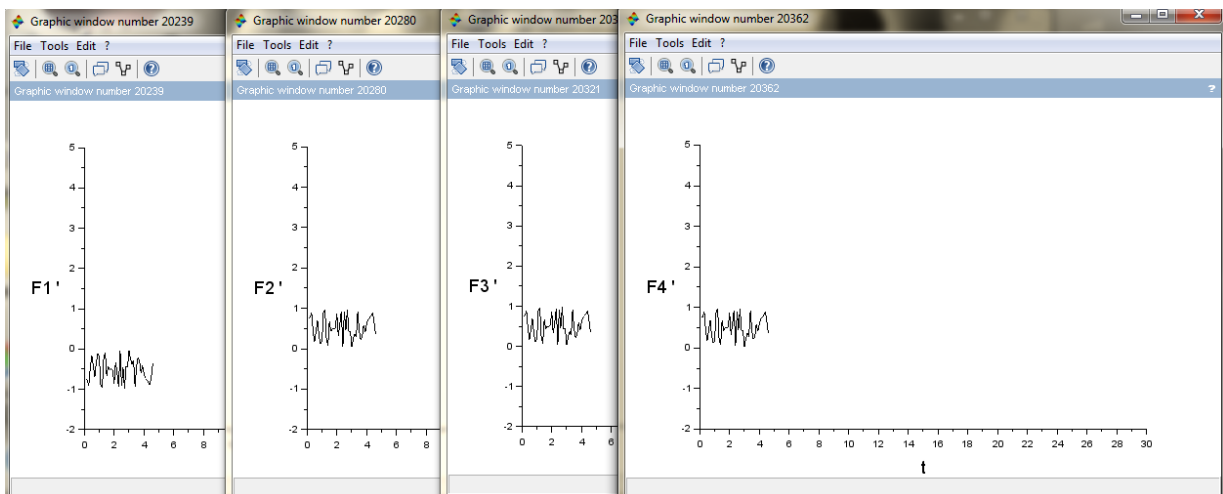
# Operation of HIL test rig



**Graph 35.20: Variation of position with time**



**Graph 35.21: Variation of angles with time**



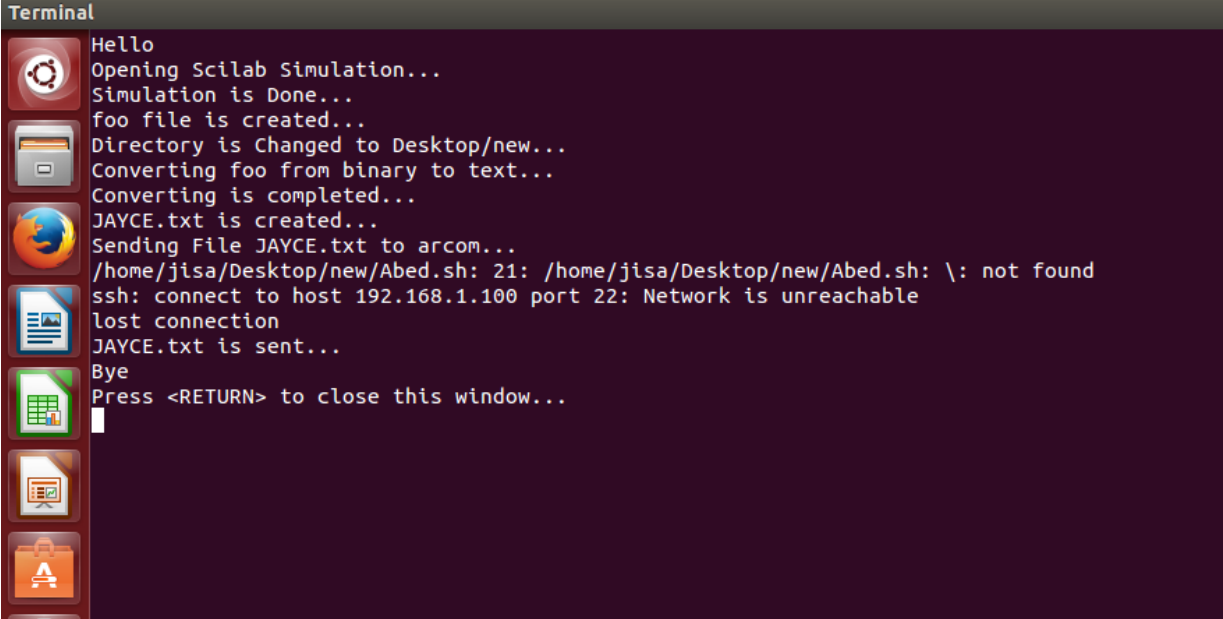
**Graph 35.22: Variation of forces with time**

Here the results are different from the other cases. We can see the difference in the graphs of position ( $X'$ ,  $Y'$  and  $Z'$ ), and we can see also the difference in the graph of the force  $F1$ . This difference is due to the nonzero value of  $F1$ , when all the others value are zero.

So, we can deduce that this simulation is really representative to the state of the satellite. Any changes in the forces given to the actuators appear in the measurement of the position and the orientation of the satellite.

### 35.1.6 Integration of the Hardware-in-the-Loop (HIL) test rig

Now, after finishing the simulation, we should integrate it with the computer board in a closed loop. The next figure (Fig. 7.1) represents the first result when we run the C-code (this result is the presence of the txt file, values of the simulation, on the board computer).



```

Terminal
Hello
Opening Scilab Simulation...
Simulation is Done...
foo file is created...
Directory is Changed to Desktop/new...
Converting foo from binary to text...
Converting is completed...
JAYCE.txt is created...
Sending File JAYCE.txt to arcom...
/home/jisa/Desktop/new/Abed.sh: 21: /home/jisa/Desktop/new/Abed.sh: \: not found
ssh: connect to host 192.168.1.100 port 22: Network is unreachable
lost connection
JAYCE.txt is sent...
Bye
Press <RETURN> to close this window...
  
```

**Figure 35.1: Results after executing the C-code**

When we run the C-code, the file `scicos` is executed automatically, its output is saved in a C binary file (`foo`); this file is converted to a txt file (`Jayce`).

Finally, the txt file `Jayce` is sent to the `arcom` board, after connecting this board and my computer to the same network.

The file `Jayce.txt` is now on the `arcom` board.

This loop is not done now. Another code is needed to let the board to check the values of position and orientation, and to regulate the values of forces which will be given to the actuators.

So, we will write a new C-code which read the txt file, compare the values with the requested one and create an impulse (as values written in txt file).

This txt file (values of forces) will be sending to my computer, where it will be transferred to a binary file. At the end, the file of simulation `.zcos` takes its input from this C binary file (Fig. 7.2).

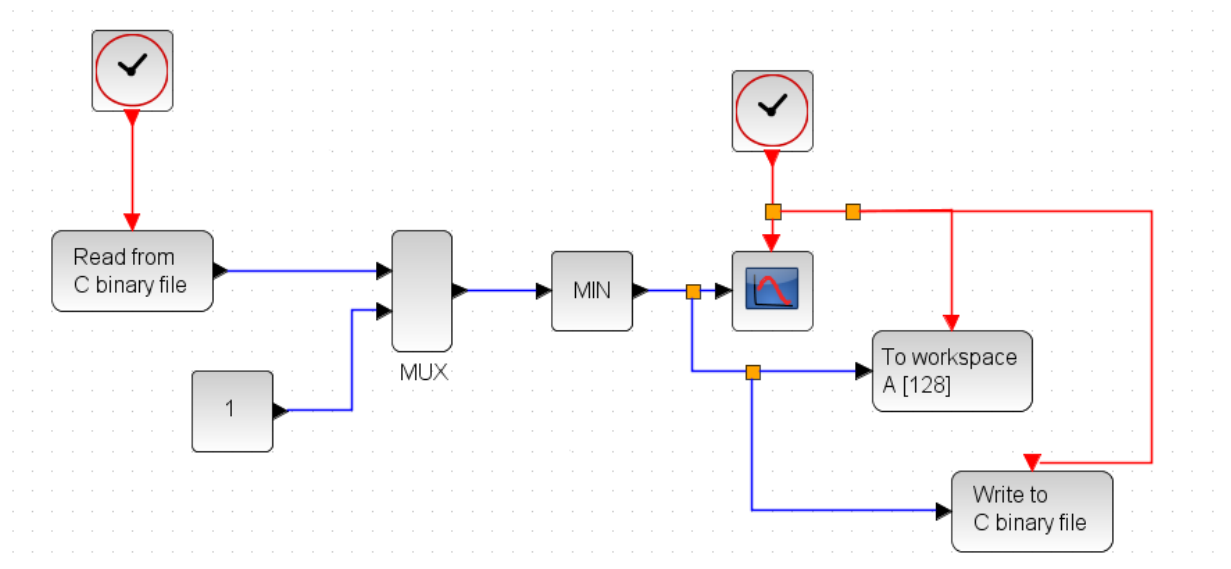


**Figure 35.2: The randomly example with input from a binary file and output to a binary file**

So the next task (to be continued) is to write the correct C-code which will create values of forces depending on the values of position and angles present in this txt file (Jayce) to read. Finally, a new txt file is created and it contains the real inputs of the file .zcoss.

When we find this C-code, the loop will be closed with integration of hardware. Using the same technique, we can connect the HP server (where the simulation of the satellite's components is) with the board computer; by writing the C-codes on the server.

After debugging, we attain the complete simulation of the satellite bus, and we can test this simulation for a long time.

### 35.2 Receiving meteorological data

After fixing the frequency to detect the meteorological satellite NOAA in the HSDR, we can see a real signal, see figures 7.3 and 7.4:



Figure 35.3: the first appearance of signal in HSDR

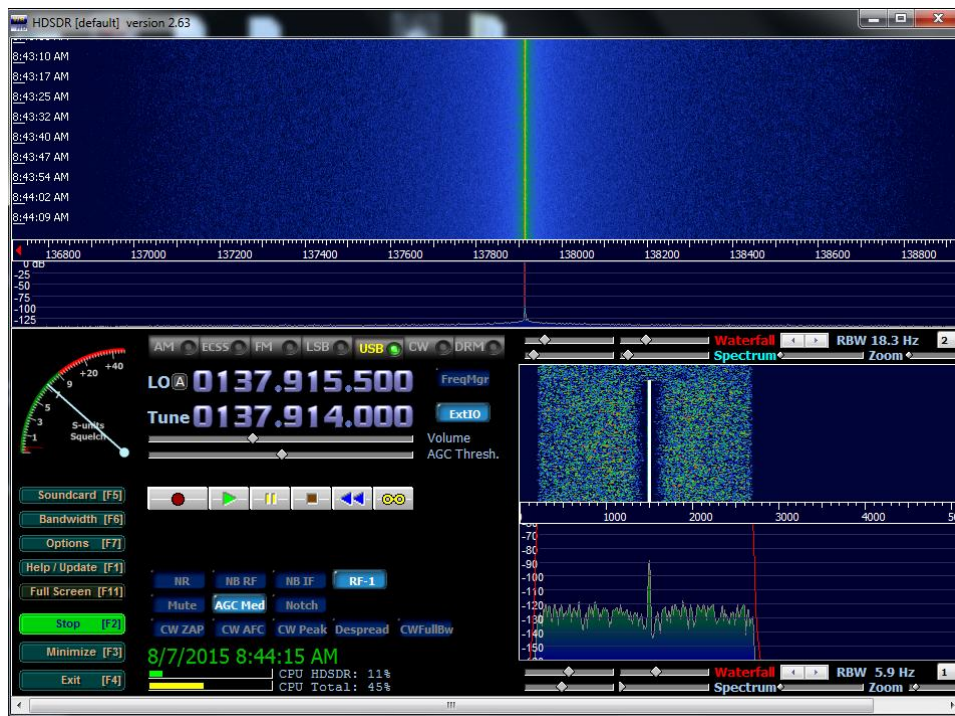
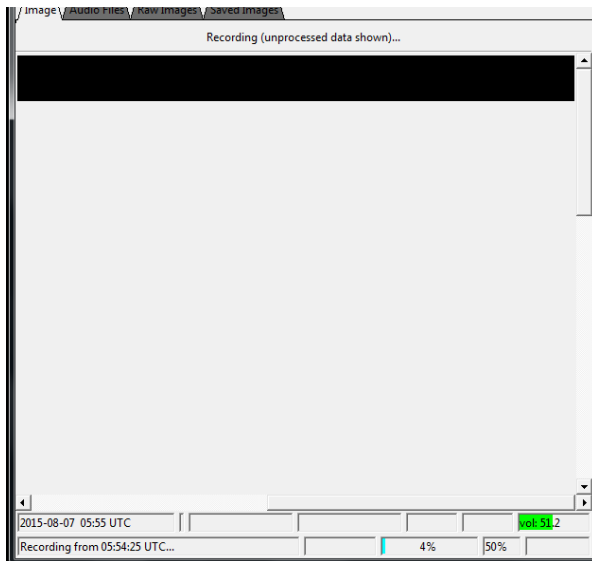
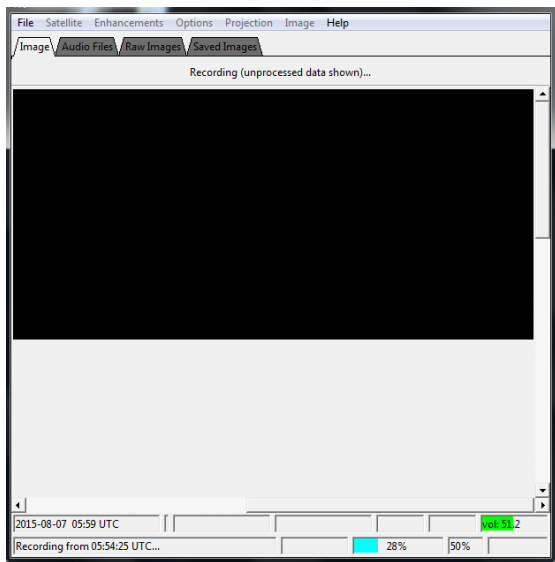


Figure 35.4: The signal received in HSDR then

And after starting WXtoImg, an image will start to appear (Fig. 7.5).



(a)



(b)

**Figure 35.5 (a, b): Appearance for a meteorological image**

This image is not representative (it is all black), because we have used an antenna with multidirectional detection, so it radiates the same pattern all around the antenna in a complete 360 degrees pattern, therefore a lot of noise are generated and the signal isn't clear and apparent.

It is necessary to use a directive antenna (Fig 7.6) very high frequency VHF to obtain the request image.

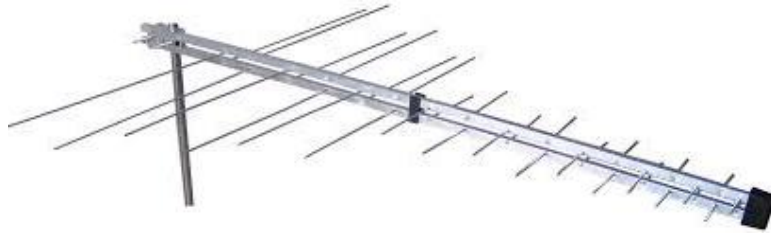


**Figure 35.6: Directive antenna**

By using this directive antenna, the image will be as the following image (Fig. 7.7):

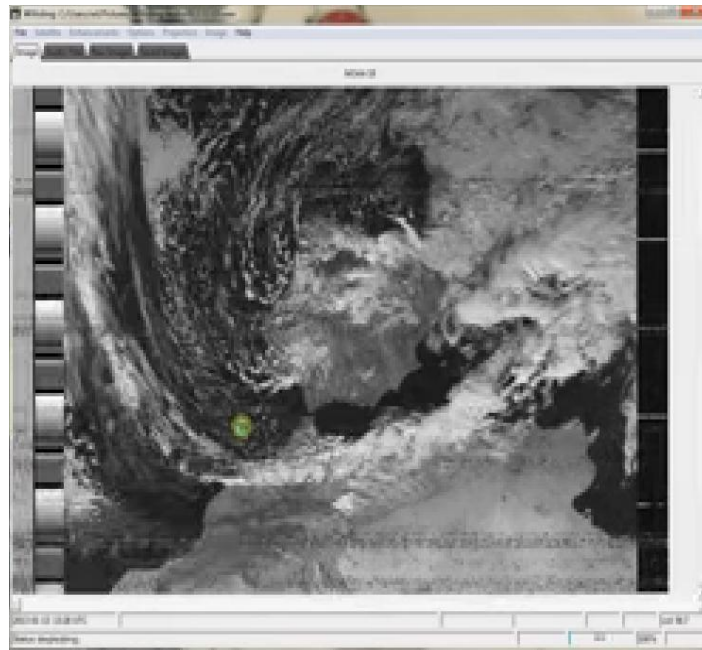


**Figure 35.7: The real meteorological image [35]**

Also, in this program, by the processing of the image, we arrive to obtain a colored image, so we can easily estimate the state of weather.

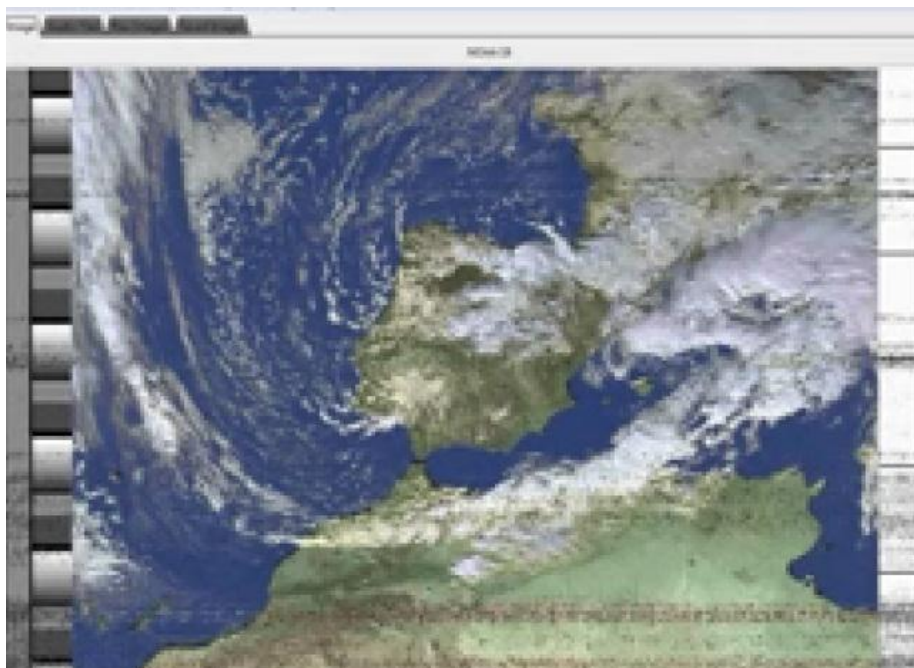


**Figure 35.8: The real colored meteorological image [35]**

Using the same methodology with the same technics, programs and steps, we arrive to take meteorological data after launching the IAP-SAT.

## Part V: Payload (Scientific Program)





## 36.2 Satellite Based Radio Astronomy Sensor

Migration of Ground Based Sensor of Suheeb Kassar Master Thesis to a Satellite based system.

## 37 Image Processing Techniques for Payload Sensors

### 37.1 Edge detection

I tried this tutorial: <http://www.semipol.de/wp-content/uploads/sites/4/2008/07/tutorial.pdf>

#### The code:

```
#include<opencv\cv.h>
#include<opencv\highgui.h>
# include <iostream >

using namespace std;

int main (int argc , char * argv []) {

    IplImage * img = cvLoadImage ( argv [1]) ;
    if (! img ) {
        cerr << " Could not load image file : " << argv [1] <<
endl ;
        exit ( EXIT_FAILURE ) ;
    }
    IplImage * binaryImage = cvCreateImage ( cvGetSize (img),
IPL_DEPTH_8U , 1);
    cvSplit (img , binaryImage , NULL , NULL , NULL );
    IplImage * normalized = cvCreateImage ( cvGetSize (img), img
->depth , 1);
    cvEqualizeHist ( binaryImage , normalized );

    // cvNamedWindow (" normalized ", CV_WINDOW_AUTOSIZE );
    // cvShowImage (" normalized ", normalized );

    IplImage * gauss = cvCreateImage ( cvGetSize (img), img ->
depth , 1);
    cvSmooth ( normalized , gauss , CV_GAUSSIAN , 13, 13);

    // cvNamedWindow (" gauss ", CV_WINDOW_AUTOSIZE );
    // cvShowImage (" gauss ", gauss );

    IplImage * canny = cvCreateImage ( cvGetSize (img), img ->
depth , 1);
    cvCanny (gauss , canny , 40, 130) ;

    // cvNamedWindow (" edges ", CV_WINDOW_AUTOSIZE );
    // cvShowImage (" edges ", canny );

    IplImage * temp = cvCreateImage ( cvGetSize (img),
IPL_DEPTH_8U , 1);
    IplImage * closed = cvCreateImage ( cvGetSize (img),
IPL_DEPTH_8U , 1);
    IplConvKernel * element = cvCreateStructuringElementEx (3,
3, 1, 1, CV_SHAPE_RECT );
    cvMorphologyEx (canny , closed , temp , element ,
CV_MOP_CLOSE );
    cvReleaseStructuringElement (& element );
    cvReleaseImage (& temp );

    cvNamedWindow (" closed ", CV_WINDOW_AUTOSIZE );
    cvShowImage (" closed ", closed );

    //cvNamedWindow (" original ", CV_WINDOW_AUTOSIZE );
    // cvShowImage (" original ", img );
    cvWaitKey (0);
}
```

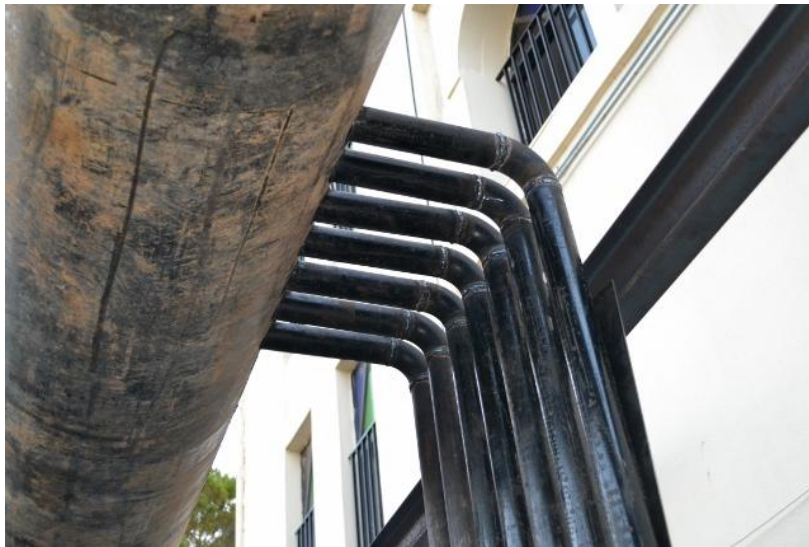
```
cvDestroyWindow (" original ");  
cvReleaseImage (& img );  
  
return EXIT_SUCCESS ;  
}
```

For compiling, this tutorial is helpful:

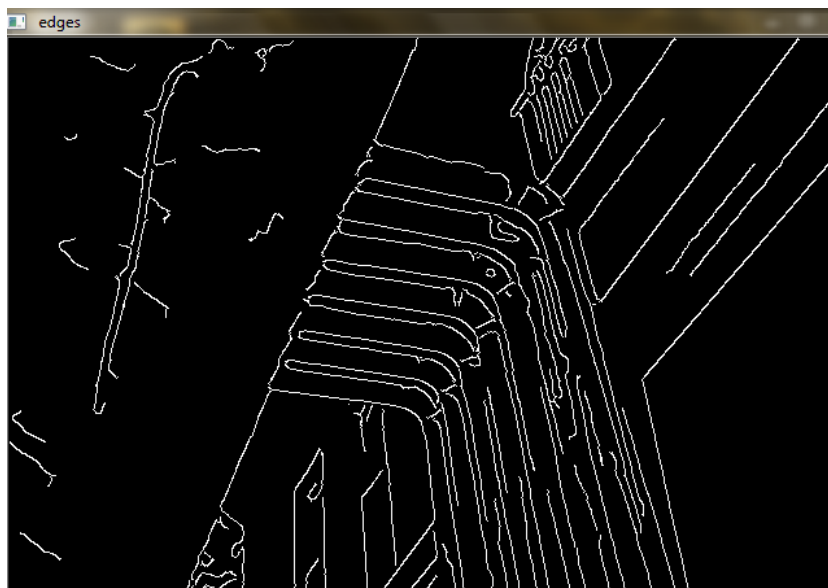
<https://www.youtube.com/watch?v=cgo0UitHfp8>

example:

Original:



Output:



## HI Line Radio Astronomy Sensor

**IAP-SWRDA**

Based on

**Prototype for a base station for supernova remnant HI line  
radio wave detector and analyzer (SRWDA)**

Master Thesis

by  
Suheeb Kassar

Supervisor: M.Sc. M.Eng. Samir Mourad, *IAP (AECENAR)*

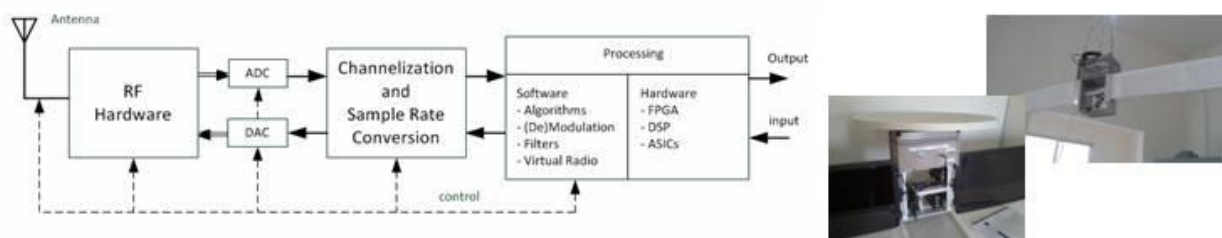
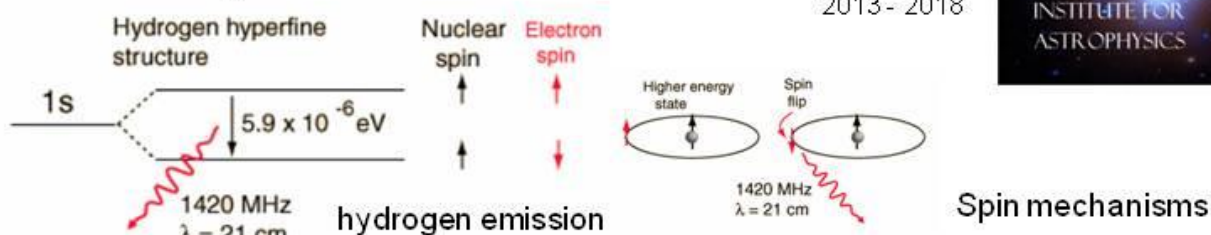
Main Referee: Prof. Dr. rer. nat. Wilhelm Stork, *ITIV (KIT)*

Abstract

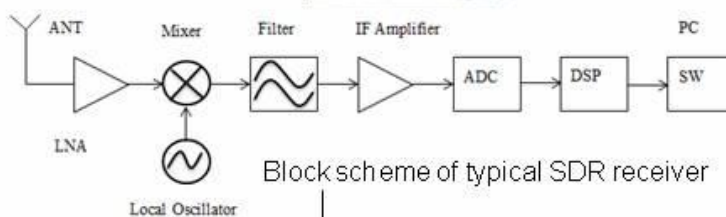


# Payload of IAP-SAT

2013 - 2018



## Model of Software Radio



## System design overview

Antenna

Hardware assembly box

- LNA Low noise amplifier
- BPF 1420 Band Pass Filter
- AMP Amplifier

DVT-RTL 820t + RTL 2832u

- ADC Analog digital converter
- DDC Digital Down Conversion
- Tuner 24-1700 Mhz

GNU-Radio

- Display signals
- Signal processing
- Synchronization

PC

USB 2.0

Antenna

Analog signal filtering

Digital signal processing

Software based signal processing

With the increasing dependence on the communication technology with wide bandwidth in more Applications and devices especially in wireless Field SDR (Software Defined Radio) is employed which

provide flexibility in technical point of view (Software) respectively market challenges. The advantages of SDR as multiband, multicarrier, multimode, Multirate and variable bandwidth enable to scan a wide range of frequencies with modified channel (modulation). On the other hand SDR concept can be implemented in different reconfigurable Hardware such as FPGA und DSP which means that replacing another analog elements for example antenna in Hardware can be effected using software design concept in reprogrammable und reconfigurable Systems .

This thesis describes the design and implementation of radio wave detector and analyzer (SRWDA) for processing supernova radio signals collected using four antennas which gives also direction information of the signals. The implemented Hardware in Software reduce the cost of station and at same time the right choice for accelerated digital signal processing. The detected signal can be displayed on GUI to observe a desired signals. The project was carried out in corporation with the Institute for Astrophysics (IAP). Some of the work was carried out in the IAP facility in Ras Nhache/Batroun/Lebanon.

### Master Thesis Task




Basmillah

**The SRWD project**

The radio astronomical IAP project supernova radio wave detector and analyzer (SRWDA) aims to detect and analyze radio signals from supernovas. At the base station a set of antennas, which gives also direction information of the signals, is aimed to be connected to a computer which acts as Software Defined Radio (SDR). Afterwards an analyzing program is aimed to be installed.

Later the detectors are planned to be installed on satellites to improve the resolution and to suppress disturbing signals from earth stations.

Master Thesis

**Initial Prototype for a base station for supernova radio wave detector and analyzer (SRWDA)**

																																																																																																																																																																																																																																																													
---	---	---	---	---	---	---	---	---	---	---	---	--	---	---	---	---	---	---	---	---	---	---	---	---	---	---	---	---	---	---	---	---	---	---	---	---	---	---	---	---	---	---	---	---	---	---	---	---	---	---	---	---	---	---	---	---	---	---	---	---	---	---	---	---	---	---	---	---	---	---	---	---	---	---	---	---	---	---	---	---	---	---	---	---	---	---	---	---	---	---	---	---	---	---	---	---	---	---	---	---	---	---	---	---	---	---	---	---	---	---	---	---	---	---	---	---	---	---	---	---	---	---	---	---	---	---	---	---	---	---	---	---	---	---	---	---	---	---	---	---	---	---	---	--	--	--	--	--	--	--	--	--	--	--	--	--	--	--	--	--	--	--	--	--	--	--	--	--	--	--	--	--	--	--	--	--	--	--	--	--	--	--	--	--	--	--	--	--	--	--	--	--	--	--	--	--	--	--	--	--	--	--	--	--	--	--	--	--	--	--	--	--	--	--	--	--	--	--	--	--	--	--	--	--	--	--	--	--	--	--	--	--	--	--	--	--	--	--	--	--	--	--	--	--	--	--	--	--	--	--	--	--	--

Presentation (May 2015)



Institut für Technik der  
Informationsverarbeitung



## MasterThesis

cand. el. **Suheeb Kassar**

### Directors

Prof. Dr.-Ing. Dr.h.c. J. Becker (speaker)  
Prof. Dr.-Ing. K. D. Müller-Glaser  
Prof. Dr. rer. nat. W. Stork

### Supervising Tutors

M.Sc. M.Eng. Samir Mourad

Institut für Technik der Informationsverarbeitung (ITV)

## Prototype for a base station for supernova remnant HI line radio wave detector and analyser (SRWDA)

KIT – University of the State of Baden-Wuerttemberg and  
National Laboratory of the Helmholtz Association

[www.kit.edu](http://www.kit.edu)

## Contents



- Thesis motivation
- Background
  - Radio astronomy and Hydrogen line1 (HL1)
  - Software defined radio(SDR) for detection HL1
- System design
- Hardware
  - Antenna
  - Analog filtering
  - SDR platform for digital processing
- Software
  - Design
  - Implementation
- Measurement
- System import on Mock-up modell

## Motivation



- Design and implementation of radio wave (Hydrogen line1) detector and analyser (SRWDA)
- Integration SRWDA with IAP Mockup model



3

17.08.2019 cand.el. [Suheeb Kassab] – [SRWDA]

Institut für Technik der Informationsverarbeitung (ITIV)

## Background



- What Radio Astronomy
  - Radio astronomy studies celestial objects at radio frequencies
  - The discovery of the cosmic microwave background radiation
  - Observation of new classes of objects (quasars, pulsars)
- Astronomical radio source
  - The Sun
  - Supernova remnants
  - Pulsars
  - Primordial black holes
  - .....

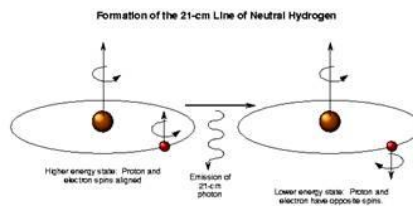
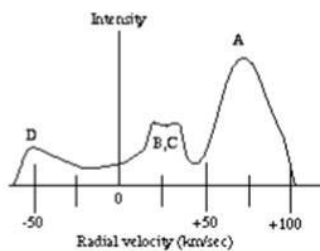
4

17.08.2019 cand.el. [Suheeb Kassab] – [SRWDA]

Institut für Technik der Informationsverarbeitung (ITIV)

## Hydrogen line 1 (HL1)

- Electromagnetic radiation spectral line (1420 MHz, 21 cm)
- HL1 is created by a change in the energy state of neutral hydrogen atoms.
- The HL1 provides the best way to map the structure of the Galaxy
- Calculate the mass of galaxies



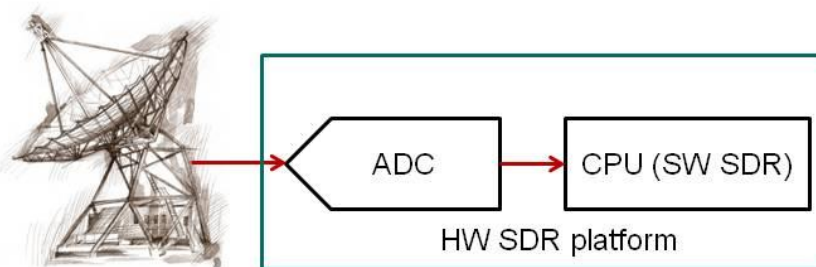
5

17.08.2019 cand.el. [Suheeb Kassab] – [SRWDA]

Institut für Technik der Informationsverarbeitung (ITIV)

## Software Defined Radio(SDR) for Detection HL

- Idea of SDR: hardware components (e.g. mixers, filters etc.) are implemented by means of software
- Radio telescope for HL can be designed using SDR
- The challenge for detection HL is a weakness of signal



Ideal SDR receiver

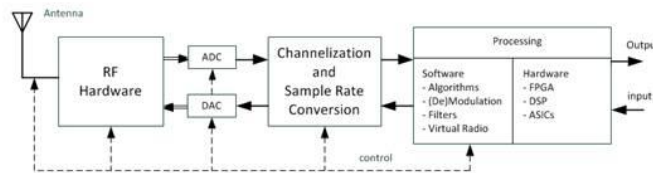
6

17.08.2019 cand.el. [Suheeb Kassab] – [SRWDA]

Institut für Technik der Informationsverarbeitung (ITIV)

## Why SDR?

- Design flexibility
- Reliability
- Upgradability
- Reusability
- Reconfigurability
- Enhanced Functionality
- Lower Cost



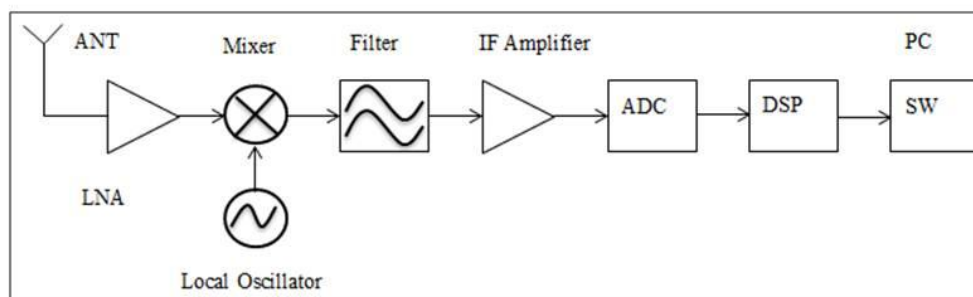
7

17.08.2019 cand.el. [Suheeb Kassar] – [SRWDA]

Institut für Technik der Informationsverarbeitung (ITIV)

## Basic SDR heterodyne receiver architecture

- The most used radio receivers use the architecture of super heterodyne receiver
- Received signal has been converted to a fixed intermediate frequency
- which can be more processed than the original radio carrier frequency.

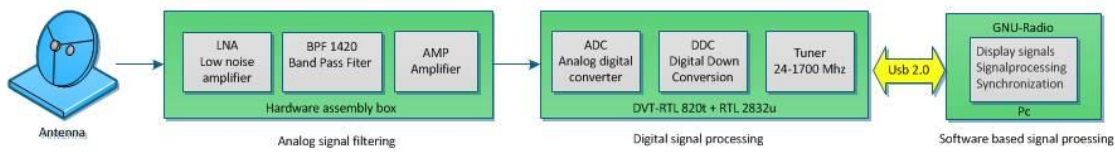


8

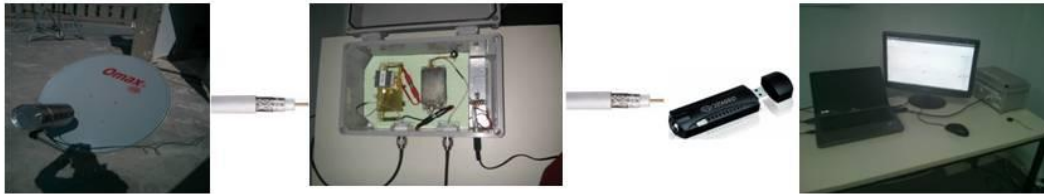
17.08.2019 cand.el. [Suheeb Kassar] – [SRWDA]

Institut für Technik der Informationsverarbeitung (ITIV)

## Telescope design



## Real system

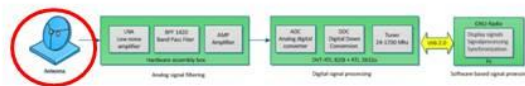


9

17.08.2019 cand.el. [Suheeb Kassab] – [SRWDA]

Institut für Technik der Informationsverarbeitung (ITIV)

## Antenna + Feeder



- Parabolic reflector antenna
- Ratio  $F/D = 0.5$ 
  - $F$  : Focal distance.  $f = 55$  cm
  - $D$  : Antenna diameter ie.  $d = 110$  cm
- Feed: dipole or crossdipole
- Feed horn  $D = 15$  cm,  $L = 20$  cm



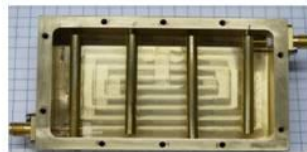
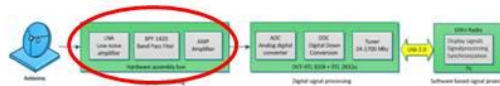
10

17.08.2019 cand.el. [NAME] – [DASA - TITEL]

Institut für Technik der Informationsverarbeitung (ITIV)

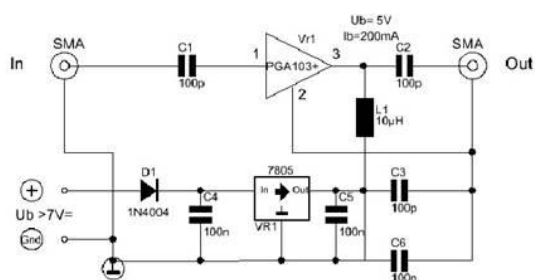
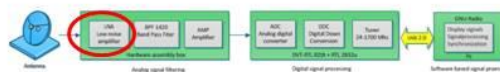
## Analog hardware

- Low noise amplifier (LNA)
- Band pass filter
- IF main amplifier & Attenuator



## Low noise amplifier (LNA)

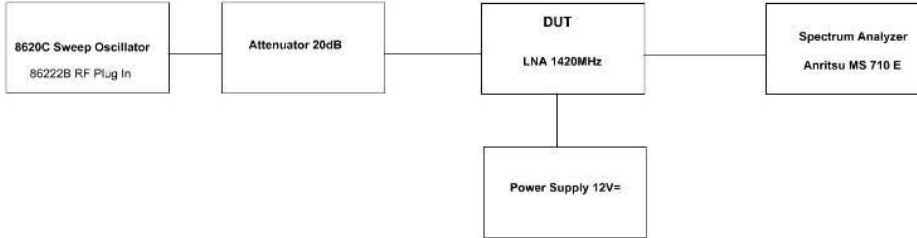
- Low noise amplifier (LNA)
  - Noise figure 12 dB
  - Gain 12 dB at 1420 MHz
  - IP1dB, 22.3dBm @ 2 GHz



## Low noise amplifier (LNA)



### ■ Test setup for LNA



### ■ Frequency response



13

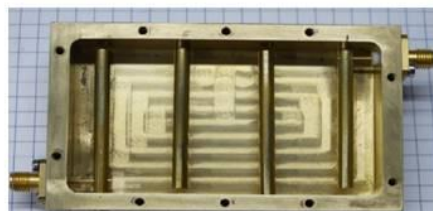
17.08.2019 cand.el. [Suheeb Kassab] – [SRWDA]

Institut für Technik der Informationsverarbeitung (ITIV)

## Hydrogen filter 1420 MHz



- Interdigital 4 Pole Filter
- frequency domain (3 dB): 1405 to 1437 MHz
- Insertion Loss: 1 dB typ.
- Input / Output impedance: 50 Ohms



14

17.08.2019 cand.el. [Suheeb Kassab] – [SRWDA]

Institut für Technik der Informationsverarbeitung (ITIV)



## Digital Hardware (SDR Platform)



Criteria for selecting a suitable platform:

- The frequency range up to 1.70 GHz.
- Suitable for low-cost experimentation
- Reconfigurability
- Fully open source platform (hardware, software)
- High resolution
- Sufficient bandwidth

## Overview of SDR platform

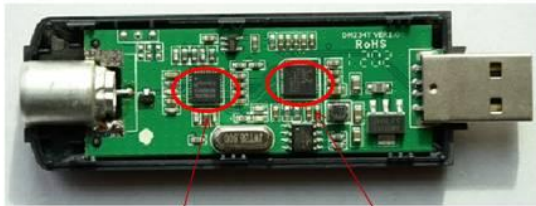
SDR Platform	Hackrf	BladeRF	USRP(B100)	Rtl_SDR(E4000)
Frequency range	30 MHz – 6 GHz	300 MHz – 3.8 GHz	50 MHz – 2.2 GHz	52 – 2200 MHz
Bandwidth	20 MHz	28 MHz	16 MHz	3.57MHz
Sample size (ADC-DAC)	8 bit	12 bit	12 bit/14 bit	8 bit
Sample rate (ADC-DAC)	20 Msps	40 Msps	64 Msps/128 Msps	3.2Msps
Transmit?	Yes	Yes	Yes	No
Interface speed	USB 2 (480M bit)	USB 3(5 gigabit)	USB 2 (480M bit)	USB (480M bit)
Open source	Everything (SW+HW)	HDL + Code Schematics	HDL + Code Schematics	Open source
Supported software	Gnu radio	Gnu radio	Gnu-radio/ Matlab	Gnu radio
Price	\$300	\$420	\$675	\$20



## SDR (RTL2832U-E4000)



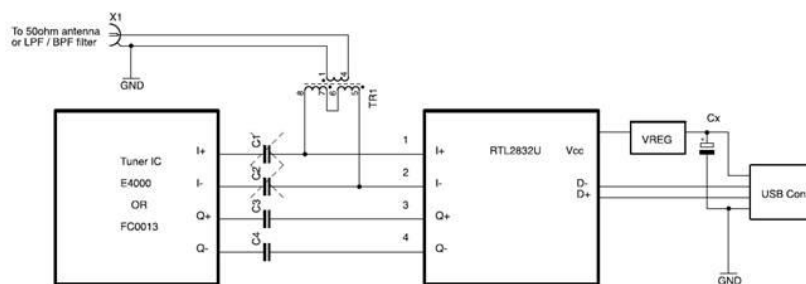
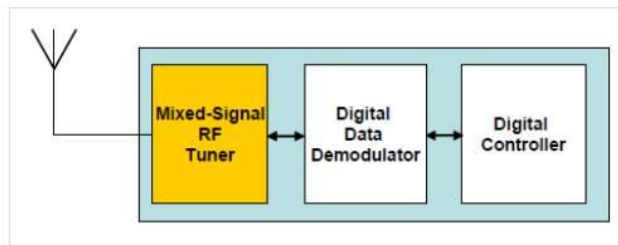
- Filtered signal is down sampled
- Frequency selecting done by The E4000 tunerchip
- Analog to digital converter (RTL2832U)
- Downconversion from IF to BF
- Output is sent to the computer by USB2.0

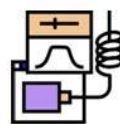


E4000

RTL2832u

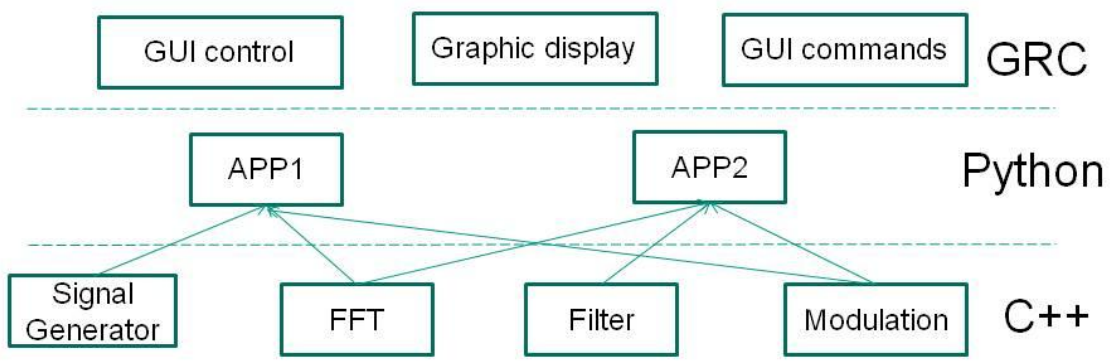
## SDR (RTL2832U-E4000)





## Software Design

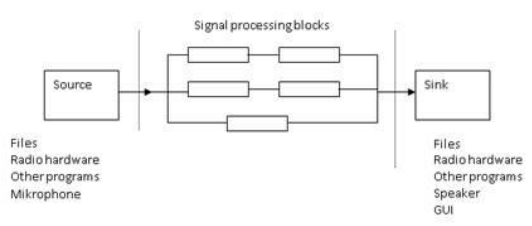
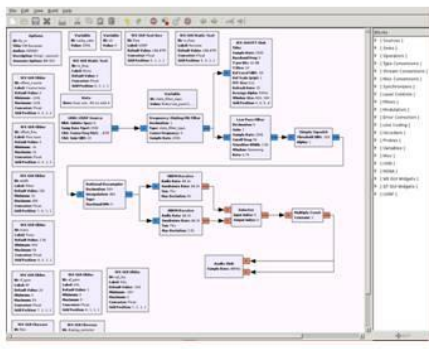
- GNU radio is an open source, Python-based architecture for building SDR projects
- C++ written signal processing blocks and python written connectors
- Available on Linux, Mac OS and Windows



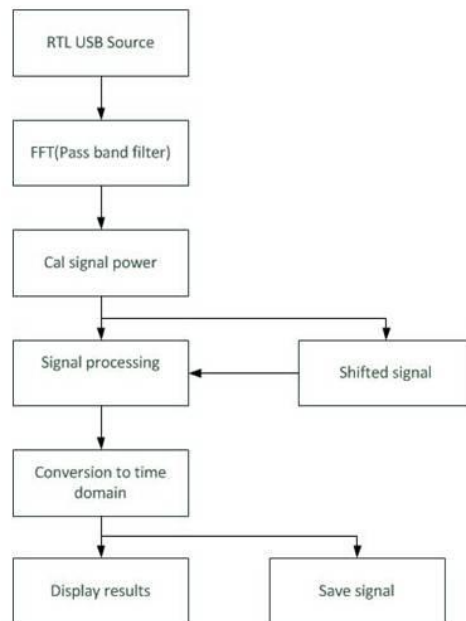
## GNU Radio Companion



- A graphical tool that Create signal flow graphs & Generate flow-graph source code



## Software Implementation



GNU Radio  
THE FREE & OPEN SOFTWARE RADIO ECOSYSTEM

23

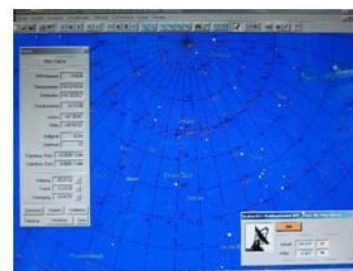
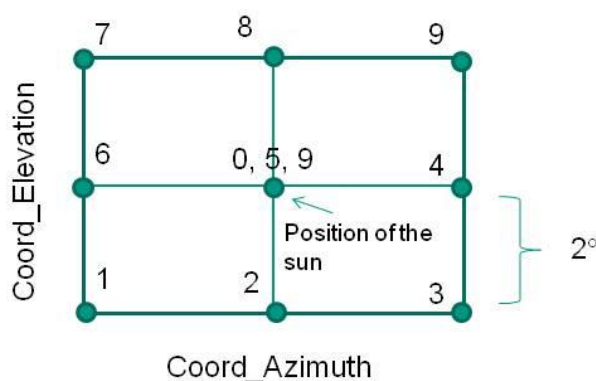
17.08.2019 cand.el. [Suheeb Kassab] – [SRWDA]

Institut für Technik der Informationsverarbeitung (ITIV)

## Software Implementation



- Scan (movement of the antenna) of area of
- Time transmission takes 2 sec between each 2 nodes
- Scanning starts from sun position (Easy Sky) and ends there
- Center of the matrix is tested 3 times



Easy Sky software

24

17.08.2019 cand.el. [Suheeb Kassab] – [SRWDA]

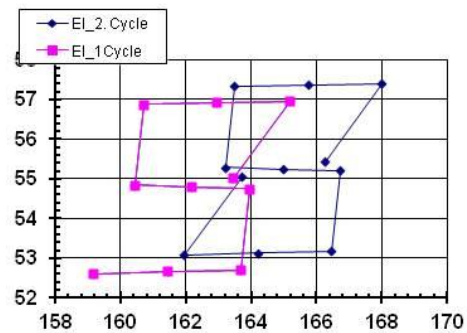
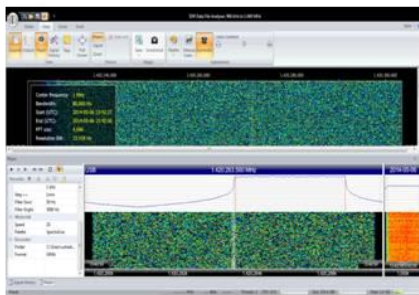
Institut für Technik der Informationsverarbeitung (ITIV)

## Measurement

### ■ First scenario



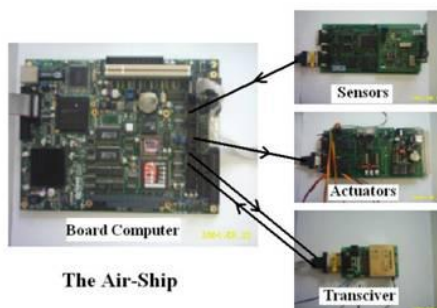
### ■ Second scenario



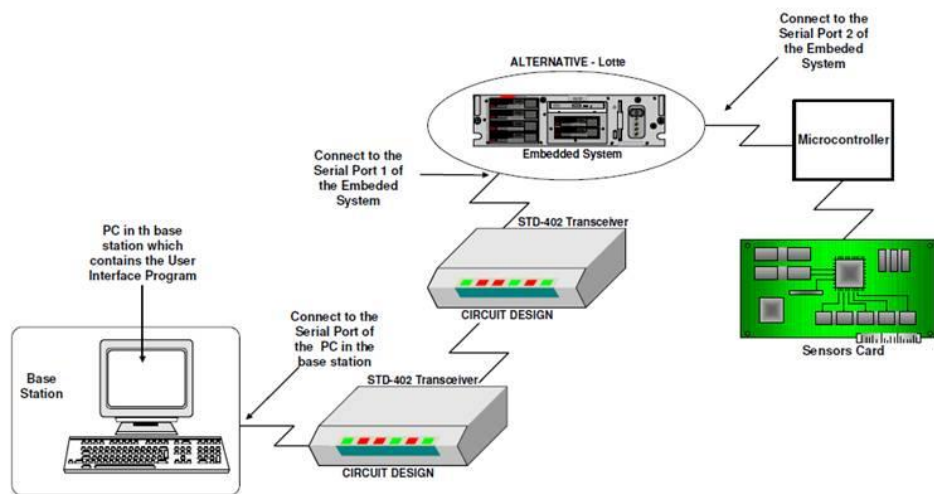
## Mock-up model of IAP-satellite (future work)

### ■ Mock-up is prototype model of IAP satellite

- Linux embedded Board computer
- Sensor card (temperature, camera,...)
- Transceiver card
- RTL SDR
- Antenna



## Communication system on Mock-up model



## Integration receiver model on Mock-up

- Import GnuRadio Model on embedded board
  - Operating system: Linux
  - Generated python\_code(GnuRadio) is compiled to C code by compiler
  - C-code will be sent by transceiver to ground station



**Table of contents**

<b>ABSTRACT .....</b>	<b>387</b>
<b>TABLE OF CONTENTS .....</b>	<b>403</b>
<b>LIST OF FIGURES .....</b>	<b>404</b>
<b>LIST OF TABLES.....</b>	<b>FEHLER! TEXTMARKE NICHT DEFINIERT.</b>
<b>LIST OF FORMULAS .....</b>	<b>FEHLER! TEXTMARKE NICHT DEFINIERT.</b>
<b>LIST OF KEYWORDS .....</b>	<b>404</b>
<b>1 INTRODUCTION .....</b>	<b>407</b>
1.1 BACKGROUND.....	407
1.2 MOTIVATION.....	407
1.3 OBJECTIVES .....	<b>FEHLER! TEXTMARKE NICHT DEFINIERT.</b>
1.4 OUTLINE.....	407
<b>2 BASICS .....</b>	<b>408</b>
2.1 21-CM RADIO ASTRONOMY BASICS .....	408
2.2 RADIO WAVE RECEIVING.....	409
2.3 SOFTWARE DESIGNED RADIO.....	409
2.4 BASIC SDR RECEIVER ARCHITECTURE .....	410
<b>3 SYSTEM DESIGN .....</b>	<b>412</b>
<b>4 MECHANICS .....</b>	<b>FEHLER! TEXTMARKE NICHT DEFINIERT.</b>
4.1 MECHANICAL DESIGN.....	<b>FEHLER! TEXTMARKE NICHT DEFINIERT.</b>
<b>5 HARDWARE CONCEPTION .....</b>	<b>414</b>
5.1 PLATFORM SELECTION .....	414
5.1.1 <i>Hackrf platform</i> .....	414
5.1.2 <i>BladeRF Platform</i> .....	415
5.1.3 <i>Ettus Research's USRP B100</i> .....	415
5.1.4 <i>Rtl_SDR(820)</i> .....	416
<b>6 HARDWARE REALIZATION.....</b>	<b>417</b>
6.1 HARDWARE OF USRP .....	419
6.1.1 <i>USRP B100 as motherboard</i> .....	419
6.1.2 <i>WBX 50-2200 MHz Rx/Tx as daughterboard</i> .....	420
6.1.3 <i>FPGA</i> .....	421
6.1.4 <i>ADC converter</i> .....	423
6.2 LOW NOISE AMPLIFIER LNA.....	423
6.3 LINE AMPLIFIER .....	426
6.4 ANTENNA.....	426
<b>7 SOFTWARE.....</b>	<b>429</b>
7.1 SOFTWARE DESIGN .....	<b>FEHLER! TEXTMARKE NICHT DEFINIERT.</b>
7.2 SOFTWARE IMPLEMENTATION .....	434
<b>8 INTEGRATION .....</b>	<b>FEHLER! TEXTMARKE NICHT DEFINIERT.</b>
<b>9 INTEGRATION TEST .....</b>	<b>FEHLER! TEXTMARKE NICHT DEFINIERT.</b>

<b>10</b>	<b>FUTURE WORK</b> .....	<b>438</b>
<b>11</b>	<b>LITERATURE</b> .....	<b>439</b>
<b>12</b>	<b>APPENDIX</b> .....	<b>440</b>
A.1	SOFTWARE .....	440
A.1.1	System Software .....	<b>Fehler! Textmarke nicht definiert.</b>
A.1.1.1	Example.c .....	<b>Fehler! Textmarke nicht definiert.</b>
A.2	HARDWARE .....	449
A.2.1	Layout motherboard USRP B100.....	449
A.3	LIST OF OFF-THE-SHELF ELECTRONIC COMPONENTS AND ASSEMBLIES.....	454
A.4	MECHANICAL COMPONENTS.....	455

### List of figures

Figure 1: hydrogen emission .....	408
Figure 2: Spain mechanisms .....	409
Figure 3: Radio system.....	409
Figure 4: Model of Software Radio [1].....	410
Figure 5: Block scheme of typical SDR receiver.....	411
Figure 8: Overview and comparison of different platforms.....	414
Figure 9:USRP Instant SDR Kit.....	419
Figure 10: Architecure of B100 .....	420
Figure 11: RF Front-End diagram.....	420
Figure 12: Receiver Blocks .....	421
Figure 13: DDC Block .....	422
Figure 14: Schematic and platine of LNA .....	423
Figure 15: Test of LNA.....	424
Figure 16: Output signal of LNA .....	424
Figure 17 .....	425
Figure 18 .....	<b>Fehler! Textmarke nicht definiert.</b>
Figure 19: Implementation of dial_tone example within Gnu Radio Companion.....	431

### List of Keywords

**ADC** Analog-to-Digital converter

**AF** Audio Frequency

**AGC** Automatic Gain Control

**AM** Amplitude Modulation

**BFO** Beat Frequency Oscillator

**CW** Continuous Wave

**DAB** Digital Audio Broadcasting

**DVB-T** Digital Video Broadcasting - Terrestrial

**RTL-SDR** Software Defeind Radio Dongle

**FFT** Fast Fourier Transform

**FM** Frequency Modulation

**FPGA** Field Programmable Gate Array

**FSF** Free Software Foundation

**GRC** GNU Radio Companion

**IF** Intermediate Frequency

**IAP** Institute for AstroPhysics

**I/O** Input/output

**ISO** International Organization for Standardization

**LNA** Low Noise Amplifier

**RDS** Radio Data System

**RF** Radio Frequency

**SRD** Software Defined Radio

**SRWDA** supernova radio wave detector and analyzer.

**USB** Universal Serial Bus



## **38 Introduction to SWRDA**

### **38.1 Background**

The gained information about the universe has been interpreted using radio frequency electromagnetic signals that can be detected through radio digital receiver. One of the most important beams is HI line 21cm that carry information about hydrogen atoms in space to get different astronomic parameters of hydrogen atom as speed, direction or distance within the galaxy etc. The rotation curve of our galaxy has also been calculated using the 21-cm hydrogen line. It is then possible to use the plot of the rotation curve and the velocity to determine the distance to a certain point within the galaxy [1].

The digital technology in communication scope made possible to measurement a spectrum line and processes to get clean signals.

### **38.2 The SRWDA Project**

The radio astronomical IAP project supernova radio wave detector and analyser (SRWDA) aims to detect and analyze HI radio signals from supernova remnants. At the base station a set of antennas, which gives also direction information of the signals, is aimed to be connected to a computer which acts as Software Defined Radio (SDR). Afterwards an analysing program is aimed to be installed.

Later the detectors are planned to be installed on satellites in the IAP SRWDA-SAT project [9] to improve the resolution and to suppress disturbing signals from earth stations.

### **38.3 Objectives**

In this thesis it is aimed to build a first prototype for a ground station for SRWDA.

### **38.4 Outline**

This thesis presents the design and implementation of SDR (Software Defined Radio) receiver to detect spectral line 21 cm of hydrogen atom for radio astronomy using reconfigurable platform and open source software for implementing Digital signal processing.

Chapter 2 gives some scientific and technical background information.

Chapters 3 until the last chapter describe the successive development process of the prototype according to the V model.

## 39 Basics

### 39.1 21-cm Radio Astronomy Basics

The hydrogen gas is one important of the main materials that can be found in throughout of the space. The 1420 MHz radiation form hydrogen pass through the Earth's atmosphere and gives us a more complete map of the hydrogen than that of the stars themselves since their visible light won't penetrate the dust clouds. The radiation comes from the transition between the two levels of the hydrogen 1s ground state, slightly split by the interaction between the electron spin and the nuclear spin. In this procedure hydrogen in its lower state will absorb 1420 MHz.

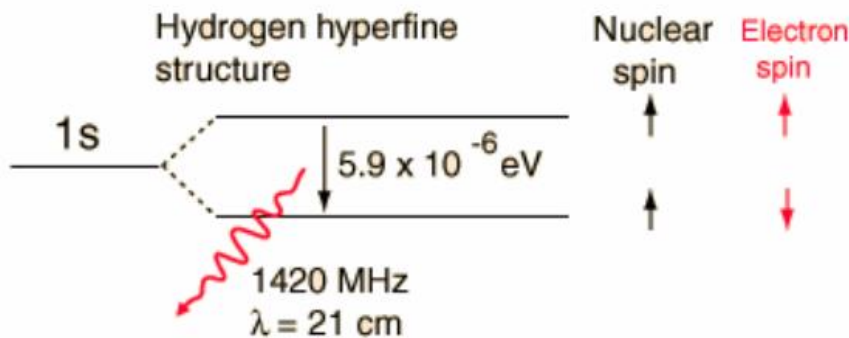


**Figure 101: hydrogen emission**

The electron moving around the proton can have a spin in the same direction as the proton's spin (i.e., parallel) or spin in the direct opposite direction as the proton's spin (i.e., anti-parallel). The energy state of an electron spinning antiparallel is slightly lower than the energy state of a parallel-spin. Since atoms always want to be in the lowest energy state possible, the electron will eventually flip to the anti-parallel spin direction if it were in the parallel spin direction. The energy difference is very small, so a hydrogen atom can wait on average a few million years before it undergoes this transition. The advantage for detecting the 21cm signal is to calculate the mass of galaxies, to put limits on any changes over time of the universal gravitational constant and to study dynamics of individual galaxies and to plot the rotation curve of our galaxy respectively the velocity [1].

This splitting of the hydrogen ground state is extremely small compared to the ground state energy of  $-13.6 \text{ eV}$ , only about two parts in a million. The two states come from the fact that both the electron and nuclear spins are  $1/2$  for the proton, so there are two possible states, spin parallel and spin antiparallel. The state with the spins parallel is slightly higher in energy (less tightly bound).

In visualizing the transition as a spin-flip, it should be noted that the quantum mechanical property called "spin" is not literally a classical spinning charge sphere. It is a description of the behaviour of quantum mechanical angular momentum and does not have a definitive classical analogy. The observation of the 21cm line of hydrogen marked the birth of spectral-line radio astronomy. It was first observed in 1951 by Harold Ewen and Edward M. Purcell at Harvard, followed soon afterward by observers in Holland and Australia.

The prediction that the 21 cm line should be observable in emission was made in 1944 by Dutch astronomer H. C. van de Hulst [2]. A radio telescope is powerful tool, which can “see” radio waves emitted by radio sources in throughout the space.

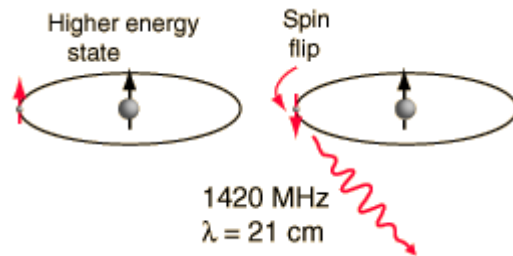


Figure 102: Spin mechanisms

### 39.2 Radio Wave Receiving

Firstly we want to present the simple radio system diagram and explain their components to get better understanding for complete system.

The electromagnetic signal has been received by an antenna and then converted into an electrical signal. This signal is normally very weak and disturbed because of many factors as atmosphere ... etc. therefor the noise must be removed from a signal amplified before it processing later. That will be happened in the next stage (RFF) that processes a signal for ADC converter. RFF consists of filter, amplifier und mixer to convert the radio frequency to lower frequency. The resulted analog signal from RFF has to be digitized using *Analog -Digital converter* for further processing in suitable hardware components as Digital Signal Processing (DSP), Field Programmable Gate Array (FPGA) or microprocessor [2].

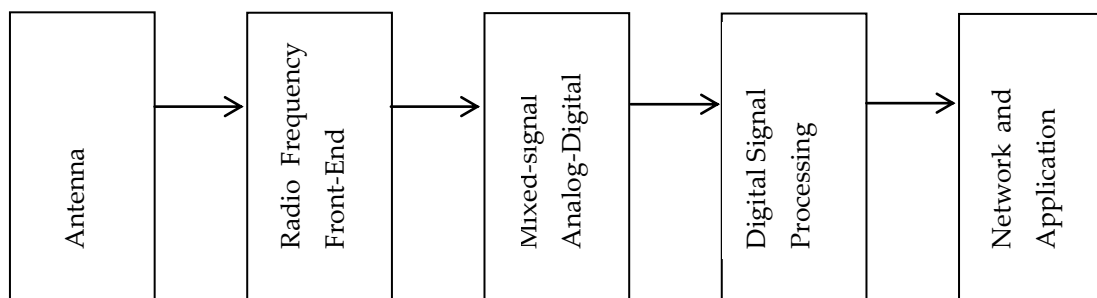


Figure 103: Radio system

Finally

a

processed radio signal can interface in modern system to a network or an application.

### 39.3 Software Designed Radio

The definition software radio was Joe Mitola in 1991 to refer to the class of reprogrammable or reconfigurable radios [3]. That means, the same hardware components can execute different functions at different times. However, a radio defines in software its modulation, error correction, and

encryption processes, exhibits some control over the RF hardware, and can be reprogrammed is clearly a software radio.

SDR is defined as a described radio in Software and whose physical layer behaviour can be significantly altered through changes to its software in which the receive digitization is performed at some stage downstream from the antenna, typically after wideband filtering, low noise amplification, and down conversion to a lower frequency in subsequent stages – with a reverse process occurring for the transmit digitization. Digital signal processing in flexible and reconfigurable functional blocks defines the characteristics of the radio [4].

Hardware components of the traditionally radio system consists of the mixers, filters, amplifiers and oscillators are replaced by software in SDR as indicated in the Figure 2.2. The hardware for signal processing should be selected for high speed signal processing for example as GGP, FPGA or DSP. The main advantage of an SDR is reconfigurability and customizable. The implementing radio functions in software are more flexible than in hardware for a radio device to be reconfigured for different use cases rather needing to redesign the hardware to support new functionality. With the rapid evolution of wireless protocols and standards, a hardware radio could be made obsolete due to the inability to conform to new standards or protocols. An SDR, however, could be reconfigured to support new standards that may not have existed at the time the device was built. Such flexibility is attractive to the manufacturers of the devices as it enables them to update their SDR product through software and not necessarily need to change the hardware of the radio. Such flexibility is helpful to fast update suchlike systems and allows manufacturer to redesign the system without changing the hardware architecture.

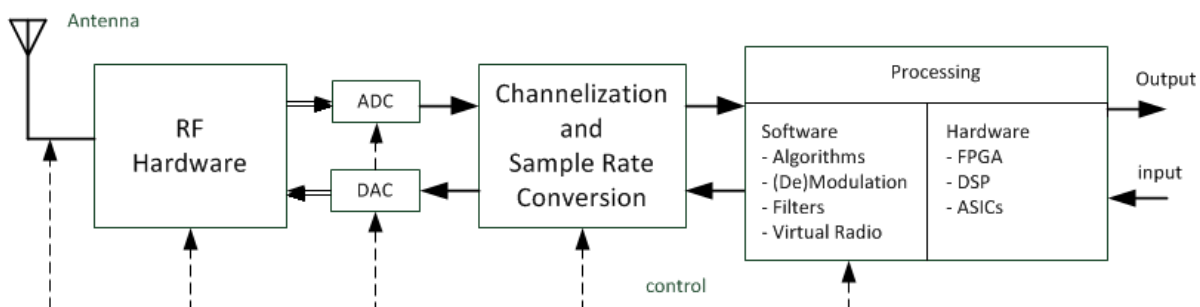


Figure 104: Model of Software Radio [1]

### 39.4 Basic SDR Receiver Architecture

The most used radio receivers use the architecture of super heterodyne receiver, in which a received signal has been converted to a fixed intermediate frequency, which can be more processed than the original radio carrier frequency. A detected signal is picked up via the antenna, mixed with local oscillator to reduce frequency of an incoming signal to intermediate frequency (IF) for further processing, filtered due unwanted signals filtered using low pass filter and finally amplified with a low noise amplifier (LNA) for accommodation to ADC converter.

The digitized IF signal repeat oneself as spectral harmonic that can be placed near the baseband frequency, helping frequency translation and digitization to be carried out simultaneously. For next processing digital filtering and downconversion of sample rate (for receiving) are needed to change a

sampled signal from high frequency to lower frequency allowing a hardware as DSP or FPGA to process it with suitable sample rate without loss of the information.

Typical SDR receivers have a simple and cheap direct-conversion or low intermediate frequency architecture. The ideal SDR receiver would have all the radio-frequency bands and modes defined software-wise, meaning it would consist only of an antenna, ADC and a programmable processor. Typically, RF front-end of a SDR will consist of antenna circuitry, amplifiers, filters, local oscillators and ADCs. When the signal is received, it is amplified and its carrier frequency downconverted to a low-intermediate frequency in order for ADC to perform digitization.

The processing is done by some of the computational resources at our disposition – mainly, General Purpose Processors (GPPs), Digital Signal Processors (DSPs) and Field Programmable Gate Arrays (FPGAs), whereas some of the future resources may include a combination of the aforementioned, thus extending the computational capacity. One of the most important aspects when deciding on a computational resource that is to be used in the system is its reprogrammability (important for implementation of new waveforms), therefore dedicated-purpose circuitry is generally avoided in SDRs.

The basic receiving process is illustrated in Figure 2.3 with its principle design constraints will be explained in this chapter.

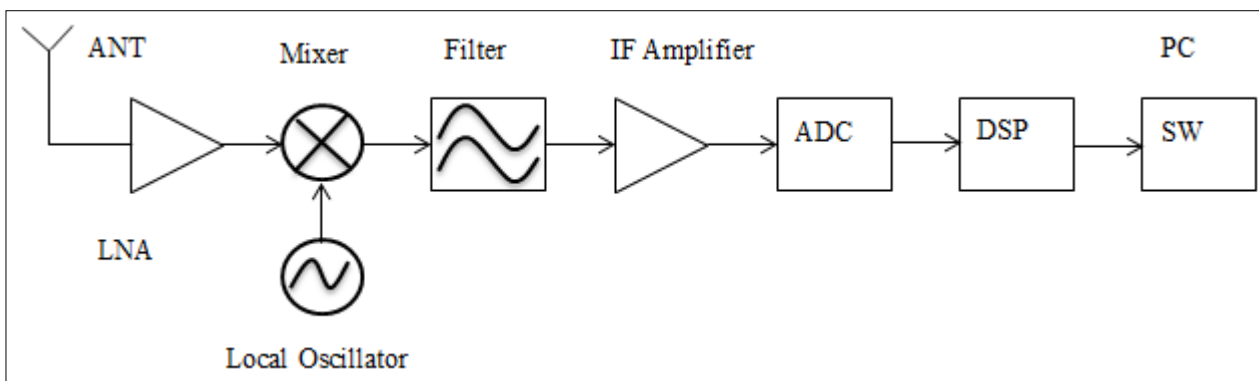


**Figure 105: Block scheme of typical SDR receiver**

The important design parameters that have to be considered during design SDR receiver system are: input sensitivity, maximum expected input signal and blocker specifications.

## 40 System Design

The HI spectrum signal will be detected by the antenna which converts the electromagnetic signal to analog signal to process with SDR system (Hardware and Software). Because of the weakness of the incoming HI spectrum signal we have to use a low noise amplifier for filtering the incoming signals and amplifying the hydrogen line signal at 1420 MHz. The filtered signal is then available for further processing phase. It is important to integrate a line amplifier in the design taking into account the signal line loss by using coaxial cable. For further high signal processing SDR platform (SDR-hardware and-software) were needed to realize **SRWDA** model. Two designs have been developed in IAP institute. The figures 6 und 7 give both alternative designs explained.

A software-defined radio (SDR) system is a hardware and software co-design system which can tune to any frequency band and preform different communication functions (modulation, demodulation, etc.) by means of a programmable hardware, which is controlled by software. SDR platform software performs various amounts of digital signal processing in PC [1]. SDR has evolved with advancement in computing machines and high-speed analog-digital (A/D) and digital-analog (D/A) converters. Thus SDR allows a single device to support a wide range of capabilities previously available only through multiple products [1].

As explained signals received by an antenna should be digitized so that SDR may processes these digitized samples at RF frequencies (around GHz frequencies) to perform further signal processing steps (IF conversion, filtering, baseband conversion etc). But due to certain limitations like unavailability of A/D converters at very high frequencies (starting from a few GHz) and very high speed general purpose computers, digitization takes place after the IF or baseband demodulator stage. That typically means that hardware is still required to convert the signals of interest into and out of the “baseband” frequencies in the digital domain, but all of the complex processing performed at baseband is handled in the digital software domain [1]. Yet, such hardware is usually fairly simple comprising of a local oscillator and mixer, and a pair of low-pass filters.

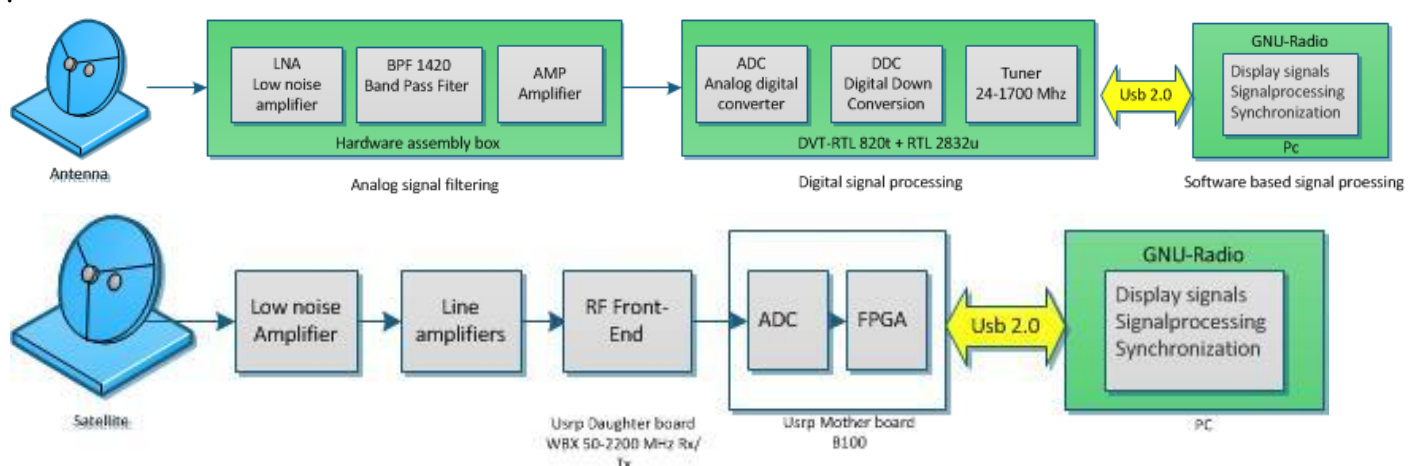


Figure 6: 1.System design overview

The digital signal will be sent via usb2.0 to host pc which software *Gnu-Radio* uses to control SDR hardware platform and transmit and receive data. GNU Radio is an open-source software toolkit. that, connected with hardware equipment such as USRP, allows for building Software Defined

Radios connect with hardware. We will later go into details also hardware components and software respectively.

## 41 Hardware Conception

### 41.1 Platform Selection

This chapter describes the core idea for selecting receiver components to implement our system and the desired environment work. These are the criteria which have to be fulfilled by a suitable platform:

- The receiver system operates in 1420 MHz.
- Suitable for low-cost experimentation.
- Reprogrammability.
- Fully open source platform (hardware, software).

Couple of weeks of research narrowed the options down to the following SDR platforms:

SDR Platform	Hackrf	BladeRF	USRP(B100)	Rtl_SDR(E4000)
Frequency range	30 MHz – 6 GHz	300 MHz – 3.8 GHz	50 MHz – 2.2 GHz	52 – 2200 MHz
Bandwidth	20 MHz	28 MHz	16 MHz	3.57MHz
Simple size (ADC-DAC)	8 bit	12 bit	12 bit/14 bit	8 bit
Simple rate (ADC-DAC)	20 Msps	40 Msps	64 Msps/128 Msps	3.2Msps
Transmit?	Yes	Yes	Yes	No
Interface speed	USB 2 (480Mbit)	USB 3(5 gigabit)	USB 2 (480Mbit)	USB (480Mbit)
Open source	Everything (SW+HW)	HDL + Code Schematics	HDL + Code Schematics	-----
Supported OS	Linux, OS X, Windows	Linux, OS X, Windows	Linux, OS X, Windows	Linux, OS X, Windows
Supported software	Gnu radio	Gnu radio	Gnu-radio/ Labview	Gnu radio
Price	\$300	\$420	\$675	\$20

**Figure 14: Overview and comparison of different platforms**

#### 41.1.1 Hackrf platform

Hackrf is open source hardware to build SDR system that has been developed by Michael Ossmann HackRF operates from 30 MHz to 6 GHz, a wider range than any SDR peripheral available today. This range includes the frequencies used by most of the digital radio systems on Earth. It can operate at even lower frequencies in the MF and HF bands when paired with the Ham It Up RF upconverter. HackRF can be used to transmit or receive radio signals. It operates in half-duplex mode: it can

transmit or receive but can't do both at the same time. However, full-duplex operation is possible if you use two HackRF devices.

HackRF is designed primarily for use with a USB-attached host computer, but it can also be used for stand-alone applications with Jared's HackRF PortaPack, an add-on that gives HackRF an LCD screen, directional buttons, and audio ports

HackRF was designed to be the most widely useful SDR peripheral that can be manufactured at a low cost. The estimated future retail price of HackRF is \$300, but you can get one for even less by backing the Kickstarter project today. The most important goal of the HackRF project is to produce an open source design for a widely useful SDR peripheral. All hardware designs and software source code are available under an open source license. The hardware designs are produced in KiCad, an open source electronic design automation tool.

### **41.1.2 BladeRF Platform**

bladeRF is a Software Defined Radio (SDR) platform make possible to enable a community of hobbyists, and professionals to explore and experiment with the multidisciplinary facets of RF communication. By providing source code modern radio systems will be simplified by covering everything from the RF, analog, and digital hardware design to the firmware running on the ARM MCU and FPGA to Linux kernel device drivers.

The bladeRF can tune from 300MHz to 3.8GHz without the need for extra boards. The current open source drivers provide support for GNURadio among other things, allowing the bladeRF to be placed into immediate use. This gives the bladeRF the flexibility to act as a custom RF modem, a GSM and LTE pico cell, a GPS receiver, an ATSC transmitter or a combination Bluetooth/WiFi client without the need for any expansion cards.

The bladeRF was designed to be highly integrated and fully reprogrammable. This means more than just providing source code to modify the host software. The USB 3.0 (Cypress FX3) microcontroller firmware is available to modify, as is the Altera Cyclone IV FPGA VHDL, bringing developers as close to the RF transceiver as possible.

### **41.1.3 Ettus Research's USRP B100**

The Universal Software Radio Peripheral (USRP) is a digital acquisition (DAQ) system containing four 64 MS/s, 12-bit A/D converters (ADCs), four 128 MS/s, 14-bit D/A converters (DACs), and supports USB 2.0 interface or Ethernet(USRP N210). The USRP is capable of processing signals with 16 MHz of bandwidth.

The USRP takes daughter-cards to map the frequency ranges of interest into the "baseband" that is visible by the A/D hardware. The USRP is a most widespread SDR's in academic environments, Ettus products still count as the best-buy platforms for research. Ettus Research offers several platforms – USRP, USRP2 and USRP N210 that differ in the level of instantaneous bandwidth they can process; reprogrammability of the FPGA; type of interface to the computer (USB or Ethernet) and, of course, price..

#### 41.1.4 Rtl\_SDR (RTL2832+ E4000):

RTL-SDR is a very cheap software defined radio, that uses a DVB-T TV tuner dongle based on the RTL2832U chipset (USB devices intended to allow you to watch over-the-air DVB-T broadcast television), had a special "mode" that allow them to be used as crude SDR receivers. In this mode, the digital base-band samples bypass the DVB-T demodulator/decoder in the RTL2832U chip, and are sent over USB. Normally, these devices send partially-decoded MPEG transport frames over the USB, but in this "SDR" mode, they send raw I/Q base-band samples instead.

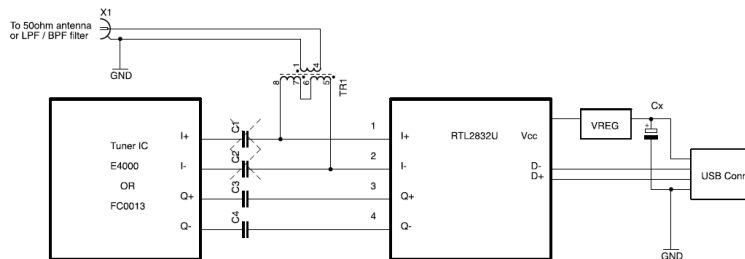
These "dongles" are typically shipped with one of two or three different tuner chips, and the most popular ones, E4000 tuner allows tuning to the hydrogen-line frequency of 1420Mhz.

A driver library was quickly produced<sup>3</sup> based on the information gleaned from datasheets and a bit of reverse engineering. The driver library can be used stand-alone, or in concert with a "plug in" for GnuRadio that allows Gnu Radio applications to use the RTLSDR devices. The disadvantages by using Rtl\_SDR outweigh his advantages because of the following reasons:

- Dynamic range is quite limited, due to use of an 8-bit ADC, roughly 45dB SFDR.
- Temperature stability is poor, leading to gain drift, and frequency drift.
- Phase and amplitude balance is quite poor, leading to image problems.
- The total cost was 30 \$.

## 42 Hardware Realization

### 42.1 Hardware of RTL SDR (RTL2832+E4000):



#### 42.1.1 RTL2832

The RTL2832U is a high-performance DVB-T COFDM demodulator that supports a USB 2.0 interface. The RTL2832U complies with NorDig Unified 1.0.3, D-Book 5.0, and EN300 744 (ETSI Specification). It supports 2K or 8K mode with 6, 7, and 8MHz bandwidth. Modulation parameters, e.g., code rate, and guard interval, are automatically detected.

The RTL2832U supports tuners at IF (Intermediate Frequency, 36.125MHz), low-IF (4.57MHz), or Zero-IF output using a 28.8MHz crystal, and includes FM/DAB/DAB+ Radio Support. Embedded with an advanced ADC (Analog-to-Digital Converter), the RTL2832U features high stability in portable reception.

The state-of-the-art RTL2832U features Realtek proprietary algorithms (patent-pending), including superior channel estimation, co-channel interference rejection, long echo channel reception, and impulse noise cancellation, and provides an ideal solution for a wide range of applications for PC-TV, such as USB dongle and MiniCard/USB, and embedded system via USB interface.

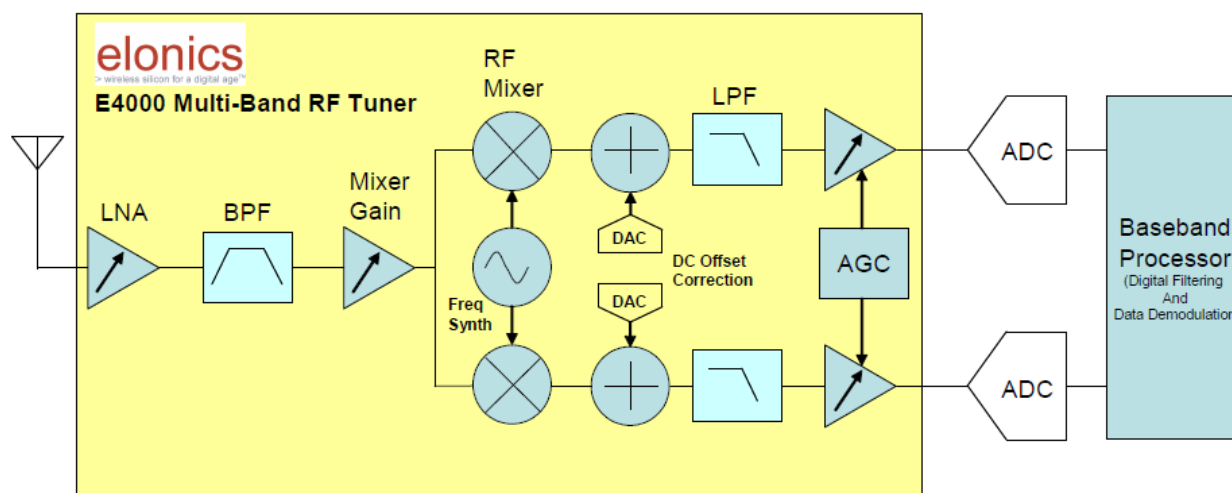
#### 42.1.2 Tuner E4000

The Elonics DigitalTune™ architecture provide solution around the ability to optimize each part of the tuner signal chain from input to output. The tuner must be able to cover the complete frequency spectrum required by the product, and output the

desired channel of interest all under control of the system controller. However, behind this apparently simple concept lies a hugely complex and challenging design problem. In order to provide such a solution, each stage in the RF tuner signal chain must be capable of being

modified to optimize the signal path characteristics for downstream processing, dependent on the broadcast standard and the desired signal characteristics chosen by the system designer.

Figure 4 shows the internal block diagram of the E4000 multi-standard RF tuner. Although the signal path looks conventional, the E4000 using the DigitalTune™ architecture provides unique flexibility at each stage in the process from input to output.



#### Benefits of Tuner E4000

- A single re-configurable RF tuner front
- Parametric performance comparable to single function tuners
- Low system power
- Small PCB
- Few external components
- Low system cost

#### Zero IF Architecture

A zero IF architecture is part of the DigitalTune™ concept. A homodyne or zero IF architecture as shown in Figure 7 employs a single stage to down convert the RF signal using a single sideband mixer to a baseband signal centred at DC. A subsequent low pass filter removes the higher frequency mixing products and attenuates unwanted out of band signals.

This filtered signal can then be digitised directly by a fast sampling ADC that has enough dynamic range to absorb both the wanted and unwanted signals. Final fine tune filtering can then be performed digitally.

The mixer output contains the sum and difference of the input signal frequencies to the mixer.

The advantages of a zero IF architecture are numerous if the intrinsic problems can be overcome.

There is no image because the signal is mixed to baseband, and therefore no image filter is needed. Because there is no intermediate IF stage, there is also no requirement for a bandpass IF filter. Finally power consumption is reduced, not only due to the simplification of the signal chain but also because the signal amplification is done at lower frequencies

## 42.2 Hardware of USRP

The Universal Software Radio Peripheral (USRP) is a low-cost SDR system developed by Ettus Research. The system consists of a motherboard with FPGA, 2 pairs of DACs and ADCs, digital downconverters and upconverters with programmable interpolation rates, and a the second part of the system is daughterboard which serve as RF front-end. The connection to the PC is done via USB2.0. Ettuscompany offers a SDR kit containing of USRP B100 as motherboard, WBX 50-2200 MHz as daughterboard which is suitable for low cost-experiment. The total price costs 590 euro. For mor details see appendix A6.



Figure 15:USRP Instant SDR Kit

### 42.2.1 USRP B100 as motherboard

A USRP motherboard is the heart of software defined system provides subsystems where can be built reconfigurable structure for many application in wireless communication systems. The B100-hardware provides low-cost RF processing capability, and up to 16 MS/s of signal streaming through the USB 2.0 host interface. As shown in figure 3.2 the B100 consists of FPGA, ADC, DAC and a USB interface.

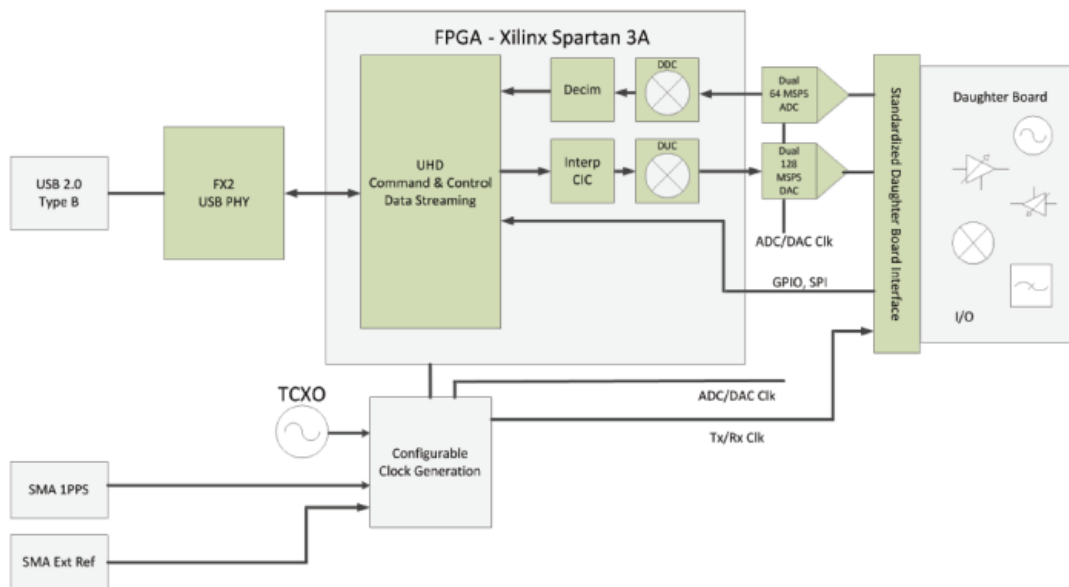


Figure 16: Architecture of B100

#### 42.2.2 WBX 50-2200 MHz Rx/Tx as daughterboard

A new front-end circuit is used for analog operations such as up/down-conversion, filtering, and other signal conditioning. This modularity allows the USRP to serve applications that operate between DC and 6 GHz. The main function of RF Front-End is to reject undesired signal using filtering it after taking the signal from antenna and then converting the signal to a center frequency with an amplitude compatible for the analog digital conversion process. The Ettus research has developed many boards as RF so called daughterboard<sup>47</sup> which achieve our requirements and cover different frequency bands. For the project, receiver boards operating in 1.4 GHz (HL spectrum line) frequency band were needed, therefore two WBX 50-2200 MHz Rx/Tx daughterboard were chosen.

The WBX is a wide bandwidth transceiver that provides up to 100 mW of output power and a noise figure of 5 dB. The LO's for the receive and transmit chains operate independently, but can be synchronized for MIMO operation. The WBX provides 40 MHz of bandwidth capability and is ideal for applications requiring access to a number of different bands within its range - 50 MHz to 2.2 GHz [5]. This receiver architecture, shown in Figure 3.3, is implemented on the daughterboard WBX.

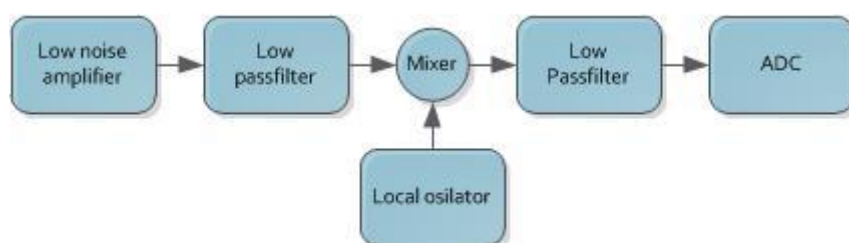


Figure 17: RF Front-End diagram

<sup>47</sup>Ettus Research Company offers different boards for various application areas. For selecting a suitable combination of boards Ettus Company recommends new users evaluate their application requirements against the specifications USRP devices.

### 42.2.3 FPGA

The FPGA plays an important role in the Radio system, providing digital signal processing, as well as timing logic for clock, chip rate and time slot synthetization . The main functionality of FPGA is to perform high bandwidth math, and to reduce the data rates to something you can squirt over USB2.0. The FPGA connects to a USB2 interface chip, the Cypress FX2. Everything (FPGA circuitry and USB Microcontroller) is programmable over the USB2 bus.

USRP B100 is powered by Xilinx Spartan 3A-1400 FPGA[5] and has the following characteristics:

- Configurable Logic Blocks (CLBs) contain flexible Look-Up Tables (LUTs) that implement logic plus storage elements used as flip-flops or latches. CLBs perform a wide variety of logical functions as well as store data.
- Input/output Blocks (IOBs) control the flow of data between the I/O pins and the internal logic of the device. IOBs support bidirectional data flow plus 3-state operation. Supports a variety of signal standards, including several high-performance differential standards. Double Data-Rate (DDR) registers are included.
- Block RAM provides data storage in the form of 18-Kbit dual-port blocks.
- Multiplier Blocks accept two 18-bit binary numbers as inputs and calculate the product.
- Digital Clock Manager (DCM) Blocks provide self-calibrating, fully digital solutions for distributing, delaying, multiplying, dividing, and phase-shifting clock signals.

The standard FPGA configuration includes digital down converters (DDC) implemented with cascaded integrator-comb (CIC) filters. CIC filters are very high-performance filters using only adds and delays. The FPGA implements 4 digital down converters (DDC). This allows 1, 2 or 4 separate RX channels. The receiver side includes 4 ADCs and 4 DDCs as shown in figure 3. Each DDC has two inputs I and Q. Each of the 4 ADCs can be routed to either of I or the Q input of any of the 4 DDCs.

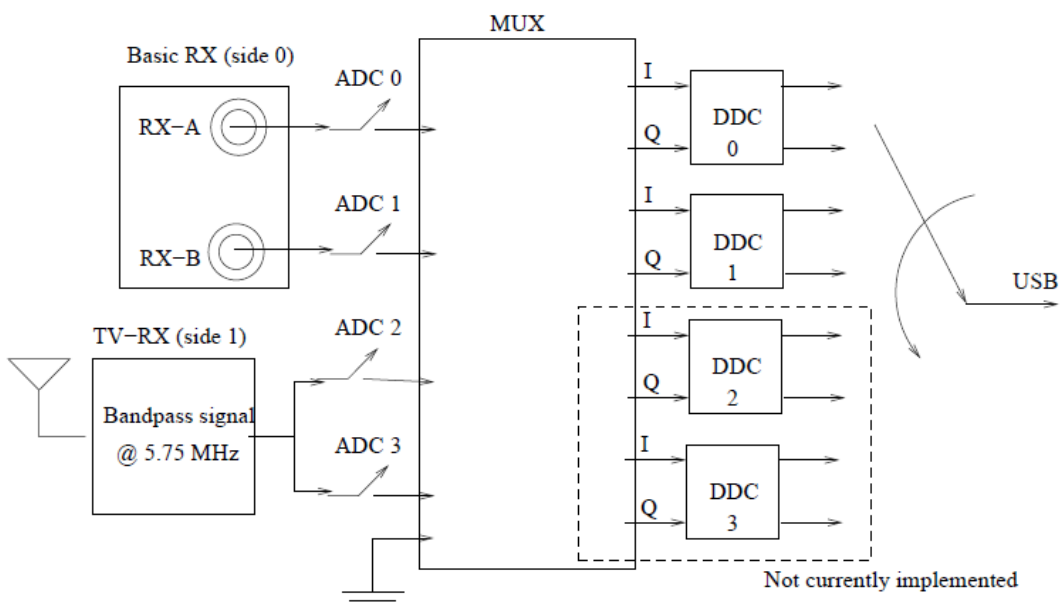


Figure 18: Receiver Blocks

The MUX is like a router or a circuit switcher. It determines which ADC (or constantzero) is connected to each DDC input. There are 4 DDCs. Each has two inputs. We can control the MUX using `usrp.set_mux ()` method in Python [6].

Each input (I0, Q0, I1 ... I3, Q3) can be connected with which ADC by using 4 bits (0, 1, 2, 3 or 0xf). For most real sampling applications, the Q input of each DDC is constant zero. So quite often we don't need to modify the standard configuration of the FPGA. Actually it is anticipated that the majority of USRP users will never need to use anything other than the standard FPGA configuration.

The platform contains two digital downconverters with programmable decimation rates, in charge of mixing, filtering and decimating arriving signals in the FPGA. Digital downconverters shift the frequency band of the incoming high sampling rate digitized signal to the baseband and lower the sampling rate without any information loss. First, the digitized stream is mixed with a digitized cosine (for I channel) and digitized sine (for Q channel), producing the sum and the difference components. These outputs are then put through the identical digital filters, filtering unwanted components. At this point, because the bandwidth of the signals we want to process has been reduced, sampling frequency can be loss lessly decimated. The DDC converts down the signal from the IF band to the base band. Second, it decimates the signal so that the data rate can be adapted by the USB 2.0 and is reasonable for the computers' computing capability. The Figure 3.4 shows the block diagram of the DDC. The complex input signal (IF) is multiplied by the constant frequency (usually also IF) exponential signal. The resulting signal is also complex and centered at 0. Then we decimate the signal with a factor N. Note that when there are multiple channels (up to 4), the channels are interleaved. For example, with 4 channels, the sequence sent over the USB would be I0 Q0 I1 Q1 I2 Q2 I3 Q3 I0 Q0 I1 Q1, etc. The FPGA's configuration data is stored externally in PROM or some other non-volatile medium, either on or off the board. After applying power, the configuration data is written to the FPGA.

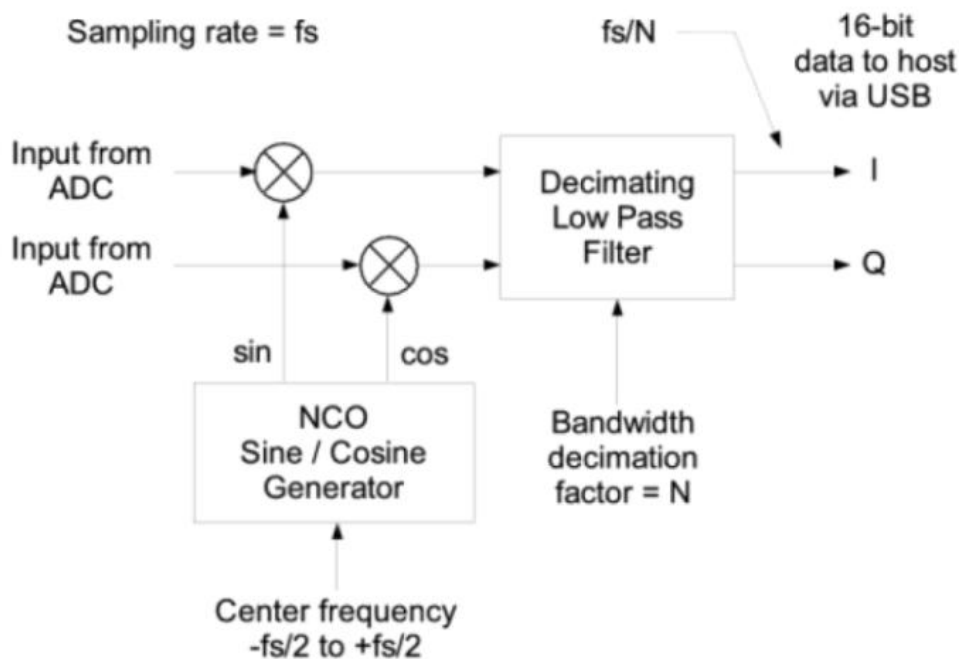


Figure 19: DDC Block

Finally I/Q complex signal enters the computer via the USB. Here starts the software fabric with signal processing.

### 42.2.4 ADC converter

In SDR system, the acquiring data via antenna has to be digitalized immediately in the receiver chain. The B100 contains two 12 bit analog digital converters with sampling rate 64 MS/s. B100 ADC's full range is 2V peak-to-peak with the input 50 ohms impedance. ADC performs sampling and quantization of incoming signal at a certain sampling rate.

### 42.3 Low Noise Amplifier LNA

In wireless communications system, low noise amplifier (LNA) plays a significant role as the critical interface between the antenna and the electronic circuits. An LNA can be considered as front-end of the receiver channel. The noise of the total receive side is reduced by using an LNA which capture and amplify a very weak signal received by antenna in addition to associated random noise which the antenna presents to it. The main parameter of LNA is noise figure (NF) that defines the degradation of the signal-to-noise ratio (SNR) due to effect of atmosphere, thermal and other sources

Low noise amplifier has been developed in the Institute IAP with typical noise figure values 0.7 dB und gain 12 dB. The figure 7 shows a schematic of an LNA using monolithic amplifier „PGA-103+“ which is characterized through high dynamic range over a broad frequency range and with low noise figure [1]. In addition, the PGA-103+ has good input and output return loss over a broad frequency range without the need for external matching components and has demonstrated excellent reliability.

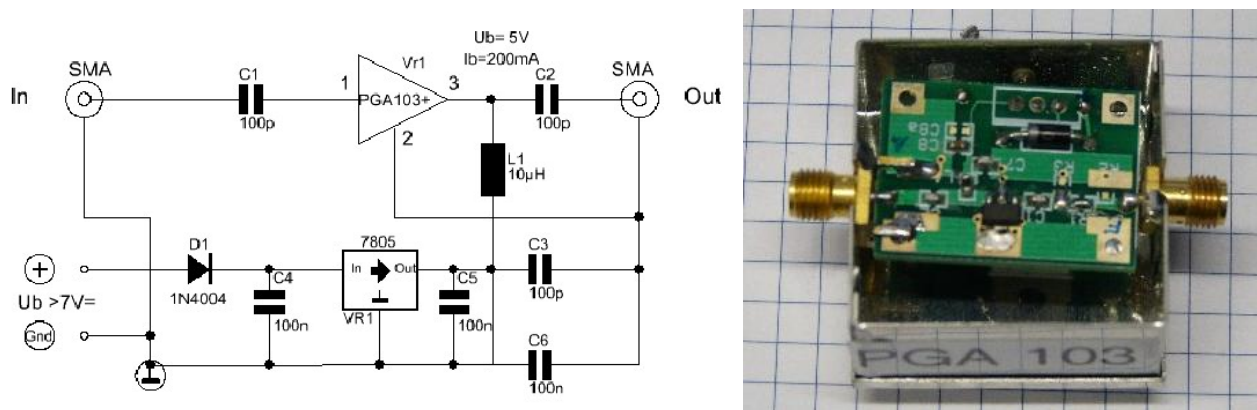


Figure 20: Schematic and platine of LNA

Furthermore, an LNA has been tested using 8620C Sweep Oscillator and the results are to see on Spectrum Analyzer (Anritsu MS 710E) as depicted in a figure 8

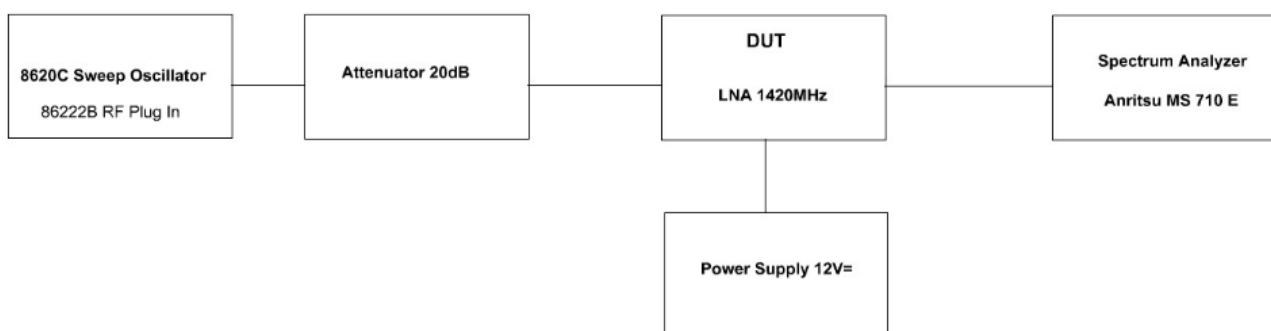


Figure 21: Test of LNA

The output signal of our test bed is to show in figure 9

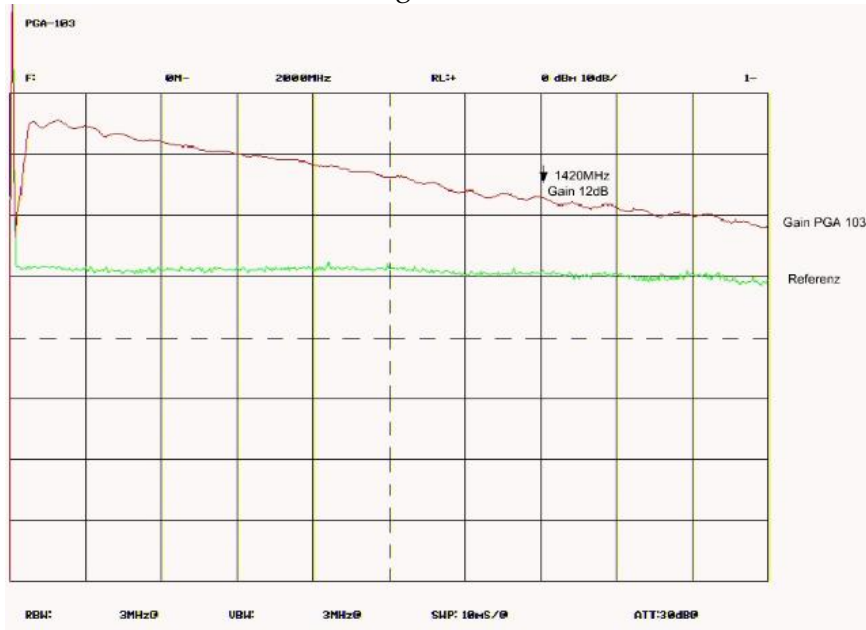


Figure 22: Output signal of LNA

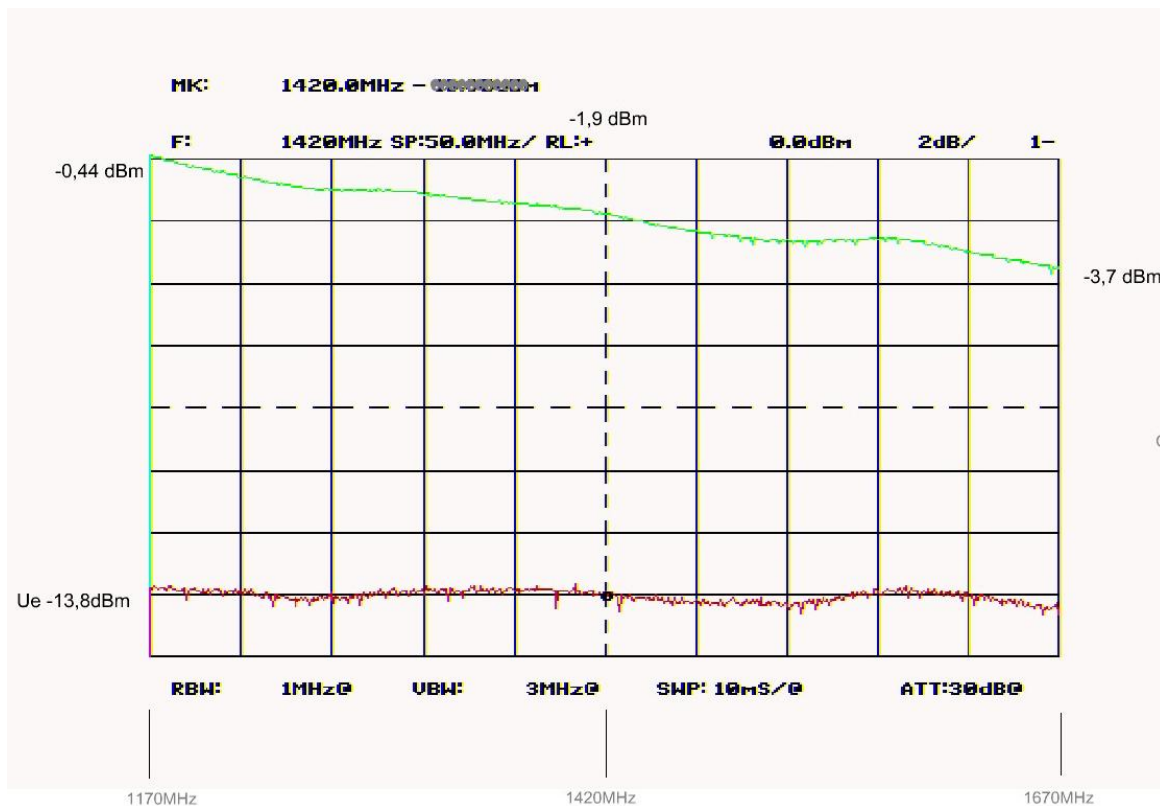
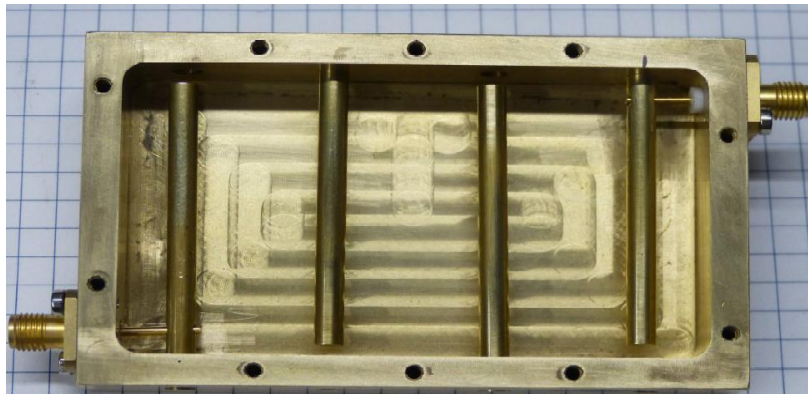


Figure 23 Output @ 2db

## 42.4 Hydrogen line filter

The frequency band to the observation of the hydrogen line which is worldwide exclusively at the radio astronomy's disposal suffices from 1400 to 1435 MHz. On the upper and lower side of this narrow frequency range strong transmitters work, such as L-band radar, mobile telephones etc.. The antennas and preamplifiers don't have the selectivity to attenuate these strong signals. This was the reason for the development of this filter. Only the frequency range around 1420 MHz passes the filter. All other frequencies become effectively attenuated. This filter is a must to prevent interferences in an H-Line receiver.

The installation of the filter should if possible be at the receiver systems input. The insertion loss



worsens however the complete noise figure of the radio astronomical receiver. The filter behind the

**Figure 116**

preamplifier therefore is as recommended in the figure 8 shown commitments. Only if strong, disturbing transmitters lead to doubtful results, the filter should be used in front of the preamplifier. Please take care furthermore that no mechanical loads on the filter and his SMA connectors work. The filter must be installed in normal atmospheric humidity at a dry place, because the filter is not water protected. The preferred mounting place is in a temperature-stabilized case direct with the preamplifier at the feed of the antenna.

The following figure shows the frequency response of hydrogen filter

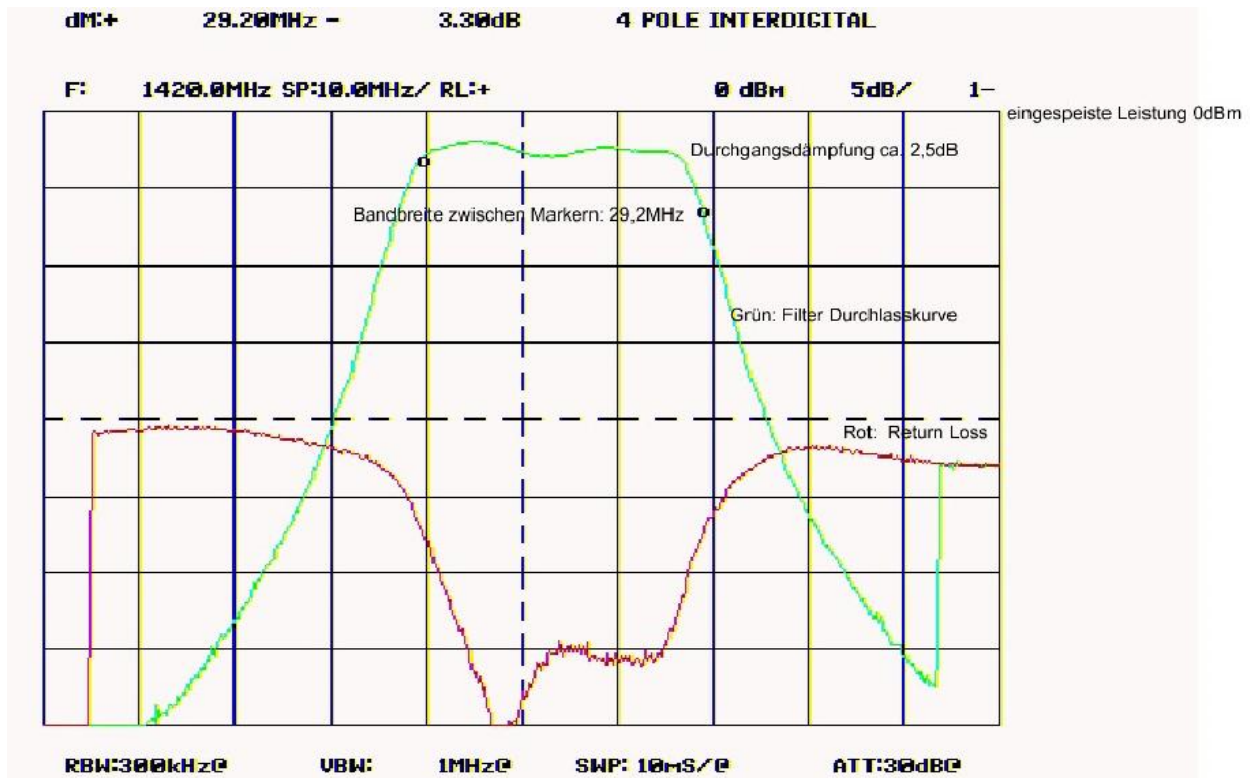


Figure 25 frequency response

## 42.5 Preamplifier:

The IF amplifier serves as adjustment the output of analog hardware with digital hardware so that adc converter can be able to work with high resolution. The next figures display the frequency response and hardware parts

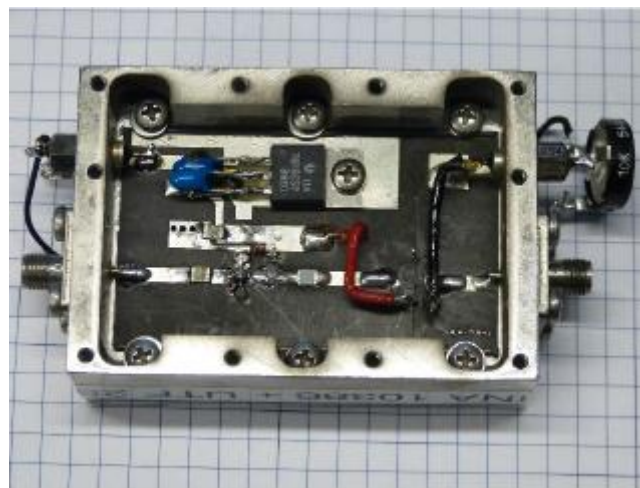


Figure 26 IF amplifier

The bandwidth of IF is 10- 1800 MHz.

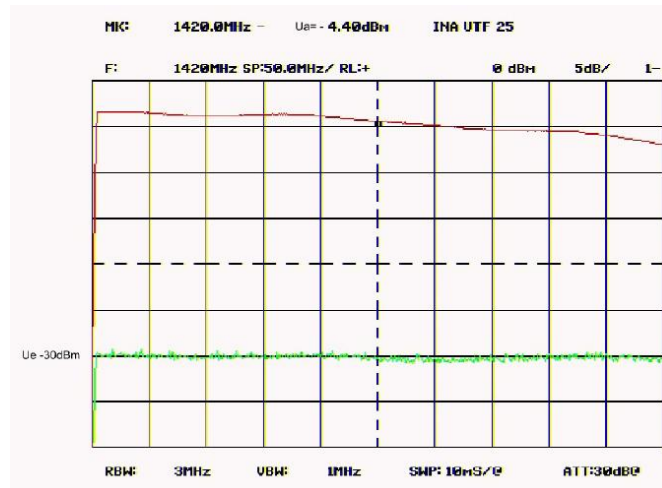


Figure 27 frequency response of IF amp

The feed horn is a corrugated aperture-controlled horn in which the phase variation over the aperture is small. By referring the design graph in [4, page 339], the directivity was calculated to be about 6 dB.

## 42.6 Antenna and Feed horn

Two parabolic mesh-surface reflector antennas were used in this project. The first antenna was thought for fixed receiver system without tracing the sun position having the diameter of 1.1 meters. Following is the parabola arc of the reflector. The F/D ratio was calculated to be about 0.5.



## 43 Software

### 43.1 Gnu radio

Radio is a free & open-source software development toolkit developed by Eric Blossom that is designed to couple PC host with hardware equipment (SDR platform) such as USRP, allowing for building SDR systems. GNU radio operates as stand-alone software package and provides signal processing blocks to implement software radios [3]. It can be used with readily-available low-cost external RF hardware to create software-defined radios, or without hardware in a simulation-like environment. Optimal operating system for building GNU Radio is Linux, but it can also be built on MS Windows using one of Linux-like environments such as Cygwin or MinGW/MSYS.

Most of GNU Radio's applications are written in Python as communicator function between functional blocks, whereas every block is programmed in C++ for implementing signal processing blocks. Python commands are used to control all of platform for software software-defined parameters, such as transmit power, gain, frequency, antenna selection, etc., some of which can be modified while the application is being executed. That means developer can implement real time radio systems in this development environment.

GNU Radio has been structured on two main levels: signal processing blocks and flow graphs. Blocks are designed to have a certain number of input and output ports, consisting of small Signal processing components. When the blocks are appropriately connected, a flow graph is made.

GNU Radio it is very straightforward to modulate and simulate SDR systems. It has a same principle as Matlab/Simulink and can be categorized as sinks, sources, filters and other functional blocks.

- Sources blocks consist of outputs have no inputs and are used as the first element in building the flow graph.
- Sinks consist of inputs and have no outputs and are typically the last element in building the flow graph.
- Filters are all the in between blocks and consist of both inputs and outputs.
- Flow-graph: the application is based on a flow-graph. Every flow-graph consists of intermediate blocks along with source and sink blocks.
- Scheduler: It is created for each active block, which is based on steady stream of data flow between the blocks. It is responsible for transferring data through the flow-graph- it monitors each block for sufficient data at I/p and O/p buffers so as to trigger processing function for those blocks.

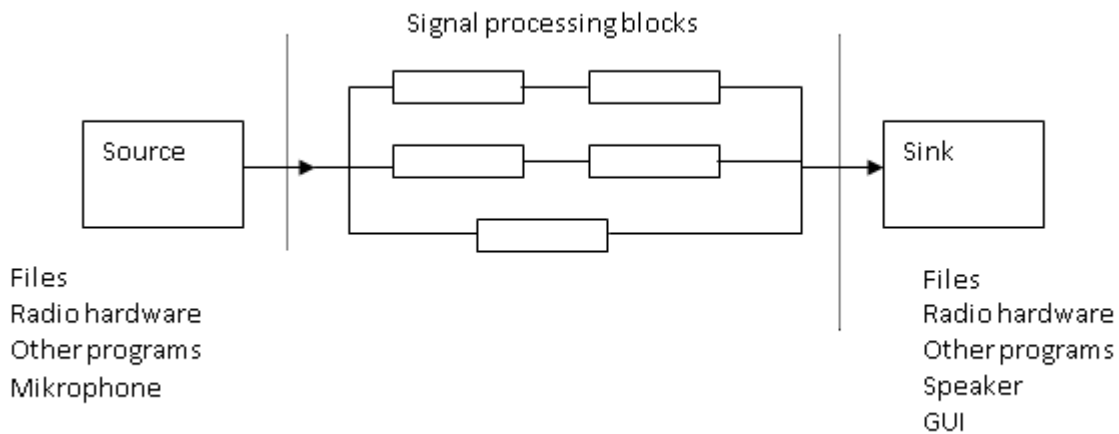


**Figure 28 functionality of gnuradio**

Various blocks such as different modulation/demodulation, filter, signal indicators, signal generator and widgets, .etc. are written in C++ and already integrated within GNU Radio, while it is also possible to write and add new blocks. Graphical interfaces are such as FFT sink and oscilloscope supported in GNU Radio.

Two kinds of Flow graphs are available in GNU Radio either as hierarchical blocks or as top blocks. Top blocks are top level flow graphs that contain all other flow graphs and have no input/output (IO) ports.

Hierarchical blocks, on the other hand, contain a certain number of IO ports (used to connect to other blocks). All of the basic signal processing blocks are connected within hierarchical blocks and can that way be used as one block. Communication between blocks is achieved using data streams considering to be connected together using same data type. It means that data types between output of one block and input of the next have to be adequately set. GNU Radio supports different data types such as byte, short, integer, float and complex (8 float byte).

## 43.2 Gnu Radio Architecture

The basic architecture of Gnuradio shows in following figure 18 containing a complex flow-graph that consists of blocks modules and low-level algorithms. Every Block or algorithm is implemented in C++ and offers various signal processing functions (Channel Coding, Filters, Modulations technique etc). These functions can be converted (generated) automatically into python modules using python "wrapper"(Simplified Wrapper) and it serves as the interface compiler allowing the integration between C++ and Python language. As mentioned, the signal processing blocks are written in C++ so that script language python connets the blocks together to form the flow graph [1]. The generated blocks are used to buid a flow-graph model with the help of python. The python framework is responsible for communication of data through module buffers and creates a simple scheduler that helps to run blocks in a sequential order for signal iteration [1]

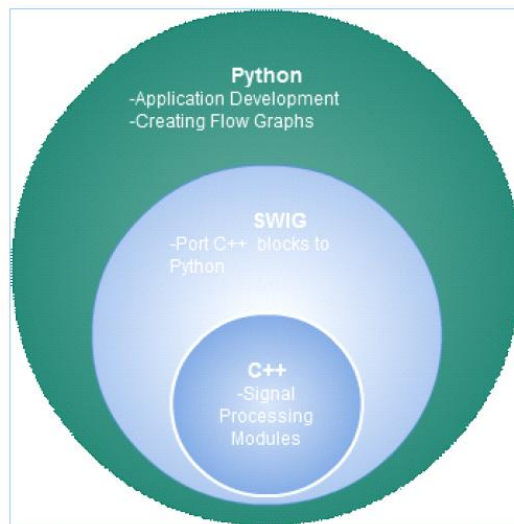


Figure 121 Software architecture

### 43.3 Gnu Radio Companion (GRC)

GNU Radio Companion is a graphical user interface for GNU Radio that allows building flow graphs by simply connecting visually-presented blocks. GRC is highly intuitive interface suitable for GNU Radio beginners that resembles Matlab Simulink's one, so anyone with some background in working with Simulink shouldn't have problems learning GRC as well.

From the Ubuntu terminal, GRC is started with command:

*gnuradio-companion* .

The dial\_tone example can be considered as “Hello world” of GNU Radio can be done using GRC as explained in Figure xx

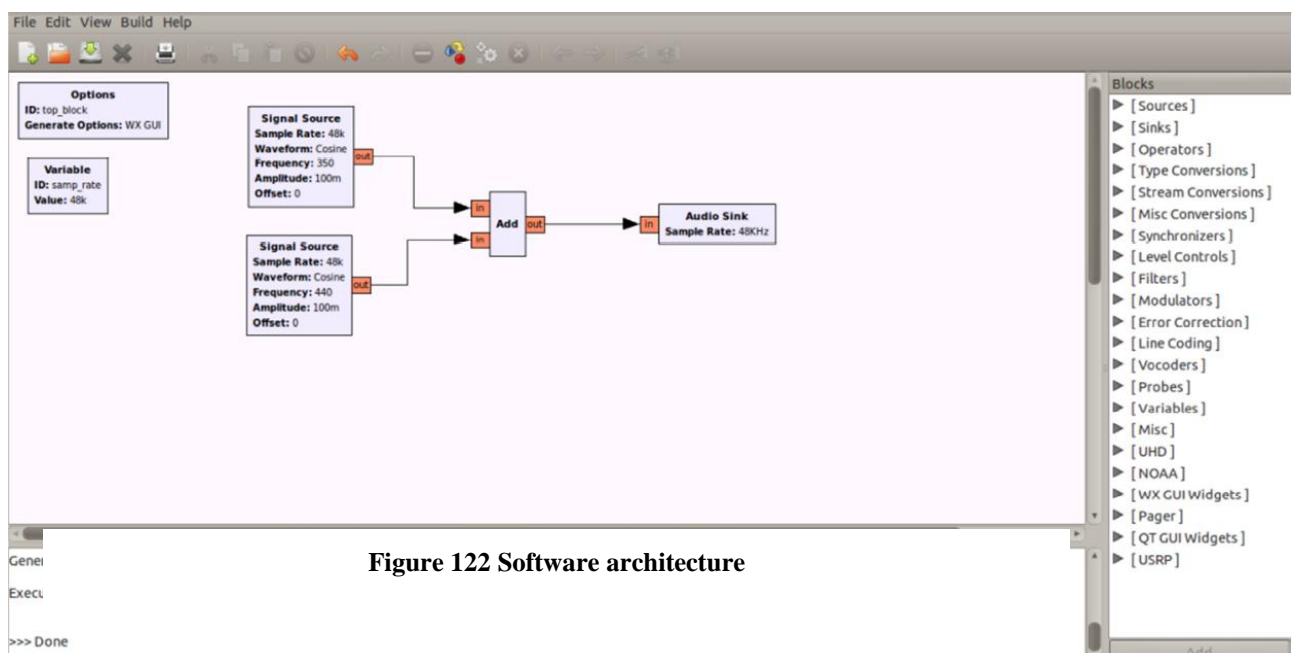


Figure 122 Software architecture

Figure 123: Implementation of dial\_tone example within Gnu Radio Companion

*Dial\_tone* example generates two sine waves of the same amplitude at frequencies 350 Hz and 440 Hz, which corresponds to the sound of US dial tone, and outputs them to the sound card.

One can translate this graph into the correspondent python code by pressing on the button “generate the flow graph ”. The  generated code will be saved in the Linux Ubuntu under home/bin and then can be executed through the button „execute the flow graph ”.

The created code source of the *dial\_tone* example is given and explained below.

```
#!/usr/bin/env python
from gnuradio import gr
from gnuradio import audio

def build_graph():
    sampling_freq = 48000
    ampl = 0.1
    fg = gr.flow_graph()
    src0 = gr.sig_source_f(sampling_freq, gr.GR_SIN_WAVE, 350, ampl)
    src1 = gr.sig_source_f(sampling_freq, gr.GR_SIN_WAVE, 440, ampl)
    dst = audio.sink(sampling_freq)
    fg.connect((src0, 0), (dst, 0))
    fg.connect((src1, 0), (dst, 1))
    return fg

if __name__ == '__main__':
    fg = build_graph()
    fg.start()
    raw_input('Press Enter to quit: ')
    fg.stop()
```

The first line, `#!/usr/bin/env python`, points python to the location of python executable, and is a line that has to be added to every program that we want to run directly from terminal (as an executable).

Then, we define which modules to import – in this case, *gr*, which is always imported, and *audio*, which allows us to use audio sink.

After that, sampling frequency is set according to sound card’s specifications (48 kHz is the sampling frequency of majority of modern sound-cards), and the amplitude to 0.1.

*gr.sig\_source\_f* is used to create sine waves at the frequencies of 350 Hz and 440 Hz, where *\_f* extension, as previously explained, indicates that the produced data is of type float.

Then, the audio sink that writes received data to the sound card is created. It is worth mentioning that audio sink only accepts float data as an input.

*fg.connect* connects the flow graph’s blocks – the first sine wave is connected to the port 0 of the audio sink, while the second sine wave is connected to port 1.

## 43.4 Basic Blocks

### 43.4.1 RTL SDR source

The purpose of the Master thesis is converting a big part of the Hardware from receiver for registration of the HL 21 cm spectrum into software using GnuRadio platform. So many algorithms for signal processing and hardware functionality (filter, modulation etc...) can be made in GRC (*gnuradio-companion*). The RTL SDR Usb(2382u) conduces as Front-End to detect HI Signal and convert it to digital signal. GnuRadio recognizes the incoming data from RTL SDR using driver implemented by Osmsann [1] in GRC in order to receive IQ data so one inputs the desired parameters as center frequency, gain, decimation etc.. through the graphic user interface driver to tune the desired frequency. The RTL driver in GRC is given and explained as follows in Figure 18.

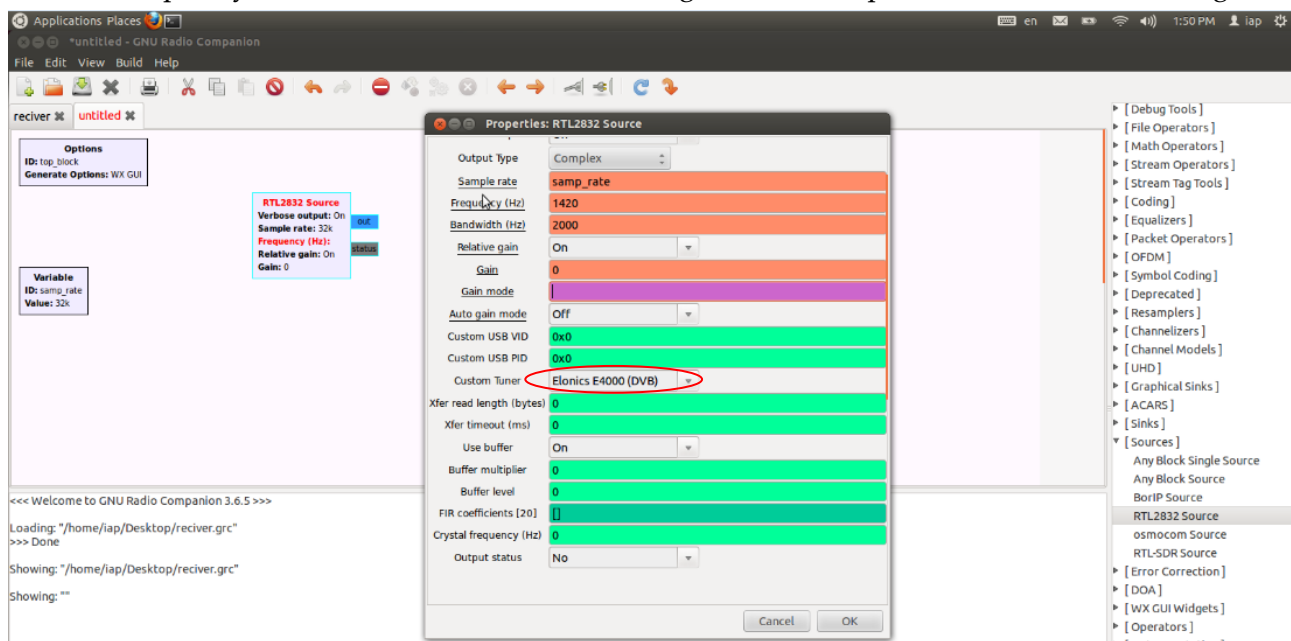


Figure 32 RTL SDR driver in GnuRadio

In the properties window of RTL2832 (our source hardware) one can select too tuner which RTL Usb contains (Elonics E4000 DVB).

### 43.4.2 WX GUI blocks

The WX GUI functions is very powerful tools to display and analyze a signal is to display in time domain and frequency domain. This block made us easy to measure and analyzes a hydrogen line 1 graphically. The python framework provides such wonderful tools in Gunradio to construct GUI tools. We used the following WX GUI blocks:

#### - FFT sink block

The function of FFT is used just as the signal sink ,based on fast Fourier transformation (FFT). It is defined in the module in python interface "wxgui.fftsink.py". The function "make\_fft\_sink\_c()"helps as the interface to create an instance of the FFT sink.

#### - Scope sink block

WX GUI scope is very useful tools in Gnu Radio to display the waveforms in the time domain. It seems as software oscillograph.

### 43.5 Software design

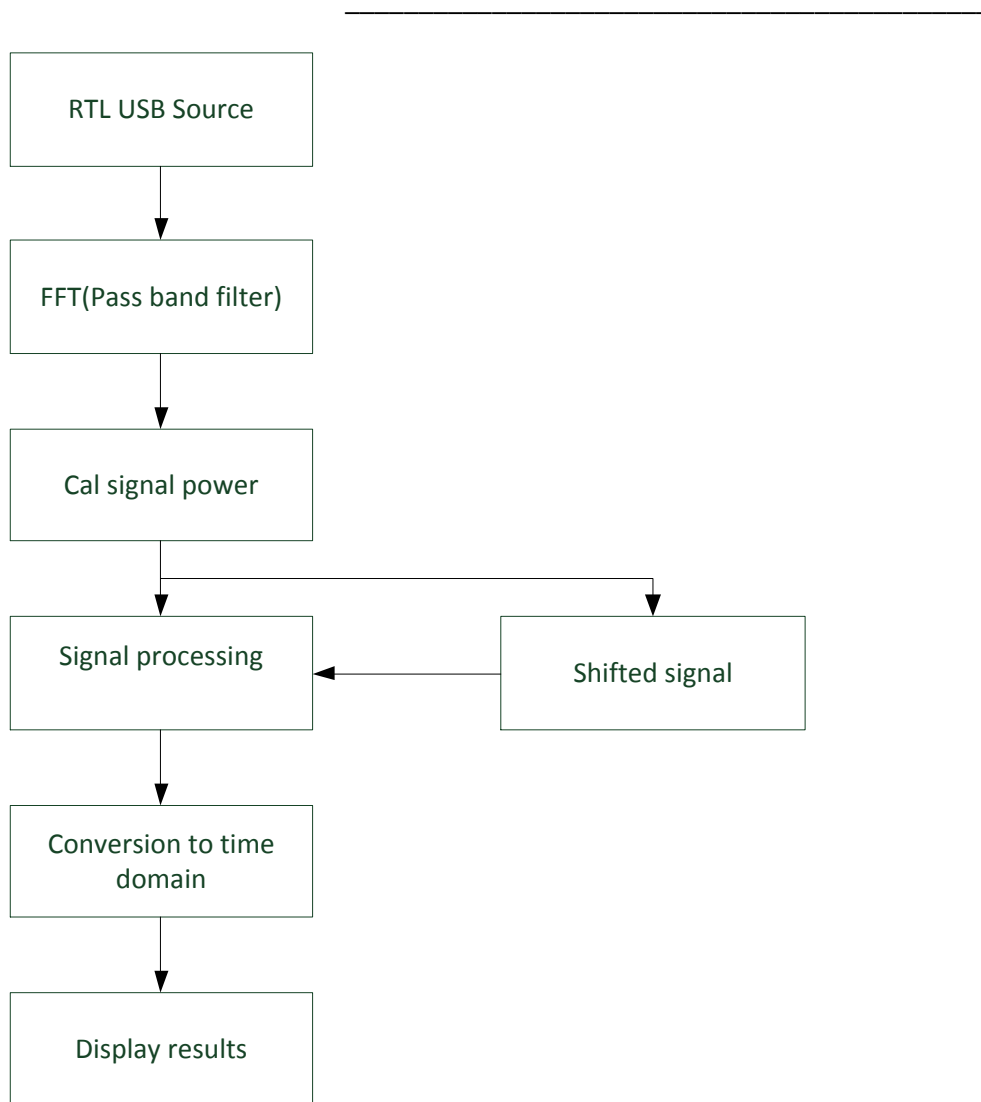
The HI 21 cm signals with other signals were obtained directly from RTL SDR Usb. The incoming digital data was filtered with FFT band-pass filter which filter the signal in frequency domain to get better removing frequently noise, whereas the parameter of this filter can be connected with GUI and then parameters of filter (center frequency, bandwidth, gain etc..) can be entered through it. Hereafter the filtered signal has been converted back to time domain then the power spectrum calculated and integrated to get average power. The averaging process ensures removing the random noise from the signal as much as possible.

To make the signal detectable within desired range and probable noise a signal processing technique is performed. The main idea of this technique is comparing the spectrum at Hydrogen line with calculated spectrum created from shift the Hydrogen line signal a few Mhz. The exact spectrum is calculated and stored for a certain period of time. The help signal comes into existence using changing the local oscillator frequency of the mixer (IF stage) to a few MHz away from Hydrogen line and then spectrum is calculated at that frequency. The Spectrum at the Hydrogen line is named Signal and spectrum at some offset frequency from Hydrogen line is named Help.

### 43.6 Software Implementation

The RF signal coming from Satellite, amplified through LNA, pass-filtered using interdigital 4 pole filter for passing signal 21 cm with bandwidth 20 Mhz finally through PGA circuit pre-amplified, is fed into RTL SDR which has E4000 chip as tuner and a RTL 2382 u chip that contains an IF stage for converting RF into IF and then baseband with a maximum bandwidth of 4 MHz This baseband signal is available through usb2.0 interface to GnuRadio running on a PC for further processing. The software for filters and FFT analyze are implemented in GnuRadio to calculate the power spectrum. In order to have two slightly different frequency signals (Signal and Reference), frequency switching is used. Instead, the whole band consisting of the signal as well as the reference was obtained for processing. In our case this was as follows Signal at 1420.4 MHz with 2.5 MHz bandwidth (1419.15 – 1421.65) MHz.

Reference at 1417.9 MHz with 2.5 MHz bandwidth (1416.65 – 1419.15) MHz. Total bandwidth comprising of Signal and Reference thus became 5 MHz. The signal and reference signals are then filtered through separate filters, their FFT is calculated, averaged and finally the above mathematical equation is applied to detect the required signal.



#### 43.6.1 RTL Source

The HL signal was acquired using determining the signal's parameters. The software diagram begins always with signal source (hardware, software). The important parameters are listed as follows.

Output type: IQ (In-phase and Quadrature) is used in signal kind of the typical kind signal in wireless communication

Frequency: Frequency: This is the frequency which will be down-converted to 0 Hz (baseband). It was set to the center of Reference frequency band i.e. 1417.9 MHz.

Sample rate:

Bandwidth: 4 MHz

Gain: 10 dB

Customer Tuner : Elonics E 4000 (DVB) is built on RTL SDR



### 43.6.2 FFT filter

As explained the goal of using FFT filter is to remove noise in frequency domain. The suitable pass band filter was implemented in FFT block.

## 43.7 Test and Measurements

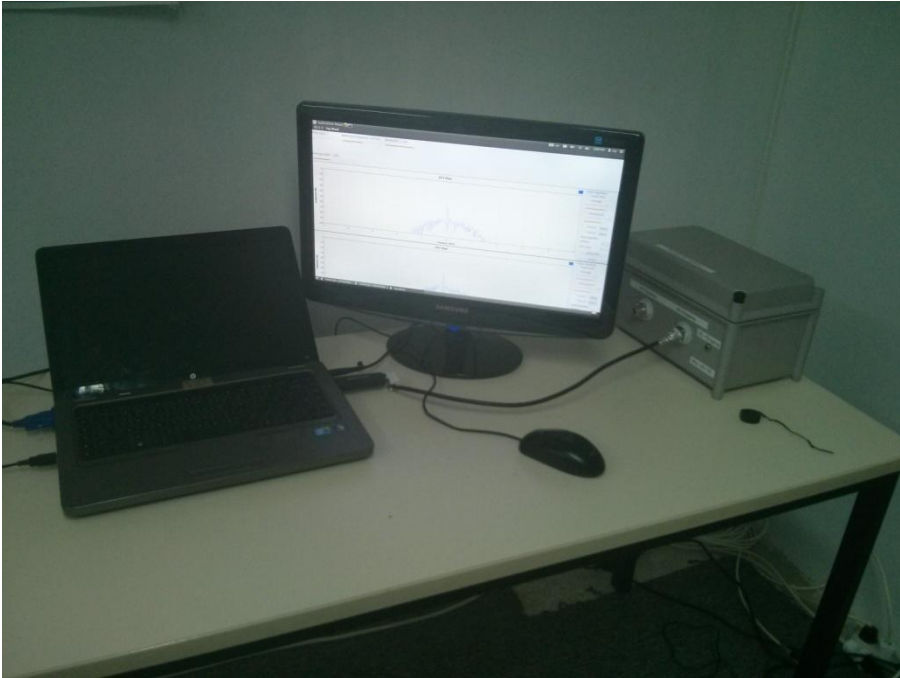
The setup of total system was realized on the high mountains for testing the whole system for HL1 detection. This testing in real environment would be validating that all the components are placed in the right order. (antenna, LNA, power supply etc).

Many experiments were carried out for the first test in different directions and then power values of the signal were measured. As next step the antenna was orient in the direction of the sun and power spectrum has been observed and that noted whereby the power values was shifted compared to spectrum taken form many astronomical observatory in Heppenheim Germany [1] and in offline environment (simulation) therefore power spectrum has been recorded regarding to changing of preamplifier gain (hardware) and filters parameters (software). The results were relative acceptable as expected. Then the antenna has scanned the sky for many angle values inclusive in the direction of hydrogen line source. Figures 3-10, 3-12, 3-13 show the setup and the difference in the spectrum of (sig-ref/ref) without and with the antenna pointed towards the Hydrogen line source respectively. It can be seen from the figures 3-12 and 3-13 that the receiver worked properly as the signal is differentiable from noise.

Comparing the spectrum taken with the old configuration of SALSA ([11], figure 3-11) pointed toward the same direction of the galactic plane (Galactic longitude  $l=120$  degrees, Galactic latitude  $b = 0$ ) and the spectrum (figure 3-13), obtained with the upgraded digital software receiver pointing in the same direction, clearly shows the functionality of the upgraded digital receiver. The difference is spectrum can be explained by the approximate pointing during our experiment, but it certainly looks like a detection! It would also have been useful to observe in a slightly larger or shifted (towards right) band [11].

The observed spectrum range seems far wider than the actual spectrum band needed to observe (within red circle in figure 3-13). This is due to the FFT Scope block of the GnuRadio, where no zooming on a particular section of the spectrum is possible; hence we have to see the whole band which is being translated from analog to digital domain through sampling. To observe only a small

part of spectrum, one could decimate the (SIGNAL-REFERENCE)/REFERENCE signal to a point where the bandwidth is half the decimated sampling rate (Nyquist Theorem). Actually, a small decimation is performed here if we compare figures 3-13 and 3-9 to see the difference.



## 44 Future Work

Parts of the system are planned to be put on a satellite in a further step in the IAP SRWDA-SAT project [9]. The Gnu Radio receiver model will be converted to python code then stored on memory of board computer



**Figure 126** Import Receiver on Mockup model



**Figure 125** Mock up model

## 45 Literature

- [1] K. Rohlfs, Tools of radio astronomy, 2004.
- [2] E. Grayver, Implementing software defined radio, 2013.
- [3] I. Joseph Mitola, Software Radio Architecture: Object Oriented Approaches to Wireless Systems Engineering., John Wiley and Sons, 2000.
- [4] W. Tuttlebee, Software Defined Radio, England, 2002.
- [5] E. Comany, „<https://www.ettus.com/product/details/WBX>“.
- [6] Xilinx, „[http://www.xilinx.com/support/documentation/data\\_sheets/ds529.pdf](http://www.xilinx.com/support/documentation/data_sheets/ds529.pdf)“.
- [7] D. Shen, „The USRP Board,“ p. 7, Augst 2005.
- [9] IAP SRWDA-SAT project, see [www.aecenar.com/research](http://www.aecenar.com/research)

[www.astronomynotes.com](http://www.astronomynotes.com)

[www.aao.gov.au](http://www.aao.gov.au)

## 46 Appendix

### A.1 Software

#### Python code

```
#!/usr/bin/env python
#####
# Gnuradio Python Flow Graph
# Title: Top Block
# Generated: Tue May 6 15:46:55 2014
#####

from gnuradio import blocks
from gnuradio import eng_notation
from gnuradio import fft
from gnuradio import filter
from gnuradio import gr
from gnuradio import window
from gnuradio.eng_option import eng_option
from gnuradio.filter import firdec
from gnuradio.gr import firdec
from gnuradio.wxgui import fftsink2
from gnuradio.wxgui import forms
from grc_gnuradio import wxgui as grc_wxgui
from optparse import OptionParser
import ConfigParser
import baz
import wx

class top_block(grc_wxgui.top_block_gui):

    def __init__(self):
        grc_wxgui.top_block_gui.__init__(self, title="Top Block")
        _icon_path = "/usr/share/icons/hicolor/32x32/apps/gnuradio-
grc.png"
        self.SetIcon(wx.Icon(_icon_path, wx.BITMAP_TYPE_ANY))

        #####
        # Variables
        #####
        self._variable_config_0_config = ConfigParser.ConfigParser()
        self._variable_config_0_config.read("default")
        try: variable_config_0 =
self._variable_config_0_config.getfloat("main", "key")
        except: variable_config_0 = 0
        self.variable_config_0 = variable_config_0
        self.samp_rate = samp_rate = 10000000
        self.low_cutoff = low_cutoff = 0.125
        self.high_cutoff = high_cutoff = 0.375
        self.gui_onoff = gui_onoff = False
        self.gain = gain = 1
        self.fft_size = fft_size = 1024
        self.dec = dec = 10
        self.avg_alpha = avg_alpha = 0.1
        self.Sig_minus_Ref = Sig_minus_Ref = 2500000
        self.Sig_freq = Sig_freq = 1420400000
        self.Ref_freq = Ref_freq = 1417900000
```

```
self.N = N = 1024
self.BW = BW = 2500000

#####
# Blocks
#####
_gain_sizer = wx.BoxSizer(wx.VERTICAL)
self._gain_text_box = forms.text_box(
    parent=self.GetWin(),
    sizer=_gain_sizer,
    value=self.gain,
    callback=self.set_gain,
    label="Filter Gain",
    converter=forms.float_converter(),
    proportion=0,
)
self._gain_slider = forms.slider(
    parent=self.GetWin(),
    sizer=_gain_sizer,
    value=self.gain,
    callback=self.set_gain,
    minimum=1,
    maximum=32,
    num_steps=100,
    style=wx.SL_HORIZONTAL,
    cast=float,
    proportion=1,
)
self.GridAdd(_gain_sizer, 0, 0, 1, 1)
_avg_alpha_sizer = wx.BoxSizer(wx.VERTICAL)
self._avg_alpha_text_box = forms.text_box(
    parent=self.GetWin(),
    sizer=_avg_alpha_sizer,
    value=self.avg_alpha,
    callback=self.set_avg_alpha,
    label="Average Alpha",
    converter=forms.float_converter(),
    proportion=0,
)
self._avg_alpha_slider = forms.slider(
    parent=self.GetWin(),
    sizer=_avg_alpha_sizer,
    value=self.avg_alpha,
    callback=self.set_avg_alpha,
    minimum=0.001,
    maximum=0.25,
    num_steps=100,
    style=wx.SL_HORIZONTAL,
    cast=float,
    proportion=1,
)
self.GridAdd(_avg_alpha_sizer, 3, 0, 1, 3)
_BW_sizer = wx.BoxSizer(wx.VERTICAL)
self._BW_text_box = forms.text_box(
    parent=self.GetWin(),
    sizer=_BW_sizer,
    value=self.BW,
```

```
        callback=self.set_BW,
        label="Bandwidth",
        converter=forms.float_converter(),
        proportion=0,
    )
    self._BW_slider = forms.slider(
        parent=self.GetWin(),
        sizer=_BW_sizer,
        value=self.BW,
        callback=self.set_BW,
        minimum=500000,
        maximum=2500000,
        num_steps=100,
        style=wx.SL_HORIZONTAL,
        cast=float,
        proportion=1,
    )
    self.GridAdd(_BW_sizer, 0, 4, 1, 1)
    self.wxgui_fftsink2_0_0_0 = fftsink2.fft_sink_c(
        self.GetWin(),
        baseband_freq=0,
        y_per_div=10,
        y_divs=10,
        ref_level=0,
        ref_scale=2.0,
        sample_rate=samp_rate,
        fft_size=1024,
        fft_rate=15,
        average=False,
        avg_alpha=None,
        title="FFT Plot",
        peak_hold=False,
    )
    self.Add(self.wxgui_fftsink2_0_0_0.win)
    self.wxgui_fftsink2_0_0 = fftsink2.fft_sink_c(
        self.GetWin(),
        baseband_freq=0,
        y_per_div=10,
        y_divs=10,
        ref_level=0,
        ref_scale=2.0,
        sample_rate=samp_rate,
        fft_size=1024,
        fft_rate=15,
        average=False,
        avg_alpha=None,
        title="FFT Plot",
        peak_hold=False,
    )
    self.Add(self.wxgui_fftsink2_0_0.win)
    self.wxgui_fftsink2_0 = fftsink2.fft_sink_c(
        self.GetWin(),
        baseband_freq=0,
        y_per_div=10,
        y_divs=10,
        ref_level=0,
        ref_scale=2.0,
        sample_rate=samp_rate,
        fft_size=1024,
```

```

        fft_rate=15,
        average=False,
        avg_alpha=None,
        title="FFT Plot",
        peak_hold=False,
    )
    self.Add(self.wxgui_fftsink2_0.win)
    self.single_pole_iir_filter_xx_0_0 =
filter.single_pole_iir_filter_ff(0.1, 1024)
    self.single_pole_iir_filter_xx_0 =
filter.single_pole_iir_filter_ff(0.1, 1024)
    self.rtl2832_source_0 = baz.rtl_source_c(defer_creation=True,
output_size=gr.sizeof_gr_complex)
    self.rtl2832_source_0.set_verbose(True)
    self.rtl2832_source_0.set_vid(0x0)
    self.rtl2832_source_0.set_pid(0x0)
    self.rtl2832_source_0.set_tuner_name("e4k")
    self.rtl2832_source_0.set_default_timeout(0)
    self.rtl2832_source_0.set_use_buffer(True)
    self.rtl2832_source_0.set_fir_coefficients([])

    self.rtl2832_source_0.set_read_length(0)

    if self.rtl2832_source_0.create() == False: raise
Exception("Failed to create RTL2832 Source: rtl2832_source_0")

    self.rtl2832_source_0.set_sample_rate(samp_rate)

    self.rtl2832_source_0.set_frequency(1420000000)

    self.rtl2832_source_0.set_auto_gain_mode(False)
    self.rtl2832_source_0.set_relative_gain(True)
    self.rtl2832_source_0.set_gain(27)

    self._gui_onoff_check_box = forms.check_box(
        parent=self.GetWin(),
        value=self.gui_onoff,
        callback=self.set_gui_onoff,
        label="check to parameter",
        true=True,
        false=False,
    )
    self.Add(self._gui_onoff_check_box)
    self.freq_xlating_fir_filter_xxx_0 =
filter.freq_xlating_fir_filter_ccc(1,
(gr.firdes.complex_band_pass(gain,samp_rate,low_cutoff,high_cutoff,BW, 0
,beta=6.76)), -2500000, samp_rate)
    self.fft_vxx_0_0_0_0 = fft.fft_vcc(1024, True,
(window.hamming(N)), False, 1)
    self.fft_vxx_0_0_0 = fft.fft_vcc(1024, True,
(window.blackmanharris(1024)), True, 1)

```

```

        self.fft_vxx_0_0 = fft.fft_vfc(1024, True,
(window.blackmanharris(1024)), 1)
        self.fft_filter_xxx_0_0_0 = filter.fft_filter_ccc(1,
(gr.firdes.complex_band_pass(gain,samp_rate,low_cutoff,high_cutoff,BW, 0
,beta=6.76)), 1)
        self.fft_filter_xxx_0_0 = filter.fft_filter_ccc(1,
(gr.firdes.complex_band_pass(gain,samp_rate,low_cutoff,high_cutoff,BW, 0
,beta=6.76)), 1)
        self.fft_filter_xxx_0 = filter.fft_filter_ccc(1,
(gr.firdes.complex_band_pass(gain,samp_rate,low_cutoff,high_cutoff,BW, 0
,beta=6.76)), 1)
        self.blocks_vector_to_stream_0 =
blocks.vector_to_stream(gr.sizeof_gr_complex*1, 1024)
        self.blocks_stream_to_vector_0_0 =
blocks.stream_to_vector(gr.sizeof_gr_complex*1, 1024)
        self.blocks_stream_to_vector_0 =
blocks.stream_to_vector(gr.sizeof_gr_complex*1, 1024)
        self.blocks_keep_one_in_n_0 =
blocks.keep_one_in_n(gr.sizeof_gr_complex*1, 5)
        self.blocks_divide_xx_0 = blocks.divide_ff(1024)
        self.blocks_conjugate_cc_0 = blocks.conjugate_cc()
        self.blocks_complex_to_mag_squared_1_0 =
blocks.complex_to_mag_squared(1024)
        self.blocks_complex_to_mag_squared_1 =
blocks.complex_to_mag_squared(1024)
        self.blocks_add_const_vxx_0 = blocks.add_const_vff((-1]*N))
        _Ref_freq_sizer = wx.BoxSizer(wx.VERTICAL)
        self._Ref_freq_text_box = forms.text_box(
            parent=self.GetWin(),
            sizer=_Ref_freq_sizer,
            value=self.Ref_freq,
            callback=self.set_Ref_freq,
            label="Reference frequency",
            converter=forms.float_converter(),
            proportion=0,
        )
        self._Ref_freq_slider = forms.slider(
            parent=self.GetWin(),
            sizer=_Ref_freq_sizer,
            value=self.Ref_freq,
            callback=self.set_Ref_freq,
            minimum=1417400000,
            maximum=1418400000,
            num_steps=100,
            style=wx.SL_HORIZONTAL,
            cast=float,
            proportion=1,
        )
        self.GridAdd(_Ref_freq_sizer, 0, 1, 1, 3)

#####
# Connections
#####
self.connect((self.fft_vxx_0_0_0_0, 0),
(self.blocks_complex_to_mag_squared_1, 0))
self.connect((self.blocks_add_const_vxx_0, 0),
(self.fft_vxx_0_0, 0))
self.connect((self.blocks_divide_xx_0, 0),
(self.blocks_add_const_vxx_0, 0))

```

---

```

        self.connect((self.single_pole_iir_filter_xx_0, 0),
(self.blocks_divide_xx_0, 1))
        self.connect((self.blocks_keep_one_in_n_0, 0),
(self.wxgui_fftsink2_0, 0))
        self.connect((self.fft_vxx_0_0, 0),
(self.blocks_vector_to_stream_0, 0))
        self.connect((self.blocks_complex_to_mag_squared_1, 0),
(self.single_pole_iir_filter_xx_0, 0))
        self.connect((self.blocks_conjugate_cc_0, 0),
(self.freq_xlating_fir_filter_xxx_0, 0))
        self.connect((self.blocks_vector_to_stream_0, 0),
(self.blocks_conjugate_cc_0, 0))
        self.connect((self.single_pole_iir_filter_xx_0_0, 0),
(self.blocks_divide_xx_0, 0))
        self.connect((self.blocks_complex_to_mag_squared_1_0, 0),
(self.single_pole_iir_filter_xx_0_0, 0))
        self.connect((self.fft_vxx_0_0_0, 0),
(self.blocks_complex_to_mag_squared_1_0, 0))
        self.connect((self.fft_filter_xxx_0, 0),
(self.blocks_keep_one_in_n_0, 0))
        self.connect((self.freq_xlating_fir_filter_xxx_0, 0),
(self.fft_filter_xxx_0, 0))
        self.connect((self.rtl2832_source_0, 0),
(self.fft_filter_xxx_0_0, 0))
        self.connect((self.fft_filter_xxx_0_0, 0),
(self.wxgui_fftsink2_0_0, 0))
        self.connect((self.rtl2832_source_0, 0),
(self.fft_filter_xxx_0_0_0, 0))
        self.connect((self.fft_filter_xxx_0_0_0, 0),
(self.wxgui_fftsink2_0_0_0, 0))
        self.connect((self.fft_filter_xxx_0_0_0, 0),
(self.blocks_stream_to_vector_0, 0))
        self.connect((self.blocks_stream_to_vector_0, 0),
(self.fft_vxx_0_0_0_0, 0))
        self.connect((self.fft_filter_xxx_0_0, 0),
(self.blocks_stream_to_vector_0_0, 0))
        self.connect((self.blocks_stream_to_vector_0_0, 0),
(self.fft_vxx_0_0_0, 0))

def get_variable_config_0(self):
    return self.variable_config_0

def set_variable_config_0(self, variable_config_0):
    self.variable_config_0 = variable_config_0

def get_samp_rate(self):
    return self.samp_rate

def set_samp_rate(self, samp_rate):
    self.samp_rate = samp_rate

self.freq_xlating_fir_filter_xxx_0.set_taps((gr.firdes.complex_band_p
ass(self.gain,self.samp_rate,self.low_cutoff,self.high_cutoff,self.BW, 0
,beta=6.76)))

```

```
self.fft_filter_xxx_0.set_taps((gr.firdes.complex_band_pass(self.gain
,self.samp_rate,self.low_cutoff,self.high_cutoff,self.BW, 0 ,beta=6.76)))

self.fft_filter_xxx_0_0_0.set_taps((gr.firdes.complex_band_pass(self.
gain,self.samp_rate,self.low_cutoff,self.high_cutoff,self.BW, 0
,beta=6.76)))
self.rtl2832_source_0.set_sample_rate(self.samp_rate)

self.fft_filter_xxx_0_0.set_taps((gr.firdes.complex_band_pass(self.ga
in,self.samp_rate,self.low_cutoff,self.high_cutoff,self.BW, 0 ,beta=6.76)))
self.wxgui_fftsink2_0.set_sample_rate(self.samp_rate)
self.wxgui_fftsink2_0_0_0.set_sample_rate(self.samp_rate)
self.wxgui_fftsink2_0_0.set_sample_rate(self.samp_rate)

def get_low_cutoff(self):
    return self.low_cutoff

def set_low_cutoff(self, low_cutoff):
    self.low_cutoff = low_cutoff

self.freq_xlating_fir_filter_xxx_0.set_taps((gr.firdes.complex_band_p
ass(self.gain,self.samp_rate,self.low_cutoff,self.high_cutoff,self.BW, 0
,beta=6.76)))

self.fft_filter_xxx_0.set_taps((gr.firdes.complex_band_pass(self.gain
,self.samp_rate,self.low_cutoff,self.high_cutoff,self.BW, 0 ,beta=6.76)))

self.fft_filter_xxx_0_0_0.set_taps((gr.firdes.complex_band_pass(self.
gain,self.samp_rate,self.low_cutoff,self.high_cutoff,self.BW, 0
,beta=6.76)))

self.fft_filter_xxx_0_0.set_taps((gr.firdes.complex_band_pass(self.ga
in,self.samp_rate,self.low_cutoff,self.high_cutoff,self.BW, 0 ,beta=6.76)))

def get_high_cutoff(self):
    return self.high_cutoff

def set_high_cutoff(self, high_cutoff):
    self.high_cutoff = high_cutoff

self.freq_xlating_fir_filter_xxx_0.set_taps((gr.firdes.complex_band_p
ass(self.gain,self.samp_rate,self.low_cutoff,self.high_cutoff,self.BW, 0
,beta=6.76)))

self.fft_filter_xxx_0.set_taps((gr.firdes.complex_band_pass(self.gain
,self.samp_rate,self.low_cutoff,self.high_cutoff,self.BW, 0 ,beta=6.76)))

self.fft_filter_xxx_0_0_0.set_taps((gr.firdes.complex_band_pass(self.
gain,self.samp_rate,self.low_cutoff,self.high_cutoff,self.BW, 0
,beta=6.76)))

self.fft_filter_xxx_0_0.set_taps((gr.firdes.complex_band_pass(self.ga
in,self.samp_rate,self.low_cutoff,self.high_cutoff,self.BW, 0 ,beta=6.76)))

def get_gui_onoff(self):
    return self.gui_onoff

def set_gui_onoff(self, gui_onoff):
```

```
self.gui_onoff = gui_onoff
self._gui_onoff_check_box.set_value(self.gui_onoff)

def get_gain(self):
    return self.gain

def set_gain(self, gain):
    self.gain = gain
    self._gain_slider.set_value(self.gain)
    self._gain_text_box.set_value(self.gain)

    self.freq_xlating_fir_filter_xxx_0.set_taps((gr.firdes.complex_band_p
ass(self.gain,self.samp_rate,self.low_cutoff,self.high_cutoff,self.BW, 0
,beta=6.76)))

    self.fft_filter_xxx_0.set_taps((gr.firdes.complex_band_pass(self.gain
,self.samp_rate,self.low_cutoff,self.high_cutoff,self.BW, 0 ,beta=6.76)))

    self.fft_filter_xxx_0_0_0.set_taps((gr.firdes.complex_band_pass(self.
gain,self.samp_rate,self.low_cutoff,self.high_cutoff,self.BW, 0
,beta=6.76)))

    self.fft_filter_xxx_0_0.set_taps((gr.firdes.complex_band_pass(self.ga
in,self.samp_rate,self.low_cutoff,self.high_cutoff,self.BW, 0 ,beta=6.76)))

def get_fft_size(self):
    return self.fft_size

def set_fft_size(self, fft_size):
    self.fft_size = fft_size

def get_dec(self):
    return self.dec

def set_dec(self, dec):
    self.dec = dec

def get_avg_alpha(self):
    return self.avg_alpha

def set_avg_alpha(self, avg_alpha):
    self.avg_alpha = avg_alpha
    self._avg_alpha_slider.set_value(self.avg_alpha)
    self._avg_alpha_text_box.set_value(self.avg_alpha)

def get_Sig_minus_Ref(self):
    return self.Sig_minus_Ref

def set_Sig_minus_Ref(self, Sig_minus_Ref):
    self.Sig_minus_Ref = Sig_minus_Ref

def get_Sig_freq(self):
    return self.Sig_freq

def set_Sig_freq(self, Sig_freq):
    self.Sig_freq = Sig_freq
```

```
def get_Ref_freq(self):
    return self.Ref_freq

def set_Ref_freq(self, Ref_freq):
    self.Ref_freq = Ref_freq
    self._Ref_freq_slider.set_value(self.Ref_freq)
    self._Ref_freq_text_box.set_value(self.Ref_freq)

def get_N(self):
    return self.N

def set_N(self, N):
    self.N = N
    self.blocks_add_const_vxx_0.set_k([-1]*self.N)

def get_BW(self):
    return self.BW

def set_BW(self, BW):
    self.BW = BW

    self.freq_xlating_fir_filter_xxx_0.set_taps((gr.firdes.complex_band_pass(self.gain,self.samp_rate,self.low_cutoff,self.high_cutoff,self.BW, 0 ,beta=6.76)))

    self.fft_filter_xxx_0.set_taps((gr.firdes.complex_band_pass(self.gain ,self.samp_rate,self.low_cutoff,self.high_cutoff,self.BW, 0 ,beta=6.76)))
    self._BW_slider.set_value(self.BW)
    self._BW_text_box.set_value(self.BW)

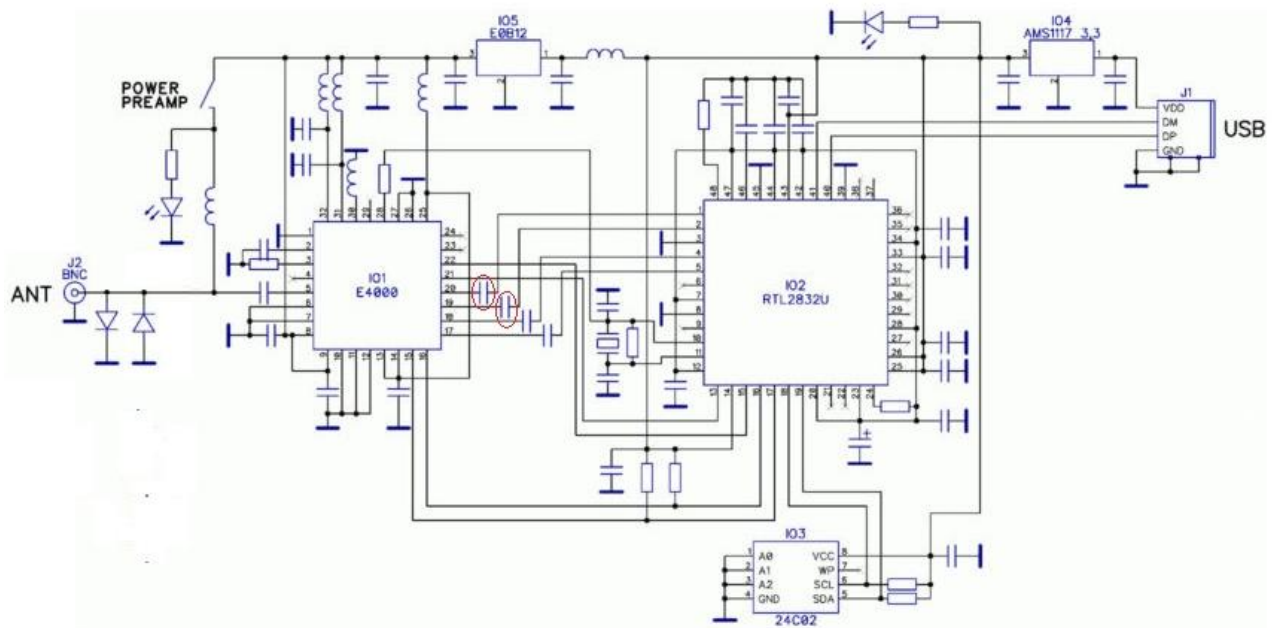
    self.fft_filter_xxx_0_0_0.set_taps((gr.firdes.complex_band_pass(self.gain,self.samp_rate,self.low_cutoff,self.high_cutoff,self.BW, 0 ,beta=6.76)))

    self.fft_filter_xxx_0_0.set_taps((gr.firdes.complex_band_pass(self.gain,self.samp_rate,self.low_cutoff,self.high_cutoff,self.BW, 0 ,beta=6.76)))

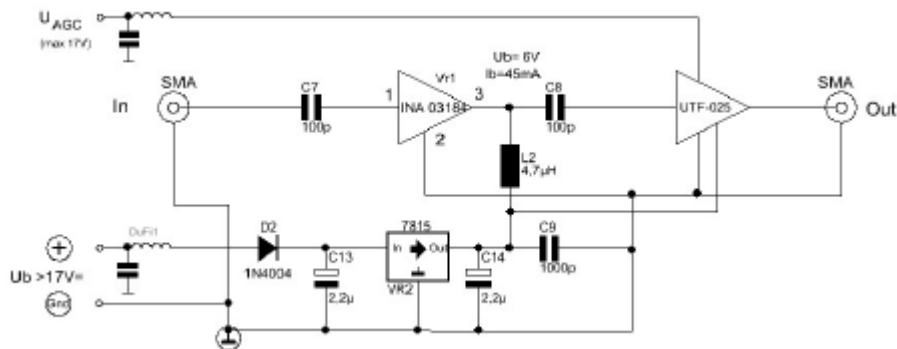
if __name__ == '__main__':
    parser = OptionParser(option_class=eng_option, usage="%prog:
[options]")
    (options, args) = parser.parse_args()
    tb = top_block()
    tb.Run(True)
```

## A.2 Hardware

### SDR RTL 2382+4000



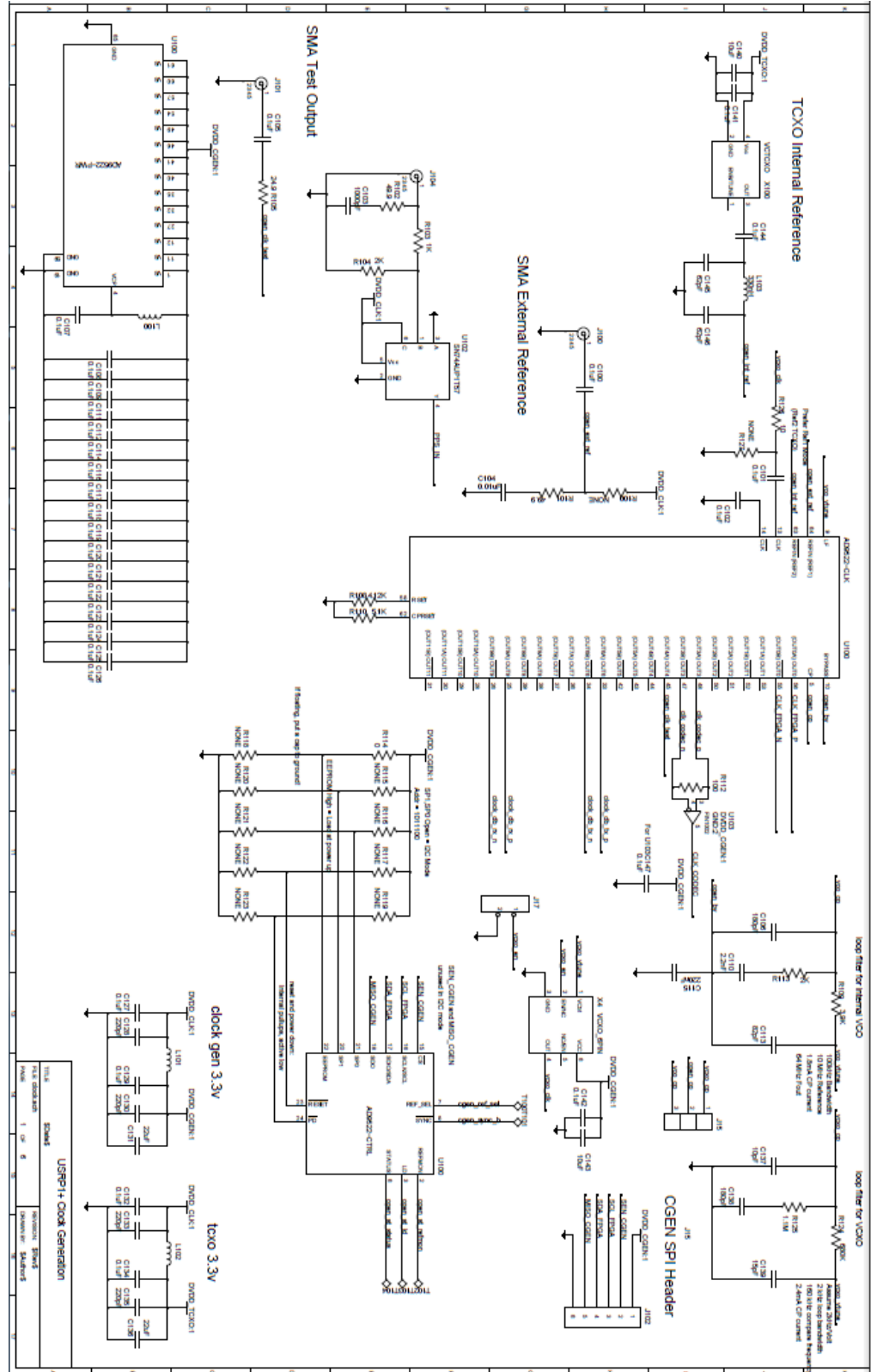
### IF Amplifier

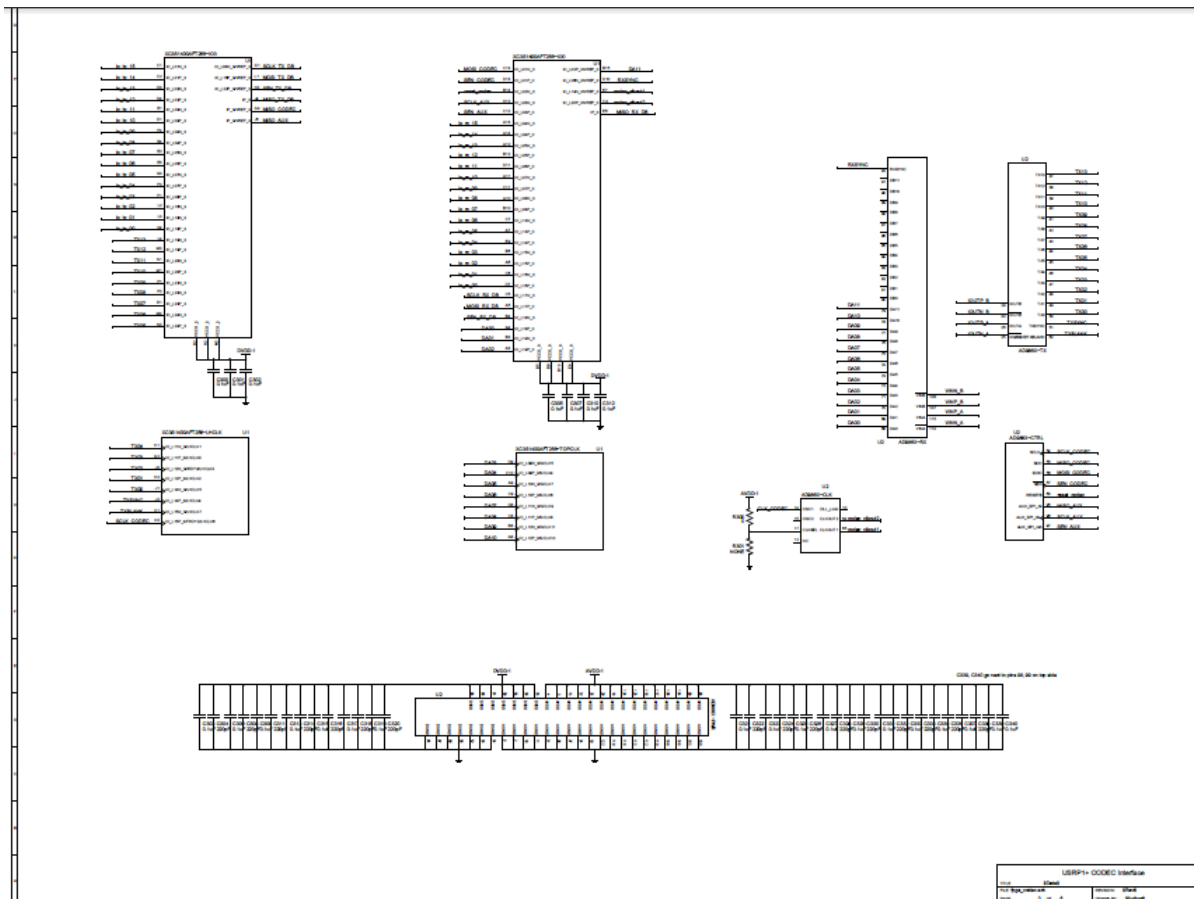
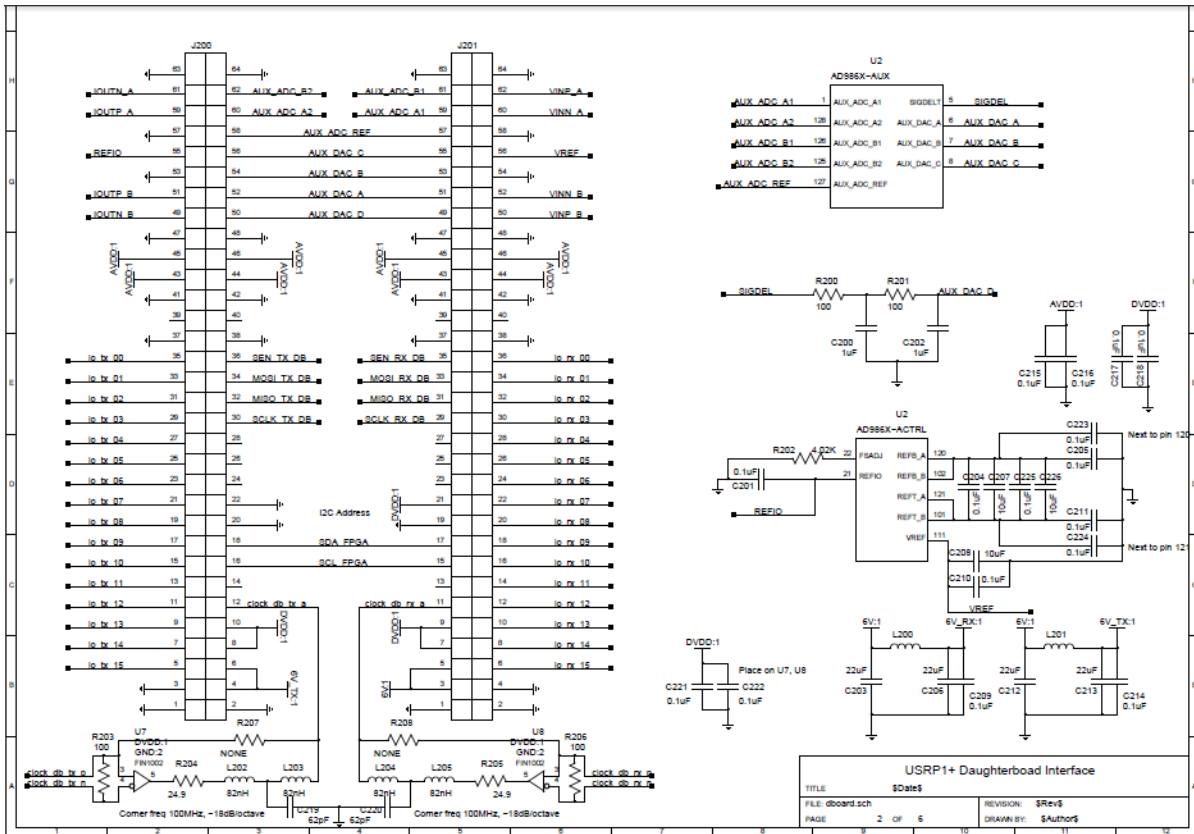


# Low noise amplifier

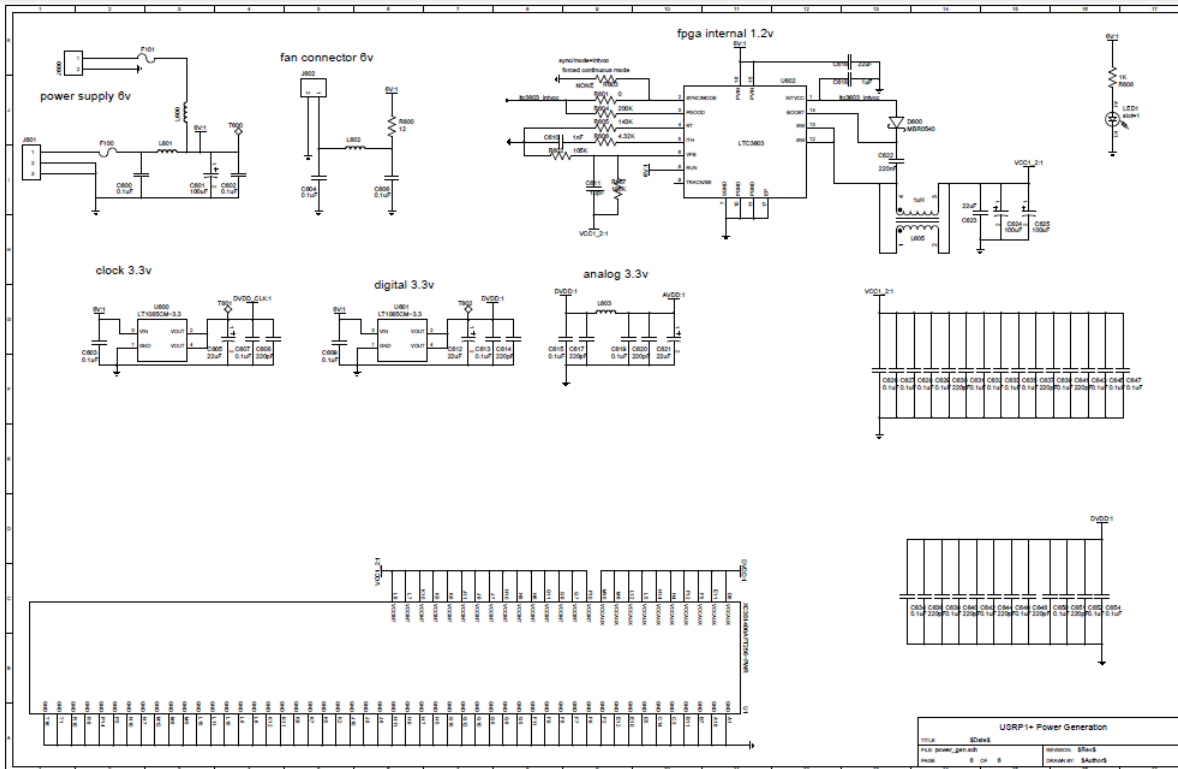
1	A	B	C	D	E	F																							
2			<p style="text-align: right;">Verstärkeroberseite</p>																										
3	<p>Low Noise Amplifier PGA 103+</p> <p>Gain @1400 MHz 12dB</p> <p>Noise Figure @1400MHz 0,7 dB</p> <p>P1dB 22,5dBm typ. @ 2 GHz @5V</p> <p>High IP3, 45dBm typ. @2GHz, 5V</p>		<p style="text-align: right;">Verstärkerunterseite</p>																										
4			<table border="1" style="width: 100%; border-collapse: collapse;"> <thead> <tr> <th colspan="2">Änderungen</th> <th>Datum</th> <th>Name</th> <th>Bezeichnung:</th> <th>Blattzahl:</th> </tr> </thead> <tbody> <tr> <td>Datum</td> <td>Name</td> <td>gez.:</td> <td></td> <td rowspan="2" style="text-align: center;">LNA PG103+</td> <td>Blatt-Nr.:</td> </tr> <tr> <td></td> <td></td> <td>gepr.:</td> <td></td> <td>Zeichnungs-Nr.:</td> </tr> <tr> <td></td> <td></td> <td></td> <td></td> <td></td> <td></td> </tr> </tbody> </table>		Änderungen		Datum	Name	Bezeichnung:	Blattzahl:	Datum	Name	gez.:		LNA PG103+	Blatt-Nr.:			gepr.:		Zeichnungs-Nr.:								
Änderungen		Datum	Name	Bezeichnung:	Blattzahl:																								
Datum	Name	gez.:		LNA PG103+	Blatt-Nr.:																								
		gepr.:			Zeichnungs-Nr.:																								

# Motherboard USRP B100

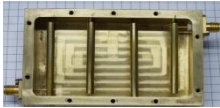








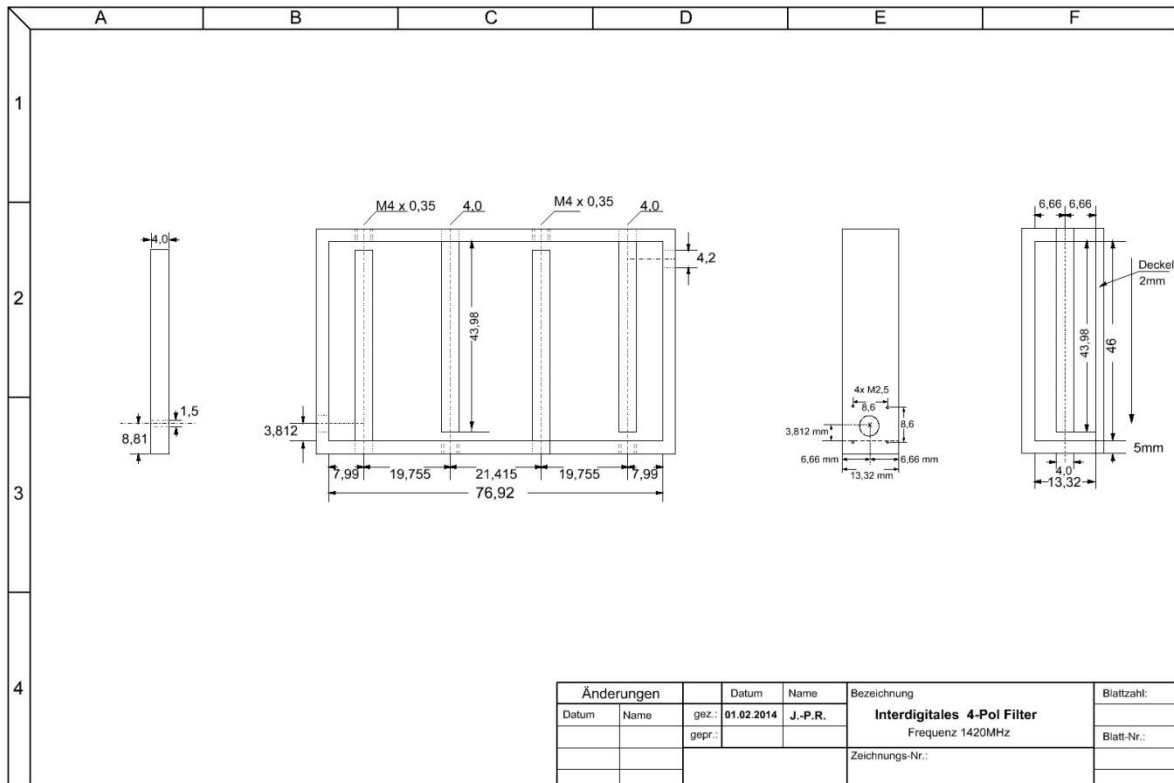
### A.3 List of off-the-shelf electronic components and assemblies

Receiver box		250 €
Hydrogen filter		
Power supply		22 €
Low noise Amplifier		120 €
Line Amplifier		3.80 €

Antenna		120 €
---------	---	-------

## A.4 Mechanical Components

### Hydrogen Filter





# IAP-OSM (Optical Spectrometer)



بِسْمِ اللَّهِ الرَّحْمَنِ الرَّحِيمِ



## Spectroscope for Visual Data

### 1-Definition of spectroscopy

Spectroscopy is the study of the interaction between matter and electromagnetic radiation. Historically, spectroscopy originated through the study of visible light dispersed according to its wavelength by a prism. Later the concept was expanded greatly to include any interaction with radiative energy as a function of its wavelength or frequency.



التحليل الطيفي هو دراسة التفاعل بين المادة والإشعاع الكهرومغناطيسي. تاريخياً، نشأ التحليل الطيفي من خلال دراسة الضوء المرئي المشتت وفقاً لطول الموجة، بواسطة المنشور. في وقت لاحق تم توسيع المفهوم إلى حد كبير ليشمل أي تفاعل مع الطاقة الإشعاعية كمدالة لطول الموجة.

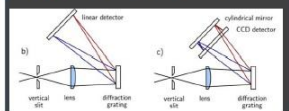
### 2-Spectrometer

A spectrometer is a scientific instrument used to separate and measure spectral components of a physical. The capability of spectroscopy to determine chemical composition drove its advancement and continues to be one of its primary uses. Much of our knowledge of the chemical makeup of the universe comes from spectroscopy.

المطياف هو أداة علمية تستخدم لفصل وقياس المكونات الطيفية. يعتبر بقدرة التحليل الطيفي لتحديد التركيب الكيميائي الأساسية الكثير من معرفتنا للتركيب الكيميائي للكون يأتي من دراسة معرفة الأطياف.

### 3-Principle:

In the horizontal plane, the incoming light must be spatially limited by a vertical slit. Then the spatial limitation is converted to angular limitation using a concave mirror or a convex lens. Ideally, we obtain a parallel beam of white light. Its width is limited either by the size of the mirror or lens used, or by the angle of the beam passing through the slit. The light components of different wavelengths separate after being reflected into different angles by a diffraction grating, delivered to the CCD. Finally, the angular separation might be converted back to spatial separation using another lens or mirror. However, this would require a big lens with diameter similar to the length of CCD. The spatial difference would be proportional to its focal length, probably resulting in a small spatial separation.



### 4-The charge coupled device, CCD:

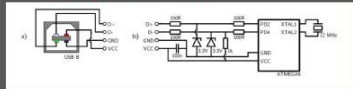
was originally designed not to be an optical detector but a memory instead. It should work as an analog shift register, storing arbitrary charge in each of its cells and reading them sequentially. Soon it was discovered that illumination causes internal photoelectric effect in the silicon substrate and fills up each memory cell with additional charge proportional to the incident light intensity.



Although CCD was rarely used as a memory, it found widespread application as a sensitive optical detector both in consumer electronics and in high-end scientific instruments such as astronomical telescopes. It should use NEB µPD3799 CCD detector.

### 5-Electronic setup

A common microcontroller The Atmega8-16PU version has 28 pins, of which 4 were occupied by DC supply, 2 by USB, 2 by oscillator, 4 by CCD driving signals and one for ADC input. The most demanding task is the USB communication.



The microcontroller should be equipped by a sufficient internal analog-to-digital converter (ADC). Many contemporary microcontrollers have an internal 10-bit converter able to perform at least 10,000 samples per second, which is sufficient for this application. The microcontroller was programmed via the serial programming interface using a USB-to-UART hardware programmer and the avrdude program. The firmware code was compiled on Linux (Ubuntu 10.04) in avr-gcc compiler and it was loaded into the microcontroller flash memory with commands.

### Properties of colors

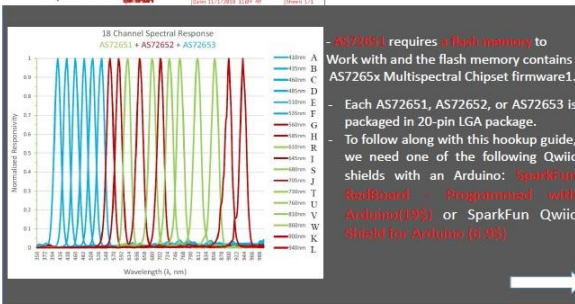
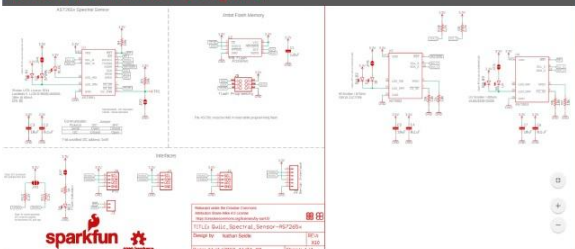
Color	Wavelength	Frequency	Photon energy
Violet	380-450 nm	668-789 THz	2.75-3.26 eV
Blue	450-495 nm	606-668 THz	2.50-2.75 eV
Green	495-570 nm	526-606 THz	2.17-2.50 eV
Yellow	570-590 nm	508-526 THz	2.10-2.17 eV
Orange	590-620 nm	484-508 THz	2.00-2.10 eV
Red	620-750 nm	400-484 THz	1.65-2.00 eV

### 6-Materials for optical setup

1. A standard aluminium L-profile 25 mm high, 2 mm thick and with 12 mm long foot.
2. The input slit was made of two razor blade segments, 15 mm long.
3. The collimating lens had 14 mm diameter, focal length  $f = 30$  mm, Plano-convex geometry.
4. The cylindrical mirror was obtained from a scrap photocopier. It is a polished metal rectangle, 42x15 mm in size. Its focal length is approximately 30 mm.
5. a blazed diffraction grating with 500 - 1000 grooves/mm, with size at least 8x8 mm.

### 7-Schematic of SparkFun Triad Spectroscopy Sensor - AS7265x (Qwiic)

AS7265x Multispectral Chipset consists of AS72651, AS72652, and AS72653 devices and each device has 6 optical filters so that AS7265x Multispectral Chipset have total 18 channels for spectral identification from 400nm to 1000nm with FWHM of 20nm. AS72651 is the main device with the smart interface to a microcontroller. The microcontroller gets the sensors data including AS72652 and AS72653 through AS72651 AT commands at I2C registers.



- AS72651 requires a flash memory to work with and the flash memory contains AS7265x Multispectral Chipset firmware.
- Each AS72651, AS72652, or AS72653 is packaged in 20-pin LGA package.
- To follow along with this hookup guide, we need one of the following Qwiic shields with an Arduino: SparkFun RedBoard Programmed with Arduino (19\$) or SparkFun Qwiic Shield by Arduino (6.9\$)

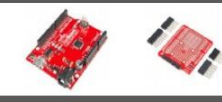
### 8-Software Design Considerations

In most of system designs, AS72651 is controlled by a microcontroller. With the UART interface, the controller could configure the devices and get the sensors data through some AT commands. The software of microcontroller design would be simple.

The following sections would focus on I2C interface and the software of microcontroller design should satisfy both I2C specification and AS7265x Multispectral Chipset register structure.



- Accessories:
- Qwiic Cable - Breadboard Jumper (4-pin) \$1.50
  - Qwiic Cable - 100mm \$1.50
  - SparkFun Qwiic Shield for Arduino \$6.95
  - SparkFun Qwiic HAT for Raspberry Pi \$5.95
  - SparkFun Qwiic Mux Breakout - 8 Channel \$11.95

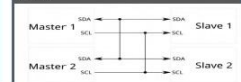


### 9-Arduino

- A computer (Windows, Mac, or Linux)
- An Arduino-compatible microcontroller (anything from this guide should work)
- A USB A-to-B cable, or another appropriate way to connect your Arduino-compatible microcontroller to your computer.
- 1-Installing Arduino IDE: <http://arduino.cc/en/Main/arduinoIDE>
- 2-The Inter-integrated Circuit (I2C) Protocol is a protocol intended to allow multiple "slave" digital integrated circuits ("chips") to communicate with one or more "master" chips. Like the Serial Peripheral Interface (SPI), it is only intended for short distance communications within a single device. Like Asynchronous Serial Interfaces (such as RS-232 or UARTs), it only requires two signal wires to exchange information.

#### I2C/Qwiic Interface:

The sensors are 3.3V compatible so don't use with a 5V Arduino Uno without proper conversion (use the Qwiic shield instead!). If you're using a 3.3V development platform that doesn't have a Qwiic connector, consider using the Qwiic Breadboard Cable.



## 47 1 Basics

In order to study the intensity of waves of stars ,we elaborate this work to built a station that facilitate the detection of waves .

### 47.1 Spectroscopy<sup>48</sup>

Spectroscopy is the study of the interaction between matter and electromagnetic radiation. Historically, spectroscopy originated through the study of visible light dispersed according to its wavelength, by a prism. Later the concept was expanded greatly to include any interaction with radiative energy as a function of its wavelength or frequency, predominantly in the electromagnetic spectrum, though matter waves and acoustic waves can also be considered forms of radiative energy; recently, with tremendous difficulty, even gravitational waves have been associated with a spectral signature in the context of LIGO and laser interferometry. Spectroscopic data are often represented by an emission spectrum, a plot of the response of interest as a function of wavelength or frequency.

Spectroscopy, primarily in the electromagnetic spectrum, is a fundamental exploratory tool in the fields of physics, chemistry, and astronomy, allowing the composition, physical structure and electronic structure of matter to be investigated at atomic scale, molecular scale, macro scale, and over astronomical distances. Important applications arise from biomedical spectroscopy in the areas of tissue analysis and medical imaging.



Figure 35: Analysis of white light by dispersing it with a prism is an example of spectroscopy.

Spectroscopy and spectrography are terms used to refer to the **measurement of radiation intensity as a function of wavelength** and are often used to describe experimental spectroscopic methods. Spectral measurement devices are referred to as spectrometers, spectrophotometers, spectrographs or spectral analyzers.

#### 47.1.1 Theory

One of the central concepts in spectroscopy is a resonance and its corresponding resonant frequency. Resonances were first characterized in mechanical systems such as pendulums. Mechanical systems

---

<sup>48</sup> from <https://en.wikipedia.org/wiki/Spectroscopy>

that vibrate or oscillate will experience large amplitude oscillations when they are driven at their resonant frequency. A plot of amplitude vs. excitation frequency will have a peak centered at the resonance frequency. This plot is one type of spectrum, with the peak often referred to as a spectral line, and most spectral lines have a similar appearance.

In quantum mechanical systems, the analogous resonance is a coupling of two quantum mechanical stationary states of one system, such as an atom, via an oscillatory source of energy such as a photon. The coupling of the two states is strongest when the energy of the source matches the energy difference between the two states. The energy ( $E$ ) of a photon is related to its frequency  $E=h\nu$ ,  $h$  is Planck's constant, and so a spectrum of the system response vs. photon frequency will peak at the resonant frequency or energy. Particles such as electrons and neutrons have a comparable relationship, the de Broglie relations, between their kinetic energy and their wavelength and frequency and therefore can also excite resonant interactions.

Spectra of atoms and molecules often consist of a series of spectral lines, each one representing a resonance between two different quantum states. The explanation of these series, and the spectral patterns associated with them, were one of the experimental enigmas that drove the development and acceptance of quantum mechanics. The hydrogen spectral series in particular was first successfully explained by the Rutherford-Bohr quantum model of the hydrogen atom. In some cases spectral lines are well separated and distinguishable, but spectral lines can also overlap and appear to be a single transition if the density of energy states is high enough. Named series of lines include the principal, sharp, diffuse and fundamental series.

#### 47.1.2 Type of radiative energy

The types of spectroscopy are distinguished by the type of radiative energy involved in the interaction. In many applications, the spectrum is determined by measuring changes in the intensity or frequency of this energy. The types of radiative energy studied include:

- Electromagnetic radiation was the first source of energy used for spectroscopic studies. Techniques that employ electromagnetic radiation are typically classified by the wavelength region of the spectrum and include microwave, terahertz, infrared, near-infrared, ultraviolet-visible, x-ray, and gamma spectroscopy.
- Particles, because of their de Broglie waves, can also be a source of radiative energy. Both electron and neutron spectroscopy are commonly used. For a particle, its kinetic energy determines its wavelength.
- Acoustic spectroscopy involves radiated pressure waves.
- Dynamic mechanical analysis can be employed to impart radiating energy, similar to acoustic waves, to solid materials.

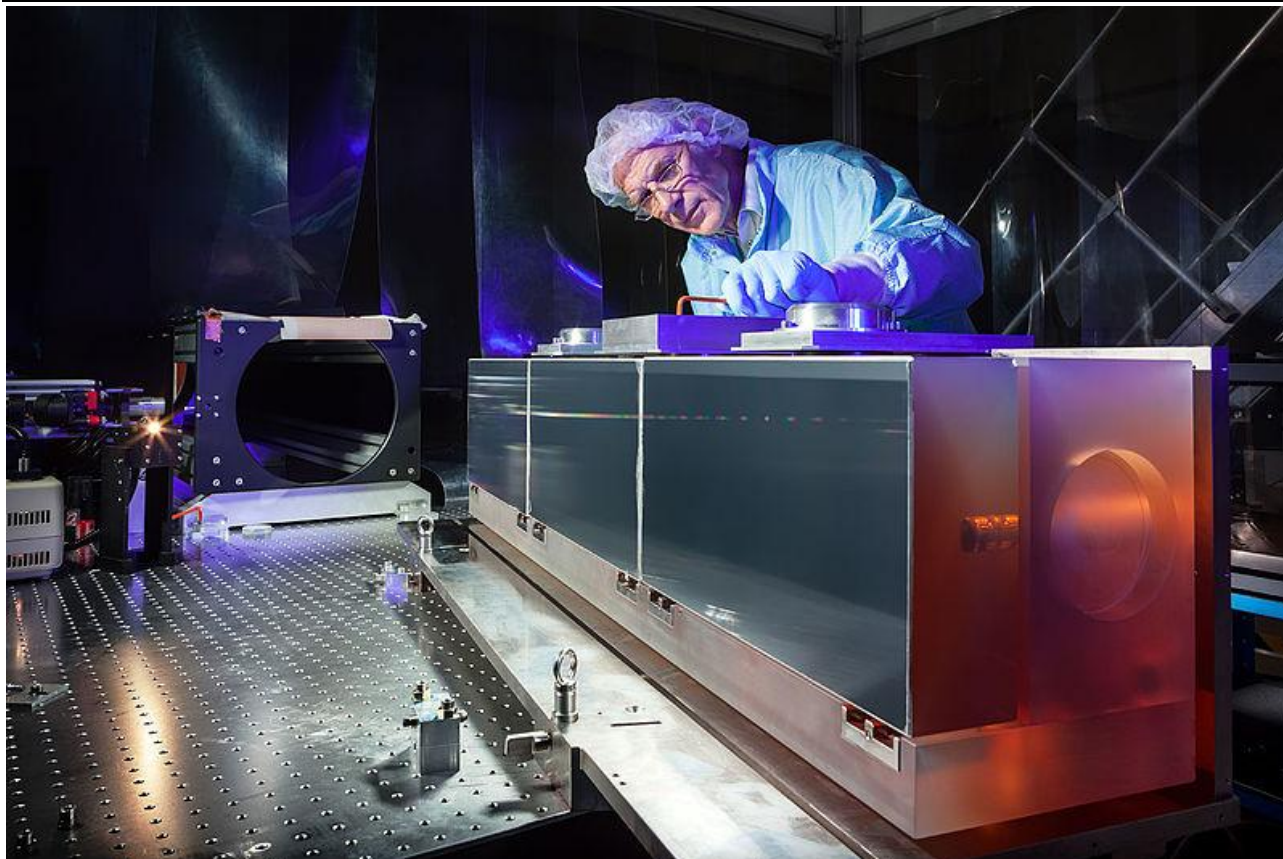


Figure 36: A huge diffraction grating at the heart of the ultra-precise ESPRESSO spectrograph.

### 47.1.3 Nature of the interaction

The types of spectroscopy also can be distinguished by the nature of the interaction between the energy and the material. These interactions include:<sup>[1]</sup>

- Absorption spectroscopy: Absorption occurs when energy from the radiative source is absorbed by the material. Absorption is often determined by measuring the fraction of energy transmitted through the material, with absorption decreasing the transmitted portion.
- Emission spectroscopy: Emission indicates that radiative energy is released by the material. A material's blackbody spectrum is a spontaneous emission spectrum determined by its temperature. This feature can be measured in the infrared by instruments such as the atmospheric emitted radiance interferometer.<sup>[4]</sup> Emission can also be induced by other sources of energy such as flames or sparks or electromagnetic radiation in the case of fluorescence.
- Elastic scattering and reflection spectroscopy determine how incident radiation is reflected or scattered by a material. Crystallography employs the scattering of high energy radiation, such as x-rays and electrons, to examine the arrangement of atoms in proteins and solid crystals.

- Impedance spectroscopy: Impedance is the ability of a medium to impede or slow the transmittance of energy. For optical applications, this is characterized by the index of refraction.
- Inelastic scattering phenomena involve an exchange of energy between the radiation and the matter that shifts the wavelength of the scattered radiation. These include Raman and Compton scattering.
- Coherent or resonance spectroscopy are techniques where the radiative energy couples two quantum states of the material in a coherent interaction that is sustained by the radiating field. The coherence can be disrupted by other interactions, such as particle collisions and energy transfer, and so often require high intensity radiation to be sustained. Nuclear magnetic resonance (NMR) spectroscopy is a widely used resonance method, and ultrafast laser spectroscopy is also possible in the infrared and visible spectral regions.

#### 47.1.4 Type of materials

spectroscopic studies are designed so that the radiant energy interacts with specific types of matter.

- Atoms

Atomic spectroscopy was the first application of spectroscopy developed. Atomic absorption spectroscopy and atomic emission spectroscopy involve visible and ultraviolet light. These absorptions and emissions, often referred to as atomic spectral lines, are due to electronic transitions of outer shell electrons as they rise and fall from one electron orbit to another. Atoms also have distinct x-ray spectra that are attributable to the excitation of inner shell electrons to excited states.

Atoms of different elements have distinct spectra and therefore atomic spectroscopy allows for the identification and quantitation of a sample's elemental composition. After inventing the spectroscope, Robert Bunsen and Gustav Kirchhoff discovered new elements by observing their emission spectra. Atomic absorption lines are observed in the solar spectrum and referred to as Fraunhofer lines after their discoverer. A comprehensive explanation of the hydrogen spectrum was an early success of quantum mechanics and explained the Lamb shift observed in the hydrogen spectrum, which further led to the development of quantum electrodynamics.

Modern implementations of atomic spectroscopy for studying visible and ultraviolet transitions include flame emission spectroscopy, inductively coupled plasma atomic emission spectroscopy, glow discharge spectroscopy, microwave induced plasma spectroscopy, and spark or arc emission spectroscopy. Techniques for studying x-ray spectra include X-ray spectroscopy and X-ray fluorescence.

- Molecules

The combination of atoms into molecules leads to the creation of unique types of energetic states and therefore unique spectra of the transitions between these states. Molecular spectra can be obtained due to electron spin states (electron paramagnetic resonance), molecular rotations, molecular vibration, and electronic states. Rotations are collective motions of the atomic nuclei and typically lead to spectra in the microwave and millimeter-wave spectral regions. Rotational spectroscopy and microwave spectroscopy are synonymous. Vibrations are relative motions of the atomic nuclei and are studied by both infrared and Raman spectroscopy. Electronic excitations are studied using visible and ultraviolet spectroscopy as well as fluorescence spectroscopy.

Studies in molecular spectroscopy led to the development of the first maser and contributed to the subsequent development of the laser.

- Crystals and extended materials

The combination of atoms or molecules into crystals or other extended forms leads to the creation of additional energetic states. These states are numerous and therefore have a high density of states. This high density often makes the spectra weaker and less distinct, i.e., broader. For instance, blackbody radiation is due to the thermal motions of atoms and molecules within a material. Acoustic and mechanical responses are due to collective motions as well. Pure crystals, though, can have distinct spectral transitions, and the crystal arrangement also has an effect on the observed molecular spectra. The regular lattice structure of crystals also scatters x-rays, electrons or neutrons allowing for crystallographic studies.

- Nuclei

Nuclei also have distinct energy states that are widely separated and lead to gamma ray spectra. Distinct nuclear spin states can have their energy separated by a magnetic field, and this allows for nuclear magnetic resonance spectroscopy.

## 47.2 Spectrometer

A spectrometer is a scientific instrument used to separate and measure spectral components of a physical phenomenon. Spectrometer is a broad term often used to describe instruments that measure a continuous variable of a phenomenon where the spectral components are somehow mixed. In visible light a spectrometer can for instance separate white light and measure individual narrow bands of color, called a spectrum, while a mass spectrometer measures the spectrum of the masses of the atoms or molecules present in a gas. The first spectrometers were used to split light into an array of separate colors. Spectrometers were developed in early studies of physics, astronomy, and chemistry. The capability of spectroscopy to determine chemical composition drove its advancement and continues to be one of its primary uses. Spectrometers are used in astronomy to analyze the

chemical composition of stars and planets, and spectrometers gather data on the origin of the universe.

Examples of spectrometers are devices that separate particles, atoms, and molecules by their mass, momentum, or energy. These types of spectrometers are used in chemical analysis and particle physics.

### 47.2.1 Types of spectrometer

#### 47.2.1.1 Optical spectrometer

An **optical spectrometer** (**spectrophotometer**, **spectrograph** or **spectroscope**) is an instrument used to measure properties of light over a specific portion of the electromagnetic spectrum, typically used in spectroscopic analysis to identify materials. The variable measured is most often the light's intensity but could also, for instance, be the polarization state. The independent variable is usually the wavelength of the light or a unit directly proportional to the photon energy, such as reciprocal centimeters or electron volts, which has a reciprocal relationship to wavelength.

A spectrometer is used in spectroscopy for producing spectral lines and measuring their wavelengths and intensities. Spectrometers may also operate over a wide range of non-optical wavelengths, from gamma rays and X-rays into the far infrared. If the instrument is designed to measure the spectrum in absolute units rather than relative units, then it is typically called a spectrophotometer. The majority of spectrophotometers are used in spectral regions near the visible spectrum.

Spectrometers are used in many fields. For example, they are used in astronomy to analyze the radiation from astronomical objects and deduce chemical composition. The spectrometer **uses a prism or a grating to spread the light from a distant object into a spectrum**. This allows astronomers to detect many of the chemical elements by their characteristic spectral fingerprints. If the object is glowing by itself, it will show spectral lines caused by the glowing gas itself. These lines are named for the elements which cause them, such as the hydrogen alpha, beta, and gamma lines. Chemical compounds may also be identified by absorption. Typically, these are dark bands in specific locations in the spectrum caused by energy being absorbed as light from other objects passes through a gas cloud. Much of our knowledge of the chemical makeup of the universe comes from spectra.

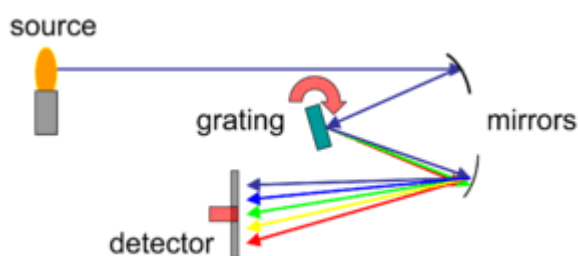


Figure 37: Grating spectrometer schematic

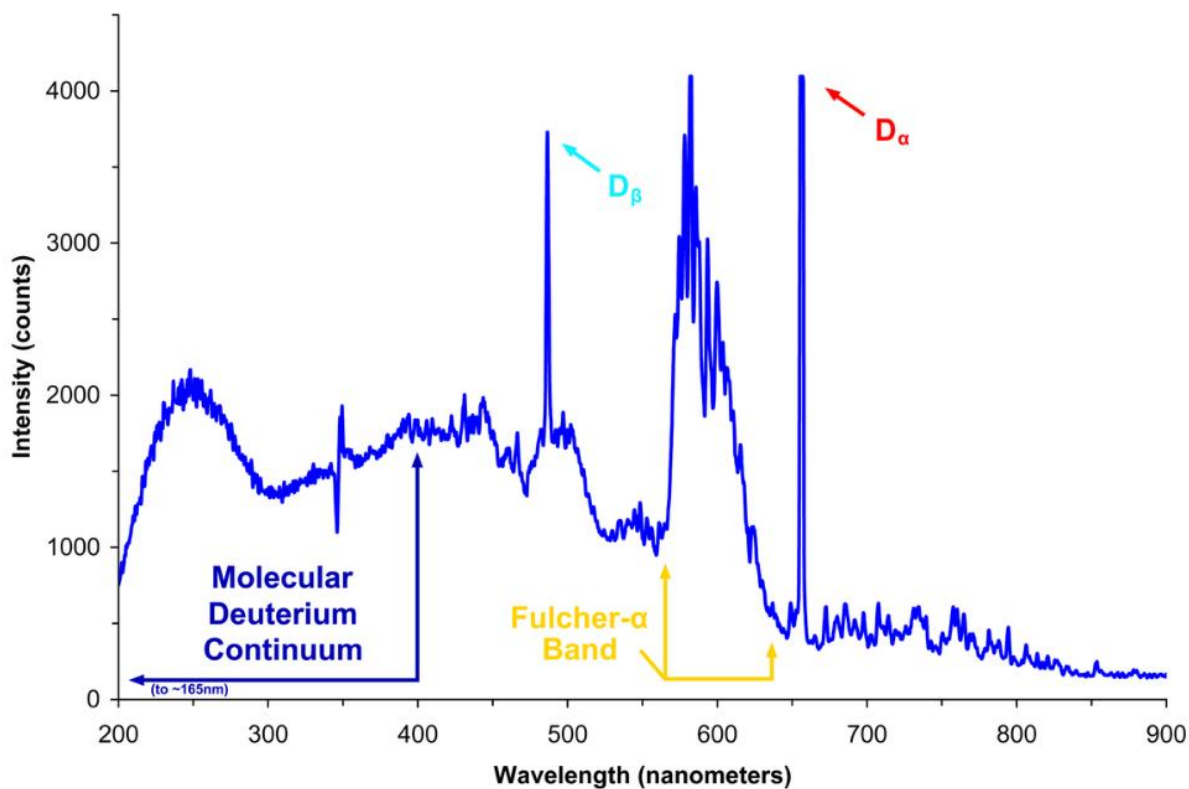


Figure 38: Spectrum of light emitted by a deuterium lamp in the UV visible and near infrared part of the electromagnetic spectrum.

#### 47.2.1.2 Spectroscopes

Spectroscopes are often used in astronomy and some branches of chemistry. Early spectroscopes were simply prisms with graduations marking wavelengths of light. Modern spectroscopes generally use a diffraction grating, a movable slit, and some kind of photodetector, all automated and controlled by a computer.

Joseph von Fraunhofer developed the first modern spectroscope by combining a prism, diffraction slit and telescope in a manner that increased the spectral resolution and was reproducible in other laboratories. Fraunhofer also went on to invent the first diffraction spectroscope.[2] Gustav Robert Kirchhoff and Robert Bunsen discovered the application of spectroscopes to chemical analysis and used this approach to discover caesium and rubidium.[3][4] Kirchhoff and Bunsen's analysis also enabled a chemical explanation of stellar spectra, including Fraunhofer lines.[5]

When a material is heated to incandescence it emits light that is characteristic of the atomic makeup of the material. Particular light frequencies give rise to sharply defined bands on the scale which can be thought of as fingerprints. For example, the element sodium has a very characteristic double yellow band known as the Sodium D-lines at 588.9950 and 589.5924 nanometers, the color of which will be familiar to anyone who has seen a low pressure sodium vapor lamp.

In the original spectroscope design in the early 19th century, light entered a slit and a collimating lens transformed the light into a thin beam of parallel rays. The light then passed through a prism (in hand-held spectroscopes, usually an Amici prism) that refracted the beam into a spectrum because different wavelengths were refracted different amounts due to dispersion. This image was then

viewed through a tube with a scale that was transposed upon the spectral image, enabling its direct measurement.

With the development of photographic film, the more accurate spectrograph was created. It was based on the same principle as the spectroscope, but it had a camera in place of the viewing tube. In recent years, the electronic circuits built around the photomultiplier tube have replaced the camera, allowing real-time spectrographic analysis with far greater accuracy. Arrays of photosensors are also used in place of film in spectrographic systems. Such spectral analysis, or spectroscopy, has become an important scientific tool for analyzing the composition of unknown material and for studying astronomical phenomena and testing astronomical theories.

In modern spectrographs in the UV, visible, and near-IR spectral ranges, the spectrum is generally given in the form of photon number per unit wavelength (nm or  $\mu\text{m}$ ), wavenumber ( $\mu\text{m}^{-1}$ ,  $\text{cm}^{-1}$ ), frequency (THz), or energy (eV), with the units indicated by the abscissa. In the mid- to far-IR, spectra are typically expressed in units of Watts per unit wavelength ( $\mu\text{m}$ ) or wavenumber ( $\text{cm}^{-1}$ ). In many cases, the spectrum is displayed with the units left implied (such as "digital counts" per spectral channel).

#### 47.2.1.3 Mass spectrometer

A mass spectrometer is an analytical instrument that is used to identify the amount and type of chemicals present in a sample by measuring the mass-to-charge ratio and abundance of gas-phase ions.<sup>[2]</sup>

#### 47.2.1.4 Time-of-flight spectrometer

The energy spectrum of particles of known mass can also be measured by determining the time of flight between two detectors (and hence, the velocity) in a time-of-flight spectrometer. Alternatively, if the velocity is known, masses can be determined in a time-of-flight mass spectrometer.

#### 47.2.1.5 Magnetic spectrometer

when a fast charged particle (charge  $q$ , mass  $m$ ) enters a constant magnetic field  $B$  at right angles, it is deflected into a circular path of radius  $r$ , due to the Lorentz force. The momentum  $p$  of the particle is then given by:

$$p = mv = qBr,$$

### 47.3 Types of optical spectrometers

Most optical spectrometers that produce a spectral waveform spanning over a selected region of wavelengths may be divided by their principle of operation into 3 most important groups:

1. Fourier-transform spectrometers use Michelson interferometer to measure how the interference signal oscillates when one of the mirrors moves. The interference function is later digitally processed to get the intensity spectrum. They can achieve very high spectral resolution and can measure even far-infrared spectra, assuming IR optics and detector are used.
2. Spectrometers with a monochromatic usually utilize rotating diffraction grating. They are simpler and less sensitive to environment, as no interference fringes are measured. The Czerny Turner setup

is often used, but other different setups may suit a particular purpose better. For example, to replace the rotating grating by a prism with moving mirror may be favorable for UV spectroscopy or when higher diffraction orders are to be eliminated.

3. The latter setup can be modified to obtain a spectrometer with multi-channel detector and no moving components. The grating is then fixed and the spectrum is projected on a broadband detector, which is usually a CCD.

The spectrometers in this category largely differ by sensitivity, resolution, application, size and price. For instance, the High Accuracy Radial Velocity Planet Searcher at La Silla Observatory in Chile is able to detect 1 m/s velocity difference in star's movement, enabling to indirectly search for extrasolar planets. On the other hand, spectrometers of this type can be made very compact and they are optimal for applications where resolution and sensitivity is not critical. Some models are available as a PCI card fitting into a computer.

This research project focuses on building a simple, cheap and compact spectrometer meeting following objectives:

1. The spectral resolution ( $\Delta\lambda$ ) should be better than 5 nm.
2. No moving components should be used.
3. The device and supplied software should be easy to use so that anybody with basic knowledge of spectroscopy can use it immediately.
4. The supplied software must run on most major operating systems with dependence on freely available programs only.
5. Except for initial calibration, no further maintenance would be required. Each device built will store its own calibration data in its permanent memory to prevent the need for recalibration when another model is connected.
6. Communication with computer and electrical supply should be performed via single USB cable.

The purpose of this research project is to decide whether such device can be built at a substantially lower price and yet remain suitable for practical tasks, as well as to present a possible way of doing that.

Additionally, the computer software is released under free license, allowing the aforementioned modifications and scripting. Last but not least, the data acquisition, processing and displaying techniques can be reused in many other applications involving measurement automation.

### **47.3.1 General dispersive spectrometer design**

A diffraction grating design with a CCD detector was used. This section describes how the light components are separated and delivered to the CCD. In the horizontal plane, the incoming light must be spatially limited by a vertical slit. Then the spatial limitation is converted to angular limitation using a concave mirror or a convex lens. Ideally, we obtain a parallel beam of white light. Its width is limited either by the size of the mirror or lens used, or by the angle of the beam passing through the slit. The light components of different wavelengths separate after being reflected into different angles by a diffraction grating. Finally, the angular separation might be converted back to spatial separation

using another lens or mirror as drawn in Fig. 5a. However, this would require a big lens with diameter similar to the length of CCD. The spatial difference would be proportional to its focal length, probably resulting in a small spatial separation. Fortunately, the second lens is not necessary, as the first lens can be shifted several millimeters away from the slit to create a real image in arbitrary distance from the grating (Fig. 5b). The beam incident on the diffraction grating becomes slightly convergent when a single lens is used. This results in nonuniform angular difference even for single wavelength and the projected image of the slit becomes slightly blurred. However, for the sharp angle of convergence this effect can be neglected.

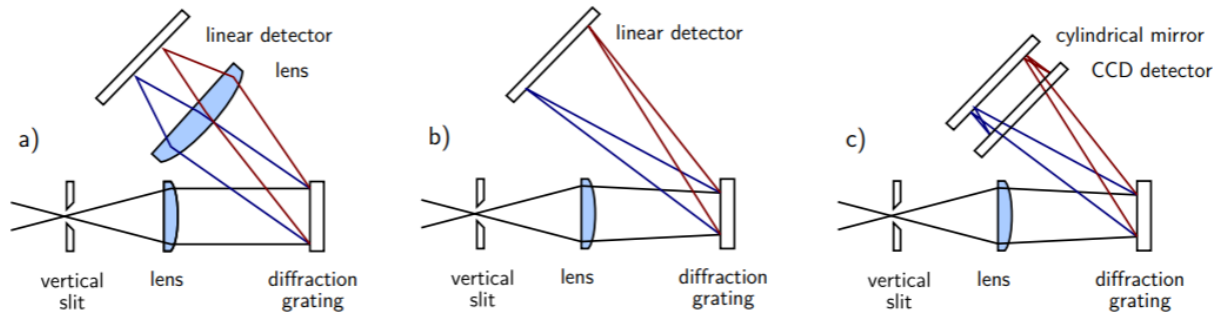


Figure 39: Horizontal schematics and light paths

There are several other phenomena limiting the spectral resolution of this setup, but assuming an ideal diffraction grating is used, the nonzero width of the input slit dominates. In the vertical projection, a single point in the slit plane is projected onto another point on the sensor as shown at Fig. 6a. As the CCD sensor is very narrow, the spectrometer would be sensitive in only one point at the slit, not depending on the incident angle. This would be optimal if either a thin optical fiber or a point source are measured. However, it was expected that the incident light would mostly be cover some area on the slit and that the spectrometer should be sensitive at nonzero length along the slit. Therefore a cylindrical mirror was inserted near to the focal plane to concentrate each spectral line (image of the input slit) into a much shorter line at the detector (Fig. 5c, 2b). If the light entered the slit at a single point and this point slightly moved in vertical axis, its image would move in vertical axis, too. When a cylindrical mirror is used, the point image would still be projected onto the CCD, albeit under different angle. The detector could not be put directly in the focal plane of this mirror, because the horizontal focus given by the lens must be maintained. Nonetheless, the sensitivity to the light entering the slit was substantially improved.

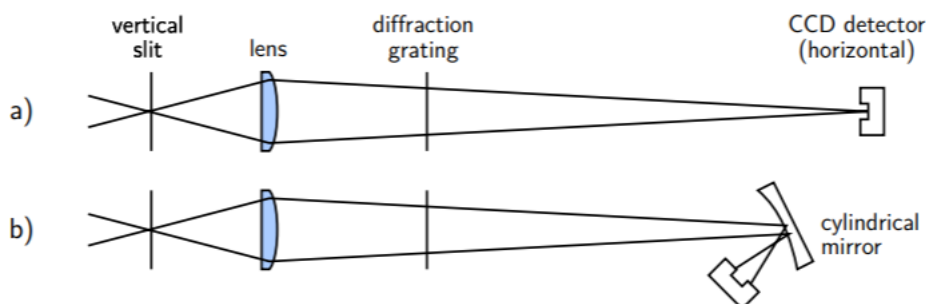


Figure 40: Vertical schematics and light paths

## 47.4 CCD detector<sup>49</sup>

### 47.4.1 Overview

The charge coupled device, CCD, was originally designed not to be an optical detector, but a memory instead. It should work as an analog shift register, storing arbitrary charge in each of its cells and reading them sequentially. Soon it was discovered that illumination causes internal photoelectric effect in the silicon substrate and fills up each memory cell with additional charge proportional to the incident light intensity. Although CCD was rarely used as a memory, it found widespread application as a sensitive optical detector both in consumer electronics and in high-end scientific instruments such as astronomical telescopes. CCD detectors may be divided into two groups: linear CCDs, where one row of pixels is shifted to the output, and matrix CCDs, where the bottom row is fully shifted out always when all columns are shifted down by one pixel. For this project, a linear CCD was chosen over a matrix CCD because only a linear detector several centimeters long was needed. Still, it would be possible to build a custom matrix CCD driver, too [1]. Another option, a CMOS sensor, was not used because of worse availability.

### 47.4.2 Driving a linear CCD

Although the internal design of the particular components may differ, the basic principle of CCD operation should remain similar. In the CCD register itself, a silicon substrate is covered by a thin layer of insulator and the electrodes. When a voltage is applied to an electrode, the electrons get trapped under the layer of insulator. By changing the voltage distribution on the surface, the charge packet can be moved with negligible loss.

In a common two-phase driven CCD, there are two electrodes on the insulating layer over each pixel. The geometry of electrodes is asymmetrical, dragging the electron packet nearer to one end of electrode . Therefore, a two-phase only signal is needed to transport the charge to the next pixel. The two phase crossing must be nearly symmetrical, which requires them to be switched at once<sup>1</sup> . The silicon surface can integrate the charge produced by internal photoelectric effect, but this is rarely used now. Instead, contemporary sensors contain an array of photodiodes, which are much more sensitive than the actual CCD register. When a transfer gate impulse comes, the charge is transferred to each corresponding pixel in the CCD register. This also eliminates blur of the image when the charges are shifted [4]. At the end of the analog register, the charge is coupled out to a pre-amplifier.

### 47.4.3 CCD output handling

Depending on the particular design, **the two CCD phases and additional one to three inputs need to be activated by an impulse so that each pixel is read. After correct pixel driving signals are input, the CCD shifts the pixel's charge to its internal preamplifier and the corresponding voltage signal occurs at one pin.** Sometimes is the output voltage stored in a sample-and-hold circuit. The CCD detector output shall depend on the illumination linearly, but the signal is inverted, at least in the CCD detectors considered, e. g., for the CCD used in this project (NEC  $\mu$ PD3799): Under no

---

<sup>49</sup> from [https://www.fzu.cz/~dominecf/electronics/usb-spect/usb\\_spectrometer\\_dominec.pdf](https://www.fzu.cz/~dominecf/electronics/usb-spect/usb_spectrometer_dominec.pdf)

illumination, the output is approximately +7 V, whereas under full saturation the output drops to +2.4 V. The influence of incident light on the CCD register itself and its supporting circuitry, along with thermal electrons, can interfere with measurement.

- **Blooming:** occurs when excess charge concentrates in one cell and it leaks into neighbouring cells. It manifests as a flat, fully saturated regions with sharp edges, effectively obscuring the signal in the vicinity of the intensively illuminated spot. Most modern CCDs address this by electronic design, but the simple linear CCDs used in this project do not. Overexposed areas must be avoided by either reducing the light intensity or integration time. For instance, the saturation exposure of the used linear CCD is lower than 0.5 lx·s [4].

- **Charge volatility:** The stored charge decays over time. This is expected to be caused by both thermal electrons and incident light. At room temperature, it was experimentally proven that the CCD must be read in  $\approx 0.5$  s after gate transfer to avoid this. This presents a time constraint to the data acquisition and transmitting time. When the CCD is read in bursts, a sawtooth-like additive bias will occur.

- **Oversaturation:** When the CCD is illuminated by common daylight for a while ( $> 10$  lx·s), the chip becomes so oversaturated that several full read-outs are needed to drain the integrated charge. Otherwise the output voltage may drop even under the saturation voltage. Sometimes this manifested as a step transition from saturation of one colour component in the middle of CCD reading, even when the CCD has been in dark for the last integration period.

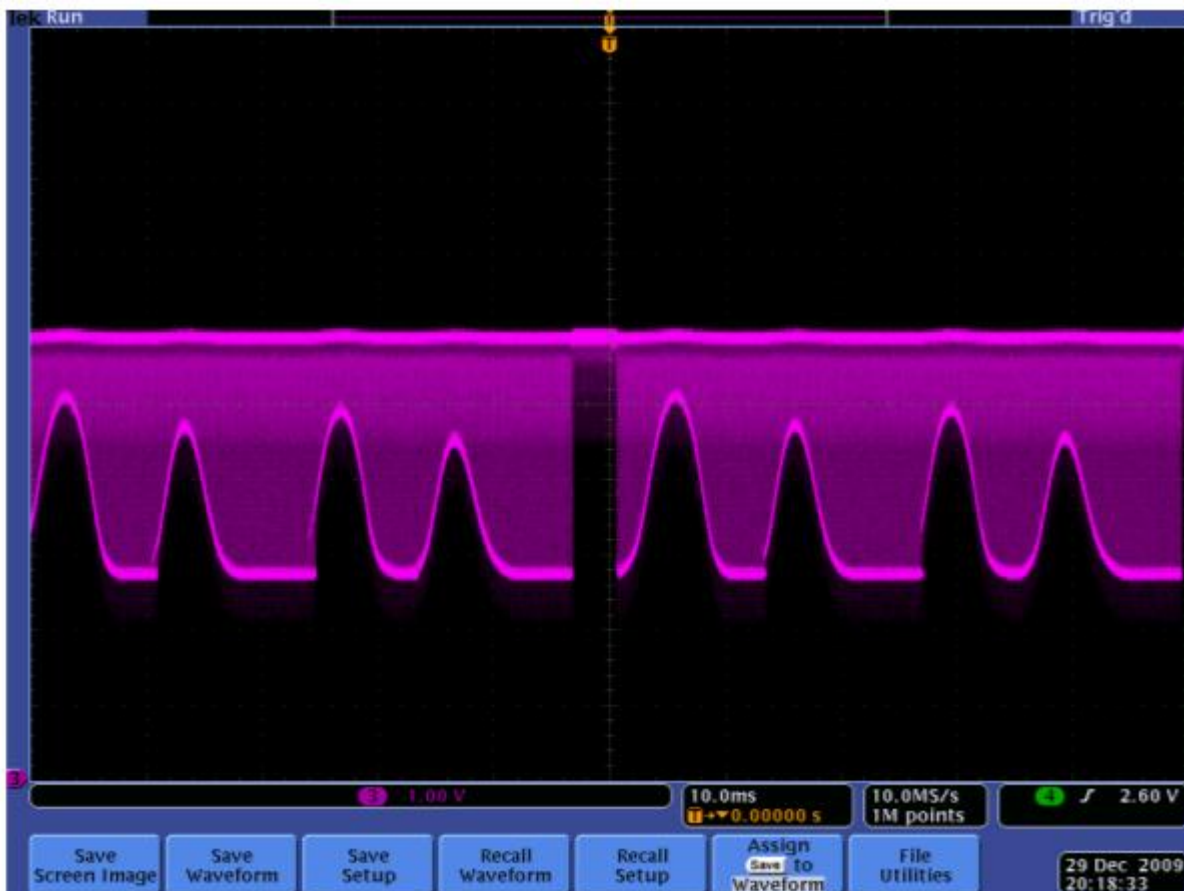


Figure 41: : One of the first measurements of the CCD output on an oscilloscope. On the screen, there are two consecutive read outs of CCD. The detector window was covered by four thin paper stripes.

Note the end of register signal in the middle of the screen and the blooming which slightly overlaps the less illuminated areas.

- **Thermal noise**

is caused by random thermal electron-hole pairs. It is probably lower than electronic noise in the sampling circuit used. Some of the mentioned issues can be addressed by thermoelectrical cooling of the sensor, as a 20 °C temperature drop is expected to effectively suppress the thermal noise and conductivity. No cooling was used in this design because of rather high power requirements of a Peltier cell. When a colour CCD is used, the red, green and blue signals must be averaged to obtain sensitivity covering the whole spectrum to be measured. This was done by inserting a 10 kΩ resistor at each channel and by connecting their second terminals together. The resulting spectral sensitivity is inhomogeneous, which was later addressed by amplitude calibration.

#### 47.4.4 Driving the CCD with a microcontroller

The proper CCD driving, analogue to digital conversion and consequent data transmission would require complicated circuitry if constructed from discrete components or TTL logic. Even such designs were constructed but most of these tasks can be easily handled by a common microcontroller of middle class. The most demanding task is the USB communication, which determines the minimum MCU computational power to approximately 12 MIPS at least. This topic is discussed later. **The microcontroller should be equipped by a sufficient internal analog-to-digital converter (ADC). Usage of an external ADC would present additional cost and complexity. Many contemporary microcontrollers have an internal 10-bit converter able to perform at least 10,000 samples per second, which is sufficient for this application.** Additionally, the need to avoid the mentioned sawtooth bias requires that the whole CCD is read at once and the spectral curve is stored in the memory until it is transmitted to the computer. Many microcontrollers come with fairly limited amount of internal RAM, which ranges from tens of bytes to 1 kB in the middle class. Taking into account that about 100 bytes are allocated by various program 10 data and that each pixel occupies 10 bits, there remains room for approximately 720 pixels if 1 kB of RAM was used. This severely limits the theoretical spectral resolution of 5300 pixels. The real spectral resolution in this case is, however, more limited by imprecise optics, and therefore the 1 kB of RAM was considered sufficient. If higher optical resolution was achieved and consequently bigger data buffer was appropriate, microcontrollers with 2 kB or 4 kB of RAM are available for approximately 5 Euro and 8 Euro, respectively. A cheaper solution would be an external RAM. As of 2010, the market is saturated by cheap parallel static RAM circuits with capacity in tens of kB. However, most of these circuits use more than 20 pins for addressing and data transmission, which would occupy all available pins of the cheaper microcontroller. The SRAM circuits communicating over the serial line are much less available, although there are plenty of rather cheap serial EEPROM circuits, which have limited number of write cycles. Possible candidates could be Microchip 23K640 and 23K256 models with 8 and 32 kB, respectively. Anyway, the use of external RAM would make the device more complicated and error prone. **Therefore no external RAM was used in this design.** As 1 kB of RAM was considered sufficient, the Atmel Atmega8 microcontroller was found to fulfill all aforementioned requirements. Moreover, this MCU supports in system

programming, which was very handy to develop and debug communication with both CCD and computer. **The Atmega8-16PU version has 28 pins, of which 4 were occupied by DC supply, 2 by USB, 2 by oscillator, 4 by** CCD driving signals and one for ADC input. There remained enough pins and capacity for a 7-segment display and simple user controls on the device, but later it was considered impractical and only the computer control was left. As for 2010, Atmega8-16PU circuit is still one of the most cost effective microcontrollers on the market, with price of about 1.5 Euro. 2.4

#### 47.4.5 Communication interfaces

##### 47.4.5.1 Comparison of different interfaces

Several different interfaces are commonly used to transfer data between a computer and external instruments.

- The serial port (RS232) can use 3 wires only, one wire for each direction and a ground. The data rate must be set on both sides. Serial line is often used in industrial applications and for older computer peripherals. **The microcontroller used in this project has hardware circuit for asynchronous serial communication, which could make this option favorable.** However, RS232 begins to disappear from newer computers and it requires the user to set the serial port options manually, too.
- The parallel port would probably require writing an own driver for data transfer and it would be too bulky for this project.
- The GPIB interface is often used to communicate with scientific instruments, but is rarely available at standard computers, let alone notebooks. Moreover, it shares the disadvantages of parallel port.
- The ethernet interface uses complicated, high-level protocol, which probably could not be processed by the microcontroller unit (MCU) and would increase the device complexity.

The Universal Serial Bus interface remains to be the most advantageous option, providing decent data rate, excellent availability and sufficient power supply. In the low-speed mode, the signalling speed is 1.5 Mb/s. This data rate can be processed by the MCU firmware, although the MCU has no hardware acceleration for USB communication. For higher data rate in full-speed mode of 12 Mb/s, a dedicated USB to RS232 converter may be used. An example is the Future Technology FT232BM circuit. According to the datasheet, it should be able to communicate with computer via USB, handle all USB protocol messages and communicate with the MCU via serial port. In this case the maximum data rate over serial port should be 2 Mb/s. [9] This may not seem as an advantage over firmware USB driver until one realizes that it is the USB protocol in the low-speed mode what presents the bottleneck, limiting the average data rate to less than one tenth of the signalling speed. Likewise, when the MCU communicates using the USART (Universal Synchronous and Asynchronous serial Receiver and Transmitter) subcircuit, less time is spent by the driver routines used to handle the messages. The USB-RS232 converter was not used here in order to keep the device simple.

##### 47.4.5.2 Hardware for USB communication

As no clock signal is sent over USB and the USB specification requires 1.5 % maximum tolerance for the timing, the MCU clock shall be timed precisely. Typically, the firmware drivers require oscillator whose frequency would be a multiple of 1.5 MHz. The minimum clock frequency is limited by the particular driver; mostly at least 8 processor steps per bit are required. A 12 MHz quartz crystal was

used in this project. **The USB cable contains 4 wires, which are listed in the table 1. The pins of the USB-B connector, used on the device side, are drawn in Fig. 8a.** The logical one voltage should fall between 2.7 and 3.6 V [16], therefore the 5 V TTL output of the MCU must be limited by Zener diodes. Additionally, the D- line must have logical one when the MCU is reset, which is ensured by the 1 k $\Omega$  pull-up resistor (Fig. 8b).

*Table 1: USB cable wires*

Wire label	Usual colour	Purpose
GND	black	ground
$U_{CC}$	red	DC power (up to 500 mA at 5 V)
D+	green	half-duplex, differential data line
D-	white	<i>dtto</i>

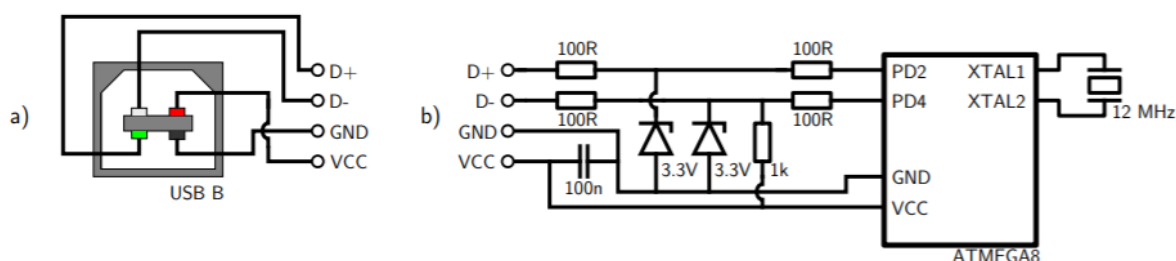


**Figure 42: : a) Pins on the USB B connector; b) Minimal circuit for connecting ATMEGA8 to USB**

The USB datasheet has some stricter requirements, e. g. for the device resistance, but the circuit from Fig. 8 worked flawlessly. Similar schematics are used in many other projects.

#### 47.4.6 Brief description of USB protocol

The data sent over USB are encoded using non-return-to-zero format: when a "0" bit is transmitted, the D- and D+ differential lines switch their state. When a "1" bit is transmitted, no change occurs. However, when more than 6 consecutive "1" bits are to be transmitted, one "0" bit is stuffed after them to enable the receiver to synchronize its clock at an edge of incoming signal. The data lines do not have to be always differential. For several low-level signals, e. g. end of packet, the D- and D+ lines may go both to logical "0" or "1". All data are sent in packets. The packet contains an initial sync sequence, the packet identification number and optionally payload or control data along with its checksum. Some packets transmit payload data, while other packets are used for handshake and identification only. Three packets, token, data and handshake, usually form a transaction. The USB protocol, mostly in a simplified, yet working form, is handled fully by the firmware driver. After being requested by the host, each USB device identifies itself by a vendor number and an USB class. Most devices fall into the human interface device or mass storage classes. Each class is handled slightly differently by the computer. The human interface device class was chosen due to its simplicity and widespread universal drivers [16]. USB protocol is rather complicated and its more

detailed description is beyond the scope of this document. There are several software implementations of the USB protocol for AVR microcontrollers. This project utilizes the V-USB driver by Christian Starkjohan [13] because of its good documentation and numerous practical examples. The driver is licensed under GNU GPL for noncommercial use. All these drivers use a hardware interrupt, which is triggered by incoming USB packet. At 1.5 Mbit/s signalling speed and 12 MHz main oscillator, only 8 clock cycles remain to receive, convert and store each bit. This requires that the microcontroller completely halts all another operation when any USB packet is received or transmitted. Besides, the USB protocol has the master-slave topology, and accordingly the MCU stops to receive or transmit packets asynchronously with its operation, which has to be taken into account when programming real-time tasks.

## 48 Design and Realization of a spectrometer prototype<sup>50</sup>

Based on:

Czech Technical University in Prague, Faculty of Nuclear Sciences and Physical Engineering  
Department of Physical Electronics, "*Design and construction of a digital CCD spectrometer*", Research  
project, Author: Filip Dominec, Supervisor: Ing. Jaroslav Pavel, Academic year: 2009/2010

([https://www.fzu.cz/~dominecf/electronics/usb-spect/usb\\_spectrometer\\_dominec.pdf](https://www.fzu.cz/~dominecf/electronics/usb-spect/usb_spectrometer_dominec.pdf))

Please note that this USB spectrometer project has a new HTML page, which may contain updates  
and further information: <http://www.fzu.cz/~dominecf/spek2/index.html>

### 48.1 Optical setup

- The optical components holders were made of **a standard aluminium L-profile 25 mm high, 2 mm thick and with 12 mm long foot**. The beam path axis was chosen to be 14 mm above the base surface. This provided optimal vertical room for the beam, maintaining enough room between the light path and the base for bolts etc.
- The input slit was made of **two razor blade segments, 15 mm long**. One of the segments was glued onto the inner side of the L-profile to cover half of the input hole. Its sharp edge was adjusted to be perpendicular to the base. The second segment was clamped next to it by a short screw with a spring bushing. This makes adjusting the slit width possible. In the final setup, the slit width of **50  $\mu\text{m}$  – 100  $\mu\text{m}$  appeared** to be appropriate
- The **collimating lens had 14 mm diameter, focal length  $f \approx 30$  mm, plano-convex geometry** and standard anti-reflex coating. (Generally, any common small lens of similar  $f$  may be used.) It was glued at the edges to a hole of similar diameter, keeping its axis at the beam axis. At the base of the L-profile, a notch instead of a hole was grinded to enable focusing.
- The reflective diffraction grating was attached nearly perpendicular to the incident beam. For the first prototype, **a 20×20 mm** segment cut from the outer edge of a blank **CD-R** was used. Notes to this solution are discussed later. The grating was rotated so that the most desired spectral range in the first diffraction order is projected on the CCD.
- The cylindrical mirror was obtained from a scrap photocopier. It is a polished **metal rectangle, 42×15 mm in size. Its focal length is approximately 30 mm**. The mirror was attached to a metal chip, which had a groove at the bottom. The groove fitted to two spikes in the bottom of the L-profile. At the top, an M3 screw allows to adjust the vertical angle of the mirror.
- The CCD detector was glued to a low profile PMMA slab. Its pins were shortened not to obscure any passing light and soldered to the controller circuit. The slab had a notch for the bolt. The output signal from three colour channels was averaged by **three 10 k $\Omega$  resistors near the CCD and** it was

---

<sup>50</sup> from [https://www.fzu.cz/~dominecf/electronics/usb-spect/usb\\_spectrometer\\_dominec.pdf](https://www.fzu.cz/~dominecf/electronics/usb-spect/usb_spectrometer_dominec.pdf)

connected using a thin shielded cable to eliminate noise from the digital wires. Between the supply voltage and ground, a 100 nF capacitor was inserted.

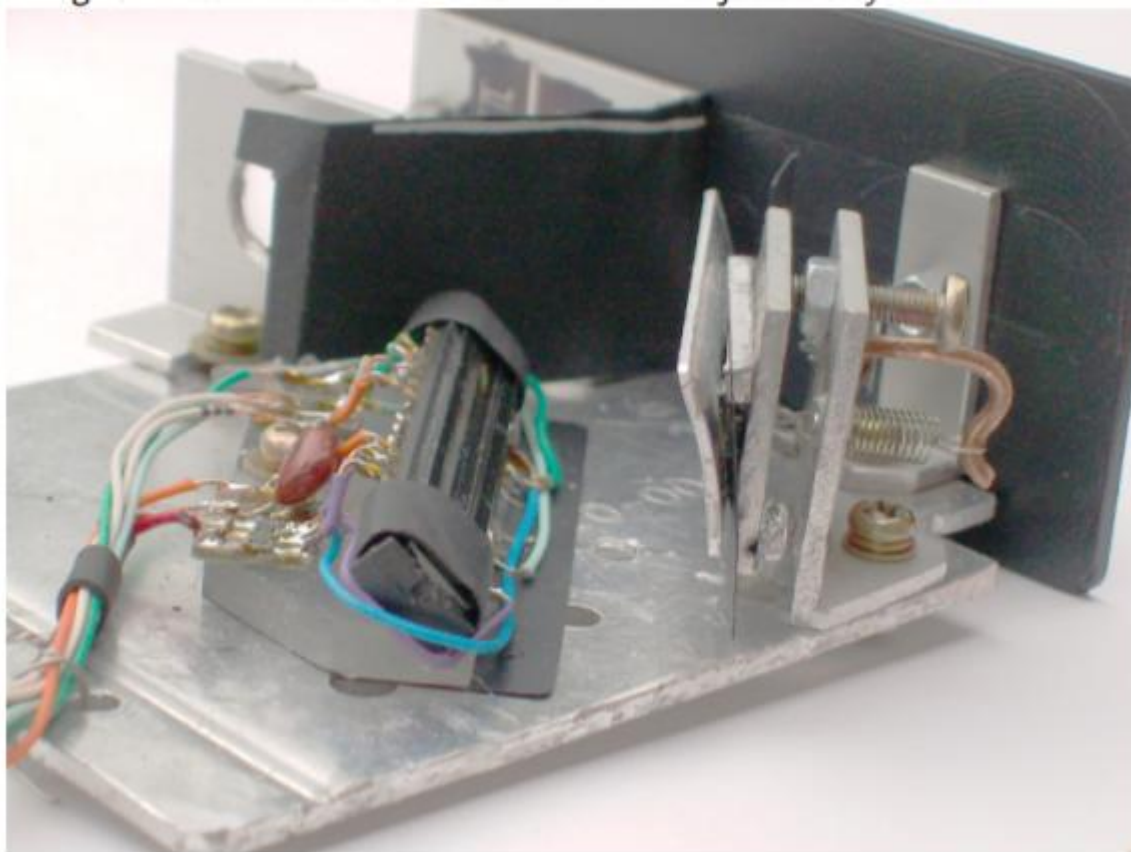


**Figure 43: Detail of the CCD mount and the adjustable cylindrical mirror**

The optical setup was mounted (by M3 bolts and nuts) to a 2 mm thick aluminium plate, of approximately 70×90 mm in size. It provided a decently rigid, yet light base. There remained 6 degrees of freedom, that had to be precisely adjusted to obtain effective and narrow spectral lines projected on the CCD.

1. The input slit width The second razor segment should limit the light entrance to an uniform, thin line.
2. The longitudinal position of the collimating lens should focus the slit onto the CCD in the horizontal plane.
3. The vertical grooves orientation of the diffraction grating should be parallel to the slit.
4. The horizontal angle of the diffraction grating: The whole desired spectral range should be projected onto the CCD.
5. The cylindrical mirror and CCD should be perpendicular to the beam coming from diffraction grating, which illuminates the center of CCD.
6. The vertical angle of cylindrical mirror and the corresponding position of the CCD detector: Along with previous setting, it should focus the spectral lines to illuminate the narrow CCD line the most effectively. The coarse setting was done visually using the light from a standard fluorescent lamp. The fine tuning of the lens position was performed when the device was connected to computer and the spectral lines were optimised to be as narrow as possible.

### 48.1.1 Diffraction grating source

The reflection diffraction grating of suitable parameters prove to be the component, that was the hardest to obtain for this project, maintaining the low price criterion. Ideally, a blazed diffraction grating with 500 – 1000 grooves/mm, with size at least 8×8 mm and with optimum efficiency in the visible range should be used. As of 2010, there is likely no shop in the Czech Republic where such gratings could be bought easily, according to the search on Internet. Future models can use a **professional grating**, which would probably cost **at least 50 Euro** [8]. This price is not limiting, however it would spoil one of the objective of minimizing the device's cost. Maybe several gratings could be replicated after one professional grating is bought. Alternatively, there is a proof that a reasonable diffraction grating may be manufactured using a nearly home-built ruling engine, taking into account the contemporary availability of MCUs, lasers and stepping motors [10]. Anyway, the precision requirements for such ruling engine are very tight. To achieve 1 nm spectrometer resolution at the 500 nm wavelength, the RMS error of groove spacing must be at most few nanometers. This limits the groove spacing error to less than 10 diameters of silver atoms! For the first prototype, the CD-R slab worked quite well. The cheapest CD-R had unexpectedly low stray light and no apparent Rowland ghosts coming from low-frequency modulation of the grating. Apart from non-optimal efficiency and fragile metallic coating on the surface, the biggest problem was caused by the grooves curvature. A monochromatic beam limited by the slit is projected into a crescent shape in the focal plane of the collimating lens. Instead, a vertical line is required, as the cylindrical mirror focuses the beam in the vertical plane.

#### 48.1.1.1 Microcontroller circuit

Aside from the CCD detector and the supply circuit mentioned later, the electronics do not require many components. The MCU is clocked by a **12.000 MHz quartz oscillator**. Some designs suppose to couple each oscillator input to **ground by two 30 pF** capacitors, but this has proven not to be necessary. The CCD driving signals use **the TTL levels**, hence the CCD inputs may be connected directly to the MCU pins. **For the used NEC  $\mu$ PD3799 CCD detector four signal wires are needed:** the phase 1 and phase 2 signals, the RB (reset gate) and the TG (transfer gate) signals. When another CCD is used, additional driving signals may have to be added, e. g., for NEC  $\mu$ PD3797, additional CLB (reset feed-through level clamp clock) negative impulse must be included after the RB impulse. According to the particular datasheet, both the firmware routines and hardware wiring can be easily modified to accomplish this. Note that one MCU clock takes only 83 ns and some minimum pulse length and delay must be maintained according to the CCD datasheet. As was noted in the 1.4.3 section, the output signal of CCD is too high to be directly connected to the analog-to-digital converter (ADC) of the MCU. **The output must be linearly inverted, amplified and shifted before passing to the ADC, which measures in the range of 0 to 5 V.** There is an older project of Paul Stoffregen, who accomplished this transformation using five operational amplifiers, of which two act as a sample-and-hold circuits, storing the two voltage levels of dark and saturated signal [14]. A circuit of two potentiometers and only one operational amplifier was used here instead, as both the dark and the saturated voltage levels both prove to be relatively stable. If only one colour component becomes saturated, the output signal gets distorted and therefore unusable. Accordingly, the signal range should be stretched so that full saturation of single colour component corresponds to full

saturation of the signal entering the ADC. In other words, the output signal must be amplified with gain enough to prevent the saturation of any colour component in CCD. The circuit with inverting preamplifier and microcontroller is shown in Fig. 10. Let us denote the CCD output voltage as  $V_{ccd}$ , the voltage reference from R1A,B as  $V_{ref} = R_{1A} / (R_{1A} + R_{1B}) \cdot 5 \text{ V}$  and the voltage at the output of the operational amplifier as  $V_{adc} = V_{adc}(V_{ccd}, V_{ref})$ . Taking into account that the operational amplifier inputs virtually no current, one obtains that

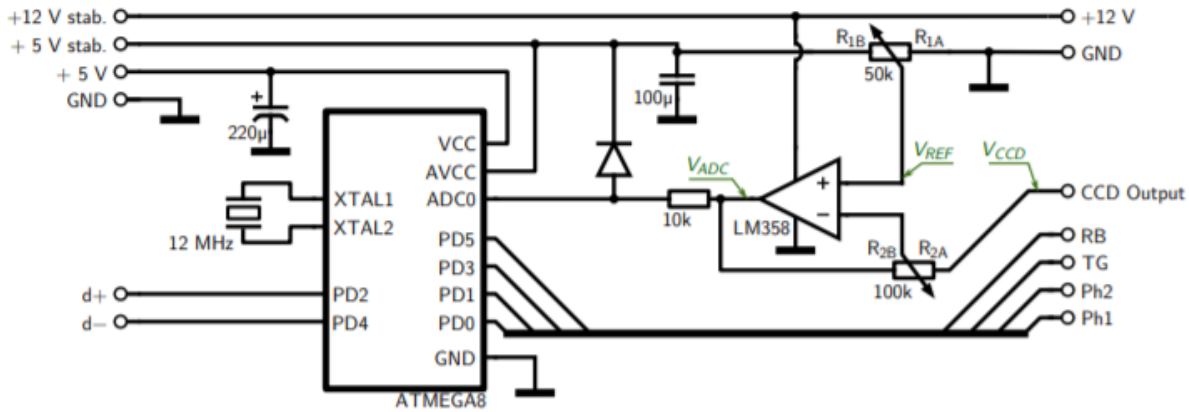


Figure 44: The microcontroller circuit. At its left side it is connected to the supply circuit, at right to the CCD detector

$$\frac{V_{ccd} - V_{ref}}{R_{2A}} = \frac{V_{ref} - V_{adc}}{R_{2B}}$$

and after simple arrangement

$$V_{adc} = \frac{R_{2A} + R_{2B}}{R_{2A}} \cdot V_{ref} - \frac{R_{2B}}{R_{2A}} \cdot V_{ccd}$$

This proves that if not saturated, the operational amplifier performs the desired linear transformation. The voltages do not have to be known precisely, as the potentiometers R1, R2 may be tuned depending on the waveform in computer. The amplification factor should be between 3 and 5. The operational amplifier supply voltage has to be 12 V, which presents a risk of destroying the ADC circuit by excess voltage, as the maximum input voltage of ADC is limited to 5.3 V in this case [3]. In order to prevent this, a 10 kΩ series resistor and a diode with low voltage drop limit the ADC input voltage, as shown at Fig. 10

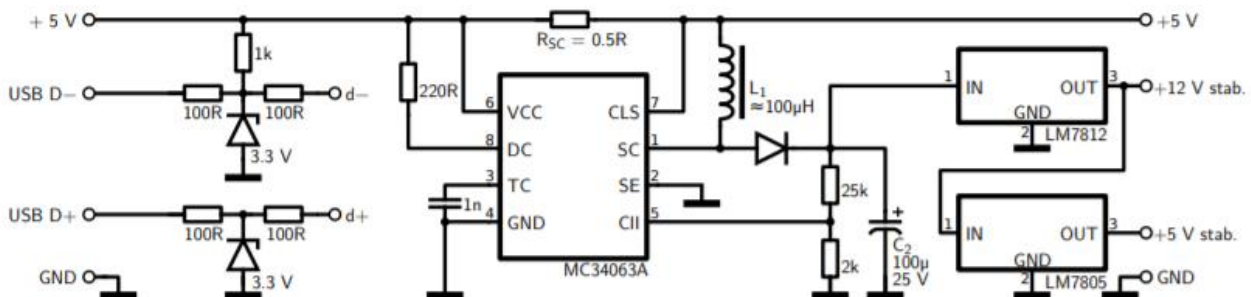


Figure 45: The supply circuit. At its left side it is connected to the computer via USB cable.

### 48.1.2 Supply circuit

The supply circuit converts the noisy 5 V USB voltage supply to stabilized 12 V required by the CCD detector and to additional stabilized 5 V for the ADC. Additionally, it limits the USB signalling levels to 3.3 V as required by the specification [16]. For the voltage conversion, a boost converter integrated circuit MC34063 was used. In short, the circuit senses the output voltage at the CII (comparator inverted input). When the voltage drops below 1.25 V, the SC (switch collector) shorts to ground, letting the current through the L1 coil and Rsc grow. The CLS (current limit sense) voltage drops as the current increases and when the voltage drop exceeds approximately 300 mV, the SC pin closes. The energy stored in the L1 coil creates an impulse of higher voltage that charges the C2 capacitor. The C1 capacitor determines the time interval of operation. The output voltage is given by the voltage divider parallel to the C2. The selected resistances of 25 k $\Omega$  and 2 k $\Omega$  set the minimum C2 voltage to 16 or 17 V. This voltage is limited by the LM7812 and LM7805 stabilizers to 12 V and 5 V, respectively. Reducing the C2 voltage would increase efficiency, but risk of negative ripple in the 12 V stabilized output would be present due to the voltage drop at LM7812. The USB signalling wires D+, D- are connected according to the figure 8.

### 48.1.3 Spectrometer casing

The spectrometer was cased in a black PVC box with dimensions 190  $\times$  90  $\times$  50 mm. About a half of the box is occupied by the optical mount, the rest contains the two circuits. The optical mount is fixed to the front panel by two M3 bolts with head containing a nut, which are common e. g. in older 17 computer connectors. This enables the user to fix some light source or cuvette in front of the input slit (or vice versa, attach the spectrometer onto a bigger device output) easily. These two bolts, as well as whole optical mount, were not connected to the USB ground to prevent accidental short-circuit or ground loop. Although the matt inner side of the plastic box has low reflection itself, the cylindrical mirror and CCD were additionally covered by a folded sheet of black paper to minimize the stray light coming directly from the input slit or any tiny hole left in the plastic case.

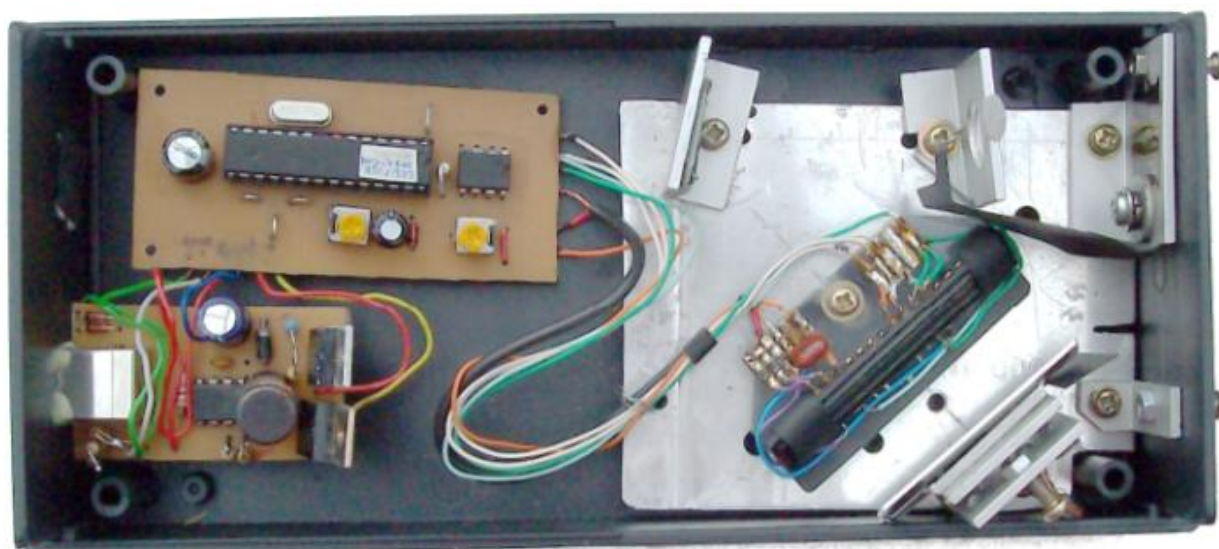
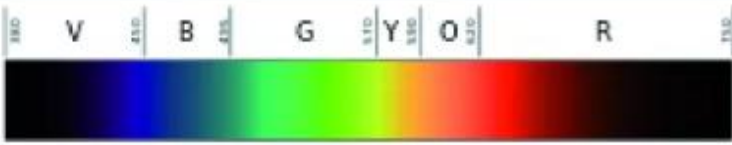


**Figure 46: A view of the assembled spectrometer without top cover and paper light shielding. The light passes through the input slit at the top right and follows the path indicated at Fig. 5. At the left, there are the converter and microcontroller circuits and USB output.**



Color	Wavelength	Frequency	Photon energy
Violet	380–450 nm	668–789 THz	2.75–3.26 eV
Blue	450–495 nm	606–668 THz	2.50–2.75 eV
Green	495–570 nm	526–606 THz	2.17–2.50 eV
Yellow	570–590 nm	508–526 THz	2.10–2.17 eV
Orange	590–620 nm	484–508 THz	2.00–2.10 eV
Red	620–750 nm	400–484 THz	1.65–2.00 eV

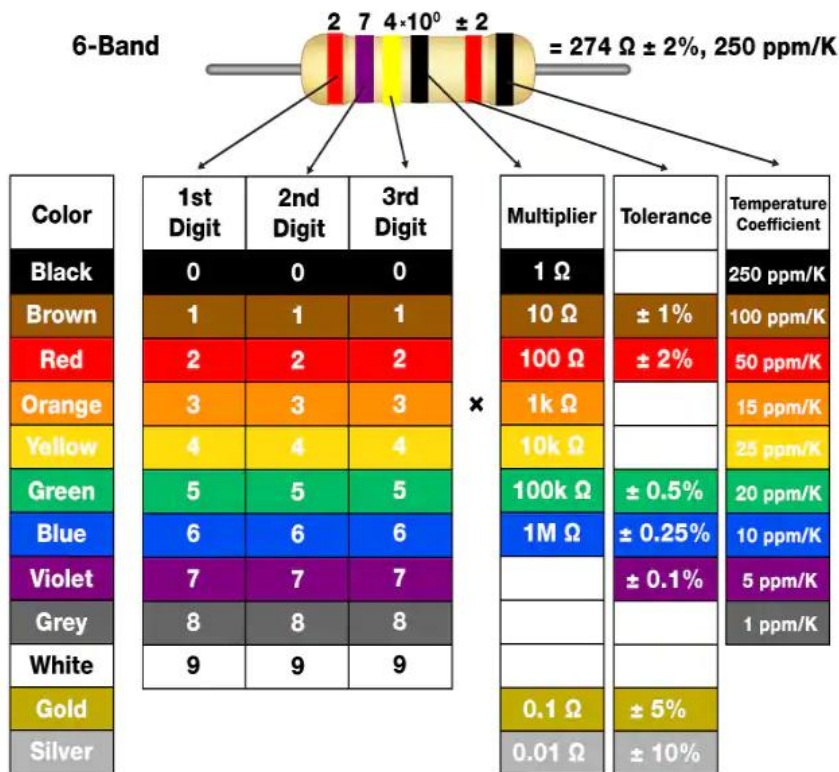
Figure 47:properties of colors

#### 48.2 Minimal circuit between USB and microcontroller

- 10-bit converter
- microcontroller:ATmega8-16PU(1 kb)
- Single USB cable :communication
- converter circuit MC34063
- 12.000 MHz quartz oscillator.
- NEC μPD3799 CCD detector (four signal wires are needed: the phase 1 and phase 2 signals, the RB (reset gate) and the TG (transfer gate) signals): silicon CCD ,400-900 nm)
- LM7812 and LM7805 stabilizers
- Resistors :25 kΩ ,2 kΩ, 1 kΩ ,100Ω(4) ,220 Ω,0.5 Ω,100k Ω ,50 kΩ,10k Ω
- Capacitor: 100 microF,100 nF,220microF
- Bobine:100microH
- Zener diodes.:3.3 V(5V),nb=2
- Circuit MC34063 w

Note :Yellow signifie that it is available in our lab.

## How to Read Resistor Color Codes



### 48.3 Microcontroller firmware

In this section, the full microcontroller firmware written in the C language (except for the USB driver) will be described, as it well illustrates the device function. The code comments were mostly maintained. The microcontroller was programmed via the serial programming interface using a USBasp hardware programmer and the avrdude program. The firmware code was compiled on Linux (Ubuntu 10.04) in avr-gcc compiler and it was loaded into the microcontroller flash memory with commands:

```
1 avr-gcc -g -Wall -O1 -mmcu=atmega8 -c main.c -o main.o
2 avr-gcc -g -Wall -O1 -mmcu=atmega8 main.o -o main.elf
3 avr-objcopy -j .text -j .data -O ihex main.elf main.hex
4 sudo avrdude -p m8 -c usbasp -U flash:w:main.hex
```

To enable the 12 MHz clock, two reserved bytes in the persistent microcontroller memory, called fuses, must be set to hexadecimal values of 0xff for lfuse and 0xd9 for hfuse.

```
1 sudo avrdude -p m8 -c usbasp -U lfuse:w:0xff:m -U hfuse:w:0xd9:m
```

During experiments, the fuses have been set wrong several times, which disabled also the serial programming needed to set fuses back. This was fixed by a parallel programming fuse resetting tool

General constants and procedures

**At the beginning, the essential header files from the avr-libc library are included.**

```
1 #include <avr/io.h>
```

```
2 #include <avr/wdt.h>
3 #include <avr/interrupt.h>
4 #include <util/delay.h>
5 #include <avr/eeprom.h>
6
7 #include <avr/pgmspace.h>
8 #include "usbdrv/usbdrv.h"
9 #include "usbdrv/oddebug.h"
```

To make the CCD driving routines clear, each CCD pin is referenced by its name from the datasheet instead of a simple port number. The CLB and SHB signals are predefined for the case that a CCD with more complicated driving signals is used. This definition enables to change the connection easily if needed.

```
1 // PORTD pins definition to comply with datasheet
2 #define PH1 BV (PD0)
3 #define PH2 BV (PD1)
4 #define TG123 BV (PD3) // Transfer gates (R+G+B)
5 #define RB BV (PD5) // Reset gate clock
6 #define CLB BV (PD6) // Reset feed-through level clamp clock (disabled)
7 #define SHB BV (PD7) // Sample and hold clock (disabled)
```

The following part contains the USB report descriptor, which is sent when the device is recognized by the computer. Further USB settings are set in the `usbdrv.h` file which is provided with the USB driver.

```
1 PROGMEM char usbHidReportDescriptor[22] = { /* USB report descriptor */
2     0x06, 0x00, 0xff, // USAGE PAGE (Generic Desktop)
3     0x09, 0x01, // USAGE (Vendor Usage 1)
4     0xa1, 0x01, // COLLECTION (Application)
5     0x15, 0x00, // LOGICAL MINIMUM (0)
6     0x26, 0xff, 0x00, // LOGICAL MAXIMUM (255)
7     0x75, 0x08, // REPORT SIZE (8)
8     0x95, 0x80, // REPORT COUNT (128)
9     0x09, 0x00, // USAGE (Undefined)
10    0x0b2, 0x02, 0x01, // FEATURE (Data, Var, Abs, Buf)
11    0xc0 // END COLLECTION
12};
```

Here we define further constants: the number of all CCD pixels and the remaining space in memory to save the buffer. The full RAM size of Atmega8 is 1 kB, of which some bytes are occupied by

variables and stack and other bytes are required for the USB driver. Approximately 920 bytes remain to store the data buffer in this configuration.

The BufMsrPos and BufBitPtr denote the position in the buffer to write the 10 bits measured by ADC. The latter variable points to the bit at which the value shall be written, as is described later.

The CCDMsrPos variable is incremented after measurement of each pixel to indicate when the CCD has been read out. The BufReadPos stores the position in the buffer which will the data transmission start from. Following variables will be described later.

```
1 #define PIXELS COUNT 5400
2 #define MSR BUF SIZE 900
3 static unsigned char buf[ MSR BUF SIZE ];
4 static int BufMsrPos ;
5 static char BufBitPtr ;
6 static int CCDMsrPos ;
7 static int BufReadPos ;
8 static unsigned int Integr Time ;
9 static char Status ; // indicates the status of measurement or transmission
```

This procedure creates a short delay of approximately  $2 \mu\text{s} \cdot \text{num}$ . It is needed to hold the minimum timings when driving the CCD.

```
1 void delay(unsigned int num)
2 {
3     unsigned int i, j;
4     for(j=0; j<2; j++)
5     for(i=0; i<num; i++)
6 ;
7 }
```

## 48.4 CCD driving

Following three procedures are used to drive the CCD. They may need to be modified if different CCD is used. The first procedure performs one CCD register shift, It both begins and ends in the phase 1 state. A minimum delay of 110 ns is required for each phase [4].

```
1 void CCDShiftReg() // expects the CCD to be in the phi2 state
2 {
3     PORTD = (PH1); // inverse RB strobe
4     PORTD = (PH1 | RB);
5     delay(0);
6     PORTD = (PH2 | RB);
7     delay(0);
8 }
```

The CCDTransferGate procedure initiates the CCD readout by transferring the charge from the photodiodes. When the transfer gate signal is activated, ten cycles of reset gate strobes are sent to the CCD, as is recommended [4].

```
1 void CCDTransferGate ()
2 {
3   int j;
4   PORTD = (PH1);
5   PORTD = (PH1 | RB);
6   delay(2);
7   for(j=0; j<10; j++) { //transfergate
8     PORTD = (PH1 | TG123);
9     PORTD = (PH1 | TG123 | RB);
10    delay(1);
11  }
12  PORTD = (PH1 | RB);
13  delay(2);
14  PORTD = (PH2 | RB);
15  delay(1);
16 }
20
```

The FlushCCD procedure first performs several full readouts to drain all excess charge from the CCD (the more sensitivity was set, the more readouts are used). When the CCD was not used for a while, this does not drain the charge at once and several such cycles are needed.

After this, an integration period begins. Its duration is determined by the IntegrTime global variable, as the delay here is accomplished by running the ADC repeatedly each 32 CCD steps. The sampling speed is approximately 10,000 samples per second. Therefore, the IntegrTime value of 32 sets the integration time to half a second. Finally, the CCDTransferGate enables the measurement.

The sensitivity is roughly proportional to the integration time. However, two effects limit the integration time to approximately one second: first, the spectrometer does not respond to USB messages, causing USB timeouts when integrating too long, and secondly, the CCD charge volatility creates a significant background signal. To improve the sensitivity, the CCD would probably have to be cooled by a Peltier element and the integration should be controlled by asynchronous timer. The best way to detect weak signals in the current setup is to set moderate sensitivity and average multiple spectral measurements.

```
1 void FlushCCD () {
2   int j, i, k;
3   PORTB |= BV(PB0);
4   CCDTransferGate(); //read the CCD to drain all charge
5   for(i=0; i<IntegrTime; i++){
```

```

6   for (j=0;j<PIXELS COUNT;j++){ CCDShi ftReg ();};
7   CCDT ran s fe rGa te ();
8   }
9   for (j=0;j<PIXELS COUNT;j++){
10  for (i=0;i<IntegrTime;i++){//delayloop
11   k++;
12   if (k%32==0){
13     ADCSRA |= BV (ADSC);
14     while (!(ADCSRA & BV (ADIF)));
15     ADCSRA |= BV (ADIF);
16     k~=0;
17   }
18 }
19 CCDShi ftReg ();
20 };
21 CCDT ran s fe rGa te ();
22 PORTB &= ~( BV (PB0));
23 }

```

#### 48.4.1 USB communication

As noted above, the USB communication is ensured by a software driver by Hans Starkjohann (Objective Development GmbH) [13]. The USB driver has relatively low requirements, as it occupies no more than 1.5 kB of program code. These definition will be used later in the following routines.

```

1 //Spectrometer commands received via USB
2 #define COMMAND SET MEASURE 100
3 #define COMMAND READ CALIB AMPLI 101
4 #define COMMAND WRITE CALIB AMPLI 111
5 #define COMMAND READ CALIB LAMBDA 102
6 #define COMMAND WRITE CALIB LAMBDA 112
7
8 //Status
9 #define STATUS IDLE 0
10 #define STATUS CCD PENDING 1
11 #define STATUS CCD INTEGRATING 2
12 #define STATUS SAMPLING 3
13 #define STATUS BUFFER READY 4
14 #define STATUS CALIB READING 10
15 #define STATUS CALIB WRITING 11
16 //Room for calibration data in EEPROM
17 #define CALIB BYTES PER POINT 4
18 //EEPROM bytes 9...410 reserved for amplitude calibration data
19 #define CALIB AMPLI POINT NUMBER MAX 100

```

```
19 #define CALIB AMPLI BUFPTR 9
20 // EEPROM bytes 411..511 reserved for lambda calibration data
21 #define CALIB LAMBDA POINT NUMBER MAX 25
22 #define CALIB LAMBDA BUFPTR 411
```

The `usbFunctionSetup` procedure is called by the driver always when a read or write packet arrives.

The type of packet can be obtained from the `rq->bRequest` structure.

```
1 usbMsgLen usbFunctionSetup(uchar data[8])
2 {
3     usbRequest *rq = (void *) data;
4     if ((rq->bmRequestType & USBRQ_TYPE_MASK) == USBRQ_TYPE_CLASS) {
5         if (rq->bRequest == USBRQ_HID_GET_REPORT) {
6             BufReadPos = 0;
7             return USB_NO_MSG; // use usbFunctionRead() to obtain data
8         }
9         else if (rq->bRequest == USBRQ_HID_SET_REPORT) {
10            return USB_NO_MSG; // use usbFunctionWrite() to receive data from host
11        }
12    } else {
13        // ignore vendor type requests, we don't use any
14    }
15    return 0;
16 }
```

The write packet contains data transmitted from the computer. Whereas the `usbFunctionSetup` is called once the packet arrives, the driver calls the following function `usbFunctionWrite` repeatedly, supplying the payload data in 8-byte chunks. All actions of the spectrometer are initiated by an incoming USB message from the computer. The first byte of the message describes the command, as is defined above in the `#define COMMAND. . .` block. Possible commands are to start spectral measurement, to read or write the wavelength or amplitude calibration. Once a `COMMAND SET MEASURE` message arrives, the spectrometer sets the integration time, flushes the CCD, starts the integration time, samples the data read from the CCD and stores the data in internal buffer. These steps can take up to several seconds and would cause USB timeout error if they were all done within the `usbFunctionWrite` procedure. Instead, only the Status variable is set here to `STATUS CCD PENDING` and all mentioned tasks are performed later in the main loop. The `COMMAND READ CALIB AMPLI` and `COMMAND READ CALIB LAMBDA` both set the Status variable into the

STATUS CALIB READING. The difference is in the initial EEPROM pointer value only.

```

1 static uchar   EEPROMPtr;
2 static uchar   CalibDataPointNumber;
3 static uchar   bytesRemaining;
4 uchar   usbFunctionWrite(uchar *data, uchar len)
5 { // Longer tasks may not be handled here. Instead, set the Status variable and
   // perform them in the main routine later.
6   if (Status == STATUS_CALIB_WRITING) {
7     if(bytesRemaining == 0)
8       return 1; // end of transfer
9     if(len > bytesRemaining) {
10      len = bytesRemaining;
11      Status = STATUS_IDLE;
12    }
13    eeprom_write_block(data, (uchar *)0 + EEPROMPtr, len);
14    EEPROMPtr += len;
15    bytesRemaining -= len;
16    if (bytesRemaining == 0) {
17      Status = STATUS_IDLE;
18      return 1; // return 1 if this was the last chunk
19    } else return 0;
20  }
21 }
22 // if first chunk of USB message, decide the command from the 1st byte
23 if (Status == STATUS_IDLE)
24   switch (data[0]) {
25     case COMMAND_SET_MEASURE: {
26       // if not zero, the two bytes set the sensitivity (integration time):
27       if (data[1]+data[2] != 0) {IntegrTime = data[1]*256 + data[2];};
28       Status = STATUS_CCD_PENDING;
29       return 1; // no additional data required
30       break;
31     }
32     case COMMAND_READ_CALIB_LAMBDA:
33     case COMMAND_READ_CALIB_AMPLI: {
34       // decide which memory location will be read
35       if (data[0] == COMMAND_READ_CALIB_AMPLI) {
36         EEPROMPtr = CALIB_AMPLI_BUFPTR;
37       } else {
38         EEPROMPtr = CALIB_LAMBDA_BUFPTR;
39       }
40       // number of points to be read
41       eeprom_read_block(&bytesRemaining, EEPROMPtr, 1);
42       bytesRemaining=bytesRemaining+CALIB_BYTES_PER_POINT+1;
43       Status = STATUS_CALIB_READING;
44       // no additional data required:
45       return 1;
46       break;
47     }
48     case COMMAND_WRITE_CALIB_LAMBDA:
49     case COMMAND_WRITE_CALIB_AMPLI: {
50       // number of points to be written
51       bytesRemaining = data[1]*CALIB_BYTES_PER_POINT;
52       if (data[0] == COMMAND_WRITE_CALIB_AMPLI) {
53         EEPROMPtr = CALIB_AMPLI_BUFPTR;
54       } else {
55
56         EEPROMPtr = CALIB_LAMBDA_BUFPTR;
57       }
58       // 1st byte of EEPROM block stores number of points:
59       eeprom_write_block(data+1, EEPROMPtr, 1);
60       EEPROMPtr++;
61       Status = STATUS_CALIB_WRITING;
62       // last 6 B of this chunk discarded, next chunk will contain data
63       return 0;
64       break;
65     }
66 }

```

The `usbFunctionRead` function is called when the computer asks the spectrometer for measured data. Naturally, the action depends on the `Status` variable: if the spectrometer finished the measurement recently, the spectral data are sent; if the microcontroller was requested for its calibration data, the corresponding EEPROM block is sent. Otherwise, no action is performed and the function returns 0 to indicate that no more data are available.

The USB specification limits the payload data length to 8 bytes for USB low-speed devices; however this would make the communication slow. Therefore, an extended length of packet up to the buffer size is used. This bigger size of packets is common for high-speed devices and it has been tested to work flawlessly, enabling to quickly transport the whole buffer in a single USB message.

```
1 uchar  usbFunctionRead(uchar *data, uchar len)
2 {
3     if (Status == STATUS_IDLE) {           // no command set
4         return 0;
5     }
6     if (Status == STATUS_BUFFER_READY) {   // Transmit the buffer with
7         spectrum to the computer.
8         if (len > (BufMsrPos - BufReadPos - 1)) { // buffer will be depleted, read
9             the left bytes
10            len = (BufMsrPos - BufReadPos);
11            if (CCDMsrPos < PIXELS_COUNT) {Status = STATUS_SAMPLING; BufBitPtr = 0;
12                BufMsrPos = 0;}
13            else {Status = STATUS_IDLE;};
14            BufMsrPos = 0;
15        }
16        int DataPos;
17        for (DataPos=0; DataPos<(len); DataPos++) {
18            data[DataPos] = buf[BufReadPos + DataPos];
19            buf[BufReadPos + DataPos] = SENT_BUF_STUFF;
20        };
21        BufReadPos += len;
22        return len;
23    }
24    if (Status == STATUS_CALIB_READING) {   // transmit the calibration data
25        from EEPROM
26        if (len > bytesRemaining) {
27            len = bytesRemaining;
28            Status = STATUS_IDLE;
29        }
30        eeprom_read_block(data, (uchar *)0 + EEPROMPtr, len);
31        EEPROMPtr += len;
32
33        bytesRemaining -= len;
34        return len;
35    }
36    return 0;
37 }
```

---

### 48.5 The main loop

This loop is called after the microcontroller starts and its clock stabilizes. During this loop the microcontroller continuously polls the USB driver for incoming packets, which is required to ensure reliable communication, and performs the action the `Status` variable describes. After the CCD readout is finished, the `Status` variable is finally set to the `STATUS_BUFFER_READY` value. In a consequent read request from computer, the spectrometer sends the data in one or more USB packets and `Status` is set back to `STATUS_IDLE`.

```

1 int main(void)
2 {
3   DDRB |= _BV(PB0) | _BV(PB1); DDRD |= (TG123 | PH1 | PH2);   DDRD |= (RB | CLB |
   SHB); // enable output pins
4   ADMUX = 0; ADCSRA |= _BV(ADEN) | _BV(ADPS2) | _BV(ADPS2); // A/D converter
   settings
5   odDebugInit(); usbInit(); usbDeviceDisconnect(); // enforce re-
   enumeration
6   unsigned char i; i = 0; while(--i){wdt_reset(); _delay_ms(5); } // fake USB
   disconnect for > 250 ms
7   usbDeviceConnect(); sei();
8   IntegrTime = 1;
9   BufMsrPos = 0;
10  CCDMsrPos = 0;
11  Status = STATUS.IDLE;
12  for(;;){
13    usbPoll();
14    int j;
15    int MeasPerPoll = 1;
16    int PixPerMeas = 8; // buffer capacity: 900 B = 7200 b = 720 px; 5400 pix
   /8 = 675 pix
17    if (Status == STATUS.CCD.PENDING) {
18      Status = STATUS.CCD.INTEGRATING;
19      // erase buffer
20      int i; for (i=0; i<MSR.BUF.SIZE; i++) {buf[i] = EMPTY_BUF.STUFF;};
21      FlushCCD();
22      BufBitPtr = 0;
23      CCDMsrPos = 0;
24      BufMsrPos = 0;
25      Status = STATUS.SAMPLING;
26    }
27    if (Status == STATUS.SAMPLING)
28      for (j=0; j<MeasPerPoll; j++)
29        if (CCDMsrPos < PIXELS.COUNT) {
30          if (BufMsrPos < (MSR.BUF.SIZE-1)) {
31            unsigned int value = 0;
32            for (i=0; i<PixPerMeas; i++) {
33              CCDShiftReg(); CCDMsrPos += 1;
34
35              ADCSRA |= _BV(ADSC);
36              while (!(ADCSRA & _BV(ADIF)));
37              ADCSRA |= _BV(ADIF);
38              // 10 bits ADC input, always read ADCL first
39              value += ADCL + 256*(ADCH&3);
40            }
41            // average from several measurements
42            value = value / PixPerMeas;
43            char BitNumber = 10;
44
45            // remove leading zeros
46            unsigned int svalue = value << (16 - BitNumber);
47            int ValBitPtr = 0;
48            // compresses 4 pixels + 10 bits to 5 bytes
49            while (ValBitPtr < BitNumber) {
50              int ChunkLen = 8 - BufBitPtr;
51              if (ChunkLen > BitNumber-ValBitPtr) {ChunkLen = BitNumber-
52                ValBitPtr;};
53              unsigned char Chunk = ((svalue << ValBitPtr) >> BufBitPtr) >>
54                8;
55              unsigned char Mask = ~(0xFF >> BufBitPtr);
56              buf[BufMsrPos] = (buf[BufMsrPos] & Mask) | (Chunk & 0xFF);
57              ValBitPtr += ChunkLen; BufBitPtr += ChunkLen;
58              if (BufBitPtr >= 8) {BufBitPtr -= 8; BufMsrPos++;}
59            }
60          } else {
61            BufBitPtr = 0;
62            Status = STATUS.BUFFER_READY; // buffer full, wait until the
63            computer reads the data
64          }
65        }
66      } else {
67        Status = STATUS.BUFFER_READY; // whole CCD read, wait
68      }
69    }
70  }
71  return 0;
72 }

```

The used CCD detector had much more pixels than the microcontroller could hold in the buffer at once.

Although full CCD data could be read and transmitted sequentially, this was problematic due to the sawtooth bias. The need to fit the full CCD readout into the 7200 bits long buffer has lead to these two measures:

1. As the microcontroller has a 10-bit analog-to-digital converter, the measured values are compressed on the fly so that each value does not occupy 16 bits as in an integer, but only the significant 10 bits. Theoretically, the 7200 bit buffer can hold 720 measured points.
2. The total pixel number was 5400. Dividing this by 8 we obtain 675 measured points, which fits the buffer the best. Accordingly, eight pixels were read sequentially and then averaged.

This reduced the noise significantly, but did not spoil the spectral accuracy much, because the optical imprecision manifested even in the reduced pixel number.

### 48.6 Computer software

The software in computer was split into two programs:

1. the backend ensures communication with the spectrometer and transforms the data according to the wavelength and amplitude calibration,
2. and the frontend, which provides graphical user interface and, calling the backend repeatedly, presents the measured spectra in real time.

#### 48.6.1 Command line backend for USB communication

The backend is written in C, compiled using the Gnu Compiler Collection (gcc, version 4.4.3). It was developed and tested under Linux 2.6, but it is designed to compile and run under Windows and other operating systems, too. Under Linux, the backend depends on libusb, on Windows it depends on the Driver Development Kit (DDK), which should be shipped along with MinGW compiler [13]. The full code is included in the attached CD and it will not be listed here. The commandline backend accepts several commands. The first parameter determines the action performed and optional parameters are in square brackets:

1. set measure [integration time] starts the measurement, integration time ranges from 1 to approx. 200
2. get spectrum receives, transforms and writes out the spectrum to the stdout
3. write calib ampli lambda1:amplitude1,[lambda2:amplitude2,...] write amplitude calibration to the EEPROM
4. write calib lambda pixel1:lambda1,[pixel2:lambda2,...] write wavelength calibration
5. read calib ampli [--short] reads amplitude calibration from the EEPROM
6. read calib lambda [--short] write wavelength calibration Usually the get spectrum command is called soon after the set measure was called. (These commands

do never have to be joint together into one command, as the spectrometer requires about half a second to measure the spectrum and much longer wait periods can occur if longer integration time is needed.

Such single command would halt the backend from responding. This would consequently either cause the frontend not to respond for a while or it would require to implement multiple threads.)

The calibration write commands use the second parameter to set the calibration points in the EEPROM. Each calibration point occupies 4 bytes in the EEPROM. See the README file for more information.

For wavelength calibration, pairs of pixel number and corresponding wavelength in picometers have to be input in the format of pairs of integers related by colon and separated by comma. First two bytes are the integer position of the pixel. Following two bytes are the wavelength divided by 32 pm. Therefore, the wavelength of  $221 = 2,097,152$  pm is encoded as the maximum integer value  $216 = 65,536$ .

For amplitude (i. e. sensitivity) calibration, the pairs of wavelength and corresponding coefficient are used, as the sensitivity curve mostly depends not on the optical geometry, but rather on the averaged spectral sensitivity of the three CCD channels. If the projected image moves slightly, only the wavelength calibration would have to be repeated. The wavelength and the coefficient are calculated similarly as above.

### **48.6.2 Data preprocessing according to calibration**

Once the data are received in the compressed raw form, they are read sequentially to convert each 10 bits to a new integer that can be dealt with easier. For each measured point, the wavelength is calculated with spline interpolation of the calibration points.

Then, the calculated wavelength is input to the second spline interpolation, which calculates the sensitivity coefficient for the given wavelength and divides the measured data by this coefficient. The spectrum is output to stdout with two columns of tab-separated numbers, and usually this output is redirected into a file. This form of communication does not cause much holdup, because the file is stored in the disk cache and possibly does not get written to the disk until it is read by frontend and rewritten by new measurement.

### **48.6.3 Python module backend**

Two versions of the backend were written: one as a standalone binary operated from command line, the second is a python module, which can be loaded dynamically into the running python program. The graphical user interface uses this module. The functions provided by the backend module are nearly the same, except for not existing equivalent for the get spectrum parameter. The SetMeasure function not only starts the measurement, but also receives the spectrum, performs calibration transformation and return it as two lists of wavelenghts and corresponding values.

### **48.6.4 Graphical user interface**

Unlike the firmware and backend, the graphical frontend was written in the Python language with Gtk widgets. Python is an interpreted language with simple syntax and many advanced features. Its

great advantage is the number of additional modules, which facilitate various tasks. Among others, the numpy and scipy modules were included to perform mathematical operations, matplotlib to plot the interactive, antialiased graphs and gtk python module to build the graphical user interface. The gtk libraries are a widget toolkit often used to create multiplatform graphical applications. The gtk libraries are commonly installed on Linux desktops by default, under Windows, one has to download and install them. Both python and gtk are released under free licenses compatible with GPL [7], [15]. Thanks to this, all the software equipment of the spectrometer can be distributed without any license costs.

The graphical user interface provides only basic functions as for now (see next Fig). It allows to switch between manual spectral measurement and automatic measurement, which runs the spectrometer repeatedly when the previous spectrum was acquired and displayed. The Sensitivity slider at the top sets the integration time to be two on the power of the value set. The most practical values are between 2 and 5. Averaging can be set either to the moving average of 2 to 64 waveforms, or to average infinitely to suppress the sampling noise. There is an option to calibrate the amplitude, which is the most important for measurement of a transmittance  $T(\lambda)$  of a sample. The calibration curves are stored in the computer memory. The spectrometer should be recalibrated always when the light source changes. It is recommended that

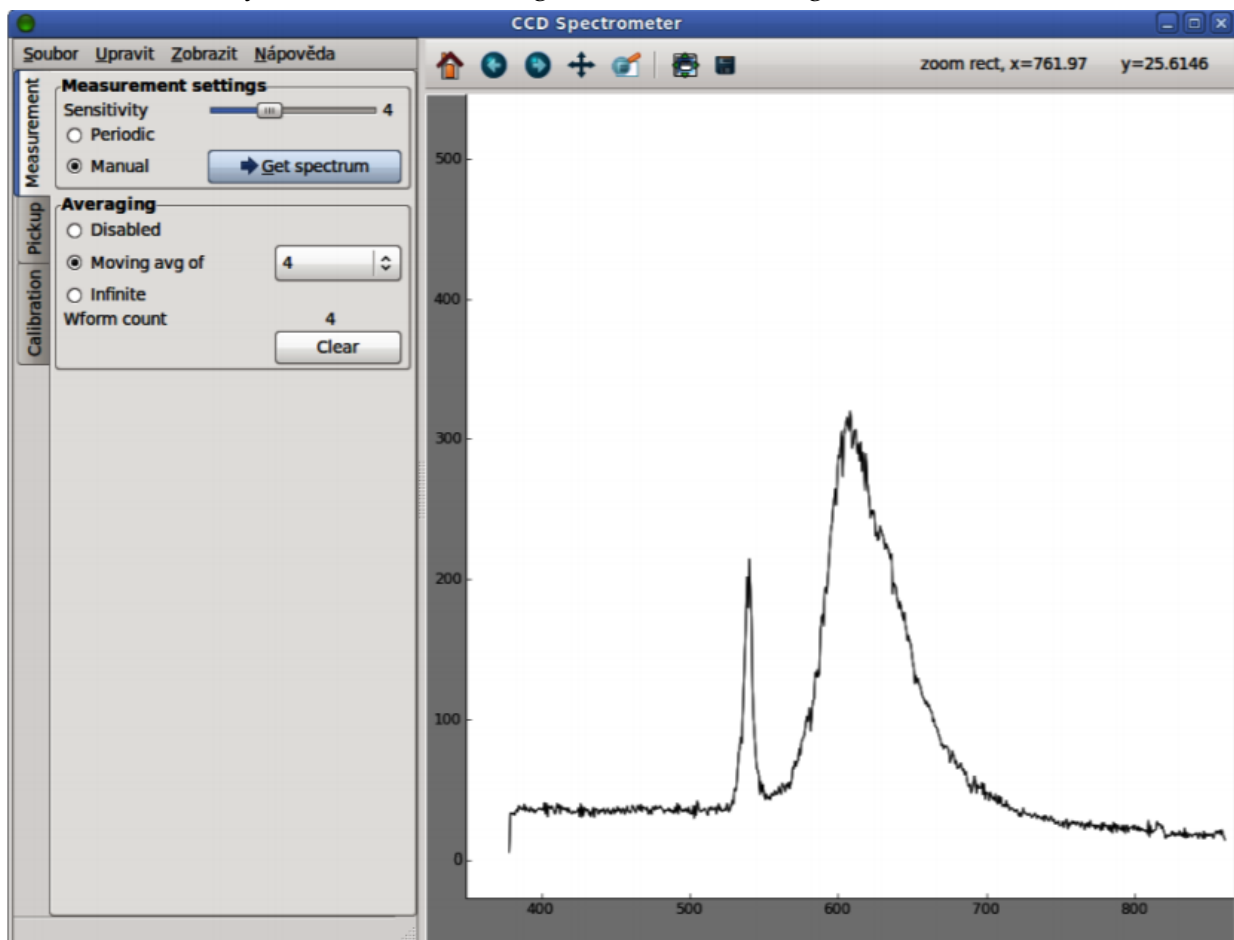


**Figure 48:** A screenshot of the graphical user interface, showing the orange-red fluorescence of a highlighter pen illuminated by a green laser pointer, whose reflection manifests as the narrow peak at 532 nm. Note also the weak component at  $\approx 810$  nm coming from the laser diode pumping the Nd:YVO4 crystal

after several minutes of CCD warm up, the source is turned off and the dark signal calibration curve  $I_D(\lambda)$  is set, then the source is turned on again without the sample and the full signal curve  $I_F(\lambda)$  is set. Long averaging time improves accuracy. When the amplitude calibration is applied to the measured signal  $I_M(\lambda)$ , the transmission  $T(\lambda)$  is calculated the following way:

$$T(\lambda) = \frac{I_M(\lambda) - I_D(\lambda)}{I_F(\lambda) - I_D(\lambda)},$$

i. e., the dark signal curve  $I_D$  is subtracted first, then the remaining extra signal is divided by the source intensity at given wavelength. To suppress noise, an intensive and broadband source, such as focused halogen bulb, is needed.

Thanks to the interactive interface of the matplotlib package, the graph may be zoomed and panned, as well as easily exported into a bitmap file.

#### 48.6.5 Calibration

The calibration procedure consists of two steps, that shall be done in the following order: the wavelength and the amplitude calibration.

For the wavelength calibration, a common compact fluorescent lamp (CFL) may be used. Such lamp contains diluted inert gas and mercury vapor and at the inner surface, a thin fluorescent layer of europium and terbium salts is sputtered. The output spectrum consists of many spectral lines

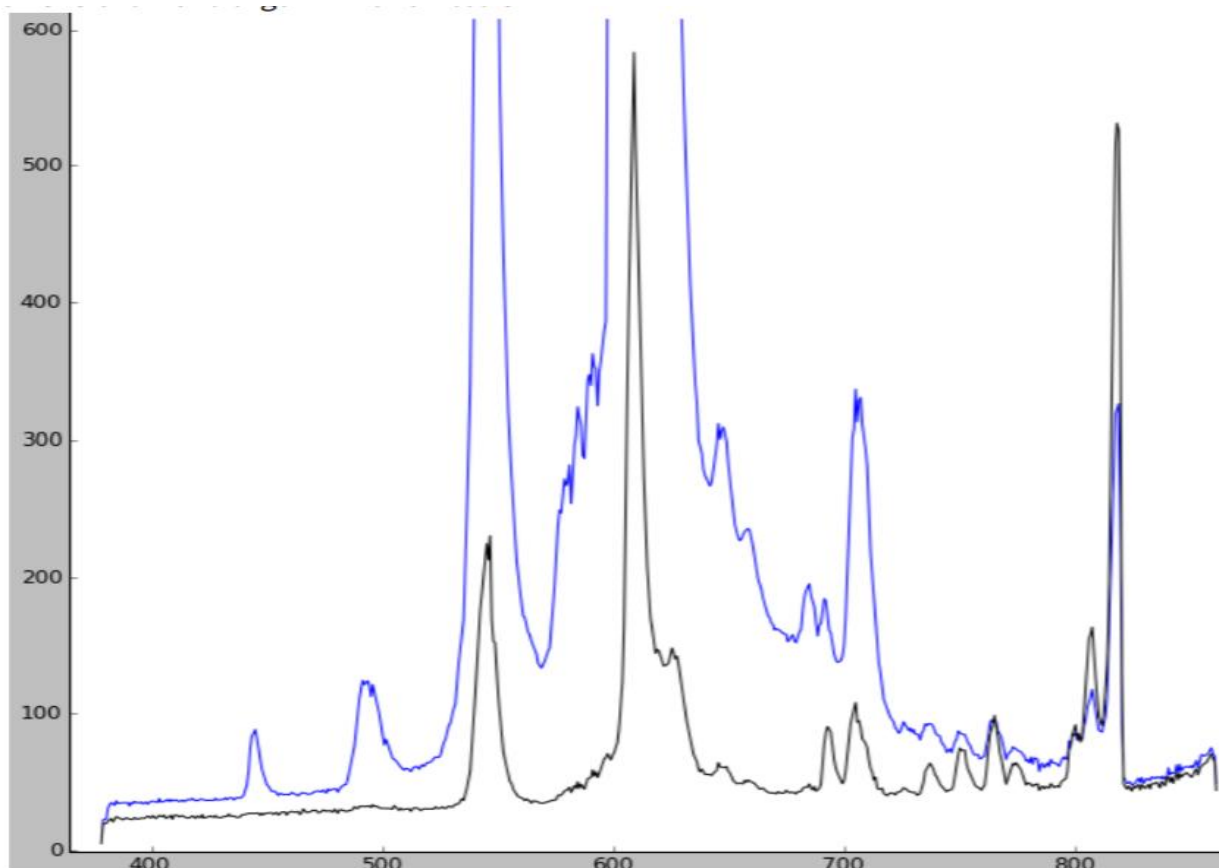


**Figure 49: Emission of a compact fluorescent lamp, 5 s after cold start (black) and  $\approx 60$  s later (blue). The horizontal axis is the wavelength in nanometer**

with different intensity and width, of which the most intensive are listed in the Table 2. The spectrum was first acquired without calibration, then the peaks were easily resolved and corresponding

calibration points were saved. As noted above, the backend uses spline interpolation/extrapolation and accordingly even for three distant enough calibration points it was possible to obtain reasonable spectral accuracy. The amplitude calibration requires a source of a broad and known spectrum. Possible candidates are a halogen bulb or common daylight. Similarly as for the wavelength calibration, several calibration points shall be calculated from the shape of uncalibrated spectrum. The value of each point is obtained as a ratio of the measured intensity to the expected real intensity of the source. It must be noted that the amplitude calibration does not take into account the linear background. This background depends on CCD temperature and sensitivity. Therefore, the background transforms to a curve that may not be easily visually subtracted without previous observation of its shape for zero input light. Additionally, it was observed that the spectrometer sensitivity varies by several percent from pixel to pixel. This can be accounted to irregularities of the cylindrical mirror or the CCD detector. Unfortunately, the corresponding compensation curves would not fit into the internal EEPROM of the microcontroller. Both unwanted effects must be compensated in the graphical user interface as the amplitude calibration curves for a particular device and light source.

*Table 2: List of the CFL spectral lines used for the wavelength calibration [17]*

Color	Origin	Peak wavelength [nm]
Dim violet	Mercury	404
Dim blue	Mercury	436
Turquoise	Terbium	485 to 490
Green doublet	Terbium and Mercury	544, 546
Red	Europium	611
Near infrared	Argon	811

## 48.7 Results

In this section, several measured spectra will be presented to illustrate the performance and shortcomings of the current design. In the Figure 11, the spectra of a starting 15 W IKEA compact fluorescent lamp is shown. This lamp was used to calibrate the spectrometer. The spectrum has been averaged from 16 measurements to suppress the noise and no amplitude calibration was used here. Initially, the argon filling emits mostly in the near infrared region. The slow start is probably caused by slow evaporation of the mercury filling, which manifests as growth of the spectral lines in visible region. Note that on the contrary, some lines intensity drops during the start. With longer averaging and proper zoom, several other lines may be resolved, such as the weak violet mercury line at 406 nm. Both the blue mercury line at 436 nm and the infrared argon line at 811 nm are emitted by diluted gas and are therefore narrow enough to assess the spectral resolution. The spectrometer measured their width at half maximum as 5 to 8 nm, which can be considered to be the maximum spectral resolution of the device. However, with proper zoom, the green peak at the 544 to 546 nm has a shallow, yet stable notch in its center. This may be accounted either to the nonuniformity of CCD response, or to the fine resolution of spectra. (Both is possible as the convolution function is probably not gaussian, but has a sharp peak instead.) The Figure 12 depicts three spectral curves measured by

passing an incandescent bulb light through a 10 mm long cuvette with pure water and two different concentrations of potassium permanganate ( $\text{KMnO}_4$ ). In low concentration, the very strong absorption in the green spectral region causes the pink tint of the solution. In higher concentration, broader spectral region from 450 to 650 nm gets absorbed. This explains the visible hue difference of different concentrations. The amplitude growth in unabsorbed regions is caused by the cuvette displacement. In this measurement, the amplitude calibration did not correct the pixel-to-pixel nonuniformity, although the spectrum was averaged from 16 measurements again. For practical application, the proper calibration for the particular source and fixed cuvette position is important.

## 48.8 Conclusion

In the above sections, a concept of a cheap, compact digital spectrometer was presented. If a CCD detector from an old scanner is used, the components cost less than 20 Euro. (A new suitable CCD can be obtained for under 10 Euro if a bigger package is requested.) The work per each next piece can be expected to be less than 5 hours, since the first prototype is tested and both the software and firmware are ready.

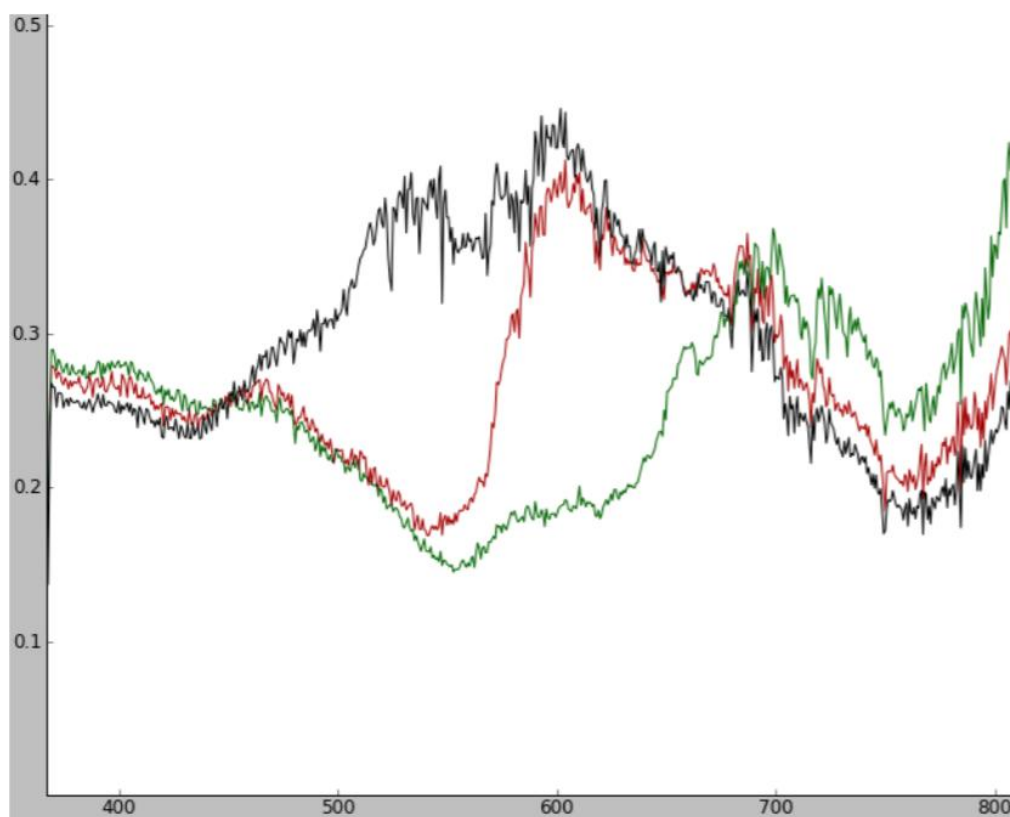
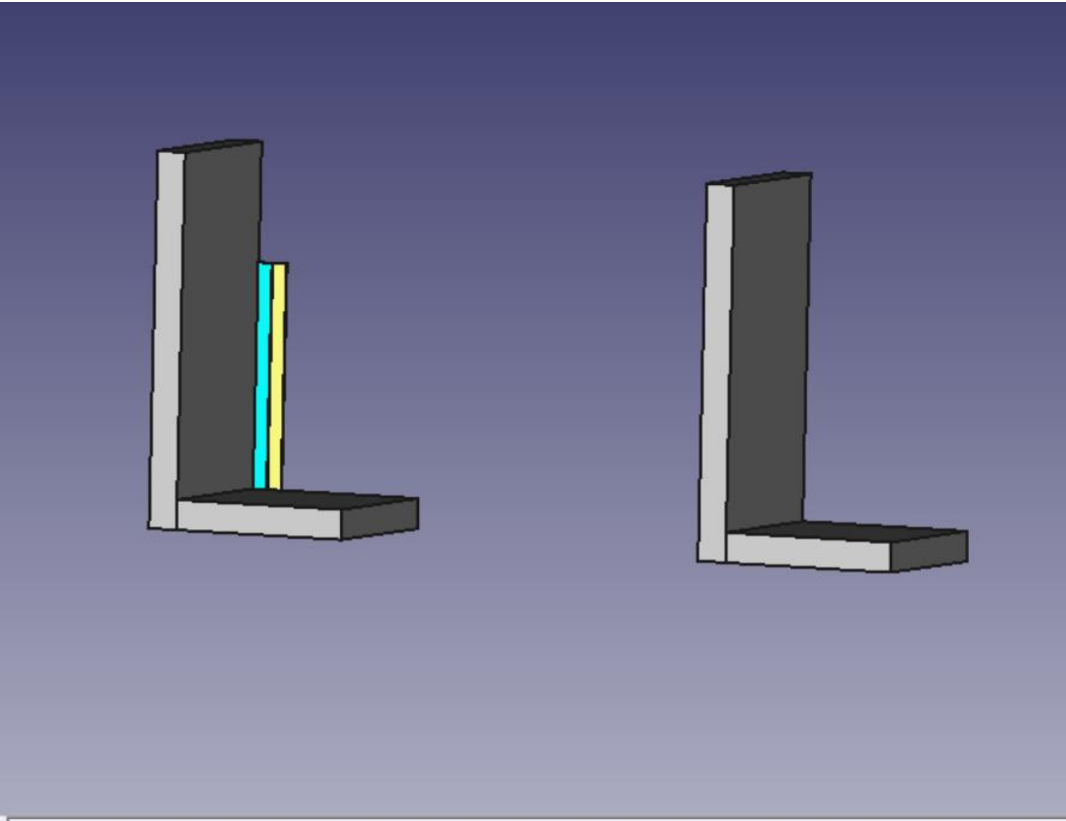
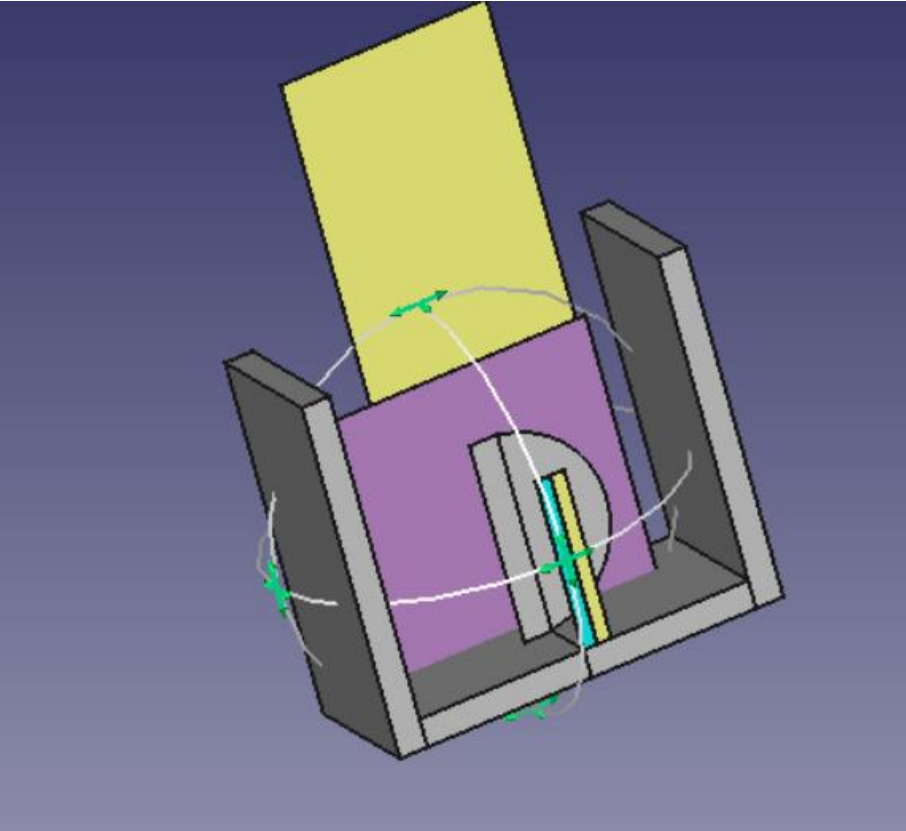


**Figure 50: Transmission of pure water (black line); of water with  $\approx 10 \mu\text{mol/l}$  solution of  $\text{KMnO}_4$  (red line) and of water with  $\approx 100 \mu\text{mol/l}$  solution thereof (green line). The horizontal axis is the wavelength in nanometers**

in the Results section it was shown that such device works with sensitivity and resolution acceptable for many tasks both in education and research. The graphical user interface makes the device relatively easy to work with. The main conclusion of this work is that it is possible to build a relatively usable, cheap and portable digital spectrometer.



# 49 Design of IAP-OSM

It was decided to use a already existing arduino kit for IAP-OSM.



بسم الله الرحمن الرحيم



## Spectroscope for Visual Data

### 1-Definition of spectroscopy

Spectroscopy is the study of the interaction between **matter** and **electromagnetic radiation**. Historically, spectroscopy originated through the study of visible light dispersed according to its wavelength, **by a prism**. Later the concept was expanded greatly to include any interaction with radiative energy as a function of its wavelength or frequency.



التحليل الطيفي هو دراسة التقاطع بين المادة والإشعاع الكهرومغناطيسي. تاريخياً، نشأ التحليل الطيفي من خلال دراسة الضوء المرئي المشتت وفقاً لطول الموجة، بواسطة المنشور. في وقت لاحق تم توسيع المفهوم إلى حد كبير ليشمل أي تقاطع مع الطاقة الإشعاعية كدالة طول الموجة.

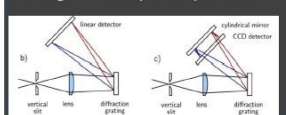
### 2-Spectrometer

A spectrometer is a scientific instrument used to **separate and measure spectral components** of a physical. The capability of spectroscopy to **determine chemical composition** drove its advancement and continues to be one of its primary uses. Much of our **knowledge** of the chemical makeup of the universe comes from **spectra**.

المطياف هو أداة علمية تستخدم لفصل وقياس المكونات الطيفية. يمكنه بقدرة التحليل الطيفي لتحديد التركيب الكيميائي الأساسية الكثير من معرفتنا للتركيب الكيميائي للكون يأتي من دراسة معرفة الأطياف.

### 3-Principle:

In the horizontal plane, the incoming light must be **spatially limited** by a **vertical slit**. Then the spatial limitation is converted to **angular limitation** using a **concave mirror** or a **convex lens**. Ideally, we obtain a parallel beam of white light. Its width is limited either by the size of the mirror or lens used, or by the angle of the beam passing through the slit. The light components of different wavelengths **separate after being reflected** into different angles by a **diffraction grating**, delivered to the **CCD**. Finally, the angular separation might be converted back to spatial separation using another lens or mirror. However, this would require a big lens with diameter similar to the length of CCD. The spatial difference would be proportional to its focal length, probably resulting in a small spatial separation.



### 4-The charge coupled device, CCD:

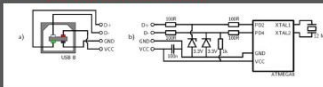
was originally designed not to be an **optical detector** but a **memory** instead. It should work as an analog shift register, storing arbitrary charge in each of its cells and reading them sequentially. Soon it was discovered that illumination causes **internal photoelectric effect** in the silicon substrate and fills up each memory cell with additional **charge proportional to the incident light intensity**.



Although CCD was rarely used as a **memory**, it found widespread application as a sensitive optical detector both in **consumer electronics** and in **high-end scientific instruments** such as **astronomical telescopes**. It should use **IMC uPD1798 CCD detector**.

### 5-Electronic setup

A common **microcontroller** The Atmega8-16PU version has 28 pins, of which 4 were occupied by DC supply, 2 by USB, 2 by oscillator, 4 by CCD driving signals and one for ADC input. The most demanding task is **the I2C communication**.



The microcontroller should be equipped by a sufficient internal analog-to-digital converter (ADC). Many contemporary microcontrollers have an internal 10-bit converter able to perform at least 10,000 samples per second, which is sufficient for this application. The microcontroller was programmed via the serial programming interface using a **USBasp hardware programmer** and the **avrduino program**. The firmware code was compiled on Linux (Ubuntu 10.04) in **avr-gcc compiler** and it was loaded into the microcontroller flash memory with commands.

### Properties of colors

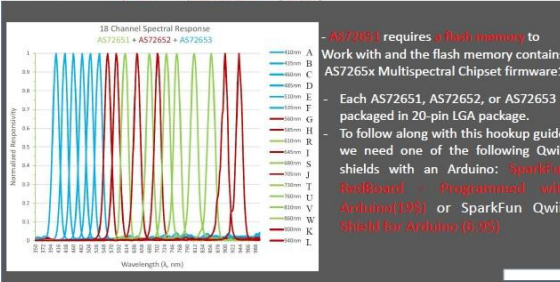
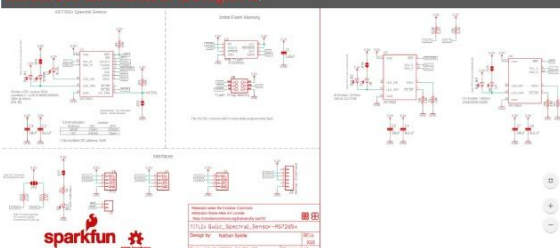
Color	Wavelength	Frequency	Photon energy
Violet	380-450 nm	668-789 THz	2.75-3.26 eV
Blue	450-495 nm	606-668 THz	2.50-2.75 eV
Green	495-570 nm	526-606 THz	2.17-2.50 eV
Yellow	570-590 nm	508-526 THz	2.10-2.17 eV
Orange	590-620 nm	484-508 THz	2.00-2.10 eV
Red	620-750 nm	400-484 THz	1.65-2.00 eV

### 6-Materials for optical setup

1. A standard aluminium L-profile 25 mm high, 2 mm thick and with 12 mm long foot.
2. The input slit was made of two razor blade segments, 15 mm long.
3. The collimating lens had 14 mm diameter, focal length  $f = 30$  mm, Plano-convex geometry
4. The cylindrical mirror was obtained from a scrap photocopier. It is a polished metal rectangle, 42x15 mm in size. Its focal length is approximately 30 mm
5. a blazed diffraction grating with 500 - 1000 grooves/mm, with size at least 8x8 mm.

### 7-Schematic of SparkFun Triad Spectroscopy Sensor - AS7265x (Qwiic)

AS7265x Multispectral Chipset consists of AS72651, AS72652, and AS72653 devices and each device has 6 optical filters so that AS7265x Multispectral Chipset have total 18 channels for spectral identification from 400nm to 1000nm with FWHM of 20nm. AS72651 is the **main device** with the **smart interface** to a microcontroller. The microcontroller gets the sensors data including AS72652 and AS72653 through **AS72651 AT commands or I2C registers**.



- AS72651 requires a **flash memory** to work with and the flash memory contains AS7265x Multispectral Chipset firmware.  
 - Each AS72651, AS72652, or AS72653 is packaged in 20-pin LGA package.  
 - To follow along with this hookup guide, we need one of the following Qwiic shields with an Arduino: **SparkFun RedBoard - Programmed with Arduino (1.95)** or **SparkFun Qwiic Shield for Arduino (1.95)**

### 8-Software Design Considerations

In most of system designs, AS72651 is controlled by a microcontroller. **With the UART interface**, the controller could **configure the devices** and get the **sensors data** through some AT commands. The software of microcontroller design would be simple. The following sections would focus on I2C interface and the software of microcontroller design should satisfy both I2C specification and AS7265x Multispectral Chipset register structure.



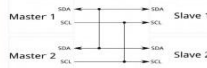
- Accessories:**
- Qwiic Cable - Breadboard Jumper (4-pin) \$1.50
  - Qwiic Cable - 100mm \$1.50
  - SparkFun Qwiic Shield for Arduino \$6.95
  - SparkFun Qwiic HAT for Raspberry Pi \$5.95
  - SparkFun Qwiic Mux Breakout - 8 Channel (\$11.95)



### 9-Arduino

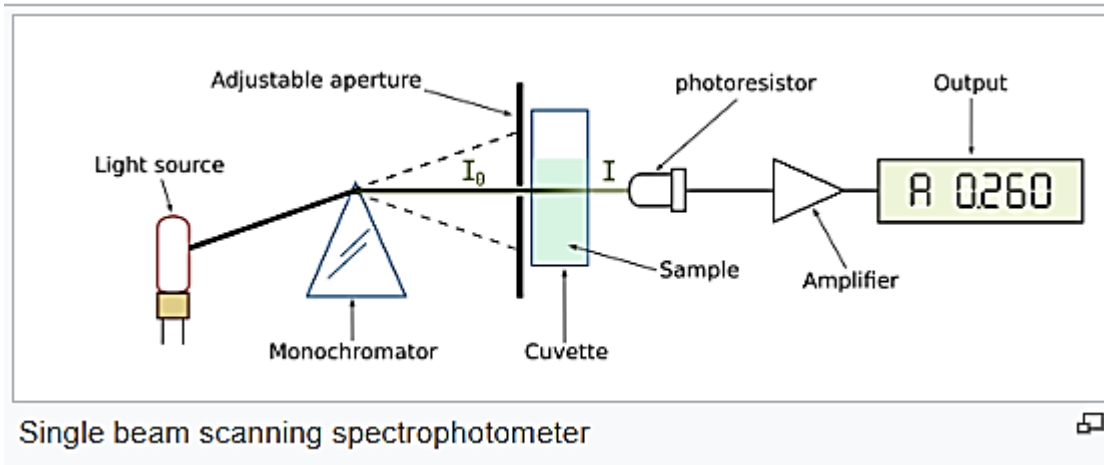
- A computer (Windows, Mac, or Linux)
- An **Arduino-compatible microcontroller** (anything from this guide should work)
- A USB A-to-B cable, or another appropriate way to connect your **Arduino-compatible microcontroller to your computer**
- **Installing Arduino IDE** (<http://www.sparkfun.com/arduino/installing-arduino-ide>)
- 2-The Inter-integrated Circuit (I2C) Protocol is a protocol intended to allow multiple "slave" digital integrated circuits ("chips") to communicate with one or more "master" chips. Like the Serial Peripheral Interface (SPI), it is only intended for short distance communications within a single device. Like Asynchronous Serial Interfaces (such as RS-232 or UARTs), it only requires two signal wires to exchange information.

**I2C-7-Qwiic-Interface:**  
 The sensors are 3.3V compatible so don't use with a 5V Arduino Uno without proper conversion (use the Qwiic shield instead!). If you're using a 3.3V development platform that doesn't have a Qwiic connector, consider using the Qwiic Breadboard Cable.



## 49.1 Optical Setup

This project aims to design, develop and build a compact digital spectrometer. The spectrum is projected with a diffraction grating on a CCD detector, sampled in a 10-bit A/D converter to the microcontroller memory and finally transmitted to the computer via USB. In the computer it is digitally processed and displayed in a graphical user interface. The spectrometer operates in the optical and near-infrared region, approximately from 400 to 900 nm, which is given by the silicon CCD detector.



## 49.2 Materials for optical setup

1. A standard aluminium L profile 25 mm high, 2 mm thick and with 12 mm long foot
2. The input slit was made of two razor blade segments, 15 mm long
3. The collimating lens had 14 mm diameter, focal length  $f \approx 30$  mm, Plano convex geometry
4. The cylindrical mirror was obtained from a scrap photocopier. It is a polished metal rectangle, 42 × 15 mm in size. Its focal length is approximately 30 mm
5. a blazed diffraction grating with 500 - 1000 grooves/mm, with size at least 8 × 8 mm

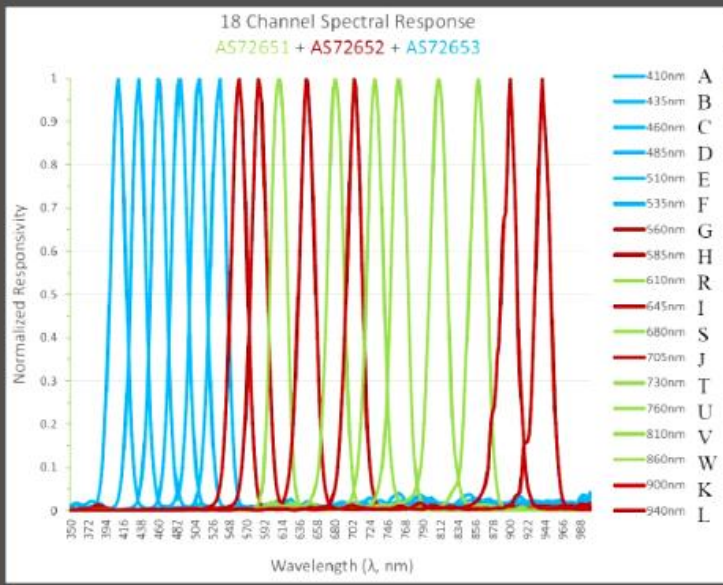
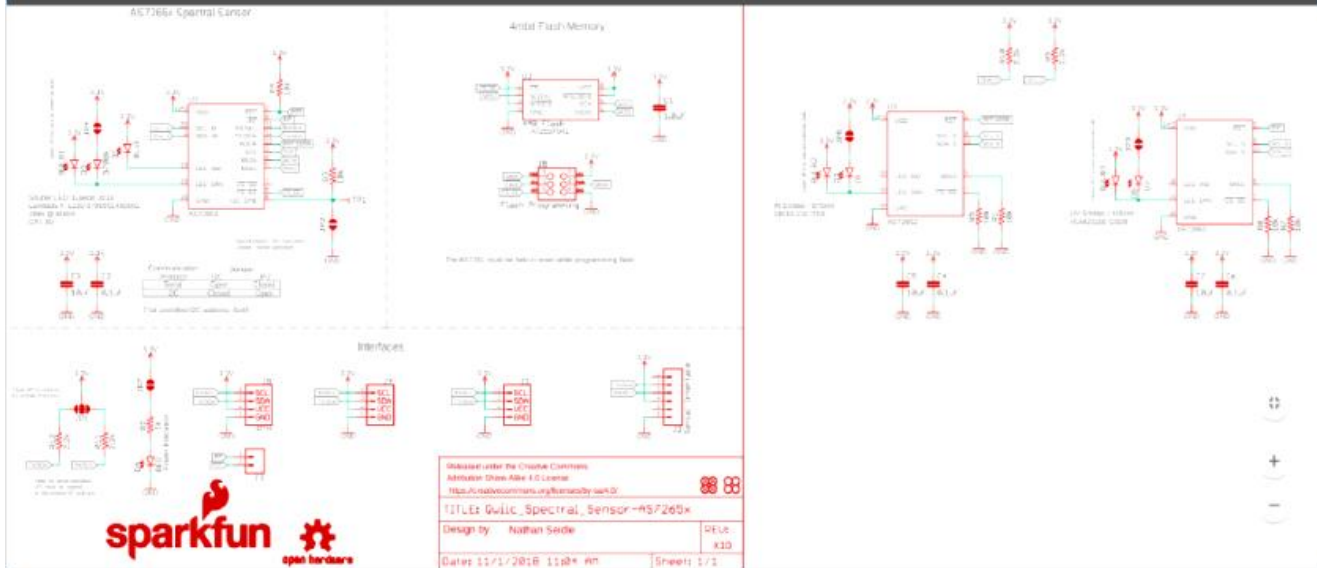
### 6-Materials for optical setup

1. A standard aluminium L-profile 25 mm high, 2 mm thick and with 12 mm long foot.
2. The input slit was made of two razor blade segments, 15 mm long.
3. The collimating lens had 14 mm diameter, focal length  $f \approx 30$  mm, Plano-convex geometry
4. The cylindrical mirror was obtained from a scrap photocopier. It is a polished metal rectangle, 42×15 mm in size. Its focal length is approximately 30 mm
5. a blazed diffraction grating with 500 – 1000 grooves/mm, with size at least 8×8 mm .

### 49.3 Schematic of SparkFun Triad Spectroscopy Sensor - AS7265x (Qwiic)

#### 7-Shematic of SparkFun Triad Spectroscopy Sensor - AS7265x (Qwiic)

AS7265x Multispectral Chipset consists of AS72651, AS72652, and AS72653 devices and each device has 6 optical filters so that AS7265x Multispectral Chipset have total 18 channels for spectral identification from 400nm to 1000nm with FWHM of 20nm. AS72651 is the **main device with the smart interface to a microcontroller**. The **microcontroller** gets the sensors data including AS72652 and AS72653 through **AS72651 AT commands or I2C registers**.



- **AS72651** requires a **flash memory** to work with and the flash memory contains AS7265x Multispectral Chipset firmware1.
- Each AS72651, AS72652, or AS72653 is packaged in 20-pin LGA package.
- To follow along with this hookup guide, we need one of the following Qwiic shields with an Arduino: **SparkFun RedBoard - Programmed with Arduino(19\$)** or **SparkFun Qwiic Shield for Arduino (6.9\$)**



### 49.4 Software Design Considerations and Arduino

In most of system designs, AS 72651 is controlled by a microcontroller with the UART interface, the controller could configure the devices and get the sensors data through some AT commands. The software of microcontroller design would be simple.

The following sections would focus on I<sup>2</sup>C interface and the software of microcontroller design should satisfy both on I<sup>2</sup>C specification and AS 7265 x Multispectral Chipset register structure.

### 8-Software Design Considerations

In most of system designs, AS72651 is controlled by a microcontroller. With the UART interface, the controller could configure the devices and get the sensors data through some AT commands. The software of microcontroller design would be simple.

The following sections would focus on I2C interface and the software of microcontroller design should satisfy both I2C specification and AS7265x Multispectral Chipset register structure.



#### Accessories:

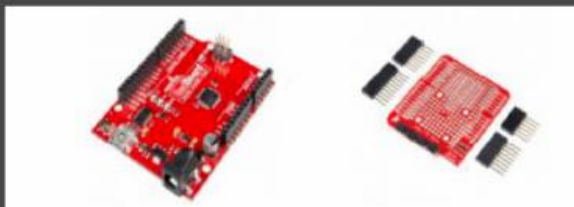
Qwiic Cable - Breadboard Jumper (4-pin) \$1.50

Qwiic Cable - 100mm \$1.50

SparkFun Qwiic Shield for Arduino \$6.95

SparkFun Qwiic HAT for Raspberry Pi \$5.95

SparkFun Qwiic Mux Breakout - 8 Channel (\$11.95)

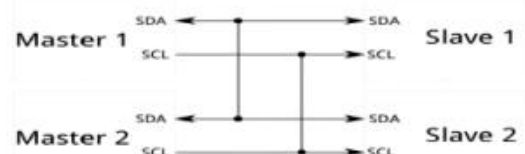


### 9-Arduino

- A computer (Windows, Mac, or Linux)
- An Arduino-compatible microcontroller (anything from this guide should work)
- A USB A-to-B cable, or another appropriate way to connect your Arduino-compatible microcontroller to your computer
- **1-installing Arduino IDE:** <https://learn.sparkfun.com/tutorials/installing-arduino-ide>
- **2-The Inter-integrated Circuit (I2C) Protocol** is a protocol intended to allow multiple "slave" digital integrated circuits ("chips") to communicate with one or more "master" chips. Like the Serial Peripheral Interface (SPI), it is only intended for short distance communications within a single device. Like Asynchronous Serial Interfaces (such as RS-232 or UARTs), it only requires two signal wires to exchange information.

#### I2C / Qwiic Interface:

The sensors are 3.3V compatible so don't use with a 5V Arduino Uno without proper conversion (use the Qwiic shield instead!). If you're using a 3.3V development platform that doesn't have a Qwiic connector, consider using the Qwiic Breadboard Cable.



## 49.5 References

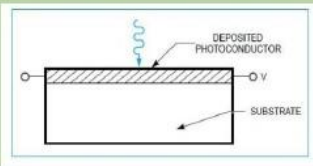
1. <https://en.wikipedia.org/wiki/Spectroscopy>
2. Czech Technical University in Prague, Faculty of Nuclear Sciences and Physical Engineering Department of Physical Electronics, "*Design and construction of a digital CCD spectrometer*", Research project, Author: Filip Dominec, Supervisor: Ing. Jaroslav Pavel, Academic year: 2009/2010  
([https://www.fzu.cz/~dominecf/electronics/usb-spect/usb\\_spectrometer\\_dominec.pdf](https://www.fzu.cz/~dominecf/electronics/usb-spect/usb_spectrometer_dominec.pdf)) Please note that this USB spectrometer project has a new HTML page, which may contain updates and further information: <http://www.fzu.cz/~dominecf/spek2/index.html>
3. Sparkfun - AS7265x (Qwiic)



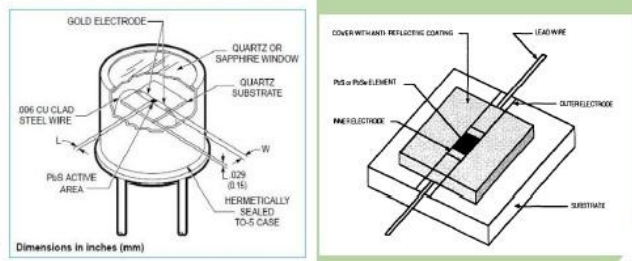
PbS cooled infrared detector (سنزور حراري)

A. Introduction

The electrical conductivity of photoconductive detectors is changed by the free-charge carriers generated by absorbed incident photons. A current starts flowing due to an applied voltage or bias. The current flow varies in proportion to the photon irradiance. Lead selenide and lead sulfide detectors fall into this category of detectors. This concept is shown in Figure .

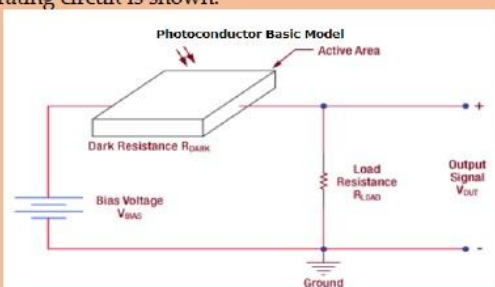


PbS and PbSe detectors are constructed through chemical deposition of polycrystalline film on a quartz substrate. Gold electrodes are plated to the film edges to provide electrical contact, and the entire assembly is sealed within a package with a suitable window, quartz or sapphire. A typical lead salt detector is depicted in Figure.



B. Theory of Operation

For photoconductive materials, incident light will cause the number of charge carriers in the active area to increase, thus decreasing the resistance of the detector. This change in resistance leads to a change in measured voltage, and hence, photosensitivity is expressed in units of V/W. An example operating circuit is shown.



The detection mechanism is based upon the conductivity of the thin film of the active area. The output signal of the detector with no incident light is defined by the following equation:

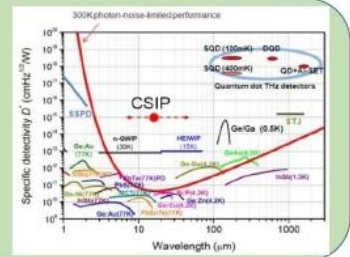
$$V_{OUT} = \frac{R_{LOAD}}{R_{DARK} + R_{LOAD}} * V_{BIAS}$$

A change  $\Delta V_{OUT}$  then occurs due to a change  $\Delta R_{Dark}$  in the resistance of the detector when light strikes the active area:

$$\Delta V_{OUT} = -\frac{R_{LOAD} V_{BIAS}}{(R_{DARK} + R_{LOAD})^2} * \Delta R_{DARK}$$

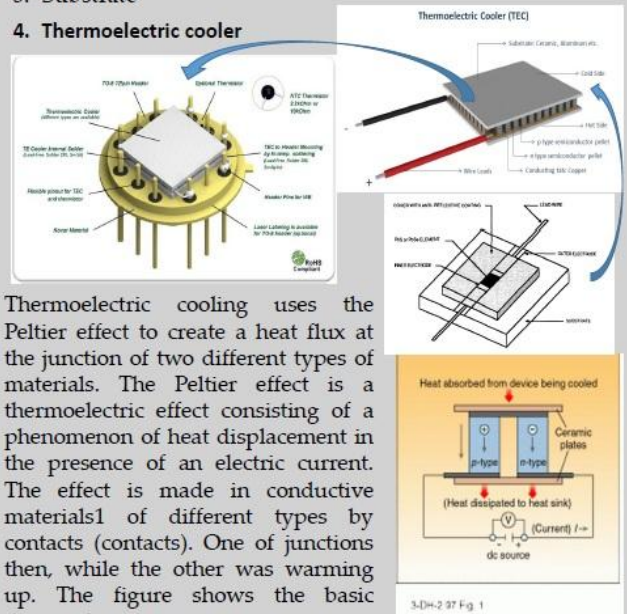
Spectral response characteristics of various infrared detectors.

(Lieda T, Komiyama S, 2010, http://open.stm.nih.gov/dataset/result.php?img=3231243\_sensors-10-08411778req=4)



C. Material

1. Thin film of PbS
2. Electrical leads
3. Substrate
4. Thermoelectric cooler



Thermoelectric cooling uses the Peltier effect to create a heat flux at the junction of two different types of materials. The Peltier effect is a thermoelectric effect consisting of a phenomenon of heat displacement in the presence of an electric current. The effect is made in conductive materials of different types by contacts (contacts). One of junctions then, while the other was warming up. The figure shows the basic thermoelectric circuit.

Two conductive materials of different natures a and b are connected by two junctions in X and W. In the case of the Peltier effect, an electric current I is imposed on the circuit, by placing for example a source of electric current between Y and Z resulting in heat release Q at one junction and heat absorption at the other junction. The Peltier coefficient relative to the material pair a and b is defined as the thermal power P released or absorbed per unit of intensity of current I. It is expressed in volts.  $\Pi_{ab}$  is then defined by:  $\Pi_{ab} = \frac{P}{I}$

If a current imposed in the direction  $Y \rightarrow W \rightarrow X \rightarrow Z$  causes a heat release in W and an absorption in X, then  $\Pi_{ab}$  is positive.

5. Sapphire window
6. Heat sink
7. Header is made of Kovar material (nickel-cobalt ferrous alloy)


**AECENAR**

 Association for Economical and Technological Cooperation  
 in the Euro-Asian and North-African Region  
[www.aecenar.com](http://www.aecenar.com)
**IAP**  
 INSTITUTE FOR  
 ASTROPHYSICS

Ras Masqa/Tripoli, Lebanon 06-11-2018

## Infrared Sensor System for IAP-SAT (IAP-IRS)

The IAP project aims to investigate a proper low cost platform to take interstellar data in IR and radio spectrum. There are the following working packages for 2018-2020:

- Detailed space infrared sensor
- Detailed Mission Planning for bringing IAP-SAT into orbit
- Collect data from IAP-SAT



Illustration 1: Caption: Black Widow nebula captured by Spitzer's IRAC.  
 Credit: NASA/JPL-Caltech/E. Churchwell (University of Wisconsin-Madison) and the GLIMPSE Team

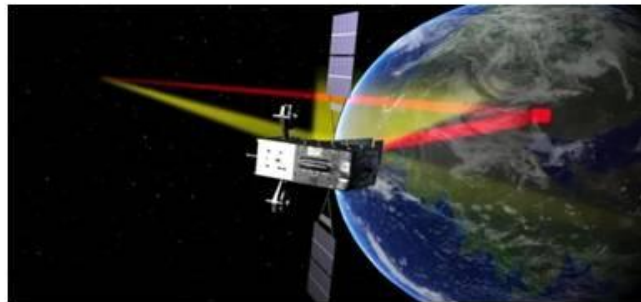


Illustration 2: The Space Based Infrared System can spot heat causing events across the world

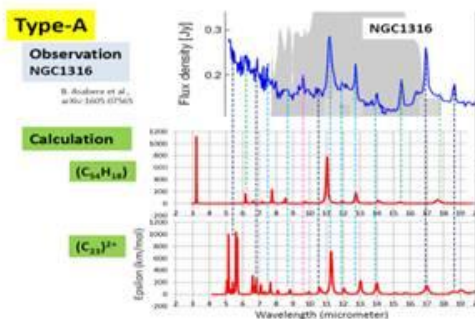


Illustration 3: Type-A spectrum. Calculated spectrum of  $(C_{54}H_{18})$  and  $(C_{23})^{2+}$  are compared with observed one of NGC1316. Blue dashed lines coincident with both molecules, whereas green with only  $(C_{54}H_{18})$ , black with  $(C_{23})^{2+}$ , pink no coincidence with both molecules.

### Tasks:

- Design of a proper infrared sensor.
- Collect IR data from satellite platform in Canopus Region.

### Contact:

Dr. Samir Mourad,  
 Mob./WhatsApp +961 76 341526  
 Email: [samir.mourad@aecenar.com](mailto:samir.mourad@aecenar.com)

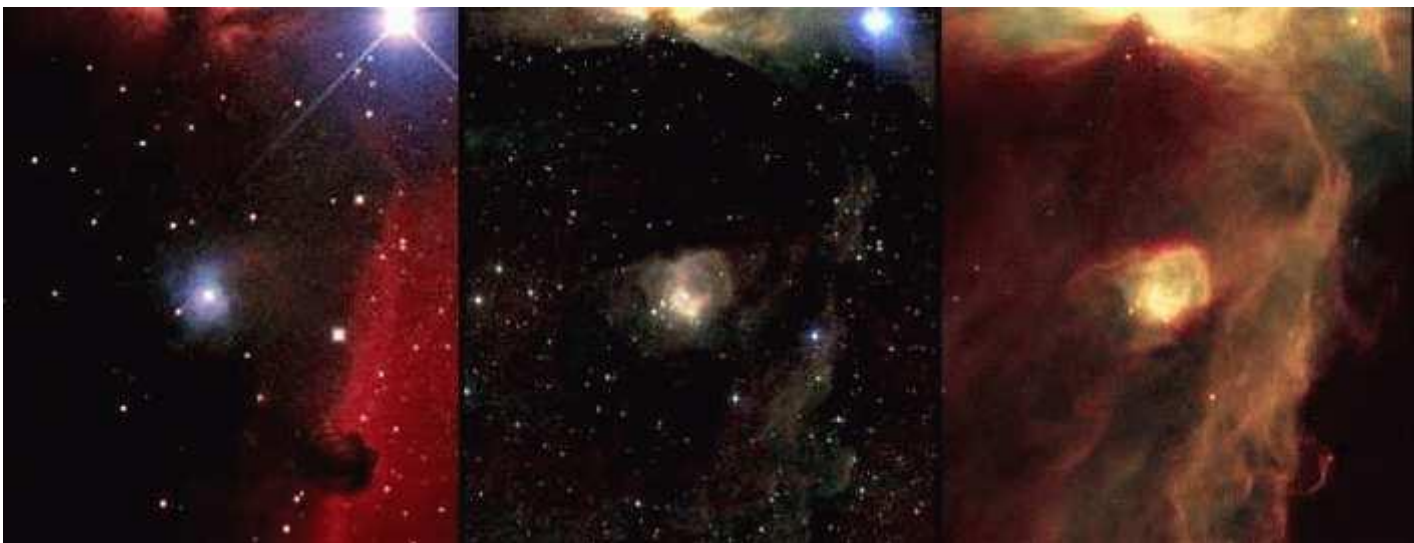
## 50 Basics of infrared science & technology

### 50.1 Infrared Astronomy (Near Infrared, Mid Infrared, Far Infrared)<sup>51</sup>

Infrared is usually divided into 3 spectral regions: near, mid and far-infrared. The boundaries between the near, mid and far-infrared regions are not agreed upon and can vary. The main factor that determines which wavelengths are included in each of these three infrared regions is the type of detector technology used for gathering infrared light.

Near-infrared observations have been made from ground based observatories since the 1960's. They are done in much the same way as visiblelight observations for wavelengths less than 1 micron, but require special infrared detectors beyond 1 micron. Mid and far-infrared observations can only be made by observatories which can get above our atmosphere. These observations require the use of special cooled detectors containing crystals like germanium whose electrical resistance is very sensitive to heat.

Infrared radiation is emitted by any object that has a temperature (i.e. radiates heat). So, basically all celestial objects emit some infrared. The wavelength at which an object radiates most intensely depends on its temperature. In general, as the temperature of an object cools, it shows up more prominently at farther infrared wavelengths. This means that some infrared wavelengths are better suited for studying certain objects than others.



Visible (courtesy of Howard McCallon), near-infrared (2MASS), and mid-infrared (ISO) view of the Horsehead Nebula. Image assembled by Robert Hurt.

As we move from the near-infrared into mid and far-infrared regions of the spectrum, some celestial objects will appear while others will disappear from view. For example, in the above image you can see how more stars (generally cooler stars) appear as we go from the visible light image to the near-infrared image. In the near-infrared, the dust also becomes transparent, allowing us to see regions

---

<sup>51</sup> <http://www.icc.dur.ac.uk/~tt/Lectures/Galaxies/Images/Infrared/Regions/irregions.html>

hidden by dust in the visible image. As we go to the mid-infrared image, the cooler dust itself glows. The table below highlights what we see in the different infrared spectral regions.

<b>SPECTRAL REGION</b>	<b>WAVELENGTH RANGE (microns)</b>	<b>TEMPERATURE RANGE (degrees Kelvin)</b>	<b>WHAT WE SEE</b>
<b>Near-Infrared</b>	<b>(0.7-1) to 5</b>	<b>740 to (3,000-5,200)</b>	<b>Cooler red stars Red giants Dust is transparent</b>
<b>Mid-Infrared</b>	<b>5 to (25-40)</b>	<b>(92.5-140) to 740</b>	<b>Planets, comets and asteroids Dust warmed by starlight Protoplanetary disks</b>
<b>Far-Infrared</b>	<b>(25-40) to (200-350)</b>	<b>(10.6-18.5) to (92.5-140)</b>	<b>Emission from cold dust Central regions of galaxies Very cold molecular clouds</b>

### 50.1.1 NEAR INFRARED

As we move away from visible light towards longer wavelengths of light, we enter the infrared region. As we enter the near-infrared region, the hot blue stars seen clearly in visible light fade out and cooler stars come into view. Large red giant stars and low mass red dwarfs dominate in the near-infrared. The near-infrared is also the region where interstellar dust is the most transparent to infrared light.



Visible (left) and Near-Infrared View of the Galactic Center

Visible image courtesy of Howard McCallon. The infrared image is from the 2 Micron All Sky Survey (2MASS)

Notice in the above images how center of our galaxy, which is hidden by thick dust in visible light (left), becomes transparent in the near-infrared (right). Many of the hotter stars in the visible image

have faded in the near-infrared image. The near-infrared image shows cooler, reddish stars which do not appear in the visible light view. These stars are primarily red dwarfs and red giants.

Red giants are large reddish or orange stars which are running out of their nuclear fuel. They can swell up to 100 times their original size and have temperatures which range from 2000 to 3500 K. Red giants radiate most intensely in the near-infrared region.

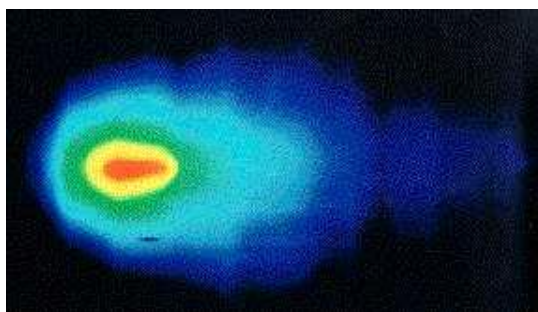
Red dwarfs are the most common of all stars. They are much smaller than our Sun and are the coolest of the stars having a temperature of about 3000 K which means that these stars radiate most strongly in the near-infrared. Many of these stars are too faint in visiblelight📡 to even be detected by optical telescopes, and have been discovered for the first time in the near-infrared.

### 50.1.2 MID INFRARED

As we enter the mid-infrared region of the spectrum, the cool stars begin to fade out and cooler objects such as planets, comets and asteroids come into view. Planets absorb light📡 from the sun and heat up. They then re-radiate this heat as infrared light. This is different from the visible light that we see from the planets which is reflected sunlight. The planets in our solar system📡 have temperatures ranging from about 53 to 573 degrees Kelvin. Objects in this temperature range emit most of their light in the mid-infrared. For example, the Earth itself radiates most strongly at about 10 microns. Asteroids also emit most of their light in the mid-infrared making this wavelength band the most efficient for locating dark asteroids. Infrared data can help to determine the surface composition, and diameter of asteroids.



An infrared view of the Earth



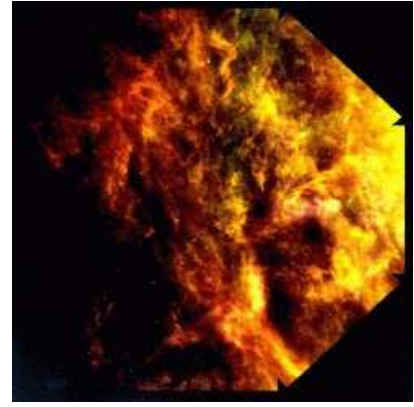
IRAS mid-infrared view of Comet IRAS-Araki-Alcock

Dust warmed by starlight is also very prominent in the mid-infrared. An example is the zodiacal dust which lies in the plane of our solar system. This dust is made up of silicates (like the rocks on Earth) and range in size from a tenth of a micron up to the size of large rocks. Silicates emit most of their radiation at about 10 microns. Mapping the distribution of this dust can provide clues about the formation of our own solar system. The dust from comets also has strong emission in the mid-infrared.

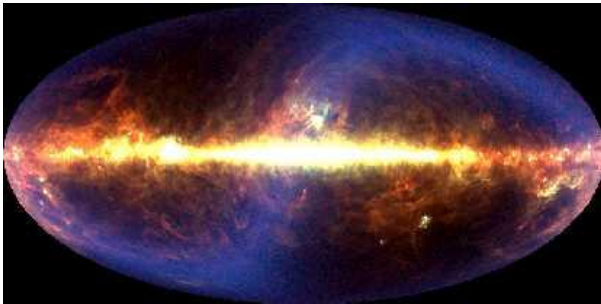
Warm interstellar dust also starts to shine as we enter the mid-infrared region. The dust around stars which have ejected material shines most brightly in the mid-infrared. Sometimes this dust is so thick that the star hardly shines through at all and can only be detected in the infrared. Protoplanetary disks, the disks of material which surround newly forming stars, also shines brightly in the mid-infrared. These disks are where new planets are possibly being formed.

### 50.1.3 FAR INFRARED

In the far-infrared, the stars have all vanished. Instead we now see very cold matter (140 Kelvin or less). Huge, cold clouds of gas and dust in our own galaxy, as well as in nearby galaxies, glow in far-infrared light. In some of these clouds, new stars are just beginning to form. Far-infrared observations can detect these protostars long before they "turn on" visibly by sensing the heat they radiate as they contract."



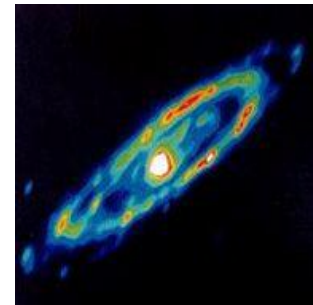
IRAS view of infrared cirrus - dust heated by starlight



Michael Hauser (Space Telescope Science Institute), the COBE/DIRBE Science Team, and NASA

The center of our galaxy also shines brightly in the far-infrared because of the thick concentration of stars embedded in dense clouds of dust. These stars heat up the dust and cause it to glow brightly in the infrared. The image (at left) of our galaxy taken by the COBE satellite, is a composite of far-infrared wavelengths of 60, 100, and 240 microns.

Except for the plane of our own Galaxy, the brightest far-infrared object in the sky is central region of a galaxy called M82. The nucleus of M82 radiates as much energy in the far-infrared as all of the stars in our Galaxy combined. This far-infrared energy comes from dust heated by a source that is hidden from view. The central regions of most galaxies shine very brightly in the far-infrared. Several galaxies have active nuclei hidden in dense regions of dust. Others, called starburst galaxies, have an extremely high number of newly forming stars heating interstellar dust clouds. These galaxies, far outshine all others galaxies in the far-infrared.



IRAS infrared view of the Andromeda Galaxy (M31) - notice the bright central region.

## 50.2 Definition of infrared and the origin of the infrared radiation<sup>52</sup>

### Table of Contents

#### 3.1 The definition of the infrared band

#### 3.2 The origin of infrared radiation

<sup>52</sup> <http://elte.prompt.hu/sites/default/files/tananyagok/InfraredAstronomy/ch03.html>

### 3.2.1 Atomic transitions

### 3.2.2 Molecular transitions

## 3.3 Radiation of molecules

### 3.3.1 Molecular hydrogen

### 3.3.2 Ices and other molecules

## 3.4 Radiation of dust

### 3.4.1 Heating and cooling of dust

### 3.4.2 Refractory dust

### 3.4.3 Silicates

### 3.4.4 Large dust grains

### 3.4.5 Polycyclic Aromatic Hydrocarbons

## References and further reading to the chapter:

In this chapter we describe the technological and observational justification of the infrared band. Atomic and molecular transitions are investigated as the origin of the infrared radiation.

**Electromagnetic radiation** is classified by wavelength into gamma rays, X-rays, ultraviolet, visible, infrared, microwave and radio, see on Figure 3.1. Infrared radiation lies between the visible and microwave part of the electromagnetic radiation.

### **50.2.1 The definition of the infrared band**

The quantum efficiency is a measure of a device's electrical sensitivity to light. It is the incident photon to converted electron ratio, i.e. the percentage of photons hitting the device's photoreactive surface that produce charge carriers. It is measured in electrons per photon or amps per watt. As we see in Figure 3.1 the quantum efficiency of the human eye is around 1% to 10%, over most conditions (see eg. <http://psych.nyu.edu/pelli/pubs/pelli1990efficiency.pdf>). It gets slightly better for red colour at low light levels (photopic vision), but our eyes lose all sensitivity beyond the red end of the visible spectrum ( $\lambda > 0.75 \mu\text{m}$ ).

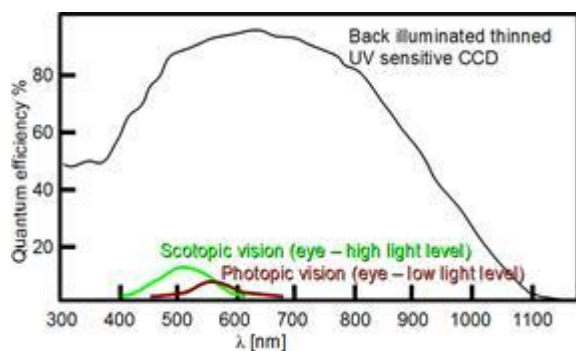


**Figure 3.1:** Quantum efficiency of human eye and CCD

The infrared quantum efficiency of typical photoemulsions is similar to the human eye, however infrared sensitive astrographic photo plates (Kodak IVN) were sensitive up to  $\lambda \approx 1 \mu\text{m}$ . We can not use any more most of the visible band technologies such as photography, CCDs and photocathodes for  $\lambda > 1.1 \mu\text{m}$ , and that wavelength limit can be considered as a technical border of infrared at the short wavelength side. Referring to Figure 3.1 we note that the CCD surface has channels used for charge transfer that are shielded by polysilicon gate electrodes which absorb light (mostly blue). Such losses are eliminated in the back-illuminated CCD, where the light falls onto the back of the CCD in a region that has been thinned so it is transparent. The wavelength dependent specific detectivity  $D^*$  is defined as reciprocal of noise-equivalent power (NEP), normalized per unit area:

$$D^* = \frac{\sqrt{\text{Area}}}{\text{NEP}}, \quad (3.1)$$

where Area is the photosensitive region of the detector. The unit of  $D^*$  is:  $\text{cmHz}^{1/2}\text{W}^{-1}$ . Figure 3.1 shows the specific detectivity  $D$  of the most common compounds used as detectors which include: Gallium Arsenide – GaAs, Lead Sulfide – PbS, Indium Antimonide – InSb, Germanium doped with Copper - Ge:Cu, Germanium doped with Zinc - Ge:Zn, Germanium doped with Gold - Ge:Au, Germanium doped with Gallium - Ge:Ga, Lead Telluride – PbTe, phosphorus-doped silicon – Si:P.

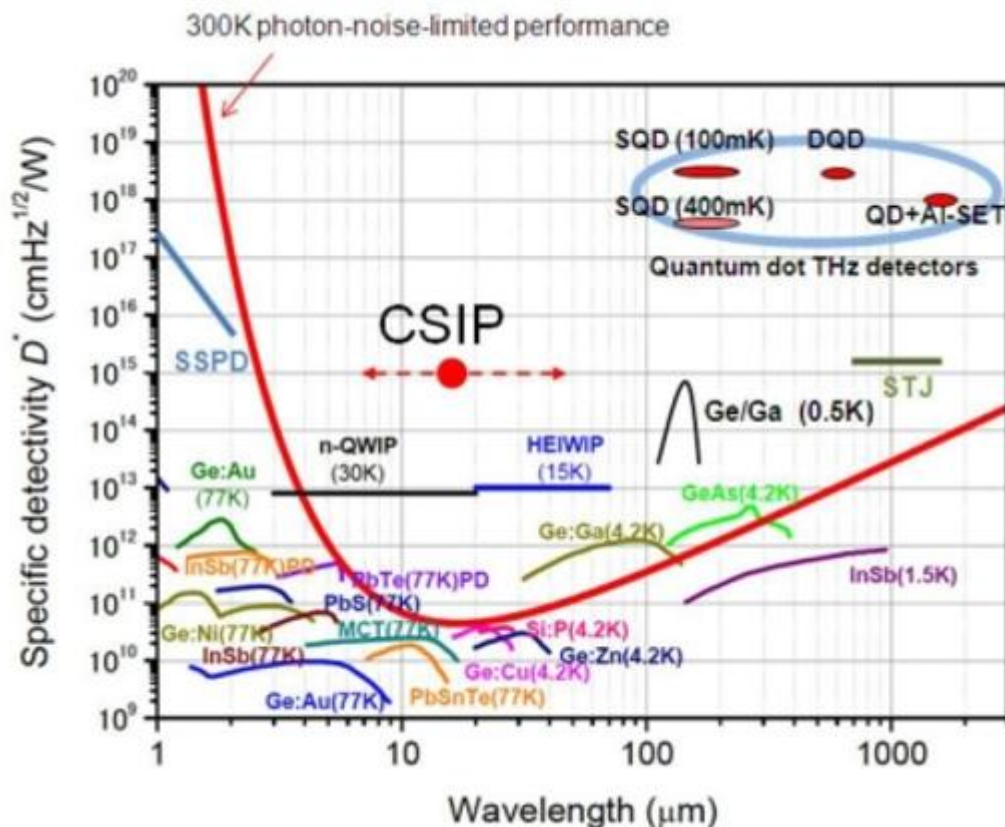


**Figure 3.2:** Spectral response characteristics of various infrared detectors. (Ueda T, Komiyama S, 2010, [http://openi.nlm.nih.gov/detailedresult.php?img=3231243\\_sensors-10-08411f7&req=4](http://openi.nlm.nih.gov/detailedresult.php?img=3231243_sensors-10-08411f7&req=4))

The highest available frequency band of terrestrial sub-mm observatories is at 810GHz (0.37mm). The "end" of the infrared region is again technologically defined: it is the wavelength ( $\approx 350\mu\text{m}$ ) where radio techniques such as superheterodyne receivers tend to be used in preference to the "optical

style” infrared approach and the incoming radiation tends to be thought of as waves rather than individual photons. The region from 0.35mm to 1mm is referred to as the sub-millimeter region. It may be regarded as a subdivision of radio astronomy.

**Astronomical justification for the definition** is that already at 2.2 $\mu$ m the sky has a significantly different appearance from the visible one. The cooler end of the stellar population becomes predominant and some objects turn out to have infrared fluxes much higher than predicted from their visible spectra.

These infrared excesses can be due to cool dust shells surrounding them or to circumstellar free-free emission for example. The most important sources of the infrared photons are Solar system objects, stars and extended galactic objects, extragalaxies. The cosmic microwave background (CMB) is the relic of the Big Bang. It is characterized by a blackbody spectrum of temperature 2.73K. The rise of its spectrum marks the end of the infrared.

The vibrational transitions of molecules results infrared photons, whereas we observe their rotational transitions spectra in the sub-mm and radio region.

Infrared is divided into three parts: near, mid and far-infrared. Near-infrared refers to the part of the infrared spectrum that is closest to visible light and far-infrared refers to the part that is closer to the microwave region. Mid-infrared is the region between these two. The boundaries between these regions are not exact and can vary. (Table 3.1. shows the general properties of the infrared ranges.)

Infrared radiation	Wavelength range [ $\mu$ m]	Astronomical objects
Near	1-5	Red giants Cooler red stars
Mid	5-30	Planets, comets and asteroids Protoplanetary disks
Far	30-400	Central regions of galaxies Emission from cold dust

**Table 3.1:** *Properties of the infrared ranges*

**A justification based on the observational conditions** can be made as well. Beyond 2.3 $\mu$ m blackbody radiation from the telescope and the atmosphere itself begins to dominate other sources of background. Measurements of faint astronomical objects have to be made by alternatively observing the field containing the source and a nearby “empty” one. This process is known as chopping. The signals are subtracted to eliminate the strong background. Alternatively the measurement is taken outside the atmosphere with a cooled observing system.

In the NIR, MIR and FIR the main sources of the background are terrestrial, Zodiacal light and galactic ISM radiation. From about 300 $\mu$ m CMB starts to dominate the background. Except bands in the NIR, the infrared sky is to be observed by air-borne or space-borne instruments.

The sub-millimeter region however can be accessed again in selected atmospheric windows by terrestrial telescopes located at high altitude, low precipitable water vapor (pwv) sites like Mauna Kea or South Pole. Precipitable water is the measure of the depth of liquid water at the surface that would result after precipitating all of the water vapor in a vertical column over a given location, usually extending from the surface to 300 mb (<http://forecast.weather.gov/glossary.php?word=precipitable%20water>).

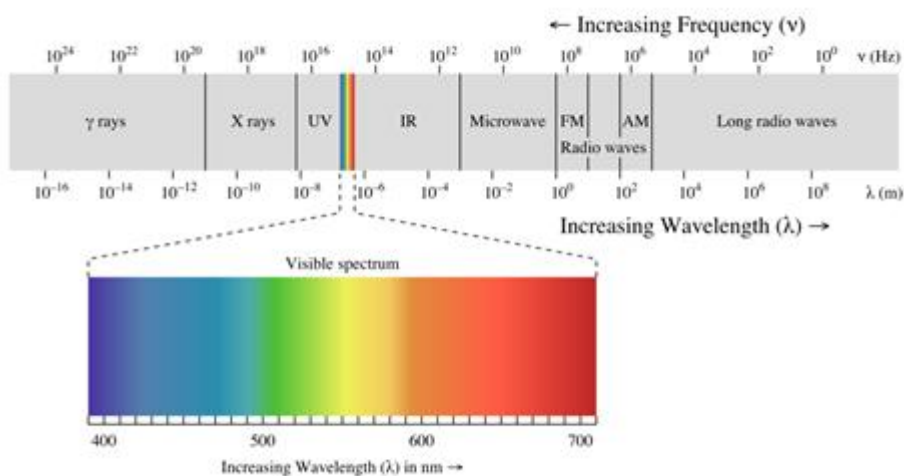


**Figure 3.3:** Electromagnetic spectrum ([http://en.wikipedia.org/wiki/File:EM\\_spectrum.svg](http://en.wikipedia.org/wiki/File:EM_spectrum.svg)) from  $10^{-16}$  to  $10^8$  m. The visible spectrum located in the middle, it covers only a small part of the spectrum.

Observations at different wavelengths reveal various pictures from astronomical objects. Figure 3.4 shows the M51 Spiral Galaxy at different wavelengths: from visible to far infrared. Observations of visible light show the stars that make up the galaxy. Infrared observations reveal the mixture of gas and dust from which new stars can be born.

**Figure 3.4:** Hubble, 2MASS, Spitzer Space Telescope, ISO and IRAS observations of M51 Spiral Galaxy. Shorter wavelengths show the star content of it, on longer wavelengths the radiation of gas and dust dominate. (<http://astromic.blogspot.de/2011/02/infrared-astronomy.html>)

Near-infrared observations have been made from ground based observatories since the 1960's. This part of the infrared radiation can be observed with similar technique as visible light, but it requires special infrared detectors. Mid and far-infrared observations, where the wavelength is longer than 20  $\mu\text{m}$ , can only be made by observatories which can get above our atmosphere. These observations require the use of special cooled detectors.

## 50.3 Instrumentation / Sensors Technology

### 50.3.1 IRAS

The Infrared Astronomical Satellite (IRAS) was initiated in 1975, designed and constructed by NASA (USA), NIVR (the Netherlands), and SERC (UK), and launched by NASA (launcher: Delta 3910) on January 25, 1983. It was the first space-borne infrared observatory to scan the entire sky. During its ten months of operation, IRAS scanned more than 96 percent of the sky four times at four infrared bands centered at 12, 25, 60 and 100 microns. Its main task was to discover and measure IR point sources. The IRAS mission has had a major impact on almost every area of astronomy.

### 50.3.1.1 The most important results of IRAS

- Detected about 350,000 infrared sources (see Figure 6.1), increasing the number of cataloged astronomical sources by about 70%.

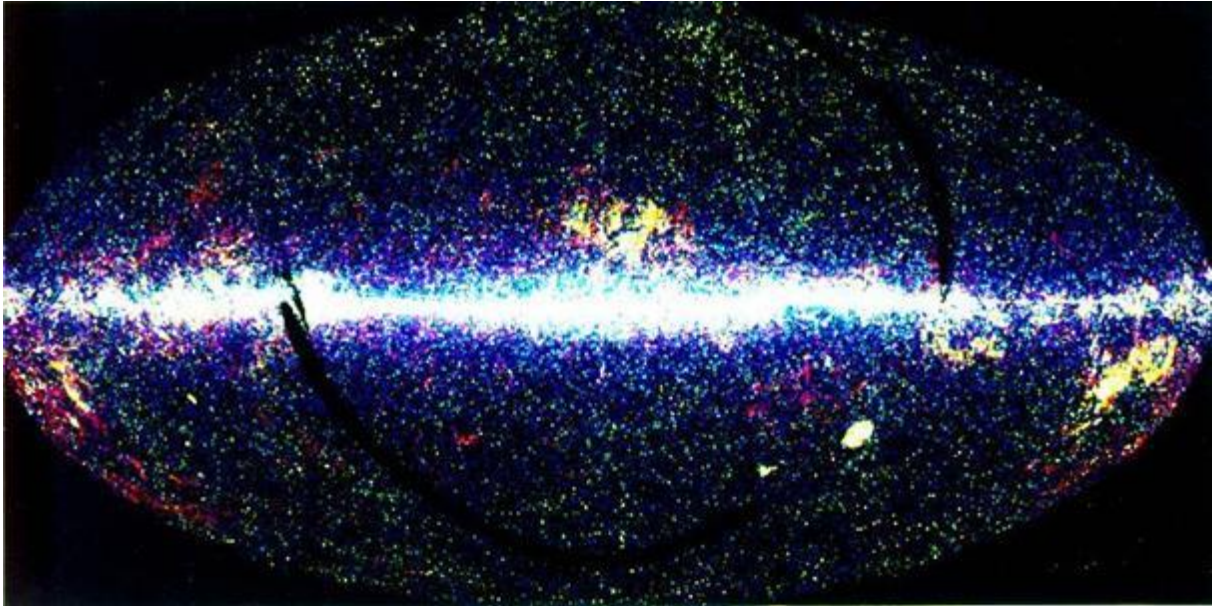


**Figure 6.1:** All sky map of IRAS sources (<http://www.iras.ucalgary.ca/~nkoning/irasDb/iras.html>)

- Discovered 6 new comets
- Found that comets are dustier than previously thought and that dust from comets fills the Solar System
- Detected useful infrared data for 2004 asteroids
- Detected the zodiacal dust bands - bands of infrared emission that girdle our solar system which are likely to be debris from asteroid collisions
- Found evidence of zodiacal dust bands around other stars
- Discovered a disk of dust grains around the star Vega, see Figure 6.2. The significant excess above the photospheric model indicates the presence of cold material around a star.

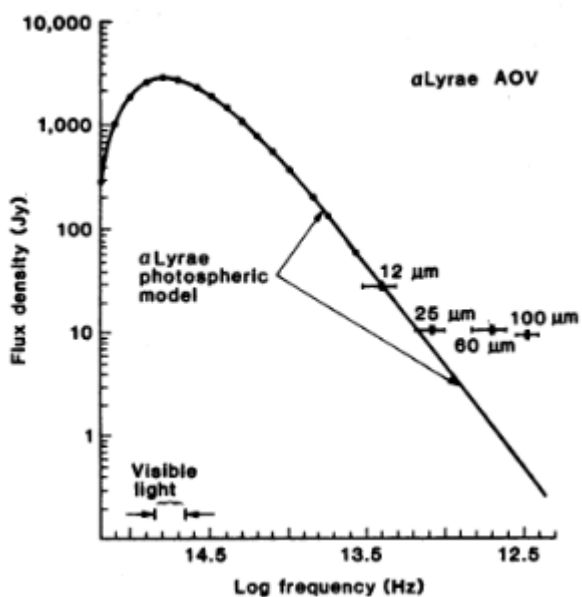


**Figure 6.2:** Observed spectral energy distribution of Vega and photospheric stellar model (Neugebauer et al.).

- Detected disks of material around several other stars.

- Detected several probable protostars embedded in clouds of gas and dust
- Found that some Bok globules contain protostars. e.g. Beichman (1984) showed that the Bok globule, Barnard 5 contains at least four protostars.
- Cataloged thousands of hot, dense cores within clouds of gas and dust which could be newly forming stars
- Cataloged over 12,000 variable stars, the largest collection known to date
- Revealed for the first time the core of our galaxy
- Found infrared cirrus (wisps of warm dust) in almost every direction of space
- Data from IRAS was used to show that our galaxy is a barred spiral galaxy - a galaxy which has an elongated central bar-like bulge from which its spiral arms unwind.
- Detected 75,000 starburst galaxies - galaxies which are extremely bright in the infrared due to intense star formation. It was found that many of these starburst galaxies have "superwinds" emerging from their centers due to the large number of supernova explosions which occur in these galaxies.
- Detected strong infrared emission from interacting galaxies
- First identified IRAS F10214+4724 - at the time, the most luminous object known in the Universe by a factor of 2. This object may be the best candidate for a forming spiral galaxy yet discovered.
- Instruments and observing strategy of IRAS

IRAS telescope system comprised the upper part of the satellite and was composed of a two mirror, Ritchey-Chretien telescope mounted within a toroidal superfluid helium tank, which in turn was mounted within the evacuated main shell. The optical system was protected from contamination before launch and during the first week of the mission by an aperture cover cooled with supercritical helium. After the cover was ejected, the sunshade limited heat flow to the aperture by blocking direct solar radiation and reflecting away terrestrial infrared radiation. The telescope orientation was constrained to prevent sunlight from striking the inner surface of the sunshade and radiation from the Earth from illuminating the radiators around the telescope aperture. The telescope was cooled by contact with the superfluid helium tank to temperatures ranging from 2 to 5 K. The surfaces of the sunshade which could be viewed by the telescope aperture were cooled by a three-stage radiator to about 95 K.

The focal plane assembly contained the infrared and visible detectors, cold electronics, and associated masks, filters and field optics. It consisted of 62 infrared channels and eight visible channels. The infrared channels were divided into eight modules, two for each color band with each module containing either seven or eight detectors. The detector masks were rectangular in aspect and infrared sources scanned across the focal plane parallel to the narrow dimension of the detectors in all observational modes.

## **50.4 Infrared satellite observatories**

### **Table of Contents**

#### 7.1 Infrared Space Observatory (ISO)

##### 7.1.1 Scientific instruments and observing strategy

##### 7.1.2 Most important results

#### 7.2 Spitzer Space Telescope

## 7.2.1 Scientific instruments

### 7.2.1 Most important scientific results

## 7.3 Herschel Space Observatory

### 7.3.1 Scientific instruments

### 7.3.2 Most important scientific results

### References and further reading to the chapter:

In this chapter we give an overview of the observing strategy, scientific instruments and main scientific result of Infrared Space Observatory, Spitzer Space Telescope and Herschel Space observatory.

#### **50.4.1 Infrared Space Observatory (ISO)**

ISO observed the infrared sky between February 1996 and April 1998. It was a European Space Agency (ESA) mission, launched in November 1995. The satellite weighed around 2500 kg and was launched with over 2000 litre of liquid helium coolant on board, which lasted for 29 months.

ISO was the first orbiting infrared observatory. It made during its lifetime more than 30 000 individual observations of all kind of astronomical objects: in the solar system and in the most distant galaxies.

The telescope operated between 2.5 and 240  $\mu\text{m}$ . Comparing to IRAS, at 12  $\mu\text{m}$  it was one thousand times more sensitive and had one hundred times better angular resolution.

Figure 7.1 shows ISO's two largely independent modules: the Payload Module and the Service Module. The Payload Module was a large cryostat containing super fluid helium which maintained the telescope and the scientific instruments at temperatures between 2 and 8 K. The Service Module contained the warm electronics of the scientific instruments and all the classical spacecraft subsystems, which are necessary to supply the basic functions. The sun-shield with solar cells always faced the Sun to provide electrical power and to protect the Payload Module from direct irradiation.

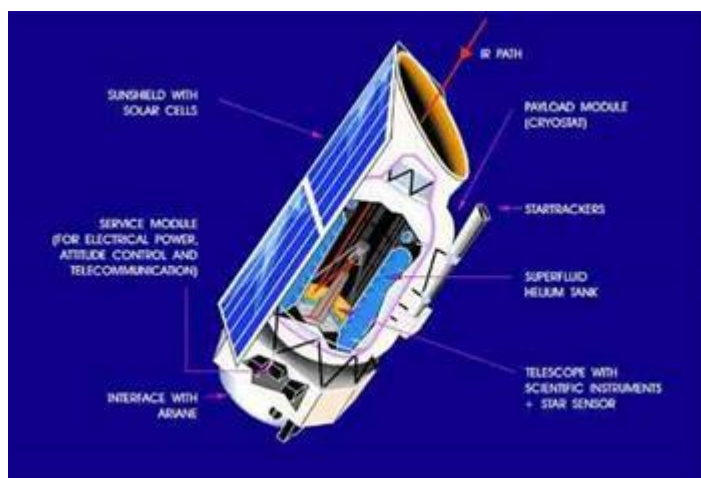


**Figure 7.1:** Schematic view of the ISO satellite, two largely independent modules are visible: the Payload Module and the Service Module

[http://vietsciences.free.fr/giaokhoa/vatly/thienvan/gsnnguyenquangrieu/images/iso\\_satellite.jpg](http://vietsciences.free.fr/giaokhoa/vatly/thienvan/gsnnguyenquangrieu/images/iso_satellite.jpg)

The ISO telescope was a 60 cm diameter Richey-Chrétien system with an overall focal ratio of  $f/15$ . This type of telescope is free from coma and spherical aberration, and they have larger field of view than the classical Cassegrain type telescopes. The optical quality of the primary and secondary mirrors provided diffraction limited performance at wavelengths beyond  $5\ \mu\text{m}$ , also limited by pointing performance.

ISO had a high Earth orbit with a period of one-to-two days. It was accustomed by previous space observatories.

#### **50.4.1.1 Scientific instruments and observing strategy**

ISO's four scientific instruments are the following: a camera, ISOCAM, an imaging photopolarimeter, ISOPHOT, and the two spectrometers, a long wavelength LWS and a short wavelength SWS.

The telescope and the scientific instruments operated at  $\sim 3\text{K}$ . Some of the infrared detectors were cooled down to  $1.8\ \text{K}$ . This low temperature enabled observations to be made at high sensitivities. Only one instrument was operational in prime mode at a time, but the camera was used in parallel mode to acquire extra astronomical data whenever it was possible. The long-wavelength channel of the photometer was used during satellite slews, this produced a partial sky survey, which covers  $\sim 15\%$  of the sky, at wavelengths around  $200\ \mu\text{m}$ . After launch, a parallel/serendipity mode was added for the LWS, in which narrow-band data were obtained at 10 fixed wavelengths in parallel with the main instrument and also during slews.

New generations of space and air-borne integral field spectrometers required large format arrays of low noise equivalent power (NEP) detectors. NEP is the radiant power that produces a signal-to-noise ratio of unity at the output of a given detector at a given data-signaling rate or modulation frequency, operating wavelength, and effective noise bandwidth. In the FIR, photoconductors still offer the higher sensitivity under low background conditions in combination with moderately low operation temperatures ( $1.7\ \text{K}$  to  $4\ \text{K}$ ) when compared to bolometers. In the  $40$  to  $200\ \mu\text{m}$  range, Gallium-doped germanium (Ge:Ga) photoconductors are commonly used because of their high sensitivity. Ge:Ga photoconductors which are mechanically stressed are used to cover the wavelength range from  $115$  to  $210\ \mu\text{m}$ . Unstressed Ge:Ga detectors are used to cover the wavelength range from  $40$  to  $115\ \mu\text{m}$ .

The ISO Camera instrument consisted of two optical channels, used one at a time, each with a  $32 \times 32$  element detector array, operated in the wavelength ranges  $2.5\text{-}5.5\ \mu\text{m}$  and  $4\text{-}17\ \mu\text{m}$ .

The ISOPHOT instrument consisted of three subsystems: ISOPHOT-C, ISOPHOT-P and ISOPHOT-S: ISOPHOT-C consists of two photometric far-infrared cameras, used one at a time, for the wavelength range  $50\text{-}240\ \mu\text{m}$ . The 'C100' camera contained a  $3 \times 3$  array of Ge:Ga detectors, each with a pixel field of view of  $43.5''$ , and 6 filters covering wavelengths up to  $105\ \mu\text{m}$ . The 'C200' camera used a  $2 \times 2$  array of stressed Ge:Ga detectors with a pixel field of view of  $89''$  and had 5 filters covering wavelengths longwards of  $100\ \mu\text{m}$ .

ISOPHOT-P was a multi-band, multi-aperture photopolarimeter for the wavelength range  $3\text{-}110\ \mu\text{m}$ . It contained 13 apertures ranging in size from  $5''$  to  $180''$  and 14 different filters. ISOPHOT-S was a

dual grating spectrophotometer which provided a resolving power of  $\sim 90$  in two wavelength bands simultaneously ( $2.5\text{-}5\mu\text{m}$  and  $6\text{-}12\mu\text{m}$ ).

The ISO Long Wavelength Spectrometer covered the wavelength range  $43\text{-}196.7\mu\text{m}$  with a spectral resolving power of  $\sim 200$ . Using also the Fabry-Pérot (FP) etalons, the resolution could be increased to around 10,000.

The ISO Short Wavelengths Spectrometer covered the wavelength range  $2.38\text{-}45.2\mu\text{m}$  with a spectral resolving power of the order of 1000-2500. Using also the Fabry-Pérot (FP) etalons, the resolution could be increased to more than 25 000 for the wavelength range  $11.4\text{-}44.5\mu\text{m}$ .

ISO was operated in a pre-planned manner without any significant routine real-time interaction.  $\sim 45\%$  of the observing time was reserved for guaranteed time programmes. But as an observatory, ESO was open to the astronomical community including expert and non-expert users.

Each of the four instruments had a number of possible operating modes. To simplify the definition of an observation and to allow users to specify their observation in terms familiar to them, a set of astronomically-useful operating modes was defined and presented to users as a set of 'Astronomical Observation Templates' (AOTs). Each AOT was designed to carry out a specific type of astronomical observation.

$\sim 65\%$  of ISO's observing time was distributed to the general community via the traditional method of proposals and peer review. The scientific programme for ISO consisted of more than 1 000 individual proposals.. About 10% of ISO's time was used for Solar System studies, 23% for the Interstellar Medium (ISM), 29% on Stellar/Circumstellar topics, 27% for Extragalactic observations and 11% for Cosmology.

#### 50.4.1.2 Most important results

ISO has delivered important results in nearly all fields of astronomical research. Nearly 1400 papers have been published in the refereed literature on ISO results. A few example from ISO's most important scientific results:

- the discovery of crystalline silicates outside our own solar system, in the atmospheres of young and old stars and also in comet Hale-Bopp. Figure 7.2 show the ISOCAM image of Hale-Bopp comet at  $15\mu\text{m}$ . This discovery shows that water is ubiquitous in the cosmos.

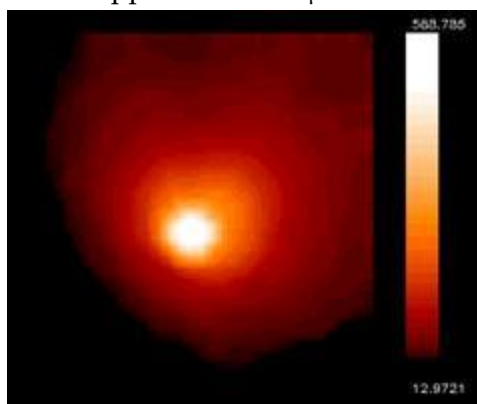


**Figure 7.2:** ISOCAM image of comet Hale-Bopp at  $15\mu\text{m}$  (<http://iso.esac.esa.int/galleries/sso/halebopp.html>)  
Credit: ESA/ISO, ISOCAM, R. Walsh, B. Altieri, P. Lamy)

- a wealth of water vapour transitions were measured e.g. in Mars, Titan, the giant planets, comets including Hale-Bopp, in shocks, in the cold interstellar medium, in circumstellar envelopes and in the ultra-luminous galaxy Arp220. The spectral resolution of most water observations was limited, but the possibility to observe the full mid- and far-infrared spectrum has opened great possibilities.
- the first detections of the lowest pure rotational lines of H<sub>2</sub> in young massive stars, HH-objects, the diffuse ISM, outer parts of edge-on galaxies. . Temperatures less than a few hundred K could be investigated.
- observing pre-main sequence stars with SWS and LWS spectrographs. These data were used for line detections and to reconstruct the spectral energy distributions. Figure 7.3 shows the spectral energy distribution of 2 Herbig Ae/Be stars. Very different SEDs were observed for Herbig Ar/Be stars, confirming the fact that these objects do not constitute a homogeneous class.

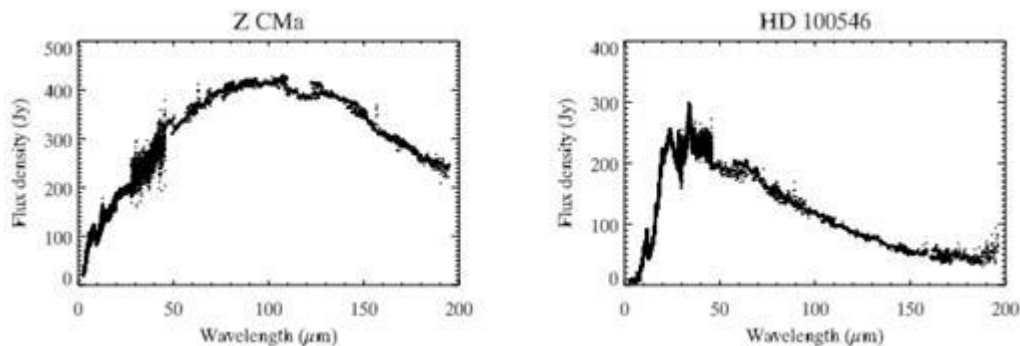


*Figure 7.3: ISO spectra of two Herbig Ae/Be stars (Lorenzetti 2004).*

- detecting planet formation around old, dying stars. E.g. in the vicinity of the Red Rectangle old binary star in the Monoceros constellation, a ring of matter constituting the first stage of planet formation was detected. This discovery contradicted theories that planet formation was only possible around young stars. Figure 7.4 shows two images in red light and the ISO LWS spectrum of the Red Rectangle. The left image was taken by H. van Winckel (Leuven) using the 90 cm Dutch telescope at the European Southern Observatory, La Silla, Chile. The right hand image was taken by G. Weigelt and R. Osterbart (Bonn) using the 2.2m Max Planck telescope, also at E.S.O.. A prominent dark lane is visible across the image, which is due to the disk surrounding the binary system. The tick marks on the spectrum indicate the position of the oxygen-rich olivine bands, suggesting that the disk contains oxygen-rich material. This disk may be the site of on-going planet formation.

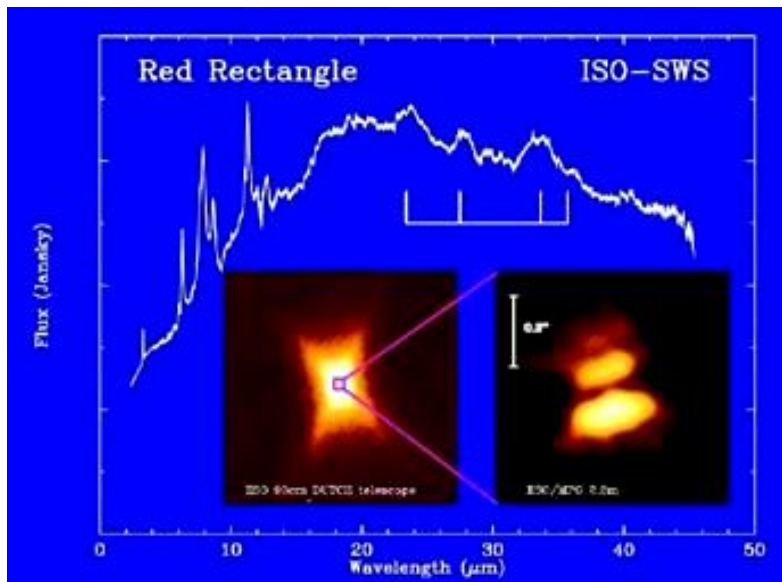


Figure 7.4: Two images in red light and ISO LWS spectrum of Red Rectangle. ([http://coolcosmos.ipac.caltech.edu/image\\_galleries/ISO/sws/redrec.html](http://coolcosmos.ipac.caltech.edu/image_galleries/ISO/sws/redrec.html))

- ISO searched for, and found several protoplanetary disks: rings or disks of material around stars which are considered to be the first stage of planet formation.
- the detailed investigations of interstellar solid state features, e.g. CO<sub>2</sub> ices. It gives the possibility to have detailed interplay between observations and laboratory spectroscopy
- obtaining spectral energy distributions of extragalactic objects, which serve as templates for cosmological studies, helped to consolidate the unified scheme or to develop quasar evolutionary scenarios. ISOPHOT SED of NGC6240 are seen on Figure 7.5.

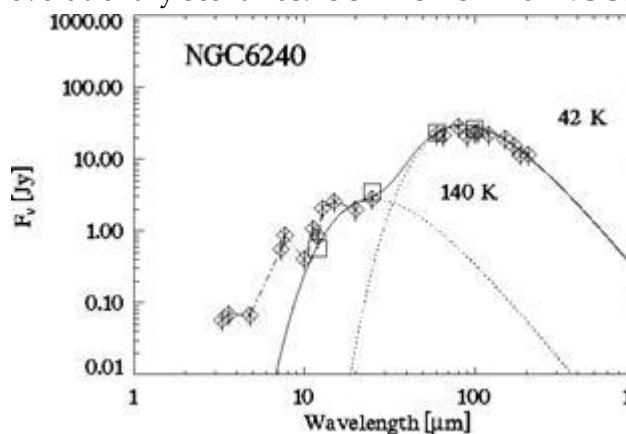


Figure 7.5: ISOPHOT spectral energy distribution of NGC6240. The SED is well fitted with two components: a 140 K and a 42 K blackbody radiation. (<http://iso.esac.esa.int/galleries/nor/ngc6240c.htm>, Credit: EAS/ISO, ISOPHOT, U. Klaas)

- making deep cosmological surveys at near- and far-infrared wavelengths. It resolved the part of the cosmic infrared background (CIB) into discrete sources and detected fluctuations in the CIB.

making the European Large Area ISO Survey to explore obscured galaxies and quantify the recent star-formation history of the Universe. This survey discovered 9 hyper luminous galaxies.

# 51 IAP-IRS Unit Design (PbS detector) Overview (Presentation)

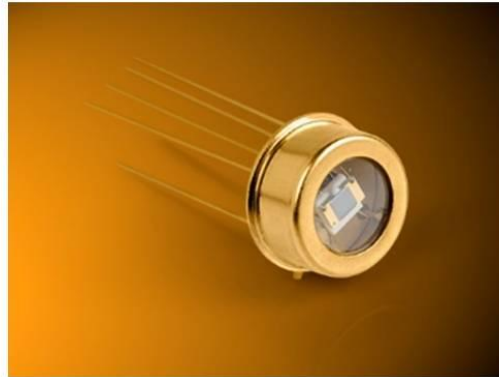
SA, Last update: 23. Jul. 2020 / 1441، الخميس، 03 ذو الحجة،



بِسْمِ اللَّهِ الرَّحْمَنِ الرَّحِيمِ



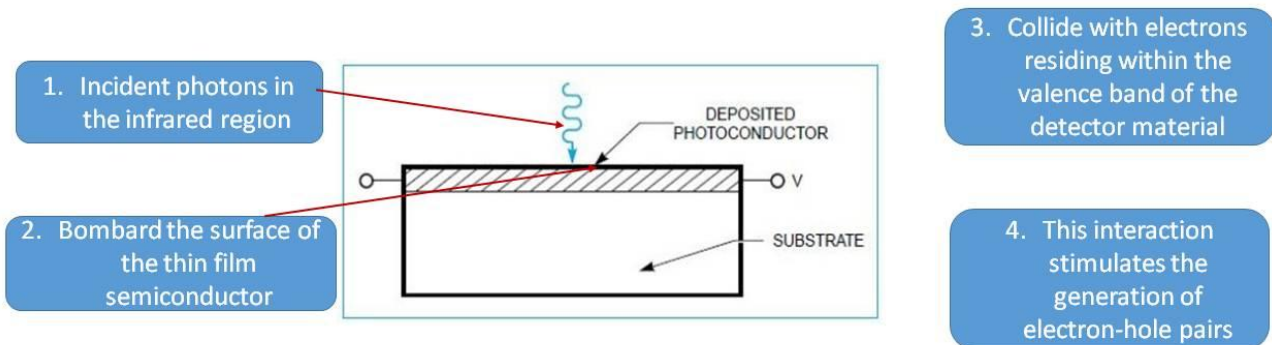
## PbS detector



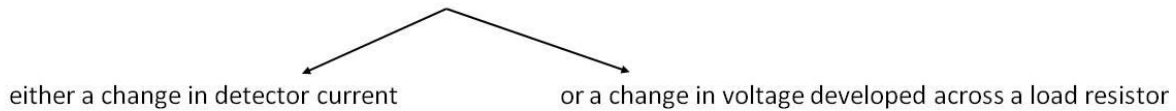
Presented by: Siham Aisha

1

### Introduction

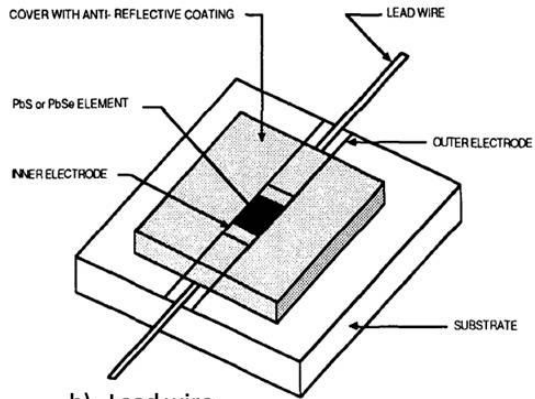


Consequently, this results in an increase in the amount of current flowing through the device. The output signal of the detector circuit is:



2

## Structure



b) Lead wire



a) Substrate

AliExpress Lianyungang Hongan Technology Ltd. 100.0% Positive feedback 68 Followers

Thin transparent quartz glass plate 10\*10\*1.5mm quartz substrate

**US \$265 / lot** (200 pieces)

US \$3.00 New User Coupon Get coupons

Quantity: 1 1000 lots available

Shipping: US \$72.80 to Lebanon via EMS - Estimated Delivery: 5-17 days

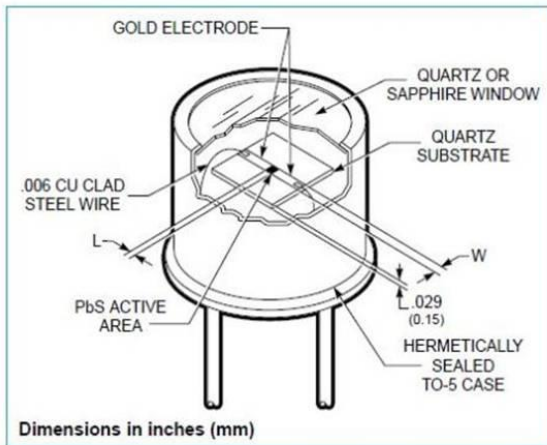
Buy Now Add to Cart

20-Day Buyer Protection Money back guarantee

c) Anti-reflective coating

An antireflective or anti-reflection (AR) coating is a type of optical coating applied to the surface of lenses and other optical elements to reduce reflection. In typical imaging systems, this improves the efficiency since less light is lost due to reflection

3



a) Sapphire window

OEM laser cutting Blank optical glass sapphire window

FOB Reference Price: Get Latest Price

**\$1.00 - \$100.00** / Pieces 1 Piece/Pieces (Min. Order)

Quantity(Pieces)	1 - 100	>100
Est. Time(days)	30	Negotiable

Contact Supplier

Chat Now!

Seller Support Trade Assurance - To protect your orders from payment to delivery

Payment: VISA T T Online Bank Payment Pay Later More

Shipping: Alibaba.com Ocean Shipping Service from China to U.S. Get shipping quote

b) Substrate

Thin transparent quartz glass plate 10\*10\*1.5mm quartz substrate

**US \$265 / lot** (200 pieces)

US \$3.00 New User Coupon Get coupons

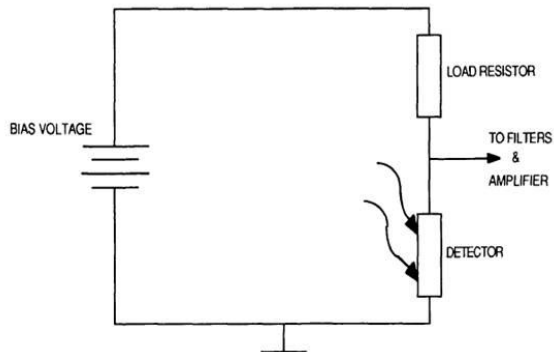
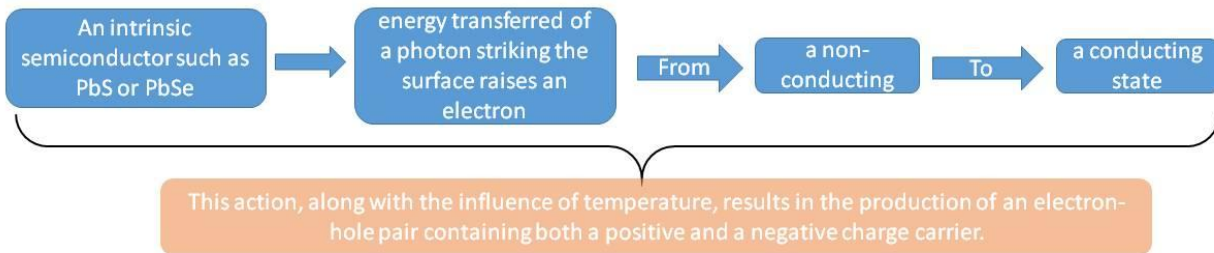
Quantity: 1 1000 lots available

Shipping: US \$72.80 to Lebanon via EMS - Estimated Delivery: 5-17 days

Buy Now Add to Cart

20-Day Buyer Protection Money back guarantee

## Theoretical background



If the detector is biased in a manner similar to that shown in figure, an electric field is developed which will increase the number of charge carriers. This phenomenon, known as the photoconductive effect, thus reduces the resistance of the device.

5

## PbS Detectors Cooled Ultimate PB30-Series

### Description

The PB30 series is a collection of TE cooled photoconductive single element PbS detectors that operate at  $-45^{\circ}\text{C}$  to  $-55^{\circ}\text{C}$  with a 20% cutoff of  $3.4\ \mu\text{m}$ . This series is widely used in analytic, safety and radiometric applications.

### Features

- Spectral range from 1 to  $3.4\ \mu\text{m}$
- State of the art performance
- 100% test data



### Applications

- Pulp and paper industry
- Non-contact temperature measurement
- Spark detection
- Flame control
- Moisture monitoring
- FTNIR

## PbS Detectors Cooled Standard PB27-Series

### Description

The PB27 series is a collection of TE cooled photoconductive single element PbS detectors that operate at  $-20^{\circ}\text{C}$  to  $-35^{\circ}\text{C}$  with a 20% cut-off of  $3.3\ \mu\text{m}$ . This series is widely used in analytic, safety and radiometric applications especially when large active areas are requested.

### Features

- Spectral range from 1 to  $3.3\ \mu\text{m}$
- State of the art performance
- 100% test data

### Applications

- Pulp and paper industry
- Non-contact temperature measurement
- Spark detection
- Flame control
- Moisture monitoring
- FTNIR



## PbS Detectors Uncooled PB25-Series

### Description

The PB25 series is a collection of uncooled photoconductive single element PbS detectors that operate at room temperature with a 20% cut-off of  $3.0\ \mu\text{m}$ . This series is widely used in analytic, safety and radiometric applications especially when large active areas are requested.

### Features

- Spectral range from 1 to  $3.0\ \mu\text{m}$
- State of the art performance
- 100% test data

### Applications

- Pulp and paper industry
- Non-contact temperature measurement
- Spark detection
- Flame control
- Moisture monitoring
- FTNIR



**PbS Photoconductor: 1.0 - 2.9  $\mu\text{m}$**



- ▶ Good Performance for 1.0 - 2.9  $\mu\text{m}$  Range
- ▶ For Detection of CW Light We Recommend an [Optical Chopper](#)
- ▶ Also Comes as a Packaged, Amplified Detector, the [PDA30G](#)

Item # <sup>a</sup>	Info	Wavelength Range	Active Area	Package Type	Rise Time <sup>b</sup>	Peak Wavelength	Peak Sensitivity <sup>c</sup>	Specific Detectivity <sup>d</sup>	Dark Resistance	Compatible Sockets
FDPS3X3		1.0 - 2.9 $\mu\text{m}$	9 mm <sup>2</sup>	TO-5	200 $\mu\text{s}$	2.2 $\mu\text{m}$ (Typ.)	2 x 10 <sup>4</sup> V/W (Min) 5.0 x 10 <sup>4</sup> V/W (Typ.)	1 x 10 <sup>11</sup> cm <sup>2</sup> Hz <sup>1/2</sup> /W (Typ.)	0.25 - 2.5 MOhm	<a href="#">STO5S</a> <a href="#">STO5P</a>

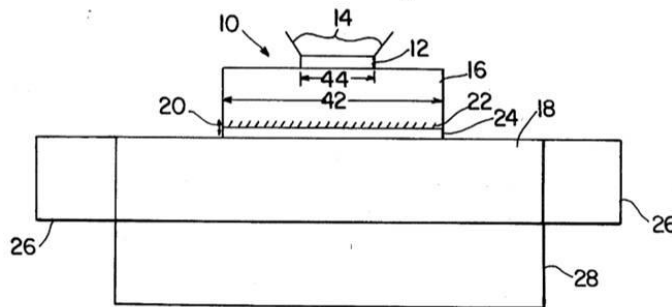
a. All measurements performed with a 50 Ohm load unless stated otherwise.  
 b. Rise Time is measured from 0 to 63% of final value.  
 c. Measured at Peak Wavelength, Chopping Frequency of 600 Hz, and Bias Voltage of 15 V,  $R_{\text{DARK}} = R_{\text{LOAD}}$   
 d. Measured at Peak Wavelength and Chopping Frequency of 600 Hz

Based on your currency / country selection, your order will ship from Newton, New Jersey

+1	Qty	Docs	Part Number - Universal	Price	Available
	<input type="text"/>		<a href="#">FDPS3X3</a> PbS Photoconductor, 3 mm x 3 mm Active Area, 200 $\mu\text{s}$ Rise Time, 1.0 - 2.9 $\mu\text{m}$	\$191.21	Today

to extract a useful signal from these detectors, we can exploit this phenomenon. As the light falls on the detector, the electron flow increases, increasing the conductivity of the materials. and conversely, reducing its resistance. By using a load resistor (typically 1 Mohm, matching the black resistance of the detectors, the best detector will be obtained as a voltage divider, and a bias voltage is applied.) When the resistance of the detector changes, the electronic characteristics of a voltage divider are used for: The debate continues on whether this mode of operation is the most appropriate method of operation for PbS detectors, the community of FPA microbolometers discussing the advantages of the S / N ratio. current associated methods.

**patent**



- 12: thin film of PbS
- 14: electrical leads
- 16: substrate
- 18: heat buffer
- 20: interface
- 22: metal
- 24: bonding layer
- 26: surround
- 28 : heat sink

**16 Substrate**

Considering first the design of substrate 16, the thermal conductivity of the substrate, the thickness of the substrate, and the surface area of the substrate:

Conductivity: for applications where thin film photoconductors will be subject to intense radiation, the substrate should be fabricated from materials such as silicon or sapphire which have large thermal conductivities.

Thickness: It is noted that the substrate must be of sufficient thickness to supply mechanical stability for the thin films.

Surface area: The heat flow in the detector will also be improved if the substrate surface area, as indicated by 42 in FIG. 1, is made large compared to the absorbing detector area, as indicated by 44 in FIG.1. This will allow transverse heat flow within the substrate 16, as well as heat flow in the direction of optical radiation, to contribute to the power dissipation of the detector.

**20 interface**

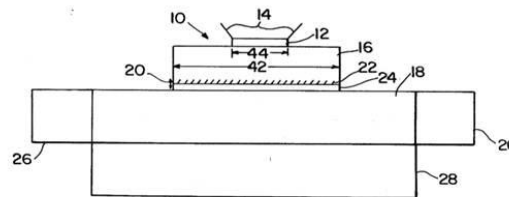
Considering now the design of the interface 20, if a thin highly-conductive material is used for the detector substrate 16, the interface 20 may become a thermal bottleneck (the thermal bottleneck is referred to the points where the temperature is excessively high mainly due to design flaws, the term being of primal importance in the Electronics Industry.)

**22 metal and 24 bonding layer**

In the preferred embodiment of detector 10, the back surface of the substrate 16 is metalized at 22 with a metal of high thermal conductivity, such as silver or copper, by conventional processes such as diffusion. This metalized surface has the effect of increasing the thermal conductivity at the back of the substrate 16, and also providing a metal layer so that a highly-thermally conductive material such as solder may be used as the bonding layer 24 between the substrate and the metal heat buffer.

It should be clear that if interface layer 20 has a higher thermal conductivity than substrate 16, the substrate should be as thin as possible considering requirements of mechanical support, electrical isolation, and formation of the metalized back surface.

Alternatively, if interface layer 20 has a lower thermal conductance than substrate 16, it is advantageous to have a substrate of a larger thickness so that the substrate may dissipate more heat itself.



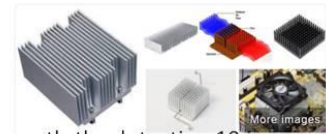
11

**18 heat buffer**

Heat buffer 18 is a high-thermal-conductivity, large-thermal mass in intimate thermal contact with the substrate 16 (via interface 20) and it has a two-fold function:

1. The first function is to remove heat from interface 20 as rapidly as possible and redistribute it throughout the entire buffer to eliminate any appreciable heat buildup in the region behind the interface.
2. The second function is to act as a high-specific-heat thermal reservoir until heat can be removed to the heat sink

Copper is a preferred material for use as the heat buffer 18.

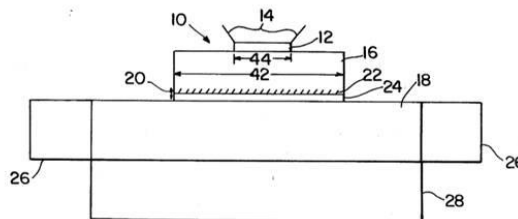


**26 surround**

The type of heat sink used with detector 10 will depend on the particular application. Frequently the detection 10 is surrounded circumferentially by a ring which acts as a heat sink as shown at 26.

**28 Heat sink**

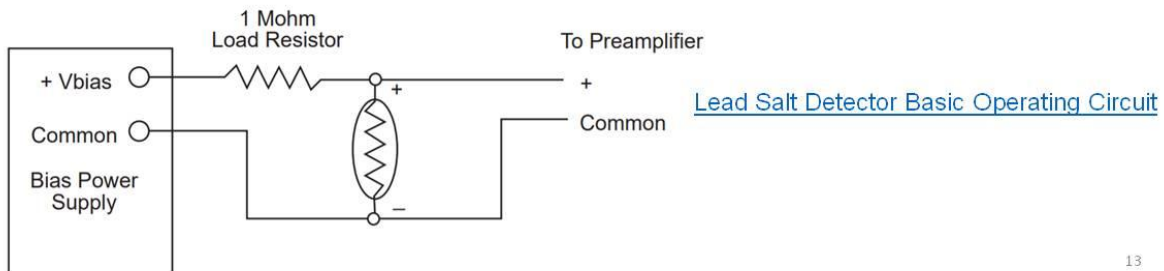
Alternatively, the detector 10 may be mounted on a heat sink such as shown at 28. In that case, the heat sink 28 and the heat buffer 18 may be combined in a single piece of highly-thermally-conductive material such as copper.



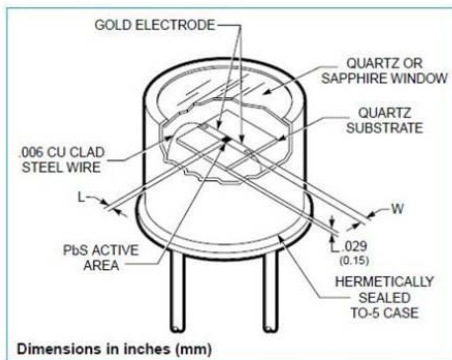
12

## Conclusion

A thin-film, photoconductive, infrared detector hardened against damage from laser irradiation comprising:  
 a thin film of photoconductor material sensitive to infrared radiation;  
 a thin substrate upon the front-surface of which said thin film is deposited,  
 substrate having a high thermal conductivity to provide efficient heat flow from said thin film through said substrate  
 substrate having a surface area that is large relative to the absorbing area of said thin film so that heat generated by said irradiation will be distributed transversely within said substrate,  
 the back surface of said substrate being metallized with a metal of high thermal conductivity;  
 a bonding layer of high thermal conductivity; and a heat buffer upon which said substrate is mounted, contact being made between said buffer and the metallized back surface of said substrate by said bonding layer said heat buffer having a high thermal conductivity to remove heat from said interface as rapidly as possible and redistribute it throughout the entire buffer to eliminate heat buildup in the region behind said interface, said heat buffer having a large thermal mass to act as a high-specific-heat thermal reservoir.



13



### Material

1. Thin film of PbS
2. Electrical leads
3. Substrate:

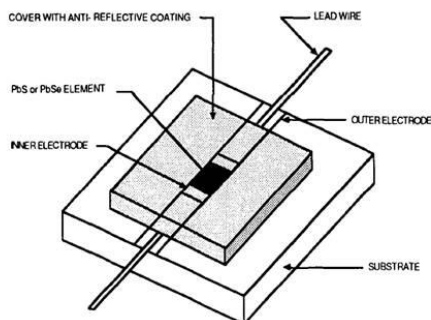
Considering first the design of substrate 16, the thermal conductivity of the substrate, the thickness of the substrate, and the surface area of the substrate:

**Conductivity:** for applications where thin film photoconductors will be subject to intense radiation, the substrate should be fabricated from materials such as silicon or sapphire which have large thermal conductivities.

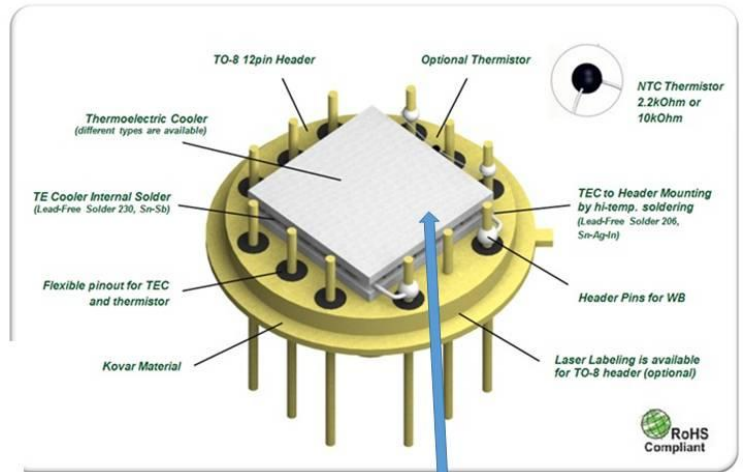
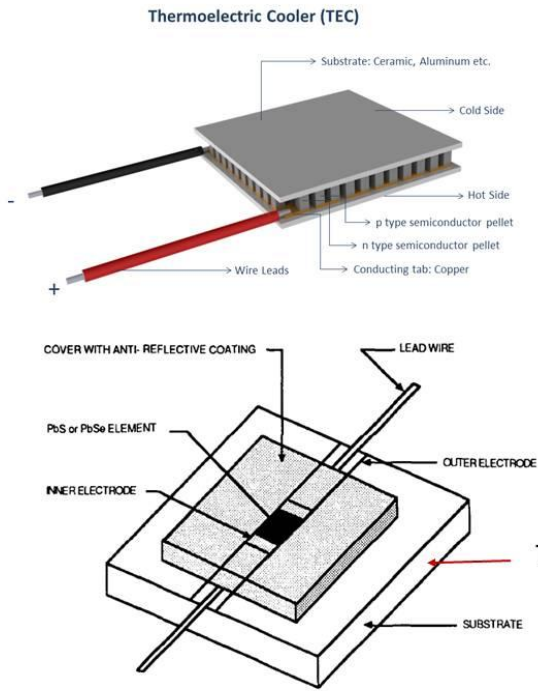
**Thickness:** It is noted that the substrate must be of sufficient thickness to supply mechanical stability for the thin films.

**Surface area:** The heat flow in the detector will also be improved if the substrate surface area, as indicated by 42 in FIG. 1, is made large compared to the absorbing detector area, as indicated by 44 in FIG.1. This will allow transverse heat flow within the substrate 16, as well as heat flow in the direction of optical radiation, to contribute to the power dissipation of the detector.

4. Thermoelectric cooler

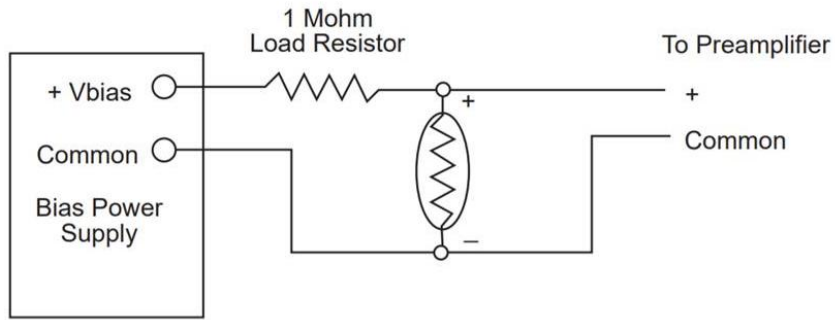


# IAP-IRS Unit Design (PbS detector) Overview (Presentation)



This area it's put above the thermoelectric cooler

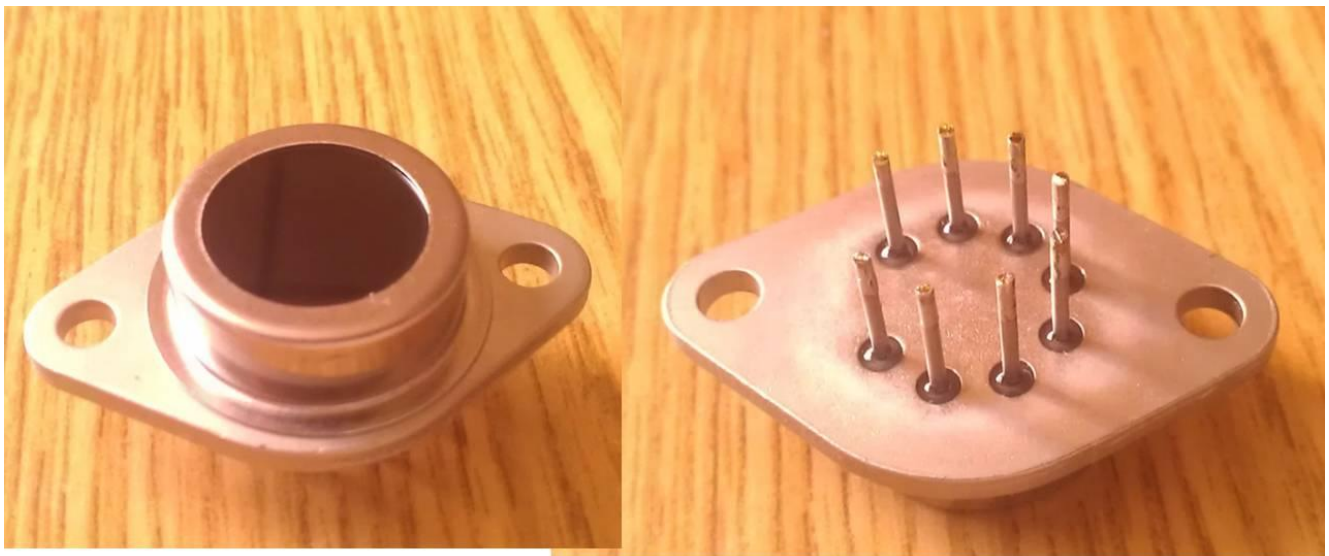
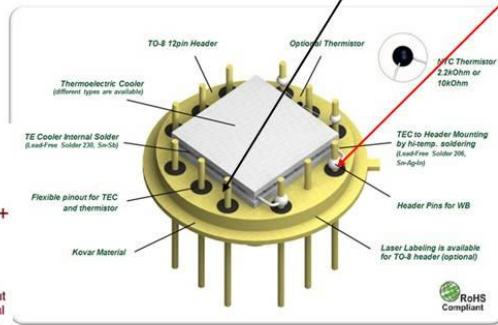
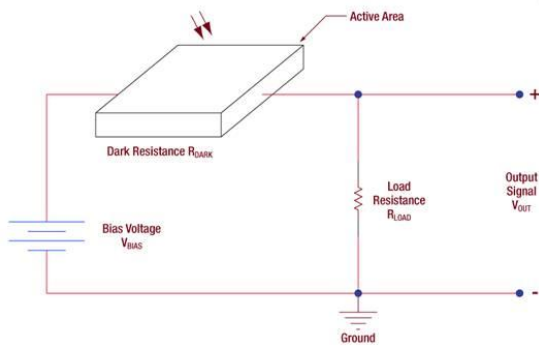




Questions:

يوجد في slide رقم 2 شكل ال detector و لديه عدة أرجل اثنين منها لل voltage and current. لم أعلم لماذا تستخدم بقية الأرجل؟

كيف يتم توصيل ال detector على المخرج ليظهر signal ؟  
 ما هو preamplifier ؟  
 كيف أطبق Bias power supply ؟



**PbS Detector - 10X10 Thermoelectrically Cooled with an IR Filter - 1-3 Microns**

Condition: **New**  
 Quantity:  More than 10 available / 12 sold

Price: **US \$100.00**

[Buy It Now](#)  
[Add to cart](#)

Best Offer: [Make Offer](#)  
 Add to watch list

Longtime Member | 18 Watchers

Shipping: May not ship to Lebanon - Read item description or contact seller for shipping options. | See details  
 Item location: Northon, Massachusetts, United States  
 Ships to: United States

Delivery: Varies

Payments:

Returns: Seller does not accept returns | See details

**Specifications:**  
 $D^*(pk, 600, 1) - 1-2 \times 10^{11}$   
 Active Area - 10mm x 10mm  
 Cooler Power - 2.2V@1.2A  
 Thermistor - 1K @25C  
 Bias - 10 - 30VDC (MAX)  
 LR - 50-100% of Detector Res.

**NOTE:**  
 Improper heat sinking will cause permanent damage  
 Over bias will cause permanent detector damage.  
 Coolers and glass seals are FRAGILE. Do not drop, twist leads or otherwise use unnecessary force.

DO NOT SCALE DRAWING	DRAWN	DATE	NEW ENGLAND PHOTOCONDUCTOR			
	CHECKED	DATE	D-10-3			
MATERIAL:	DESIGNER	DATE				
	ENGINEER	DATE				
FINISH SPEC:	PROJECT ENGINEER	DATE	SIZE	CODE IDENT. NO.	TYPE	REV
	PROJECT APPROVAL	DATE	A		1412A	
PMB 7/21			SCALE	3-1	SHEET	

20

## Thermoelectric cooler (TE)



n/p type semiconductor element bismuth telluride pellet

FOB Reference Price: [Get Latest Price](#)

**\$150.00 - \$250.00** / Kilograms | 1 Kilogram/Kilograms (Min. Order)

[Contact Supplier](#)

[Leave Messages](#) [Request FREE Sample](#)

Seller Support: Trade Assurance - To protect your orders from payment to delivery

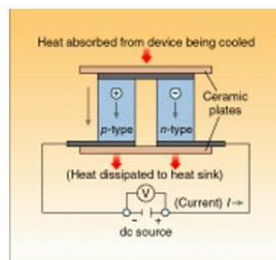
Payment:

Shipping: Alibaba.com Ocean Shipping Service from China to U.S  
[Get shipping quote](#)



Thermoelectric materials on the basis of bismuth telluride  $Bi_2Te_3$

1. A single-stage TE cooler consists of a matrix of thermoelectric couples connected electrically in series, and thermally in parallel.
    - The couples themselves consist of bismuth telluride p- and n-type semiconductor material.
    - These couples are sandwiched between ceramic plates
  2. When a positive dc voltage is applied to the n-type material, electrons pass from the p- to the n-type material
    - The temperature on the cold side decreases because heat is being absorbed from it
    - This heat pumped from the cold side plus the heat generated by the input power is conducted through to the hot side of the cooler, where it is dissipated by a heat sink
  3. **Choosing a cooler**
    - the advantage of TE cooler is that you can integrate the detector and the cooler into one housing
    - The detector chip itself will generally be cooled below 0°C, so hermetic sealing is necessary to block out moisture that would otherwise precipitate and freeze on the cold detector surface.
  4. The total heat load on the top cooler stage plays a critical role in determining the minimum achievable temperature.
    - Gas convection inside the hermetic housing is a major source of heat-loading.
    - Convection can be reduced by filling the package with a high-molecular-weight gas (such as xenon) or by evacuating the package.
  5. Finally, standard glass windows transmit wavelengths only to 2.5 μm.
    - For detectors that respond beyond this point, the package must incorporate sapphire windows or antireflection-coated germanium (Ge) windows, soldered or fused into the package cap.
- ☐ For detectors that respond beyond this point, the package must incorporate sapphire windows or antireflection-coated germanium (Ge) windows, soldered or fused into the package cap.
- ☐ Thermoelectrically cooled detectors are reliable and simple to operate
- The most critical aspect of the design is proper heat-sinking, without which a cooler will be inefficient or may even be damaged by overheating



3-DH-2 37 Fig. 1

- For small two- and three-stage coolers, good thermal connection of the device to a metal plate with several square inches or more of surface area is usually sufficient; forced-air cooling is rarely needed

## 52 Basics<sup>53</sup>

The electrical conductivity of photoconductive detectors is changed by the free-charge carriers generated by absorbed incident photons. A current starts flowing due to an applied voltage or bias. The current flow varies in proportion to the photon irradiance. Lead selenide and lead sulfide detectors fall into this category of detectors. This concept is shown in Figure 51.

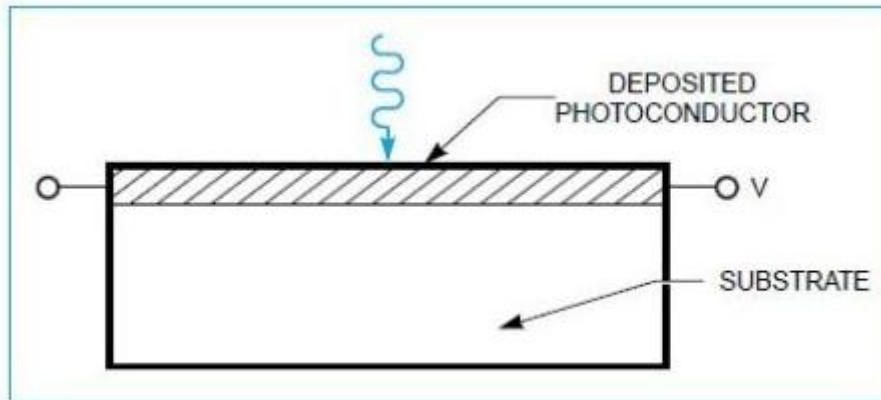


**Figure 51: Schematic of a photoconductive detector**

PbS and PbSe detectors are constructed through chemical deposition of polycrystalline film on a quartz substrate. Gold electrodes are plated to the film edges to provide electrical contact, and the entire assembly is sealed within a package with a suitable window, quartz or sapphire. A typical lead salt detector is depicted in Figure 52.

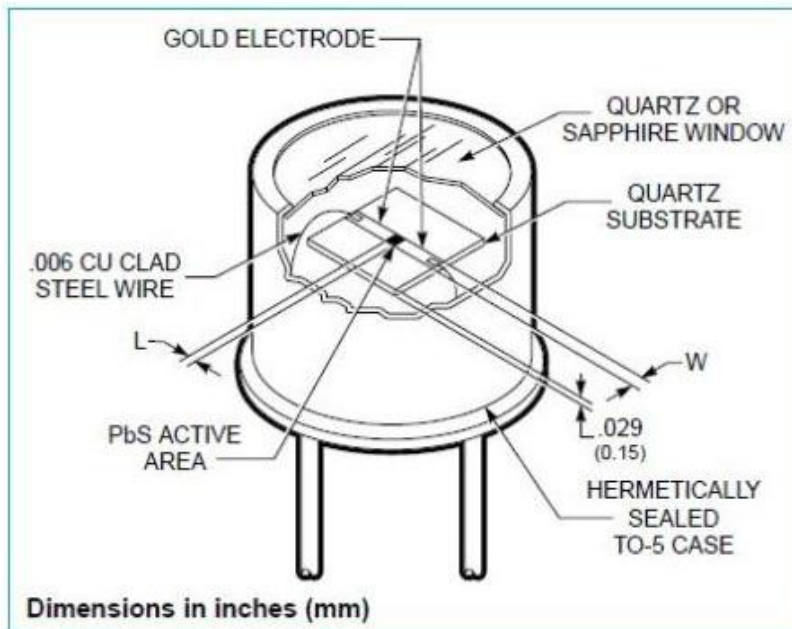


**Figure 52: Typical lead salt detector**

<sup>53</sup> <https://www.azooptics.com/Article.aspx?ArticleID=886>

## 52.1 Introduction to lead salt infrared detectors<sup>54</sup> (Kondas, February 1993)

Infrared detectors are generally classified as being either thermal or photon (quantum) detectors. Among the photon detectors there are two major types: photoconductors and photovoltaics (ref. 1). As shown in Figure 53, PbS and PbSe detectors are both members of the lead salt family of photoconductive infrared detectors. Photoconductive detectors are thin film semiconductor devices which undergo a change in conductivity when exposed to varying quantities of radiation. In the case of both detectors, incident photons in the infrared region bombard the surface of the thin film semiconductor and collide with electrons residing within the valence band of the detector material. This interaction stimulates the generation of electron-hole pairs. Consequently, this results in an increase in the amount of current flowing through the device. The output signal of the detector circuit is either a change in detector current or a change in voltage developed across a load resistor. Thus, when the device is incorporated as part of a sensor system, it is these current or voltage changes which are interpreted by the detector circuit processor as being the target of interest or not.

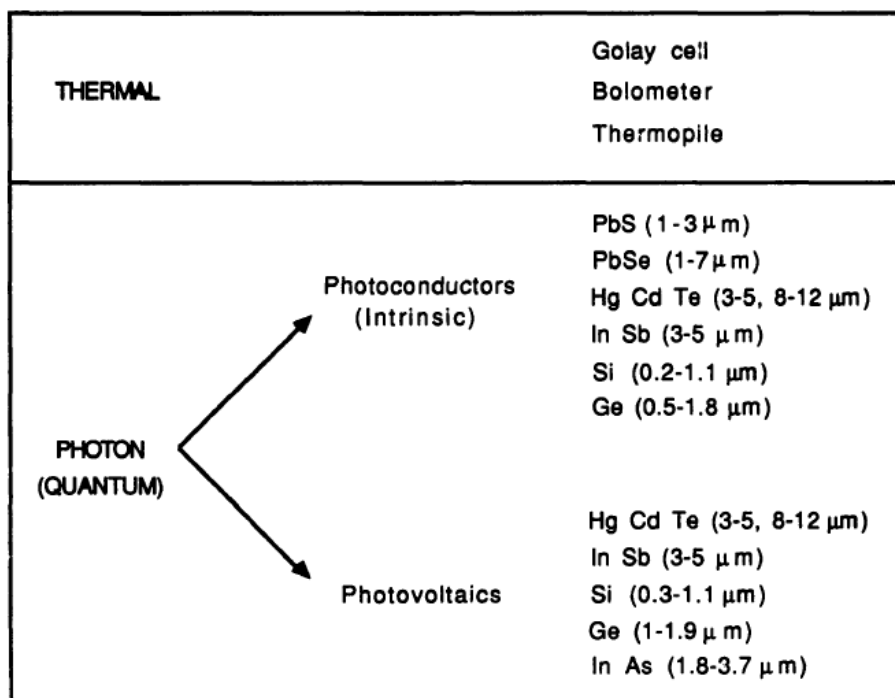


Figure 53: Types of infrared detectors

<sup>54</sup> <https://apps.dtic.mil/dtic/tr/fulltext/u2/a260781.pdf>

## 52.2 Structure

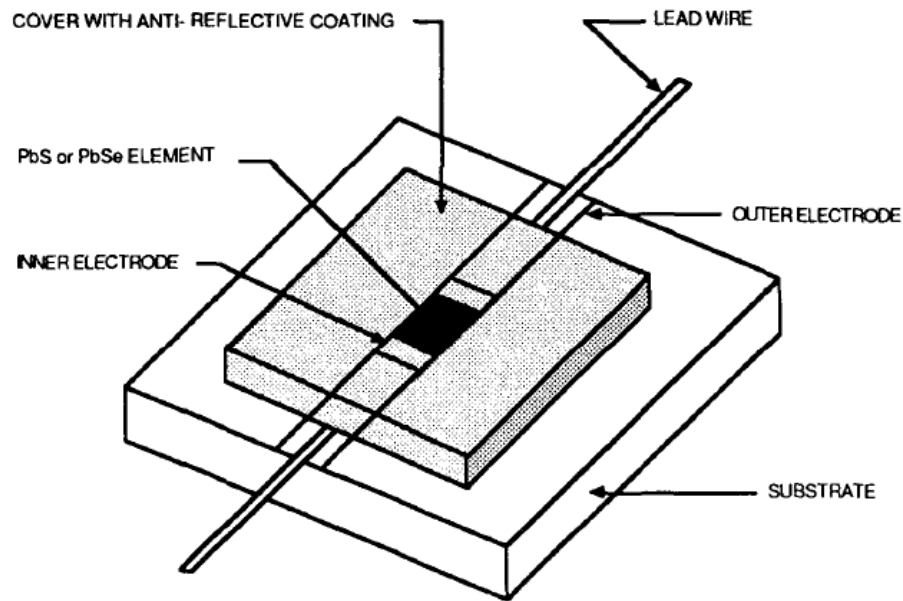


Figure 54:A single element lead salt detector

The structure of a lead salt infrared detector is that of a thin film semiconductor. These thin films are polycrystalline in nature, with individual PbS crystals ranging in size from 0.1  $\mu\text{m}$  to approximately 1.0  $\mu\text{m}$  in diameter, and PbSe crystals ranging in size from 0.2  $\mu\text{m}$  to 0.8  $\mu\text{m}$  in diameter. Lead salt detectors are manufactured as either single element detectors or multi-element detector arrays, the latter for which there are several array designs. A single element detector, which usually possesses the geometry of a thin plate, is shown in Figure 54. The fabrication and basic structure of both of these detector configurations have many similarities. Both configurations utilize chemical deposition techniques to precipitate photosensitive thin films on a flat, cylindrical or spherical substrate surface. However, the most widely used fabrication method is to chemically deposit a lead salt solution onto a flat surface substrate. The major differences between single element detectors and detector arrays are the overall detector sizes, patterns and overall complexity.

### a) Substrate<sup>55</sup>

<sup>55</sup> <https://www.sumibe.co.jp/english/product/it-materials/package/prepreg/index.html>

Thin transparent quartz glass plate 10\*10\*1.5mm quartz substrate



**US \$265 / lot** (200 pieces)

US \$3.00 New User Coupon [Get coupons](#)

Quantity:

– 1 + 1000 lots available

**Shipping: US \$72.80** to Lebanon via EMS ▾

Estimated Delivery: 5-17 days ⓘ

[Buy Now](#) [Add to Cart](#) ♥ 2

 **20-Day Buyer Protection**  
Money back guarantee

The most widely used fabrication method is to chemically deposit a lead salt solution onto a flat surface substrate

### b) Lead wire



Several kinds of lead wires. A lead wire is a metal wire connected from the electric pole of an electronics part or an electronic component. The lead wire is a coated copper wire, a tinned copper wire or another electrically conductive wire used to connect two locations electrically.

### c) Cover with anti-reflective coating

An antireflective or anti-reflection (AR) coating is a type of optical coating applied to the surface of lenses and other optical elements to reduce reflection. In typical imaging systems, this improves the efficiency since less light is lost due to reflection. In complex systems such as telescopes and microscopes the reduction in reflections also improves the contrast of the image by elimination of stray light. This is especially important in planetary astronomy. In other applications, the primary benefit is the elimination of the reflection itself, such as a coating on eyeglass lenses that makes the eyes of the wearer more visible to others, or a coating to reduce the glint from a covert viewer's binoculars or telescopic sight.

### d) Sapphire window



OEM laser cutting Blank optical glass sapphire window

FOB Reference Price: [Get Latest Price](#)

**\$1.00 - \$100.00** / Pieces | 1 Piece/Pieces (Min. Order)

Lead Time:

Quantity(Pieces)	1 - 100	>100
Est. Time(days)	30	Negotiable

[Contact Supplier](#)

[Chat Now!](#)

Seller Support: Trade Assurance – To protect your orders from payment to delivery

Payment: [Online Bank Payment](#) [Pay Later](#) More

Shipping: Alibaba.com Ocean Shipping Service from China to U.S  
[Get shipping quote](#)

### 52.3 Theoretical background

As previously mentioned, the operation of a photoconductive lead salt detector relies heavily on the transfer of infrared energy from incoming photons to electrons residing within the detector material. This transfer results in an electronic reorganization within the atomic structure of the semiconductor. In the case of an intrinsic semiconductor such as PbS or PbSe, energy transferred from a photon striking the surface raises an electron from a non-conducting to a conducting state. This action, along with the influence of temperature, results in the production of an electron-hole pair containing both a positive and a negative charge carrier. If the detector is biased in a manner similar to that shown in Figure 55, an electric field is developed which will increase the number of charge carriers. This phenomenon, known as the photoconductive effect, thus reduces the resistance of the device. Consequently, this will result in an increase in the amount of current flowing through the device. The measured output signal can be either the change in current through the detector or the change in voltage developed across the load resistor in series with the detector. In most cases, the signal detected is the change in voltage developed across the load resistance which is matched to the dark resistance of the detector.

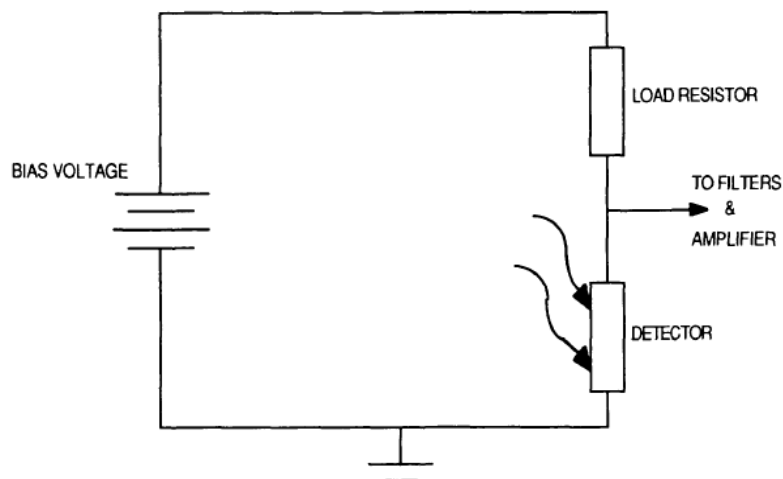


**Figure 55: Photoconductive Detector Bias Circuit**

### 52.3.1 Basic principle

To extract a useful signal from these detectors, we can exploit this phenomenon. As light falls on the detector the electron flow increases increasing the materials conductivity; and inversely, reducing its resistance. By using a load resistor (typically 1Mohm, as matching the detectors dark resistance will ensure the best detector as a voltage divider, and a bias voltage is applied. as the resistance of the detector changes, the electronic characteristics of a voltage divider are used to measure the "output". debate continues as to whether this mode of operation is the most suitable operation method for PbS and PbSe detectors, with the Microbolometer FPA community discussing the S/N ratio advantages of current related methods.

### 52.3.2 Biasing

our PbS and PbSe detectors are photoconductive and require a biasing voltage to operate, increasing the bias voltage increases signal and noise respectively. A minimum bias voltage is needed to overcome system noise and a maximum voltage cannot be exceeded due to runaway thermal effects. Historically the optimum biasing voltage has been 50V/mm with the maximum being roughly double, but progress in modern electronics means that lower voltages can now be used without making compromises in the performance. LASER COMPONENTS corporate research is looking into the trade-offs.

### 52.3.3 Noise

the two dominant types of noise in a PbS or PbSe detector are generation-recombination noise and 1/f noise, which is why historically detector specifications are given at 1 KHz to represent optimum performance. However, we understand that more often than not these detectors are used at lower operation frequencies which is why LASER COMPONENTS lists D\* values for operation at 90 Hz as well. As a rule of thumb, you can expect a threefold increase in noise at 90 Hz when compared to 1 KHz.

## 53 Overview (William V. Cummings Jr., 1951)<sup>56</sup>

The infrared region of the spectrum was first discovered in 1800 by Sir William Herschel. While checking the heating power of the various colors in the solar spectrum, he found that the greatest heating effect was not inside the visible portion, but just beyond the red edge of the spectrum. Thus a simple heat detecting instrument, the thermometer, became the first infrared detector. (3) Sensitive heat detecting devices such as bolometers, thermocouples, and various other radiometers have been used as means of detecting and studying infrared radiation down to the present time. In fact, above 3.5 microns, thermal detection is used almost exclusively in infrared spectrometers.

For that part of the spectrum below 3.5 microns, other special techniques have been discovered and developed. Among these methods is the detection and measurement of spectra by photocells. Three types of photoelectric phenomena have been adapted to spectroscopy: (4) the photo emissive effect, which is the ejection of electrons from matter when energy is imparted to it by radiation; the photovoltaic effect, which is the generation of a potential difference between two electrodes when one of them is irradiated; and the photoconductive effect, which is the change of electrical conductivity of a material caused by radiation falling upon it. Cells incorporating these properties have been developed and used, but only the photoconductive cells have an appreciable response in the infrared. Detectors using various photoconductive materials have been developed, but at the present time those which have photosensitive elements composed chiefly of lead sulfide appear to be superior. Figure 56 illustrates the spectral sensitivities of various photocells and the visibility curve of the eye. (5) It should be pointed out that in this graph the maximum of sensitivity for each curve is arbitrarily set at 100. The two typical curves shown for lead sulfide surfaces indicates that the spectral response of cells of this type will vary somewhat in each individual case.

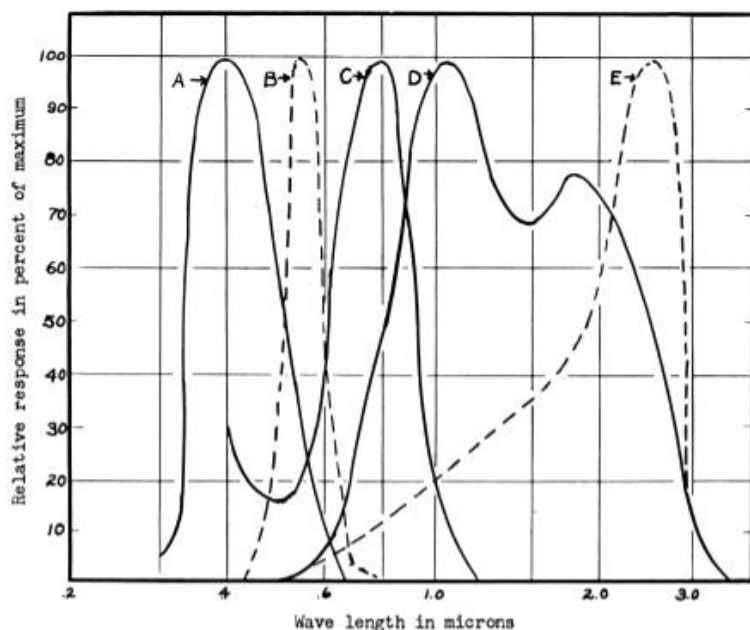
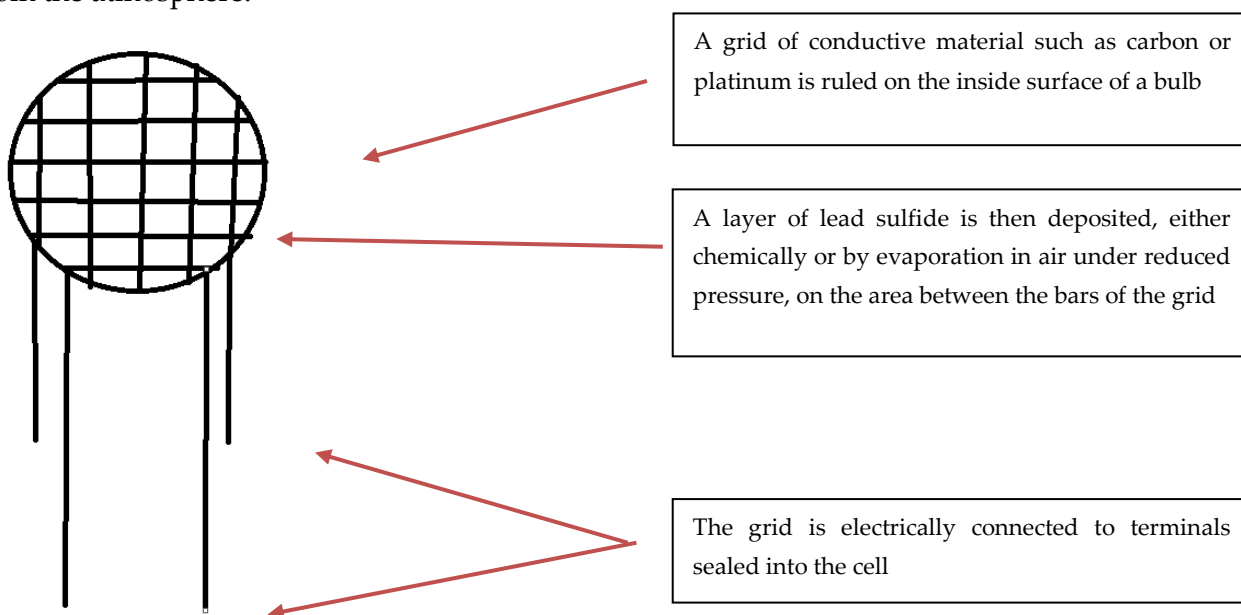


Figure 56: Spectral Response Curves of Various Photocells

<sup>56</sup> [https://scholarsmine.mst.edu/cgi/viewcontent.cgi?article=5150&context=masters\\_theses](https://scholarsmine.mst.edu/cgi/viewcontent.cgi?article=5150&context=masters_theses)

The photoconductive properties of lead sulfide when irradiated by wave lengths between 1 and 3.5 microns were first utilized by the Germans during world War II as a means of detecting infrared radiation. During the latter stages of the conflict PbS cells were developed by the United States and Great Britain, for it was noted that within their response range they were far superior to any other detector in speed of response and sensitivity. To the physicist, this indicated a powerful tool for infrared spectroscopy. Experiments by Sutherland and others (6) indicate that the signal-to-noise ratio for the PbS cell at its point of maximum sensitivity is increased to such an extent that slit widths can be reduced by a factor of 10 in going from thermocouple to lead sulfide detector. This, in turn, gives a corresponding increase in resolving power. Advantage is also derived from the exceptional speed of response of the lead sulfide detector which has a time constant of less than .001 sec. compared to times of about .1 sec. and .01 sec. for the thermocouple and bolometer, respectively. This permits the use of faster "chopping" rates for the incident radiation, which in turn simplifies the problem of amplification. <7>

The methods of manufacturing these cells are variable, but, all manufacturers seem to follow the same general procedure. A grid of conductive material such as carbon or platinum is ruled on the inside surface of a bulb and the grid is electrically connected to terminals sealed into the cell. A layer of lead sulfide is then deposited, either chemically or by evaporation in air under reduced pressure, on the area between the bars of the grid. (At the present time, the evaporation process seems to produce cells with more desirable characteristics.) A heat treatment then follows at determined temperature and pressure conditions. Finally, the activated surface is sealed off in vacuum or otherwise protected from the atmosphere.



As a result of this procedure, the original lead sulfide lattice has lost the sulfur in some small regions and consequently has an excess of lead. In other regions of the material, the sulfur has been replaced by oxygen, which had been contained in the lattice or absorbed interstitially, leaving as a final product a homogeneous mixture of both types. A layer of oxygen atoms also may be absorbed on the surface and barrier layers may be formed at the contact surface of the grid material. The characteristics of the cell will, to a great extent, depend upon this formation. [8]

## 54 IR photoconductive detectors<sup>57</sup>

- ▶ PbSe and PbS Photoconductive Detectors
- ▶ Linear Response for 1.0 - 2.9  $\mu\text{m}$  or 1.5 - 4.8  $\mu\text{m}$
- ▶ TO-5 Package Style



Lead Sulfide (PbS) and Lead Selenide (PbSe) photoconductors are widely used for the detection of infrared radiation from 1.0 to 4.8  $\mu\text{m}$ . Photoconductors detect light in a broader wavelength range, offer higher detection capability, and provide better linear response in the IR than typical PIN junction photodiodes.

### 54.1 Photoconductors vs. Photodiodes

Unlike PIN junction photodiodes, which generate a photocurrent when light is absorbed in the depleted region of the junction semiconductor, the photoconductive material in these devices exhibits a decrease in electrical resistance when illuminated with IR radiation. Photoconductive detectors typically have a very linear response when illuminated with IR radiation.

### 54.2 Usage Notes

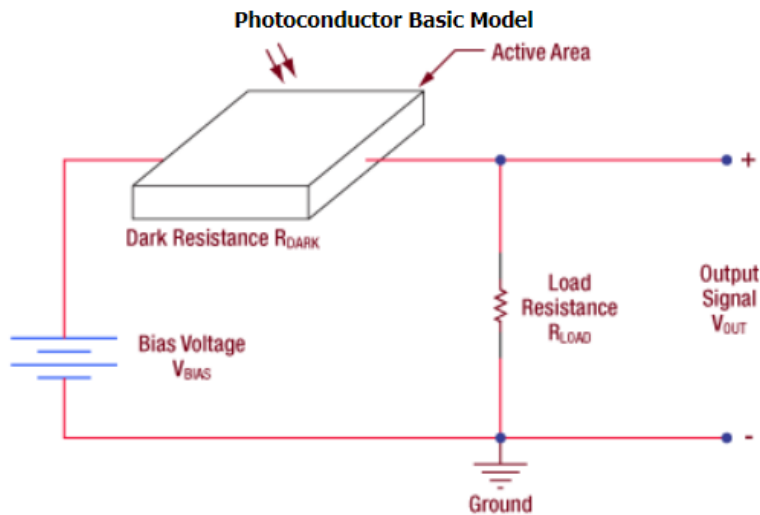
Photoconductors function differently than typical PIN junction photodiodes. We recommend that an optical chopper be employed when using these detectors with CW light, due to signal noise issues. PbS and PbSe detectors can be used at room temperature. However, temperature fluctuations will affect dark resistance, sensitivity, and response speeds (see the Temperature Considerations section in the Tutorial tab for details).

Theory

### 54.3 Theory of Operation

For photoconductive materials, incident light will cause the number of charge carriers in the active area to increase, thus decreasing the resistance of the detector. This change in resistance leads to a change in measured voltage, and hence, photosensitivity is expressed in units of V/W. An example operating circuit is shown. Please note that the circuit depicted is not recommended for practical purposes since low frequency noise will be present.

<sup>57</sup> [https://www.thorlabs.com/newgrouppage9.cfm?objectgroup\\_ID=6479](https://www.thorlabs.com/newgrouppage9.cfm?objectgroup_ID=6479)



The detection mechanism is based upon the conductivity of the thin film of the active area. The output signal of the detector with no incident light is defined by the following equation:

$$V_{OUT} = \frac{R_{LOAD}}{R_{DARK} + R_{LOAD}} * V_{BIAS}$$

A change  $\Delta V_{OUT}$  then occurs due to a change  $\Delta R_{Dark}$  in the resistance of the detector when light strikes the active area:

$$\Delta V_{OUT} = -\frac{R_{LOAD}V_{BIAS}}{(R_{DARK} + R_{LOAD})^2} * \Delta R_{DARK}$$

## 54.4 Frequency Response

Photoconductors must be used with a pulsed signal to obtain AC signals. Hence, an optical chopper (shown in Figure 57) should be employed when using these detectors with CW light. The detector responsivity ( $R_f$ ) when using a chopper can be calculated using the equation below:

$$f_c = \frac{1}{2\pi\tau_r}$$

Here,  $f_c$  is the chopping frequency,  $R_0$  is the response at 0 Hz, and  $\tau_r$  is the detector rise time.



**Figure 57: The SR540 optical beam chopper from Stanford Research Systems**

An optical chopper is a device that interrupts a light beam at periodic intervals. By varying the frequency of operation of the chopper it can be used for various applications. The first ever optical chopper was invented in the 1800s and was used to measure the speed of light.

The chopper consists of a mechanical disc that rotates at a certain speed. In order to improve the performance of the chopper high precision and stable mechanical components must be chosen. This worksheet will provide details on the working principle, construction and applications of optical beam choppers.

### 54.5 Temperature Considerations

These detectors consist of a thin film on a glass substrate. The effective shape and active area of the photoconductive surface varies considerably based upon the operating conditions, thus changing performance characteristics. Specifically, responsivity of the detector will change based upon the operating temperature.

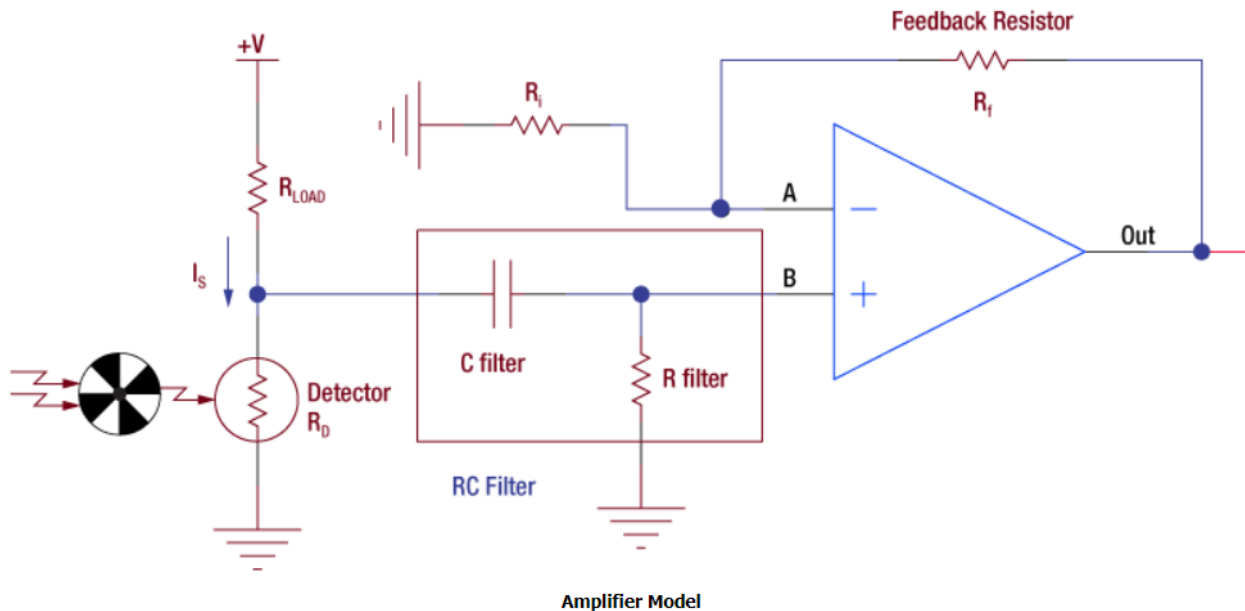
Temperature characteristics of PbS and PbSe bandgaps have a negative coefficient, so cooling the detector shifts its spectral response range to longer wavelengths. For best results, operate the photodiode in a stable controlled environment. See the Operating Manuals for characteristic curves of Temperature vs. Sensitivity for a particular detector.

### 54.6 Typical Photoconductor Amplifier Circuit

Due to the noise characteristic of a photoconductor, it is generally suited for AC coupled operation. The DC noise present with the applied bias will be too great at high bias levels, thus limiting the practicality of the detector. For this reason, IR detectors are normally AC coupled to limit the noise. A pre-amplifier is required to help maintain the stability and provide a large gain for the generated current signal.

Based on the schematic below, the op-amp will try to maintain point A to the input at B via the use of feedback. The difference between the two input voltages is amplified and provided at the output. It is also important to note the high pass filter that AC couples the input of the amplifier blocks any DC signal. In addition, the resistance of the load resistor (RLOAD) should be equal to the dark resistance of the detector to ensure maximum signal can be acquired. The supply voltage (+V) should be at a level where the SNR is acceptable and near unity. Some applications require higher voltage levels; as a result, the noise will increase. Provided in chapter 4 of the Operating Manual is a SNR vs. Supply Voltage characteristic curve to help determine best operating condition. The output voltage is derived as the following:

$$V_{out} = \left(1 + \frac{R_f}{R_i}\right) * I_s R_D$$



### 54.7 Signal to Noise Ratio

Since the detector noise is inversely proportional to the chopping frequency, the noise will be greater at low frequencies. The detector output signal is linear to increased bias voltage, but the noise shows little dependence on the bias at low levels. When a set bias voltage is reached, the detector noise will increase linearly with applied voltage. At high voltage levels, noise tends to increase exponentially, thus degrading the signal to noise ratio (SNR) further. To yield the best SNR, adjust the chopping frequency and bias voltage to an acceptable level.

### 54.8 Noise Equivalent Power

The noise equivalent power (NEP) is the generated RMS signal voltage generated when the signal to noise ratio is equal to one. This is useful, as the NEP determines the ability of the detector to detect low level light. In general, the NEP increases with the active area of the detector and is given by the following equation:

$$NEP = \frac{\text{Incident Energy} * \text{Area}}{\frac{S}{N} * \sqrt{\Delta f}}$$

Here, S/N is the Signal to Noise Ratio,  $\Delta f$  is the Noise Bandwidth, and Incident Energy has units of W/cm<sup>2</sup>. For more information on NEP, please see Thorlabs' Noise Equivalent Power White Paper.

### 54.9 Dark Resistance

Dark Resistance is the resistance of the detector under no illumination. It is important to note that dark resistance will increase or decrease with temperature. Cooling the device will increase the dark resistance.

### 54.10 Detectivity (D) and Specific Detectivity (D\*)

Detectivity (D) is another criteria used to evaluate the performance of the photodetector. Detectivity is a measure of sensitivity and is the reciprocal of NEP.

$$D = \frac{1}{NEP}$$

Higher values of detectivity indicate higher sensitivity, making the detector more suitable for detecting low light signals. Detectivity varies with the wavelength of the incident photon.

NEP of a detector depends upon the active area of the detector, which in essence will also affect detectivity. This makes it hard to compare the intrinsic properties of two detectors. To remove the dependence, Specific Detectivity ( $D^*$ ), which is not dependent on detector area, is used to evaluate the performance of the photodetector. In the equation below,  $A$  is the area of the photosensitive region of the detector and  $\Delta f$  is the effective noise bandwidth.

$$D^* = \frac{\sqrt{A \cdot \Delta f}}{NEP}$$

**PbS Photoconductor: 1.0 - 2.9  $\mu\text{m}$**



Zoom

- ▶ Good Performance for 1.0 - 2.9  $\mu\text{m}$  Range
- ▶ For Detection of CW Light We Recommend an [Optical Chopper](#)
- ▶ Also Comes as a Packaged, Amplified Detector, the [PDA30G](#)

Item # <sup>a</sup>	Info	Wavelength Range	Active Area	Package Type	Rise Time <sup>b</sup>	Peak Wavelength	Peak Sensitivity <sup>c</sup>	Specific Detectivity <sup>d</sup>	Dark Resistance	Compatible Sockets
FDPS3X3	<a href="#">Info</a>	1.0 - 2.9 $\mu\text{m}$	9 mm <sup>2</sup>	TO-5	200 $\mu\text{s}$	2.2 $\mu\text{m}$ (Typ.)	2 x 10 <sup>4</sup> V/W (Min) 5.0 x 10 <sup>4</sup> V/W (Typ.)	1 x 10 <sup>11</sup> cm <sup>2</sup> Hz <sup>1/2</sup> /W (Typ.)	0.25 - 2.5 MOhm	<a href="#">STO5S</a> <a href="#">STO5P</a>

a. All measurements performed with a 50 Ohm load unless stated otherwise.  
 b. Rise Time is measured from 0 to 63% of final value.  
 c. Measured at Peak Wavelength, Chopping Frequency of 600 Hz, and Bias Voltage of 15 V,  $R_{\text{DARK}} = R_{\text{LOAD}}$   
 d. Measured at Peak Wavelength and Chopping Frequency of 600 Hz

Based on your currency / country selection, your order will ship from Newton, New Jersey

+1	Qty	Docs	Part Number - Universal	Price	Available
	<input type="text"/>		<a href="#">FDPS3X3</a> PbS Photoconductor, 3 mm x 3 mm Active Area, 200 $\mu\text{s}$ Rise Time, 1.0 - 2.9 $\mu\text{m}$	\$191.21	Today

## 55 Room-temperature, thin-fil, PbS photoconductive detector hardened against laser damage<sup>58</sup>

FIG. 1 shows a thin-film, photoconductive, infrared detector 10 incorporating the laser hardening techniques of the present invention. The active detecting layer is a thin film 12 of photoconductive material which is sensitive to infrared radiation at ordinary room temperatures (approximately 290 K. to 310 K.), such as a thin film of PbS, typically 1  $\mu\text{m}$  in thickness and 0.25-10mm in surface area. Electrical connection is made to the thin film in a conventional manner as indicated by electrical leads 14. The thin film 12 is deposited by conventional techniques on a substrate 16, which as previously noted, provides mechanical stability and electrical isolation for the thin film. The substrate 16 is mounted on a metal heat buffer 18 by means of an interface 20 of negligible thermal impedance. The interface 20 includes a metalized back-surface 22 of substrate 16 and a bonding layer 24. As will be described hereinafter, the characteristics of the substrate 16, the heat buffer 18, and the interface 20 are very important in hardening the detector against damage due to laser irradiation and constitute novel features of the present detector. The detector 10 (specifically heat buffer 18) is mounted on a conventional heat sink as shown conceptually at 26 and 28. Since laser irradiation may result in high thermal loading of thin-film detectors, the thermal configuration of a detector is important in determining its susceptibility to damage from optical radiation. To prevent irreversible detector damage, the heat generated by the laser irradiation must be dissipated so that the thin film does not reach the critical temperature where detector degradation begins. This is approximately 600 K. in a PbS detector. The detector of the present invention is designed to provide efficient heat flow from the thin film to prevent such detector degradation. Considering first the design of substrate 16, the thermal conductivity of the substrate, the thickness of the substrate, and the surface area of the substrate relative to the detector absorbing area are important factors in hardening the detector against laser irradiation. FIG. 2 shows the calculated power density  $P$  for heating thin films of PbS on substrates of quartz, strontium titanate and silicon (shown by curves 30, 32, and 34, respectively) from 300 K. to 600 K. (the damage threshold temperature) as a function of irradiation time  $t$ . The substrates are of the same thickness and have very good thermal contact with a heat sink so that heat flow within the detector is not limited by an interface layer which might confine the heat within the substrate. Further explanation of the calculations referred to herein may be found in "Thermal Analysis of Laser Damage in the Thin-film Photoconductors", Journal of Applied Physics, Vol. 47, No. 7, July 1976, authored by the inventors of the present application.

As shown in FIG. 2,  $P$  is strongly dependent on substrate material over a wide range of irradiation times. For times between 10 and 10-sec, the damage thresholds for detectors on silicon substrates are about seven times those for detectors on quartz and about two times those for detectors on strontium titanate. A comparison of the magnitudes of the damage thresholds for the different substrates at a specific irradiation time in this range indicates that  $P$  is approximately proportional to the square root of substrate thermal conductivity. (For example, the thermal conductivity of silicon is about 50 times that of quartz). For long times, the ratio of damage thresholds for silicon and quartz increases to 50

---

<sup>58</sup> <https://patentimages.storage.googleapis.com/c5/3c/aa/789099fb49e8e4/US4117329.pdf>

indicating the  $P$  is proportional to thermal conductivity. This analysis indicates that, for applications where thin film photoconductors will be subject to intense radiation, the substrate should be fabricated from materials such as silicon or sapphire which have large thermal conductivities. The advantages of using a silicon or sapphire substrate over quartz become even greater for detectors operating at intermediate or low temperatures. For example, at 77 K., the thermal conductivity of silicon is three orders of magnitude greater than that of quartz, as compared to the factor of 50 at room temperature. Accordingly, materials that have high thermal conductivities such as silicon (1.5 W/cm K) and sapphire (0.33 W/cm-K) are preferred materials for use as substrate 16 in the present invention.

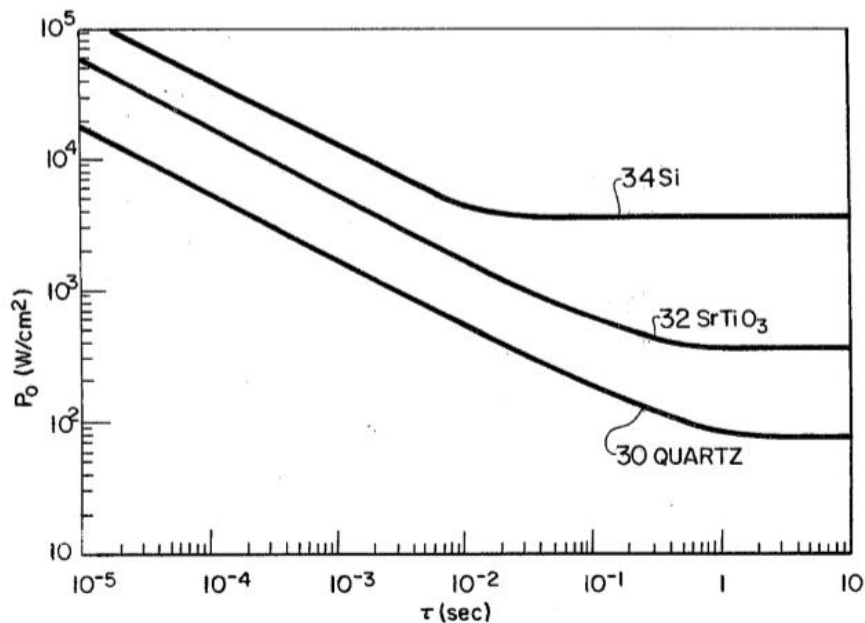


**FIG. 2**

The substrate thickness also has an effect on heat flow in the detector. Consider a detector on a quartz substrate which is bonded to a heat sink by an adhesive layer with a large thermal conductance per unit area ( $h = 10$  W/cmK) so that the bonding layer does not limit heat flow. The calculated power density  $P$  required to heat a thin film from 300' to 600 K. is shown in FIG. 3 as a function of irradiation time for three different substrate thicknesses. The thicknesses used in the calculation to generate curves 36, 38 and 40 are 0.01 0.03 and 0.1 cm, respectively. For sufficiently short times ( $t(10$  msec), heat does not diffuse to the rear of the substrate and  $P$  is independent of substrate thickness. The substrate thickness can have a large effect on  $P$  if the pulse duration is longer than 50 msec. For very large  $T$ , heat is conducted to the heat sink at the same rate it is deposited by the optical radiation. In this limit,  $P$ , asymptotically approaches a constant value independent of  $T$  and is inversely proportional to substrate thickness.

Therefore, decreasing the substrate thickness will improve detector resistance to laser irradiation if the thermal conductivity between the substrate and the heat sink is better than the thermal conductivity within the substrate. It is noted that the substrate must be of sufficient thickness to supply mechanical stability for the thin films.

The heat flow in the detector will also be improved if the substrate surface area, as indicated by 42 in FIG. 1, is made large compared to the absorbing detector area, as indicated by 44 in FIG.1. This will

allow transverse heat flow within the substrate 16, as well as heat flow in the direction of optical radiation, to contribute to the power dissipation of the detector.

Considering now the design of the interface 20, if a thin highly-conductive material is used for the detector substrate 16, the interface 20 may become a thermal bottleneck (the thermal bottleneck is referred to the **points where the temperature is excessively high mainly due to design flaws**, the term being of primal importance in the Electronics Industry.). This bottleneck becomes important at long times when heat has had time to diffuse to the rear of the substrate. FIG. 4 shows the calculated power density thresholds  $P_0$  for PbS thin films on silicon substrates assuming several values for the thermal conductance per unit area ( $h$ ) of the interface 20. The damage thresholds depicted by curves 46, 48, 50, and 52 were calculated using values of the  $h$  equal to 10, 1, 10, and 10  $W/cm^2K$ , respectively. For  $t < 10$  msec, the thermal conductance of the interface 20 is not important and the calculated threshold is the same for the four values of  $h$  used. For irradiation times  $t < 1$  sec, the above variation in  $h$  changes the calculated power density threshold  $P_0$  by several orders of magnitude.

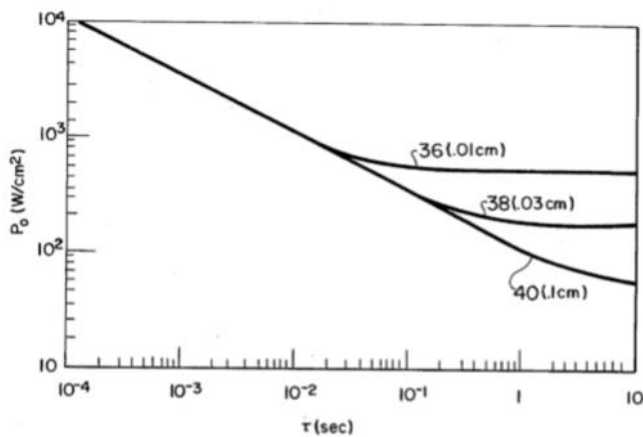


FIG. 3

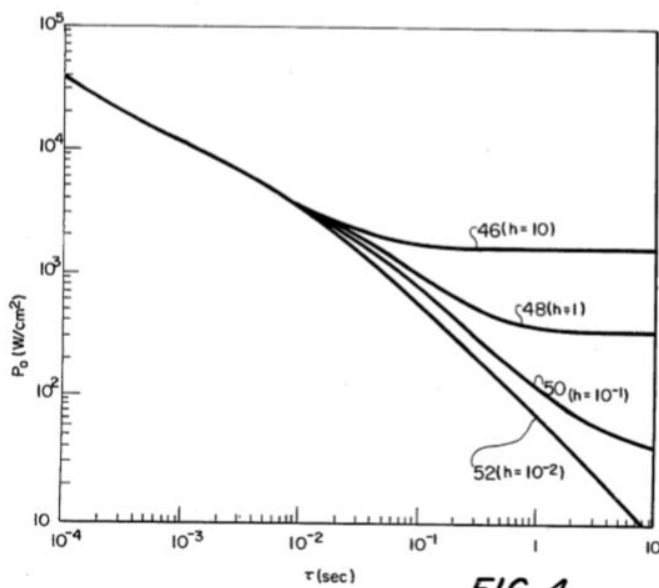
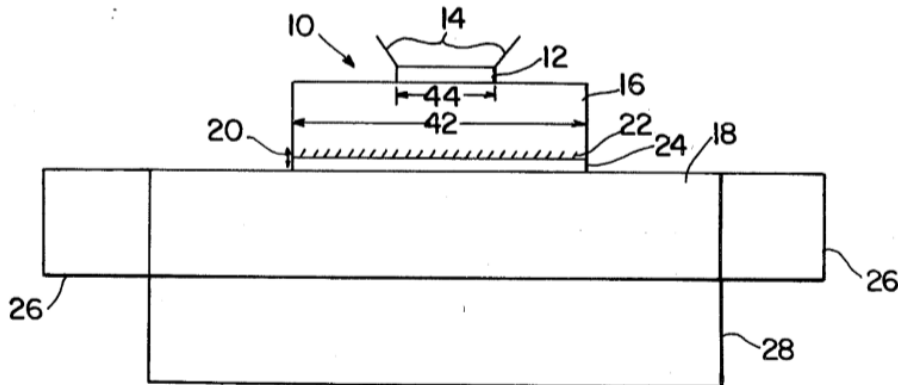


FIG. 4

In the preferred embodiment of detector 10, the back surface of the substrate 16 is metalized at 22 with a metal of high thermal conductivity, such as silver or copper, by conventional processes such as diffusion. This metalized surface has the effect of increasing the thermal conductivity at the back of

the substrate 16, and also providing a metal layer so that a highly-thermally conductive material such as solder may be used as the bonding layer 24 between the substrate and the metal heat buffer.

It can be seen that thermal conductance of the interface 20 is relatively more important if the substrate is efficient in transferring heat from the absorbing surface of the detector. If the interface layer 20 is less efficient in transferring heat than the substrate 16, the heat generated by the laser radiation will build up in the substrate.



It should be clear that if interface layer 20 has a higher thermal conductivity than substrate 16, the substrate should be as thin as possible considering requirements of mechanical support, electrical isolation, and formation of the metalized back surface. These factors require a minimum substrate thickness of approximately 0.005 cm. Alternatively, if interface layer 20 has a lower thermal conductance than substrate 16, it is advantageous to have a substrate of a larger thickness so that the substrate may dissipate more heat itself.

The use of a heat buffer 18 is the final novel feature of a detector according to the present invention. Heat buffer 18 is a high-thermal-conductivity, large-thermal mass in intimate thermal contact with the substrate 16 (via interface 20) and it has a two-fold function. The first function is to remove heat from interface 20 as rapidly as possible and redistribute it throughout the entire buffer to eliminate any appreciable heat buildup in the region behind the interface. This requires a high thermal conductivity material. The second function is to act as a high-specific-heat thermal reservoir until heat can be removed to the heat sink. The large thermal mass of the heat buffer maintains the heat buffer (and therefore the detector) at a low temperature. For long optical irradiation times, heat can be effectively conducted into the heat sink and the function of the heat buffer becomes simply an effective conduit for heat transport. Copper is a preferred material for use as the heat buffer 18.

The type of heat sink used with detector 10 will depend on the particular application. Frequently the detector 10 is surrounded circumferentially by a ring which acts as a heat sink as shown at 26 in FIG. 1. Alternatively, the detector 10 may be mounted on a heat sink such as shown at 28. In that case, the heat sink 28 and the heat buffer 18 may be combined in a single piece of highly-thermally-conductive material such as copper.

The preceding analysis shows that thin-film photoconductors can withstand laser irradiation of much higher power if they are fabricated on thin, highly thermally conductive substrates which are efficiently coupled to heat sinks. These results are summarized in FIG. 5. Curve 54 is the threshold for onset of damage of PbS photoconductors on a quartz substrate assuming the thermal conductance per unit area of the bonding layer is 0.01 W/cmK. This thermal configuration is typical of that found in

many prior PbS applications. Curve 56 refers to thresholds for PbS detectors on quartz substrates with higher thermal conductance per unit area of the bonding layer. Curve 58 is the calculated threshold for a silicon substrate with a bonding layer having the same thermal conductance per unit area as the bonding layer in curve 56. These calculations show that an optimized thermal design can significantly increase the damage threshold for all irradiation times shown. In particular, for a 10-second irradiation time, the damage thresholds can be increased by more than two orders of magnitude. These considerations are particularly important for detectors exposed to chopped radiation or repetitively pulsed lasers where the energy of one pulse may not damage the detector but the integrated power may.

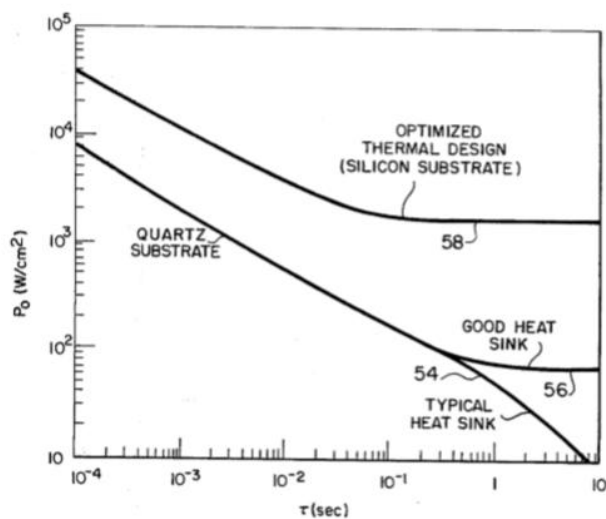


**FIG. 5**

Although the present invention has been described with application to room temperature PbS detectors, it is noted that other thin-film photoconductive detectors may be hardened against laser damage by using the techniques of the present invention. For example, a thin-film lead selenide (PbSe) detector (which operates at liquid nitrogen temperature) may be hardened against laser irradiation by fabrication on a thin, highly-conductive substrate which is mounted on a heat buffer by means of a highly-conductive interface. The heat sink in this case must be capable of maintaining the required operating temperature in the liquid-nitrogen Dewar.

It is also noted that when the word 'high' is used to describe the thermal conductivity of the substrate 16 in the present specification, a thermal conductivity of approximately 0.25W/cm-K to 15 W/cm-K is denoted. When the term "high" is used to describe the thermal conductivity of the heat buffer 18 or the bonding layer 24, a thermal conductivity of approximately 0.5 W/cm K to 20 W/cm-K is denoted. For example, silicon would be a material having a thermal conductivity within the former range and copper would be a material within the latter range. It is further noted that when the word 'thin' is used to describe the substrate 16, a substrate of approximately 0.005 cm to 0.025 cm in thickness is denoted.

Obviously, many modifications and variations of the present invention are possible in light of the above teachings. It is therefore to be understood that within the scope of the appended claims, the invention may be practiced otherwise than as described.

What is claimed and desired to be secured by Letters Patent of the United States is:

1. A thin-film infrared detector hardened against damage from laser irradiation comprising: a thin film of material sensitive to infrared radiation; a thin substrate upon the front-surface of which said
2. thin film is deposited, said substrate having a high thermal conductivity to provide efficient heat flow from said thin film through said substrate, said substrate having a surface area that is large relative to the absorbing area of said thin film so that heat generated by irradiation will be distributed transversely within said substrate; a heat sink; and an interface of negligible thermal impedance between said substrate and said heat sink for removing heat from said substrate.
3. The detector of claim 1 wherein said thin film comprises lead sulfide.
4. The detector as recited in claim 1, wherein said interface of negligible thermal impedance comprises: a metalized back surface of said substrate, said back surface being metallized with a metal of high thermal conductivity; and a bonding layer of high thermal conductivity between said back-surface and said heat sink.
5. The detector of claim 3 wherein said bonding layer comprises solder.
6. The detector of claim 3 wherein said thin substrate is sapphire.
7. The detector of claim 3 wherein said thin substrate is silicon.
8. A thin-film, photoconductive, infrared detector hardened against damage from laser irradiation comprising: a thin film of photoconductor material sensitive to infrared radiation; a thin substrate upon the front-surface of which said thin film is deposited, said substrate having a high thermal conductivity to provide efficient heat flow from said thin film through said substrate, said substrate having a surface area that is large relative to the absorbing area of said thin film so that heat generated by said irradiation will be distributed transversely within said substrate, the back surface of said substrate being metallized with a metal of high thermal conductivity; a bonding layer of high thermal conductivity; and a heat buffer upon which said substrate is mounted, contact being made between said buffer and the metalized back surface of said substrate by said bonding layer said heat buffer having a high thermal conductivity to remove heat from said inter face as rapidly as possible and redistribute it throughout the entire buffer to eliminate heat buildup in the region behind said interface, said heat buffer having a large thermal mass to act as a high-specific-heat thermal reservoir.
9. The detector of claim 7 further comprising a heat sink in good thermal contact with said heat buffer for removing heat from said heat buffer.
10. The detector of claim 7 wherein said thin substrate is sapphire.
11. The detector of claim 7 wherein said thin film comprises lead sulfide.
12. The detector of claim 10 wherein said heat buffer comprises copper.
13. The detector of claim 10 wherein said thin substrate is silicon.
14. A thin-film, photoconductive, infrared detector hardened against damage from laser irradiation comprising: a thin film of photoconductor material sensitive to infrared radiation; a thin substrate upon the front-surface of which said thin film is deposited, said substrate having a high thermal conductivity to provide efficient heat flow from said thin film through said substrate, said substrate having a surface area that is large relative to the absorbing area of said thin film so that heat generated by said irradiation will be distributed transversely

within said substrate; an interface of negligible thermal impedance located on the back-surface of said substrate; and a heat buffer upon which said substrate is mounted, contact being made with said buffer by said inter face, said heat buffer having a high thermal conductivity to remove heat from said interface as rapidly as possible and redistribute it throughout the entire buffer to eliminate heat buildup in the region behind said interface, said heat buffer having a large thermal mass to act as a high-specific heat thermal reservoir.

15. The detector of claim 13 further comprising a heat sink in good thermal contact with said heat buffer for removing heat from said buffer.
16. The detector as recited in claim 13 wherein said interface of negligible thermal impedance comprises: a metalized back-surface of said substrate, and a bonding layer of high thermal conductivity between said back-surface and said heat sink.
17. A detector of claim 15 wherein said bonding layer comprises solder.

## 56 PbS Synthesis<sup>59</sup>

### 56.1 Prepare Reactants

Prepare reaction mixture with 14 g of octadecene, 1.4 grams of oleic acid, 450 mg of lead oxide. When it mixes up it is murky yellow at first and then becomes clear when it is heated up.

### 56.2 Degas the mixture

The Schlenk line is used to degas the reaction mixture. Remove the nitrogen bubbler and replace with a pipette bulb. Slowly turn the stopcock from nitrogen flow to vacuum. First watch the pipette bulb when it collapses vacuum is being pulled on the solution. Now slowly turn the stopcock while watching the reaction mixture making sure not over-boil. Once the boiling mixture has stabilized fully-open the vacuum valve. Leave the mixture under vacuum for approximately 1 hour. Slowly turn the stopcock back to nitrogen while holding a finger over the bubbler to prevent pulling the silicon fluid into the Schlenk line. Remove the pipette bulb and replace the nitrogen bubbler. Increase the reaction mixture to 180 degrees

### 56.3 Injection

Prepare the injection mixture from 4 gms of octadecene in 210 mL of hexylmethylidisilazane (HMDS). Once the reaction mixture has stabilized purge a syringe with nitrogen. Draw up the injection mixture and quickly insert it into the reaction vessel. Within second the mixture should turn a turbid black color. Let it react for 5 minutes and then quench the reaction in an ice bath. After it comes to room temperature transfer it to a separatory funnel.

### 56.4 Cleaning

After the synthesis is quenched it is necessary to remove excess oleic acid and other impurities. Two methods are shown:

A) Separatory Funnel:

1. pour PbS QDs (dissolved in minimal amount of hexanes) into sep. funnel
2. precipitate with methanol (MeOH)
3. Add back small amounts of hexanes and shake funnel vigorously between additions. If there is still precipitated product clinging to the walls of the funnel between hexanes additions, continue to add more hexanes. Once the product stops sticking to the walls, let the funnel sit for a minute or so to see if any phase separation occurs. If not, continue adding small amount of hexanes until it does. Note that only a small amount of separation will be seen at the bottom of the funnel at first, and the mixture will have to sit for at least 30 mins to fully separate. If no phase separation is observed after a few additions, the funnel can be placed in the freezer to speed the process.
4. Drain off the clear bottom MeOH layer into the waste

---

<sup>59</sup> <https://youtu.be/bKLDkjV6Mbc>

5. Drain small amounts (~1 or 2 mL portions) of PbS into a centrifuge tube.
6. Precipitate by filling the tube with MeOH
7. Centrifuge the tube (5 min, 3000 RPM), and pour off clear MeOH layer
8. Pour another addition of PbS into the same tube and repeat steps 6) and 7). Note: for the first two cycles, multiple tubes can be used rather than just one, but on the third (last) cleaning step, it is generally preferred to use a single tube to consolidate product.
9. Dissolve the product in minimal amount of hexanes, vortex, sonicate (5 mins, or until dissolved) and add PbS back to the separatory funnel. Repeat the above steps for the first two cleaning cycles.

B) Simply use multiple centrifuge tubes:

- (1) Dissolve the product in small amount of hexanes, then vortex and sonicate until QDs dissolve.
- (2) Precipitate by filling each centrifuge tube with MeOH
- (3) Centrifuge each tube (5 min, 3000 RPM)
- (4) Discard clear supernatant
- (5) For the first two cleaning cycles, repeat the above steps

To consolidate into a single tube, just choose one tube to keep and repeat step 1) above for the other tubes. Then successively add the dissolved QDs of ONE of the other tubes to to the dry product in the tube you chose to keep and repeat steps 2-4 above until all tubes have been combined into one (only add the contents of one tube for each step precipitation-centrifuge cycle-do not combine the contents of all remaining tubes at once)

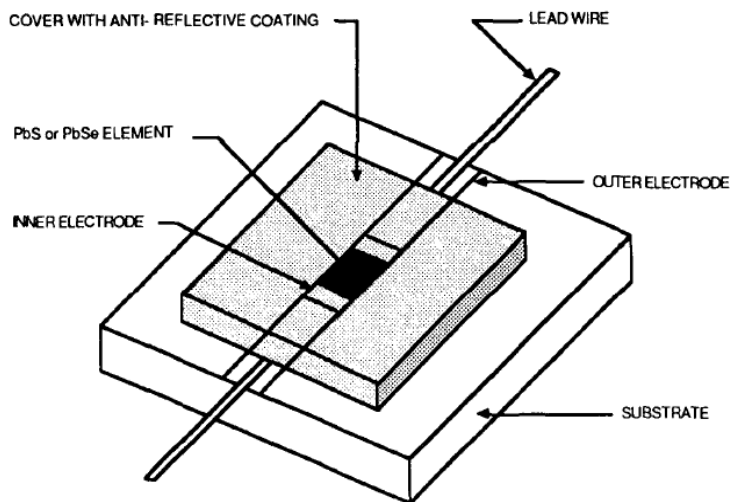
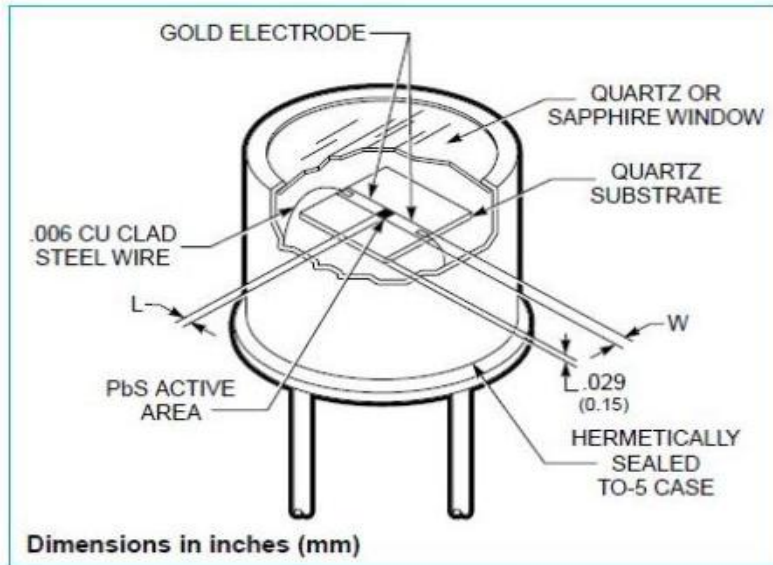
In both cases, once the cleaning cycles are complete, the QDs can be dissolved in hexanes or toluene and left to sit. Alternatively, a septum cap can be placed on the centrifuge tube which can then be placed on the Schlenk line to dry.

## 56.5 PbS/Polymer Nanocomposite Optical Materials with High Refractive Index

High refractive index nano-PbS/polymer composites were fabricated from reactive lead-containing precursors and polythiourethane (PTU) oligomer terminated with isocyanate group, followed by in situ gas/solid reaction. The lead-containing precursor with a chemical formula of  $\text{Pb}(\text{SCH}_2\text{CH}_2\text{OH})_2$  was synthesized in water phase at  $\text{pH} = 5.9$  and exhibited an absorption at 317 nm in dimethyl sulfoxide (DMSO) in UV-vis spectra. PbS nanoparticles can be formed in DMSO after treatment with  $\text{H}_2\text{S}$ . TEM studies indicated that the PbS nanoparticles were smaller than 10 nm and aggregated seriously in DMSO. After the precursors were incorporated into PTU oligomer, the obtained composite films were treated with  $\text{H}_2\text{S}$  to obtain PbS nanoparticles/PTU nanocomposite films. TEM showed that the nanocomposites exhibited interesting phase behaviors depending on the precursor content in films. A uniform spherical aggregate of PbS nanoparticles (nanospheres) with a size smaller than 100 nm formed in the nanocomposite films below 26.3 wt % of lead-containing precursors. When the precursor content was larger than 59.3 wt %, the PbS.

## 57 Conclusion

### PbS detector design



### Material

1. **Thin film of PbS**
2. **Electrical leads**
3. **Substrate:**

Considering first the design of substrate 16, the thermal conductivity of the substrate, the thickness of the substrate, and the surface area of the substrate:

Conductivity: for applications where thin film photoconductors will be subject to intense radiation, the substrate should be fabricated from materials such as silicon or sapphire which have large thermal conductivities.

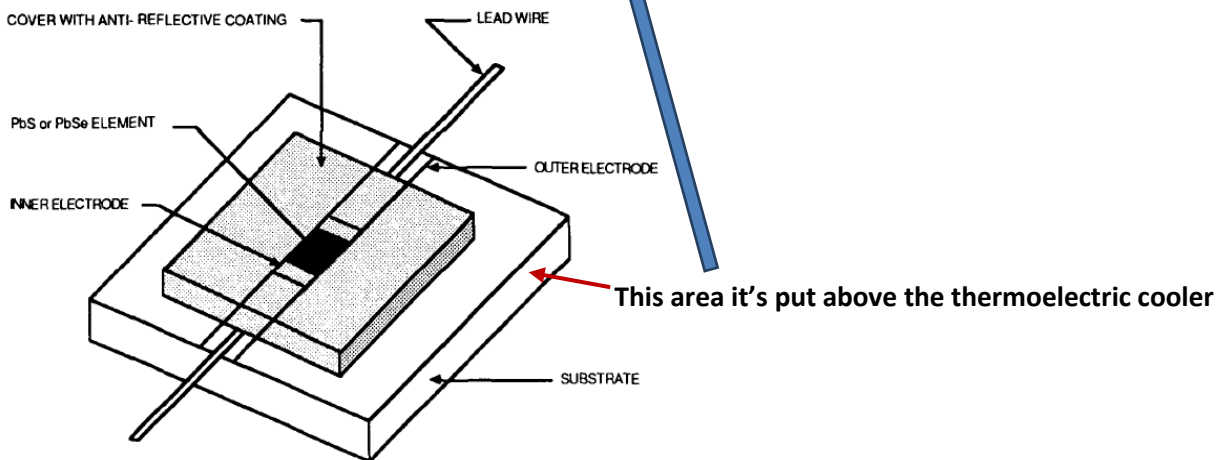
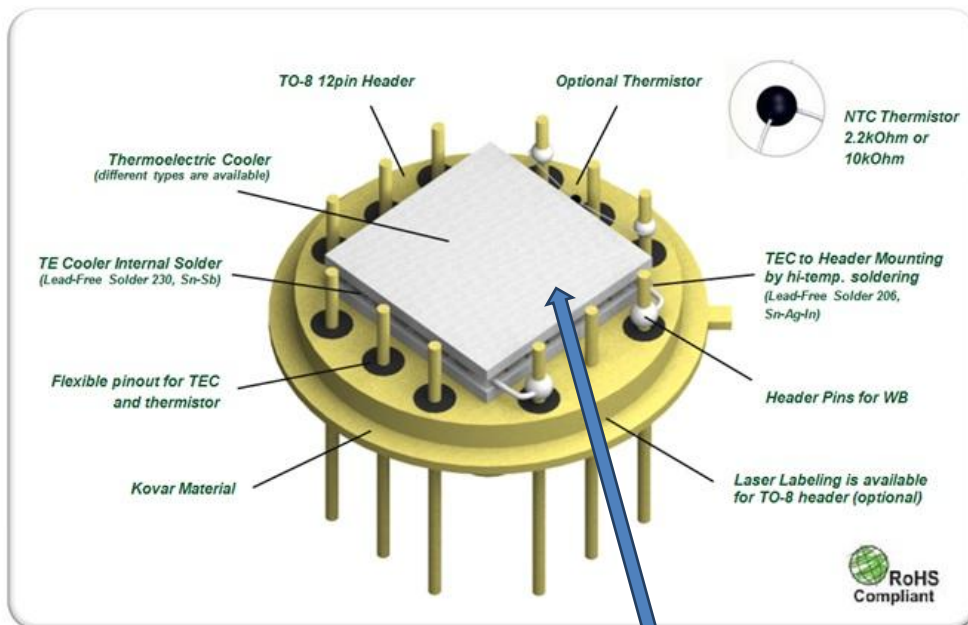
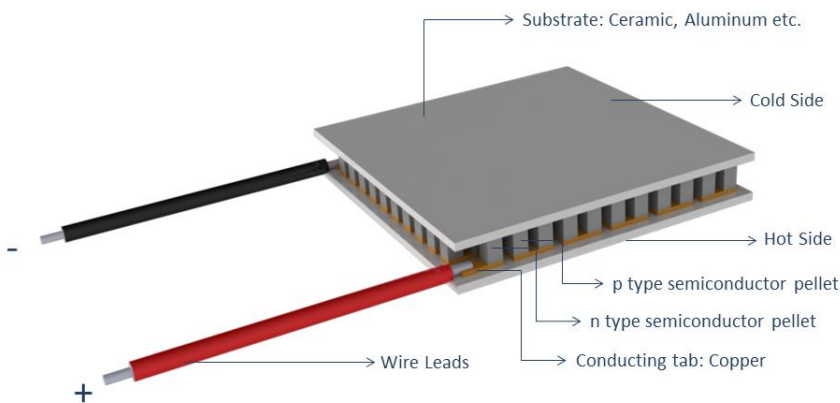
Thickness: It is noted that the substrate must be of sufficient thickness to supply mechanical stability for the thin films.

Surface area: The heat flow in the detector will also be improved if the substrate surface area, as indicated by 42 in FIG. 1, is made large compared to the absorbing detector area, as indicated by 44 in

FIG.1. This will allow transverse heat flow within the substrate 16, as well as heat flow in the direction of optical radiation, to contribute to the power dissipation of the detector.

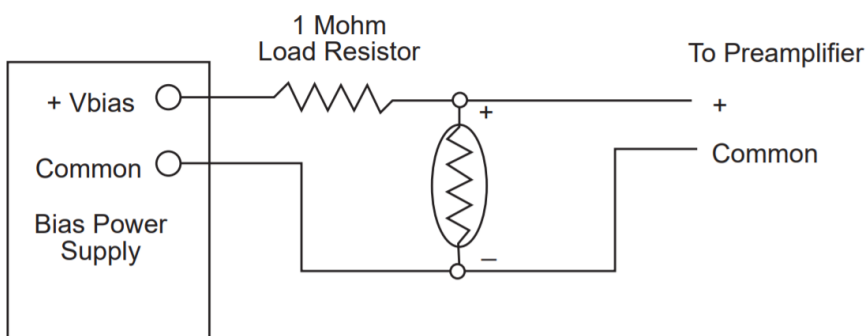
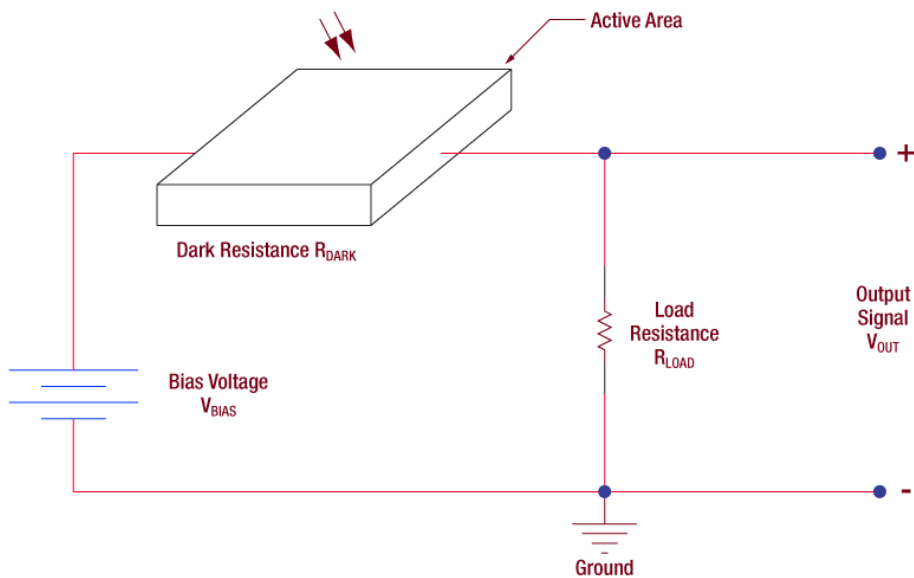
4. Thermoelectric cooler

Thermoelectric Cooler (TEC)



Finally, the detector will be supplied power

## Conclusion



Material	Supplier
PbS thin element film	
Thermoelectric cooler	<p style="text-align: right;"><a href="http://www.ekt2.com">www.ekt2.com</a> قطرنخي</p> <p style="text-align: center;"><a href="http://www.ekt2.com/products/productdetails/14_SENSOR_PELTIER_TEC1-12706">http://www.ekt2.com/products/productdetails/14_SENSOR_PELTIER_TEC1-12706</a></p> <p>Alibaba</p> <p><a href="https://www.alibaba.com/product-detail/Multistage-Peltier-Thermoelectric-Cooler-TEC2-127_1968756161.html?spm=a2700.7724838.2017115.26.11a72476ZW5aqT&amp;s=p">https://www.alibaba.com/product-detail/Multistage-Peltier-Thermoelectric-Cooler-TEC2-127_1968756161.html?spm=a2700.7724838.2017115.26.11a72476ZW5aqT&amp;s=p</a></p>
Substrate quartz	<p>Alibaba</p> <p><a href="https://www.alibaba.com/product-detail/SUCCESS-Polished-Quartz-Slides-Clear-Optical_60697516047.html?spm=a2700.galleryofferlist.normalList.69.2be0ffc5HIpEP3">https://www.alibaba.com/product-detail/SUCCESS-Polished-Quartz-Slides-Clear-Optical_60697516047.html?spm=a2700.galleryofferlist.normalList.69.2be0ffc5HIpEP3</a></p>
Sapphire window	<p>Alibaba</p> <p><a href="https://www.alibaba.com/product-detail/25-4mm-Anti-Reflection-Coated-Optical_60830570102.html?spm=a2700.7724838.2017115.25.4b4d6ebe2KQix&amp;s=p">https://www.alibaba.com/product-detail/25-4mm-Anti-Reflection-Coated-Optical_60830570102.html?spm=a2700.7724838.2017115.25.4b4d6ebe2KQix&amp;s=p</a></p>
Heat sink	<p style="text-align: right;"><a href="http://www.ekt2.com">www.ekt2.com</a> قطرنخي</p> <p style="text-align: center;"><a href="http://www.ekt2.com/products/productdetails/412_3D_PRINTER_EXTRUDER_HEAT_SINK">http://www.ekt2.com/products/productdetails/412_3D_PRINTER_EXTRUDER_HEAT_SINK</a></p>
Kovar material	

### Heat sink:



## 412 3D PRINTER EXTRUDER HEAT SINK

40x40x11 Aluminum Radiator Black

Original No:  
In Stock: confirmed after order

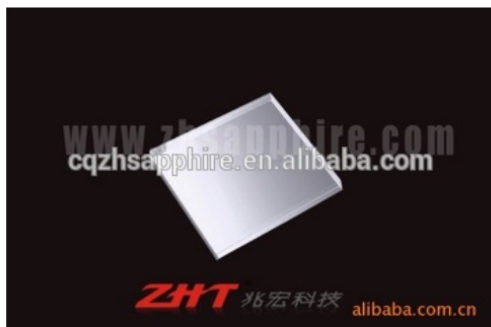
Quantity:  Price 3.30627 USD

[Buy Now](#)

[Download PDF](#) [Download Excel](#) [YouTube](#) [Product Video](#)

### Sapphire window overview:

[https://www.alibaba.com/product-detail/square-sapphire-window\\_60473688791.html?spm=a2700.7724838.2017115.66.7003110fs2bxd2](https://www.alibaba.com/product-detail/square-sapphire-window_60473688791.html?spm=a2700.7724838.2017115.66.7003110fs2bxd2)



[View larger image](#)



Add to Compare [Share](#)

square sapphire window

FOB Reference Price: [Get Latest Price](#)

**\$1.00 - \$15.00** / Pieces | 1 Piece/Pieces (Min. Order)

[Contact Supplier](#)

[Leave Messages](#)

Seller Support: Trade Assurance protect your orders from payment to delivery

Payments: [Online Bank Payment](#) [Pay Later](#) More

Shipping: Alibaba.com Ocean Shipping Service from China to U.S  
[Get shipping quote](#)

# Conclusion

## Quick Details

Place of Origin:	Chongqing, China (Mainland)	Brand Name:	ZHT
Model Number:	ZHT-Round Sapphire Window	Material:	Synthetic Sapphire Optical Grade
Usage:	Infrared, optical, UV	Structure:	Round
Shape:	Plano	Product name:	sapphire window
Description:	optical grade	Surface Quality:	S/D 10/5, 20/10, 40/20, 80/50

## Supply Ability

Supply Ability: 50000 Piece/Pieces per Month

## Packaging & Delivery

Packaging Details ZHT sapphire products are packed within vacuumed plastic bag.  
ZHT packing is anti-dust. And, more customized packing demand can be met.

Port Chongqing, China

## Product Description

Sapphire possesses nice light transmission in 0.20-5.50um wave band, and its infrared ray transmission is hardly influenced by temperature, so the optical components made of sapphire are fully applied to infrared equipments, low-temperature laboratory viewing aperture, and high precise apparatus of navigation and aviation, etc.

We can fabricate miniature size as well as super large size: diameter 1mm to 300mm, with thickness 0.2mm to 200mm.

## Substrate quartz:

[https://www.alibaba.com/product-detail/Polishing-thin-optical-clear-quartz-substrate\\_60729729793.html?spm=a2700.galleryofferlist.normalList.64.144867c876zxgm](https://www.alibaba.com/product-detail/Polishing-thin-optical-clear-quartz-substrate_60729729793.html?spm=a2700.galleryofferlist.normalList.64.144867c876zxgm)



[View larger image](#)



[Add to Compare](#) [Share](#)

Polishing thin optical clear quartz substrate

FOB Reference Price: [Get Latest Price](#)

**\$3.00 - \$50.00** / Pieces | 5 Piece/Pieces (Min. Order)

[Contact Supplier](#)

[Chat Now!](#)

Seller Support: [Trade Assurance](#) protect your orders from payment to delivery

Payments: [VISA](#) [MasterCard](#) [TT](#) [Online Bank Payment](#) [Pay Later](#) [More](#) ▾

Shipping: Alibaba.com Ocean Shipping Service from China to U.S  
[Get shipping quote](#)

Value-added services: [Production View](#)

## Overview

### Quick Details

Type:	Clear Quartz Plate	Application:	semiconductor material
Thickness:	1-3mm	Shape:	Square
Place of Origin:	Jiangsu, China (Mainland)	Brand Name:	HIGHBORN
Model Number:	HBC	Material:	Fused Quartz Glass/JGS1/JGS2/JGS3/GE
purity:	99.99%	density:	2.2kg/cm3
working temperatur...	1100 degree celsius	annealing point:	1180 degree celsius
softening point:	1680 degree celsius	process:	polishing or grind
Keywords:	optical quartz substrate	keywords 2:	Clear quartz substrate

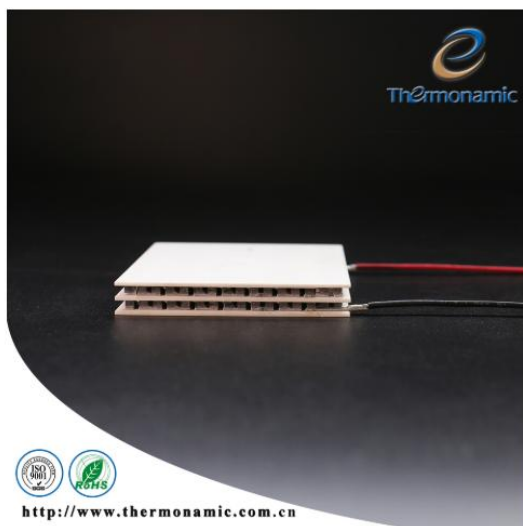
### Supply Ability

Supply Ability: 500 Kilogram/Kilograms per Month

### Packaging & Delivery

Packaging Details 1.pearl cotton 2.bubble pad 3.carton 4.standard wooden case  
Port Shanghai,Qingdao,Ningbo,Shenzhen,Tianjin

## Thermoelectric cooler



[View larger image](#)



### Multistage Peltier Thermoelectric Cooler TEC2-127-127-06

FOB Reference Price: [Get Latest Price](#)

**\$10.00 - \$100.00** / Pieces | 1 Piece/Pieces (Min. Order)

[Contact Supplier](#)

[Chat Now!](#)

Payments: [VISA](#) [MasterCard](#) [TT](#) [Online Bank Payment](#) [Pay Later](#) [More](#) ∨

Shipping: Alibaba.com Ocean Shipping Service from China to U.S  
[Get shipping quote](#)

## Overview

### Quick Details

Place of Origin:	Jiangxi, China (Mainland)	Brand Name:	Thermonamic
Model Number:	TEC2-127-127-06	Couples:	127+127
DTmax:	93	Umax (Voltage):	14.6
I <sub>max</sub> (amps):	6.5	QCmax (Watts):	40.6
AC resistance (oh...):	2.1~2.4	Size (mm):	40*40(top) /40*40 (bottom).
Appearance:	Cube and White	Certification:	ROHS, REACH, SGS, A&V, ISO9001

### Supply Ability

Supply Ability: 100000 Piece/Pieces per Month

### Packaging & Delivery

Packaging Details Inner packing: hard foam box, Outer packing: carton  
Port Shanghai, Guangzhou

## DESCRIPTION

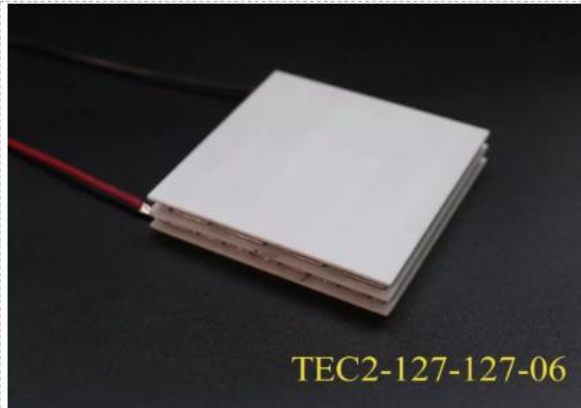
*Thermonamic Electronics(Jiangxi) Corp., Ltd.*



TEC2-127-127-06

The TEC2-127-127-06 is a multistage module designed for greater temperature differential cooling, good for cooling and heating up to 100 °C applications. It is a 127-127 couples module in size of 40mm×40mm (top)/40mm ×40mm (bottom). If higher operation or processing temperature is required, please specify, we can design and manufacture according to your special requirements.

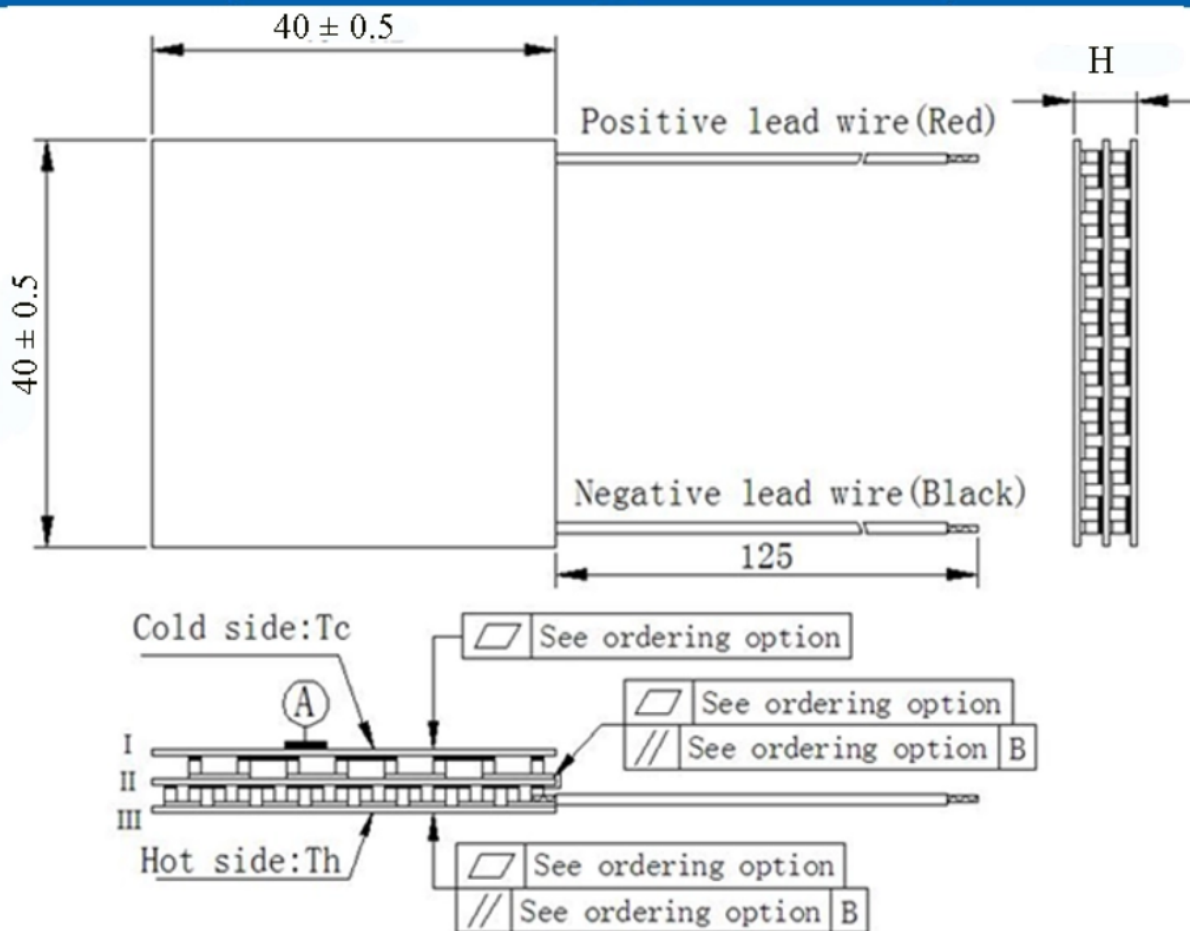
- Environmental friendly
- RoHS compliant
- Precise temperature control
- Exceptionally reliable in quality
- High performance
- High Temperature Differential
- No moving parts, no noise, and solid-state
- Compact structure
- Small in size, light in weight



TEC2-127-127-06

**GEOMETRIC CHARACTERISTICS**

*Thermonamic Electronics(Jiangxi) Corp., Ltd.*



## Specification of Thermoelectric Module

TEC2-127-127-06

## Description

The TEC2-127-127-06 is a multistage module designed for greater temperature differential cooling, good for cooling and heating up to 100 °C applications. It is a 127-127 couples module in size of 40 mm × 40 mm (top) / 40 mm × 40 mm (bottom). If higher operation or processing temperature is required, please specify, we can design and manufacture according to your special requirements.

## Features

- High Temperature Differential
- No moving parts, no noise, and solid-state
- Compact structure, small in size, light in weight
- Environmental friendly
- RoHS compliant
- Precise temperature control
- Exceptionally reliable in quality, high performance

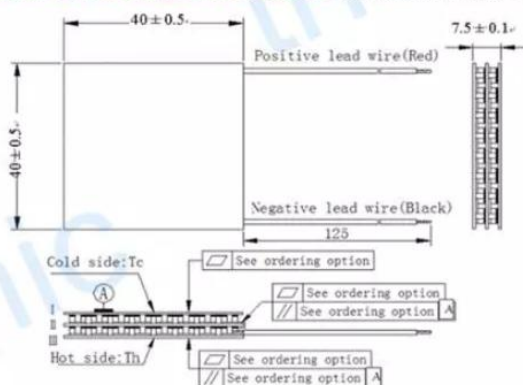
## Application

- Infrared (IR) Sensors
- CCD Sensor
- Gas Analyzers
- Calibration Equipment
- CPU cooler and scientific instrument
- Photonic and medical systems
- Guidance Systems

## Performance Specification Sheet

Th (°C)	27	50	Hot side temperature at environment: dry air, N <sub>2</sub>
DT <sub>max</sub> (°C)	93	104	Temperature Difference between cold and hot side of the module when cooling capacity is zero at cold side
U <sub>max</sub> (Voltage)	14.6	16.4	Voltage applied to the module at DT <sub>max</sub>
I <sub>max</sub> (amps)	6.5	6.5	DC current through the modules at DT <sub>max</sub>
Q <sub>Cmax</sub> (Watts)	40.6	42.2	Cooling capacity at cold side of the module under DT=0 °C
AC resistance (ohms)	2.25	2.45	The module resistance is tested under AC
Tolerance (%)	± 10		For thermal and electricity parameters

## Geometric Characteristics Dimensions in millimeters



## Ordering Option

Suffix	Thickness (mm)	Flatness/ Parallelism (mm)	Lead wire length(mm) Standard/Optional length
TF	0: 7.5±0.1	0: Face II 0.010/0.010, Face III 0.015/0.015	125±1/Specify
TF	1: 7.5±0.08	1: Face II 0.008/0.008, Face III 0.01/0.01	125±1/Specify

Eg. TF0: Thickness 7.5±0.1(mm) and Face II 0.008/0.008, Face III 0.01/0.01

## Manufacturing Options

## A. Solder:

1. T100: BiSn (Melting Point=138°C)
2. T200: CuSn (Melting Point= 227 °C)

## B. Sealant:

1. NS: No sealing (Standard)
2. SS: Silicone sealant
3. EPS: Epoxy sealant
4. Customer specify sealing

## C. Ceramics:

1. Alumina (Al<sub>2</sub>O<sub>3</sub>, white 96%)(AlO)
2. Aluminum Nitride (AlN)

## D. Ceramics Surface Options:

1. Blank ceramics (not metalized)
2. Metalized (Copper-Nickel plating)

## Naming for the Module

TEC2-127-127-06-X-X-X-X



TEC2-127-127-06-T100-NS-TF01-AlO

T100: BiSn(Tmelt=138°C)

NS: No sealing

AlO: Alumina white 96%

TF01: Thickness ±0.2(mm) and Face II 0.008/0.008, Face III 0.01/0.01

Creative technology with fine manufacturing processes provides you the reliable and quality products  
Tel: +86-791-88198288 Fax: +86-791-88198308 Email: [sales@thermonamic.com.cn](mailto:sales@thermonamic.com.cn) Web Site: [www.thermonamic.com.cn](http://www.thermonamic.com.cn)

Or other supplier [www.ekt2.com](http://www.ekt2.com)



### 14 SENSOR PELTIER TEC1-12706

Thermoelectric Cooler Senso

4.32 USD

Quantity:

 Add To Cart

 Details

## 58 Thermoelectrically cooled IR detectors beat the heat<sup>60</sup>

High-performance solid-state infrared (IR) detectors are at the heart of a wide variety of military, industrial, and medical electro-optical systems. As in visible-wavelength-sensitive silicon photodetectors, IR detectors can be made from semiconductor materials. To absorb IR photons, the detector material must have band-gap energy less than the energy of the incoming photon; thus, sensing longer wavelengths requires the use of small band gap materials. Such materials yield devices sensitive to low-energy IR photons, but the electron carriers are then more easily generated in the semiconductor from random thermal excitation, and this degrades performance through increased dark current and noise.

One way to reduce these effects is to reduce the operating temperature of the detector, for example by thermoelectric (TE) cooling. Thermoelectric coolers are simply low-power, miniature heat pumps that are small enough to be easily integrated into compact optical systems. When properly packaged, TE coolers can efficiently cool small detector chips (3, 3 mm) to temperatures below  $-70^{\circ}\text{C}$ . Thermoelectric coolers can provide temperature control to better than  $0.1^{\circ}\text{C}$ , ensuring stable detector performance. The devices operate under direct current (dc), minimizing electrical noise, and can be used for heating or cooling by reversing the direction of current flow. Because both the detector and cooler are solid-state components, operating lifetimes are greater than 10 years.

Thermoelectric coolers have not entirely replaced cryogenic coolers for IR applications. Background-limited performance in the mid- or long-wave IR spectral regions still requires operating temperatures of 100 K or less, which can be attained only by liquid-nitrogen-filled Dewars or closed-cycle refrigerators. But for many applications at near- and mid-IR wavelengths, thermoelectric cooling is appropriate.

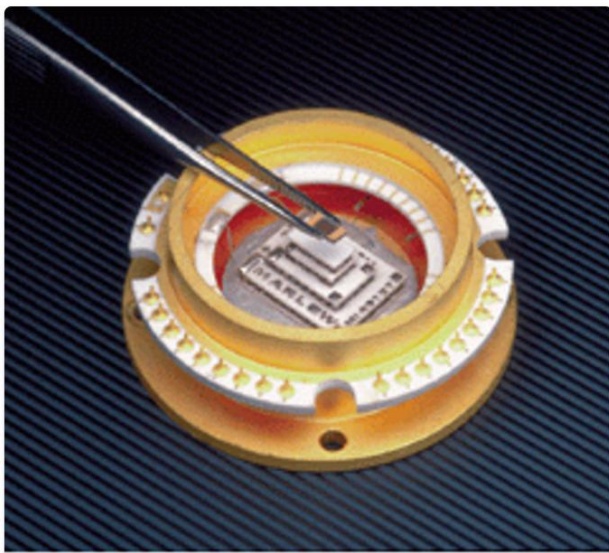
### 58.1 Thermoelectric coolers

The development of thermoelectric (TE) cooling can be traced back to the early 1800s when Jean Peltier noted a heating or cooling effect when electrical current passed through two conductors. Thomas Seebeck later found that two dissimilar conductors at different temperatures created a voltage. William Thomson (Lord Kelvin) concluded that over a temperature gradient, a single conductor with current flow will demonstrate reversible heating and cooling. Based on these principles and the development of certain semiconductor materials in the late 1950s, thermoelectric cooling has developed into a viable technology for many IR detector applications.

A single-stage TE cooler consists of a matrix of thermoelectric couples connected electrically in series, and thermally in parallel (see Fig. 1). The couples themselves consist of bismuth telluride p- and n-type semiconductor material. Depending on performance requirements, a TE cooler incorporates anywhere from one to several hundred couples. These couples are sandwiched between ceramic plates, which provide structural integrity as well as electrical insulation between the heat sink and the object being cooled.

---

<sup>60</sup> <https://www.laserfocusworld.com/detectors-imaging/article/16550903/thermoelectrically-cooled-ir-detectors-beat-the-heat>



When a positive dc voltage is applied to the n-type material, electrons pass from the p- to the n-type material. The temperature on the cold side decreases because heat is being absorbed from it. This heat pumped from the cold side plus the heat generated by the input power is conducted through to the hot side of the cooler, where it is dissipated by a heat sink. The degree of cooling achieved is proportional to the current and the number of thermoelectric couples. For more extensive cooling requirements, multiple cooler assemblies can be stacked to accommodate additional heat pumping for both active and passive heat loads. Thermoelectric coolers with as many as four stages are typically used in many IR detector applications.

## 58.2 Choosing a cooler

One of the main advantages of TE coolers compared to bulk liquid nitrogen or mechanical refrigerators is their small size, which allows the detector and cooler to be incorporated in a single housing (see bottom photo on p. S15). Selecting the proper package for TE-cooled IR detectors requires some special considerations. The detector chip itself will generally be cooled below 0°C, so hermetic sealing is necessary to block out moisture that would otherwise precipitate and freeze on the cold detector surface. This is especially critical for near-IR spectroscopy in the 3- $\mu\text{m}$  wavelength region, where ice has a strong absorption band. Proper cleaning and bake out of the coolers and packages eliminate moisture that might introduce this spurious absorption feature.

The colder the operating temperature desired, the more TE cooler stages are required. This increases the size of the device and hence the housing; power consumption also rises. For single-element detectors in the near-IR spectral region, TO-37 or TO-8 headers are sufficient to accommodate small two-stage TE coolers. Array detectors require larger coolers with more complex packages.

The total heat load on the two cooler stage plays a critical role in determining the minimum achievable temperature. Gas convection inside the hermetic housing is a major source of heat-loading. Convection can be reduced by filling the package with a high-molecular-weight gas (such as xenon) or by evacuating the package.

Finally, standard glass windows transmit wavelengths only to 2.5  $\mu\text{m}$ . For detectors that respond beyond this point, the package must incorporate sapphire windows or antireflection-coated germanium (Ge) windows, soldered or fused into the package cap.

### 58.3 Near-infrared detectors

Over the spectral range from 0.8 to 3.0  $\mu\text{m}$ , IR detectors are used for applications as diverse as fiber optic communications, agricultural sorting, environmental monitoring, chemical analysis, and Fourier-transform spectroscopy. Typical photovoltaic detector materials are germanium for the 0.8- to 1.6- $\mu\text{m}$  wavelength region, indium gallium arsenide (InGaAs) for the 1- to 2.5- $\mu\text{m}$  region, and indium arsenide (InAs) for the 1- to 3.4- $\mu\text{m}$  region. For wavelengths up to 1.6  $\mu\text{m}$ , cooling is often unnecessary. Both germanium and InGaAs offer high shunt resistance, low dark currents, and stable response at 25°C (see Fig. 2). However, dark currents are higher for detectors sensitive to longer wavelengths. Detectors are often cooled for wavelengths beyond 2  $\mu\text{m}$ .

Indium arsenide has the longest wavelength response in the near-IR spectral range. With TE cooling, InAs exhibits dark currents below 10 nA, with noise-equivalent powers (NEPs) of less than 1 pW. InAs offers linear performance from the Pico watt to the mill watt regime, response times below 1  $\mu\text{s}$ , dc response stability, and good uniformity of response. Lead sulfide (PbS) detectors are also available for near-IR wavelengths, but these devices operate in the photoconductive mode and can suffer from poor response stability, high bias voltages, and slow response times.

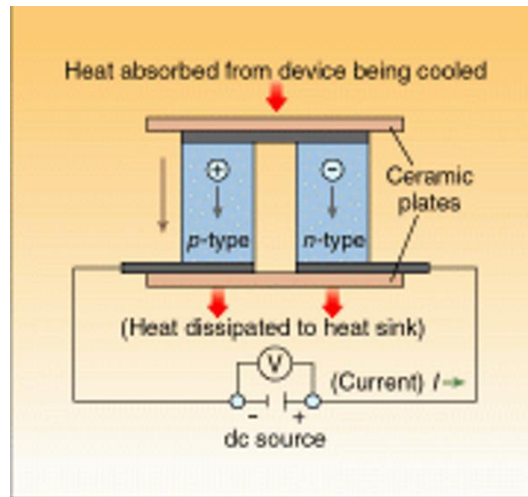
Further into the IR region (from 2 to 5  $\mu\text{m}$ ), applications for IR detectors include noncontact temperature sensing, thermal imaging, and gas analysis for pollution control. Indium antimonide (InSb) is the highest-performance detector for this region, but unfortunately, InSb cannot be used with TE coolers because the large number of thermally generated carriers shorts out the p-n junction in InSb.

Photoconductive devices do not incorporate a p-n junction and can operate successfully over a wider temperature range. Lead selenide (PbSe) and mercury cadmium telluride (HgCdTe) photoconductive detectors are widely used in industrial and medical instruments. When mounted on two-stage thermoelectric coolers, PbSe detectors are economical alternatives to InSb and offer sufficient performance for many applications. For high-performance applications such as thermal imaging and radiometry, photoconductive HgCdTe provides better sensitivity, faster response, and lower bias voltage. Three-stage or even four-stage cooling is used for maximum performance.

The long-wave IR spectral region spans the wavelength range from 8 to 13  $\mu\text{m}$ , which corresponds to a peak for thermal emission at ambient temperature. The 8-13- $\mu\text{m}$  range also has high transmission through the atmosphere. This spectral region is thus optimal for such applications as thermal imaging, noncontact temperature sensing, security sensing, and environmental monitoring. Photoconductive HgCdTe detectors can provide background-limited performance at these wavelengths, but only at operating temperatures below 100 K.

Thermoelectrically cooled HgCdTe photoconductive detectors for the 8- to 12- $\mu\text{m}$  region do not necessarily offer better sensitivity than low-cost thermal detectors (thermopiles, pyroelectrics, or bolometers) that convert heat energy to an electrical signal. Such devices require no cooling and can achieve NEPs of 100 pW/ $\sqrt{\text{Hz}}$ . The major drawbacks of pyroelectrics and thermopiles are the slow response time and reduced sensitivity at higher frequencies. Thermoelectrically cooled HgCdTe detectors maintain their sensitivities up to very high frequencies (10 MHz), making them suitable for fast-pulsed applications such as CO<sub>2</sub> laser detection.

Thermoelectrically cooled detectors are reliable and simple to operate. The most critical aspect of the design is proper heat-sinking, without which a cooler will be inefficient or may even be damaged by overheating (see Fig.). For small two- and three-stage coolers, good thermal connection of the device to a metal plate with several square inches or more of surface area is usually sufficient; forced-air cooling is rarely needed. Once properly integrated into an electro-optical system, TE-cooled IR detectors should give years of continuous, maintenance-free operation.



3-DH-2 97 Fig. 1

#### 58.4 Principle of thermoelectric cooling

Thermoelectric cooling uses the Peltier effect to create a heat flux at the junction of two different types of materials. A Peltier cooler, heater, or thermoelectric heat pump is a solid-state active heat pump which transfers heat from one side of the device to the other, with consumption of electrical energy, depending on the direction of the current. Such an instrument is also called a Peltier device, Peltier heat pump, solid state refrigerator, or thermoelectric cooler (TEC). It can be used either for heating or for cooling, [1] although in practice the main application is cooling. It can also be used as a temperature controller that either heats or cools.

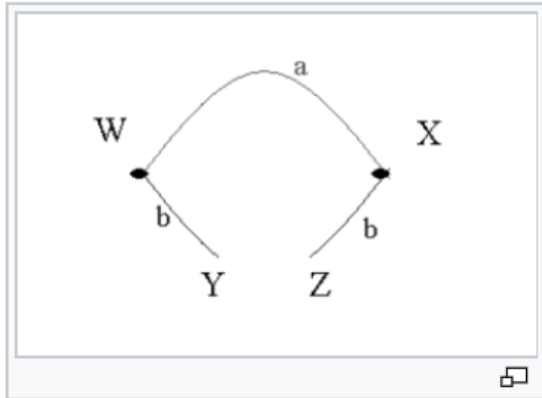
This technology is far less commonly applied to refrigeration than vapor-compression refrigeration is. The primary advantages of a Peltier cooler compared to a vapor-compression refrigerator are its lack of moving parts or circulating liquid, very long life, invulnerability to leaks, small size, and flexible shape. Its main disadvantages are high cost and poor power efficiency. Many researchers and companies are trying to develop Peltier coolers that are cheap and efficient. (See Thermoelectric materials.)

A Peltier cooler can also be used as a thermoelectric generator. When operated as a cooler, a voltage is applied across the device, and as a result, a difference in temperature will build up between the two sides. When operated as a generator, one side of the device is heated to a temperature greater than the other side, and as a result, a difference in voltage will build up between the two sides (the Seebeck effect). However, a well-designed Peltier cooler will be a mediocre thermoelectric generator and vice versa, due to different design and packaging requirements.

### 58.4.1 Peltier effect

The Peltier effect is a thermoelectric effect consisting of a phenomenon of heat displacement in the presence of an electric current. The effect is made in conductive materials<sup>1</sup> of different types by contacts (contacts). One of junctions then, while the other was warming up. This effect was discovered in 1834 by physicist Jean-Charles Peltier.

The figure shows the basic thermoelectric circuit.



Two conductive materials of different natures a and b are connected by two junctions in X and W. In the case of the Peltier effect, an electric current  $I$  is imposed on the circuit, by placing for example a source of electric current between Y and Z resulting in heat release  $Q$  at one junction and heat absorption at the other junction<sup>2</sup>. The Peltier coefficient relative to the material pair a and b is defined as the thermal power  $P$  released or absorbed per unit of intensity of current  $I$ . It is expressed in volts.

$\Pi_{ab}$  is then defined by:

$$\Pi_{ab} = \frac{P}{I}$$

If a current imposed in the direction  $Y \rightarrow W \rightarrow X \rightarrow Z$  causes a heat release in W and an absorption in X, then  $\Pi_{ab}$  is positive.

## 59 Lead Sulfide Quantum Dots Synthesis

### 59.1 Overview

Quantum dots are semiconductor nanocrystals on the scale of a few nanometers, or several hundred atoms. At this size quantum effects dominate and the electrons are quantum confined to narrow energy levels determined by the size of the particle. This means that the absorption wavelength the light can be fine-tuned and that quantum dots can be used to adjust the bandgap of the materials they are associated with. Quantum dots being explored for use in photovoltaics and in signal processing.

### 59.2 Significance

Quantum dots can be used increase the efficiency of solar cells by tapping different portions of the spectrum and by increasing the number of excitons that be formed per photon, resulting in higher quantum efficiency.

### 59.3 Procedure

**Link:** <https://youtu.be/bKLdkjV6Mbc>

- **Prepare Reactants:**

Prepare reaction mixture with 14 g of octadecene, 1.4 g of oleic acid, 450 mg of lead oxide. When it mixes up it is murky yellow at first and then becomes clear when it is heated up.

- **Degas the mixture:**

The Schlenk line is used to degas the reaction mixture. Remove the nitrogen bubbler and replace with a pipette bulb. Slowly turn the stopcock from nitrogen flow to vacuum. First watch the pipette bulb when it collapses vacuum is being pulled on the solution . Now slowly turn the stopcock while watching the reaction mixture making sure not over-boil. Once the boiling mixture has stabilized fully-open the vacuum valve. Leave the mixture under vacuum for approximately 1 hour. Slowly turn the stopcock back to nitrogen while holding a finger over the bubbler to prevent pulling the silicon fluid into the Schlenk line. Remove the pipette bulb and replace the nitrogen bubbler. Increase the reaction mixture to 180 degrees

- **Injection**

Prepare the injection mixture from 4 gms of octadecene in 210 mL of hexylmethylidisilazane (HMDS).

Once the reaction mixture has stabilized purge a syringe with nitrogen. Draw up the injection mixture and quickly insert it into the reaction vessel. Within second the mixture should turn a turbid black color. Let it react for 5 minutes and then quench the reaction in an ice bath. After it comes to room temperature transfer it to a separatory funnel.

- **Cleaning**

After the synthesis is quenched it is necessary to remove excess oleic acid and other impurities. Two methods are shown.

### **I. Separatory Funnel:**

1. pour PbS QDs (dissolved in minimal amount of hexanes) into sep. funnel
2. precipitate with methanol (MeOH)

Add back small amounts of hexanes and shake funnel vigorously between additions. If there is still precipitated product clinging to the walls of the funnel between hexanes additions, continue to add more hexanes. Once the product stops sticking to the walls, let the funnel sit for a minute or so to see if any phase separation occurs. If not, continue adding small amount of hexanes until it does. Note that only a small amount of separation will be seen at the bottom of the funnel at first, and the mixture will have to sit for at least 30 mins to fully separate. If no phase separation is observed after a few additions, the funnel can be placed in the freezer to speed the process.

3. Drain off the clear bottom MeOH layer into the waste
4. Drain small amounts (~1 or 2 mL portions) of PbS into a centrifuge tube.
5. Precipitate by filling the tube with MeOH
6. Centrifuge the tube (5 min, 3000 RPM), and pour off clear MeOH layer
7. Pour another addition of PbS into the same tube and repeat steps 6) and 7). Note: for the first two cycles, multiple tubes can be used rather than just one, but on the third (last) cleaning step, it is generally preferred to use a single tube to consolidate product.
8. Dissolve the product in minimal amount of hexanes, vortex, sonicate (5 mins, or until dissolved) and add PbS back to the separatory funnel. Repeat the above steps for the first two cleaning cycles.

### **II. Simply use multiple centrifuge tubes:**

1. Dissolve the product in small amount of hexanes, then vortex and sonicate until QDs dissolve.
2. Precipitate by filling each centrifuge tube with MeOH
3. Centrifuge each tube (5 min, 3000 RPM)
4. Discard clear supernatant
5. For the first two cleaning cycles, repeat the above steps

To consolidate into a single tube, just choose one tube to keep and repeat step 1) above for the other tubes. Then successively add the dissolved QDs of ONE of the other tubes to to the dry product in the tube you chose to keep and repeat steps 2-4 above until all tubes have been combined into one (only add the contents of one tube for each step precipitation-centrifuge cycle-do not combine the contents of all remaining tubes at once)

In both cases, once the cleaning cycles are complete, the QDs can be dissolved in hexanes or toluene and left to sit. Alternatively, a septum cap can be placed on the centrifuge tube which can then be placed on the Schlenk line to dry.

## **59.4 PbS/Polymer Nanocomposite Optical Materials with High Refractive Index**

High refractive index nano-PbS/polymer composites were fabricated from reactive lead-containing precursors and polythiourethane (PTU) oligomer terminated with isocyanate group, followed by in situ gas/solid reaction. The lead-containing precursor with a chemical formula of  $\text{Pb}(\text{SCH}_2\text{CH}_2\text{OH})_2$  was synthesized in water phase at  $\text{pH} = 5-9$  and exhibited an absorption at 317 nm in dimethyl sulfoxide (DMSO) in UV-vis spectra. PbS nanoparticles can be formed in DMSO after treatment with

H<sub>2</sub>S. TEM studies indicated that the PbS nanoparticles were smaller than 10 nm and aggregated seriously in DMSO. After the precursors were incorporated into PTU oligomer, the obtained composite films were treated with H<sub>2</sub>S to obtain PbS nanoparticles/PTU nanocomposite films. TEM showed that the nanocomposites exhibited interesting phase behaviors depending on the precursor content in films. A uniform spherical aggregate of PbS nanoparticles (nanospheres) with a size smaller than 100 nm formed in the nanocomposite films below 26.3 wt % of lead-containing precursors. When the precursor content was larger than 59.3 wt %, the PbS nanoparticles about 3 nm dispersed uniformly in the whole polymer matrix. Ellipsometric measurement indicated that the precursors/PTU composite films before being treated with H<sub>2</sub>S had a refractive index in the range 1.57–1.665 and after reaction with H<sub>2</sub>S, the obtained PbS/PTU nanocomposite films had a higher refractive index in the range 1.57–2.06 with the varied content of precursors from 0 to 67 wt %.

## 60 Synthesis and Optical Properties of the Semiconductor PbS Nanobelts

### 60.1 Introduction

Due to its unique structure and superior optoelectronic properties, nanobelts have surpassed nanowires and nanotubes and attracted a lot of interest in nanomaterials research. The controlled synthesis of no-defective, oxide nanobelts under high temperature and the solid gas phase method was first described by Pan et al. Since the one-dimensional nanobelts with wide band gap were expected to have vital applications in areas such as high-efficiency electricity transmission, a series of nanobelts have been fabricated, most of which were oxides, such as ZnO, SnO<sub>2</sub>, GaO<sub>2</sub>, MoO<sub>3</sub>, etc. There have also been a lot of interests in making nanobelts with non-oxide materials and potentially utilizing them in areas such as electronics, biology, pigment and pharmaceuticals. The most commonly study of nonoxide semiconductors focus on sulfides, such as CdS, ZnS, Bi<sub>2</sub>S<sub>3</sub>, Ti<sub>2</sub>S, etc. However, synthesis of nanobelts has proven to be difficult because reactions are often performed at very high temperature and require the addition of catalysts. Therefore, it is important to explore the simple and mild methods to achieve the controlled synthesis of nanobelts, preferably under room temperature.

As typical narrow band gap semiconductors, PbS nanomaterials possess special optoelectronic properties, which have vital applications in optical information storage, optical communication apparatus, radioactivity detector, etc. A number of PbS nanomaterials with different morphologies and structures such as nanoparticles, nanorods, nanowires, nanoflakes, and nanocubes have been synthesized. However, so far there is no report so far on the synthesis of nanobelts by employing using the reverse micelles under a mild chemical reaction condition and at room temperature.

The reverse micelle soft-template method represents a simple and unique way to make nanomaterials with desired nano-sizes and two- or three-dimensional tropism. Compared with nanomaterials obtained from physical-chemical methods, the products prepared in reverse micelles are widely considered to show superior structures and physical properties. Herein, this paper describes a successfully selfcontrolled synthesis of PbS nanobelts in a reverse micelle system by employing the surfactant of C<sub>12</sub>E<sub>9</sub> as the soft template. The optical properties of PbS nanobelts are investigated and the potential mechanism of reaction is also proposed.

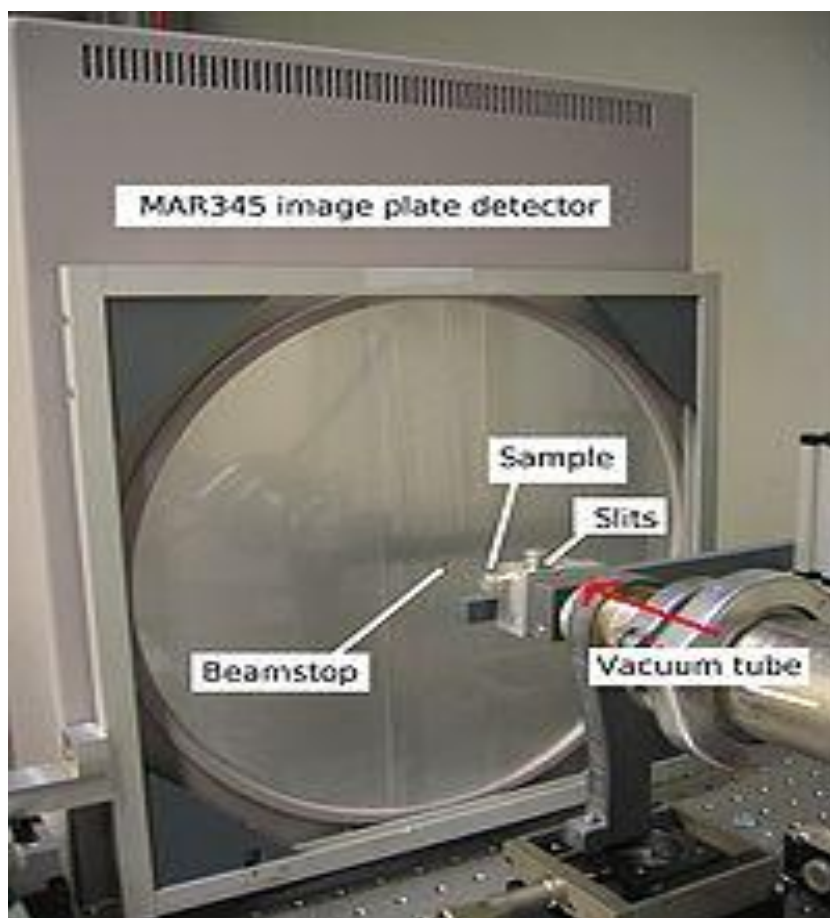
### 60.2 Experimental Section

#### 60.2.1 Reagents & Equipments:

C<sub>12</sub>E<sub>9</sub> [polyoxyethylene (9) dodecy ether], cyclohexane, absolute ethanol, n-pentanol, Na<sub>2</sub>S·9H<sub>2</sub>O and Pb(CH<sub>3</sub>COO)<sub>2</sub>·3H<sub>2</sub>O were purchased from Shanghai Chemical Reagent Factory, China. All the reagents are of analytical grade.

The morphologies of the products were observed through transmission electron microscopy (TEM). The crystal phase and structure of the products were determined by X-ray powder diffraction (XRD) using Hitachi-800 diffractometer with graphite monochromatized Cu-Kα radiation ( $\lambda = 0.15418$  nm, 50 kV, 100 mA). Optical properties of products were studied by Agilent 8453 UV-Visible spectrophotometer, Perking Elmer LS-55 fluorescent spectroscopy.

A **diffractometer** is a measuring instrument for analyzing the structure of a material from the scattering pattern produced when a beam of radiation or particles (such as X-rays or neutrons) interacts with it.



### **Preparation of PbS Nanobelts:**

The reverse micelle system was prepared by adding into a 250 mL volumetric glass in sequence of 28 mL cyclohexane, 3 mL  $C_{12}E_9$ , 1 mL of 0.1 mol/L aqueous  $Pb(CH_3COO)_2 \cdot 3H_2O$  and 1 mL n-pentanol.

The same experiment was also performed in parallel by adding into another 250 mL volumetric glass in sequence of 28 mL cyclohexane, 3 mL  $C_{12}E_9$  and 1 mL of 1.0 mol/L aqueous  $Na_2S \cdot 9H_2O$ .

Both solutions were mixed vigorously at approximately 3000 rpm for 15 minutes, and kept at room temperature for another five minutes.

After that an equal volume of two microemulsions, one containing  $S^{2-}$  and the other containing  $Pb^{2+}$ , was mixed together followed by gentle shaking for another 5 to 10 minutes. The final solution was kept at room temperature for 12 hours to result in the formation of nanobelts.

A volume of 3 mL acetone was then added to the solution to break up the micelles.

Finally, the supernatant was removed from the solution described above, the bottom solution was centrifuged at 2000 rpm for 10 minutes, washed sequentially with acetone, ethanol and water 2-3 times each.

The final product should be black precipitate insoluble in water and ethanol.

The morphology of the final product was observed using TEM. One to two drops of the microemulsion solutions containing the PbS products were transferred onto a copper grid that was placed on filter paper followed by air-drying. The structure of the final product was studied using X-ray diffraction, while the optical properties of the product was determined by photoluminescence (PL) and UV-Vis spectrophotometers.

### 60.3 Results and Discussions

**Morphologies and Structures.** The TEM micrograph and electron diffraction of the PbS nanoproducts formed are shown in Figure 1. The products have belt shape (Figure 1a). The single layer nanobelts were very thin and nearly transparent. There were also some other nanobelts shown in Figure 1a, which were likely made of a few overlapping layers. The width of the nanobelt was found to be between 50 and 120 nm and the length over 3  $\mu\text{m}$ . The exact thickness of the nanobelts can't be easily measured. However, it was concluded that nanobelts should be approximately 3 nm thick based on: (1) As pointed in the arrow in Figure 1a, the particles were still visible even when they were underneath the nanobelt. This has clearly demonstrated the transparent nature of the nanobelt and subsequently shown the thickness of the nanobelt was under 5 nm. (2) As shown in Figure 1b, the nanobelts could be penetrated by 100 kv electron beam. This has proven the nanobelt was less than 20 nm in thickness. (3) "Blue Shift" was observed on the UV-Vis absorption spectrum of the PbS nanobelts (in Figure 3). The thickness of the nanobelts was thus determined to be around 3 nm based on literature report. (4) As shown in Figure 5, the gap between different layers of micelles was normally 1-4 nm. This has in turn limited the nanobelt thickness to 1-4 nm.

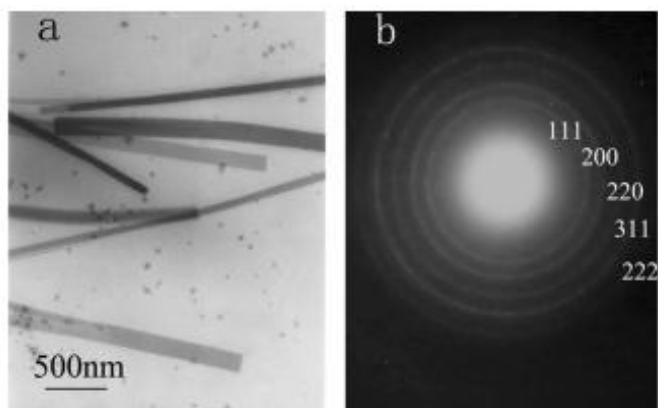


**Figure 1.** The TEM micrograph (a) and ED image (b) of PbS nanobelts.

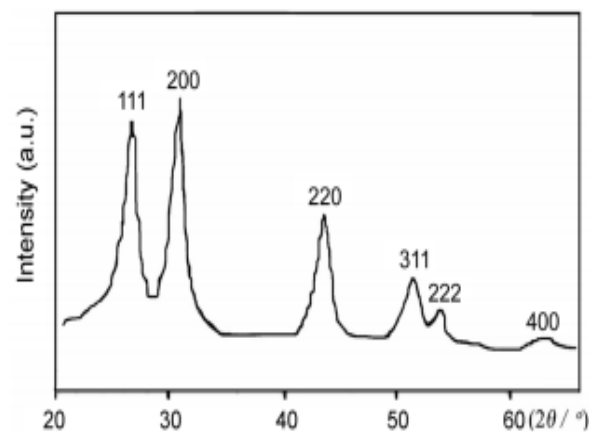


**Figure 2.** The XRD pattern of the PbS nanobelts.

The corresponding electron diffraction pattern has shown the presence of clear diffraction circles, indicative of polycrystal structure. No impurity peaks were observed from the XRD spectral of the nanobelts (Figure 2). All the peaks found in Figure 2 matched with the ones listed in JCPDS file (No: 5-592) for the cube galena structure. The lattice constant was then calculated to be 5.9378 Å, close to the JCPDS file. Therefore, it was concluded that very pure PbS nanobelts were synthesized in this experiment and the nanobelts possessed cube galena polycrystal structure.

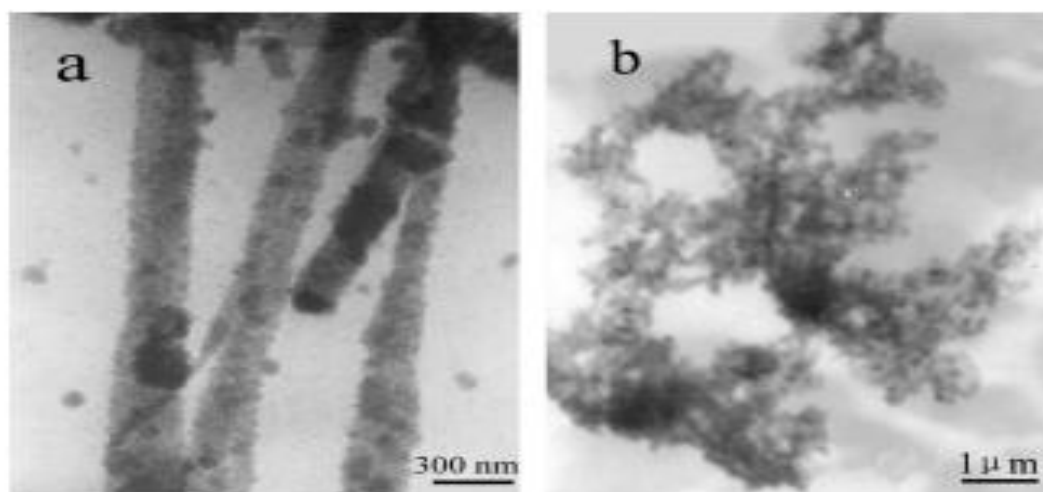


**Figure 3.** The TEM micrograph of PbS products (When the concentration of  $\text{Pb}^{2+}$  and  $\text{S}^{2-}$  were a 0.1 mol/L; b When the concentration of  $\text{Pb}^{2+}$  and  $\text{S}^{2-}$  were 1.0 mol/L)

**Experimental Conditions.** Experimental conditions have been optimized in order to produce the PbS nanomaterial with the desired dimension, morphologies and structures. (1) It was found that the concentrations of reactant have influence on morphologies and structures of the products. When the concentration of  $\text{Pb}^{2+}$  and  $\text{S}^{2-}$  were 0.1 mol/L respectively, the products were nanorods (shown in Figure 3a), not nanobelts. When the concentration of  $\text{Pb}^{2+}$  and  $\text{S}^{2-}$  were 1.0 mol/L respectively, the products were large particulates (shown in Figure 3b), not nanorods or nanobelts. The excess amount of  $\text{S}^{2-}$  was important. It not only improved the morphologies of the final nanobelts, but also ensured the complete depletion of  $\text{Pb}^{2+}$  to avoid the environmental pollutions from heavy metal waste. In this paper the concentration ratio of  $\text{S}^{2-}$  to  $\text{Pb}^{2+}$  was 10. A concentration of 0.1 mol/L for  $\text{Pb}(\text{CH}_3\text{COO})_2 \cdot 3\text{H}_2\text{O}$  and that of 1.0 mol/L of  $\text{Na}_2\text{S} \cdot 9\text{H}_2\text{O}$  were used in the experiments described in this paper. (2) Molar ratio of the water to the surfactant was ten on the experiments described in this paper. Theoretically, surfactant to n-pentanol volume ratio ( $\delta$ ) had no effect on the reverse micelle system containing  $\text{C}_{12}\text{E}_9$ . However, a  $\delta$  value of three was selected here for the solution containing  $\text{Pb}(\text{CH}_3\text{COO})_2 \cdot 3\text{H}_2\text{O}$  to improve emulsion, and no n-pentanol was added to the solution containing  $\text{Na}_2\text{S} \cdot 9\text{H}_2\text{O}$  as determined to be unnecessary.

**Optical Properties.** As shown in the UV-Vis absorption spectra in Figure 3, a strong absorption peak was observed at the wavelength about 347 nm for the PbS nanobelts. Due to its semiconductor nature, the PbS nanobelts have demonstrated excellent photoluminescence (PL) properties. When excited at 390 nm, nanobelts have shown a significant “blue shift” with the new emission wavelength

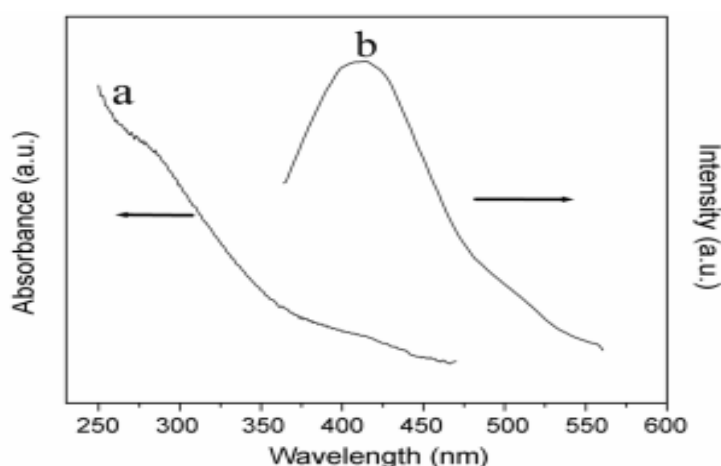


**Figure 4.** The UV-Vis spectra (a) and PL spectra (b) of the PbS nanobelts.

peaking at 423 nm. Unlike the bulk materials,<sup>23</sup> the PbS nanobelts have shown narrow gap band (0.41 eV) and large Bohr exciton radius. This has resulted in strong quantum confinement effect, unique three stage non-linear optical properties and properties of optical band restriction found on the PbS nanobelts.

**Formation Mechanism of Nanobelts.** The process of nanobelts synthesis is relatively complexed. A microemulsion template based mechanism is proposed below to explain the formation process of nanobelts in the reverse micelle system containing C12E9. It has been reported previously that different surfactants or even the same surfactant at different concentrations may have provided different microemulsion soft templates that resulted in the formation of nanomaterials with different morphologies and structures, such as spheres, rods, layers, etc. The surfactant of C<sub>12</sub>E<sub>9</sub> is a relatively simple and symmetric molecule (Figure 4). The hydrophilic oxy-ethylene chain tended to arrange along the surface and formed the colloids of layer shape. This has subsequently provided the microemulsion template leading to the directional aggregation of PbS colloid nanoparticles. PbS nucleuses were formed as soon as the reverse micelles containing S<sup>2-</sup> and Pb<sup>2+</sup> were mixed. The nucleuses would penetrate each other and amalgamate; the PbS nanoparticles were then produced. Guided by the microemulsion soft template, the nanoparticles aligned along the plane surface. The gap between different layers would shrink due to the interaction between the hydrophilic groups of C12E9 molecules. Finally, a very thin layer of nanobelt was obtained after removing template (Figure 5).

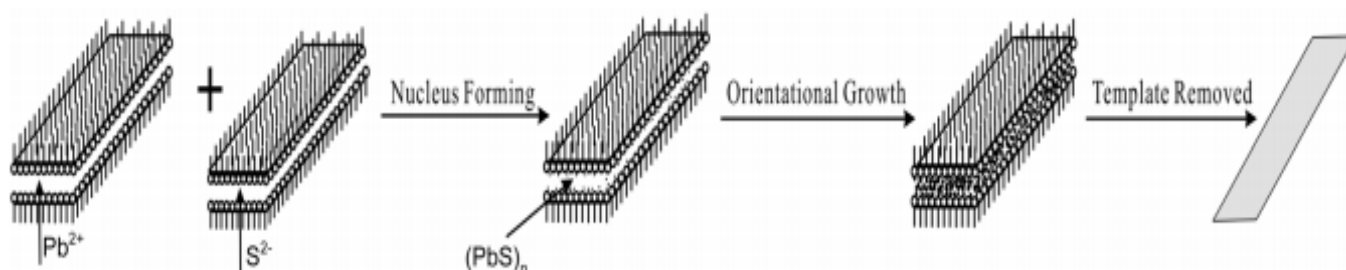


Figure 6. The proposed formation mechanism of PbS nanobelts.

## 60.4 Conclusion

The synthesis of the non-oxide nanobelts is traditionally considered to be technically very challenging. Although the reverse micelle systems have been employed to prepare nanomaterials with various morphologies and structures, the synthesis of the nanobelts using the reverse micelles isn't still reported. As described in this paper, PbS nanobelts were formed at the room temperature using the reverse micelles technique that included the surfactant of C<sub>12</sub>E<sub>9</sub>. The method used is simple, easy, mild and controllable.

Significant "blue shift" was observed on the PbS nanobelts when analyzed by photoluminescence and UV-Vis spectroscopy. Nanobelts have thus demonstrated even more superior optoelectronic properties than nanowires and nanotubes. Therefore, they are expected to show vital applications in many important areas. A microemulsion templates based assembling process was proposed as the mechanism of synthesis. However, a lot more studies are still needed in order to fully understand the mechanism for the formation of nanobelts in the reverse micelle systems containing the surfactant of C12E9.

**Acknowledgements.** The authors are grateful to the financial support of the National Natural Science Foundation of China (Grant No: 20471042 and 20571051); NanoFoundation of Shanghai in China (Grant No: 0452nm075) and the Doctoral Program Foundation of the Ministry of Education (Grant No: 20040247045).

## 61 Materials

قد استحصلت اليوم على:

Acetate plomb كمية قليلة

Poudre

وعلى haxane ربع ليتر

بسعر اجمالي \$68 ثمن المادتان

منى ترغب استلامها

## 62 References to IAP-IRS

### 62.1 References and further reading to the 2.6

- Beichman, C. A. et al.** 1984, “*The formation of solar type stars - IRAS observations of the dark cloud Barnard 5*”, ApJ, 278, 45
- Cohen, M.,** Walker, R. G., Carter, B., Hammersley, P., Kidger, M., Noguchi, K., 1999: “*Spectral Irradiance Calibration in the Infrared. X. A Self-Consistent Radiometric All-Sky Network of Absolutely Calibrated Stellar Spectra*”, AJ, 117, 1864
- Cohen, M.,** Megeath, S. T., Hammersley, P. L., Martin-Luis, F. & Stauffer, J., 2003a: “*Spectral Irradiance Calibration in the Infrared. XIII. “Supertemplates” and On-Orbit Calibrators for the SIRTf Infrared Array Camera*”, AJ, 125, 2645
- Cohen, M.,** Wheaton, W. A., Megeath, S. T., 2003b: “*Spectral Irradiance Calibration in the Infrared. XIV. The Absolute Calibration of 2MASS*”, AJ, 126, 1090
- Cutri R. M. et al.,** 2012: “*WISE All-Sky Data Release*”, NASA/IPAC Infrared Science Archive , 2012yCat,2311,0C
- Hauser, M. G. et al.** 1998: “*The COBE Diffuse Infrared Background Experiment Search for the Cosmic Infrared Background. I. Limits and Detections*”, ApJ, 508, 25
- Kataza, H. et al.,** 2010: “*AKARI/IRC All-Sky Survey Point Source Catalogue Version 1.0- Release Note (Rev.1)*”
- Kawada, M.,** Baba, H., Barthel, P.D., et al., 2007: “*The Far-Infrared Surveyor (FIS) for AKARI*”, PASJ, 59, S389
- Kim, H.-J. et al.** 2012: „*Star Formation in the Long Filamentary Infrared Dark Cloud at  $l \sim 53^\circ.2$* ”, Proceedings of the International Astronomical Union, Symposium 292, Volume 8, pp 46
- Kim, H.-J. et al.** 2013: „*Star Formation Activity in the Long Filamentary Infrared Dark Cloud IRDC G53.2*”, poster at Protostars and Planets VI, Heidelberg, July 15-20, 2013, <http://www.mpia-hd.mpg.de/homes/ppvi/posters/1S015.pdf>
- Müller, T. G., & Legerros, J. S. V.,** 1998: “*Asteroids as far-infrared photometric standards for ISOPHOT*”, A&A, 338, 340
- Müller, T. G.; Lagerros, J. S. V.,** 2002: “*Asteroids as calibration standards in the thermal infrared for space observatories*”, A&A, 381, 324
- Murakami, H.,** Baba, H., Barthel, P. et al., 2007: “*The Infrared Astronomical Mission AKARI*”, PASJ, 59, S369
- Nakagawa, T. et al.** 2007: “*Flight Performance of the AKARI Cryogenic System*” PASJ, 59, 377
- Neugebauer, G. et al.** “*Early Results from the Infrared Astronomical Satellite*”, (<http://www.sciencemag.org/content/224/4644/14.long>)

**Planck Collaboration**, 2011: “*Planck early results. I. The Planck mission*”, A&A, 536, A1

**Schlegel, D. J., Finkbeiner, D.P., & Davis, M.**, 1998: “*Maps of Dust Infrared Emission for Use in Estimation of Reddening and Cosmic Microwave Background Radiation Foregrounds*”, ApJ, 500, 525

**Schulz, B., et al.** 2002: “*ISOPHOT - Photometric calibration of point sources*”, A&A, 381, 1110

**Simon, R., et al.**, 2006: “*A Catalog of Midcourse Space Experiment Infrared Dark Cloud Candidates*”, ApJ, 639, 227

**Wright, E.L., Eisenhardt, P.R.M., Mainzer, A.K. et al.**, 2010: “*The Wide-field Infrared Survey Explorer (WISE): Mission Description and Initial On-orbit Performance*”, AJ, 140, 1868

**Yamamura, I., Makiuti, S., Ikeda, N. et al.**, 2010, “*AKARI/FIS All-Sky Survey Point Source Catalogues*”, 2010yCat,2298,0Y

<http://astron.berkeley.edu/davis/dust/index.html>

<http://irsa.ipac.caltech.edu/Missions/msx.html>

<http://lambda.gsfc.nasa.gov/product/cobe/>

## 62.2 For PbS Sensor

Kondas, D. A. (February 1993). *INTRODUCTION TO LEAD SALT INFRARED DETECTORS*. U.S.: ARMY ARMAMENT RESEARCH, DEVELOPMENT AND.

William V. Cummings Jr. (1951). *A lead sulfide near infrared detection system*. U.S.: missouri university of science and technology.

<https://cdn.embedded.com/contenteetimes/images/My%20Pictures/>

# Suppliers Data

## Electronics, Control

- CNCLab
- قطرنجي للإلكترونيات EKT Beirut
  - Number: 01 820020
  - Website: www.ekt2.com



- البشير للإلكترونيات - Bashir electronics

## Satellite Parts

Specification form © Surrey Satellite Technology Ltd., Tycho House, 20 Stephenson Road, Surrey Research Park, Guildford, Surrey, GU27YE, United Kingdom, Tel: +44(0)1483803803 | Fax: +44(0)1483803804 | Email: info@sstl.co.uk | Web: www.sstl.co.uk

Remark: No answer to email has come.

## CNC Fine Mechanics (2D)

**Hard Steel Digits**

Hi-Tech Fab is specialized in manufacturing brass and hardened steel stamps. We make various types of marking heads for food packing and pharmaceutical industries.

We use the most advanced CAD/CAM software with our CNC milling machines. Our state of the art CNC machines enable us to produce quality parts with utmost precision.

We also manufacture custom parts that are designed according to customer's drawings. We carry printing heads that fit on Markem, Image, and Allen coding printers (Rotary and flat holders).

In the case of difficult jobs our clients are supported by qualified engineers to develop a solution and satisfy their needs. Our facilities are prepared for delivering large custom jobs in a timely manner.

**Brass Digits**

**HI-TECH FABRICATION**  
Mahjar Suhi  
P.O. Box 1274  
Tripoli, Lebanon  
Tel 00961-6-442787  
www.hitechfabrication.com  
info@hitechfabrication.com  
sirfawaz@yahoo.com

"You will find our products in every packing factory"

**HI-TECH FABRICATION**  
Precision Mechanical Parts Manufacturing  
Brass & Steel Marking Heads Maker

**M. Fawaz Abdul Hadi**  
Mechanical Engr

Mahjar Suhi  
P.O. Box 1274  
Tripoli, Lebanon  
Tel/Fax 00961-6-442787  
www.hitechfabrication.com  
info@hitechfabrication.com  
sirfawaz@yahoo.com

The company HI-TECH Fabrication takes CAD Data (in .dxf format) -> Changing to CAM Data.

Satellite Parts are in Alluminium Alloy.

**3D Printing (Plastics)**

<http://www.cnclablb.com/>

**CNC**

Company	Phone number	Description	Address	E-mail web site
CNC LAB	06 412 895 03 476 916	Manufacture 3D design in plastic & open source hardware	Tripoli, Lebanon Bahsas, Behind Haykalieh Hospital, Harba Bld.	<a href="http://www.cnclab.com">www.cnclab.com</a> <a href="mailto:info@cnclablb.com">info@cnclablb.com</a>
Hasan Al Baba	03 828 256	Manufacture and casting	Tripoli, Lebanon Mina, Industry and Commerce street	
HI-Tech fabrication Fawaz Abdel Hadi	06 442 787 70 751 522	Precision mechanical parts manufacturing brass & steel marking heads maker	Tripoli, Lebanon Mahjar suhi P.O. Box 1274	<a href="http://www.hitechfabrication.com">www.hitechfabrication.com</a> <a href="mailto:info@hitechfabrication.com">info@hitechfabrication.com</a> <a href="mailto:sirfawaz@yahoo.com">sirfawaz@yahoo.com</a>
Hannuf mechanical 'Corporation for casting and art construction	06 387 723 03 717 107	Manufacture and casting	Tripoli, Lebanon Al Badawi	
GPS Steel	03 196 225	Uses electric discharge machining process to shape any metal material rapidly by using desired modeled electrodes	Beirut, Lebanon Burj Hammoud	<a href="mailto:Gps.steel.co@gmail.com">Gps.steel.co@gmail.com</a>
Riyako factory	79 118 779	3D CNC machine, manufacture cupboard for cars	Tripoli, Lebanon Badawi, behind Al Ridani bakery	

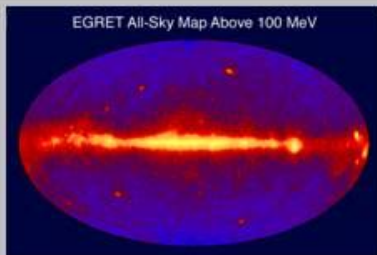
# IAP-GAMS (Gamma Astronomy Sensor)



**AECENAR**  
Association for Economical and Technological Cooperation  
in the Euro-Asian and North-African Region  
[www.aecenar.com](http://www.aecenar.com)

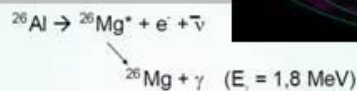
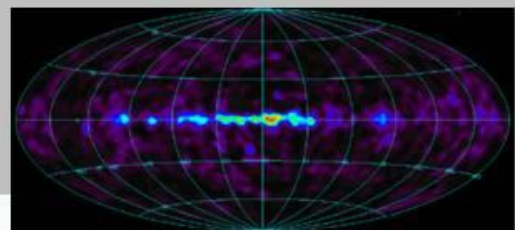


## Gamma Astronomy Measurement System (IAP-GAMS) 2018–2021 (planned)



The sky at energies above 100 MeV observed by the Energetic Gamma Ray Experiment Telescope (EGRET) of the Compton Gamma Ray Observatory (CGRO) satellite (1991–2000)

The sky at 1.8 MeV (COMPTEL Telescope)



Scintillators	Density (g/cm <sup>3</sup> )	Emission Intensity (NaI(Tl) normalized at 100)	Emission Time (ns)	Peak Emission Wavelength (nm)	Applications
NaI(Tl)	3.67	100	230	410	Surveymeter, area monitor, gamma camera
BGO	7.13	15	300	480	PET
CsI(Tl)	4.51	45 to 50	1000	530	Surveymeter, area monitor
Pure CsI	4.51	<10	10	310	High energy physics
BaF <sub>2</sub>	4.88	20	0.9/330	229/325	TOF, PET, high energy physics
GSO:Ce	6.71	20	30	319/420	Area monitor, PET
Plastic	1.02	25	2	400	Area monitor, neutron detection
LSO:Ce	7.35	70	40	420	PET
PWO	8.28	0.7	15	470	High energy physics
YAP:Ce	5.55	40	30	380	Surveymeter, compact gamma camera

Table 7-1: Typical characteristics and applications of scintillators

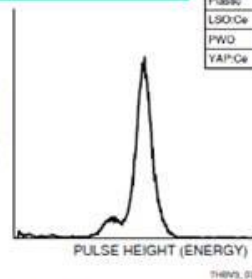
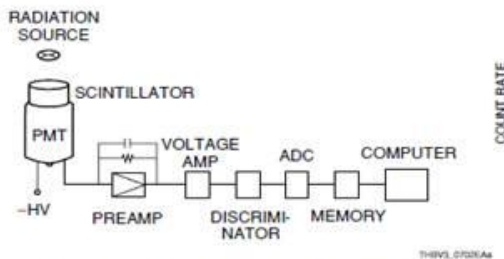


Figure 7-2: Block diagram for scintillation counting and pulse height distribution

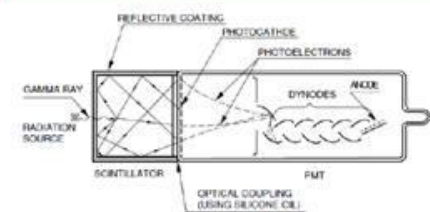
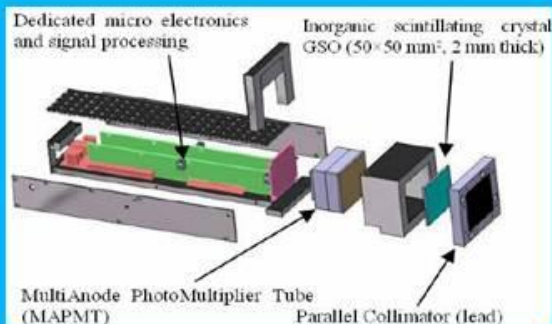
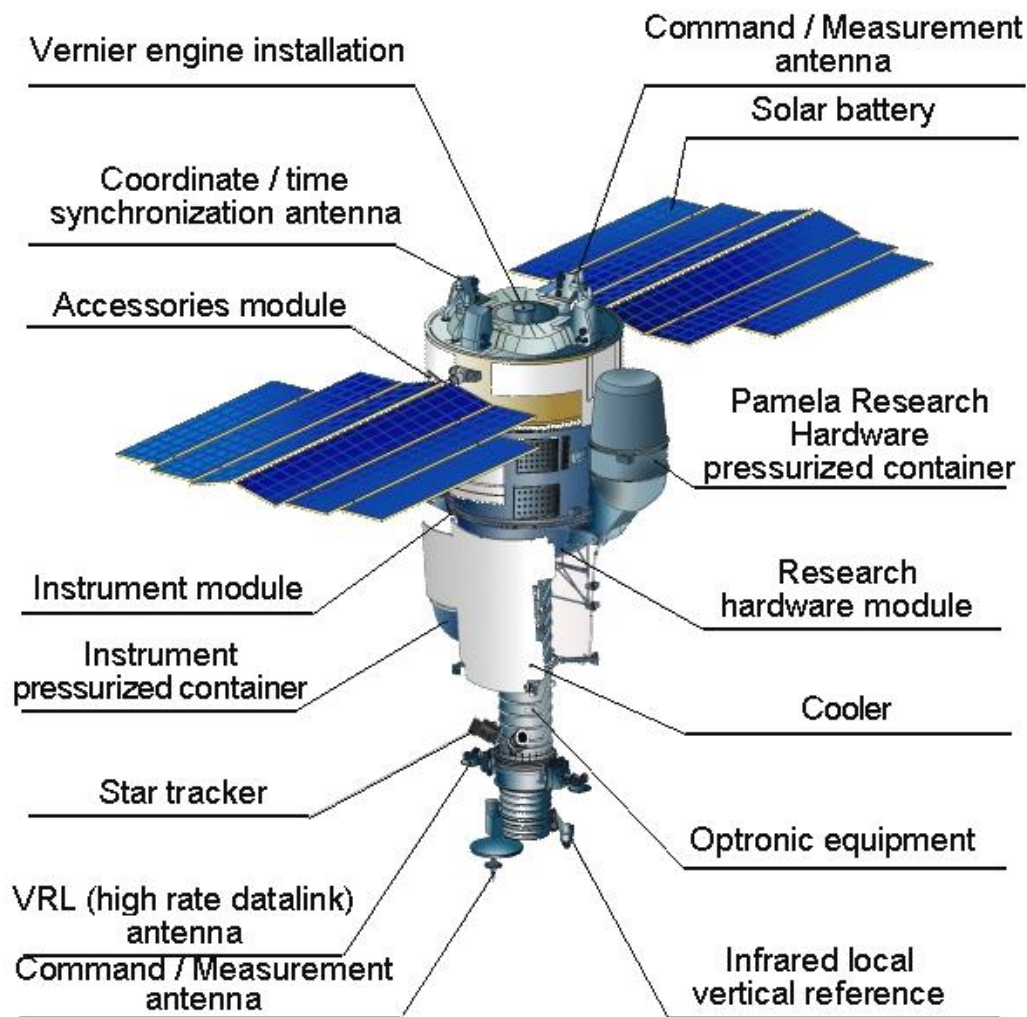


Figure 7-3: Gamma-ray detection using a NaI(Tl) scintillator and a photomultiplier tube



## Project Status at Beginning of actual project phase

Initial Goals of actual phase: Predevelopment of a gamma astronomy satellite - similar to satellite of PAMELA experiment:



and as:

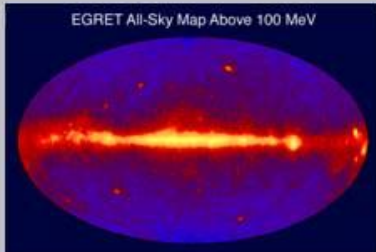




**AECENAR**  
 Association for Economical and Technological Cooperation  
 in the Euro-Asian and North-African Region  
[www.aecenar.com](http://www.aecenar.com)

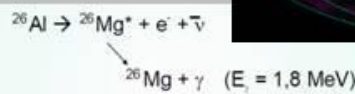
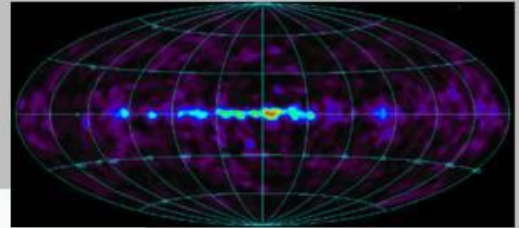


**Gamma Astronomy Measurement System (IAP-GAMS) 2018–2021 (planned)**



The sky at energies above 100 MeV observed by the Energetic Gamma Ray Experiment Telescope (EGRET) of the Compton Gamma Ray Observatory (CGRO) satellite (1991–2000)

The sky at 1.8 MeV (COMPTEL Telescope)



Scintillators	Density (g/cm <sup>3</sup> )	Emission Intensity (NaI(Tl) normalized at 100)	Emission Time (ns)	Peak Emission Wavelength (nm)	Applications
NaI(Tl)	3.67	100	230	410	Surveymeter, area monitor, gamma camera
BGO	7.13	15	300	480	PET
CaI(Tl)	4.51	45 to 50	1000	530	Surveymeter, area monitor
Pure CsI	4.51	<10	10	310	High energy physics
BaF <sub>2</sub>	4.88	20	0.9/330	229/325	TOP, PET, high energy physics
GSO:Ce	5.71	20	30	310/420	Area monitor, PET
Plastic	1.03	25	2	400	Area monitor, neutron detection
LSO:Ce	7.35	70	40	420	PET
PWO	8.28	0.7	15	470	High energy physics
YAP:Ce	5.55	40	30	380	Surveymeter, compact gamma camera

Table 7-1: Typical characteristics and applications of scintillators

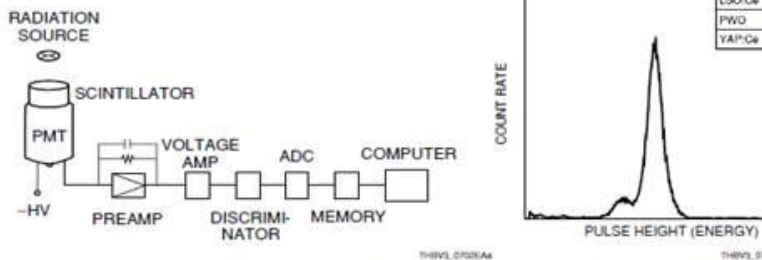


Figure 7-2: Block diagram for scintillation counting and pulse height distribution

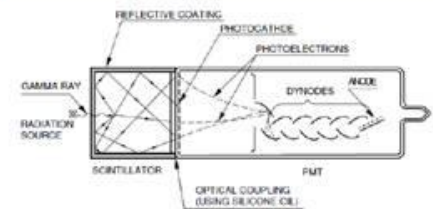
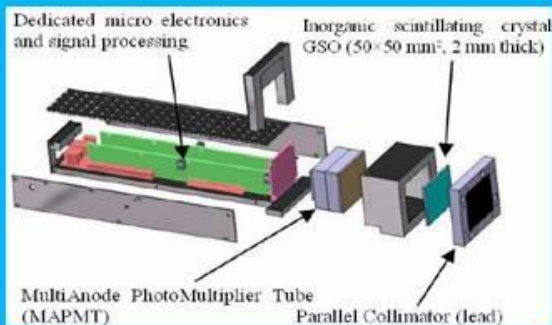
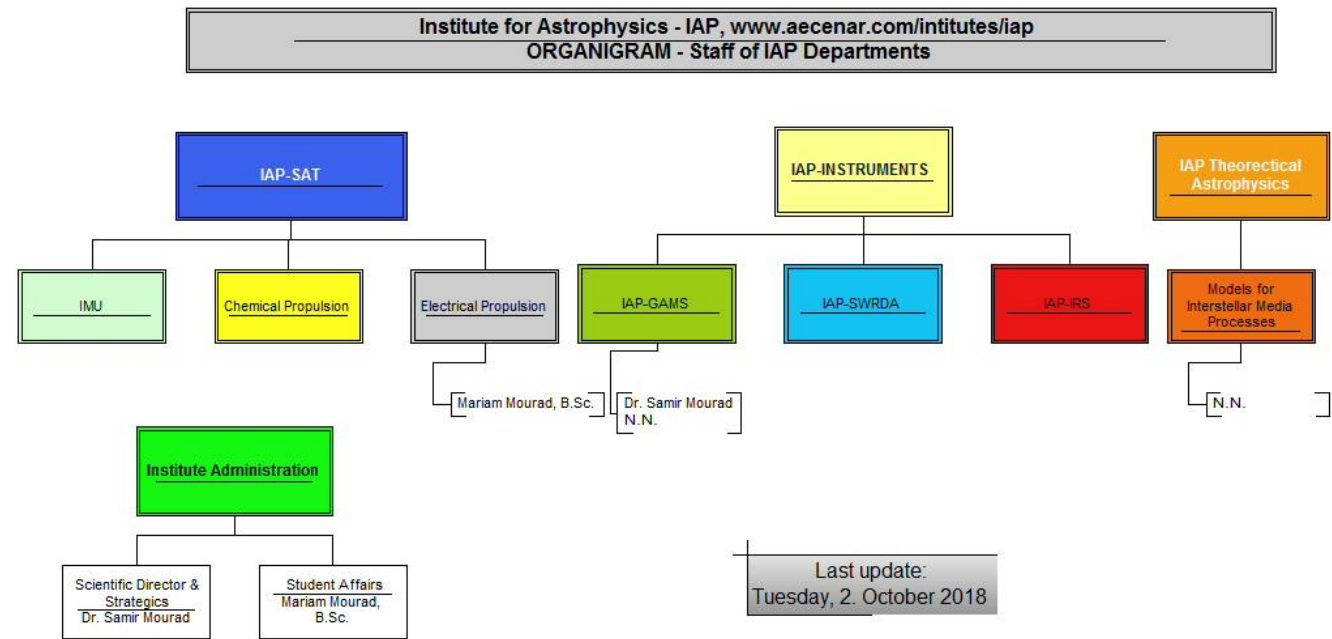


Figure 7-3: Gamma-ray detection using a NaI(Tl) scintillator and a photomultiplier tube



## 63 Project Management

### 63.1 Organisation within IAP




### 63.2 Working Packages and Time Plan

#### 63.2.1 To do with internal resources

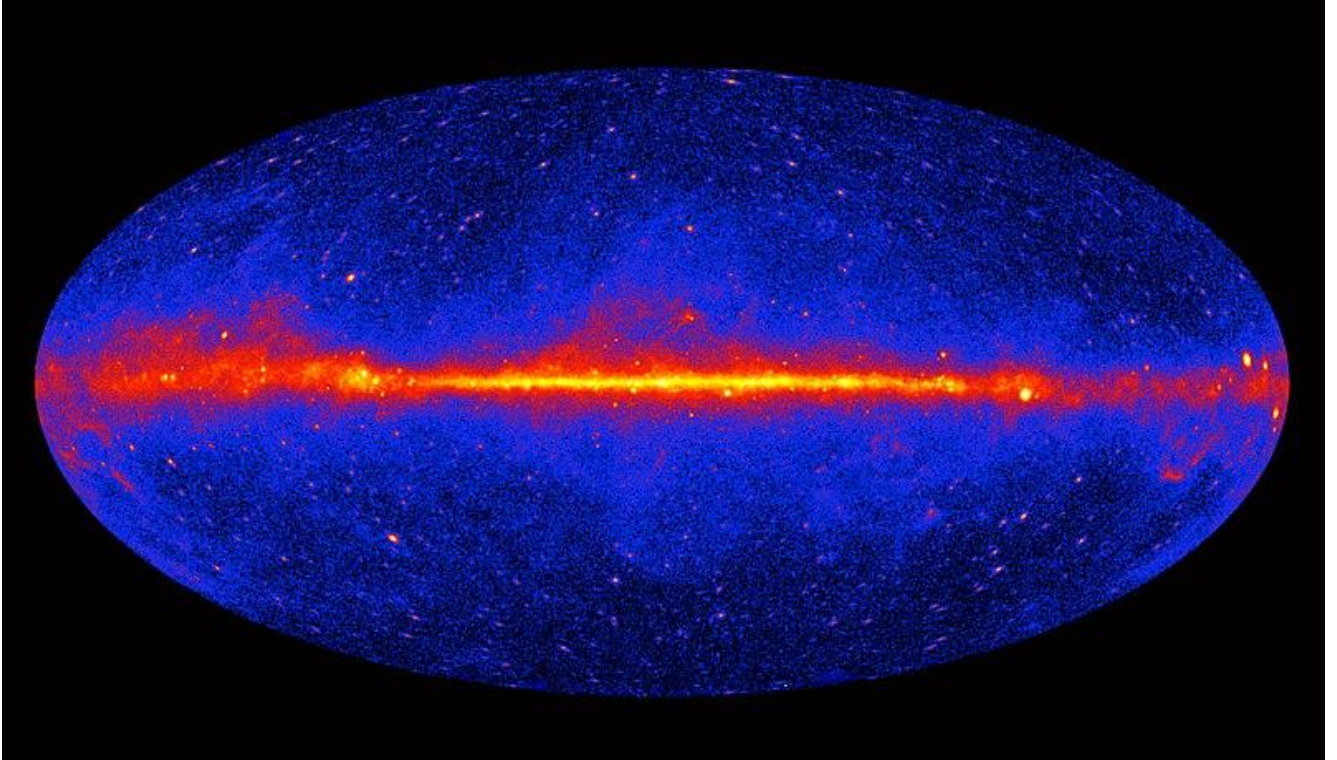
WP No.	Working package content	Time span, costs	Development environment (HW, SW)	Responsible	Status

#### 63.2.2 To do with external resources

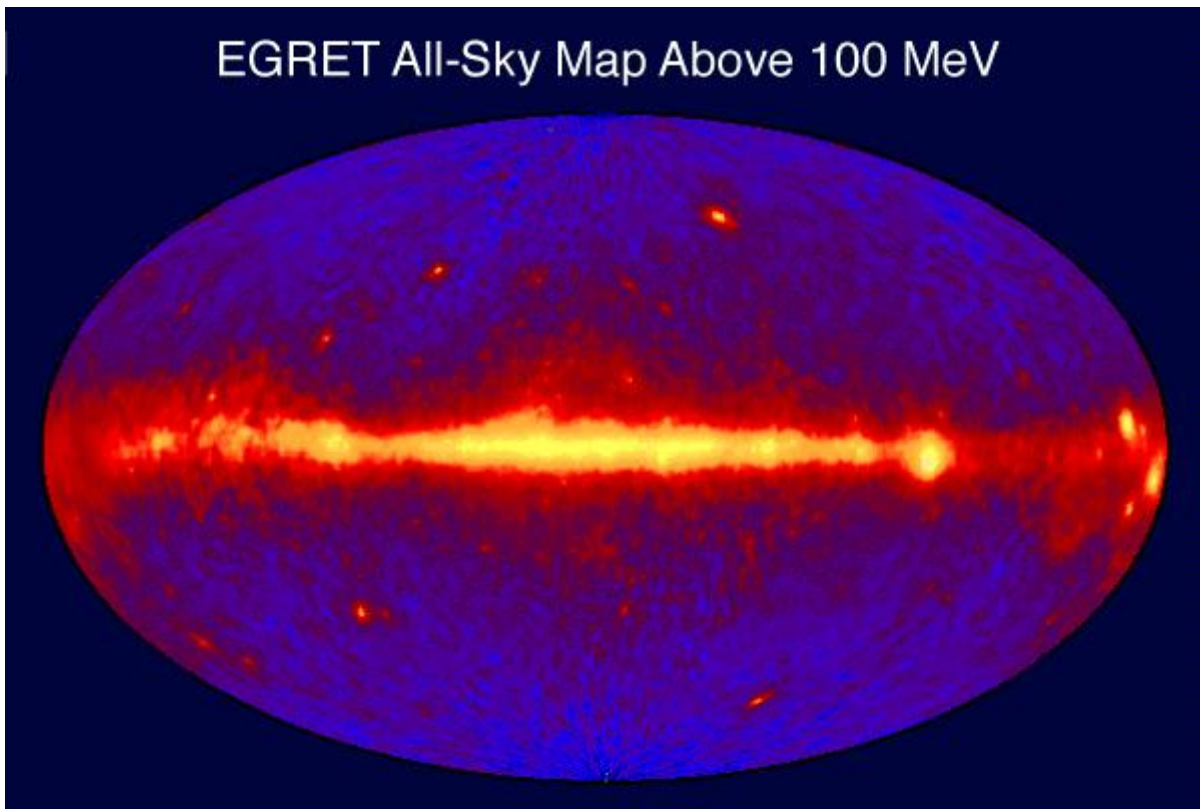
WP No.	Working package content	Time span, costs	Development environment (HW, SW)	Responsible	Status

## 64 Basics

### 64.1 Gamma Astronomy

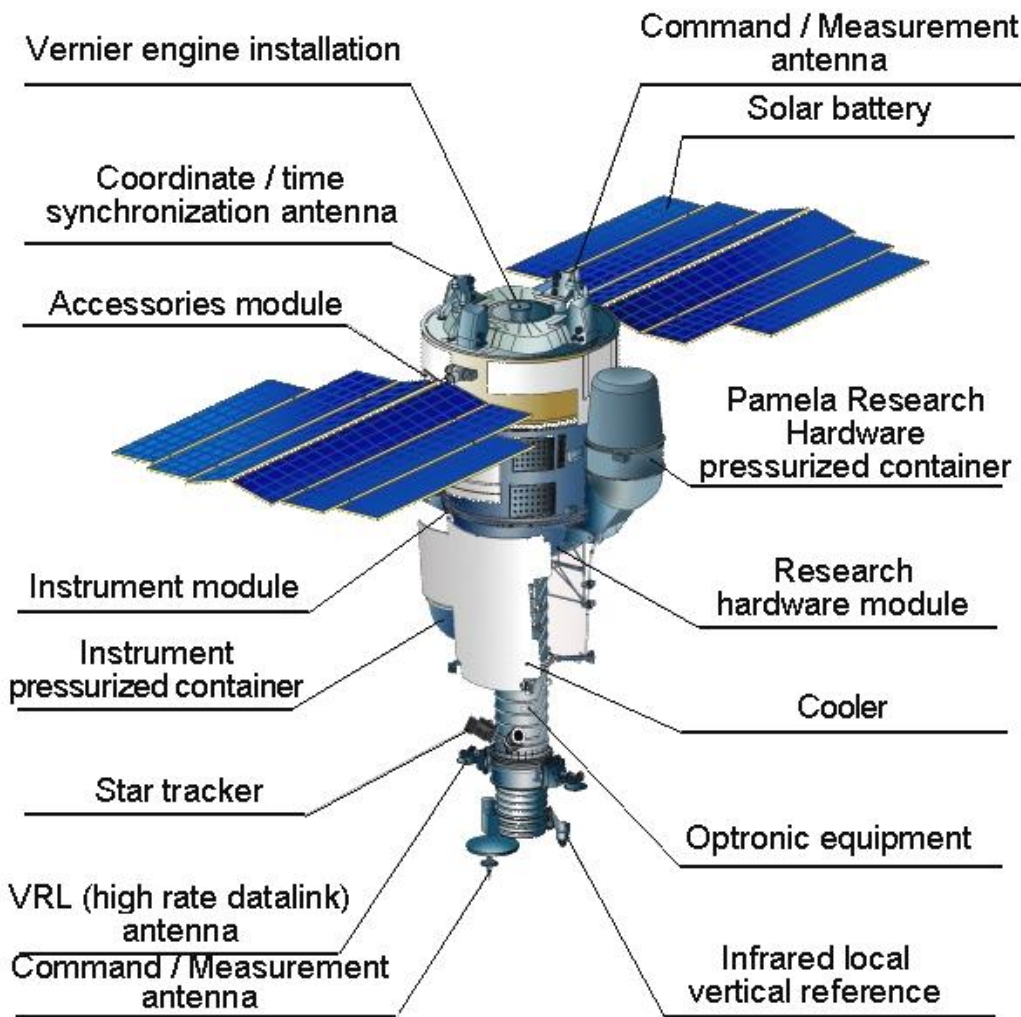


First survey of the sky at energies above 1 GeV, collected by the [Fermi Gamma-ray Space Telescope](#) in three years of observation (2009 to 2011)



The sky at energies above 100 MeV observed by the [Energetic Gamma Ray Experiment Telescope](#)(EGRET) of the [Compton Gamma Ray Observatory](#)(CGRO) satellite (1991–2000)

### 64.1.1 PAMELA Experiment



## 64.2 Nuclear Processes, Neutron and Gamma Ray Physics<sup>61</sup>

### 64.2.1 Introduction

Energy production in an operating nuclear reaction is mainly the result of fission reactions initiated by neutrons. Following these reactions, radiation is produced in the form of alpha particles, electrons (beta -articles), photons, and neutrons, as well as a large number of unstable nuclei (including actinides and fission products) that may decay, thereby producing additional radiation and energy. The neutrons generated directly in the fission reaction as well as those resulting from fission product decay are a key factor in maintaining and controlling the chain reaction as discussed in Chapters 4 and 5. Radiation also has an impact on the properties of the various materials in the core as well as on living cells. It is therefore important to understand how radiation interacts with matter if one needs, for example, to evaluate the radiotoxicity of burned fuel (Chapter 19) or to determine the kind of

<sup>61</sup> from [Essential], Ch.3

barrier that must be put in place to protect the public, the environment, or the personnel in a nuclear power plant (Chapter 12). Moreover, the energy produced by these decays contributes to heating the fuel, whether it is still in the core or in the spent fuel pools. This section provides an overview of the nuclear processes.

### 64.2.1.1 Overview

Several very important processes take often place simultaneously, including neutron slowdown as a result of collisions with nuclei, nuclear fission, and decay of radioactive nuclei with radiation emissions that subsequently lose energy or are absorbed.

To understand how all these physical processes take place, it is important to possess a general knowledge of the physics of the nucleus, including its composition and the fundamental forces that affect its behaviour. Although one rarely uses a description of the nucleus in terms of elementary particles and their interaction in power-reaction core applications, such a description provides a practical background for a study of nuclear structure. In fact, the nucleus is such a complex object that it can be described only through simplified models that provide useful information. For example, the liquid drop model (Section 2.4) gives an empirical description of how one can extract energy from a nucleus by breaking it into smaller components (fission or decay) or by combining nuclei (fusion). These models are also used to predict the stability of a nucleus under various decay processes, the energy associated with its excited states, and the associated gamma-ray spectrum. In Section 2, an overview of the structure of the nucleus is provided, starting from a fundamental description and progressing to more practical models.

We will also introduce some language specific to nuclear physics. The majority of the fission reactions taking place in a reaction core are initiated following the absorption of a neutron by a heavy nucleus. Radioprotection also involves the interaction between radiation, in the form of alpha particles, electrons, photons, and neutrons, and matter. Two important points must then be addressed before describing the physics of neutrons in a nuclear reaction core: the source of this radiation and its behaviour over time, and the interaction of the emitted particles with matter. Therefore, Section 3 is divided into three parts: it starts with a description of radioactivity and the decay of nuclei, continues with a description of the interaction of ionizing radiation with matter (everything but neutrons), which is a very important topic for radiation protection studies, and ends with a brief discussion of the interaction of neutrons with matter.

The last section of this chapter is dedicated to the nuclear chain reaction. It starts by giving an extensive description of the fission reaction and discusses the need to slow down neutrons.

This is followed by a description of the neutron transport equation that can be used to characterize the behaviour of neutrons inside a reaction core.

### 64.2.1.2 Learning Outcomes

The goal of this chapter is for the reader to:

- Understand the fundamental forces in nature and the structure of the nucleus;

- Learn how to compute the mass of a nucleus based on the liquid drop model and to evaluate the energy released by the fission and fusion processes;
- Understand how to evaluate the activity and radio-toxicity of spent fuel from nuclear energy generating devices;
- Become familiar with nuclear cross-section databases for neutrons and ionization radiation and the computation of reaction rates between particles and matter;
- Recognize the need to slow down neutrons in thermal reaction cores and to evaluate the effectiveness of a moderator.

## 64.2.2 Structure of the Nucleus

### 64.2.2.1 Fundamental Interactions and Elementary Particles

Four forces, or interactions, are currently sufficient to understand and explain nature from particle physics to astrophysics, including chemical and biological processes. These forces are classified relative to their intensity at the nuclear level (distances of the order of 1 fm) as follows:

- The strong force: responsible for the cohesion of the proton as well as the nucleus. This force is always attractive.
- The electromagnetic force: governs the physics of the atom and the associated chemical and biological processes. This force can be both attractive and repulsive.
- The weak force: responsible for the existence of the neutron as well as many other radioactive nuclei. This force is always attractive.
- The gravitational force: governs the large-scale structure of the universe. This force ensures the stability of the solar system as well as the fact that people can keep their feet on the ground. This force is always attractive.

From the point of view of physics, these forces arise from the specific intrinsic properties of the particles on which they act. For example, the electromagnetic force arises between two particles that have electric charges, while the gravitational force appears between two particles with masses (or more generally, between two particles with energy). For the strong force, the so-called “colour” of the particle plays a role equivalent to that of electric charge in electromagnetic interactions, while the weak force is the result of the interaction of two particles having a “weak” charge. Table 1 provides a brief description of the general properties of the four fundamental forces, where the alphas are dimensionless coupling constants related to the intensity of the interaction and the spatial dependence of the force is the distance between the two interacting particles [Halzen1984]. For example, the electromagnetic force between two particles of charge  $ze$  and  $Ze$  is given by:

$$|\vec{F}(\vec{r})| = \left( \frac{e^2}{4\pi\epsilon_0} \right) \frac{zZ}{|r|^2} = (\alpha_e \hbar c) \frac{zZ}{|r|^2}, \quad (1)$$

where  $e = 1.6 \times 10^{-19}$  C is the charge of an electron,  $\epsilon_0 = 8.854 \times 10^{-12}$  F/m is the electric permittivity of vacuum,  $\hbar = 1.0546 \times 10^{-34}$  J  $\times$  s is the reduced Planck constant, and  $c = 2.9979 \times 10^8$  m/s is the speed of light. For the gravitational force, the coupling constant is expressed in terms of proton masses. One can immediately see that the range of the gravitational and electromagnetic forces is substantially larger than that of the weak force due to their  $\frac{1}{r^2}$  dependence. Accordingly, the weak force is important only when two particles with weak charges are in close contact. On the other hand,

the strong (colour) force remains significant irrespective of the distance between particles with colour charge. This observation led to the concept of colour confinement, meaning that it is impossible to isolate a particle having a net colour charge different from zero [Halzen1984].

**Table 1 Properties of the four fundamental forces**

Force	Equivalent charge	Coupling constant	Spatial dependence
Strong	Colour charge	$\alpha_s \approx 1$	$\approx r^0$
Electromagnetic	Electric charge	$\alpha_e \approx 1/137$	$r^{-2}$
Weak	Weak charge	$\alpha_w \approx 10^{-6}$	$r^{-5}$ to $r^{-7}$
Gravitational	Mass	$\alpha_G \approx 10^{-39}$	$r^{-2}$

In the standard model of particle physics [Halzen1984, Le Sech2010], these forces are represented by 12 virtual particles of spin 1 called “gauge bosons”:

- the massless photon that carries the electromagnetic interaction;
- eight massless gluons that carry the strong (colour) force;
- three massive bosons ( $W^\pm$  and  $Z^0$ ) that mediate the weak interaction.

These bosons are exchanged between the 12 “physical fermions” (spin 1/2 particles) that make up all the matter in the universe:

- six light fermions or leptons that have a weak charge. Three of these have no electric charge (the neutrinos), while three are charged (electron, muon, and tau);
- six heavy fermions or quarks that have colour, weak, and electric charges. These fermions cannot exist freely in nature because of colour confinement and must be combined in triplets of quarks or quark-antiquark pairs to form respectively baryons (protons, neutrons) and mesons (pion, kaon) that have no net colour charge.

**Table 2 Properties of leptons and quarks**

Leptons			Quarks		
Particle	Mass (GeV/c <sup>2</sup> )	Charge	Particle	Mass (GeV/c <sup>2</sup> )	Charge
$e$	0.000511	-1	$u$	$\approx 0.003$	2/3
$\nu_e$	$< 2.5 \times 10^{-9}$	0	$d$	$\approx 0.006$	-1/3
$\mu$	0.1057	-1	$c$	$\approx 1.2$	2/3
$\nu_\mu$	$< 0.000170$	0	$s$	$\approx 0.1$	-1/3
$\tau$	1.7777	-1	$t$	$\approx 173$	2/3
$\nu_\tau$	$< 0.018$	0	$b$	$\approx 4.1$	-1/3

**Table 2** provides a description of the main properties of leptons and quarks with the masses given in  $\text{GeV}/c^2$ , with  $1 \text{ GeV}/c^2 \approx 1.782661 \times 10^{-27} \text{ kg}$ , and the charges in terms of the charge of one electron [Le Sech2010].

#### 64.2.2.2 Protons, Neutrons, and the Nuclear Force

The two lightest baryons that can be created out of a quark triplet are the positively charged proton, which is composed of two u quarks and one d quark, and the neutral neutron, made up of two d quarks and one u quark. These are present in the nucleus of all the elements present naturally in the universe. The main properties of the proton and the neutron are provided in Table 3 [Basdevant2005]. One can immediately see that the masses of the proton and neutron are very large compared with those of the u and d quarks. In fact, most of their mass is a result of the strong colour force (gluon interaction). One can also observe that protons are stable, while neutrons are unstable and decay relatively rapidly into protons through the weak interaction. A second observation is that the magnetic moment, which is created by the movement of charged particles, is negative for the neutron. This confirms, at least partially, the theory that neutrons are made of quarks because even though the neutron is neutral, the distribution of charge inside it is not uniform.

**Table 3 Main properties of protons and neutrons.**

Property	Proton	Neutron
Mass ( $\text{GeV}/c^2$ )	$m_p = 0.938272$	$m_n = 0.939565$
Charge (electron charge)	1	0
Magnetic moment ( $\mu_N$ )	$\mu_p = 2.792847$	$\mu_n = -1.913042$
Spin	1/2	1/2
Mean-life (s)	$\tau_p > 10^{36}$	$\tau_n = 881.5$

Although the proton and neutron have a neutral colour, they interact through the nuclear force, which is a residual of the strong colour force. However, instead of exchanging gluons directly, as do the quarks inside the proton or neutron, they interact by exchanging of virtual pion. As a result, the nuclear force is much weaker than the strong force in the same way that the Van der Waals force between neutral atoms is weaker than the electromagnetic force.

Moreover, in contrast to the strong colour force, the magnitude of the nuclear force decreases rapidly with distance, the nuclear interaction being given approximately by the Yukawa potential:

$$V_{\text{Yukawa}}(r) = -\alpha_N \hbar c \frac{e^{-\frac{m_\pi r}{\hbar}}}{r}, \quad (2)$$

where  $m_\pi$  is the mass of the pion ( $140 \text{ MeV}/c^2$ ) and  $\alpha_N \approx 14.5$  is a constant that controls the strength of the nuclear interactions between baryons (protons or neutrons). The minus sign here indicates that the resulting force ( $\vec{F} = -\vec{\nabla}V$ ) is always attractive. This potential is identical for proton-proton, proton-neutron, and neutron-neutron interactions.

The strength of this force at short distances is so intense that it can compensate for the repulsive electromagnetic force between protons, leading to the formation of bonded nuclei as well as inhibiting neutron decay. For example, the helium nucleus, which is composed of two protons and two neutrons, is stable. Similarly, the stable deuteron is composed of one proton and one neutron. The absence in nature of a nucleus composed of two protons is not a result of the fact that the electromagnetic force is greater than the strong force, but rather due to the exact structure of the nuclear force. In addition to having a spatial behaviour provided by the Yukawa potential, this potential is also spin-dependent and repulsive between particles with anti-parallel spins (a nucleus with two protons having parallel spins is not permitted because of Pauli's exclusion principle). This also explains why stable nuclei containing only neutrons are not seen in nature.

### 64.2.2.3 Nuclear Chart

As indicated in the previous section, not all combinations of neutrons and protons can lead to bonded states. Figure 1 provides a list of all bonded nuclei [Brookhaven2013, KAERI2013]. The points in red represent stable nuclei, while those in green indicate radioactive nuclei. The straight black line indicates nuclei having the same number of neutrons and protons. Note that this chart is quite different from the periodic table, where the classification of the elements is based on the number of electrons surrounding the nucleus. Because the number of electrons surrounding the nucleus is identical to  $Z$ , the number of protons inside the nucleus, each element corresponds to a combination of the nuclei that are found on a horizontal line of the nuclear chart. The nomenclature used to classify these nuclei is the following:

- The number of protons in the nucleus is used to identify the element. For example, all nuclei with  $Z = 8$  are known as oxygen (atomic symbol O), independently of the number of neutrons present in the nucleus.
- For a given element, the specific isotope is identified by  $A = Z + N$ , where  $A$  is known as the mass number and  $N$  is the number of neutrons in the nucleus. For example, oxygen-17, denoted by  $^{17}\text{O}$ , corresponds to an oxygen atom where the nucleus has eight protons and nine neutrons. Instead of the notation  $^{N+Z}\text{X}$ , with X the element associated with  $Z$ , the notation  $^{N+Z}_{Z}\text{X}$  is also found in the literature.
- Two other terms are less frequently used: isobars, corresponding to nuclei having the same mass numbers, but different values for  $Z$  and  $N$ ; and isotones, corresponding to nuclei having the same number of neutrons, but a different number of protons.

Several conclusions can be reached from Figure 1:

- Isotopes containing a small number of protons ( $Z < 20$ ) will generally be stable only if  $N$  and  $Z$  are nearly equal. If the difference  $|N - Z|$  is slightly too large, the nucleus becomes unstable. For combination of protons and neutrons with large values of  $|N - Z|$ , no nuclei can be formed.
- For nuclei with values of  $Z$  ranging from 20 to 82, the number of excess neutrons ( $N - Z$ ) required to create bonded nuclei increases steadily. One can also observe that for a specific value of  $Z$ , several stable nuclei can be produced with different numbers of neutrons.
- No stable nucleus exists with  $Z > 83$ , although some radioactive nuclides with  $Z < 93$  can still be found in nature because they decay at a very slow rate. No isotope with  $Z$  above 92 remains in nature.

Approximately 3200 bonded nuclei have been identified, out which 266 are stable. The stability of a nucleus is ensured by the presence of a sufficient number of neutrons to compensate for the effect of the Coulomb force between protons. Because the nuclear force acts only at short distances, while the Coulomb force has a longer range, additional neutrons are required when the radius  $R$  of the nucleus increases because of the presence of more nucleons (proton and neutrons):

$$R \propto A^{1/3} R_0, \quad (3)$$

where  $R_0$  is the average radius of a single nucleon.

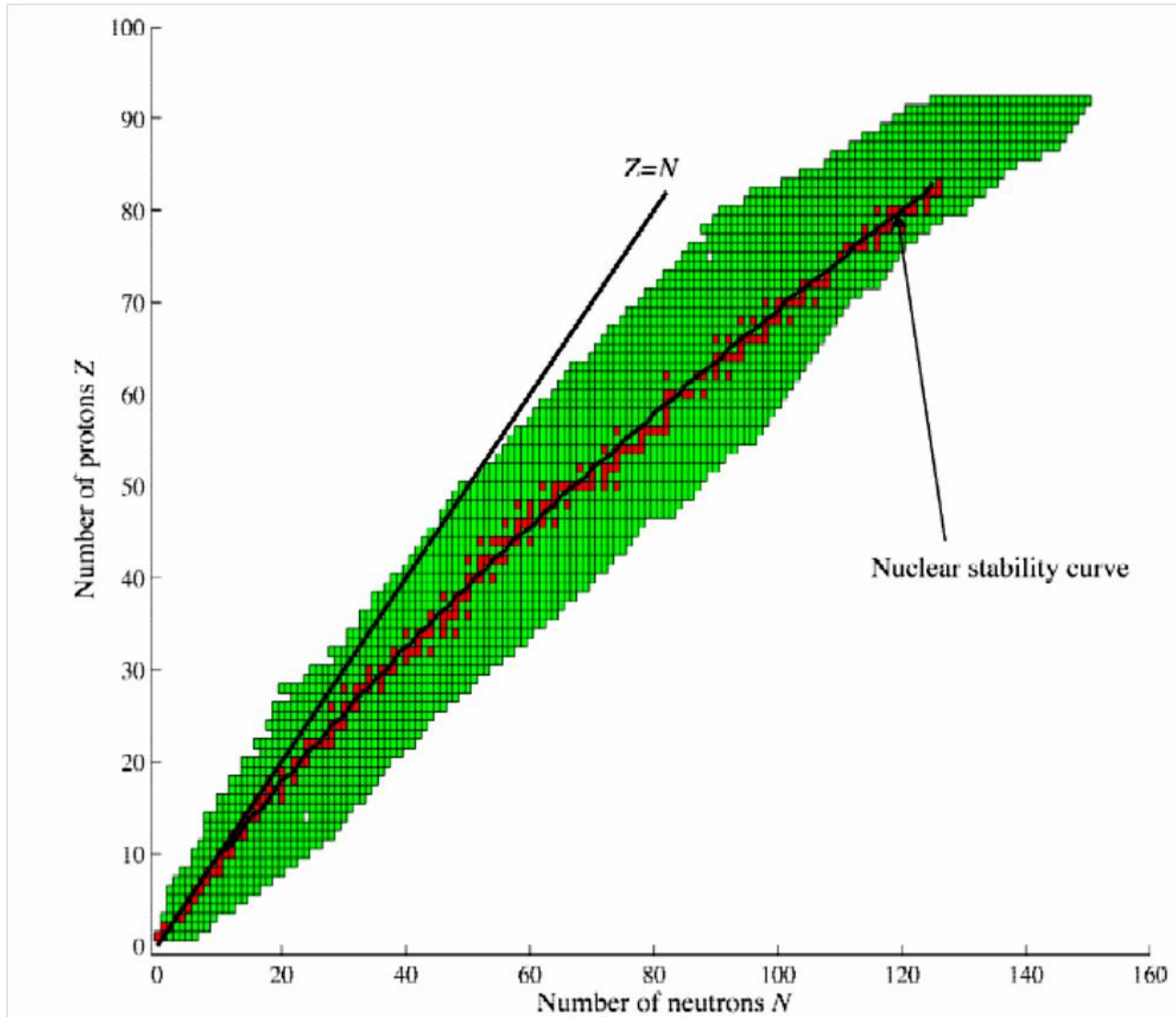


**Figure 1** Nuclear chart, where  $N$  represents the number of neutrons and  $Z$  the number of protons in a nucleus. The points in red and green represent respectively stable and unstable nuclei. The nuclear stability curve is also illustrated.

The stability of a nucleus does not only depend on the number of nucleons it contains but also on how these protons and neutrons are paired. For example, out of the 266 stable nuclei:

- 159 contain an even number of protons and of neutrons,
- 53 have an even number of protons, but an odd number of neutrons
- 50 have an odd number of protons and an even number of neutrons, and

- only 4 are made up of an odd number of protons and of neutrons.

In addition, for values of Z or N equal to 8, 20, 50, 82, and 126, the number of stable nuclei is very high. These numbers are known as “magic numbers”. They suggest that the neutrons and protons, just like electrons in atoms, are more tightly bonded when they fill a quantum energy shell (see Section 2.5). The mass  $m_{N+Z_X}$  of a nucleus produced by combining Z protons and N neutrons is less than the sum of the masses of its constituents:

$$m_{N+Z_X} = Z m_p + Nm_n - AB / c^2, \tag{4}$$

where  $B > 0$ , the average binding energy per nucleon, is the result of the negative potential that binds the nucleons inside the nuclei. As can be seen in Figure 2, where a plot of B as a function of A is provided for stable nuclei, B first increases rapidly for low mass numbers, reaching a maximum around  $A = 60$ , and then decreases slowly with A. This means that, on the average, nucleons are more tightly bonded inside nuclei having intermediate values of A ( $20 < A < 120$ ) than for very high values.

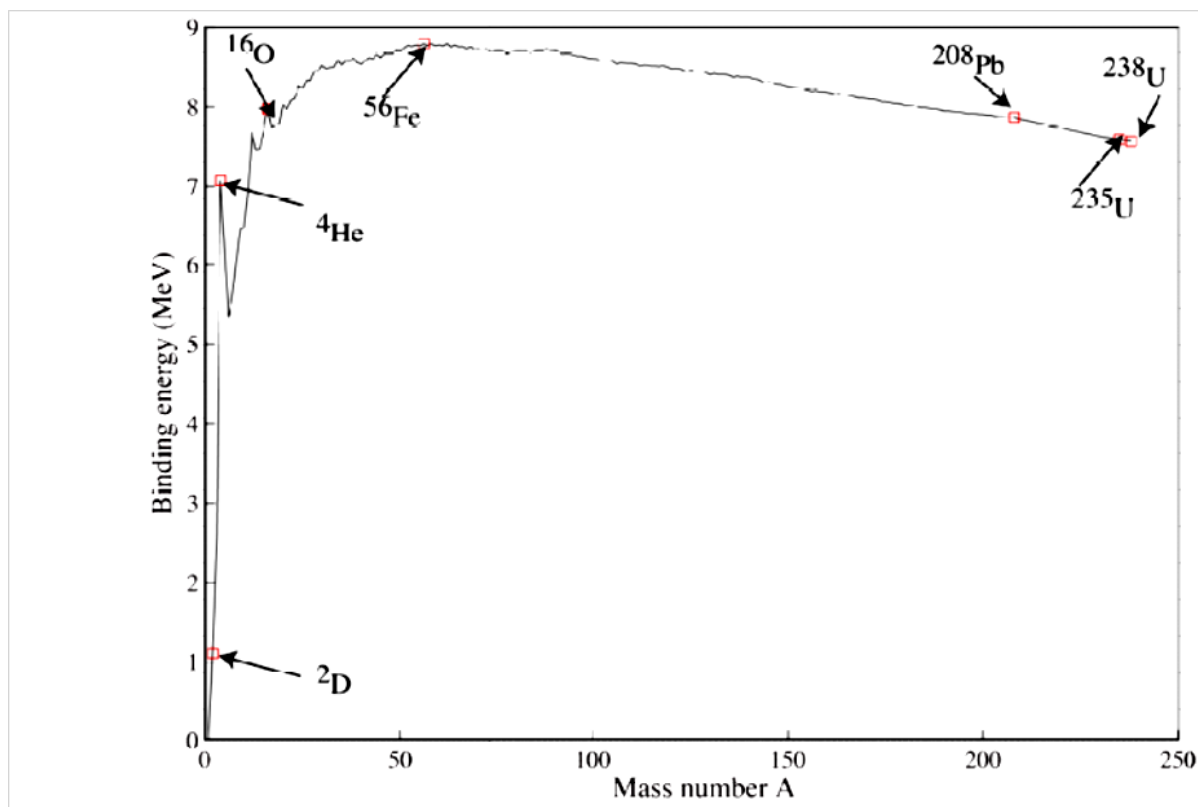


**Figure 2 Average binding energy per nucleon (MeV) as a function of the mass number (number of nucleons in the nucleus).**

Information on the atomic mass of over 3000 isotopes is available in [Livermore2013]. Note that the atomic mass is different from the nuclear mass of an isotope because it includes both the mass and the binding energy of the Z electrons gravitating around the nucleus. One simple way to compute the atomic mass is using

$$M_{N+Z_X} \approx Z M_{1H} + Nm_n - AB / c^2, \tag{5}$$

where the mass of the proton has been replaced by that of the hydrogen atom, which includes the electron mass as well as its binding energy. The approximation sign comes from the fact that the

binding energy of each of the  $Z$  electrons around a heavy nucleus is different from that of a single electron attached to a proton in the hydrogen atom.

Finally, the natural composition of a given element will include stable as well as some radioactive isotopes. Assuming that the relative atomic abundance of isotope  $i$  of atomic mass  $M_i$  in the natural element is  $\gamma_i$ , then the mass of the natural element is given by:

$$M_X = \sum_i \gamma_i M_i. \quad (6)$$

In reactor physics, one often works with the mass (or weight) fraction for the abundance of an isotope, defined as:

$$w_i = \frac{\gamma_i M_i}{M_X}. \quad (7)$$

For completeness, one can compute the isotopic concentration  $N_X$  of an element (atoms/cm<sup>3</sup>) with atomic mass  $M_X$  (g/moles) and density  $\rho$  (g/cm<sup>3</sup>) using:

$$N_X = \frac{\rho}{M_X} N_A, \quad (8)$$

where  $N_A = 6.022 \times 10^{23}$  atoms/moles is the Avogadro number. The concentration of isotope  $i$  is then given by:

$$N_i = \gamma_i \frac{\rho}{M_X} N_A = \gamma_i N_X. \quad (9)$$

More information related to the isotopic contents of natural elements can be found in [KAERI2013,WebElements2013].

#### 64.2.2.4 Nuclear Mass and the Liquid Drop Model

As discussed in Section 2.3, the mass of the nucleus is smaller than its classical mass (the mass of its constituents) because the strong force linking the nucleons reduces the global energy of the nuclear system, the binding energy being related to the missing mass  $\Delta m_x$  according to

$$\Delta m_x c^2 \approx AB. \quad (10)$$

This missing mass is very difficult to compute based on theoretical models because the form of the nuclear potential is known only approximately and because quantum models involving more than two particles in interaction cannot be solved exactly. For evaluation of the missing mass, one generally relies on a semi-empirical model known as the liquid drop model. The main assumption used in this model is that the nuclear force is identical for protons and neutrons.

The liquid drop model first assumes that each of the  $A$  nucleons in the nucleus sees the same nuclear potential [Basdevant2005]. Moreover, this potential is independent of the number of nucleons in the nucleus. This second assumption can be justified by the fact that the range of the nuclear force is small, and therefore each nucleon feels the effect of only the limited number of nucleons that are close by. Accordingly, the contribution to the missing mass from the  $A$  nucleons is given by:

$$\Delta m_p c^2 = a_v A. \quad (11)$$

where the constant  $a_V \approx 15.753 \text{ MeV}$  has been determined experimentally. This contribution is known as the volume effect because the volume of a nucleus can be assumed to be proportional to the number of nucleons it contains. This term would be sufficient if the nucleus had an infinite size. However, this is not the case, and the protons and neutrons that are located near the boundary of the nucleus will interact with a smaller number of nucleons. If the surface of the nucleus is given by  $4\pi R^2 \propto A^{2/3}$ , one can assume that the  $A^{2/3}$  nucleons near the outer surface of the nucleus see a reduced uniform potential. This leads to a negative surface contribution to the mass defect of the form:

$$\Delta m_S c^2 = -a_S A^{2/3}, \quad (12)$$

where  $a_S \approx 17.804 \text{ MeV}$ .

Until now, only the nuclear force has been taken into account. However, the protons present inside the nucleus repel each other through the Coulomb force, thereby decreasing the binding energy. Because the potential associated with this force is long-range ( $V(R) \propto 1/R \propto 1/A^{1/3}$ ), each of the  $Z$  protons will interact with the remaining  $Z - 1$  protons, leading to a contribution of the form:

$$\Delta m_C c^2 = -a_C \frac{Z(Z-1)}{A^{1/3}} \approx -a_C \frac{Z^2}{A^{1/3}}, \quad (13)$$

where only the dominant term in  $Z$  has been preserved, and  $a_C \approx 0.7103 \text{ MeV}$ . It can be observed in the nuclear chart that stable nuclei with a low mass number generally contain an equal number of protons and neutrons. As the number of excess neutrons or protons in a nucleus increases, it becomes more and more unstable until no bonded state can be produced. This means that nuclear binding should decrease as a function of  $|N - Z| = |2N - A|$ , the form of the contribution being

$$\Delta m_A c^2 = -a_A \frac{(A - 2Z)^2}{A}, \quad (14)$$

where  $a_A \approx 23.69 \text{ MeV}$  is known as the asymmetry term. The nuclear chart also shows that few stable nuclei with an odd number of neutrons and protons (odd-odd nuclei) can be found in nature, while the number of isotopes with an even number of protons and neutrons (even-even nuclei) dominates. This means that the binding energy should be large for even-even and small for odd-odd nuclei. Assuming that the contribution to the missing mass presented previously remains valid only for odd-even or even-odd nuclei ( $A$  odd), an additional empirical correction of the form

$$\Delta m_P c^2 = (-1)^Z a_P \frac{(1 + (-1)^A)}{2A^{3/4}} \quad (15)$$

is required. Here,  $a_P \approx 33.6 \text{ MeV}$  is known as the pairing term. The final formula for the missing mass is therefor

$$\Delta m_X c^2 \approx a_V A - a_S A^{\frac{2}{3}} - a_C \frac{Z^2}{A^{\frac{1}{3}}} - a_A \frac{(A - 2Z)^2}{A} + (-1)^Z a_P \frac{(1 + (-1)^A)}{2A^{3/4}}, \quad (16)$$

which is known as the Bethe-Weizsäcker or semi-empirical mass formula (SEMF). Even if this mechanistic model is relatively simple, it provides a very good approximation to the mass of the nuclei found in nature. It can also be used to determine the value of A that minimizes the mass of a nucleus for a specific value of Z thereby maximizing the probability that it is stable. Neglecting the pairing term, one then obtains

$$Z(A) = \frac{4Aa_A + A(m_n - m_p)c^2}{8a_A + 2a_C A^{\frac{2}{3}}}. \quad (17)$$

This equation, which is also illustrated in Figure 1 (the nuclear stability curve), closely follows the nuclear stability profile. The main weakness of the liquid drop model is its lack of predictive power. For example, it neither explains the presence of “magic numbers”, nor the gamma-ray absorption spectrum, nor the decay characteristics of different nuclei. These explanations can be obtained only by looking at the interactions between protons and neutrons using quantum theory, as explained in the next section.

#### 64.2.2.5 Excitation Energy and Advanced Nuclear Models

All chemists and physicists are familiar with atomic “magic numbers”, even though the explicit term is rarely used. For example, the number of electrons in noble gases could be considered “magic” because these gases are odourless, colourless, and have very low chemical reactivity. For such atoms, all the states associated with principal quantum energy levels 1 to n are occupied by electrons (closed or filled shells). In addition, the absorption (emission) spectrum of light by different atoms is the result of electrons being excited (de-excited) from one electronic shell to another. One can therefore expect nuclear magic numbers to have a similar nature, namely, that only specific energy levels are permitted for the protons and neutrons when they are bonded inside a nucleus (which would explain also the photon emission and absorption spectra). These energy levels are not uniformly distributed, but occur in bands called shells. The fact that all the quantum states in a shell (a neutron or proton shell) are occupied by a nucleon increases the stability of the nucleus compared to nuclides with partially filled shells. To obtain the energy levels permitted for protons and neutrons inside the nucleus, one needs to solve the quantum-mechanics Schrödinger equation for A strongly coupled nucleons [Griffiths2005]. However, when trying to solve this equation, two problems arise:

- the Schrödinger equation has no analytic solution for problems where three or more particles are coupled;
- the interaction potential between nucleons is not known exactly.

As a result, this many-body problem is generally simplified using the following assumptions that are inherent to the shell model [Basdevant2005]:

- each nucleon in the nucleus is assumed to move independently without being affected by
- the displacement of other nucleons;
- a nucleon moves in a potential V(r) that is relatively uniform inside the nucleus and increases sharply near its outer surface, namely when  $r \approx R$  (mean field approximation).

Note that in this model, there are no one-to-one interactions between the nucleons. This means that instead of solving the Schrödinger equation for  $A$  strongly coupled nucleons, the problem is reduced to the solution of  $A$  independent Schrödinger equations for a single nucleon with an averaged potential. The conventional nuclear potential used in the shell model is the Saxon-Wood potential (see Figure 3), which has the form [Basdevant2005]:

$$V(r) = -V_0 \left( \frac{1}{1 + e^{(r-R)/R}} \right), \quad (18)$$

where  $V_0 \approx 30 \text{ MeV}$  is the potential depth and  $R \propto A^{1/3}$  is the radius of the nucleus in fm.

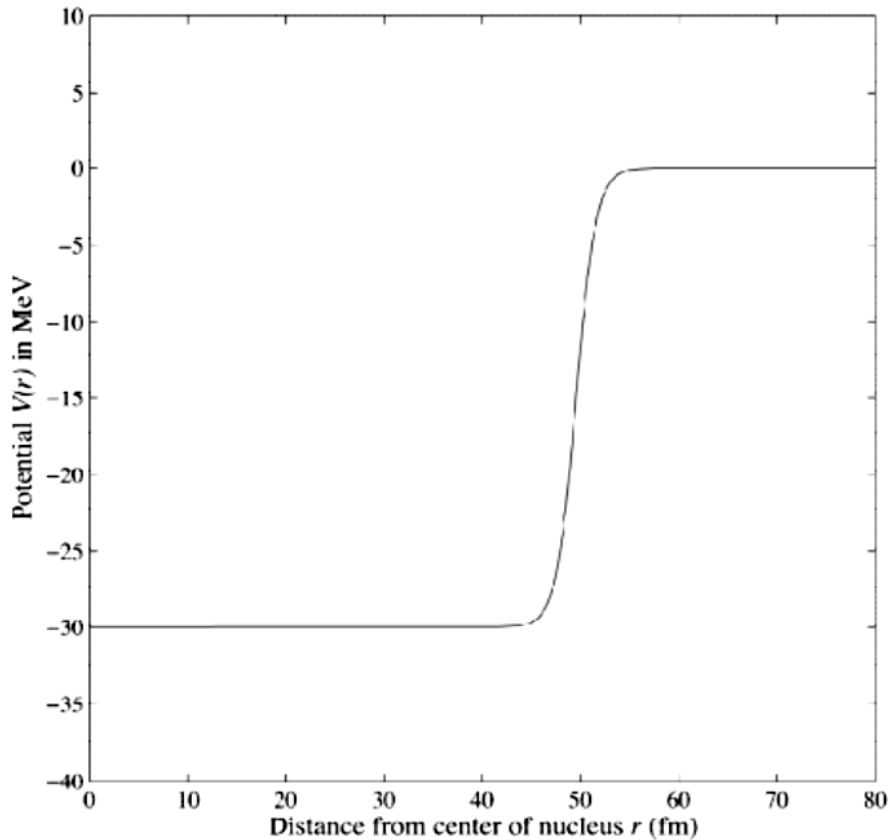


**Figure 3 Saxon-Wood potential seen by nucleons inside the uranium-235 nucleus.**

The energy levels are the very similar to those associated with the harmonic potential, namely

$$E_N = \frac{\hbar\sqrt{2V_0}}{R\sqrt{m_n}} \left( N + \frac{3}{2} \right), \quad (19)$$

where  $m_n$  is the mass of a nucleon (proton or neutron),  $N = (2n + l - 2) = 0, 1, 2, \dots$  with  $n = 1, 2, \dots$  the principal quantum number, and  $l = 0, 1, 2, \dots$  the angular momentum quantum number that takes into account spin-orbit coupling. In general, one assumes that the energy is independent of the magnetic quantum number  $m$ . The spin  $j$  of each of the nucleons, which is important when determining the probability of interaction between a nucleus (spin  $J$ ) and other particles, is a combination of its internal spin and its angular momentum:

$$j = \left( l \pm \frac{1}{2} \right). \tag{20}$$

The energy states of the shell model are presented in Table 4, whereas the association between the magic numbers and these states is illustrated in Figure 4. The model is never used to evaluate the mass of nuclei (the SEMF model is used for this purpose), but it is useful for classifying the energy levels of excited nuclei (denoted as  $({}^{N+Z}_Z X)^*$ ) and for determining the magic numbers.

**Table 4 Energy states in the shell model, where  $g$  is the degeneracy level of a state.**

$N$	0	1	2	2	3	3	4	4	4
$n$	1	1	1	2	1	2	1	2	3
$l$	0	1	2	0	3	1	4	2	0
$g$	2	6	10	2	14	6	16	10	2
orbital	1s	1p	1d	2s	1f	2p	1g	2d	3s

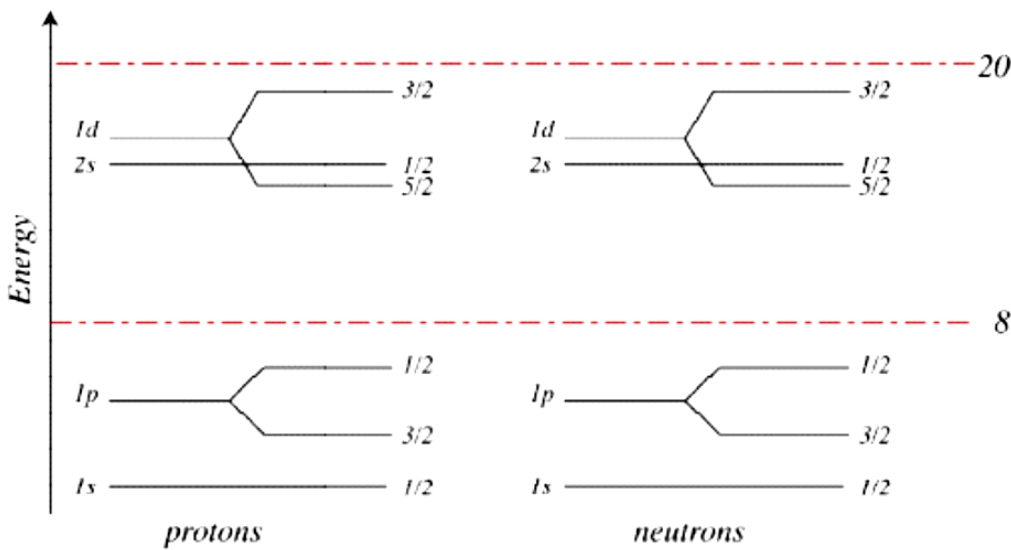


**Figure 4 Shell model and magic numbers.**

The second model that is often used is the collective model of the nucleus. Here, instead of looking at the motion of the individual nucleons, one considers the overall rotation and vibration movement of the nucleus. The justification for this model is that most nuclei take the shape of an ellipsoid (only nuclei that contain magic numbers of protons and neutrons are spherical). Distorted nuclei can then acquire rotational and vibrational motions, to which quantized energy levels can be associated. In classical mechanics, the energy of a rotating solid having a moment of inertia  $I$  and an angular momentum  $J$  is given by [Basdevant2005, Wong2004]:

$$E = \frac{J^2}{2I}, \tag{21}$$

In quantum mechanics, the angular momentum is quantized, with the energy levels being given by

$$E_J = \hbar^2 \frac{J(J+1)}{2I}, \quad (22)$$

with  $J = 0, 1, 2, \dots$ . For nucleus having an ellipsoid shape, only even values of  $J$  are allowed, and the energies satisfy the following relation:

$$E_2 = \frac{3}{10} E_4 = \frac{1}{17} E_6 = \frac{1}{12} E_8, \quad (23)$$

with

$$E_2 = \frac{15\hbar^2}{2MR^2}, \quad (24)$$

where  $M$  and  $R$  are respectively the mass and radius of the nucleus. These energy levels are generally much smaller than those associated with the shell model.

#### 64.2.2.6 Nuclear Fission and Fusion

Let us look back at Figure 2, where the average binding energy per nucleon is provided as a function of mass number. As mentioned previously, this curve indicates that the total binding of one heavy nuclide containing  $A > 180$  nucleons, which is given by

$$E_A = AB(A), \quad (25)$$

is larger than that of two identical nuclides containing  $A/2$  protons and neutrons:

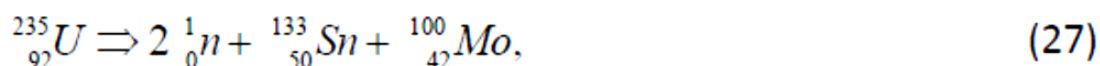
$$2E_{A/2} = AB\left(\frac{A}{2}\right) > E_A. \quad (26)$$

In physical terms, this means that two lighter nuclides generally represent a lower energy state than a heavier nucleus. Accordingly, a spontaneous reaction where the heavy nuclide,  $H$ , breaks down into

two smaller components ( $L_1$  and  $L_2$ ) is permitted from an energy-conservation point of view,

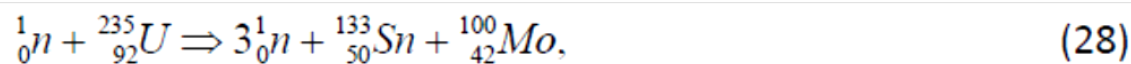
with the energy released by the reaction given by  $E_{L_1} + E_{L_2} - E_H$ .

This spontaneous reaction, called fission, has been observed experimentally for long-lived actinides such as  $^{232}\text{Th}$ ,  $^{235}\text{U}$ , and  $^{238}\text{U}$ , even through this is not their preferential decay mode (seven in  $10^9$  decays of  $^{235}\text{U}$  follow this path. For example, the spontaneous fission reaction



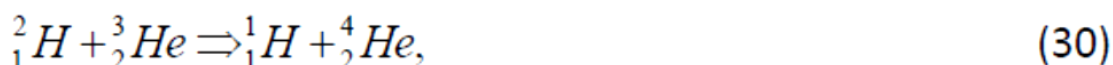
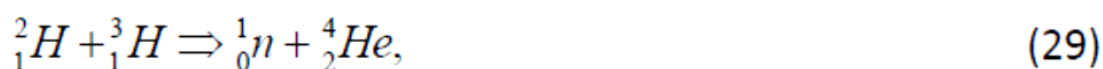
which releases 116 MeV, has been observed.

A second observation is that, even if a spontaneous fission reaction is very improbable, the fission process can be initiated externally by an absorption collision between a projectile and a heavy nuclide. For example, the neutron-induced reaction,



is possible even with very low-energy neutrons and produces the same amount of energy as the spontaneous fission reaction above. This reaction is facilitated by the fact that the main interaction between the neutron and a nucleus is the attractive nuclear force. The fact that several neutrons are generally produced following such reactions finally leads to the concept of a controlled chain reaction, if sufficient neutrons are produced following a fission reaction to initiate another fission reaction. The conditions required to achieve and maintain such a chain reaction are discussed in Section 4.

Figure 2 also indicates that the nucleons inside very light nuclides are loosely bonded compared to intermediate-mass nuclei. Combining two such nuclides could therefore result in a nucleus that is more strongly bonded, again releasing energy. This process is called nuclear fusion. Examples of such exothermal fusion reactions are



which release respectively 17.6 and 18.3 MeV in the form of kinetic energy for the final fusion products. Producing such reactions is much more difficult than neutron-induced fission because the two initial nuclides have positive charges and must overcome the Coulomb force to come into close contact. This can be achieved by providing sufficient kinetic energy (plasma temperature) for a sufficient long time (confinement) to ensure that the energy released by fusion is greater than the energy required to reach these conditions (the break-even point). The two main technologies that are currently able to attain the conditions necessary for controlled nuclear fusion are based respectively on confinement by magnetic fields (Tokamak) and inertial confinement (fusion by laser).

### 64.2.3 Nuclear Reactions

From the nuclear chart (**Figure 1**), it is clear that only 266 nuclides are stable. This means that most of the bonded nuclei that can be created will decay. This raises two questions:

- How do they decay?
- How are they created?

Another observation is that if one succeeds in creating a nucleus (stable or not), it may not necessarily be in its fundamental (ground) energy state (see Section 2.5). These are the main questions to answer in the first part of this section. We start by discussing the decay process before continuing with a description of nuclear reactions. The second topic involves the interaction of particles with matter, with most of these particles being produced during the decay process.

#### 64.2.3.1 Radioactivity and Nuclear Decay

Nuclear decay, the emission of radiation from an unstable nucleus or radioisotope, is a stochastic process controlled by the laws of statistics and physics. Therefore, it cannot take place unless several fundamental quantities are conserved [Basdevant2005, Smith2000]:

- total energy (including mass, which is a form of energy according to special relativity);

- linear momentum;
- angular momentum;
- electric charge;
- leptonic charge; and
- baryonic charge.

The latter two are required because of the intrinsic properties of quarks and leptons. For common nuclear reactions, these last two conservation relations can be translated to:

- conservation of electrons and neutrinos where the electron and the neutrino have a leptonic charge of +1 and the positron (anti-electron) and anti-neutrino have a leptonic charge of -1; and
- conservation of the total number of protons plus neutrons (mass number).

A decay process transforms, through emission of particles, a parent nucleus into a more stable daughter nucleus (a nucleus with a lower mass where the nucleons are more strongly bonded or equivalently have a lower mass). In fact, if one considers a nucleus at rest that decays according to the following reaction:



then total energy conservation implies that

$$m_{{}^A_Z X} c^2 = \left( m_{{}^B_W Y} c^2 + T_{{}^B_W Y} \right) + \sum_{i=1}^N \left( m_{{}^{C_i}_{V_i} b} c^2 + T_{{}^{C_i}_{V_i} b} \right), \quad (32)$$

where  $T$  is the kinetic energy of the different decay products. This reaction can take place spontaneously only if

$$T_{{}^B_W Y} + \sum_{i=1}^N T_{{}^{C_i}_{V_i} b} = m_{{}^A_Z X} c^2 - m_{{}^B_W Y} c^2 - \sum_{i=1}^N m_{{}^{C_i}_{V_i} b} c^2 > 0, \quad (33)$$

$$Z = W + \sum_{i=1}^N V_i, \quad (34)$$

$$A = B + \sum_{i=1}^N C_i, \quad (35)$$

that is, when the energy balance is favourable (the last two equations are for mass number and charge conservation). For a nucleus in an excited state, the daughter nucleus will often be the same as the parent nucleus, but at a different energy level (ground or lower-lying excited state), the secondary particle being a photon (a  $\gamma$ -ray because the photon is produced following a nuclear reaction).

Nuclear decay is characterized by a constant  $\lambda$  defined according to [Smith2000, Nikjoo2012]:

$$\lambda = \lim_{\Delta t \rightarrow 0} \frac{-\Delta N(t) / N(t)}{\Delta t}, \quad (36)$$

...

The most common decay reactions are the following:

$\gamma$ -ray emission for an excited nucleus:



Internal conversion for an excited nucleus:



This process corresponds to the direct ejection of an orbital electron leaving the nucleus in an ionized state ( $[{}_Z^A X]^+$ ).

$\beta^-$  decay (weak interaction) for a nucleus containing too many neutrons:



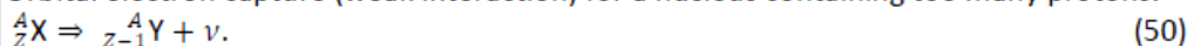
Neutron emission (nuclear interaction) for a nucleus having a very large neutron excess:



$\beta^+$  decay (weak interaction) for a nucleus containing too many protons:



Orbital electron capture (weak interaction) for a nucleus containing too many protons:



Proton emission (nuclear interaction) for a nucleus having a very large proton excess:



This process corresponds to the ejection of an atom of hydrogen.

$\alpha$ -emission for heavy nuclei (nuclear interaction):



This process corresponds to the ejection of an atom of helium.

Spontaneous fission for heavy nuclei (nuclear interaction):



This process corresponds to the fragmentation of a heavy nucleus into two or more smaller nuclei with the emission of several neutrons. For heavy or very unstable nuclei (see, for example, Figure 5 for uranium-238), several of these reactions must often take place before a stable isotope is reached.

The free Janis software from OECD-NEA can be used to retrieve and process the decay chain for all isotopes [OECD-NEA2013]<sup>62</sup>.

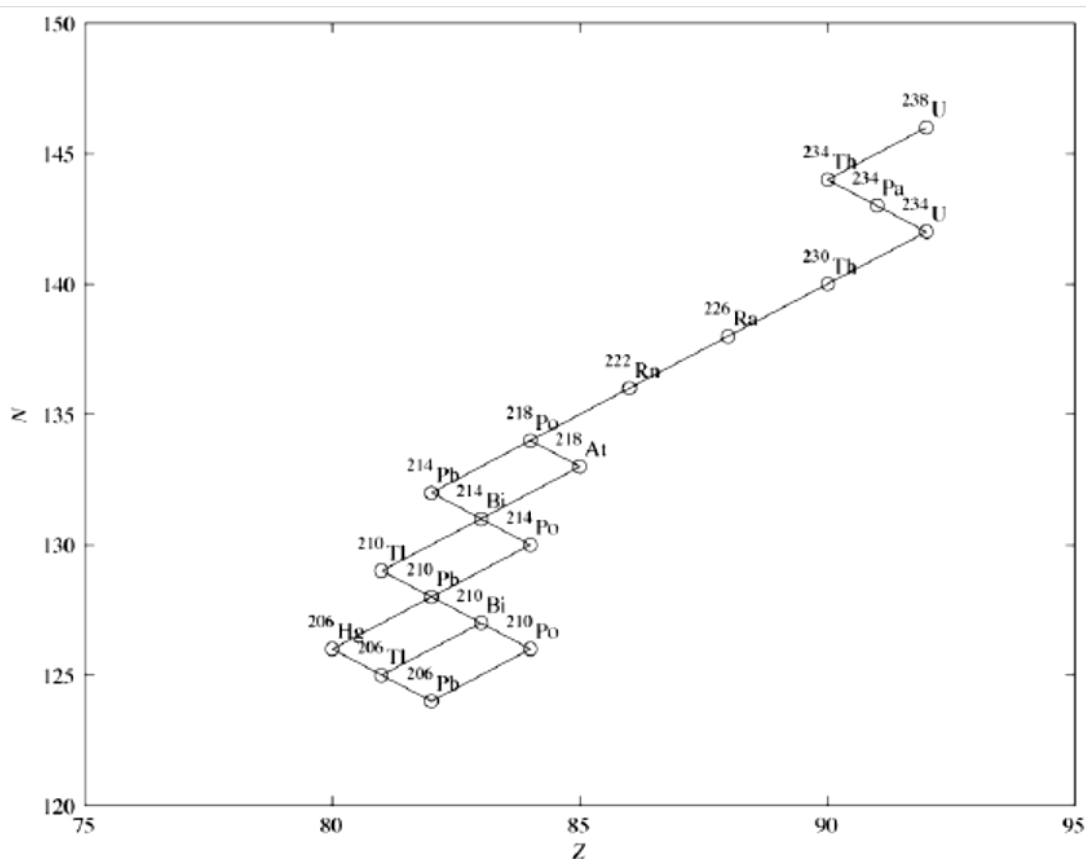


**Figure 5 Decay chain for uranium-238 (fission excluded). The type of reaction ( $\beta$  or  $\alpha$ -decay) can be identified by the changes in N and Z between the initial and final nuclides.**

### 64.2.3.2 Nuclear Reactions

As we saw in the previous section, several types of particles are produced through decay of radioactive nuclides. These particles have kinetic energy, and as they travel through matter, they interact with orbital electrons and nuclei. A nuclear reaction takes place if these particles produce after a collision one or more nuclei that are different from the original nucleus (an excited state of the original nucleus or a new nucleus). Otherwise, the collision gives rise to a simple scattering reaction where kinetic energy is conserved.

For the case where charged particles are traveling through a material, scattering collisions with the orbital electrons or the nucleus are mainly observed (also called potential scattering). More rarely, the charged particles are captured by the nucleus to form a compound nucleus (a very short-lived, semi-bonded nucleus) that can decay through various channels. Similarly, the electric and magnetic fields associated with the photons interact mostly with the nucleus or the orbital electrons. They can also

<sup>62</sup> [OECD-NEA2013] OECD-NEA Janis 3.0, Java-Based Nuclear Data Display Program. <https://www.oecd-nea.org/janis>, visited April 2013.

initiate nuclear reactions after being absorbed in the nucleus. Finally, neutrons rarely interact with electrons because they are neutral particles and the electrons are not affected by the nuclear force (electromagnetic interaction with the quarks inside the nucleon, magnetic interactions with unpaired electrons, and weak interactions are still present). However, they can be scattered (nuclear potential scattering) or absorbed (nuclear reaction) by the nucleus. Again, this absorption can lead to the formation

of a very unstable compound nucleus that will decay rapidly. The main nuclear reactions of photons, electrons, neutrons, and charged heavy particles with nuclei are often the inverses of the decay reactions presented earlier:

**$\gamma$  – ray absorption:**



**$\gamma$ -ray scattering (elastic and inelastic):**



**electron capture:**



**positron capture:**



**proton capture:**



**$\alpha$  capture:**



**neutron capture:**



**neutron scattering (elastic and inelastic):**



**photon-induced fission:**



**neutron-induced fission:**



These reactions must obey the same conservation laws as those described earlier for the decay reaction. For most reactions (except elastic scattering), the final nucleus will be in a

highly excited state and will decay rapidly by  $\gamma$ -ray emission (prompt photons).

The probability that any given reaction will take place between a nucleus and a particle is represented by the microscopic cross section  $\sigma$ .

Much like the decay constant, the cross sections have a quantum mechanical interpretation and can be expressed in terms of the wave function  $|i\rangle$  associated with the initial state (the product of the wave functions of the projectile and the nucleus), the wave function  $\langle f|$  associated with the final state, and  $H'$ , the interaction potential. The differential cross section is then given by Fermi's first golden rule, which can be written as:

$$\frac{d\sigma}{d\Xi} = \frac{2\pi V}{\hbar v_i} \langle f|H'|i\rangle^2 \rho(f), \quad (64)$$

where  $V$  is the volume of the system,  $v_i$  is the velocity of the projectile (assuming that the initial nucleus is at rest), and  $\rho(f)$  is again the density of states in the phase space  $\Xi$  for final particles. The cross section, which is then the integration over the final phase space of the differential cross section, has units of surface. The most common unit used for the microscopic cross section is the barn (b), with  $1 \text{ b} = 10^{-24} \text{ cm}^2 = 10^{-28} \text{ m}^2$ .

These cross sections are very difficult to evaluate explicitly because of the complexity of the wave functions (the wave function for a nucleus is the product of the wave functions of all the nucleons in the nucleus bonded by the nuclear potential) and the interaction potential. These are generally evaluated experimentally, and the results are stored in evaluated nuclear data files. A software package such as Janis can be used to retrieve and analyze these cross sections [OECD-NEA2013]. For computational reaction core physics, the NJOY program is generally used to process the cross-section databases for neutron-induced reactions [MacFarlane2010]<sup>63</sup>.

#### 64.2.3.3 Interactions of Charged Particles with Matter

As mentioned earlier, charged particles traveling through matter interact mainly with atomic electrons because they are much more numerous than nuclei ( $Z$  electrons for a nucleus with atomic number  $Z$ ) and also because the wave functions associated with these electrons have a very large spatial extension (the size of an atom) compared to that associated with the nucleus. Heavy particles, such as protons, alpha-particles, and ions, are scattered by the Coulomb potential produced by the electron, with the cross section given by the Mott scattering formula [Leroy2009, Bjorken1964]. As a result, a heavy particle loses a very small quantity of energy and momentum to secondary electrons and travels mainly in a straight line as it slows down. The secondary electrons, on the other hand, can gain enough energy to be knocked loose from the atom, leaving it in an ionized state.

For electrons and positrons traveling through matter, the problem is somewhat more complex. The cross section for electron-electron collisions is given by the Möeller scattering formula, while Bhabha

<sup>63</sup> R. E. MacFarlane, A. C. Kahler, "Methods for Processing ENDF/B-VII with NJOY", *Nuclear Data Sheets*, 111, 2739-2890, 2010.

scattering is used for positron-electron collisions [Leroy2009, Bjorken1964]. Positrons lose, on average, half their energy in collision with atomic electrons, and their trajectory is somewhat erratic. Positron-electron annihilation reactions can also take place, producing two gamma-rays. Finally, the electrons and positrons that are accelerated in the strong electromagnetic field of a heavy nucleus lose some of their energy by gamma-ray emission due to synchrotron radiation (also known as Bremsstrahlung) [Leroy2009, Bjorken1964].

One can approximate the energy loss of a particle of charge  $z$  and mass  $m$  inside a material of density  $\rho$ , atomic number  $Z$ , and atomic mass  $M$ , using the continuous slowing-down approximation (CSDA), where one assumes that the particle is interacting constantly with an electron gas of density  $n$  given by

$$n = Z \frac{\rho}{M} N_A. \quad (65)$$

The energy loss per unit distance traveled by the particle inside the material ( $-dE/dx$ ), known as the stopping power, is then given by the Bethe-Block formula [Smith2000, Leroy2009]:

$$\left( -\frac{dE}{dx} \right)_{\text{collision}} = 4\pi n \frac{(z\alpha_e \hbar c)^2}{mv^2} (L(v) - F(v)), \quad (66)$$

where  $v$  is the speed of the particle and  $L(v)$  the stopping number, which can be written as

$$L = \ln \left( \frac{2mv^2}{I(1 - (v/c)^2)} \right) - (v/c)^2, \quad (67)$$

where  $I$  is the mean excitation potential for the atomic electrons in this material. The correction term,  $F(v)$ , takes into account the fact that the atomic electrons are bonded as well as

other quantum effects. For electrons, one must also consider the energy lost by synchrotron radiation, which is given approximately by [Leroy2009]:

$$\left( -\frac{dE}{dx} \right)_{\text{radiation}} \approx Zn \frac{\alpha_e^3 \hbar^2}{m_e}, \quad (68)$$

where  $m_e$  is the mass of the electron. Here, it is assumed that the kinetic energy of the electrons  $T_e \ll m_e c^2$ .

For heavy particles (protons,  $\alpha$ -particles), nuclear slowing-down,  $(-dE/dx)_{\text{nuclear}}$ , becomes important when they reach a low energy.

The CSDA range  $R$  of a particle is defined as the distance (path of flight) that it must travel to lose all its kinetic energy. It is computed as

$$R = \int_0^T \frac{1}{\left( -\frac{dE}{dx} \right)_{\text{total}}} dE, \quad (69)$$

where  $T$  is the initial kinetic energy of the particle and

$$\left(-\frac{dE}{dx}\right)_{total} = \left(-\frac{dE}{dx}\right)_{collision} + \left(-\frac{dE}{dx}\right)_{radiation} + \left(-\frac{dE}{dx}\right)_{nuclear}. \quad (70)$$

These CSDA expressions are helpful to understand the general behaviour of particles slowing down in a material. However, for practical applications, tabulated values for  $-dE/dx$  and  $R$  are more useful.

This type of information for electrons, protons, and alpha-particles can be found on-line for various elements and different material compositions on the National Institute of Standard and Technology Web sites [Berger2013a]. The databases available are:

- ESTAR, for electrons;
- PSTAR, for protons;
- ASTAR, for alpha-particles.

For heavy particles, this site also provides information on nuclear stopping power. Also note that the stopping power and range are defined in a somewhat different way from the notation above. The following expressions are used instead:

$$-dE/dx(\text{MeV} \times \text{cm}^2/\text{g}) = -\frac{1}{\rho} dE/dx(\text{MeV}/\text{cm}) \quad (71)$$

and

$$R(\text{g}/\text{cm}^2) = \rho R(\text{cm}) \quad (72)$$

because these are the conventional units used in radiation shielding studies. Note that the number of electron/ion pairs produced per unit distance in a material is given approximately by

$$\frac{dn_{pairs}}{dx} = \frac{1}{W} \left(-\frac{dE}{dx}\right)_{total}, \quad (73)$$

where  $W$  is the average energy required to ionize an atom in this material.

#### 64.2.3.4 Interactions of Photons with Matter

The behaviour of photons as they travel in a material is somewhat different from that of charged particles, which lose their kinetic energy mainly by continuously interacting with electrons and nuclei, the Coulomb field being a long-range force. The photon is the quantum particle that carries the

energy  $E = h\nu$  and momentum  $\vec{p} = \vec{n}h/\lambda$  of an electromagnetic field of frequency  $\nu$

and wavelength  $\lambda = c/\nu$  travelling in direction  $\vec{n}$ . Depending on its wavelength, the photon behaves as a wave (diffraction and interference for low-energy photons) or as a particle (photoelectric effect for high-energy photons) when it interacts with matter.

Here, we will consider only the interactions with matter of the relatively high-energy photons ( $E > 1\text{keV}$ ) as found in nuclear reaction cores. In this case, the photon behaves as a particle that is first absorbed by the atomic electrons of the nucleus. Following this absorption, secondary particles are

produced, including photons (scattering reactions), electrons and positrons (pair creation), and neutrons (photonuclear reaction).

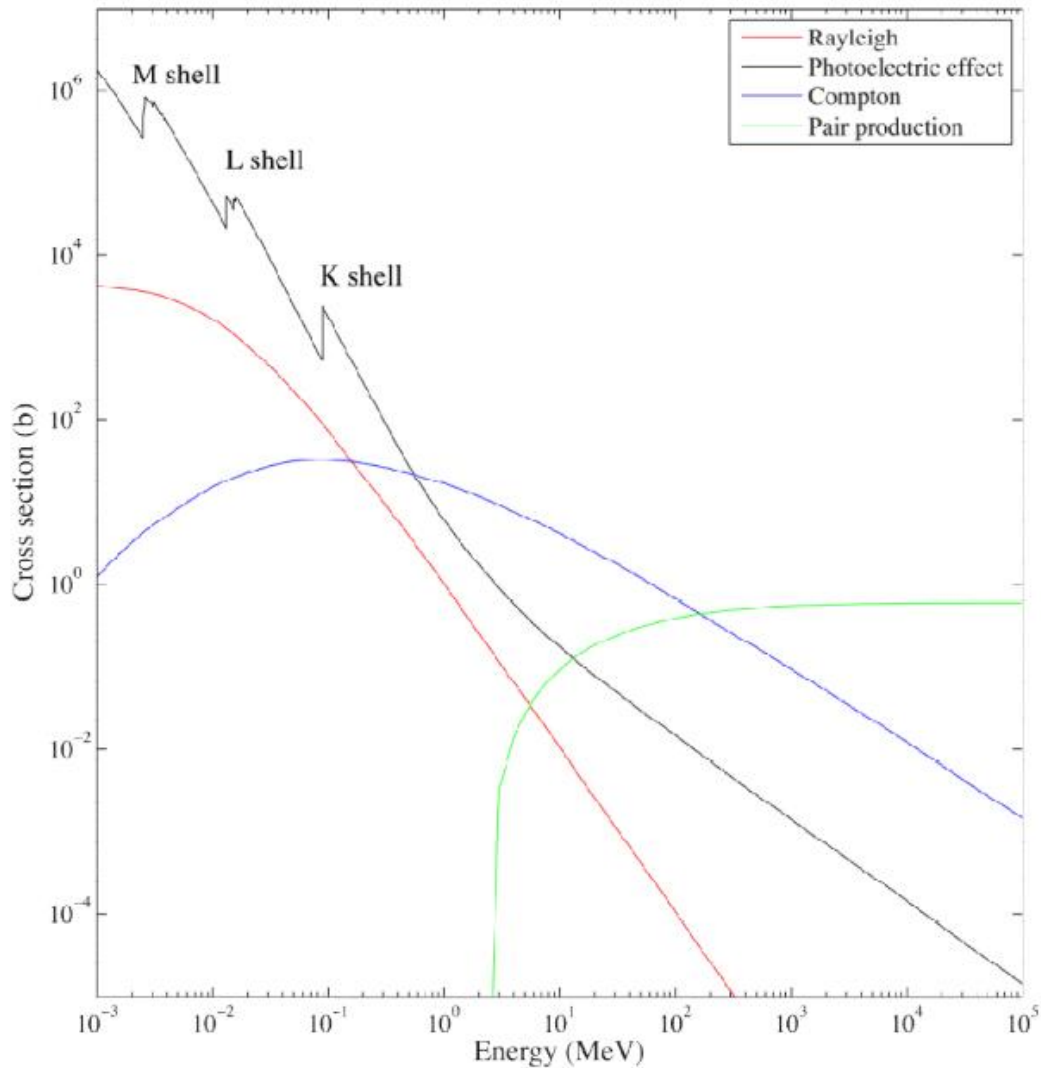


**Figure 6 Microscopic cross section of the interaction of a high-energy photon with a lead atom**

The five main reactions taking place between high-energy photons and matter that are of interest in nuclear reaction core-related studies are:

- Photoelectric effect;
- Rayleigh scattering;
- Compton scattering;
- Pair production; and
- Photonuclear reactions.

With each such reaction is associated a macroscopic cross section  $\Sigma_{m,x}(E)$  representing the probability per unit distance travelled by a photon of energy  $E$  that an interaction of type  $x$  has taken place in material  $m$ . The macroscopic cross section takes into account the probabilities of interaction both between single photons and between particles and the fact that the material contains  $N_{m,i}$  particles of type  $i$  per unit volume:

$$\Sigma_{m,x}(E) = \sum N_{m,i} \sigma_{i,x}(E), \tag{74}$$

where  $\sigma_{i,x}(E)$  is the microscopic cross section of the interaction of a photon of energy  $E$  with a particle of type  $i$  through reaction  $x$  (see Section 3.2). The total microscopic photon cross section can be expressed as:

$$\sigma(E) = \sigma_{\text{Photoelectric}}(E) + \sigma_{\text{Rayleigh}}(E) + \sigma_{\text{Compton}}(E) + \sigma_{\text{Pair production}}(E) + \sigma_{\text{Photonuclear}}(E). \quad (75)$$

Examples of microscopic cross sections for the interaction of photons with a lead atom are presented in Figure 6. Let us now describe in detail the five reactions contributing to  $\sigma(E)$  and discuss their respective dependences on the energy of the incident photon.

**Photoelectric effect**

This effect is illustrated in Figure 7. A photon with an energy  $E = h\nu$  that is greater than the binding energy  $W$  of atomic electrons around the nucleus is absorbed. Following the absorption, the electron becomes free, leaving behind an ion. The energy balance for this reaction is

$$T_e + T_N = E - W, \quad (76)$$

where  $T_e$  is the kinetic energy of the final electron and  $T_N$  that of the recoil nucleus (general very small compared with  $T_e$ ).

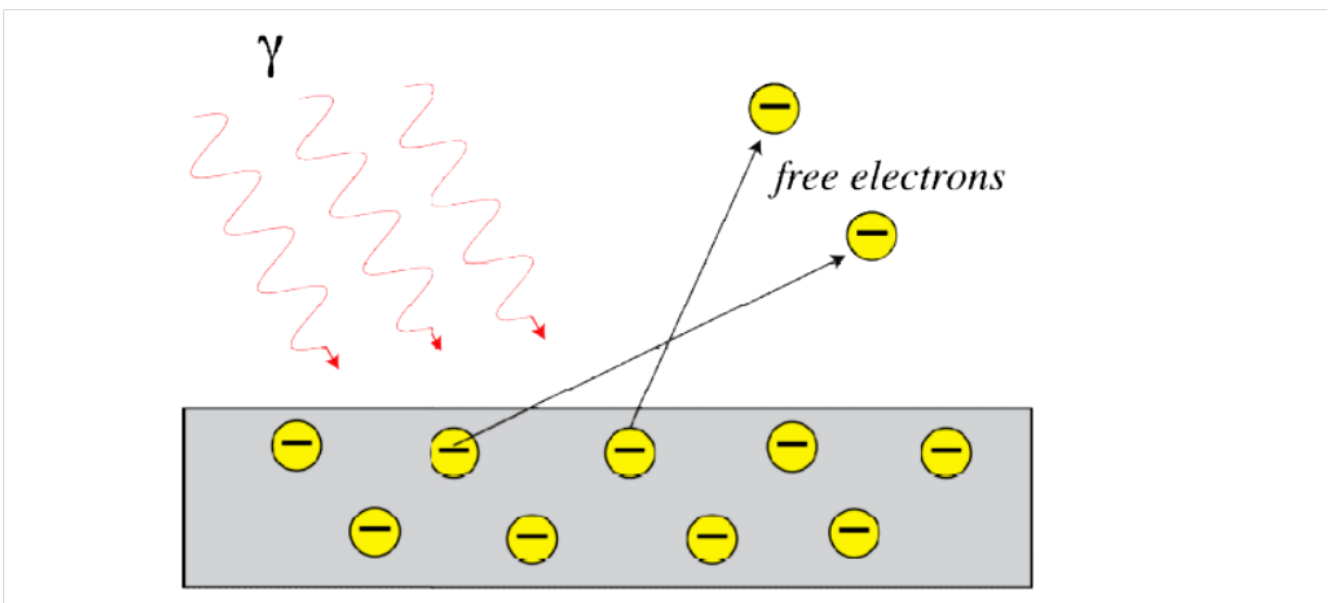


Figure 7 Photoelectric effect

From quantum mechanics, the binding energy of electrons around a nucleus of charge  $Ze$  can be approximated using [Griffiths2005]:

$$W_n = \frac{13.61 Z^2}{n^2} eV, \quad (77)$$

[...]

Several processes can take place after this reaction. If the electron ejected from the atom was initially in the valence band, the ionized atom is in its ground state, and no further radiation emission is observed. When electrons coming from more tightly bonded energy levels are ejected, the ionized atom is left in an excited state. This excited ion can then decay to its ground state by two different

means. First, an electron in a much higher energy state (i.e., a valence electron) can emit a photon and fill the vacant energy level, leaving the ion in a less excited state that will further decay before reaching its ground state. When the photons emitted in these successive decays are absorbed by less-bonded electrons, so-called soft Auger electrons are ejected from the atom, producing an Auger electron cascade.

### Raleigh scattering

This **elastic scattering reaction** takes place when a photon, after being absorbed by a bound atomic electron, is re-emitted with the same energy, but in a different direction, by the electron, returning the atom to its original state [Leroy2009, Jauch1976]. The cross section for this reaction is very difficult to evaluate because it depends strongly on the wave function of the bonded electrons surrounding the nucleus. It is generally written as an integral of the form

$$\sigma_{\text{Rayleigh}}(E) = \pi \left( \frac{\alpha_e \hbar c}{m_e c^2} \right)^2 \int_0^\pi (1 + \cos^2(\theta)) [F(E, \theta, Z)]^2 \sin(\theta) d\theta, \quad (80)$$

where  $F(E, \theta, Z)$  is the atomic form factor that represents the effect of the  $Z$  electrons surrounding the nucleus on the scattering of a photon at an angle  $\theta$  with respect to the initial

photon direction. Several theoretical expressions for  $F(E, \theta, Z)$  are available in the literature for different values of  $Z$  and various energy ranges. For example, when the photon energy is greater than 100 keV, the main contributors to Rayleigh scattering are the electrons in the Kshell, and the relativistic Bethe-Levinger form factor is used [Hubbell1975]:

$$F(E, \theta, Z) = \frac{\sin(2\gamma \arctan(Q))}{\gamma Q(1+Q^2)^\gamma}, \quad (81)$$

with

$$Q(E, \theta, Z) = \frac{2E \sin(\theta/2)}{\alpha_e Z m_e c^2}, \quad (82)$$

$$\gamma(Z) = \sqrt{1 + (\alpha_e Z)^2}. \quad (83)$$

Because Rayleigh scattering is never the dominant photon reaction (see Figure 6) for the photon energy range considered in nuclear reaction cores, its contribution to the total cross section is often neglected.

### Compton scattering

The Compton effect is the **incoherent inelastic scattering** of a photon by an electron that is weakly bonded to a nucleus (see Figure 8).

[...]

This cross section decreases with energy, but much more slowly than for the photoelectric effect. It dominates the photoelectric reaction for energies above approximately 0.5 MeV.

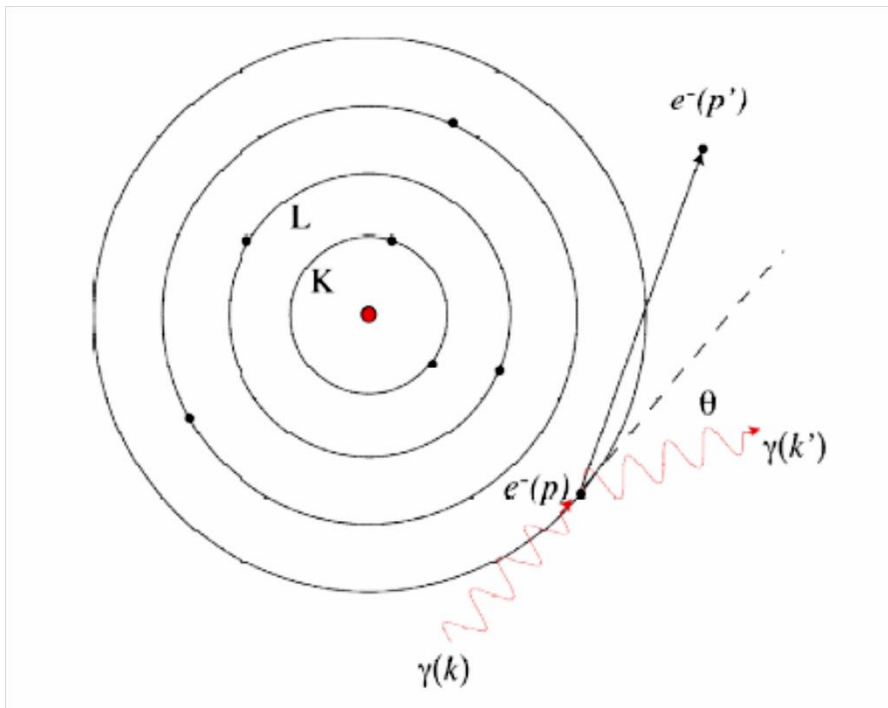


Figure 8 Compton effect

### Pair production

A photon with energy  $E = h\nu > 2m_e c^2$  traveling through the Coulomb field of a nucleus of charge  $Z$  (or an electron) can be converted into an electron-positron pair. After the reaction, the nucleus carries a small part of the kinetic energy of the photon, with the bulk of the energy being transferred in the form of mass and kinetic energy to the pair.

for  $E > 1$  keV

$$\sigma_{\text{Pair production}}(E) \approx \alpha_e Z^2 \left( \frac{\alpha_e \hbar c}{m_e c^2} \right)^2 \left[ \frac{28}{9} \ln(2\varepsilon) - \frac{218}{17} + \frac{129}{20\varepsilon} \right], \quad (86)$$

### Photonuclear reactions

Photonuclear reactions are the result of photons being absorbed by a nucleus to form an excited nucleus, which gets rid of its energy through different decay processes, namely the emission of a secondary photon, the ejection of one or more nucleons (proton and neutrons), the ejection of alpha-particles, or through a fission reaction. Photonuclear reactions occur only above a threshold, which lies between 7 and 9 MeV for heavy nuclides, but is considerably lower for very light isotopes (1.666 MeV and 2.226 MeV respectively for beryllium and deuterium). The absorption cross section for these reactions (see Figure 9) are generally very difficult to evaluate, and only approximate expressions are available.

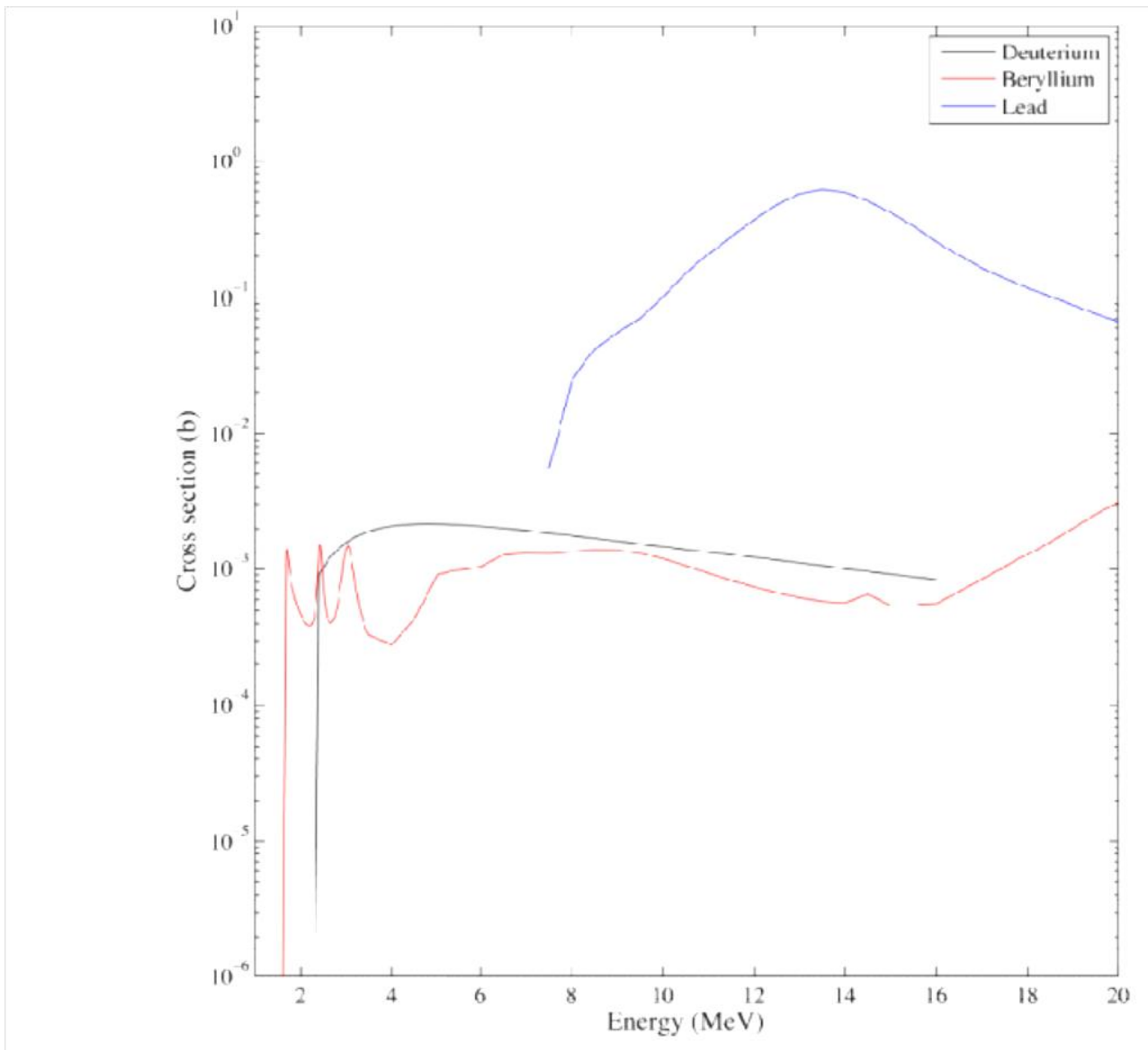


**Figure 9 Photonuclear cross-sections for deuterium, beryllium, and lead.**

For deuterium, which is important to some reaction cores because they use large amounts of heavy water, the expression [Leroy2009]

$$\sigma_{{}^2\text{D,Photonuclear}}(E) \approx C_{{}^2\text{D}} \frac{(\sqrt{E - 2.226})^3}{E^3} \quad (87)$$

is often used, where  $E$ , the photon energy, is given in MeV,  $C_{{}^2\text{D}}$  varies between 0.061 and 0.0624 and  $\sigma_{\text{D}}(E)$  is in barns. The end result of such a photonuclear reaction is a hydrogen atom and a fast neutron that can initiate a fission reaction (see Section 2.6).

Tabulated values for Rayleigh scattering (coherent scattering), photoelectric effect, Compton scattering (incoherent scattering), and pair production cross sections with different atoms or materials and for energies ranging from 1 keV to 100 GeV are available on-line on the Web site of the National Institute of Standards and Technology (NIST) [Berger2013b]. For photonuclear reactions, the energy-dependent cross sections for various isotopes can be obtained using the OECS-NEA Janis OECD-NEA Janis software [OECD-NEA2013].

For each reaction presented above, the photons first transfer all their energy to an electron or a nucleus following a collision. As a result, starting with  $n(E, \vec{r}, \vec{\Omega})$  photons of energy E and

direction  $\vec{\Omega}$  incident at point  $\vec{r}$  on a material of uniform macroscopic cross section  $\Sigma(E)$ , the number of initial photons  $n(E, \vec{r} + s\vec{\Omega}, \vec{\Omega})$  still present after a distance  $s$  has been crossed is given by [Basdevant2005]:

$$n(E, \vec{r} + s\vec{\Omega}, \vec{\Omega}) = n(E, \vec{r}, \vec{\Omega}) e^{-\Sigma(E)s}. \quad (88)$$

The number of photons therefore decreases exponentially with distance. This behaviour is similar to what is observed when light is attenuated by passing through a material with a linear attenuation coefficient  $\mu(E) = \Sigma(E)$ . Secondary photons produced with energy E and direction  $\vec{\Omega}$  following the absorption of photons of energy E' and direction produces a photon of energy E and direction  $\vec{\Omega}$ .

### 64.2.3.5 Interactions of Neutrons with Matter

Neutron interaction with matter is the result of the nuclear force, although weak and electromagnetic interactions, the latter being the result of anomalous magnetic moment, are also possible. As a result, only neutron-nucleus interactions are generally considered, including

- elastic potential scattering with cross section  $\sigma_{\text{elastic}}$ ;
- inelastic scattering with cross section  $\sigma_{\text{inelastic}}$ ;
- neutron absorption with cross section  $\sigma_{\text{absorption}}$ ; and
- spallation reactions,  $\sigma_{\text{spallation}}$ .

In the first three reactions, the neutron interacts with the nucleus as a whole. In spallation reactions, the neutrons interact directly with the nucleons in the nucleus. The latter reaction can take place only

when the energy of the incident neutron  $E_{n,i}$  is sufficiently high (threshold reactions with  $E_{n,i} > 0.1$  MeV), and therefore  $\sigma_{\text{spallation}}$  is either neglected, because it is too small, or simply included in the absorption cross section. The probability that the neutron interacts with a nucleus is then given by the total cross section,  $\sigma$ , where

$$\sigma(E_{n,i}) = \sigma_{\text{absorption}}(E_{n,i}) + \sigma_{\text{scattering}}(E_{n,i}), \quad (90)$$

$$\sigma_{\text{scattering}}(E_{n,i}) = \sigma_{\text{elastic}}(E_{n,i}) + \sigma_{\text{inelastic}}(E_{n,i}). \quad (91)$$

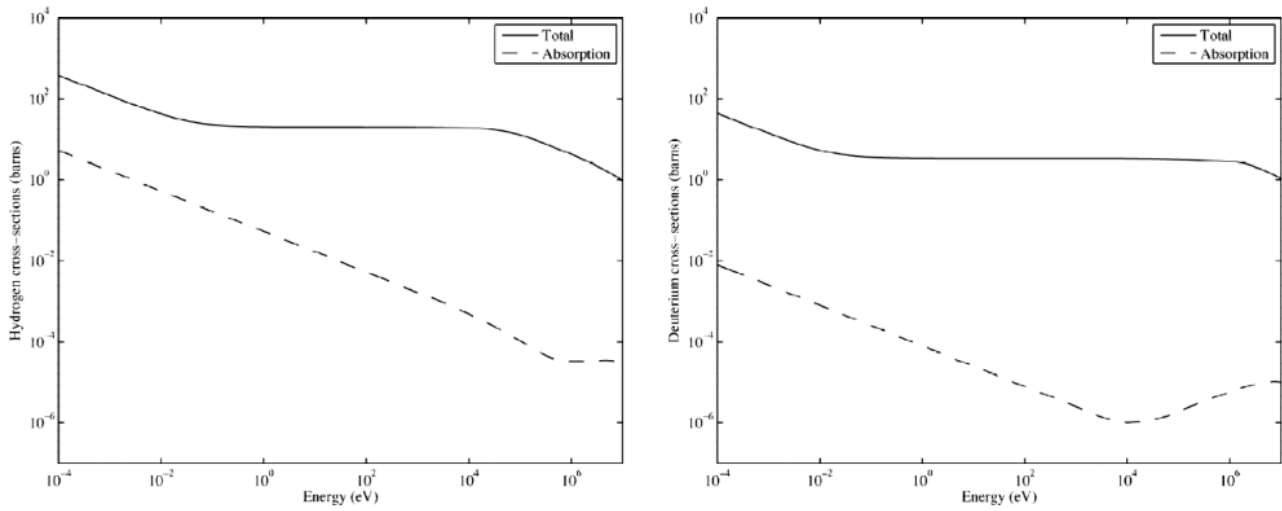


**Figure 10 Cross sections for hydrogen (left) and deuterium (right) as functions of energy.**

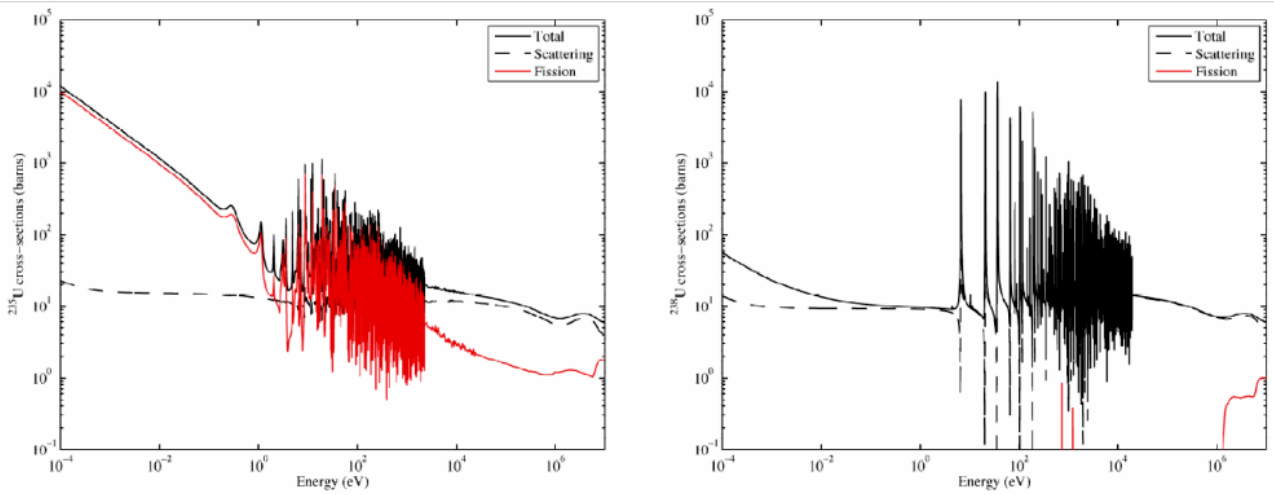


**Figure 11 Cross sections for  $^{235}_{92}\text{U}$  (left) and  $^{238}_{92}\text{U}$  (right) as functions of energy.**

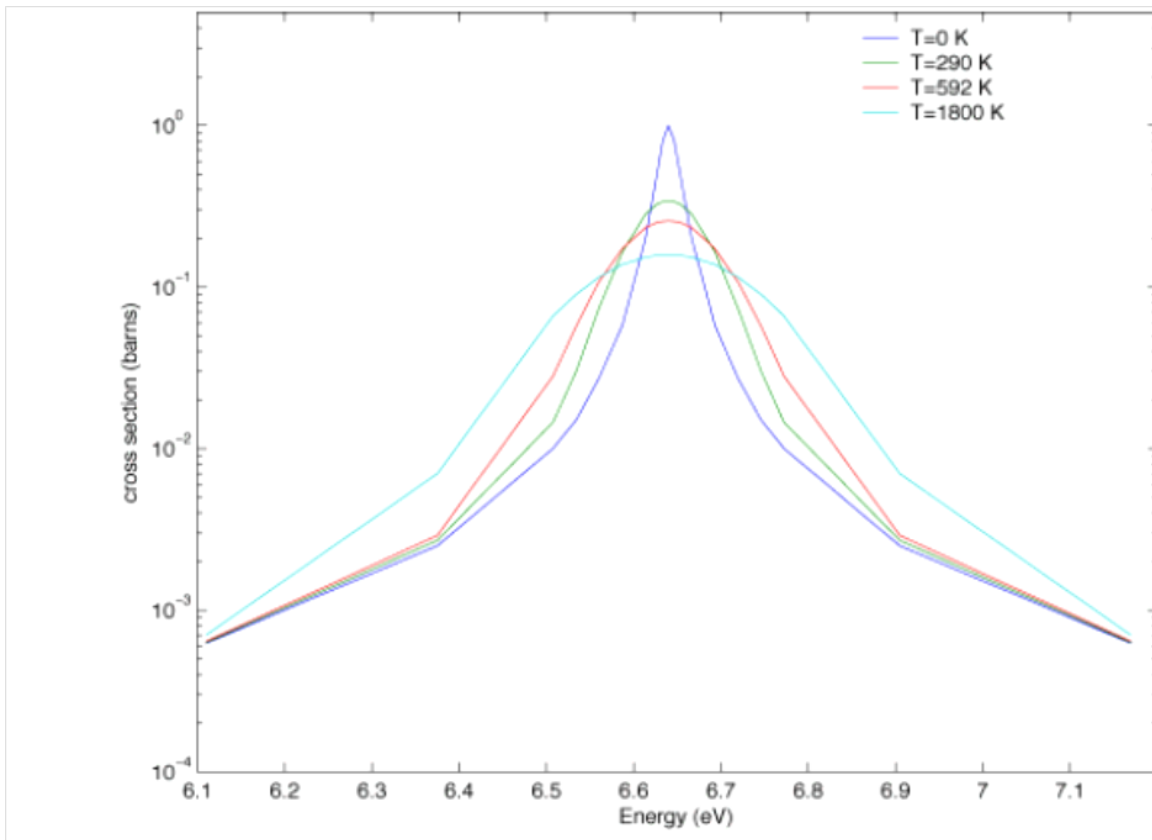


**Figure 12 Effect of temperature on  $U^{238}$  absorption cross section around the 6.64-eV resonance.**

The neutron-nucleus interaction cross sections are very complex and in most cases are evaluated using a combination of theory and experiment. They are generally tabulated in evaluated nuclear data files that can be read by nuclear calculation software (NJOY, for example) [MacFarlane2010]. They can also be extracted on-line from nuclear databases or off-line using the Janis software [KAERI2013, Livermore2013, OECD-NEA2013].

Once the energy-dependent cross sections are known, one can easily evaluate the number of reactions of type  $x$  per second (the reaction rate  $R_{m,x}(v)$ ) taking place inside a region of volume  $V$  containing  $N_m$  nuclei per  $\text{cm}^3$  of a material  $m$  (cross section  $\sigma_{m,x}(v)$ ) with a population of  $n(v)$  neutrons per  $\text{cm}^3$  having a velocity  $v = \sqrt{2E_n/m}$ :

$$R_{m,x}(v) = V \frac{N_m \sigma_{m,x}(v) n(v)}{v} = V \Sigma_{m,x}(v) \phi(v), \quad (108)$$

where  $\phi(v) = n(v)/v$  is the neutron flux and  $\Sigma_{m,x}(v) = N_m \sigma_{m,x}(v)$  the macroscopic cross section for a reaction of type  $x$  in this material.

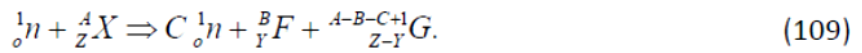
#### 64.2.4 Fission and Nuclear Chain Reaction

The concept of controlled energy production in a nuclear reaction core is based on three fundamental ideas that were discussed in Sections 2.6, 3.1, and 3.2, namely:

- energy is released if a heavy nucleus is fragmented into lighter nuclei, the fragmentation process being called nuclear fission;
- the spontaneous nuclear fission process, which has a very low yield for several heavy nuclei, generates neutrons in addition to the light nuclei as end products;

- the nuclear fission process can be initiated by neutrons and photons.

Accordingly, a neutron of kinetic energy  $T_n$  travelling through a medium containing heavy nuclei at rest could initiate a fission reaction:



The kinetic energy  $T_R$  released by this reaction is then

$$T_R = T_n + (1 - C)m_n c^2 + m_{{}_Z^AX} c^2 - m_{{}_Y^BF} c^2 - m_{{}_{Z-Y}^{A-B-C+1}G} c^2, \tag{110}$$

### 64.2.4.1 Fission Cross Sections

**Table 5 Comparison of the energy,  $U$ , required for a fission reaction in a compound nucleus with the energy,  $Q$ , available after a neutron collision with different isotopes.**

Isotope	$Q$ (MeV)	$U$ (MeV)
${}_{90}^{232}\text{Th}$	5.1	5.9
${}_{92}^{233}\text{U}$	6.6	5.5
${}_{92}^{235}\text{U}$	6.4	5.8
${}_{92}^{238}\text{U}$	4.9	5.9
${}_{94}^{239}\text{Pu}$	6.4	5.5

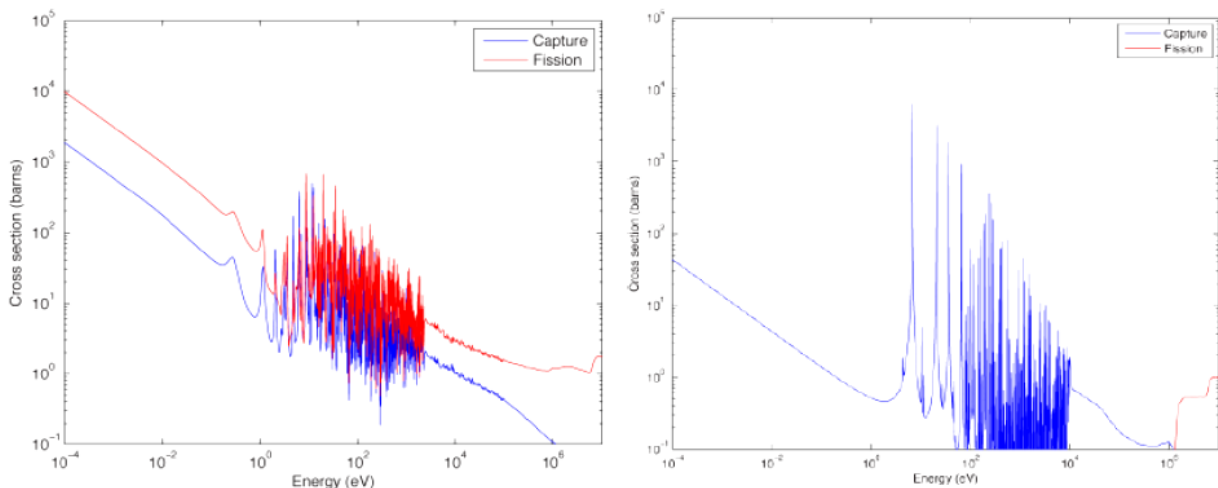


**Figure 13 Capture and fission cross sections of  ${}_{92}^{235}\text{U}$  (left) and  ${}_{92}^{238}\text{U}$  (right) as functions of energy.**

### 64.2.4.2 Fission Products and the Fission Process

The fission process generally produces two light nuclei, called fission products, although three or more nuclei can also be generated. The relative rate of production of a given nuclide  $I$ , called the fission yield, is denoted by  $Y_I$  and satisfies

$$\sum_I Y_I = 2. \quad (111)$$

assuming that only two nuclei are produced by each fission reaction. As one can see in **Figure 14**, where the fission yields of all the nuclei resulting from the fission of  ${}^{235}_{92}\text{U}$  are plotted as a function of their mass number, the fission process favours the production of relatively light nuclides ( $90 < A < 105$ ) combined with heavier isotopes ( $130 < A < 145$ ).

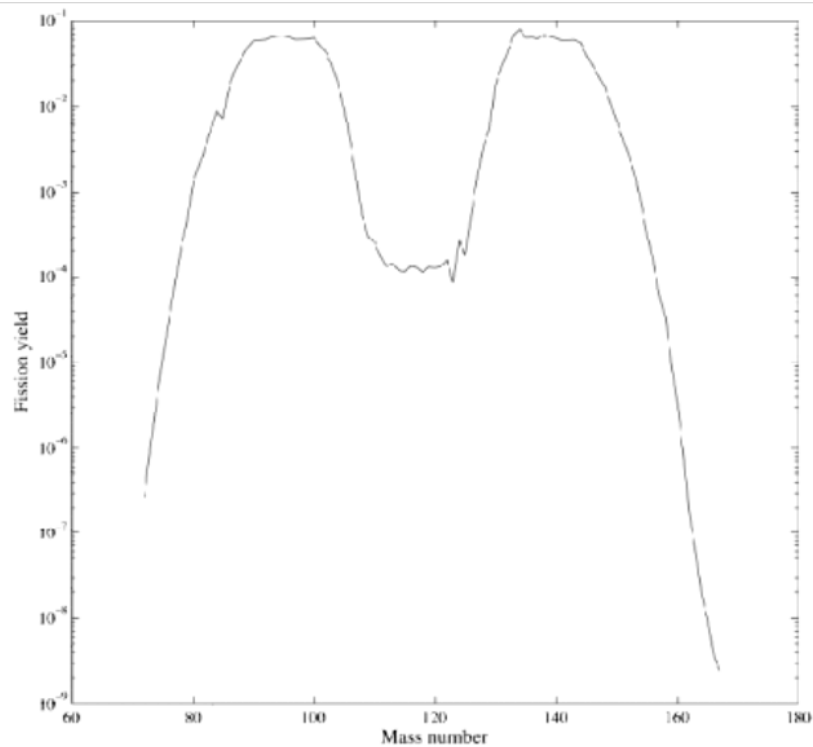


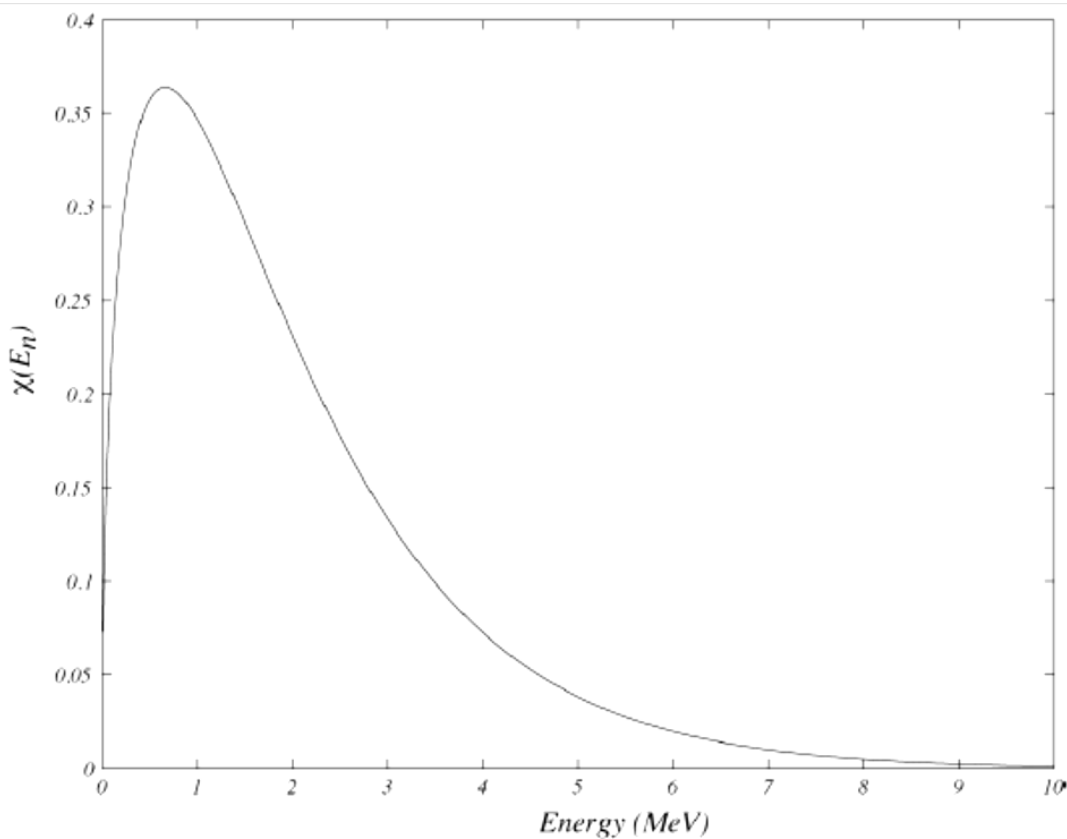
**Figure 14** Relative fission yield for  ${}^{235}_{92}\text{U}$  as a function of mass number.

**Table 6** Average numbers of neutrons produced by the fission of common heavy nuclides.

Isotope	$\nu(E_n < 1 \text{ eV})$	$\nu(E_n > 1 \text{ MeV})$
${}^{232}_{90}\text{Th}$	0	2.2
${}^{233}_{92}\text{U}$	2.50	2.6
${}^{235}_{92}\text{U}$	2.43	2.6
${}^{238}_{92}\text{U}$	0	2.6
${}^{239}_{94}\text{Pu}$	2.89	3.1

**Table 7 Distribution of kinetic energy among the particles produced by a fission reaction.**

Particles	Kinetic energy (MeV)
Fission products	168
Prompt $\gamma$ -rays	7
Delayed $\gamma$ -rays	7
Electrons	8
Neutrinos	12
Neutrons	7
Total	207

**Figure 15 Fission spectrum for  $^{235}_{92}\text{U}$ .**

Finally, we must address the problem of the changes in the composition of a material exposed to a neutron flux. In Section 3.1, we introduced the Bateman equation, which takes the form [Smith2000, Nikjoo2012, Magill2005]:

$$\frac{dN_I(t)}{dt} = -\lambda_I N_I(t) - L_I(t) + P_I(t), \quad (115)$$

where  $\phi(E)$  is the neutron flux. The production term has two contributions: decay from other nuclei, and transformation of a different nucleus into  $I$  following a neutron-induced nuclear reaction:

$$P_I(t) = \sum_J Y_{J,I}^d \lambda_J N_J(t) + \sum_J \sum_x Y_{J,I}^x N_J(t) \int_0^\infty \sigma_{J,x}(E) \phi(E) dE, \quad (117)$$

where  $Y_{J,I}^d$  is the yield for the production of isotope  $I$  from the decay of isotope  $J$ , while  $Y_{J,I}^x$  is the isotope  $I$  production yield from a reaction of type  $x$  (fission, capture, etc.) between a neutron and isotope  $J$ .

#### 64.2.4.3 Nuclear Chain Reaction and Nuclear Fission Reaction cores

The previous sections have introduced all the concepts required to design a conceptual nuclear fission reaction core:

- The nuclear fuel contains heavy isotopes that are broken into lighter nuclides (fission products) following a neutron-induced fission reaction. Such a reaction also generates energy and secondary neutrons that can be used to maintain a chain reaction.
- Most of the energy released as a result of the fission process is carried away by the fission products and deposited in the fuel from nuclear energy generating devices because of the short range of these nuclei.
- The secondary neutrons produced in the fission process are fast neutrons.
- These neutrons can lose their energy through scattering collisions with the various materials present in our conceptual reaction core. Neutron slowing-down by collisions with light isotopes is more efficient than by collision with heavy isotopes (see Section 3.5).
- This energy deposition increases the temperature of the fuel, which must then be cooled to make use of the heat and avoid damage to the reaction core. For a power reaction core, this heat is collected in a coolant (generally gas or liquids circulating around the fuel) and used to generate electricity. Now let us look at the fuel and coolant materials that are the most readily available.

Three heavy fissionable isotopes are present in nature:  ${}_{90}^{232}\text{Th}$ ,  ${}_{92}^{238}\text{U}$ , and  ${}_{92}^{235}\text{U}$ . Of these, only  ${}_{92}^{235}\text{U}$  is fissile by neutrons of all energies. Because the density of thorium is  $11,000 \text{ kg/m}^3$  and it has a microscopic fission cross section of 0.1 barn for 1 MeV neutrons, the mean free path of a neutron for fission in this material is 3.5 m. The mean free path for neutron capture in thorium is very similar in magnitude. Therefore, nearly half the 2.2 neutrons emitted by fission in thorium will be lost to unproductive capture. For  ${}_{92}^{238}\text{U}$ , which represents 99.27% of all the atoms found in natural uranium (density of  $18,000 \text{ kg/m}^3$ ), the odds are slightly better, with mean free paths for fission and capture respectively of 50 and 300 cm and fewer neutrons emitted per fission are lost to capture.

The main advantage of  ${}_{92}^{235}\text{U}$ , even though it represents only 0.72% of natural uranium composition, is that its fission cross section is quite high (1000 barns at 0.01 eV), giving a mean free path for fission of 2 cm. The capture cross section of  ${}_{92}^{235}\text{U}$  at this energy is also six times smaller than the fission cross section. It is possible to decrease the mean free path for fission with  ${}_{92}^{235}\text{U}$  by increasing its relative concentration in uranium-based fuel (fuel enrichment). The ratio of capture to fission in uranium-enriched fuels remains small even if the fuel contains a large amount of  ${}_{92}^{238}\text{U}$  (capture cross section less than 1 barn).

The heat produced in the fuel can then easily be extracted by conventional means (by circulating

a fluid such as water). The main problem is to slow down the secondary fission neutrons to low energies ( $< 1$  eV) while ensuring that few are lost by capture inside other materials or by leaving the reaction core. A neutron slowing-down material, the moderator, must therefore be introduced into the reaction core to serve this purpose.

**Table 8 Maximum values of the elastic scattering and absorption cross sections for  $^1_1\text{H}$ ,  $^2_1\text{D}$ , and  $^{12}_6\text{C}$  in the energy range  $0.1 \text{ eV} < E < 0.1 \text{ MeV}$ .**

Isotope	$\sigma_{\text{scattering}}$ (b)	$\sigma_{\text{absorption}}$ (b)
$^1_1\text{H}$	18	0.17
$^2_1\text{D}$	3.4	0.00025
$^{12}_6\text{C}$	4.6	0.0016

#### 64.2.4.4 Reaction core Physics and the Transport Equation

When designing a nuclear power reaction core, physicists have two main objectives:

- controlling the nuclear chain reaction;
- extracting the energy produced inside the fuel to avoid damage to the core and to use this energy to produce electricity.

Because most of the energy produced in a nuclear reaction core is the result of the fission process, the power produced in the core can be expressed by:

$$P(t) = \int_V d^3r \int_0^\infty dE \sum_J \kappa_J \Sigma_{f,J}(\vec{r}, t, E) \int_{4\pi} \phi(\vec{r}, t, E, \vec{\Omega}) d^2\Omega, \quad (118)$$

where  $V$  is the reactor volume,  $\phi(\vec{r}, t, E, \vec{\Omega})$  is the flux of neutrons with energy  $E$  and direction  $\vec{\Omega}$  at a point  $\vec{r}$  in space and a time  $t$ , and  $\Sigma_{f,J}(\vec{r}, t, E)$  is the macroscopic fission cross section for isotope  $J$  given by

$$\Sigma_{f,J}(\vec{r}, t, E) = N_J(\vec{r}, t) \sigma_{f,J}(E), \quad (119)$$

where  $N_J(\vec{r}, t)$  is the time-dependent concentration of  $J$ , the solution of the flux-dependent Bateman equations (see Section 4.2). Finally,  $\kappa_J$  represents the average energy produced by the fission of isotope  $J$ , which we assume to be energy-independent.

Now let us consider the flux, which is a measure of the neutron population in the reactor (Section 3.5). For a given time interval  $dt$ , the change of the neutron population  $dn(\vec{r}, t, E, \vec{\Omega}) = d\phi(\vec{r}, t, E, \vec{\Omega})/v$  due to loss of neutrons by collisions is [Bell1982, Duderstadt1979, Hébert2009, Lewis1993]:

$$L_C(\vec{r}, t, E, \vec{\Omega}) dt = -\Sigma(\vec{r}, t, E) \phi(\vec{r}, t, E, \vec{\Omega}) dt, \quad (120)$$

where  $\Sigma$  is the total cross section and  $L_C(\vec{r}, t, E, \vec{\Omega})$  the rate of collision per unit volume of neutrons with energy  $E$  and direction  $\vec{\Omega}$  at point  $\vec{r}$  and time  $t$ . This term includes both absorbed and scattered neutrons. Some neutrons will be lost to migration when the net flow of neutrons reaching a region in space of volume  $d^3r$  is different from that leaving this same region. This rate of neutron loss due to migration is given by

$$L_M(\vec{r}, t, E, \vec{\Omega}) dt = -\vec{\Omega} \cdot \vec{\nabla} \phi(\vec{r}, t, E, \vec{\Omega}) dt, \quad (121)$$

meaning that neutrons, which can be considered to form a gas, tend to move towards regions of low neutron population (the kinetic theory of gas). Neutron with energy  $E$  and direction  $\vec{\Omega}$  can also be produced in this region of space due to scattering of neutrons with different directions and energies:

### 64.2.5 Bibliography

[Basdevant2005] J.-L. Basdevant, R. James, S. Michel, *Fundamentals in Nuclear Physics*. Springer, New York, 2005.

[Berger2013a] M. J. Berger, J. S. Coursey, M. A. Zucker, J. Chang, J., *ESTAR, PSTAR, and ASTAR: Computer Programs for Calculating Stopping-Power and Range Tables for Electrons, Protons, and Helium Ions*, <http://physics.nist.gov/Star>, visited April 2013.

[Berger2013b] M. J. Berger, J. H. Hubbel, S. M. Seltzer, J. Chang, J. S. Coursey, R. Sukumar, D. S. Zucker, K. Olsen, *XCOM: Photon Cross Section Database*, <http://www.nist.gov/pml/data/xcom>, visited April 2013.

[Bjorken1964] J. D. Bjorken, S. D. Drell, *Relativistic Quantum Mechanics*, McGraw-Hill, New York, 1964.

[Brookhaven2013] National Nuclear Data Center at Brookhaven National Laboratory: <http://www.nndc.bnl.gov/chart/>, visited April 2013.

[Griffiths2005] D. J. Griffiths, *Introduction to Quantum Mechanics*, Pearson Canada, Toronto, 2005.

[Duderstadt1979] J. J. Duderstadt, W. R. Martin, *Transport Theory*. Wiley, New York, 1979.

[Halzen1984] F. Halzen, A. Martin, *Quarks and Leptons: An Introductory Course in Modern Particle Physics*. Wiley, New York, 1984.

[Hubbell1975] J. H. Hubbell, W. J. Veigele, E. A. Briggs, R. T. Brown, D. T. Cromer, and R. J. Howerton, "Atomic form factors, incoherent scattering functions, and photon scattering cross sections", *J. Phys. Chem. Ref. Data*, 4, 471-538, 1975.

[Jauch1976] J. M. Jauch, F. Rohrlich, *The Theory of Photons and Electrons*. Springer-Verlag, New York, 1976.

[KAERI2013] Nuclear Data Center at Korea Atomic Energy Research Institute: <http://atom.kaeri.re.kr/ton/>, visited April 2013.

[Leroy2009] C. Leroy, P.-G. Rancoita, *Principle of Radiation Interaction in Matter and Detection*, 2nd edition. World Scientific, Singapore, 2009.

[Le Sech2010] C. Le Sech, C. Ngô, *Physique nucléaire : Des quarks aux applications*. Dunod, Paris, 2010.

- [Lewis1993] E. E. Lewis and W. F. Miller, Jr., *Computational Methods of Neutron Transport*, 2nd edition. Wiley, New York, 1993.
- [Livermore2013] *Isotope Evaluation at Lawrence Livermore National Laboratory*: <http://ie.lbl.gov/toi2003/MassSearch.asp>, visited April 2013.
- [MacFarlane2010] R. E. MacFarlane, A. C. Kahler, "Methods for Processing ENDF/B-VII with NJOY", *Nuclear Data Sheets*, 111, 2739-2890, 2010.
- [Magill2005] J. Magill and J. Galy, *Radioactivity, Radionuclides, Radiation*. Springer: Heidelberg, 2005.
- [Nikjoo2012] H. Nikjoo, S. Uehara, D. Emfietzoglou, *Interaction of Radiation with Matter*. CRC Press, Boca Raton, FL, 2012.
- [OECD-NEA2013] OECD-NEA Janis 3.0, *Java-Based Nuclear Data Display Program*. <https://www.oecd-nea.org/janis>, visited April 2013.
- [Pomraning1991] G. C. Pomraning, *Linear Kinetic Theory and Particle Transport in Stochastic Mixtures*. World Scientific, London, 1991.
- [Schiff1968] L. I. Schiff, *Quantum Mechanics*. McGraw-Hill, New York, 1968.
- [Smith2000] F. A. Smith, *A Primer of Applied Radiation Physics*. World Scientific, Singapore, 2000.
- [Watt1952] B. E. Watt, "Energy spectrum of neutrons from thermal fission of  $^{235}\text{U}$ ", *Phys. Rev.* 87, 1037-1041, 1952.
- [WebElements2013] *WebElements: The Periodic Table on the Web*. <http://www.webelements.com/isotopes.html>, visited April 2013.
- [Wong2004] S. S. M. Wong, *Introductory Nuclear Physics*. Wiley-VCH, Weinheim, 2004.

### 64.3 Dosimetry, Dose Limitations, and Guidance

The underlying principle of any process that uses ionizing radiation is that the benefit from potential exposure outweighs the potential risk from exposure. Radiation protection is guided by regulations that eliminate deterministic effects and limit stochastic effects from exposure.

The relationship between scientific discovery, international synthesis of data, and adoption of national regulations is illustrated in Figure 16.



**Figure 16 Radiation protection regulation pyramid**

Scientific knowledge and discovery is the broad base from which we derive fundamental radiation-protection quantities. This knowledge is disseminated through national reports, industrial reports, peer-review publications, conferences, and many other scientific venues.

International bodies periodically synthesize the available data from the scientific literature and produce recommendations on various aspects of radiation protection. International recommendations form the basis of national standards, but are not themselves regulations. National regulations are adopted by government bodies country by country, and although these bodies tend to follow international recommendations, they are not obligated to do so. In Canada, there are various governmental agencies involved in establishing radiation-protection guidelines, with different areas of responsibility depending upon the source of radiation. For example:

- Radioactive sources and waste – Canadian Nuclear Safety Commission (CNSC)
- Uranium mining and milling operations – Canadian Nuclear Safety Commission (CNSC)
- High-energy particle accelerators – Canadian Nuclear Safety Commission (CNSC)
- X-ray regulations – each province regulates independently
- X-ray use – Health Canada (HC) guidelines
- Naturally Occurring Radioactive Material (NORM) - each province regulates independently
- NORM mitigation – Health Canada (HC) guidelines.

Other agencies that have input into radiation protection regulations.

This section discusses fundamental definitions related to ionizing-radiation dose, background radiation, and national/international guidance regarding dose and dose limitations. Background information on the historical development of the radiation protection-system can be found in [Inkret1995] [Lindell1996] [Jones2005] [Clarke2005] [Walker2000].

### 64.3.1.1 Dose Definitions

The concepts of absorbed dose, equivalent dose (radiation weighting factors), and effective dose (tissue weighting factors) are discussed here in relation to risk concepts. In addition, radon guidance will be introduced.

#### Exposure

Before discussing dose, it is worthwhile to discuss, in a historical sense, exposure. In the early days of X-rays, a common dosimeter was a piece of dental film attached to a paper clip. The daily allowable exposure was an exposure that was just enough so that some “fogging” of the film could be observed on processing. This was known as a “paper-clip unit” of radiation exposure and amounted to an early dosimeter. For larger doses such as might be used in therapeutic medicine, a “skin erythema unit” was used, which was an exposure that would just cause visible reddening of the skin. Neither unit was what could be considered biologically meaningful, although they did provide a measure of protection.

Exposure was defined for X- (and gamma) radiation in terms of air ionization, and the original unit of air ionization established in 1928 was the Roentgen ( $R$ ). The current definition is given

as:

$$1R \equiv 2.58 \times 10^{-4} \text{ C kg}^{-1} \text{ of air} .$$

Absorbed dose was subsequently defined as the energy absorbed per unit mass from any kind of ionizing radiation in any target. As such, the absorbed dose is a physical quantity. To calculate the absorbed dose in air from a given exposure, the ionization potential of air (which is 33.7 eV/ion pair or 33.7 J/C) can be used. Using this value, the absorbed dose in air from an exposure of 1 Roentgen can be calculated as:

$$1R \equiv \left( 2.58 \times 10^{-4} \frac{\text{C}}{\text{kg}} \right) \left( 33.7 \frac{\text{J}}{\text{C}} \right) = 8.7 \times 10^{-3} \frac{\text{J}}{\text{kg}} .$$

A similar calculation of the soft-tissue ionization potential yields  $9.5 \times 10^{-3} \text{ J kg}^{-1}$ .

Because energy deposition per unit mass was deemed to be close to actual biological damage, a new unit was developed, called the Rad (standing for Radiation Absorbed Dose). The Rad was defined as an energy deposition of 100 erg per gram of material, where  $10^7 \text{ erg} = 1 \text{ Joule}$ . The Roentgen could therefore be defined as 87 erg/g in air (or 95 erg/g in soft tissue), and the Rad was defined as 100 erg/g. For regulatory purposes, it was therefore assumed that if one could measure the ionization of air in Roentgen ( $R$ ), this would be approximately equivalent to the absorbed dose in tissue ( $\text{Rad}_{\text{tissue}}$ ). To convert exposure to absorbed dose for any medium, Eq. (14) can be used:

$$D(\text{Rad}) = \frac{87}{100} \times \frac{\rho_m}{\rho_a} \times \frac{\mu_m}{\mu_a} \times E(\text{Roentgen}) , \quad (14)$$

where

$D$  = absorbed dose in Rad

$E$  = exposure in Roentgen

$\mu_m$  = energy-absorption coefficient for tissue (or any medium)

$\mu_a$  = energy-absorption coefficient for air

$\rho_m$  = tissue density (or density of any medium)

$\rho_a$  = air density.

Although the historical unit of Rad is still used in some instances, SI units are more common internationally and are promulgated through all major international guidance bodies such as IAEA, ICRP, and UNSCEAR.

### Absorbed, equivalent, and effective dose

Three fundamental quantities are required when considering radiation protection:

- Absorbed dose ( $D$ ) is energy absorbed per unit mass. 1 gray (Gy) = 1 joule per kilogram (J/kg)
- Equivalent dose ( $H_T$ , units of Sievert, Sv) takes into account the relative biological effectiveness of different radiation types
- Effective dose ( $E$ , units of Sievert, Sv) takes into account the potential for detrimental effects to the various organs and tissues.

It is important to realize that absorbed dose is a physical quantity, whereas equivalent and effective dose are derived quantities used for radiological-protection purposes. In addition, these derived quantities use reference "individuals" and assigned factors, roughly approximate risk on a population basis, and are not useful for accurate estimation of risk on an individual basis.

The absorbed dose can be expressed as in Eq. (15):

$$D_{T,r} = \frac{E_T}{m_T}, \quad (15)$$

where

$D_{T,r}$  is the absorbed dose to target  $T$  from radiation  $r$  (J/kg, or Gy)

$E_T$  is the energy deposited in target  $T$  (Joule)

$m_T$  is the mass of target  $T$  (kg).

The equivalent dose is calculated by summing over all different radiations interacting in the target material using Eq. (16):

$$H_T = \sum w_r D_{T,r}, \quad (16)$$

where

$H_T$  is the equivalent dose to target  $T$  (Sv)

$w_r$  is the radiation weighting factor for the radiation type.

Radiation weighting factors are related to the relative biological effectiveness (RBE) of different kinds of radiation, which is an indication of the relative amount of radiation damage done to tissue for a given absorbed dose. The recommended radiation weighting factors from ICRP103 are provided in Table 7.

**Table 7 Radiation weighting factors [ICRP2007]**

Radiation	Radiation weighting factor, $w_r$
Photons (X- and gamma)	1
Electrons (incl. beta)	1
Protons	2
Alpha particles and fission fragments	20
Neutrons (continuous function of energy) N.B.: in ICRP60 [ICRP1990], the centre expression represented all $w_r$ )	$2.5 + 18.2e^{-\frac{(\ln E)^2}{6}} \quad E < 1 \text{ MeV}$ $5.0 + 17.0e^{-\frac{(\ln(2E))^2}{6}} \quad 1 \text{ MeV} \leq E \leq 50 \text{ MeV}$ $2.5 + 3.25e^{-\frac{(\ln(0.04E))^2}{6}} \quad E > 50 \text{ MeV}$

$$E = \sum w_T H_T, \quad (17)$$

where  $w_T$  is the tissue weighting factor for target  $T$ .

Tissue weighting factors have been established as indicators of the relative sensitivities of different tissues to radiation exposure. The ICRP103 tissue weighting factors, along with ICRP60 and ICRP26, are given in Table 8. Blank entries mean that the organ was not uniquely identified in the guide and was included in "remainder". The sum of tissue weighting factors over all tissues is unity.

**Table 8 Tissue weighting factors [ICRP1977,1990,2007]**

Organ	Tissue weighting factor, $w_T$		
	ICRP26 (1977)	ICRP60 (1990)	ICRP103 (2007)
Gonads	0.25	0.20	0.08
Red Bone Marrow	0.12	0.12	0.12
Lung	0.12	0.12	0.12
Breast	0.15	0.05	0.12
Thyroid	0.03	0.05	0.04
Bone surface	0.03	0.01	0.01
Remainder	0.30	0.05	0.12
Colon		0.12	0.12
Stomach		0.12	0.12
Bladder		0.05	0.04
Liver		0.05	0.04
Esophagus		0.05	0.04
Skin		0.01	0.01
Salivary glands			0.01
Brain			0.01
Sum	1.00	1.00	1.00

Unfortunately, ICRP adopted the same base unit (Sv) for both equivalent dose and effective dose, which has the potential to lead to confusion in dose representation. The equivalencies between classical and SI dose units (and activity, which was discussed in Chapter 3) are provided in Table 9. Dose rate units are the same base units as a function of time (for example, Gy/h).

**Table 9 Dose units**

Unit	Classical unit	SI unit	Unit conversion
Activity	Curie (Ci)	Becquerel (Bq)	1 Ci = $3.7 \times 10^{10}$ Bq
Absorbed dose	Radiation absorbed dose (Rad)	Gray (Gy)	100 Rad = 1 Gy
Equivalent dose	Roentgen equivalent man (Rem)	Sievert (Sv)	100 Rem = 1 Sv
Effective dose	Roentgen equivalent man (Rem)	Sievert (Sv)	100 Rem = 1 Sv

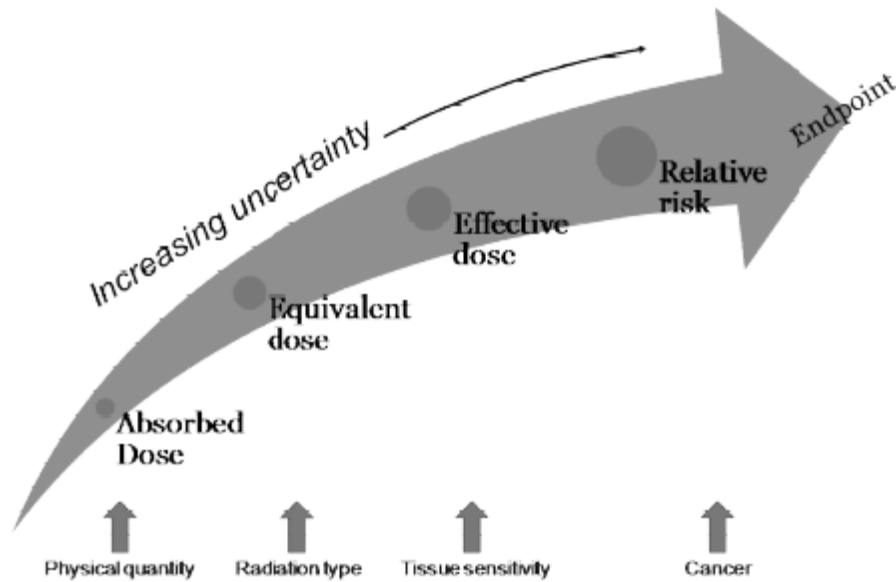


**Figure 17 Relationship between dose and endpoint**

**Committed dose**

The committed effective dose (CED) is the effective dose that an individual will eventually receive after having taken a radionuclide into the body (inhalation, ingestion, injection skin/wound absorption). Committed usually means to 50 years, although 70 years is used when a childhood intake has occurred.

**Derived quantities**

Derived quantities are values or results that are made up, or derived, from other values. Often, derived quantities are made up of other fundamental quantities. Four primary derived quantities are discussed in this section: (i) dose-conversion factors (DCF), (ii) annual limits on intake (ALI), (iii) derived air concentration (DAC), and (iv) radon progeny (WL; WLM).

**Dose-conversion factors (DCF)**

Dose-conversion factors (DCF) are tabulated derived values that enable conversion from one quantity to another. For example, dose-conversion factors are tabulated for inhalation and ingestion for workers in ICRP68 [ICRP1994] and the public in ICRP72 [ICRP1996a]. A doseconversion factor for an internalized radionuclide typically has units of Sv/Bq committed effective dose (CED), and therefore if the intake (in Bq) is known, the estimated CED in Sv can be immediately calculated. In the case of internalized radionuclides, values are available for inhalation and ingestion, for differing particle sizes, and for the different chemical forms of many radionuclides. Examples of tabulated dose conversion factors for <sup>14</sup>C are shown in Table 10.

**Table 10 Sample inhalation dose coefficients [ORNL2013]**

Inhalation dose coefficients (Sv / Bq) from ICRP 68				
Chemical form=	CO <sub>2</sub>	CO	CH <sub>4</sub>	Vapour
Effective (ICRP 60)	6.5E-12	8E-13	2.9E-12	5.8E-10

These conversion factors are derived using compartmental biokinetic models for internal dosimetry. Other dose-conversion factors can include external DCFs such as those found in ICRP74 [ICRP1996b] and discussed in Section 5.

**Annual limit on intake (ALI)**

The annual limit on intake (ALI) is the activity (Bq) of a radionuclide which, if taken internally, would result in a dose equal to the annual limit. As such, the ALI is normally defined as the dose limit divided by the effective dose per unit intake. Both equivalent and effective doses are considered; the more restrictive limit is used. Note that simply multiplying the number of ALIs taken in by 20 mSv to calculate committed effective dose may not be a correct estimate because some ALIs are based on effective dose and some on equivalent dose. The ALI is calculated using Eq. (18):

$$ALI(Bq) = \frac{D_{\text{limit}}(Sv)}{\sum w_T H_T \left( \frac{Sv}{Bq} \right)} = \frac{0.02 Sv}{DCF \frac{Sv}{Bq}} \quad (18)$$

**Derived air concentration (DAC)**

The derived air concentration (DAC) is defined as the air concentration (Bq/m<sup>3</sup>) that would lead to the inhalation of 1 ALI by a reference person over 2000 hours (50 weeks x 40 h/week) assuming that the reference person inhales 1.2 m<sup>3</sup>/h (light work). The DAC is calculated using

Eq. (19):

$$DAC \left( \frac{Bq}{m^3} \right) = \frac{ALI(Bq)}{2000 \text{ hr} \cdot 1.2 \frac{m^3}{\text{hr}}} = \frac{ALI(Bq)}{2400 m^3} \quad (19)$$

DACs enable rapid estimation of committed effective dose rate because the DAC represents 1 ALI (in the case of Canadian regulations, 20 mSv) in 2000 h, or stated in another manner, 1 DAC = 10 µSv/h. The number of DAC-h corresponds to the CED.

**Radon-derived quantities (WL;WLM)**

Radon gas (<sup>222</sup>Rn) is considered harmful primarily because it has numerous short-lived daughters such as polonium, bismuth, and lead which are solids and readily adsorbed on particles of fine dust than can be inhaled. When air containing radon is breathed in, it can be readily expelled without inducing any damage whatsoever. However, the radon daughters, both from gas decay and dust, can be trapped in lung tissue, where they can induce local damage to lung tissue through alpha-particle interactions. The combined alpha energies of the daughters per unit volume of air are the most important parameters to be considered when estimating damage to lung tissue. There is a special unit used to define this quantity, called the working level (WL).

The working level (WL) is defined as any combination of the short-lived decay products of radon (<sup>218</sup>Po, <sup>214</sup>Pb, <sup>214</sup>Bi, and <sup>214</sup>Po) in one dm<sup>3</sup> (1 litre) that will result in the ultimate emission of 1.3x10<sup>5</sup> MeV of alpha energy (or 2.08x10<sup>-5</sup> J/m<sup>3</sup>). An atmosphere containing 3.6 Bq/dm<sup>3</sup> (~100 pCi/L) of radon in equilibrium with its daughters is 1 WL. Note that the short-lived daughters are not necessarily in equilibrium with the radon parent, and for this reason, conversion of radon concentration to daughter concentrations uses a factor of about 0.7 for uranium mines (0.4 for homes). For example, finding 3.6 Bq/dm<sup>3</sup> in a mine is approximately equivalent to 0.7 WL. It is common practice to use an equilibrium factor of 0.5, and therefore a WL would be equal to 100 pCi/L (3.7 Bq/L).

A working-level month (WLM) is defined as the exposure to the equivalent radon daughter concentration of 1 WL for a time period of 170 hours. For regulatory purposes, an abundance of

data was obtained from uranium miners, which showed that miners exposed to 100 or more WLM had an increased risk of developing lung cancer. A regulatory limit of 4 WLM per year was therefore set for uranium workers. This was set to correspond to the fact that a 25-year work duration at a level of 4 WLM would lead to a cumulative exposure of 100 WLM. Doseconversion factors for radon are presented in ICRP50 [ICRP1987]. A worker dose-conversion factor of 5 mSv/WLM is often used for radiation-protection purposes.

### 64.3.1.2 Background Radiation Exposure

The Earth is radioactive and has been since its formation. The Earth contains radioisotopes that originated from planetary formation (primordial radioisotopes) and also from extra-terrestrial origins (cosmogenic radioisotopes produced continuously in the upper atmosphere through cosmic-ray interactions which deposit on Earth through atmospheric dispersion, deposition, and precipitation). Some important primordial and cosmogenic radioisotopes are listed in Table 11.

**Table 11 Primordial and cosmogenic radioisotopes**

Primordial			Cosmogenic	
<sup>40</sup> K	<sup>142</sup> Ce	<sup>174</sup> Hf	<sup>10</sup> Be	<sup>22</sup> Na
<sup>50</sup> V	<sup>144</sup> Nd	<sup>180</sup> Ta	<sup>26</sup> Al	<sup>35</sup> S
<sup>87</sup> Rb	<sup>147</sup> Sm	<sup>187</sup> Re	<sup>36</sup> Cl	<sup>7</sup> Be
<sup>113</sup> Cd	<sup>148</sup> Sm	<sup>190</sup> Pt	<sup>14</sup> C	<sup>33</sup> P
<sup>115</sup> In	<sup>152</sup> Gd	<sup>204</sup> Pb	<sup>32</sup> Si	<sup>32</sup> P
<sup>123</sup> Te	<sup>156</sup> Dy	<sup>238, 235</sup> U	<sup>39</sup> Ar	<sup>28</sup> Mg
<sup>138</sup> La	<sup>176</sup> Lu	<sup>232</sup> Th	<sup>3</sup> H	<sup>24</sup> Na

In addition to the two natural source categories, radioisotopes are introduced into the environment from anthropogenic sources such as nuclear medicine, certain industrial processes, routine nuclear power operations, historical nuclear weapons testing, and nuclear reaction core accidents. Theoretically, all radioisotopes on the nuclide chart can be introduced into the environment through anthropogenic processes. In practice, only a few anthropogenic radioisotopes are persistent in the environment, for example, <sup>137</sup>Cs. All the above-listed sources contribute to the ubiquitous background that constantly surrounds us [Waller2013].

The most recent analysis of U.S. population dose due to natural and anthropogenic radionuclides was conducted by the NCRP and published in Report No. 160 [NCRP2009]. The report indicated that roughly half the yearly exposure to a member of the U.S. population is from natural background radiation, primarily radon (originating from uranium in the ground) and thoron (originating from thorium in the ground) gases, whereas the other half is from anthropogenic (human-made) sources, of which the majority is due to medical procedures (see Figure 18). In Canada, it can be expected that the ratios will be similar to the U.S. values.

Note that in the U.S. report [NCRP2009], the average estimated yearly dose corresponding to Figure 18 is approximately 6.2 mSv. The data indicated a large increase in average yearly dose, which was exclusively due to medical procedures. Before the release of NCRP Report No. 160, the average yearly dose was estimated to be approximately 3.6 mSv from all sources [NCRP1987]. Therefore, the dose increase of 3.6 mSv to 6.2 mSv (almost 75% greater) due to medical procedures is significant and worthy of increased surveillance.

Because Canada is a country in which advanced medical procedures such as computer tomography (CT) are widely used, it is likely that our yearly average dose is proportionally similar to that shown in Figure 18.

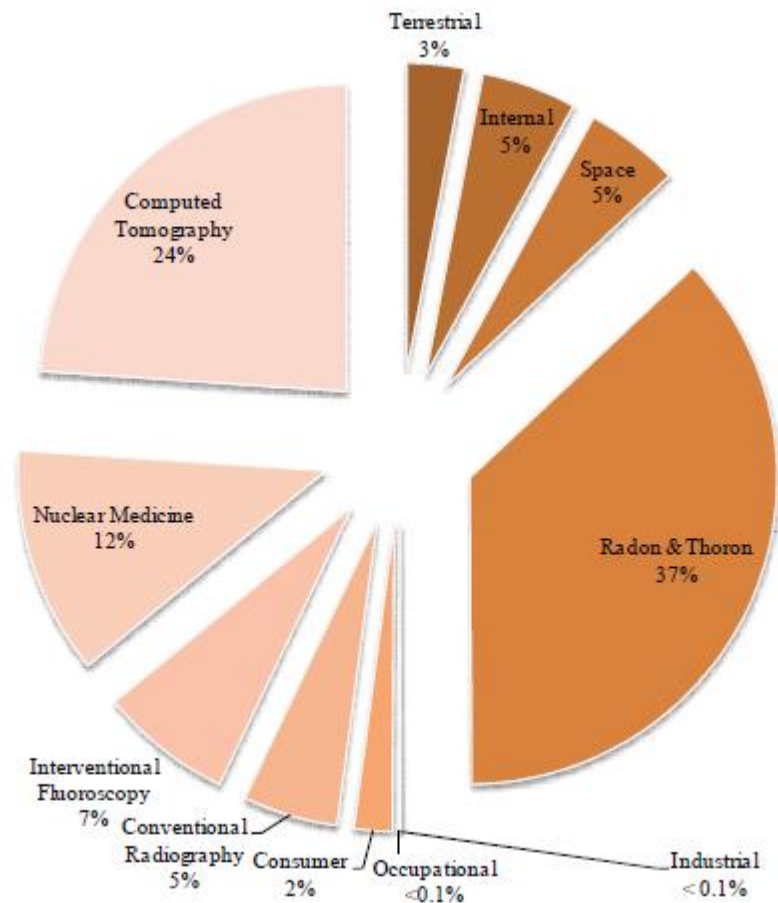


**Figure 18 Origin of average yearly radiation exposure (adapted from [NCRP2009])**

However, since the use of radiation for medical procedures is more strictly controlled in Canada, it is also likely that the average yearly dose is proportionally smaller than U.S. values, with a correspondingly higher percentage assigned to radon and thoron compared to, for example, CT. A study done by [Grasty2004] for natural background radiation in Canada indicated that the average annual radon and thoron component of the dose is 926  $\mu\text{Sv}$ , compared to the [NCRP2009] U.S. estimate of 2294  $\mu\text{Sv}$ . In fact, taking into account all sources of natural (not anthropogenic) radiation, it was found [Grasty2004] that the average yearly effective dose from natural sources was 1769  $\mu\text{Sv}$ , which is significantly smaller than the 2422  $\mu\text{Sv}$  worldwide average reported by [UNSCEAR2000]. Note, however, that the natural background can vary greatly from location to location in Canada (and, of course, world-wide).

### 64.3.1.3 International Guidance

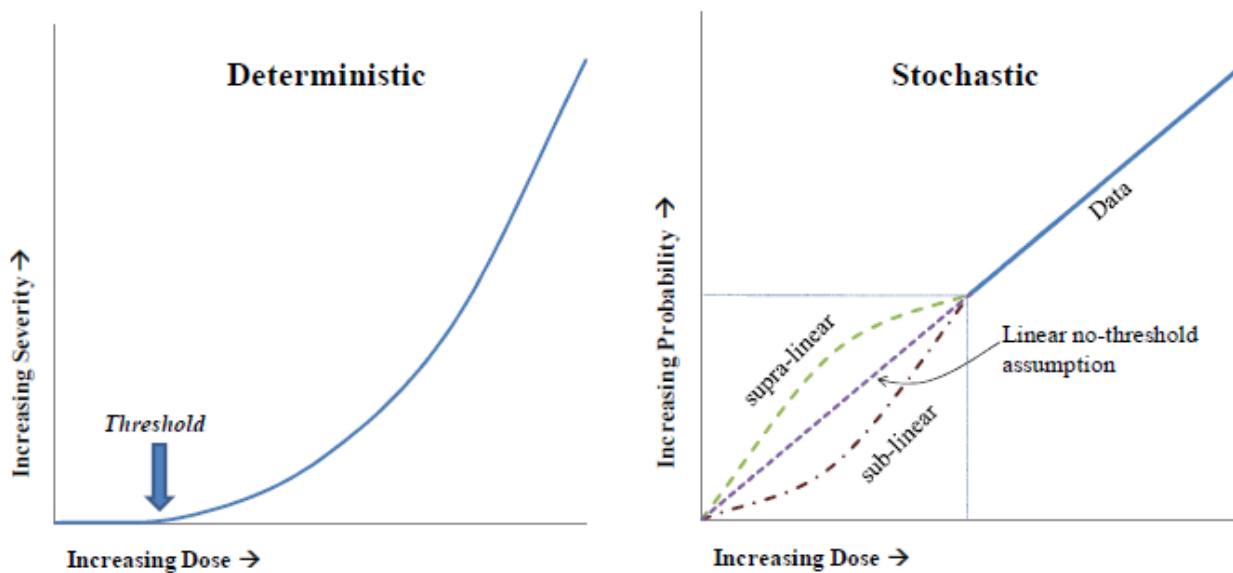
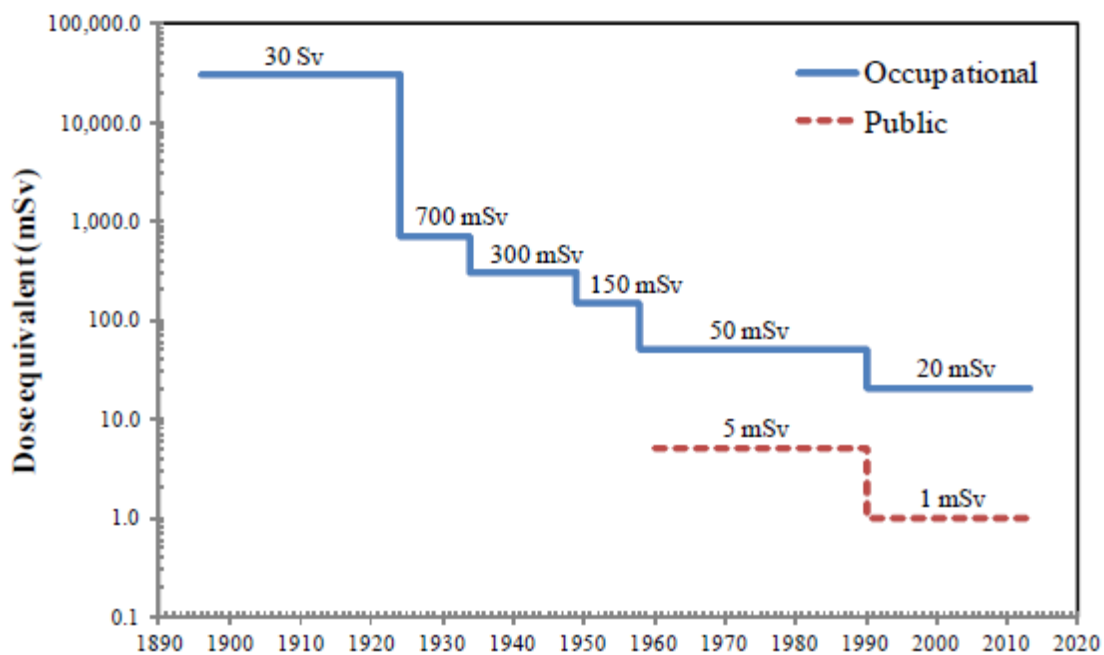
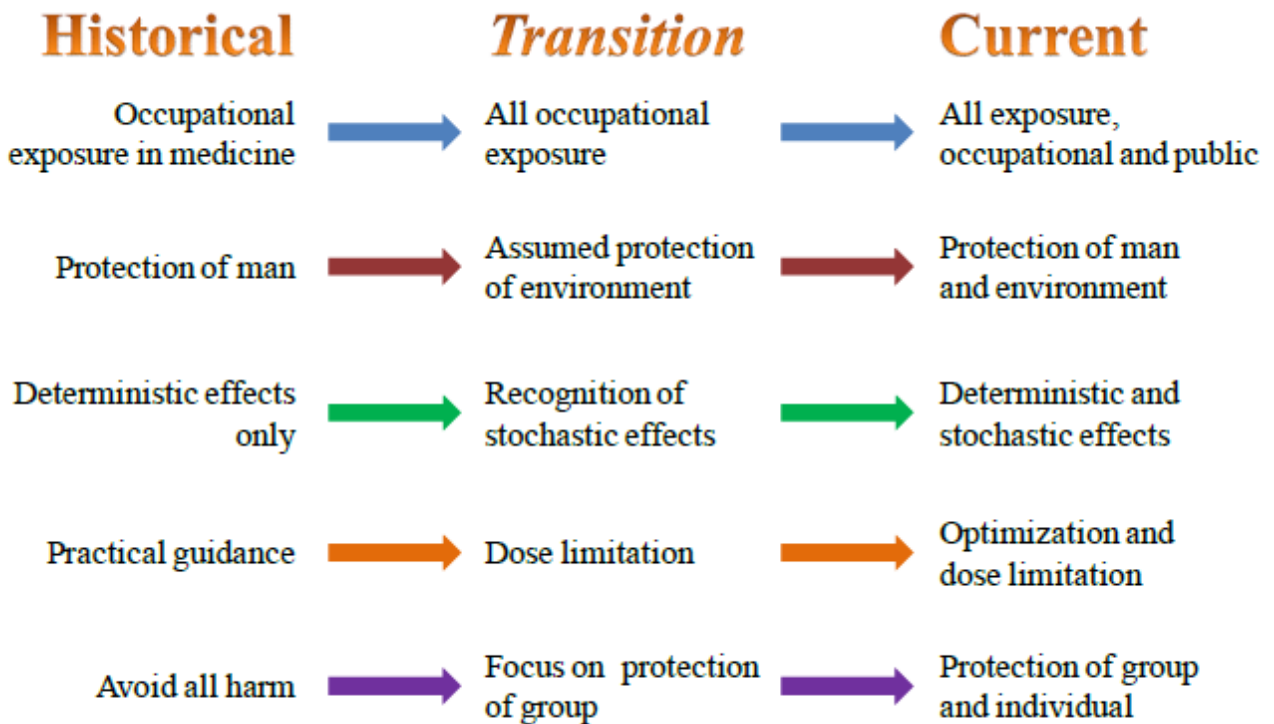
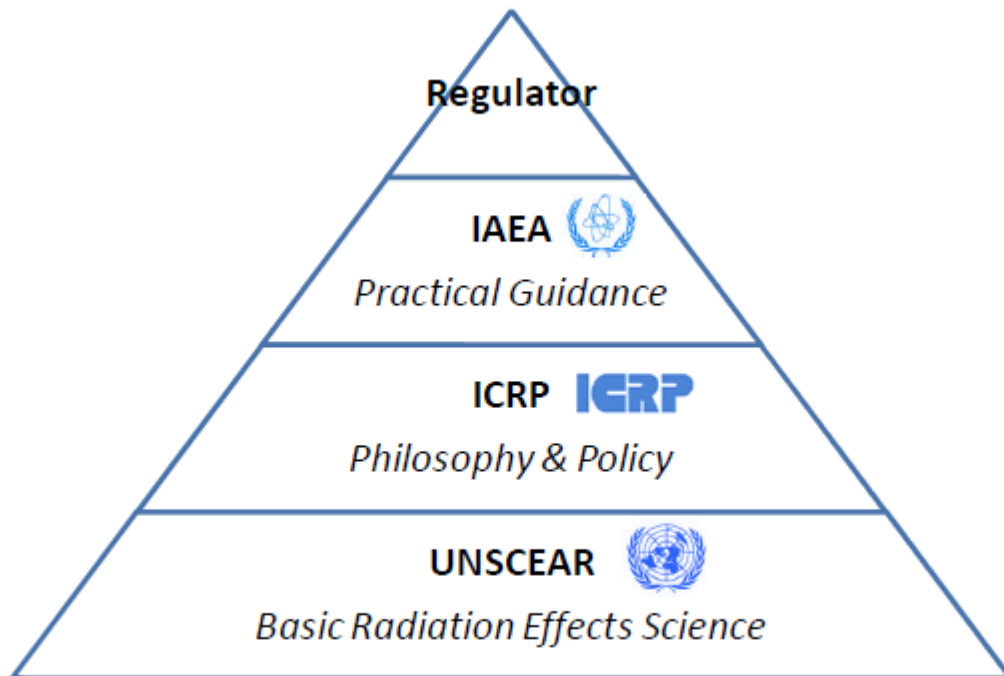


Figure 20 Paradigm shift from deterministic to stochastic effect protection



**Figure 21 Progression of radiation protection principles (adapted from [Clement2009])**

A number of international organizations are pivotal in setting radiological protection standards and providing guidance. The essential organizations that provide input to national regulatory standards are depicted in Figure 22. These organizations are discussed in the following sections.



**Figure 22 Relationship of international bodies for radiation protection regulations**

### UNSCEAR

UNSCEAR is the United Nations Scientific Committee on the Effects of Atomic Radiation, which was established by the United Nations in 1955 to assess and report levels and effects of exposure to ionizing radiation and provides the scientific basis for evaluating radiation risk and for

establishing protective measures. UNSCEAR provides the scientific guidance that is consulted when developing ICRP recommendations. UNSCEAR publications can be found online at:

<http://www.unscear.org/unscear/en/publications.html> .

## **ICRP**

ICRP is the International Commission on Radiological Protection, established in 1928 to advance for the public benefit the science of radiological protection, in particular by providing recommendations

and guidance on all aspects of protection against ionizing radiation. The main objective of the Commission's recommendations is to provide an appropriate standard of protection for humans without unduly limiting the beneficial practices giving rise to radiation exposure. The ICRP produces recommendations on radiological protection that are adopted worldwide based on science and value judgements. The ICRP guidance documents form the basis for IAEA regulatory recommendations. ICRP publications can be found online at:

<http://www.icrp.org/publications.asp>.

## **ICRP 103**

The current recommendations of the ICRP [ICRP2007] form the basis for the radiation protection system. The primary aim of the recommendations is to provide an appropriate level of protection for people and the environment without unduly limiting the desirable human activities that may be associated with radiation exposure. The three primary goals of radiation protection are:

- Justification – more benefit than detriment from exposure
- Optimization – exposure has been optimized to be as low as reasonably achievable
- Dose limitation – limit the dose (except for medical exposures).

The three goals form the core of the radiation-protection system and apply to three different situations:

- Existing situations – natural events, past practices, past events; the situation already exists when a decision on control is required, including natural background and residues from past practices.
- Planned situations – practices, medical exposures; the situation involves planned operation of sources, including decommissioning and disposal of radioactive waste.
- Emergency situations – preparedness, response; the situation is unexpected and requires urgent action to mitigate consequences.

In ICRP103, three exposure types are also considered:

- Occupational exposure - all exposure incurred by workers in the course of their work, with the exception of (i) excluded exposures and exposures from exempt activities involving radiation or exempt sources, (ii) medical exposure, and (iii) normal local natural background radiation.
- Public exposure - exposure incurred by members of the public from radiation sources, excluding any occupational or medical exposure and the normal local natural background radiation.
- Medical exposure - exposure incurred by patients as part of their own medical or dental diagnosis or treatment; by persons, other than those occupationally exposed, knowingly, while voluntarily helping in the support and comfort of patients; and by volunteers in a programme of biomedical research involving their exposure.

Dose limits corresponding to planned public and occupational exposure are provided in Table 12. Note that the numerical values are essentially the same as reported in ICRP60 [ICRP1990],

from which the current CNSC regulations are derived. Note that the dose-limit guidance refers to exposures above background radiation (as discussed in Section 3.2) and as such may be considered as an additional dose over background. It should also be noted that, operationally, action levels are often used that are a fraction of the dose limit. Exceeding an action level would initiate an investigation into the reason for the dose and may initiate a review of procedures to make doses as low as reasonably achievable, social and economic factors being taken into account (ALARA). The ALARA principle is also found in CNSC document G-129, Rev1 [CNSC2004].

**Table 12 ICRP103 dose limits for planned exposure scenarios [ICRP2007]**

	Occupational	Public
Effective Dose (Whole Body)	20 mSv/a averaged over 5 years (50 mSv/a max)	1 mSv/a
Equivalent Dose (Lens of the Eye)	150 mSv/a	15 mSv/a
Equivalent Dose (Skin)	500 mSv/a	50 mSv/a
Equivalent Dose (Hands and Feet)	500 mSv/a	n/a

ICRP103 also considers the target for exposure in defining a “representative person”. A representative person is an individual receiving a dose that is representative of the more highly exposed individuals in the population. This term is the equivalent of, and replaces the notion of, the “average member of the critical group” described in prior ICRP documents (for example, [ICRP1990]).

Finally, ICRP103 considers explicitly the need for protection of the environment by delineating the requirement for scientific evidence to demonstrate that protection is adequately afforded and the need for improved protection as required. Further guidance is provided by ICRP108 [ICRP2008].

### **IAEA**

The IAEA is the International Atomic Energy Agency, established within the United Nations framework in 1956 as the world’s “Atoms for Peace” organization to promote safe, secure, and peaceful nuclear technologies. The Agency works with its member states and multiple partners world-wide to promote safe, secure, and peaceful nuclear technologies. Three main areas of work underpin the IAEA’s mission: Safety and Security; Science and Technology; and Safeguards and Verification. The IAEA has a wide range of programmes, including development of safety standards in regulatory language. IAEA Safety Series documents are often used as the principal references for national regulatory policy. The most fundamental IAEA radiation protection standard was the “International Basic Safety Standards for Protection against Ionizing Radiation and for the Safety of Radiation Sources” [IAEA1996], which has been superseded by an interim General Safety Requirements Part 3 report [IAEA2011]. IAEA publications can be found online at: <http://www-pub.iaea.org/books/>.

### 64.3.2 Summary

Radiation-protection standards have evolved over the years to provide increased levels of protection for workers and the public. Dose limits are established on the basis of scientific knowledge which forms policy, best practices and guidance, and then national regulations. The basic dose quantities used are absorbed dose, equivalent dose, and effective dose. Although nuclear power plant operations often use obsolete units (such as Ci, Rad, and Rem) in their plants, most of the nuclear industry uses SI units. Dose quantities for regulatory purposes, as promulgated through the Nuclear Safety and Control Act, use SI units. Dose limits derived from International Commission on Radiological Protection guidance are established in Canada, and derived quantities are used in operations.

Background radiation is made up of natural and anthropogenic components. Dose limits are established to provide protection above the ubiquitous background level, which has a wide annual dose range world-wide. In Canada, the background dose is estimated to be approximately 3.6 mSv per year. Evidence from U.S. estimates indicates that increased use of advanced medical imaging procedures such as computed tomography is resulting in a larger estimated background dose; however, no such study has indicated that this is the case in Canada. As research continues into large epidemiological studies and low-dose rate radiation effects, dose-limit guidance may change in the future.

## 64.4 Radiation Instrumentation

Detection of ionizing radiation is vitally important to all aspects of the nuclear energy industry. The ability to identify sources of radiation, quantities of radiation, and specific radioisotopes enables the administration of comprehensive radiation protection, environmental monitoring, and security programs.

Before discussing the mechanisms of how radiation interacts with detection materials, the basics of radiation interactions with matter must be understood. These concepts were discussed in 2.3 (Nuclear Processes and Neutron Physics). The basics of detection, as well as gas-filled, scintillation, and semiconductor detectors, are discussed. **Dosimetry detectors**, are explored.

### 64.4.1.1 Basics of Detection

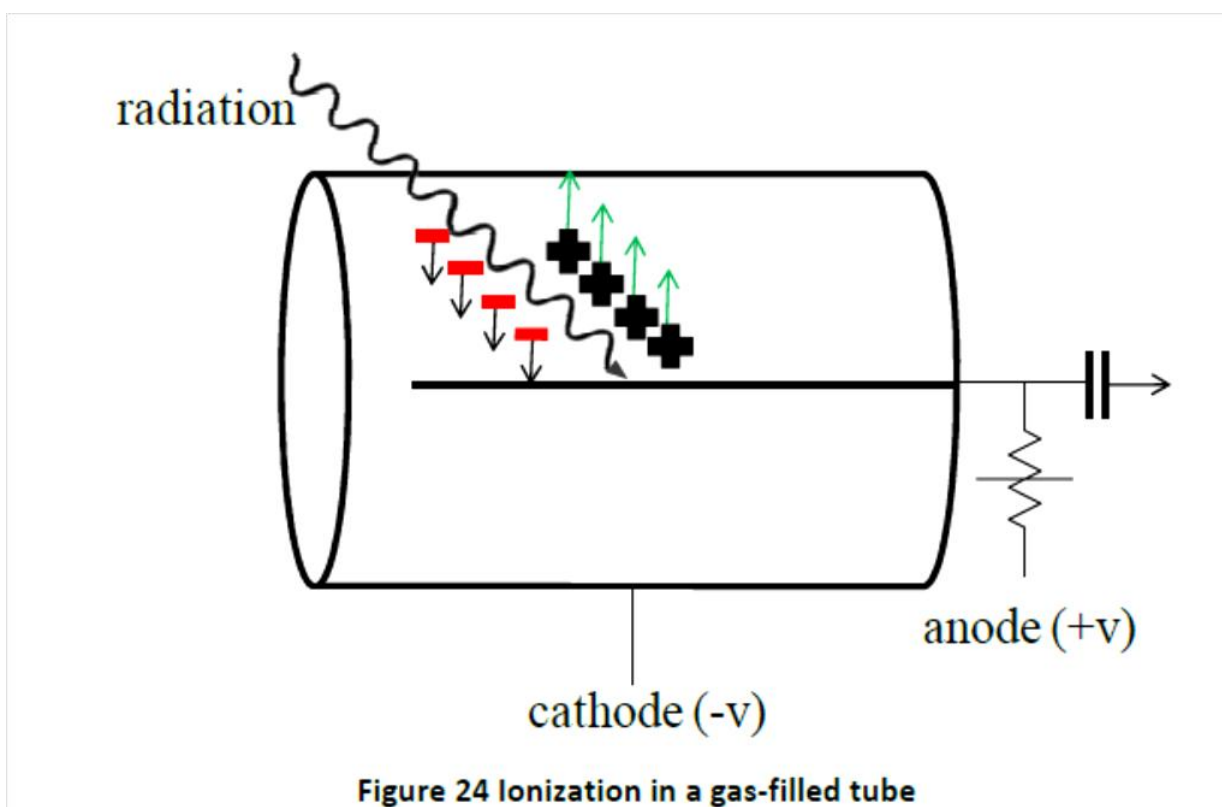
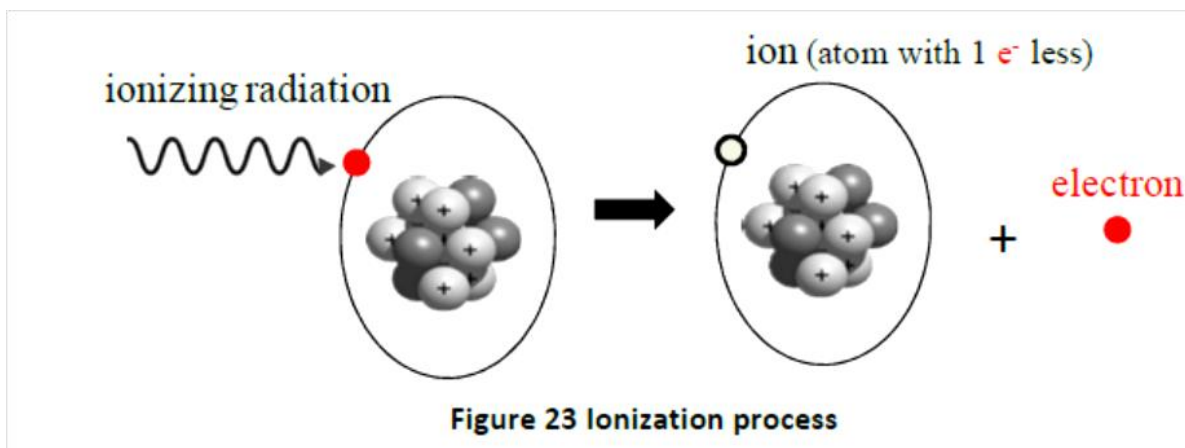
Ionizing radiation is tasteless, odourless, and colourless and cannot be detected by the human senses. Therefore, devices to aid in detection and identification of ionizing radiation are required for safety purposes. Anything that responds to ionizing-radiation interactions can be considered a radiation detector. In fact, the mechanisms of radiation interactions with tissue and the human body, as discussed in Section 2, are fairly closely related to radiation detectors.

The primary differences are in the observable endpoints, where radiation detectors are designed to provide an indication of radiation level through chemical/electric/electronic indications, whereas the endpoints in radiation biology tend to be deterministic or stochastic health effects. That being said, the human body itself is a radiation detector of sorts. The first “radiation dosimeters” used were based on skin reddening (or erythema). The variability in individual human response to radiation (and of course the fact that skin reddening occurs only at unsafe moderate to high radiation doses) makes this type of radiation detector impractical.

Radiation detectors work on one of two basic principles: (i) ionization and (ii) excitation.

## Ionization

In an ionization-based detector, electrons bound to the atoms or molecules of the material through which charged particles such as alpha and beta particles pass are released. The separated electrons and ions (Figure 23) can be collected at two electrodes by imposing a potential difference across the detector space; their presence is then measured as pulses or a current. An example of generation of electron-ion pairs in a gas-filled counter (for example, a Geiger-Müller tube) is depicted in Figure 24.



## Excitation

In an excitation-based detector, part of the radiation energy is transferred to bound electrons and raises them to an excited state in the atom or molecule. When the excited species returns to its ground-state energy level, the excited atom or molecule may emit electromagnetic energy in the ultraviolet to visible region (Figure 25). This light can be detected by a photomultiplier tube (PMT), which generates secondary electrons using a photocathode and multiplies them to generate a detectable signal. This process is depicted in the scintillation-type counter system shown in Figure 26.

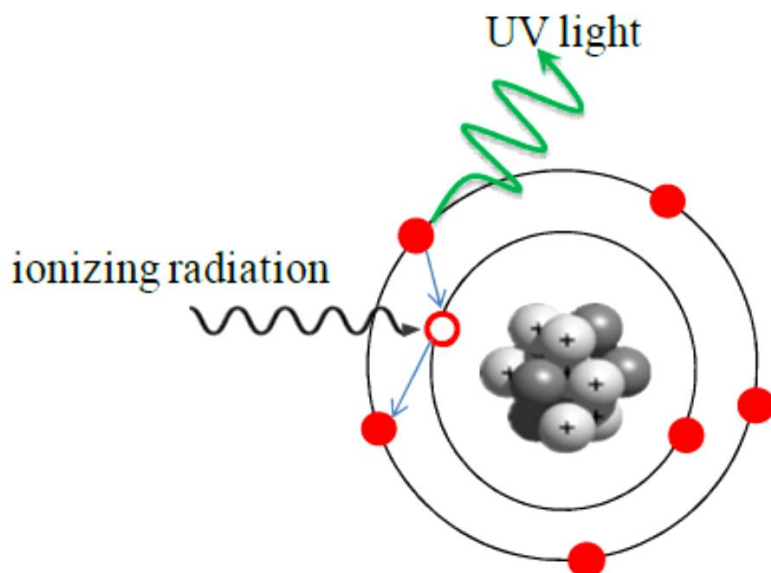


**Figure 25 Excitation process**

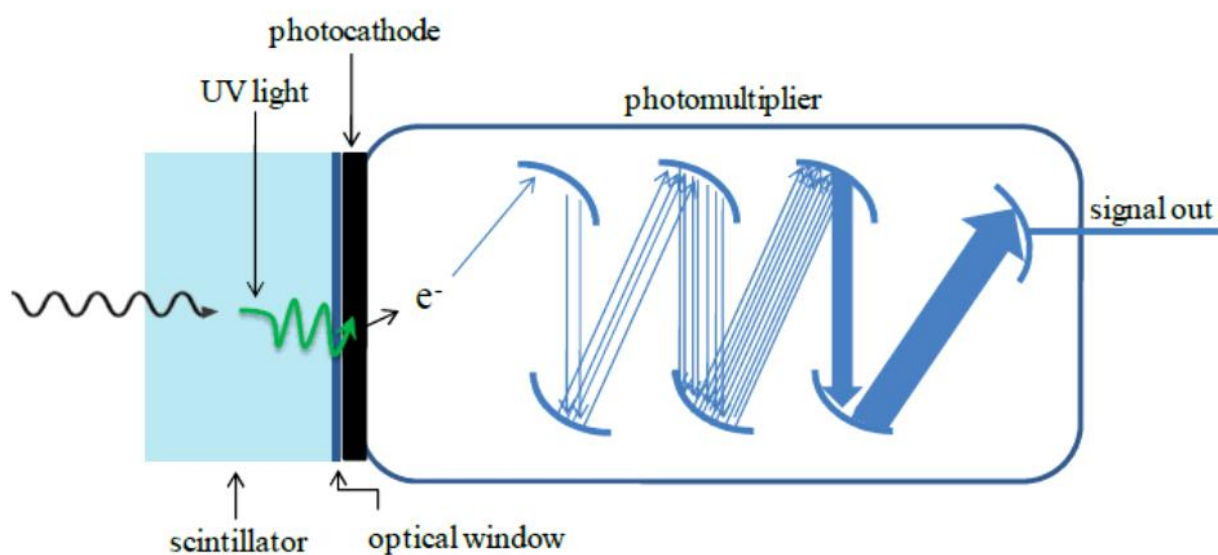


**Figure 26 Excitation in a scintillator-type detector**

Advances in radiation-detection instrumentation took place in the 1920s and have continued ever since. A concise discussion of the history of radiation-detection instrumentation is provided by [Frame2005]. Important operational characteristics for all detector types include resolving time and efficiency and are discussed below. An excellent reference on particle counting is ICRU Report 52 [ICRU1994].

### Resolving time

When ionizing radiation interacts with a detector, a signal in the detector material (whether it be a gas, scintillator, or solid-state device) is produced that is related to the radiation event that generated it. During the time it takes the system to process a pulse that is generated in the detector, the detector may be unavailable to process additional events. For example, during the time it takes for positive ions in a GM tube to reach the cathode, the tube is insensitive to any radiation. During this time, if a second ionizing ray interacts with the detector, it will not be observed because the tube cannot distinguish that there is another electron avalanche present; the system observes only one large electron avalanche until it has been reset after detection. In

essence, the counter cannot produce pulses for more than one event because the counter is “occupied” with the first event. This phenomenon is sometimes called coincidence, and as a result, the observed counts are always lower than the true counts. The “resolving time” is often referred to as “dead time”, because in essence the detector is “dead” and cannot detect any other radiation in this time window. Note, however, that the resolving time is actually the sum of the dead time and recovery time. In terms of definitions, dead time is the time required in a detector before another unique pulse can form; recovery time is the time required after the dead time until the pulse size is large enough to pass a discriminator; and resolving time is the minimum time from the detection of one interaction until the next detection can occur. True resolving times span a range from a few microseconds to 1000 microseconds, depending on the detector. The loss of particles is important, especially when high count rates are involved and the losses accumulate into large numbers.

For a counting rate,  $R$ , from a radioactive source, the presence of coincidence will mean that the rate actually measured,  $r$ , will be less than the expected value ( $r < R$ ). If the detector has a dead time of  $T$ , then the true count rate is given by Eq. (21):

$$R = r + rRT . \quad (21)$$

The counting rate can therefore be corrected for dead time using Eq. (22):

$$R = \frac{r}{1 - rT} . \quad (22)$$

The value of dead time,  $T$ , can be determined using a two-source method by measuring the activity from two known sources  $r_1$  and  $r_2$ . In theory, the measurement,  $r_3$ , should be the simple sum of the two sources as given by Eq. (23):

$$r_1 + r_2 = r_3 + b , \quad (23)$$

where  $b$  is the background counting rate. If each of these counting rates is corrected for dead time, then Eq. (23) becomes Eq. (24):

$$\frac{r_1}{1 - r_1T} + \frac{r_2}{1 - r_2T} = \frac{r_3}{1 - r_3T} + b . \quad (24)$$

Because the background count rate may be considered negligible for this measurement, Eq. (24) can be expressed in the form of a quadratic equation:

$$r_1r_2r_3T^2 - 2r_1r_2T + r_1 + r_2 - r_3 = 0 . \quad (25)$$

$T$  should be on the order of microseconds, thereby making  $T^2$  negligible, enabling the simple solution for the dead time,  $T$ , given by Eq. (26):

$$T = \frac{r_1 + r_2 - r_3}{2r_1r_2} . \quad (26)$$

The above expressions are useful in the limit of low interaction rates and are considered part of what is known as the non-paralyzable model. If the dead time approaches 30% or more, the

above model fails, and the paralyzable model must be used (which is not developed here; the reader is referred to [Knoll2010]). The significance of non-paralyzable versus paralyzable, from a practical perspective, relates to ability to count radiation in extreme fields. An ideal detector will have a linear response of count rate with interaction rate. A non-paralyzable detector will have an increasing count rate with interaction rate (but not necessarily linear at high interaction rate), but will tend to flatten out at high interaction rate. A paralyzable detector is one which has an increasing response at lower interaction rate, a peak response, and then a decreasing response with higher interaction rate. Essentially, in a paralyzable system, an interaction that occurs in the detector during the dead time will extend the dead time. The danger of a paralyzable detector is that if the count rate goes down as the interaction rate goes up, a person entering a progressively higher radiation field will think that he is moving into an area of lower radiation. For example, a GM counter in a high radiation field will tend to become paralyzed and may severely under-predict the radiation hazard.

### Energy response and efficiency

All radiation detectors respond to energy deposition differently, based upon the type of radiation interacting with the detector and the energy of the radiation. For example, in a thinwindow GM tube, beta particles interact best with the filling gas, followed by alpha particles and then gamma rays. This is due to the range of the respective particles in the gas in relation to the anode and cathode of the GM detector.

No radiation detector counts all the particles which are emitted from a source for various reasons. For example, resolving time affects the registered counts. In addition, many of the particles do not strike the tube at all because they are emitted uniformly in all directions from the source. The combination of effects that prevent the detector from counting all particles is known as the efficiency. Efficiency of a radiation counting system is achieved by comparing the measured count rate in the system to the disintegration rate (activity) of the source when the activity is given in units of disintegrations per second (dps; 1 dps = 1 Bq), where the conversion factor is 1 Ci = 3.7x10<sup>10</sup> Bq.

The formula for determining the absolute efficiency is straightforward and is given as Eq. (27):

$$\% \text{ Efficiency} = \varepsilon = \frac{C_{\text{measured}}}{A} \times 100\%, \quad (27)$$

where  $C_{\text{measured}}$

is the measured count rate and  $A$  is the calculated source activity. Note that the time units of the numerator and denominator must be the same.

In fact, the absolute efficiency is a product of two separate phenomena, known as the geometric efficiency and the intrinsic (or quantum) efficiency. The relationship for absolute efficiency,  $\varepsilon$ , is given by Eq. (28):

$$\begin{aligned} \varepsilon &= \frac{\text{Number detected}}{\text{Number emitted}} \times 100\% \\ &= \frac{\text{Number reaching detector}}{\text{Number emitted}} \times \frac{\text{Number detected}}{\text{Number reaching detector}} \times 100\%. \end{aligned} \quad (28)$$

$\uparrow$   
*Geometric efficiency*

$\uparrow$   
*Intrinsic efficiency*

The intrinsic efficiency is determined by the energy of the particles, atomic number of the

detector, density of the detector, thickness of the detector, and other factors. A variety of geometrical efficiency examples are depicted in Figure 27. In the left figure, the source is a certain distance from the detector, and the geometrical efficiency will be low and based upon the angle subtended by the source to the detector edge. In the centre figure, the geometrical efficiency approaches optimal for a planar detector (often called a “ $2\pi$  geometry” because the solid angle of a cone intersecting with the detector is approximately  $\Omega = 2\pi(1 - \cos(\pi/2)) = 2\pi$ ). In the right figure, the geometrical efficiency approaches unity because the source is surrounded by detector material. This configuration is called a well detector (often called a “ $4\pi$  geometry” because the solid angle of a cone intersecting with the detector is approximately  $\Omega = 2\pi(1 - \cos(\pi)) = 4\pi$ ). In practice, detector efficiencies are specified as a function of radioisotope (or energy) for a given geometry.

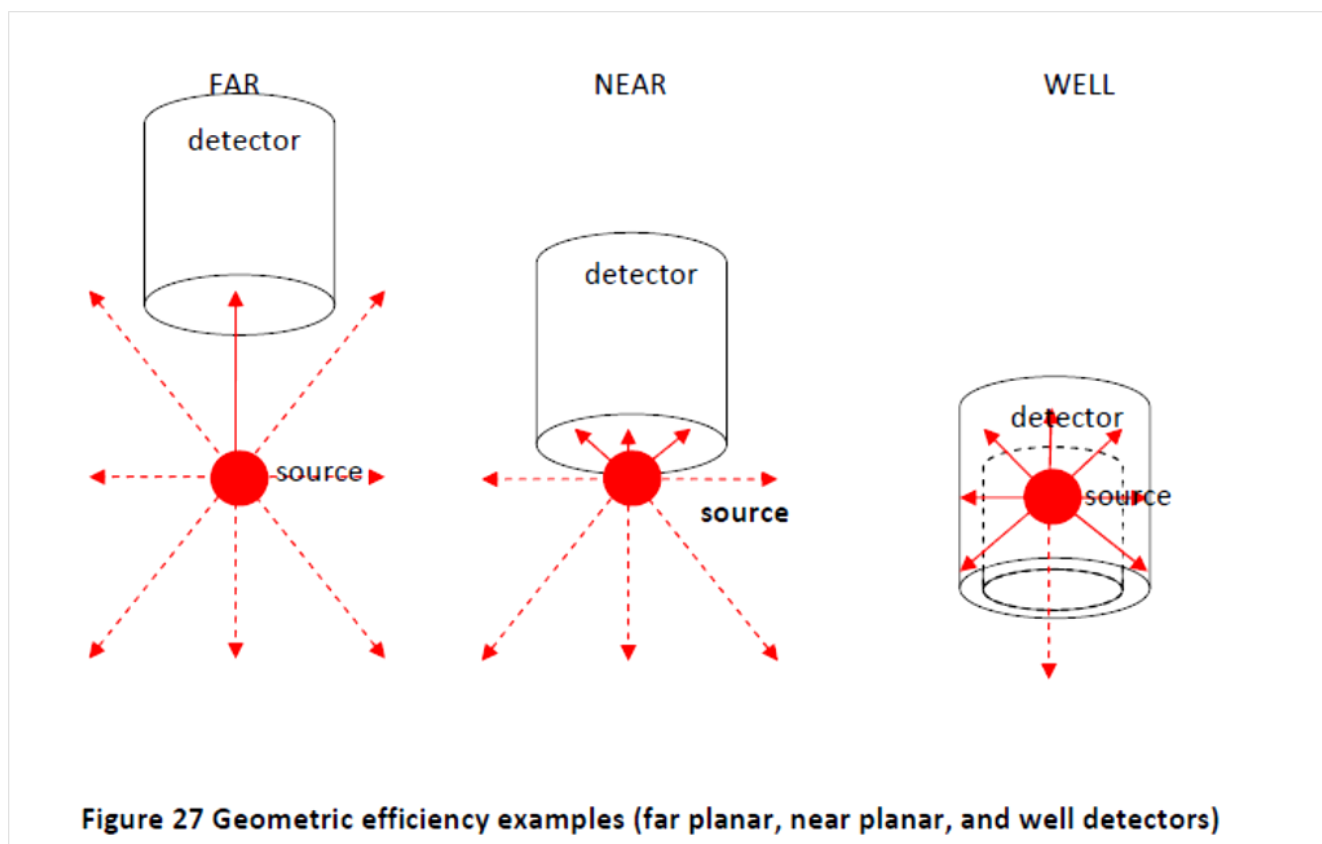


**Figure 27 Geometric efficiency examples (far planar, near planar, and well detectors)**

For detectors that perform spectroscopy (measurement of incident radiation spectra), both energy and efficiency calibration are generally required. As an example of how this calibration is performed, consider a simple scintillation (sodium iodide) gamma spectroscopy system. When a gamma ray (emitted during a change in an atom's nucleus) interacts with a sodium iodide crystal, NaI(Tl), the gamma ray will frequently give all its energy to an atomic electron through the photoelectric effect (PE). This electron travels a short, erratic path in the crystal, converting its energy into photons of light by colliding with many atoms in the crystal. The more energy the gamma ray has, the more photons of light will be created. A photomultiplier tube (PMT) converts each photon interaction into a small electrical current, and because the photons arrive at the PMT at about the same time, the individual currents combine to produce a larger current pulse. This pulse is converted into a voltage pulse with size proportional to the gamma-ray energy. The voltage pulse is amplified and measured by an analog-to-digital conversion (ADC) process. The result of this measurement is an integer between 1 and 1024 for a 10-bit ADC. One

is the measured value for a voltage pulse less than a hundredth of a volt, and 1024 is the measured value for a pulse larger than approximately 8 volts (or the largest voltage pulse in the ADC). Pulses between 0V and 8V are proportionately assigned an integer measured value between 1 and 1024. This measure is called the channel number. The analog-to-digital conversion process is performed, and the computer records the measurements as the number of gamma rays observed for each integer measurement or channel number.

The spectrum is a visual display of the number of gamma rays as a function of the channel number. In the case of known sources (location of the energy peak(s) is well known), then a correlation of channel number with gamma-ray energy can be generated. The result is a graph of the channel number (memory location) as a function of gamma-ray energy (photopeak). The slope of this graph (energy/channel) is the energy calibration (a fitted equation may also be used if the relationship is not linear over all energy values). An example of energy calibration is shown in Figure 28.

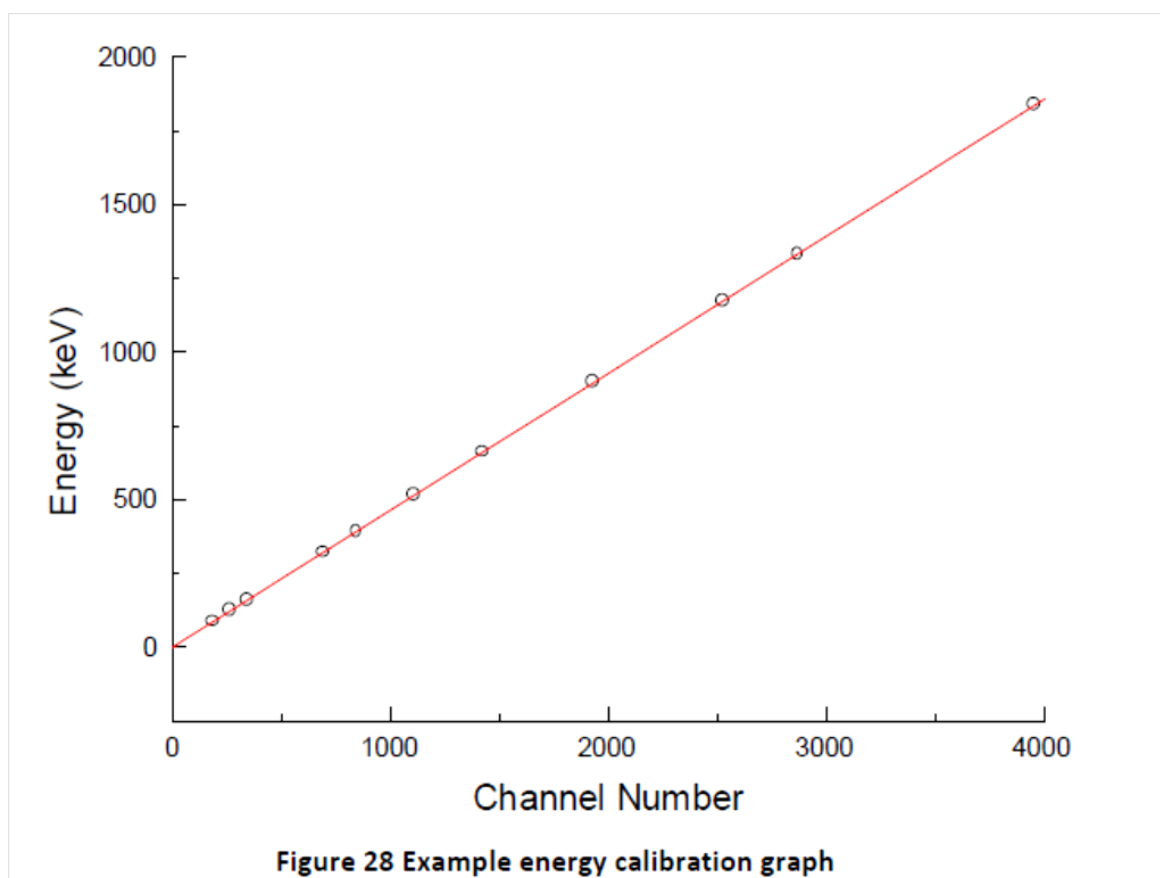


**Figure 28 Example energy calibration graph**

If the geometry is fixed and the activity of the calibration source is known, the peak area (integral counts) can be correlated with activity to determine the efficiency for each photopeak, as determined by Eq. (27). The efficiency can be plotted as a function of photopeak energy to obtain an efficiency curve, as depicted in Figure 29. This curve enables determination of the activity of an unknown source in a spectroscopic system.

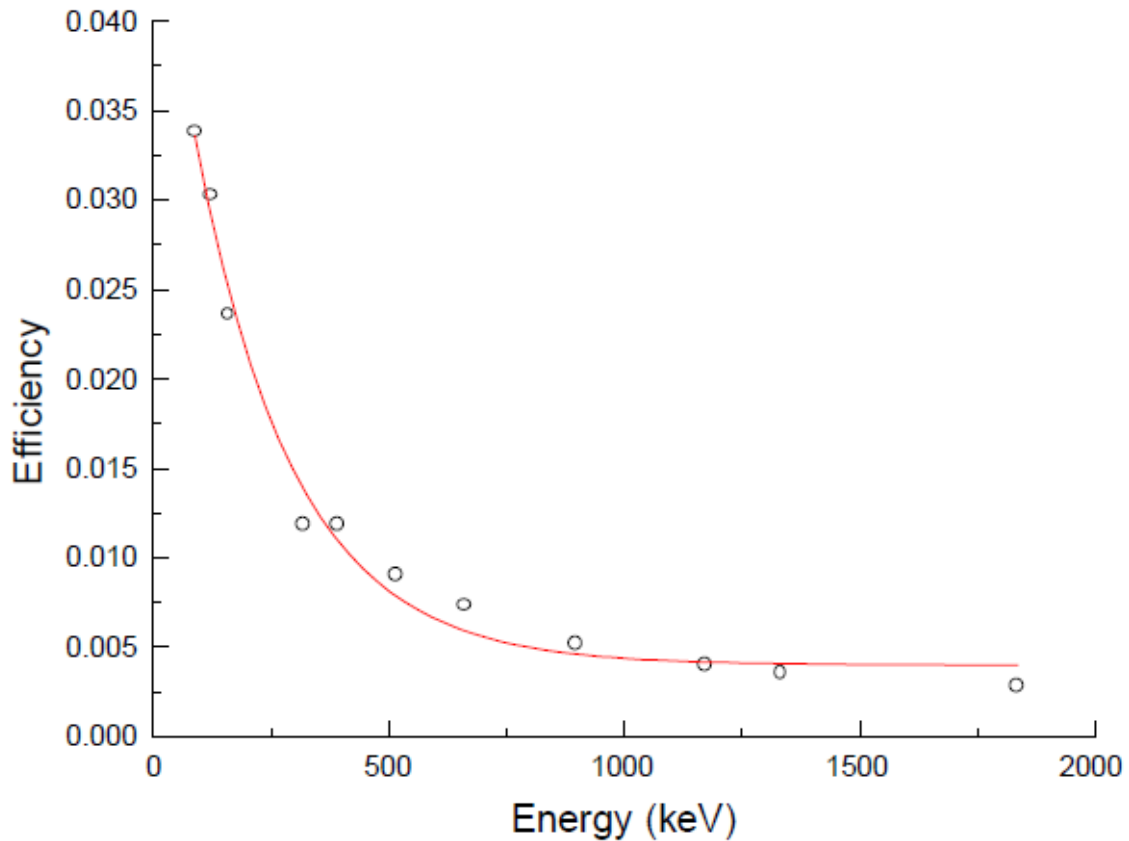


**Figure 29 Example efficiency calibration graph**

Energy calibration is essential for isotope *identification*, and efficiency is essential for *activity* determination.

### Counting statistics and decision levels

Statistics play a very important role in particle counting because atomic concentrations are on the order of Avogadro's number. Therefore, it is impossible to deal with atoms individually, and statistics are used to assist in prediction of behaviour. Statistics uses two main quantities in predicting behaviour, the *mean* and the *standard deviation*.

The mean ( $\bar{x}$ ) is computed as in Eq. (29):

$$\bar{x} = \sum_{i=1}^N \frac{x_i}{N}, \quad (29)$$

where the number of measurements ( $x_i$ ) ranges from 1 to N.

The standard deviation of the data is computed as in Eq. (30):

$$\sigma = \sqrt{\frac{\sum_{i=1}^N (\bar{x} - x_i)^2}{N-1}}. \quad (30)$$

The standard deviation is a measure of the variation of the data without regard to position above or below the mean (that is, an absolute value using the square). Because most measurements

tend to follow a Gaussian distribution about the mean (i.e., they are symmetrical), the mean and standard deviation are widely used measures to predict behaviour. However, particle counting is not symmetrical about a mean. Radioactive decay is a random process that occurs very infrequently for low-activity samples and very frequently for high-activity samples. Three statistical distributions useful in particle counting will be discussed below.

### Binomial distribution

The binomial distribution is used when there are two possible outcomes of an event. The probability of an outcome is a constant independently of the number of trials, and the selection of either outcome does not affect the outcome of subsequent trials. Assume an experiment where there are only two outcomes: (A) and (B). In a binomial distribution,  $p$  is defined as the probability of obtaining one of the outcomes (A), and  $q$  is the probability that the other (B) outcome occurs. Occasionally, statistical references use  $1-p$  in place of  $q$  (which is how  $q$  is calculated). The binomial distribution gives the probability,  $P(n)$ , that  $n$  out of  $N$  objects are A, is given by Eq. (31):

$$P(n) = \frac{N!}{(N-n)!n!} p^n q^{N-n} = \frac{N!}{(N-n)!n!} p^n (1-p)^{N-n} . \quad (31)$$

For this distribution, the mean,  $m$ , is given by Eq. (32):

$$m = pN , \quad (32)$$

and the standard deviation is calculated using Eq. (33):

$$\sigma = \sqrt{mq} = \sqrt{Npq} = \sqrt{Np(1-p)} . \quad (33)$$

To study radioactive decay, a distribution is required that represents a large number of counts and a small probability of success (large  $N$  and small  $p$ ). The Poisson distribution is appropriate for this purpose.

### Poisson distribution

The Poisson distribution is a special case of the binomial distribution given:

1. large number of counts, and
2. small probability of success.

The Poisson distribution, described by Eq. (34), gives the probability,  $P(n)$ , that  $n$  out of  $N$  objects are outcome (A):

$$P(n) = \frac{m^n}{n!} e^{-m} , \quad (34)$$

where  $m$  is the mean of the distribution ( $m = Np$ ). A primary feature of the Poisson distribution is the ease of calculating the standard deviation using Eq. (35):

$$\sigma = \sqrt{m} . \quad (35)$$

For individual measurements, the standard deviation is the square root of the number of counts, ( $N$ ), as given by Eq. (36):

$$\sigma = \sqrt{N}. \quad (36)$$

For large values of  $m$  ( $m > 20$ ), a more appropriate distribution, called the Gaussian distribution, is used.

### Gaussian distribution

The Gaussian (normal, or bell) distribution is used when the sample size is large. An important feature of this distribution is that it uses continuous variables, unlike the Poisson and binomial distributions which use discrete variables. The Gaussian distribution is described by Eq. (37):

$$P(n) = \frac{1}{\sigma\sqrt{2\pi}} e^{-\frac{(x-m)^2}{2\sigma^2}}. \quad (37)$$

For a large number of measurements, the data should follow a Gaussian distribution and yield the mean and standard deviation presented by Eqs. (29) and (30).

### Decision level

An important circumstance involving counting statistics is when low levels of radiation are present (which is often the case, for example, in environmental measurements). When a detector measurement is made at low counts, it must be determined whether the measurement is indicative of anthropogenic radiation or due to fluctuations in the natural background which is also being measured by the radiation-detection system.

The background can be estimated using two approaches. The first is a Poisson approach using Eqs. (29) and (30) for the mean and standard deviation of the measurements and making a judgement as to what multiple of the background measurement indicates a reading that is not due to background radiation. For example, it may be decided that the background mean + 3 standard deviations of the mean is appropriate.

The second, more rigorous approach is to use detection limit statistics. A full discussion is beyond the scope of this chapter, and the user is referred to [Currie1968] and [Chambless1992] for broad discussions of detection limit statistics.

The decision criterion (sometimes called the detection limit,  $L_D$ ) is a value above some critical level ( $L_C$ ) in which there is a quantifiable confidence that, if exceeded, you have actually measured radioactivity. The primary indicator is the critical level ( $L_C$ ), which is defined as the go/nogo value above which a measurement is considered to represent radiation above a blank (or background) sample. The critical level ( $L_C$ ) is defined by Eq. (38):

$$L_C = \sqrt{2}k\sigma_b, \quad (38)$$

where  $k$  is the Gaussian parameter related to area under the curve (sometimes termed "z") and  $\sigma_b$  is the standard deviation of the background radiation. Consider a normal distribution of background counts, a 95% confidence level, and the fact that for a normal distribution, the 95% confidence level occurs at  $k = 1.645$ ; in this case, the critical level is defined as in Eq. (39):

$$L_C = \sqrt{2} \cdot 1.645 \cdot \sigma_b = 2.33\sigma_b. \quad (39)$$

Therefore, the procedure to determine the critical level (the decision criterion) is:

1. Obtain numerous background measurements (for example, 20), spatially and temporally separated, but NOT near contamination or radioactive sources.
2. Determine the mean and standard deviation of the measurements
3. Multiply the standard deviation by 2.33 and add it to the mean to obtain the decision criterion.

For example, if the background-count rate mean is 30 cpm and the standard deviation is 5 cpm, the decision criterion is  $30 \text{ cpm} + 12 \text{ cpm} = 42 \text{ cpm}$ . If a measurement above 42 cpm is obtained, it can be attributed to non-background radiation.

### Particle counting versus spectroscopy

Generally speaking, gas-filled detectors are used for counting applications. In these, ionizing radiation interacts within the detection material to create a pulse that is counted by an electronic counting system. Scintillation and semiconductor detectors can also be used strictly as particle counters as well. In pulse mode, the signal from each interaction is processed individually. In current mode, the electrical signals from individual interactions are averaged together, forming a net current signal. In current mode, all information regarding individual interactions is lost. If the amount of electrical charge collected from each interaction is proportional to the energy deposited by that interaction, then the net current is proportional to the dose rate in the detector material. This mode is used for detectors subjected to very high interaction rates. The output from a particle-counting system will typically be counts per second (cps) or counts per minute (cpm). It is also possible through calibration to convert the pulses counted to dose rate or to integrated dose (Sv/h; Sv). A simple depiction of a particle-counting system is shown in Figure 30. Radiation interacts in the detector and creates pulses. If the pulses are above a discrimination threshold, they are passed to an integrator or counter circuit, and then if being used with a digital display, through an analog-to-digital converter and digital display. In addition, the count rate may be converted to dose rate using a calibrated radiation source and mapping count rate against known dose rate. The important aspect of a particle-counting system is that single values of count (rate) and/or dose (rate) are presented to the user as a function of time. The user does not generally have any direct information about the radioisotope or the activity being measured. To perform radioisotope identification and quantification, spectroscopy is normally used.

Spectroscopy is strictly defined as the identification of a radioisotope using the energy of emission of the decay particles. Spectrometry, on the other hand, is the quantification (i.e., activity determination) of a radioisotope using the intensity of the decay particle signal. For all practical purposes, spectroscopy is used to denote identification and quantification.

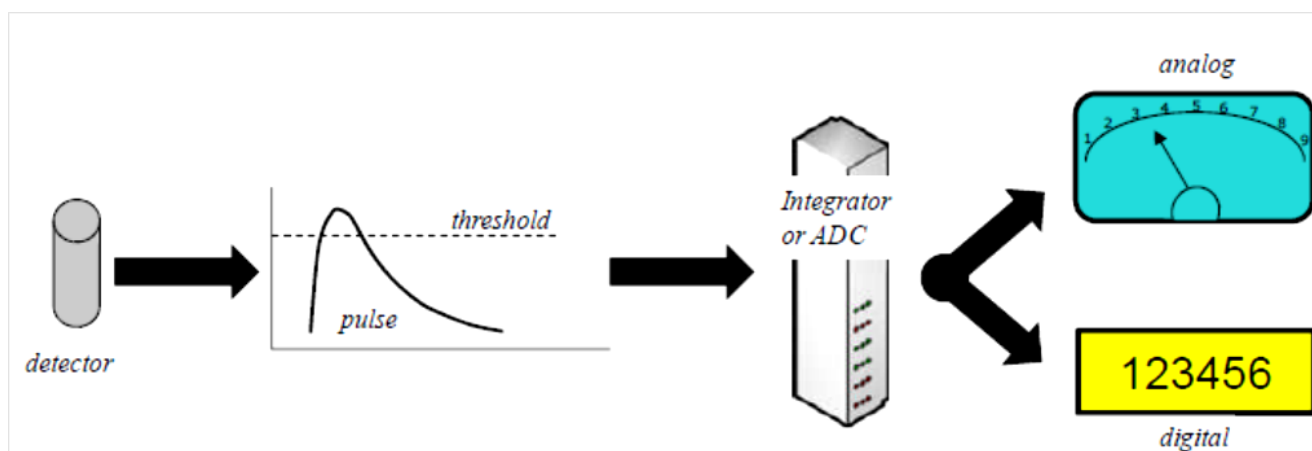


**Figure 30 Simple particle-counting system**

A simple depiction of a spectroscopy system is provided in Figure 31. In the system, radiation is emitted from the source and interacts with a material that responds to radiation with pulse

heights that vary with, and are proportional to, the incident radiation energy. The various pulse heights, which are represented by a range of voltages, are processed in a multi-channel analyzer (MCA). The purpose of the multi-channel analyzer is to process the pulse heights into bins that are determined by memory allocation units (typically called channels). For example, if the pulses are amplified to have a maximum voltage of 10 volts and there are 1024 memory locations, then each memory location is 9.8 mV wide. The first channel is 0–9.8 mV, the second is 9.8–19.6 mV, and so on. It is normal to use a threshold discriminator to eliminate noise that would otherwise be counted as real events, and event logging can be controlled by a lower-level discriminator (LLD) and an upper-level discriminator (ULD). Events that fall within the window will be processed by the multi-channel analyzer. Each pulse is counted within its respective bin (analog-to-digital conversion) and as more counts accumulate, a spectrum is produced which is displayed with counts on the y-axis and channel number on the x-axis. The spectrum produced is characteristic of the radioisotope, and therefore identification is possible.

It can be readily seen that spectroscopy systems can also be used for particle counting. It is not unusual for portable spectroscopy systems to use a scintillation detector for both dose rate and spectral ID functions.

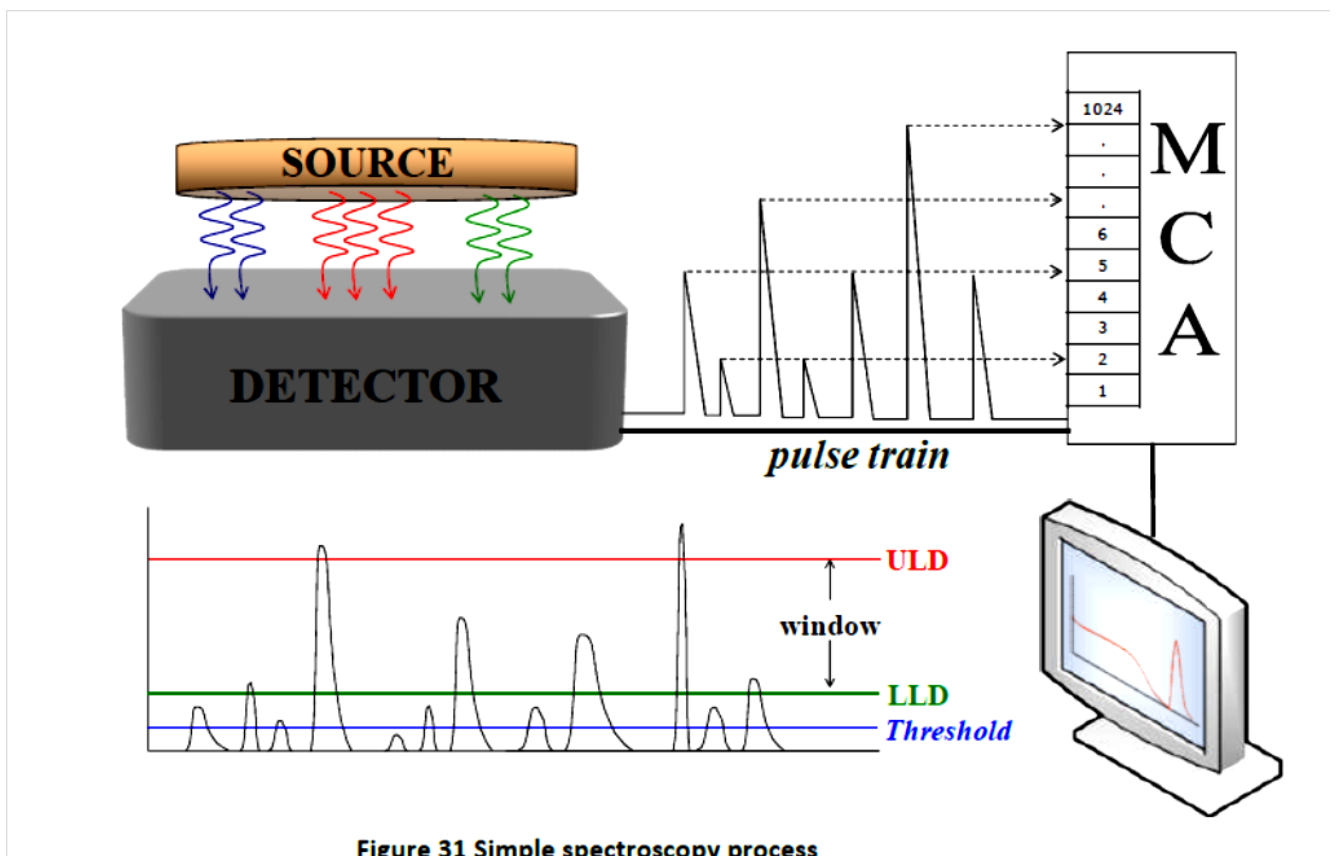


**Figure 31 Simple spectroscopy process**

Spectrometer systems can be summarized by the following steps:

- When a gamma ray interacts with a detector, a pulse is produced. For gamma spectroscopy, the pulses are produced when gamma rays interacting in the detector create electrons through the photoelectric effect, Compton scattering, or pair production.
- The size of the pulse reflects the energy deposited in the detector.
- An analog-to-digital converter (ADC) sorts the pulses into bins according to size.
- The results of the ADC analysis are displayed. The display, a plot of number of pulses (counts) versus pulse size (channel number), is referred to as a spectrum.
- If a large number of pulses have a similar size, they are sorted into adjacent channels and appear on the spectrum as a peak. A peak represents a number of pulses of similar size.

In an ideal spectrometer system, a peak would be produced that corresponds to the photopeak energy(ies) of the radioisotopes being measured, and the peak would be very narrow (approaching a delta function). In reality, a number of processes can occur within (a) the detector and (b) the shielding that is often present around the system. These processes generally produce undesirable effects in the spectrum, and therefore attempts are made to minimize the impact of these effects. The important aspect of that energy deposited in the detector (which is what the spectrometer measures and displays) is simply the energy in minus the energy out ( $E_{\text{dep}} = E_{\text{in}} - E_{\text{out}}$ ).

### Detector Interactions

The primary interactions of importance in the detector are as follows:

- **Photopeak.** A photopeak is generated in the spectrum when gamma rays deposit all their original energy in the detector through the photoelectric (PE) interaction. This is the primary signature in a gamma spectroscopy system and is used both to identify and to quantify the radiation.
- **X-Ray Escape Peak.** An X-ray escape peak is generated in the spectrum when gamma rays deposit all their original energy in the detector through the photoelectric effect (PE), except for the energy of an iodine or germanium X-ray that leaves the detector.
- **Compton Continuum.** The Compton continuum is produced when gamma rays interact in the detector through Compton scattering (CS) and then leave the detector.
- **Double Escape Peak.** The double escape peak is produced when gamma rays interact in the detector through pair production (PP) and two 511-keV annihilation photons escape the detector.
- **Single Escape Peak.** The single escape peak is produced when gamma rays interact in the detector through pair production (PP) and one 511-keV annihilation photon escapes the detector.

### Shield interactions

If there is significant shielding around a spectroscopy system (for example, environmental radioactivity gamma spectroscopy systems often use a scintillator or semiconductor detection system in a lead shield, which is sometimes called a “castle”), then interaction occurring in the shield can produce scattered or secondary radiation in the detector that will be logged in the spectrum.

- **Lead X-Rays.** Lead X-rays are generated in the spectrum when gamma rays interact with a lead shield through the photoelectric effect (PE) and the resulting X-rays produced in the shield interact with the detector. The lead X-rays are around an energy level of 75 keV (73, 75, and 85 keV). If the shield were made of steel, iron X-rays might be seen, but these would be of such low energy that they would probably go undetected.
- **Backscatter Peak.** A backscatter peak is generated in the spectrum when gamma rays interact with the shield through Compton scattering (CS) and the 180°-scattered gamma rays interact with the detector.
- **Annihilation Peak.** An annihilation peak is generated in the spectrum when gamma rays interact with the shield through pair production (PP) and the resulting annihilation photons at 511 keV interact with the detector.
- **Summation Peak.** A summation peak occurs when two gamma rays deposit all their energy in the detector at the same time. The energy of this peak is the sum of the two photopeak energies.
- **Bremsstrahlung.** Bremsstrahlung (“braking” radiation) is observed in the spectrum when high-energy beta particles are produced and slow down in the sample.

### 64.4.1.2 Gas-Based Detectors

The various operating regions for gas-filled detectors are shown in Figure 32.

At low applied voltage, below the ion-saturation region, there is a region called the recombination region. Many electrons and ions produced in the gas recombine because the voltage applied between cathode and anode is not large enough to collect all the electrons. This region is not useful for counting radiation.

The next region is the ion-saturation region. The potential difference is sufficient to collect all freed electrons. A detector working in the saturation region is called an ionization chamber, and its output is proportional to the deposited radiation energy. Internal or thin-window ionization chambers are used as alpha-particle and fission-fragment detectors.

The next important region is the proportional region. The applied voltage is large enough that the electrons freed by the initial radiation are accelerated, so that they in turn ionize additional atoms or molecules (secondary ionization) to free more electrons. This electron multiplication generates an avalanche toward the anode for each primary electron that was freed. The applied voltage domain is called the proportional region because each avalanche is characterized by the same electron multiplication at a given applied voltage. The output signal is directly proportional to the deposited energy, although each pulse is many times larger than in the ionization region. The limited proportional region is at slightly higher applied voltage, and the proportionality of the output signal to the deposited energy no longer applies. Amplification of the greater deposited energy reaches its limit while that for the lesser deposited energy continues to increase. This region is usually avoided as a detection region.

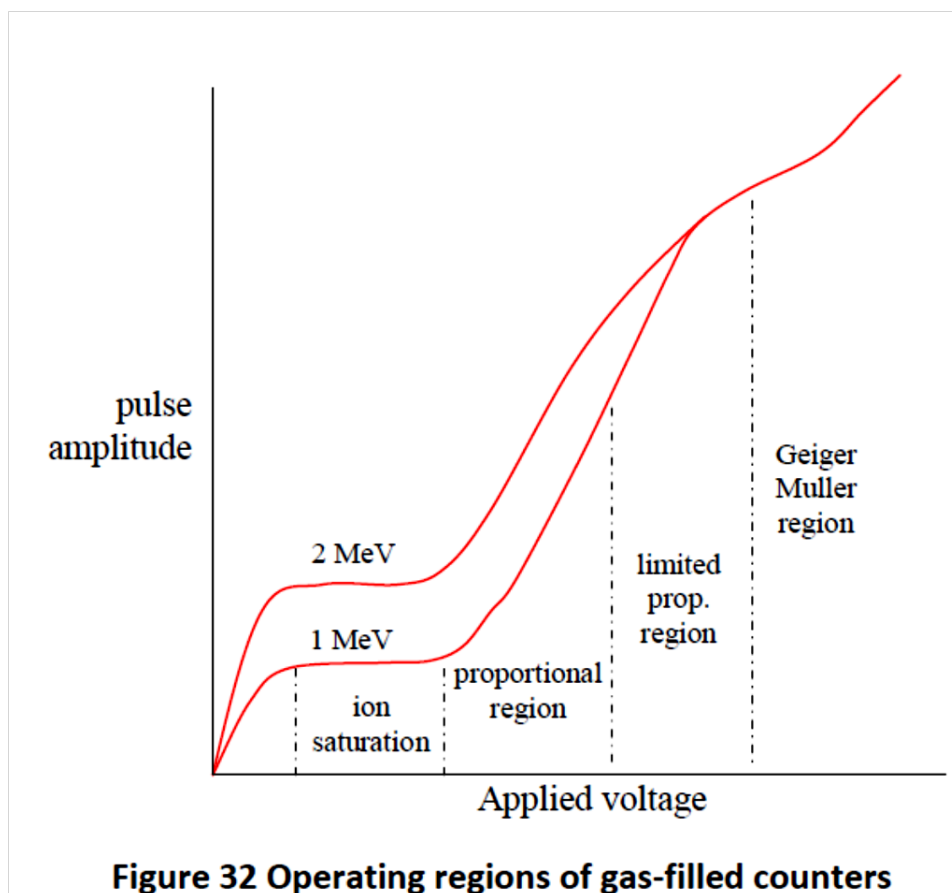


**Figure 32 Operating regions of gas-filled counters**

The next usable region is the Geiger-Müller region, which is characterized by an applied voltage high enough that any deposited energy produces sufficient secondary electrons to discharge the entire counting gas. A linear amplifier is no longer needed because there is sufficient

electron production to generate a usable signal. In this region, it is not possible to distinguish between small and large depositions of energy. At higher applied voltages, electrical discharge occurs between the electrodes. This voltage region, called the continuous-discharge region, has been used for some purposes, but generally is avoided because the discharge can disable the detector.

Details about the two most common types of radiation detectors used in nuclear operations, namely the proportional counter and the Geiger-Müller (GM) counter, are discussed in the following sections.

### **Proportional counters**

The proportional counter is a type of gas-filled detector introduced in the late 1940s. These counters are similar to GM counters in that they rely on gas multiplication to generate a signal. The primary difference between a GM and a proportional counter is that a GM counter produces a pulse when radiation interacts with it, irrespective of incident particle type or energy. A proportional counter generates different-size pulses that are dependent on the incident particle energy. It is, therefore, possible to distinguish between alpha and beta particles using a proportional counter, or between two different energies. Although proportional counters do not have the resolution required to perform spectroscopy, they are extremely useful for discriminating between alpha and beta particles.

The primary use of proportional counters in the nuclear industry is therefore in alpha-beta counters (for example, swipe counters), where it is desirable to discriminate between alpha and beta particles.

### **Geiger-Müller counters**

Geiger-Müller (GM) counters were invented by H. Geiger and E.W. Müller in 1928 and are used to detect radioactive particles ( $\alpha$  and  $\beta$ ) and rays ( $\gamma$  and  $x$ ). A GM tube usually consists of an airtight metal cylinder closed at both ends and filled with a gas that is easily ionized (usually neon, argon, or a halogen). One end consists of a "window" made of a thin material, mica, which allows alpha particles to enter (these particles can be shielded easily). A wire, which runs lengthwise down the centre of the tube, is positively charged with a relatively high voltage and acts as an anode. The tube itself acts as the cathode. The anode and cathode are connected to an electric circuit that maintains the high voltage between them.

When the radiation enters the GM tube, it will ionize some of the atoms in the gas. Because of the large electric field created between the anode and the cathode, the resulting positive ions and negative electrons accelerate toward the cathode and the anode. Electrons move or drift through the gas at a speed of about  $10^4$  m/s, which is about  $10^4$  times faster than the positive ions move. The electrons are collected a few microseconds after they are created, while the positive ions take a few milliseconds to travel to the cathode. As the electrons travel toward the anode, they ionize other atoms, producing a cascade of electrons called a gas multiplication or avalanche. The multiplication factor is typically  $10^6$  to  $10^8$ . The resulting discharge current causes the voltage between the anode and cathode to drop. The counter (electric circuit) detects this voltage drop and recognizes it as a signal of a particle's presence. There are additional discharges triggered by UV photons liberated in the ionization process that start avalanches away from the original ionization site. These short-lived discharges are called GM discharges and do not affect performance. Once the avalanche of electrons is started, it must be stopped (quenched) because the positive ions may still have enough energy to start a new cascade. One early method was external quenching, which was done electronically by quickly ramping down the voltage in the GM tube after a particle was detected. This meant that any more electrons or positive ions created were not accelerated towards the anode or cathode.

The electrons and ions would recombine and no more signals would be produced. The modern method is called internal quenching. A small concentration of a polyatomic gas (organic or halogen) is added to the gas in the GM tube. The quenching gas is selected to have a lower

ionization potential ( $\sim 10$  eV) than the fill gas (26.4 eV). When the positive ions collide with the molecules of the quenching gas, they are slowed or absorbed by giving their energy to the quenching molecule. They break down the gas molecules in the process (dissociation) instead of ionizing the molecule. Any quenching molecule that may be accelerated to the cathode dissociates upon impact, producing no signal. If organic molecules are used, GM tubes must be replaced periodically because they permanently break down over time (about one billion counts). GM tubes can also use a halogen molecule, which naturally recombines after breaking apart.

Different Geiger-Müller (GM) tubes have varying operating characteristics due to differences in their fabrication. Consequently, each GM counter has a different high voltage that must be applied to obtain optimal performance from the instrument. If a source of ionizing radiation is positioned beneath a tube and the voltage of the GM tube is ramped up (slowly increased by small intervals) from zero, the tube does not start counting right away. The tube must reach the starting voltage where the electron "avalanche" can begin to produce a signal. As the voltage is increased beyond that point, the counting rate increases quickly before it stabilizes. Where the stabilization begins is a region commonly referred to as the knee, or threshold value. Past the knee, further increases in voltage produce only small increases in the count rate. This region is the plateau we are seeking. Determining the optimal operating voltage starts with identifying the plateau. The end of the plateau is found when increasing the voltage produces a second large rise in count rate. This last region is called the discharge region. To preserve the life of the tube, the operating voltage is selected near the middle, but towards the lower half of the plateau (closer to the knee). If a GM tube operates near the discharge region and there is a change in its performance, the tube will operate in a "continuous-discharge" mode, which can damage it. Figure 33 shows a typical plateau shape for a GM tube. Above approximately 1100 volts, the tube enters the continuous-discharge region.

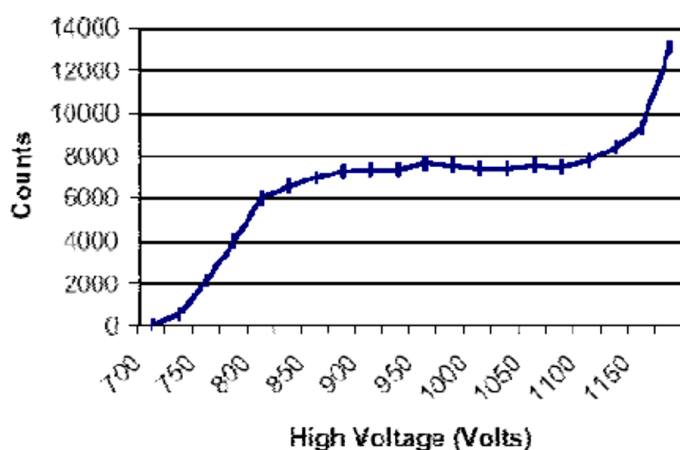


Figure 33 GM counter sample plateau

For hand-held radiation detection instrumentation commonly used in nuclear power operations, GM counters are the most common type of detectors; they can be found in radiation survey instruments, contamination detectors (e.g. pancake detectors), and in personal dosimeters.

### 64.4.1.3 Scintillation-Based Detectors

Scintillation detectors are the most commonly used detectors for field applications because they do not require bulky cooling strategies. There are two stages in a scintillation detector unit: the scintillator and the photomultiplier. The scintillation detection process is outlined as follows:

1. Ionizing radiation deposits energy in the scintillator.
2. A portion of the absorbed energy causes electrons in the scintillator to move to a higher energy level.
3. A portion of these electrons immediately fall back down to a lower energy level. As they do, they emit a photon of light. Collectively, the photons of light form a flash, or scintillation.
4. Scintillations are converted into an electronic pulse by a photomultiplier tube (PMT). The brighter the scintillation, the larger is the pulse.

One particle of radiation (alpha, beta, gamma ray, X-ray, or neutron) interacting in the scintillator results in one scintillation (flash) of light and therefore one pulse. The greater the energy transferred to the scintillator, the greater is the number of excited electrons and the greater is the number of photons of light emitted in the scintillation. In other words, the greater the deposition of energy, the brighter is the flash of light and the larger is the pulse.

#### Scintillators

Scintillators are categorized as fluors as opposed to phosphors. Fluorescence has a lifetime in the excited state from  $10^{-7}$  to  $10^{-10}$  s, whereas phosphorescence has a lifetime in the excited state of  $10^{-3}$  s or longer. It is desirable to have a material with a short excited-state lifetime to achieve a shorter resolving time. Scintillation materials can be classified as solid, liquid, or gas, as detailed below.

- **Gas scintillators:** The radiation energy excites the electrons of the gas molecules, and light photons are emitted when the electrons de-excite. Because these photons are typically in the UV range, a PMT must be chosen that is UV-sensitive. Gas scintillators are extremely fast, but their light output is poor (low efficiency). The most extensively investigated gas scintillators use the noble gases xenon and helium.
- **Liquid scintillators:** Liquid scintillators consist of an organic scintillator dissolved in an appropriate solvent. Normally, the sample to be counted is also dissolved in the scintillator. The advantage of this arrangement is a high counting efficiency for beta particles, even for betas of the lowest energies (e.g.,  $^3\text{H}$ ). In some cases, the liquid scintillator is used to measure external radiation sources (e.g., cosmic rays). In such cases, the liquid scintillator is packaged and treated as if it were a solid crystal. One advantage of liquid scintillators is the fact that extremely large detectors can be constructed. This is the basis of the commonly found liquid scintillation counter (LSC).
- **Solid scintillators:** This is the most common type of material used for gamma spectroscopy. Aside from their physical form, scintillators may also be classified chemically as organic or inorganic:
  - **Inorganic:** gas scintillators (e.g., He, Xe), inorganic crystals (e.g., NaI, ZnS, CsI, LiI, BGO), glass scintillators.
  - **Organic:** liquid scintillators (e.g., PPO, Bis-MSB, POPOP), organic crystals (e.g., anthracene, stilbene), plastic scintillators.

Two extremely common solid scintillation materials used in the nuclear industry are ZnS and NaI, which are discussed below.

#### Zinc Sulfide

Zinc sulfide is often doped (activated) with silver in the form of ZnS(Ag). It is typically used in

alpha detectors and for heavy-particle detection.

In the past, ZnS was combined with  $^{226}\text{Ra}$  to form radium paint, which was used to paint clock and aircraft dials so that they would “glow in the dark”. ZnS is fairly opaque and has high scintillation efficiency (~40%) with a long decay time.

### *Sodium Iodide*

Sodium iodide is an alkali halide. Its use as a scintillator dates back to the late 1940s, and it is often activated using thallium in the form NaI(Tl). Thallium is added in trace amounts, at a level of approximately one atom in one thousand. NaI is used primarily for photon (X- or gamma) radiation detection. NaI has a high light yield with a scintillation efficiency of approximately 12%. In other words, approximately 12% of the gamma-ray energy deposited in the crystal will be emitted as light. The average energy of a photon emitted by NaI activated with thallium is 3 eV (which has a wavelength of approximately 415 nm, a wavelength readily detected by most photomultiplier tubes). For a hypothetical 1-MeV gamma ray that deposits all its energy in the NaI scintillator, one would expect 120 keV (12% of 1 MeV) to be emitted as light. With an average photon energy of 3 eV, this would be equivalent to 40,000 photons of light. NaI crystals can be grown to relatively large sizes for application in airborne/carborne spectroscopy systems or portal monitors.

Scintillators produce photons of light in the UV to near-visible region and require photomultiplier tubes (PMT) as part of the detection process (Figure 26).

### **Photomultiplier tubes (PMT)**

A photomultiplier tube is used to detect very weak light signals. It is a photoemissive device in which the absorption of a photon results in the emission of an electron. It works by amplifying electrons generated by a photocathode impinged upon by a UV or near-visible light source.

Photomultipliers acquire light through a glass or quartz window that covers the photosensitive surface (photocathode), which then releases electrons that are multiplied by electrodes known as metal channel dynodes. At the end of the dynode chain is an anode or collection electrode.

The current flowing from the anode to ground is directly proportional to the photoelectron flux generated by the photocathode.

Electrons emitted by the photocathode are accelerated toward the dynode chain, which may contain in excess of 14 elements. Focussing electrodes are usually present to ensure that photoelectrons emitted near the edges of the photocathode will be likely to land on the first dynode. Upon impacting the first dynode, a photoelectron will invoke the release of additional electrons that are accelerated toward the next dynode. Note that photomultipliers produce a signal even in the absence of light due to dark current arising from thermal emissions of electrons from the photocathode, leakage current between dynodes, or background high-energy radiation.

#### **64.4.1.4 Semiconductor-Based Detectors**

Electrons in a solid can occupy some energy levels, but not others. These levels are not single discrete energies, but ranges of energies called bands. The highest energy band occupied by electrons is referred to as the valence band. The conduction band is of even higher energy than the valence band, but it is normally nearly void of electrons. The range of energies between the valence and conduction bands (forbidden to electrons) is called the band gap (forbidden band). When the valence band is full,

the electrons in the band are essentially fixed in place, i.e., tied to a particular site in the solid. Such a material will not conduct electricity unless electrons in the valence band can be given the energy to reach the conduction band where they would be free to move. If the valence band is not completely full, the electrons in it are free to move, and the solid will conduct electricity.

Solids can be divided into the following three categories:

- **Conductor.** A material in which the valence band is partly, but not completely, full.
- **Insulator.** A material in which the valence is completely full and for which the band gap is greater than 3–5 electron volts.
- **Semiconductor.** A material for which the valence band is completely full and for which the band gap is less than 3–5 electron volts. Semiconductor materials will not normally conduct electricity. However, the band gap is small enough that it is possible to lift enough electrons up into the conduction band for electrical conduction to occur.

When alpha or beta particles enter a semiconductor detector, they create positive and negative ion pairs (electron-hole pairs). Under the influence of an applied electric field, the positive members of the ion pairs (called holes) and the negative members of the ion pairs (electrons) move to the cathode and anode respectively. The result is an electronic pulse.

In the case of gamma detection, the gamma rays must first interact with the solid to produce secondary electrons (through the photoelectric effect, pair production, or Compton scattering). The secondary electrons then move through the detector and create electron-hole pairs which are collected at the electrodes. A semiconductor detector is often considered to be the solid equivalent of an ionization chamber.

Germanium is one of the most common semiconductor detector materials. A very common semiconductor detector used for environmental investigation is the high-purity germanium detector (HPGe). This detector needs to be cooled to near-liquid-nitrogen temperatures ( $\sim 77^{\circ}\text{K}$ ) to operate. This type of spectrometer is normally found in a health physics laboratory and is used when high-resolution gamma spectroscopy is required. In general, for higher efficiency, scintillation detectors are used because they tend to be much larger-volume detectors, whereas semiconductor detectors are used when higher resolution is required. A typical commercial HPGe spectroscopy system is shown in Figure 34. At the bottom of Figure 34, the details of the opened lead castle can be seen, with the cylindrical HPGe detector element in the castle. The castle is designed to hold cylindrical geometries. For environmental sample analysis, it is very common to use a Marinelli beaker, which is a one-litre geometric design which covers the HPGe detector element for maximum efficiency.

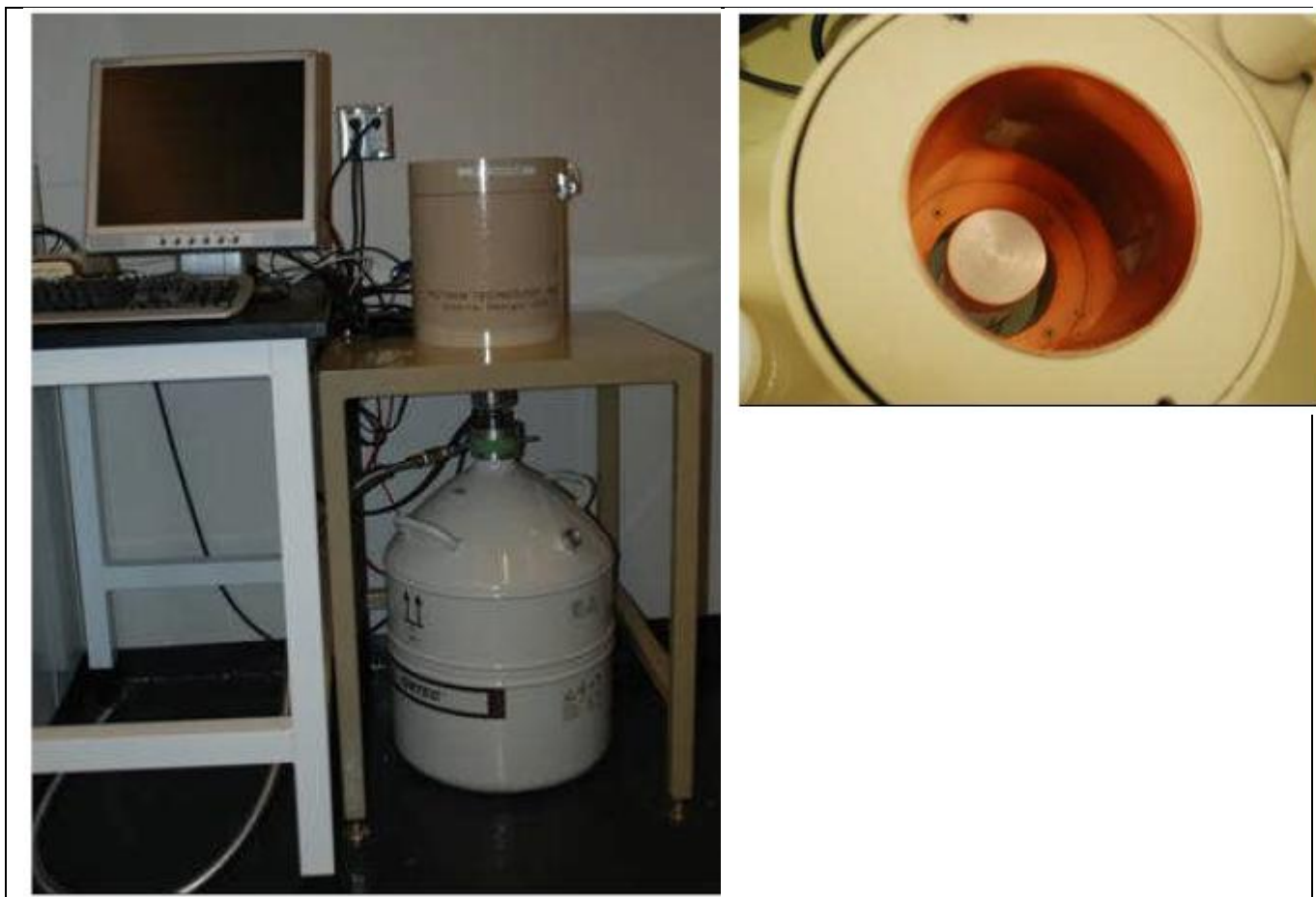


Figure 34 Commercial HPGe system (left) and detail of lead castle (right)

#### 64.4.1.5 Portable Instrumentation

All nuclear facilities make use of various types of portable instrumentation. Portable or handheld instruments can be fabricated based on any detector technology, although some are more suited than others to the mission. Broad categories of portable instrumentation include: (a) general-purpose survey meter, (b) area contamination meter, (c) neutron meter, and (d) portable spectrometer.

##### General-purpose survey meter

A general-purpose survey meter (GPSM) is almost always a gamma detection system using scintillator, GM, or proportional detectors. This type of instrument is often called a gamma survey meter and is used to detect and quantify ambient gamma-radiation fields. The instruments have wide response to both incident photon energy and direction and provide readings

in counts per minute, counts per second, or both. If the instruments are calibrated, readings are in dose rate ( $\mu\text{r}$ , mSv, or Gy per hour) and if they have an integration function, in total dose.

##### Area contamination meter

An area contamination meter (ACM) is an instrument used to detect and quantify alpha or beta/gamma surface contamination. It must be capable of detecting small quantities of radioactive material, but is not capable of determining whether contamination is fixed to a surface or loose. An ACM must be held very close to the surface to ensure accurate readings; however, there are no suitable portable instruments for detecting small quantities of tritium ( $^3\text{H}$ ). A common type of area contamination detector is the pancake probe (see Figure 35), which is a relatively small-area thin-window GM tube that is very useful for frisking personnel for contamination.

ACMs are usually based on a GM or other gas-filled tube. A common alpha detector uses a ZnS screen to convert alpha-particle interactions to UV photons, which are then detected by a photomultiplier tube. In this case, no gas is required.

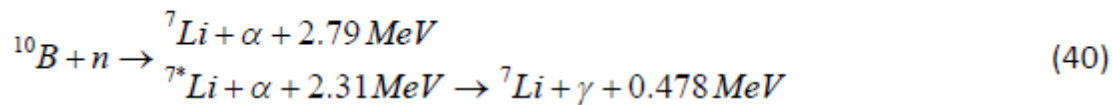


**Figure 35 Portable contamination meter with pancake probe**

##### Neutron meter

Portable neutron meters are commonly proportional counters which use neutron detection reactions depending on the filling gas and generate charged particles. Two common reactions (and hence,

detection-tube types) are  $\text{BF}_3$ - and  $^3\text{He}$ -based respectively according to the reactions in Eqs. (40) and (41):



These reactions are most likely to occur at low neutron energies, and therefore the counters are wrapped in hydrogenous (neutron-moderating) material. Detector-response functions can be altered using various techniques, such as perforated cadmium sleeves, so that a flat response over a wide energy range of incident neutrons can be achieved. There are also a variety of physical configurations, such as cylindrical, spherical, or even rectangular. Portable neutron detectors have historically been called “neutron REM-meters”, “long counters”, “Bonner spheres” (see Figure 36), “REM balls”, or by other names, depending on their origin and other physical characteristics.



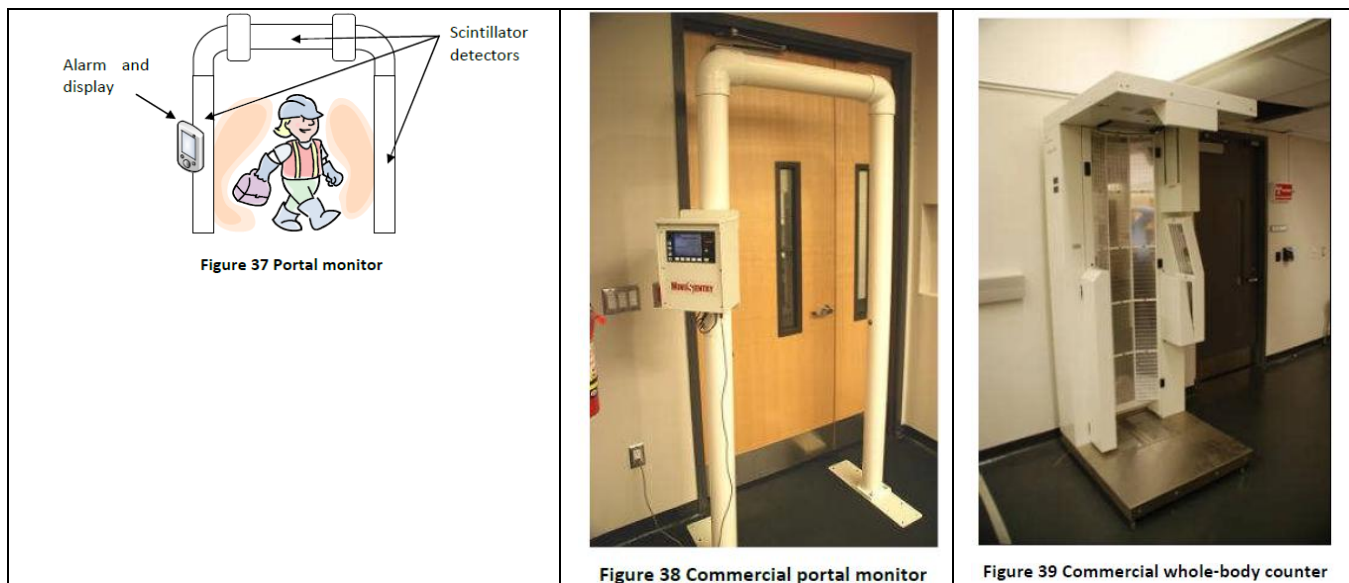
Figure 36 Neutron Bonner sphere

### Portable gamma spectrometer

The possibility of portable gamma spectroscopy became a reality as electronics, processors, microprocessors, and computers in general became smaller. Portable gamma spectrometers typically use scintillation-type detectors with small photomultiplier tubes. Some “portable” spectroscopy systems in the past have used semiconductor detectors; however, these are actually quite bulky and heavy, and their true portability is doubtful. Although portable spectroscopy generally cannot give the same performance as a laboratory system, these instruments can perform simplified radioisotope identification and typically offer count, count rate, dose, and dose rate functions.

#### 64.4.1.6 Specialized Detectors

A number of specialized detector systems are commonly used in nuclear facilities to process personnel for potential internal or external contamination. These detection systems include portal monitors, whole-body counters, hand/cuff/foot counters, and thyroid counters.



#### 64.4.1.7 Dosimetry Techniques

This section will consider thermo-luminescent dosimeters (TLD, as dosimeter of record), electronic personal dosimeters (EPD), and liquid scintillation counting (LSC) for bioassay dose estimation.

##### Thermo-luminescent dosimetry (TLD)

Thermo-luminescence (TL) is a thermally stimulated phenomenon; that is, material absorbs energy from ionizing radiation or light. This energy is stored, and part of it is released in the form of light when the material is heated. This phenomenon was first formally reported by Robert Boyle in his address to the Royal Society of London on October 28, 1663, when he described, "*observation of a glimmering light when he heated a diamond in the dark*" [Uchrin1988]. In the 1950s, research suggested the possibility of applications of thermoluminescent properties, including radiation dosimetry, which led to development of more sophisticated TL phosphors and commercially available TL readers, making thermo-luminescent dosimetry (TLD) for ionizing radiation widely possible in the 1960s.

The main advantages of thermo-luminescent dosimeters (TLD) are their applicability over a wide dose range ( $10^{-6}$  –  $10^5$  Gy), their usability for various types of radiation including mixed fields, and their small physical size, which enables them to be readily worn as personal dosimeters.

One of the fundamental disadvantages of TLDs is that the act of reading the dosimeter effectively "zeros" the dosimeter (through a process called annealing), which means that there is no permanent record of the dose.

The thermo-luminescence mechanism is highly complex and based on solid-state physics. TL materials are insulators with a crystalline structure. In a perfect crystal lattice, the atomic electronic levels are broadened into a series of continuous bands (the conduction band) separated by a several electron volt-wide "forbidden" energy region from the highest filled band, called the valence band. Usually, the conduction band is empty, and the valence band is filled. Crystals always contain

imperfections: thermal or intrinsic defects, extrinsic defects, or substitutional impurities and radiation-induced defects [Uchrin1988]. The presence of lattice imperfections and impurities is essential for thermo-luminescent processes. The energy levels presented by them are situated in the forbidden region and act as traps or recombination centres for electrons and holes created in the crystal due to an excitation from interaction with ionizing radiation.

Electrons and holes will remain in traps provided that they do not acquire sufficient energy to escape. The number of trapped states is directly proportional to the number of ionizing radiation interactions with the material and hence the total dose. When the temperature of the material is raised, the trapped charge carriers are given sufficient energy to escape from their traps to the conduction band, where they recombine at a luminescence centre, and the excess energy is radiated as visible or UV light, which is recorded by a photomultiplier tube (see Section 4.3.2). The TLD reader unit provides a correspondence between the signal generated from the measured light and the radiation exposure of the TL material.

Reading a TLD chip is relatively simple. The TL material is heated from the ambient temperature up to 300°C–400°C, and the emitted light is collected and measured quantitatively. The TLD reader consists of four components: (i) heating unit, (ii) light collection and detection system (PMT), (iii) signal measuring system, and (iv) data recording system. The emission of light from heated TLD material is often called a “glow”, and the resulting spectrum from heating the material to release the traps is called a “glow curve”. A typical glow curve obtained from a Harshaw model 3500 TLD reader for LiF TLD material irradiated to 500  $\mu$ Sv total dose from a 1 Ci  $^{137}\text{Cs}$  irradiator is depicted in Figure 40. The portion of the curve corresponding to the delivered dose is denoted by the region of interest marked with vertical lines.

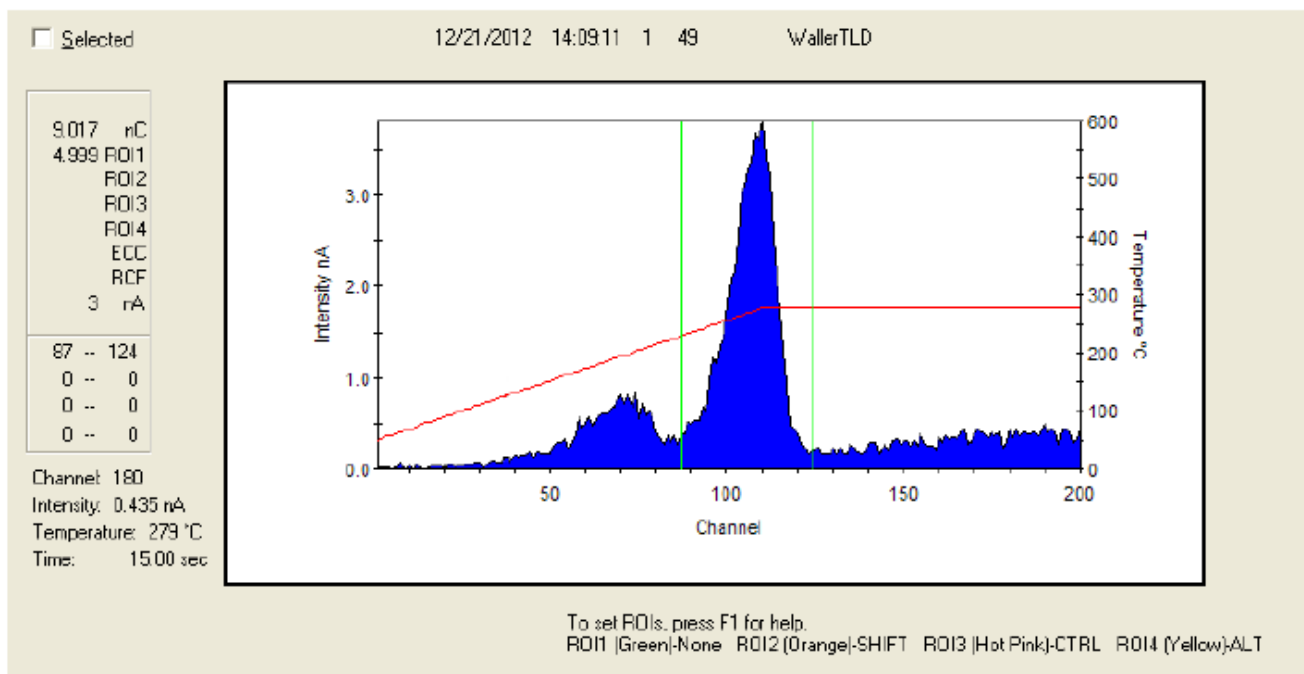


**Figure 40 TLD glow curve from irradiated LiF chip**

A variety of physical and chemical forms of thermo-luminescent dosimeters are used for different radiations and dose ranges. For example, physical forms of TLDs can include chips, disks, powders, and rods; a subset of materials used as dosimeters include LiF,  $\text{Li}_2\text{B}_4\text{O}_7$ ,  $\text{CaF}_2$ ,  $\text{CaSO}_4$ , and  $\text{Al}_2\text{O}_3$ . TLDs are characterized by their dose-response properties, energy dependence,

sensitivity, and fading characteristics (fading is unintentional loss of stored signal due to thermal or optical release of traps). The observed glow curve from reading TLDs may be affected by chemo-luminescence (luminescence due to chemical reactions from material impurities) and tribo-luminescence (luminescence caused by mechanical effects in material preparation). These effects can be greatly reduced by inert gas (typically N<sub>2</sub>) flushing. A commercial TLD reader and LiF chips are shown in Figure 41.



**Figure 41 Commercial TLD reader (top) and tray of LiF chips (bottom)**

The TLD is the dosimeter of record for nuclear energy workers (NEW) in Canada (National Dose Registry, Radiation Protection Bureau, Health Canada), as it is in most countries world-wide. All nuclear energy workers in Canada wear TLD dosimeters if they are working around sources of radiation exposure and as directed by the health physics department.

#### **Electronic personal dosimeter (EPD)**

An electronic personal dosimeter (EPD) is a detector calibrated to provide dose rate and dose readings in real time. The readings may be present on a display directly on the dosimeter,

stored for later retrieval, or transmitted to a base station. The primary advantage of an electronic personal dosimeter is that it can be set with alarm points to warn the user (through audible and visual alarms) in real time if a dose or dose rate is being exceeded. This makes it a very useful tool for ALARA adherence. Key features of EPDs include: small size, light weight, fast response, continuous update and display, and timer/stay time functions. EPDs are generally made from small GM tube or semiconductor detectors, and although the most common are sensitive to X- and gamma radiation, some have neutron-detection capabilities. Although EPDs do not provide a legal dose of record, they are often worn in conjunction with TLDs by personnel working in nuclear-facility radiation environments, especially in nonhomogeneous fields or in areas where exposure may be in excess of action or regulatory limits.

### Liquid scintillation counting (LSC)

Liquid scintillation counting (LSC) is a radioanalytical technique developed in the 1950s and defined by incorporation of a radioisotope analyte into a scintillating liquid. It is a very sensitive and widely used technique for detection and quantification of radioactivity and is applicable to most forms of nuclear decay emissions (alpha and beta particles, electron capture, and gamma-ray-emitting radionuclides).

Consider the case of a beta-emitting radioisotope in a liquid scintillation material. The beta particle dissipates energy by collisions in the liquid, and the energy is absorbed by the medium in three forms: heat, ionization, and excitation of the molecules in the solution. Excitation of the solution molecules is the mechanism of the liquid scintillation technique. Facilitation of efficient transfer of energy between beta particles and the solution is accomplished using a solvent material and a scintillation solute solution (together called a “cocktail”). The scintillation solute is a fluor, and excited solvent molecules can transfer energy to one another and also to the solute. An excited solvent molecule creates an excited state in the solute, and as the excited orbital electrons of the solute molecule return to the ground state, a photon of UV or nearvisible light is generated, which can be detected by a photomultiplier tube. The intensity of light from the scintillation process is proportional to the initial energy of the beta particle. The detection process for beta decay is summarized in Figure 42.

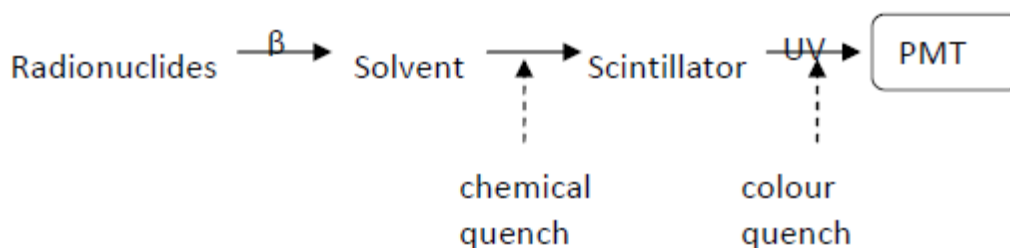


**Figure 42 LSC detection process**

The counting efficiency of the solvent-scintillator system is affected by many different factors that may reduce detection efficiency. Two dominant factors are: (i) chemical quenching (sometimes called impurity quenching), which causes energy losses in the transfer from solvent to solute, and (ii) colour quenching, which is the attenuation of UV light photons in the solution. Both quench factors can be compensated for through calibration. Other effects that may degrade LSC performance include: (a) thermionic effects, which are noise pulses that are extraneous to the true signal, yet resemble electronic pulses resulting from nuclear decay events; (b) photoluminescence, which results in activation of the cocktail or vial by ultraviolet light, which can occur by exposure to sunlight (LSCs rely on light-tight counting chambers); and (c) static electricity, which is a very common source of counting interference due to buildup and

subsequent discharge of static electricity on LSC vials.

The electronic process of light detection and pulse generation in an LSC analyzer is depicted in Figure 43. In most scintillation counters, two photomultiplier tubes collect the total light produced within the scintillation vial that either (a) falls directly onto the two photocathodes or (b) is reflected onto each photocathode by a reflector centrally mounted between the two PMTs. Radioactive decay events produce approximately 10 photons per keV of energy. Beta decay yielding a multiplicity of photons will stimulate both PMTs at the same instant in time, and the signal from each PMT is fed into a summing circuit which produces an output only if the two signals occur simultaneously, which is called coincidence. Because electrical noise from the PMTs is produced randomly over time, it occurs at a sufficiently low rate to be excluded by the coincidence circuit (below the equivalent of 1 keV). The sample in the counting chamber and the PMTs are surrounded by lead, typically about 5 cm in all directions, which generally reduces the background radiation to low levels.

The output from the analog-to-digital converter is processed with a spectrum analyzer calibrated in keV, and regions between 0 and 2000 keV are used for sample analysis. For example, the region of interest for  $^3\text{H}$  is 0–18.6 keV ( $^3\text{H}$  maximum beta energy = 18.6 keV) and for  $^{14}\text{C}$  is 0–156 keV ( $^{14}\text{C}$  maximum beta energy = 156 keV).

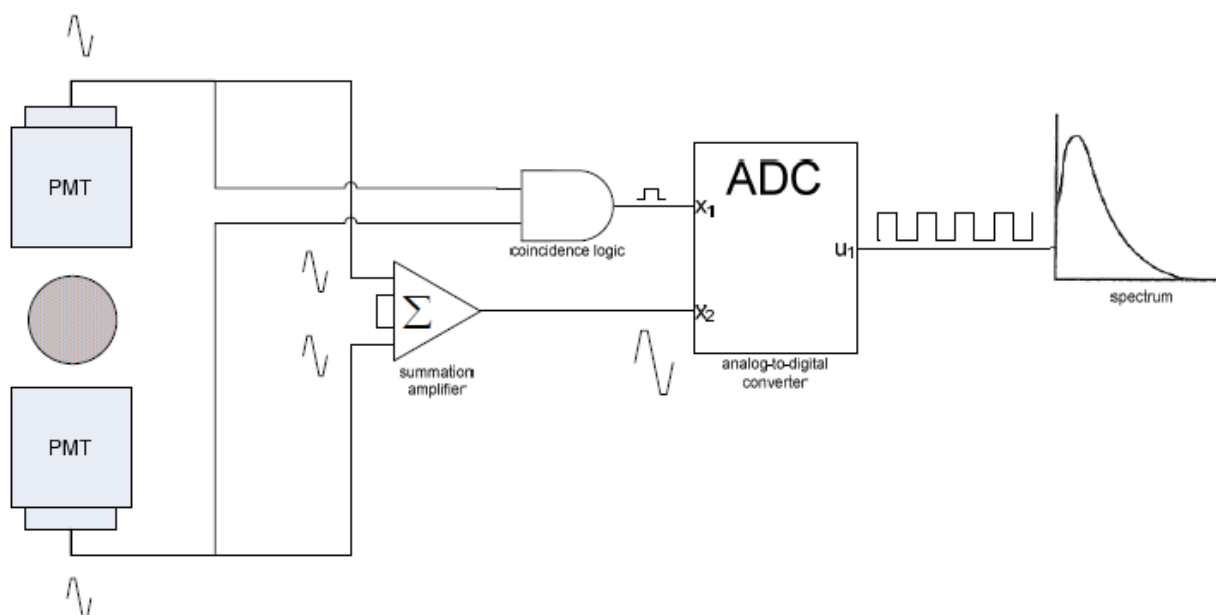


**Figure 43 LSC electronics**

Liquid scintillation counting is used in the nuclear industry for swipe analysis, environmental sample analysis, and urine (bioassay) analysis. LSC is vitally important to detection of one important radionuclide in HEAVY WATER nuclear power stations: tritium ( $^3\text{H}$ ). Tritium is extremely hard

to detect with field-portable instrumentation because the average energy of the beta particles emitted is very low (5.6 keV). In nuclear plants, LSC is routinely used for determining tritium intake through urine analysis. When tritium contamination is suspected on surfaces, quartz fibre or paper swipes can be used to wipe down a surface and then be analyzed in an LSC. Likewise, when performing environmental sample analysis for tritium, especially on water samples, LSC is the analytical technique of choice for tritium. A commercial LSC (for urine bioassay) is shown in Figure 44.



**Figure 44 Commercial LSC counter (top) and detail of trays with vials (bottom)**

#### 64.4.1.8 Summary

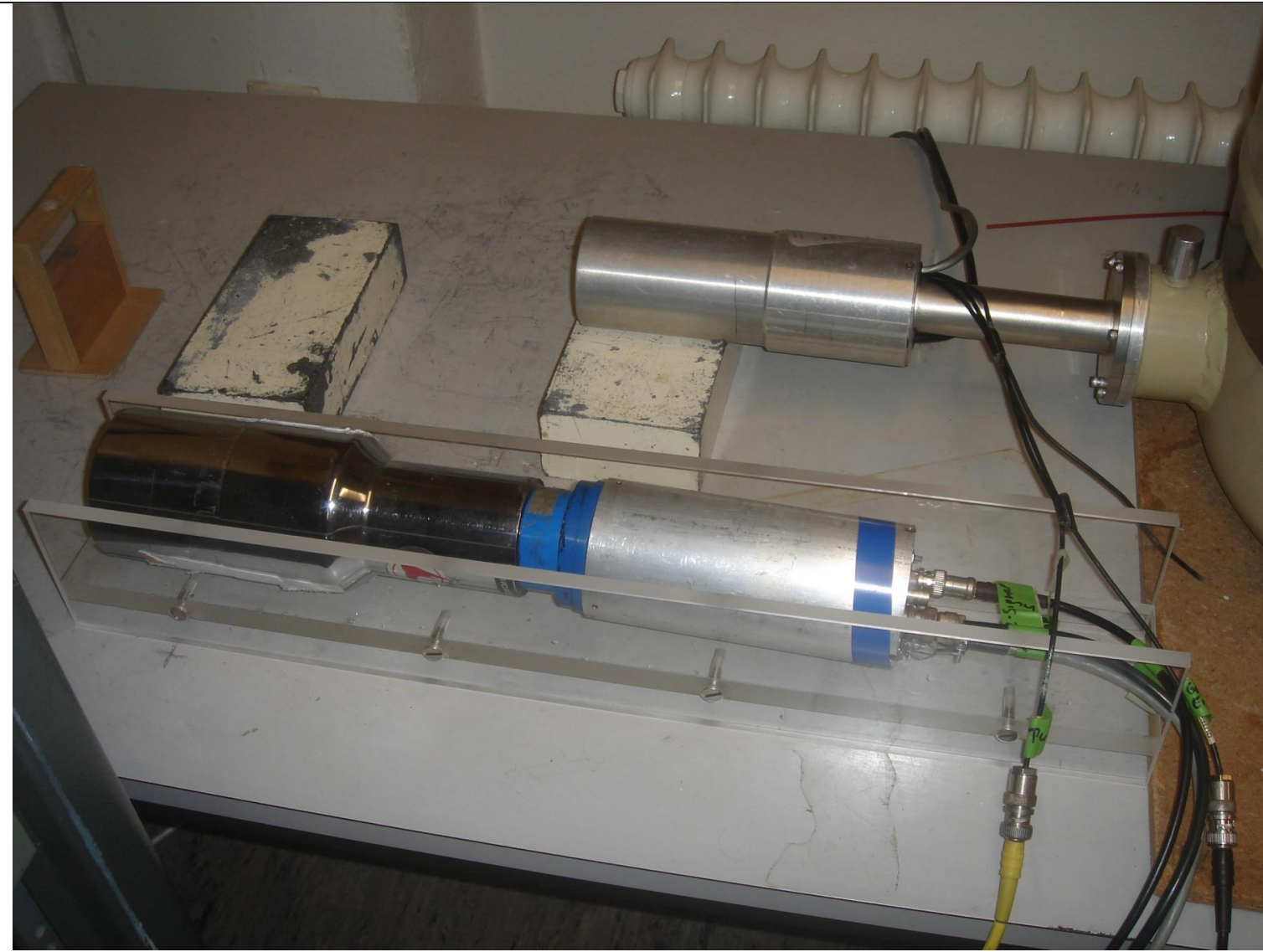
Ionizing radiation cannot be detected by the human senses, and therefore instrumentation is required. A variety of radiation detection instruments is used in nuclear facilities to support routine operations such as dosimetry, radiation protection, and environmental monitoring.

Instrumentation is selected by health physics personnel based on its applicability to the mission design. Radiation fields to be measured in nuclear facilities may be in the form of external fields, water effluent, airborne gases, or particulates. Instrumentation is of critical importance for the safe operation of nuclear facilities such as nuclear reaction cores and therefore is an integral part of the radiation-safety management plan.

#### 64.5 Gamma decay

## 64.6 Gamma Spectroscopy

### 64.6.1 Detektor



Ein Halbleiterdetektor, der als "Arm" aus einem Dewar(Kühlgefäß) herausragt (im Hintergrund) und ein Szintillationsdetektor (im Vordergrund).



## 64.6.2 Gamma-Gamma Coincidence Spectroscopy using Fast Scintillators<sup>64</sup>

## 64.6.3 Detectors for neutron scattering<sup>65</sup>

### Nomenclature

Category	Energy [meV]	Temperature [K]	$\lambda$ [Å]
Ultra-cold	< 0.1	< 1	< 30
Cold	0.1 – 10	1 – 120	30 – 3
Thermal	10 – 25-100	120 – 1000	3 – 1
Epithermal	> 500	> 6000	> 0.4
Fast	> $\sim 10^5$	> $10^6$	> 0.03

2

---

<sup>64</sup> [Alruhaili]

<sup>65</sup> [Tardocchi], M. Tardocchi, *Detectors for neutron scattering*



## **64.7 Scintillators in Deep**

### **64.7.1.1 Overview**

## 64.7.2 Scintillation Materials and their applications

Materials	Important Properties	Major Application
Nal(Tl)	Very high light output, good energy resolution	General scintillation counting, Health Physics, environmental monitoring, high temperature use
CsI(Tl)	Non-hygroscopic, rugged	Particle and high energy physics, general radiation detection, photo diode readout, phoswiches
CsI(Na)	High light output, rugged	Geophysical, general radiation detection
CsI(undoped)	Fast, non-hygroscopic	Physics (calorimetry)
CaF <sub>2</sub> (Eu)	Low Z, high light output	β detectors, α/β phoswiches
LaCl <sub>3</sub> :Ce(0.9)	Very high light output, very good energy resolution	High resolution scintillation spectroscopy, Health Physics environmental monitoring
CeBr <sub>3</sub>	Very high light output, very good energy resolution, low background	High resolution spectroscopy, low background applications
<sup>6</sup> LiI(Eu)	High neutron cross-section, high light output	Thermal neutron detection and spectroscopy
<sup>6</sup> Li-glass	High neutron cross section, non-hygroscopic	Thermal neutral detection
BaF <sub>2</sub>	Ultra-fast sub-ns UV emission	Positron life time studies, physics research, fast timing
YAP(Ce)	High light output, low Z, fast	MHz-X-ray spectroscopy, synchrotron physics
LYSO	High density and Z, fast	Physics research, PET, High Energy Physics
BGO	High density and Z	Particle physics, geophysical research PET, anti-Compton spectrometers.
CdWO <sub>4</sub>	Very high density, low afterglow Slow decay times	DC measurement of X-rays (high intensity), readout with photodiodes, Computerized Tomography (CT)
PbWO <sub>4</sub>	Fast, high density, low afterglow	Physics research (calorimetry)
Plastics	Fast, low density and Z high light output	General counting, particle and neutron detection.



Berkeley Nucleonics Corporation - 2955 Kerner Blvd - San Rafael CA 94901  
800-234-7858 or Live Chat @ [www.Berkeleynucleonics.com](http://www.Berkeleynucleonics.com)

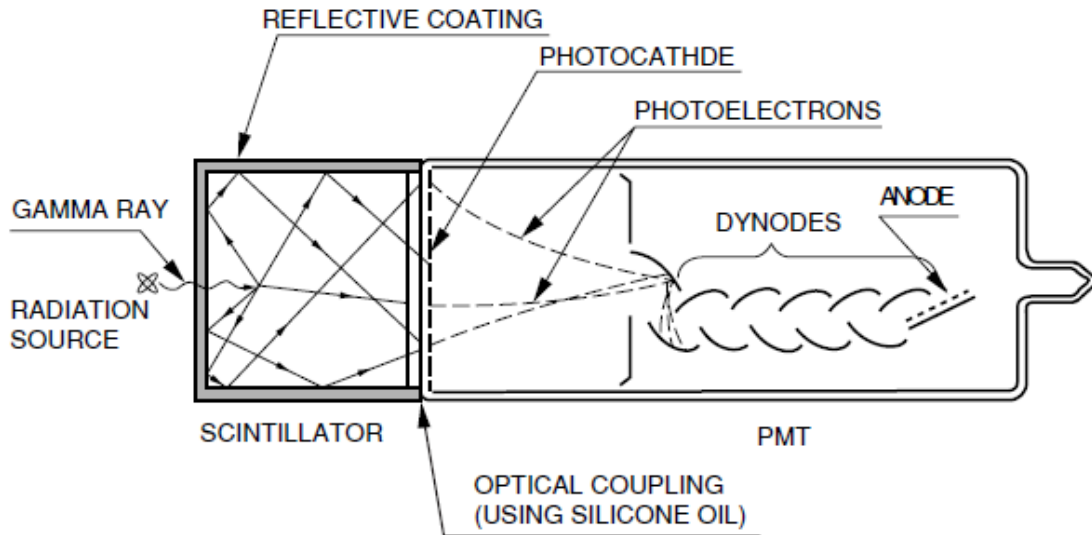
Table 7-1 shows typical characteristics and applications of major scintillators which have been developed up to the present.

Scintillators	Density (g/cm <sup>3</sup> )	Emission Intensity (NaI(Tl) normalized at 100)	Emission Time (ns)	Peak Emission Wavelength (nm)	Applications
NaI(Tl)	3.67	100	230	410	Surveymeter, area monitor, gamma camera
BGO	7.13	15	300	480	PET
CsI(Tl)	4.51	45 to 50	1000	530	Surveymeter, area monitor
Pure CsI	4.51	<10	10	310	High energy physics
BaF <sub>2</sub>	4.88	20	0.9/630	220/325	TOF, PET, high energy physics
GSO:Ce	6.71	20	30	310/430	Area monitor, PET
Plastic	1.03	25	2	400	Area monitor, neutron detection
LSO:Ce	7.35	70	40	420	PET
PWO	8.28	0.7	15	470	High energy physics
YAP:Ce	5.55	40	30	380	Surveymeter, compact gamma camera

Table 7-1: Typical characteristics and applications of scintillators

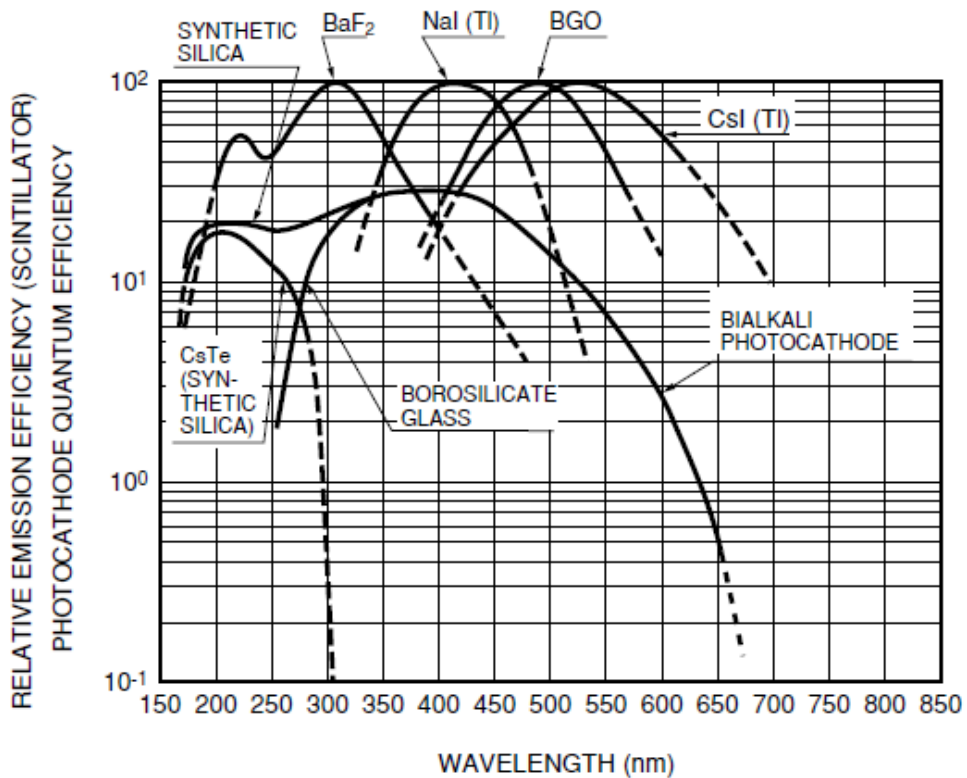
## Plastics

A scintillator is attached to a photomultiplier tube with coupling material as shown in Figure 7-3. The coupling material is used in place of an air layer in order to minimize optical loss between the scintillator and the photocathode faceplate. Silicone oil having an index of refraction close to that of the glass faceplate is most widely used as a coupling material. However, selecting the proper material which provides good transmittance over the emission spectrum of the scintillator is necessary. Figure 7-4 indicates typical emission spectra of major scintillators and photocathode spectral responses of photomultiplier tubes.



THBV3\_0703EA

Figure 7-3: Gamma-ray detection using a NaI(Tl) scintillator and a photomultiplier tube



THBV3\_0704EA

Figure 7-4: Photocathode quantum efficiency and emission spectra of major scintillators

### 64.7.2.1 Radiation Detection with Plastic scintillators

#### Background

It has been established opinion since the 1950s that organic crystals and liquid scintillators can work for detecting neutrons, but that plastics are not suitable for neutron detection.

For years, plastic materials have been used in large, low-cost detectors for portals and high-energy physics facilities, and while they could detect neutrons and gamma rays, they have been incapable of distinguishing one from the other, which is key to identifying nuclear substances such as uranium and plutonium from benign radioactive sources.

Organic crystals serve as one of the best neutron detectors, but the crystals can be difficult to grow and obtain in large volumes. Liquid scintillators present some hazards that hinder their use.

Gas detectors that rely on helium-3, a byproduct of tritium's radioactive decay, have run into problems because the United States now produces markedly less tritium.

However, plastics have more flexibility in their composition and structure than crystals, as well as having none of the hazards associated with liquid scintillators.

---

#### Description

Scientists at Lawrence Livermore National Laboratory have developed a plastic that can detect neutrons, something previously thought impossible.

Livermore scientists demonstrated a plastic scintillator that can discriminate between neutrons and gamma rays with a polyvinyltoluene (PVT) polymer matrix loaded with a scintillating dye, 2,5-diphenyloxazole (PPO). They have found that plastic scintillators have a roughly 20 percent finer resolution for neutron-gamma ray discrimination than liquid scintillators.



---

#### Advantages

New plastic that detects neutrons could be far cheaper and more flexible than traditional detectors. Given the material's low cost, huge plastic sheets could be formed easily into dramatically larger surface areas than other neutron detectors currently used and could aid in the protection of ports, stadiums and other large facilities.

---

The plastic scintillators may turn out to be best for detecting neutrons once the factors of usage in the field, cost, and performance are taken into consideration

---

### Potential Applications

Plastic scintillators could assist in detecting nuclear substances such as plutonium and uranium that might be used in improvised nuclear devices. As well as help in detecting neutrons in major scientific projects.

#### 64.7.2.2 Multi-anode photomultiplier tube: Phillips XP1704

#### 64.7.2.3 Proton beam Scintillator-CCD camera system<sup>66</sup>

The purpose of this study is to investigate the luminescence light output response in a plastic scintillator irradiated by a 67.5 MeV proton beam using various dosimetry parameters. The relationship of the visible scintillator light with the beam current or dose rate, aperture size and the thickness of water in the water-column was studied. The images captured on a CCD camera system were used to determine optimal dosimetry parameters for measuring the range of a clinical proton beam. The method was developed as a simple quality assurance tool to measure the range of the proton beam and compare it to (a) measurements using two segmented ionization chambers and water column between them, and (b) with an ionization chamber (IC-18) measurements in water.

We used a block of plastic scintillator that measured 5×5×5 cm<sup>3</sup> to record visible light generated by a 67.5 MeV proton beam. A high-definition digital video camera Moticam 2300 connected to a PC via USB 2.0 communication channel was used to record images of scintillation luminescence. The brightness of the visible light was measured while changing beam current and aperture size. The results were analyzed to obtain the range and were compared with the Bragg peak measurements with an ionization chamber. The luminescence light from the scintillator increased linearly with the increase of proton beam current. The light output also increased linearly with aperture size. The relationship between the proton range in the scintillator and the thickness of the water column showed good linearity with a precision of 0.33 mm (SD) in proton range measurement. For the 67.5 MeV proton beam utilized, the optimal parameters for scintillator light output response were found to be 15 nA (16 Gy/min) and an aperture size of 15 mm with image integration time of 100 ms. The Bragg peak depth brightness distribution was compared with the depth dose distribution from ionization chamber measurements and good agreement was observed. The peak/plateau ratio

---

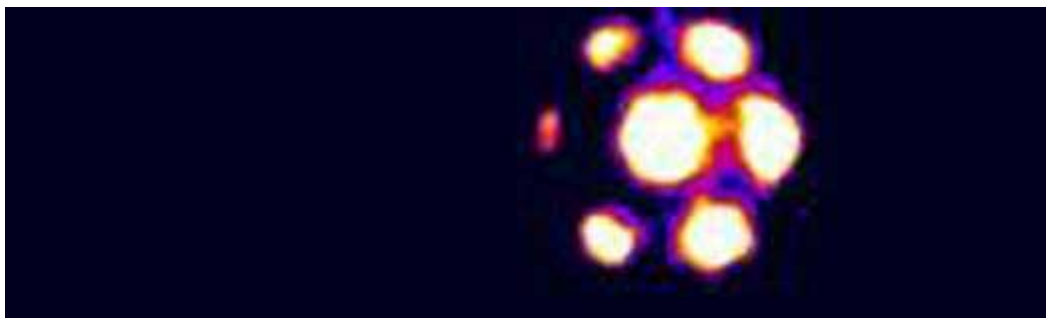
<sup>66</sup> Scintillator-CCD camera system light output response to dosimetry parameters for proton beam range measurement, [Nuclear Instruments and Methods in Physics Research Section A: Accelerators, Spectrometers, Detectors and Associated Equipment, Volume 686](#), 11 September 2012, Pages 7-14, [Inder K.Daftari<sup>a</sup>](#) [Carlos M.Castaneda<sup>b</sup>](#) [TimothyEssert<sup>b</sup>](#) [Theodore L.Phillips<sup>a</sup>](#) [Kavita K.Mishra<sup>a</sup>](#),

<sup>a</sup> Department of Radiation Oncology, 1600 Divisadero Street, Suite H1031, University of California-San Francisco, San Francisco, CA 94143, USA; <sup>b</sup> Crocker Nuclear Laboratory, 1 Shields Avenue, University of California-Davis, Davis, CA 95616, USA

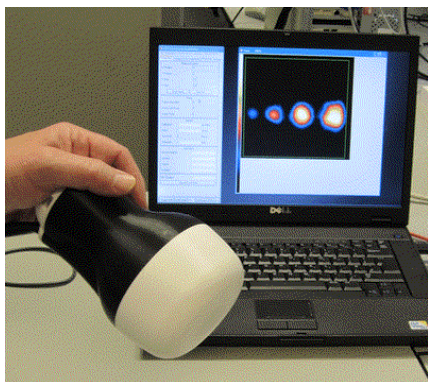
observed for the scintillator was found to be 2.21 as compared to the ionization chamber measurements of 3.01. **The response of a scintillator block–CCD camera in 67.5 MeV proton beam was investigated.** A linear response was seen between light output and beam current as well as aperture size. The relation between the thickness of water in the water column and the measured range also showed linearity. The results from the scintillator response was used to develop a simple approach to measuring the range and the Bragg peak of a proton beam by recording the visible light from a scintillator block with an accuracy of less than 0.33 mm. Optimal dosimetry parameters for our proton beam were evaluated. It is observed that this method can be used to confirm the range of a proton beam during daily treatment and will be useful as daily QA measurement for proton beam therapy.

#### 64.7.2.4 The Mini Gamma-Ray Camera<sup>67</sup>

Scintillator coated CCD



The Mini Gamma-Ray Camera (MGRC) has been developed for use in Nuclear Medicine employing solid state detector technology originally developed for x-ray astronomy applications. The MGRC has been developed as a collimated, **scintillator-coated**, low noise device which compliments whole-body gamma cameras as a generic low cost, high performance, hand held gamma camera. These cameras have an intrinsic **sub-mm spatial resolution (~0.5 mm)** and excellent energy resolution over the **energy range 30 – 160 keV**.



The MGRC is based on an existing class of detector, incorporating a scintillator which converts gamma-rays into photons, made from CsI(Tl) in a columnar layer placed in direct contact with a silicon CCD. The specific goal is to image, with high spatial resolution and good scatter-rejection, the 140.5 keV gamma-ray emissions from <sup>99m</sup>Tc-labelled tracers.

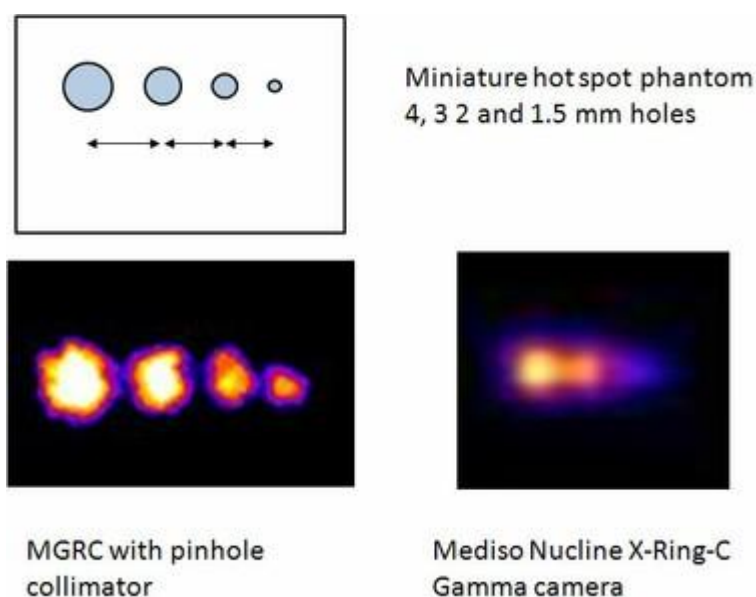
---

<sup>67</sup> <https://www2.le.ac.uk/departments/physics/research/src/res/bioimaging-unit/the-mini-gamma-ray-camera>

Key application for the MGRC will be the detection and imaging of sentinel lymph nodes which forms part of the diagnosis of cancer. Current procedures can require investigative surgery to assess the spread of primary tumours. The device, will help to reduce the cost and trauma of surgery. Other non-intrusive techniques are coming to the market, however an assessment of these indicates they do not achieve the projected performance of the Space Research Centre MGRC systems.

### Comparison of MGRC with Standard Gamma Camera

These images were taken of a  $^{99m}\text{Tc}$  phantom (i.e. a model of a tumour) consisting of 4 hot spots source. The image on the right was taken using a large field of view Mediso Nucline X-Ring-C gamma camera. The image on the left was taken using the MGRC. It is evident from the images that the standard camera only shows two distinct spots whereas the MGRC shows there are actually four.



Standard whole body gamma cameras are expensive and offer only a moderate spatial resolution (approx. 10mm). The cost of such systems often precludes their widespread use. MGRC cameras will be significantly cheaper than the standard gamma cameras.

Small gamma cameras will be a natural complement to Whole Body Gamma Cameras by offering imaging of small volumes of tissue, joints etc. at higher spatial resolutions (~0.4mm cf. 4mm).

### Publications

1. J E Lees, DJ Bassford, OE Blake, PE Blackshaw, AC Perkins, *A high resolution Small Field Of View (SFOV) gamma camera: a columnar scintillator coated CCD imager for medical applications*, J. Inst. 6 (2011) C12033
2. J E Lees, DJ Bassford, PE Blackshaw, AC Perkins, *Design and use of mini-phantom for high resolution planar gamma cameras*, Applied Radiation and Isotopes, 68 (2010) 2448-2451

Bioimaging Unit,  
Space Research Centre,  
Department of Physics,

- e2v CCD 97 BI
- 16  $\mu\text{m}$  pixels
- 512 x 512 pixels
- 8 mm x 8 mm

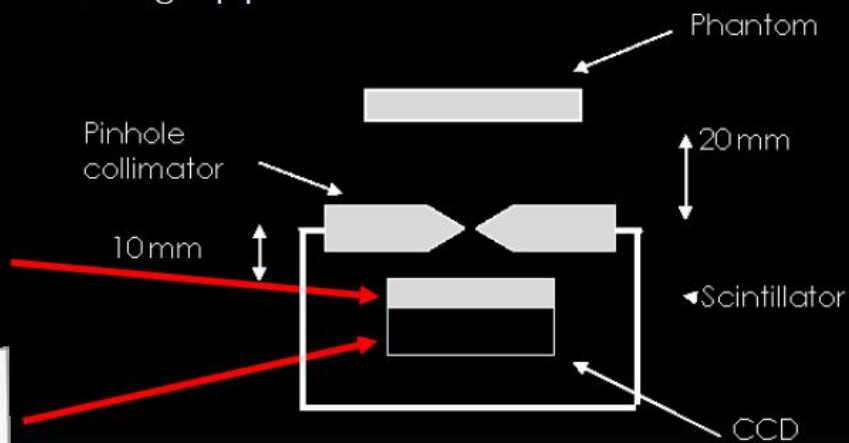
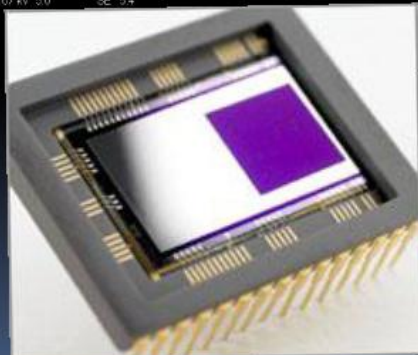
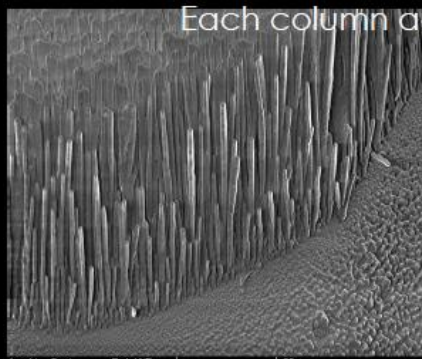
Pinhole collimators:  
FOV 40mm x 40mm



## Camera Schematic

Columnar CsI

Each column acts as a "light pipe"



The mini gamma camera

# Phantoms

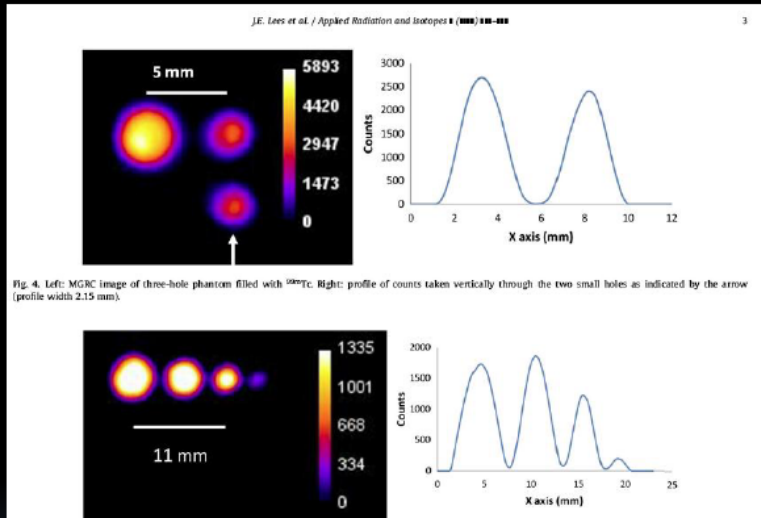


Fig. 4. Left: MGRIC image of three-hole phantom filled with  $^{99m}\text{Tc}$ . Right: profile of counts taken vertically through the two small holes as indicated by the arrow (profile width 2.15 mm).

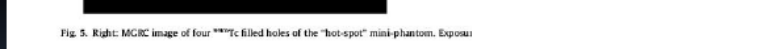


Fig. 5. Right: MGRIC image of four  $^{99m}\text{Tc}$  filled holes of the "hot-spot" mini-phantom. Exposure

Applied Radiation and Isotopes 68 (2010) 2448–2451



Contents lists available at ScienceDirect

Applied Radiation and Isotopes

journal homepage: [www.elsevier.com/locate/apradiso](http://www.elsevier.com/locate/apradiso)

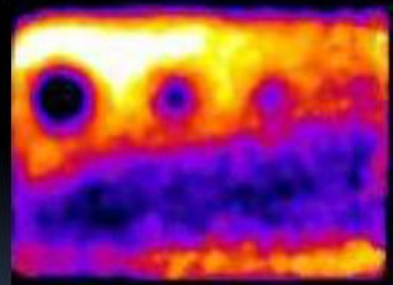
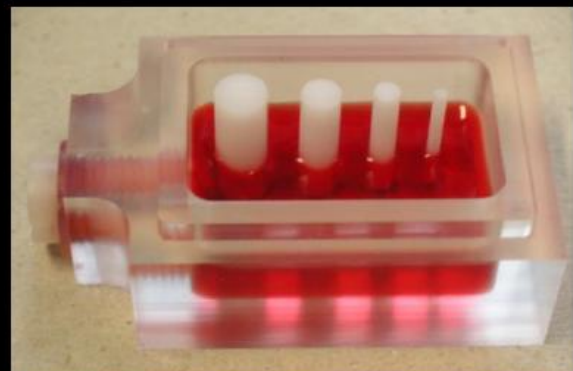
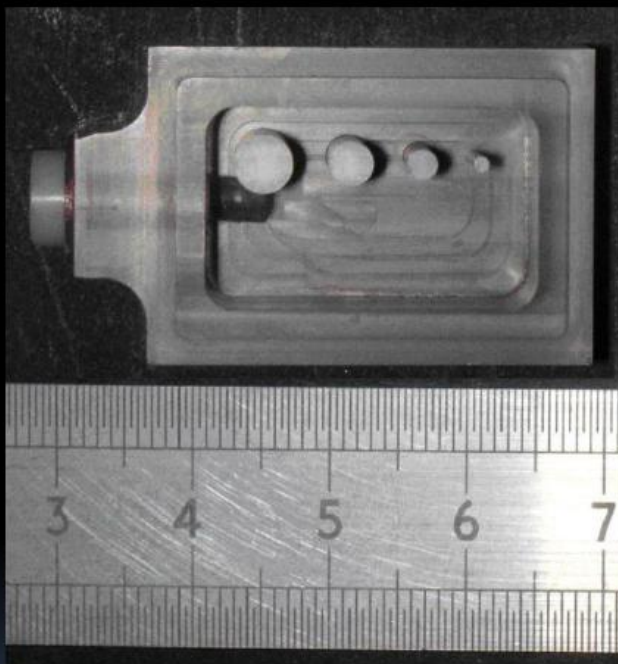


Design and use of mini-phantoms for high resolution planar gamma cameras

J.E. Lees <sup>a,\*</sup>, D.J. Bassford <sup>a</sup>, P.E. Blackshaw <sup>b</sup>, A.C. Perkins <sup>b</sup>

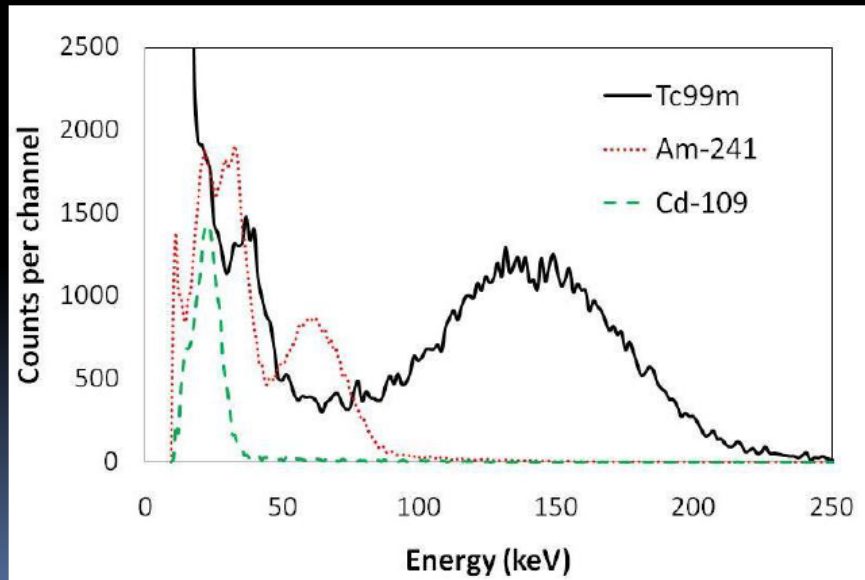
<sup>a</sup> *Biomedical Unit, Space Research Centre, Michael Atiyah Building, University of Leicester, Leicester LE1 7RH, UK*  
<sup>b</sup> *Academic Medical Physics, Medical School, University of Nottingham, Nottingham NG7 2UH, UK*

# Mini-Phantom



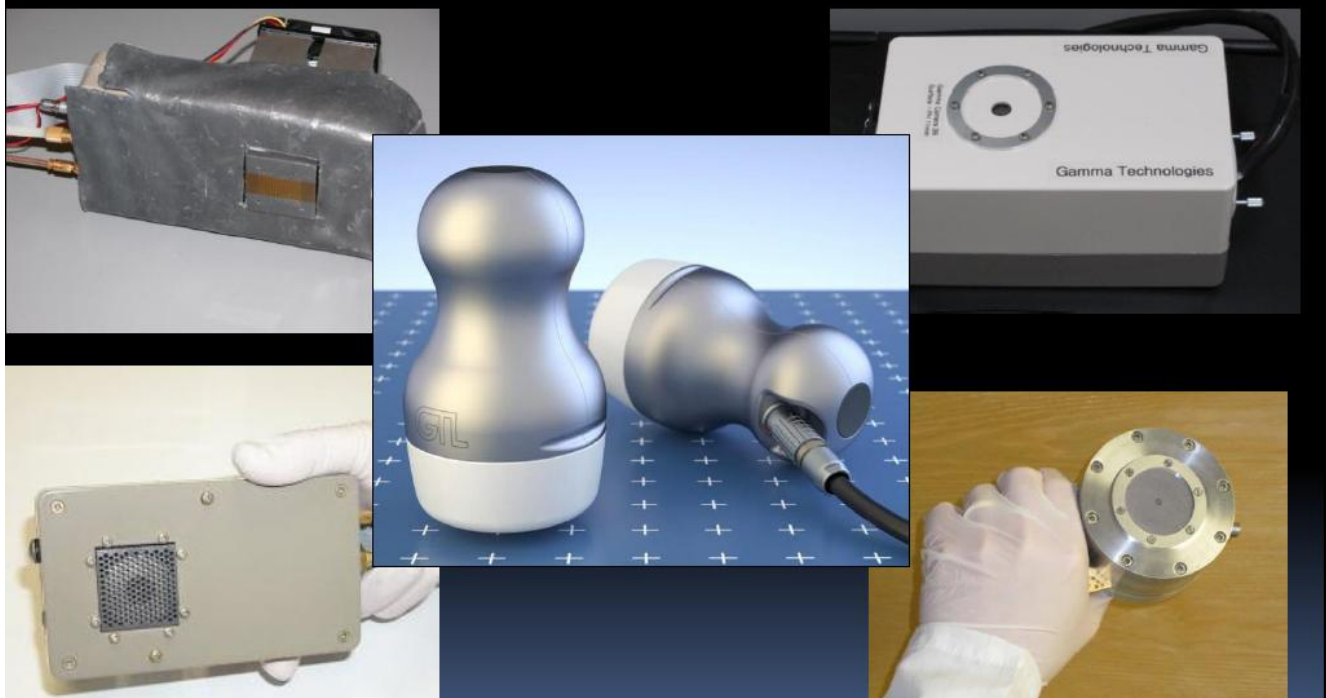
# MGRC performance

- Sub-mm spatial resolution  $\sim 0.9\text{mm}$  @  $25\text{mm}$
- Interesting Energy Resolution



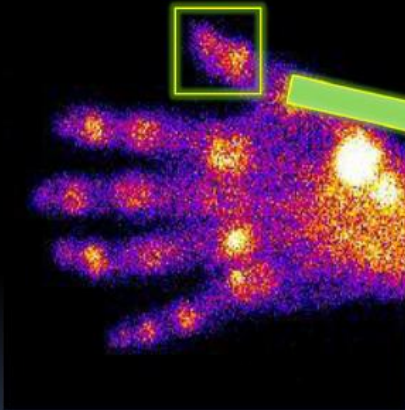
University of

# Design evolution - MGRC

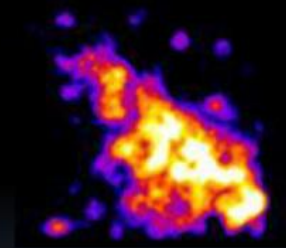


# Clinical trial, QMC Nottingham

Tc-99m-HDP bone imaging in patient



Conventional gamma camera



HR Mini gamma camera

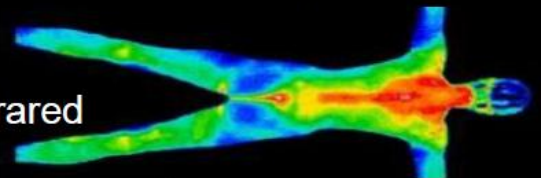
# Multi-wavelength approach

The Milky Way

Man



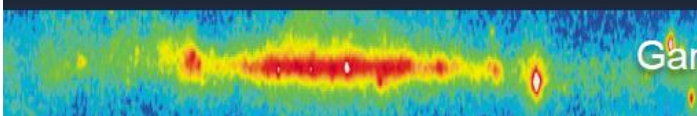
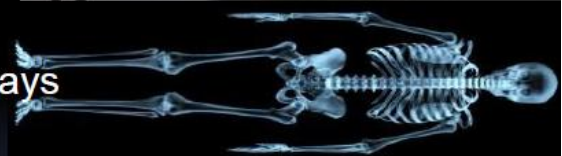
Near-Infrared



Optical



X - rays

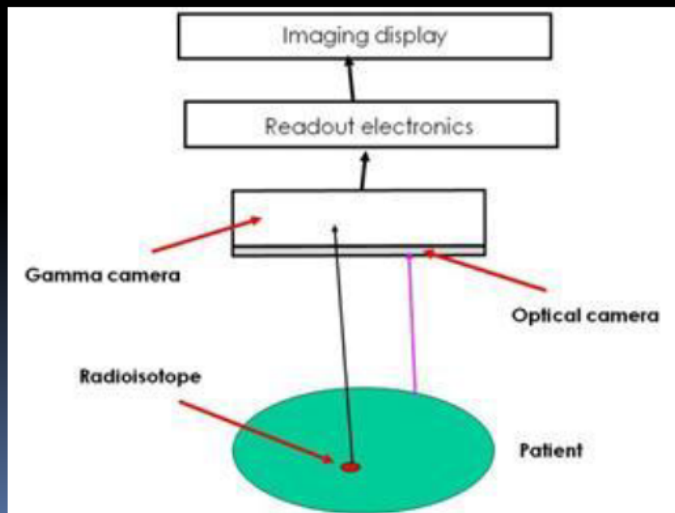


Gamma rays

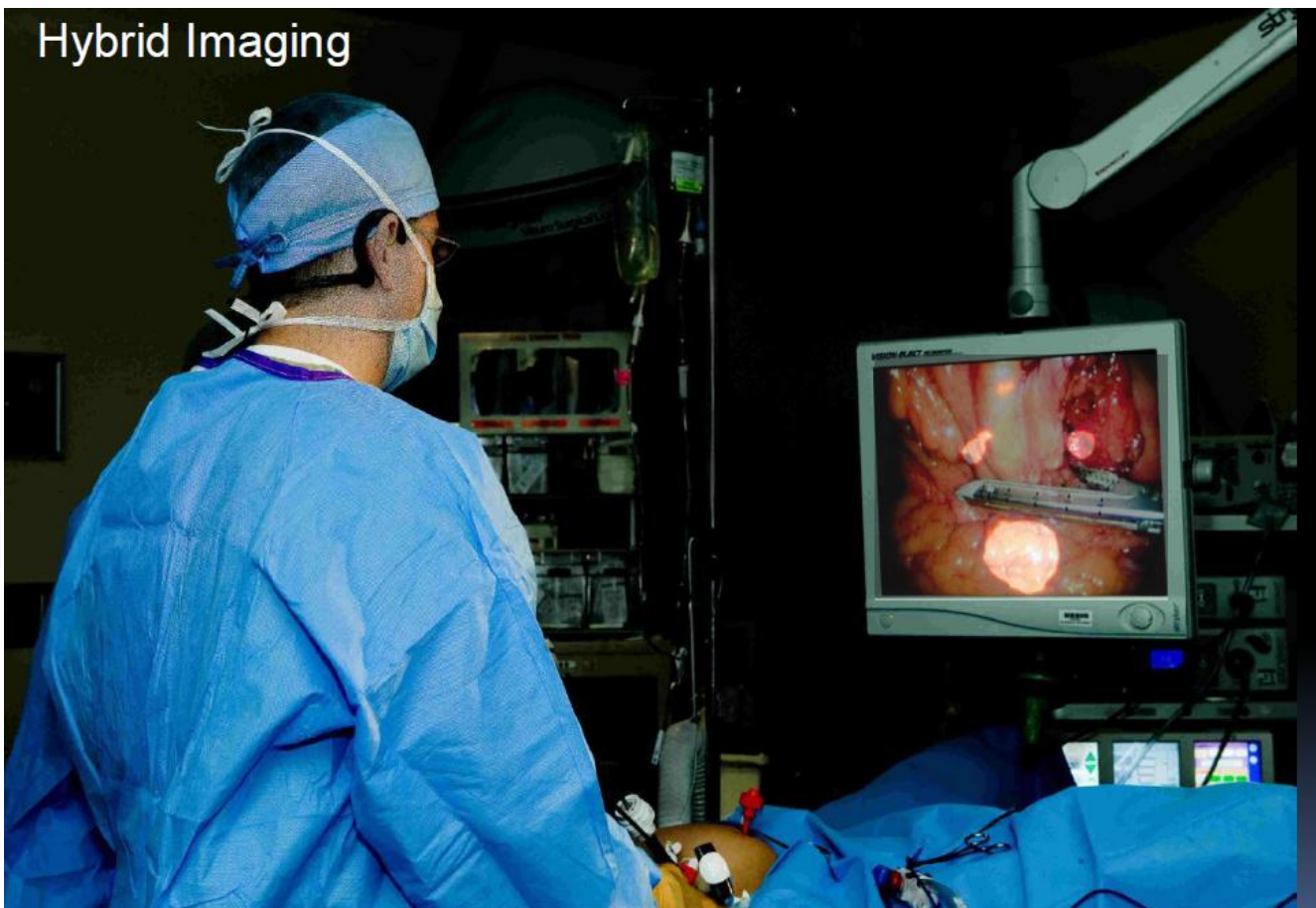


# Hybrid camera

- A combined optical and gamma camera system
- Co-aligned optical and gamma camera
- Minimises parallax
- Minimises image registration problems



## Hybrid Imaging



Acknowledgements

- Space Research Centre, Leicester

David Bassford, Oliver Blake, Tony Abbey,

George Fraser, Duncan Ross, Chris Bicknell

Massimiliano Canali

- University of Nottingham

Alan Perkins and Elaine Blackshaw

- De Montfort University

Peter Ford and Lee Cottrell

#### 64.7.2.5 Q&A

The following question was answered by an expert in the appropriate field:

Q

I have disassembled various consumer-grade digital cameras with CMOS (complementary metal-oxide semiconductor) and CCD (charge-coupled device) image sensors and (after removing the plastic and glass optics) experimented with holding the **image-sensing silicon wafer** up to various sources. When I held it ~1 cm from a **smoke detector's <sup>241</sup>Am source foil**, I see the tons of randomly flickering white dots. But a piece of copy paper fully blocks this effect, and a bottle of <sup>40</sup>K containing salt substitute (KCl) fails to excite the CCD sensor at all. So, apparently this CCD system only works as an alpha scintillator. My question is, why? Americium-241 should also be giving off a 60 keV gamma photon that would penetrate a sheet of copy paper, and the beta particle from <sup>40</sup>K-decay in the salt substitute has a pretty high peak energy as I recall. But my CCDs don't register even a single "blip" for either of these scenarios. Are CCD sensors somehow insensitive to ionizing photons and betas?

P.S. It goes without saying, but all of my experiments are conducted with careful attention to safety, e.g., double gloves, respirator, personal dosimeter to check for source leakage onto work surfaces, etc. I verified with the smoke detector manufacturer's consumer affairs that as long as I fully reassemble the detector housing and do not puncture or separate the foil from its steel block, there would not be any problem accepting the detector for recycling.

A

Sounds as if you're having some fun with these imaging devices. As you have observed, it is true that **both the charge-coupled silicon devices and the metal-oxide semiconductors may produce visible light scintillations in response to ionizing radiation**. Just as visible light will set free electrons through photoelectric interactions in silicon, higher-energy radiations such as alpha, beta, and gamma radiation also have the ability to free electrons in the material. The subsequent light emission normally occurs when free electrons combine with the holes that represent the positive charge carriers; this recombination process sometimes results in the emission of energy as visible light photons. In silicon the process is relatively inefficient so that relatively few of the ionization events

that set free electrons lead to light emission. If the frequency and density of recombination events is sufficiently high, however, some of the light pulses may be sufficiently intense to be visible to the naked eye, especially in a darkened environment.

I believe the major reason you see the flashes when the detector is exposed to alpha radiation from the  $^{241}\text{Am}$  but not from the gamma and beta radiations has to do with the nature of the energy deposition process by the alpha radiation compared to the other types of radiation. As you have demonstrated, using a piece of paper as a shield, the alpha particles have a very short range in condensed materials. Most alpha particles from  $^{241}\text{Am}$  have individual energies of about 5.5 million electron volts (MeV), and when one of these alpha particles enters the silicon, it will deposit all of its energy within approximately 20 micrometers (this is not much different from the thickness of silicon used in many CCDs), thus producing a track of very dense ionization, a single alpha particle producing likely between four and five million ionization events. The electrons (and holes) produced may recombine, and this provides the potential to produce a burst of light photons in sufficient intensity to be visualized.

The situation is quite different for beta and gamma radiation. The maximum energy beta radiation from  $^{40}\text{K}$  is about 1.3 MeV, and the approximate distance such a beta particle could travel in silicon is about 3 mm, a dimension much greater than the thickness of the active material in a CCD or CMOS. The average beta particle traversing the same 20 micron path length as the alpha particle would produce approximately 5,000 to 10,000 ionization events. Thus, the ionization density, as well as the total ionization per particle, would be much less for the beta radiation than for the alpha particle. This makes it much less likely that one would be able to see the light emission with the naked eye. There are optical microscopy enhancement techniques that might make these weaker scintillations visible.

Gamma rays will also interact in silicon to set free electrons that may lead to recombination and light emission, but the situation with respect to the gamma radiation is even more restrictive as regards the possibility of viewing the light emission. The probability that a 60 keV gamma ray will interact within a 20 micron thickness of silicon is about  $1.4 \times 10^{-3}$ . This compares to the probability of 1.0 for the alpha particle (and the beta particle). Additionally, the photon energy is much less than the alpha or beta energy and only about half of the photon energy, on average, would be deposited in the silicon per interaction. Thus, one would have an even more difficult time trying to visualize light emissions from gamma-ray interactions.

Other factors, such as the intensity of the various sources, also play some part in the likelihood of producing enough interactions to yield visible light output. You don't specify the thickness of the bottle holding the KCl or whether the CCD was exposed to the bare KCl (the bottle walls could produce considerable attenuation of beta radiation). In any event, the rate of incidence of beta particles on the CCD would likely be considerably less than the alpha particles from the  $^{241}\text{Am}$  source. The  $^{40}\text{K}$  also emits 1.46 MeV gamma rays in about 11 percent of its disintegrations, but again you would not have sufficient source intensity to yield an interaction density sufficient to produce light pulses visible to the unaided eye.

It's good to hear that you are aware of potential hazards associated with some radioactive sources, and I expect that you will continue to invoke appropriate safety measures and to seek guidance as necessary if your experimentation expands to include other radioactive sources. Good luck.

George Chabot, PhD, CHP

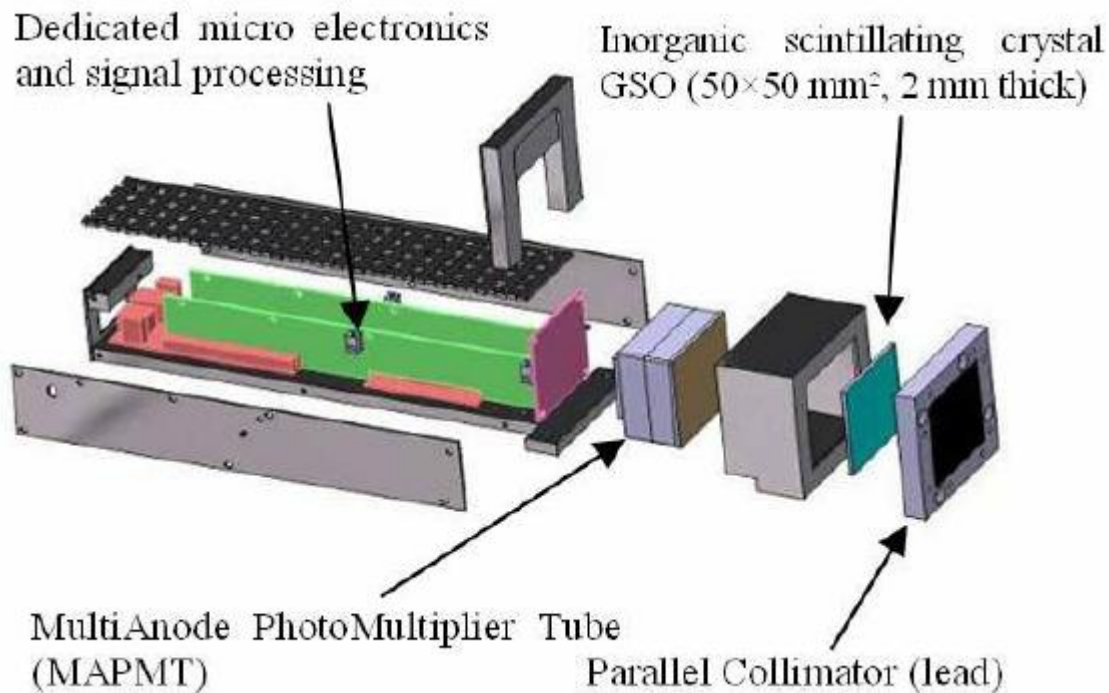
#### **64.7.2.6 Manufacturing mini gamma-ray camera**

Design optimization, manufacturing, and tests, both laboratory and clinical, of a portable gamma camera for medical applications are presented. This camera, based on a continuous scintillation crystal and a position-sensitive photomultiplier tube, has an intrinsic spatial resolution of approximately 2 mm, an energy resolution of 13% at 140 keV, and linearities of 0.28 mm (absolute) and 0.15 mm (differential), with a useful field of view of 4.6 cm diameter. Our camera can image small organs with high efficiency and so it can address the demand for devices of specific clinical applications like thyroid and sentinel node scintigraphy as well as scintimammography and radio-guided surgery. The main advantages of the gamma camera with respect to those previously reported in the literature are high portability, low cost, and weight (2 kg), with no significant loss of sensitivity and spatial resolution. All the electronic components are packed inside the minigamma camera, and no external electronic devices are required. The camera is only connected through the universal serial bus port to a portable personal computer (PC), where a specific software allows to control both the camera parameters and the measuring process, by displaying on the PC the acquired image on "real time." In this article, we present the camera and describe the procedures that have led us to choose its configuration. Laboratory and clinical tests are presented together with diagnostic capabilities of the gamma camera.

#### **Abstract:**

We have tested a concept of a mini gamma camera based on monolithic arrays of MPPCs from Hamamatsu. CsI(Tl), and Cs(Na) arrays and a thin scintillation GSO plate were tested with 122 keV gammas from  $^{57}\text{Co}$  sources. The planned application requires placement of this mini-camera in an endorectal probe and thus needs to be very compact and possess high spatial resolution. The high sensitivity and high granularity collimator and gamma shield made out composite material (tungsten powder with epoxy) completes the detector package. We are developing the dual modality (hybrid) imaging prostate probe combining in one compact device a high resolution and high efficiency single gamma imager with an Ultrasound (US) sensor. The US component will typically provide not only the usual structural 3D information, as the standard TransRectal Ultrasound (TRUS) probe, but also the tissue differentiating information through proper US signal analysis, such as elastography. The mini gamma probe will provide the direct metabolic information related to the biological state of the prostate and specifically about the presence of any cancerous structures exhibiting increased metabolic activity, when used with the single gamma labeled dedicated imaging agents for prostate cancer. In addition to cancer diagnosis, the dual-modality Gamma/US prostate probe can be used in biopsy and in surgical guidance.

**Published in:** [2011 IEEE Nuclear Science Symposium Conference Record](#)



#### 64.7.2.7 GSO scintillator

### GSO / GSO(Ce) Gadolinium Orthosilicate

Gadolinium Orthosilicate -  $Gd_2SiO_5(Ce)$  is a effective all round gamma-ray absorber. It is referred to both as GSO and GSO(Ce), it is only available with Ce doping.

GSO scintillator crystals have:

Mechanically robust characteristics and are non-hygroscopic

Good energy resolution up to 150°C

Good radiation hardness

No intrinsic radiation background

GSO scintillator crystals have the following issues which should be noted. They:

Have have limited light output

Gadolinium Orthosilicate - GSO scintillator crystals are useful in diverse applications such as:

Positron Emission Tomography (PET)

Geological logging

Specialist applications in high energy, nuclear, space and medical physics

<b>Properties</b>	<b>Units</b>	<b>Value</b>
<b>Optical/Scintillation</b>		
Wavelength (Max. Emission)	nm	430
Lower Wavelength Cut-off	nm	TBA
Decay Time	ns	30 - 60
Light Yield	photons/keV	8 to 10
Photoelectron Yield	% of NaI(Tl)	20
Radiation Length	cm	1.38
Optical Transmission	$\mu\text{m}$	TBA
Attenuation	$\text{cm}^{-1}$	0.67
Transmittance	%	TBA
Refractive Index		1.85
Reflection Loss/Surface	%	TBA
Neutron Capture X-section	barns	TBA
Radiation Hardness	Gy	$>10^6$

<b>Properties</b>	<b>Units</b>	<b>Value</b>
<b>Mechanical</b>		

Chemical Formula

Density	$\text{g/cm}^3$	6.7
Atomic Number (Effective)		58
Melting Point	$^{\circ}\text{K}$	1900
Thermal Expansion Coeff.	$\text{C}^{-1}$	$4 - 12 \times 10^{-6}$
Crystal Structure		Mono
Hardness	Mho	5.7
Hygroscopic		No

Solubility	g/100gH <sub>2</sub> O	N/A
------------	------------------------	-----

64.7.3 Scintillators and Photomultipliers<sup>68</sup>

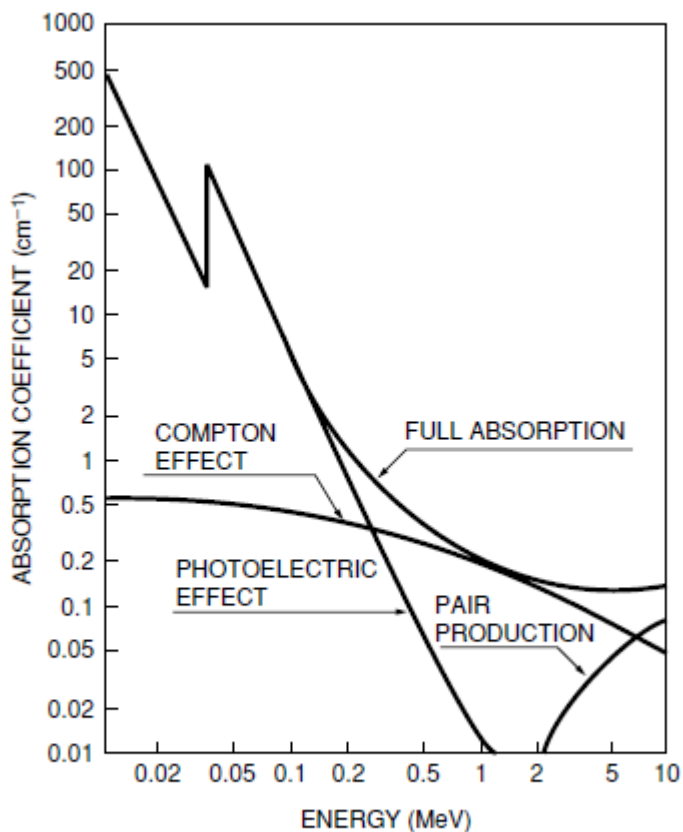


Figure 7-1: Gamma-ray absorption characteristics of NaI(Tl) scintillator

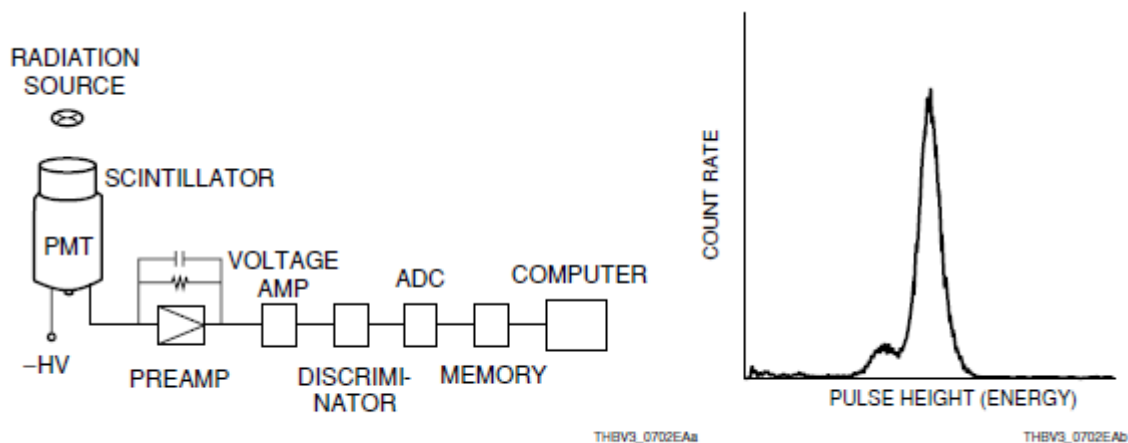


Figure 7-2: Block diagram for scintillation counting and pulse height distribution

<sup>68</sup> PMT Handbook, Photomultiplier Tubes, Basics and Applications, Hamamatsu, 3rs Ed.

## 65 GAMS Unit Design

### 65.1 Concept

Candidates:

Scintillator

Gas-based (He)

Scintillator: Plastic

## 66 Realization





**68 Next working packages**

## 69 Suppliers Data

### 69.1 Electronics, Control

- CNCLab
- قطرنجي للإلكترونيات EKT Beirut
  - Number: 01 820020
  - Website: www.ekt2.com



- البشير للإلكترونيات - Bashir electronics

### 69.2 Satellite Parts

Specification form © Surrey Satellite Technology Ltd., Tycho House, 20 Stephenson Road, Surrey Research Park, Guildford, Surrey, GU27YE, United Kingdom, Tel: +44(0)1483803803 | Fax: +44(0)1483803804 | Email: info@sstl.co.uk | Web: www.sstl.co.uk

Remark: No answer to email has come.

### 69.3 CNC Fine Mechanics (2D)

**HI-TECH FABRICATION**  
Precision Mechanical Parts Manufacturing  
Brass & Steel Marking Heads Maker

**M. Fawaz Adul Hadi**  
Mechanical Engr

Mahjar Suhi  
P.O. Box 1274  
Tripoli, Lebanon  
Tel 00961-6-442787  
www.hitechfabrication.com  
info@hitechfabrication.com  
sirfawaz@yahoo.com

"You will find our products in every packing factory"

**HI-TECH FABRICATION**  
Precision Mechanical Parts Manufacturing  
Brass & Steel Marking Heads Maker

**M. Fawaz Adul Hadi**  
Mechanical Engr

Mahjar Suhi  
P.O. Box 1274  
Tripoli, Lebanon  
Tel/Fax 00961-6-442787  
www.hitechfabrication.com  
info@hitechfabrication.com  
sirfawaz@yahoo.com

The company HI-TECH Facrification takes CAD Data (in .dxf format) -> Changing to CAM Data.

Satellite Parts are in Alluminium Alloy.

### 69.4 3D Printing (Plastics)

<http://www.cnclablb.com/>

### 69.5 CNC

Company	Phone number	Description	Address	E-mail web site
CNC LAB	06 412 895 03 476 916	Manufacture 3D design in plastic & open source hardware	Tripoli, Lebanon Bahsas, Behind Haykalieh Hospital, Harba Bld.	<a href="http://www.cnclab.com">www.cnclab.com</a> <a href="mailto:info@cnclablb.com">info@cnclablb.com</a>
Hasan Al Baba	03 828 256	Manufacture and casting	Tripoli, Lebanon Mina, Industry and Commerce street	
HI-Tech fabrication Fawaz Abdel Hadi	06 442 787 70 751 522	Precision mechanical parts manufacturing brass & steel marking heads maker	Tripoli, Lebanon Mahjar suhi P.O. Box 1274	<a href="http://www.hitechfabrication.com">www.hitechfabrication.com</a> <a href="mailto:info@hitechfabrication.com">info@hitechfabrication.com</a> <a href="mailto:sirfawaz@yahoo.com">sirfawaz@yahoo.com</a>
Hannuf mechanical Corporation for casting and art construction	06 387 723 03 717 107	Manufacture and casting	Tripoli, Lebanon Al Badawi	
GPS Steel	03 196 225	Uses electric discharge machining process to shape any metal material rapidly by using desired modeled electrodes	Beirut, Lebanon Burj Hammoud	<a href="mailto:Gps.steel.co@gmail.com">Gps.steel.co@gmail.com</a>
Riyako factory	79 118 779	3D CNC machine, manufacture cupboard for cars	Tripoli, Lebanon Badawi, behind Al Ridani bakery	

## References

[Essential] [www.unene.ca/education/CANDU-textbook](http://www.unene.ca/education/CANDU-textbook), Editor-in-Chief: Wm. J. Garland, Professor Emeritus, McMaster University, Hamilton, Ontario

[Alruhaili] Aied S. Alruhaili, *Gamma-Gamma Coincidence Spectroscopy using Fast Scintillators*, Master Thesis in Radiation Detection & Instrumentation, University of Surrey, 2010,

[http://personal.ph.surrey.ac.uk/~phs1pr/msc\\_dissertations/msc-diss-2010/Aied%20Alruhaili%20dissertation.pdf](http://personal.ph.surrey.ac.uk/~phs1pr/msc_dissertations/msc-diss-2010/Aied%20Alruhaili%20dissertation.pdf)

For 2.4 and 2.5:

### 69.6 Further Reading

F. H. Attix, *Introduction to Radiological Physics and Radiation Dosimetry*. Toronto, ON: Wiley-Interscience, 1986.

V. Baryakhtar, V. Kukhar, I. Los, V. Poyarkov, V. Kholosha, and V. Shestopalov, *Comprehensive Risk Assessment of the Consequences of the Chernobyl Accident. Science and Technology*

*Centre in Ukraine – Ukrainian Radiation Training Centre*. Project No. 369, Kiev, Ukraine, 1998.

R. Bailey, H. Clark, J. Ferris, S. Krause, and R. Strong, *Chemistry of the Environment*, 2<sup>nd</sup> Edition. New York: Academic Press, 2002.

E. Baum, H. Knox, T. Miller, *Nuclides and Isotopes*, 16<sup>th</sup> ed. Schenectady, NY: Lockheed Martin, Knolls Atomic Power Laboratory, 2002.

J. J. Bevelacqua, *Health Physics in the 21<sup>st</sup> Century*. New York: Wiley-VCH, 2008.

A. Brodsky, *Review of Radiation Risks and Uranium Toxicity with Application to Decisions Associated with Decommissioning Clean-Up Criteria*. Hebron, CT: RSA Publications, 1996.

Chernobyl Forum, *Chernobyl's Legacy: Health, Environmental, and Socio-Economic Impacts and*

*Recommendations to the Governments of Belarus, the Russian Federation, and Ukraine*.

The Chernobyl Forum: 2003-2005, 2<sup>nd</sup> revised edition, 2005.

CIBA, *Health Impacts of Large Releases of Radionuclides*. Toronto: John Wiley, CIBA Foundation

Symposium 203, 1997.

J. Cooper, K. Randall, and R. Sokhi, *Radioactive Releases in the Environment—Impact and Assessment*. Etobicoke, ON: John Wiley, 2003.

M. Eisenbud and T. Gesell, *Environmental Radioactivity from Natural, Industrial, and Military Sources*, 4<sup>th</sup> Edition. Toronto, ON: Academic Press, 1997.

M. Gomez, *Radiation Hazards in Mining: Control, Measurement, and Medical Aspects*. New York: Society of Mining Engineers, American Institute of Mining, Metallurgical, and Petroleum Engineers, 1981.

E. M. A. Hussein, *Radiation Mechanics—Principles and Practice*. New York: Elsevier, 2007.

IAEA. *Protection of the Environment from the Effects of Ionizing Radiation—A Report for Discussion*.

Vienna, Austria: International Atomic Energy Agency, IAEA-TECDOC-1091, 1999.

IAEA, *Classification of Radioactive Waste*. Vienna, Austria: International Atomic Energy Agency, General Safety Guide GSG-1, 2009.

*Journal of Environmental Radioactivity*, Elsevier, ISSN: 0265-931X.

- R. L. Kathren, *Radioactivity in the Environment—Sources, Distribution and Surveillance*. London, U.K.: Harwood, 1984.
- J. Lehr, M. Hyman, T. Gass, and W. Seevers, *Handbook of Complex Environmental Remediation Problems*. Toronto, ON: McGraw-Hill, 2002.
- K. H. Lieser, *Nuclear and Radiochemistry—Fundamentals and Applications*, 2<sup>nd</sup> ed. Toronto, ON: Wiley-VCH, 2001.
- J. Louvar and B. Louvar, *Health and Environmental Risk Analysis*. Toronto, ON: Prentice-Hall, 1998.
- J. Magill and J. Galy, *Radioactivity, Radionuclides, Radiation*. New York: Springer, 2005.
- J. E. Martin and C. Lee, *Principles of Radiological Health and Safety*. Toronto, ON: Wiley-Interscience, 2003.
- D. Moeller, *Environmental Health*, 3<sup>rd</sup> Edition. Cambridge, MA: Harvard University Press, 2005.
- T. Moore and D. Dietrich, "Chernobyl and its Legacy", *EPRI Journal*, 5:21 (1987).
- G. Paić, *Ionizing Radiation: Protection and Dosimetry*. Boca Raton, FL: CRC Press, 1988.
- J. Turner, *Atoms, Radiation, and Radiation Protection*, 2<sup>nd</sup> Edition. Toronto, ON: Wiley Interscience, 1995.
- R. Tykva and D. Berg (eds.), *Man-Made and Natural Radioactivity in Environmental Pollution and Radiochronology*. Dordrecht, The Netherlands: Kluwer, 2004.
- UNSCEAR, *Sources, Effects, and Risks of Ionizing Radiation*. New York: United Nations Scientific Committee on the Effects of Atomic Radiation (UNSCEAR), Report to the General Assembly, with scientific annexes, 1988.
- UNSCEAR, *Sources and Effects of Ionizing Radiation*, Volumes I and II. New York: United Nations, 2000.
- V. Valković, *Radioactivity in the Environment*. Amsterdam, The Netherlands: Elsevier Science, 2000.
- X. G. Xu and F. K. Eckerman, *Handbook of Anatomical Models for Radiation Dosimetry*. Boca Raton, FL: CRC Press, 2010.

### 69.7 References from [Essential]

- [ANS1991] ANS, *Gamma Ray Attenuation Coefficients and Buildup Factors for Engineering Materials*. La Grange IL: ANSI/ANS-6.4.3-1991.
- [ANSI2001] ANSI, *American National Standard – Respirator Fit Testing Methods*. Fairfax, VA: American National Standards Institute, ANSI/AIHA Z88.10-2001.
- [ANSI2003] ANSI, *American National Standard – Laboratory Ventilation*. Fairfax, VA: American National Standards Institute, ANSI/AIHA Z9.5-2003.
- [ANSI2006] ANSI, *American National Standard – Fundamentals Governing the Design and Operation of Local Exhaust Ventilation Systems*. Fairfax, VA: American National Standards Institute, ANSI/AIHA Z9.2-2006.
- [ANSI2007] ANSI, *American National Standard – Recirculation of Air from Industrial Process Exhaust Systems*. Fairfax, VA: American National Standards Institute, ANSI/AIHA Z9.7-2007.

- [Aydogdu2013] K. Aydogdu, Personal communication via email with Kam Aydogdu, February 20, 2013.
- [BEIRVII2006] BEIR VII, *Health Risks from Exposure to Low Levels of Ionizing Radiation: Phase 2*. Washington DC: National Research Council of the National Academies, National Academies Press, 2006.
- [Bentur1991] Y. Bentur, N. Horlatsch, and G. Koren, "Exposure to Ionizing Radiation during Pregnancy: Perception of Teratogenic Risk and Outcome", *Teratology* 43: 109-112 (1991).
- [Bergonie1906] J. Bergonie and L. Tribondeau, "De quelques resultats de la radiothérapie et essai de fixation d'une technique rationnelle", *Comptes Rendus des Séances de l'Académie des Sciences* 143: 983-985 (1906).
- [Bond1996] V. P. Bond, L. Wielopolski, and G. Shani. "Current Misinterpretations of the Linear No-Threshold Hypothesis", *Health Phys.* 70: 877-882 (1996).
- [Brenner2003] D. J. Brenner, R. Doll, D. T. Goodhead, E. J. Hall, C. E. Land, J. B. Little, J. H. Lubin, D. L. Preston, R. J. Preston, J. S. Puskin, E. Ron, R. K. Sachs, J. M. Samet, R. B. Setlow, and M. Zaider, "Cancer Risks Attributable to Low Doses of Ionizing Radiation: Assessing What We Really Know", *PNAS* 100: 13761-13766 (2003).
- [Burnham1992] J. U. Burnham, *Radiation Protection*, Rev. 3. Point Lepreau Generating Station, NB: New Brunswick Power Corporation, 1992.
- [Cember2009] H. Cember and T. Johnson, *Introduction to Health Physics*, 4th Edition. Toronto, ON: McGraw-Hill, 2009.
- [Chambless1992] D. A. Chambless, S. S. Dubose, and E. L. Sensintaffar, "Detection Limit Concepts: Foundations, Myths, and Utilization", *Health Phys.* 63(3): 338-340 (1992).
- [Clarke2005] R. Clarke and J. Valentine, "A History of the International Commission on Radiological Protection", *Health Phys.* 88(6): 201-216 (2005).
- [Clement2009] C. Clement, *Radiological Protection Standards*. Seminar at University of Ontario Institute of Technology, March 17, 2009.
- [CBSC2004] CNSC, *Keeping Radiation Exposures and Doses "As Low as Reasonably Achievable (ALARA)"*. Ottawa, ON: Canadian Nuclear Safety Commission, Regulatory Guide G-129, Revision 1, 2004.
- [Cole1997] D. Cole and E. Waller, *Environmental Radionuclide Baseline Study*. Department of National Defence, Maritime Command Headquarters, prepared by SAIC Canada, 1997.
- [CSA2004] CSA, *Fume Hoods and Associated Exhaust Systems*. Mississauga, ON: Standards Council of Canada, Canadian Standards Association, CAN/CSA-Z316.5-04, 2004.
- [CSA2008] CSA, *Guidelines for Calculating Derived Release Limits for Radioactive Material in Airborne and Liquid Effluents for Normal Operation of Nuclear Facilities*. Mississauga, ON: Standards Council of Canada, Canadian Standards Association, CAN/CSA-N288.1-08, 2008.
- [CSA2010] CSA, *Environmental Monitoring Programs at Class I Nuclear Facilities and Uranium Mines and Mills*. Mississauga, ON: Standards Council of Canada, Canadian Standards Association, CAN/CSA-N288.4-10, 2010.
- [CSA2012] CSA, *Selection, Use, and Care of Respirators*. Mississauga, ON: Standards Council of Canada, Canadian Standards Association, CAN/CSA-Z94.4-11, 2012.
- [Currie1968] L. A. Currie, "Limits for Qualitative Detection and Quantitative Determination:

- Application to Radiochemistry". *Anal. Chem.* 40: 586-593 (1968).
- [Deichmann1986] W. B. Deichmann, D. Henschler, B. Holmstedt, and G. Kell, "What Is There that is Not Poison? A Study of the Third Defense by Paracelsus". *Arch. Toxicol.* 58: 207-213 (1986).
- [DoseResponse2013] Dose-Response, *Dose-Response, an International Journal – Assessing the Nature, Mechanisms, and Implications of Dose-Response Relationships*. ISSN 1559-3258, <http://www.dose-response.com/>, 2013 .
- [Faw1999] R. E. Faw and J. K. Shultis, *Radiological Assessment: Sources and Doses*. La Grange, IL: American Nuclear Society, 1999.
- [Frame2005] P. W. Frame, "A History of Radiation Detection Instrumentation", *Health Phys.* 88(6): 97-121 (2005).
- [Goans1997] R. E. Goans, E. C. Holloway, M. E. Berger, and R. C. Ricks, "Early Dose Assessment Following Severe Radiation Accidents", *Health Phys.* 72: 513-518 (1997).
- [Grasty2004] R. L. Grasty and J. R. LaMarre, "The Annual Effective Dose from Natural Sources of Ionizing Radiation in Canada", *Rad. Prot. Dos.* 108(3): 251-226 (2004).
- [Gusev2001] I. A. Gusev, A. K. Guskova, and F. A. Mettler, *Medical Management of Radiation Accidents*, 2<sup>nd</sup> Edition. New York: CRC Press, 2001.
- [IAEA1995] IAEA, *The Principles of Radioactive Waste Management*. Vienna, Austria: International Atomic Energy Agency, IAEA Safety Series No. 111-F, 1995.
- [IAEA1996] IAEA, *International Basic Safety Standards for Protection against Ionizing Radiation and for the Safety of Radiation Sources*. Vienna, Austria: International Atomic Energy Agency, IAEA Safety Series No. 115, 1996.
- [IAEA2009] IAEA, *INES – The International Nuclear and Radiological Event Scale User's Manual*, 2008 Edition. Vienna, Austria: International Atomic Energy Agency, IAEA-INES-2009.
- [IAEA2011] IAEA, *Radiation Protection and Safety of Radiation Sources: International Basic Safety Standards*. Vienna, Austria: International Atomic Energy Agency, IAEA Safety Standards Series No. GSR, Part 3 (Interim), 2011.
- [ICRP1977] ICRP, *Recommendations of the International Commission on Radiological Protection*. International Commission on Radiological Protection, ICRP Publication 26; *Annals of the ICRP* 1(3), 1977.
- [ICRP1987] ICRP, *Lung Cancer Risk from Indoor Exposures to Radon Daughters*. International Commission on Radiological Protection, ICRP Publication 50; *Annals of the ICRP* 17(1), 1987.
- [ICRP1990] ICRP, *Recommendations of the International Commission on Radiological Protection*. New York: International Commission on Radiological Protection, ICRP Publication 60, Pergamon, 1990.
- [ICRP1994] ICRP, "Dose Coefficients for Intakes of Radionuclides by Workers", ICRP Publication 68; *Annals of the ICRP* 24(4) (1994).
- [ICRP1996a]. ICRP, "Age-Dependent Doses to Members of the Public from Intake of Radionuclides: Part 5: Compilation of Ingestion and Inhalation Dose Coefficients", ICRP Publication

- 72; *Annals of the ICRP* 26(1) (1996a).
- [ICRP1996b] ICRP, "Conversion Coefficients for Use in Radiological Protection against External Radiation", ICRP Publication 74; *Annals of the ICRP* 26(3/4) (1996b).
- [ICRP2003a] ICRP, *A Framework for Assessing the Impact of Ionizing Radiation on Non-Human Species*. Toronto, ON: International Commission on Radiological Protection, ICRP Publication 91, Elsevier, 2003a.
- [ICRP2003b] ICRP, *Basic Anatomical and Physiological Data for Use in Radiological Protection*. Toronto, ON: International Commission on Radiological Protection, ICRP Publication 89, Elsevier, 2003b.
- [ICRP2007] ICRP, *Recommendations of the International Commission on Radiological Protection*. Toronto, ON: International Commission on Radiological Protection, ICRP Publication 103, Elsevier, 2007.
- [ICRP2008] ICRP, *Environmental Protection: Concept and Use of Reference Animals and Plants*. Toronto, ON: International Commission on Radiological Protection, ICRP Publication 108, Elsevier, 2008.
- [ICRU1994] ICRU, *Particle Counting in Radioactivity Measurements*. Bethesda, MD: International Commission on Radiation Units and Measurements, ICRU Report 52, 1994.
- [IMBA2010] IMBA, *IMBA Professional Plus Computer Code for Internal Dosimetry Calculations* – Version 4.1.3 HPA. Chilton, UK: <http://www.imbaprofessional.com>, 2010.
- [Inkret1995] W. C. Inkret, C. B. Meinhold, and J. C. Tascher, "A Brief History of Radiation Protection Standards", *Los Alamos Science* 23: 116-123 (1995).
- [Jones2005] C. G. Jones, "A Review of the History of U.S. Radiation Protection Regulations, Recommendations, and Standards", *Health Phys.* 88(6): 181-200 (2005).
- [Knoll2010] G. F. Knoll, *Radiation Detection and Measurement*, 4th Edition. New York: Wiley, 2010.
- [Lamarsh2001] J. R. Lamarsh and A. J. Baratta, *Introduction to Nuclear Engineering*, 3rd Edition. Upper Saddle River, NJ: Prentice-Hall, 2001.
- [Lindell1996] B. Lindell, "The History of Radiation Protection", *Rad. Prot. Dos.* 68(1/2): 83-95 (1996).
- [Mattson2008] M. P. Mattson, "Hormesis Defined", *Aging Res. Rev.* 7(1): 1-7 (2008).
- [Miller1992] K. Miller (ed.), *Handbook of Management of Radiation Protection Programs*, 2nd Edition. Boca Raton, FL: CRC Press, 1992.
- [MIRD1978] MIRD, "Estimates of Specific Absorbed Fractions for Photon Sources Uniformly Distributed in Various Organs of a Heterogeneous Phantom". In: Society of Nuclear Medicine, Medical Internal Radiation Dose Committee, MIRD Pamphlet No. 5, W. S. Snyder, M. R. Ford, and G. G. Warner (eds.), New York, 1978.
- [Moeller2005] D. W. Moeller, "Environmental Health Physics: 50 Years of Progress", *Health Phys.* 88(6): 160-180 (2005).
- [Mosby1990] C. V. Mosby, *Mosby's Medical, Nursing, and Allied Health Dictionary*, 3rd Edition. Toronto, ON: C. V. Mosby, 1990.
- [NCRP1987] NCRP, *Radiation Exposure of the U.S. Population from Consumer Products and Miscellaneous Sources*. Bethesda, MD: National Council on Radiation Protection and

- Measurements, Report No. 95, 1987.
- [NCRP2001] NCRP, *Management of Terrorist Events Involving Radioactive Material*. Bethesda, MD: National Council on Radiation Protection and Measurements, NCRP Report No. 138, 2001.
- [NCRP2009] NCRP, *Ionizing Radiation Exposure of the Population of the United States*. Bethesda, MD: National Council on Radiation Protection and Measurements, Report No. 160, 2009.
- [NDR2013] NDR, *National Dose Registry, Radiation Protection Bureau, Health Canada*. <http://www.hc-sc.gc.ca/ewh-semt/occup-travail/radiation/regist/index-eng.php>, 2013.
- [NSCA1997] NSCA, *Nuclear Safety and Control Act. Government of Canada, S.C. 1997, c.9*. Available at <http://laws-lois.justice.gc.ca/eng/acts/N-28.3/>. 1997.
- [NSCA2000] NSCA, *Radiation Protection Regulations*. Government of Canada, SOR/2000-203. Available at <http://laws-lois.justice.gc.ca/eng/regulations/SOR-2000-203/index.html>. 2000.
- [OPG2012] OPG, *2011 Results of Radiological Environmental Monitoring Programs*. Ontario Power Generation, N-REP-03481-10010. Downloadable at: <http://www.opg.com/news/reports/index.asp>. 2012.
- [ORNL2013] ORNL, *RadToolbox*. Downloadable from the Centre for Biokinetic and Dosimetric Research, <http://ordose.ornl.gov/downloads.html>. 2013.
- [Poston2005] J. W. Poston, "External Dosimetry and Personnel Monitoring", *Health Phys.* 88(6): 41-48 (2005).
- [Potter2005] C. A. Potter, "Internal Dosimetry: A Review", *Health Phys.* 88(6): 49-62 (2005).
- [Preston2005] R. J. Preston, "Radiation Biology: Concepts for Radiation Protection", *Health Phys.* 88(6): 29-40 (2005).
- [Scott2008] B. R. Scott, "It's Time for a New Low-Dose Radiation Risk-Assessment Paradigm—One that Acknowledges Hormesis", *Dose-Response*, 6: 333-352 (2008).
- [Scott2012] B. R. Scott, V. R. Bruce, K. M. Gott, J. Wilder, and T. March, "Small  $\gamma$ -Ray Doses Prevent Rather than Increase Lung Tumors in Mice", *Dose-Response* 10: 527-540 (2012).
- [Shultis2000] J. K. Shultis and R. E. Faw, *Radiation Shielding*. La Grange Park, IL: American Nuclear Society, 2000.
- [Shultis2005] J. K. Shultis and R. E. Faw, "Radiation Shielding Technology", *Health Phys.* 88(6): 71-96 (2005).
- [Siegel2012] J. A. Siegel and M. G. Stabin, "RADAR Commentary: Use of Linear No-Threshold Hypothesis in Radiation Protection Regulation in the United States", *Health Phys.* 102: 90-99 (2012).
- [Till2008] J. Till and H. Grogan, *Radiological Risk Assessment and Environmental Analysis*. Toronto, ON: Oxford University Press, 2008.
- [Uchirin1988] G. Uchirin and M. Ranogajec-Komor, "Thermoluminescent Dosimetry". In: *Ionizing Radiation: Protection and Dosimetry*, Paić, G., (ed.), Boca Raton, FL: CRC Press, 1988.
- [UNSCEAR2000] UNSCEAR, *United Nations Scientific Committee of the Effects of Atomic Radiation – Report to the General Assembly*. New York: United Nations, 2000.
- [UNSCEAR2008] UNSCEAR, *Sources and Effects of Ionizing Radiation*. New York: United Nations

Scientific Committee on the Effects of Atomic Radiation, Report to the General Assembly (A/63/46), 2008.

[Walker2000] J. S. Walker, *Permissible Dose – A History of Radiation Protection in the Twentieth*

*Century*. Berkeley, CA: University of California Press, ISBN 0-520-22328-4, 2000.

[Waller2013] E. J. Waller, “Sources of Radiation in the Environment, Including Natural Radiation, Naturally Occurring Radioactive Materials (NORM), Technically Enhanced Materials, Weapons Tests, and Nuclear Accidents”. In: *Encyclopedia of Sustainability Science and Technology*, ISBN 978-0-387-89469-0, New York: Springer, 2013.

**IR Sensor (Basics and Concept)**

## Optical Spectroscopy

## **Gamma Astronomy Sensor (Basics and Concept)**

## 70 References

- [Yassir 2010] Muhammad Yassir, *Development and Implementation of the attitude control algorithms for the e micro-satellite Flying Laptop*, PhD thesis, IRS, University of Stuttgart, 2010
- [1] Satellite Power Systems Solar energy used in space; BR-202 May 2003; European Space Agency; Published by: ESA Publications Division ESTEC, PO Box 299 2200 AG Noordwijk; The Netherlands; Editors: Niels E. Jensen & Bruce Battrick)
- [2] The Space Grid; Sun-synchronous orbiting SBSP Satellites with Equatorial orbiting Reflector Satellites for Earth and Space Energy By Royce Jones.
- [3] Goddard Space Flight Center. SpaceRef Interactive Inc. June 16, 2009, Retrieved 2009-
- [4] Introduction to Spacecraft Propulsion; Peter Erichsen, September 2006
- [5] Satellite orbits; Kidder and Vonder Haar: chapter 2; Stephens: chapter 1, pp. 25-30; Rees: chapter 9, pp. 174-192.
- [6] A thesis accepted by the Faculty of Aerospace Engineering and Geodesy of the Universität Stuttgart in partial fulfillment of the requirements for the degree of Doctor of Engineering Sciences (Dr.-Ing.), By Muhammad Yassir.
- [7] Prototype for a base station for supernova remnant HI line radio wave detector and analyzer (SRWDA), Master Thesis, Suheeb Kassar. Supervisor: Samir Mourad, IAP/AECENAR, KIT, Karlsruhe, April 2014
- [8] STAR is an accelerometer system provided by CNES and developed by ONERA (Office National d'Etudes ET de Recherches Aérospatiales), France.
- [9] Narayan, K. Lalit (2008). Computer Aided Design and Manufacturing. New Delhi: Prentice Hall of India. p.3. ISBN 812033342X'.
- [10] Hess.M, Martin.K.K, Rachul.L.J.; (February 7, 2002). "Thrusters Precisely Guide EO-1 Satellite in Space First", NASA, Archived from the original on 2007-12-06.
- [11] U.S. Department of Commerce National Oceanic and Atmospheric Administration National Environmental Satellite, Data, and Information Service Suitland, Maryland; National Aeronautics and Space Administration Goddard Space Flight Center Greenbelt, Maryland
- [12] S`adhan`a Vol. 29, Part 2, April 2004, pp. 189–203. © Printed in India
- [13] Gpredict User Manual; by Alexandru Csete OZ9AEC; 12 Oct 2010.
- [14] Satellite Attitude Determination with Low-Cost Sensors By John C. Springmann in the University of Michigan 2013.

- [15] European space agency; science and technology; electrical space craft propulsion; September 2003.
- [16] 2006 Springer Science + Business Media, Inc, Printed in the United States of America.
- [17] Saturday, May 21, 2011; Control Systems- Block Diagrams and Signal Flow Graphs; by ramesh akula).
- [18] INTECH; 2014, Modelling and Simulation Based Matlab/Simulink of a Strap-Down Inertial Navigation System' Errors due to the Inertial Sensors; Teodor Lucian Grigorie and Ruxandra Mihaela Botez; <http://dx.doi.org/10.5772/57583>
- [19] Precise Orbit Determination for Low Earth Orbit Satellites, David Hobbs, Lund Observatory, Sweden; <http://www.astro.lu.se>.
- [20] DUBAISAT-1: MISSION OVERVIEW, DEVELOPMENT STATUS AND FUTURE APPLICATIONS; by Adnan Al Rais, Ali Al Suwaidi, and Hosni Ghedira. Associate Research Engineer, DubaiSat-1 Program; Emirates Institution for Advanced Science & Technology (EIAST), Dubai, UAE.
- [21] SHELDAHL; A Multek brand; WWW.SHELDAHL.COM | 1150 SHELDAHL ROAD, NORTHFIELD, MINNESOTA 55057 USA.
- [22] Choueiri, Edgar Y. (2009) <http://.alfven.princeton.edu/papers/sciam2009.pdf>
- [23] <http://www.srh.noaa.gov/images/bro/outreach/pdf/CareerOpportunitiesMeteorology.pdf>
- [24] <http://www.imd.gov.in/section/satmet/dynamic/satfaq.pdf>
- [25] <http://www.astro.washington.edu/users/smith/Astro150/Tutorials/Kepler/>
- [26] Sun-Synchronous Orbit dictionary entry, from U.S. Centennial of Flight Commission
- [27] Radio-Electronics.com: resources and analysis for electronics engineers (<http://www.radio-electronics.com/info/satellite/satellite-orbits/low-earth-orbit-leo.php>)
- [28] <http://history.nasa.gov/conghand/propulsn.htm>.
- [29] <http://www.scicos.org/book/ScilabScicosBook-Ch7.pdf> (Scicos Block; By Fady NASSIF).
- [30] Texas Instruments; satellite payload: gyro sensor.
- [31] <http://www.wxtoimg.com/>
- [32] VGB Congress Power Plants 2001, Brussels, October 10 to 12, 2001
- [33] 6 Factors that Effect Solar PV System Efficiency; Posted on March 6, 2013 by Goodpal
- [34] Technical information, SMA, performance ratio, Quality factor for the PV plant, Perfratio-UEN100810
- [35] <http://www.youtube.com/watch?v=fopnIkYnFPI>; 2 jan. 2013 - Ajouté par themrworf1701.

- [Kassar 2014] Suheeb Kassar, *Prototype for a base station for supernova remnant HI line radio wave detector and analyzer (SRWDA)*, IAP, AECENAR / KIT, Karlsruhe/Ras Nhache, April 2014 (planned)
- Space Mission Analysis and Design**, W. Larson, J. Wertz, Kluwer, 1999
- Elements of Spacecraft Design**, C.D. Brown, AIAA, 2002
- Space Vehicle Mechanisms**, P. Conley, New York, 1998
- Spacecraft Structure and Mechanisms**, T.P. Sarafin, Kluwer, 1995
- Raumfahrtsysteme: eine Einführung mit Übungen und Lösungen**, E. Messerschmidt ; S. Fasoulas. - Berlin u.a.: Springer, 2000. 533 S.
- Handbuch der Raumfahrttechnik**, W. Hallmann; W. Ley, München, Wien, Hanser 1999, 792 S.
- [Laufer 2009] Lunar Mission BW1: Scientific Objectives and Small Satellite Concept, Rene Laufer, 2010
- [Mourad et. al. 2006] Mourad S.(Ed.): Mourad S., Forstmann S., Subhan M., E.J., Farkh R., Abdelhaq N., Faquir M., Mikou M.Y., Ammar A., Flight Control System for an Wind Data Measuring Airship (Project Report for 2000 - 2006), Karlsruhe, 2006
- [Nawaz et al. 2005] Investigation and Optimization of an Instationary MPD Thruster at IRS, IEPC-2005-2008, *Presented at the 29<sup>th</sup> International Electric Propulsion Conference, Princeton University, October 31 – November 4, 2005*, Anusheh Nawaz\*, Monika Auweter-Kurtz, Georg Herdrich and Helmut L. Kurtz. *University of Stuttgart, Institut für Raumfahrtsysteme, 70550 Stuttgart, Germany*
- [Böhrk et. al. 2007] Elektrostatische Sonden im I-MPD Simp-LEX, Hannah Böhrk, Anusheh Nawaz, Uwe Bauder, Bastian Steiner, Oliver Troll, IRS Stuttgart, 2007
- [Inalhan 2009] Applied Space Education and Research at ITU CAL Assoc. Prof. Gokhan Inalhan, Istanbul Technical University, Faculty of Aeronautics and Astronautic, Director of Controls and Avionics Laboratories
- [Thirion] Pierre THIRION, Design and Implementation of On-board Electrical Power Supply of Student Nanosatellite OUFTI-1 of University of Liège (Master Thesis)
- [IAP\_ECS] Emergency Control System, IAP 2013
- [IAP\_SBEP] Zohby, Mahmoud; *Concept for Stratospheric Ballon Control System*, IAP, 2013
- [Maral et. al. 2009] SATELLITE COMMUNICATIONS SYSTEMS - Systems, Techniques and Technology, Fifth Edition, Gerard Maral, Ecole Nationale Superieure des Telecommunications, Site de Toulouse, France, Michel Bousquet, Ecole Nationale Superieure de l'Aeronautique et de l'Espace (SUPAERO), Toulouse, France, Revisions to fifth edition by Zhili Sun, University of Surrey, UK, with contributions from Isabelle Buret, Thales Alenia Space, 2009
- [Yassir 2010] Muhammad Yassir, *Development and Implementation of the attitude control algorithms for the e micro-satellite Flying Laptop*, PhD thesis, IRS, University of Stuttgart, 2010

## 71 Suppliers Data

### 71.1 Electronics

- قطرنجي للإلكترونيات EKT Beirut
  - Number: 01 820020
  - Website: www.ekt2.com



- Bashir electronics - البشير للإلكترونيات

### 71.2 Satellite Parts

Specification form © Surrey Satellite Technology Ltd., Tycho House, 20 Stephenson Road, Surrey Research Park, Guildford, Surrey, GU27YE, United Kingdom, Tel: +44(0)1483803803 | Fax:+44(0)1483803804 | Email: info@sstl.co.uk | Web:www.sstl.co.uk

Remark: No answer to email has come.

### 71.3 CNC Fine Mechanics (2D)

The company HI-TECH Fabrication takes CAD Data (in .dxf format) -> Changing to CAM Data.

Satellite Parts are in Alluminium Alloy.

## 71.4 3D Printing (Plastics)

<http://www.cnclablb.com/>

### 71.5 تصنيع قطع (...CNC)

Company	Phone number	Description	Address	E-mail web site
CNC LAB	06 412 895 03 476 916	Manufacture 3D design in plastic & open source hardware	Tripoli, Lebanon Bahsas, Behind Haykalieh Hospital, Harba Bld.	<a href="http://www.cnclab.com">www.cnclab.com</a> <a href="mailto:info@cnclablb.com">info@cnclablb.com</a>
Hasan Al Baba	03 828 256	Manufacture and casting	Tripoli, Lebanon Mina, Industry and Commerce street	
HI-Tech fabrication Fawaz Abdel Hadi	06 442 787 70 751 522	Precision mechanical parts manufacturing brass & steel marking heads maker	Tripoli, Lebanon Mahjar suhi P.O. Box 1274	<a href="http://www.hitechfabrication.com">www.hitechfabrication.com</a> <a href="mailto:info@hitechfabrication.com">info@hitechfabrication.com</a> <a href="mailto:sirfawaz@yahoo.com">sirfawaz@yahoo.com</a>
Hannuf mechanical 'Corporation for casting and art construction	06 387 723 03 717 107	Manufacture and casting	Tripoli, Lebanon Al Badawi	
GPS Steel	03 196 225	Uses electric discharge machining process to shape any metal material rapidly by using desired modeled electrodes	Beirut, Lebanon Burj Hammoud	<a href="mailto:Gps.steel.co@gmail.com">Gps.steel.co@gmail.com</a>
Riyako factory	79 118 779	3D CNC machine, manufacture cupboard for cars	Tripoli, Lebanon Badawi, behind Al Ridani bakery	